ISFEH10

University of South-Eastern Norway

Proceedings of the Tenth International Seminar on

# Fire and Explosion Hazards

*Edited by*
Vågsæther K.
Lach A.W.
Bradley D.
Lundberg J.


University of South-Eastern Norway 2022

**Proceedings of the Tenth International Seminar on Fire and Explosion Hazards**

22-27 May 2022, Oslo, Norway

**Edited by** K. Vågsæther, A. W. Lach, D. Bradley, and J. Lundberg



ISBN: **978-82-7206-721-1**

Porsgrunn
University of South-Eastern Norway
2022

# Seminar Committees

## International Organizing Committee

Chair: *A. Snegirev (Russia)*

Co-Chairs: *D. Bradley (UK), D. Drysdale (UK), V. Molkov (UK), F. Tamanini (USA)*

Members: *N. Chaumeix (France), R. Dobashi (Japan), N.A. Liu (China), B. Merci (Belgium), E. Oran (USA), J. Torero (USA), K. Vågsæther (Norway) A. Pękalski (UK), J.G. Quintiere (USA),*

## Scientific Advisory Board

*K. Vågsæther (Norway),*
*F. Tamanini (USA),*
*A. Snegirev (Russia),*
*T. Skjold (Norway),*
*G. Rein (UK),*
*J.G. Quintiere (USA),*
*V. Molkov (UK),*
*B. Merci (Belgium),*
*J. Lundberg (Norway),*
*Ch. Fleischmann (New Zealand),*
*R. Dobashi (Japan),*
*N. Chaumeix (France),*
*D. Bradley (UK),*
*Y. Nakamura (Japan),*

Reviewers:

*Abdulrahman Shehu*
*Agarwal Gaurav*
*Arntzen Bjorn*
*Babrauskas Vyto*
*Bauwens C. Regis*
*Beji Tarek*
*Hisken Helene*
*Hostikka Simo*
*Hu Longhua*
*Huang Xinyan*
*Husted Bjarne*
*Jallais Simon*
*Novozhilov Vasily*
*Oka Yasushi*
*Oran Elaine*
*Pau Dennis Su Wee*
*Phylaktou Herodotos*
*Proust Christophe*

*Bergthorson Jeff*
*Beyer Michael*
*Bhattacharjee Subrata*
*Bjerketvedt Dag*
*Boeck Lorenz*
*Brohez Sylvain*
*Cantizano Alexis*
*Chaos Marcos*
*Chen Haixiang*
*Cirrone Donatella*
*Cracknell Roger*
*Delichatsios Michael*
*Dembele Siaka*
*Dorofeev Sergey*
*Dufaud Olivier*
*Farahani Hamed*
*Fernandez-Anez Nieves*
*Gao Wei*
*Gollner Michael*
*Gopala Yogish*
*Guo Haiqing*
*Gupta Vinny*
*Gaathaug André Vagner*
*Hansen Olav Roald*
*Hansen Per Morten*
*Henriksen Mathias*
*Ji Jie*
*Johnsen Stig Ole*
*Kapusta Łukasz*
*Kashkarov Sergii*
*Kesana Netaji*
*Khattri Sanjay*
*Kim Wookyung*
*Kuwana Kazunori*
*Kuznetsov Mike*
*Lach Agnieszka W.*
*Lautenberger Chris*
*Lazaro Mariano*
*Lázaro David*
*Li Junyi*
*Lundberg Joachim*
*Makarov Dmitriy*
*Maragkos Georgios*
*Markus Ekaterina*
*Matsuyama Ken*
*McAllister Sara*
*McDermott Randall*
*McGrattan Kevin*
*McLaggan Martyn S*
*Melguizo Gavilanes Josue*
*Mogi Toshio*
*Nakamura Yuji*
*Runefors Marcus*
*Santoso Muhammad Agung*
*Shentsov Volodymyr*
*Skjold Trygve*
*Stankovic Ivana*
*Stoliarov Stanislav*
*Sunderland Peter*
*Suzuki Masataro*
*Suzuki Sayaka*
*Swedosh William*
*Thomsen Maria*
*Torero Jose*
*Tsuruda Takashi*
*Ustolin Federico*
*van Hees Patrick*
*Venetsanos Alexandros*
*Vermina Plathner Frida*
*Viitanen Alexandra*
*Welahettige Prasanna*
*White James*
*Winters Caroline*
*Yakush Sergey*
*Yu Hong-Zeng*
*Zeng Dong*
*Åkervik Espen*

## Local Organizing Committee

Chair: *K. Vågsæther*

Co-Chairs: *J. Lundberg, A.W. Lach*

Members: *M. Henriksen, D. Bjerketvedt, P.K Welahettige, O.M. Ibrahim, A. Gaathaug, R. Sikka, P.M. Hansen,*

# Preface

The International Seminar on Fire and Explosion Hazards has become one of the important international events for fire and explosion engineering and science. The long-term traditions were established by the past successful events in St. Petersburg, Russia (2019), Hefei, China (2016), Providence, USA (2013), Leeds, UK (2010), Londonderry, UK (2003), Lake Windermere, UK (2000), and Moscow, Russia (1997, 1995). The Tenth International Seminar on Fire and Explosion Hazards (ISFEH10) organized in Oslo, Norway from 22 to 27 May 2022, is a place to share research on the physical effects of hazards, prediction methods for consequences, applied safety analysis methods, mitigiation methods, emergency response strategies, and many other topics.

It is a pleasure to present the Proceedings of the the Tenth International Seminar on Fire and Explosion Hazards (ISFEH10). In total 63 papers and 17 posters' abstracts are included in the Proceedings, after careful evaluation and selection by the Scientific Advisory Board with help of the reviewers.

The Organizers and Editors express thanks to all who have contributed to the success of the Seminar and helped to make this conference possible, including the following supporting organizations:

University of South-Eastern Norway
FM Global

Sincere thanks are extended to numerous professionals for their involvement in the evaluation and selection of the submissions.

The work done by the Local Organizing Committee created opportunities and solutions during the difficult times the conference was held in. This is well acknowledged with appreciation.

The Editors,

May 2022

Norway

# Contents

# Combustion Fundamentals of Fires

# Theoretical study of solid laminar combustion under forced flow

**Fuhai Gou, Huahua Xiao*, Mi Li, Manman Zhang, Jinhua Sun***

*State Key Laboratory of Fire Science, University of Science and Technology of China, Hefei, Anhui, China.*
**Corresponding author's email: xiaoh@ustc.edu.cn; sunjh@ustc.edu.cn*

## ABSTRACT

In this paper, the laminar combustion characteristics of solid plates under forced flow have been studied. The steady combustion experiments of PMMA plates of different sizes under forced flow have been carried out. The theory of solid plate combustion under forced flow is developed based on the boundary layer theory. It can also be seen from the experiments that the combustion state of PMMA plate is stable laminar combustion. Based on the boundary layer theory, the flow function equation is solved and the theoretical expressions of flame thickness and Nusselt number are obtained. Based on the experimental results, flame thickness, flame length, the relationship between Nusselt number and Reynolds number, and the mass loss rate are discussed. Flame standoff distance is related to the wind speed, position, and mass transfer number. The relationship of Nusselt number and Reynolds number under forced flow can be obtained through experimental data and calculated using boundary layer theory. And, the result shows that Nu and $\sqrt{Re}$ are not simply proportional, which is different from previous studies. In analysis, the mass transfer number is found not to be constant for different positions in the flame area.

**KEYWORDS:** Laminar combustion, boundary layer, flame, heat transfer.

## NOMENCLATURE

| | |
|---|---|
| $B$ | mass transfer number |
| $c_P$ | constant pressure specific heat (J/(kg·K)) |
| $f$ | modified flow function (-) |
| $F$ | dimensionless function (-) |
| $\Delta H_C$ | combustion heat (J/g) |
| $h$ | heat transfer coefficient (W/(m$^2$·K)) |
| $k$ | thermal conductivity (-) |
| $L$ | heat of gasification (J/g) |
| $\dot{m}_i'''$ | mass loss rate per volume (g/(m$^3$s)) |
| $Nu$ | Nusselt number (-) |
| $q''$ | heat flux (W/m$^2$) |
| $q'''$ | heat release rate (W/m$^3$) |
| $Q$ | heat (J) |
| Re | Reynolds number (-) |
| $r$ | reflectivity of PMMA surface (-) |
| $T$ | temperature (K) |
| $u$ | horizontal velocity (m/s) |
| $v$ | vertical velocity (m/s) |
| $x$ | characteristic length (m) |
| $x_f$ | flame length (m) |
| $y_f$ | flame standoff distance (m) |
| $Y$ | mass concentration (-) |

**Greek**

| | |
|---|---|
| $\eta$ | similarity variable (-) |
| $\nu$ | viscosity (m$^2$/s) |
| $\nu_s$ | mass stoichiometric ratio (-) |
| $\mu$ | dynamic viscosity (N s/m$^{-2}$) |
| $\rho$ | density (g/m$^3$) |
| $\psi$ | stream function (-) |
| $\chi$ | fraction of flame radiation (-) |

**Subscripts**

| | |
|---|---|
| $f$ | flame |
| $\infty$ | ambien |

## INTRODUCTION

The combustion of solid fuel is one of the most common phenomena in real fire scenarios and the key research content in the fire area. The forced wind affects the burning of solid, making combustion

more complicated and unpredictable. The theoretical analysis of solid combustion under forced convection is more difficult than that under natural convection. However, the burning of solid fuel under force wind is more consistent with the actual fire scene than that under a static environment. Hence, the study has great practical value and significance.

In fire research, whether the fuel is gas, liquid, or solid, the fire behavior under forced flow is always a research hotspot. The diffusion flame of solid combustion may be laminar or turbulent under forced flow, which is an important research direction of flame reaction dynamics theory. The research can help people to understand and master the combustion mechanism of solid fuel more clearly.

Some researchers studied fire behavior under forced flow. Spalding[1] carried out experiments on liquid fuel combustion and analyzed the combustion behavior of liquid fuel under force flow. The mass transfer number was demonstrated by Spalding in his study, so it was also called Spalding B number, which can well solve the problem of mass and heat transfer between solid and liquid in the combustion process. Based on Spalding's study, Emmons[2] proposed the boundary layer theory about the fire under forced flow by solving approximate solutions of Navier-Stokes equations, which also provided an important theoretical basis for the value of mass transfer number. Sibulkin et. al[3] studied the combustion of vertical fuel under natural convection driven by buoyancy, and the stud showed that even considering the finite reaction rate, they still got a solution similar to the study of Emmons. Based on boundary layer theory, Loh et. al[4] carried out experiments of PMMA plate flame spread under forced flow. Without considering the influence of radiation heat transfer, they found that there is a linear positive correlation between flame spread rate and wind speed. Ananth et. al[5] and Ndubizu et. al[6] measured the regression rate of PMMA surface burning under a forced flow boundary layer flame and obtained local mass loss rate. Their study found that the local mass loss rate of PMMA plate in upstream and downstream present different rules, while the local mass loss rate of upstream is always transient and the local mass loss rate of downstream trends to steady-state. Zhao et. al[7] discussed the influence of width on flame spread under forced convection by solving the flow function equations based on boundary layer theory. Their study found that flame spread rate increases with the increase of width, but does not increase when the width exceeds 10 cm and the mass transfer number affects the mass and heat transfer process. Zhu el. al[8] found the steady-state flame spread process goes through a transitional process to a new steady-state when the wind speed changes. Although some previous studies on fire behavior under forced flow have been carried out, and also have some shortcomings. Many researchers have carried out some experiments on solid plate flame spread. However, the boundary layer theory is established based on the assumption of stable combustion, and the flame spread process is unstable combustion process. The boundary layer theory is more suitable for stable combustion without spreading, which is the research content of this paper. In addition, the calculation method of Nusselt number based on boundary layer theory will be discussed.

Based on laminar boundary layer theory, this paper will analyze the stable combustion of PMMA plate under forced flow, combining with previous studies and experimental results. The burning process is recorded by DV camera and the video is processed by MATLAB. The mass data of PMMA plate in burning is obtained by electronic balance. The experimental data are combined with theoretical analysis to further enrich the theory of flame reaction kinetics.

## THEORETICAL DEVELOPMENT

### Laminar Boundary Layer Theory

Laminar boundary layer theory is the basic theory that is widely applied to fluid mechanics and combustion research. Figure 1 shows a two-dimensional reacting boundary layer to depict the steady burning of the solid plate under forced flow. Because of the forced flow, the effects of buoyancy can be ignored to simplify model and calculation. Hence, the study assumes that burning of PMMA plate is stable two-dimensional laminar boundary layer flow which is ignoring buoyancy. Besides, it

assumes the mixed gas is ideal gas that the specific heat and molecular weight are constants in the burning area. Thus, the conservation equations for the burning of PMMA plate can be expressed by:

Mass conservation equation

$$\frac{\partial\ \rho u}{\partial x}+\frac{\partial\ \rho v}{\partial y}=0\ , \tag{1}$$

where $\rho$ , $u$ , and $v$ are density, horizontal velocity parallel to the airflow and vertical velocity perpendicular to the airflow.

Momentum conservation equation

$$\rho u\frac{\partial u}{\partial x}+\rho v\frac{\partial v}{\partial y}=\frac{\partial}{\partial y}\mu\frac{\partial u}{\partial y}\ , \tag{2}$$

where $\mu$ is the dynamic viscosity of the mixed gas in the reaction zone.

Energy conservation equation

$$\rho u\frac{\partial h}{\partial x}+\rho v\frac{\partial h}{\partial y}=\frac{\partial}{\partial y}\frac{k}{C_p}\frac{\partial h}{\partial y}+\dot{q}'''\ , \tag{3}$$

where $h$ is the specific enthalpy, $C_p$ is the specific heat, $\dot{q}'''$ is heat release rate per volume.

Species conservation equation

$$\rho u\frac{\partial Y_i}{\partial x}+\rho v\frac{\partial Y_i}{\partial y}=\frac{\partial}{\partial y}\left(\rho D_i\frac{\partial Y_i}{\partial y}\right)+\dot{m}_i'''\ , \tag{4}$$

where $Y_i$ is mass concentration, $\dot{m}_i'''$ is mass loss rate per volume.

In this study, an overall one-step irreversible chemical reaction mechanism adopted to describe the combustion reaction can be expressed as:

$$v_F\mathrm{PMMA}+v_O\mathrm{O}_2\rightarrow v_p\mathrm{Products}+Q \tag{5}$$

where $v_F$ , $v_O$ , $v_p$ are stoichiometric coefficients of the fuel, oxygen, and production, $Q$ is the heat released by the reaction.

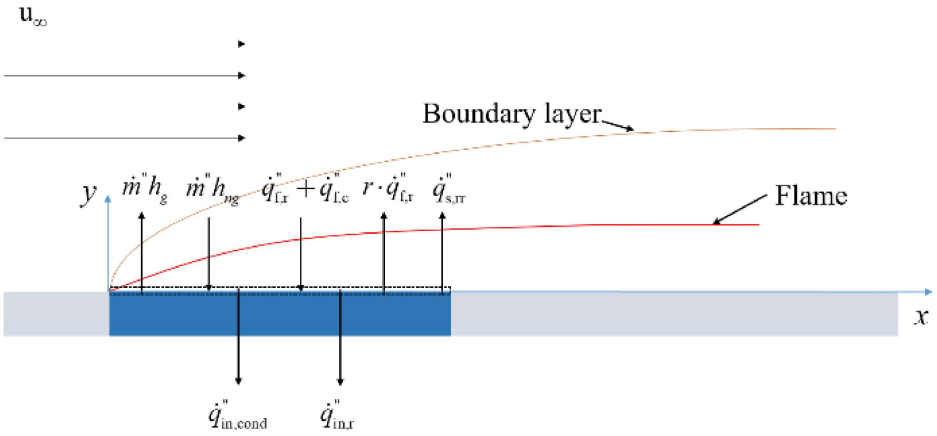


**Fig. 1.** Diagram of solid laminar combustion under forced flow.

Coupling Eq. (1-5), by using the Shvab-Zeldovich transformation[9] and boundary layer theory[2], the combustion of solid fuel under forced flow can be described by the following equations:

$$\begin{aligned} f''' + ff'' &= 0 \\ F'' + \Pr fF' &= 0 \end{aligned}, \tag{6}$$

where $f$ is the modified flow function that can be expressed by $f\ \eta\ = \frac{\psi}{x/\mathrm{Re}^{1/2}}$, where $\psi$ is primitive flow function, Re is Reynolds number, $x$ is characteristic length, $F\ x,y\ $ is the dimensionless function defined in solving. The boundary condition of Eq.(6) is expressed as:

$$\begin{aligned} f'\ 0\ &= 0, f\ 0\ = BF'\ 0\ /\Pr, F\ 0\ = 1; \\ f'\ \infty\ &= 2, F\ \infty\ = 0 \end{aligned}, \tag{7}$$

where $\eta$ is self-similar variable, expressed as

$$\eta = \tfrac{1}{2} x^{-1/2} Re \int_0^y \tfrac{\rho}{\rho_\infty} dy\ , \tag{8}$$

$F_f = \ B+1\ r/B\ \ r+1\ $ is the solution of Eq. (6) on the flame location in the reaction zone, when the self-similar variable $\eta$ is equal to $\eta_f$. Using the inverse of the Howarth-Dorodnitsyn transformation, $x,\eta\ $ can be transformed to $\ x,y\ $, thus Eq. (8) can be written as:

$$y = 2xRe^{-1/2} \int_0^\eta \tfrac{\rho_w}{\rho} d\eta\ , \tag{9}$$

where $\rho_w/\rho$ is expressed by $\frac{\rho_w}{\rho} = \frac{B+\tau-BF}{\tau}\ \frac{T_w-T_\infty}{T_\infty}\ +1$ and $\tau = h_w/L$. Thus, the flame standoff distance can be calculated by integrating from 0 to $\eta_f$:

$$y_{\mathrm{f}} = 2xRe^{-1/2} \int_0^{\eta_{\mathrm{f}}} \left[ \tfrac{B+\tau-BF}{\tau}\ \tfrac{T_w-T_\infty}{T_\infty}\ +1 \right] d\eta \tag{10}$$

In Eq. (10), $F$ is the solution of Eq. (6-7). Figure 2 shows all solutions of Eq. (6-7) when $B$ is equal to 1.3.

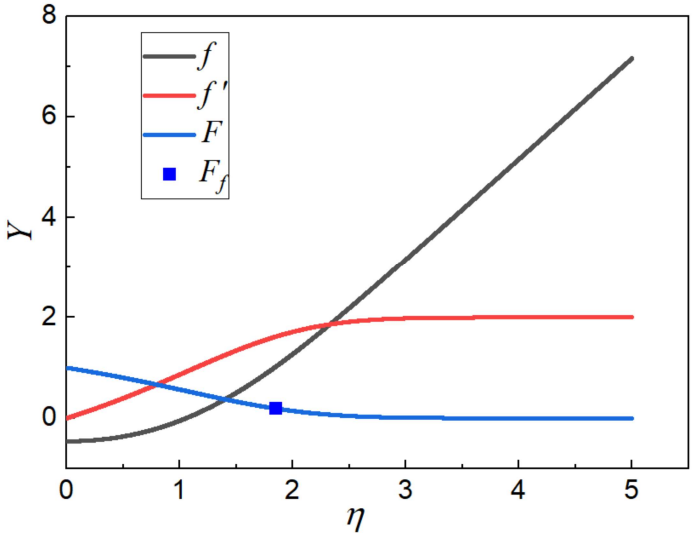


**Fig.2.** Solutions of Eq. (6-7) when B is equal to 1.3.

The flame standoff distance can be calculated using Eq. (10) if the value of the B number is determined. On the contrary, the experimental value of the B number at any position can be obtained by measuring the flame standoff distance.

**Mass transfer number**

Mass transfer number, also called Spalding-B number, was proposed by Spalding in the study of liquid fuel burning to characterize the relationship between chemical energy released and heat loss in combustion[1]. A more accurate expression of mass transfer number was proposed by Emmons in the study[2]. Then, Torero et. al[10] conducted a special study and discussion on mass transfer number, and proposed the modified mass transfer number, the adiabatic mass transfer number, the leading edge mass transfer number, and the critical mass transfer number. The expressions of these four forms are shown in Table 1.

**Table 1. Four expressions of mass transfer number**

| Type of mass transfer number | Expression |
|---|---|
| modified mass transfer number | $B = \frac{1-\chi \quad \Delta H_C Y_{O_2,\infty}/\nu_s \quad - C_{p,\infty} \quad T_p - T_\infty}{L+Q}$ |
| adiabatic mass transfer number | $B_A = \frac{\Delta H_C Y_{O_2,\infty} \quad - C_{p,\infty} \quad T_p - T_\infty}{L}$ |
| leading edge mass transfer number | $B_R = \frac{1-\chi \quad \Delta H_C Y_{O_2,\infty} \quad - C_{p,\infty} \quad T_p - T_\infty}{L}$ |
| critical mass transfer number | $B_C = \frac{1-\chi \quad \Delta H_C Y_{O_2,\infty} \quad - C_{p,\infty} \quad T_p - T_\infty}{L+Q_C}$ |

In this study, it is assumed that only convective heat transfer exists in combustion. However, radiation exists in the actual combustion, so the modified mass transfer number is used in the study, which is expressed as:

$$B = \frac{1-\chi \quad \Delta H_C Y_{O_2,\infty}/\nu_s \quad - C_{p,\infty} \quad T_p - T_\infty}{L_v + Q} \quad , \tag{11}$$

where $\chi$ is the radiant fraction of flame, $\Delta H_C$ is combustion heat, $\nu_s$ is the mass stoichiometric ratio, $L_v$ is the heat of gasification, $Q$ is the non-convective heat loss at the surface. As shown in Fig.1, the surface energy conservation of PMMA in combustion can be expressed as:

$$\dot{m}'' h_g = \dot{q}''_{f,c} + \ 1-r \ \dot{q}''_{f,r} + \dot{m}'' h_{ng} - \dot{q}''_{s,rr} - \dot{q}''_{in,cond} - \dot{q}''_{in,r} \ , \tag{12}$$

where $\dot{m}'' h_g$ is the heat carried by fuel vapors away from the surface, $\dot{q}''_{f,c}$ is the convective heat from the flame to fuel surface, $\dot{q}''_{f,r}$ is radiative heat from the flame to fuel surface, $r$ is the reflectivity of PMMA surface, $\dot{m}'' h_{ng}$ is the heat carried by solid fuel to the surface, $\dot{q}''_{s,rr}$ is the surface re-radiative heat, $\dot{q}''_{in,cond}$ is the conductive heat loss into solid, and $\dot{q}''_{in,r}$ is the radiative heat loss into solid. In previous studies[11, 12], the heat carried by solid fuel to the surface is approximately equal to the sum of the conductive heat loss into solid and the radiative heat loss into solid for thermal-thickness solid plate, which is expressed as:

$$\dot{m}'' h_{ng} = \dot{q}''_{in,cond} + \dot{q}''_{in,r} \tag{13}$$

Therefore, the non-convective heat loss at the surface can be calculated by:

$$Q = \frac{\dot{q}''_{\mathrm{s,rr}} - \dot{q}''_{\mathrm{f,r}}}{\dot{m}''} \tag{14}$$

**Nusselt number**

Nusselt number (Nu) is a physical quantity representing the dimensionless temperature gradient, which can be applied to measure and calculate the convective heat transfer at the interface between the fluid and solid fuel[13]. In the combustion process of PMMA plate, the convective heat from the flame to fuel surface at any value of $x$ can be expressed as[6]:

$$\dot{q}''_{\mathrm{f,c}} = h\Delta T = \frac{Nu \cdot k_{\mathrm{f}}}{x}\Delta T \simeq k_{\mathrm{f}}\frac{\Delta T}{y_{\mathrm{f}}}, \tag{15}$$

where $h$ is the convective heat transfer coefficient, $\Delta T$ is the temperature difference between flame and fuel surface, $k_{\mathrm{f}}$ is the thermal conductivity of gas near the solid surface. Hence, the Nusselt number can be calculated by the following formula:

$$Nu = \frac{x}{y_{\mathrm{f}}} = \frac{1}{2\int_0^{\eta_{\mathrm{f}}}\left[\frac{B+\tau-BF}{\tau}\ \frac{T_w-T_\infty}{T_\infty}+1\right]d\eta} Re^{1/2} \tag{16}$$

## EXPERIMENTS

Figure 3 is the schematic diagram of the experimental device used in this study. Before the experiment, the mica plate with good insulation is put on the experimental device support placed on the electronic balance. The mica plate can play a supporting role and reduce the conduction heat loss from the lower surface of PMMA plate to the experimental device during burning. The PMMA plate used in the experiment is placed inside the hollow insulation board to ensure that the upper surface of PMMA plate is flush with the upper surface of the insulation board. The whole composed of PMMA plate and insulation plate is placed on the mica plate to obtain stable burning during the experiment. The experimental device is positioned in the hollow area of the wind tunnel, ensuring that the fuel surface is flush with the inner surface of the wind tunnel. In this way, it can not only ensure the wind blows evenly over the PMMA surface but also prevent the wind leakage from the lower of the wind tunnel to affect the flow field. To avoid the influence of DV camera on the flow field, the camera was installed on the outside of the wind tunnel with transparent glass, and the lens of the camera is close to the surface of the glass. The lens is installed to the same level as the flame center in the pre-experiment, to ensure the DV camera can truly record the flame shape in the burning.

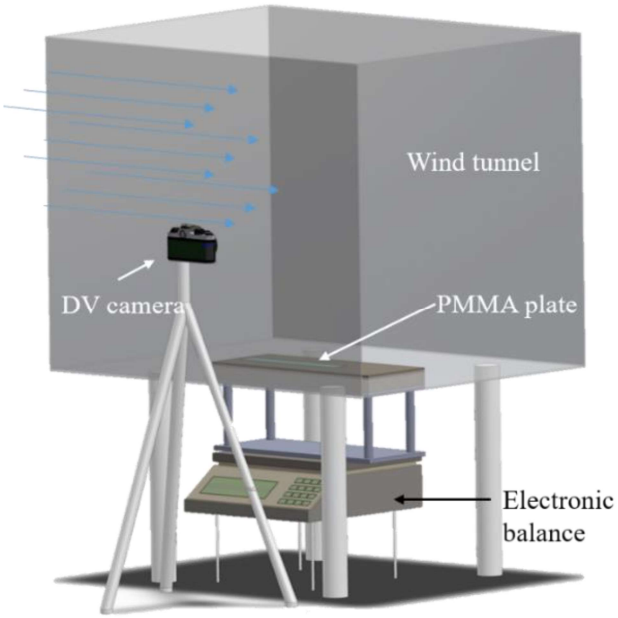


**Fig.3.** Schematic diagram of the experimental device

The experimental fuel samples are PMMA plates produced by Qingdao SDM building materials company. Table 2 shows the sizes of PMMA plates used in the experiment, and the thickness of all samples is 2 cm. The length direction is defined as the same direction as the flow, while the width direction is defined as the direction perpendicular to the flow. In the experiments, 2 m/s is adopted for all cases.

**Table 2. Sizes of PMMA plates used in the experiment**

| Case number | Length (cm) | Width (cm) |
|---|---|---|
| 1 | 5 | 10 |
| 2 | 10 | 10 |
| 3 | 15 | 10 |
| 4 | 10 | 5 |
| 5 | 10 | 15 |

When the experimental facilities and fuel sample have been installed, the linear ignitor is used to ignite the PMMA plate. The linear ignitor is powered by butane with an exothermic power of 1.8 kW and can provide an ignition temperature of approximately 1550 K. When the whole surface of PMMA plate is ignited by the linear ignitor, the ignitor is removed. Meanwhile, the fan fills the wind tunnel with uniform airflow and the load cell (Mettler Toledo XP10002S) with a maximum load of 14000 g and precision of 0.01 g began to record the mass loss data instantly. Camera with a spatial resolution of 1980*1080 and frame rates of 25 fps were set to guarantee the flame shape to be recorded clearly. Each case was repeated three times in this study to ensure that the experiment is repeatable. When the experiments are finished, MATLAB is used to intercept the video and identify the flame.

## RESULT AND DISCUSSION

### Flame appearance

After the whole surface of PMMA is ignited, the combustion process reaches a steady-state in a short time. Figure 4 shows the images of the flame of PMMA plates with five sizes in the steady combustion process. As shown in Fig.4, the combustion flame of PMMA plate presents a laminar flow state basically at a wind speed of 2 m/s. Reynolds number (Re) is a dimensionless parameter describing the relationship between the inertia force and the viscous force, which can determine whether the flow state is laminar or turbulent. Reynolds number is calculated by

$$\mathrm{Re} = \frac{ux}{\nu} \tag{17}$$

According to Eq. (17), the values of Re of all cases is less than $10^5$, thus, combustion of PMMA plate with all sizes is laminar flow state.


**Fig.4.** Image of stable combustion of PMMA plates with different sizes under forced flow

As shown in Fig.4, the combustion flame of the PMMA plate under forced flow appears blue in upwind. The flame in the middle is bright, while the downwind flame appears yellow. In upwind, the air is sufficient enough for combustion. The combustion state in this area is fuel-lean, and the combustible vapor pyrolyzed from the PMMA plate is fully burning. Therefore, fewer soot particles are produced in burning and the flame is blue. In downwind, the concentration of combustible vapor pyrolyzed from the PMMA plate is higher than that of air so that the combustion state is fuel-rich. There are three main reasons for the fuel-rich in this area. One is that the combustible gas pyrolyzed from upstream fuel travels downstream with the airflow increasing the concentration of combustible gas. The second reason is that this area pyrolyzes more combustible gas than upwind area owing to the flame. The third reason is that the gas products from upstream in burning are mixed downstream , resulting in reduced air concentration. Hence, the combustion is inadequate in the downwind area, that more soot particles are produced in burning and flame appears yellow.

**Flame standoff distance**

Flame standoff distance is the distance between the flame surface and the burning surface of solid fuel plate, which is related to the wind speed, position, and mass transfer number according to Eq. (10). In the experiment, the wind speed is the same for all cases, so the main influences on flame standoff distance are position and mass transfer number. Based on the video of the combustion process, the image of flame shape can be captured and the flame standoff distance can be obtained By MATLAB. Figure 5 shows the flame standoff distance data of five sizes of PMMA plates in burning obtained from the video. As shown in Fig.5, there are some differences in the flame standoff distance of five PMMA plates during combustion under the condition of constant wind speed. In the comparison of the plates with the same area, the flame standoff distance of the wider PMMA plate is slightly larger than that of the longer PMMA plate at the same position. In addition, the flame standoff distance is increasing with $x$. The flame standoff distance is proportional to $x^{0.5}$ according to Eq. (10), which can be fitted by the following equation.

$$y_f = Ax^{1/2} \tag{18}$$

In the previous study[7], another parameter related to flame standoff distance is mass transfer number. From Fig.5, there is some deviation between the experimental data of flame standoff distance and the fitting curve. This demonstrates that the values of $A$ in different positions are different.

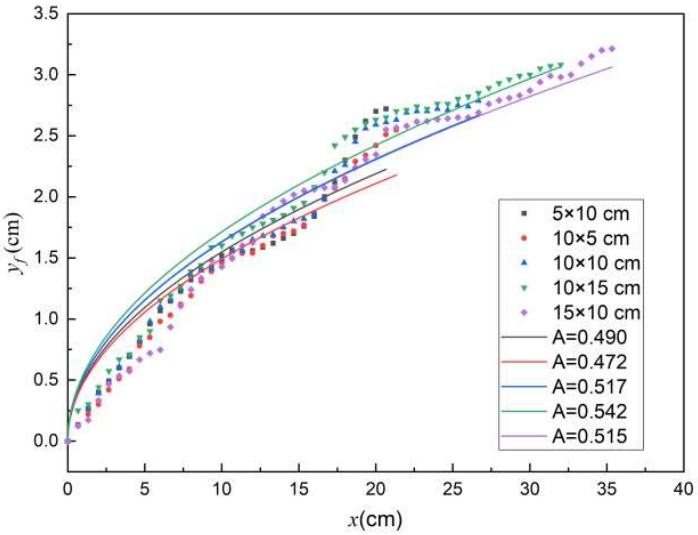


**Fig.5.** The flame standoff distance of five sizes of PMMA plates

## Flame length

Figure 6 shows data on the flame length of PMMA plate stable combustion under forced flow. As shown in Fig.6, the effect of the length is greater than that of width. With the increase in length and width of PMMA plate, the flame length increases obviously. However, with the increase of PMMA plate length direction, the increase of flame length is more obvious. In comparison with PMMA plates of the same area, it can be seen that the flame length of the longer PMMA plate is greater than that of the wider plate.

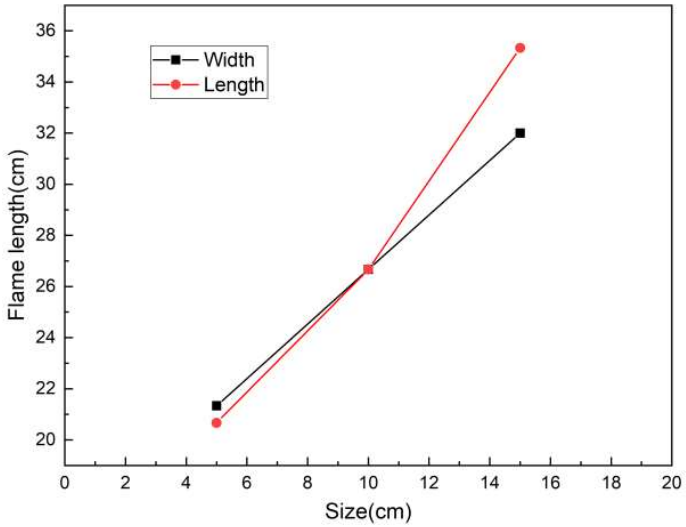


**Fig. 6.** The flame length of PMMA plate stable combustion under forced flow

## Heat transfer and mass loss rate

Figure 7 is the experimental data relationship between Nusselt number and Reynolds number of PMMA plates with different sizes in stable combustion under forced flow. Previous scholars studied the relationship of Nusselt number and Reynolds number under forced flow. The research results of Singh et. al[14] show that the relationship between Nusselt number and Reynolds number under forced flow is as follows:

$$Nu = 0.1148\sqrt{Re} \tag{19}$$

Ananth et. al[5] concluded that: when the wind speed is greater than 1.2 m/s, the relationship between Nusselt number and Reynolds number can be expressed by the following formula:

$$Nu = 0.1\sqrt{Re} \tag{20}$$

According to Eq. (16), the relationship between Nusselt number and Reynolds number can be fitted by

$$Nu = C\sqrt{Re} \tag{21}$$

As shown in Fig. 7, there is some deviation between the fitting curve and experimental data. Hence, $C$ of Eq. (21) is not constant.

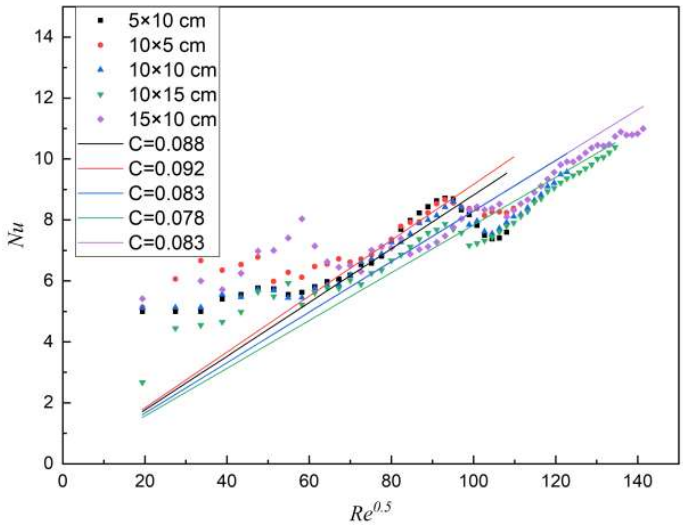


**Fig. 7.** The relationship between Nusselt number and Reynolds number of PMMA plates with different sizes in stable combustion under forced flow

## Mass loss rate

Figure 8 shows the relationship between mass loss rate per unit area and size of PMMA plates of different sizes in the stable combustion under forced flow. As shown in Fig.8, the mass loss rate per unit area decreases with the increase of length and width of samples and the length has a more obvious effect than width.

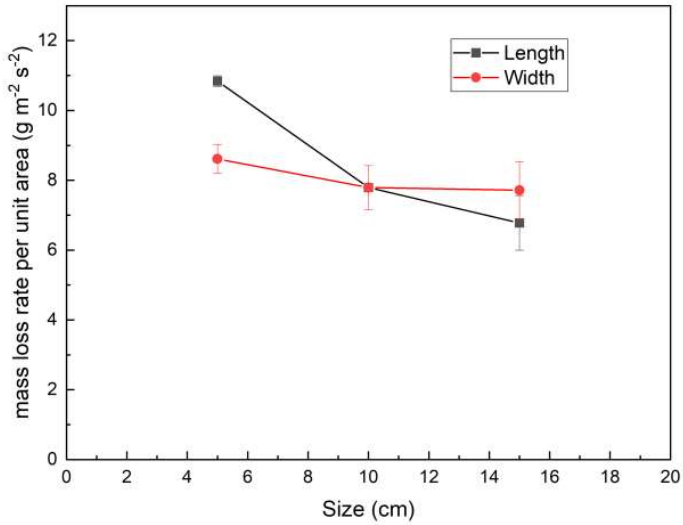


**Fig. 8.** Mass loss rate per unit area of PMMA plates of different sizes in burning under forced flow

## CONCLUSIONS

The study analyzed the stable combustion characteristics of PMMA plates under forced flow using laminar boundary layer theory. The theoretical expression of flame standoff distance is obtained by solving the flow function equation. According to the experimental results, it can be seen that the flame standoff distance of the wider PMMA plate is larger than that of the longer PMMA plate in the same size in the steady combustion process. And with the change of the characteristic length ($x$), the flame standoff distance also changes constantly because the mass transfer number has a great influence on it. According to experimental data, the flame length increases with the increasing length and width of the PMMA plate, and the effect of increasing the length of the plate is more obvious. Based on boundary layer theory, the theory relationship between Nusselt number and Reynolds number have been analyzed, while the result is different from previous studies. The reason is the mass transfer number is not constant in every position. The experimental results show mass loss rate per unit area decreases with the increasing length and width of the PMMA plate and the effect of increasing the length of the plate is more obvious.

## ACKNOWLEDGMENT

The authors would like to thank the Fundamental Research Funds for the Central Universities (Grant Nos. WK2320000043 and WK2320000048).

## REFERENCES

[1] D.B. Spalding, The combustion of liquid fuels, Symposium (International) on Combustion 4 (1953) 847-864.

[2] H. Emmons, The film combustion of liquid fuel, ZAMM - Journal of Applied Mathematics and Mechanics/Zeitschrift für Angewandte Mathematik und Mechanik 36 (1956) 60-71.

[3] M. Sibulkin, A.K. Kulkarni, K. Annamalai, Burning on a vertical fuel surface with finite chemical reaction rate, Combustion and Flame 44 (1982) 187-199.

[4] H.T. Loh, A.C. Fernandez-Pello, A study of the controlling mechanisms of flow assisted flame spread, Symposium (International) on Combustion 20 (1985) 1575-1582.

[5] R. Ananth, C.C. Ndubizu, P.A. Tatem, Burning rate distributions for boundary layer flow combustion of a PMMA plate in forced flow, Combustion and Flame 135 (2003) 35-55.

[6] C.C. Ndubizu, R. Ananth, P.A. Tatem, Transient burning rate of a noncharring plate under a forced flow boundary layer flame, Combustion and Flame 141 (2005) 131-148.

[7] L.-y. Zhao, J. Fang, X.-z. He, J.-w. Wang, S.-q. Tao, Y.-m. Zhang, An analysis of width effects on flame spread in conjunction with concurrent forced flow using a variable B-number, Combustion and Flame 194 (2018) 334-342.

[8] N. Zhu, X. Huang, J. Fang, L. Yang, L. Hu, Transitional flame-spread and fuel-regression behaviors under the change of concurrent wind, Fire Safety Journal, (2020) 103015.

[9] J.S. Kim, J. de Ris, F. William Kroesser, Laminar free-convective burning of fuel surfaces, Symposium (International) on Combustion 13 (1971) 949-961.

[10] J. Torero, T. Vietoris, G. Legros, P. Joulain, Estimation of a total mass transfer number from the standoff distance of a spreading flame, Combustion Science and Technology 174 (2002) 187-203.

[11] L. Orloff, A.T. Modak, R. Alpert. Burning of large-scale vertical surfaces. In: editor^editors. Proceedings of the Combustion Institute; 1977: Elsevier. p. 1345-1354.

[12] Y. Pizzo, C. Lallemand, A. Kacem, A. Kaiss, J. Gerardin, Z. Acem, P. Boulet, B. Porterie, Steady and transient pyrolysis of thick clear PMMA slabs, Combustion and Flame 162 (2015) 226-236.

[13] F.P. Incropera, A.S. Lavine, T.L. Bergman, D.P. DeWitt, Fundamentals of heat and mass transfer, Wiley2007.

[14] A.V. Singh, M.J. Gollner, A methodology for estimation of local heat fluxes in steady laminar boundary layer diffusion flames, Combustion and Flame 162 (2015) 2214-2230.

# Three-Dimensional Numerical Simulation of Smoldering in Granular Biomass Fuel Beds

**Meraner C.[1,*], Mikalsen R.F.[1], Fernandez-Anez N.[2], Hagen B.C.[2], Zhang J.[3], Li T.[1,3*]**

*[1] RISE Fire Research AS, Trondheim, Norway.*
*[2] Western Norway University of Applied Science, Bergen, Norway.*
*[3] Norwegian University of Science and Technology, Trondheim, Norway*
**Corresponding author's email: christoph.meraner@risefr.no, tian.li@risefr.no*

## ABSTRACT

Economic, societal and environmental consequences from smouldering fires may be significant, and there is a need for improved models to understand the smouldering dynamics and mitigate the risk associated with this type of fire. A comprehensive three-dimensional numerical model is presented and compared with an experimental study of self-sustained smouldering in a granular biomass fuel bed. The model considers the complex heterogeneous bed structure of wood pellets storage, describing the interaction between the granular fuel pellets and heat and oxygen transfers. It includes a Lagrangian description of the fuel bed, which enables the characterisation and modelling of the individual particle in the fuel bed. As a result, the model is capable of reviewing the localised hotspots in the fuel bed, which is also observed in the experiment. Moreover, the model provides a platform to evaluate the delicate heat balance inside the fuel bed. Various sub-models are discussed and compared in the study highlighting the difference between simulations of combustion and smouldering as well as the impact of the char oxidation model, radiation heat transfer model, and particle-fluid-particle conductive heat transfer model. The developed numerical solver aims to form a basis for a tool that may predict the smouldering dynamics in industrial material storages, and by extent, increase industrial fire safety.

**KEYWORDS:** smouldering, CFD-DEM, bulk granular biomass, industrial fires.

## INTRODUCTION

Smouldering is a complex phenomenon representing significant risks to people, homes, industry, and the wildland [1,2]. Smouldering usually results in high yields of carbon monoxide (CO) and other complex fuel vapour combinations. CO is often found to cause death in residential house fires [3]. In addition, the complex vapours from smouldering fires may cause a transition to flaming and explosions in industries such as grain elevators [4], silos containing sawdust [5] and wood pellets [6]. Wildland is also subjected to smouldering fires [7], and where both significant emissions of toxic gasses [8] and transition to flaming [9] cause substantial damage to wildlife, eco-systems and global warming [10]. The development of smouldering fires depends on different factors such as the amount and state of combustible material, access to oxygen, surrounding boundaries, and other constraints [11,12]. Large variations in material properties, geometrical constraints, and overall scale etc., makes it challenging to carry out controlled experiments for representative scenarios. Therefore, one needs reliable and validated models for the evolution of smouldering fires, and these models have been the focus of various research through the years.

To the authors' knowledge, the complexity of smouldering is not reflected in the current models used to simulate smouldering, where relatively simple assumptions are made especially with regard to the treatment of the fuel bed. Most of the existing smouldering models treat the phenomenon as a one-dimensional situation [13–15], while two- [16] and three-dimensional [17] models are scarcer. And finally, the porous fuel bed is typically represented as a continuum, employing volume-averaged macro-scale values for the description of the smouldering fire, instead of resolving the pores at a micro-scale. Macro-scale continuum approaches cannot account for nonequilibrium conditions at the micro-scale [18]. There has been developed micro-scale models [17], which was applied in two-dimensional [19] and three-dimensional simulations [20]. However, in general, there is a need for

more complex models, including two- and three-dimensional models, to improve the description of different heat transfer processes, the occurrence of non-centrosymmetric hotspots and temperature gradients perpendicular to the propagation direction. The importance of this has been shown, for example, in the horizontal propagation of smouldering peat fires, which was recently investigated by Yang et al. [21], employing a two-dimensional model. The study identified three smouldering types with different overhang structures, dependent on the wind speed and oxygen mass fractions. A unique two-dimensional model, utilising a cellular automaton, was recently proposed by Fernandez-Anez et al. [22] and was employed to study the roles of different ignition locations and airflow directions on smouldering combustion of generic biomass.

Currently, Gpyro [23], Comsol [24] and special purpose models, which are detailed in a recent review article by Zanoni et al. [2], are mostly used when simulating smouldering fires. Typically, all these models use simple kinetics, one- or two-dimensional combustion zones and continuous fuels. The work presented in this article will expand on the traditional approach of modelling smouldering fire by using a three-dimensional configuration, where the fuel is represented by discrete particles. The model builds on an existing model, which has successfully been employed to simulate fixed-bed combustion of biomass by Zhang et al. [25,26]. The objective of the present work is to investigate which assumptions and submodels need to be modified to make the previously developed model suitable for the special case of a smouldering fire. The focus of this article is on the char conversion process, radiation as well as heat transport between particles.

## EXPERIMENTAL BACKGROUND

Experiments with self-sustained smouldering wood pellets from Mikalsen et al. [27,28] are used as a reference for the model validation. The fuel sample was bulk and granular biomass, consisting of wood pellets (1.25 kg, 1.8 litres) of pine/spruce mixture, 8.2 ± 0.2 mm diameter, 13.5 ± 6 mm length, elemental analysis 48% carbon, 39% oxygen, 6% hydrogen, 0% nitrogen, proximate analysis 6.3 % moisture, 77 % volatiles, 0.46 % ash (more material properties can be found in [27,28]). The sample was added to a vertical steel cylinder (330 mm height, inner diameter 150 mm) with insulated sidewalls, which was open at the top and placed on top of a heater, as shown in Fig. 1.

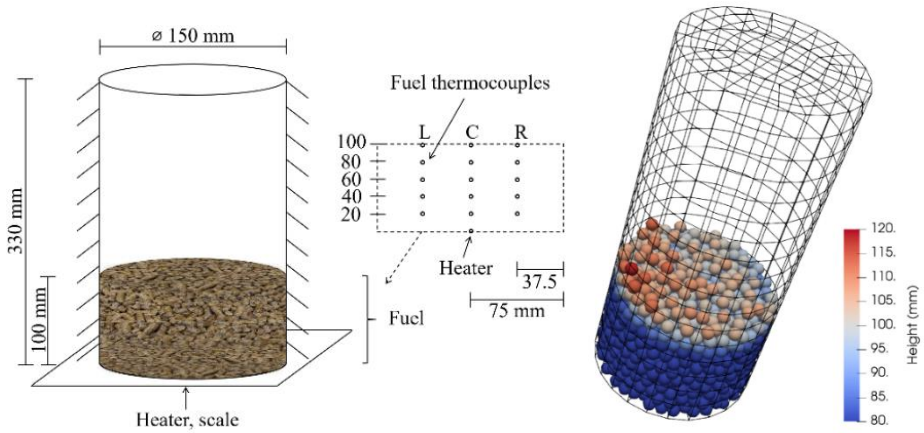


**Fig. 1.** Illustration of the experimental setup (left) and numerical domain (right), with the colour showing the particle height.

A filling height of 100 mm was used for the wood pellets sample. The sample was exposed to external heating for a predetermined time, after which self-sustained smouldering or self-extinguishment was

observed, and the system was left undisturbed until all temperatures reached ambient. Temperatures within the sample and on the heater were measured using 0.5 mm encapsulated type K thermocouples. Self-sustained smouldering was indicated by fuel bed temperature increase after the external heating was switched off, while self-extinguishing was indicated by temperatures decreasing to ambient. During self-sustained smouldering, a key feature was non-centrosymmetric smouldering propagation, displayed both by temperatures and by irregular fuel consumption (fuel height). A total of ten experiments of self-sustained smouldering formed the basis of the numerical work in this study.

## NUMERICAL METHODS

The computational fluid dynamics (CFD)–discrete element method (DEM) used in this study is primarily based on the OpenFOAM solver developed in the previous works [25,26]. The gas phase is described in an Eulerian framework based on the Navier-Stokes equations, whereas the biomass pellets are modelled in a Lagrangian manner and are tracked individually.

### Gas phase

The governing equations for gas phse are detailed in the previous works [25,26], thus are omitted here. In general, continuity, momentum, energy, and species transport equations are solved in the CFD-DEM solver. Moreover, the discrete ordinates model is applied to resolve the radiative transfer equation for the gas phase. It should be noted that some modifications and simplifications are made in the current solver to enable a prompt evaluation of the smouldering conditions. One major change is that the sources from the particle are added to the gas-phase transport equations based on the particle centroid method [29]. In addition, gas-phase combustion is not taken into account, which is common for smouldering simulation.

### Discrete particle phase

The biomass pellets are modelled as spheres with volume equivalent diameter as the pellets used in the experiments. However, the surface areas of the spheres are replaced by the surface area of the cylindrical pellets for better predictions of heat transfer and char reaction processes.

The motion of the discrete particle is obtained by solving Newton’s equation of motion. The fluid-particle drag is calculated based on Wen and Yu correlations [30]. Both particle-particle and particle-wall interactions are resolved by a soft-sphere method proposed by Cundall and Strack [31]. The soft-sphere method is particularly suitable for handling densely packed granular systems. However, different from the previous particle treatment [25,26], the shrinkage is not considered as minor height changes of the fuel bed were observed in the experiment [27,28]. Therefore, the particle movement is only activated during the bed forming process. However, as shown in the previous works [25,26], it is possible to include the shrinkage effect during the particle conversion process using the soft-sphere method despite the high computational cost. A compromise can be made to reduce the calculation frequency of the particle collisions. Since the particle's velocity is relatively small, the collision update can only be performed at the chosen time interval, e.g., 60 s, instead of every time step.

The biomass particles contain specific fractions of moisture, dry wood, and ash at the beginning of the simulation. These fractions were set according to the experimental values. The conversion of the biomass is simulated by three successive steps: drying, pyrolysis, and oxidation. The drying process is calculated using a single first-order kinetic model with an Arrhenius type rate expression (a pre-exponential factor of $5.13\times10^{10}$ 1/s and activation energy of 88 kJ/mol [32]). Pyrolysis is modelled with a two-stage model, the same model used in our previous works [25,26]. Wood converts to light gases, char and tar in the first stage of pyrolysis. And tar can further decompose to light gases and char. Regarding the heat of pyrolysis of wood, various values can be found in the literature reviewed by Ström and Thunman [33]. Typically, the pyrolysis process is modelled as heat neutral or slightly endothermic. In this study, only heat neutral pyrolysis is considered.

Only oxidation is considered for char conversion as the rate of char gasification is much lower than the char oxidation at the relatively low temperature during the smouldering fire. The char is assumed to contain only reactive carbon and nonreactive ash, and the oxidation of the char is modelled as

$$\Omega C + O_2 \rightarrow 2(\Omega - 1)CO + (2 - \Omega)CO_2, \quad (1)$$

where $\Omega$ is a temperature sensitive correlation, which is calculated based on the model introduced byTognotti [34]. Both diffusion and kinetic rates are considered in the calculation of char oxidation rate. Various char oxidation kinetics have been tested. But only the results obtained using the kinetics applied in our previous works [25,26] are detailed in the later section. This char oxidation kinetics was originally proposed by Evans and Emmons [35] and successfully implemented into a bed model by Thunman and Leckner [36]. Depending on the cases, a multiplier ranging from 0.5 to 1.5 is multiplied by the obtained char oxidation rate to assess the effect of char conversion. Details regarding the char conversion model can be found in previous works [25,26].

The particle temperature is calculated from the equation below

$$m_p c_p \frac{dT_p}{dt} = hA_p\left(T_g - T_p\right) + PA_p\varepsilon\left(G - 4\sigma T_p^4\right) + Q_r + Q_{cont}, \quad (2)$$

where $m_p$ is the mass of the particle, $c_p$ is the specific heat of the particle, $A_p$ is the surface area of the particle, $T_g$ is the temperature of the gas phase, $h$ is the heat transfer coefficient estimated by Ranz-Marshall correlation [37], $PA_p$ is the projection area of the particle which is estimated as the mean projection area of the equal-volume cylinder [38], $\varepsilon$ is the emissivity of the particle, $\sigma$ is the Stefan-Boltzmann constant, $Q_r$ is the energy source term caused by the drying, pyrolysis and char oxidation processes, $Q_{cont}$ is the energy source term caused by the conductive heat transfer between particles. Compared to the previous developed model [25,26], one key difference in this work is the thermally thin treatment of the particle, considering the relatively low temperature and slow heating process. The second term on the right-hand side of Eq. (2) is related to the radiative heat transfer, which may not be included depending on the simulation settings. The heat exchange rate between particles $i$ and $j$ ($Q_{cont,i,j}$) is calculated based on the presvious works [39,40]. Two different conductive contributions are considered, including particle-fluid-particle conduction heat transfer and particle-particle conduction transfer detailed elsewhere [39–41]. The numerical implementation of the particle-fluid-particle conduction in the solver is based on the open-source code MFiX-DEM [42], which was developed at NETL in US. The required parameters for calculating the two modes of conductive heat transfer are obtained from the above-mentioned collision model. As our first attempt to resolve the smouldering in a granularly packed bed, only the particle-fluid-particle conduction heat transfer between two contacting particles is included. It is possible to include such heat transfer between two particles that are not in contact by enlarging the search diameter for the neighbouring particles in the collision model. However, as indicated in the previous work [41], the contribution from such heat conduction is comparatively small.

**Computational methodology**

As shown in Figure 1, the computational domain is a cylinder that is discretised into 1836 hexahedral cells. The corresponding boundary conditions used in the simulation are listed in Table 1. An electric heater in the experiment heats the bottom surface. The temperature of the bottom varies slightly between different experiments. Therefore, we use the mean measurements as inputs to set the boundary temperature for the bottom in the simulation. In the first 20 seconds of the simulation, the fuel bed is formed. Particles are injected randomly from the top surface until the fuel bed reaches a similar height as reported in the experiment [27,28]. During these 20 seconds, all the models related to reactions and heat transfer are temporally turned off. And the bottom surface is set to be at a constant temperature of 300 K. The time step used in the simulation is estimated by limiting the max Courant number to 1. A maximum time step of 0.01 s is chosen to ensure numerical stability. The first order implicit Euler method is adopted for the time discretisation. Spatial discretisation is

achieved using the so-called “Gauss limitedLinear” scheme with a coefficient of 1, which is the OpenFOAM implementation of the total variation diminishing (TVD) scheme. Pressure and velocity equations are coupled and solved by the pressure-implicit method for the pressure-linked equations (PIMPLE) algorithm.

**Table 1. Boundary conditions for the reactive simulation**

| Boundaries | Velocity | Pressure | Temperature |
|---|---|---|---|
| Side wall | No slip | Zero gradient | Zero gradient |
| Bottom wall | No slip | Zero gradient | Experimental input |
| Top surface | Outflow: Zero gradient | 101325 Pa | Outflow: Zero gradient |
| | Inflow: Velocity based on the flux | | Inflow: 300 K |

## RESULTS AND DISCUSSION

The results are presented in two sections, char conversion and heat transfer. The first section presents the results from a parameter study with different char conversion rate multipliers. The latter presents the results for different variations in the heat transport modelling.

### Char conversion

Char oxidation is, besides the heater, the only energy source in the present model. Hence, it is important to describe this process accurately. Three different kinetic models, Thunman and Leckner [36], Anca et al. [43], and Sven and Thunman [44] have been investigated. However, only the model from Thunman and Leckner is shown here. There are many fuel-specific models available in the literature, and it is at this stage not possible to evaluate which model is the most accurate. Furthermore, the energy balance of the char conversion is not only dependent on the Arrhenius coefficients but also on other parameters such as the ratio between CO and $CO_2$ yield, as seen in Eq. (1). It is, thus, more interesting to evaluate the sensitivity of the smouldering combustion to variations in the char conversion model. Therefore, a parameter study was conducted in which the char conversion rate has been multiplied with different factors (1, 0.7, 0.6 and 0.5).

The results from this study are presented in Fig. 2, which shows the gas temperature development overtime at the fuel bed centreline on three different elevations. All simulations underpredict the temperature within the first hours. However, this is not related to the char conversion, as it is already observed before char conversion starts after approximately two hours. The three simulations with the highest char conversion rates show a temperature increase that also continues after the heater is turned off at the six-hour mark. This indicates that these simulations would lead to a transition to flaming if gas-phase reactions had been included in the model. The simulation, which uses 50% of the original char conversion rate, shows, on the other hand, a temperature decay that follows the temperature profile of the heater once the heater is turned off. Hence, self-sustained smouldering was not achieved. Note that a few simulations in Fig. 2 were stopped before 10 hours. As mentioned in the previous section, the time step was set according to a maximum Courant number of 1. However, due to the low fluid velocity, the maximum Courant number in the simulation was, in general, smaller than 1. Therefore, all conducted simulations were conducted mainly with a time step of 0.01 seconds, which is relatively large. Such a large time step caused convergence issues resulting from the rapid increase of the temperature.

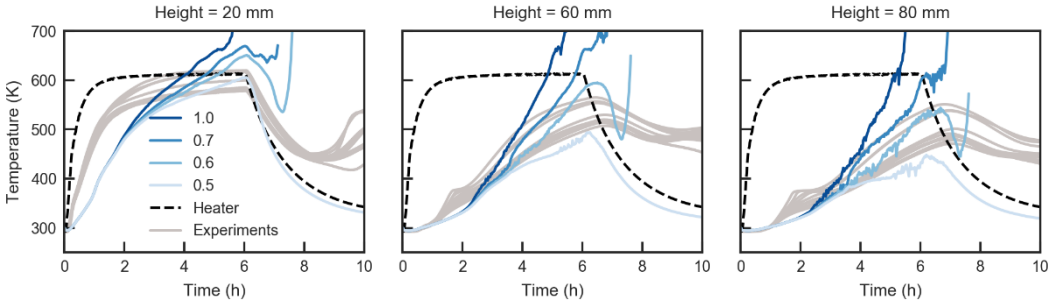


**Fig. 2.** Gas temperature development over time as predicted by the model with different char conversion rate multipliers (solid blue lines) and measured in the experimental campaign (solid grey lines) at different heights (20 mm, 60 mm, and 80 mm from left to right). The heater temperature, which is used as input to the model, is shown as a reference (dashed black line).

It is important to note that only the centerline temperature is shown in Fig. 2 due to the limited spatial resolution of the experimental data. However, the simulations show the appearance of hotspots adjacent to the outer wall. This is related to the adiabatic boundary condition, which reduces the heat loss compared to a particle located further to the centre of the fuel bed.

Once the heater is turned off, the bottom plate turns practically into a heat sink as it follows a prescribed curve to lower temperatures. If a simulation shows only hotspots close to the bottom plate at this point, smouldering will be quenched due to heat losses and reduced oxygen concentration. Hotspots at slightly higher elevations were observed in the simulations that led to a temperature increase also after the heater was turned off. An example is given in Fig. 3, which shows the explicit particle enthalpy source. Since only the char oxidation releases heat, a positive enthalpy source indicates the char oxidation is undergoing.

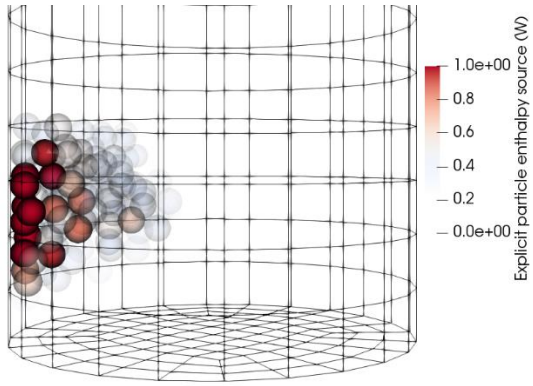


**Fig. 3.** Particles are coloured by the explicit particle enthalpy source based on the simulation with a char conversion multiplier of 0.6 after 7 hours and 14 minutes. Note that the colour scale is limited to a narrow range of 0–1W, and opacity is employed to visualise the hotspot.

## Heat transport

The results presented in Fig. 2 clearly show that further adaptations need to be made to the combustion model to make it suitable for modelling smouldering combustion. The simulations have, furthermore, shown that heat transport is a key factor for the formation of local hotspots and the potential onset of

self-sustained smouldering. The three main heat transfer mechanisms, convection, conduction and radiation, have therefore been addressed.

In a first step, the radiation model was disabled in the simulation as the temperature in the fuel bed will be largely below 550 °C and is therefore not expected to have a significant contribution to the heat transport as indicated in previous work [41]. However, the significant lower temperature (see Fig. 4 no particle-fluid-particle heat transport) compared to the same simulation with radiation (see Fig. 2 with multiplier 1.0) indicates that other heat transport mechanisms are underpredicted in the model.

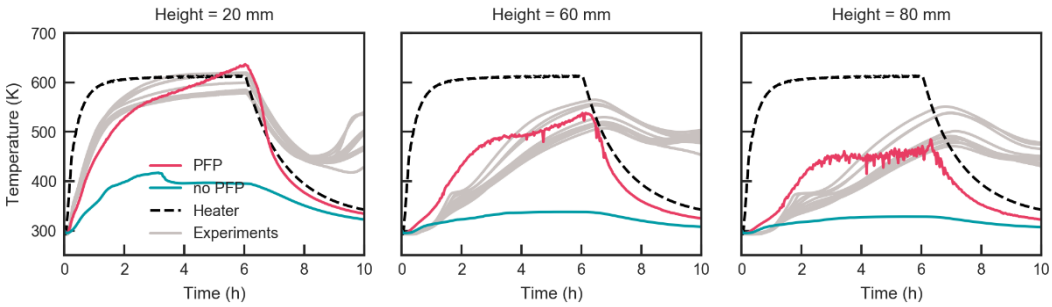


**Fig. 4.** Gas temperature development over time as predicted by the model with and without particle-fluid-particle (PFP) heat transport and measured in the experimental campaign (solid grey lines) at different heights (20 mm, 60 mm, and 80 mm from left to right). The heater temperature, which is used as input to the model, is shown as a reference (dashed black line).

The present model treats convection by employing the classic Ranz-Marshall correlation [37]. The gas-phase conductivity is modelled as a constant. Due to the relatively low gas velocity of the buoyancy-driven flow at low temperatures, it can be expected that conduction between particles will be a dominant heat transport mechanism [39]. The original model for flaming combustion in a packet bed with forced convection [25,26] includes a particle-particle conductive heat transport model for particles in direct contact with each other. However, the particle-particle conduction was deemed neglectable due to the forced flow. For smouldering combustion without forced flow, this is not true. Indeed, it has been shown [39,45] that not only direct particle-particle conduction should be considered for packed beds without forced convection, but also indirect (i.e., particle-fluid-particle) conduction. The present model was therefore extended with a particle-fluid-particle conduction model for contacting particles. The heat transfer from particle-fluid-particle of non-contacting particles, which contributes slightly less to the total heat transfer at low velocities, is not modelled explicitly. It should, however, be noted that the coarse grid solution, containing several particles within a single control volume, leads to an increased heat transfer (particle-fluid-particle for non-contacting particles) as all particles within a control volume see the same gas temperature.

The results from the simulation with particle-fluid-particle conduction (Fig. 4) and without radiation show a clear improvement compared to the earlier model (Fig. 2). This is especially evident in the early stage of the simulation and lower elevations in the fuel bed.

## CONCLUSION

A CFD-DEM solver previously developed for simulating packed-bed combustion was modified and used to investigate the self-sustained smouldering inside a granular bed of wooden pellets, a scenario that is representative of industrial smouldering fires. The main features of the model are as follows:

- The smouldering process is treated in a three-dimensional framework, which allows accounting for its random nature, including localised hotspots.
- The solid phase is described based on a Lagrangian approach instead of the commonly employed volume averaged continuum assumption. This makes the individual treatment of the particle shrinkage possible and consequently, together with the DEM, enables the model to reflect the changing fuel bed structure.
- The solver provides a platform that can be used to test sub-models. Particularly, the inclusion of the DEM solver enables the possibility to include particle-particle and particle-fluid-particle conductive heat transfer.

The comparison of in total six CFD-DEM simulations with experimental data showed that the char conversion rate has a strong impact on the potential to obtain self-sustained smouldering. Too high rates may cause a transition to flaming combustion, while low rates lead to extinguishment once the external heat source is turned off. It has, furthermore, been shown that, in order to model self-sustained smouldering in packed granular fuel beds, it is important to employ a model that can predict localised hotspots. The location of the hotspots in relation to the external boundaries has been identified as an important factor for self-sustained smouldering.

The need to modify some of the assumptions and submodels of the combustion model for flaming combustions with forced convections have been highlighted to employ the model for smouldering combustion. One key difference is the contribution of the conductive heat transfer. Particle-particle and particle-fluid-particle conduction need to be taken into consideration for the simulation of smouldering in a granular fuel bed.

The conducted simulations show that the CFD-DEM model has the potential to describe some important characteristics of smouldering in granular fuel beds, such as localised hotspots and their random nature. However, the model failed to predict the self-sustained smouldering after the heater turned off, as the selection of sub-models and related parameters are challenging, which requires further studies.

## ACKNOWLEDGEMENTS

This study was funded by the Research Council of Norway, project 238329: Emerging Risks from Smoldering Fires (EMRIS), project 294649: Fire Research and Innovation Centre (FRIC), and project 267916: GASPRO. Virginia Rebaque Valdes is gratefully acknowledged for performing the experimental work as part of a master thesis with the Norwegian University of Science and Technology (NTNU).

## REFERENCE

[1] G. Rein, Smouldering combustion phenomena in science and technology, Int. Rev. Chem. Eng. 1 (2009) 3–18.

[2] J. L. Torero, J. I. Gerhard, M. F. Martins, M. A. B. Zanoni, T. L. Rashwan, J. K. Brown, Processes defining smouldering combustion: Integrated review and synthesis, Prog. Energy Combust. Sci. 81 (2020) 100869.

[3] J. L. McAllister, D. J. Carpenter, R. J. Roby, D. Purser, The Importance of Autopsy and Injury Data in the Investigation of Fires, Fire Technol. 50 (2014) 1357–1377.

[4] R. A. Ogle, S. E. Dillon, M. Fecke, Explosion from a smoldering silo fire, Process Saf. Prog. 33 (2014) 94–103.

[5] P. Russo, A. De Rosa, M. Mazzaro, Silo explosion from smoldering combustion: A case study, Can. J. Chem. Eng. 95 (2017) 1721–1729.
[6] D. Botnen, Hallingdal trepellets 5.juli 2010 (in Norwegian), 2010. available at: https://rib.msb.se/Filer/pdf/26258.pdf (accessed 6 June 2021).
[7] G. Rein, Smouldering Fires and Natural Fuels, in: C. Belcher, Fire Phenomena and the Earth System- An interdisciplinary Approach to Fire Science, John Wiley & Sons, Ltd, Chichester, 2013, pp. 15–34.
[8] Y. Hu, N. Fernandez-Anez, T. E. Smith, G. Rein, Review of emissions from smouldering peat fires and their contribution to regional haze episodes, Int. J. Wildland Fire 27 (2018) 293–312.
[9] M. A. Santoso, E. G. Christensen, J. Yang, G. Rein, Review of the Transition From Smouldering to Flaming Combustion in Wildfires, Front. Mech. Eng. 5 (2019) 49.
[10] P. E. Higuera, Taking time to consider the causes and consequences of large wildfires, Proc. Natl. Acad. Sci. USA 112 (2015) 13137–13138.
[11] G. Rein, Smoldering Combustion, in: M. J. Hurley et al., SFPE Handbook of Fire Protection Engineering, 5th edition, Springer, New York, 2016, pp. 581–603.
[12] R. K. Eckhoff, Dust explosions in the process industries: identification, assessment and control of dust hazards, 3rd edition. Gulf professional publishing, USA, 2003.
[13] C. Zaccone, G. Rein, V. D'Orazio, R. M. Hadden, C. M. Belcher, T. M. Miano, Smouldering fire signatures in peat and their implications for palaeoenvironmental reconstructions, Geochim. Cosmochim. Acta 137 (2014) 134–146.
[14] B. W. Benscoter et al., Interactive effects of vegetation, soil moisture and bulk density on depth of burning of thick organic soils, Int. J. Wildland Fire 20 (2011) 418.
[15] X. Huang, G. Rein, H. Chen, Computational smoldering combustion: Predicting the roles of moisture and inert contents in peat wildfires, Proc. Combust. Inst. 35 (2015) 2673–2681.
[16] T. Hasan, J. I. Gerhard, R. Hadden, G. Rein, Self-sustaining smouldering combustion of coal tar for the remediation of contaminated sand: Two-dimensional experiments and computational simulations, Fuel 150 (2015) 288–297.
[17] G. Debenest, V. Mourzenko, J. Thovert, Smouldering in fixed beds of oil shale grains. A three-dimensional microscale numerical model, Combust. Theory Model. 9 (2005) 113–135.
[18] A. A. M. Oliveira M. Kaviany, Nonequilibrium in the transport of heat and reactants in combustion in porous media, Prog. Energy Combust. Sci. 27 (2001) 523–545.
[19] G. Debenest, V. V. Mourzenko, J.-F. Thovert, Smouldering in fixed beds of oil shale grains: governing parameters and global regimes, Combust. Theory Model. 9 (2005) 301–321.
[20] G. Debenest, V. V. Mourzenko, J.-F. Thovert, Three-Dimensional Microscale Numerical Simulation of Smoldering Process in Heterogeneous Porous Media, Combust. Sci. Technol. 180 (2008) 2170–2185.
[21] J. Yang, N. Liu, H. Chen, W. Gao, R. Tu, Effects of atmospheric oxygen on horizontal peat smoldering fires: Experimental and numerical study, Proc. Combust. Inst. 37 (2019) 4063–4071.
[22] N. Fernandez-Anez, K. Christensen, G. Rein, Two-dimensional model of smouldering combustion using multi-layer cellular automaton: The role of ignition location and direction of airflow, Fire Saf. J. 91 (2017) 243–251.
[23] C. Lautenberger, H. Hall, Gpyro – A Generalized Pyrolysis Model for Combustible Solids Users' Guide, University of California, Berkeley, California, USA, 2009.
[24] *COMSOL Multiphysics*®. Stockholm, Sweden: COMSOL AB.
[25] J. Zhang, T. Li, H. Ström, T. Løvås, Grid-independent Eulerian-Lagrangian approaches for simulations of solid fuel particle combustion, Chem. Eng. J. 387 (2020) 123964.
[26] J. Zhang, T. Li, H. Ström, T. Løvås, Computationally efficient coarse-graining XDEM/CFD modeling of fixed-bed combustion of biomass, Combust.Flame (accpted).
[27] R. F. Mikalsen, B. C. Hagen, A. Steen Hansen, U. Krause, V. Frette, Extinguishing smoldering fires in wood pellets with water cooling- an experimental study, Fire Technol. 55 (2019) 57–284.

[28] R. F. Mikalsen, Fighting flameless fires - Initiating and extinguishing self-sustained smoldering fires in wood pellets, PhD thesis, Otto von Guericke University Magdeburg, Magdeburg, Germany, 2018.
[29] R. Sun, H. Xiao, Diffusion-based coarse graining in hybrid continuum–discrete solvers: Theoretical formulation and a priori tests, Int. J. Multiph. Flow 77 (2015) 142–157.
[30] C. Y. Wen, Y. H. Yu, Mechanics of fluidization, Chem. Eng. Prog. Symp. Ser. 62 (1966) 100–111.
[31] P. A. Cundall, O. D. L. Strack, A Discrete Numerical Model for Granular Assemblies, Géotechnique 29 (1979) 47–65.
[32] K. M. Bryden, M. J. Hagge, Modeling the combined impact of moisture and char shrinkage on the pyrolysis of a biomass particle, Fuel 82 (2003) 1633–1644.
[33] H. Ström, H. Thunman, CFD Simulations of Biofuel Bed Conversion: A Submodel for the Drying and Devolatilization of Thermally Thick Wood Particles, Combust. Flame 160 (2013) 417–431.
[34] L. Tognotti, J. P. Longwell, A. F. Sarofim, The products of the high temperature oxidation of a single char particle in an electrodynamic balance, Symp. (int.) Combust. 23 (1991) 1207–1213.
[35] D. D. Evans, H. W. Emmons, Combustion of Wood Charcoal», Fire Saf. J. 1 (1977) 57–66.
[36] H. Thunman, B. Leckner, F. Niklasson, F. Johnsson, Combustion of Wood Particles—a Particle Model for Eulerian Calculations, Combust. Flame 129 (2002) 30–46.
[37] W. E. Ranz, W. R. Marshall, Evaporation from Drops, Chem. Eng. Prog. 48 (1952) 141–146.
[38] G. T. Vickers, D. J. Brown, The Distribution of Projected Area and Perimeter of Convex, Solid Particles, Proc. R. Soc. Lond. A 457 (2001) 283–306.
[39] Z. Y. Zhou, A. B. Yu, P. Zulli, Particle scale study of heat transfer in packed and bubbling fluidized beds, AIChE J. 55 (2009) 868–884.
[40] A. B. Morris, S. Pannala, Z. Ma, C. M. Hrenya, A conductive heat transfer model for particle flows over immersed surfaces, Int. J. Heat Mass Tran. 89 (2015) 1277–1289.
[41] Z. Peng, E. Doroodchi, B. Moghtaderi, Heat transfer modelling in Discrete Element Method (DEM)-based simulations of thermal processes: Theory and model development, Prog. Energy Combust. Sci. 79 (2020) 100847.
[42] *MFiX-DEM*. National Energy Technology Laboratory, aviable at https://mfix.netl.doe.gov/products/mfix/.
[43] A. Anca-Couce, N. Zobel, A. Berger, F. Behrendt, Smouldering of pine wood: Kinetics and reaction heats, Combust. Flame 159 (2012) 1708–1719.
[44] S. Hermansson, H. Thunman, CFD modelling of bed shrinkage and channelling in fixed-bed combustion», Combust. Flame 158 (2011) 988–999.
[45] Z. Y. Zhou, A. B. Yu, P. Zulli, A new computational method for studying heat transfer in fluid bed reactors, Powder Technol. 197 (2010) 102–110.

# Exploratory comparative study of the impact of simplified finite-rate chemistry in LES-EDC simulations of the UMD line burner

**At Thabari J. *, Maragkos G. , Merci, B.**

*[1] Ghent University - UGent, Department of Structural Engineering and Building Materials, Ghent, Belgium.*
**Corresponding author's email: Jeri.Atthabari@UGent.be*

## ABSTRACT

This study focuses on incorporating finite-rate chemistry in turbulent combustion modelling in CFD simulations of the UMD line burner, a scenario considered to be representative of fire-induced flows. In this exploratory research, the use of EDC (finite rate chemistry) is compared with predictions obtained with EDM (infinitely fast chemistry) and validated against experimental data involving first and second order statistics. A sensitivity study of the different reaction mechanisms on different grid sizes reveals a stronger grid dependency and, particularly on coarse grids, higher maximum flame temperatures with the EDC model and finite-rate chemistry. It is also found that the Arrhenius reaction parameters have a significant impact on the numerical predictions, particularly on coarser grids. The consideration of finite-rate chemistry resulted in an increased computational cost, compared to infinitely fast chemistry simulations, by a maximum factor of about 4.

**KEYWORDS:** LES, fast-chemistry, finite-rate chemistry, fire modelling.

## INTRODUCTION

The use of Large Eddy Simulations (LES) along with the Eddy Disspation Model (EDM) [1] or Eddy Dissipation Concept (EDC) [2] is common practice in Computational Fluid Dynamics (CFD) simulations of fire scenarios. Chemical reactions are usually assumed to be infinitely fast with the turbulent combustion reaction rate then only determined by a turbulent mixing time scale (i.e., 'mixed-is-burnt'). While this is an appealing approach, minor species cannot be readily obtained with a high level of accuracy in such simulations. Even though minor species are usually considered unimportant in the context of fire dynamics (e.g., flame spread scenarios), they can play an important role in assessing the toxicity in dedicated spaces, especially in under-ventilated conditions. With the use of finite-rate chemistry, the prediction of minor species is in principle possible. When it comes to incomplete combustion or flame extinction, with the introduction of finite rate chemistry in EDC, these phenomena can be, in principle, better predicted without additional modelling as required with infinitely fast chemistry (i.e., such as the use of a temperature or enthalpy-based flame extinction model [3]). An assessment of the performance of EDM and EDC with infinitely fast chemistry was previously performed in [4] and it was concluded that the EDC performed better in terms of predictive simulations of a turbulent methanol pool fire. Also in [5], numerical predictions with EDC were shown to be in a good agreement with the experimental data while reasonably predicting the radiative fractions as well. The latter is important in the context of fire-related flows. Presently, this study is not yet focusing on capturing extinction or re-ignition phenomena. Rather, the study aims to to assess the inclusion of finite-rate chemistry combined with the EDC combustion model as a first step, before flame extinction is considered in the future.

The main objective is the evaluation of the impact of the EDC/finite-rate chemistry approach in CFD simulations for the UMD line burner [6]. The influence of the reaction mechanism (i.e., 1 and 2-steps), as a function of grid size, is analyzed and compared against predictions obtained with EDM using infinitely fast chemistry. The resulting flame temperatures, flow fields and reaction rates with EDC and EDM are discussed, both in the near and far field of the plume. A simple radiation modelling approach is employed (i.e., constant radiative fraction) in order to decouple radiation from combustion modelling as the former can strongly affect the accuracy of the predicted flame temperatures.

## MODELLING

The CFD code FireFOAM, based on the OpenFOAM v1912 package, is utilized here. The code solves the Navier-Stokes equations, along with transport equations for species mass fractions and sensible enthalpy, assuming a unity Lewis number. The governing equations read [7]:

$$\frac{\partial \bar{\rho}}{\partial t} + \nabla \cdot \left( \bar{\rho} \tilde{u} \right) = 0 \tag{1}$$

$$\frac{\partial \left( \bar{\rho} \tilde{u} \right)}{\partial t} + \nabla \cdot \left( \bar{\rho} \tilde{u} \tilde{u} \right) = -\nabla \bar{p} + \nabla \cdot \left[ \mu_{eff} \left( \nabla \tilde{u} + \left( \nabla \tilde{u} \right)^T - \frac{2}{3} \left( \nabla \cdot \tilde{u} \right) I \right) \right] + \bar{\rho} g \tag{2}$$

$$\frac{\partial \left( \bar{\rho} \tilde{Y}_k \right)}{\partial t} + \nabla \cdot \left( \bar{\rho} \tilde{u} \tilde{Y}_k \right) = \nabla \cdot \left[ \bar{\rho} \left( D_k + \frac{\nu_{sgs}}{Sc_t} \right) \nabla \tilde{Y}_k \right] + \overline{\dot{\omega}_k'''} \, , \left( k = 1, \ldots, N_s - 1 \right) \tag{3}$$

$$\frac{\partial \left( \bar{\rho} \tilde{h}_s \right)}{\partial t} + \nabla \cdot \left( \bar{\rho} \tilde{u} \tilde{h}_s \right) = \frac{\overline{Dp}}{Dt} + \nabla \cdot \left[ \bar{\rho} \left( D_{th} + \frac{\nu_{sgs}}{Pr_t} \right) \nabla \tilde{h}_s \right] - \nabla \cdot \overline{\dot{q}_r''} + \overline{\dot{q}_c'''} \tag{4}$$

where $\bar{\rho}$ is the density (obtained from the ideal gas law), $\tilde{u}$ is the velocity vector, $\bar{p}$ is the pressure, $\mu_{eff} = \mu + \mu_{sgs}$ is the effective dynamic viscosity, $I$ is the identity tensor, $g$ is the gravitational acceleration, $\tilde{Y}_k$ is the species mass fraction, $D_k$ is the species mass diffusivity, $Sc_t$ is the turbulent Schmidt number, $\overline{\dot{\omega}_k'''}$ is the species source term, $\tilde{h}_s$ is the sensible energy, $D_{th}$ is the thermal diffusivity, $Pr_t$ is the turbulent Prandtl number, $\overline{\dot{q}_r''}$ is the radiative heat flux, $\overline{\dot{q}_c'''} = \Delta H_c \overline{\dot{\omega}_k'''}$ is the heat release rate per unit volume due to combustion and $\Delta H_c$ is the heat combustion of the fuel. Finally, $Pr_t = Sc_t$ is considered.

### Turbulence Modelling

The Smagorinsky model [8] is used to model turbulence calculating the sub-grid scale viscosity as:

$$\mu_{sgs} = C_k \Delta \sqrt{k_{sgs}} \tag{5}$$

where the model constant is assigned the value $C_k = 0.05$ [9] and $\Delta = \left( \Delta x \Delta y \Delta z \right)^{\frac{1}{3}}$ is the filter width. The sub-grid kinetic energy, $k_{sgs}$, is calculated considering a local equilibrium as:

$$k_{sgs} = \frac{C_k \Delta^2 \left| \tilde{S} \right|^2}{C_\varepsilon} \tag{6}$$

where $\tilde{S}$ is the resolved strain rate while the sub-grid scale dissipation rate, $\varepsilon_{sgs}$, is modelled as:

$$\varepsilon_{sgs} = C_\varepsilon \frac{k_{sgs}^{\left( \frac{3}{2} \right)}}{\Delta} \tag{7}$$

where $c_\varepsilon = 1.048$ is a model constant [4]. The sub-grid scale thermal diffusivity is calculated as $\alpha_{sgs} = \mu_{sgs} / Pr_t$ with the $Pr_t$ set to 0.5. The sub-grid scale dissipation rate is used in the combution modelling presented below.

**Combustion Model**

Two combustion models, namely EDM [1] and EDC [2] are used to model turbulence-chemistry interactions in this study. The EDM is used together with infinitely fast chemistry, employing a 1-step irreversible chemical reaction for the fuel. On the other hand, a finite rate chemistry scheme is employed for EDC considering both 1-step and 2-step global chemical reactions.

Within EDM, the fuel reaction rate is expressed as:

$$\overline{\dot{\omega}_k'''} = \bar{\rho} \frac{min\left( \tilde{Y}_k, \frac{\tilde{Y}_{O_2}}{s} \right)}{\tau_{EDM}} \tag{8}$$

where $s$ is the stoichiometric oxygen-to-fuel ratio and the mixing time scale, $\tau_{EDM}$, is calculated as:

$$\tau_{EDM} = min\left( \frac{k_{sgs}}{C_{EDM}\varepsilon_{sgs}}, \frac{\Delta^2}{C_{diff}\alpha_{eff}} \right) \tag{9}$$

which considers the mixing under turbulent and laminar flow conditions, respectively. $C_{EDM}$ and $C_{diff}$ are model parameters, both set to 4 [4].

Within EDC, the species source term is calculated as:

$$\overline{\dot{\omega}_k'''} = \bar{\rho} \frac{\gamma^2 \chi}{\tau_{EDC}\left(1-\gamma^2\chi\right)} \left( \tilde{Y}_k - Y_k^* \right) \tag{10}$$

where $\gamma$ is the size of fine structures, $\tau_{EDC}$ is the EDC mixing time scale, $\chi$ is the reacting fraction of the fine structures, while $\tilde{Y}_k$ and $Y_k^*$ are the filtered mass fractions of species $k$ and the mass fractions of that species in the fine structures, respectively. The latter is calculated considering a Perfectly Stirred Reactor (PSR) [10], through equations for enthalpy, pressure and chemical species:

$$\frac{dh}{dt} = 0 \tag{11}$$

$$\frac{dp}{dt} = 0 \tag{12}$$

$$\frac{dY_k^*}{dt} = \frac{\omega_k'''^*}{\rho^*} + \frac{1}{\tau_{EDC}} \left( Y_k^0 - Y_k^* \right) \tag{13}$$

Where $\omega_k'''^*$ is evaluated from a chemical kinetics mechanism (Eq. 16). When finite-rate chemistry is employed, the reacting fraction of the fine structures is generally set to be $\chi = 1$, indicating that the reacting fraction of the fine structures is controlled by chemistry [11].

The size of the fine structures can be expressed as:

$$\gamma = C_\gamma \left( \frac{\nu \varepsilon_{sgs}}{k_{sgs}^2} \right)^{\frac{1}{4}} \tag{14}$$

with the model parameter set to $C_\gamma = 2.1377$ while $\gamma \leq 1$ [5].

The EDC mixing time scale ( $\tau_{EDC}$ ), based on the original energy cascade model, is taken in the order of the Kolmogorov time scale as:

$$\tau_{EDC} = C_\tau \left( \frac{\nu}{\varepsilon_{sgs}} \right)^{\frac{1}{2}} \tag{15}$$

where $C_\tau = 0.4803$ is a model constant [12].

**Chemistry mechanisms**

Four chemistry mechanisms are compared, i.e., two 1-step and two 2-step, in order to analyze the influence of finite-rate chemistry in the numerical predictions. The kinetic parameters as described in Tables 1 and 2 refer to Arrhenius expressions for the PSR calculations in EDC (see above):

$$\omega_k^{'''*} = A T^\beta e^{-Ea/RT} \left[ Fuel \right]^a \left[ Oxidizer \right]^b \tag{16}$$

- 1-step mechanism: $CH_4 + 2O_2 \rightarrow CO_2 + 2H_2O$

**Table 1. Kinetic parameters for 1-step mechanisms**

| PS-mod 1-step [13] | | | | | CERFACS 1-step. [14] | | | | |
|---|---|---|---|---|---|---|---|---|---|
| *A* | *Ea* | *a* | *b* | *β* | *A* | *Ea* | *a* | *b* | *β* |
| 3 x $10^{22}$ | 45000 | 1 | 2 | - | 1.1 x $10^{10}$ | 20000 | 1 | 0.5 | - |

PS-mod is the modified version of original Puri – Seshadri [15]. The 'CERFACS 1-step' mechanism is not 'recommended' in [14], but is included here anyway for comparison purposes.

- 2-step mechanism: (1) $CH_4 + 1.5O_2 \rightarrow CO + 2H_2O$,
  (2) $CO + 0.5O_2 \leftrightarrow CO_2$

**Table 2. Kinetic parameters for 2-step mechanisms**

| | WD 2-step [16] | | | | | CERFACS 2-step [17] | | | | |
|---|---|---|---|---|---|---|---|---|---|---|
| | *A* | *Ea* | *a* | *b* | *β* | *A* | *Ea* | *a* | *b* | *β* |
| (1) | 1.5 x $10^{12}$ | 48400 | 0.3 | 1.3 | 0 | 4.9 x $10^9$ | 35500 | 0.5 | 0.65 | 0 |
| (2) for | 3.98 x $10^{14}$ | 40000 | 1 | 0.2 | 0 | 2 x $10^8$ | 12000 | 1 | 0.5 | 0.8 |
| (2) rev | 5 x $10^8$ | 40000 | 1 | - | 0 | | | | | |

### Radiation Modelling

The radiation modelling approach adopted treats the radiative intensity as a function of spatial location and angular direction. It is acquired by solving the radiative transfer equation (RTE) by the finite volume discrete ordinates model (fvDOM), assuming a non-absorbing optically thin medium. Subsequently, the radiative heat fluxes in the sensible enthalpy equation (Eq.(4)) are calculated as:

$$\nabla \cdot \overline{\dot{q}_r''} = \chi_r \overline{\dot{q}_c'''} \tag{17}$$

where $\chi_r$ is the radiative fraction set to be 0.24 [6]. This simple approach aims at bypassing the uncertainties related to modeling the radiation-turbulence interaction (RTI) as well as minimizing the dependency of the source term of the RTE on the filtered temperature (i.e., $\tilde{T}^4$) that can lead to significant errors in the calculations if coarse grids are employed in the numerical simulations.

## TEST CASE DESCRIPTION

The UMD line burner [6] (Fig. 1) is chosen as a validation test case for the numerical simulations. It is one of the well-documented experiments within the MacFP workshop [18]. Only a case with $CH_4$ as fuel is considered in the present study, in order to avoid any complexities associated with soot modelling. The fuel is injected at a mass flow rate of 1 g/s, resulting in a heat release rate value of 50 kW for an unsuppressed flame. The co-flowing oxidizer is introduced with a mass flow rate of 85 g/s. More details are found in [6] and the well-documented experimental data can be accessed from [18].

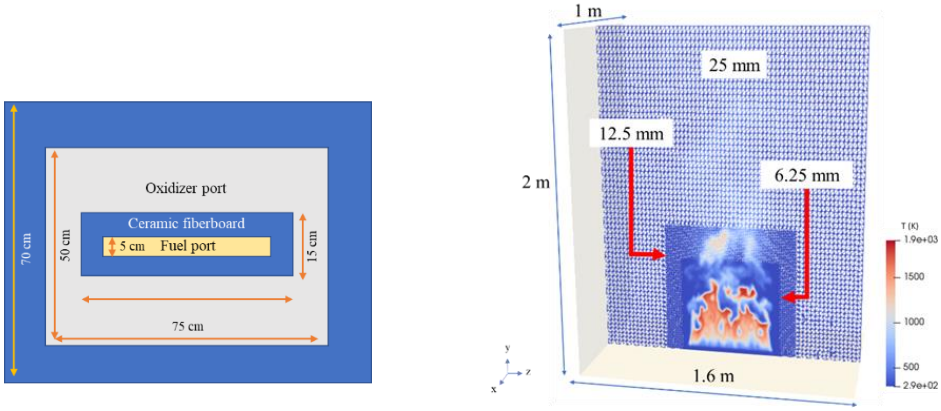


**Fig 1**. Left: Top view of the UMD line burner (adapted from [5]). Right: Computational domain, illustrating the different levels of grid refinement and an instantaneous temperature plot in the vertical mid-plane.

## NUMERICAL SET-UP

The computational domain used in this study is a rectangular box of 1.6 m x 1 m x 2 m (length x width x height), shown in Fig 1. The mesh labeled '25 mm' below is uniform, using 25 mm cubic cells. In order to improve the grid resolution in the flame region, a refinement strategy was implemented in a region around the center of the burner, starting from the floor and up to a height of 0.6 m, which is higher than the flame height as reported in the experiments (i.e., 0.5 m). More specifically, 12.5 mm cells are used in a 0.8 m x 0.8 m x 0.6 m region on the '12.5 mm' mesh, and additionally 6.25 mm cells are used on the '6.25 mm' mesh in a 0.6 m x 0.6 m x 0.4 m region (see Fig 1). The total number of cells is then approximately 739500. A previous numerical study [3] on the same test case has indicated that cell sizes in the order of 5 mm are needed to accurately simulate this scenario. The chosen grid size in our study is of the same order of magnitude. The fuel and co-flowing oxidizer mass flow rates were set equal to the corresponding experimental values. The

ambient temperature and pressure were 293 K and 101325 Pa, respectively. The ceramic fiberboard plate (separating the fuel inlet and co-flow air at y = 0) was treated as an isothermal wall with a no-slip boundary condition for the velocity. For the solution of the RTE, 72 solid angles were used for angular discretization. All simulations were set to run for 35 s (averaged over the last 30 s to produce mean results), with a varying time step, based on a maximum CFL number of 0.9. The equations were advanced in time using a second order backward scheme. The convective terms were discretized with a second order filtered linear scheme while for scalar transport a second order TVD scheme, using a Sweby limiter, was applied. The bottom plane (y = 0), outside the co-flowing air, along with the sides of the computational domain were set to be open allowing for air to be entrained inside the domain.

## RESULTS

The mean and rms centerline and radial (i.e., at height $y = 0.25$ m) temperature profiles are presented in Fig. 2 for the different combustion models on three different meshes.

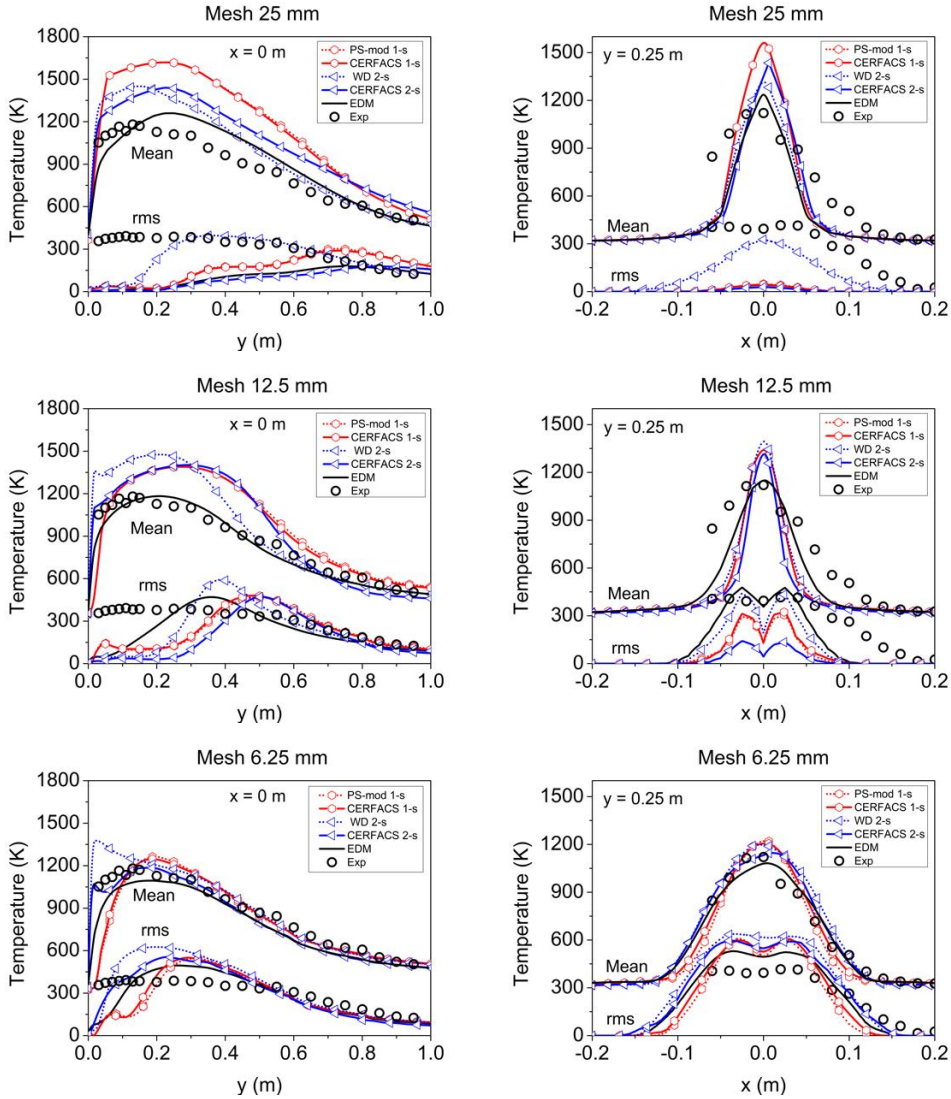


**Fig 2.** Left: Mean and rms centerline temperatures. Right: Mean and rms radial temperatures at y = 0.25 m.

Overall, the EDM approach with infinitely fast chemistry performs better than EDC with finite-rate chemistry on coarse grids. The EDM predictions follow the experimental profiles fairly well and remain within 8% of the experimental data close to the fuel source on the finest grid size. Compared to EDC, the EDM approach with infinitely fast chemistry is significantly less grid sensitive. In the EDC simulations , the centerline mean temperature is over-predicted on the coarse grids (25 mm and 12.5 mm). The use of coarser grid sizes tends to dissipate turbulence and results in a flame with laminar-like structure (as confirmed in the significant differences in rms values on the different meshes), causing the fuel to react fast with oxidizer and producing high temperatures, as reported in [5]. At the finest grid (6.25 mm), EDM still outperforms most of the EDCs except, CERFACS 2-s which has the best agreement to the experimental data. This leads to the idea that the kinetic parameters strongly affect the EDC results with the 2-step mechanisms, specifically in the flame region where the scalar dissipation rate is believed to be high [19]. The width of the mean radial temperature profiles, at height of 0.25 m above the burner, is reasonably well captured by the numerical simulations on the finest grid size (6.25 mm). This is the case for both EDM and EDC with different chemical mechanisms. Overall, the numerical predictions of CERFACS 2-s and EDM agree better with the experimental data than the other EDC mechanisms, in terms of maximum flame temperature and profile width. Overall, different maximum temperatures are predicted for each chemistry mechanism. In addition, the maximum temperatures occur further downstream, compared to the experiments, indicating lack of turbulence near the burner (i.e., see also the lower rms values above the burner in Figure 2). The implemented static turbulence model might also be the cause for these lower rms values. An overview of the numerical predictions is presented in Table 3.

**Table 3**. Maximum mean flame temperature and its recorded position on the 6.25 mm grid size.

| Model | Position (m) | Temperature (K) |
|---|---|---|
| Experiment | 0.130 | 1180 |
| PS – mod 1-s | 0.194 | 1263 |
| CERFACS 1-s | 0.188 | 1247 |
| WD 2-s | 0.019 | 1365 |
| CERFACS 2-s | 0.181 | 1185 |
| EDM | 0.181 | 1094 |

As previously mentioned, the differences between the centerline temperature predictions obtained with the two 2-step mechanisms (Figure 2) are striking and are attributed to be the effect of the Arrhenius parameters. Compared to CERFACS 2-s, the WD has a higher pre-exponential factor (see Table 2), hence, results in a higher reaction rate as well. A previous study [19] has indicated that the region along the centerline, up to 0.05 m, is the region where the scalar dissipation rate is the highest, which also results in higher mixing rates and faster chemical reactions to occur.

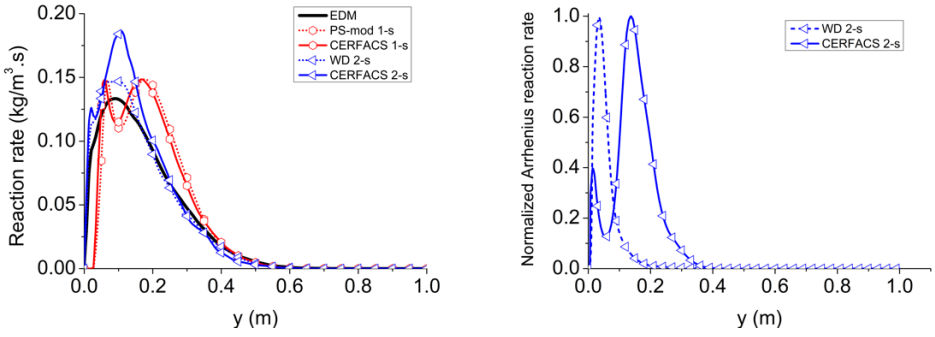


**Fig 3.** Left: Calculated reaction rates from the simulations. Right: Normalized reaction rates (by their maximum value) from the Arrhenius expression (Eq. 13). Results presented on the 6.25 mm mesh.

In order to illustrate this, the predicted reaction rates from the numerical simulations are presented in Fig 3. This is only done for the 2-step mechanisms, because the differences between the 1-step EDC results in Fig. 2 are very small (suggesting that inclusion of finite-rate chemistry is less influential for 1-step EDC for temperature predictions). The reaction rate on the left figure is acquired by dividing the heat release rate (HRR) per unit volume ( $\overline{\dot{q}_c'''}$ ) from the simulations with the heat of combustion ( $\Delta H_c$ ). In case of the 1-step mechanisms, the reaction rates represent the fuel ($CH_4$) consumption rate ( $\overline{\dot{\omega}_F'''}$ ). It is observed that the maximum reaction rate of EDM is lower compared to all EDCs. This is in line with the lower mean temperatures predicted by EDM, compared to EDCs. However, in the case of 2-step reaction mechanisms, $\overline{\dot{\omega}_F'''}$ depends on both reactions. Therefore, the result shown on Fig 3.-Left cannot explicitly explain the temperature differences observed very close to the burner with the 2-step mechanisms in Fig. 2. For this reason, the fuel reaction rates from the Arrhenius expression (Eq. 16), normalized by their maximum value, are presented in Fig 3.-Right. The profiles of the normalized reaction rate values on Fig 3. have a very close resemblance to the temperature profile of the two EDC 2-step models. The WD normalized reaction rate reaches its maximum value very close to the burner, which correlates to the steep temperature increase for the model as seen in Fig. 2. Also the CERFACS 2-s experiences a fluctuation that has a very similar profile as its temperature. An in-depth analysis of the enthalpy changes from the chemical reactions and of the spatial variation of the species mass fractions would help to further explain the temperature differences observed in Fig. 2 and will be considered in the future.

The predicted mean centerline axial velocities and the radial profiles of the mean axial velocities at height 25 cm above th burner are presented in Fig. 4 for the different combustion models on the three different meshes. Overall, a decrease in the predicted axial velocities with decreasing grid size is observed due to the fire becoming increasingly more turbulent. The predictions with EDM and EDCs are comparable for the finest grid size (6.25 mm) but significantly differ on the coarser grids (12.5 mm, 25 mm). It is observed that the WD on the finest grid size has a higher axial velocity close to the burner as a result of its higher temperature. This further strengthens the idea that the kinetic parameters can affect the development of the flow field, and as such the mixing and the evolution of SDR.

One drawback when it comes to the use of EDC with finite rate is the increased computational cost compared to EDM with infinitely fast chemistry. When finite rate chemistry was taken into account, the computational cost increased by 18.5% for 1-step and by up to 409% for 2-steps (for the finest grid of 6.25 mm) compared to EDM. The implementation of more detailed chemistry alongside the TDAC [20] method is deemed promising in order to reduce the computational time of simulations with multiple steps and will be explored in the future.

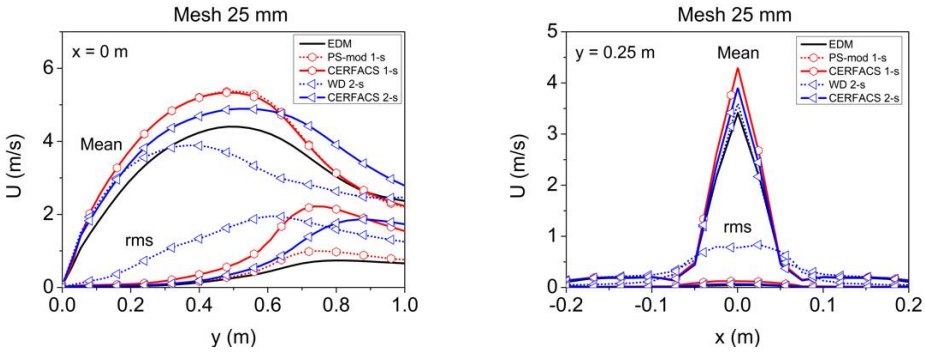

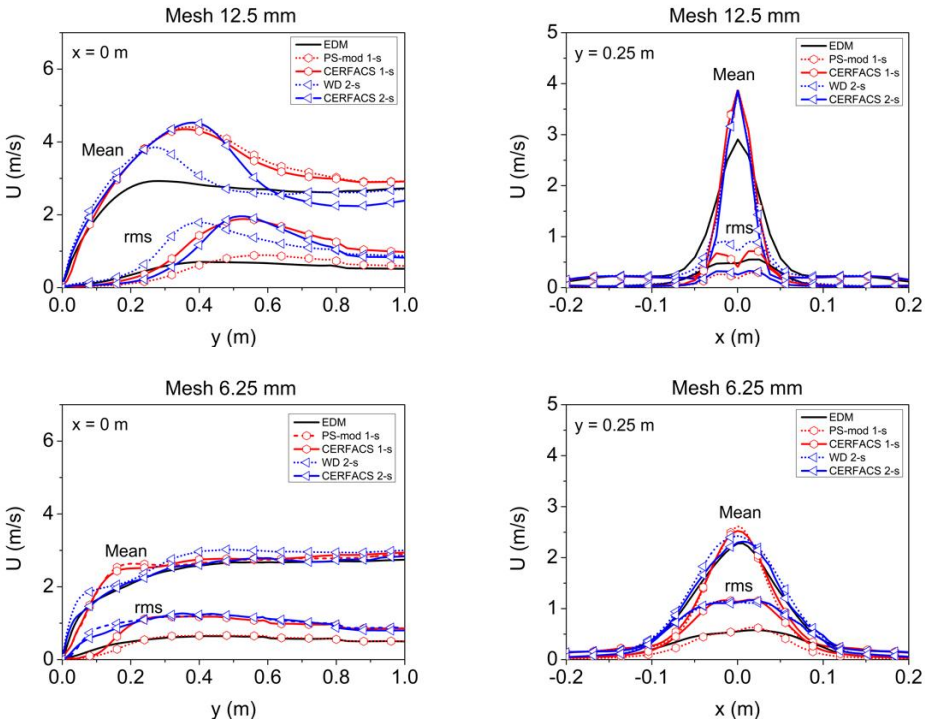


**Fig 4.** Left: Mean and rms centerline axial velocity. Right: Mean and rms axial velocity at height y = 0.25 m.

## CONCLUSION

Large eddy simulations of a buoyant turbulent line burner, focusing on combustion modelling with EDC and finite rate chemistry, were presented. Focus was given on the influence of the employed chemical reaction mechanism and the results were compared against experimental data and with results obtained with EDM with infinitely fast chemistry. In total, four reaction mechanisms were considered with EDC: two 1-step and two 2-step mechanisms. In general, the predictions with EDC and finite rate chemistry were more grid sensitive compared to EDM at all the different grid sizes considered.

In general, the simulations with EDC predicted higher temperatures, compared to the EDM, regardless of the reaction mechanism used. The EDC, combined with the CERFACS 2-step mechanism for finite-rate chemistry, revealed the best agreement on the finest mesh. However, when it comes to 2-step mechanisms, the EDC were strongly affected by the kinetic parameters. The significant differences in temperature evolutions have been explained through the evolutions of the reaction rates. As the simulated test case is a buoyant driven flame, these kinetic parameters also influenced the flow field given its correlation with the temperature. Lastly, the computational cost was increased up to four times when the 2-step reaction mechanisms were employed. A further assessment of the use of more complex reaction mechanisms and computational load improvements is considered as next step.

## ACKNOWLEDGEMENT

This research is funded by The Research Foundation – Flanders (FWO – Vlaanderen) through project G023221N.

## REFERENCES

[1] B. F. Magnussen, B. H. Hjertager, On mathematical modeling of turbulent combustion with special emphasis on soot formation and combustion, Symposium (international) on Combustion (1977) 719-29.

[2] B. F. Magnussen, The eddy dissipation concept: A bridge between science and technology, ECCOMAS thematic conference on computational combustion (2005) 24.

[3] J. P. White, S. Vilfayeau, A. W. Marshall, A. Trouvé, R. J. McDermott, Modeling flame extinction and reignition in large eddy simulations with fast chemistry, Fire Safety Journal 90 (2017) 72-85.

[4] G. Maragkos, T. Beji, B. Merci, Advances in modelling in CFD simulations of turbulent gaseous pool fires, Combustion and Flame 181 (2017) 22-38.

[5] G. Maragkos, B. Merci, Large eddy simulations of flame extinction in a turbulent line burner, Fire Safety Journal 105 (2019) 216-26.

[6] J. P. White, E. D. Link, A. C. Trouvé, P. B. Sunderland, A. W. Marshall, J. A. Sheffel, M. L. Corn, M. B. Colket, M. Chaos, H. Z. Yu, Radiative emissions measurements from a buoyant, turbulent line flame under oxidizer-dilution quenching conditions, Fire Safety Journal 76 (2015) 74-84.

[7] G. Maragkos, B. Merci, On the use of dynamic turbulence modelling in fire applications, Combustion and Flame 216 (2020) 9-23.

[8] J. Smagorinsky, General circulation experiments with the primitive equations: I. The basic experiment, Monthly Weather Review 91 (1963) 99-164.

[9] S. Menon, P. K. Yeung, W. W. Kim, Effect of subgrid models on the computed interscale energy transfer in isotropic turbulence, Computers & Fluids 25 (1996) 165-80.

[10] M. Bösenhofer, E.-M. Wartha, C. Jordan, M. Harasek, The Eddy Dissipation Concept—Analysis of Different Fine Structure Treatments for Classical Combustion, Energies 11 (2018) 1902.

[11] A. Shiehnejadhesar, R. Mehrabian, R. Scharler, G. M. Goldin, I. Obernberger, Development of a gas phase combustion model suitable for low and high turbulence conditions, Fuel 126 (2014) 177-87.

[12] A. Parente, M. R. Malik, F. Contino, A. Cuoci, B. B. Dally, Extension of the Eddy Dissipation Concept for turbulence/chemistry interactions to MILD combustion, Fuel 163 (2016) 98-111.

[13] P. Bitala, M. Kozubková, P. Kadeřábek, V. Nevrlý, J. Dlabka, E. Kozubek, O. Štěpánek, M. Bojko, P. Kubát, Z. Zelinger, Experimental investigations and numerical simulations of methane cup-burner flame, EPJ Web of Conferences 45 (2013) 01067.

[14] CERFACS. "Methane/Air Combustion." https://www.cerfacs.fr/cantera/mechanisms/meth.php, (accessed 30 December 2021).

[15] I. K. Puri, K. Seshadri, Extinction of diffusion flames burning diluted methane and diluted propane in diluted air, Combustion and Flame 65 (1986) 137-50.

[16] C. K. Westbrook, F. L. Dryer, Simplified reaction mechanisms for the oxidation of hydrocarbon fuels in flames, Combustion science and technology 27 (1981) 31-43.

[17] B. Franzelli, E. Riber, L. Y. M. Gicquel, T. Poinsot, Large Eddy Simulation of combustion instabilities in a lean partially premixed swirled flame, Combustion and Flame 159 (2012) 621-37.

[18] MaCFP. https://github.com/MaCFP, (accessed 29 December 2021).

[19] B. Kruljevic, I. Stankovic, B. Merci, Large eddy simulations of the UMD line burner with the conditional moment closure method, Fire Safety Journal 116 (2020) 103206.

[20] F. Contino, H. Jeanmart, T. Lucchini, G. D'Errico, Coupling of in situ adaptive tabulation and dynamic adaptive chemistry: An effective method for solving combustion in engine simulations, Proceedings of the Combustion Institute 33 (2011) 3057-64.

# Gas and Dust Explosions

# Study of Simplified Models and Influencing Parameters of the Minimum Ignition Energy of Dust Clouds

**Chen T.[1,*], Berghmans J.[2], Degrève J.[3], Verplaetsen F.[3,4], Van Caneghem J.[5], Vanierschot M. [1]**

*[1] KU Leuven, Department of Mechanical Engineering, Group T Leuven Campus, Leuven, Belgium.*
*[2] KU Leuven, Department of Mechanical Engineering, Leuven, Belgium.*
*[3] KU Leuven, Department of Chemical Engineering, Leuven, Belgium.*
*[4] Adinex NV, Herentals, Belgium.*
*[5] KU Leuven, Department of Materials Engineering, Group T Leuven Campus, Leuven, Belgium.*
**Corresponding author's email: tengfei.chen@kuleuven.be & chentf19946@163.com*

## ABSTRACT

In this study, simplified models for the prediction of the minimum ignition energy (MIE) of dust clouds based on the ignition of a single dust particle are studied. The MIE results from the simplified models are compared with the obtained data from a more complex model which considers propagation of ignition within multiple particles in the dust cloud. Comparison between these models verifies the feasibility of using the MIE of only a single particle at the ignition center as a prediction of the dust cloud MIE. A parametric study is then performed using the simplified single central particle model, which shows that most dust cloud and spark parameters have rather simple power function relationships with the MIE results, except for the ambient, the spark and the dust cloud minimum ignition temperature (MIT), whose influence on the dust cloud MIE is too complex to be analytically expressed. Nevertheless, piecewise function approximations for the influence of the three temperatures on the MIE are derived, and based on these functions simple MIE calculation equations are established as an alternative for the numerical solution of the simplified single central particle model.

**KEYWORDS:** Minimum ignition energy, dust cloud, single particle, theoretical modelling.

## NOMENCLATURE

| | |
|---|---|
| $Cp$ | constant pressure specific heat (J/(kg·K)) |
| $d_p$ | particle diameter (m) |
| $E_0$ | initial spark energy (J) |
| $f$ | undetermined function |
| $h$ | heat transfer coefficient (W/(m$^2$·K)) |
| $k$ | thermal conductivity (W/(m·K)) |
| $L$ | cylindrical spark length (m) |
| $MIE$ | minimum ignition energy (J) |
| $MIT$ | minimum ignition temperature (K) |
| $Nu$ | Nusselt number |
| $r$ | radial coordinate (m) |
| $S$ | particle surface area (m$^2$) |
| $T$ | temperature (K) |
| $T_{spark}$ | spark temperature (K) |
| $t$ | time (s) |
| $V$ | particle volume (m$^3$) |

**Greek**

| | |
|---|---|
| $\alpha$ | thermal diffusivity (m$^2$/s) |
| $\delta(t)$ | the Dirac delta function in time (1/s) |
| $\delta(\vec{r})$ | the Dirac delta function in space (1/m$^2$ in cylindrical coordinates and 1/m$^3$ in spherical coordinates) |
| $\theta$ | specific temperature difference ratio |
| $\rho$ | density (kg/m$^3$) |

**Subscripts**

| | |
|---|---|
| $cyli$ | under cylindrical coordinates with the cylindrical spark |
| $g$ | gas |
| $i$ | initial/ambient |
| $ig$ | ignition |
| $One$ | Model One |

| | |
|---|---|
| *Three* | Model Three |
| *s* | particle/solid |
| *sphe* | under spherical coordinates with the spherical spark |
| max | maximum |

## INTRODUCTION

The minimum ignition energy ( *MIE* ) of a dust cloud is a measure of the spark ignition sensitivity of the cloud. Therefore, accurate prediction of this parameter is crucial to the explosion risk control of related industrial processes. The earliest attempt of the theoretical prediction of the dust cloud *MIE* can be dated back to Kalkert & Schecker [1]. They derived an equation for a single dust particle *MIE* located in the center of a spherical spark based on gas-particle heat transfer. This *MIE* was taken as a prediction of the dust cloud *MIE* . However, this model rather arbitrarily assumes that the criterion for the successful ignition of a dust particle is to reach a particle temperature of 1000 °C regardless of the particle type, and does not take the influence of the spark temperature into consideration. Hosseinzadeh et al. [2] further developed the Kalkert & Schecker model [1], solving the same governing equations but with a new assumption for the ignition of a dust particle: the particle is ignited when its temperature reaches the dust cloud minimum ignition temperature ( *MIT* ). Hosseinzadeh et al. [2] also limited the spark temperature to 2000 K. However, the resulted predictive equation for the dust cloud *MIE* by Hosseinzadeh et al. [2] was non-analytical because it contained imaginary parts. Moreover, both the Kalkert & Schecker model [1] and the Hosseinzadeh et al. model [2] adopted the single dust particle *MIE* to predict the dust cloud *MIE* .

Chen et al. [3] developed a model for the dust cloud *MIE* calculation considering not just the ignition of a single dust particle, but including the particle to particle propagation of ignition in a dust cloud. The self-sustaining character of the particle ignition propagation is used as the criterion for the successful ignition of the dust cloud. With this model the influence of the dust concentration and the dust material heat of combustion on the *MIE* can also be studied which is not possible with [1] and [2]. Moreover, in this model both the spherical spark and the cylindrical spark were studied (the cylindrical spark having a shape closer to that of the electric arc used in the *MIE* testing experiment), and the model can be extended directly for the *MIE* calculation of dust mixtures. However, the Chen et al. model [3] is more complex so it does not result in a single *MIE* prediction formula as in the previous two models. Chen et al. [3] discussed the influence of particle diameter and dust concentration on the dust cloud *MIE* , but did not provide an analysis of the influence of other important parameters such as particle and gas densities and specific heats, spark temperature, and the cylindrical spark length.

In this study simplified models based on the Chen et al. model [3] will be studied to explore the feasibility of using the *MIE* of a single particle at the spark center to predict the *MIE* of a whole dust cloud. In addition, more thorough analysis of the *MIE* influencing parameters will be provided. Inspired by the Kalkert & Schecker model [1] and the Hosseinzadeh et al. model [2], this work will also attempt to derive more accurate simple *MIE* prediction equations.

## METHODOLOGY

In this section, different physical models for the dust cloud ignition processes and their governing equations will be introduced and compared. The models are mainly based on previous models developed in [1], [2] and [3].

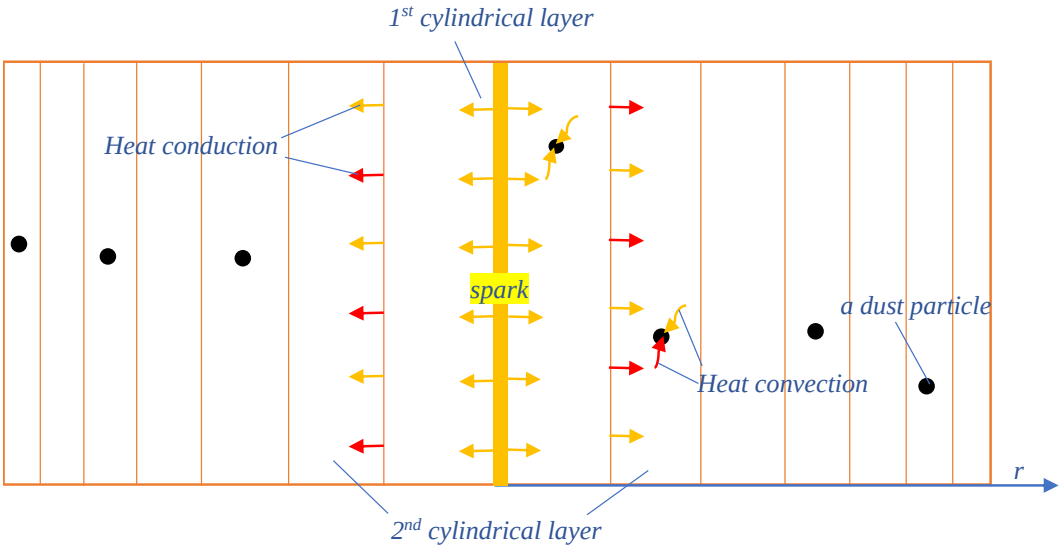


(a)

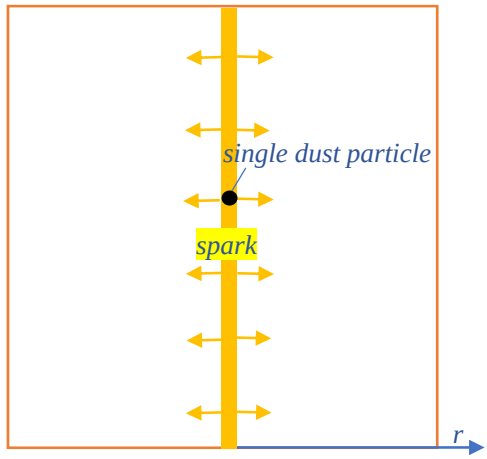


(b)

**Fig. 1.** Physical models. (a) Model One: complex physical model from Chen et al. [3]) and Model Two: the same physical model but considering only ignition of the particle nearest to the spark center; (b) Model Three: further simplified model with only a single particle at the spark center.

## Physical models

The following physical models for the dust cloud ignition processes are considered in this study:

(1) The complex physical model from Chen et al. [3] (called Model One) as illustrated in Fig. 1(a) considers the particle to particle ignition propagation process. The *MIE* calculated with this model is the minimum spark energy to sustain the spontaneous propagation of particle ignition from particle to particle throughout the dust cloud.

(2) A simplification (called Model Two) of this complex physical model considers only the ignition of the particle nearest to the spark center in Fig. 1(a). The *MIE* calculated with this model is the minimum spark energy to ignite this nearest particle, but not necessarily the outer particles in the dust cloud, so it is expected to give rather conservative *MIE* results compared with Model One.

(3) A further simplification (called Model Three) of the complex model is shown in Fig. 1(b) where only a single particle's presence at the spark center is considered like in the Kalkert & Schecker [1] and Hosseinzadeh et al. [2] models. In Model Two, multiple particles in the dust cloud are still included as in Model One, so although only the ignition of the nearest particle to the ignition center is considered, heat transfer between the gas and the outer particles still affects the *MIE* results, which means the outer particles only act as heat sinks. However in Model Three, only a single central particle is included in the physical model and the influence of all the other particles is completely neglected. The *MIE* calculated with Model Three will be the minimum energy to ignite only this single particle at the spark center, which is an even more conservative prediction of the dust cloud *MIE* than with Model Two.

It must be noted that the particle nearest to the spark center in Fig. 1(a) is not put exactly at the center in Model One and Model Two [3] mainly because of a possible blast effect at the moment of the spark releasing [2], so it is likely that no particle is present exactly at the spark center during the ignition process. In Model One and Model Two, the space around the spark is divided into cylindrical or spherical layers, each containing a single particle. The dust particles distribution is assumed to be uniform, thus the divided layers also has the same volume. Each particle is assumed to be located at the middle radius position of the corresponding layer. Therefore, in Fig. 1(a) the nearest particle to the spark center is at the position of half the radius of the first cylindrical layer. With this assumption, the position of the particles in this model depends on both the particle properties and the dust concentration. Usually the distance between the nearest particle and the spark center is within the range of 1 $\mu$m ~1 mm . Higher dust concentrations result in the nearest particle closer to the spark center and lower dust concentrations result in the opposite, which is also to be expected in reality. Further details regarding the particle arrangements in Model One and Model Two and the position of the nearest particle can be found in [3]. Moreover, Fig. 1 only illustrates the physical model with a cylindrical spark, the corresponding model for a spherical spark can be derived with the same approach. Other basic assumptions for the dust particles can be found in [3].

**Governing equations**

The governing equations for Model One and Model Two are consistent with [3]. For Model Two, since only the ignition of the particle nearest to the spark center is considered, it is no longer required to include the heat of combustion in its governing equations. On the other hand, for Model Three with only a single particle in the spark center, the *MIE* depends only on the temperature profile of this particle. For the spherical spark, the governing equations for this model are already given in [2], and the governing equations for a cylindrical spark can be derived similarly. The temperature distributions in the gas phase with an initial spark energy of $E_0$ are as follows [4]:

cylindrical spark (in cylindrical coordinates):

$$\rho_g Cp_g \frac{\partial T_g(r,t)}{\partial t} = \frac{1}{r}\frac{\partial}{\partial r}(k_g r \frac{\partial T_g(r,t)}{\partial r}) + \frac{E_0}{L}\delta(t)\delta(\vec{r}), \tag{1a}$$

spherical spark (in spherical coordinates):

$$\rho_g Cp_g \frac{\partial T_g(r,t)}{\partial t} = \frac{1}{r^2}\frac{\partial}{\partial r}(k_g r^2 \frac{\partial T_g(r,t)}{\partial r}) + E_0\delta(t)\delta(\vec{r}), \tag{1b}$$

with initial condition: $T_g(r,0) = T_i$,

and boundary conditions: $T_g(\infty,t) = T_i$ and $\frac{\partial T_g(0,t)}{\partial r} = 0$.

With only a single central particle, the analytical solution to Eqs. (1a) and (1b) can be simplified into the following forms considering only the gas temperature evolution at the spark center [2][3][5]:

$$T_g(0,t) = T_i + \frac{E_0}{4\pi\alpha_g t \rho_g Cp_g L} \ , \tag{2a}$$

$$T_g(0,t) = T_i + \frac{E_0}{(4\pi\alpha_g t)^{1.5} \rho_g Cp_g} \ , \tag{2b}$$

where $\alpha_g = \frac{k_g}{\rho_g Cp_g}$.

In order to avoid an infinite spark temperature [2][3], the initial time of the heat transfer between the gas and the central particle is not set at $t = 0$ but at $t = t_i$ when the central gas temperature drops to an assumed spark temperature $T_{spark}$, which is set as 3300 K in the air according to [6]. The central particle temperature is then governed by [7]:

$$\rho_s Cp_s \frac{\partial T_s(0,t)}{\partial t} = \frac{h_s S}{V}(T_g(0,t) - T_s(0,t)) \ , \tag{3}$$

With initial condition: $T_s(0,t_i) = T_i$,

where $h_s = \frac{Nuk_g}{d_p}$, $S = 4\pi(\frac{d_p}{2})^2$, $V = \frac{4}{3}\pi(\frac{d_p}{2})^3$.

Combining Eqs. (2a) and (2b) with Eq. (3) results in the following equations for the central particle temperature evolution:

$$\rho_s Cp_s \frac{\partial T_s(0,t)}{\partial t} = \frac{6Nuk_g}{d_p^{\,2}}(T_i + \frac{E_0}{4\pi\alpha_g t \rho_g Cp_g L} - T_s(0,t)) \, , \tag{4a}$$

$$\rho_s Cp_s \frac{\partial T_s(0,t)}{\partial t} = \frac{6Nuk_g}{d_p^{\,2}}(T_i + \frac{E_0}{(4\pi\alpha_g t)^{1.5} \rho_g Cp_g} - T_s(0,t)) \, . \tag{4b}$$

Unfortunately, with the complex form of the gas temperature profile Eqs. (4a) and (4b) can not be solved analytically. Hosseinzadeh et al. [2] attempted to solve Eq. (4b) directly with $T_{spark}$ assumed to be 2000 K, but resulted in a non-analytical solution of $T_s(0,t)$ with imaginary parts. Nevertheless, these two equations are no longer space dependent so they are still much simpler compared with the governing equations for Model One and Model Two, and the numerical algorithm used in Chen et al. [3] becomes unnecessary. Therefore in this study, Eqs. (4a) and (4b) are solved directly with the ode45 solver in MATLAB [8] to find the maximum central particle temperature $T_{s,\max}$ and the time when this temperature is reached. If the maximum particle temperature $T_{s,\max}$ equals the $MIT$, the assumed spark energy $E_0$ is regarded as the $MIE$. The time at which this occurs is the ignition time $t_{ig}$.

## RESULTS AND DISCUSSION

In this section, the *MIE* results calculated with Model One, Two and Three will be compared to discuss the feasibility of using the single particle *MIE* as the prediction of the dust cloud *MIE*; then the influencing patterns of the dust cloud and spark parameters on the *MIE* will be discussed by means of a parametric study.

**Comparison between the single particle and the dust cloud *MIE* results**

Figure 2 compares the *MIE* results calculated with Model One, Model Two and Model Three for the same 38 dust samples as used in [3]. The 38 dust samples include both metal dusts (magnesium, Aluminum, Zirconium and Titanium) and organic dusts (PE-HD, Corn starch, Wood, Niacin and Lycopodium), with $d_p$ within 10 ~ 163 $\mu$m, $\rho_s$ within 940 ~ 7000 kg·m$^{-3}$, $Cp_s$ within 278 ~ 2390 J·(kg. K)$^{-1}$, heat of combustion of the dust material within 15302 ~ 42704 kJ·kg$^{-1}$, and the *MIT* within 503 ~ 1023 K. The figure clearly shows that the calculated *MIE* values with the three models have very similar variation trends. Model One and Model Two generate almost identical *MIE* values as shown in Fig. 2. Since Model Two is a direct simplification of Model One by only considering the ignition of the particle nearest to the spark center, Fig. 2 also implies that the ignition of the particle closest to the spark center requires the highest marginal spark energy input. Once this particle is ignited, the dust cloud is likely to also be ignited with rather trivial extra spark energy requirement: for the studied 38 dust samples, generally less than 5% of extra spark energy is required to ignite the dust cloud once the particle nearest to the spark center is ignited. This confirms the feasibility of using only the *MIE* of the particle nearest to the spark center as a prediction of the *MIE* of the dust cloud. On the other hand, compared with Model Two, Model Three generates more conservative *MIE* values: with the cylindrical spark, the Model Three *MIE* values are on average 88.5% of the Model One *MIE* values, and for the spherical spark this proportion even decreases to 68.2%. This deviation is due to the difference in particle position as shown in Fig. 1: in Model Three the single particle is placed exactly at the spark center, while in Model One and Model Two there is some distance between the spark center and the nearest particle. This distance is relatively larger for spherical coordinates with the particle arrangement approach in [3], which is why the deviation is also bigger for the spherical spark under spherical coordinates. Therefore, it can also be concluded that the exact position of the particle nearest to the spark center has a much stronger influence on the *MIE* values than the ignited particle number considered. Nevertheless, Model Three can still serve as a decent alternative for Model One with a proportional correction: $MIE_{cyli,One} \approx 1.13 MIE_{cyli,Three}$ and $MIE_{sphe,One} \approx 1.47 MIE_{sphe,Three}$. Also it must be noted that in practice at the moment of spark ignition, the exact particle positions are actually unknown, in this sense Model Three is perhaps the safest *MIE* prediction model as it gives the most conservative *MIE* results.

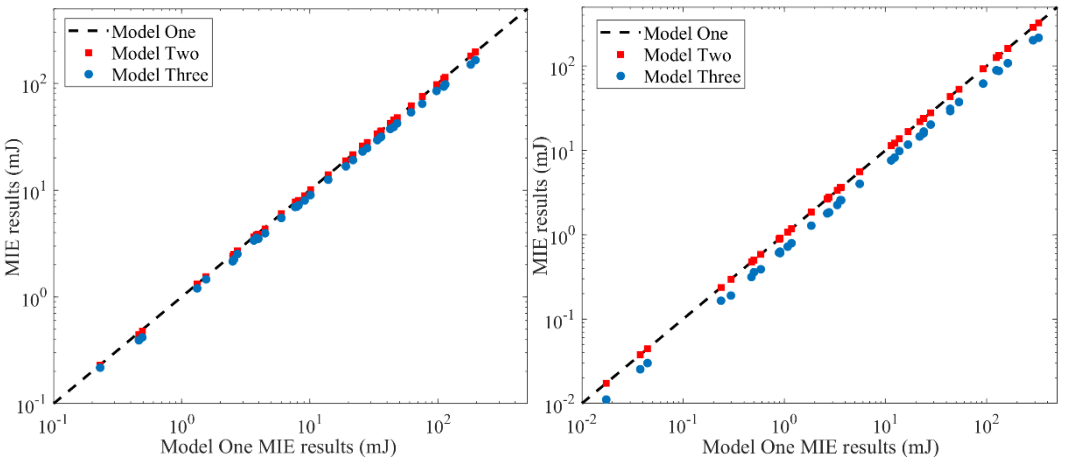


**Fig. 2.** Comparison of *MIE* results calculated with Model One, Model Two and Model Three (a) cylindrical spark; (b) spherical spark.

**Simple *MIE* calculation equations derivation**

The above comparison verifies the usage of the single central particle *MIE* values obtained with Model Three as alternatives of the dust cloud *MIE* values obtained with Model One and Model Two. However, for all these three models the *MIE* results can only be solved numerically. Numerical approaches not only require more sophisticated calculation tools, but also make it complicated to identify the influencing patterns of the parameters involved. Therefore, this study attempts to find simple equations that can give a rather precise prediction of the Model Three *MIE* results.

When $E_0 = MIE$, at the time of the central particle ignition $t_{ig}$, the particle temperature reaches $T_{s,\max} = MIT$, which also implies that at this moment the gas temperature also has to be the *MIT*, otherwise $E_0$ is either not enough to raise $T_{s,\max}$ to the *MIT* resulting in ignition failure, or higher than the *MIE* and can increase $T_s$ to an unnecessary high value. Therefore, Eqs. (2a) and (2b) lead to the following equalities:

$$MIE_{cyli} = 4\pi\alpha_g t_{ig} \rho_g Cp_g L(MIT - T_i), \tag{5a}$$

$$MIE_{sphe} = (4\pi\alpha_g t_{ig})^{1.5} \rho_g Cp_g (MIT - T_i). \tag{5b}$$

In the above Eqs. (5a) and (5b) the only unknown parameter on the right hand side is $t_{ig}$ whose analytical form is unavailable. However, by assuming $T_g(0,t) - T_s(0,t)$ as a constant of $\frac{MIT - T_i}{A}$ ( $A$ is assumed as an unknown dimensionless constant) Eq. (3) will become

$$\frac{\partial T_s(0,t)}{\partial t} = \frac{6Nuk_g}{A\rho_s Cp_s d_p{}^2}(MIT - T_i), \tag{6}$$

Solving Eq. (6) at $t = t_{ig}$ results in

$$t_{ig} = \frac{A\rho_s Cp_s d_p{}^2}{6Nuk_g} + t_i. \tag{7}$$

Comparing with $t_{ig}$, $t_i$ is expected to be very small, therefore by replacing $t_{ig}$ with $\frac{A\rho_s Cp_s d_p{}^2}{6Nuk_g}$, Eqs. (5a) and (5b) turn into

$$MIE_{cyli} = 4\pi\alpha_g \frac{A\rho_s Cp_s}{6Nuk_g} \rho_g Cp_g L(MIT - T_i) d_p{}^2, \tag{8a}$$

$$MIE_{sphe} = (4\pi\alpha_g \frac{A\rho_s Cp_s}{6Nuk_g})^{1.5} \rho_g Cp_g (MIT - T_i) d_p{}^3. \tag{8b}$$

If $MIT - T_i = 1000K$, $A = \ln(2)$ and $Nu = 2$, then Eq. (8b) becomes exactly the *MIE* prediction equation derived by Kalkert and Schecker [1]. However, the problem is that $A$ is unlikely to be constant but complexly related to the three temperatures $T_i$, *MIT* and $T_{spark}$. Clearly, here it is not the absolute temperatures but the temperature differences $MIT - T_i$ and $T_{spark} - MIT$ that really affect the *MIE* variation, and the *MIE* is also expected to increase as $MIT - T_i$ increases or $T_{spark} - MIT$ decreases. Therefore, it can be assumed that $A$ is actually a function of $\theta$ which is the

specific temperature difference ratio of $\frac{MIT - T_i}{T_{spark} - MIT}$. Moreover, this relationship is also likely to be different for $MIE_{cyli}$ and $MIE_{sphe}$:

$$MIE_{cyli} = \frac{4\pi\rho_s Cp_s L(MIT - T_i)d_p^{\,2}}{6Nu} f_{cyli}(\theta) \ , \tag{9a}$$

$$MIE_{sphe} = \frac{(4\pi)^{1.5}(\rho_s Cp_s)^{1.5}(MIT - T_i)d_p^{\,3}}{(6Nu)^{1.5}(\rho_g Cp_g)^{0.5}} f_{sphe}(\theta) \ . \tag{9b}$$

Whether Eqs. (9a) and (9b) are decent alternatives for the numerical *MIE* solver of Model Three requires verification with a parametric study between the numerical *MIE* values and all parameters involved in Eqs. (9a) and (9b). Moreover, mathematical expressions of the $f$ functions are needed to make Eqs. (9a) and (9b) solvable in practice.

**Influence of the dust cloud and spark parameters on the *MIE***

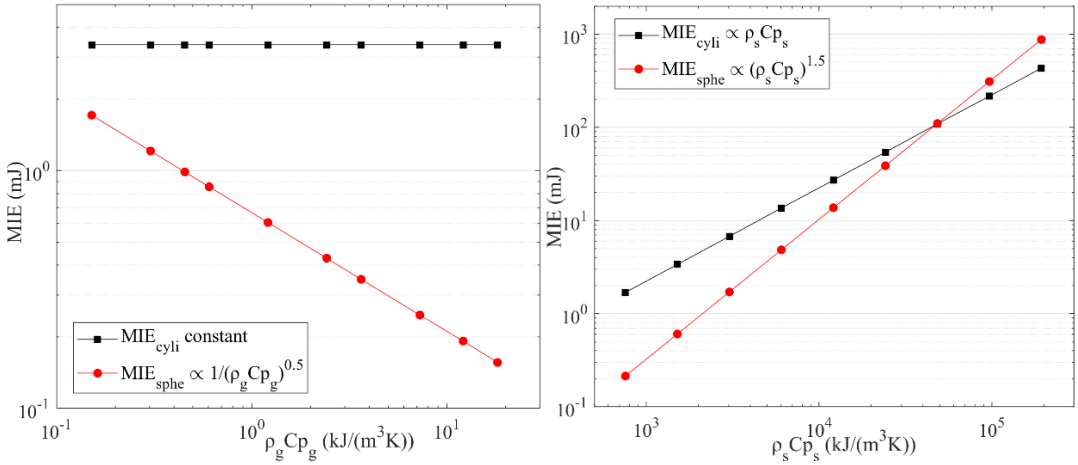

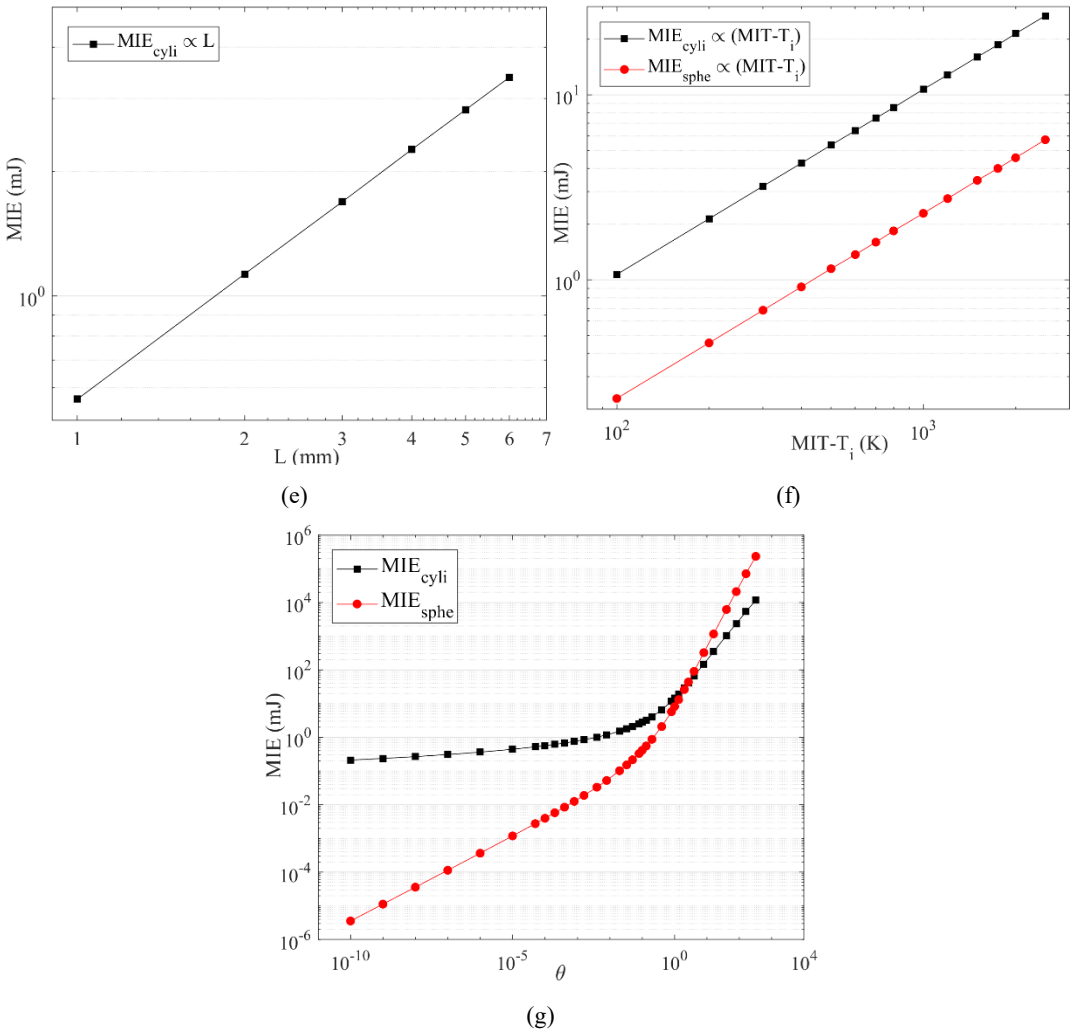


**Fig. 3.** Parametric study of the influence of (a) gas volumetric specific heat $\rho_g Cp_g$, (b) particle volumetric specific heat $\rho_s Cp_s$, (c) Nusselt number $Nu$, (d) particle diameter $d_p$, (e) cylindrical spark length $L$, (f) temperature difference $MIT - T_i$ and (g) temperature difference ratio $\theta$ on the Calculated *MIE* results with Model Three (base material lycopodium).

Figure 3 shows a parametric study of the influence of the particle and spark parameters on the $MIE$ results with Model Three to verify Eqs. (9a) and (9b). The influencing factors involved are gas volumetric specific heat $\rho_g Cp_g$, particle volumetric specific heat $\rho_s Cp_s$, Nusselt number $Nu$, particle diameter $d_p$, cylindrical spark length $L$, temperature difference $MIT - T_i$ and temperature difference ratio $\theta$. Each of these factors is studied independently with all the other factors kept constant and with the same base material lycopodium. The resulted influencing patterns in Fig. 3 fit accurately with the derived relationships in Eqs. (9a) and (9b) where all parameters except for $\theta$ have simple power function relationships with the $MIE$ results, while the influence of $\theta$ is clearly more complicated.

To further verify that $f_{cyli}$ and $f_{sphe}$ are indeed functions of $\theta$ and have universal forms for different dust materials, $f_{cyli}$ and $f_{sphe}$ are calculated for another two different base materials: magnesium and

zirconium, and the results are compared with base material lycopodium in Fig. 4. This figure clearly reveals that $f_{cyli}$ and $f_{sphe}$ are very consistent for all these three base materials and are indeed universal functions of only $\theta$. However, while Eqs. (9a) and (9b) require mathematical forms of $f_{cyli}(\theta)$ and $f_{sphe}(\theta)$ to be operational in practice, the analytical solutions of $f_{cyli}(\theta)$ and $f_{sphe}(\theta)$ are not available, so the numerical data of $f_{cyli}(\theta)$ and $f_{sphe}(\theta)$ are analyzed for $\theta$ between $10^{-200}$ and 300. Analysis of the numerical data shows that the asymptotes of $f_{cyli}(\theta)$ and $f_{sphe}(\theta)$ when $\theta$ approaches 0 are $f_{cyli}(\theta) = -(\ln\theta)^{-1}$ and $f_{sphe}(\theta) = e^{-1}\sqrt{\theta}$, with deviations from the numerical data below 10% for $\theta < 10^{-5}$; however, for $\theta$ above $10^{-5}$, these equations are not accurate anymore: for $10^{-5} \le \theta < 0.05$, the corrections of the above asymptotes ( $f_{cyli}(\theta) = -1.41(\ln\theta)^{-1} - 0.0341$, $f_{sphe}(\theta) = e^{-1}\sqrt{\theta} + e^{-0.921}\theta$ ) can still generate rather accurate predictions of $f_{cyli}(\theta)$ and $f_{sphe}(\theta)$. However, for $0.05 \le \theta \le 1$, $f_{cyli}(\theta)$ becomes linear and $f_{sphe}(\theta)$ becomes quadratic polynomial. Finally for $1 < \theta \le 300$, both $f_{cyli}(\theta)$ and $f_{sphe}(\theta)$ fit better with simple power functions. Summarizing the above analysis, the following Eqs. (10a) and (10b) are piecewise function approximations of $f_{cyli}(\theta)$ and $f_{sphe}(\theta)$:

$$f_{cyli}(\theta) \approx \begin{cases} -(\ln\theta)^{-1} & \theta < 10^{-5} \\ -1.41(\ln\theta)^{-1} - 0.0341 & 10^{-5} \le \theta < 0.05 \\ 2.76\theta + 0.315 & 0.05 \le \theta \le 1 \\ e^{1.06}\theta^{1.17} & 1 < \theta \le 300 \end{cases}, \tag{10a}$$

$$f_{sphe}(\theta) \approx \begin{cases} e^{-1}\sqrt{\theta} & \theta < 10^{-5} \\ e^{-1}\sqrt{\theta} + e^{0.921}\theta & 10^{-5} \le \theta < 0.05 \\ 0.0484 + 3.08\theta + 4.97\theta^2 & 0.05 \le \theta \le 1 \\ e^{2.05}\theta^{1.79} & 1 < \theta \le 300 \end{cases}. \tag{10b}$$

Calculated results with Eqs. (10a) and (10b) are also compared with the numerically calculated $f_{cyli}(\theta)$ and $f_{sphe}(\theta)$ data as shown in Fig. 4, and the deviations between them are below 10% for $\theta \le 300$. Therefore, with the combination of Eq. (9) and Eq. (10), the *MIE* with Model Three can be predicted simply without the requirement of numerical calculations. It should also be noted that in standard ambient air conditions, $T_{spark}$ is usually 3300 K [6] and $T_i$ is approximately 300 K, and the experimental *MIT* results of the 38 dust samples studied generally lie between 500 ~ 1100 K, which means that under most conditions in practice, $\theta$ ranges between 0.07 and 0.5. According to Eqs. (10a) and (10b), within this range $f_{cyli}(\theta)$ has a simple linear expression of $f_{cyli}(\theta) \approx 2.76\theta + 0.315$, and $f_{sphe}(\theta)$ can be expressed polynomially with the equation of $f_{sphe}(\theta) \approx 0.0484 + 3.08\theta + 4.97\theta^2$, thus for usually encountered dust clouds with a $\theta$ in the range of $0.05 \le \theta \le 1$, their *MIE* values can be predicted with the following equations:

$$MIE_{cyli} = \frac{4\pi\rho_s Cp_s L(MIT - T_i){d_p}^2(2.76\theta + 0.315)}{6Nu}, \tag{11a}$$

$$MIE_{sphe} = \frac{(4\pi)^{1.5}(\rho_s Cp_s)^{1.5}(MIT - T_i){d_p}^3(0.0484 + 3.08\theta + 4.97\theta^2)}{(6Nu)^{1.5}(\rho_g Cp_g)^{0.5}}. \tag{11b}$$

It must be admitted that the parametric study performed here is under very ideal conditions and it assumes that all the studied parameters influence the *MIE* independently and stay constant during

the ignition process. According to Eq. (9a), $\rho_g Cp_g$ does not have any influence on the $MIE_{cyli}$ results of Model Three, which is a direct result of Eq. (2a) where $\alpha_g$ eliminates $\rho_g Cp_g$, while in Eq. (2b) the $\alpha_g^{1.5}$ results in $MIE_{sphe} \propto 1/(\rho_g Cp_g)^{0.5}$. It is understandable that $\rho_g Cp_g$ has a complex relationship with the $MIE$: on the one hand, increasing $\rho_g Cp_g$ obstructs the gas temperature rise which is a disadvantage for the gas-particle heat transfer, while on the other hand, this also increases the heat storage ability of the gas which favors the particle temperature rise. It is possible that the $\rho_g Cp_g$ increase boosts the gas heat storage ability more significantly for the three dimensional gaseous heat conduction under spherical coordinates comparing with the two dimensional gaseous heat conduction under cylindrical coordinates, which is why with Model Three $MIE_{sphe}$ drops when $\rho_g Cp_g$ rises but $MIE_{cyli}$ does not change. However, in reality, heat conduction in space is always in three dimensions. Moreover, it must be noted that $T_{spark}$ is also likely to be related to $\rho_g Cp_g$, so the assumption of parameter independence is also questionable. Another very ideal assumption in the models is that for dust particles, phase change and devolatilization are neglected during the ignition process, while in reality metal dust particles can melt and organic dust particles will devolatilize, so the real particle ignition processes are much more complex. One possible argument for this assumption is that the ignition time $t_{ig}$ of spark ignition is usually within a short time scale of 1 ~ 100 ms[2], during which it is likely that the dust particles do not experience significant state and property change before ignited. However, this argument also awaits further verification. Therefore, to what extent will the simplified model stays representative is still to be tested in practice.

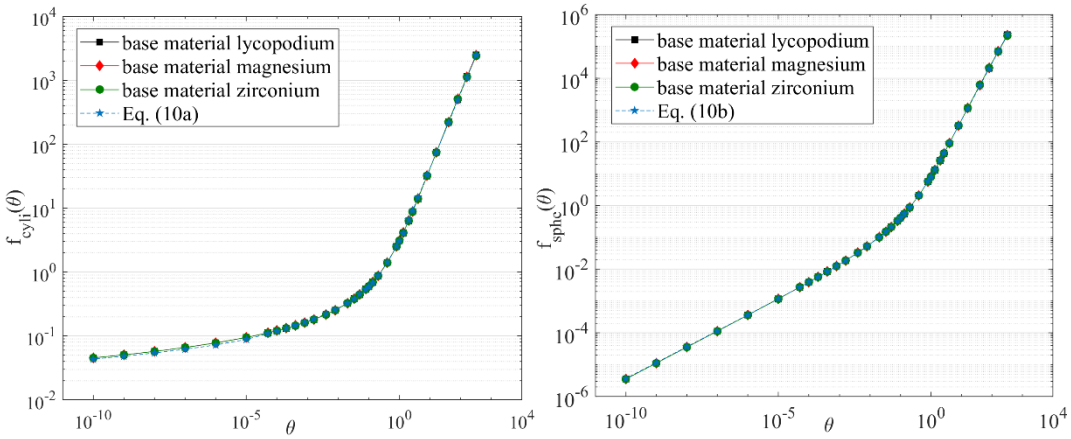


**Fig. 4.** Functions $f_{cyli}(\theta)$ and $f_{sphe}(\theta)$ calculated numerically for three base materials lycopodium, magnesium and zirconium comparing with the predictions with Eqs. (10a) and (10b).

## CONCLUSIONS

In this study, the numerical model developed by Chen et al. [3] (Model One) for dust cloud *MIE* calculation was further simplified into Model Two, considering only the ignition of the particle nearest to the spark center and Model Three, which considers only a single particle at the spark center. *MIE* results with these three models were compared; then a parametric study was presented for Model Three and simple *MIE* prediction equations were also derived based on the governing equations of Model Three. The following conclusions can be drawn:

(1) Comparison of the *MIE* results from the three models for 38 dust samples shows that the ignition of the particle nearest to the spark center is the most important threshold for the dust cloud ignition; the position of this particle has a stronger influence on the dust cloud *MIE* than the

ignited particle number. Therefore, it is feasible to use the $MIE$ of a single particle at the spark center as the prediction of the $MIE$ of a dust cloud.

(2) A parametric study of the influencing patterns of gas volumetric specific heat $\rho_g Cp_g$, particle volumetric specific heat $\rho_s Cp_s$, Nusselt number $Nu$, particle diameter $d_p$, cylindrical spark length $L$, temperature difference $MIT - T_i$ and temperature difference ratio $\theta$ on the Model Three $MIE$ results reveals that for all these factors except $\theta$, their relationships with the $MIE$ results are simple power function relationships, while for $\theta$ the relationship is too complex to be expressed analytically, which also implies the complex influence of the three temperatures $T_i$, $MIT$ and $T_{spark}$ on the $MIE$.

(3) Simple $MIE$ calculation equations derived from the governing equations of Model Three are clearly verified by a parametric study: all the relationships between the studied parameters and the numerical $MIE$ results are predicted by these two equations; the assumed function $f$ in these equations is indeed only a function of $\theta$. Although analytical forms of the $f_{cyli}(\theta)$ and $f_{sphe}(\theta)$ functions are not available, simple piecewise function approximations of $f_{cyli}(\theta)$ and $f_{sphe}(\theta)$ are derived with deviations below 10% from the numerical data. A combination of the simple $MIE$ prediction equations and the piecewise function approximations $f_{cyli}(\theta)$ and $f_{sphe}(\theta)$ allows the prediction of the $MIE$ of dust clouds without the requirement of numerical calculations.

## ACKNOWLEDEGMENTS

The authors gratefully acknowledge the financial contribution from China Scholarship Council (No. 201806030181).

## REFERENCES

[1] H.G. Kalkert, N. Schecker, Theoretische Überlegungen zum Einfluß derTeilchengröße auf die Mindestzündenergie von Stäuben, Chem. Ing. Tech. 51(12) (1979) 1248–1249.

[2] S. Hosseinzadeh, J. Berghmans, J. Degrève, F. Verplaetsen, A model for the minimum ignition energy of dust clouds, Process Saf. Environ. Protect. 121 (2019) 43–49.

[3] T. Chen, J. Berghmans, J. Degrève, F. Verplaetsen, J. Van Caneghem, M. Vanierschot, A theoretical model for the prediction of the minimum ignition energy of dust clouds, J. Loss Prev. Process. Ind. 73 (2021) 104594.

[4] J. Taler, P. Duba, Approximate analytical methods for solving transient heat conduction problems, in: Solving Direct and Inverse Heat Conduction Problems, Springer Berlin Heidelberg, Berlin, Heidelberg, 2006, pp: 587-604.

[5] A. Mills, Heat Transfer, CRS Press, Boston, 1992.

[6] Y.M. Zhang, Q.M. Liu, Experimental study of transient response of spark discharge ignition temperature, High. Volt. Eng., 41 (2) (2015) 547-553.

[7] L.P. Yarin, G. Hetsroni, Dynamics of a Single Particle. In: Combustion of Two-Phase Reactive Media, Springer Berlin Heidelberg, Berlin, Heidelberg, 2004.

[8] MATLAB ode45. https://www.mathworks.com/help/matlab/ref/ode45.html, (accessed 18th December 2020).

# Vented dust explosions: comparing experiments, simulations and standards

**Huang C.[1,*], Bloching M. [2], Lipatnikov A. N.[3]**

*[1] RISE Research Institutes of Sweden, Division Safety and Transport, Safety Research Department, Gothenburg, Sweden*
*[2]IND EX® - Intercontinental Association of Experts for Industrial Explosion Protection e.V. Friedrich-Ebert-Anlage 36, 60325 Frankfurt am Main, Germany*
*[3]Chalmers University of Technology, Department of Mechanics and Maritime Sciences, Gothenburg, Sweden.*
**Corresponding author's email: chen.huang@ri.se*

## ABSTRACT

A vented corn starch dust explosion in an 11.5 $m^3$ vessel is studied by comparing experiments, simulations and the standards. The reduced explosion overpressure inside the vessel is recorded using two pressure sensors installed on the inner wall of the vessel. 3D Unsteady Reynolds-Averaged Navier-Stokes simulations of the experiment are performed using the Flame Speed Closure (FSC) model and its extended version. The FSC model predicts the influence of turbulence on premixed combustion, and the extended version allows for self-acceleration of a large-scale flame kernel, which is associated with the combustion-induced thermal expansion effect. Such an extension is highly relevant to large-scale industrial application. The explosion overpressure-time trace computed using the extended FSC model agrees reasonably well with the experimental data. Furthermore, the effect of vent size and ignition location on the explosion overpressure is studied by comparing the simulation results and the standards. The developed numerical tool and model is especially useful for scenarios, which are not addressed in the standards, and it deserves further study in simulations of other large-scales dust or gaseous explosions together with comparison with experiments.

**KEYWORDS:** Simulations, experiments, standards, vent size, ignition position, corn starch, vented dust explosions, Computational Fluid Dynamics, turbulent combustion, flame self-acceleration, open source, OpenFOAM.

## INTRODUCTION

Dust explosion is a constant threat to the physical working environment of industries worldwide, especially among countries and regions with high industrial output, which deal with combustible powders. Examples of representative industries are woodworking, metal processing, food and feed, pharmaceuticals and additive industries. This complicated process involves ignition of very fine combustible particles well mixed with air in a confined equipment, followed by a violent and explosive combustion. Once dust explosion occurs, the generated high-pressure waves, hot flames and flying fragments can cause loss of lives and huge economic consequences associated with destroy of process plants and stop in the productions.

Dust explosion risk is commonly mitigated by following regulations, e.g., using appropriate equipment, housekeeping, safety routine and so on. In the research field, experimental testing is a dominant method. At the same time, numerical simulations have become more and more requested due to high cost associated with large-scale experiments and limited application conditions in the standards.

A dust explosion is a more difficult process to model as compared to that of a gas explosion. First, there is limited knowledge on the fundamental burning properties of dust, e.g., laminar burning velocities. Furthermore, unlike gas, the laminar burning velocities of dust depend not only on dust concentration, but also on dust particle size distribution and the moisture content. In such a challenging situation, Computational Fluid Dynamics (CFD) research into dust explosion were still carried out by different research groups [1-4].

This paper presents a part of results obtained in a project aiming at developing physics-based models and an efficient numerical tool for simulating dust explosions. The current approach assumes that a dust explosion resembles that of a premixed turbulent gaseous flame. Such an assumption is reasonable for fine organic dust particles with high volatile content because the flame propagation is determined by the gas phase reactions not by the devolatilization process [5-7]. Furthermore, such an assumption is commonly adopted in CFD simulations of dust explosions [8]. In a previous study [9], a well-validated premixed turbulent combustion model Flame Speed Closure (FSC) model [10,11] was implemented into the OpenFOAM code. The code including the model was validated against corn starch dust explosion experimental data obtained using a small-scale fan-stirred vessel [6]. The current paper aims (i) to compare simulation results with data measured by investigating large-scale industrial dust explosions and (ii) to demonstrate the practical usages of the numerical tool in a parametric study performed by varying either vent size or ignition location.

In the following section, the experimental method and setup are briefly described. Then, the numerical method and setup are reported, followed by results and conclusions.

## EXPERIMENTAL METHOD AND SETUP

An 11.5 m³ vessel at the REMBE® Research + Technology Center in Brilon, Germany was used to perform the vented corn starch dust explosions. The corn starch was characterized by a $K_{St}$-value of 220 bar·m/s ± 15 %, a median diameter $D_{50}$ of 97 µm and a moisture content of 9.87%. The calculated and applied vent area was set to $A_v$= 0.5 m² in a circular shape. The vent opening was closed with a layer of 70 µm low mass aluminium foil with a static activation pressure ($p_{stat}$) of 0.1 ± 15 %.

To create an explosive atmosphere inside the vessel two pressurized dust containers were used for blowing the dust into the test vessel. A dust concentration of 750 g/m³ was chosen. An ignition delay of 800 ms was selected via multiple tests in order to achieve the required $K_{St}$-value with the above dust concentration.

The resulting explosive atmosphere was ignited using a pair of pyro-technique igniters with a total ignition energy of 10 kJ in the center of the test vessel. Two pressure detectors P1 and P2 were installed to measure the reduced maximum explosion overpressures ($p_{red}$) inside the vessel (see Fig. 1). The data was recorded using an oscilloscope (Tektronix TDS 2014C). A snapshot of the vented corn starch dust explosion is shown in Fig. 2.

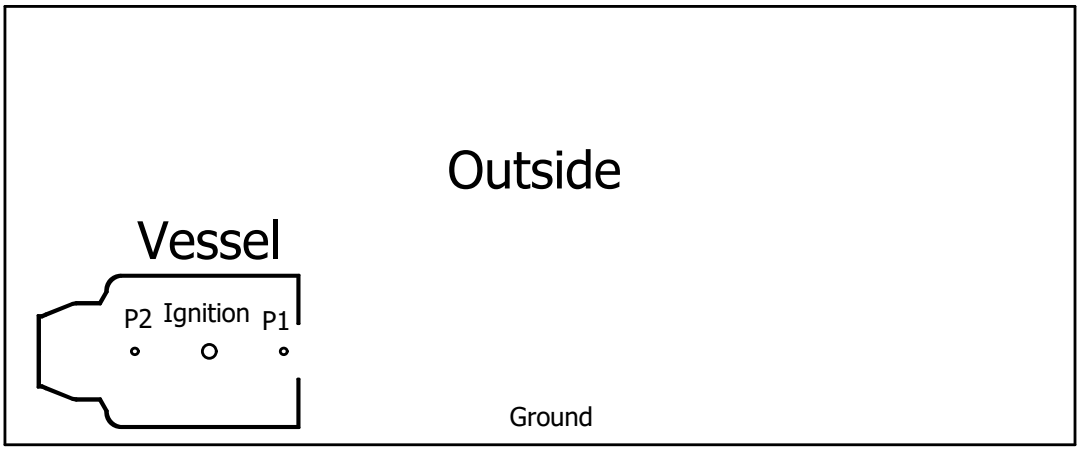


**Fig. 1.** Illustration of the 11.5 m³ explosion vessel and the computational domain.

**Fig. 2.** A snapshot of the vented corn starch dust explosion in the 11.5 m³ vessel with a circular vent opening.

## NUMERICAL METHOD AND SETUP

In this section, the used combustion model, the input data for the simulation, and the numerical method are briefly discussed.

**FSC turbulent combustion model**

The FSC model [10,11] deals with the following transport equation

$$\frac{\partial \bar{\rho}\tilde{c}}{\partial t} + \nabla \cdot (\bar{\rho}\tilde{\mathbf{u}}\tilde{c}) = \nabla \cdot [\bar{\rho}(\kappa + D_t)\nabla\tilde{c}] + \rho_u U_t |\nabla\tilde{c}| + \frac{\bar{\rho}(1-\tilde{c})}{t_r(1+D_t/\kappa_b)} \exp\left(-\frac{\Theta}{\tilde{T}}\right), \quad (1)$$

for the Favre-averaged combustion progress variable $\tilde{c}$. Here, $t$ is the time; $\mathbf{u}$ is the flow velocity vector; $\kappa$ is the molecular heat diffusivity of the mixture; the Favre-averaged temperature $\tilde{T}$ is evaluated using the simplest form $\bar{\rho}\tilde{T} = \rho_u T_u$ of the ideal gas state equation; $\Theta$ is the activation temperature for a single reaction that the combustion chemistry is reduced to ($\Theta = 20000$ K in the present work); over-lines designate the Reynolds average, while $\tilde{q} = \overline{\rho q}/\bar{\rho}$ is the Favre-averaged value of $q$ with $q'' = q - \tilde{q}$; subscripts $u$ and $b$ designate unburned and burned gas, respectively; $t_r$ is the reaction time scale, which is calculated according to Ref. [12].

The turbulent diffusivity $D_t$ and burning velocity $U_t$ are closed as follows [10,11]

$$D_t = D_{t,\infty}\left[1 - \exp\left(-\frac{t_{fd}}{\tau_L}\right)\right], \quad (2)$$

$$U_t = U_{t,ISP} \underbrace{\left[1 - \frac{\tau_L}{t_{fd}} + \frac{\tau_L}{t_{fd}} \exp\left(-\frac{t_{fd}}{\tau_L}\right)\right]}_{T_1}^{1/2} \underbrace{\left(\frac{t}{t_{flacc}}\right)^{1/2}}_{T_2}, \quad (3)$$

where $t_{fd}$ is the flame development time counted starting from ignition; $D_{t,\infty}$ is the fully developed turbulent diffusivity given by a turbulence model; $\tau_L = D_{t,\infty}/u'^2$ is the Lagrangian time scale of turbulence; term $T_1$ belongs to the original FSC model [10]; term $T_2$ is based on a study by Gostintsev et al. [13] who discovered a self-similar regime of flame kernel growth by analysing large-scale gaseous flames; $t_{flacc}$ is the timing for activating the flame acceleration mechanism in simulations. Due to the lack of a model or empirical formula, which could be adopted to evaluate the onset of the self-similar regime, $t_{flacc}$ requires tuning. In this work, $t_{flacc}$ is chosen for a time instance, which corresponds to a flame position characterized by $\bar{c} = 0.5$ at a distance of 1.85 m away from the vent opening.

$$U_{t,ISP} = Au'Da^{1/4}, \quad (4)$$

is an intermediately steady turbulent burning velocity [14]; $Da = \tau_t/\tau_f$ is the Damköhler number; $\tau_t = L/u'$ and $L$ are turbulent time and length scales, respectively; $\tau_f = \delta_L/S_L$ and $\delta_L = \kappa_u/S_L$ are the laminar flame time scale and thickness, respectively; $A$=0.4 is the sole constant of the FSC model. The interested reader is referred to references [10,11,15,16] for detailed information.

**Thermophysical properties of corn starch dust**

Thermophysical properties are required to calculate the combustion and heat transfer process in the dust explosion simulation. They include the chemical formula, heat of reaction, standard heat of formation, specific heat capacity, and adiabatic flame temperature. The chemical formula of $C_6H_{7.88}O_{4.98}$ and the heat of reaction $\Delta H_{reaction}$=-2 521 kJ/mol for corn starch are taken from a paper by Bradley et al. [6], whereas the specific heat capacity is taken from the work by Tan et al. [17]. Accordingly, the absolute enthalpy $H_a$ [J/kg] is evaluated using the following NIST-JANAF polynomial equation

$$H_{a,cs} = R_{spec,cs}\left(\frac{a_{4,cs}}{5}T^5 + \frac{a_{3,cs}}{4}T^4 + \frac{a_{2,cs}}{3}T^3 + \frac{a_{1,cs}}{2}T^2 + a_{0,cs}T + a_{5,cs}\right). \quad (5)$$

Here, $R_{spec,cs}$ is the specific gas constant for corn starch measured in J/(kg·K); $a_{0,cs}$, $a_{1,cs}$, $a_{2,cs}$, $a_{3,cs}$, $a_{4,cs}$ and $a_{5,cs}$ are the JANAF coefficients of corn starch. A summary of the thermophysical properties of corn starch dust is shown in Table 1.

**Table 1. Summary of thermophysical properties of corn starch dust.**

| Name | Symbol | Value |
|---|---|---|
| Chemical formular | $C_6H_{7.88}O_{4.98}$ | - |
| Molecular weight | $W_{cs}$ | 0.16 kg/mol |
| Standard heat of formation | $H^{\Theta}_{f,cs}$ | -792.6 kJ/mol |
| JANAF coefficients | $a_{0,cs}$ | -3.2726 |
| | $a_{1,cs}$ | 0.10056 |
| | $a_{2,cs}, a_{3,cs}, a_{4,cs}$ | 0 |
| | $a_{5,cs}$ | -9 9808 |

**The laminar burning velocity of corn starch dust**

Contrary to gaseous flames, available data on the laminar burning velocities for corn starch dust is limited and controversial. In the present study, the laminar burning velocity $S_L$ measured by Dahoe et al. [18] is used, and the data is fitted using Gülder's correlation [19] (see Fig. 3) as follows

$$S_L = W\phi^{\eta}e^{-\xi(\phi-\sigma)^2}. \quad (6)$$

Here, the coefficients $W = 0.2145$, $\eta = -0.2774$, $\xi = 39.1832$, $\sigma = 0.6$ for corn starch dust. Note that the corrected equivalence ratio includes only the dust which participated in the explosion. The dust concentration is converted to a corrected equivalence ratio using data on burnt mass fraction reported by Skjold et al. [1, 20].

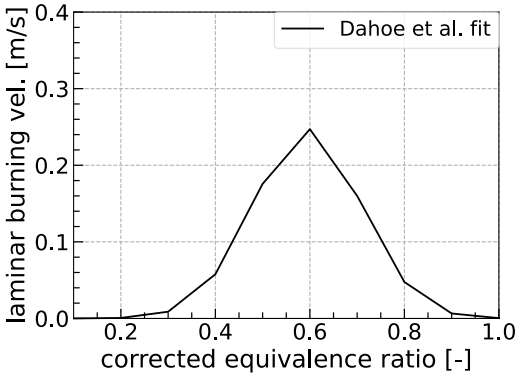


**Fig. 3.** Laminar burning velocity measured by Dahoe et al. [18], and fitted using Gülder's correlation versus corrected equivalence ratio.

**Numerical setup**

The vented corn starch dust explosion was simulated in two stages. First, the dust explosion was simulated in a closed vessel. When the computed overpressure in the vessel reached a critical value of 0.1 bar (recall that, in the experiments, the vent panel ruptured at a static activation pressure $p_{stat}$ equal to 0.1 bar ± 15%), the simulation was stopped, and the results were saved. These computed results were then mapped to a new computational mesh created for a larger computational domain to simulate the venting process. The computational mesh covering the closed vessel (see the vessel part in Fig. 1) has a mesh number of 1.4 million and a mesh size of 6.25 – 25 mm; the computational mesh covering the whole domain (see Fig. 1) has a mesh number of 2.4 million and a mesh size of 12.5 – 100 mm. One simulation of the initial flame growth and the flame venting process of a duration 0.35 s took around three days using 2 nodes with 56 cores on a supercomputer. The initial temperature and pressure are 273 K and 1 atm., respectively. The initial turbulence velocity fluctuation $u'$ and the integral length scale $L$ are 0.75 m/s and 0.1 m, respectively. Such initial turbulence characteristics are chosen by comparing measured and computed pressure curves during the first stage of the dust explosion, i.e., $t < 0.1$ s in Fig. 4. This method is motivated by the lack of experimental data on the flow characteristics in the large-scale dust explosion experiments. This method also offers an opportunity to handle uncertainties of the data on laminar burning velocities, because the computed turbulent burning velocity is affected by the Damköhler number, i.e., by a combination of the laminar flame and turbulence characteristics. The dust dispersion process was not modelled. A homogenous corn starch dust/air cloud was assumed, with a dust concentration being equal to 750 g/m$^3$ and the corrected equivalence ratio being equal to 0.62 at the time of ignition.

## RESULTS AND DISCUSSIONS

### Comparison with the experiments

Fig. 4 compares the measured overpressure inside of the vessel wall at P2 (see Fig. 1) and the calculated value. The k-omega-SST turbulence model [21-23] is chosen instead of the standard k-epsilon turbulence model due to better agreement in terms of overpressure curve as compared to the experiment. A detailed discussion of the effect of turbulence models on the computed explosion overpressure can be found in Ref. [24]. The experimental curve can be studied in four stages: (i) an increase in the overpressure during dust explosion in the closed vessel before the rupture of the vent panel, i.e., at $t < 0.1$ s, (ii) a decrease in the overpressure after the rupture of the vent panel, i.e., at $0.1 < t < 0.12$ s, followed by a slow increase in the overpressure at $0.12 < t < 0.16$ s, (iii) a rapid increase in the overpressure at $0.16 < t < 0.30$ s, and (iv) a decrease in the overpressure at $t > 0.31$ s. The simulated pressure curve follows the experimental data closely.

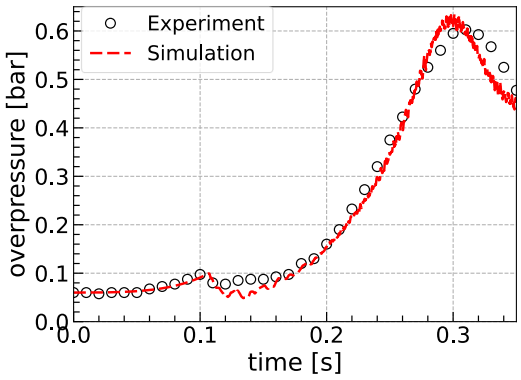


**Fig. 4.** Comparison between measured and simulated explosion overpressures. $u'$=0.75 m/s, $L$=0.1 m, $t_{flacc}$=0.15 s, k-omega-SST turbulence model.

### Effect of grid size

Grid size is a constant concern for CFD simulations. Figure 5 compares explosion overpressures computed using two different grid size resolutions in the vessel. The red dashed curve in Fig. 5 shows results computed using a mesh size of 25 mm inside the vessel, whereas the cyan dash-dotted curve in Fig. 5 shows results computed using a refined mesh size of 12.5 mm in a 0.7 m radius sphere inside the vessel. A finer grid size yields lower pressure as compared to a coarser grid size (c.f. red dash-dotted line and cyan dashed lines in Fig. 5). Figure 6 compares the explosion overpressures computed using two different grid size resolutions at the walls. The red dashed curve in Fig. 6 shows results computed using five layer mesh at the wall of the vessel and the venting wall, whereas the cyan dash-dotted curve in Fig. 6 shows results computed without mesh refinement at the walls of the vessel. A finer grid size at the wall yields a higher explosion overpressure as compared to a coarser grid size at the vent wall (c.f. red dash-dotted line and cyan dashed line in Fig. 6). It is recommended to have a finer grid size in the vessel and at the walls (especially at the vent wall) to better capture the propagation of the flame and the flow through the vent opening. Such a finer mesh was used in the case setups in Fig. 4.

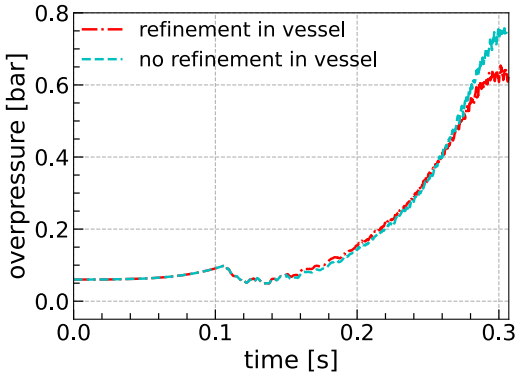


**Fig. 5.** The effect of the mesh refinement on the explosion overpressure computed using k-omega-SST turbulence model.

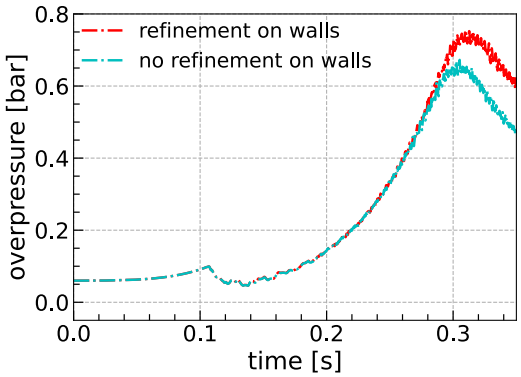


**Fig. 6.** The effect of the mesh refinement at the walls on the explosion overpressures computed using k-omega-SST turbulence model.

### Effect of vent size

In this section, the numerical model is applied to study the effect of vent size on the maximum reduced explosion overpressure, $p_{red}$. Since the standard EN 14491:2012 [25] invokes the same correlations as those in the standard VDI 3673:2002 [26] for calculating the required vent areas for isolated enclosures, only results yielded by EN 14491:2012 [25] are shown here. The parameters used in calculations in the standards and simulations are summarized in Table 2. Both standards (i.e., EN 14491:2012 [25] for Europe and NFPA 68:2018 [27] for the US) and the simulations show that the maximum reduced explosion overpressure decrease with an increase of vent area (see Fig. 7). Furthermore, both the estimations done using the standards and the RANS simulations closely follow each other, with the simulation results being slightly closer to the estimations for the NFPA 68:2018 standard. For the current case, the calculations using the NFPA 68:2018 standard are slightly less conservative for a vent area larger than 0.35 m$^2$ as compared to the results yielded by the EN 14491:2012. Similar finding was reported by Tascon et al. [28]. However, for a vent area smaller than 0.35 m$^2$, EN 14491:2012 standard yields a less conservative result than that by NFPA 68:2018 standard.

**Table 2. Summary of the parameters used in the calculations in the standards and simulations.**

| Name | Symbol | Value | Unit |
|---|---|---|---|
| Vessel volume | $V$ | 11.5 | m$^3$ |
| Static activation pressure | $p_{stat}$ | 0.1 | bar |
| Vent area | $A_v$ | 0.28, 0.50, 0.79 | m$^2$ |
| Deflagration index | $K_{St}$ | 220 | bar m/s |
| Maximum explosion overpressure | $p_{\max}$ | 8.7 | bar |

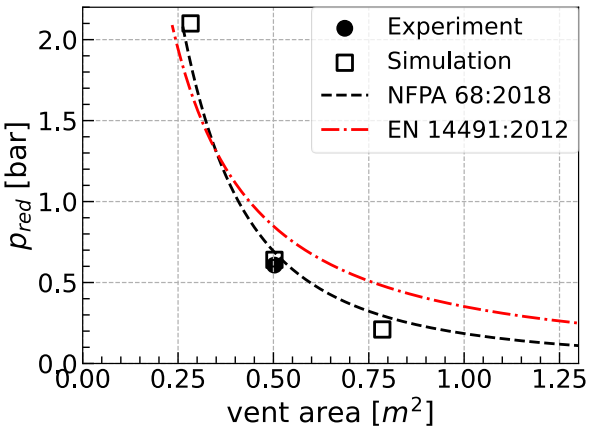


**Fig. 7.** Comparison of the maximum reduced explosion overpressure versus vent area among simulations, standards, and experiments. NFPA 68:2018 invokes $L/D$ = 1.86, and EN 14491:2012 invokes $L/D$ = 1.41.

**Effect of ignition locations**

The developed model and tool can be used not only for parametric studies covered in the standards (see the previous example), but can also be used for parametric studies that are partly addressed in the standards. Ignition location is a factor which can affect the vented explosions. Experiments from Bauwens et al. [29] showed that a back-wall ignition yielded a substantially higher explosion overpressure than that for a central ignition for gaseous explosions. Castellanos et al. [30] also found that a rear ignition led to a higher explosion overpressure for coal dust using simulations. For dust explosions EN 14491:2012 and NFPA 68:2018 indirectly consider the ignition location by applying the correction factors involving $L/D$, usually calculating the longest path that the flame can travel to the vent opening. A higher $L/D$ usually lead to a higher explosion overpressure. Especially for gas explosions the equations are more limited and less precise.

In this study, four ignition positions are studied, i.e., back, center, upper and lower, as illustrated in Fig. 8. All the ignition points are chosen in a vertical plane cutting through the center of the vessel. The back ignition point is located at 0.5 m from the back wall of the vessel. The upper and lower ignition positions are located at 0.6 m away from the horizontal center line of the vessel (see Fig. 8). Figure 9 compares the computed explosion overpressure for four ignition locations using the original FSC model (i.e., Eq. 3 without the term $T_2$) and the model with acceleration effect (see Eq. 3). Due to the lack of experimental data on the ignition locations other than center ignition, the flame acceleration timing is chosen by assuming that the flame position characterized by $\bar{c} = 0.5$ reaches a distance of 1.85 m away from the vent opening. Accordingly, the $t_{flacc}$ for back, center, upper and lower ignition positions is equal to 0.193 s, 0.15 s, 0.143 s and 0.143 s, respectively.

To reflect different ignition locations, the $L/D$ value was adapted for the vent area calculations when applying the standards. $L/D$ = 1 reflects center ignition or ignition close to the vent opening for both standards. Back ignition is calculated considering $L$ to be the length from the back ignition location to the vent opening. Accordingly, for the back ignition vent area calculations EN 14491:2002 and NFPA 68:2018 invoke $L/D$ being 1.31 and 1.56, respectively. Note that for the NFPA 68:2018 standard, the effect of $L/D$ starts to play a role for $L/D \geq 2$. Furthermore, the $L/D$ calculations between NFPA 68:2018 and EN 14491:2002 slightly differ due to a different approach in the calculation of the conical part of the vessel.

The simulations clearly show that the back ignition position yields the highest explosion overpressure, whereas the upper and lower ignition positions yield the lowest pressure. This is also reflected in the vent area calculation using the EN 14491:2012 standard (c.f. red dotted line and cyan dash dotted line in Fig. 9). Note that the simulated explosion overpressure using the extended FSC model with the flame acceleration term $T_2$ in Eq. 3 yields substantially higher values than those computed using the original FSC model for the center, upper and lower ignition positions, but not for the back ignition position (c.f. slash filled bars and backslash filled bars in Fig. 9).

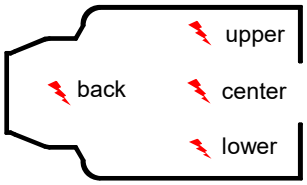


**Fig. 8.** Illustration of the ignition locations.

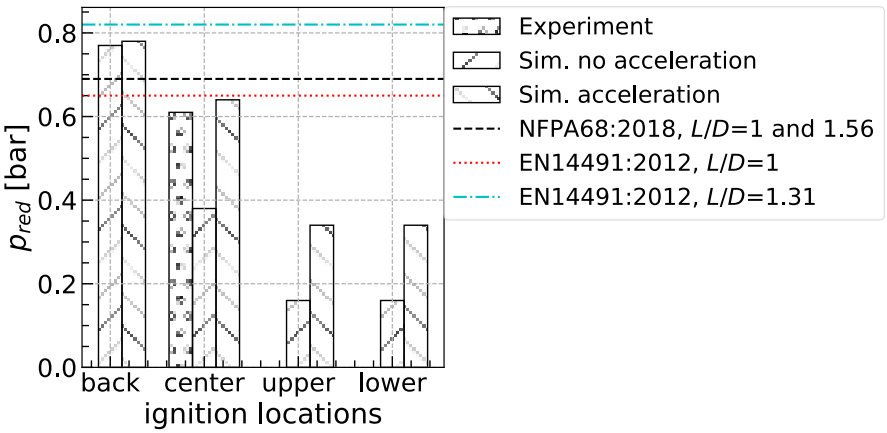


**Fig. 9.** Maximum reduced explosion overpressures versus ignition locations.

### Effect of buoyancy force

The effect of buoyancy force is studied by introducing an extra source term in the Favre-averaged Navier-Stokes equations. Results are shown in red dashed line in Fig. 10. Before 0.29 s, the buoyancy force has no influence on the computed results, and after 0.29 s, the buoyancy force reduces the calculated explosion overpressure.

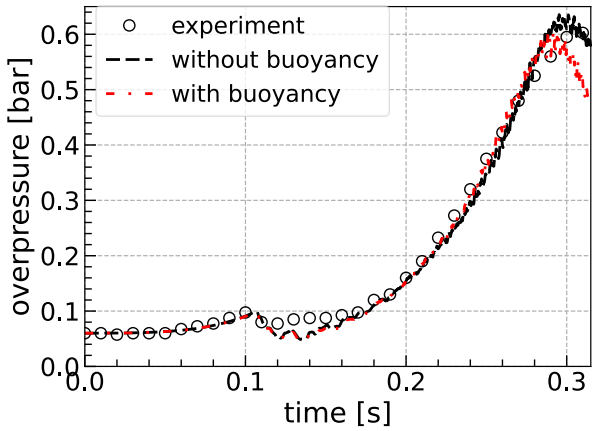


**Fig. 10.** Effect of buoyancy force on the computed explosion overpressures.

## CONCLUSIONS

The vented corn starch dust explosion in an 11.5 $m^3$ vessel was investigated experimentally and numerically. The numerical approach is based on unsteady 3D RANS simulations using the extended FSC model of the influence of turbulence on combustion implemented into OpenFOAM. Good agreement between measured and computed overpressures is obtained. Parametric studies are performed by varying vent area and ignition location using the developed model and numerical tool. The well calibrated numerical model is especially useful for scenarios which are not covered in the standards. The numerically efficient extension of the FSC model is promising and deserves further study in simulations of other experiments with large-scales dust or gaseous explosions.

## ACKNOWLEDGEMENTS

The authors would like to acknowledge AFA-Försäkring for financial support of this project (grant number 180028). The computations were enabled by resources provided by the Swedish National Infrastructure for Computing (SNIC) at HPC2N partially funded by the Swedish Research Council through grant agreement no. 2018-05973 and RISE Simulation Lab. The SNIC projects SNIC2021-22-217, SNIC2021-5-185 and SNIC2021-22-821 are acknowledged. Åke Sandgren and Erik Andersson at HPC2N are specially acknowledged. The authors would like to acknowledge IND EX® for providing the real scale test data of the IND EX® research project "Influence of the Explosion Relief Device Geometry on its Venting Efficiency".

## REFERENCES

[1] T. Skjold, B.J. Arntzen, O.R. Hansen, O.J. Taraldset, I.E. Storvik, R.K. Eckhoff, Simulating Dust Explosions with the First Version of DESC, Process Saf. Environ. Prot. 83(2) (2005) 151-160.
[2] T. Skjold, Review of the DESC Project, J. Loss Prev. Process Ind. 20(4-6) (2007) 291-302.
[3] H.T. Li, X.K. Chen, J. Deng, C.-M. Shu, C.-H. Kuo, Y.C. Yu, X.Y. Hu, CFD Analysis and Experimental Study on the Effect of Oxygen Level, Particle Size, and Dust Concentration on the Flame Evolution Characteristics and Explosion Severity of Cornstarch Dust Cloud Deflagration in a Spherical Chamber. Powder Technol. 372(2020) 585-599.
[4] P. Pico, N. Ratkovich, F. Muñoz, O. Dufaud, Analysis of the Explosion Behaviour of Wheat Starch/Pyrolysis Gases Hybrid Mixtures Through Experimentation and CFD-DPM Simulations. Powder Technol. 374(2020) 330-347.
[5] D. Bradley, S. El-Din Habik, J.R. Swithenbank, Laminar burning velocities of CH4—air-graphite mixtures and coal dusts. Proc. Combust. Inst. 21 (1988), 249-256.
[6] D. Bradley, Z. Chen, J. Swithenbank, Burning Rates in Turbulent Fine Dust-Air Explosions. Proc. Combust. Inst. 22(1) (1989) 1767-1775.
[7] D., Bradley, G., Dixon-Lewis, S., El-Din Habik. Lean flammability limits and laminar burning velocities of CH4-air-graphite mixtures and fine coal dusts. Combust. Flame,77 (1989) 41-50.
[8] T. Skjold, Simulating vented maize starch explosions in a 236 m3 silo. Fire Saf. Sci. 11 (2014) 1469-1480.

[9] C. Huang, A.N. Lipatnikov, K. Nessvi, Unsteady 3-D RANS Simulations of Dust Explosion in a Fan Stirred Explosion Vessel Using an Open Source Code. J. Loss Prev. Process Ind. 67(2020) 104237.
[10] A. Lipatnikov, J. Chomiak, Turbulent Flame Speed and Thickness: Phenomenology, Evaluation, and Application in Multi-Dimensional Simulations. Prog. Energy Combust. Sci. 28(1) (2002) 1-74.
[11] A.N. Lipatnikov, J. Chomiak, A Simple Model of Unsteady Turbulent Flame Propagation. SAE transactions, Section 3, Journal of Engines, 106 (1997) 2441-2452.
[12] C. Huang, E. Yasari, L.C.R. Johansen, S. Hemdal, A.N. Lipatnikov, Application of Flame Speed Closure Model to RANS Simulations of Stratified Turbulent Combustion in a Gasoline Direct-Injection Spark-Ignition Engine. Combust. Sci. Technol. 188(1) (2016) 98-131.
[13] Y.A. Gostintsev, A. Istratov, Y.V. Shulenin, Self-similar Propagation of a Free Turbulent Flame in Mixed Gas Mixtures. Combust. Explos. Shock Waves, 24(5) (1998) 563-569.
[14] V.L. Zimont, Gas Premixed Combustion at High Turbulence. Turbulent Flame Closure Combustion Model. Exp. Therm. Fluid Sci., 21(1) (2000) 179-186.
[15] A. Lipatnikov, Fundamentals of Premixed Turbulent Combustion. 2012, CRC Press.
[16] A.N. Lipatnikov, RANS Simulations of Premixed Turbulent Flames,in Modeling and Simulation of Turbulent Combustion. Springer. 2018, pp.181-240.
[17] I. Tan, C.C. Wee, P.A. Sopade, P.J., Halley, Estimating the Specific Heat Capacity of Starch‐water‐glycerol Systems as a Function of Temperature and Compositions. Starch‐Stärke, 56(1) (2004) 6-12.
[18] A.E. Dahoe, K. Hanjalic, B. Scarlett, Determination of the Laminar Burning Velocity and the Markstein Length of Powder–air Flames. Powder Technol. 122(2) (2002) 222-238.
[19] Ö.L. Gülder, Correlations of Laminar Combustion Data for Alternative SI Engine Fuels. SAE Technical Paper 841000, 1984.
[20] T. Skjold, B.J. Arntzen, O.R. Hansen, I.E. Storvik, R.K. Eckhoff, Simulation of Dust Explosions in Complex Geometries with Experimental Input from Standardized Tests. J. Loss Prev. Process Ind. 19(2-3) (2006) 210-217.
[21] A. Hellsten, Some Improvements in Menter's K-omega SST Turbulence model, in: 29th AIAA, Fluid Dynamics Conference, pp. 2554, 1998.
[22] F. Menter, T. Esch, Elements of Industrial Heat Transfer Predictions, in: 16th Brazilian Congress of Mechanical Engineering (COBEM), pp. 650, 2001.
[23] F.R. Menter, M. Kuntz, R. Langtry, Ten Years of Industrial Experience with the SST Turbulence Model. Turbulence, heat and mass transfer 4 (2003) 625-632.
[24] C., Huang, M., Bloching, A.N., Lipatnikov, A vented corn starch dust explosion in an 11.5 m3 vessel: Experimental and numerical study. J. Loss Prev. Process Ind. 75 (2022) 104707.
[25] EN14491, Dust Explosion Venting Protective Systems. European Committee for Standardization, Brussels. 2012.
[26] VDI3673, Guideline VDI 3673 Part 1: Pressure Release of Dust Explosions, VDI. 2002.
[27] NFPA68. NFPA 68 Standard on Explosion Protection by Deflagration Venting. 2018.
[28] A. Tascón, P.J. Aguado, A. Ramírez, Dust Explosion Venting in Silos: A Comparison of Standards NFPA 68 and EN 14491. J. Loss Prev. Process Ind. 22(2) (2009) 204-209.
[29] C.R. Bauwens, J. Chaffee, S.B. Dorofeev, Vented Explosion Overpressures from Combustion of Hydrogen and Hydrocarbon Mixtures. Int. J. Hydrog. 36(3) (2011) 2329-2336.
[30] D. Castellanos, T. Skjold, K.V. Wingerden, R.K. Eckhoff, S. Mannana. Simulating Dust Explosion Venting Through Ducts. in 23rd ICDERS. 2011. Irvine, USA.

# Deflagration, DDT, Detonation and Their Mitigation

# Numerical investigations on dust explosion process in MIKE 3 apparatus

**Pan Yangyue[1,*], Spijker Christoph [1], Raupenstrauch Harald [1]**

*[1] 1 Montanuniverstitaet Leoben, Thermal Processing Technology, Leoben, Styria, Austria.*
**Corresponding author's email: yangyue.pan@unileoben.ac.at*

## ABSTRACT

In this paper the flame structure and propagation of coal particles are studied experimentally and numerically. The measurements were conducted in a Hartmann tube and a high-speed camera was used to record the process of the dust explosion. The results show the complex flame shape of coal dust explosion due to the devolatilization process. The particle clusters are identified as a result of the unevenly distributed dust cloud prior to ignition. The particle clusters produce more volatile content in the reaction which leads the flame propagation. In order to understand the particle behaviors in the combustion, the coal particle content is applied to its characters in the simulation. High temperature is found near the ignition source as well as high particle load. The number of coal particles in the upper part of the tube gradually decreases over time, and the flame is mainly maintained by the pyrolysis gas of the middle and lower particles. When the flame spreads to the top of the tube, a large number of unburned particles are concentrated at the bottom of the tube. This is due to the lack of oxygen. When the flame at the top of the tube is extinguished, sufficient oxygen is supplied to the bottom of the tube and the combustion will continue.

**KEYWORDS:** Hartmann tube, dust explosion, flame propagation, CFD.

## INTRODUCTION

In the new and sophisticated process lines, dust explosion is a potential disaster. The fast explosion process makes it hard to observe the chemical reactions and transport phenomena. Small explosion chambers such as Hartmann tube and 20 L sphere were designed to do laboratory-scale experiments [1]. Some recent research has focused on the flame propagation of different particles, including nano and microscale particles. The flame shape is affected by particle size. In the dust explosion study of octadecanol particles [2], when increasing the smaller particle content of the test sample from three particles (D50 are 43.64 μm, 62.88 μm and 101.95 μm), a smoother flame shape was identified. Besides, the flame leading zone is supported by the volatile gases, and it tends to decompose the smaller particles in the propagation. The flame propagates more rapidly when the particle consists of more volatiles [3]. The flame shape is also influenced by turbulence flow when considering the dust propagation period before the ignition. The uneven flame shape and large numbers of folds and vortices occur during the combustion process [4].

The experimental instruments are able to provide repeatable results, but also many stays unknown to us. For example, in the previous study [5], the dust concentration along the MIKE 3 tube prior to ignition varies due to different particle sizes. A possible way to understand the fundamental combustion principles and combustion behavior is using CFD simulation. However, the simulation of dust explosion still faces challenges due to the complexity of phase change and chemical reactions [6]. To investigate the process, proper simulation models should be used accordingly. The simulation methods for multi-phase phase flow are Eulerian and Lagrangian approaches. For the Eulerian method, particles and air are both described as continuum phase, where the solid particle is implemented with a pseudo liquid model. The percentage of each phase in a cell is defined with a coefficient alpha. This method is able to determine the flow field properties such as flame propagation profile out of the embedded chemical reaction model. However, the particle trajectories are not predicted due to the assumption of the pseudo-liquid model. The Lagrangian method provides the possibility of a detailed investigation of particle effects. The particles are seen as individuals and data

such as components and reaction rate is available. While the biggest drawback of this method is the high requirement of computation time.

In this study, continuous work is carried out to study the explosion process of dust explosion in the MIKE 3 apparatus in experimental and simulation methods. The open-source toolkit OpenFOAM version 5 was used in the simulation work.

## EXPERIMENT SETUP

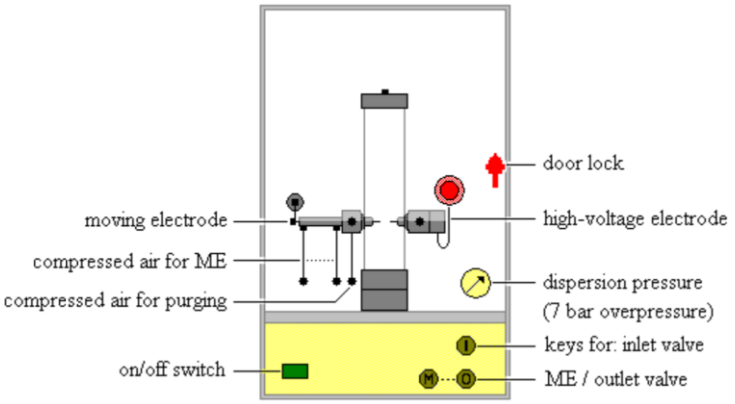


**Fig. 1.** MIKE-3 apparatus from Kuehner AG [7].

The experimental apparatus used in the study is shown in Fig. 1. MIKE 3 is a modified Hartmann tube that is widely used in laboratories to test the minimum ignition energy of powders. The apparatus consists of the dispersion tube, dispersion system, pneumatic system, high-voltage electrodes, measurement and detection system. An additional high-speed video camera was set to record the experiment process. For each dust class, tests were repeated five times to assure consistency of the measurement results. All the tests are carried out under ambient pressure and temperature condition.

**Table 1. Element analysis of the coal sample, air-dry basis**

| | Element analysis (wt.%) | | | | |
|---|---|---|---|---|---|
| | C | H | O | N | S |
| Coal | 73.9 | 4.87 | 4.81 | 1.47 | - |

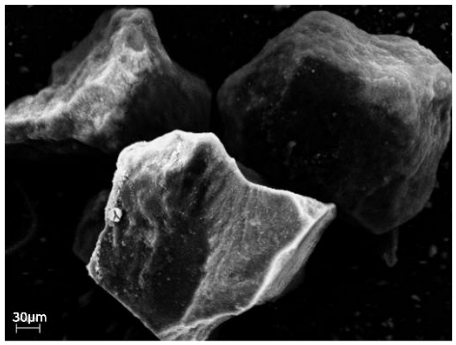


**Fig. 2.** SEM image of the coal sample.

The sample used in the experiment is black coal with a density of 1007 kg/m$^3$. The bulk coal was processed into smaller particle sizes. A ball mill was used firstly to grind the bulk coal and then the coal dust was sieved into a particle size range of 71 - 125 μm. The pulverized coal was dried in an oven at 100 ℃ for 12 hours. The element analysis result of the coal sample is shown in Table. 1. The scanning elctron microscopy (SEM) image of the coal sample is shown in Fig. 2. In the experiment, 900 mg of dust sample was put on the curved bottom under the nozzle. When the experiment started, an air blast was released from a high-pressure container into the dispersion tube. The dust is lifted with the high turbulence flow and forms a cloud in the dispersion tube. According to the test standard in dust explosion, the spark discharge is drawn from the electrodes at the height of 100 mm above the tube bottom after a certain time from the dust dispersion. The delay of the discharge time from the onset of air blast is the ignition delay time, which is 60 ms in the tests. The ignition delay time decides the turbulence level, dust cloud concentration in the flow domain at the instant of spark ignition. The ignition energy is set at 1000 mJ to ensure dust ignition. A detailed introduction and result analysis of the dust explosion experiment can be found in documents [8,9].

## MODEL DESCRIPTION

Current study is based on OpenFOAM 5.x version, in which the solver coalChemistryFoam was employed. The coalChemistryFoam is a transient, compressible solver with the utility of chemical reaction and multiphase flow. The solver uses RANS (Reynolds-Averaged Navier Stokes) model as the turbulence model and closed up with k-epsilon model. The evaporation and devolatilization of the particles were also modelled. The Lagrangian particles was used to couple with the gas, which the trajectories are tracked in the combustion process.

To track the particle movement, the Newton's second law was used as considering all the forces exerting on each particle.

$$m_p \frac{\partial^2 x_p}{\partial t^2} = m_p \left[ F_D(u - u_p) + \frac{g(\rho_p - \rho)}{\rho_p} \right] \quad (1)$$

where $m_p$, $u_p$, $\rho_p$ are the particle mass (kg), velocity (m/s) and density (kg/m$^3$), respectively. The terms on the right hand side of the Eq. (1) are the drag force and gravity. The drag force $m_p F_D(u - u_p)$ is calculated depending on the particle Reynolds number ($Re_p$) and drag coefficient ($C_D$) [10].

$$F_D = \frac{0.75 \mu C_D Re_p}{\rho_p d_p^2} \quad (2)$$

$$Re_p = \frac{\rho_p d_p |u - u_p|}{\mu} \quad (3)$$

$d_p$ represents the particle diameter (m), and $\mu$ is the dynamic viscosity (kg/m·s) of the fluid. Due to the interaction of the two phases, more forces are taking part in the dispersion. In this study, the forces in the two-phase system, such as the pressure difference on particles owing to the difference of velocity (lift force), are not considered. The lift force has a negligible influence on the trajectories of particles [10]. Considering the micro size of particles, the buoyancy force and drag forces have a significant influence on the dispersed phase.

Due to the coal samples being dried prior to the experiment, the adsorbed water content is zero. Therefore, the liquidEvaporation models are deactivated. According to the Thermogravimetric analysis, the coal particles have 34.77% of the volatile gas component until 1200 K, which includes 52.71% $CH_4$, 47.29% $CO_2$. The solid part of the coal at 1200 K consists of 16% incombustible ash and 84% carbon molecules. The constantRateDevolatilization model was used to calculate the coal decomposition with a constant rate in the form of a single-step Arrhenius expression:

$$\dot{m}_{Yi}^{p} = m_{Yi}^{p} A_v \exp\left(-\frac{E_{a,v}}{RT_p}\right) \tag{4}$$

$A_v$ and $E_{a,v}$ are the pre-exponential coefficient (kg/s) and activation energy (J/kg·K). $Yi$ represents the gas components in the coal particles. In calculating the Lagrangian particles, the numerical scheme loops through all Lagrangian particles, the pyrolysis gases from the particles are updated by using the Eq. (4), which uses the temperature and particle mass in the cell where the particle is located. These become the source term of the gas phase equation. Other properties such as velocities, temperature, gas-phase density are also calculated by the mass and energy conservation equations.

The surface reaction considers the direct reaction of carbon and oxygen on the surface of the particle:

$$\mathrm{C(s)+O_2 \rightarrow CO_2} \tag{5}$$

where the oxygen from the gas phase is consumed and carbon dioxide is produced from the heterogeneous reaction. The diffusion-limited surface reaction model is used to specify the surface reaction rate, which is limited by the oxygen diffused to the particle surface [11,12].

$$\frac{dm_p}{dt} = -4\pi d_p D_{i,m} \frac{Y_{O_2} T_\infty \rho}{T_p + T_\infty} \tag{6}$$

where $D_{i,m}$ represents the diffusion coefficient for oxygen ($m^2/s$). $Y_{O_2}$ is the local mass fraction of oxygen in the gas at the surface of the particle.

The devolatilization process is followed by a series of chemical reactions due to the release of combustible gases. The evolved gases take part in the computational cell in the gas phase and participate the homogeneous reaction. One chemical reaction mechanism for $CH_4$ was considered in the simulation.

$$\mathrm{CH_4 + 2O_2 \rightarrow CO_2 + H2O} \tag{7}$$

The reaction rate is represented by an irreversible Ahrrenius equation, where only $CH_4$ is combusted in the gas phase:

$$\dot{m}_{CH_4}^{g} = m_{CH_4} A_v \exp\left(-\frac{E_{a,v}}{RT_\infty}\right) \tag{8}$$

The reaction model in the gas phase used PaSR (Partially Stirred Perfect Reactor) model. In each simulation cell, the reactants are perfectly mixed only in part of cell. This model considered the chemical scale and time scale to prevent overpredicting of the chemical reaction process. A robust chemical reaction solver Seulex was used.

According to the movement momentum, chemical reaction, heat transfer from the particles, the momentum, chemical component, and energy level in each computation cell are affected by the particle sources. The sources are registered as source terms in the conservation equations in the gas phase transportations.

$$\frac{\partial \rho}{\partial t} + \nabla \cdot \phi = S_\rho^p \tag{9}$$

$$\frac{\partial \rho u}{\partial t} + \nabla \cdot (\phi u) - \nabla^2(\mu_{eff} u) + \nabla \cdot p = S_{\rho u}^p \tag{10}$$

where $\rho$ is the density of the fluid (kg/m$^3$). $u$ is the fluid velocity (m/s). $\phi$ is mass flux (kg/m$^2$·s). $\mu_{eff}$ is effective viscosity (kg/m·s). p is fluid pressure (Pa). $S_\rho^p$ and $S_{\rho u}^p$ are the source terms from the solid phase.

## NUMERICAL DOMAIN

The three-dimensional numerical domain for the current model is shown in Fig. 3, which has the exact dimensions as the explosion tube in MIKE 3 apparatus. It is a 1.2 L verticle cylinder with a dimension of 300 mm in height and 68 mm in diameter. The spark ignition source is located at the center of the tube at the height of 100 m. The geometry is discretized into 600 000 hexahedra cells. The grid sizes range from 1 mm to 2 mm, which is enough to capture the intensive heat transport. The top of the tube is outlet, and the others are walls as the boundary condition. The initial temperature in the internal field is 300 K.

Fig. 3(b) indicates the particle positions at the instant of spark ignition. The positions are obtained from previous simulation results in the particle propagation simulation [13]. The spark ignition is set as a sphere region with a 6 mm radius. The temperature in the ignition source is 2000 K. It starts from 0.001s and lasts for 0.01s in order to ignite the particles. The particles are set as monodispersed with a diameter of 125 μm. The total ignited particle mass is 900 mg, and the mass parcel basis is used. The solid particles are two-way coupled with the flow domain. A summary of the simulation parameters used in the present study is shown in Table 1.

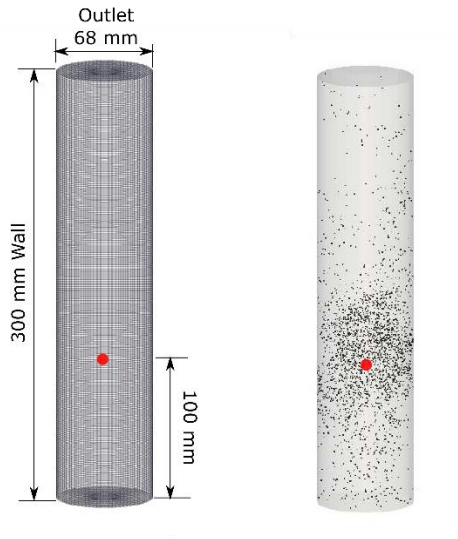


**Fig.3.** Schematic of three-dimensional computational domain indicated the ignition source position. (a) the geometry scale and boundary conditions; (b) the initial position of the dust cloud.

**Table 1. Simulation parameters used in the model.**

| Parameter | Value |
|---|---|
| Fluid | Air |
| Solid | Coal dust |
| Particle size (μm) | 125 |
| Dust concentration (g/m$^3$) | 750 |
| Particle density (kg/m$^3$) | 1007 |

| | |
|---|---|
| Ambient pressure (Pa) | 100 000 |
| Temperature (fluid) (K) | 300 |
| Temperature (solid) (K) | 300 |
| Ignition temperature (K) | 2000 |
| Cell size (m) | 0.001 ~ 0.002 |
| Simulation time (ms) | 180 |
| Ignition period (ms) | 1 ~ 11 |

## RESULTS

### Flame propagation in the experiment

Figure. 4 shows a series of recorded images of the flame propagation of coal dust at a concentration of 750 g/m$^3$ and particle diameter of 125 μm. At 0.001 s, a faint flame shows after the spark ignition which propagates slowly during several milliseconds, which could be due to the burning of small and easily released volatile particles of coal particles which leads to weight loss. The particles are separated by the volatiles released from the heated particles. When the oxygen diffused to the surrounding of the particle, the combustible volatile gases react. The heat from combustion continues to heat up the separated particles. The flame starts to be luminous, which is a diffusion-controlled reaction. The flame shape is irregular due to the particle suspension conditions at the instance of ignition. As seen in 0.03 s, the flame has a direction towards the left wall because more particle accumulation means more reactant. The flame propagates along the wall and continues to heat up particles nearby. Therefore, the particles on the right side of the tube are ignited. The flame has a very luminous part in the active reaction center due to the high volatile content released from particles. This also explains the discontinuous flame front. The flame top front is hard to capture as a result of scattering burning particles, which can be observed in 0.07 s. Similar irregular flames were also observed by Kern [14], who did flame propagation experiments using lycopodium particles in a 2-meter long cylindrical tube. Different from his result, the flame in the MIKE 3 does not propagate to the bottom of the tube intensely due to the lack of oxygen. Only part of the dust is combusted, which can be identified from 0.04 s to 0.08 s. Similarly, the particle concentration towards the right bottom of the tube is higher and more combustion heat is produced, indicating a lower temperature gradient in the neighborhood of the particle. The high particle concentration part is named particle clusters in the study of Hosseindach [9]. The flame reached the top of the tube at 0.08 s. After that, the flame still burns as the flame extinct and more oxygen is diffused to the tube bottom.

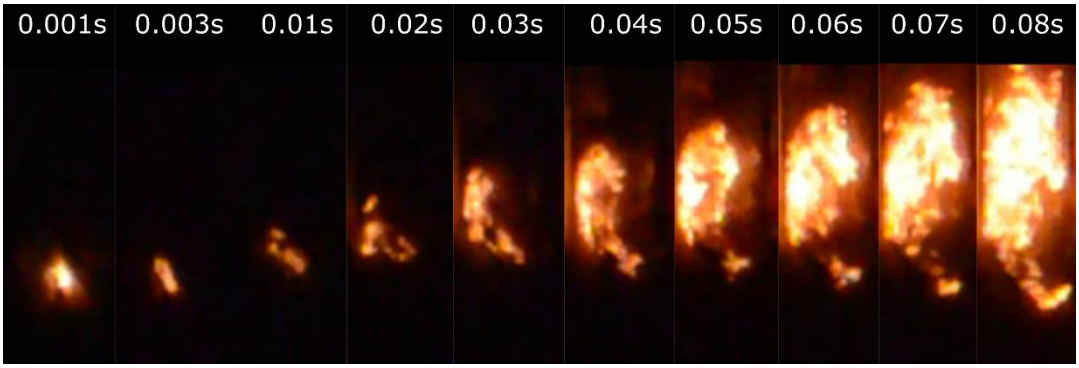


**Fig. 4.** High-speed images of coal cloud flame.

### Flame propagation in simulation

Figure. **Fig. 5**5 shows the flame propagation in the simulation with the experimental results on the left of each group of subfigures. The yellow dashed line marks the height of the ignition source. The particle starts to form a flame at 0.1 s due to the lower heat transfer from the ignition source. It is different from the experiment, where the flame forms at 0.003 s right after the spark discharge because of high energy transfer. Such a high energy transfer condition is hard to achieve in the simulation due to the instability and unknown material property at very high temperatures [15]. This problem arises in the Lagrangian method because the heat exchange of gas phase and particles is calculated. The temperature of the gas phase is limited by the Janaf thermal model.

It can be observed from Fig. 5 that the flame gradually spreads to the top of the tube. At 0.18 s, the flame front reaches the outlet. The propagation lasts for 0.08 s, which is in good agreement with the experiment result. At 0.1 s, the coal particles near the ignition source start to lose volatile content. The volatiles in the surroundings of the particle combusts due to the high temperature. After that, the ignition source is removed, and the heat transfer continues with the heat of combustion. The presence of darker coal particles can be found near the yellow line. The particle temperature is lower due to the release of volatile content. There is also a temperature gradient around the particles. The highest temperature in the field locates neighboring the particles, where active homogeneous combustion takes place. Due to air expansion and buoyancy, the flame spreads upward. In the meantime, the burning particles simultaneously drive the flame to the bottom of the tube as a result of gravity. The particle concentration is higher near the yellow line compared to the upper part of the tube. These particle clusters yield more combustible gases and higher combustion heat. The particle in the simulation are concentrated near the electrodes (see Fig. 3) and settle down during the combustion when no initial velocity field exists. Therefore, the flame has a different shape from the experiment.

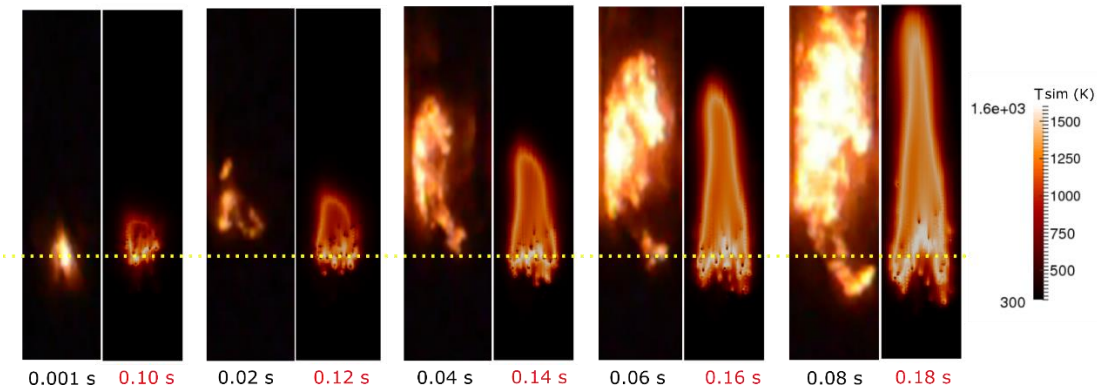


**Fig. 5.** Coal cloud flame propagation of simulation and experiment over time with the ignition height marked by the yellow dashed line.

### Particle combustion behavior

The coal particle decomposition level is shown in Fig. 6. The Ygas represents the particle volatile content varying from 0 to 1. When the Ygas equals 0, all the volatiles from one particle is released by the devolatilization. At 0.1 s, the particles in the ignition source region are heated up and release a large percentage of gas volatiles. The particles decrease into a lower location due to gravity. The high-temperature volatile gas moves upwards due to the buoyancy and is combusted when the oxygen is diffused to the particle surrounding. The fully decomposed particles become more in the lower part of the tube, where more active combustion happens due to the high particle concentration. At 0.16 s, the particle number is low in the upper part of the tube and the particles are mostly maintained undecomposed. This indicates that the fuel in the flame front is raised from the middle of the tube. At

0.18 s, the flame reaches the outlet, while high particle accumulation is found at the bottom of the tube. Those particles are not combusted due to the lack of oxygen.

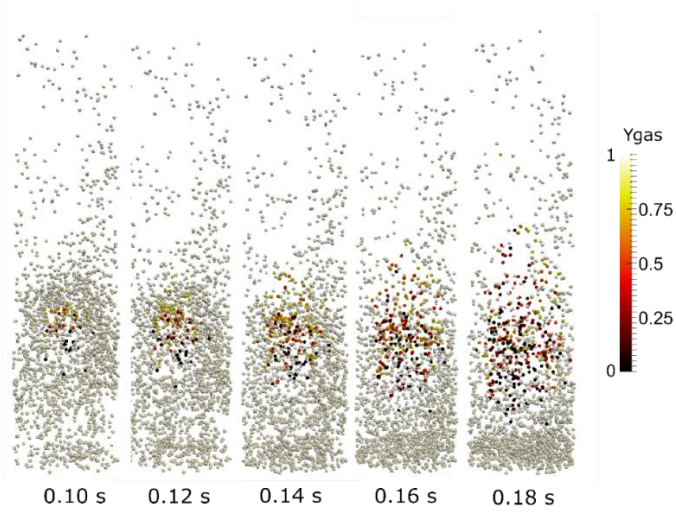


**Fig. 6** Coal particle volatile content over time.

## CONCLUSION

The flame structure and propagation in the dust/air mixture flames are hard to capture due to the fast reaction process. The particle trajectories and devolatilization behavior are rarely investigated in the dust explosion. In this study, experimental and simulation work has been conducted in order to understand the flame propagation and dust behavior in the MIKE 3 apparatus.

The coal sample with narrow size distribution was used in order to do further research in comparing the particle size influence in the dust explosion. The other reason is to prepare the experiment in order to simplify the particle size distribution in the simulation. The volatile content was obtained by a Thermogravimetric analysis and was applied to the CFD (computational fluid dynamics) simulation.

In the experiment, the flame propagates in the direction of particle clusters where more combustible gases are present. As a result, the flame direction is more or less uncertain, and the flame shape is irregular. The flame propagates mainly upward, where there is more oxygen entrainment. At the bottom of the explosion tube, the flame also propagates to the particle clusters but at a very slow speed due to lower oxygen diffusion.

The simulation flame starts at 0.01 s, which is slower than the experiment because of the limitation of the energy source term in the model. It takes the same time as the experiment for the flame to reach the top of the tube. The flame shape is not exactly matching the experiment results. It can be explained by the reasons:

(1) The particle position in the simulation used is mostly accumulated near the electrodes. During the combustion, the particles settle down. Therefore, fewer particles are combusted in the simulation than in the experiment. The particle clusters in the experiment are random, and the flame shape can not be exactly reproduced. The distributed particle concentrations over the domain can be studied.

(2) The initial field of the fluid domain is assumed with no velocity. This will result in less heat and mass transport. However, in reality, there exists high turbulence flow in the fluid domain during ignition.

(3) The monodispersed particles lead to the same sedimentation speed. With the overall constant devolatilization rate, the gas volatiles are not accurately predicted. However, this is hard to be improved. This simplification is to reduce the computation time.

Further studies will be carried out to investigate the gas species consumption in the explosion. The different particle sizes and initial particle positions are in consideration for parameter analysis. New models would be implemented in order to obtain more accurate results.

## REFERENCES

[1] Janes, A., Chaineaux, J., Carson, D., & Le Lore, P. A. (2008). MIKE 3 versus HARTMANN apparatus: Comparison of measured minimum ignition energy (MIE). Journal of Hazardous Materials, 152(1), 32–39. https://doi.org/10.1016/j.jhazmat.2007.06.066

[2] Gao, W., Mogi, T., Sun, J., Yu, J., & Dobashi, R. (2013). Effects of particle size distributions on flame propagation mechanism during octadecanol dust explosions. Powder Technology, 249, 168–174. https://doi.org/10.1016/J.POWTEC.2013.08.007

[3] Cao, W., Gao, W., Peng, Y., Liang, J., Pan, F., & Xu, S. (2014). Experimental and numerical study on flame propagation behaviors in coal dust explosions. Powder Technology, 266, 456–462. https://doi.org/10.1016/J.POWTEC.2014.06.063

[4] Zhang, H., Chen, X., Zhang, Y., Niu, Y., Yuan, B., Dai, H., & He, S. (2017). Effects of particle size on flame structures through corn starch dust explosions. Journal of Loss Prevention in the Process Industries, 50, 7–14. https://doi.org/10.1016/j.jlp.2017.09.002

[5] Pan, Y., Spijker, C., & Raupenstrauch, H. (2022). CFD modeling of particle dispersion behavior in the MIKE 3 apparatus. Alexandria Engineering Journal, 61(12), 9305–9313. https://doi.org/10.1016/j.aej.2022.03.039

[6] Skjold, T., Larsen, Ø., & Hansen, O. R. (2006). Possibilities, limitations, and the way ahead for dust explosion modelling. Institution of Chemical Engineers Symposium Series, (151), 1–16.

[7] C.Cesana, R. Siwek, Manual MIKE 3 apparatus, Kuehner AG (2010).

[8] CEN, Potentially explosive atmospheres, explosion prevention and protection, determination ofminimum ignition energy ofdust/air mixtures, European Standard EN 13821, 2003 (Brussels).

[9] S. Hosseinzadeh, M. Vanierschot, F. Norman, F. Verplaetsen, J. Berghmans, Flame propagation and flow field measurements in a Hartmann dust explosion tube, Powder Technol. 323 (2018): 346-356.

[10] S. A. Morsi, A. J. Alexander, An investigation of particle trajectories in two-phase flow systems. J. Fluid Mech. 55(2) (1972) 193–208.

[11] M.A. Field, Rate of combustion of size-graded fractions of char from a low-rank coal between 1 200 K and 2 000 K. Combustion. Flame (1969) 237-52.

[12] C. T. Cloney, R. C. Ripley, M. J. Pegg, P. R. Amyotte, Laminar burning velocity and structure of coal dust flames using a unity Lewis number CFD model, Combustion. Flame 190 (2018) 87–102.

[13] Y. Pan, C. Spijker, H. Raupenstrauch, Investigations on the effect of particle size on dust dispersion in MIKE 3 apparatus, In: Proceedings of the 13th International Symposium on Hazards, Prevention and Mitigation of Industrial Explosions (ISHPMIE 2020), Braunschweig, Germany, pp, 654-662, 2020.

[14] H. Kern, G.J. Wieser, H. Raupenstrauch, Flame propagation in lycopodium/air mixtures below atmospheric pressure, J. Loss Prev. Process Ind. 36 (2015) 281–286.

[15] W. Pollhammer, C. Spijker, H. Kern, H. Raupenstrauch, Numerical investigation on heat transport while the ignition process of a dust/air mixture, In: The 26th International Symposium on Transport Phenomena, pp, 2–6, 2015.

# Hybrid-Mixture Explosions: Large-Scale Testing and Estimation of Reactivity Parameters

**Boeck L.R., Bauwens C.R.L., Dorofeev S.B.**

*FM Global, Research Division, Norwood, MA, USA.*
**Corresponding author's email: lorenz.boeck@fmglobal.com*

## ABSTRACT

Hybrid mixtures of combustible dusts with flammable gases/vapors present explosion hazards across various industries. To evaluate these hazards, and design appropriate explosion protection, it is often necessary to characterize reactivity parameters of hybrid mixtures, such as the deflagration index and the maximum explosion pressure. When test data for reactivity parameters are unavailable, simple methods are needed to estimate these parameters for engineering purposes.

Recently, a large-scale test setup was developed at FM Global to study hybrid-mixture explosions, and the initial results examining cornstarch-propane-air mixtures are discussed in this paper. These results, along with experimental literature data, are compared with existing estimation methods for reactivity parameters included in the NFPA 68 and EN 14491 standards and an improved method is proposed to reduce overly conservative estimates at gas/vapor concentrations below the lower flammability limit.

**KEYWORDS:** Explosions; Hybrid mixtures; Large-scale testing

## INTRODUCTION

Hybrid mixtures of combustible dusts with flammable gases/vapors and oxidizer pose explosion hazards in industries such as mining, power generation, pharmaceutical, agriculture and food, and other manufacturing (e.g., polymer, paint) [1]. Hybrid-mixture explosion hazards can exist both within process equipment, for example when a combustible dust is suspended and mixed with a vaporized solvent, or in larger enclosures, such as in mines where coal dust and methane gas may both be present.

### Reactivity parameters for explosion protection design

Reactivity parameters considered in the design of explosion protection for combustible dusts, such as explosion venting, include the dust deflagration index, $K_{St}$, and the maximum explosion pressure, $P_{max}$. The former represents the maximum rate of pressure rise, $(dP/dt)_{max}$, observed in a 1-m$^3$ vessel. The scaling to test volumes $V$ other than 1 m$^3$ is accounted for using the following relation [2]:

$$K_{St} = \left(\frac{dP}{dt}\right)_{max} V^{1/3} \quad (1)$$

Test standards including ASTM E1226 [3] provide methods for measuring $K_{St}$ of dust samples using standardized test equipment such as 20-L or 1-m$^3$ spheres. Dust reactivity is typically classified in groups, that is, St-1 ($K_{St}$ < 200 bar·m/s), St-2 (200 bar·m/s ≤ $K_{St}$ < 300 bar·m/s), or St-3 ($K_{St}$ ≥ 300 bar·m/s). Equation (1) is also often used to evaluate dust explosion tests performed in non-standard equipment, such as large-scale vessels, to obtain the test-specific effective deflagration index, $K_{eff}$. Although there are limitations to the use of empirical parameters such as $K_{St}$ and $K_{eff}$ in characterizing explosion reactivities, current explosion protection guidance largely relies on these parameters. The development of alternative methods for characterizing reactivity is an active area of research.

To determine the reactivity parameters of hybrid mixtures, standardized test equipment can be modified to pre-charge the explosion vessel with flammable gas/vapor before injecting dust and

igniting the hybrid mixture. While these small-scale tests provide an important relative comparison of reactivity between different hybrid mixtures for engineering purposes, the deflagration physics differ significantly between these tests and large-scale explosions. Additional tests need to be performed at realistic scales to study the phenomena governing industrial explosions.

For hybrid mixtures where test data are not available, methods are needed to estimate reactivity parameters for engineering purposes. NFPA 68 [4] and EN 14491 [5] provide such methods:

1. NFPA 68 estimates the deflagration index and maximum explosion pressure of hybrid mixtures at $K_h$ = 500 bar·m/s and $P_{max}$ = 10 bar(g), respectively, under the following conditions:
   - The flammable gas/vapor has a laminar burning velocity ≤1.3 times that of propane (according to NFPA 68: 1.3 × 0.46 m/s = 0.60 m/s), and
   - The combustible dust is characterized as St-1 or St-2.
2. EN 14491 allows for estimating the reactivity parameters at $K_h$ = 500 bar·m/s and $P_{max}$ = 10 bar(g), under the following conditions:
   - The flammable gas/vapor has a $K_g$ < 100 bar·m/s ($K_g$ is the deflagration index of the gas/vapor, obtained under initially quiescent conditions according to EN 15967 [6], where a value of 100 bar·m/s is representative of propane), and
   - The combustible dust has a $K_{St}$ < 300 bar·m/s, and
   - The "main component" of the hybrid mixture is the combustible dust.

**Published experimental studies on hybrid-mixture reactivity**

Previous studies on hybrid-mixture explosions and their reactivity parameters have evaluated a wide range of gases/vapors and dusts using mostly small-scale (20-L) and medium-scale (1-m$^3$) test equipment. Table 1 summarizes the test volumes, combustible dusts, and flammable gases/vapors used in published studies, whose data will be used in this work to evaluate methods for estimating reactivity parameters.

**Table 1:** Published experimental studies on hybrid-mixture explosions.

| Reference | Test volume | Dust | Gas/vapor |
|---|---|---|---|
| Bartknecht [2] | 1 m$^3$ | Cellulose,<br>Pea flour,<br>Optical brightener | Propane |
| Chatrathi [7] | 1 m$^3$ | Cornstarch | Propane |
| Kosinski et al. [8] | 20 L | Carbon black | Propane |
| Amyotte et al. [9,10] | 20 L | Polyethylene | Propane, Ethylene |
| Ji et al. [11] | 20 L | Lycopodium | Methane |
| Garcia-Agreda et al. [12] | 20 L | Nicotinic acid | Methane |
| Addai et al. [13] | 20 L | Lycopodium | Methane, Hydrogen |
| Sanchirico et al. [14] | 20 L | Nicotinic acid | Acetone |
| Hossain et al. [15] | 20 L | Microcrystalline cellulose (MCC),<br>Lactose | Ethanol, Methanol,<br>Isopropanol |
| Dufaud et al. [16] | 20 L | Magnesium stearate,<br>Nicotinic acid,<br>Antibiotic | Ethanol, Diisopropyl ether,<br>Toluene |

### Scope of this study

A large-scale test setup was developed at FM Global to study explosions of hybrid mixtures. A first series of tests with cornstarch-propane-air mixtures is discussed in this paper with a focus on reactivity parameters. Methods provided by NFPA 68 and EN 14491 standards for estimating reactivity parameters are then evaluated against experimental literature data and the data obtained in this study. Using these results, an improved method is proposed to reduce overly conservative estimates of deflagration indices at gas/vapor concentrations below the lower flammability limit.

## EXPERIMENTAL METHODOLOGY

This section introduces the test setup and procedure, discusses the choice of ignition source, provides the properties of the gas and dust fuels used, and summarizes the diagnostics.

### Test setup and procedure

Figure 1 shows a schematic of FM Global's 8-m$^3$ explosion vessel used in the present study, equipped with four dust injectors. Each injector assembly comprises a 150-L air cannon, a manifold that accepts a dust container, a fast-acting valve that isolates the injector from the vessel shortly before ignition, and a hemispherical perforated injection nozzle protruding into the vessel. Further connections at the vessel include supply lines for gaseous fuel and dry air, gas sampling, and vacuum. This system can perform dust, gas, or hybrid-mixture explosions.

To prepare for a hybrid-mixture explosion test, the vessel is flushed with dry air, supplied with gaseous fuel, and mixed using a circulation pump. The mixture composition is verified using gas sampling. Dust is loaded into the dust containers, all air cannons are pressurized with air, and the vessel is partially evacuated. All air cannons are fired to inject dust and generate turbulence inside the vessel, and ignition is triggered after a desired delay that controls the turbulence intensity at the time of ignition and therefore the effective reactivity of the mixture. Since air injection from the air cannons dilutes the gaseous fuel-air mixture, the mixture prepared before injection contains a pre-determined fuel concentration that exceeds the desired final concentration. Preliminary testing and gas sampling showed that the desired final fuel concentration is reached with an uncertainty of ±0.1% by volume.

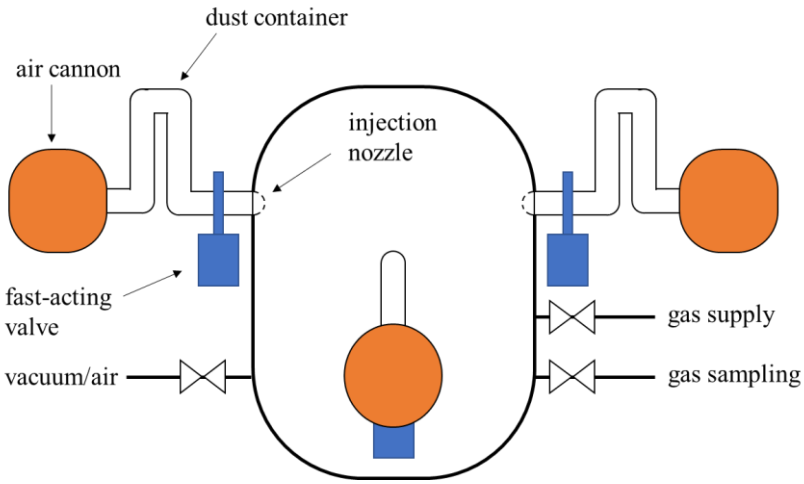


**Fig. 1:** Schematic of 8-m$^3$ vessel used in this study, including injection system and gas lines.

### Ignition source

This study used a standard ignition source commonly used for dust reactivity testing, which consists of two 5-kJ Sobbe chemical igniters, located at the center of the vessel. The igniters were oriented horizontally, facing the vessel side-walls in opposite directions. Tests were also performed where the total ignition energy was varied in a range between 2 kJ and 10 kJ, and no significant changes in the measured values of $K_{eff}$ or $P_{max}$ for turbulent cornstarch-air or propane-air mixtures were found.

### Gas and dust fuels

This study used propane and cornstarch as representative gas and dust fuels, respectively. Propane was instrument-grade, with a minimum purity of 99.5%. The cornstarch dust was submitted for reactivity testing according to ASTM E1226, resulting in a $K_{St}$ value of 155–166 bar m/s and $P_{max}$ of 7.9–8.1 bar(g), at an optimum concentration of 750 g/m$^3$. The dust was dried before large-scale testing to a maximum moisture content of 1% by weight.

### Diagnostics

Measurements of explosion pressure were taken using a piezoresistive pressure transducer (Kistler 4260A) located at the side of the vessel. Additional transducers near the top and bottom of the vessel were used to verify the measurement. The gas sampling system included a custom-built infrared absorption measurement and a speed-of-sound measurement (SRS BGA244) to measure the gas concentration in the vessel prior to dust injection.

## LARGE-SCALE EXPLOSION TEST RESULTS

The following sections discuss two series of explosion tests conducted at two different ignition delay times, 650 ms and 550 ms. In this test setup, these delays produce explosions representative of St-1 and St-2 hazards, i.e., the $K_{eff}$ of cornstarch at an optimum concentration (750 g/m$^3$) reaches values of 200 bar·m/s and 300 bar·m/s for 650 ms and 550 ms ignition delays, respectively. The concentrations of cornstarch (0 g/m$^3$; 100 g/m$^3$; 750 g/m$^3$) and propane (0%; 1.05%; 2.1%; 3.0%; 4.0%; 5.0% by volume) were varied for each ignition delay to investigate the effect of the hybrid-mixture composition on the reactivity parameters $K_{eff}$ and $P_{max}$.

### Reactivity parameters at 650 ms ignition delay

The reactivity parameters $K_{eff}$ and $P_{max}$ at 650 ms ignition delay are shown in Figs. 2(a) and 2(b), respectively, for propane-air mixtures without dust (0 g/m$^3$ CS), mixtures with a low concentration of dust (100 g/m$^3$ CS), and an optimum dust concentration (750 g/m$^3$ CS). Two tests were performed for each condition.

The optimum concentration of dust shows $K_{eff} \approx 200$ bar·m/s at 0% propane, see Fig. 2(a), and a moderate increase with increasing propane concentration, peaking at about 3% propane and 253–285 bar·m/s, and decreasing toward higher propane concentrations. The series of tests at low dust concentration show a strong increase in $K_{eff}$ with increasing propane concentration, from 30–34 bar·m/s at 0% to 407–459 bar·m/s at 5% propane, which is driven by the reactivity of the gas component. Hybrid mixtures with low dust concentration exceed the deflagration indices of pure propane-air mixtures throughout the entire range of tested concentrations. At 100 g/m$^3$ dust concentration and 5% propane, the value of $K_{eff}$ averaged between the two tests conducted at this condition exceeds the average value of $K_{eff}$ for pure propane by 9%.

Figure 2 (b) summarizes $P_{max}$ values. At optimum dust concentration, addition of propane leads to a decrease of $P_{max}$, whereas at low dust concentration, addition of propane increases $P_{max}$. Likewise, $P_{max}$ increases for pure propane-air mixtures with increasing propane concentration. The peak value of $P_{max}$ within this series of tests occurs at the optimum dust concentration and 0% propane.

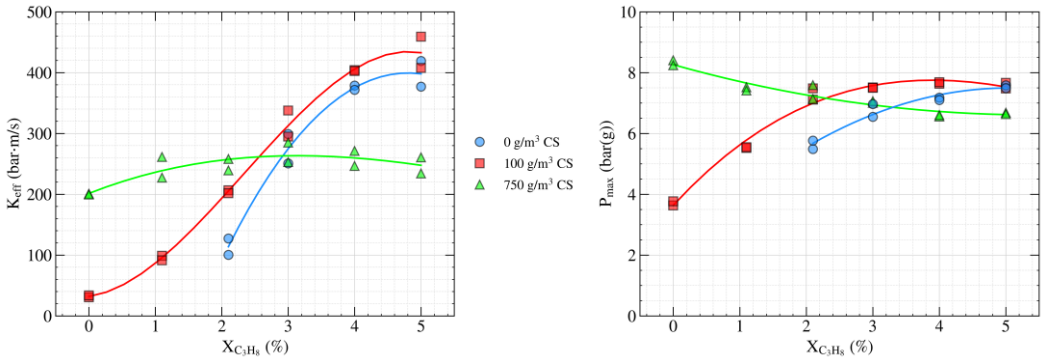


**Fig. 2:** Reactivity parameters at 650 ms ignition delay. $K_{eff}$, left panel (a), and $P_{max}$, right panel (b).

**Reactivity parameters at 550 ms ignition delay**

Selected mixture compositions were tested at a shorter ignition delay time of 550 ms, to investigate the effect of initial turbulence. Reactivity parameters are shown in Fig. 3.

As expected, the values of $K_{eff}$ at a delay of 550 ms, see Fig. 3(a), exceed those observed at 650 ms delay due to higher initial turbulence. The optimum concentration of dust shows $K_{eff} \approx 300$ bar·m/s at 0% propane and a slightly lower value of 272–284 bar·m/s at 5% propane. Further testing would be needed to investigate the cause of this decrease in $K_{eff}$, compared to the relative increase observed at 650 ms delay. At 100 g/m$^3$ dust concentration, $K_{eff}$ ranges from 37–45 bar·m/s at 0% propane to 526–585 bar·m/s at 5% propane. Pure propane at a 5% concentration reaches comparable $K_{eff}$ values of 532–559 bar·m/s.

Values of $P_{max}$ shown in Fig. 3 (b) are generally similar to the values observed at 650 ms ignition delay, which indicates that the faster rate of combustion at 550 ms delay does not lead to significant changes in the magnitude of heat loss experienced during the explosion.

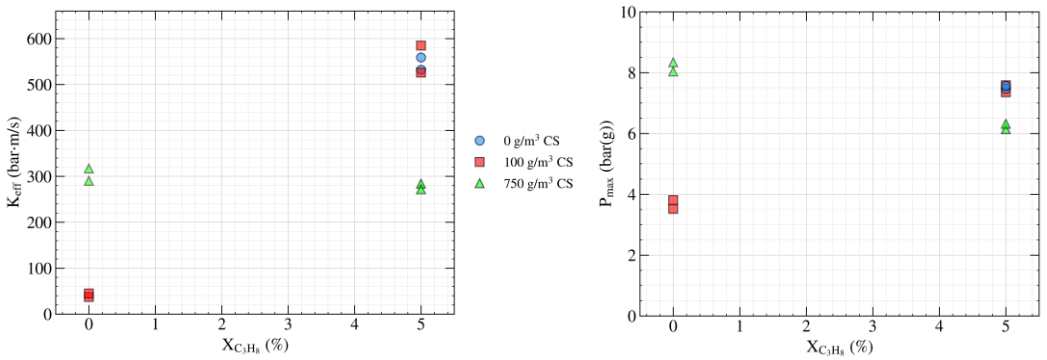


**Fig. 3:** Reactivity parameters at 550 ms ignition delay. $K_{eff}$, left panel (a), and $P_{max}$, right panel (b).

## DISCUSSION

This section evaluates the methods provided in NFPA 68 and EN 14491 for estimating the hybrid-mixture deflagration index against experimental data, proposes an improved method that reduces overly conservative estimates at low gas/vapor concentrations and, lastly, discusses representative values of maximum explosion pressure.

### NFPA 68 and EN 14491 estimates of the deflagration index

Figure 4 shows a comparison between experimental data ($_{EXP}$) and estimates from NFPA/EN standards ($_{NFPA/EN}$) for the deflagration indices of hybrid mixtures, $K_h$, as a function of volumetric gas/vapor concentration, $X$, normalized by the concentration at the lower flammability limit, $X_{LFL}$, of each gas/vapor in air. Estimates are conservative for gas/vapor concentrations below the LFL where experimental values are over-estimated by up to 470%. Above the LFL, NFPA/EN estimates are conservative for 71% of all considered data points. The maximum under-prediction of 34% occurs for a hybrid mixture of carbon black with propane [8].

Overall, the NFPA/EN estimates provide a reasonable upper bound to the experimental deflagration indices for the present hybrid mixtures. At low gas/vapor concentrations, however, the methods can significantly over-predict $K_h$, which can lead to unnecessarily conservative and potentially infeasible explosion protection designs and excessive cost.

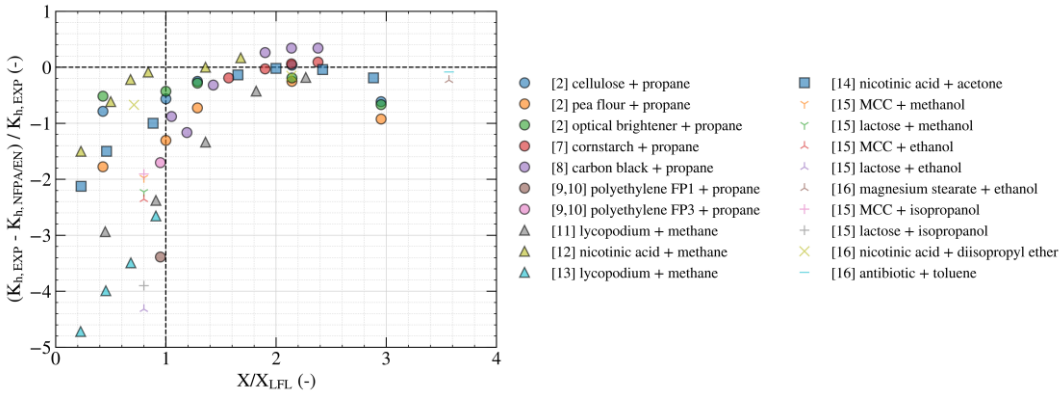


**Fig. 4:** Comparison between experimental literature values of $K_h$ and estimates from NFPA/EN methods.

### Improved engineering method for estimating the deflagration index

An improved engineering method is proposed for estimating hybrid-mixture deflagration indices, which reduces the overly conservative estimates of the NFPA/EN methods at low gas/vapor concentrations. The method estimates $K_h$ based on the deflagration index of the dust involved, $K_{St}$, by increasing the $K_{St}$ value by empirical margins that depend on the concentration of the flammable gas/vapor.

The hybrid-mixture deflagration index, $K_h$, is estimated as follows:

1) When the hybrid mixture has a gas/vapor concentration less than the gas/vapor LFL, assume $K_h = K_{St} + 150$ bar·m/s.
2) When the hybrid mixture has a gas/vapor concentration between the gas/vapor LFL and 1.5 times the LFL, assume $K_h = K_{St} + 300$ bar·m/s.
3) When the hybrid mixture has a gas/vapor concentration greater than 1.5 times the gas/vapor LFL and the gas/vapor has a fundamental burning velocity of 0.5 m/s or less, assume $K_h$ = max ($K_{St} + 300$ bar·m/s ; 500 bar·m/s).

To prevent under-conservative estimates, this method should not be applied for metal dusts or gas/vapor concentrations higher than 1.5 times the gas/vapor LFL if the fundamental burning velocity of the gas/vapor at optimum concentration exceeds 0.5 m/s.

Figure 5 compares the estimates from the proposed method ($_{FM}$) against experimental data ($_{EXP}$). Below the LFL, the proposed method yields significantly more realistic predictions than the NFPA/EN methods. Above the LFL, predictions are comparable to NFPA/EN. Additional data are included in this comparison for hybrid mixtures containing hydrogen [13] and ethylene [9,10] at concentrations below the LFL, showing conservative estimates using the proposed method.

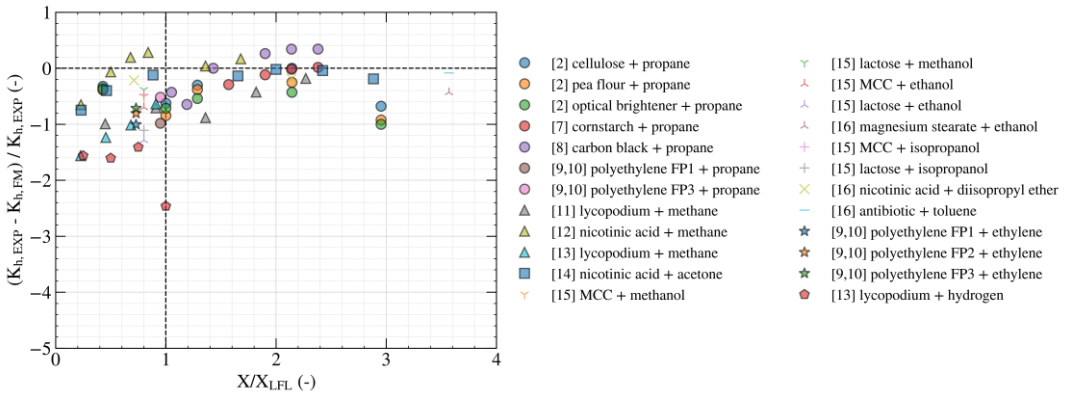


**Fig. 5:** Comparison between experimental literature values of $K_h$ and estimates from the proposed method.

Similar to the comparison against small-scale and medium-scale literature data, the proposed method can be evaluated against the large-scale experimental data obtained in this work for cornstarch-propane-air mixtures. To consider the inherent differences between standardized small-scale setups and large-scale tests, including the differences in initial turbulence at different ignition delays, the effective deflagration index $K_{eff}$ of the dust at 0% propane measured in the large-scale test is used in lieu of the dust $K_{St}$ to exercise the estimation method. Figure 6 compares experimental ($_{EXP}$) and estimated ($_{FM}$) values of $K_{eff}$. The proposed method provides conservative estimates, accounting for the effects of dust and gas concentrations and ignition delay.

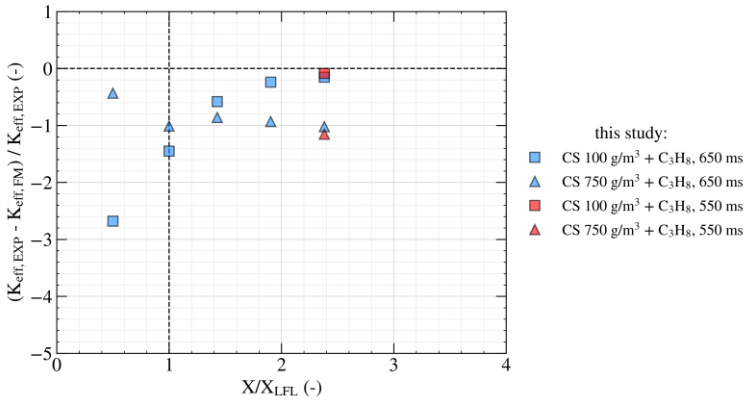


**Fig. 6:** Comparison between large-scale experimental values of $K_{eff}$ (averaged between pairs of tests for each condition) and estimates from the proposed method.

While the proposed method can be used to estimate deflagration indices of hybrid mixtures for a wide range of gases/vapors and dusts, it remains preferable to obtain reactivity parameters of hybrid mixtures experimentally, using standardized test equipment.

**Representative values of maximum explosion pressure**

Experimental values of maximum explosion pressure, $P_{max}$, were collected from the literature and the present large-scale explosion tests and are summarized in Fig. 7 with values ranging between about 6 bar(g) and 10 bar(g) and a most representative value of about 8 bar(g). NFPA 68 and EN 14491 standards estimate $P_{max}$ at 10 bar(g), which provides an upper bound to the present experimental data.

Whether this upper bound is a reasonable value to be used for explosion protection design, depends on the application:

- Designs of explosion containment should generally be based on a high estimate of $P_{max}$; the NFPA/EN methods therefore provide a reasonable estimate for the mixtures included in Fig. 7, and similar mixtures with comparable energetics.
- For designing explosion venting, the specific mathematical vent-sizing method used should be reviewed to determine whether a high or low estimate of $P_{max}$ results in a conservative vent size.

Metal dusts, which often produce values of $P_{max}$ exceeding 10 bar(g), are not covered by the NFPA/EN methods or the present experimental data and should be addressed individually.

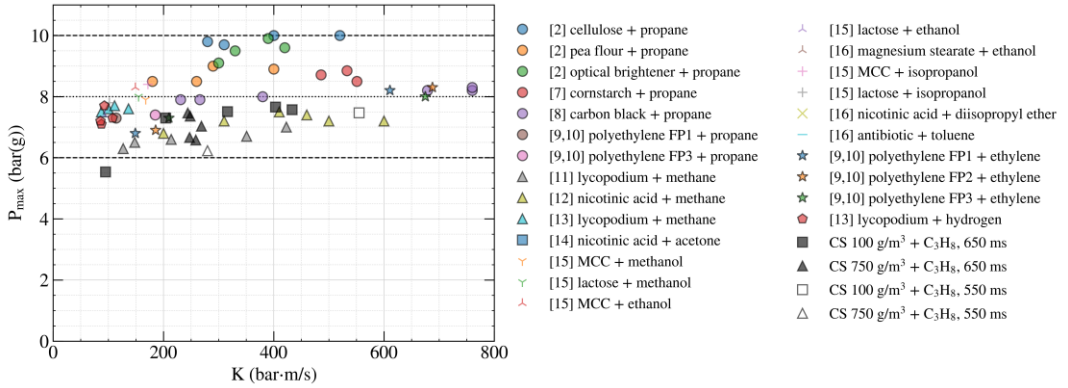


**Fig. 7:** Summary of maximum explosion pressures from literature studies and present large-scale tests.

## CONCLUDING REMARKS

This study examined hybrid-mixture explosions with a focus on reactivity parameters, i.e., the deflagration index and maximum explosion pressure, using large-scale experiments in an 8-m$^3$ explosion vessel and a survey of literature studies. These reactivity parameters are needed when assessing explosion hazards and designing explosion protection, and are obtained either from standardized testing or estimated when test data are unavailable. Available methods for estimating these parameters were evaluated and an improved method was proposed in this paper.

Large-scale experiments were performed with cornstarch-propane-air mixtures in a wide range of propane (1.05%–5.0%) and cornstarch (0 g/m$^3$; 100 g/m$^3$; 750 g/m$^3$) concentrations. A worst-case composition of 5% propane and 100 g/m$^3$ cornstarch produced deflagration indices of 407–459 bar·m/s and 526–585 bar·m/s for ignition delays of 650 ms and 550 ms, respectively. The maximum explosion pressure among all conditions was 8.4 bar(g) for a mixture of 750 g/m$^3$ cornstarch and 0% propane.

The comparison of methods from the NFPA 68 and EN 14491 standards, used to estimate reactivity parameters for hybrid mixtures, with experimental literature data showed that these methods are overly conservative for mixtures with gas/vapor concentrations below the lower flammability limit. An improved method was presented that considers the concentration of gas/vapor and the reactivity of the dust to estimate the deflagration index. This method significantly improves the quality of predictions especially below the lower flammability limit, which will result in more accurate explosion risk assessments and allow for more feasible explosion protection designs.

Future work should continue to address the gap between small-scale reactivity testing and the significantly larger scales of industrial hybrid-mixture explosions at realistic turbulence conditions. Advanced reactivity concepts should be developed that allow for predicting the dynamics of hybrid-mixture explosions and their consequences.

## REFERENCES

[1] R. K. Eckhoff, Dust Explosions in the Process Industries, Gulf Professional Publishing, 2003.

[2] W. Bartknecht and G. Zwahlen, Dust Explosions: Course, Prevention, Protection, Springer, New York, 1989.

[3] ASTM E1226-19 Standard Test Method for Explosibility of Dust Clouds, ASTM International, West Conshohocken, PA, 2019.

[4] NFPA 68 Standard on Explosion Protection by Deflagration Venting, National Fire Protection Association, Quincy, MA, 2018.

[5] EN 14491 Dust Venting Protective Systems, European Committee for Standardization, Brussels, 2012.

[6] EN 15967 Determination of Maximum Explosion Pressure and the Maximum Rate of Pressure Rise of Gases and Vapours, European Committee for Standardization, Brussels, 2011.

[7] K. Chatrathi, Dust and Hybrid Explosibility in a 1 $m^3$ Spherical Chamber, Process Saf Prog. 3 (1994) 183–189.

[8] P. Kosinski, R. Nyheim, V. Asokan and T. Skjold, Explosions of Carbon Black and Propane Hybrid Mixtures, J Loss Prevent Proc. 26 (2013) 45–51.

[9] P. Amyotte, M. Lindsay, R. Domaratzki, N. Marchand, A. Di Benedetto and P. Russo, Prevention and Mitigation of Dust and Hybrid Mixture Explosions, Process Saf Prog. 29 (2010) 17–21.

[10] P. Amyotte, N. Marchand, A. Di Benedetto and P. Russo, Influence of Particle Size and Ethylene Admixture on Polyethylene Dust Explosions, in Proceedings of Seventh International Symposium on Hazards, Prevention, and Mitigation of Industrial Explosions, St. Petersburg, Russia, 2008.

[11] W. Ji, J. Yu, X. Yu, Y. Hou and X. Yan, Explosion Venting of Hybrid Mixtures: A Comparison of Standards NFPA 68 and EN 14491, J Loss Prevent Proc. 54 (2018) 325–332.

[12] A. Garcia-Agreda, A. Di Benedetto, P. Russo, E. Salzano and R. Sanchirico, Dust/Gas Mixtures Explosion Regimes, Powder Technol. 205 (2011) 81–86.

[13] E. K. Addai, A. Aljaroudi, Z. Abbas, P. Amyotte, A. Addo and U. Krause, Investigation of the Explosion Severity of Multiphase Hybrid Mixtures, Process Saf Prog. 39 (2020).

[14] R. Sanchirico, A. Di Benedetto, A. Garcia-Agreda and P. Russo, Study of the Severity of Hybrid Mixture Explosions and Comparison to Pure Dust-Air and Vapour-Air Explosions, J Loss Prevent Proc. 24 (2011) 648–655.

[15] M. N. Hossain, P. Amyotte, M. Abuswer, A. Dastidar, F. Khan, R. Eckhoff and Y. Chunmiao, Influence of Liquid and Vapourized Solvents on Explosibility of Pharmaceutical Excipient Dusts, Process Saf Prog. 33 (2014) 374–379.

[16] O. Dufaud, M. Perrin, M. Traore, S. Chazelet and D. Thomas, Hybrid Mixtures Explosions: When Vapours Met Dusts, in IChemE Symposium Series No. 153, 2007.

# Micro-explosions: Simple Models of Complex Phenomena

**Sazhin S.S.[1,*], Bar-Kohany T.[2,3], Antonov D.V. [4], Strizhak P.A.[4]**

*[1] Advanced Engineering Centre, School of Architecture, Technology and Engineering, University of Brighton, Brighton, BN2 4GJ, UK.*
*[2] School of Mechanical Engineering, Tel Aviv University, Tel Aviv, Israel.*
*[3] Mechanical Engineering Department, nrcn, Israel.*
*[4] National Research Tomsk Polytechnic University, Lenin Avenue, Tomsk 634050, Russia*
**Corresponding author's email: S.Sazhin@brighton.ac.uk*

## ABSTRACT

Recent developments in the modelling of puffing and micro-explosions are reviewed. The focus is on relatively simple models, compared with Direct Numerical Simulations, which, despite their simplicity, are able to capture the most important features of the phenomena. The most recent model is based on the analytical solution to the one-dimensional heat transfer equation in a composite droplet, assuming that a spherical water sub-droplet is placed exactly in the centre of a spherical fuel droplet. The analytical solution to this equation with the Robin boundary condition at the droplet surface was obtained, implemented into the numerical code, and used at each time step of the calculations. The effects of thermal swelling and evaporation, using the Abramzon and Sirignano model, are considered. The radiative heating of the droplet is considered assuming that the droplet is semi-transparent. The effect of a supporting wire is taken into account assuming that heat supplied from the wire is distributed instantaneously and homogeneously throughout the whole droplet volume. The effect of relative movement between the droplet and gas is taken into account considering a non-self-consistent model, in which this effect on the Nusselt and Sherwood numbers was considered but not on the recirculation inside the droplet. The start of puffing/micro-explosion is linked with the time instant when the temperature at the water/rapeseed oil interface reaches the water nucleation temperature. The model predictions are shown to agree with experimental data referring to times to puffing/micro-explosion for droplets placed in ethanol (temperature 1,120 K) and propane/butane mixture (temperature 1,400 K) flames.

**KEYWORDS:** Droplets, puffing, micro-explosion, nucleation temperature.

## NOMENCLATURE

$c$ specific heat capacity (J/(kg·K))
$h$ heat transfer coefficient (W/(m$^2$·K))
$k$ thermal conductivity (W/(m·K))
$Ja$ Jakob number
$L$ latent heat of evaporation (J/kg)
$P$ source (radiation) term in Eq. (1) (K/s)
$R$ distance from the droplet centre (m)
$R_d$ droplet radius (m)
$T$ temperature (K)
$t$ time (s)

**Greek**
$\kappa$ thermal diffusivity (m$^2$/s)
$\rho$ density (kg/m$^3$)
$\tau_p$ time to puffing/micro-explosion (s)

**Subscripts**
$B$ boiling
$d$ droplet
$eff$ effective
$g$ gas
$f$ liquid fuel
$N$ nucleation
$s$ surface
$v$ vapour
$w$ water
0 initial

## INTRODUCTION

Adding water into fuel droplets is known to lead to their puffing (partial disintegration into relatively large child droplets) and micro-explosion (complete disintegration leading to the formation of a cloud of aerosols). Typical images of these processes are shown in Figure 1. The experiments were performed in a heated furnace in which the droplets were supported by a nickel-chromium alloy wire of 0.2 mm diameter as in the experimental setup described in [1]. The initial droplet temperatures were 300 K; the initial droplet radii were about 0.95 mm. The ambient pressure was atmospheric, assumed to be equal to 101325 Pa; the ambient temperature was 850 K.

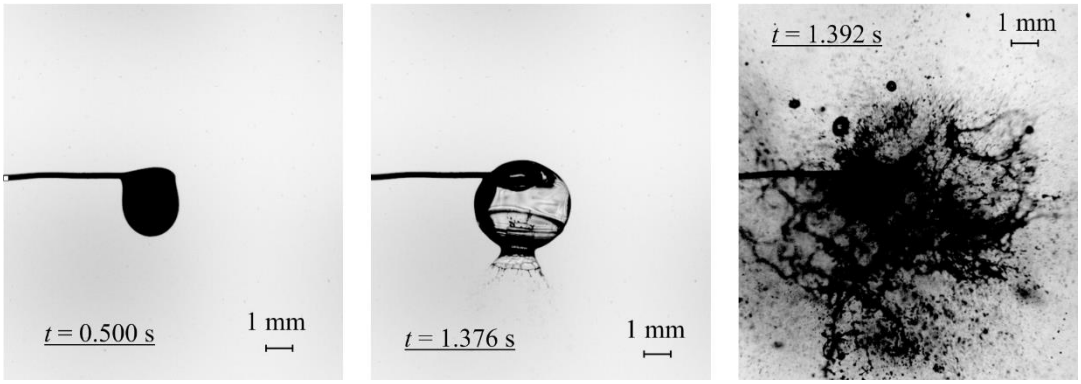


**Fig. 1.** Typical dynamics of puffing/micro-explosion in the experiments performed at National Research Tomsk Polytechnic University (rapseed oil (90%) + water (10%)).

The processes shown in Figure 1 can be considered within the wider framework of explosions, which are the focus of this seminar. The main motivations for investigating these processes have been the need to understand the underlying physics, and also the volume of potential engineering applications which include the control of combustion and fire extinguishing processes.

Puffing and micro-explosion lead to a rapid increase in the liquid fuel surface area. This in turn leads to an increase in the fuel evaporation rate and the formation of a homogeneous fuel vapour/air mixture. The latter is important for improving the efficiency of combustion technologies including those used in internal combustion engines [2,3]. The effects produced by puffing and micro-explosion lead to a reduction in fuel consumption, improved fuel/air mixing and reduction of harmful emissions [4].

The contributions of puffing and micro-explosion in the extinguishing of fires have been discussed in many papers including [5-7].

The importance of these processes in these and many other applications led to extensive experimental and theoretical studies of the phenomena, the results of which are presented in numerous research papers, including [8,9]. The most advanced models of the phenomena are based on Direct Numerical Simulation (DNS) (e.g. [10,11]). Although these models are essential for understanding many of the fine details of the processes they also have many well known limitations. The predictions of these models depend on the initial and boundary conditions, which are difficult to accurately specify in most applications. Also, the underlying physics of individual processes becomes hidden behind the complexity of the whole event.

In a series of our previous papers, starting with [12,13], an alternative approach to modelling puffing and micro-explosion was developed. In this approach, relatively simple models of the phenomena were developed which, nevertheless, were able to capture the underlying physics of the processes and predict the parameters that were measureable in the experiments (e.g. times to puffing/micro-

explosion). This approach complements similar approaches to the modelling of other processes in droplets and sprays described in [14,15] and summarised in a presentation by one of the author (SSS) at ISFEH 9 in St Petersburg [16].

This paper primarily summarises the results of the developments of these models since 2019.

## SIMPLE ANALYTICAL MODEL

The model for the puffing/micro-explosion of water-fuel droplets, suggested in [12], assumes that a spherical water sub-droplet is in the centre of a larger n-dodecane droplet, as schematically presented in Figure 2.

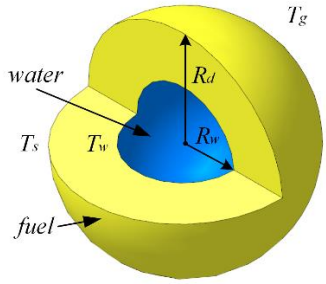


**Fig. 2.** Scheme showing the location of a water sub-droplet of radius $R_w$ inside a fuel droplet of radius $R_d$. $T_w$ is the temperature at the interface between the water and the fuel, $T_s$ is the droplet surface temperature.

The following heat conduction equation for temperature $T(t,R)$ inside this composite droplet was solved:

$$\frac{\partial T}{\partial t} = \frac{\kappa}{R^2}\frac{\partial}{\partial R}\left(R^2\frac{\partial T}{\partial R}\right) + P(t,R), \quad (1)$$

where $\kappa$ ($\kappa = \kappa_w = k_w/(c_w\ \rho_w)$ when $R \le R_w$ and $\kappa = \kappa_f = k_f/(c_f\ \rho_f)$ when $R_w < R \le R_d$) is the liquid thermal diffusivity, $k_{w(f)}$, $c_{w(f)}$, and $\rho_{w(f)}$ are the water (liquid fuel) thermal conductivity, specific heat capacity, and density, respectively, $R$ is the distance from the centre of the spherical droplet, $t$ is time. $P(t,R)$ takes into account the contribution of the volumetric heating (e.g. by thermal radiation).

The Dirichlet boundary condition
$T(R= R_d) = T_s$ (2)
and the initial condition
$T(t=0) = T_{d0}(R)$, (3)
were used to solve Equation (1). The temperature dependence of transport properties was ignored. These properties were taken equal to those at the initial values of temperature. Droplet evaporation was not considered.

These assumptions allowed the authors of [12] to obtain the analytical solution to Equation (1) describing the distribution of $T(t,R)$ in the form of a quickly converging series. The time instant when $T = T_B$, where $T_B$ is the boiling temperature of water, was associated with the start of the puffing/micro-explosion process. The contribution of $P(t,R)$ was not considered in the initial application of the model.

An example of the application of this approach is given in Figure 3. In the case shown in Figure 3, the time to puffing/micro-explosion is predicted equal to 0.5 ms. This prediction and similar predictions for other values of input parameters were shown to be in qualitative agreement with experimental data in some cases [12]. In many other practically important cases, however, the difference between the predictions of the model and experimental data was too large to justify the

usefulness of the model for practical applications. This stimulated further developments of this model leading to the simple numerical model described in the next section.

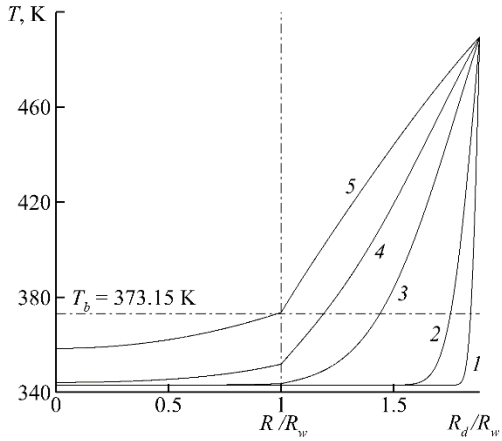


**Fig. 3.** Typical plots of temperatures inside the composite droplet ($T$) versus normalised distance from the droplet centre at 5 instants of time: 1.1 μs (curve 1), 11 μs (curve 2), 0.11 ms (curve 3), 0.25 ms (curve 4) and 0.5 ms (curve 5). Reprinted from [12], Copyright Elsevier (2019).

## SIMPLE NUMERICAL MODEL

The authors of [13] relaxed several important assumptions of the model described in the previous section, which limited its practical applicability, although the models developed in both [12] and [13] are based on the same geometry as shown in Figure 2.

First, the model in [13] is based not on the Dirichlet boundary condition, as in the model described above, but on the Robin boundary condition at the surface of the fuel droplet:

$$h\left(T_g - T_s\right) = k_f \frac{\partial T}{\partial R}|_{R=R_d}, \quad (4)$$

where $T_g = T_g(t)$ is the ambient gas temperature, $h = h\ (t)$ is the convective heat transfer coefficient. This allowed the authors of [13] to obtain an analytical solution to Equation (1) which was different from the one obtained in [12].

Second, the effects of evaporation and the temperature dependence of thermodynamic and transport properties of water and liquid fuel were considered. The effect of swelling was taken into account. The Abramzon and Sirignano model (see [14] for the details) was used assuming that the droplet was stationary. To consider the effect of evaporation in the analytical solution obtained in [13], the gas temperature $T_g$ was replaced with the so-called effective temperature:

$$T_{eff} = T_g + \rho_f L \frac{dR_d}{dt} / h,$$

where $L$ is the latent heat of evaporation and $\frac{dR_d}{dt}$ is the rate of change of droplet radius due to evaporation.

Third, the assumption made in [12], that puffing/micro-explosion starts when the temperature at the water/fuel interface reaches the water equilibrium boiling (saturation) temperature $T_B$, was replaced in [13] with a more realistic assumption, that it starts when this temperature reaches the heterogeneous nucleation temperature $T_N$, which is higher than $T_B$. The Onset of Nucleate Boiling temperature, referred to here as the nucleation temperature, pertains to quasi-steady processes, where the liquid is in the metastable region, which means it is kinetically stable, rather than thermodynamically stable

**Error! Reference source not found.**. A higher nucleation temperature implies a higher Jakob number $\left(Ja \equiv \frac{\rho_f c_f (T_N - T_B)}{\rho_v L}\right)$, which equates to a greater driving force for bubble growth **Error! Reference source not found.**. This, along with the effect on the time to nucleation, and hence the growth duration, may affect the size of the bubbles that will eventually cause micro-explosions and puffing.

In contrast to the model described in [12], the second assumption of the model described in [13] does not allow the application of the analytical solution during the whole period preceeding the onset of puffing/microexplosion. This solution, however, can be incorporated into a numerical code and used at each individual time step of the calculation. The prediction of the solution at the end of each time step is used as the initial condition for the following time step with adjusted values of droplet radius and thermodynamic and transport properties. Thus the model is called the simple numerical model. The following approximations of $T_N$ for water were given in [13]:

$$T_N = T_B + 0.37\,\dot{T}^{10/626} \quad \text{when} \quad 10^5 \le \dot{T} \le 10^9 \tag{5}$$

$$T_N = 375 + 160\tanh(\dot{T}/10^5) \quad \text{when} \quad 10^2 \le \dot{T} \le 10^6 \tag{6}$$

$$T_N = T_B + 12\tanh(\dot{T}/50) \quad \text{when} \quad 0 \le \dot{T} \le 300, \tag{7}$$

where $\dot{T}$ is the heating rate (in K/s).

The plots of $T_N$ versus $\dot{T}$ predicted by (5) – (7) are shown in Figures 4 and 5. The experimental data presented in [13] and by other groups (see the references in [13]) are shown in the same figures.

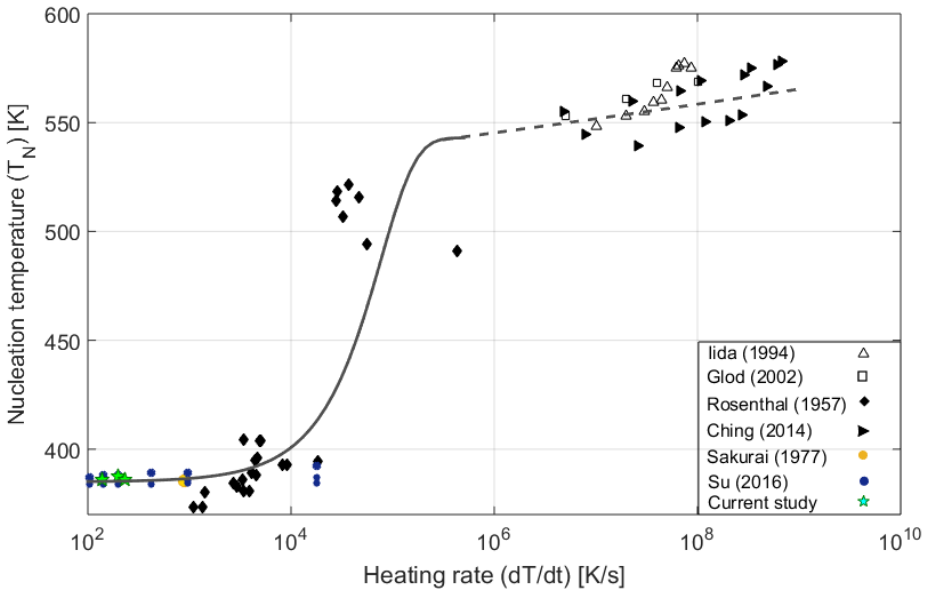


**Fig. 4.** Nucleation temperature $T_N$ versus heating rate $\dot{T} = dT/dt$. – A comparison between predictions by Expressions (5) (dashed) and (6) (solid), experimental data obtained in [12] (Current study), and six other groups (references are given in [13]). Reprinted from [13], Copyright Elsevier (2020).

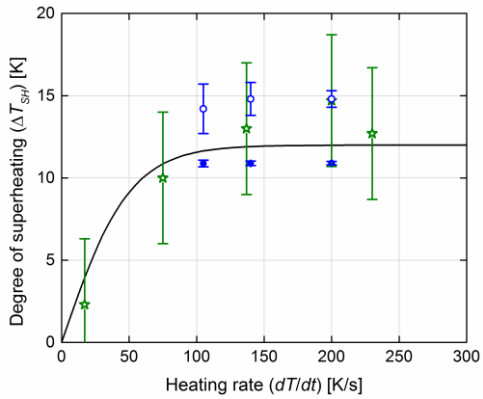


**Fig. 5.** Nucleation temperature $T_N$ versus heating rate $\dot{T} = \frac{dT}{dt}$. A comparison between predictions by Expression (7), experimental data presented in [13] (stars) and another group (filled and empty circles) (the reference is given in [13]). Reprinted from [13], Copyright Elsevier (2020).

As follows from Figures 4 and 5, approximations (5)-(7) agree reasonably well with experimental data in a wide range of $\dot{T}$ from zero to $10^9$. The main attraction of Formulae (5)-(7) for our application is that in all cases $T_N$ depends on a single parameter $\dot{T}$. On the other hand, the analytical solution to (1), subject to the initial condition (3) and boundary condition (4), predicts not only the values of $T$ at all points inside the droplet but also the values of $\dot{T}$ at these points. Remembering (5)-(7), this means that this solution predicts both $T$ and $T_N$ at all points, including the water-fuel interface.

It should be noted that composite droplets in our experiments contain micron-sized organic dye particles (Rhodamine B). These particles pose as nucleation sites ("ready-centres"), and thus lower the energy boundary that must be reached for the formation of a new phase. These colloids and other impurities determine the nucleation site density and limit the maximal heating rate and the maximal heterogeneous nucleation temperature. Having said this, the values of $T_N$ inferred from Correlations (5)-(7) are not expected to be very sensitive to these effects and they can be used for the analysis of our experimental data. Correlations (5)-(7) implicitly take into account the presence of impurities in the system.

Assuming that puffing/micro-explosion is initiated at the water/fuel interface when the temperature at this interface $T_w$ becomes equal to $T_N$, this opens the way to the estimation of the time to puffing/micro-explosion. The procedure is illustrated in Figure 6, where the time dependencies of the surface temperature $T_s$, temperature at the water/fuel interface $T_w$, water nucleation temperature $T_N$ and water boiling temperature $T_B$ are shown for n-dodecane/water droplets with initial radii and temperature equal to 5 μm and 300 K, respectively, and with the volume fraction of water equal to 15%, placed in gas at atmospheric pressure and temperature 700 K.

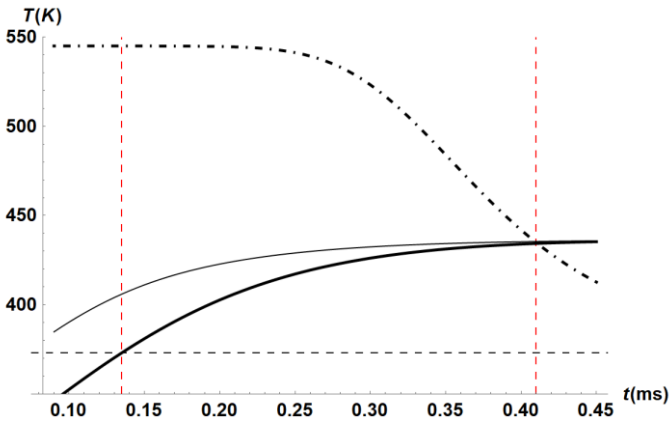


**Fig. 6.** The plots of time evolution of $T_w$ (thick solid), $T_s$ (thin solid), $T_N$ (dashed-dotted) and $T_B$ (horizontal dashed line); the vertical dashed lines show the time instant when $T_w = T_B$ and $T_w = T_N$. Reprinted from [13], Copyright Elsevier (2020).

The intersection between the curves $T_w(t)$ and $T_N(t)$ in Figure 6 shows the time to puffing/micro-explosion if these processes start when $T_w(t)=T_N(t)$. As follows from this figure, this time is more than three times longer than the time to puffing/micro-explosion predicted when $T_w(t)=T_B(t)$. This supports the need to use the model in which puffing/micro-explosion is predicted when $T_w(t)=T_N(t)$.

## FURTHER DEVELOPMENTS OF THE SIMPLE NUMERICAL MODEL

The model described in [13] was generalised in a non-self-consistent way by the authors of [16] to consider the effect of gas velocity around droplets. In this generalisation the convection heat and mass transfer coefficients were inferred from the Abramzon and Sirignano model considering the non-zero velocity between droplets and gas [14]. At the same time the recirculation of the liquid inside the droplet was ignored.

The authors of [20] generalised the model to the case of up to three droplets following one another in a flow, based on the above-mentioned non-self-consistent model.

The authors of [21] further generalised the model to consider the effects of thermal radiation and droplet support. In the latter case, the model developed earlier in [22] was used. The contribution of thermal radiation from remote flames is particularly important in the case of droplet ignition in Diesel engines during late injection and in the process of extinguishing fire.

The authors of [23] suggested a simple model for the puffing and micro-explosion of composite multi-component water/liquid fuel droplets. As in the case of the earlier suggested models, the new model is based on the assumption that a spherical water sub-droplet is located in the centre of a spherical fuel droplet. The equation for species diffusion inside the fuel shell is solved analytically, and this solution is incorporated into the numerical code and used at each time step of the calculations.

The model developed in [13] was verified based on a comparison of the predictions of this model with those of a numerical code for solving the same heat transfer problem in a fuel-water droplet (using the heat transfer module available from COMSOL software) [24]. Almost perfect agreement between the predictions of both codes supported the validity of both approaches to the problem [24].

The above-mentioned numerical code, based on COMSOL, was generalised to consider a shift of the water sub-droplet away from the centre of the fuel droplet. The heat transfer equation was solved in

the cylindrical coordinate system with the *z*-axis being the line joining the centre of the fuel droplet to that of the water sub-droplet, using a simplifying assumption that the surface temperature of the fuel droplet is uniform although it can change with time [24].

The size of the shift $L$ (distance between the centres of the fuel droplet and water sub-droplet) was inferred from experimental observations. It was demonstrated that in most cases the time to puffing/micro-explosion predicted by the model with a shift is closer to experimental results than that predicted by the model based on the assumption that the water sub-droplet is located in the centre of the fuel droplet. The shift was quantified by the normalised shift, defined as $S=L/L_{max}$, where $L_{max}$ is the maximal value of $L$. It was shown that, for typical values of input parameters for $S \leq 0.2$, the predictions of the original (based on the assumption that the water sub-droplet is located exactly in the centre of the fuel droplet) and new models differ by less than 1% [24].

## MODELLING VERSUS EXPERIMENTAL DATA

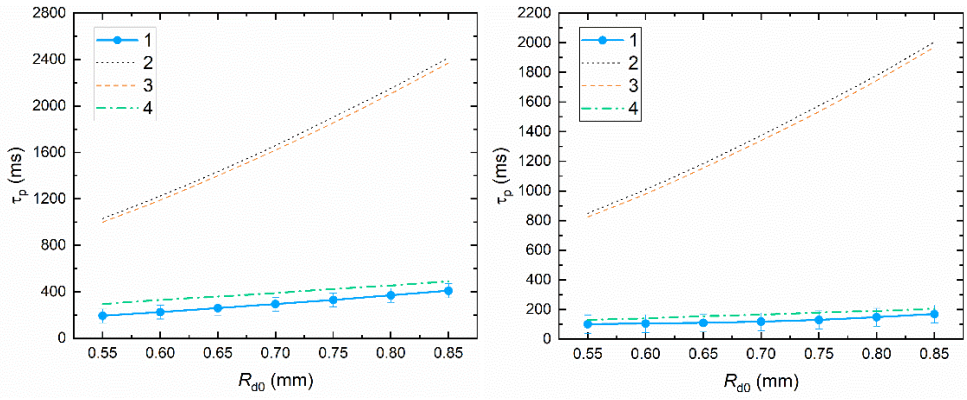


(a) (b)

**Fig. 7.** The times to puffing/micro-explosion of composite rapeseed oil/water droplets introduced into ethanol (a) and propane/butane mixture (b) flames versus droplet radii. Curves 1 show the experimental data; curves 2 show the predictions of the model when the effects of radiation and support were ignored; curves 3 show the predictions of the model when the effects of the support were taken into account but the effects of radiation were ignored; curves 4 show the predictions of the model when the effects of radiation and support were taken into account. Reprinted from [21], Copyright Elsevier (2021).

A comparison between experimentally observed and predicted times to puffing/micro-explosion ($\tau_p$) for droplets placed in ethanol (temperature 1,120 K) and propane/butane mixture (temperature 1,400 K) flames is shown in Figure 7. Composite droplets with volume fractions of rapeseed oil and water equal to 90% and 10%, respectively, were used in the experiments. The efficiency factor of absorption in the model was assumed equal to one.

Since the measurements took place inside the flames, where gas is optically thick, it was assumed that the radiative temperature was equal to the gas temperature in both experiments. As follows from Figure 7, the effect of the support was relatively small, while the effect of thermal radiation led to a reduction in the values of $\tau_p$ for both flames. When the effects of both radiation and support were considered, the model predictions and experimental data were very close.

Note that the models described in the paper are still based on many assumptions, the applicability of which to the analysis of experimental data is far from obvious. For example, Figure 1 shows a noticeable time difference between the starts of droplet puffing and micro-explosion, while the model assumes that these processes start at the same time.

## ACKNOWLEDGEMENTS

The authors are grateful for: financial support received from the Russian Science Foundation (Grant 21-19-00876), which supported S.S. Sazhin (who contributed to the development of the physical and mathematical models, analysis of the results and preparation of the text of the paper); a Scholarship from the President of the Russian Federation (Grant SP-447.2021.1), which supported D. Antonov (who performed the experiments and applied the model to their analysis); and to National Research Tomsk Polytechnic University (project VIU-ISHFVP-60/2019), which supported P.A. Strizhak (who contributed to the preparation of the experiments and the analysis of the results).

## REFERENCES

[1] D.V. Antonov, G.S. Nyashina, P.A. Strizhak, D.S. Romanov, Micro-explosive droplet fragmentation of environmentally promising coal-water slurries containing petrochemicals, Fuel 283 (2021) 118949

[2] X. Zhang, T. Li, B. Wang, Y. Wei, Superheat limit and micro-explosion in droplets of hydrous ethanol-diesel emulsions at atmospheric pressure and diesel-like conditions. Energy 154 (2018) 535-543.

[3] E.A. El Shenawy, M. Elkelawy, H.A.-E. Bastawissi, M.M. Shams, H. Panchal, K. Sadasivuni, N. Thakar, Investigation and performance analysis of water-diesel emulsion for improvement of performance and emission characteristics of partially premixed charge compression ignition (PPCCI) diesel engines. Sustain. Energy Technol. Assessments 36 (2019) 100546.

[4] H. Watanabe, Y. Suzuki, T. Harada, Y. Matsushita, H. Aoki, T. Miura, An experimental investigation of the breakup characteristics of secondary atomization of emulsified fuel droplet. Energy 35 (2010) 806-813.

[5] G.V. Kuznetsov, M.V. Piskunov, P.A. Strizhak, How to improve efficiency of using water when extinguishing fires through the explosive breakup of drops in a flame: Laboratory and field tests. Int. J. Therm. Sci. 121 (2017) 398-409.

[6] M. Gupta, R. Rajora, S. Sahai, R. Shankar, A. Ray, S.R. Kale, Experimental evaluation of fire suppression characteristics of twin fluid water mist system, in: Fire Safety J 2012.

[7] X.K. Xiao, B.H. Cong, X.S. Wang, K.Q. Kuang, R.K.K. Yuen, G.X. Liao, On the behavior of flame expansion in pool fire extinguishment with steam jet, J. Fire Sci. 29 (2011).

[8] M.M. Avulapati, T. Megaritis, J. Xia, L. Ganippa, Experimental understanding on the dynamics of micro-explosion and puffing in ternary emulsion droplets. Fuel 239 (2019) 1284-1292.

[9] D.V. Antonov, G.V. Kuznetsov, P.A. Strizhak, O. Rybdylova, S.S. Sazhin, Micro-explosion and autoignition of composite fuel/water droplets. Combustion and Flame 210 (2019) 479-489.

[10] J. Shinjo, J. Xia L. C. Ganippa, A. Megaritis. Puffing-enhanced fuel/air mixing of an evaporating n-decane/ethanol emulsion droplet and a droplet group under convective heating. J. Fluid Mech. 793 (2016)

[11] J. Shinjo, J. Xia, Combustion characteristics of a single decane/ethanol emulsion droplet and a droplet group under puffing conditions. Proc. Combust. Inst. 36 (2017) 2513-2521.

[12] S.S. Sazhin, O.D. Rybdylova, C. Crua, M. Heikal, M.A. Ismael, Z. Nissar, A.R.B.A. Aziz, A simple model for puffing/micro-explosions in water-fuel emulsion droplets. Int. J Heat Mass Transfer 131(2019) 815-821.

[13] S.S. Sazhin, T. Bar-Kohany, Z. Nissar, D. Antonov, P. Strizhak, O. Rybdylova, O. A new approach to modelling micro-explosions in composite droplets. Int. J of Heat Mass Transfer 161 (2020) 120238.

[14] S.S. Sazhin, Droplets and Sprays, Springer, London, 2014.

[15] S.S. Sazhin, Modelling of fuel droplet heating and evaporation: recent results and unsolved problems. Fuel 196 (2017) 69-101.

[16] S.S. Sazhin, Modelling of hydrocarbon fuel droplet heating and evaporation: recent results. Proceedings of the Ninth International Seminar on Fire and Explosion Hazards (ISFEH9), Vol. 1, pp. 125-134, 2019. Edited by Snegirev A., Liu N.A., Tamanini F., Bradley D., Molkov V., and Chaumeix N. Published by St. Petersburg Polytechnic University Press. ISBN 978-5-7422-6496-5.

[17] T. Bar-Kohany, Y. Amsalem, Nucleation temperature under various heating rates. Int. J Heat and Mass Transfer, 126 (2018) 411-415.

[18] V.P. Carey, Liquid-Vapor Phase-Change Phenomena: an Introduction to the Thermophysics of Vaporization and Condensation Processes in Heat Transfer Equipment. CRC Press, 2020.

[19] D.V. Antonov, P.A. Strizhak, R.M. Fedorenko, Z. Nissar, S.S. Sazhin, Puffing and micro-explosions in rapeseed oil/water droplets: the effects of coal micro-particles in water. Fuel 289 (2021) 119814.

[20] D.V. Antonov, R.S. Volkov, R.M. Fedorenko, P.A. Strizhak, G. Castanet, S.S. Sazhin, Temperature measurements in a string of three closely spaced droplets before the start of puffing/micro-explosion: experimental results and modelling. Int. J Heat Mass Transfer, 181 (2021) 121837.

[21] D.V. Antonov, R.M. Fedorenko, P.A. Strizhak, Z. Nissar, S.S. Sazhin, Puffing/micro-explosion in composite fuel/water droplets heated in flames. Combustion and Flame 233 (2021) 111599.

[22] P.A. Strizhak, R.S. Volkov, G. Castanet, F. Lemoine, O. Rybdylova, S.S. Sazhin, Heating and evaporation of suspended water droplets: experimental studies and modelling. Int. J Heat Mass Transfer 127 (2018) 92-106.

[23] S.S. Sazhin, E. Shchepakina, V.A. Sobolev, D.V. Antonov, P.A. Strizhak, Puffing/micro-explosion in composite multi-component droplets. Int. J Heat Mass Transfer 184 (2022) 122210.

[24] G. Castanet, D.V. Antonov, P.A. Strizhak, S.S. Sazhin, Effects of water subdroplet location on the start of puffing/micro-explosion in composite fuel-water droplets. Int. J of Heat Mass Transfer 186 (2022) 122466.

# Blast Wave Overpressures From $CO_2$ Depressurization In A Conical-Shaped Vessel

**M. brahim O.[1,*], Hansen P.M[1], Bjerketvedt D.[1], Vågsæther K.[1]**

*[1] The University of South-Eastern Norway, Faculty of Technology, Natural Sciences, and Maritime Sciences, Department of Process, Energy and Environmental Technology, Kjølnes Ring 56, 3918, Porsgrunn, Norway .*
**Corresponding author's email: osama.k.ibrahim@usn.no*

## ABSTRACT

The primary hazards arising from boiling liquid expanding vapor explosion (BLEVE) during liquid $CO_2$ transport are the pressure waves, flying fragments, and sizeable $CO_2$ discharges to the surroundings. Risk assessment and process safety analyses are crucial aspects to tackle these hazards. This paper studies release of liquid $CO_2$ from a double-membrane conical apparatus to a tube opened to atmospheric conditions. It aims to characterize the effects of a blast wave arising from the phase transition process in the existing test geometry. Results from measured peak overpressures and calculated impulses indicate that the rapid liquid evaporation significantly impacts the leading overpressure positive phase. Besides, they increase with an increase in liquid volume fraction (LVF). Based on analysis of high-speed videos, the estimated fragments' velocity and their corresponding kinetic energy increase with an increase in LVF, and observed velocity up to 112 m/s for LVF of 73.6%. Comparison of estimated fragment velocity from the test with LVF of 52.7% and calculated velocity based on the initial fragment velocity model at the same initial conditions show a difference of about 16 m/s.

**KEYWORDS:** Peak overpressure, Impulse, Expansion, Fragment velocity.

## INTRODUCTION

In increasingly developing Carbon Capture and Storage (CCS) technologies, there are growing apprehensions over unintended release during $CO_2$ transport and storage. A container carrying liquid $CO_2$ at a temperature significantly above its atmospheric boiling point might be exposed to harmful conditions, resulting in its breaking. Such conditions include exposure to higher temperatures, projectile impact, or corrosion. The Boiling Liquid Expanding Vapor Explosion ( BLEVE) is a primary hazard, wherein a storage tank filled with liquified $CO_2$ could fail catastrophically, and a sizeable mass of saturated liquid and vapor exploded into the surroundings. Besides, it is instantaneously generating destructive pressure loads on adjacent structures, and perilous rocketed fragments [1]. The discharge of large $CO_2$ volumes also represents a major health threat as it is toxic at high concentrations, causing suffocation and frostbite burns. Several $CO_2$ BLEVE accidents have been reported, including the 1988 $CO_2$ tank BLEVE in Worms, Germany. Where three people died, eight suffered frost burns, and nearby buildings crumbled. An investigation report concluded that the leading causes were overheating and fracturing [2]. There were two casualties, and the sinking of two ships carrying chemicals resulted from a catastrophic rupture of the $CO_2$ ship tank in 2008, Yuhang, China. The reasons were believed to be overfilling and technical faults [3]. The presented $CO_2$ BLEVE examples clearly show its strength and seriousness. Therefore, process safety analyses and risk assessment are the essential elements to ensure the detection, prevention, and mitigation of such disastrous events.

Key parameters that characterize the shock wave strength and evaluate its impact on the surrounding structures and living beings include overpressure and the wave's positive impulse [4]. Birk et al. [5] described overpressure results from BLEVE tests conducted in tanks filled with propane at various levels. The study concluded that liquid energy content had an insignificant effect on generated shock overpressure. However, in the case of tank disintegration, the energy of expanded multiphase flow generated powerful dynamic overpressure loads on the surrounding surfaces. Based on the contained

energy in the vessel and energy released in the explosion, several models have been proposed to estimate the overpressures during the BLEVE incident [6, 7, 8]. Van der Voort et al. [9] tested overpressures during CO2 BLEVE utilizing 40-l CO2 cylinders. The experimental results were applied to validate the inertia-limited prediction model proposed by Van den Berg [8], and good agreement was reported. Hansen et al. [10] studied the effects of liquid volume fraction and the vent size on originated overpressures during CO2 depressurization in a rectangular duct. The obtained results were compared with simulations of one-phase gas dynamics in a confined chamber, and they showed good correspondence.

This paper demonstrates the results of the laboratory-scale experiments on blast waves consequences during $CO_2$ decompression into an atmospheric vented cylindrical tube. It analyzes overpressure and impulse resulting from rapid $CO_2$ liquid evaporation in a conical-shaped vessel for different liquid levels. Additionally, it determines the velocity and kinetic energy of the flying fragments in four explosion experiments. This study also evaluates a model for calculating initial fragment velocity and compares it with the experimental results.

## EXPERIMENTAL SETUP AND PROCEDURE

Laboratory-scale experiments were conducted in a double-membrane arrangement comprising a conical-shaped vessel as a high-pressure driver section (HPS). A slip-on flange is designed as a medium-pressure section (MPS) set between the HPS and another slip-on flange on the top. Furthermore, The three sections are separated by two membranes that seal the HPS and the MPS. The upper flange is connected to a tubular duct opened to atmospheric conditions. Fig. 1 shows an experimental setup sketch and an image.

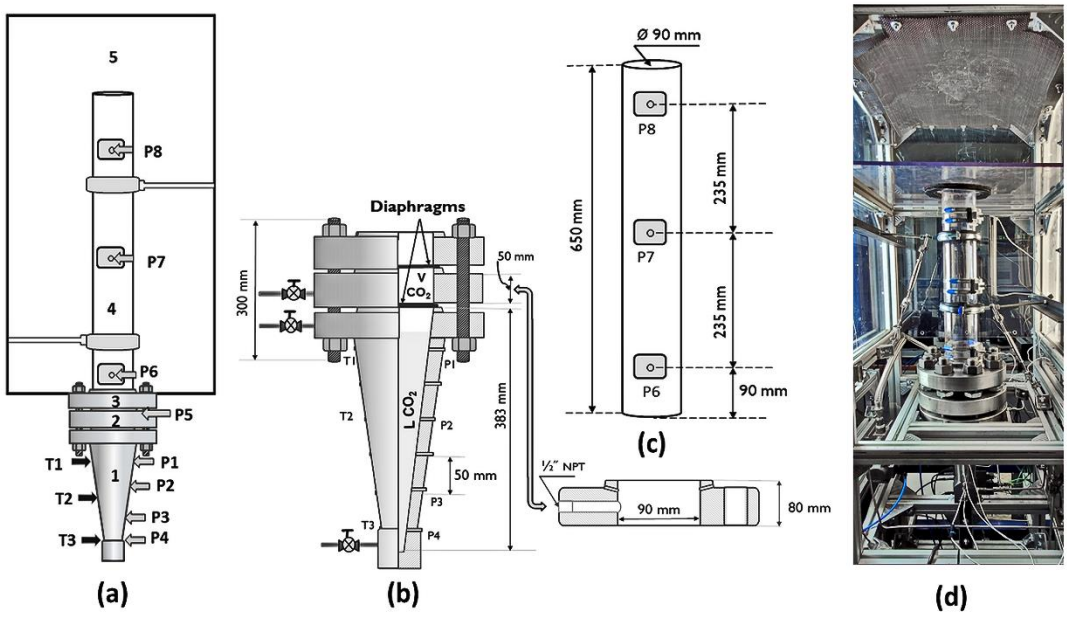


**Fig. 1.** Schematic drawing of the setup: (a) main installed parts: 1- HP conical vessel, 2- MP slip-on flange, 3- upper flange opened to atmospheric pressure, 4- polycarbonate tube, 5- chamber. (b) Conical shaped vessel's detail with the MPS slip-on flange closed up. (c) polycarbonate tube dimensions. (d) An image of the installation.

The conical vessel and the two slip-on flanges are fabricated from stainless steel AISI 316 and installed on an aluminum frame. The HP vessel has an inner volume of $480 \cdot 10^3$ mm$^3$, while the MP slip-on flanges' cylindrical section volume is $510 \cdot 10^3$ mm$^3$. The HP vessel wall has an angle of 4° to

the central axis and a top diameter of 90.7 mm, similar to the MP slip-on flange and polycarbonate tube diameters. Besides, it has a flat bottom diameter of 9.37 mm. Two industrial graded cylinders separately supplied the HP vessel with liquid $CO_2$ up to 5.2-5.6 MPa, and the MP section with gaseous $CO_2$ up to 2.6-2.8 MPa. Before vessel's and duct's filling, they were flushed by 1 MPa vapor $CO_2$. All experiments were carried out at ambient temperature. The vessel has unsighted walls. Therefore the vessel filling to the desired level is achieved with the help of an auxiliary HP duct with glass windows. The atmospherically opened tube is made of transparent polycarbonate and has a height of 650 mm and a cross-section area of about 0.184 $m^2$. The inner cylindrical rim of the upper atmospheric flange was excavated to place in the polycarbonate tube at a depth of 60 mm. Grooves were carved on its side to prevent potential leaks during the multiphase release. A detailed description of the HP vessel, MPS slip-on flange, and the release mechanism is provided in a previous study [11]

The tests were initiated by increasing the pressure in the medium pressure section by triggering a three-way valve. As a result, the MP diaphragm ruptured, and the pressure fell to atmospheric. Following the increase in the pressure difference between the HP and MP sections, the second diaphragm burst. Subsequently, a multiphase mixture spurted out in the atmospherically vented tube. HP vessel is equipped with four Kulite XTM-190-2000G transducers to record the pressure during the decompression process. The distance between pressure transducers' positions is 100, 100, and 50 mm from top to bottom. Besides, The resulting overpressures from the explosion were measured with three transducers types Kulite XTM-190-100G and Kulite XTM-190-50G. They attached to the cylindrical tube's sidewall at an equal distance of 235 mm and 90 mm from the bottom. The temperature inside the HP vessel is measured using three K-type thermocouples assigned as T1-T3 in Fig. 1 (a). However, this study excluded their records because they have a slow response time. Diaphragm rupturing and erupted multiphase mixture evolution captured by a high-speed camera (Photron Fastcam SA-1). A digital pulse generator unit (Quantum Composers 9500) simultaneously triggered the three-way valve, data acquisition system, and high-speed camera at the test start.

## RESULTS AND DISCUSSION

### Overpressure and impulse

Overpressure description required knowledge about the factors influencing the processes in the HP test section. Fig. 2. shows pressure records inside the HP conical vessel during depressurization of liquid $CO_2$ with 35.2% liquid volume fraction (LVF). Time zero signifies the HP diaphragm rupture. The MP diaphragm ruptured by increasing the medium section pressure to about 3.7 MPa. As a result, the HP diaphragm responded with bulging seen as oscillations that faded out through about 18 ms, and the pressure stabilized before the HP diaphragm was ruptured. The duration between the two ruptures was 109 ms, while the pressure decreased from pre-ruptured 5.4 MPa to 5 MPa.

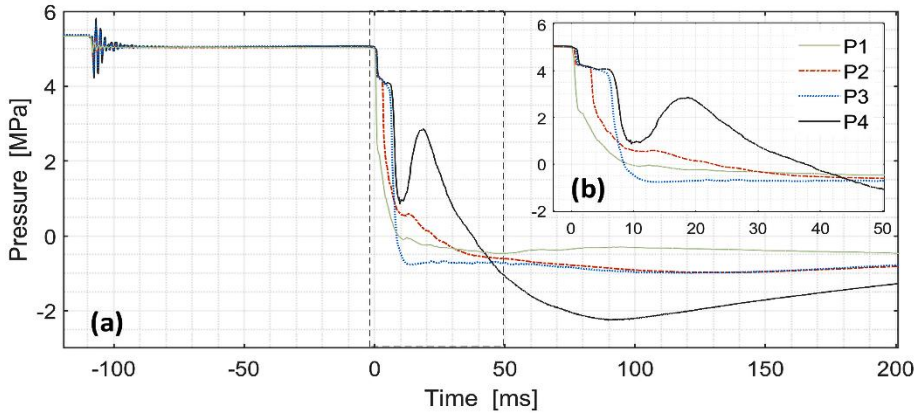


**Fig. 2.** (a) Pressure sensors record P1-P4 (top to bottom) during 200 MS of $CO_2$ depressurization for LVF of 35.2%. (b) a close-up Graph covers 50 ms after the rupture of the HP diaphragm

After the HP diaphragm ruptured, a rarefaction wave moved downward through the saturated liquid resulting in isentropic expansion with reduced temperature and pressure. The calculated rarefaction wavefront average velocity is 358.7 m/s. Whereas the local speed of sound is determined from SW-EOS tabulated data is 350.5 m/s for the liquid phase and 197.5 m/s for the vapor phase. The liquid was kept temporarily in the metastable state when the pressure reached about 4.3 MPa. The evaporation wave required roughly 6 ms to pass across the liquid volume. The first shock wave was generated once the MP diaphragm ruptured, releasing the vapor from the MP section. The second shock followed the HP diaphragm rupture and release of multiphase flow. The observed decrease in pressure reading P3 below zero while the two-phase mixture was expanding could be attributed to the drift due to the rapid temperature drop.

Fig. 3. shows measured peak overpressure (MPO) in the tube at 180/100 mm (bottom) and 650/570 mm (top) from the HP/MP diaphragms, respectively. Also, it illustrates overpressure records during explosive $CO_2$ depressurization from a conical vessel filled with 15 (a), 35.2 (b), and 52.7 % (c) LVF. Time zero signalizes the HP diaphragm rupture. Graphs (a'), (b'), and (c') in Fig.3. are corresponding enlarged segments covering 100 ms from the upper raw graphs. The first peak overpressure indicates the blast wave produced by vapor decompression in the MP section. While the second denotes the waves followed the depressurization in the HP vessel. As the blast signals are measured parallel to the direction of pressure waves, there is no account for reflected pressures from impinging on any surface except the tube wall and the champer's ceiling. The MPOs in Fig. 3. specify two peaks of overpressure in the leading positive phase with a higher second peak following the first lower peak. The expanded headspace vapor produces the first pressure wave, while the second peak results from the expansion due to liquid evaporation.

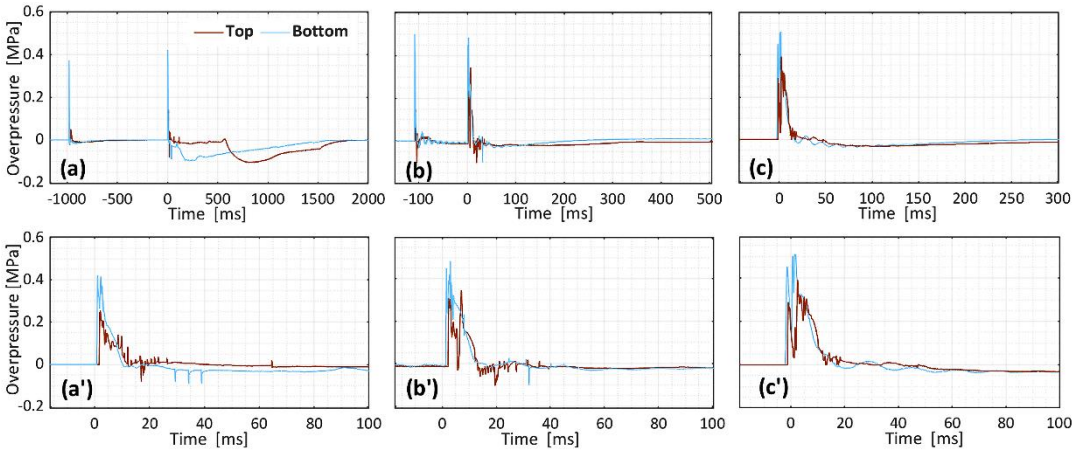


**Fig. 3.** Measured overpressures at the top and bottom alongside the tube at 180 and 650 mm from the HP diaphragm. For LVF of 15 (a), 35.2 (b), and 52.7% (c). graphs (a'), (b'), and (c') are the corresponded enlarged segments.

The graphs above show that the period between MP and HP diaphragm ruptures decreases as the LVF increases. Similarly, the measured peak overpressure from the top and bottom sensors increases with an increase in LVF. These overpressures peaked at 0.42, 0.48, and 0.51 MPa from the bottom sensor's records and 0.25, 0.35, and 0.38 MPa from the top sensor's histories. The blast wave signal shape primarily depends on the expansion development, particularly the evaporation process pace [12]. Ciccarelli et al. [13] have measured overpressures generated from $CO_2$ decompression in a polycarbonate tube. The signals are typified by a gradual increase in pressure at two different positions, while graphs in Fig. 3. show a steep increase. It is interesting to note that these results indicate a rapid evaporation process in this geometry as the downstream mixture flows towards a regularly increasing cross-section in the conical-shaped vessel. Additionally, the MPOs are much higher than those measured during $CO_2$ decompression in a constant cross-section duct done by

Hansen et al. [10]. The correlations between MPOs and the LVFs (0, 15, 20, 25, 35.2, 52.7, and 73.6 %) are presented in Fig.4.

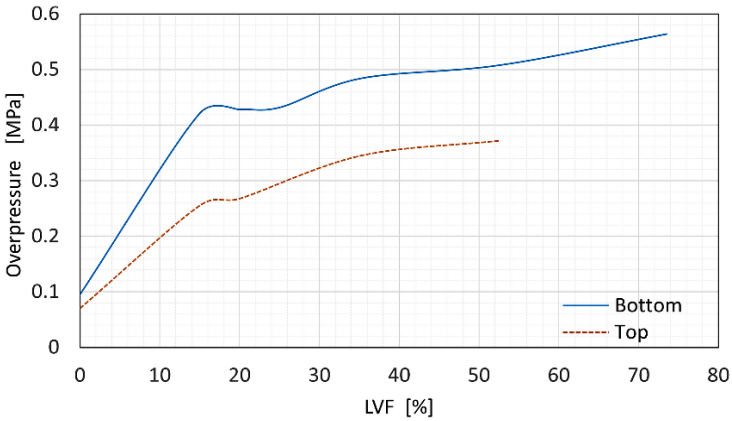


**Fig. 4.** Measured peak overpressure at the top (180 mm) and bottom (650 mm) of the atmospheric tube versus LVF during $CO_2$ depressurization in the conical-shaped vessel.

The energy quantity from the explosion potentially transferred to the structure is illustrated as a calculated impulse over 40 ms in Fig. 5. The impulse computations have been executed by integration of the pressure histories. Graph (a) represent the calculated impulse for pressure records at the bottom tube cite. In comparison, graph (b) shows them at the top transducer position. After 40 ms, all impulse curves fade out, and there is no positive phase. Besides, there are no significant differences in the lines' behavior during approximately 2 ms from the start

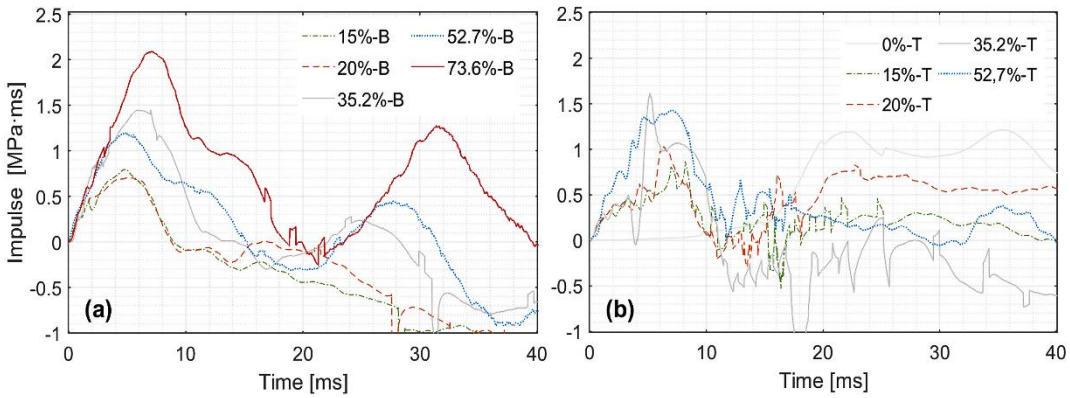


**Fig. 5.** The calculated impulse from the measured overpressure records at the tube's bottom (a) and top (b).

Interestingly, in Fig. 5. (a), the curve with 35.2 % LVF peaked higher than the one with 52.7%. Then the curves traversed twice before the latter curve peaked higher in the second positive phase. This behavior may be due to the expansion of higher vapor volume in the vessel's headspace and subsequent expansion of multiphase mixture after the evaporation wave has passed. The impulse curves in Fig. 5. (b) have inverse behavior, wherein the lines with lower LVF peak higher in the second positive phase. This trend can be observed from the 0% and 15% LVF curves pattern.

**Fragments' initial velocity and kinetic energy**

The analysis of flying fragments and missiles is essential in estimating BLEVE incident effects. The fragmentation of the pressure vessel constitutes a severe hazard to surrounding living beings and structures. Therefore, it is necessary to assess the consequences impacts of such risk for better safety

management. Generally, the explosion-released energy is an aggregate of pressure wave's energy, fragments' kinetic and potential energy, and the surrounding heating. The pressure wave energy has been suggested to be around 80% of the explosion energy in the case of fragile vessel fracture [14]. Several methods were proposed to quantify the fragments' hazard. Birk [15] has offered experimental data showing that the projectile hazard from shattering a tank filled with pressurized propane in terms of mass x range (kg·m) increased with an increase in average liquid temperature before the explosion. Baum [16] has measured the end-cap velocity during experiments with pressurized water in a horizontal vessel. According to obtained data, he proposed a formula to calculate the fragment's initial velocity ($v_f$) as:

$$v_f = \left(\frac{2 \cdot k_q \cdot Q_{ex}}{m_f}\right)^{0.5} \quad (1)$$

$$Q_{ex} = m_l \cdot C_p \cdot \left(T_{rupt} - T_b\right) = \left(V_V \cdot \phi \cdot \rho_l\right) \cdot C_p \cdot \left(T_{rupt} - T_b\right) \quad (2)$$

where $m_f$ is the fragment mass [kg], $Q_{ex}$ is the excess heat stored in the liquid before the explosion [J], and $k_q$ is the fraction of the excess heat transformed to the fragment kinetic energy, and the most suitable value noticed to be 0.00126. $C_p$ is the pre-ruptured liquid specific heat at constant pressure [kJ/kg·K], $T_{rupt}$ is superheated liquid temperature [K], $T_b$ is the liquid boiling temperature at atmospheric pressure [K]. $V_V$ is the vessel volume [$m^3$]. $\phi$ is liquid volume fraction. $\rho_l$ is the Liquid density at the superheated state [kg/ $m^3$].

This section compares fragments' velocities analyzed based on experimental results with fragment velocity calculation results from the above relationship. $CO_2$ properties at pre-ruptured saturation state were found from tabulated data built from the Span-Wagner equation of state (SW-EOS) and NIST [17, 18]. Based on Baum's equation, the fragment velocity from the rupture of a vessel containing $CO_2$ with 52.7% LVF at pre-ruptured conditions 5.58 MPa and 292 K is:

$$Q_{ex} = 0.25 \cdot 4.0145 \cdot (292 - 194.69) = 97.66 \text{ kJ} \quad (3)$$

$$v_f = \left(\frac{2 \cdot 0.00126 \cdot 97660}{0.0282}\right)^{0.5} \approx 93.4 \text{ m/s} \quad (4)$$

During the explosion experiments in the HP conical vessel, the flying fragment is a circular diaphragm consisting of three aluminum layers with 0.8, 0.5, and 0.3 mm thicknesses. Fragments velocities were estimated by processing the high-speed videos from four experiments of $CO_2$ depressurization in the conical vessel filled with LVF of 25,35.2, 52.7, and 73.6%. The videos were captured at 7200 frames per second (fps) and a 256 x 1024 pixels resolution. Velocity calculations have been done along two equal tube heights, each covering 235 mm, by tracking the diaphragm trajectories with a height to pixel conversion of 0.94 mm/pixel. Fig. 6 (on the top) shows cropped images from the sequence of video frames during 10.4 ms covering the evolution of the ruptured HP diaphragm through the atmospheric tube. The images are cut from the video captured in the test with 35.2 % LVF. The cropped images resolution was minimized to 119 x 901 pixels, and the variance between one image and the followed image is three frames (about 0.42 ms). A light line is drawn underneath the trajectory of the diaphragm movement. In addition, Fig. 6. (on the bottom) shows the pressure records corresponding to the duration of the image sequence.

From the data in Fig. 6., the emergence of the diaphragm in the tube required about 1 ms and took nearly 7 ms to propagate through the tube length. The liquid remained in a metastable state during this period, as shown in Fig. 6. (bottom). This trend reveals that the ruptured diaphragm is propelled mainly by the expanded vapor in the vessel's headspace

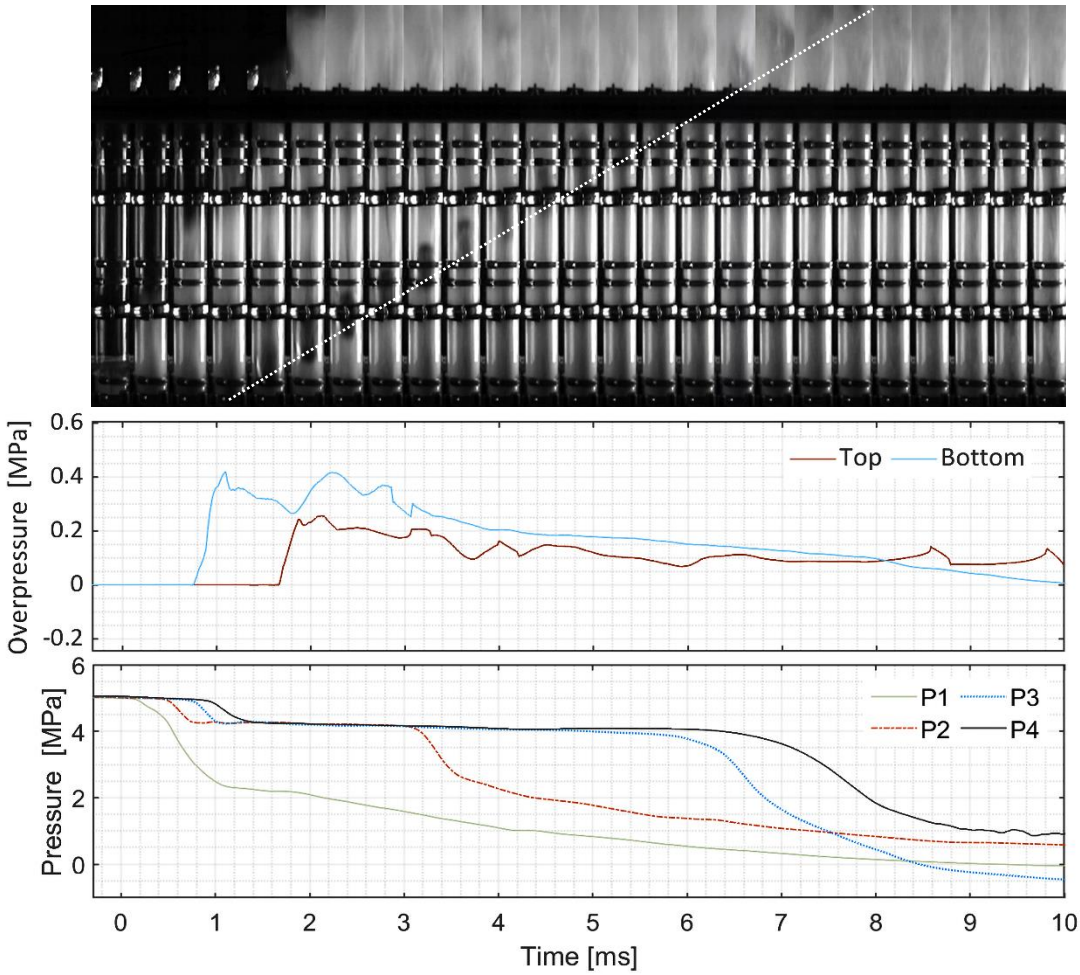


**Fig. 6.** Top: sequence of cropped images from a high-speed video of $CO_2$ depressurization test with LVF of 35.2% (time step of 0.416 ms). Middle: synchronized overpressure records on the top and bottom of the polycarbonate tube. Bottom: corresponding pressure histories from HP vessel during 10.4 ms.

Interestingly, the force of the released expanded multiphase mixture acting on the diaphragm should likely result in parabolic path motion. However, its movement is described by a constant velocity ( as the linear trajectory shows in Fig. 6). It could be argued that it moves with about the same velocity as the released multiphase mixture, but further research might explore its movement without net force.

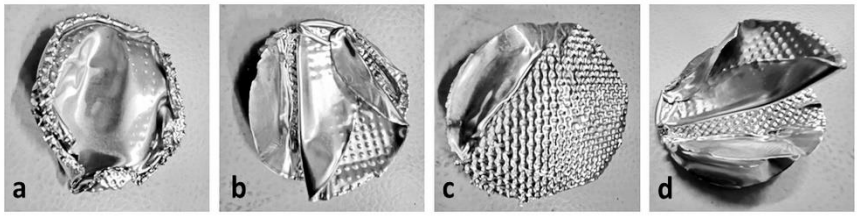


**Fig. 7.** Fragments' (HP diaphragm layers) shape after they are propelled through the tube and hit the protective mesh at the chamber's ceiling. The VLF in the vessel was 73.6 in (a), 52.7 in (b), 35.2 in (c), and 25% in (d).

The rocketed fragments from four experiments with different LVFs were collected, classified, and weighed (see Table 1). Pictures showing the diaphragms' shape after hitting the protective mesh at the chamber ceiling are presented in Fig. 7. After the propelled diaphragms' weights were determined, their kinetic energy was calculated, and the results are set out in Table 1.

**Table 1. Characteristics of the fragments from HP diaphragm rupture**

| LVF, % | Weight, g | Velocity, m/s | Kinetic energy, J |
|---|---|---|---|
| 73.6 | 27.9 | 121.1 | 204.9 |
| 52.7 | 28.2 | 109.3 | 168.6 |
| 35.2 | 28.5 | 112.0 | 177.1 |
| 25 | 28.5 | 94,6 | 127.4 |

## CONCLUSION

Laboratory-scale experiments have been conducted to study the release of liquified $CO_2$ from a conical-shaped vessel sealed with double-membrane apparatus to an atmospherically vented tube. The research goal is to describe the blast wave consequences during the $CO_2$ depressurization in such geometry. Analysis of measured overpressure at the top and bottom of the tube shows that rapid evaporation significantly influences the leading overpressure positive phase. This positive phase combines a second higher peak from expansion due to liquid evaporation and an initial lower peak driven by the expanded headspace vapor content. The peak overpressure increases with an increase in LVF. The measured peak overpressures in the tests with LVF of 15, 35.2, and 52.7% are 0.42, 0.48, and 0.51 MPa, respectively.

In addition, this research estimates the flying diaphragms' velocity and their kinetic energy by analyzing high-speed videos. Results indicate that the propelled diaphragm's velocity and the corresponding kinetic energy increase with increasing LVF. The highest values obtained from the test with 73.6% LVF are about 121 m/s and 205 J. Comparing the obtained velocity from the test with LVF of 52.7% with the calculated model for initial fragment velocity at the same initial conditions indicates conservative divergence. It is 109.3 m/s for the former and 93.4 m/s for the latter.

## REFERENCES

[1] CCPS, Guidelines for Vapor Cloud Explosion, Pressure Vessel Burst, BLEVE, and Flash Fire Hazards. AIChE-Wiley, pp. 311-360, 2010.

[2] W. E. Clayton, M. L. Griffin, Catastrophic failure of a liquid carbon dioxide storage vessel. Process Safety Progress. vol. 13, no. 4, (1994) pp. 202-209, doi: doi.org/10.1002/prs.680130405.

[3] Y. Zhang, J. Schork, K. Ludwig, Revisiting the conditions for a $CO_2$ tank explosion. Proceedings of the Ninth Global Congress on Process Safety, San Antonio, Texas: AIChE, pp. 109-120, 2013.

[4] A. C. Van den Berg, M. M. Van der Voort, J. Weerheijm, N. H. A. Versloot, BLEVE blast by expansion-controlled evaporation. Process Safety Progress, vol. 25, no. 1, (2006) pp. 44-51, doi: 10.1002/prs.10116.

[5] A. M. Birk, C. Davison, M. Cunningham, Blast overpressures from medium-scale BLEVE tests. Journal of Loss Prevention in the Process Industries, vol. 20, no.3, (2007) pp.194-206, doi: doi.org/10.1016/j.jlp.2007.03.001.

[6] R. W. Prugh, Quantitative Evaluation of "Bleve" Hazards. Fire Protection Engineering, vol. 3, no. 1, (1991) pp. 9-24, doi: 10.1177/104239159100300102.

[7] E. Planas-Cuchi, J. M. Salla, J. Casal, "Calculating overpressure from BLEVE explosions. Loss Prevention in the Process Industries, vol. 17, no. 6, (2004) pp. 431-436, doi: doi.org/10.1016/j.jlp.2004.08.002.

[8] A. C. van den Berg, Blast charts for explosive evaporation of superheated liquids. Process Safety Progress, vol. 27, no. 3, (2008) pp. 219-224, doi: doi.org/10.1002/prs.10252.

[9] M. M. van der Voort, A. C. van den Berg, D. J. E. M. Roekaerts, M. Xie, P. C. J. de Bruijn, Blast from explosive evaporation of carbon dioxide: experiment, modeling, and physics. Shock Waves, vol. 22, no. 2, (2012) pp. 129-140, doi: 10.1007/s00193-012-0356-0.

[10] P. M. Hansen, A. V. Gaathaug, D. Bjerketvedt, K. Vaagsaether, "Blast from pressurized carbon dioxide released into a vented atmospheric chamber" *Shock Waves,* vol. 28, no. 5, pp. 1053-1064, Art no., doi: 10.1007/s00193-018-0819-z.

[11] O. M. Ibrahim, P. M. Hansen, D. Bjerketvedt, and K. Vågsæther, "Release mechanisms and waves interaction during liquified $CO_2$ depressurization in a double-membrane conical vessel," SN Applied Sciences, vol. 4, no. 4, p. 89, 2022/03/02 2022, doi: 10.1007/s42452-022-04975-4.

[12] J. C. A. M. v. Doormaal and R. M. M. v. Wees, 2005 , Rupture of vessels. in Methods for the calculation of physical effects: due to releases of hazardous materials (liquids and gases), The Hague: Min. VROM, ch. 7, 2018, pp. 7.1 - 7.78.

[13] G. Ciccarelli, J. Melguizo-Gavilanes, J. E. Shepherd, Pressure field produced by the rapid vaporization of a CO2 liquid column. 30th International Symposium on Shock Waves, Tel-Aviv, Israel, 2015.

[14] J. Casal, J. Arnaldos, H. Montiel, E. Planas-Cuchi, J. A. Vı´lchez, Modeling and understanding BLEVEs. in The Handbook of Hazardous Materials Spills Technology. NY: McGraw-Hill, pp. 22.1-22.27, 2002.

[15] A. M. Birk, Hazards from propane BLEVEs: An update and proposal for emergency responders. *Loss* Prevention in the Process Industries, vol. 9, no. 2, (1996) pp. 173-181, doi: doi.org/10.1016/0950-4230(95)00046-1.

[16] M. R. Baum, Failure of a horizontal pressure vessel containing a high temperature liquid: the velocity of end-cap and rocket missiles. Loss Prevention in the Process Industries, vol. 12, no. 2, (1999) pp. 137-145, Art no., doi: doi.org/10.1016/S0950-4230(98)00051-5

[17] R. Span, W. Wagner, A New Equation of State for Carbon Dioxide Covering the Fluid Region from the Triple‐Point Temperature to 1100 K at Pressures up to 800 MPa. Physical and Chemical Reference Data, vol. 25, no. 6, (1996) pp. 1509-1596, doi: doi.org/10.1063/1.555991.

[18] Eric W. Lemmon, Mark O. McLinden, D. G. Friend. Thermophysical Properties of Fluid Systems. in NIST Chemistry WebBook, NIST Standard Reference Database Number 69, Eds. P.J. Linstrom and W.G. Mallard, National Institute of Standards and Technology, Gaithersburg MD, 20899, https://doi.org/10.18434/T4D303 (accessed, 2021).

# Simulation of One Dimensional Detonation in OpenFOAM using Detailed Chemistry and Adaptive Mesh Refinement

**Shahanaghi A.[1], Karimkashi S.[1], Kaario O.[1], Vuorinen V.[1], Tripathi R.[2], and Sarjovaara T.[2]**

[1]*Aalto University, Department of Mechanical Engineering, School of Engineering, Otakaari 4, 02150 Espoo, Finland*

[2]*Neste Oyj, Finland*

## ABSTRACT

A combination of numerical tools developed by Aalto University CFD group is used in order to make a high fidelity numerical investigation on one dimensional planar detonations. ARC (Adaptive, Runge-Kutta, Central)Foam is developed based on OpenFOAM to simulate denotative combustion. ARCFoam uses an efficient solution of detailed chemistry (DLBfoam) with high (2nd and 4th) order time discretization, and shock capturing convective schemes (Kurganov-Tadmor and HLLC). One dimensional (1D) adaptive grid refinement is implemented for the first time for OpenFOAM to enhance the numerical resolution in 1D simulations. The effect of utilizing different forms of energy equation on detonative combustion is examined using 1D constant volume (*n*-heptane/iso-octane/air) and shock induced detonation (hydrogen/argon/oxygen) simulations and detailed chemistry. Direct initiation of detonation in hydrogen mixtures with air is studied. Effect of equivalence ratio on the propagation of 1D detonation is studied and shows a reliable conformation with ZND (Zeldovich, von Neumann and Doring) detonation wave. Moreover, the sensitivity of the predicted detonation propagation to mesh resolution is investigated. Studies show that unresolved 1D detonation front can result in wrong steady propagation for a pulsating detonation or quenching under steady detonation conditions. A coarse grid can result in thickening the reaction zone and therefore, false stability. In addition, a coarse grid can result in under-prediction of heat release from the exothermic zone, which leads to false decay of propagating detonation.

## KEYWORDS

Adaptive mesh refinement, computational fluid dynamics, detonation, detailed chemistry

## INTRODUCTION

Understanding detonative combustion in gases has a great importance in engineering (e.g. spark engines) and safety (e.g. explosion) practices. Numerical analysis of compressible flows coupled with finite rate chemical reactions can provide understanding on the causes and consequences of detonations in technically relevant problems.

OpenFOAM [1], an open source CFD package, has proved to be versatile and accurate in modelling various fluid mechanics problems, including high speed reacting flows[2, 3, 4] . Based on OpenFOAM, Ettner et al. [5] developed a solver (ddtFoam), by incorporating Harten–Lax–van Lee (HLLC) [6] method alongside with reaction progress variable equation for simulation of deflagration to detonation phenomenon (DDT). As a part of OpenFOAM, rhoCentalFoam [7] is a density based solver utilizing second order central Kurganov and Tadmor (KT)[8] scheme for capturing shock waves in high speed non-reacting flows. In recent years, rhoCentralFoam, is extended by a number of authors to model detonative combustion. Marcantoni et al. [3] included the species transport and chemical reaction source in the solver and examined

the one dimensional detonation propagation of $H_2$/air mixtures. More recently, Huang et al. [4] extended the solver for two-phase gas-droplet detonations.

In a detonative combustion mode, due to the presence of intense reactions in proximity of the shock front, it is necessary to use very fine meshes in this region. Therefore, in order to maintain the computational feasibility of the simulations Adaptive Mesh Refinement (AMR) procedure is used in the previous studies on 1D detonation [9, 10, 11]. However, to this date, the mentioned method is not applied for 1D problems in OpenFOAM. The effect of mesh resolution on capturing the 1D detonative combustion behavior has been studied in both classical studies considering reaction progress variable [10] and more recent studies using finite rate chemistry [9, 12]. The main disadvantage of progress variable method is that it cannot predict the exothermic thickness correctly due to lack of knowledge on chemical kinetic reactions. Therefore, Half Reaction Length (HRL/ $l_{\frac{1}{2}}$), considered as the distance between the leading shock and maximum heat release [13], has been used as a measure to spatially resolve detonation waves [10, 4, 2]. HRL does not provide information about the detonation's induction length and exothermic length separately, while the ratio between these two length affects the detonation stability. Moreover, the mentioned ratio varies significantly between different fuels. Meanwhile, in recent studies [3, 4, 9] a mesh resolution range of $0.5\ mm - 1\mu m$ was considered for simulating 1D hydrogen detonation propagation. The mentioned range changes from approximately 0.005 to 0.5 size of exothermic zone for a ZND (Zeldovich, von Neumann and Doring) $H_2$ detonation wave with pre-shock condition at 300 K and 1 atm. According to the above mentioned literature, there is no specific criteria for mesh resolution in 1D detonation simulation using realistic detailed chemistry. Moreover, the utilized mesh resolution varies significantly between recent studies.

Therefore, the present study aims to develop a high fidelity numerical solver, ARCFoam, for detonative combustion using efficient and accurate computations with help of DLBfoam [14] and 1D AMR. We study the effect of coupling between different forms of energy equation and chemical source term. Moreover, we investigate the mesh resolution effect on the prediction of 1D planar detonations, using detailed chemistry.

## METHODOLOGY

In this section, more information on the selected computational methods used in present work are provided.

### Adaptive Mesh Refinement

The OpenFOAM code solves three dimensional Navier Stokes equations. In order to reduce the dimensions of a problem, the approach is to use empty boundaries. Therefore, for a 1D problem, the geometry should have only one row of cells extended in an specific direction. However, the AMR engine in OpenFOAM is isotropic and it is limited to Octree refinement of hexahedral mesh. In other words, it refines a cubic cell, in 3 directions in a uniform way, to 8 cells with half size. As a result, a 1D problem turns into a 3D problem after using standard OpenFOAM's AMR engine. In the present work, the AMR engine has been extended to refine the grid in only one direction without slicing the surfaces perpendicular to the fluxes. Moreover, density gradient is considered as the criteria for locating the refinement regions in the studied problems.

### Chemistry model/solver

In OpenFOAM, the system of ODEs governing the evolution of thermochemical composition which is solved coupled with the flow solution is:

$$\frac{\partial T}{\partial t} = \frac{-1}{\rho c_p} \sum h_k W_k \dot{\omega}_k, \tag{1}$$

$$\frac{\partial Y_k}{\partial t} = \frac{W_k}{\rho} \dot{\omega}_k, \tag{2}$$

where $c_p$ is constant pressure specific heat, $h_k$ is enthalpy of the kth species and $\dot{\omega}_k$ is production rate. Above formulation considers a constant pressure reactor and calculates the change in sensible enthalpy, Eq.(1). The present solver utilizes an efficient chemistry solver (DLBfoam) [14] to take the effect of finite rate chemistry into account in reacting simulations.

### CFD solver

Transport of mass, momentum, energy and species mass fractions are solved by ARCFoam solver using finite volume method. The solver combines the explicit 2nd and 4th order Runge Kutta [15] time differencing with shock capturing central convective schemes, Harten–Lax–van Leer (HLLC) [6] and Kurganov and Tadmor (KT) [8] methods.

*Energy equation*

Forms of energy equation (total energy or enthalpy) in OpenFOAM solvers can change considering the solver's application. rhoCentralFoam and solvers based on that [7, 3, 4] use the total energy (E) form of equation since it can be numerically solved in a more simple and accurate manner,

$$\frac{\partial(\rho E)}{\partial t} + \nabla \cdot [u(\rho E)] + \nabla \cdot [up] - \nabla \cdot [T \cdot u] + \nabla \cdot j = \dot{\omega}_T, \tag{3}$$

where $E = e_s + K$, wherein $K$ is kinetic energy and $e_s$ is sensible internal energy, $T$ is the viscous stress tensor, $j$ is diffusive heat flux and $\dot{\omega}_e$ is combustion heat release . The enthalpy form of energy also reads

$$\frac{\partial(\rho h)}{\partial t} + \nabla \cdot [u(\rho h)] - \frac{\partial p}{\partial t} - \nabla \cdot [T \cdot u] + \nabla \cdot j = \dot{\omega}_T, \tag{4}$$

in which $h = h_s + K$, where $h_s$ is sensible enthalpy. It has been seen that in order to take into account In the present paper, we examined effect of using both of these forms on detonative combustion. $\frac{\partial p}{\partial t}$ term in Eq. (4) has been calculated in an explicit way. It should be noted that chemical source term added to different forms of energy equation can be subject to change considering the chosen form of energy equation[16]. OpenFOAM implementation of sensible energy ($e_s = h_s - p/\rho$) enables to use the same chemical source term in both forms of energy equation theoretically. However, numerical implementation (e.g. $\frac{\partial p}{\partial t}$ term in sensible enthalpy or $p$ in sensible energy) can lead to appearance of differences in the results of these equations.

### ZND model

In the present paper in order to study detonation structure, Zeldovich, von Neumann and Doring (ZND) model is used. The calculations are done using Shock and Detonation Toolbox (SD Toolbox) [17]. ZND model consists of a set of steady one-dimensional ordinary differential equations including species exchange rates. As a result, when using a detailed chemistry mechanism, the ZND ODEs form a stiff system of equations. Therefore, to address this issue, SD Toolbox ODE integrator is extended by a including a stiff ODE integrator (VODE). It is notable that present implementation in the code supports usage of BDF method which is capable of solving stiff chemistry. However it is shown that VODE has better performance due to implemented algorithmic improvements [18].

## RESULTS AND DISCUSSIONS

### Solver validation

In this section, different benchmarks have been studied in order to examine the validity of the solver's numerical methods and their implementations in the solver. Initially, the ability of the solver for capturing and preserving the discontinuities is tested in non-reacting cases. Furthermore, reacting cases including detonative mode have been simulated and validated with the numerical results from available solvers.

*Case I: Sod shock tube*

Sod shock tube is chosen to evaluate the capability of the numerical approaches in predicting the displacement of discontinuities. Details about case configuration, including initial density ($\rho$), pressure (P), velocity (U), molecular weight (MW), length of the domain (L) and number of gridpoints, are mentioned in Table 1.

**Table 1:** Case I configuration.

| $\rho_1$ [Kg/m$^3$] | $\rho_2$ [Kg/m$^3$] | $P_1$ [pa] | $P_2$ [pa] | U [m/s] | MW | L [m] | Gridpoints |
|---|---|---|---|---|---|---|---|
| 1 | 0.125 | 1 | 0.1 | 0 | 28.9 | 1 | 1000 |

Figure 1 demonstrates pressure, velocity, density and speed of sound at 0.0016 s. Different combinations of implemented numerical methods are compared to the analytical solution. The profiles include a right propagating shock, a contact discontinuity and a left propagating rarefaction wave. The timesteps have been adjusted to achieve convective courant number of 0.02 (acoustic courant number $\approx$ 0.04).

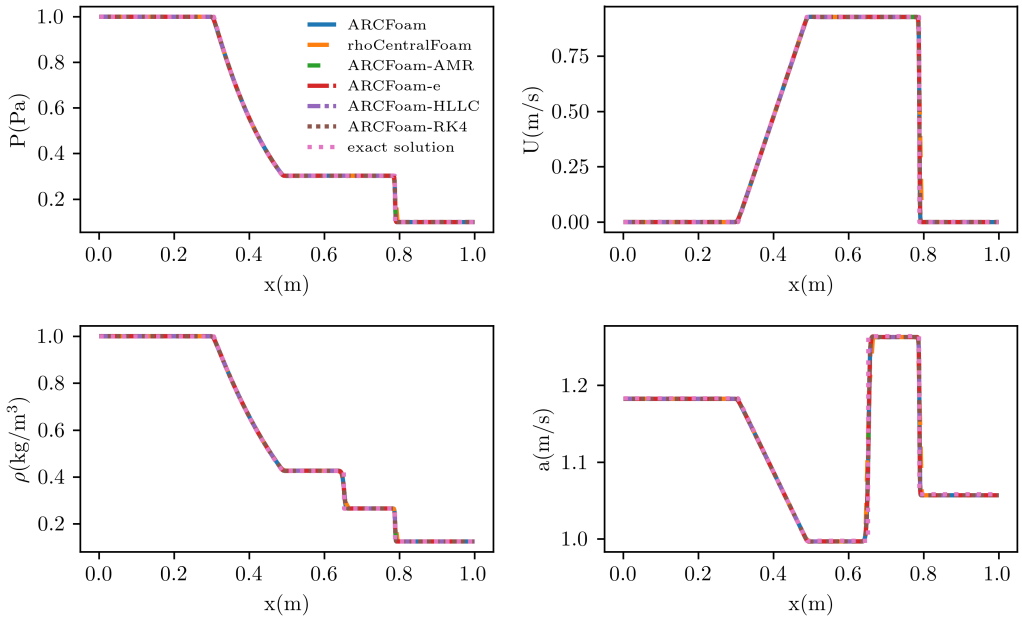


**Figure 1:** Pressure, velocity, density and temperature distribution of sod shock-tube problem at 0.0016s

As it is shown in Fig. 1, all tested approaches are in agreement with the analytical solution of the problem. Hereafter, RKSSP time discretization with sensible enthalpy energy formulation and KT method are considered as the main configuration for the solver, i.e. the solid line in Fig. 1. From Fig. 1, it is observable that results for two energy equation formula (dash-dotted and solid lines) match which verifies the implementation for sensible enthalpy. Moreover, results from HLLC scheme (dash-dot-dotted line) match with rhoCentralFoam and base method (solid and long dashed lines) with KT scheme. Results from using 1D-AMR method with two levels of refinement are also inline with the rest of methods. To be consistent with other simulations, initial number of cells were set to 250 and cell count during simulation (i.e. with 2 level refinements applied) was 456.

*Case II: Constant Volume reactor*

A 1D constant volume reactor filled with homogeneous mixture of PRF 87, 87% volume iso-octane and 13% volume n-heptane, using a skeletal mechanism [19], at 830 K and 20 bar is studied. The purpose is

to compare the coupling between chemical source term and flow properties in two different solvers. In this case, the contribution of convection and diffusion terms in transport equation is negligible. Figure 2 shows the the profiles of temperature, pressure and heat release rate during the ignition period. To avoid generation of spurious waves in the domain, the acoustic courant number is kept less than 0.1 ($\delta$t = 1e-7) and non reflecting boundary conditions is applied for pressure. Moreover, simulation results from the present solver using internal energy and sensible enthalpy forms of energy equation are compared with Cantera's zero dimensional (0D) constant volume (CV) reactor with the same initial conditions.

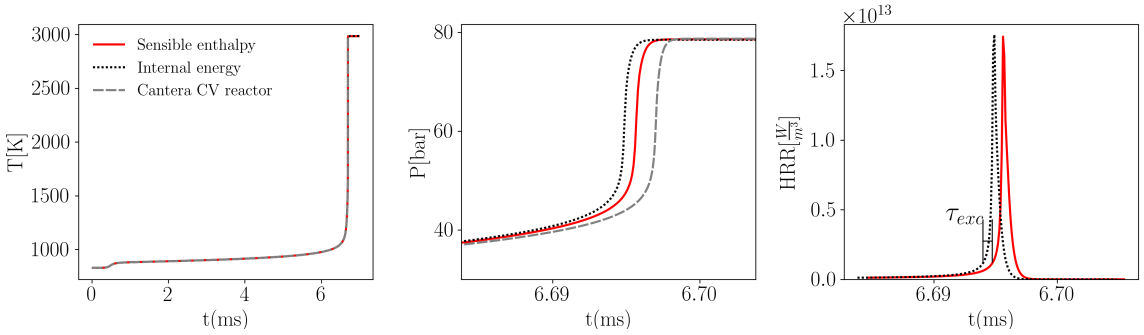


**Figure 2:** Temperature, pressure and heat release rate profiles vs time. Red, black and gray lines represent sensible enthalpy, internal energy form of energy equation and Cantera's 0D CV reactor respectively.

Overall, considering the whole IDT period, predicted temporal evolution of temperature and pressure (in Fig. 2 left) are in agreement. Moreover, Fig. 2 left shows that prediction of low temperature heat release at about 0.5 $\mu s$ matches well for the tested approaches. However, a closer inspection of the main heat release instance, Fig 2 middle and right, reveals that the main heat release occurs in advance in results from OpenFOAM compared with Cantera's result. The difference between Cantera's and OpenFOAM result could arise from the fact that OpenFOAM uses constant pressure assumption for chemical kinetic solution sub-step. Next, excitation times, $\tau_{exc}$, defined as the time between 5% and the maximum heat release are calculated in Fig. 2 right. The values of $\tau_{exc}$ obtained from the simulations are the same using both methods: 1.1 $\mu s$. However, as it is depicted in Fig. 2-right, the difference between heat release instance using enthalpy and total energy forms is about $\tau_{exc}$. In general, small induction times result in resonance between the sound and reaction waves and yet formation of detonation [20, 21]. Therefore, the present results show that using the internal energy form of energy equation may result the appearance of detonation by advancing heat release and increasing the rate at which the chemical energy is being released to a traveling acoustic wave. Nevertheless results from OpenFOAM are consistent. Observed deviation between the OpenFOAM results could be due to the indirect calculation of temperature for internal energy implementation, explicit assumption utilized for pressure derivative in sensible enthalpy implementation or boundary conditions effect.

*Case III: Shock induced detonation*

In this section, the shock induced detonation first studied by Oran et al. [22] is investigated. The mixture considered is 2/1/7 molar concentration of $H_2/O_2$/Ar, respectively. Initial conditions for the left and right sides of diaphragm is mentioned in table 1. In this example, the generated shock travels to the left wall and the reflected shock increases the temperature to above auto-ignition limit. After a delay, detonation wave kicks in and merges with the right propagating shock wave.

**Table 2:** Case III configuration.

| $\rho_l$ [Kg/m$^3$] | $\rho_r$ [Kg/m$^3$] | $P_l$ [pa] | $P_r$ [pa] | $U_l$ [m/s] | $U_r$ [m/s] | L [m] |
|---|---|---|---|---|---|---|
| 0.072 | 0.18075 | 173 | 594 | 0 | -487.34 | 0.12 |

In order to evaluate the accuracy of the numerical methods in compressible reactive flows, a mesh size in the

range of 400 - 9600 gridpoints is used in previous studies [4, 23, 24]. In this study, we used 200 gridpoints as the base mesh with 3 levels of refinement ($\delta x_{min} = 75\mu m$). The convective CFL number of 0.1 as well as GRI3.0 mechanism are considered for solving the coupled flow/chemical kinetic sets of equations. Figure 3 visualizes the H mass fraction, velocity and temperature profiles at three instances compared to Martínez Ferrer et al. [23] numerical results. Three combinations of flux scheme/energy equation, namely KT/enthalpy, KT/internal energy and HLLC/enthalpy, are chosen for studying the effect of these methods on the reactive compressible flow conditions.

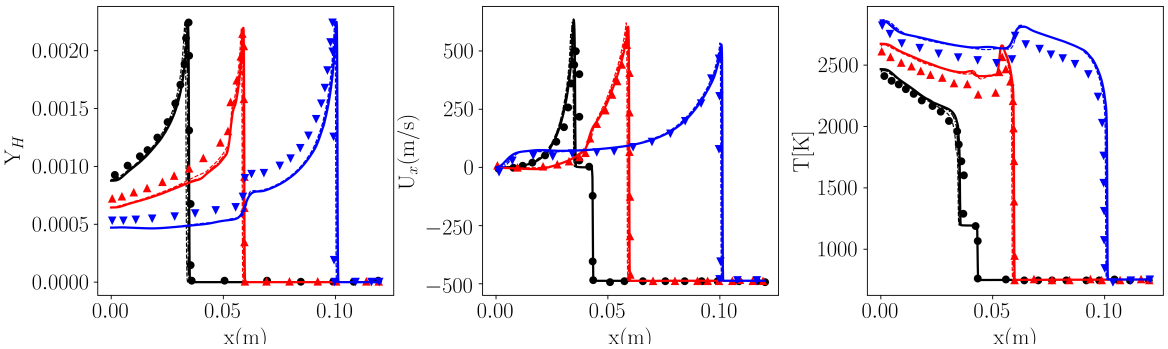


**Figure 3:** H mass fraction, velocity and temperature distribution at 170 $\mu s$ (black), 190 $\mu s$ (red) and 230 $\mu s$ (blue). The symbols are from Martínez Ferrer et al. [23]. Solid, dashed and dotted-dashed lines show KT/enthalpy, KT/internal energy and HLLC/enthalpy combination results.

Initiated detonation wave first accelerates towards CJ speed at the post shock conditions, Fig 3 black lines, and after merging with the shock, Fig 3 red lines, detonation decelerates to CJ speed which reads new unburnt state ahead of leading shock. The differences between the present and Martínez Ferrer et al. [23] simulation results in H mass fraction and combustion temperature can be related to different chemical mechanisms that are in use. The present paper utilizes GRI3.0 mechanism while a 9 species and 18 reactions reduced mechanism [25] has been used in Ref. [23]. Figure 3 shows that all three method combinations resulted in the similar profiles. This observation is majorly due to the high temperatures behind the reflected shock and later the detonation wave. However, looking more closely, small deviation between the approaches is observable from temperature profiles at 170 $\mu s$. Figure 4 shows the temperature profiles during the initial stages of ignition of the compressed mixture close to the wall. Compared to KT/enthalpy, KT/internal energy combination shows higher local temperature gradients while the ignition kernel is formed.

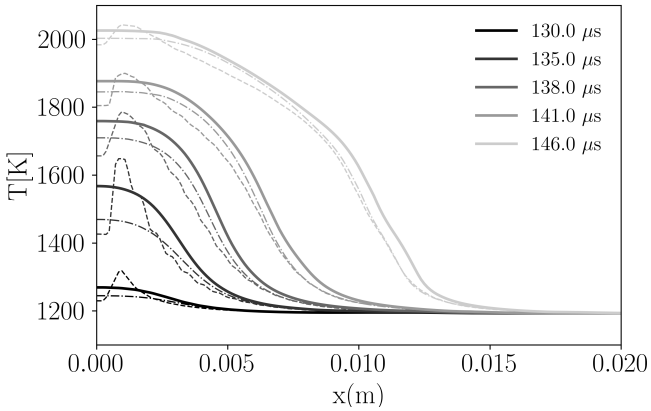


**Figure 4:** Temperature distribution during the ignition. Solid, dashed and dotted-dashed lines show KT/enthalpy, KT/internal energy and HLLC/enthalpy combination results.

### One dimensional direct initiation of detonation

In the following sections, we first validate the solver against the result from Marcantoni et al. [3] study with the same case configuration. Furthermore, we study the effect of mesh resolution on the results.

*Hydrogen one dimensional direct initiation of detonation*

Direct initiation of detonation in premixed hydrogen/air mixtures with different equivalence ratios is studied. The aim is to evaluate the solver in simulating planar detonation phenomenon. The studied case is a close end vessel, with a wall boundary on the left and an non reflective boundary on the right side. The detonation is ignited by a hotspot filled with helium. Details of the initial conditions and case configuration are listed in Table 3. Burke et al. [26]'s detailed mechanism with 13 species and 27 reaction is chosen for solving the chemistry problem.

**Table 3:** Case configuration.

| $T_h$ [K] | $T_0$ [K] | $P_h$ [Mpa] | $P_0$ [Mpa] | U [m/s] | $L_h$ [m] | $L_t$ [m] | $\Delta x$ [mm] |
|---|---|---|---|---|---|---|---|
| 3000 | 300 | 2 | 0.02 | 0 | 0.05 | 0.5 | 0.5 |

Simulation starts by a blast wave initiated by an igniter close to the wall. Shortly after, the blast wave generates an overdriven detonation propagating with speeds higher than CJ velocity through the unburnt mixture. Figure 5 shows, temperature, $H_2O$ mass fraction, pressure and density profiles at 228 $\mu s$. The present simulation results are also compared with the Marcantoni et al. [3] numerical simulation results.

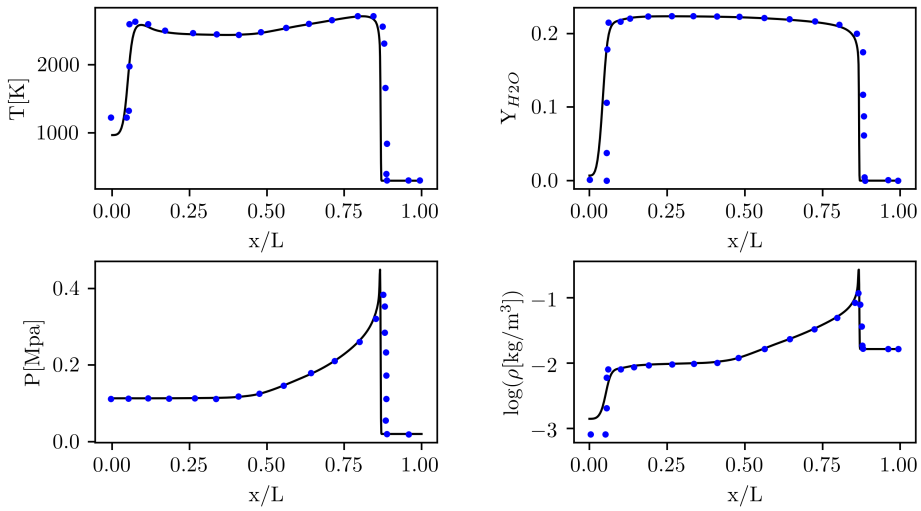


**Figure 5:** Temperature, H2O mass fraction, pressure and density distribution at 228 $\mu s$. The symbols are from Marcantoni et al. [3]. Solid, lines show KT/enthalpy combination, results.

Figure 5 shows that results predicted by the present solver are in agreement with results from ref. [3]. The early strong shock wave after formation of detonation wave travels as a contact discontinuity and indicates the interface between the igniter mixture and combustion products. The over-driven detonation wave later converges to velocities close to CJ speed. According to Fig 5, the pressure profile resembles a Taylor expansion wave, with a peak at the location of detonation and minimum values at the end of detonation zone.

Furthermore the estimated detonation displacement speeds from 1D simulations versus equivalence ratios in range 0.4-1.5 are compared with CJ velocities. Figure 6 shows the comparison between the theoretical CJ speed and simulated detonation wave speeds. Simulation of detonating combustion in leaner mixtures than considered above is not possible since the induction and excitation times are significantly affected

by equivalence ratio and consequently diffusion will affect the induction zone before auto-ignition of the mixture.

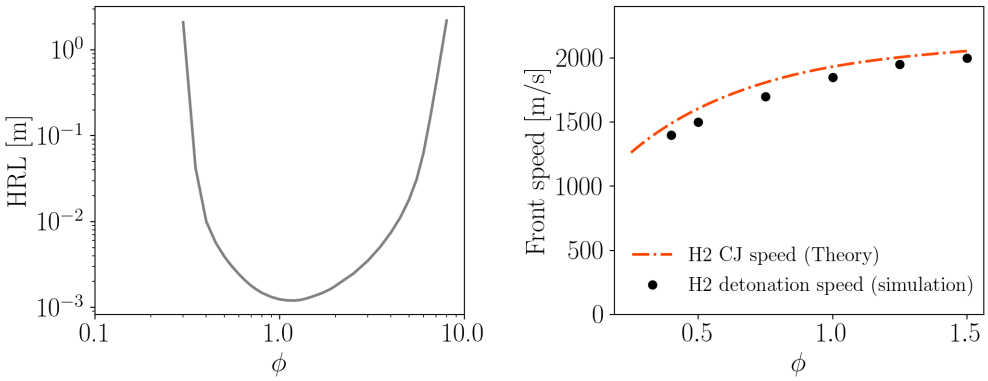


**Figure 6:** CJ velocity and HRL profiles of $H_2$ under different equivalence ratio. Symbols are estimated propagation speeds from 1D simulations.

Figure 6-left, illustrates the effect of equivalence ratio on detonation Half Reaction Length (HRL), defined as distance between leading shock to maximum heat release location (calculated with SD Toolbox). As it can be seen from Fig 6-left, equivalence ratios less than 0.4 increase the HRL to above 2 meters length. The planar detonation is stable when its structure is dominated by the heat release zone and such a long induction length is prone to instabilities initiated from variations in the strength of leading shock and subsequently variations in heat release which leads to an unstable detonation front. Moreover, ratio of the induction zone to the reaction zone length is an indicator of detonation stability [11], where $\chi \leq 1$ and $\chi \gg 1$ qualitatively demonstrate a stable and unstable detonation propagation, respectively. Details on the ZND structure of detonation, i.e. post shock pressure, maximum heat release, CJ speed, induction length ($\delta_{ind}$), exothermic length ($\delta_{ext}$) and their ratio ($\chi = \delta_{ind}/\delta_{ext}$), are mentioned in Table 4. The exothermic length has been defined as the distance between two points on the heat release pulse with 5% of maximum value.

**Table 4:** $H_2$ ZND detonation information.

| $\Phi$ | $P_{ps}$ [bar] | $HRR_{max}$ [W/m$^3$] | $U_{CJ}$ [m/s] | $\delta_{ind}$ [mm] | $\delta_{ext}$ [mm] | $\chi$ |
|---|---|---|---|---|---|---|
| 1.5 | 5.282 | 1.12e+12 | 2056.44 | 1.1 | 2.7 | 0.395 |
| 1.25 | 5.36 | 1.18e+12 | 2009.82 | 0.9 | 2.6 | 0.375 |
| 1 | 5.315 | 1.11e+12 | 1937.63 | 0.9 | 2.7 | 0.362 |
| 0.75 | 5.002 | 8.42e+11 | 1815.9 | 1.2 | 2.9 | 0.441 |
| 0.5 | 4.247 | 3.84e+11 | 1613.2 | 3 | 4.4 | 0.683 |
| 0.4 | 3.762 | 2.01e+11 | 1495.59 | 7 | 6.7 | 1.06 |

*Mesh sensitivity study*

While the CJ speeds estimated from 1D were in agreement with calculated values, the number of cells inside the exothermic zone in the results presented in the above section was only between 4 - 12 based on the equivalence ratio. Table 3 demonstrates the ZND induction and exothermic lengths for the considered equivalence ratios. Therefore, here we study the dependency of the result on the mesh size.

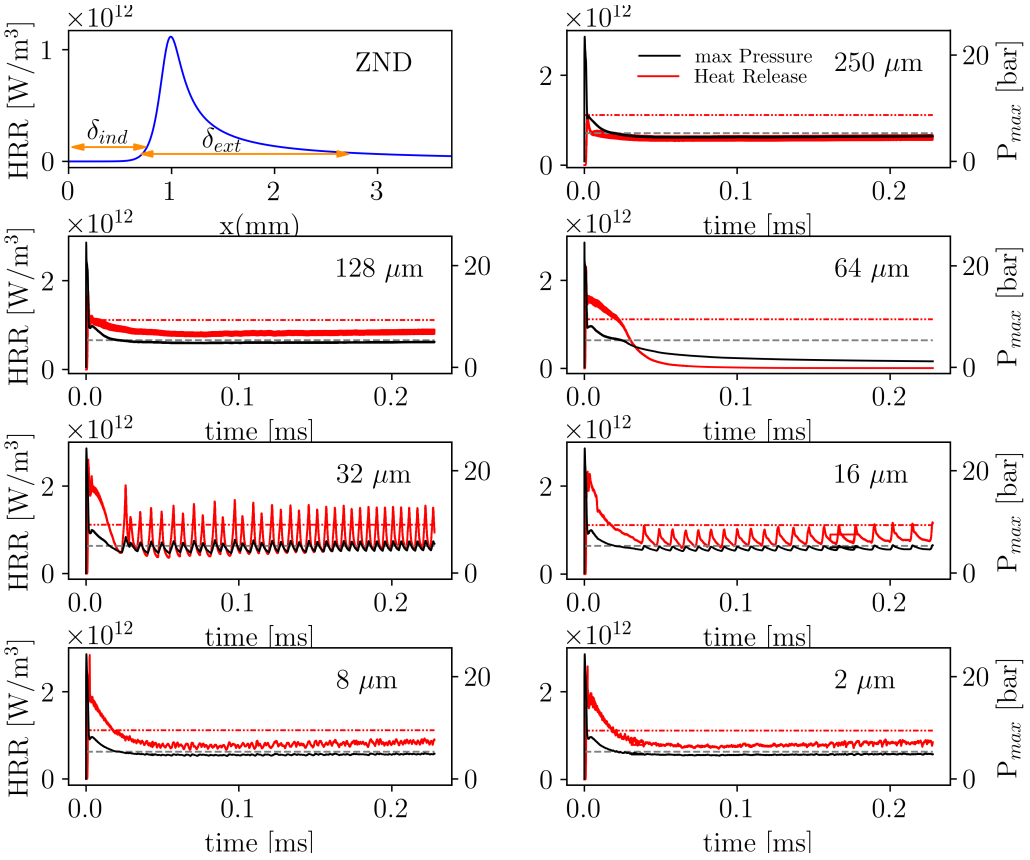


**Figure 7:** H2 detonation maximum heat release and pressure trace at $\phi = 1$. Solid lines show 1d simulation data, dashed line and dash-dotted lines show pressure and heat release of respective ZND detonation wave.

The results show that using a considerably coarse mesh will result in under-prediction of the initial heat release from over-driven detonation. However, the heat release and pressure fluctuate around a constant average value. Further decreasing the mesh size to 128 $\mu$m will result in gradual increase in initial and average heat release. However reducing mesh size to 64 $\mu$m results in a bifurcation between reaction and pressure waves which lead to decaying from a detonation wave to an subsonic reaction and shock fronts. By further decreasing the mesh size to 32 $\mu$m the decaying detonation turns into a pulsating detonation with high amplitudes and high frequency. Similar results is observed for 16 $\mu$m mesh while the amplitude and frequency of the pulses reduced to half. Finally, reducing the mesh size to 8 and 2 $\mu$m resulted in a stable detonation with low amplitude oscillations of pressure and heat release.

The result suggest that for a very coarse mesh, the reduced initial heat release will be compensated with diffused reaction zone due to the larger cell sizes and yet a stable detonation. Further decrease in mesh size increases the initial and average heat release but it results in narrower reaction zone and yet more unstable detonation. Due to the mentioned effect at certain cell sizes a bifurcation between the reaction front and shock wave can be observed. Once the grid refinement reached a certain value, due to the increase in initial heat release and later on will result in an stable propagation of detonation.

Comparison between the non-pulsating results in Fig. 7 (i.e. 250, 128, 8, 2 $\mu m$ mesh) suggest that using a coarse mesh will result in faster transition of heat release to steady form compared to finer mesh results. The steady heat release observed in these figures is expected due to the dominant exothermic zone for a stoichometric mixture of $H_2$/air, Fig.7 upper-left. The above trend suggests that considering the exothermic thickness about 100 cells in $\delta_{ind}$ (340 cells in $\delta_{ext}$) are required in order to correctly predict the detonation propagation.

Table 4 shows that at $\phi = 0.5$, the ratio of the induction zone to the reaction zone length is double the amount at stoichometric value which suggests that detonation propagates more unsteadily. Same study is done on the lean mixture and the result are show in Fig 8. Figure 8, demonstrates that in the mesh independent results

(i.e. mesh sizes below 16 $\mu m$), detonation undergoes a low frequency, high amplitude pulses. Compared to the previous case, the result suggests that the diffusive effect of the coarse mesh is now only limited to 500 ($\mu$m) case. Moreover, the results become independent to the mesh resolution at one level coarser mesh, i.e 16 $\mu$m (190 cells in $\delta_{ind}$ and 300 cells in $\delta_{ext}$)). These observations can be addressed by the fact that the induction and exothermic width are increased compared to the stoichometric case. Moreover, decaying happened in a wider range of mesh sizes, i.e. 250 - 64 $\mu m$, which may be due to the increased instability of the lean mixture's detonation ($\chi = 0.683$).

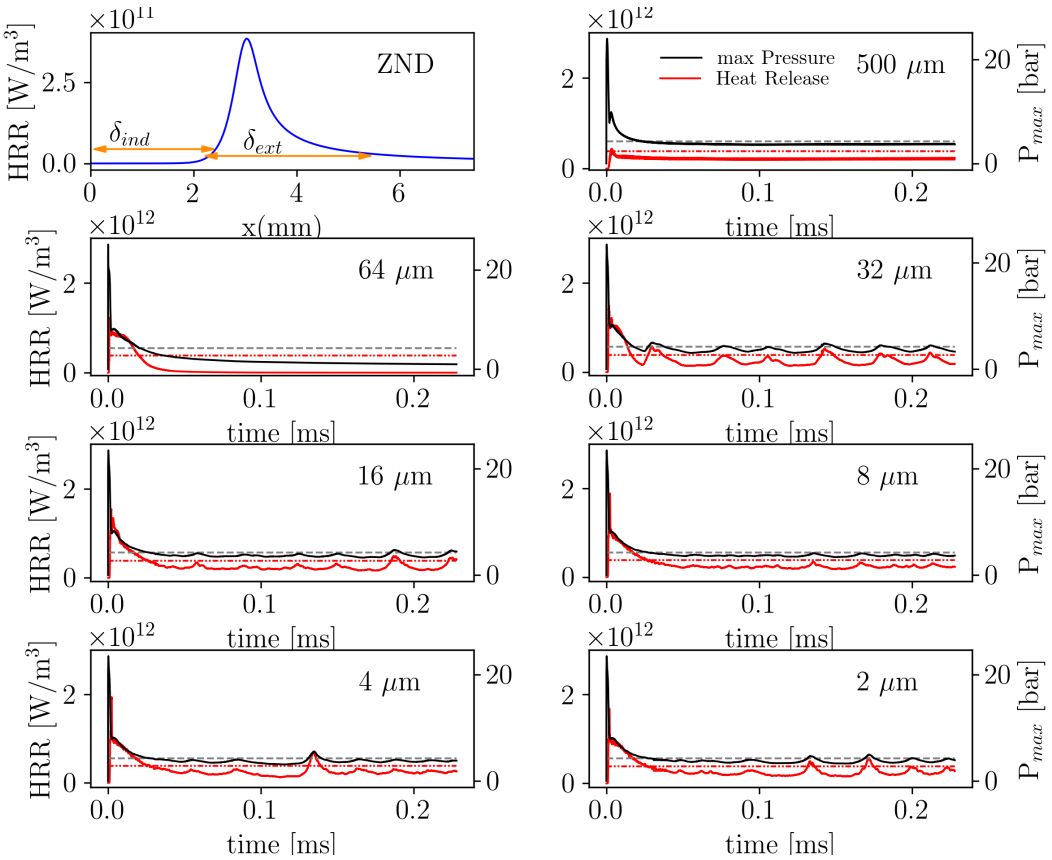


**Figure 8:** H2 detonation maximum heat release and pressure trace at $\phi = 0.5$. Solid lines show 1d simulation data, dashed line and dash-dotted lines show pressure and heat release of respective ZND detonation wave.

## CONCLUSIONS

The present results indicate the validation and verification of ARCFoam, based on OpenFOAM, in simulation of detonative combustion. ARCFoam combines, the adaptive mesh refinement approach, 2nd and 4th order time discretization with 2nd order central convective schemes (KT and HLLC) and efficient chemistry solution (DLBfoam) to simulate detonative combustion. 1D constant volume reactor and shock induced detonation simulations illustrated the sensitivity of the results to the selected form of energy equation (enthalpy or total energy) in reacting simulations. In general and in present implementation using total energy form of equation lead to earlier heat release compared to enthalpy form. This may result in higher temperature gradients during early stages of ignition and in presence a shock front it may affect the dynamics of detonation propagation. Results from mesh sensitivity study of direct initiated detonation of Hydrogen mixtures showed that above 300 mesh in $\delta_{ext}$ is required for correctly capturing the Hydrogen detonation propagation. Furthermore, results indicated that unresolved mesh resolution can lead to detonation quenching at both lean and stoichometric mixtures. Moreover, it was shown that coarse mesh can result in false stability in propagation of detonation at lean mixtures of Hydrogen with air.

## References


[1] Henry G Weller, Gavin Tabor, Hrvoje Jasak, and Christer Fureby. A tensorial approach to computational continuum mechanics using object-oriented techniques. *Computers in physics*, 12(6):620–631, 1998.

[2] Majie Zhao, Zhuyin Ren, and Huangwei Zhang. Pulsating detonative combustion in n-heptane/air mixtures under off-stoichiometric conditions. *Combustion and Flame*, 226:285–301, 2021.

[3] LF Gutiérrez Marcantoni, José Tamagno, and Sergio Elaskar. rhocentralrffoam: An openfoam solver for high speed chemically active flows–simulation of planar detonations–. *Computer Physics Communications*, 219:209–222, 2017.

[4] Zhiwei Huang, Majie Zhao, Yong Xu, Guangze Li, and Huangwei Zhang. Eulerian-lagrangian modelling of detonative combustion in two-phase gas-droplet mixtures with openfoam: Validations and verifications. *Fuel*, 286:119402, 2021.

[5] Florian Ettner, Klaus G Vollmer, and Thomas Sattelmayer. Numerical simulation of the deflagration-to-detonation transition in inhomogeneous mixtures. *Journal of Combustion*, 2014, 2014.

[6] Eleuterio F Toro, Michael Spruce, and William Speares. Restoration of the contact surface in the hll-riemann solver. *Shock waves*, 4(1):25–34, 1994.

[7] Christopher J Greenshields, Henry G Weller, Luca Gasparini, and Jason M Reese. Implementation of semi-discrete, non-staggered central schemes in a colocated, polyhedral, finite volume framework, for high-speed viscous flows. *International journal for numerical methods in fluids*, 63(1):1–21, 2010.

[8] Alexander Kurganov and Eitan Tadmor. New high-resolution central schemes for nonlinear conservation laws and convection–diffusion equations. *Journal of Computational Physics*, 160(1):241–282, 2000.

[9] Shaye Yungster and Krishnan Radhakrishnan. Pulsating one-dimensional detonations in hydrogen–air mixtures. *Combustion Theory and Modelling*, 8(4):745, 2004.

[10] Anne Bourlioux, Andrew J Majda, and Victor Roytburd. Theoretical and numerical structure for unstable one-dimensional detonations. *SIAM Journal on Applied Mathematics*, 51(2):303–343, 1991.

[11] Hoi Dick Ng. *The effect of chemical reaction kinetics on the structure of gaseous detonations*. PhD thesis, McGill University Montreal, Canada, 2005.

[12] Shaye Yungster and Krishnan Radhakrishnan. Structure and stability of one-dimensional detonationsin ethylene-air mixtures. *Shock Waves*, 14(1):61–72, 2005.

[13] Fan Zhang. *Shock wave science and technology reference library*. Springer, 2009.

[14] Bulut Tekgül, Petteri Peltonen, Heikki Kahila, Ossi Kaario, and Ville Vuorinen. Dlbfoam: An open-source dynamic load balancing model for fast reacting flow simulations in openfoam. *Computer Physics Communications*, page 108073, 2021.

[15] John R Dormand and Peter J Prince. A family of embedded runge-kutta formulae. *Journal of computational and applied mathematics*, 6(1):19–26, 1980.

[16] Thierry Poinsot and Denis Veynante. *Theoretical and numerical combustion*. RT Edwards, Inc., 2005.

[17] S Kao and JE Shepherd. Numerical solution methods for control volume explosions and znd detonation structure. *Galcit report fm2006*, 7:1–46, 2008.

[18] Peter N Brown, George D Byrne, and Alan C Hindmarsh. Vode: A variable-coefficient ode solver. *SIAM journal on scientific and statistical computing*, 10(5):1038–1051, 1989.

[19] Alessandro Stagni, ALESSIO Frassoldati, ALBERTO Cuoci, TIZIANO Faravelli, and ELISEO Ranzi. Skeletal mechanism reduction through species-targeted sensitivity analysis. *Combustion and Flame*, 163:382–393, 2016.

[20] Ya B Zeldovich. Regime classification of an exothermic reaction with nonuniform initial conditions. *Combustion and Flame*, 39(2):211–214, 1980.

[21] D Bradley, C Morley, XJ Gu, and DR Emerson. Amplified pressure waves during autoignition: relevance to cai engines. *SAE Transactions*, pages 2679–2690, 2002.

[22] ES Oran, TR Young, JP Boris, and A Cohen. Weak and strong ignition. i. numerical simulations of shock tube experiments. *Combustion and Flame*, 48:135–148, 1982.

[23] Pedro José Martínez Ferrer, Romain Buttay, Guillaume Lehnasch, and Arnaud Mura. A detailed verification procedure for compressible reactive multicomponent navier–stokes solvers. *Computers & Fluids*, 89:88–110, 2014.

[24] Ralf Deiterding. A parallel adaptive method for simulating shock-induced combustion with detailed chemical kinetics in complex domains. *Computers & Structures*, 87(11-12):769–783, 2009.

[25] Joseph F Grcar, Robert J Kee, Mitchell D Smooke, and James A Miller. A hybrid newton/time-integration procedure for the solution of steady, laminar, one-dimensional, premixed flames. In *Symposium (International) on Combustion*, volume 21, pages 1773–1782. Elsevier, 1988.

[26] Michael P Burke, Marcos Chaos, Yiguang Ju, Frederick L Dryer, and Stephen J Klippenstein. Comprehensive h2/o2 kinetic model for high-pressure combustion. *International Journal of Chemical Kinetics*, 44(7):444–474, 2012.

# Deflagration-to Detonation Transition of Hydrogen-Air Mixture in a Highly Congested, Open-ended Channel

**Henriksen, M.[1,*], Vaagsaether K.[1], Bjerketvedt D[1]**

*Faculty of Technology, Natural Sciences and Maritime Sciences, University of South-Eastern Norway, Kjølnes Ring 56, Porsgrunn, 3901, Norway*

**Corresponding author's email: mathias.henriksen@usn.no*

## ABSTRACT

The stochastic nature of the deflagration-to-detonation transition (DDT) is investigated in a 1-meter-long explosion channel partly filled with a mesh of 40 cylinders with a hydrogen-air gas mixture. The cylinder mesh/geometry was placed approximately in the center of the channel. In the cylinder geometry, the flame accelerates rapidly, and as the flame exits the cylinder geometry, the flame can propagate at velocities above 1000 m/s relative to the stationary observer. Out of the 20 experiments with the same initial conditions and a fuel-air equivalence ratio of 1.2, DDT occurred in half of the experiments, yielding a probability of 50% for DDT to occur in this experimental setup. Analysis of the high-speed images revealed that an initial hot spot had to form slightly downstream from the cylinder geometry for DDT to occur. The hypothesis is that the collision of two opposite transverse pressure waves causes a hot spot to form. The two opposite pressure waves are generated by two local explosions, which occur as the flame exits the top and bottom of the cylinder geometry. All experiments where DDT occurred showed the hot-spot formation, and no hot-spot formation was observed in the experiments where DDT did not occur.

**KEYWORDS:** DDT, Deflagration, Detonation, Turbulent Flames, Fast Flames, Explosions

## INTRODUCTION

Accidental explosions are one of the major potential hazards in the process industry; they can lead to large economic losses and, in the worst case, severer injuries and fatalities. It is crucial to understand the physics and mechanisms for these explosions to implement explosive preventive and safety measures appropriately. Significant advances have been made within numerical models; however, studies have shown that the results can vary in accuracy compared to experimental results. Therefore, experiments are essential for understanding the underlying physics and validating and improving numerical methods.

If a flame is sufficiently accelerated under the right conditions, it can transition into a detonation wave. This process is referred to as the deflagration-to-detonations transition (DDT). Earlier experimental and numerical studies have shown that during a DDT, shock focusing and reflection, turbulent mixing, and boundary layer effects generate a "hot spot" that initiates a detonation [1–11]. Although there have been significant advances in the numerical simulations and experimental studies of DDT, it is still one of the more challenging pheromones within combustion theory.

The generation of turbulence and turbulent combustion's effect on flame acceleration has an essential role in the DDT process. Pinos and Ciccarelli [12] studied the flame acceleration and DDT of stoichiometric hydrogen in a closed channel filled with a staggard and a non-stagger mesh of cylinders. Their study saw that the flame was accelerated mainly due to turbulence generation. Before DDT occurred, the measured flame velocity approached the sonic velocity relative to the burnt gas. The DDT process happened outside the schlieren imaging and was therefore not captured. The velocity of the detonation wave fluctuated significantly around the Chapman-Jouguet velocity due to the detonation quenching and re-initiation.

In this study, the stochastic nature of DDT is analyzed in a 1-meter, highly congested open-ended explosion channel. The explosion channel is filled with 40 cylinders with a diameter of 18 mm approximately in the center of the channel. The initial flame propagation is close to a laminar but becomes highly turbulent as it enters the cylinder geometry. In the geometry, the flame accelerates

rapidly and exits the cylinder geometry with a flame speed (from a laboratory frame of reference) of approximately 1000 m/s. Although the flame accelerates up to velocities at which DDT can occur, it does not always happen. 20 parallel (same initial conditions) experiments of hydrogen-air at a fuel-air equivalence ratio of 1.2 at atmospheric conditions have been studied to gain knowledge of this phenomenon.

## METHODS AND MATERIALS

The experimental setup and procedure have been described in previous studies [13–15]. The explosion channel's length, width, and height are 1000.0 mm, 65.0 mm, and 116.5 mm, respectively. In the explosion channel, there are 40 cylinders evenly placed approximately in the center of the channel. Each cylinder has a diameter of 18 mm and a length of 650 mm. Furthermore, the distance between the cells in the vertical and horizontal direction is 4.6 mm (±0.1 mm), creating a 0.5 void ratio and maximum blockage ratio of 0.77 in the obstructed part of the channel. The first column of cells was 400 mm from the closed end of the channel. Figure 1 a) shows a photo of the explosion channel with the 40 cylinders, and Fig. 1 b) shows a schematic illustration of the experimental setup with dimensions.

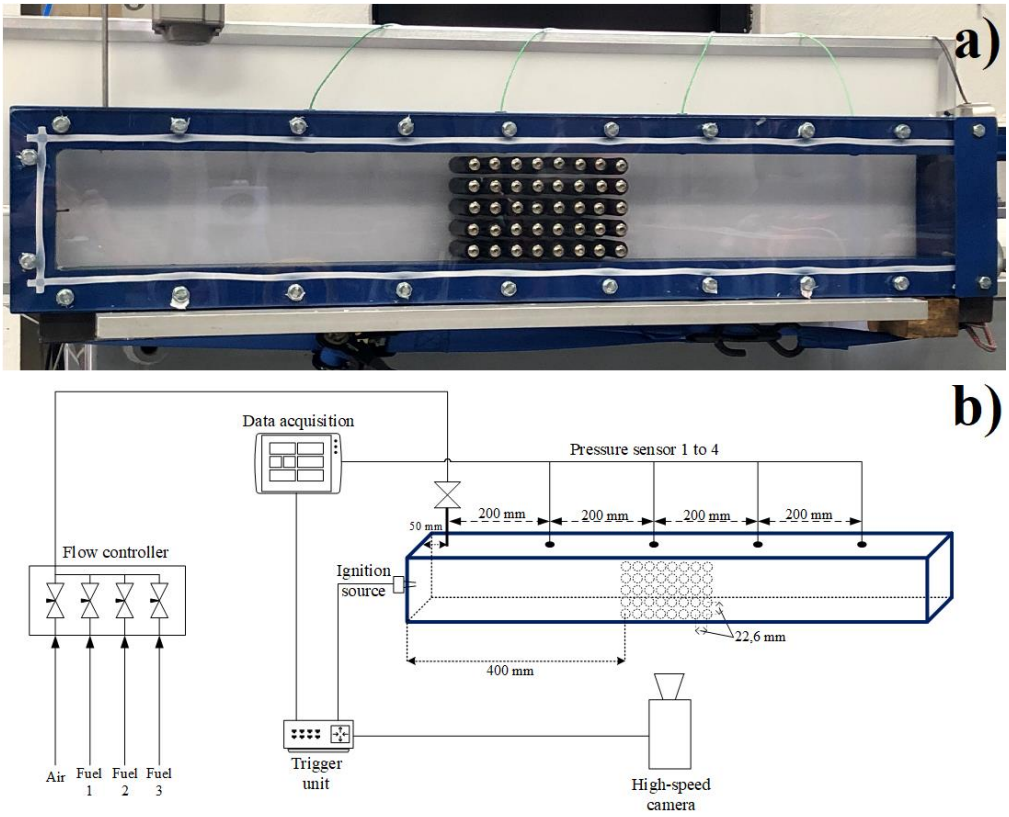


**Fig. 1.** Photo and schematic illustration of the 1-meter explosion channel. a): Photo of explosion channel with the cylinder geometry in the center of the channel; b): Schematic illustration of the experimental setup with dimensions.

The premixed hydrogen-air inlet is located 50 mm from the closed end of the channel. With a porous lid attached to the open end of the channel, the channel's volume was exchanged eight times to ensure a homogenous mixture. After filling, there was a 20-second delay before ignition to reduce convective flow. Moreover, the ignition duration was 0.02 s, which gives two sparks generated from an AC

transformer with an output voltage of 10 kV and a current of 20 mA. At the top of the channel, four Kistler pressure transducers spaced 250, 450, 650, and 850 mm from the closed end of the channel measures the explosion pressure. A Photron SAZ high-speed camera records the flame propagation at 75 000 to 200 000 frames per second. The flame front position and velocity were determined using an in-house developed image processing code from the high-speed video images. The pressure data, flame front position, and velocity were post-processed by a Savitzky-Golay filter [16] before further analysis. The Savitzky-Golay filter width and order for the pressure data were 9 and 1, respectively. For the flame front position and the velocity, the filter width and order were 7 and 1, respectively.

## RESULTS AND DISCUSSION

Table 1 shows the maximum pressure for all sensors and the maximum flame front velocity for the experiments. Of the 20 experiments, detonation occurred in half of the experiments, thus, resulting in a 50% probability of DDT in this explosion channel geometry. The detonation was determined by the recorded pressure, the calculated flame front velocity, and visually from the recorded high-speed video.

**Table 1. Summary of the main results for all experiments.**

| Experiment | $\phi$ | DDT | Max. Pressure PS 1 [kPa (gauge)] | Max. Pressure PS 2 [kPa (gauge)] | Max. Pressure PS 3 [kPa (gauge)] | Max. Pressure PS 4 [kPa (gauge)] | Max. Flame Front Velocity [m/s] |
|---|---|---|---|---|---|---|---|
| experiment 1 | 1.21[2] | No | 328 | 868 | 533 | 635 | 1080 |
| experiment 2 | 1.21[2] | Yes | 425 | 1257 | 1268 | 1926 | N/A |
| experiment 3 | 1.21[2] | No | 391 | 1189 | 554 | 455 | 1123 |
| experiment 4 | 1.21[2] | Yes | 391 | 726 | 1199 | 1787 | 1969 |
| experiment 5 | 1.21 | No | 325 | 966 | 745 | 468 | 1450 |
| experiment 6 | 1.21 | Yes | 304 | 1706 | 1409 | 1592 | 3253[3] |
| experiment 7 | 1.21 | No | 322 | 1348 | 700 | 326 | 1514 |
| experiment 8 | 1.21 | Yes | 322 | 1272 | 1359 | 1050 | 2126 |
| experiment 9 | 1.21 | No | 323 | 837 | 739 | 316 | 1591 |
| experiment 10 | 1.21 | No | 294 | 1164 | 655 | 482 | 1615 |
| experiment 11 | 1.21 | No | 277 | 718 | 823 | 260 | 1521 |
| experiment 12 | 1.21 | Yes | 331 | 1059 | 1016 | 955 | 2736 |
| experiment 13 | 1.21 | Yes | 331 | 956 | 2316 | 1068 | 2104 |
| experiment 14 | 1.21 | Yes | 344 | 1262 | 1136 | 1325 | 2146 |
| experiment 15 | 1.21 | Yes | 318 | 918 | 1329 | 1400 | 2326 |
| experiment 16 | 1.20 | No | 311 | 1503 | 651 | 420 | 1820 |
| experiment 17 | 1.22 | Yes | 339 | 850 | 1150 | 1203 | 2141 |
| experiment 18 | 1.22 | No | 290 | 1275 | 558 | 583 | 1622 |
| experiment 19 | 1.21 | Yes | 329 | 1810 | 1113 | 1190 | 2154 |
| experiment 20 | 1.22 | No | 247 | 1178 | 649 | 504 | 1398 |

[1] Not recorded by the high-speed camera1
[2] Concentration from volume flowmeters
[3] Over-exposed high-speed video

For the initial four experiments, separate volume flow meters for hydrogen and air were used to fill the channel with premixed hydrogen-air at a fuel-air equivalence ratio of 1.2. Due to the variation between the parallel experiments, the accuracy of the volume-flow meters and the filling time were considered a potential source of possible variation. Therefore, the volume-flow meters were replaced with two Bronkhorst mini cori-flow coriolis mass flow meters. The hydrogen concentration was measured during filling for five separate tests. With mass flows of 10.6 g/h of hydrogen and 300 g/h of air, the channel reached the desired hydrogen-air concentration after approximately 4 minutes. The filling time was set to 8 minutes for experiments 5 to 20. The fuel-air equivalence ratio was calculated from the mean mass flow rate from the last 4 minutes of filling. Any slight variation in the fuel-air equivalence ratio could not be correlated with the experiments where DDT occurred.

The initial flame propagation was first analyzed to see if any discrepancies between the parallel experiment could be found, which could explain why some of the experiments achieved DDT. Figure 2 a) compares the initial pressure build-up recorded at pressure sensor 1, located upstream from the cylinders. The experiments show that the pressure build-up upstream of the cylinders is between 60 to 90 kPa (gauge) for all experiments before the flame reaches the cylinders. The spatial flame front velocity before the flame reaches the cylinders is compared in Fig. 2 b). Figure 2 b) shows that it is also little to no difference in flame front velocity between experiments that later achieved DDT and those that did not. The flame front velocity for the three experiments is remarkably similar when they reach the cylinders at a distance of 400 mm. Based on the results presented in Fig. 2, we concluded that the initial flame propagation does not seemingly influence the DDT process. Furthermore, there were no distinct differences in the flame shape until the flame reached the cylinder geometry.

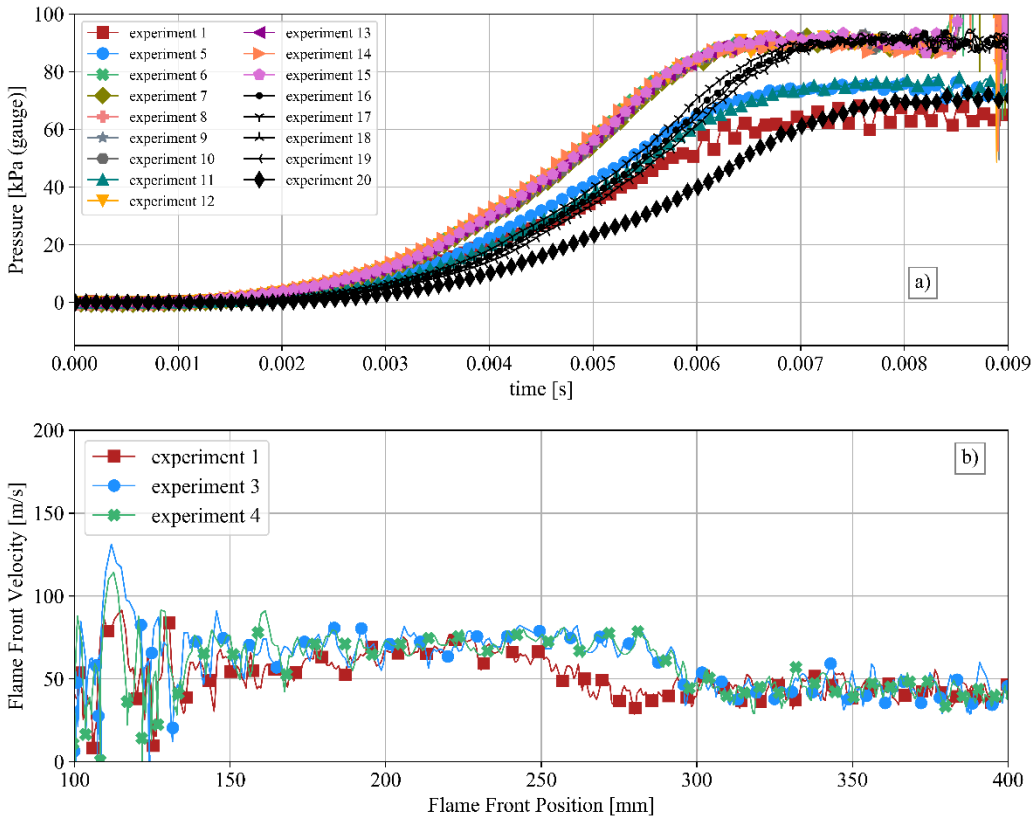

**Fig. 2.** The flame front velocity and the initial flame propagation pressure build-up upstream from the cylinder geometry. a): The recorded pressure from sensor 1 of all experiments; b) the spatial flame front velocity of all experiments 1, 3, and 4.

There is a considerable variation in recorded maximum pressure for pressure sensors 2, 3, and 4, as seen in Table 1. However, no evident trends in the dataset could explain why DDT occurred in 50% of the experiment. In Table 2, the experiments are divided into two groups/categories, one for those where DDT occurred and one for those where DDT did not; hereafter referred to as the detonation experiments and the deflagration experiments, respectively. Table 2 shows the maximum, minimum, standard deviation, and mean maximum explosion pressure for the four pressure sensors for the two groups of experiments. For pressure sensors 1 and 2, the minimum, maximum, and mean explosion pressure is in the same range for both groups of experiments. Comparing the pressure history for pressure sensors 1 and 2 for all experiments shows no apparent trends in the time of arrival or pressure peaks. It may indicate that the DDT process is not dependent on the pressure before and in the cylinder geometry. In the experiments where DDT occurred, the mean maximum pressure at sensors 3 and 4 is slightly lower than the Chapman-Jouguet (CJ) pressure of 1490 kPa (gauge) [17].

**Table 2. Statistical properties of the maximum explosion pressure for the detonation and the deflagration experiments**

| The detonation experiments | | | | |
|---|---|---|---|---|
| | PS 1 [kPa (gauge)] | PS 2 [kPa (gauge)] | PS 3 [kPa (gauge)] | PS 4 [kPa (gauge)] |
| Max. Maximum Pressure | 425 | 1810 | 2316 | 1926 |
| Mean Maximum Pressure | 343 | 1182 | 1330 | 1350 |
| Min Maximum Pressure | 304 | 726 | 1016 | 955 |
| The standard deviation | 37 | 356 | 368 | 326 |
| **The deflagration experiments** | | | | |
| | PS 1 [kPa (gauge)] | PS 2 [kPa (gauge)] | PS 3 [kPa (gauge)] | PS 4 [kPa (gauge)] |
| Max. Maximum Pressure | 391 | 1503 | 823 | 635 |
| Mean Maximum Pressure | 311 | 1105 | 661 | 445 |
| Min Maximum Pressure | 247 | 718 | 553 | 260 |
| The standard deviation | 38 | 249 | 94 | 118 |

A distinction was found when comparing the high-speed videos for the two experimental groups (the detonation and deflagration experiments). In the experiments where DDT occurred, the formation of a small hot-spot head or at the tip of the flame was observed. The hot spots were consistently observed in the center of the channel and 30 to 80 mm downstream from the end of the cylinder geometry. The flame accelerated from the hot spot, and the onset of DDT occurred when the flame reached the upper and lower walls of the channel. In the detonation experiments, planar detonation fronts could be detected approximately 200 to 270 mm downstream from the end of the cylinders. By contrast, no visible hot spots were detected in all the deflagration experiments, indicating that an initial hot spot is needed in the proximity of the cylinder geometry to initiate the DDT process. In Fig. 3. a series of high-speed images illustrate the hot-spot formation, the onset of DDT, and a flat detonation wave propagation.

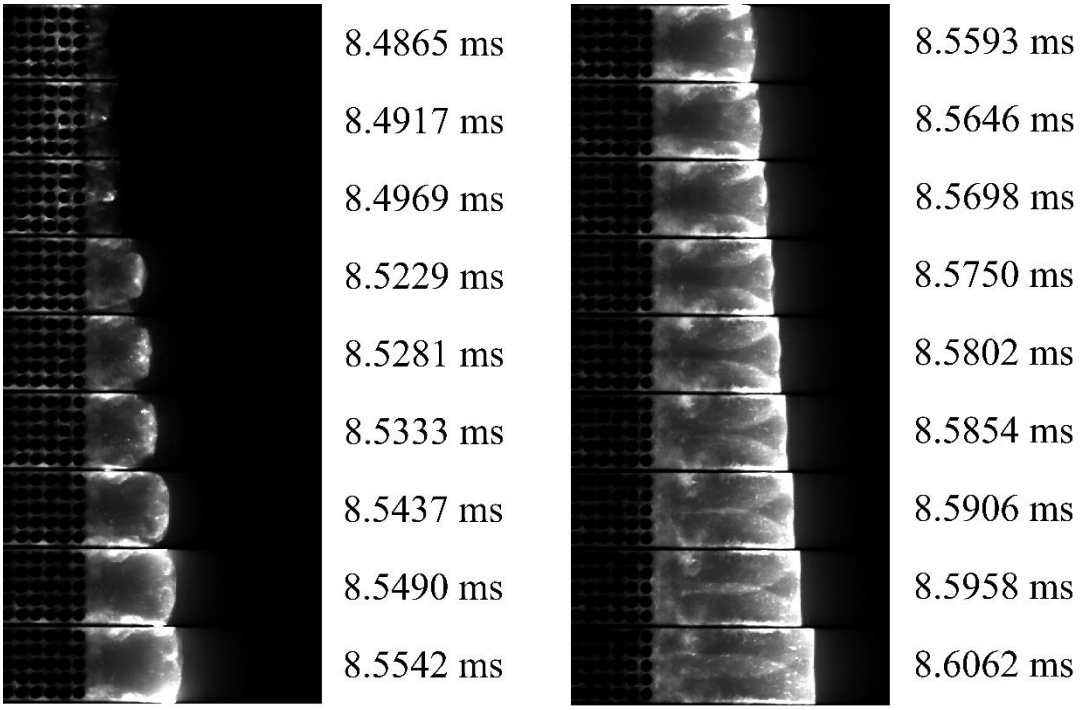


**Fig. 3.** Series of high-speed images from experiment 14.

Figure 3 shows a series of high-speed images of experiment 14. The first three images (8.4865 to 8.4969 ms) show the hot-spot formation, which occurs almost in the channel's center, approximately 31 mm downstream from the cylinders. The fourth image at 8.5229 ms shows the flame front accelerates from the hot spot, which leads to the onset of DDT at image 8.5490 ms, approximately 144 mm downstream from the cylinders. After the onset of DDT, a flat detonation front can be observed at 8.5854 ms, about 212 mm downstream from the cylinders. For all detonation experiments, similar hot-spot formation, flame propagation, and the onset of DDT, as shown in Fig. 3. were observed.

The flame front position and the recorded pressures from experiment 14 are compared in Fig. 4. Figure 4 show that the onset of DDT occurs between pressure sensor 3 and 4. The onset of DDT occurred between pressure sensors 3 and 4 for all the detonation experiments. No significant pressure peaks were found, which could be associated with the hot-spot formation. Comparing the events illustrated in Fig. 3 and described in the previous paragraph is in close agreement with the pressure and flame front position shown in Fig 4.

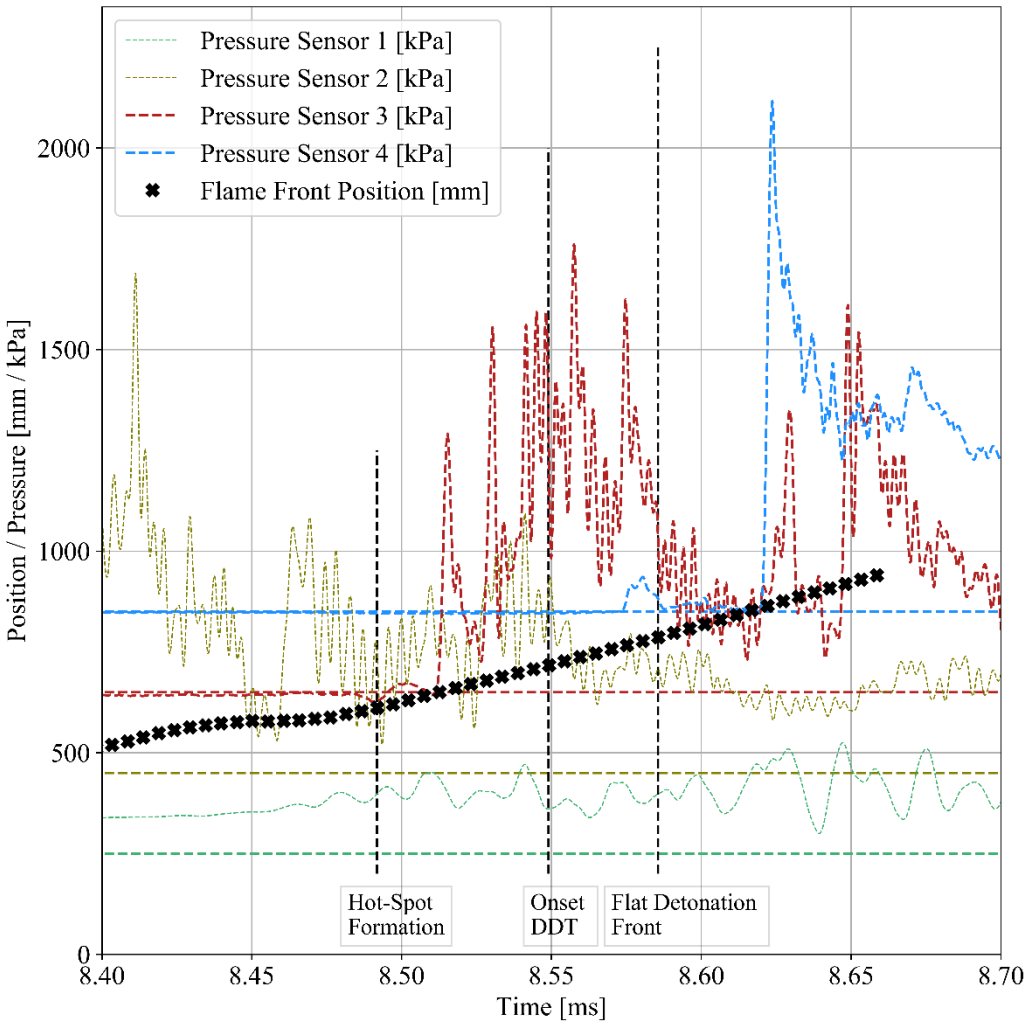


**Fig. 4.** The measured flame front position and pressure for the four pressure sensors for experiment 14.

A hypothesis on the initial hot-spot formation is that two opposite and local explosions occur as the flame exits the top and bottom of the cylinder geometry. The pressure waves from these two explosions collide near the center of the channel and ignite a small volume ahead or at the tip of the flame. If the flame exits the top and bottom at slightly different times, or there is only one local explosion either in the top or bottom, there is no initial hot-spot formation in the center of the channel. It is impossible to confirm this hypothesis with the current high-speed images. In further work, shadowgraphy and schlieren imaging will be used to study the flame propagation and pressure wave formation as the flame exits the cylinder geometry.

Since the gap between the cylinders, which is 4.6 mm, is less than the detonation cell size for a hydrogen-air mixture at a fuel-air equivalence ratio of 1.2, it is unlikely that a steady detonation wave would propagate through the cylinder geometry [6,18–20]. However, quenching and re-initiating quasi-detonation could have occurred within the cylinder geometry. Pinos and Ciccarelli [6] found detonation quenching and re-initiation in a study with similar channel geometry. Experiments 6, 16, and 18 with a maximum explosion pressure of 1706 kPa, 1503 kPa, and 1810 kPa at pressure sensor 2 may indicate that quasi-detonations inside the cylinder geometry occur. It is difficult to determine

if a detonation was initiated or quenched in the cylinder geometry based on the high-speed images. In further work, shadowgraphy and schlieren imaging will be used to study the flame propagation and shock formation as the flame within the cylinder geometry

## CONCLUSION

In this study, stochastic nature DDT has been studied in an open-ended explosion channel filled with a cylinder mesh/geometry with a void ratio and maximum blockage ratio of 0.5 and 0.78, respectively. A total of 20 experiments with the same initial conditions were conducted to determine the likelihood of DDT. Out of 20 experiments, DDT occurred in 10 of the experiments, yielding a probability of 50% of DDT.

The initial flame propagation (before the flame reached the cylinders) appeared not to affect whether or not a DDT occurred. Similarly, comparing the pressure from pressure sensors 1 and 2 for all experiments, no apparent trends could be found that explained why DDT only occurred 50% of the time. Moreover, the pressure, flame front velocity, and flame shape were remarkably similar for all experiments until the flame reached the cylinder geometry.

In all experiments where DDT occurred, the high-speed images revealed that the flame needed to be accelerated from an initial hot spot slightly downstream from the cylinder geometry for DDT to occur. The onset of DDT was observed when the accelerated flame reached the channel's upper and lower walls. The current hypothesis is that two opposite local explosion needs to occur when the flame exits the cylinder geometry for the hot spot to form. However, it is difficult to confirm this hypothesis with the current high-speed images, and further work with shadowgraphy and schlieren imaging is needed to confirm this hypothesis.

## ACKNOWLEDGMENT

This work was performed within MoZEES, a Norwegian Centre for Environment-friendly Energy Research (FME), co-sponsored by the Research Council of Norway (project number 257653) and 40 partners from research, industry and public sector.

## REFERENCES

[1] Urtiew PA, Oppenheim AK. Experimental observations of the transition to detonation in an explosive gas. Proc R Soc Lond A 1966;295:13–28. https://doi.org/10.1098/rspa.1966.0223.

[2] Knystautas R, Lee JH, Moen I, Wagner HGg. Direct initiation of spherical detonation by a hot turbulent gas jet. Symposium (International) on Combustion 1979;17:1235–45. https://doi.org/10.1016/S0082-0784(79)80117-4.

[3] Oran ES, Gamezo VN. Origins of the deflagration-to-detonation transition in gas-phase combustion. Combustion and Flame 2007;148:4–47. https://doi.org/10.1016/j.combustflame.2006.07.010.

[4] Gamezo VN, Ogawa T, Oran ES. Numerical simulations of flame propagation and DDT in obstructed channels filled with hydrogen–air mixture. Proceedings of the Combustion Institute 2007;31:2463–71. https://doi.org/10.1016/j.proci.2006.07.220.

[5] Xiao H, Oran ES. Shock focusing and detonation initiation at a flame front. Combustion and Flame 2019;203:397–406. https://doi.org/10.1016/j.combustflame.2019.02.012.

[6] Kellenberger M, Ciccarelli G. Propagation mechanisms of supersonic combustion waves. Proceedings of the Combustion Institute 2015;35:2109–16. https://doi.org/10.1016/j.proci.2014.08.002.

[7] Houim RW, Ozgen A, Oran ES. The role of spontaneous waves in the deflagration-to-detonation transition in submillimetre channels. Combustion Theory and Modelling 2016;20:1068–87. https://doi.org/10.1080/13647830.2016.1249523.

[8] Gaathaug AV. Experimental Study of Deflagration to Detonation Transition in Hydrogen-Air Mixtures n.d.:191.
[9] Vaagsaether K. Modelling of gas explosions. Telemark University College, 2010.
[10] Bjerketvedt D, Sonju OK, Moen IO. The Influence of Experimental Condition on the Reinitiation of Detonation Across an Inert Region. Progress in Astronautics and Aeronauticsamic 1985;106.
[11] Dziemińska E, Hayashi AK. Auto-ignition and DDT driven by shock wave – Boundary layer interaction in oxyhydrogen mixture. International Journal of Hydrogen Energy 2013;38:4185–93. https://doi.org/10.1016/j.ijhydene.2013.01.111.
[12] Pinos T, Ciccarelli G. Combustion wave propagation through a bank of cross-flow cylinders. Combustion and Flame 2015;162:3254–62. https://doi.org/10.1016/j.combustflame.2015.05.013.
[13] Henriksen M. A study of premixed combustion of gas vented from failed Li-ion batteries. University of South-Eastern Norway, 2021.
[14] Henriksen M, Vaagsaether K, Lundberg J, Forseth S, Bjerketvedt D. Simulation of a premixed explosion of gas vented during Li-ion battery failure. Fire Safety Journal 2021:103478. https://doi.org/10.1016/j.firesaf.2021.103478.
[15] Henriksen M, Vaagsaether K, Lundberg J, Forseth S, Bjerketvedt D. Numerical study of premixed gas explosion in a 1-m channel partly filled with 18650 cell-like cylinders with experiments. Journal of Loss Prevention in the Process Industries 2022:15. https://doi.org/10.1016/j.jlp.2022.104761.
[16] Savitzky A, Golay MJE. Smoothing and Differentiation of Data by Simplified Least Squares Procedures. Analytical Chemistry 1964;36:1627–39. https://doi.org/10.1021/ac60214a047.
[17] Kaneshige M, Shepherd JE. Detonation database. GALCIT - Caltech; 1997.
[18] Peraldi O, Knystautas R, Lee JH. Criteria for transition to detonation in tubes. Symposium (International) on Combustion 1988;21:1629–37. https://doi.org/10.1016/S0082-0784(88)80396-5.
[19] Cross M, Ciccarelli G. DDT and detonation propagation limits in an obstacle filled tube. Journal of Loss Prevention in the Process Industries 2015;36:380–6. https://doi.org/10.1016/j.jlp.2014.11.020.
[20] Guirao CM, Knystautas R, Lee JH. A Summary of Hydrogen-Air Dentonation Experiments. McGill University; 1989.

# The explosion length as a measure of detonability: Review of data in methane and hydrogen

**Radulescu M.I.[1,*], Pekalski, A.[2], S. Zangene, F.[1]**

*[1] University of Ottawa, Mechanical Engineering, Ottawa, Ontario, Canada.*
*[2] Shell, United Kingdom.*
**Corresponding author's email:matei@uottawa.ca*

## ABSTRACT

We review the concept of critical explosion length $R_0$ as a unique length scale characterizing the detonability of a reactive mixture. Review of empirical data for methane and hydrogen fuels in various compositions with air or $O_2/N_2$ supports that this length scale in critically initiated detonations by a strong energy source (direct initiation) coincides with the distance required for a choked Chapman Jouguet deflagration to accelerate to a detonation wave in deflagration to detonation transition (DDT) experiments. For all mixtures investigated, it is found that the critical explosion length $R_0$ is approximately $25\pm2\lambda$. Correlations with the ZND induction zone lengths yield mixture specific correlations: $R_0 \cong 1900 t_i u_{VN}$ for methane mixtures and $R_0 \cong 290 t_i u_{VN}$ for hydrogen mixtures, kinetic based limitations are noted for detonations lying beyond the chain branching cross-over limit. This occurs for fuel-air equivalence ratios less than approximately 0.5 (18% H) and for sufficiently high pressures. Kinetic predictions are found to be severely underpredicting the detonability of these mixtures. Experiments are suggested to measure this unique length scale in tubes and large scale non-confined with line energy deposition.

**KEYWORDS:** explosion length, detonation, initiation, hydrogen, methane.

## INTRODUCTION

Detonations can be established by direct initiation from the decaying blast wave originating from a strong energy source [1, 2] or through the acceleration of deflagration waves to detonations [3, 4]. In accident scenarios, the latter is usually the norm, given the very large energies required for direct initiation in common fuel-air mixtures. While the two initiation processes are usually treated differently and separately in the literature , this review suggests that the two modes of initiation can indeed be characterized by the same length scale of amplification of a fast deflagration wave to a detonation, the *explosion length*. This unique length scale offers a unique measure of the detonability of a reactive mixture. In this paper, we review the meaning of the explosion length and compile data for hydrogen and methane, highlighting the relevant knowledge gaps.

## THE LENGTH SCALES OF DIRECT INITIATION AND DDT

### Direct Initiation

In the context of blast wave theory [5], the explosion length $R_0$ provides a characteristic length scale for the decay of a blast wave originating from a point, line or plane source of energy

$$R_0 = \left(\frac{E_{sph}}{p_0}\right)^{\frac{1}{3}} \text{ in the spherical geometry} \quad (1)$$

$$R_0 = \left(\frac{E_{cyl}}{p_0}\right)^{\frac{1}{2}} \text{ in the cylindrical geometry} \quad (2)$$

$$R_0 = \left(\frac{E_{plan}}{p_0}\right) \text{ in the planar geometry} \quad (3)$$

For a fixed explosion length, when blasts decay in a reactive gas, the local time scale of blast wave decay is nearly identical in the three geometries at conditions of hot spot ignition [6]. Under *critical* initiation conditions, one thus expects that there would be a unique dependence of the decay rate time scale with a time scale denoting the detonation sensitivity. This argument relating the energies in different geometries for a fixed explosion length leads to the concept of explosion length scaling:

$$R_0^* = \left(\frac{E_{sph}^*}{p_0}\right)^{\frac{1}{3}} = \left(\frac{E_{cyl}^*}{p_0}\right)^{\frac{1}{2}} = \left(\frac{E_{plan}^*}{p_0}\right) \quad (4)$$

a relation postulated by Lee [1]. Previous experiments, mostly in the spherical or cylindrical geometries, suggest that the critical explosion length in a wide range of mixtures can be well correlated with the detonation cell size $\lambda$, yielding empirical estimates $R_0 = 20 - 30\lambda$ for a wide range of mixtures [1, 7, 8].

The invariance of the explosion length with geometry can also be interpreted in terms of length scales. The critical explosion length was found to be comparable with the detonation formation length scale [7] itself, a finding of central importance in our discussion. Fig. 1 shows, for example, the formation of a quasi-cylindrical detonation from a line source of energy through merging of explosion centers, culminating in a self-sustained detonation wave after a travel distance comparable to the explosion length of 0.8m. The invariance of the explosion length with geometry also permits to simply scale between different geometries and also consider hybrid geometries. For example, a non-confined planar or line source of physical dimension less than the critical explosion length acts as an effective point source[1, 7].

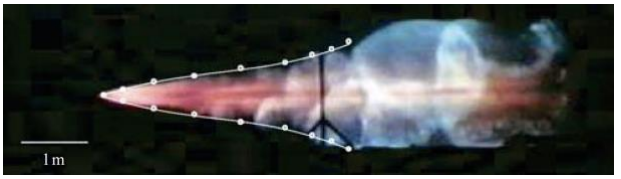


**Fig. 1** Critical detonation initiation from a line source of energy consisting of a high explosive detonation cord in a stoichiometric mixture of $C_2H_4$-air; explosive products are red and blue chemical emission is associated with detonative combustion in the gas [6].

**Deflagration to detonation transition (DDT)**

Deflagration to detonation transition (DDT) usually involves two phases. The first is the acceleration of a laminar flame through the mechanism of surface area increase by hydrodynamically induced flame deformations. This phase usually saturates into a Chapman-Jouguet deflagration, where the turbulent reaction wave propagates with sonic velocity relative to its products [9-13]. The second phase is the acceleration of these "choked" flames to a detonation wave. In non-sensitive fuel-air mixtures where auto-ignition is difficult, this acceleration takes on a finite distance, during which transverse waves are amplified and both auto-ignition and diffusively dominated combustion participate[11]. An example is shown in Fig. 2. The shock-flame complex dynamically reforms into fewer modes with stronger transverse waves, a process reminiscent of the acceleration of Fig. 1.

In congested geometries, these fast flames also benefit from interactions with obstacles, which locally favor shock-flame interactions and auto-ignition events through wave reflections. At present, there is no guideline to model this amplification process. Empirically, however, it is expected that the characteristic length scale of amplification be proportional to the cell size. Dorofeev et al. [14-16], suggest that this is related to the spontaneous wave amplification concept, at least in a stochastic sense, and advocate for a characteristic length scale of approximately $7\lambda$. Typically, a pore size greater than this length scale is required for the transition to be possible. Nevertheless, the amplification distance from choked flames to detonations has not been quantified to date.

**This study**

It is thus of interest to determine how the amplification length of choked flames in DDT experiments compares with the critical explosion lengths derived from direct initiation experiments, given these length scales monitor the amplification of deflagration waves, following local ignition spots, into a fully developed detonation. In the remainder of the paper, we compile the available data for direct initiation and DDT in hydrogen-air and methane-air and compare with the available amplification lengths in DDT experiments, in order to draw some insight into the controlling mechanisms, while also providing useful correlations for the practitioner.

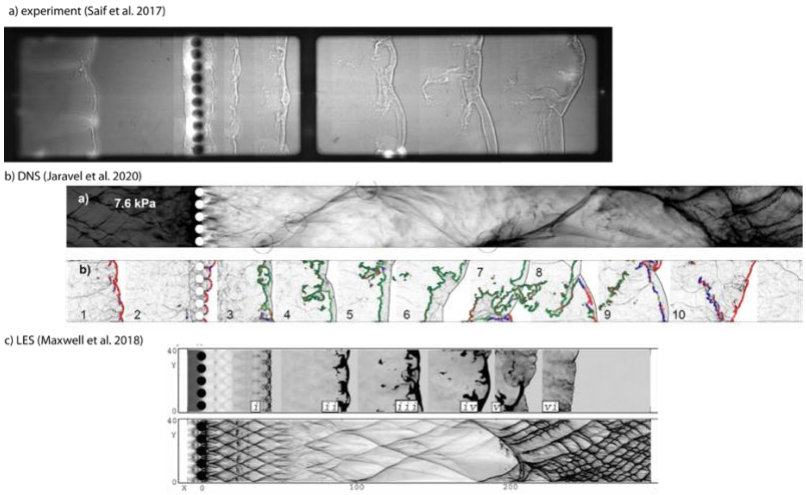


**Fig. 2** The decoupling of a $CH_4$-$O_2$ detonation across a row of cylinders into a shock-fast flame complex and its subsequent re-acceleration to a detonation via the amplification of transverse modes; a) schlieren experiments from [11], b) DNS simulations from [16] and c) LES simulations from [15]. The color coded reaction zones in b) indicate diffusion controlled flames (green) and auto-ignition controlled (red) using Chemical explosive mode analysis.

## HYDROGEN

Elsworth et al. measured the critical mass of Tetryl high explosive required to initiate non-confined hydrogen-air detonations at atmospheric conditions; tabulated results are provided by Guirao et al.[17]. To reduce their data, we used the heat of detonation of 4.56MJ/kg reported by Dobratz and Crawford measured experimentally with water in vapor form. Their data is reported as an explosion length via (1) in Fig. 3. Note that the experiments were performed in a 1.5m$^3$ vessel (radius 0.7 m). Data with explosion radii larger than this rely on experiments in which the initiation limits may be affected by the walls and should be discarded [17].

Benedick also measured the mass of C4 high explosive required to initiate non-confined hydrogen-air detonations in the unconfined, but a reduced pressure of 0.83 atm. Tabular data is provided by Guirao et al. [17] to reduce their data, we used the heat of detonation of 4.87MJ/kg reported by Guirao et al.[17]. In order to correct for the non-atmospheric conditions, we assumed

$$\frac{R_0^*}{\lambda} \equiv \left(\frac{E_{sph}^*}{p_0}\right)^{\frac{1}{3}} \frac{1}{\lambda} = \text{const.} \qquad (5)$$

and the usual dependence $\lambda \sim p_0^{-1}$, yielding the scaling relation $E_{sph}^* p_0^2 = \text{const.}$ Their data is also reported as an explosion length in Fig. 3.

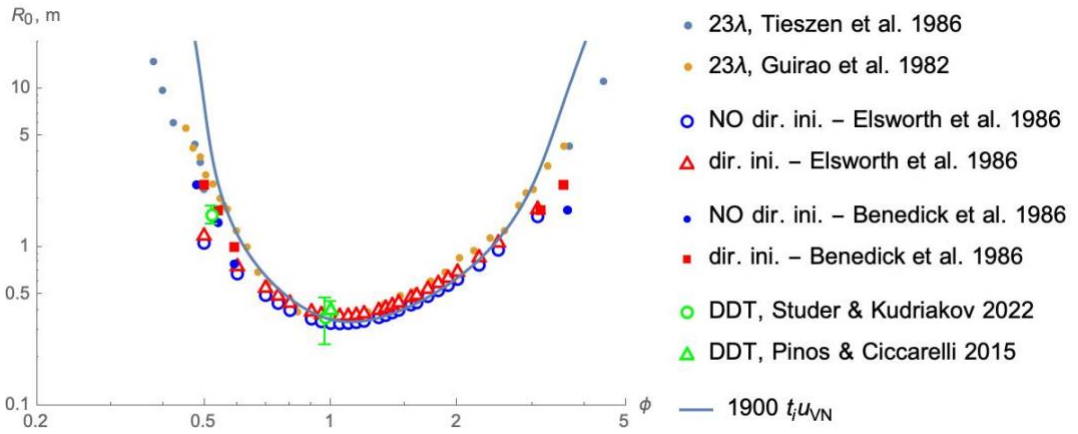


**Fig. 3** The explosion length dependence on fuel-air equivalence ratio in $H_2$-air.

Fig. 3 also reports the result of DDT length in $H_2$-air mixtures at ambient conditions. In a stoichiometric mixture, Pinos and Cicarrelli [18] measured a choked flame acceleration distance of 40 cm in a tight arrangement of staggered obstacles. This is found in excellent agreement with the explosion length data obtained from direct initiation.

More recently, Studer et al. [19] measured the acceleration of flames in a 120 cm diameter tube with periodic orifice rings placed 1 tube diameter apart and providing a 0.3 area blockage ratio. Their flame acceleration in an 18%$H_2$ mixture ($\phi = 0.52$) is shown in Fig. 4. Repeat experiments reproducibly recover a unique amplification distance of approximately 1.6$\pm$0.2m. Their data for the run up distance is also in excellent agreement with the explosion length data of Fig. 3. This may seem quite surprising at first glance, since their geometry is very different from that of Pinos and Cicarelli. Nevertheless, it supports the view of a unique length scale for detonation formation from fast flames.

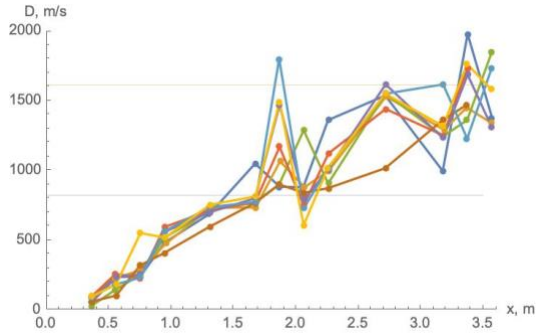


**Fig. 4** Flame speed in a 120 mm diameter tube with orifice plate blockage [19], lines denote the CJ deflagration (below) and CJ detonation (above) speeds.

The explosion length data was correlated with the cell size data available in the literature. Also shown in Fig. 3 is the cell size data of Guirao et al.[20] and Tieszen et al.[21], multiplied by a factor of 23. An $R_0^* \approx 23\lambda$ correlation appears to capture well the available data for direct initiaion and DDT, although some experimental scatter is clearly evident on the lean side near an equivalence ratio of 0.5 (correspoding to approximately 18%$H_2$ on a molar basis) – see above dicussion on expeimental limitations.

We have also attempted to correlate the available data with an estimate of the induction zone length $u_{VN}t_i$. We calculated the ignition delay $t_i$ at constant volume for each mixture composition at the post shock Von Neumann state and evaluated the flow speed $u_{VN}$ at that state using real gas

calculations with Cantera [22] and the San Diego chemical kinetic mechanism [23]. ZND calculations yielded very similar results. For equivalence ratios between 0.6 and 3, a correlation $R_0^* \approx 1900 u_{VN} t_i$ provides a good fit. Nevertheless, outside these limits, this correlation is not expected to hold, as the cell size is no longer proportional to the induction zone length. Unfortunately, data available for these conditions is limited and displays significant scatter.

The point where the correlation breaks down corresponds to when the shock temperature drops below the chain-branching cross-over limit [23]. Below this temperature, the global activation energy grows significantly and the induction to reaction time ratio also grows, as shown in Fig. 3. At these conditions, the detonation waves are expected to be significantly more unstable, as the stability parameter

$$\chi \equiv \frac{E_a}{RT_{VN}} \frac{t_i}{t_r} \tag{6}$$

grows considerably, as shown in Fig. 5. More unstable detonations are known to be more easily initiated [24, 25], as indicated by the significant drop in the ratio $R_0^*/(u_{VN} t_i)$. Clearly, more experiments are required to assess the detonability of these lean detonations in $H_2$-air, where a significant amount of scatter exists, and which are of particular interest for safety considerations.

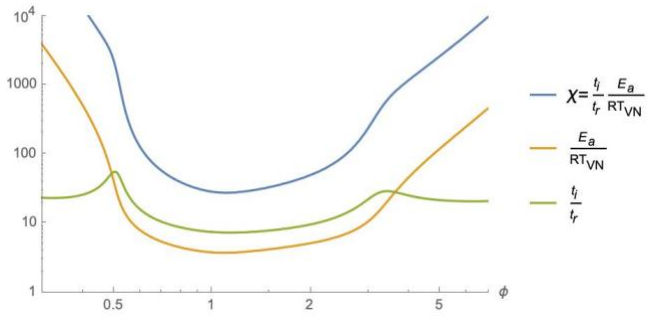


**Fig. 5** Variation of the global activation energy $\frac{E_a}{RT_{VN}}$, induction to reaction time ratio and stability parameter $\chi \equiv \frac{E_a}{RT_{VN}} \frac{t_i}{t_r}$ in $H_2$-air mixtures.

## METHANE

The direct initiation of methane-air mixtures is much more difficult and more limited data is available. Fig. 6 shows our compilation of experiments of direct initiation in the stoichiometric mixture $CH_4+2(O_2+\beta N_2)$ where $\beta$ varies from 0 to 3.76, which corresponds to air. Bull et al. initiated spherical detonations using Tetryl high explosive charges [26]. Aminallah et al. [27] initiated cylindrical detonations bounded between two walls using exploding wires. Extrapolation to walls infinitely far apart was required in order to account for wall loss effects, which tended to increase the critical energy per unit length required. The explosion length was evaluated using (2). Benedick [28] performed large scale initiation in methane-air mixtures using planar sheets of high explosive. Since the dimensions of the span of these sheets were less than the explosion length, the initiator was equivalent to a hemi-spherical initiation and the explosion length was formed using twice the total energy deposition with (1).

More recently, Pekalski performed a similar experiment using 6 charges of high explosive in a 3 m by 6 m by 20 m plastic tent enclosure filled with stoichiometric methane-air [29]. Given the charges were contained within the explosion length, the total energy of the charges was considered to arrive at the energy deposition for hemi-spherical initiation and arrive at an explosion length of $R_0^* = 8 \pm 0.5$ m via (1). Frames for the critical initiation experiments are shown in Fig. 7. From discrete explosion centers, the detonation forms approximately half way in the bag (10 m). Given the charges

were placed 0.75m into the gas, the resulting detonation formation distance is in agreement with the explosion length derived from the total energy of the ignition charges.

Ohyagi et al. [30] performed experiments experimens in tubes, using a gaseous $H_2$-$O_2$ driver. The explosion length reported is given by (3), using the energy equivalence per unit area reported by Ohyagi et al.

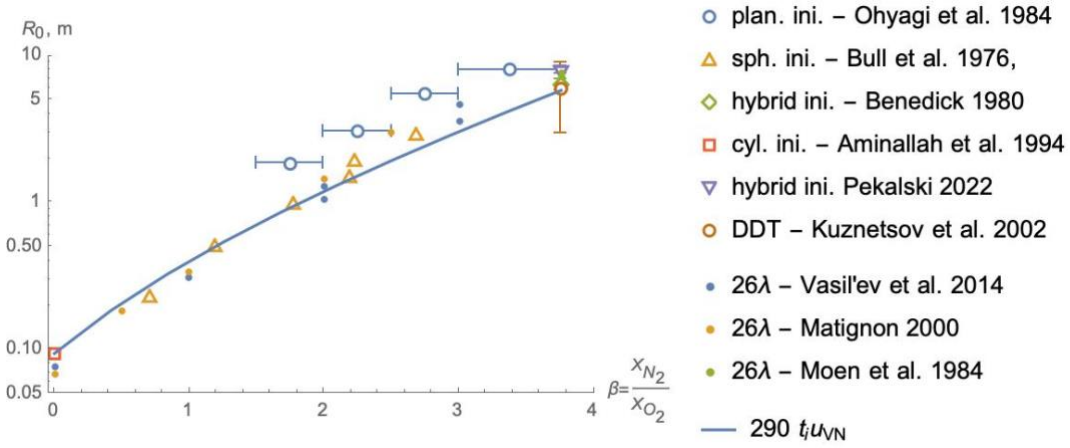


**Fig. 6** The explosion length dependence on the composition of $CH_4+2(O_2+\beta N_2)$.

All the data available appear to collapse to a single curve (except the experiments of Ohyagi) hence substantiating the concept of explosion length scaling. The slight discrepancy with Ohyiagi's data can be accounted by the relatively small tube diameter of 3 cm (!) used. The mixtures tested has nominal cell sizes between 5 to 20 cm, signifying that severe wall losses were present. These were not accounted for in the data reduction.

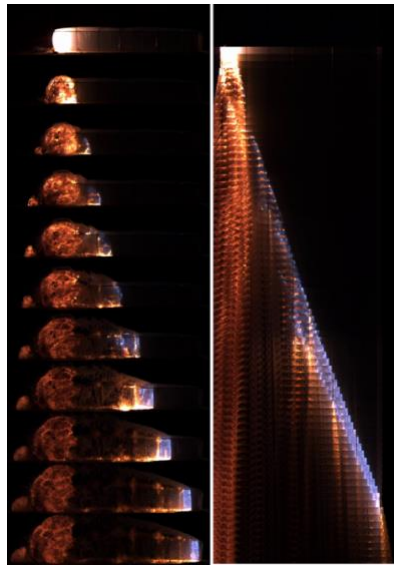

**Fig. 7** Individual frames and space-time diagram from successive frame splicing of the direct initiation of methane-air [29].

Also shown in Fig. 6 is the single result we could find for the choked flame acceleration length from the experiments of Kuznetsov et al.[31] These experiments were performed in two different tubes of 0.52 m and 0.174 m diameter tubes. From the single experiments reported for each tube diameter,

choked flame acceleration distances of $6 \pm 3$m were apparent. The DDT length is in good agreement with the explosion length derived from the direct initiation experiments discussed above.

The critical explosion lengths were correlated with the available cell size data for these mixtures obtained by Vasil'ev et al.[32], Matignon [33] and Moen et al. [34]. The correlation $R_0^* \approx 26\lambda$ captures approximately the entire range of experiments, as shown in Fig. 6. It is noteworthy that recently Zhang et al. [8] found the same correlation over a wide range of fuel-oxygen mixtures.

Correlations with the ZND induction zone lengths were also attempted for this mixture. Calculations were performed using the San Diego mechanism, as outlined above. The correlation $R_0^* \approx 290 u_{VN} t_i$ captures well the experimental data. Note that the numerical coefficient is an order of magnitude lower than for the hydrogen mixtures, indicative of the role of instability promoting the detonability of this fuel [24].

Recently, we have performed a large suite of experiments of fast flame accelerations by passing a detonation across a perforated plate or a column of equally spaced obstacles [11]. Fig. 2 shows an example of such an experiment. Fig. 8 provides the measured DDT length for a high speed CJ deflagration in $CH_4$+$2O_2$ mixture for a 90% plate blockage, for which the transmitted deflagration has a speed comparable to that of choked flames in closed ended tubes. The data provided agrees well with the direct initiation experiment of Aminallah et al.[27]. Using the cell sizes are from Laberge et al.[35], Manzhalei et al.[36] and Abid et al.[37], the same correlation $R_0^* \approx 26\lambda$ applies. Likewise, the same correlation with induction zone length $R_0^* \approx 290 u_{VN} t_i$ also applies. This observation further suggests that the DDT length of a choked flame, which relies on self-amplification, provides the same length scale as the explosion length for characterising the detonability of a given mixture.

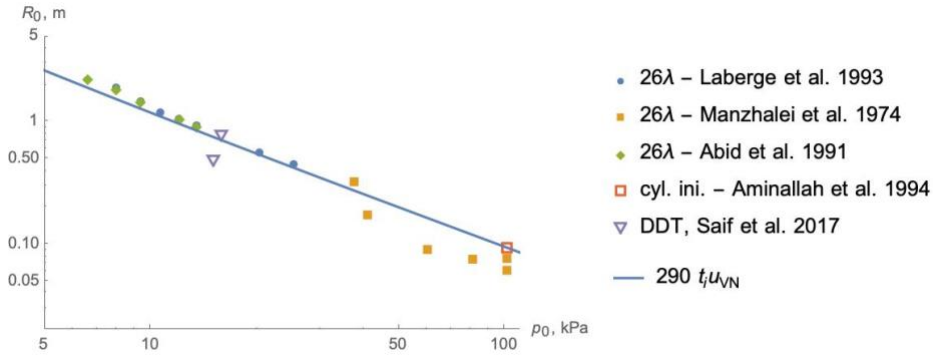


**Fig. 8** The explosion length dependence on initial pressure of $CH_4$+$2O_2$.

## METHANE-HYDROGEN BLENDS

Blending hydrogen with methane is currently envisioned for reducing carbon emissions while retaining the technology and infrastructure associated with natural gas, for which methane is the main component. We consider the stoichiometric fuel blend of composition:

$$(1-x)\ \mathrm{CH_4} + x\ \mathrm{H_2} + \left(2 - \tfrac{3}{2}x\right)(\mathrm{O_2} + 3.76\mathrm{N_2}) \qquad (10)$$

To date, the only experimental data available for these blends is for cell sizes. Using these data, an attempt to predict the explosion length for intermediate blends is shown in Fig. 8. Note that if the cell size data of Matignon [33] is made to fit the Aminallah et al. direct initiation data in pure $H_2$, the cell size correlation changes to $R_0^* \approx 35\lambda$. This is indicative of the inherent diffuculty of ascribing a single cell size.

We have also extended the correlations using the ZND induction zone length by assuming, for lack of a better model, a blending function of the form:

$$R_0^* \approx (290(1-x) + 1900\,x)\,u_{VN} t_i \tag{11}$$

This correlation, shown in Fig 9, remains to be verified with direct initiation or DDT experiments.

## BEST PRACTICES FOR EVALUATING THE EXPLOSION LENGTH

The preferred method to evaluate the explosion length for characterizing the detonability of a given mixture is by direct initiation, since the energy of the source to directly initiate can be determined by bisection to any degree of accuracy. Spherical initiation, although appearing as the most elegant, is very difficult to conduct. The detonation of a spherical charge of explosive is very difficult, as fragments are ejected in random directions, rapidly braking the desired spherical geometry. On the other hand, cylindrical initiation with a line source of energy delivered by detonating cords, as shown in Fig. 1, permits to have a clean energy deposition and conduct experiments retaining the desired symmetry. Both cylindrical and spherical experiments require gas clouds at least the size of the explosion length, making them difficult to implement for insensitive mixtures.

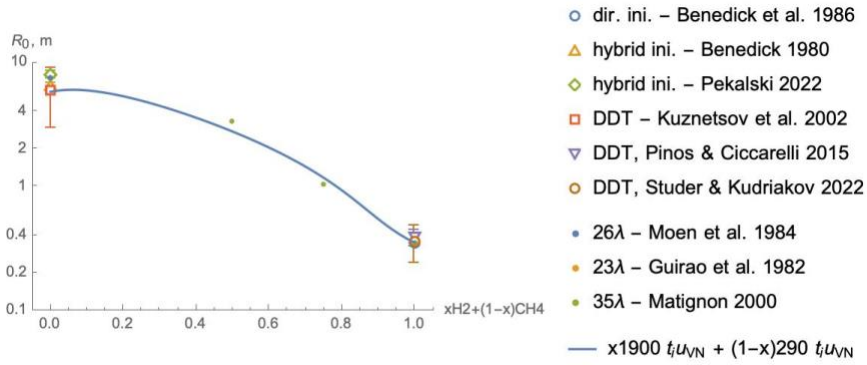


**Fig. 9** The explosion length of detonations in $(1-x)\ CH_4 + x\ H_2$ fuel blends in stoichiometric proportion with air.

Confined experiments in a tube, using planar energy sources are much more easily achieved. Tube diameters of only a few cell sizes in diameter are required, and gaseous drivers are easily implemented using fuel-oxygen mixtures, like in the experiments of Ohyagi et al. [30] and Gamezo et al.[38]. Care is needed, however, to accurately establish the energy equivalence and to eliminate possible wall effects. Alternatively, high explosive charges can be used.

## CONCLUSIONS

The critical explosion length $R_0$ derived from direct initiation experiments provides a unique length scale characterizing the detonability of a reactive mixture. It is the length scale over which a fast deflagration accelerates to a detonation. Review of empirical data for methane and hydrogen support the view that this length scale is the same in critically initiated detonations by a strong energy source (direct initiation) in any geometry and in deflagration to detonation experiments, as the distance required for a choked Chapman Jouguet deflagration to accelerate to a detonation wave. For all mixtures investigated, it is found that the critical explosion length $R_0$ is approximately $25 \pm 2\lambda$. Correlations with the ZND induction zone lengths yield mixture specific correlations: $R_0 \cong 1900 t_i u_{VN}$ for hydrogen mixtures and $R_0 \cong 290 t_i u_{VN}$ for methane mixtures. Future experiments should verify these observations through a systematic comparison between DDT experiments and direct initiation data. The good agreement between these two length scales suggests that future characterization of detonability of mixtures should be obtained in direct initiation, either in the unconfined using line sources of energy for the cleanest experiments, or in tubes with energetic gaseous drivers.

## REFERENCES


[1] J. H. S. Lee, "INITIATION OF GASEOUS DETONATION," *Annual Review of Physical Chemistry,* vol. 28, pp. 75-104, 1977, doi: 10.1146/annurev.pc.28.100177.000451.

[2] J. H. S. Lee and A. J. Higgins, "Comments on criteria for direct initiation of detonation," (in English), *Philosophical Transactions of the Royal Society a-Mathematical Physical and Engineering Sciences,* Article vol. 357, no. 1764, pp. 3503-3521, Dec 1999, doi: 10.1098/rsta.1999.0506.

[3] G. Ciccarelli and S. Dorofeev, "Flame acceleration and transition to detonation in ducts," *Progress in Energy and Combustion Science,* vol. 34, no. 4, pp. 499-550, Aug 2008, doi: 10.1016/j.pecs.2007.11.002.

[4] E. S. Oran, G. Chamberlain, and A. Pekalski, "Mechanisms and occurrence of detonations in vapor cloud explosions," *Progress in Energy and Combustion Science,* vol. 77, Mar 2020, Art no. 100804, doi: 10.1016/j.pecs.2019.100804.

[5] J. H. S. Lee, *The Gas Dynamics of Explosions*. Cambridge, 2016.

[6] M. I. Radulescu, A. J. Higgins, S. B. Murray, and J. H. S. Lee, "An experimental investigation of the direct initiation of cylindrical detonations," *Journal of Fluid Mechanics,* vol. 480, pp. 1-24, 2003, doi: 10.1017/s0022112002003154.

[7] M. I. Radulescu, A. J. Higgins, J. H. S. Lee, and S. B. Murray, "On the explosion length invariance in direct initiation of detonation," *Proceedings of the Combustion Institute,* vol. 28, pp. 637-644, 2000.

[8] B. Zhang, H. D. Ng, and J. H. S. Lee, "Measurement and scaling analysis of critical energy for direct initiation of gaseous detonations," *Shock Waves,* vol. 22, no. 3, pp. 275-279, May 2012, doi: 10.1007/s00193-011-0351-x.

[9] R. S. Chue, J. F. Clarke, and J. H. Lee, "Chapman-Jouguet deflagrations," *Proceedings of the Royal Society of London Series a-Mathematical Physical and Engineering Sciences,* vol. 441, no. 1913, pp. 607-623, Jun 8 1993, doi: 10.1098/rspa.1993.0082.

[10] A. Eder, "Brennverhalten schallnaher und überschall-schneller Wasserstoff-Luft Flammen " Ph.D., Technischen Universität München, 2001.

[11] M. Saif, W. T. Wang, A. Pekalski, M. Levin, and M. I. Radulescu, "Chapman-Jouguet deflagrations and their transition to detonation," *Proceedings of the Combustion Institute,* vol. 36, no. 2, pp. 2771-2779, 2017, doi: 10.1016/j.proci.2016.07.122.

[12] W. Rakotoarison and M. I. Radulescu, "Model for Chapman-Jouguet deflagrations in open ended tubes with varying vent ratios," in *27th International Colloquium on the Dynamics of Explosions and Reactive Systems*, 2019, p. 186.

[13] A. Y. Poludnenko, T. A. Gardiner, and E. S. Oran, "Spontaneous Transition of Turbulent Flames to Detonations in Unconfined Media," (in English), *Physical Review Letters,* Article vol. 107, no. 5, p. 4, Jul 2011, Art no. 054501, doi: 10.1103/PhysRevLett.107.054501.

[14] S. B. Dorofeev, V. P. Sidorov, M. S. Kuznetsov, I. D. Matsukov, and V. I. Alekseev, "Effect of scale on the onset of detonations," *Shock Waves,* vol. 10, no. 2, pp. 137-149, 2000.

[15] B. Maxwell, A. Pekalski, and M. Radulescu, "Modelling of the transition of a turbulent shock-flame complex to detonation using the linear eddy model," *Combustion and Flame,* vol. 192, pp. 340-357, Jun 2018, doi: 10.1016/j.combustflame.2018.02.013.

[16] T. Jaravel, O. Dounia, Q. Male, and O. Vermorel, "Deflagration to detonation transition in fast flames and tracking with chemical explosive mode analysis," *Proceedings of the Combustion Institute,* vol. 38, no. 3, pp. 3529-3536, 2021, doi: 10.1016/j.proci.2020.09.020.

[17] C. M. Guirao, R. Knystautas, and J. H. Lee, "A summary of hydrogen-air detonation experiments," Office of Nuclear Regulatory Research, Washington, DC, 1989.

[18] T. Pinos and G. Ciccarelli, "Combustion wave propagation through a bank of cross-flow cylinders," *Combustion and Flame,* vol. 162, no. 9, pp. 3254-3262, Sep 2015, doi: 10.1016/j.combustflame.2015.05.013.

[19] E. Studer, S. Kudriakov, and D. L. C. Fernando, "Detailed Examination of Deformations Induced by Internal Hydrogen Explosions ", M. I. Radulescu, Ed., ed: Note technique CEA/DES, 2021.

[20] C. M. Guirao, R. Knystautas, J. Lee, W. Benedick, and M. Berman, "Hydrogen-air detonations," presented at the 19th Sym. (Int.) Combust., 1982.

[21] S. R. Tieszen, M. P. Sherman, W. B. Benedick, J. E. Shepherd, R. Knystautas, and J. H. S. Lee, "Detonation cell size measurements in hydrogen-air-steam mixtures," *Prog. Astronaut. Aeronaut.,* vol. 106, pp. 205-219, 1986.

[22] D. G. Goodwin, H. K. Moffat, and R. L. Speth, "Cantera: An object- oriented software toolkit for chemical kinetics, thermodynamics, and transport processes," 2014.

[23] A. L. Sanchez and F. A. Williams, "Recent advances in understanding of flammability characteristics of hydrogen," (in English), *Progress in Energy and Combustion Science,* Review vol. 41, pp. 1-55, Apr 2014, doi: 10.1016/j.pecs.2013.10.002.

[24] Q. Xiao and M. I. Radulescu, "Role of instability on the limits of laterally strained detonation waves," *Combustion and Flame,* vol. 220, pp. 410-428, Oct 2020, doi: 10.1016/j.combustflame.2020.06.040.

[25] M. I. Radulescu, "The propagation and failure mechanism of gaseous detonations : experiments in porous-walled tubes," Thesis (Ph D ), 2003.

[26] D. C. Bull, J. E. Elsworth, G. Hooper, and C. P. Quinn, "A study of spherical detonation in mixtures of methane and oxygen diluted by nitrogen," *J. Phys. D,* vol. 9, no. 13, pp. 1991-2000, 1976.

[27] M. Aminallah, J. Brossard, and A. Vasiliev, "Cylindrical detonations in methane-oxygen-nitrogen mixtures," *Prog. Astronaut. Aeronaut.,* vol. 153, 1993.

[28] W. B. Benedick, "HIGH-EXPLOSIVE INITIATION OF METHANE-AIR DETONATIONS," *Combustion and Flame,* vol. 35, no. 1, pp. 87-93, 1979.

[29] A. Pekalski, "Direct initiation of unconfined methane-air detonations," M. I. Radulescu, Ed., ed, 2016.

[30] S. Ohyagi, T. Yoshihashi, and Y. Harigaya, "Direct initiation of planar detonation waves in methane/oxygen/nitrogen mixtures," *Prog. Astro. Aero.,* vol. 94, pp. 1-22, 1984.

[31] M. Kuznetsov, G. Ciccarelli, S. Dorofeev, V. Alekseev, Y. Yankin, and T. H. Kim, "DDT in methane-air mixtures," *Shock Waves,* vol. 12, no. 3, pp. 215-220, Nov 2002, doi: 10.1007/s00193-002-0155-0.

[32] A. A. Vasil'ev *et al.*, "The damping of detonation wave with the help of dust cloud of inert particles," presented at the Tenth International Symposium on Hazards, Prevention, and Mitigation of Industrial Explosions, Bergen, Norway, 2014.

[33] C. Matignon, "Etude de la détonation de deux mélanges stoechiométriques (CH4/H2/O2/N2 et CH4/C2H6/O2/N2) Influence de la proportion relative des deux combustibles et de la température initiale élevée " Ph.D., Université de Poitiers, 2000.

[34] I. O. Moen, J. W. Funk, S. A. Ward, G. M. Rude, and P. A. Thibault, "Detonation length scales for fuel-air explosives," *Prog. Astronaut. Aeronaut.,* vol. 94, pp. 55-79, 1984.

[35] S. Laberge, R. Knystautas, and J. H. S. Lee, "Propagation and extinction of detonation waves in tube bundles," *Prog. Astronaut. Aeronaut.,* vol. 153, pp. 381-396, 1993.

[36] V. I. Manzhalei, V. V. Mitrofanov, and V. A. Subbotin, "Measurement of inhomogeneities of a detonation front in gas-mixtures at elevated pressures," *Combustion Explosion and Shock Waves,* vol. 10, no. 1, pp. 89-95, 1974.

[37] S. Abid, G. Dupré, and C. Paillard, "Oxidation of gaseous unsymmetrical dimethylhydrazine at high temperatures and detonation of UDMH/O2 mixtures," *Prog. Astronaut. Aeronaut.,* vol. 153, pp. 162-181, 1991.

[38] V. N. Gamezo *et al.*, "Detonability of natural gas-air mixtures," *Combustion and Flame,* vol. 159, no. 2, pp. 870-881, Feb 2012, doi: 10.1016/j.combustflame.2011.08.009.

# Hydrogen Safety

# Tactical depressurization of hydrogen containers with civilian rifle and ammunition

**Gehandler J.[1,*], Lönnermark A.[1,*], Runefors M.[2], Madsen D.[2], Egardt E.[3]**

[1] *RISE Research Institutes of Sweden, Safety Research, Borås, Sweden.*
[2] *Lund University, Division of Fire Safety Engineering, Lund, Sweden.*
[3] *Swedish Civil Contingencies Agency (MSB), Karlstad, Sweden.*
**Corresponding author's email: jonatan.gehandler@ri.se*

## ABSTRACT

There can be situations, for example if gas containers have been damaged in a vehicle crash, when the fire and rescue service would like to depressurize the gas containers through shooting with a civilian rifle. Modern high-pressure hydrogen containers are designed for a working pressure of 700 bars. This means that they have a very thick and strong shell made of composite material. At the same time the fire and rescue service only have access to civilian rifles and ammunition that can be bought for hunting purposes. Thus, tactical and safe depressurization of hydrogen containers is a big challenge. RISE have, together with the Södra Älvsborgs Fire and Rescue Services (SÄRF), Swedish Civil Contingency Agency, and Lund University conducted shooting tests of gas tanks mounted on a hydrogen gas vehicle and three stand-alone hydrogen gas tanks. The shooting tests were conducted at Remmene shooting field in Sweden. Thirteen shooting tests with hydrogen tanks placed in favouarable positions were performed. Out of these, only four tests were succesful in puncturing the individual gas tank in a single shot. Furthermore, two unwanted events occurred; one rupture (after 7 shots) and two powerful jets (after 20 and one shot respectively). This shows that further development and research is required in order to develop a method to safely depressurize high pressure hydrogen tanks.

**KEYWORDS:** Depresurization, puncture, hydrogen, civilian rifle, shooting, winchester.

## INTRODUCTION

With the projected increase in hydrogen vehicles in the coming years, more such vehicles can be expected to be involved in traffic accidents. In some accidents, there might be situations when the gas containers have been damaged, making it too dangerous to tow these vehicles from the scene without first depressurizing the containers. One technique, that has been successfully applied in Sweden over several decades to depressurize gas containers, is by using rifles. This technique has primarily been developed for use in industrial fires with gas containers filled with, for example, acetylene for welding. However, the technique has also been applied in a few recent accidents involving CNG-vehicles [1, Runefors].

When it comes to research on how this can be effectively and safely performed, a few tests on the penetration of CNG containers [1, Runefors] and industrial containers [2, Hora et al.] can be found in the literature, but the number of experiments is very low. Also, modern high-pressure hydrogen containers are designed for a working pressure of 700 bars. This means that they have a very thick and strong shell made of composite material making them difficult to penetrate.

Only one study on the penetration of such high yield containers has been found in the literature, and that is from a study by U.S. Army [3, Paczkowski et al.]. However, they primarily used military-grade ammunition with armour piercing capabilities. Such ammunition is not available on the civilian market and, therefore, not for the fire and rescue services. The only ammunition used in the study that is available on the civilian market was the 7.62 Ball, and this was found to not be able to penetrate the tanks. Therefore, no guidance on the selection of combination of rifles and ammunition for the fire and rescue service when depressuzing hig-pressure hydrogen containers can be found in the literature.

Therefore, to fill this gap, RISE Research Institutes of Sweden have, together with the Södra Älvsborg fire and rescue services (SÄRF), Swedish Civil Contingency Agency, and Lund University conducted shooting tests of gas tanks mounted on a hydrogen gas vehicle and three stand-alone hydrogen gas tanks. The first steps have been taken to develop a safe method to depressurize high-pressure hydrogen tanks using civilian rifles and ammunition.

## METHOD

### Test objects

Three different designs of compressed hydrogen gas containers for passenger car usage were used in the shooting tests. Two tanks (103 l and 50 l) mounted on a Hyundai ix35, and 3 stand-alone hydrogen tanks (52 l) from a Hyundai Nexo. The ix35 vehicle tanks were filled with a mixture of methane and hydrogen to a pressure of 700 bar. The reason was that the vehicle was accidently filled with methane at a refueling station which was the reason for decomissioning the vehicle and making it avaliable for testing. The vehicle was before the tests refuelled (to 700 bar) with hydrogen. The small ix35 tank had a material thickness of 30 mm. The big ix35 tank had a material thicknes of 50 mm. Of the stand-alone tanks, two were exposed to fire such that the TPRD released and they were thus empty and damaged by fire at the time of shooting. The third stand-alone tank was not exposed to any fire and was filled with hydrogen to a pressure of 410 bar at the time of shooting. The stand-alone tanks had a material thickness of 30 mm. All tanks were composite tanks with a plastic container that is wrapped in carbon fibre reinforced polymer composite material (Type 4). All tanks were fitted with valves and a TPRD at one end.

The fire and shooting tests were conducted at Remmene shooting field in Sweden, 30th of august and 1st of September 2021, see Fig. 1. The ix35 passenger car was tilted unto its side and fixed unto the ground with metal bars to keep it steady, see Fig. 2 (left) The stand-alone gas cylinders were fixed approximately 0.7 m above ground level on metal bars, see Fig. 2 (right).

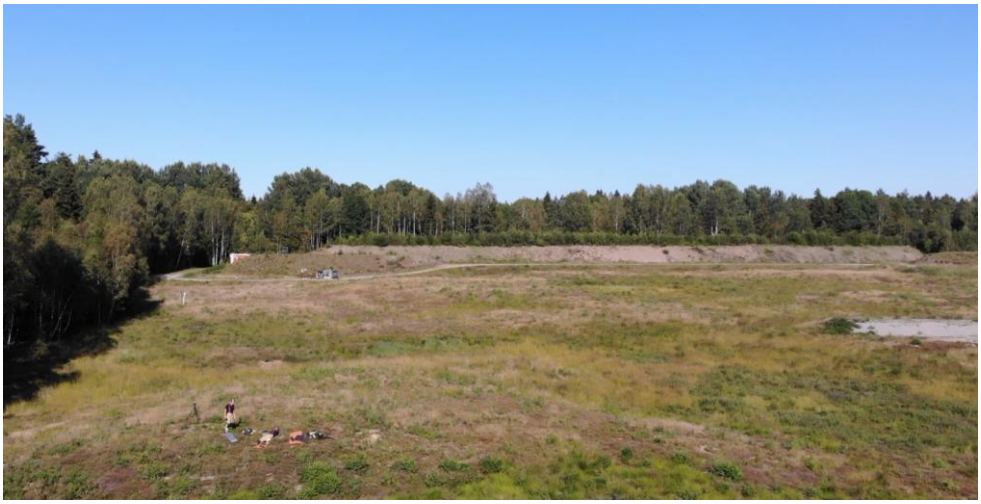

**Fig. 1.** Shooters (in the foreground) and the hydrogen vehicle (120 m away) at Remmene shooting field. (Photo: Marcus Aronsson, SÄRF)

### Rifle, ammunition and balistic calculations

A pre-condition for the shooting tests was to use civilian weapons that can be bought for hunting purposes in class 1 according to the The Swedish Environmental Protection Agency (Swedish EPA) publication NFS 2002:18 [4]. This is the highest class where the pre-conditions of the derived rifle and ammunition allow for hunting of the largest species in Sweden, i.e. mooses, bears etc. Different

rifles and ammunition were tested. Balistic calculations of bullet speed were based on the Pejsa model[1] using the software tool JBM ballistics.

**Fig. 2.** The target: rear of the tilted hyrogen vehicle with the small and large tank (left) and a stand-alone tank (right) (Photo: RISE)

## Test set-up

The shooters were placed on a small elevation at around 120 m distance from the target in north-east. The tank was placed with the aim that the shooter should be positioned perpendicular to the tank mantle surface. In reality this was not always achieved and deviations with up to 14° angle between a perpendicular axis from the cylinder mantle surface and shooter were estimated, see Fig. 3 and Table 1.

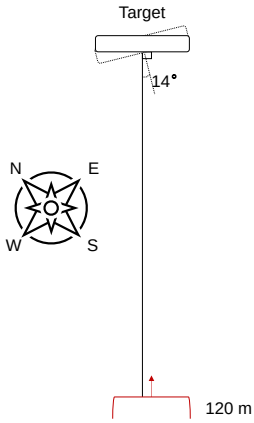


**Fig. 3.** The shooter was placed about 120 m from the target. The target, i.e. the gas tank, was up to 14° from its perpendicular position.

[1] https://en.wikipedia.org/wiki/External_ballistics

**Table 1. Hydrogen tank shooting tests, overview**

| Test no. | Target | Date | Fire exposed | Distance [m] | H2 Pressure [bar] |
|---|---|---|---|---|---|
| 1 | 50 l tank iX35 | 30th aug 2021 | No | 117 | 700 |
| 2 | 103 l tank iX35 | 30th aug 2021 | No | 117 | 700 |
| 3 | Stand-alone 52 l tank | 1st sep 2021 | Yes, 22 min | 127 | 0 |
| 4 | Stand-alone 52 l tank | 1st sep 2021 | Yes, 5 min | 127 | 0 |
| 5 | Stand-alone 52 l tank | 1st sep 2021 | No | 127 | 410 |
| 6 | 50 l tank iX35[a] | 1st sep 2021 | No | 124 | 0 |
| 7 | 103 l tank iX35[a] | 1st sep 2021 | No | 124 | 0 |

[a]Tanks were disabled and placed on the ground.

### Measurements and documentation

The tests were recorded with video cameras. Bullet speed of each rifle and ammunition combination was measured with a balistic chronograph, e.g. Chrony M1, before or after the shooting. Weather data was measured or retrieved from weather stations nearby.

The pressure inside the stand-alone gas containers was measured. The free field blast pressure were measured with two pressure probes (from PCB/ICP) positioned at 5 m and 10 m distance from the tank centre, see Fig. 4. At 5 m the 137B24B probe was equiped with one piezoelectric element and at 10 m, the 137B25 probe was equipped with two piezoelectric elements, Front and Rear respectively.

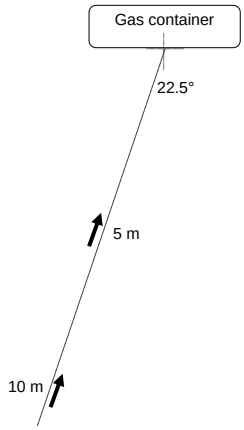


**Fig. 4.** Placement of free field blast pressure probes relative to the stand-alone gas tank.

## RESULTS

In Table 2, the weather data are presented. In Table 3, balistic data for calculation of bullet speed are presented, and in Table 4 the results from the shooting tests can be seen. The ballistic coefficient in Table 3 of a bullet is a measure of its ability to overcome air resistance in flight. The kinetic energy of the bullet when it hits the tank surface is in the order of 250 J for all combinations in table 4.

**Table 2. Hydrogen tank shooting tests, weather data**

| Test # | Temperature [°C] | Wind speed [m/s] | Wind direction[a] | Relative humidity [%] | Air-pressure [kPa] |
|---|---|---|---|---|---|
| 1 & 2 | 21 | 1,5 | NE | 47 | 100.9 |
| 3 | 18 | 1 | N | 50 | 102.4 |
| 4 | 19 | 1 | NW | 45 | 102.4 |
| 5 | 20 | 1 | NW | 47 | 102.3 |
| 6 & 7 | 20 | 1 | NW | 47 | 102.3 |

[a]N=North, NW= North West, NE=North East.

**Table 3. Inner and outer ballistic data.**

| Rifle, bullet | Projectile weight [g] | Balistic coefficient |
|---|---|---|
| Remington 700 .308W 580 mm barrel 1:12 twist, Sako Powerhead Blade | 10.5 | 0.39[a] |
| Remington 700 .308W 580 mm barrel 1:12 twist, Barnes Vor-Tx | 10.9 | 0.47[b] |
| Antonio Zoli .300 WM, 510 mm barrel twist unknown, Winchester Supreme Elite | 11.7 | 0.527[c] |
| Sauer 202 .300 WM, 600 mm barrel 1:11 twist, Barnes Vor-Tx | 10.7 | 0.442[d] |

[a]www.sakosverige.se/ammunition/solida-kulor/powerhead-blade
[b]www.raytrade.com.au/products/category/EYMMVAGC-centrefire-rifle-ammunition/BB308W2--barnes-vor-tx-308-win-168gr-ttsx-bt-cartridges
[c]www.ableammo.com/catalog/ammo_charts/Winchester_Ammunition_Ballistic.pdf
[d]www.raytrade.com.au/products/category/EYMMVAGC-centrefire-rifle-ammunition/BB300WM2--barnes-vor-tx-300-win-mag-165gr-ttsx-bt-carts

**Table 4. Hydrogen tank shooting tests, results**

| Test # | Target | Rifle, bullet | Measured speed at 1.8 m [m/s] | Calculated speed at target [m/s] | Impact |
|---|---|---|---|---|---|
| 1 | 50 l tank iX35 | Remington 700 .308W, Powerhead Sako | 888 | 800 | Started to leak after 3 shots. Rupture after 7 shots |
| 2a | 103 l tank iX35 | Remington 700 .308W, Powerhead Sako | 888 | 800 | No leaking after 8 shots |
| 2b | 103 l tank iX35 | Antonio Zoli .300WM, Winchester Supreme Elite | 953 | 884 | No leaking after 6 shots (of which 4 where clustered) |
| 2c | 103 l tank iX35 | Remington 700 .308W, Powerhead Sako | 888 | 800 | Gas jet after 7 shots |
| 3a | 52 l tank (fire exposed) | Remington 700 .308W, Barnes Vor-Tx | 833 | 756 | 2 shots, one penetration |
| 3b | 52 l tank (fire exposed) | Sauer 202 .300WM, Barnes Vor-Tx | 893 | 808 | 2 shots, one penetration |
| 4a | 52 l tank (fire exposed) | Remington 700 .308W, Barnes Vor-Tx | 833 | 756 | Penetration at first shot |
| 4b | 52 l tank (fire exposed) | Sauer 202 .300WM, Barnes Vor-Tx | 893 | 808 | Penetration at first shot |
| 5a | 52 l tank | Remington 700 .308W, Barnes Vor-Tx | 833 | 756 | Penetration at first shot. Minor leakage. |
| 5b | 52 l tank | Sauer 202 .300WM, Barnes Vor-Tx | 893 | 821 | Penetration at first shot. Major jet flame with blast wave. |
| 6a | 50 l tank | Remington 700 .308W, Barnes Vor-Tx | 833 | 758 | No penetration. Bullet entered 9 mm into the tank. |
| 6b | 50 l tank | Sauer 202 .300WM, Barnes Vor-Tx | 893 | 810 | No penetration. Bullet entered 29 mm into the tank. |
| 7a | 103 l tank | Remington 700 .308W, Barnes Vor-Tx | 833 | 758 | No penetration. Bullet entered 13 mm into the tank. |
| 7b | 103 l tank | Sauer 202 .300WM, Barnes Vor-Tx | 893 | 810 | No penetration. Bullet entered 15 mm into the tank. |

**Test #1 and #2 on the hydrogen vehicle with pressurized tanks**

The combination of rifle and ammunition was not very succesfull in these first two shootings on the big and small iX35 tanks. At the same time, these tanks were very challenging to penetrate, see Fig. 5 & Fig. 6. All the hits from the Remington 700 rifle was contained in a surface with a diameter of 33 mm, indicating that a high level of accuracy can be achieved at the used distance. For the Antonio Zoli rifle (Test #2b) the accuracy was worse, only the first 4 shots were clustered. Most likely the barrel was heated from the 4 first shots resulting in a worse shooting. Therefore the shooters switched back to the Remington 700 rifle (Test #2c). From the sound recording of a video camera placed nearby the vehicle, a squezing sound is clearly heard indicating leaking gas after three shoots in test #1. Unfortunatley the only camera that was available for test #2 was the drone which did not record any sound. However, according to the shooters (who also heard the leaking gas in test #1, it was not leaking until the gas jet (see Fig. 5 right hand side) apeared after 19 clustered shots.

**Fig. 5.** The rupture of the small tank (left, test #1), and the puncture of the big tank (right, test #2). (Photo: Marcus Aronsson, SÄRF)

**Fig. 6.** Punctured big tank (left, test #2) and ruptured small tank (right, test #1). (Photo: RISE)

### Test #3 and #4 on fire exposed tanks at low pressure

In these tests, the fire had caused the TPRD to release. In test 3a and 3b, two shots were required for penetration. In test 4a and 4b, one shot was enough for penetration, which was captured on video as there still was some gas left in the container, see Fig. 7.

**Fig. 7.** A small jetflame following the penetration on the first shot in 4a (left) and 4b (right). (Photo: RISE)

### Test #5 shooting on pressurized unexposed stand alone tank

The impact from shooting #5a on the pressurized stand-alone tank resulted in a small leakage. The pressure dropped from 408 bar to 407 bar in 5 s. Shoting #5b resulted in a violent release, see Fig. 8. The hole from shooting #5a measured 6 mm and from shooting #5b it was 13 mm, see Fig. 9. The fast release resulted in a blast wave that is seen in Fig. 10 - 12 below.

**Fig. 8.** A sequence of pictures showing the penetration on the first shot in #5b, from left to right.

**Fig. 9.** Two successful penetrations at first shot; one big hole to the left (#5b that resulted in a large jet flame) and a small to the right (#5a that resulted in minor leakage). (Photo: RISE)

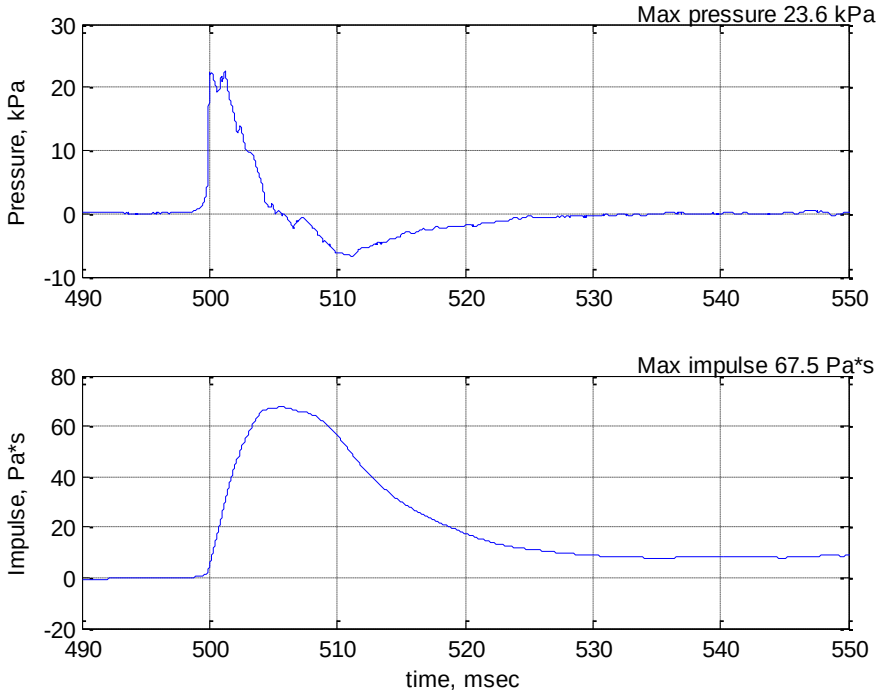


**Fig. 10.** Blast wave at 5 m distance, 137B24B sensor.

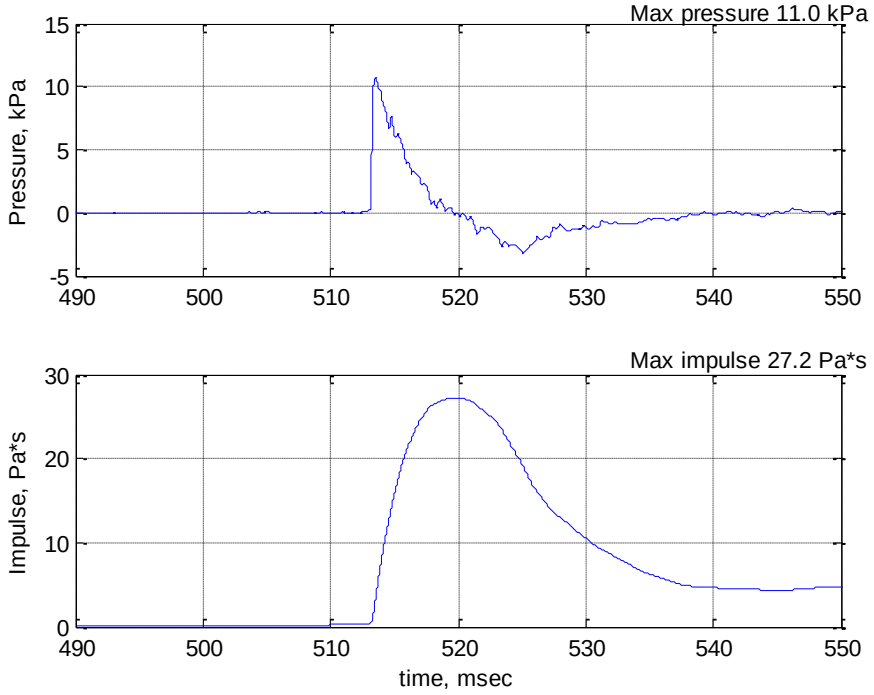


**Fig. 11.** Blast wave at 10 m distance, 137B25 Front sensor.

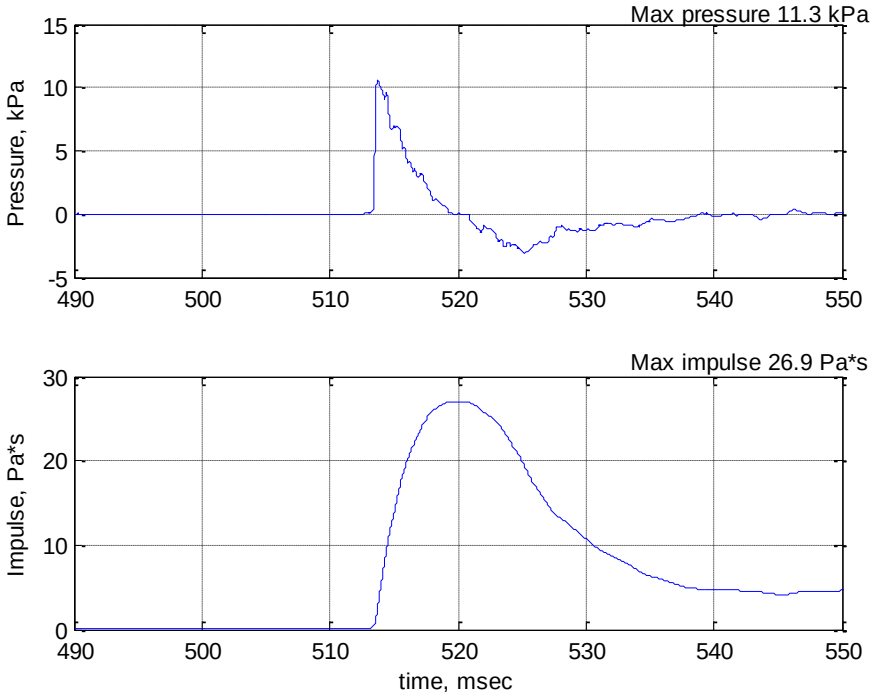


**Fig. 12.** Blast wave at 10.1 m distance, 137B25 Rear sensor.

### Test #6 and #7 shooting on empty iX35 tanks

As the iX35 tanks apeared to be stronger, the rifle and ammunition used in test #5 was tested on the empty small and large iX35 tanks from test #1 and #2. No penetration at first shoot was achieved which confirm that the iX35 tanks were stronger and more difficult to penetrate. The same rifle and ammunition (Sauer 202 .300 WM, Barnes Vor-Tx) that caused a sudden release in test #5 penetrated deepest into the iX35 tanks.

## DISCUSSION

### Method

Depressurization of gas storage tanks in a safe and verified way is hard to achieve for vehicles with hidden fuel tanks. Nevertheless, it is the most suitable method we have to secure the working environment for staff working at accidents where potentially weakened gas tanks might occur. The available literature on this topic is scarse. This paper handles a series of tests of different combinations of rifles and ammunition to puncture exposed hydrogen fuel tanks of different types in a favorable orientation. The storage tanks have in all tests been placed to optimize the shooting conditions. In test #1-#2, the vehicle had been tilted and the protective plastic plate beneath the storage tank had been removed to expose the tanks. In test #3-#5, the storage tanks were placed as standalone objects in a favourable shooting orientation. This was also the case in Test #6-#7, where the tanks in Test #1-#2 were removed from the vehicle and placed on the ground. Standing at an accident scene, where the deformed vehicle is still standing on four wheels, makes the depressurization more difficult and also more difficult to verify if the shot punctured the tank or not. Nevertheless, as the experience in this matter is scarse, the performed tests in this study give valuable information of appropiate measures to the ongoing work to secure the working environment for staff working at accident sites.

The shooting distance in the order of 100 m is a trade off between safety, weather conditions, effects of the ammunition and accuracy in shooting (Runefors et al., 2021). In fact, the actual distance of these tests is within what eventually could be the distance of flying debris. Stronger means, as more powerful rifle/ammunition, would make it possible to increase the distance between the shooter and the gas tank, and thereby increase the safety.

The tanks were hit by three different bullets from two different types of rifles, The two rifle types, 0.308 Winchester and 0.300 Winchester Magnum are commonly used for hunting of the largest species and therefore the most appropiate arms for puncture of high pressure containers with a thick and strong shell. This rifle and ammunition combination has shown until now to be suitable means for puncturing gas tanks at scenes of accidents.

Ammunition for hunting purposes are designed to penetrate and expand as it enters the flesh of the animal. The expansion leads to a larger wound canal that shortens the suffering of the animal. This expanding design for hunting purposes is desribed as mandatory in The Swedish Environmental Protection Agency (Swedish EPA) publication NFS 2002:18. Unfortunately, the expanding property takes the power of the penetrating ability that is desired in the performed tests of this study. The chosen ammunition, 0.308 Powerhead, 0.308 Barnes Vor-Tx, 0.300 Barnes Vor-Tx and 0.300 Winchester Supreme Elite, have all bullets made to expand to fulfill its purpose in a hunting situation.

When the results were analysed, it was realized that hearing was the best indicator of minor leakages. From the visual video camera or IR-camera it was not possible to detect minor leakages. However, on video recordings with sound in the vicinity of the tank (within 10-15 m), a squezing sound is clearly heard after some of the hits. The shooters at a distance of 120 m could sometimes also hear the squezing sound, but at more safe positions, e.g., at 600 m or behind proteciton, no sound from leakages could be heard. In real shooting situations, the rescue service should be equipped with a live or similar so that they can know when the tank begins to leak so that further shooting can be avoided.

### Results

The gained experience from this study clarifies that the used rifles/ammunition for hunting purposes, the 308W/0.300 WM, is not in general able to penetrate the hydrogen storage tanks in one shot. Out of 13 tests, only 4 tests were succesful in puncturing the individual gas tank in a single shot. It should also be noted here that the tanks were placed in a favorable exposed position.That leaves the remaining opportunity to shoot hole-in-hole at the tanks that withstand the single shot. Shooting repeatably at the same spot gives a larger hole, that in the case of test #1 eventually led to an undesired rupture of the tank. So instead of a more controlled leakage, the tank opened in a instant explosion. It should be noted though that after analysing the videomaterial from test #1, a squezing sound was heard after

three shots, indicating a leakage before the following four shots caused the rupture. The larger tank in test #2 had to be shot with even more bullets before puncture, releasing a massive outflow of gas that led to strong reaction forces on the vehicle. These reaction forces rotated the vehicle despite that it was stabilised with steel bars. Minimizing reaction forces through minor holes as the gas leaves the tank is of course of interest. There is also a need to get more knowledge of this effect on the vehicle during the discharge to avoid further implications.

It would be expected some difference between the fire arms of 0.308W and 0.300WM as the 0.300 WM has substantially higher velocity than the 0.308W together with a more favourable balistic coefficient. This was shown in test #6-#7 where the depth of single holes were measured and the 0.300WM had deeper penetration ability although it did not succed in penetrating the gas tank.

The used rifles and ammunition are, as earlier described, normally used for hunting purposes as this is the usual available means for the fire and resue service. Military ammunition with higher penetration ability (which has previously shown to be able to penetrate hydrogen tanks [3]) are normally not allowed to be handled by the municipial fire and rescue service as the ammunition for hunting purposes have shown enough penetrating properties to punture normal gas tanks as for CNG, LPG and acetylene. However, the introduction of high pressure hydrogen tanks seem to require stronger means.

The EU project HYPACTOR [6] finds that the energy of the impactor was an important factor for the reuslting damage to hydrogen composite tanks. The study used energies between 1 kJ and 10 kJ, where 1 kJ seldom damaged the tank, while higher energies, above 3 kJ often did. The energies used in these tests were in the order of 0.25 kJ, and should therefore not damage the tank. The larger mass impactor that was used in [6] does not seem to be comparable with bullets. Likely, bullets have a smaller impact area and therefore creates a greater damage at lower kinetic enrgies.

Apparently the choice of rifles and ammunition that is suitable for pressure relief of gas bottles containing CNG, acetylene and LPG can not be validated for puncturing 700 bars hydrogen gas tanks. For this, a higher penetrating effect is needed from the combination of rifle and ammunition. The Swedish Police states in their regulation RPSFS 2009:13FAP 551-3 Chapter 2 [5] that weapon license is admitted for “Udda ändamål” (Odd purposes in English), e.g., for puncturing of gas containers. In Chapter 10, it is stated that you do not need any more permit or license to buy ammunition as long as the ammunition has the same purpose as the weapon license admits. So in fact, this can be interpreted as that any ammunition might be available as long as it is needed to fulfill the purpose given in the license conditions. With this knowledge, it is important that in future applications for weapon licenses for shooting at hydrogen containers, well-founded reasons for ammunition that offers higher penetration are given.

Future project should clarify the shooting positions and complexity in puncturing hydrogen gas storage tanks as they are mounted on the vehicle. Drawings of tank installations are needed and references to what ammunition is required to penetrate tires, protection plates, fenders or what else is in the way of shooting at the tank. A large reference bank is needed as well with recommendations of ammunition required for the specific case.

## CONCLUSIONS

Thirteen shooting tests with the ambition to safely depressurize high pressure hydrogen containers with civilian rifles and ammunition were performed. In these tests the tanks were placed in favourable shooting positions. Out of these 13 tests, only 4 tests were succesful in puncturing the individual gas tank in a single shot. Furthermore, two unwanted events occurred; one rupture (after 7 shots) and two powerful jets (after 20 and one shot respectively). This shows that further development and research is required in order to develop a method suitable for the municipal fire and rescue service to safely depressurize these tanks.

## ACKNOWLEDGEMENTS

Anders Jönsson & Per Gullander from SÄRF are acknowledged for the shooting.

Anders Toresson with staff at Torsbo Handels (www.torsbohandels.com) are acknowledged for their assistance with rifles and ammunition.

## REFERENCES

[1] M. Runefors, E. Egardt, Tactical Depressurization of Hydrogen and CNG Tanks using Rifles and Other Projectiles, Proc. of the International Conference on Hydrogen Safety (2021) 1615–1626.

[2] J. Hora, K. Karl, O. Suchy, Pressure Cylinders under Fire Condition, Perspectives in Science 7 (2016), 208-221

[3] B. Paczkowski, D. Maslach, M. Radiwon, S. Caito, K. Centeck, Compressed Hydrogen Storage Cylinder Ballistic and Explosive Test Results, United States Army Tank Automotive Research, Development and Engineering Center (TARDEC)

[4] Naturvårdsverkets författningssamling NFS 2002:18. Available at https://lagen.nu/nfs/2002:18

[5] Rikspolisstyrelsens författningssamling RPSFS 2009:13 FAP 551-3. Available at https://polisen.se/lagar-och-regler/vapen-regler-och-tillstand/

[6] F. Nony, Final Report Summary - HYPACTOR Pre-normative research on resistance to mechanical impact of composite overwrapped pressure vessels (2018).
Available at https://cordis.europa.eu/project/id/621194/reporting

# Analysis of hydrogen incidents and accidents database HIAD 2.0

Jennifer X. Wen[1,*], Marta Marono[2], Pietro Moretto[3], Ernst-Arndt Reinecke[4], Pratap Sathiah[5], Etienne Studer[6], Elena Vyazmina[7] and Daniele Melideo[8]

[1] *Warwick FIRE, School of Engineering, University of Warwick, Coventry CV4 7AL, United Kingdom*
[2] *Research Centre for Energy, Environment and Technology (CIEMAT), Energy Department, Av. Complutense, 40, 28040 Madrid, Spain*
[3] *European Commission, Joint Research Centre (JRC), Petten, Netherlands*
[4] *Forschungszentrum Juelich GmbH, IEK-6, 52425 Juelich, Germany*
[5] *Shell Technology Centre Bangalore, Shell India Markets Private Limited, Bangalore Hardware Park, Devanahalli, Mahadeva Kodigehalli, Bangalore - 562 149, Karnataka, India*
[6] *CEA Direction des Energies, Service de Thermohydraulique et Mécanique des Fluides, Université Paris-Saclay, 91191 Gif-sur-Yvette, France*
[7] *Air Liquide R&D – Innovation Campus Paris, 1 chemin de la Porte des Loges – 78354 Les Loges-en-Josas, France*
[8] *Dipartimento di Ingegneria dell'Energia, dei Sistemi, del Territorio e delle Costruzioni, Università di Pisa, Largo Lucio Lazzarino, 56122 Pisa, Italy*
**Correspondence Jennifer.wen@warwick.ac.uk*

**ABSTRACT**
The Hydrogen Incidents and Accidents Database (HIAD 2.0) is an international open communication platform collecting systematic data on hydrogen-related incidents or accidents. It is jointly maintained and updated by the Joint Research Centre of the European Commission (JRC) and the European Hydrogen Safety Panel (EHSP), established by the Fuel Cells and Hydrogen 2 Joint Undertaking (FCH 2 JU) of the European Commission. The EHSP and JRC work together to enlarge the database with newly occurred events as well as adding high-quality historic events which were not previously uploaded to HIAD 2.0. This activity has facilitated the number of validated events in HIAD 2.0 to increase from 272 in 2018 to currently 706. JRC has also reviewed all previously input events to improve accuracy, traceability of sources and quality of the text. Furthermore, the overall quality of the published events has also been improved. Recently, EHSP has conducted statistical analysis to identify trends in the type of incident/accident, origin, causes, severity, etc; and analysed the lessons learnt and key recommendations that can be drawn from the newly added events which were consolidated before May 2021. This paper summarises the key developments and findings from the analysis.

**KEYWORDS:** Hydrogen incidents and accidents, database, statistics, lessons learnt.

## INTRODUCTION

In the last two decades, at least two incident databases dedicated to hydrogen safety have emerged, i.e. the Hydrogen Incidents and Accidents Database (HIAD 2.0) [1] and H2LL [2] within the Hydrogen Tools portal [9]. HIAD 2.0 is a publicly available database collecting systematic data and lessons learnt an international open communication platform collecting systematic data on hydrogen-related undesired events (incidents or accidents). The database was initially developed by the Joint Research Centre of the European Commission (JRC) in the frame of HySafe, an EC co-funded Network of Excellence in the 6th Framework Programme. It was updated by JRC as HIAD 2.0 in 2016 with the support of the Fuel Cells and Hydrogen 2 Joint Undertaking (FCH 2 JU). Since the launch of the European Hydrogen Safety Panel (EHSP), an initiative started up in 2017 by FCH 2 JU, the EHSP has worked closely with JRC to improve the quality and accuracy of the information compiled in HIAD 2.0 by adding the information available through other international databases, incident/accidents reports and by uploading additional/new events to HIAD 2.0.

This paper summarises the continuous efforts of EHSP and JRC to enlarge HIAD 2.0 database and analyse the incidents to gather lessons learnt and formulate recommendations. Two conference

presentations have been presetned about HIAD 2.0 at ICHS 2019 [3] and ICHS 2021[4]. The joint efforts have resulted in an increase in the number of validated events in HIAD 2.0 as well as a new report summarising the statistics, lessons learnt and recommendations which has been published by FCH 2 JU [5].

## ENLARGEMENT AND IMPROVEMENT OF HIAD 2.0

JRC and the EHSP have continuously worked together to add newly occurred incidents as well as quality historic incidents which were not previously uploaded to HIAD 2.0. This has facilitated the number of validated incidents in HIAD 2.0 to increase from 272 in 2018 to currently 706. This number is also dynamic and continues to increase as new incidents are being continuously added by EHSP and validated by JRC. For the newly occurred events, experts used their professional networks to gather information and the JRC and EHSP hold discussions internally via emails and meetings before uploading the description to the database.

## OVERVIEW OF THE INCIDENTS AND THE ANALYSIS PROCEDURE

Six members of the EHSP formed a working group under Task Force 3 (TF3). The template used previously to collect individual analysis of the allocated incidents was firstly modified to facilitate statistics analysis and distinguish recommendations from lessons learnt. The "European scale of industrial incidents" used in ARIA database [6] and the "Accidentology involving hydrogen" [7] are used to help to provide some quantification wherever possible on the amount of hydrogen involved, the human, social, environmental and economic consequences.

## STATISTICS

As explained earlier, the number of incidents in HIAD 2.0 is dynamic as new incidents are being continuously added, validated and published. The analysis reported here is based on the 706 incidents which were in the database in May 2021 2020. During the individual analysis, the experts were asked to identify whether an event is worth including in the statistics. 576 of these incidents were considered to be statistically relevant because it contains meaningful information. These incidents form the basis for the statistical analysis. As the spreadsheet contains several sub-sheets which are dynamically linked to produce some statistics, e.g. timeline, locations, industrial sector, etc. while other statistics, e.g. severity, were manually produced by examining the consolidated spreadsheet for all the 576 incidents.

As shown in Fig.1., most of the incidents included in this analysis occurred in the period from the years the 1990s to 2000s. This is merely a reflection that some of the more recent incidents imported by the experts were still in the process of being validated at the time and not included in this report.

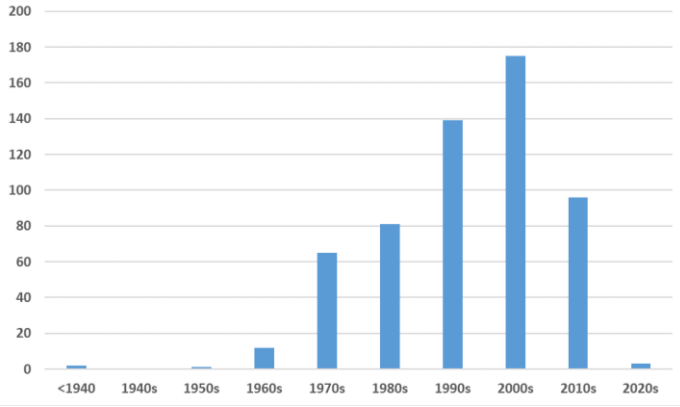


Fig.1. Distribution over time of the cases included in these statistics.

As illustrated in Fig.2, among the 576 incidents considered, apart from the 6 % near misses and 15 % un-ignited releases, hydrogen was ignited in 79 % of the incidents with 48 % involved explosions and 31 % of the incidents resulted in only hydrogen fires. The 15 % incidents without ignition were attributed to a number of reasons, e.g. the unintended releases being promptly stopped, the occurrence of minor releases, etc. The 6 % near misses indicate that early detection and prompt action to mitigate any potential releases can successfully avoid major hydrogen releases.

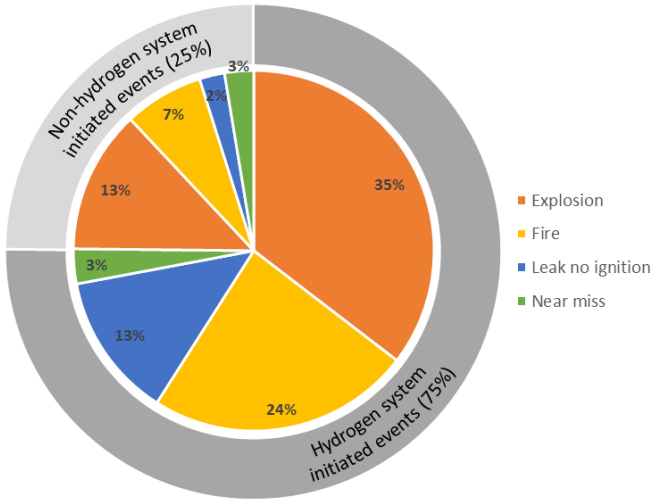


Fig. 2. Consequences of the reported incidents.

Aalysis was also conducted about whether the incidents occurred during normal operation or outside. While one-third of the incidents occurred during normal operation, one third occurred outside normal operation i.e., during maintenance, special services or immediately after returning from maintenance to normal routine operation [2].

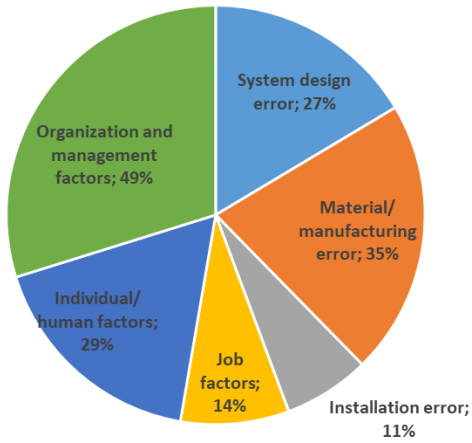


Fig. 3. Causes of hydrogen incidents considering multiple causes per event.

Fig. 3 illustrates the statistics concerning the causes. Most incidents had multiple causes, the individual percentages here add up to more than 100 %. It is important to note that almost in half of the incidents considered, organization and management factors were identified as at least one of the key responsible factors. Material/manufacturing errors are second in relevance with a share of 35 %

in the root causes. Individual and human factors with 29 %, system design errors with 27 % as well as job factors with 14 % play another significant role. Only 11 % of the incidents were related to installation error. Overall, it can be concluded that the so-called soft factors play just as big a role in the causes of incidents as technical factors.

In 2019, the EHSP published a guidance document for "Safety Planning for Hydrogen and Fuel Cell Projects" [8], in which the EHSP experts extracted ten safety principles from the actions required to prevent an escalation of a prototypical hydrogen accident. The derived safety principles (SP), as listed in Table 1, state simple objectives, being widely understandable and acting as preventive barriers or at least as risk-reducing measures on the various elements of the chain of events.
The 576 incidents in HIAD 2.0 considered to be of statistical value as of May 2021 were individually analysed by six safety experts based on the available incident information. The recommendations were provided against each incident based on Safety Principles (SP0-SP11). However, it is noted that for some events, the safety principle suggested by an individual expert is the best guess based on the information available from HIAD 2.0 database. The EHSP plans to devise a consistent methodology to determine the relevance of the incidents to specific safety principles.

During the analysis, it was found that for various incidents, a common cause was the poor design of the hydrogen system or the use of material that is not compatible with hydrogen. A new safety principle SP0 was hence added to account for the poor design of hydrogen system and/or material selection.

**Table 1 The Safety Principles [8]**

| Number | Safety Principle | Explosion Protection Tier |
|---|---|---|
| 0 | Perform proper design and material selection for hydrogen applications. | 1st Tier |
| 1 | Limit hydrogen inventories, especially indoors, to what is strictly necessary. | |
| 2 | Avoid or limit formation of flammable mixture, by applying appropriate ventilation systems, for instance. | |
| 3 | Carry out ATEX zoning analysis. | |
| 4 | Combine hydrogen leak or fire detection and countermeasures. | 2nd Tier |
| 5 | Avoid ignition sources using proper materials or installations in the different ATEX zones, remove electrical systems or provide electrical | |
| 6 | Avoid congestion, reduce turbulence promoting flow obstacles (volumetric blockage ratio) in respective ATEX zones. | 3rd Tier |
| 7 | Avoid confinement. Place storage in the free, or use large openings which are also supporting natural ventilation. | |
| 8 | Provide efficient passive barriers in case of active barriers deactivation by whatever reason. | |
| 9 | Train and educate staff in hydrogen safety. | Organi-sational Safety Principles |
| 10 | Report near misses, incidents and accidents to suitable databases and include lessons learned in your safety plan. | |
| 11 | Perform periodic maintenance and audits. | |

The results of the analysis are shown in Fi. Out of the 576 incidents considered, the major contributing factors were from SP9 (23 %), SP10 (14 %) and SP11 (11 %). The data clearly shows that lack of training of operators/plant personnel and lack of understanding of hydrogen hazards is key area that need further improvement. In addition, the lack of a system to report near misses/incidents and apply learning from it for further development of a safety plan is another area that has contributed to these incidents. Finally, 11 % of the incidents show that the poor design of the hydrogen system and the use of incompatible material are the root cause.

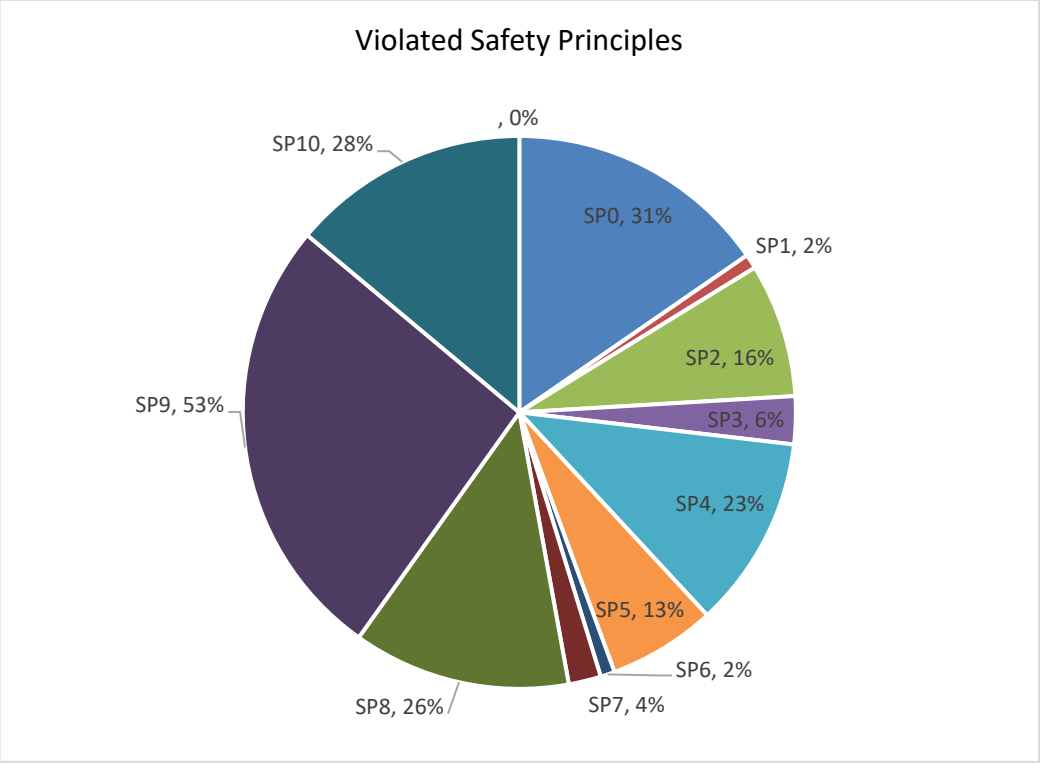


Fig. 5. Statistics showing the number of incidents classified according to the 10 Safety Principles (SP) in [8].

## LESSONS LEARNT

This section is devoted to experiences distilled from the incidents added to HIAD 2.0 databases since the release of our previous report in 2019. An overarching lesson is that some incidents might consist of several causal events that, if occurred separately, might have little consequences; but if these minor incidents occurred simultaneously, they could result in extremely serious consequences. Some incidents were caused by multiple reasons while some involve cascading effects. Although some key information relevant to the description of lessons learnt was extracted in the paper, the readers are recommended to consult the original event description in HIAD 2.0, where there are more details for specific incidents of interest.

### Lessons learnt related to system design

Some design issues were identified being the causes of numerous incidents. In the following, these are grouped according to the categories which were identified as being most relevant. It should, however, be recognised that many incidents were caused by multiple malfunctions, which were included in the description.

*Corrosion related:* Considerable amount of incidents were found to be related to corrosion, the occurrence of which was not detected through regular inspection, prevented from maintenance, or

lack of due consideration of the hydrogen compatibility of materials used. For example, incident ID95 was caused by the corrosion of the heat exchanger. Other incidents caused by corrosion include incidents IDs: 83, 104, 122, 131, 179, 194, 196, 208, 210, 246, 261, 478, 546, 567, 568, 615, 616, 648, 707.

*Design related:* Lack of precaution during the design stage to limit hydrogen inventory, place the inventory outside and protect vessels against thermal attacks, etc. were all found to result in some incidents. For example, incident ID734 was partially caused by a lack of clear separation of combustible gas from the oxidizer and ignition source; incident ID542 was traced back to piping system leaks which could have been avoided by welding the piping system with the exception of flanged joints. Some incidents were caused by a combination of design issues and human error, e.g. incident ID179, in which hydrogen was accidentally released during the filling of a 28 bottles rack. It was found that the feeding pipe was still connected to the rack in the process and resulted in the rupture of the pipe to cause a hydrogen leak. The design of the connection between the stand and the bottles was not sufficiently visible. As a result, when the operator removed the rack, he could not see that the feeding pipe was still connected.

*Venting:* Some incidents were caused by the lack of provision for safe venting of hydrogen and some were attributed to inappropriate ventilation and detection system as well as the latter not directly linked to an automatic alarm, e.g. a temperature controller on the pipe directly connected to an emergency shut down. For example, incident ID670 was caused by inadequate ventilation of the stack base space and the lack of equipment installed to monitor explosive gas concentrations within the enclosed; incident ID674 was suspected to be due to the ventilation system has not been activated; and in incident ID680, the cylinders were stored indoor without adequate ventilation and detections system. It is suggested to safely site the vents such that the hydrogen plume does not reach the ignition source.

*Fatigue:* The fatigue of components could result in partial loss of mechanical integrity, e.g. incident ID498, which involved an explosion in a factory manufacturing nitrogen fertilizers was suspected to be related to the possible failure of welded components due to fatigue. A series of incidents were caused by a lack of periodic verification/audit of the structural integrity of the hydrogen tank. This is an important lesson to learn.

*Extreme weather conditions:* Icing could result in blockage and cause over-pressurization in some systems. In incident ID552, the blockage resulted in the fracture of the second stage cylinder of a hydrogen compressor. Heavy rains could lead to water accumulation, e.g. the explosion incident ID558 which occurred during the cleaning of a blast furnace was caused by accidentally generated hydrogen due to dissociation of the accumulated water after hot slag and was poured into a pit. Lack of consideration during the design stage for adequate protection against extreme weather incidents such as lightning and heavy rains could trigger initiating incidents such as thermal stresses on pipes, e.g. incident ID572.

*Second-order redundancy on critical systems:* Provision of second-order redundancy in some hydrogen facilities could have prevented some incidents, e.g. for incident ID553 which involved incorrectly calibrated transmitters, secondary stops fitted to key controllers/valves could have limited the gas flows due to malfunction (ID553). In this incident, the investigation of the incident was hampered by the loss of the relevant instrument record charts.

*Pressure relief valves:* Some incidents indicated inadequate design and/or installation of pressure relief valves in some pressure systems, e.g. incident ID808. Incident ID562 was also caused by the absence of a pressure relief valve at the recycle compressor's injection point upstream of the isolation valve and failure to operate the system valves in the correct sequence.

*Hydrogen accumulation in confined/semi-confined spaces:* Several lessons can be learnt in relation to this: (1) Explosive mixture with hydrogen in the stagnant zone of pipe systems could result in incidents such as those in incidents ID533 and ID571 concerning radiolytic gases in nuclear power plants; (2) Internal pump might create a vacuum inside tanks with possible air ingress to form an explosive atmosphere, e.g. incident ID551; (3) Dead legs, which are sections of process piping that have been isolated and no longer maintain a flow of liquid or gas, were identified as weak points in

ID568; and (4) Pipe trench with hydrogen pipes near other hot pipes is a potential hazard, e.g. in incident ID544 and requires clear separation with due consideration for specific firefighting.
*Hydrogen generation due to malfunction:* ID522 hydrogen explosion in the core spray system of a nuclear power plant was traced back to the design which was vulnerable to hydrogen generation due to water splitting by the neutron radiation from the reactor core. Event ID492 in a nuclear power plant was due to the formation of hydrogen by radiolysis of reactor water in a core, which exploded and possibly transited to the detonation in the pipe. The explosion in event ID510 which was related to the cleaning agent indicated that chemical decomposition of the heavy alcohol component could release hydrogen at temperatures much lower than previously assumed. ID525 was also caused by accidentally generated hydrogen. Event ID514 was linked to a ruptured seal on a valve in the blast furnace gas pipework that caused the release.
*Equipment factor:* The explosion and fire in incident ID 609 were due to reverse flow in the raw material tank caused by the excessive opening of the valve, which was suspected to be related to maintenance issues or inappropriate materials. Equipment factor and poor apparatus were also mentioned in incident ID612 involving two workers being injured when an explosion and fire occurred at a plant during shutdown operations for routine maintenance. Similarly, these factors were also mentioned in incident ID613.
*Miscellaneous:* An important lesson is to ensure inherently safe design. Some incident was caused by a design problem. For example, the explosion in ID687 was caused by the release of about 30 kg of hydrogen gas into a compressor shed from a burst flange operating at about 47 bar after the unit was being restarted following a regular semi-annual turnaround. Although the specific design issues were not identified, the operator has to implement plant modifications to prevent recurrences of similar incidents.
*Interoperability:* While transferring hydrogen it is necessary the systems fittings work perfectly on both side of the transfer; it has be noted, in same cases, the safety design has in first instance focussed on the safety of the stand-alone system and not to the interconnections

**Lessons learnt related to system manufacturing/installation/modification**
System manufacturing issues were identified being the causes of numerous incidents. In the following, these are grouped according to the categories which were identified as being most relevant. It should, however, be recognised that many incidents were caused by multiple malfunctions and some system manufacturing issues were indeed also related to design. Wherever possible, the description below endeavoured to point such multiple issues out.
*Material compatibility:* Incident ID534 in 1994 was the first reported of such incidents related to the use of materials incompatible with hydrogen. This incident triggered the development of the German pressure vessel code and standards. Incident ID615 involving vapour cloud explosion was traced back to the crack in a storage tank releasing gaseous hydrogen to the atmosphere. The likely cause was the use of materials not compatible with hydrogen and the lack of periodic audit and maintenance to detect the defect promptly.
*Venting system:* Hydrogen venting system malfunctioning could lead to severe consequences, e.g. in ID536, a road tanker carrying 125,000 cubic feet of liquid hydrogen caught fire when the tankers vent stack malfunctioned. The area within a one-mile radius had to be evacuated.
*Weak points:* Some weak points resulted in numerous incidents. Examples include gauge glass for liquid tank level monitoring, flange connections, welded junctions, etc.

**Lessons learnt related to operator errors**
Everyone can make mistakes regardless of their skills or training. However, when handling hydrogen or any other flammable gases, the consequences of these mistakes can be severe. Sometimes, several small mistakes can combine and result in more serious incidents. Human errors, as well as technical errors, were quite often the cause of incidents. In the following, for lessons learned from past incidents, the classification [9] proposed by the Health and Safety Executive (HSE) is adapted, which identifies the factors that make operator errors more or less likely to occur. The three categories that influence human performance are the job itself, the individual and the organisation.

**Lessons learnt related to job factors**

Most incidents reported under this category were initially caused by a lack of regular and appropriate maintenance and inspection. Some could also be attributed to unclear instructions. The lessons learnt related to these two most representative sub-categories are detailed below.

*Lack of maintenance or inspection:* Considerable number of incidents were caused because maintenance and inspection were not carried out regularly and in timely.

*Special attention for safety devices during maintenance:* Fittings, gaskets, flanges, valves, etc. are often identified as weak points of hydrogen systems. Some incidents were caused by a lack of special care on these components during maintenance and inspections or the lack of periodic audit on such devices. As a result, their malfunctioning led to some dramatic consequences, e.g. the fire in event IDs 156 and the severe explosion in ID 475, which resulted from the lack of maintenance on an emergency shut-off valve of a tube trailer.

*Individual/human factors:* In event ID 679, the pipe was incorrectly installed, which led to shutdown valves failed to operate. Some incidents were caused by the lack of compliance with company procedure, e.g. in event ID 675, the compressor manufacturer did not comply with the company's practice for reciprocating compressors in $H_2S$ applications.

*Lack of clear instructions:* Some incidents were caused by a lack of adequate process instructions or such instructions were not readily available.

*Accidentally generated hydrogen:* In several incidents, the flammable gas was not initially present but was produced during a chemical reaction without detection and ventilation. This mainly concerns reactions between acids and metals (event IDs 49, 192, 234 and 321) or unexpected chemical reactions (event ID 123). Wrong identification of chemical components was found to accidentally produce a strong explosion in event ID 530.

*Reoperation after repair:* The fire in event ID 579, which resulted from an escape of liquid hydrogen from a joint between an isolating block valve and a relief valve on one of the separation column preheater, occurred when the relief valve was firstly brought back into operation following repair. The lack of proper checking to confirm that it was safe to resume operation in the section of the plant could have prevented this incident.

*Re-use of tanks or pipes previously contained flammable liquid or gas:* Lessons from event IDs 531, 631, 750 and 752 suggested that without complete degasification supported by instruction for the appropriate procedure, such re-use could incur incidents. The explosion in event ID 673, for example, was because the furnace was not fully purged/ventilated, the employer did not have a portable gas detector and the safety procedure was not followed.

**Lessons learnt related to individual/human factors**

Lack of adequate staff training was identified to be the cause of many incidents. Some incidents occurred because the training procedure was insufficiently stringent and updated at regular intervals in line with operational changes. These resulted in a significant number of incidents being caused by human error.

**Lessons learnt related to organization and management factors**

Management and organization factors are also significant cause of incidents. Among all the incidents whose cause originates from these factors, the following lessons need to be learnt:

- Some incidents were traced back to the lack of up to date inspection plan, infrequent inspection frequency and insufficient scope of the inspected components.
- The maintenance procedures were modified following some incidents, indicating insufficient check of safety equipment, leakage tests and lack of inspection for hydrogen embrittlement.
- Some incidents occurred because the security processes prescribed for the modification and /or improvement of the plants, especially when external companies were used, were not sufficiently stringent.

- Some incidents indicated the lack of safety supervision during certain repairing works and the need for extreme precautions when soldering, using a grinding machine or impact wrench (e.g. ID 631).
- Some incidents could have been preventing by procedures for fast isolation of the release sources.
- Some incidents were traced back to a lack of clear guidance about the lifetime of critical components in addition to their regular inspection and replacement.

**RECOMMENDATIONS**

In formulating the recommendations, links are made to the relevant safety principles [8] wherever possible.

**Recommendations for different operational modes**

Approximately two-thirds of the incidents considered happened during normal operations, while around one third took place outside normal operations, for example during testing, maintenance, starting after maintenance, etc. An analysis of the incidents provided the following recommendations:

- Adequate training of personnel is key (SP9).
- Both passive and active safety measures should be given a crucial role.
- It is necessary to keep the equipment and systems up to date and clean with appropriate surveillance and maintenance. Updating maintenance procedures to consider changes is crucial.
- A final recommendation is to perform a thorough risk/hazards assessment during the design phase and before any process or equipment change.

**Recommendations for different industry sectors**

*Hydrogen energy applications*

The ultimate target of the EHSP is to ensure safety for the FCH 2 JU program including projects but also to facilitate the large deployment of hydrogen energy applications with safe considerations. This section is focused on specific hydrogen applications of interest for the FCH community that have been selected. Note that these are the high-level preliminary recommendations given by the sector of the highest interest of FCH JU applications. These recommendations will be improved in future investigations.

*Hydrogen transport and distribution*

Among the 576 incidents considered, 85 incidents were linked with hydrogen transport and distribution representing 32 un-ignited hydrogen releases, 16 explosions and 23 fires, only 14 near-misses were found.

The general recommendations applied to almost all incidents is that effective safety training of the personnel should be enforced (SP9). Learning from incidents and near misses in the past (SP10) is essential to avoid new incidents (see an example of ID 519, where the second accident led to an explosion and one injured person).

*Recommendations to improve system design*

- Perform Process Hazard Analysis for the new/updated installations (SP1-10);
- Use materials that are compatible with hydrogen services. It should be noted that in certain incidents, this resulted in the need to change standards/codes for pressure vessel (SP11); and
- Install high fidelity leak detection and other extra mitigation barriers (e.g., SP4, SP8).

*Recommendations related to material failure*

- Regular check and maintenance and inspections should be carried out (SP10);
- The operator should consider the installation mitigation barriers such as hydrogen sensors (ID 42, ID 270), pressure sensors (ID 58, ID 156), so that any hydrogen leak can be detected promptly for mitigation measures to be implemented; (SP4, SP8)
- Take all possible measures to avoid any ignition sources to come close to the leaked hydrogen (ID 42, ID 139) (SP3, SP5); and

- Control the proper functioning of hydrogen venting devices (ID 536).

*Hydrogen-powered vehicles*

Special interest in hydrogen safety represents incidents occurred with hydrogen-powered vehicles. There are now 9 declared incidents in HIAD 2.0 involving mainly FCE buses (near misses) and 1 Hydrogen leak on a fuel cells bus in confined space. This event does not correspond to an accident, it represents a near-miss corresponding to a traffic accident including an experimental hydrogen-powered vehicle. This near-miss demonstrates that both safety principles were followed. Recommendations are mainly dedicated to organization safety principles:

- The corresponding staff should be trained and educated about hydrogen safety (SP9)
- All near-misses should be declared (SP10)

*Laboratory / R&D*

Attention must be paid to R&D installations and laboratories involving hydrogen. Among the incidents considered, thirteen were reported by the Laboratory/R&D sector. Among them, only two occurred outside normal operation and explosion was the most frequent consequence.

Recommendations to minimize the occurrence of such incidents in laboratory/R&D installations that handle hydrogen can be grouped in three categories:

- Perform an exhaustive risk analysis for each specific activity to identify safety measures required, including leak detection.
- Periodically update safety procedures and provide adequate training for personnel involved to follow them.
- Carry out periodic surveillance and maintenance of equipment, especially safety devices (valves) and testing protocols.

## CONCLUDING REMARKS

The continuous joint efforts of the EHSP and JRC have facilitated the number of validated events in HIAD 2.0 to increase from 272 in 2018 to currently 706. JRC has also reviewed all previously input events to improve accuracy, traceability of sources and quality of the text. Furthermore, the overall quality of the published events has also been improved. Recently, EHSP has also conducted statistical analysis to identify trends in the type of incident/accident, origin, causes, severity, etc; and analysed the lessons learnt and key recommendations that can be drawn from the newly added events which were consolidated before May 2021. This paper summarises the key developments and findings from the analysis. Readers should consult the original database [1] and the newly published report by FCH 2 JU [2] for further details.

## REFERENCES

[1] European Hydrogen Incidents and Accidents Database (latest accessed 30 November 2020): https://odin.jrc.ec.europa.eu/giada/. The JRC web-platform hosting HIAD 2.0 is currently offline for maintenance. Those who are interested to gain access should contact Pietro MORETTO at JRC pietro.moretto@ec.europa.eu
[2] https://www.fch.europa.eu/sites/default/files/documents/Lessons%20learnt%20from%20HIAD%202.0-Final.pdf
[3] Daniele Melideo, Pietro Moretto, Jennifer Wen, HIAD 2.0- Hydrogen Incident and Accident Database, Proc. 8th Int. Conf. on Hydrogen Safety, Yokohama, Adelaide, Australia, Sep.2019.
[4] Jennifer X. Wen, Marta Marono, Pietro Moretto, Ernst-Arndt Reinecke, Pratap Sathiah, Etienne Studer and Elena Vyazmina, Statistics, lessons learnt and recommendations from analysis of HIAD 2.0 database, Proc. International Conference on Hydrogen Safety, Edinburgh, UK, Sep. 2021.
[5] https://h2tools.org/
[6] https://www.aria.developpement-durable.gouv.fr/wp-content/uploads/2014/08/European-scale-of-accidents.pdf
[7] https://www.aria.developpement-durable.gouv.fr/wp-content/files_mf/SY_hydrogen_GB_2009.pdf
[8] https://www.fch.europa.eu/sites/default/files/Safety_Planning_for_Hydrogen_and_Fuel_Cell_Projects_Release1p31_20190705.pdf
[9] https://www.hse.gov.uk/humanfactors/topics/humanfail.html

# QRA methodology of hydrogen tank rupture in a fire in a tunnel

**Kashkarov S.[1,*], Dadashzadeh, M.[2], Sivaraman S.[1], Molkov V.[1]**

[1] *Ulster University, HySAFER centre, Newtownabbey, Co. Antrim, BT37 0QB, UK.*
[2] *Efectis UK/Ireland, The Bower Stockley Park, Uxbridge, UB11 1AF.*
**Corresponding author's email: s.kashkarov@ulster.ac.uk*

## ABSTRACT

This paper aims to develop a quantitative risk assessment (QRA) methodology for a fire incident with fuel cell vehicles in a tunnel. The methodology is applied to a road tunnel. The consequence analysis of 70 MPa, 62.4 litre hydrogen tank rupture in a fire is considered for two states of charge, i.e. 99% and 59%. The risks in terms of fatalities per vehicle per year and a cost per accident are assessed. To reduce the risk to the acceptable level of $10^{-5}$ fatality/vehicle/year, the fire-resistance rating (FRR) of the onboard storage tank should be above 58 min in the tunnel. The increase of FRR to 91 min reduces both risks to acceptable levels in terms of fatality/vehicle/year and £/accident, i.e. £300 per accident. It is suggested for inherently safer use of hydrogen-powered vehicles in tunnels to increase the FRR accordingly or to use explosion free in fire self-venting thermally activated pressure relief device (TPRD)-less tanks.

**KEYWORDS:** Risk assessment, hydrogen safety, tunnel, hydrogen storage, self-venting container.

## NOMENCLATURE

| | |
|---|---|
| $E$ | Energy (J) |
| $EP$ | Escalation probability (-) |
| $F$ | Frequency (accident/$10^6$ vehicle-mile/year; rupture/vehicle/year) |
| $HRR/A$ | Fire specific heat release rate (W/m$^2$) |
| $L$ | Length (m) |
| $m$ | Mass (kg) |
| $N$ | Number of individuals affected (fatality/rupture) |
| $P$ | Probability (-) |
| $Risk$ | Risk (fatality/vehicle/year; £/accident) |
| $V$ | Tank volume (m$^3$) |

**Subscripts**

| | |
|---|---|
| $ch$ | Chemical (energy) |
| $fat.$ | Fatality |
| $fire\ init.$ | Initiation of a fire |
| $H2$ | Hydrogen |
| $loc.fire$ | Localised fire |
| $m$ | Mechanical (energy) |
| $no\ leak$ | No hydrogen leak |
| $p-crash\ fire$ | Post-crash fire |
| $sev.accident$ | Severe accident |
| $ser.injury$ | Serious injury |
| $sl.injury$ | Slight injury |
| $tot$ | Total |
| $TPRD\ fail.$ | Failure of TPRD |
| $tun.accident$ | Accident in a tunnel |
| $t.rupt.$ | Hydrogen tank rupture |

## INTRODUCTION

Many countries throughout the world are deploying hydrogen fuel cell vehicles (HFCV), including cars, buses, trucks, trains, marine vessels and aeroplanes. A fire incident such as a flammable liquid spill, hydrogen jet fire, smouldering fire, could cause a hydrogen tank rupture. The current onboard composite high-pressure tanks have a low fire-resistance rating (FRR) of 4-8 min in gasoline/diesel/hydrogen fires with intensity HRR/A=1-4 MW/m$^2$ [1–4]. An incident in a confined space like a tunnel with HFCV could escalate to fire and lead to a catastrophic onboard tank rupture with consequences for life, property and the built environment. The severity of an incident and the value of risk will depend on the storage tank volume and pressure, tunnel and traffic parameters.

While the models for the quantitative risk assessment (QRA) in tunnels [5] focus on the societal risk and safety measures of the tunnel, a QRA methodology in a tunnel considering the safety issues relevant to HFCV is lacking. Indeed, when it comes to public and first responders' safety, the individual risk level is of primary importance. The study [6] has shown that increasing the FRR of

onboard storage can reduce the risk to the acceptable level of $10^{-5}$ fatality/vehicle/year using innovative engineering solutions.

The specific heat release rate (HRR) of a fire, HRR/A, directly affects the tank FRR [4]. The current standard tanks may withstand about 4-8 minutes in a fire, considering the higher is the HRR/A, the bigger is the FRR value. One of the reasons for the scatter of FRR values obtained in different laboratories found in the literature is the present fire test protocol of GTR#13 [7] with no specified control of HRR/A. Other factors influencing the FRR are the tank design and the state of charge (SoC). Driving a vehicle in-between the fuellings would be always characterised by the SoC below 100%. It was observed for the selection of 17 hydrogen-powered cars where the SoCs before refuelling the tanks varied from 17% to 59% on average [8]. Hence, looking at consequence analysis of a tank with SoC=100% would be a worst-case scenario. With the decrease of SoC to a certain level, for example below 54% in the numerical study [4], the tank does not rupture in a fire, but leaks.

The detailed comprehensive analysis of different hazards, including jet fires from thermally activated pressure relief devices (TPRD), possible pressure and thermal effects from deflagrations and detonations, and projectiles emanating from a tank explosion, is out of the scope of this study. This QRA study is performed to address the risk associated with the blast waves after the tank rupture in the tunnels. The QRA methodology is demonstrated on a typical tunnel to calculate the blast wave decay and define hazard distances for fatality, injury and no-harm. The risk in terms of fatalities per vehicle per year and the cost per accident (accounting for the loss of human lives only) are assessed for SoC=99% and SoC=59%.

## THE QRA FOR ONBOARD HYDROGEN TANK RUPTURE IN TUNNELS

A flowchart of the QRA methodology is shown in Fig. 1. The risk in terms of fatalities per vehicle per year (Fig. 1a) is calculated based on the consequence analysis of hydrogen tank rupture and the frequency of ruptures per vehicle per year in road tunnels. Following a similar consequence analysis procedure, the risk in terms of cost per accident (Fig. 1b) is evaluated using the tank rupture probability with an additional extension to account for losses of human lives in the incident scenario.

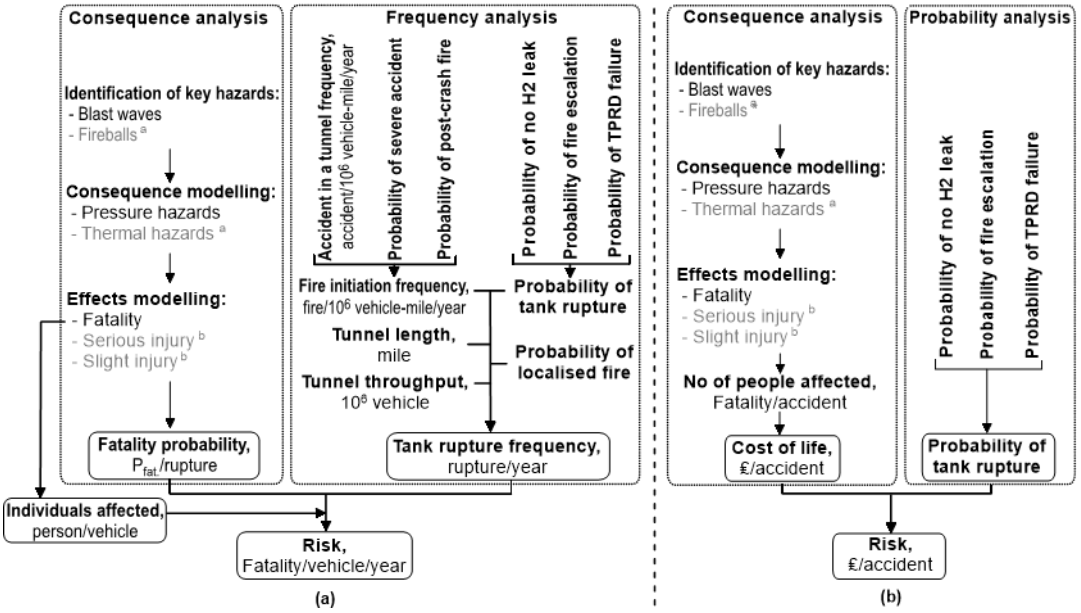


**Fig. 1.** The QRA methodology flowchart for HFCV in a tunnel: (a) risk in terms of fatality per vehicle per year; (b) risk in terms of monetary losses per accident.

[a] Fireball and thermal hazards are excluded from consideration in this study due to the current unavailability of the tool for assessment of fireballs propagation inside tunnels.
[b] Serious and slight injury are excluded from consideration in this study; only fatalities are taken into account.

The main hazards after tank rupture in a tunnel are considered to be the blast wave, which has little decay with distance due to the one-dimensional character of the problem, and the fireball (not taken into account in this study), which propagates with velocity up to 20-25 m/s in a tunnel behind the shock wave due to a preliminary computational study.

The harmful effects on humans from the blast wave inside the tunnel (see Fig. 2) are based on the pre-defined harm criteria [9]:

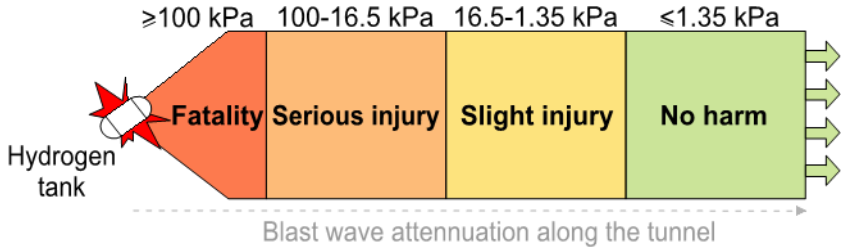


**Fig. 2.** Schematic representation of possible overpressure thresholds inside a tunnel and hazard zones.

The zones describing "Serious" and "Slight" injuries are a product of dividing the spectrum of overpressures in the tunnel by the thresholds.

The frequency analysis (see Fig. 1) includes the estimation of the tank rupture frequency (rupture/year) by multiplying the following parameters: the fire initiation frequency, the probability of tank rupture, tunnel parameters (i.e. tunnel length and tunnel throughput) and the probability of a localised fire mode (among all the fires occurred).

Here the fire initiation frequency is calculated by multiplying: accident in a tunnel frequency, severe accident probability and post-crash fire probability.

The probability of tank rupture includes the probability of no hydrogen leak (as no leak is considered before the tank rupture), following [10], the probability of fire escalation and the TPRD failure probability.

There are no, and probably cannot be, any statistics on the probability of a localised (in the sense of affecting or not the TPRD) fire type among all fires. Indeed, each fire could be both a localised fire, e.g. when an edge of a liquid spill is affecting a tank, or a fire engulfing the tank. Moreover, the fire could start as localised due to a small initial portion of the combustion area and develop into engulfing fire (as per the GTR#13 fire test protocol). Thus, in our study, we assume that half of all fires would affect the storage tank as an engulfing fire and half as a localised fire. Therefore, the probability of a localised fire, $P_{loc.fire}$, is taken as 0.5.

The consequence analysis includes the estimation of the fatality probability ($P_{fat.}$/rupture) and the individuals, i.e. passengers of the vehicles (person/vehicle).

Finally, the risk in terms of fatality/vehicle/year is calculated as a product of the fatality probability, the tank rupture frequency and the individuals affected (due to fatal effects) inside the tunnel (see Fig. 1a).

The risk in terms of cost per accident is estimated as a product of the cost of life (based on the individuals affected) and the tank rupture probability. The latter is calculated by multiplying the no hydrogen leak probability, the fire escalation probability and the TPRD failure probability.

## EXAMPLE OF QRA METHODOLOGY APPLICATION

The suggested dimensions for this study's hypothetical tunnel are analogous to those of Dublin Tunnel of 2.89 miles length (4650 m), from the available information on different tunnels in UK and Ireland [11]. The tunnel has 2 tubes with 2 lanes each. A tube has the traffic travelling in the same direction on both lanes. In the example of the QRA methodology application, the consequence analysis will be performed for 1 tube. The proposed scenario includes the following assumptions:

- An HFCV is trapped in a severe accident inside the tunnel, that has escalated to a fire. The car has two onboard storage tanks, whereas only the rupture on the larger tank of 62.4 L, NWP=70 MPa, $m$=2.5 kg of hydrogen [12] in a fire will be considered for the reason of conservatism. The rupture of the larger tank does not provoke the rupture of a smaller tank. The latter assumption is taken into account as an isolated case of rupture of one tank.
- The blast wave decay in the tunnel is calculated for a case of stand-alone tank rupture, i.e. without spending mechanical energy of compressed gas on vehicle destruction, body frame translation, etc. [13]. The reasoning is justified as in the far-field, being practically the entire tunnel length, the blast wave strengths for a stand-alone or an under-vehicle tank are similar [14].
- The car incident location is 50 m away from the tunnel tube exit. Both lanes in the tube for the same direction of traffic are blocked by an incident. This makes all the vehicles, that have entered the tunnel, trapped inside and unable to carry on driving to leave the tunnel. This gives the affected tunnel length of (4650–50) m = 4600 m.
- Considering the onboard hydrogen tank's SoC will normally be from 17% to 59% on average before refuelling [8], the value of SoC=59% (the equivalent of storage pressure of 35.5 MPa and 1.5 kg of hydrogen at 20°C) is selected for the consequence analysis. The tank filled up to NWP=70 MPa at 20°C would have SoC=99% (or SoC=100% at a temperature 15°C). The SoC=59% is considered an attempt to approach reality as close as possible.

Table 1 shows mechanical, $E_m$, and chemical, $E_{ch}$, energy fractions contributing to the blast wave strength and calculated using the methodology [14].

**Table 1. Fractions of mechanical and chemical energies contributing to the blast strength after 62.4 L tank rupture in a fire for two different SoC.**

| Tank SoC, % | Storage pressure, MPa | $\boldsymbol{E_m}$, MJ | $\boldsymbol{E_{ch}}$, MJ | $\boldsymbol{E_{tot}}$, MJ |
|---|---|---|---|---|
| 99 | 70 | 13.6 | 15.6 | 29.2 |
| 59* | 35.5 [a] | 8.1 [a] | 9.3 [a] | 17.4 [a] |

[a] Will be used for the consequence analysis in the methodology application example.

Table 2 presents the parameters of the tunnel and the assumed number of cars and the average number of people per car for this study.

**Table 2. Tunnel and vehicle parameters and the average number of passengers per vehicle.**

| Tunnel and vehicle parameters | Values | Units |
|---|---|---|
| Overall tunnel length [11] | 4650 | m |
| Tunnel cross-section area [13] | 39.5 | $m^2$ |
| Tunnel length used in calculations | 4600 | m |
| Tunnel throughput [11] | 5.5 [a] | $10^6$ vehicle |
| Car length (calculated average from [15]) | 4.5 | m |
| Length of the gap between cars (assumption) | 5 | m |
| Average No of passengers per vehicle [16] | 1.55 | person/vehicle |

[a] $5.5\times10^6$ vehicle throughput is for two tubes of the tunnels, for one tube the value $5.5\times10^6/2=2.75\times10^6$, which will be used in our study.

## Consequence analysis

The rupture of a tank occurs due to exposure of the tank to the initiating fire given that both safety barriers, i.e. TPRD initiation by the fire and the fire extinction by emergency actions, fail. Fig. 3 shows the sequence of events for an incident.

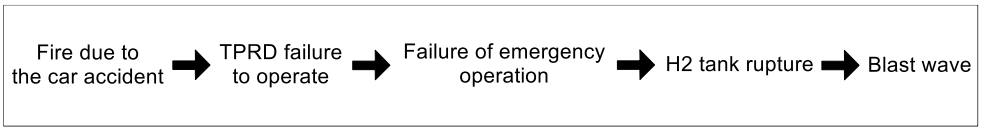


**Fig. 3.** The sequence of events leads to tank rupture in a fire and results in the blast wave.

The experimental [17–19] and numerical [4] studies on the performance of hydrogen storage tanks in a fire, consequences of tank rupture and mechanism of the blast waves formation and decay have been carried out for the open atmosphere only. Only partial data is available on high-explosive charges with the mass equivalent to that of trinitrotoluene (TNT). The TNT blast wave, on the other hand, differs from the blast wave generated by a hydrogen tank rupture in a fire, in particular by the process of how the chemical energy is released. The original dimensionless correlation [13] is applied in this study to calculate the blast wave decay in the tunnel after the rupture of 62.4 L, 70 MPa tank at SoC=99% (70 MPa at 20°C) and SoC=59% (35.5 MPa at 20°C). The correlation [13] allows for consequence assessment for the rupture of any hydrogen tank in a fire inside a tunnel of any cross-section area, aspect ratio and length. The calculated overpressure decay along the hypothetical tunnel is shown in Fig. 4 together with three thresholds (fatality, injury and no-harm).

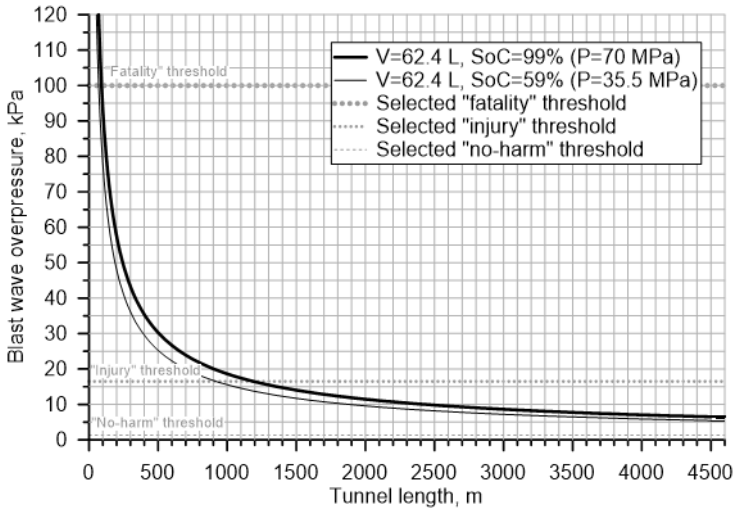


**Fig. 4.** Blast wave decay in the tunnel for the 62.4 L tank for SoC=99% and SoC=59% (T=20°C).

The four hazard zones, i.e. fatality, serious injury, slight injury, and no-harm due to a blast wave together with corresponding probabilities are shown in Table 3.

**Table 3. Hazard zones from the blast wave after the tank rupture inside one tube of the tunnel.**

| Harm to people | Blast wave hazard zone for tank rupture at different SoC | |
|---|---|---|
| | For tank SoC=99% (70 MPa) | For tank SoC=59% (35.5 MPa) |
| Fatality | 0-90 m | 0-70 m |
| Serious Injury | 90-1150 m | 70-900 m |
| Slight Injury | 1150-4600 m (end of the tunnel) | 900-4600 m (end of the tunnel) |
| No harm | Does not exist | Does not exist |

Therefore, for the tank rupture at SoC=59% (35.5 MPa) within the first 70 m from the car, the number of people affected is estimated as follows. Given the vehicle length of 4.5 m and the assumed gaps between vehicles of 5 m, the number of vehicles in 2 lanes within the fatality zone is [70 m/(4.5 m+5 m)]×2 = 15. Given the average number of passengers per vehicle 1.55, the average number of people in the fatality zone is 15×1.55 = 23.25.

The cost of fatality, serious injury, and slight injury are £1,336,800, £207,200, and £300 respectively as introduced by the UK's Health and Safety Executive (HSE). In this study, only the cost of fatality is accounted for in the risk calculations. By multiplying the single fatality cost by the number of fatalities the cost of losses of people due to fatality in an accident involving an HFCV inside the tunnel is calculated as 23.25×£1,336,800=31,080,600 £/accident.

## Frequency analysis

### *Frequency of the initiating fire event*

The number of hydrogen-powered vehicles is currently very small compared to conventional fuel vehicles. There are no statistics on fire accidents with HFCV. It was assumed here that the parameters relevant to assessing the frequency of initiating fire events associated with HFCVs are the same as for fossil fuels cars. The frequency of fires due to a vehicle accident in the tunnel was estimated using data [10,20,21] as:

$$F_{fire\ init.} = F_{tunn.accident} \times P_{sev.accident} \times P_{p-crash\ fire}. \quad (1)$$

Using the data available from [10,20,21], it is calculated as $F_{fire\ init.}$=3.1×10$^{-1}$ accident/10$^{6}$ vehicle-mile/year × 5.94×10$^{-2}$ × 3.17×10$^{-1}$ = 5.84×10$^{-3}$ fire/10$^{6}$ vehicle-mile/year.

### *Failure probability of TPRD*

There is no published data and data on the failure rate of TPRD for hydrogen-powered vehicles. The conservative characteristic value for the random mechanical failure probability of pressure relief devices (PRD) was proposed in the publicly available database NPRD [22] as $6.04 \cdot 10^{-3}$. This value is used in the calculation of TPRD failure probability similar to Dadashzadeh et al. [6]. The FireComp project [23] suggested the TPRD failure probability in fire conditions as 0 for the engulfed fire and 0.5 for the localised fire. Hence, the failure probability of TPRD in our study can be calculated as (1-0)×(6.04×10$^{-3}$)+0=6.04×10$^{-3}$ for the engulfing fire, and (1-0.5)×(6.04×10$^{-3}$)+0.5=5.03×10$^{-1}$ for the localised fire. Dadashzadeh et al. [6] demonstrated that the highest risk for a hydrogen-powered vehicle on London roads is due to a localised fire. This study focuses solely on the localised fire scenario being the worst-credible one for tank rupture in a fire.

### *Escalation probability*

A probability of failure of emergency operations to extinguish a fire that leads to tank rupture, i.e. the escalation probability, $EP$, could be assessed by implementing a probit function, $Y$ [24,25]. For

avoiding the complications of the integration, the EP was expressed in the following form using the error function ($erf$) following [26]:

$$EP = \frac{1}{2}\left[1 + erf\left(\frac{Y-5}{\sqrt{2}}\right)\right], \quad (2)$$

where $Y$ is the probit function, previously used as the general equation in the probit analysis [24,25,27] which assumes log-normal distribution. The probit function in a scenario of a fire brigade arrival at an accident involving a fire considering a 90% failure probability for 5 mins response time and 10% for 20 mins response time with a hydrogen-powered vehicle can be written as [6]:

$$Y = 9.25 - 1.85 \times ln(FRR), \quad (3)$$

where the $FRR$ is the time from fire initiation until the tank rupture in a fire in case of failed TPRD. For example, for 36 L, 70 MPa Type IV tank the FRR is 8 min [4,28]. The use of Eqs. (2) and (3) allows for the calculation of the EP value as: $Y$ =9.25-1.85×ln(8)=5.403, hence $EP$ =1/2[1+ $erf\left(\frac{5.403-5}{\sqrt{2}}\right)$]=6.57×10$^{-1}$.

***Probability of a tank rupture***

The tank rupture probability is calculated as:

$$P_{t.rupture} = P_{TPRD\ fail.} \times EP \times P_{no\ leak}. \quad (4)$$

Using the value of 9×10$^{-1}$ [10] for the "No $H_2$ leak probability", the tank rupture probability is obtained as $P_{t.rupture}$=5.03×10$^{-1}$ × 6.57×10$^{-1}$ × 9×10$^{-1}$ = 2.97×10$^{-1}$.

***Frequency of a tank rupture***

Having already calculated the values of the fire initiation frequency, Eq. (1) and the probability of tank rupture, Eq. (4), the tank rupture frequency can be obtained as follows:

$$F_{t.rupture} = F_{fire\ init.} \times P_{loc.fire} \times P_{t.rupture} \times L_{tunnel} \times TH_{tunnel}. \quad (5)$$

Hence, the tank rupture frequency for the considered accident scenario is:

$F_{t.rupture}$ =5.84×10$^{-3}$ fire/10$^6$ vehicle-mile/year ×0.5×2.97×10$^{-1}$×2.89 mile×2.75 10$^6$ vehicle = 6.89×10$^{-3}$ rupture/year.

***Risk***

The risk of fatality is calculated as:

$$Risk = P_{fat.} \times F_{t.rupture} \times N, \quad (6)$$

where we assume that the fatality probability, $P_{fat.}$, for people in the fatality zone in the tunnel would be taken as 1 (as all the people in this zone would be subject to overpressure equal to or above the fatal overpressure threshold), the tank rupture frequency. $F_{t.rupture}$, is obtained from Eq. (5) and the affected individuals (passengers per vehicle), $N$, are presented in Table 3. The fatality probability strongly depends on a tank's $FRR$. The $FRR$ of an unprotected hydrogen tank in a realistic fire, e.g. gasoline/diesel spill fire source of $HRR/A$=1 MW/m$^2$, is as low as 4-6 min. It can reach tens of minutes for the quite low $HRR/A$=0.2 MW/m$^2$ [4]. The tank $FRR$ can be significantly increased, e.g. beyond 1 hour, by using intumescent paint [28]. However, it should be noted that this will not guarantee the exclusion of the tank rupture in a fire. The results of risk calculations are presented in the next section.

## QRA RESULTS AND DISCUSSION

Fig. 5a presents the risk of fatality as a function of $FRR$ of the onboard hydrogen storage tank. The risk acceptance criteria value was defined as $10^{-5}$ fatality/vehicle/year which is proposed by [29] as an acceptable level of risk for the first responders in a hydrogen refuelling station. Fig. 5b shows that the risk in terms of the cost per accident can be as high as about £9.24M for the aforementioned tank with $FRR$=8 min.

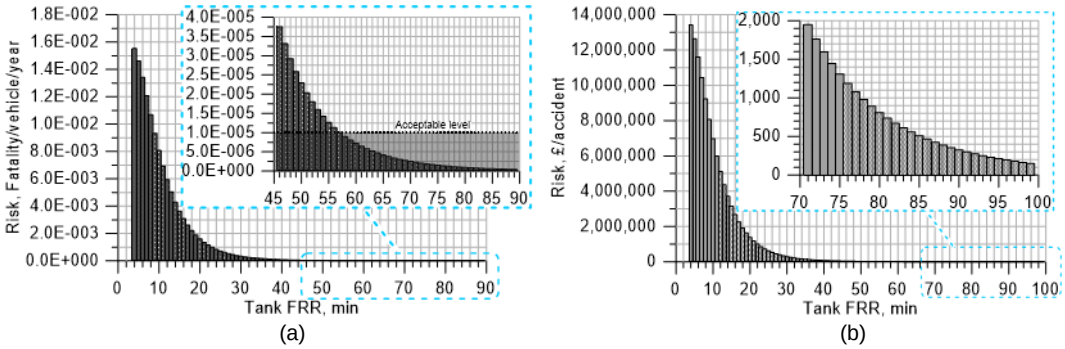


**Fig. 5.** Risks as a function of hydrogen storage tank FRR in a fire for 62.4 L tank rupture at SoC=59%: (a) Risk (Fatality/vehicle/year), (b) Risk (£/accident).

It can be seen in Fig. 5a that for a hydrogen tank with $FRR$=8 min [28] the risk is $1.07\times10^{-2}$ fatality/vehicle/year, which is 3 orders of magnitude bigger than the acceptable level (shown with a black dotted line with a grey transparent filling under it in the graph insert). The increase of the tank $FRR$ for a localised fire reduces the fatality rate progressively until the risk becomes below the acceptable level at the $FRR$ as long as 58 min. The monetary cost of an incident, however, can be significantly reduced down to as low as only £300, but only if the $FRR$ can be as long as at least 91 min, as can be seen in Fig. 5b.

One of the possible solutions to achieve such FRR could be intumescent paint. However, the available experimental studies, e.g. [28], have shown that the increase of FRR beyond 1.5 hours would be possible if the intumescent paint layer thickness is of the order of 1 cm, which is hardly acceptable due to the additional volume of storage tanks on board of a vehicle. Fortunately, the breakthrough safety technology of microleak-no-burst (μLNB) explosion free in fire self-venting (TPRD-less) tank is invented and successfully tested for hydrogen storage tanks of Type IV [30]. The technology allows manufacturing tanks with the same wall thickness as an original tank but with unprecedented safety features to exclude rupture in a fire and avoid TPRD as a potential source of failure.

## CONCLUSIONS

Considering previously unavailable knowledge on the risk and hazards of catastrophic hydrogen tank rupture in a fire inside a tunnel, this study carries out the QRA for hydrogen-powered vehicles in the road tunnel analogous to the Dublin Tunnel. This promotes hydrogen technologies and inherently safer designs of the fuel cell vehicles, informs the stakeholders and the public on the specific hazards and the acceptable risks and elucidates the available solution for prevention and mitigation of the hazards. This supports the significance of our study.

This study further develops the QRA methodology, its application alongside the novel correlation of the blast wave decay in a tunnel for an incident with a hydrogen-powered vehicle. The QRA for the tunnel incident is demonstrated as a holistic analysis of safety and risk reduction measures such as the increase of fire-resistance rating of onboard storage tanks. The “new” hazard to people in a tunnel, i.e. the blast wave after tank rupture in a fire, and associated risks are estimated in terms of fatalities per vehicle per year and cost per accident. The risks were assessed for the cases of a 62.4 L, NWP=70

MPa hydrogen tank rupture in a fire with SoC=99% and SoC=59%. The frequency analysis is carried out by using existing statistical datasets for road tunnel accidents. The probability analysis resources provided by the Health and Safety Executive (UK) were used to assess the risk in terms of costs per accident.

The study's rigour was supported by the authors' use of the relevant data from a number of safety science and engineering sources. The described QRA methodology is applied to a hypothetical tunnel fire involving a hydrogen-powered vehicle with the aforementioned contemporary Type IV hydrogen storage tank. The QRA is based on statistics on car accidents and vehicle fires in the UK. The cost of an accident was assessed using data from the UK Health and Safety Executive. The increase of FRR to 91 min reduces both risks to acceptable levels below $10^{-5}$ fatality/vehicle/year and 300 £/accident. The competing technology to increase fire-resistance rating and exclude tank rupture in a fire is mentioned. The conservative characteristic values for the failure rate of PRD available from industry and the European hydrogen project FireComp are taken as the TPRD failure frequency.

## ACKNOWLEDGEMENTS

The authors are grateful to the Engineering and Physical Sciences Research Council (EPSRC) of the UK for funding through the EPSRC Centre for Doctoral Training in Sustainable Hydrogen “SusHy” (EP/S023909/1), the SUPERGEN Hydrogen and Fuel Cell Hub project (EP/P024807/1) and to Fuel Cells and Hydrogen 2 Joint Undertaking (FCH2 JU) for funding this research through the HyTunnel-CS project “Pre-normative research for safety of hydrogen driven vehicles and transport through tunnels and similar confined spaces” and SH2APED project “Storage of hydrogen: alternative pressure enclosure development”. The HyTunnel-CS and SH2APED projects have received funding from the FCH2 JU under grant agreements No.826193 and No.101007182 respectively. This Joint Undertaking receives support from the European Union's Horizon 2020 research and innovation programme, Hydrogen Europe and Hydrogen Europe Research.

## REFERENCES

[1] H. Ingason, Y.Z. Li, Spilled liquid fires in tunnels. Fire Saf. J. 91 (2017) 399–406.
[2] H. Ingason, Y.Z. Li, A. Lönnermark, Tunnel Fire Dynamics. New York: Springer; 2015.
[3] H. Ingason, R. Hammarström, Fire test with a front wheel loader rubber tyre. 2010.
[4] V. Molkov, M. Dadashzadeh, S. Kashkarov, D. Makarov, Performance of hydrogen storage tank with TPRD in an engulfing fire, Int. J. Hydrog. Energy 46 (2021) 36581-36597.
[5] B. D. Ehrhart, D. M. Brooks, A. B. Muna, C. B. LaFleur, Risk Assessment of Hydrogen Fuel Cell Electric Vehicles in Tunnels, Fire Technol. 56 (2020) 891–912.
[6] M. Dadashzadeh, S. Kashkarov, D. Makarov, V. Molkov, Risk assessment methodology for onboard hydrogen storage, Int. J. Hydrog. Energy (2018) 6462–75.
[7] UNECE. Global Registry. Addendum 13: Global technical regulation No. 13. Global technical regulation on hydrogen and fuel cell vehicles. UNECE; 2013.
[8] V. Mattelaer, Private communication. Toyota Eur., 2020.
[9] S. Kashkarov, Z. Li, V. Molkov, Blast wave from a hydrogen tank rupture in a fire in the open: Hazard distance nomograms, Int. J. Hydrog. Energy 45 (2020) 2429–46.
[10] C. Lafleur, G. Bran-Anleu, A. Muna, B. Ehrhart, M. Blaylock, W. Houf, Hydrogen Fuel Cell Electric Vehicle Tunnel Safety Study, United States: 2017.
[11] Road Tunnel Association (RTA), UK & Eire Road Tunnel Directory. 2019.
[12] A. Yamashita, M. Kondo, S. Goto, N. Ogami, Development of High-Pressure Hydrogen Storage System for the Toyota “Mirai”, SAE Tech Pap 2015.
[13] V. Molkov, Dery W. The blast wave decay correlation for hydrogen tank rupture in a tunnel fire, Int. J. Hydrog. Energy 45 (2020) 31289–302.
[14] V. Molkov, S. Kashkarov, Blast wave from a high-pressure gas tank rupture in a fire: Stand-alone and under-vehicle hydrogen tanks, Int. J. Hydrog. Energy 40 (2015) 12581–603.

[15] What Are The Average Dimensions Of A Car In The UK? 2021. https://www.nimblefins.co.uk/cheap-car-insurance/average-car-dimensions (accessed October 12 2021).
[16] Average car and van occupancy England 2002-2018 Statistic. https://www.statista.com/statistics/314719/average-car-and-van-occupancy-in-england/ (accessed October 12 2021).
[17] N. Weyandt, Vehicle bonfire to induce catastrophic failure of a 5,000-psig hydrogen cylinder installed on a typical SUV. Southwest Research Institute report for the Motor Vehicle Fire Research Institute; 2006.
[18] N. Weyandt, Analysis of Induced Catastrophic Failure Of A 5000 psig Type IV Hydrogen Cylinder. Southwest Research Institute report for the Motor Vehicle Fire Research Institute; 2005.
[19] J. Zheng, H. Bie, P. Xu, H. Chen, P. Liu, X. Li, et al. Experimental and numerical studies on the bonfire test of high-pressure hydrogen storage vessels, Int. J. Hydrog. Energy 35 (2010) 8191–8.
[20] S. Bassan, Overview of traffic safety aspects and design in road tunnels. 2016.
[21] U.S. DOT National Highway Traffic Safety Administration (NHTSA). Traffic safety facts 2015: a compilation of motor vehicle crash data from the fatality analysis reporting system and the general estimates system. 2015.
[22] Reliability Analysis Center. Non electronic parts reliability data. 1991.
[23] J. L. Saw, Y. Flauw, M. Demeestere, V. Naudet, P. Blanc-Vannet, K. Hollifield, et al. The EU FireComp Project and Risk Assessment of Hydrogen Composite Storage Applications using Bow-tie Analysis, Proc. Hazards, vol. 26, 2016.
[24] G. Landucci, G. Gubinelli, G. Antonioni, V. Cozzani, The assessment of the damage probability of storage tanks in domino events triggered by fire, Accid. Anal. Prev. 41 (2009) 1206–15.
[25] G. Landucci, F. Argenti, A. Tugnoli, V. Cozzani, Quantitative assessment of safety barrier performance in the prevention of domino scenarios triggered by fire, Reliab. Eng. Syst. Saf. 143 (2015) 30–43.
[26] A. Papoulis, Probability, random variables, and stochastic processes. 3rd ed. New York: McGraw-Hill; 1965.
[27] D. J. Finney, Probit analysis. 1971.
[28] D. Makarov, Y. Kim, S. Kashkarov, V. Molkov, Thermal protection and fire resistance of high-pressure hydrogen storage, Hefei, China: 2016.
[29] Norsk Hydro ASA, DNV. Risk acceptance criteria for Hydrogen Refuelling Stations. YumpuCom 2003. https://www.yumpu.com/en/document/view/29767890/risk-acceptance-criteria-for-hydrogen-refuelling-stations (accessed October 14 2021).
[30] V. Molkov, D. Makarov, S. Kashkarov, Composite Pressure Vessel for Hydrogen Storage. WO 2018/149772 A1, 2018.

# Numerical modelling of sustained hydrogen combustion and flame blow-off from a TPRD

**Kazemi M.[1], Brennan S.[1,*], Molkov V.[1]**

*[1] HySAFER Centre, Belfast School of Architecture and the Built Environment, Ulster University, Newtownabbey, BT37 0QB, United Kingdom*
**Corresponding author's email: sl.brennan@ulster.ac.uk*

## ABSTRACT

This work focuses on numerical modelling of hydrogen non-premixed combustion from an under-expanded jet to accurately predict the conditions, i.e. storage pressure and nozzle diameter, for flame blow-off from a thermally activated pressure relief device (TPRD). Computational Fluid Dynamics (CFD) had been used to reproduce experimentally observed conditions for hydrogen sustained flame and flame blown-off for storage pressures in the range 3-100 bar (0.3-10 MPa) through round nozzles with diameters of 0.1 mm through to 2 mm. Flame behaviour, specifically the existence of either sustained flame or its blow-off, and flame lift-off height were compared with experimental data. The model was found to predict blow-off and sustained flame behaviour in line with experimental observations in the studied range of parameters. The lift-off heights of sustained flames were within 10% of the values available from the literature. The work has implications for TPRD design where blow-off, particularly in a confined space, is undesirable.

**KEYWORDS:** hydrogen safety, blow-off, sustained flame, lift-off height, numerical modelling

## NOMENCLATURE

| | |
|---|---|
| $c_p$ | constant pressure specific heat (J/(kg·K)) |
| $p$ | pressure (Pa) |
| $U$ | velocity (m/s) |
| $E$ | total energy (J/kg) |
| h | enthalpy (J/kg) |
| $g$ | gravity acceleration (m/s$^2$) |
| $t$ | time (s) |
| $Sc$ | Schmidt number (-) |
| $Pr$ | Prandtl number (-) |
| $Y$ | mass fraction (-) |
| D | molecular diffusivity (-) |

**Greek**

| | |
|---|---|
| $\rho$ | density (W/m$^2$/K) |
| $\mu$ | dynamic viscosity (W/m$^2$) |

**Subscripts**

| | |
|---|---|
| *i, j, k* | cartesian coordinate indexes |
| *m* | chemical species |
| *t* | turbulent |

**Superscripts**

| | |
|---|---|
| * | fine-scale quantities |
| ′ | Sub-filtered scales |

## INTRODUCTION

Climate change, scarcity of fossil fuels and the associated concerns have accelerated the move to alternative fuels, particularly in the transportation sector, and in this regard, hydrogen presents a viable alternative. However, there is a need to understand the characteristics specific to hydrogen, particularly from a safety perspective. The associated infrastructure should be at least as safe as that for conventional fuels. Hydrogen is typically stored as a compressed gas at high pressures up to 700 bar for onboard storage in vehicles to overcome the low gravimetric density of hydrogen. Otherwise, significant tank volumes would be needed to ensure an acceptable vehicle range. From a safety point of view, high-pressure onboard hydrogen tanks need a thermally activated pressure relief device (TPRD) to reduce overpressure and prevent tank rupture in conditions of high temperature. Therefore, TPRDs play an important role in the prevention and mitigation of catastrophic tank rupture. A TPRD is a type of pressure relief device, which will be activated if the hydrogen temperature inside the tank exceeds about 110°C [1]. When a TPRD activates, the compressed hydrogen will be released, causing pressure in the tank to blow down thus preventing tank rupture. TPRDs are vital devices for high-pressure hydrogen vehicles [1]. A hydrogen release from a TPRD results in a high momentum under-expanded hydrogen jet. The jet entrains air forming a flammable envelope that can be easily ignited by an ignition source, e.g. static electricity. The ignition can initiate a jet flame with the potential to damage property and causes injury to people [2]. Our previous and recent studies have included the recommendation that the TPRD diameters be reduced to minimise the effect of the pressure peaking phenomenon in confined spaces [3] that were implemented in the international standard ISO 19882 "Gaseous hydrogen land vehicle fuel tanks and TPRDs" However, reducing the diameter of the TPRD increases the potential

for the flame to blow-off and the hazard of hydrogen accumulation followed by deflagration and deflagration-to-detonation transition (DDT) with devastating pressure and thermal effects. Thus, the blow-off phenomenon, which may occur for hydrogen releases from TPRDs with diameters less than 1.5 mm [2], has the potential to be considered a hazardous phenomenon and thus needs more investigation to inform the design of inherently safer TPRDs. Research on the development of a CFD model able to accurately predict conditions for hydrogen sustained flame or its blow-off is important for the hydrogen safety engineering discipline. The jet flame stability can be characterised by two phenomena, i.e. lift-off and blow-off. They have to be understood for the conditions of hydrogen blowdown from the storage tanks to improve TPRD design with implications for hydrogen vehicle safety.

## BACKGROUND

When considering the hydrogen jet flame stability limit which is a safety consideration: lift-off height, lift-off velocity, and blow-off velocity can be used as parameters to determine the flame stabilisation mechanism. In general, a lower release velocity will lead to a stable flame, subsequently, if the flow velocity increases and exceeds a critical velocity which is defined as the lift-off velocity, the flame will detach from the nozzle exit and restabilises at a distance downstream from the nozzle exit which is known as the lift-off height. The flame stabilises where flow velocity at the flame base is equal to turbulent burning velocity (this happens at distance from the nozzle at lift-off height). However, if the release rate increases, even more, the flame is pushed further downstream of the nozzle and reaches the point that the turbulent burning velocity is not enough in comparison with the value of local jet flow velocity to support combustion. The flow velocity at which the flame is extinguished is known as the blow-off velocity [4], [5]. It is important to underline that the last statement is valid when the flow velocity is increasing starting from very low velocities characteristic for releases at very low pressures below 0.2 MPa abs. As the pressure is further increased, and the release velocity moves towards sonic and supersonic, the upper limit of blow-off velocity is reached and a lifted, sustained flame is again observed. i.e. at high storage pressures of tens and hundreds of atmospheres an increase in pressure leads to sustained flame compared to flame blow-off at pressures just a few atmospheres less.

Different models and physical mechanisms have been presented to explain the lift-off behaviour and blow-off limits. In 1965, the early premixed flame propagation model was proposed by Vanquickenborne and Van Tiggelen [6] to predict lift-off height and the structure of the turbulent lifted diffusion flame. In this model, the stabilisation point of flame was defined as a distance from the burner exit where turbulent burning velocity is equal to the mean gas velocity. In 1978, a semi-empirical formula was presented by Annushkin and Sverdlov [4] to calculate blow-off and lift-off velocity as well as the blow-off limit for three different fuels of propane, methane, and hydrogen and various nozzle diameters. The velocity for hydrogen, methane, and propane ranged from approximately 600-2000, 20-160, and 5-50 m/s, respectively. Later, the dimensionless blow-off velocity was plotted against the Reynolds number in 1981 by Kalghatgi [5] which presented a single curve that was described by a universal formula for blow-off limit of jet diffusion flames. In another study by Kalghatgi [7] published in 1984, lift-off height for hydrogen, propane, methane, and ethylene diffusion flames was measured experimentally. The results demonstrated that there is a linear correlation between lift-off height and jet exit velocity regardless of nozzle diameter for each gas. However, this cannot be applied to the non-premixed turbulent combustion of hydrogen jets at high storage pressures.

In 2009, conditions for hydrogen sustained flame and blow-off limits were extensively investigated by Mogi et al. [2] through a series of experiments with different nozzle diameters and release pressures. Indeed, it is this seminal piece of experimental work that is the basis for the numerical study presented here. In the cases considered experimentally by Mogi et al. [2] when the release pressure is lower than defined by the critical pressure ratio of 1.9, a lifted flame was observed regardless of nozzle diameter. The limits separating zones of sustained flame and flame blow-off for hydrogen jet flames are presented for low and high pressures. It was concluded that the lower limit of blow-off release pressure was almost constant and independent of nozzle diameter, but the upper ("inverted") limit of blow-off pressure was reduced with the increase of nozzle diameter [2].

To characterise blow-off limits, a correlation between experimental dimensionless flame lengths and flame lift-off distances with dimensionless jet velocity before blow-off occurrence was proposed by Palacios et al. [8]. Results demonstrated that unstable flames can be observed at both low and high velocities (due to blow-off). Despite these correlations regarding flame lengths and lift-off distances, the onset of the blow-off phenomenon should be studied more.

In 2018, the blow-off process of hydrogen under-expanded non-premixed turbulent jet flames was studied experimentally by Yamamoto et al. [9]. The results demonstrated how the lift-off heights of stable under-expanded jet flames depend on nozzle diameter and decrease with the increase of nozzle diameter. However, the lifted flame heights were not affected by storage pressure in the range of the studied pressures of 6.0-13.1 MPa Also, the blow-

off process of subsonic and under-expanded jet flames was proposed. It was concluded that if the nozzle diameter is constant, the maximum waistline position of the stoichiometric contour for the stable flame jet is constant, but the flame base position will vary with flow velocity variation. If the flame base position (along the jet axis) becomes larger than the maximum waistline position, blow-off will occur. On the other hand, regarding stable under-expanded jet flames, the flame base position is almost constant, but the maximum waistline position would vary because of Mach disk diameter variation due to different reservoir pressure. Thus, the Mach disk variation stemming from the reservoir pressure change would give rise to different maximum waistline positions. Therefore, decreasing the reservoir pressure can cause the flame base height to become larger than the maximum waistline position and blow-off occurs.

The effect of shock structure on lift-off and blow-off of non-premixed hydrogen jet flames was experimentally studied by Takeno et al. [10] for a range of nozzle geometries. As the first point, it was found that a higher mass flow rate is needed to stabilize a jet flame when shock structures were observed in the range of pressure ratio smaller than 2.45. The minimum mass flow rate for a stable jet flame was shown to depend on the nozzle shape, specifically the ratio of nozzle exit cross-section to nozzle inlet cross-section and the pressure ratio. Tests were completed for highly under-expanded jets through to over-expanded jets which occur when the pressure at the nozzle exit is lower than the atmospheric pressure.

Whilst there have been several experimental studies on the blow-off phenomenon, there is limited numerical work and no validated Computational Fluid Dynamics (CFD) models available for hydrogen safety engineering. ANSYS Fluent is used here as a CFD engine to numerically model sustained flame and flame blow-off phenomena for hydrogen releases. In the present study, to gain a deeper understanding of the lift-off and blow-off phenomenon, experimental work [2] has been used to estimate the capability of numerical simulations to reproduce hydrogen jet flame stability limits.

## PROBLEM DESCRIPTION

Dispersion and subsequent ignition of a series of constant pressure hydrogen releases through a round nozzle have been investigated numerically. The releases and associated geometry were chosen to allow comparison with experimental data [2]. However, it should be noted that pressure losses in the experimental piping system were not accounted for in this study. The cases considered numerically are shown in Table 1. In all cases the hydrogen jet flame stability was examined with time, specifically to see if a sustained flame was established or if blow-off behaviour was observed after the ignition source was removed.

**Table 1. Nozzle diameters (D) and release pressures used in the numerical experiments.**

| D, mm | Release pressure, bar |
|---|---|
| **0.1** | 70.0 |
| **0.2** | 2.0, 5.0 |
| **0.3** | 200.0 |
| **0.5** | 0.8, 2.0, 3.0, 10.0, 40.0, 100.0 |
| **0.8** | 0.6, 0.8, 2.0, 4.0, 10.0, 20.0 |
| **2** | 2.0 |

## EXPERIMENTAL SETUP

A series of experiments were performed by Mogi et al. [2] to study the hazards of hydrogen jet flame and these were used for comparison with the numerical studies described here. Mogi et al. [2] reported blow-off limits based on nozzle diameter and release pressure for hydrogen releases up to 400 bar through diameters up to 4 mm. In the experiments, compressed hydrogen gas was ejected horizontally through a circular nozzle. A pilot burner was used to ignite spouted hydrogen and it was turned off when the gas was ignited. A pressure transducer that was located on the header measured the release pressure $P_0$ of hydrogen (different from the stagnant storage pressure). In the experiments, an aqueous $Na_2CO_3$ solution was applied to visualise the hydrogen jet flame. The flame length and width were determined from camera images. The release pressure ranged from 0.1 to 400 bar and the nozzle diameter was changed from 0.1 mm to 4 mm in the experiments. A key output of the study was the definition of stability limits for hydrogen jet flames. These flame stability limits have been used to validate the numerical model presented here.

## MODEL AND NUMERICAL APPROACH

For all simulations, ANSYS Fluent versions 17.2, 19.2, and 20.2.was used as a computational engine to solve the governing equations. A pressure-based solver has been utilised. To capture the compressibility effects of the flow the ideal gas law was applied because pressure range used in this study was lower than 200 bar in which either ideal gas or real gas law leads to approximately the same results. The SIMPLE method was used for pressure-velocity coupling in this study. A second-order upwind scheme was used to descretize density, momentum, energy and species transport equations. A second-order implicit scheme was used for temporal discretization. Moreover, to interpolate pressure values at cell faces, a second-order scheme was considered. The mass, momentum, energy, and species transport equations solved are:

$$\frac{\partial \rho}{\partial t} + \frac{\partial \rho U_i}{\partial x_i} = 0, \tag{1}$$

$$\frac{\partial (\rho U_i)}{\partial t} + \frac{\partial (\rho U_i U_j)}{\partial x_i} = -\frac{\partial P}{\partial x_i} + \frac{\partial}{\partial x_j}(\mu + \mu_t)\left(\frac{\partial U_i}{\partial x_j} + \frac{\partial U_j}{\partial x_i} - \frac{2}{3}\frac{\partial U_k}{\partial x_k}\,\delta_{ij}\right) + \rho g_i, \tag{2}$$

$$\frac{\partial (\rho E)}{\partial t} + \frac{\partial}{\partial x_i}\big(U_i(\rho E + p)\big) = \frac{\partial}{\partial x_i}\left[\left(k + \frac{\mu_t\, c_p}{Pr_t}\right)\frac{\partial T}{\partial x_i} - \sum_m h_m\left(-\left(\rho D_m + \frac{\mu_t}{Sc_t}\right)\right) + U_i\,(\mu + \mu_t)\left(\frac{\partial U_i}{\partial x_j} + \frac{\partial U_j}{\partial x_i} - \frac{2}{3}\frac{\partial U_k}{\partial x_k}\,\delta_{ij}\right)\right] + S_E, \tag{3}$$

$$\frac{\partial (\rho\, Y_m)}{\partial t} + \frac{\partial}{\partial x_i}(\rho U_i Y_m) = \frac{\partial}{\partial x_i}\left[\left(\rho D_m + \frac{\mu_t}{Sc_t}\right)\frac{\partial Y_m}{\partial x_i}\right] + S_m, \tag{4}$$

where $i, j$ and $k$ are the Cartesian coordinates. Parameters $t, \rho, \mu_t, p, T, U, E, c_p, k, g_i, Y, D$ and $S$ are time, density, turbulent dynamic viscosity, pressure, temperature, velocity, total energy, specific heat at constant pressure, thermal conductivity, gravity acceleration, mass fraction, molecular diffusivity, and source term, respectively. Subscript m refers to the species. $Sc_t$ and $Pr_t$ are the turbulent Schmidt and Prandtl numbers, which are taken as 0.7 that was used in combusting simulations [11] and 0.85 that was identified as a good prediction for turbulent flows with moderate and high $Pr$ number [12], respectively. Subscript m stands for the species involved in chemical reactions. The Kronecker symbol and defined as:

$$\delta_{ij} = \begin{cases} 1 & i = j \\ 0 & i \neq j \end{cases}. \tag{5}$$

### Turbulence and combustion approach

The large eddy simulation (LES) technique which is a promising CFD approach for simulating turbulent flows was applied in this study. It was successfully used to simulate hydrogen jet flames in our previous studies [13]. To explain more, two filtering operations, LES filter and mass-weighted filter (see equation (6) and (7)) is applied to the Navier-Stokes equations (1-4) to decompose each dependant function such as U, E and $Y_m$ into resolved and Subgrid-scale components. Subgrid-scale which stem from scales of motions smaller than the grid size are filtered out and resolved components stemming from flow structures larger than the grid size are solved explicitly.

$$\bar{\varphi}(x) = \int G(x, x')\,\varphi(x')dx' \tag{6}$$

$$\bar{\rho}(x)\tilde{\varphi}(x) = \int \rho(x')G(x, x')\,\varphi(x')dx' \tag{7}$$

The Smagorinsky-Lilly Subgrid-scale (SGS) model was used to model Subgrid-scale components generated in filtered governing equations.

The eddy dissipation concept (EDC) model was applied to simulate combustion. EDC is an extension of the eddy dissipation model with an extensive chemical reaction mechanism for turbulent flow [14]. In this study, 1 chemical reaction with 4 species was used for the reaction of hydrogen with air, so that water is the only product of the hydrogen-air combustion. Considering the EDC method, the source term in equation (4) called the net rate of production of species by chemical reactions is defined as below [15]:

$$R_i = \frac{\rho(\xi^*)^2}{\tau^*[1-(\xi^*)^3]}(Y_i^* - Y_i). \tag{8}$$

The time scale and length scale of small scale motions are calculated as follow [16]:

$$\tau^* = C_\tau \left(\frac{\nu}{\varepsilon}\right)^{1/2}, \quad (9)$$

$$\xi^* = C_\xi \left(\frac{\nu\varepsilon}{k^2}\right)^{1/4}, \quad (10)$$

where $C_r$ and $C_\xi$ are the time scale and volume fraction constants, which are equal to 0.4082 and 2.137 respectively [16], $R_i$ is the net rate of production/destruction of species $i$ by chemical reactions, $Y_i$ is the species $i$ mass fraction in the surrounding fine-scales state, $Y_i^*$ is the fine-scale mass fraction of species $i$ after reacting over the time $\tau^*$.

## SIMULATION DETAILS

### Computational domain and mesh

The geometry of the nozzle was designed to replicate the experimental apparatus. However, the conjunction angles of different parts of the nozzle were not mentioned in the experimental paper. Therefore all dimensions that are shown in Fig. 1 are according to the experimental set-up instead of two conical conjunction parts that were not detailed in the experimental paper[2]. The computational domain was a cylinder with a diameter of 150 mm and a length of 200 mm.

One computational hexahedral grid which contained approximately 220k control volumes (CVs) is shown in Fig. 1 as an example. Nozzle diameters up to 0.8 mm were resolved by 18 CVs along the diameter. The minimum size of CVs in each simulation was (D)/(number of meshes along D) which gives the size of 0.0055 0.01, 0.016, 0.027, 0.04, and 0.1 mm for 0.1, 0.2, 0.3, 0.5, 0.8, and 2 mm diameter nozzles respectively. The small size of the CVs in the nozzle and the vicinity of the nozzle exit is necessary to resolve the shock structure which was captured in all simulations. The sensitivity of the simulation results to the grid resolution in the vicinity of the nozzle was studied, specifically grid resolutions of 6, 12 and 18 cells along diameter were simulated for comparison, resolution of 12 cells was found to give results comparable to the resolution of 18 cells  The simulations were computationally expensive, each taking several weeks of high-performance computing power.

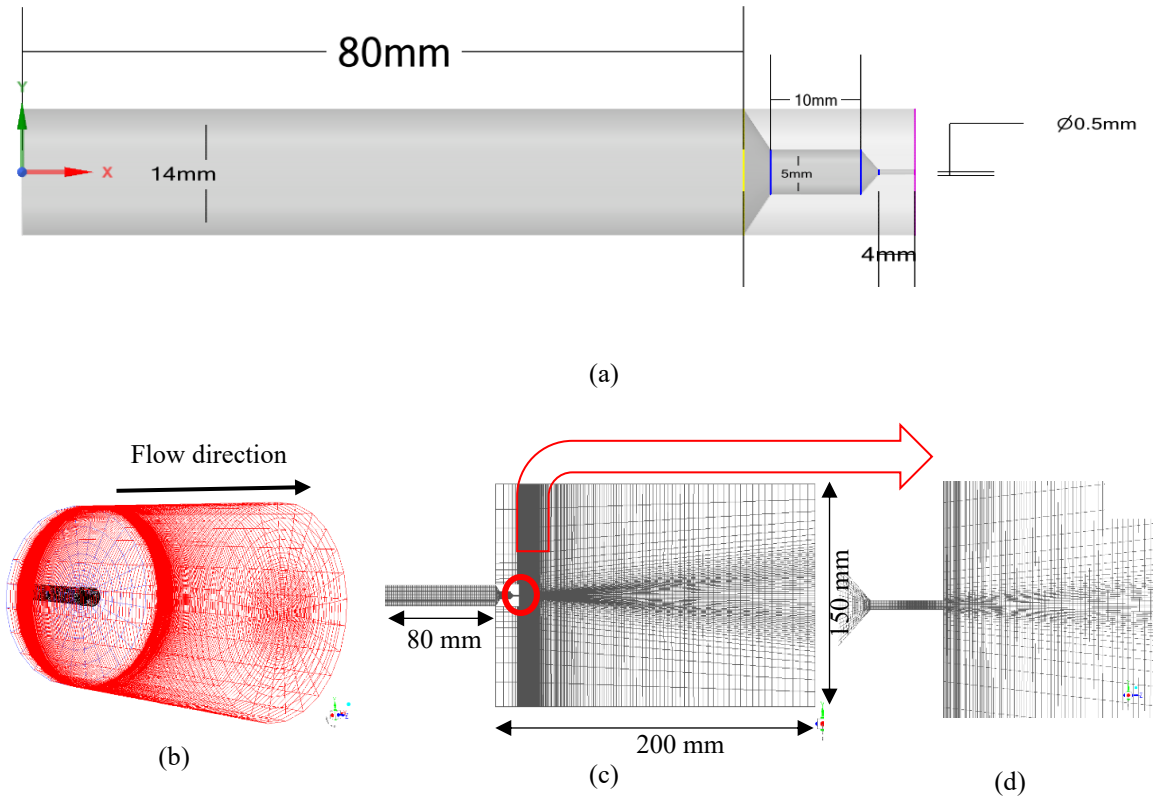


**Fig. 1** Simulation grid: a) Nozzle geometry b) 3D computational domain with the hexahedral grid; c) 2D centreline cross-section; d) 2D zoomed-in schematic of cross centreline near the nozzle exit.

### Boundary and initial conditions

The hydrogen inlet boundary condition which was a pressure inlet was located at the distance from the nozzle exit where the pressure transducer in the experiments was mounted. A pressure outlet condition was applied for the radial and downstream boundary of the domain. A pressure inlet condition was applied for the upstream boundary of the domain. Non-reflecting boundary conditions were imposed for the domain boundaries (inlet and outlet). The hydrogen temperature and mass fractions were 300 K and 1 respectively at the hydrogen inlet boundary. Moreover, temperature, absolute pressure, and oxygen mass fraction were 300 K, 1 atm, and 0.23 respectively at the domain boundaries. A no-slip condition was employed for all solid wall boundaries.

To decrease computational cost, a steady-state solution of the unignited release using RANS was first simulated. Once the unignited jet had been established these results were used as an input for unsteady simulations. The pressure-based steady-state solver, the renormalization group (RNG) k-ε turbulence model and COUPLED scheme were used in this initial unignited release stage.

The steady-state results were used to estimate the initial time step size by extracting the steady-state velocity under no ignition condition and considering an initial Courant-Friedrichs-Lewy (CFL) number less than 1. A time step size of 1 ns which met the CFL number less than 0.5 for all cases was selected in all scenarios until a flame was formed. The CFL number was then gradually increased up to more than 1 to accelerate simulation speed. However, it was considered that the CFL number was maintained below 1 inside the flame zone until a quasi-steady-state has been reached.

### Ignition simulation

To ignite the hydrogen-air mixture, a static temperature of 2400 K was patched in the calculation domain which is shaped like a cube with dimensions of e.g. x: 70 to 80 mm, y: -20 to 20 mm, and z: -20 to 20 mm. This hot spot was in place of the pilot burner which was used in the experiments. Since the location of the pilot burner was not mentioned in the experimental study, care was taken to ensure the ignition source was appropriately located to ensure ignition would happen Considering hydrogen concentration between 4-75% (hydrogen flammability limits), to make sure that ignition source position does not affect flame extinguishment, the ignition source was located such that the hydrogen concentration at the domain centreline was larger than 11% vol. of hydrogen in the air so that the flame could be propagated downstream and upstream of the ignition source position [17]. In comparison, if the ignition source were to be located where hydrogen concentration is less than 11%, experimental studies have shown that the flame may be unstable and propagates just downstream when the ignition source is present or quenches if the ignition source is removed [17]. Therefore, the position of the numerical ignition source (hot spot patch) in each simulated scenario was determined according to the hydrogen concentration at the centreline where it was more than 11% which was different for each scenario.

The water concentration was checked before ignition source deactivation to make sure the hydrogen-air mixture has been ignited. The behaviour of the hydrogen fire was investigated following the removal of the ignition source.

## RESULTS AND DISCUSSION

### Blow-off

Blow-off was reproduced for several scenarios in line with experimental observations. In all cases, the same behaviour was observed (which was in contrast to the behaviour of sustained flames described in the next section). On removal of the ignition source, as shown in Fig. 2, the temperature in the vicinity of the ignition source could be seen to continuously drop, and the hot products of combustion, namely water vapour could be seen to propagate downstream of the domain. Blow-off is shown in Fig. 2 for a release pressure of 4 bar and a 0.8 mm diameter nozzle.

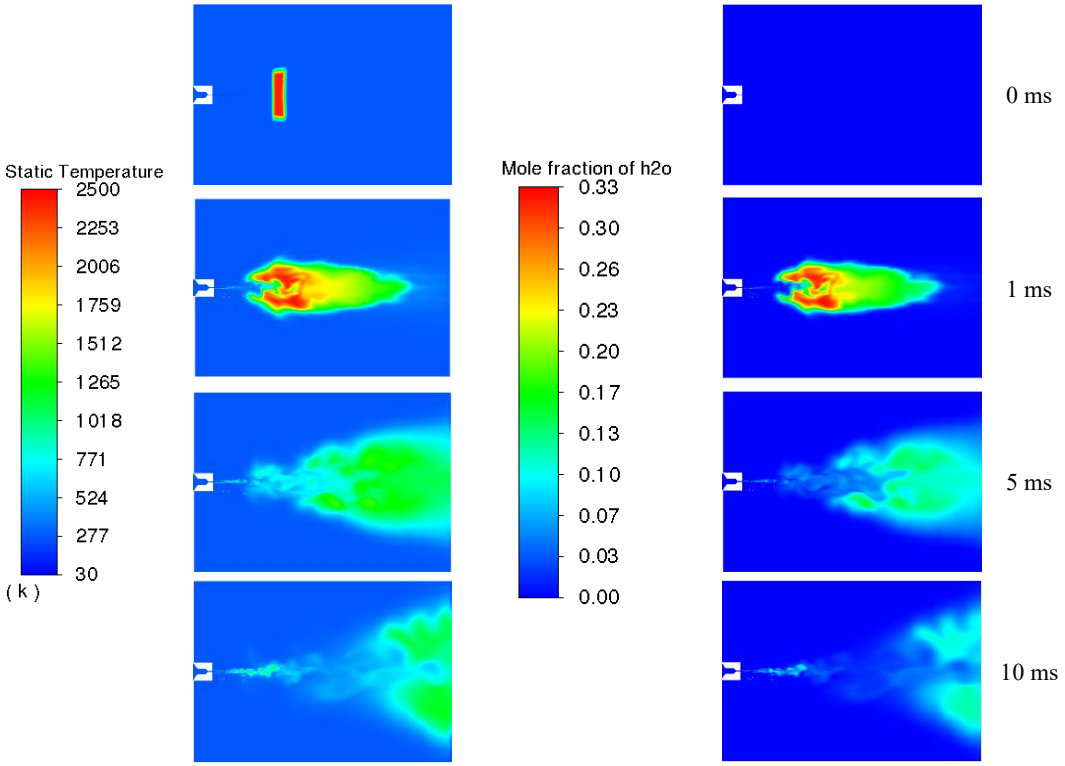


**Fig. 2** Contour plots along the jet axis showing blow-off following a release from 4 bar through a 0.8 mm nozzle: a) temperature (K); b) water mole fraction.

The time for the hot products to travel along the computational domain was estimated to ensure that the behaviour was physical. It was clear within 5 ms of flow time in all cases where blow-off could be numerically predicted to occur, and the majority of simulations where blow-off was expected were stopped at this time to reduce computational expense. However, to ensure the indication of blow-off was accurate, the scenario of a release from 5 bar through a 0.2 mm diameter nozzle was run for 20 ms, as shown in Fig. 3 and propagation of the hot products through the computational domain can be seen. It should be noted that the influence of ignition position and duration was checked as described earlier, to ensure that this did not influence the flame behaviour.

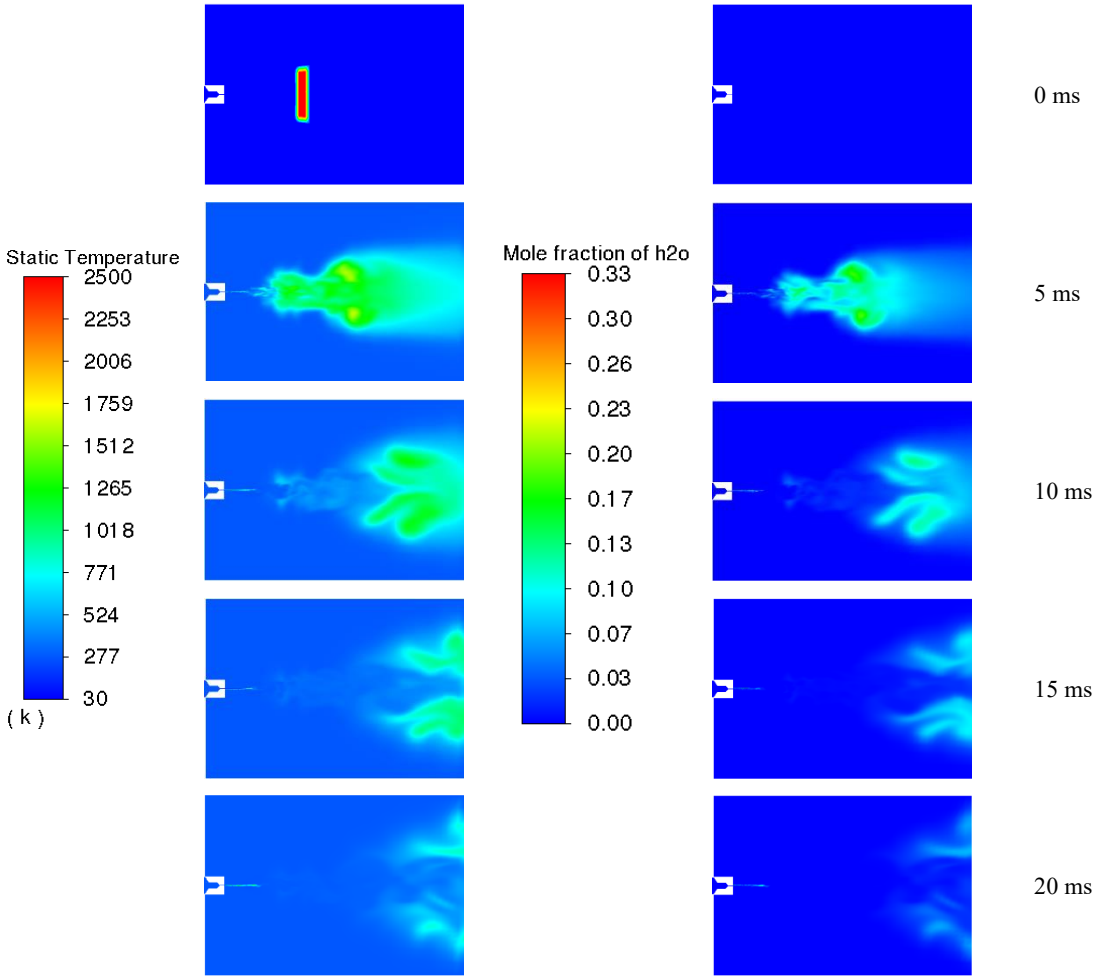


**Fig. 3** Contour plots along the jet axis showing blow-off following a release from 5 bar through a 0.2 mm nozzle: a) temperature (K); b) water mole fraction.

### Sustained flame

The simulations were carried out for conditions where a sustained flame is expected to occur [2]. Within several ms of flow-time, it was clear if a sustained flame was likely to occur. Unlike the blow-off, the combustion region could be seen to grow, and a sustained flame is established.

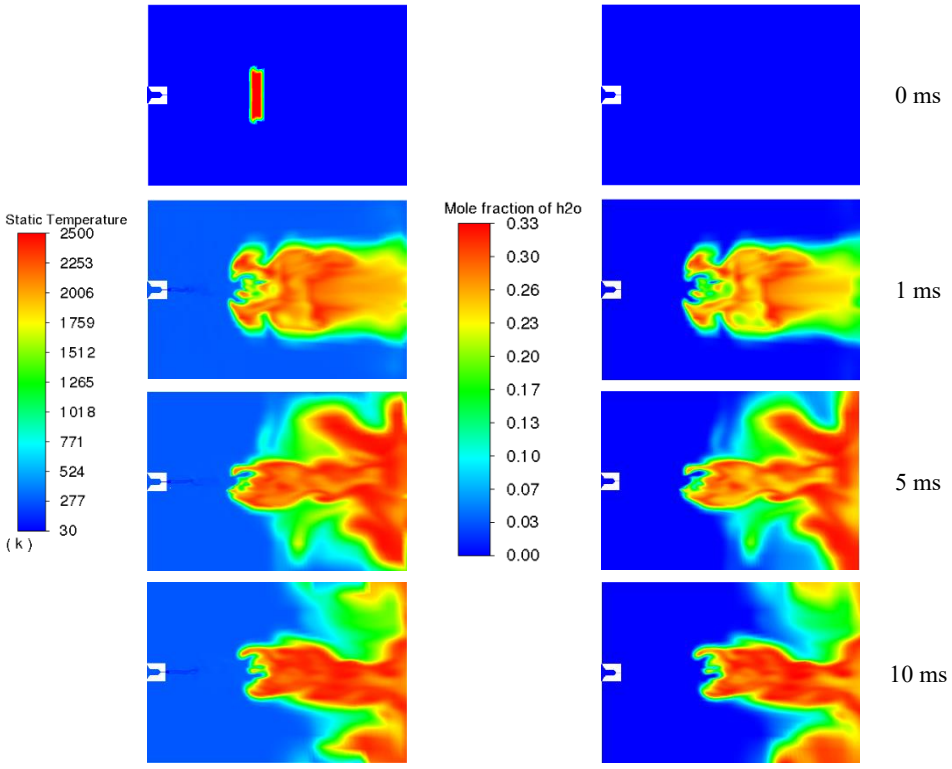


**Fig. 4** Contour plots along the jet axis showing a sustained flame following a release from 100 bar through a 0.5 mm nozzle: a) temperature (K); b) water mole fraction.

The flame can be seen to fluctuate at a lift-off height. An example of sustained flame simulations is given in Fig. 4 for a release from 100 bar through a 0.5 mm nozzle. The variance of simulated lift-off height with time is shown for this case in Fig. 5. To determine lift-off height, a temperature between 1200 K and 1400 K was chosen as an indicator for the visible flame. The lift-off distance for different nozzle diameters and reservoir pressures was measured by Yamamoto et al. [9] in which it was concluded lift-off height depended on nozzle exit diameter and remained almost constant for a particular nozzle exit diameter even with different reservoir pressures. In their work, lift-off distance was reported by a graph showing a variation of lift-off height versus pressure in which lift-off distance for 0.53 mm nozzle exit diameter and two different pressures of 95 bar and 131 bar was almost the same at approximately 55.2 mm. It is worth mentioning that flame will fluctuate over time with a period of fractions of a millisecond. Therefore, the time-averaged lift-off height from 4 ms (when the flame has been established) to 10 ms is compared with experimentally-measured lift-off distance. The estimated lift-off height from simulations was within 10% of that predicted by Yamamoto et al [9].

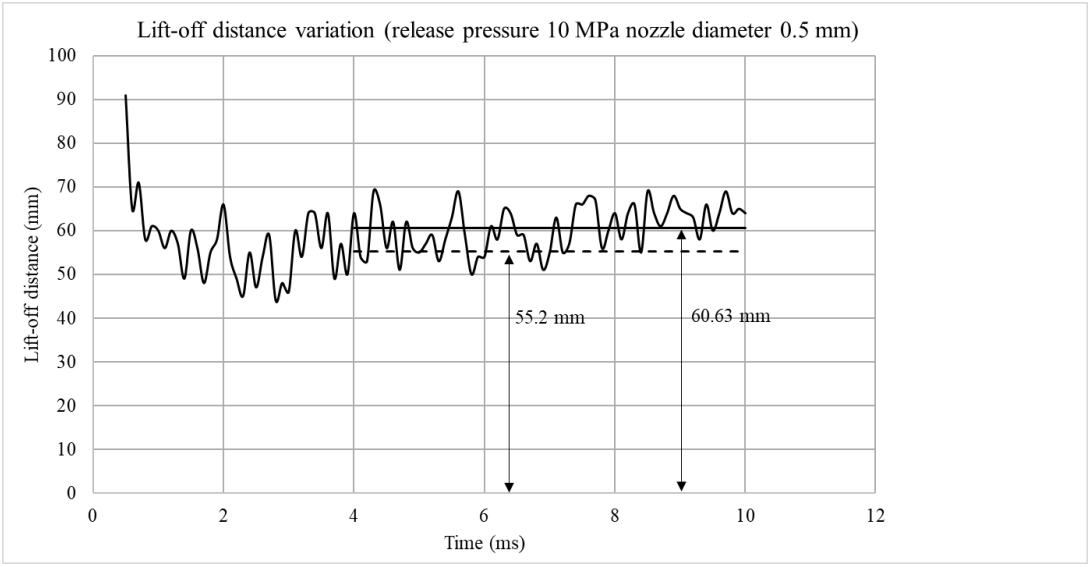


**Fig. 5** Lift-off height for a sustained flame following a release from 100 bar through a 0.5 mm nozzle.

### Blow-off limits

A series of scenarios were simulated and compared with the experimentally determined blow-off limits presented by Mogi et al. [2]. Fig. 6 includes the simulation data from this study, mapped against the experimentally determined flame behaviour curve developed by Mogi et al. [2]. The flame behaviour observed numerically is broadly in line with that observed experimentally.

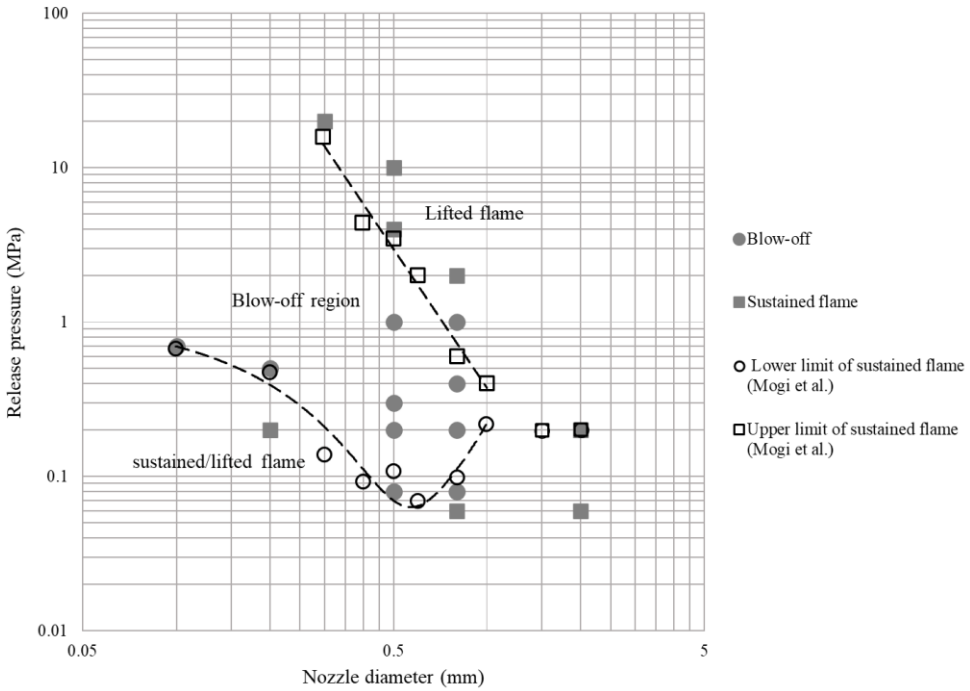


**Fig. 6** Sustained hydrogen flame domain and blow-off limits as a function of pressure and nozzle diameter: simulations (this study) and experimental data [2].

## CONCLUSIONS

A numerical study has been undertaken to investigate blow-off prediction for hydrogen releases through nozzles characteristic of TPRDs. Diameters from 0.1 to 2 mm and pressure from 0.6 to 200 bar have been considered. The model has been found to successfully predict the potential for blow-off to occur and a sustained lifted flame has been observed at conditions in line with experimental data. As experiments have shown that blow-off does not occur in in diameters larger than 1.5 mm, diameters greater than 2 mm have not been investigated. In addition an application of this work is TPRDs where smaller diameters have been shown to be inherently safer.. Lift-off heights predicted for sustained flames are within 10% of values reported in the literature.

A new modelling approach has been taken in this study, which has been compared against experimental data with the intention that a validated model can subsequently be applied to further practical applications. Specifically, blow-off has implications from a safety perspective, particularly where it occurs in a confined space resulting in the accumulation of a flammable atmosphere. Thus, this study and the numerical model can be subsequently be utilised to inform TPRD design and ultimately improve vehicle safety including TPRD design.

## ACKNOWLEDGMENTS

The authors are grateful to the Engineering and Physical Sciences Research Council (EPSRC) of the UK for funding through the EPSRC Centre for Doctoral Training in Sustainable Hydrogen “SusHy” (Grant EP/S023909/1), and performing simulations using the Tier 2 High-Performance Computing resources provided by the Northern Ireland High Performance Computing (NI-HPC) facility funded by the EPSRC (grant EP/T022175/1, https://www.ni-hpc.ac.uk/Kelvin2/).

## REFERENCES

[1] Z. Li and K. Sun, “Mitigation measures for intended hydrogen release from thermally activated pressure relief device of onboard storage,” *Int. J. Hydrogen Energy*, vol. 45, no. 15, pp. 9260–9267, 2020.

[2] T. Mogi and S. Horiguchi, “Experimental study on the hazards of high-pressure hydrogen jet diffusion flames,” *J. Loss Prev. Process Ind.*, vol. 22, no. 1, pp. 45–51, 2009.

[3] S. Brennan and V. Molkov, “Pressure peaking phenomenon for indoor hydrogen releases,” *Int. J. Hydrogen Energy*, vol. 43, no. 39, pp. 18530–18541, Sep. 2018, doi: 10.1016/j.ijhydene.2018.08.096.

[4] Y. M. Annushkin and E. D. Sverdlov, “Stability of submerged diffusion flames in subsonic and underexpanded supersonic gas-fuel streams,” *Combust. Explos. Shock Waves*, vol. 14, no. 5, pp. 597–605, 1978.

[5] G. T. Kalghatgi, “Blow-out stability of gaseous jet diffusion flames. Part I: in still air,” *Combust. Sci. Technol.*, vol. 26, no. 5–6, pp. 233–239, 1981.

[6] L. Vanquickenborne and A. Van Tiggelen, “The stabilization mechanism of lifted diffusion flames,” *Combust. Flame*, vol. 10, no. 1, pp. 59–69, 1966.

[7] G. Kalghatgi, “Lift-off Heights and Visible Lengths of Vertical Turbulent Jet Diffusion Flames in Still Air,” *Combust. Sci. Technol.*, vol. 41, pp. 17–29, Sep. 1984, doi: 10.1080/00102208408923819.

[8] A. Palacios, D. Bradley, and M. Lawes, “Blow-off velocities of jet flames,” in *Proceedings of the Eighth International Seminar on Fire and Explosion Hazards (ISFEH8)*, 2017, pp. 650–657.

[9] S. Yamamoto, R. Sakatsume, and K. Takeno, “Blow-off process of highly under-expanded hydrogen non-premixed jet flame,” *Int. J. Hydrogen Energy*, vol. 43, no. 10, pp. 5199–5205, 2018.

[10] K. Takeno *et al.*, “Effect of shock structure on stabilization and blow-off of hydrogen jet flames,” *Int. J. Hydrogen Energy*, vol. 45, no. 16, pp. 10145–10154, 2020.

[11] S. W. Churchill, “A Reinterpretation of the Turbulent Prandtl Number,” *Ind. Eng. Chem. Res.*, vol. 41, no. 25, pp. 6393–6401, Dec. 2002, doi: 10.1021/ie011021k.

[12] R. A. Baurle, “Hybrid Reynolds-averaged/large-eddy simulation of a scramjet cavity flameholder,” *AIAA J.*, vol. 55, no. 2, pp. 544–560, 2017.

[13] S. L. Brennan, D. V. Makarov, and V. Molkov, “LES of high pressure hydrogen jet fire,” *J. Loss Prev. Process Ind.*, vol. 22, no. 3, pp. 353–359, May 2009, doi: 10.1016/j.jlp.2008.12.007.

[14] B. Magnussen, “On the structure of turbulence and a generalized eddy dissipation concept for chemical reaction in turbulent flow,” in *19th aerospace sciences meeting*, 1981, p. 42.

[15] B. F. Magnussen, “Modeling of pollutant formation in gas turbine combustors based on the eddy dissipation concept,”

1989.

[16] I. R. GRAN and B. F. MAGNUSSEN, “A Numerical Study of a Bluff-Body Stabilized Diffusion Flame. Part 2. Influence of Combustion Modeling And Finite-Rate Chemistry,” *Combust. Sci. Technol.*, vol. 119, no. 1–6, pp. 191–217, Oct. 1996, doi: 10.1080/00102209608951999.

[17] A. Veser *et al.*, “The structure and flame propagation regimes in turbulent hydrogen jets,” *Int. J. Hydrogen Energy*, vol. 36, no. 3, pp. 2351–2359, Feb. 2011, doi: 10.1016/J.IJHYDENE.2010.03.123.

# Water Mist Characteristics for Explosion Mitigation

**Lundberg J.*, Sikka R., Vaagsaether K. Bjerketvedt D.**

*University of South-Eastern Norway, Faculty of Technology, Natural Sciences and Maritime Sciences, Porsgrunn, Vestfold and Telemark, Norway.*
**Corresponding author's email: joachim.lundberg@usn.no*

## ABSTRACT

This work aims to characterize a mist nozzle for hydrogen explosion mitigation purposes. The emphasis is on the fraction of the larger droplets in the spray. One of the reasons is that the mechanisms for the flame/droplet interactions are droplet size-dependent. Smaller droplets can evaporate fully in the flame, while the larger ones evaporate post the flame zone. However, if the flame propagation is sufficiently fast, a pressure wave can occur before the flame, resulting in droplet breakup and finer droplets. Current research characterizes a typical commercial mist nozzle (Danfoss HNMP-5-10-1.19-00) to give averaged diameters, flow patterns, and droplet size distributions, among other parameters. The novelty of the work is to investigate the fraction of the larger droplets in the mist spray using a laser-based imaging technique. The technique gives the possibility to estimate the fraction of the smallest droplets. When using spray data for simulation purposes, the size distribution (and other characteristics) is essential due to multiple mechanisms of flame droplet interactions in an explosion.

**KEYWORDS:** Mist Spray, Droplet Size Distribution, Explosion Mitigation, Experimental

## INTRODUCTION

Today's transportation depends on fossil fuels, where petrol and diesel power passenger cars. Due to the Norwegian government's ambitious goals for reducing emissions from road transport, they have a plan that all new passenger cars sold should be zero-emission by 2025, among other purposes. By 2020 54 % of all new vehicles sold in Norway aims to be electric [1]. The high percentage can address to economic benefits of electric cars. Furthermore, hydrogen cars predict to have the same benefits as electric cars. As a result, electric and hydrogen vehicles prospects to dominate the passenger car fleet in the future. Similar trends can exist worldwide.

Hydrogen fuels are typically stored onboard cars as a pressurized gas at 70 MPa [2], while the fuel is a liquid in traditional fossil cars. The energy stored in both fuels is quite similar, but the accidental scenarios are different. Since hydrogen is a light, explosive gas, an accidental release in confined or partially confined spaces is of great concern. A prospected scenario is a high-pressure gas release inside a tunnel leading to rapid mixing of fuel and air with delayed ignition. In this case, the flame can propagate as a premixed/partially premixed flame. In addition, the flame can propagate as a deflagration or detonation, depending on the reaction rate. The consequence of such a scenario can be severe damage to structures, people, and other vehicles.

Given the hazards of hydrogen fuel, systems for the suppression of flammable gas or mitigation of overpressure in an explosion are not fully developed. Water is the most widely used in fire-fighting because of its thermal characteristics [3]. However, the recommendations are not clear regarding gas explosion mitigation. Thomas [4] investigated mitigation by water spray for hydrocarbon explosions. Among the findings, water droplet below about 50 µm is most effective due to the ability to evaporate inside the combustion zone. Larger droplets continue to evaporate in the burned gas, decreasing the mitigation efficiency. However, the larger droplets can break up into smaller fragments due to hydrodynamic forces resulting in a fine mist. Bjerketvedt and Bjørkhaug [5] pointed at two mechanisms in water spray mitigation of gas explosions, one that accelerates the flame in the early phase and another that can reduce explosion pressure in the later stage of the explosion. van Wingerden et al. [6] found turbulence generated by large droplets (>50 µm) to increase the flame

speed. A theoretical approach combined with experience from experiments van Wingerden et al. [6] formulated a most efficient mitigation water-spray system with droplet sizes less than 10 µm or above 200 µm for a hydrocarbon explosion.

For premixed hydrogen/air explosions, Ingram et al. [7] found the limit for the droplet size to evaporate in the flame zone to be 2 – 5 µm. The density of the mist was also crucial for the burning velocity.

Gai [8] illustrates the different combustion mechanisms of a premixed flammable gas/air combustion. Fig. 1 a illustrates small droplets entering a slow flame evaporating in the flame zone. Fig. 1 b shows large droplets on a slow flame that corrugates the flame front, increasing the flame area and reaction rate. Finally, Fig. 1 c shows a fast flame with a leading pressure front or shock, atomizing the large droplets, providing small droplets to the flame zone.

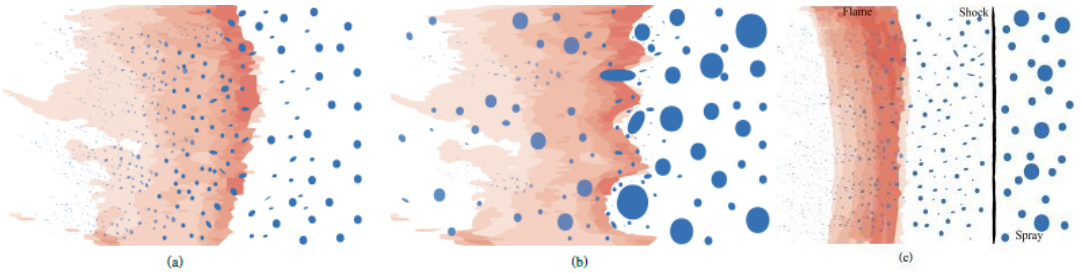


**Fig. 1.** Mechanisms of flame droplet interactions from [8].

When modeling a scenario from an accidental release of hydrogen investigating the benefit of water droplets, the mechanisms can be determined by the initial droplet size distribution of the spray.

Commonly used water sprays in the industry can be sprinkler/deluge sprays characterized in Lundberg [9] or mist sprays characterized in Fan et al. [10].

The measurement of droplet sizes can be demanding due to the complexity of the flow field. Industrial-sized sprays are often dense and have many droplets ranging over several orders of magnitude in size. The measurement techniques for droplet size measurements are often based on scattering (phase doppler anemometry, Mie-scattering, light-induced fluorescence, e.c.) or shadow imaging.

Husted et al. [11] performed measurements using phase Doppler anemometry (PDA) to measure mist spray from one micro nozzle, reporting difficulties using the technique in the dense region of the spray and capturing larger droplets. Husted et al. [11] measured the droplet size distribution of 10 to 80 µm at 100 bar pressure. The data is on a specific nozzle provided by a commercial manufacturer.

However, the spray data is often from a generalized nozzle, making it difficult to reproduce without the manufacturer of the nozzles.

The current research aims to characterize high-pressure mist spray from a typical industrial mist spray with five individual micro nozzles (nozzle head). The micro nozzles are similar to the work by Husted et al. [11], but the amount of water in the complete nozzle head is approximately five times more, aiming to reproduce the behavior of an authentic industrial mist spray system. The spray density increases, focusing on the fraction of the larger droplets in the spray. The quantity of the smallest droplets is presented in the results.

## MATERIALS AND METHOD

The measurements are performed on the spray from a typical multipurpose high-pressure mist spray. Water for the spray is provided to the nozzle using a high-pressure water supply pump equipped with

a pressure sensor. The characteristics of the spray are determined using a commercial laser-based shadow-imaging system equipped with image processing software.

The measurements are performed on a Danfoss HNMP-5-10-1.19-00 nozzle with five separate micro nozzles attached to a joint nozzle head. The micro nozzles are mounted at a half cone angle of 56° and an azimuthal angle of 72° with adjacent nozzles. The nozzle head gives a hollow cone spray. The micro nozzles of the type 1934 have an independent spray cone angle of 60° and a capacity of 2.38 $dm^3$/min at 100 bar (for each of the five nozzles).

The nozzle head with five micro nozzles have a K-factor =1.19 that gives the relation between flow and pressure using

$$q[dm^3/min] = K \cdot \sqrt{p[bar(g)]}$$

where $q$ is the volumetric flow rate, $K$ is the discharge coefficient, and $p$ is the supply water pressure. An illustration of the nozzle head is presented in Fig. 2 a.

The Danfoss mist nozzle is recommended at 45, 80, or 100 bar pressures. The high-pressure water supply system used in the experiments is of the type Kränzle HD 10/122 TS displacement pressure washer pump with the max pressure of 135 bar. Working pressure is about 100 bar, giving about 10 $dm^3$/min. The pump has a manometer and a pressure control valve.

The measurement technique used to measure the characteristics of the mist spray is a laser-based shadow-imaging technique provided by LaVision. The image-based technique capture images of the droplets in small regions are to be analyzed by image processing. The technique develops from the work by Kashdan et al. [12, 13], but the algorithms' details are limited due to commercial software. The main components of the setup are a dual cavity pulsed laser fitted with front optics (beam expander and a diffusor plate), a long-distance microscope, and a high-speed camera. A step-motor-driven traverse controls the radial position of the nozzle. The setup is shown in Fig. 2 b.


**Fig. 2.** Experimental setup with a)Danfoss mist nozzle [14], b) high-speed camera, c) microscope lens, d) laser front optics, e) mist nozzle with mount, f) traverse, g) Kränzle HD 10/122 TS high-pressure washer pump.

The laser light is transferred through a fiber optical cable to the front optics, where the light exposes a fluorescent plate. The fiber optic cable and fluorescent plate remove coherent optical effects making

the background uniformly distributed over the plate. The high-speed camera, fitted with a long-distance microscope, captures images of the droplets in the spray. The microscope lens has a short depth of field, isolating only the droplets in a sheet close to the focused region of the setup. In addition, the setup utilizes a dual cavity pulsed laser giving the possibility of capturing droplets in adjacent frames used for velocity determination.

The laser is Photonic industry DM60-532 DH dual-head (dual cavity) laser with a wavelength of 532 nm (green). The laser is of the type DPSS (diode-pumped solid-state) Nd:YAG laser with two independently controlled laser cavities, both with a repetition rate of 1.0 – 35.0 kHz and adjustable power. The pulse jitter of cavity 1 (laser head 1) and 2 is 14.1 ns and 13.2 ns, respectively. The high-speed camera is a Photron SA-Z type 2100K-M-32GB with a high resolution and sensitivity CMOS (Complementary Metal-Oxide Semiconductor) sensor. The sensor resolution is 1024 x 1024 pixels recording 12-bit monochrome images. The physical sensor size is 20.48 mm x 20.48 mm with a fill factor of 58 %. The Questar QM-1 by LaVision used for the experiments is a long-distance microscope lens designed to operate with 500-1500 mm focal lengths. The magnification of the lens is controlled by the configuration of macro rings and lenses. The N.A. of the QM-1 is typically 0.04 with a distance to the focal plane of 1000 mm.

A given lens with a given magnification gives a field of view (FOV) and depth of field (DOF). The FOV is dependent on the setup, but the DOF is also droplet size-dependent. Calibration of the DOF is performed by traversing a sizing reticle throughout the FOV. The calibration is performed before the experiment with the same camera, lens, and laser settings.

The calibration reticle gives four calibration ranges of droplet sizes. Current research uses 20 – 400 µm to ensure to capture all the largest droplets of the spray. For the current experiment, the $DOF[mm] = 0.01643 \cdot d[\mu m]$. The magnification is approximately 2.5 giving a field of view of 8.228 mm x 8.228 mm. The pixel resolution with the current setup is 8.04 µm/pixel.

The laser settings were adjusted by trial and error to give a proper measurement range of droplets and velocities. The repetition rate of the laser was set to 1.000 kHz and 20.00 µs spacing between image pairs. For every position, 1000 frames were recorded (1.0 seconds). The current of the laser was set to 27.7 A and 27.5 A for cavity 1 and 2, respectively. The current setting gave average power of 7.9 and 8.2 W and a peak duration of about 140 and 160 ns. Using these numbers, the peak power of cavity 1 and 2 was 56 and 58 kW. The pulse energy was 7.9 and 8.2 mJ, respectively.

The in-frame movement during one exposure of droplets for a velocity of 10 m/s is 1.4 and 1.6 µm, which is much less than one image pixel.

The inter-frame movement of droplets for a velocity of 10 m/s is 200 µm which is about 25 pixels with current magnification.

## RESULTS AND DISCUSSION

Twenty-five measurements of the mist spray were performed at a single azimuth 940 mm below the tip of the nozzle. The location of the measurements ranged from center to radius 600 mm with 25 mm intervals. This distance to the nozzle was in the post-breakup region.

The supply water pressure was set to 100 bar with a water temperature of 12 °C and an ambient air temperature of 20 °C.

The measurement was performed using a shadow-imaging setup from LaVision using Davis version 10.1. The results were analyzed using Particle Master with the settings in Table 1. The maximum velocity and excentricity(reciprocal of the ratio of the short axis to the long axis of an ellipsoidal droplet) were determined by visual consideration of the shadow images.

**Table 1. Settings for Particle Master**

| Property | Value |
|---|---|
| Normalization radius | 75 pixels |
| Reduce Pixel Noise | Weak |
| Binarization Threshold | 50 % |
| Minimum Slope | 3.00 % |
| Minimum Shadow Area | 3 pixels |
| Maximum velocity | 10 m/s |
| Maximum excentricity | 120 % |

Fig. 3 a shows the mist spray and illustrates the spray's unitless optical depth (O.D.). An estimate of the O.D. of the mist spray is made using an expression by Payri [15]. The expression is

$$OD = \frac{3}{2}\phi_f Q_e l \frac{1}{d_{32}}$$

where $\phi_f$ is the volume fraction of water in the spray, $Q_e$ is the extinction efficiency of the droplet and is assumed similarly equal here to 2.1, $l$ is the path length, and $d_{32}$ is the Sauter-mean diameter.

In the current research, the droplet density and Sauter-mean diameter was measured for radial positions. Summarizing the contribution of all the intervals, the O.D. was found to be 2.4.

According to Payri [15], pure laser-based techniques like PDA, Mie scattering, and LIF generally perform well with O.D. less than unity but can give inaccurate measurements above due to multiple scattering. On the other hand, shadow imaging is not equally dependent on O.D. other than providing blurred images.

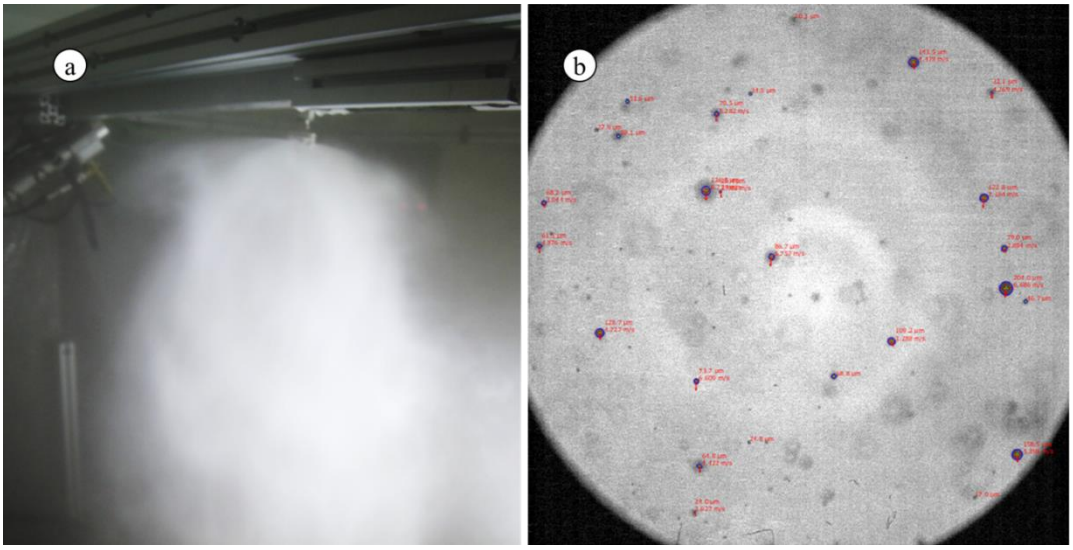


**Fig. 3.** a) Overview of mist spray, b) shadow image with droplet data overlay from Particle Master by Davis

LaVision Particle Master measures the droplet diameter based on a single frame, Depth of Field (DOF) of every droplet, and velocity of droplets from adjacent frames. Automatically, this is used to calculate the properties: droplet size distributions, averaged diameters, droplet density, velocity, and fluxes from a given experiment. An example of the output of the image-processing tool Particle Master is shown in Fig. 3 b.

Due to the high density of droplets in the mist spray and the droplet size range expected, a quantitative measure of the capabilities of the measurement method was performed. For the larger droplets of the spray, visual considerations were performed on the shadow images. Since this is a high-pressure spray, no droplets above 400 µm were observed or expected in the spray. The measurement method was expected to incorrectly account for the small droplets due to the density of the spray. Particle Master provides the mass flux of droplets of the measured locations in the spray. By integrating these measurements over the entire cross-section of the spray, the overall measured mass flow of water can be determined and compared with the actual mass flow of water to the nozzle. For the current experiment, about 50% of the water was registered by the shadow imaging system. The remaining 50 % can be assumed to be contained in the smallest-sized droplets.

The following figures give the results from the measurements.

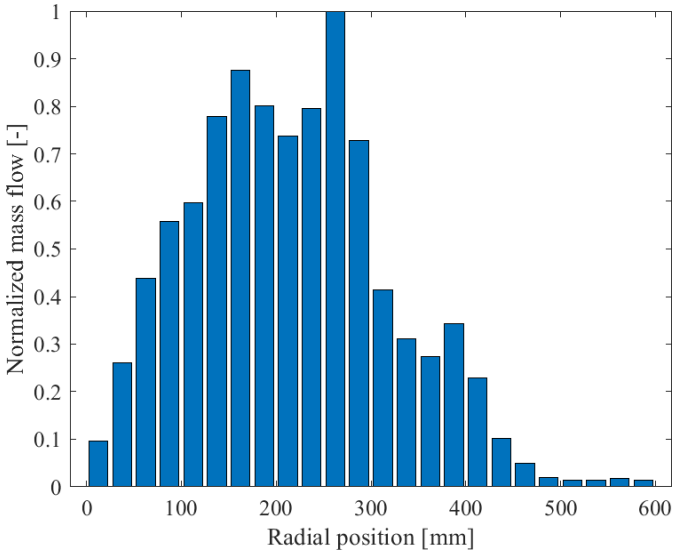


**Fig. 4.** Normalized mass flow for 100 bar supply water pressure, 940 mm below mist nozzle.

As an indication of the performance of the mist nozzle, the mass flow of water is presented in Fig. 4. The unit of the y-axis in the figure is arbitrary but indicates where the majority of the water is present radially in the mist spray. The majority is 100 to 300 mm from the center, and just a minor portion of the water is outside 500 mm. It is assumed the azimuthal independence of the nozzle in the measurement. The spray is more narrow than expected due to the size limitations of the room geometry.

The properties were averaged for all the 1000 frames to get the averaged values for each location. The measured values changed minimally after about 500 frames were analyzed, where 1000 frames ensure properly averaged results.

Figures 5 a and 5 b show the number-mean and Sauter-mean diameters. The Sauter-mean diameter of the mist spray represents the entire spray's averaged volume to surface ratio. The diameter is often in use when representing fire phenomena.

The number-mean- and Sauter-mean diameter measurements are the same for a monodisperse droplet size distribution, and the difference of 40 µm to 90 µm indicates a wide range of droplet sizes.

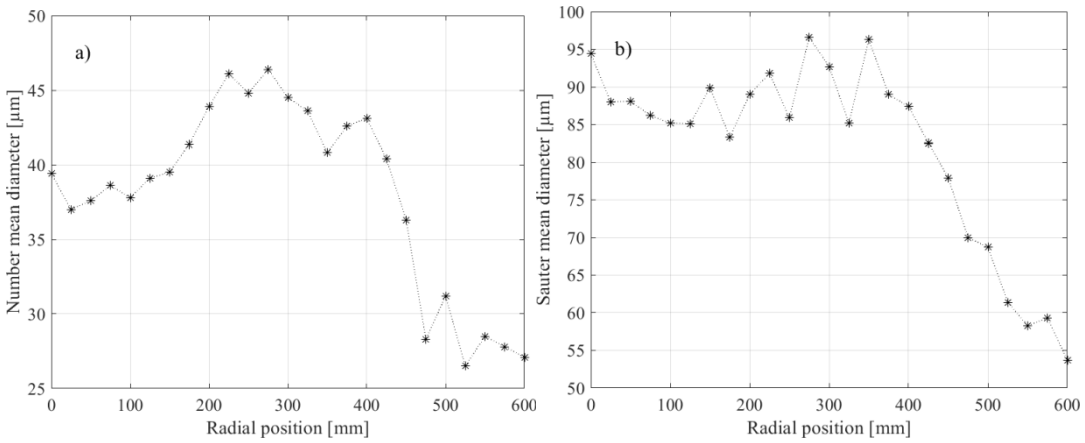


**Fig. 5.** a) Number-mean diameter, b) Sauter-mean diameter of measured droplets for 100 bar supply water pressure, 940 mm below mist nozzle.

A measure of the uniformity of the droplets is the span ($\Delta$) of the distribution. The relative span is calculated using

$$\Delta = \frac{DV90 - DV10}{DV50}$$

where DV90 is the droplet diameter such that 90 % of the water (volumetric) is below this diameter. The DV10 and DV50 are defined in the same manner. A low value of span indicates a uniform size distribution. In Fig. 6 a, the span is shown for the different radial positions in the mist spray. The average value in the previously discussed range is $\Delta = 1.2$.

The total number of droplets used to measure the characteristics for every position (for one second or 1000 frames at a framerate of 1.0 kHz) in the spray is shown in Fig. 6 b.

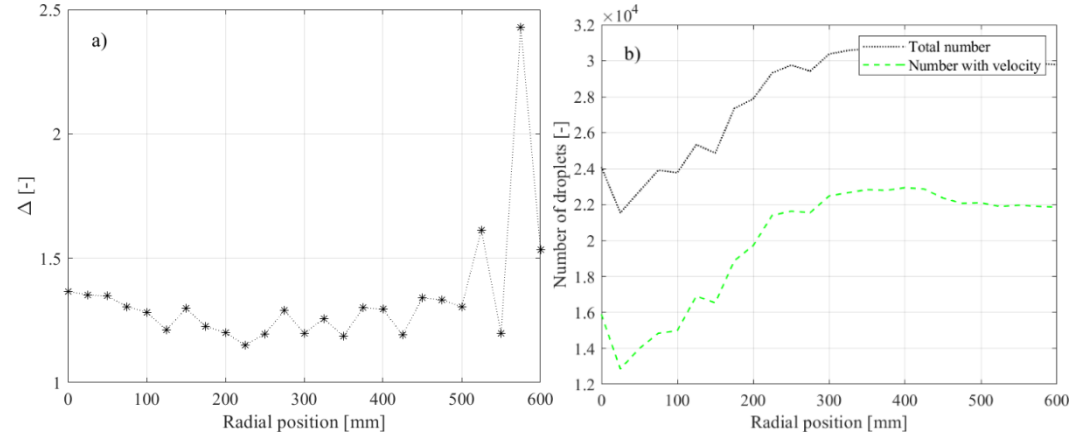


**Fig. 6.** a) Relative span factor- and b) the number of measured droplets for 100 bar supply water pressure, 940 mm below mist nozzle.

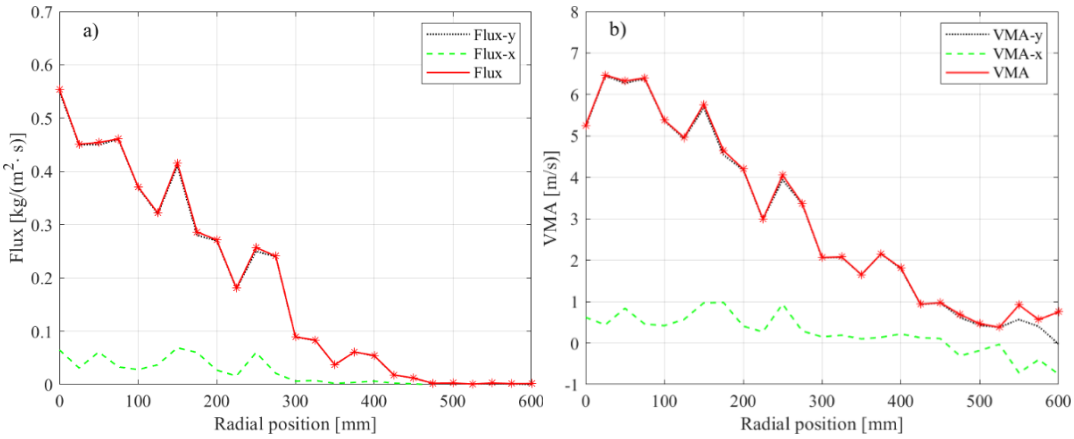


**Fig. 7.** a) Mass flux of water droplets- and b) Mass averaged velocity of measured droplets for 100 bar supply water pressure, 940 mm below mist nozzle.

The mass flux of water measures the amount of water per area and time in an area perpendicular to the mist nozzle. The mass of water is found by summing up the volume of all recorded droplets and multiplying by the density of water. The measurements are compensated for the DOF of droplets. The measurements show the mass flux to be highest at the center of the spray, decreasing to the periphery (see Fig. 7 a). It is essential to consider that the measurement is performed without fire or external wind. Convection can change the mass flux dramatically for given positions.

The mass-averaged velocity gives the velocity of the droplets. This velocity accounts for larger droplets moving faster than smaller droplets, shown in Fig. 7 b. In a fire or explosion situation, the velocity can contribute to increased turbulence, but the momentum of the individual droplets is not likely to affect the momentum of a fire or explosion.

In the case of a fire or a gas explosion, the droplet density can influence the propagation of the flame. In Fig. 8, the droplet density is shown for various radial positions. The measurements show a decreasing density for increasing radial position. We can convert droplet density to the volume fraction of water by dividing by $10^6$, assuming the density of water to be $1000\ kg/m^3$.

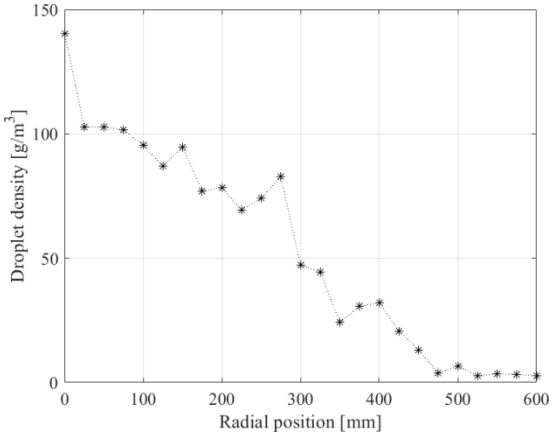


**Fig. 8.** Droplet density for 100 bar supply water pressure, 940 mm below mist nozzle.

The measured mist spray's number- and volume distribution (averaged by mass flow and radially compensated) are shown in Fig. 9 a and Fig. 9 b, respectively. The number distribution shows a high end to the lowest detectable diameters indicating the method is likely to under-predict the number of

the smallest droplets. The mode of the volume distribution is the approximate Sauter-mean diameter. Comparing the two figures, most of the mass or volume of water in the spray exists as droplets around the Sauter-mean diameter, though the highest number of droplets is skewed to the smallest sizes.

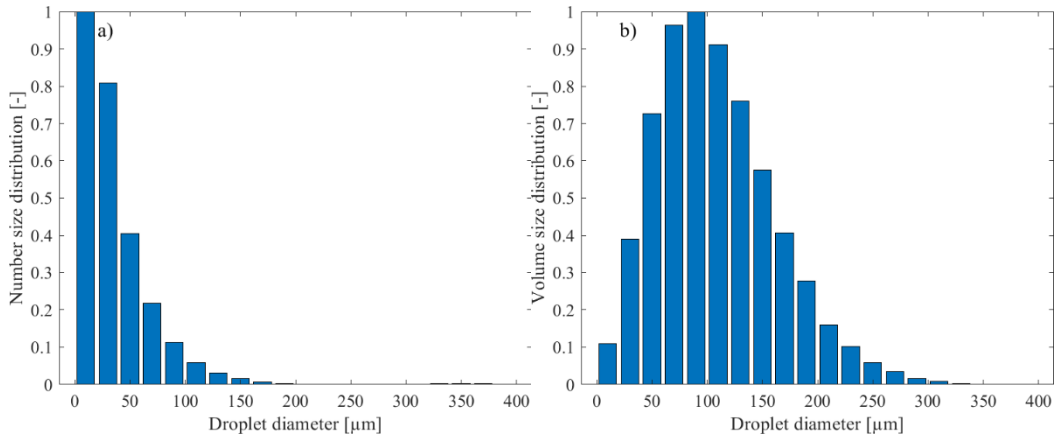


**Fig. 9.** a) Number size distribution- and b) Volume distribution of measured droplets for 100 bar supply water pressure, 940 mm below mist nozzle.

The properties of the measured droplets of the entire spray compensated for radial mass flow differences are in Table 2, and the numerical values of the distributions of Fig. 9 are in Table 3.

Visual investigation of the spray and the measured data in Fig. 9 indicates the measurement technique to measure the droplets above 100 µm correctly but cannot determine the low end of the distribution. The size composition of the undetected water spray is at the low end of the distribution. For mitigation purposes, the overall surface area of the water droplets contributes to evaporation leading to the extraction of energy from the flame front. Gai [8] reported that a decreasing droplet size increases the evaporation rate following the $d^2$-law.

The droplet density can be assumed to be higher than the measured values. Regarding Ingram et al. [7], increasing the droplet density decreases the burning velocity.

In a premixed combustion/explosion, the larger droplets can increase the turbulence by perturbating the flame front and increasing flame propagation speed [6]. However, if the flame propagation is sufficiently fast and generates a pressure wave in front, the sudden increase in velocity can make the droplets atomize to microscopic mist. The atomization process depends on the Weber number of the droplets, where increased values generally give decreased droplet sizes. Dependent on the strength of the pressure wave, the larger droplets can break up and mitigate the flame/explosion.

**Table 2. Averaged properties of the measured droplets**

| Averaged property | Value |
|---|---|
| $d_{10}$ | 42 µm |
| $d_{32}$ | 88µm |
| $v_{MA}$ | 4.0 m/s |
| Droplet density | 73 $g/m^3$ |

**Table 3. Numerical values for droplet size distributions of measured droplets.**

| Diameter [µm] | Number distribution | Volume distribution |
|---|---|---|
| 10 | 37.6 % | 1.7 % |
| 30 | 30.4 % | 6.0 % |
| 50 | 15.2 % | 11.2 % |
| 70 | 8.2 % | 14.8 % |
| 90 | 4.3 % | 15.4 % |
| 110 | 2.2 % | 14.0 % |
| 130 | 1.1 % | 11.7 % |
| 150 | 0.6 % | 8.8 % |
| 170 | 0.3 % | 6.2 % |
| 190 | 0.1 % | 4.3 % |
| 210 | 0.1 % | 2.5 % |
| 230 | 0.0 % | 1.6 % |
| 250 | 0.0 % | 0.9 % |
| 270 | 0.0 % | 0.5 % |
| 290 | 0.0 % | 0.3 % |
| 310 | 0.0 % | 0.1 % |

## CONCLUSION

The characteristics of a general multipurpose mist nozzle with a K-factor=1.19 were measured with a laser-based shadow-imaging technique. The experiments were performed with supply water pressure equal to 100 bar at an axial distance of 940 mm for radial positions ranging from center to 600 mm at a single azimuth. The mist nozzle is a general pendent nozzle head with 5 micro nozzles.

The experiments were difficult to perform due to the high density of the water droplets. The optical depth (O.D.) was estimated to be about 2.4.

The number size distribution and number averaged diameter ($d_{10}$) of 42µm was low for the entire spray, but the volume distribution shows the occurrence of droplets of 300+ µm. The droplet density was averaged to be 73 g/m$^3$ for the applied area with a radius of 600 mm.

By considering the limitations of the measurement method, the full droplet size distribution is not determined. However, the method shows the existence of droplets ranging from 50 µm to 300 µm. Furthermore, in faster combustion regimes with high-velocity flow regimes, the secondary breakup of these droplets can occur, decreasing the droplet size and enhancing the mitigation efficiency.

The acquired data in this work proves the existence of larger droplets in high-pressure mist sprays, which needs to be considered when analyzing the mitigation mechanisms of hydrogen gas explosions. However, current findings indicate that most water is in the smallest droplets, even if the method does not detect this. Future work can combine the current data set with measurements of an isolated part of the spray to determine the full-size distribution of all the droplets in the commercial high-pressure mist spray.

## ACKNOWLEDGEMENT

This project has received funding from the Fuel Cells and Hydrogen 2 Joint Undertaking (now Clean Hydrogen Partnership) under Grant Agreement No 826193. This Joint Undertaking receives support

from the European Union's Horizon 2020 Research and Innovation program, Hydrogen Europe and Hydrogen Europe Research.

## REFERENCES

[1] Norwegian Ministry of Transport, Norway is Electric, Government.no, (accessed 3. January 2022).

[2] H. Hussein, S. Brennan, and V. Molkov, Hydrogen Jet Fire from a Thermally Activated Pressure Relief Device (TPRD) from Onboard Storage in a Naturally Ventilated Covered Car Park, Hydrogen 2(3) (2021) 343–361.

[3] G. Grant, J. Brenton, and D. Drysdale, Fire suppression by Water Sprays, Prog. Energy Combust. Sci. 26(2) (2000) 79–130.

[4] G. O. Thomas, On the Conditions Required for Explosion Mitigation by Water Sprays, Trans I Chem E: Part B - Process Saf. Environ. Prot. 78 (2000) 339-354.

[5] D. Bjerketvedt, M. Bjørkhaug, Experimental Investigation — Effect of Water Sprays on Gas Explosions. Prepared by Chr. Michelsen Institute for the Department of Energy. U.K. OTH 90 316. HMSO. London, 1991.

[6] K. van Wingerden, B. Wilkins, J. Bakken, and G. Pedersen, The Influence of Water Sprays on Gas Explosions. Part 2: Mitigation, J. Loss Prev. Process Ind. 8(2) (1995) 61–70.

[7] J. M. Ingram, A. F. Averill, P. N. Battersby, P. G. Holborn, and P. F. Nolan, Suppression of Hydrogen-Oxygen-Nitrogen Explosions by Fine Water Mist: Part 1. Burning Velocity, Int. J. Hydrogen Energy 37(24) (2012) 19250–19257.

[8] G. Gai, Modeling of Water Sprays Effects on Premixed Hydrogen-Air Explosion, Turbulence and Shock waves, Ph.D. thesis, Normandie University, Normandie, France, 2020.

[9] J. Lundberg, Characterization of a Medium Velocity Deluge Nozzle for Offshore Installations, J. Loss Prev. Process Ind. 71 (2021) 104510.

[10] C. Fan, R. Bu, X. Xie, and Y.Zhou, Full-scale Experimental Study on Water Mist Fire Suppression in a Railway Tunnel Rescue Station: Temperature Distribution Characteristics, Process. Saf. Environ. Prot. 146 (2021) 396-411.

[11] B.P. Husted, P. Petersson, I. Lund, and G. Holmstedt, Comparison of PIV and PDA Droplet Velocity Measurement Techniques on Two High-Pressure Water Mist Nozzles, Fire Saf. J. 44(8) (2009) 1030-1045.

[12] J. Kashdan, J. Shrimpton, and A. Whybrew, Two-Phase Flow Characterization by Automated Digital Image Analysis. Part 1: Fundamental Principles and Calibration of the Technique, Part. Part. Syst. Charact. 20 (2003) 387-397.

[13] J. Kashdan, J. Shrimpton, and A. Whybrew, Two-Phase Flow Characterization by Automated Digital Image Analysis. Part 2: Application of PDIA for Sizing Sprays, Part. Part. Syst. Charact. 21 (2004) 15-23.

[14] Danfoss Fire Safety A/S, SemSafe Watermist Systems Product Catalog, Nozzle Type HNMP-5-10-1.19-00 P, Odense, Denmark, 2013.

[15] F. Payri, J. V. Pastor, R. Payri, and J. Manin, Determination of the Optical Depth of a DI Diesel Spray, J. Mech. Sci. Technol. 25(1) (2011) 209–219.

# Experimental study of self-ignition induced by high-pressure hydrogen release through a tube with obstacles

Qian Zeng, Mengyuan Zhu, Jing Tang, Yunfan Wu, Qiangling Duan*, Jinhua Sun*

*State Key Laboratory of Fire Science, University of Science and Technology of China, Hefei 230026, P. R. China*

**Corresponding authors' email: duanql@ustc.edu.cn; sunjh@ustc.edu.cn*

**ABSTRACT**

The self-ignition and flame propagation during high-pressure hydrogen release through a tube with obstacles are experimentally investigated using direct high-speed photographs, pressure records and flame detection. Experimental results show that the presence of obstacles exhibit great effect on shock wave propagation and flame evolution inside the tube. When the shock travels through obstacles, the shock intensity becomes weaken. While the maximum pressure behind the reflected shock wave is about 1.5 as large as the overpressure behind leading shock wave, providing more favorable conditions for self-ignition. The critical pressure for self-ignition decreases with an increase in axial distance to the diaphragm and then remains at an almost constant value of 2.72 MPa in obstructed tube, lower than that of 3.98 MPa in straight tube. In obstructed tube, self-ignition initiates in the near-wall region or the centerline of the tube near obstacle location. Besides, the flame area and its increase rate in tube unblocked section is significantly higher than that in straight tube. After self-ignition initiates, the flame front propagation velocity and the increase rate of flame area are first attenuated when the flame passes through the obstacles, then quickly restored with further propagation downstream. This may be attributed to the complex dynamic flow and ignition structure induced by obstacles.

**KEYWORDS:** High-pressure hydrogen; self-ignition; flame propagation; obstacle

## Introduction

Motivated by present efforts to mitigate environmental impacts, pure hydrogen is currently attracting attention due to its potential as a clean and efficient energy carrier. In recent years, hydrogen energy utilization such as hydrogen-fueled vehicles and hydrogen-based energy storage is advancing rapidly. The internal pressure in the reservoirs and piping of hydrogen systems have been designed to be up to 100 MPa [1]. Under such high pressure, the accidental fire and explosion accidents during hydrogen storage, transportation and utilization cannot be ignored because of its extremely low ignition energy and wide flammability range. Especially, self-ignition induced by sudden hydrogen release from the reservoirs or pipelines is one of the key causes for fire and explosion accidents, producing a great threat to people and property safety [2].

For the special phenomenon of pressurized hydrogen self-ignition, a large number of

experimental and numerical studies have been conducted, and the diffusion ignition mechanism has always been the focus of researches. In this mechanism, a shock wave is generated instantly when the high-pressure hydrogen release into the air. Then, self-ignition is initiated by an increase in the temperature of hydrogen-air mixture produced by diffusion due to heat flux from shock-heated oxidizer [3]. It has been proposed that multi-dimensional transient flow can facilitate the mixing of expansion hydrogen and shock-heated air, playing an important role in promoting self-ignition initiation and the development of the ignition kernel to a flame [4, 5]. Shock-induced vortices and turbulence at contact surface promote the molecular diffusion and provide more combustible mixture for the initiation of hydrogen self-ignition [6]. After the high-temperature hydrogen-air mixture meets the requirement of self-ignition, the duration of combustible mixture in the mixing zone becomes another key factor affecting self-ignition onset [4, 7]. The previous studies have showed several factors affecting self-ignition occurrence, including burst pressure, release tube dimensions and geometries, diaphragm rupture process, different gases additions and etc. The result showed that the critical burst pressure necessary for self-ignition decreases with increasing dimensionless parameter L/D (tube length/tube diameter) [8]. Besides, a slower rupture was suggested to increase ignition delay time and thus mitigate the self-ignition possibility [5]. As the opening area is reduced, the minimum burst pressure of self-ignition is promoted exponentially [9]. The diffusion self-ignition of pressurized accidentally released $H_2/CH_4$ or $H_2/N_2$ binary fuels were discussed in the experiments [10, 11]. It was found that the minimum burst pressure for self-ignition is significantly affected by the impurity gases addition. Based on these findings, the correlation to quantitatively define the critical conditions for hydrogen self-ignition onset was derived using the similitude analysis [12]. Furthermore, evolution of ignition spot initiation and transition to a stably propagating flame inside the tube were reported by several studies. In flow visualization studies using shadowgraph and high-speed direct photography [13], the ignition spot was always observed first in the boundary layer of the mixing zone and then spread to the whole mixing zone along with the boundary layer.

As it is known that there is often the presence of obstacles inside the tube, such as the inevitably installation discrepancies or monitoring equipment installed along the tube [14]. Over the decades, several studies have been conducted on the obstacle effects on the occurrence of self-ignition. Especially, studies mainly focused on the effect of obstacles on the self-ignition onset and flame development for pre-mixed hydrogen-air mixture in a closed tube. Research results showed that different positions [15], different shapes [16] and different blockage ratios [16, 17] of obstacles showed different evolution processes in self-ignition onset, flame acceleration and deflagration to detonation transition (DDT). Different from previous work, this study is conducted with the objective of clarifying the effect of obstacle existence on shock wave, self-ignition onset, and subsequent flame evolution inside the tube, which is the diffusion combustion. The study is of great significance for providing a valuable theoretical guidance for practical tube equipment design and application.

## Experimental apparatus

**Fig. 1** shows the schematic diagram of the main experimental setup, mainly consisting of a 0.79 l high-pressure tank, a diaphragm holder, a visualization downstream tube, and an exhaust chamber. Nickel burst disk with cross scores in the middle is used to separate pressurized hydrogen in the tank from the ambient air in the tube. According to the thickness and the notching depth of the burst disk, the storage pressure in compressed hydrogen cylinder can be controlled to vary from 2 MPa to 8 MPa. A strain gauge pressure sensor (Kulite, ETM-375M-20MPa) is installed at the top of the tank to record the accurate rupture pressure ($P_b$). Rectangular release tube with three pairs of obstacles is used in the experiments, as shown in **Fig. 2**. The tube is 400 mm in length and 15 mm in diameter, with two glass windows on sidewalls ranging from 65 mm to 315 mm away from the burst disk. Several pressure transducers P*n* (PCB Piezotronics, 113B22) and light sensors L*n* (Thorlabs, Si photodiode, FDS010) are mounted spaced by 80 mm on upper and lower sidewalls to record the pressure dynamics and self-ignition process. A high-speed camera (Phantom v710) is adopted to capture the ignited hydrogen flame inside the tube at a frame rate of 79069 fps. Triangular obstacles are set in the middle of the positions of two adjacent sensors, made of 304 stainless steel with a base of 4 mm, a height of 3.6 mm and a length of 15 mm. Each group of obstacles is composed of two triangular obstacles arranged symmetrically, respectively defined as $O_1$, $O_2$, $O_3$. At the end of the release tube, there is an exhaust chamber (600 mm × 470 mm × 500 mm) attached to the tube. The experimental procedure can be found in our previous study [18]. For each designed burst pressure of the burst disk, repeat tests (at least three times) are carried out in this study.

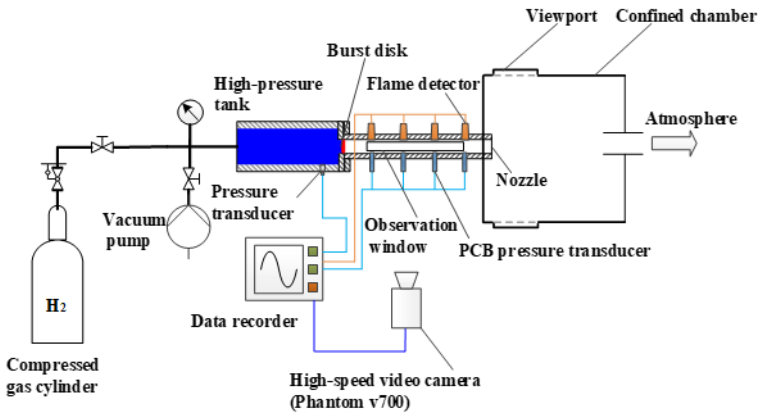


**Fig. 1.** Schematic diagram of the experimental setup.

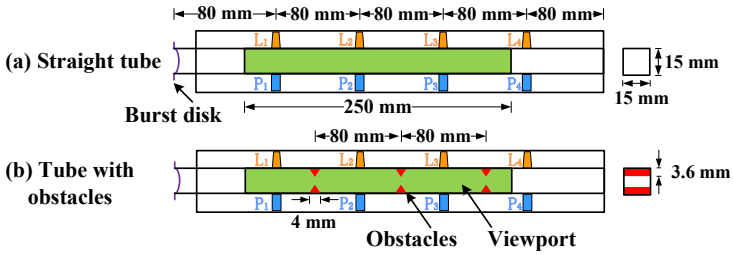


**Fig. 2.** Drawings of the visualized rectangular tube with obstacles, P*n* (*n* = 1, 2, 3, 4): Pressure transducer, L*n* (*n* = 1, 2, 3, 4): Light sensor, (a) straight tube, (b) tube with obstacles.

## Results and discussion

### Pressure dynamics in the tube with obstacles

From the diffusion ignition mechanism, a shock wave produced at the moment of disk rupture is considered as one of the essential prerequisites for self-ignition. Here the pressure dynamics under the effect of obstacles is described first. **Fig. 3** shows the typical time history of pressure and light signals at different positions in obstructed tube. A sharp pressure rise is detected by $P_1$-$P_4$ successively, indicating a leading shock is generated and travels downstream the tube. After a period of time, a secondary pressure rise is detected by the pressure transducers $P_1$, $P_2$, and $P_3$ behind the obstacles. This is because the leading shock is partly reflected from the obstacles and then the produced reflected shock propagates upstream.

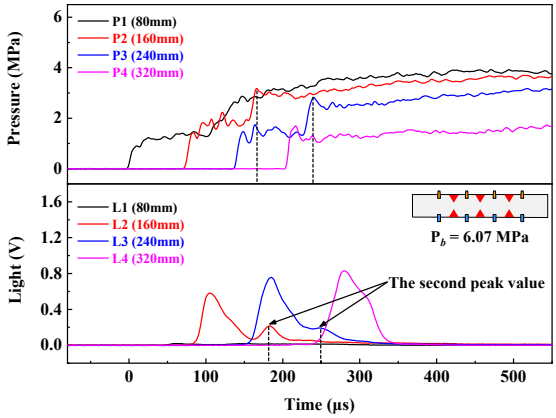


**Fig. 3.** Time history of pressure and light signals at different positions for the tube with obstacles.

**Fig. 4** plots the relationship of shock overpressure in tube with and without obstacles versus burst pressure and distance away from diaphragm. The plotted cases are all non-ignition cases to eliminate

the influence of combustion wave. It is shown in **Fig. 4**(a) that the shock overpressure increases with increasing distance along the tube. Due to the complicated shock reflection and interaction in the rectangular tube [13, 19], a stable shock is generated as the shock passes through the pressure transducer $P_1$ and the shock intensity continues to strengthen as propagating along the straight tube. After the obstacles are placed in the tube, the leading shock experiences more complicated variation. When obstacles placed at location $O_1$, $O_2$, and $O_3$, the shock overpressure, i.e. the shock intensity, first increases when passing through $O_1$ and then decreases significantly when passing through $O_2$ and $O_3$ in **Fig. 4**(b). In previous work [20], results showed that the formation of a stable shock requires a certain propagation distance. As the shock travels this distance, the shock overpressure first rises due to the compression wave superposition. Nevertheless, the shock overpressure in **Fig. 4**(b) decreases at the position of 160 mm, 240 mm, and 320 mm for burst pressure $P_b$ = 2-4 MPa compared with that in tube without obstacles. This indicates that the shock intensity undergoes a reduction when the leading shock passes through obstacles, which may be due to the flow divergence and the momentum losses when the shock impacts on the obstacles [6, 14].

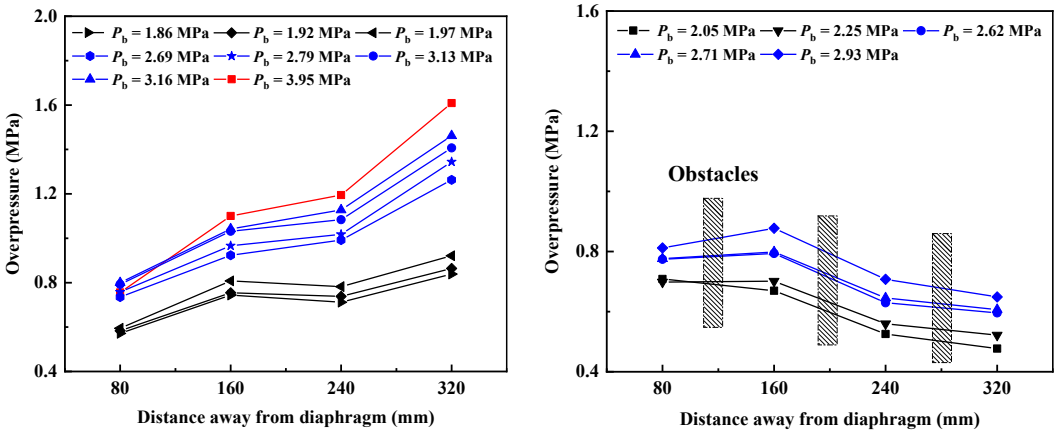


(a) (b)

**Fig. 4.** Relationship of shock wave overpressure with burst pressure and distance away from diaphragm for different tubes, (a) straight tube, (b) tube with obstacle.

**Fig. 5** shows relationship of the maximum shock overpressure in tube with and without obstacles versus burst pressure. From **Fig. 3**, the maximum shock overpressure in obstructed tube appears after the secondary pressure rise caused by the reflected shock. It is found that the maximum shock overpressure increases with burst pressure in tube either with or without obstacles. Besides, the maximum pressure behind the reflected shock is about 1.5 times of that behind leading shock in straight tube. Following the one-dimensional transient shock theory, the air temperature behind the

shock increases with the shock overpressure. The increase in pressure resulted from the reflected shock will cause the temperature of shock-heated air to rise. Meanwhile, the presence of reflected shock will facilitate the formation of hydrogen-air mixture by turbulent mixing [21]. Therefore, it is inferred that the presence of obstacles in tube provides more favorable conditions for self-ignition.

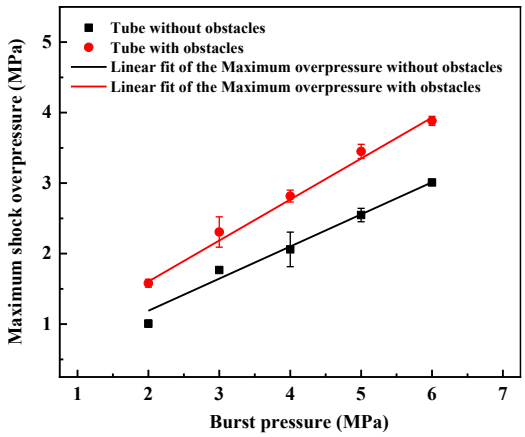


**Fig. 5.** Relationship of maximum shock overpressure in tube with and without obstacles versus burst pressure.

**Self-ignition boundary in the tube with obstacles**

According to the measurement of light signal inside the tube, two experimental phenomena observed are classified as self-ignition and non-ignition. Typical light signals at different positions for obstructed tube is shown in **Fig. 3**. Three light signals show a significant rise successively, indicating that self-ignition initiates and flame propagates downstream the tube. It is worth noting that light detectors $L_2$ and $L_3$ detect the second light peak value at the time when the reflected shock passes through their positions. It implies that the combustion of hydrogen is intensified under the effect of the reflected shock. As discussed above, the temperature of hydrogen-air mixture and the mixing of the combustible mixture can be increased by the reflected shock, and thus the combustion is enhanced.

**Fig. 6** plots self-ignition onset associated with burst pressure and axial position along the tube with obstacles. The measurement for the locations of self-ignition onset plotted in **Fig. 6** is through high-speed images. There exists a minimum burst pressure resulting in the self-ignition of hydrogen-air mixture, illustrated by a self-ignition critical line in **Fig. 6**. It can be seen that the critical release pressure for self-ignition decreases with the axial position to a length of 160 mm. Then it remains at a constant value of 2.72 MPa with further rise in axial position. Owing to the limited hydrogen-air mixture formed and the short time that the mixture maintains at a high temperature in the early stage of hydrogen release, self-ignition requires stronger leading shock to induce its occurrence [22]. After the shock propagates downstream for a certain distance, the amount of the hydrogen-air mixture and its remaining time under high temperature state continue to rise, and gradually they are no longer the

main factors affecting self-ignition onset. Hence, the shock intensity required for self-ignition first decreases and then remains at approximately the same value. Besides, once the ignition occurs inside obstructed tube and the ignited flame propagates to tube exit, almost all ignited flame finally forms a self-sustained flame in the air. This will bring great risks to the ambient environment.

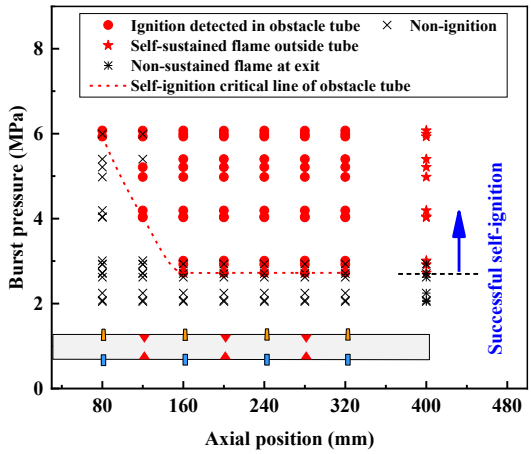


**Fig. 6.** Self-ignition occurrence associated with burst pressure ($P_b$) and axial position along the obstructed tube.

**Fig. 7** shows a comparison of self-ignition critical release pressure versus axial position in tube with and without obstacles. For the cases of straight tube, the critical pressure for self-ignition first maintains at a high value of 5.96 MPa. Then it starts to decrease at the axial position of 160 mm and soon reaches a certain value of 3.98 MPa. The overall variation of critical pressure versus axial position for self-ignition have similar features in tube with and without obstacles, but differs in some details. For the case of obstructed tube, the critical pressure for self-ignition is the same as that in straight tube at about 6 MPa before the shock reaches the location $O_1$. Then the critical value first decreases at the axial position of 120 mm, i.e. the location $O_1$, closer to the burst disk than the position in straight tube. It infers that shock focusing, shock-shock, and shock-wall interactions when the shock passes through obstacles can provide required conditions for self-ignition, inducing self-ignition to occur near obstacles. After the shock propagates to the axial position of 160 mm, the critical pressure for self-ignition remains at a certain value of 2.72 MPa, lower than that in straight tube. It indicates that the presence of obstacles can promote self-ignition onset, decreasing the critical release pressure for self-ignition occurrence. From **Fig. 6**, some tests present non-ignition for burst pressure above the critical pressure for axial position equal to 120 mm. While excellent reproducibility of tests providing ignition and non-ignition for axial position equal or lager than 160 mm. This shows that obstruction-induced self-ignition occurs at different positions, e.g. before or after the obstacle position. If it is before the obstacles, no ignition initiates at the location of the obstacles, so it cannot be measured.

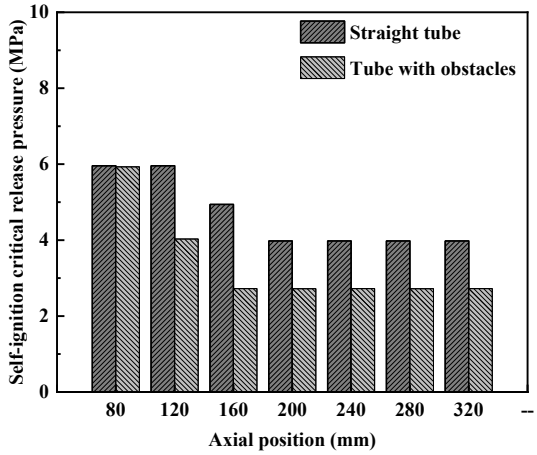


**Fig. 7.** Self-ignition critical release pressure versus axial position in tube with and without obstacles.

### Effects of obstacles on flame propagation

A sequence of direct photographs of self-ignition and flame propagation for typical cases in tube with and without obstacles at similar burst pressure of 8 MPa is shown in **Fig. 8**. For the case of straight tube (**Fig. 8**a), weak luminescence is photographed near the tube wall in front of obstacles (about 160 mm away from the diaphragm) at time $t$ = 119.36 μs. Then within the observation window, hydrogen ignited flame spreads along the sidewall and gradually develops to the center of the tube. For the case of obstructed tube (**Fig. 8**b), two strong hydrogen self-ignition kernel are photographed at both tube sidewalls near obstacle location $O_1$. On the basis of all experimental results, self-ignition may initiate before or after the obstacle. Besides, it can occur at the boundary layer near tube sidewalls or at the centerline of the tube with obstacles. The position of self-ignition initiation observed in our experiment is consistent with the numerical results of Morri et al. [21]. In their numerical work, there are three high-temperature regions that may cause hydrogen self-ignition. The first high-temperature region is produced by the reflected shock, which are generated by the interaction between the leading shock and obstacles. When the two reflected shock from both obstacles are focused at the tube centerline, the second high-temperature region is produced. The third high-temperature region is created near both sidewalls because each reflected shock wave interacts on the opposite wall. When the hydrogen-air contact surface propagates to these three high-temperature regions, self-ignition may be triggered. As shown in **Fig. 8**(b), clear shock structure, i.e. shock-wall reflection and shock-shock interaction can be seen within time t = 228.15 μs to 238.15 μs, verifying the above discussion.

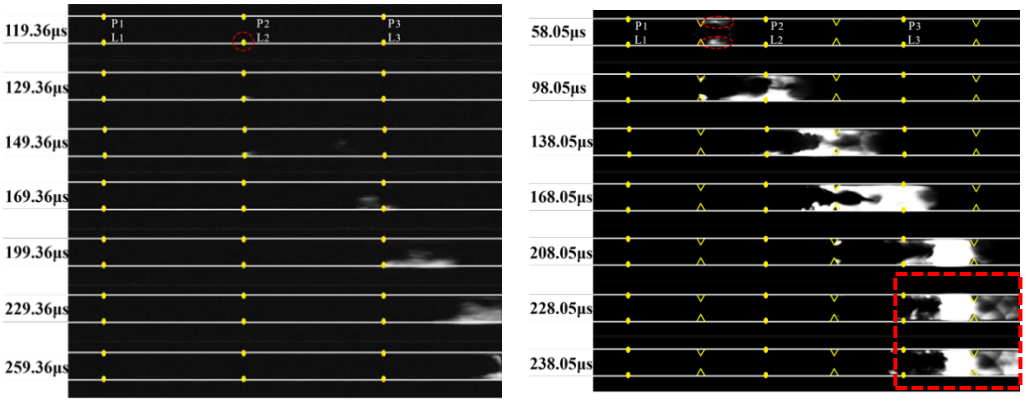


(a) straight tube (b) tube with obstacles

**Fig. 8.** The x-t diagram from direct photograph on the self-ignition cases at the burst pressure of 6 MPa.

**Fig. 9** presents the location of the flame front and flame front propagation velocity for the typical cases of straight tube and obstructed tube at burst pressure of 6 MPa. The flame front velocity is defined as the velocity relative to tube wall. It can be observed in **Fig. 9** that the propagation velocity of the flame front along tube with and without obstacles mostly exhibits fluctuations in the range of 1000 m/s -1500 m/s. For tube with obstacles, the flame front propagation velocity experiences a drastic deceleration as the flame reaches the obstacle location. Then the flame front velocity after further propagation restores to the same as the one propagates in unblocked section of obstructed tube.

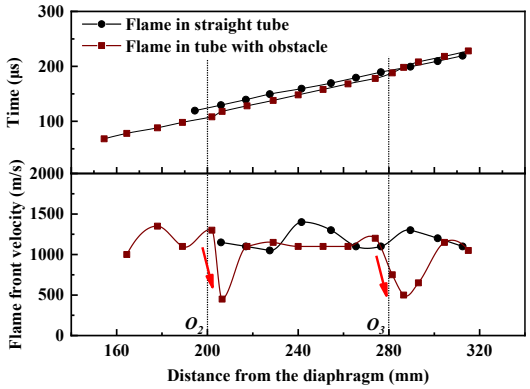


**Fig. 9.** Location of the flame front and flame front propagation velocity ($P_b$ = 6.07 MPa).

Furthermore, the visible flame area and its growth rate inside the two kinds of tube are analyzed in **Fig. 10**. It can be seen that obstacles great promote the flame area, i.e. flame development in the tube. According to the direct photographs in **Fig. 8**(a), the ignited flame at lower wall of straight tube spreads only to the mixing front and tail along with the boundary layer within the observation window

[13]. While for case in obstructed tube (**Fig. 8**b), the flames in boundary layer quickly converge into a complete flame across the tube width, which significantly improves the flame area. Besides, the flame area increase rate in straight tube varies within a small range of 0 $mm^2/\mu s$ – 10 $mm^2/\mu s$. The development of flame surface area shows relative stability within observation window. For the case in obstructed tube, the flame area increase rate along the tube exhibits great fluctuations in the range of -15 $mm^2/\mu s$ – 20 $mm^2/\mu s$. When the flame front reaches the obstacle location, the increase rate of the flame area attenuated to a negative value, resulting in the dramatic reduction of flame area. After passing through the obstacles, the increase rate of flame area significantly rises, resulting in the rapid rise of flame area. Besides, it is observed that the flame area increase rate in the unblocked section of tube is generally higher than that in straight tube. It is inferred that the complicated evolution of flame inside obstructed tube is mainly attributed to the variation of the flow and ignition structures caused by the shock-shock interaction and shock-vertex interaction near obstacle location [21, 23].

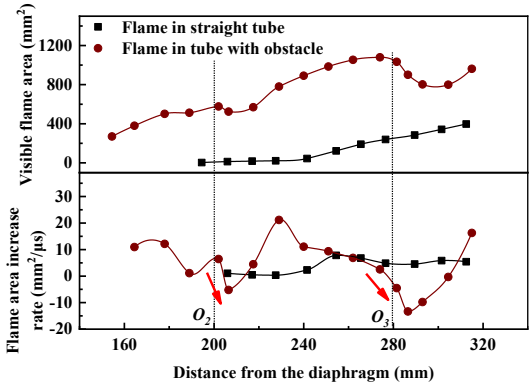


**Fig. 10.** Visible flame area and its growth rate as a function of distance ($P_b$ = 6.07 MPa).

## Conclusions

The self-ignition onset and flame propagation during pressured hydrogen release into tube with obstacles have been studied. The high-speed direct photography as well as simultaneous pressure and flame acquisition are performed in the experiments. The main findings are as follows.

The strength of the leading shock is weakened when the shock travels through obstacles, showing a negative effect on the onset of self-ignition. While the maximum pressure behind the reflected shock wave is about 1.5 as large as the overpressure behind leading shock wave. It exhibits a positive effect on self-ignition onset.

The critical release pressure for self-ignition decreases with an increase in axial distance to the burst disk and then remains at an almost constant value for tube with and without obstacles. However, the position where the critical pressure for self-ignition starts to decrease in obstructed tube appears

near first obstacle location. Besides, the critical pressure for self-ignition finally remains at a constant value of 2.72 MPa in obstructed tube, lower than that of 3.98 MPa in straight tube. It indicates that the presence of obstacles can promote self-ignition onset near the obstacle location and decrease the critical pressure for self-ignition.

In obstructed tube, self-ignition initiates in the near-wall region or the centerline of the tube, verifying the self-ignition mechanism proposed in numerical work [21]. According to the evolution process of flame microstructure, the flame area and its increase rate (in the unblocked section) is significantly higher than that in straight tube. Besides, flame front propagation velocity and increase rate of flame area first attenuate when passing through the obstacles, then quickly restored with further propagation downstream. This may be attributed to the variation of the flow and ignition structures caused by the shock-shock interaction and shock-vertex interaction near obstacle location.

## Acknowledgments

This study is supported by National Natural Science Foundation of China (No. U21A20144, 52104227,), National Natural Science Foundation of Anhui Province (No. 2108085ME157), , and USTC Research Funds of the Double First-Class Initiative.

## References

[1] R. Singh, M. Singh, S.J.M.T.P. Gautam, Hydrogen economy, energy, and liquid organic carriers for its mobility, 46 (2021) 5420-5427.
[2] B.P. Xu, J.X. Wen, S. Dembele, V.H.Y. Tam, S.J. Hawksworth, The effect of pressure boundary rupture rate on spontaneous ignition of pressurized hydrogen release, J Loss Prevent Proc, 22 (2009) 279-287.
[3] P. Wolanski, S. Wojcicki, Investigation into the mechanism of the diffusion ignition of a combustible gas flowing into an oxidizing atmosphere, P Combust Inst, 14 (1972) 1217-1223.
[4] F.L. Dryer, M. Chaos, Z.W. Zhao, J.N. Stein, J.Y. Alpert, C.J. Homer, Spontaneous ignition of pressurized releases of hydrogen and natural gas into air, Combust Sci Technol, 179 (2007) 663-694.
[5] J.X. Wen, B.P. Xu, V.H.Y. Tam, Numerical study on spontaneous ignition of pressurized hydrogen release through a length of tube, Combust Flame, 156 (2009) 2173-2189.
[6] B.P. Xu, J.X. Wen, The effect of tube internal geometry on the propensity to spontaneous ignition in pressurized hydrogen release, Int J Hydrogen Energ, 39 (2014) 20503-20508.
[7] V. Golub, V. Volodin, D. Baklanov, S. Golovastov, D. Lenkevich, Experimental investigation of hydrogen ignition at the discharge into channel filled with air, Physics of extreme states of matter, (2010) 110-113.
[8] Q. Duan, H. Xiao, L. Gong, K. Jin, W. Gao, H. Chai, J. Sun, Experimental study on spontaneous

ignition and subsequent flame development caused by high-pressure hydrogen release: Coupled effects of tube dimensions and burst pressure, Fire Safety J, 97 (2018) 44-53.
[9] S.-W. Cha, T.-S. Roh, H.J. Lee, Effect of opening area on the suppression of self-ignition of high-pressure hydrogen gas leaking in the air by an extension tube, Int J Hydrogen Energ, 46 (2021) 5904-5915.
[10] W. Rudy, A. Dabkowski, A. Teodorczyk, Experimental and numerical study on spontaneous ignition of hydrogen and hydrogen-methane jets in air, Int J Hydrogen Energ, 39 (2014) 20388-20395.
[11] W. Rudy, A. Teodorczyk, J. Wen, Self-ignition of hydrogen–nitrogen mixtures during high-pressure release into air, Int J Hydrogen Energ, 42 (2017) 7340-7352.
[12] L. Gong, Q. Duan, J. Sun, V. Molkov, Similitude analysis and critical conditions for spontaneous ignition of hydrogen release into the atmosphere through a tube, Fuel, 245 (2019) 413-419.
[13] Y.R. Kim, H.J. Lee, S. Kim, I.-S. Jeung, A flow visualization study on self-ignition of high pressure hydrogen gas released into a tube, P Combust Inst, 34 (2013) 2057-2064.
[14] P. Li, Q. Duan, K. Jin, Q. Zeng, J. Sun, Experimental study on shock waves, spontaneous ignition, and flame propagation produced by pressurized hydrogen release through tubes with varying obstacle location, Fuel, 290 (2021).
[15] L. Zhou, L. Zhong, J. Zhao, J. Pan, Z. Xu, H. Wei, Flame Propagation and Combustion Phenomena in a Confined Space with the Perforated Plate at Different Positions, Combust Sci Technol, 192 (2019) 493-512.
[16] H. Xiao, E.S. Oran, Flame acceleration and deflagration-to-detonation transition in hydrogen-air mixture in a channel with an array of obstacles of different shapes, Combust Flame, 220 (2020) 378-393.
[17] N.N. Smirnov, V.F. Nikitin, S.A. Shurekhdeli, Investigation of Self-Sustaining Waves in Metastable Systems: Deflagration to Detonation Transition, J Propul Power, 25 (2009) 593-608.
[18] Q. Zeng, Q. Duan, D. Sun, P. Li, M. Zhu, Q. Wang, J. Sun, Experimental study of methane addition effect on shock wave propagation, self-ignition and flame development during high-pressure hydrogen sudden discharge from a tube, Fuel, 277 (2020) 118217.
[19] V.N. Gamezo, T. Ogawa, E.S. Oran, Numerical simulations of flame propagation and DDT in obstructed channels filled with hydrogen–air mixture, P Combust Inst, 31 (2007) 2463-2471.
[20] B.P. Xu, J.X. Wen, Numerical study of spontaneous ignition in pressurized hydrogen release through a length of tube with local contraction, Int J Hydrogen Energ, 37 (2012) 17571-17579.
[21] Y. Morii, H. Terashima, M. Koshi, T. Shimizu, Numerical study of the effect of obstacles on the spontaneous ignition of high-pressure hydrogen, J Loss Prevent Proc, 34 (2015) 92-99.
[22] S.B. Dorofeev, V.P. Sidorov, A.E. Dvoinishnikov, W. Breitung, Deflagration to detonation transition in large confined volume of lean hydrogen-air mixtures, Combust Flame, 104 (1996) 95-110.
[23] P. Halder, S. De, K.P. Sinhamahapatra, N. Singh, Numerical simulation of shock–vortex

interaction in Schardin's problem, Shock Waves, 23 (2013) 495-504.

# Thermal effects from downwards hydrogen impinging jet – experimental results from high-pressure releases in a carpark.

**Lach A.W* , Vaagsaether K., Gaathaug A.V**

*University of South-Eastern Norway, Department of Process, Energy and Environmental Technology, Porsgrunn, Vestfold and Telemark, Norway.*
**Corresponding author's email: Agnieszka.Lach@usn.no*

## ABSTRACT

The study of hydrogen releases from high-pressure storage systems is important for practical applications for 1) hydrogen driving vehicles: technology and safety, and 2) validation of computational fluid dynamic models. The focus of this paper is on accidental releases that occur due to for example a failure of the TPRD (thermal pressure-activated relief device) with immediate ignition. The physics and dynamics of such releases have to be understood and the importance of the resulted effects needs to be implemented into the development of RCS (regulations, codes, and standards) and mitigation systems. In this paper the real scale experimental results are presented. Releases from the hydrogen tank with storage pressure 350 and 700 bar through 0.5 mm and 1.0 mm diameter into a container with an installed forced ventilation system are presented. The thermal effects resulting from a different angle of the TPRD exhaust pipe were tested. The resulting hydrogen jet fires showed direct dependence on the mass flow rates. Higher mass flow rates resulted from the bigger TPRD diameter or higher storage pressure caused higher temperatures in the ventilation pipe and in the container. A more detailed analysis of the thermal consequences related to TPRD size, storage pressure, and ventilation rate is presented. Results from all the experiments showed temperatures below specified in the regulations, 300 °C, in the ventilation pipe. Low temperatures measured at the front of the car and high temperatures behind will be used for the mitigation strategies and first response guidance. Generally decreasing TPRD diameter to 0.5 mm decreased max temperature behind the car from 500 °C to 250 °C from the same storage pressure, and decreasing harm distance.

**KEYWORDS:** Hydrogen safety, impinging $H_2$ jet, thermal effects, compressed hydrogen, jet fire,

## INTRODUCTION

The change in the transportation system from conventional vehicles (gasoline, diesel, LPG) to zero-emission vehicles (battery/hydrogen driven or hybrid) needs a revaluation of the mitigation system used today. The consequences of accidental hydrogen releases from a high-pressure tank (commonly used from 200 bar to 700 bar) varied from conventional ones. Hence the Regulation Codes and Standards (RCS) which remain unchanged in many aspects of fire safety engineering need to be reevaluated.

The hydrogen cars are equipped with a thermally activated relief device (TPRD) in order to avoid tank rupture in case of exposure to fire. Other causes of the TPRD activation can be a collision with another car/object or a failure of the TPRD. One of the scenarios (study presented in this work) is that released hydrogen will automatically ignite, creating a jet flame. In closed or semi-closed enclosures the thermal and pressure effects of jet flames are greater than in the open air. The size and direction of the jet flame are determined by the tank pressure; the size of the TPRD opening, and the direction of the released hydrogen.

The experimental investigation described in this paper was focusing on comparing the temperature effects resulting from the turbulent hydrogen jet fires to existing RCS (human factors and principle to the building design). The temperature tolerance limit for unprotected skin (in the literature) varied depending on the water concentration in the atmosphere. The time limits of exposure to convected heat with less than 10% $H_2O$ is 5 min for 115 °C and up to 30 min for 68 °C according to BSI PD 7974-6:2004 and CFPA_E Guidelines No19 [1,2]. The same limits were described in a book of

Fundamentals of Hydrogen Safety Engineering [3]. The temperature limit for the saturated atmosphere is 60 °C for no longer than 30 min. In different sources (ISO/TR 16576:2017 considering open jets) the 45 °C was the pain limit [4]. The study on the skin burns with exposure to hot water resulted in less than 10 min exposure time for 50 °C water temperature causing injury which will not fully recover within 21 days [5]. The same pain limits are given in several sources [6–8].

In a building like a carpark, the temperature limitation is 300 °C classified as class F300 [9,10]. The required ventilation system varied from 3 air changes per hour (ACH) with natural ventilation possibilities (2.5% of the floor area), 6 ACH for carpark which don't have natural ventilation and 10 ACH when the cars in a carpark stay in a queue with running engine.

The prediction of the flame length and resulting thermal effects can be used to increase the effectiveness of fire protection measures. Previous work described mainly vertical and horizontal jets [11–17] while impinging jets are investigated in a few studies [18,19]. The experimental results with turbulent hydrogen jet impinging with the floor from short distances are not available to the authors' knowledge. Experimental investigation of hydrogen jet fires presented in [19] focused on horizontal impinging jets with a barrier wall used as a mitigation technique. The hydrogen jet was impinging 90° with the wall. The most effective mitigation method was to use a three wall (135°) configuration. Experimental results from horizontal high-pressure hydrogen fires [17] were used to validate the simulation of thermal hazards presented by Cirrone et al.[14]. Short time hydrogen releases from 900 bar through 2.0 mm nozzle resulted in temperature from 200 °C to 1500 °C depending on the sensor location.

The TPRD in personal cars is usually placed under the car with a 45° exhaust pipe 25 cm above the floor. The CFD study investigated hydrogen dispersion from impinging jets with the floor from different angles in a carpark and vertical jets [20]. Three TPRD diameters were compared resulting in a smaller flammable cloud from releases through 0.5 mm and 45° compared to higher diameters and releases through 0° and 30°. The simulations were done in a scenario with natural ventilation. The authors continued their investigation on hot gases from ignited hydrogen jets [21]. Results showed that downward hydrogen jet flames through 30° and 45° exhaust pipes were safer for 0.5 mm TPRD diameter and recommendation for experiments was suggested.

In the present article, the investigation of thermal effects resulting from the under-expanded hydrogen jet fire impinged with the floor is presented based on the experimental work. The large-scale carpark geometry and instrumentation setup are described in detail. The goal of this work is to investigate the temperature effects from under-expanded hydrogen jet fires and to develop recommendations for the Regulation Codes and Standards (RCS) for the safe use of hydrogen vehicles in the enclosed transportation system. The study was part of the HYTUNNEL-CS European project sponsored by FCH-JU. The produced experimental data, presented in this work, will be used for benchmarking studies using CFD codes.

The thermal characteristics near the hydrogen jet fire resulting from the activation of TPRD are important for the escape possibilities not only for the passengers of the car but people around as well. The information about temperature effects can be used by firefighters and construction engineers. One of the most important uses of data presented in this work will be to validate the models for the thermal effects resulting from 45° impinging hydrogen jet fires with the floor. To the author's knowledge,no other experimental test on such a impinging jet fires were performed in a underground car park scenarios The model validation is not part of the work presented in this study.

## JET FIRE EXPERIMENTS

In this section, the detailed description of the experimental setup and instrumentation is presented first. Then the results are discussed and analyzed.

## Experimental setup

All experiments were carried out in a 40 ft ISO container (summer 2021). The container had isolated walls and inner dimensions of LxWxH: 11.885 x 2.240 x 2.285 m gives a total volume of 60.8 $m^3$ (Fig. 1). The walls and ceiling isolation thickness was approximately 0.07 m. On the floor were mounted cement-based, non-combustible building plates, 6 mm thick. After the first two experiments, two extra layers were added to protect the container floor from burning, those layers were replaced after each second experiment. To compare dimensions, the real-scale carpark/underground parking has the standard 2.25 m minimum free height accordingly to Norwegian Standard [22].

**Fig. 1.** Container and instrumentations

The table imitating a hydrogen car was scaled against the Toyota Mirai with a scaling factor of 0.4 resulting in dimensions: LxWxH: 1.965 x 0.73 x 0.25 m. The table, further called 'car', consists of steel legs and a 1 mm steel plate. The hydrogen outlet was mounted vertically through the steel plate. For the first two experiments, hydrogen was vertically discharged (90°) with a nozzle 230 mm above the floor (Fig. 2 left). For the rest of the experiments, hydrogen was discharged with a 45° nozzle, 180 mm above the floor (Fig. 2 right). All but one experiment were conducted with a 0.5 mm nozzle. The last experiment was conducted with a 1.0 mm nozzle.

**Fig. 2.** Nozzle: left 90°, right 45°.

A Hexagon type IV hydrogen tank (operating pressure up to 700 bar) with a carbon composite wall was used during all experiments (36.8 l). The hydrogen was compressed from a 200 bar hydrogen pack consisting of 12 hydrogen bottles. All pipes were 6x1.5 mm 316 steel with ID 3.0 mm.

The ventilation outlet with ID 315 mm was located 0.050 m from the ceiling (0.2075 m from the ceiling to centre) on the ventilation wall (Fig. 3). The ventilation pipe consists of two sections, 4 m long in total. One section with 0.315 m diameter pipe with outlet into the container and second section with 0.2 m diameter with airfan at the end. The ventilation was suction-type ventilation provided from an air fan.

Before the hydrogen ignition, a small propane pilot flame was ignited. The hydrogen was released into the propane flame and hence automatically ignited. The thermal effect from the propane flame is assumed to be negligible (propane flame was shut down seconds after hydrogen ignited).

**Instrumentation**

For the mass flow measurements the coriolis mass flow meter, model HPC010P ultra-high pressure from Emerson Micromotion with connected transmitter model 5700 with a pressure range up to 1043 bar was used during all experiments. The total pipe length from the hydrogen tank to the nozzle was 3.86 m. At the tank outlet, a pressure transmitter ESI model HP1003-1000DE with a pressure range from 0 to 1000 barg was installed. The same type of pressure transmitter was mounted at the outlet of the coriolis mass flow meter.

The airflow rate was controlled by an IRIS 200 damper and voltage speed controller for the fan. The air change per hour (ACH) for the experiments was according to BSI 7346-7:2013 [9]: 10 ACH and 6 ACH. The airflow was measured by the differential pressure of the IRIS 200 damper with the GAMS Sensor differential pressure transmitter model 5266. For the container geometry that means 608 $m^3/h$ and 365 $m^3/h$ for 10 and 6 ACH respectively.

10 sensors were installed to measure temperature change during experiments: 9 thermocouples inside the container and 1 in the ventilation pipe. All 10 thermocouples were fast response Type 'K' thermocouples with grounded hot junction. The sensor locations are presented in Fig. 3 and Table 1.

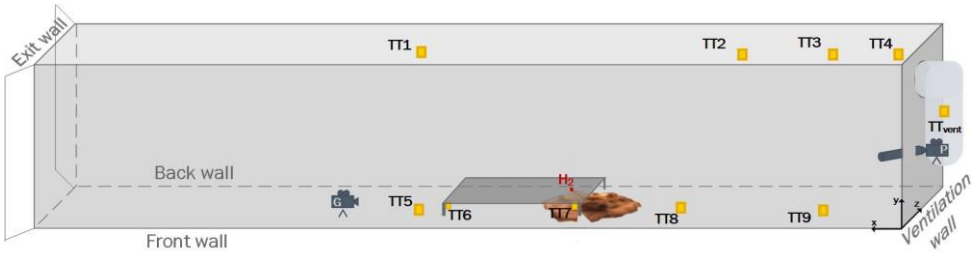


**Fig. 3**. Thermocouples locations inside the 40 ft container and ventilation pipe.

Four thermocouples (TT1-TT4) were mounted 180 mm from the ceiling along the centre axis (z=1120 mm) to measure temperature change under the ceiling and the effect of ventilation rate. Two thermocouples were mounted in the corners under the car (close to the 'wheels') at the front (TT6) and in the back (TT7) of the car. Three thermocouples were mounted at the front wall: 735 mm at the front of the car (TT5), and two behind the car: 1190 mm and 3470 mm (TT8 and TT9 respectively) (Fig. 3). The temperature inside the ventilation pipe was measured 510 mm from the top of the pipe and 130 from the pipe wall.

**Table 1. Location parameters [mm]**

| | y | x | z |
|---|---|---|---|
| TT1 | 2105 | 6250 | 1120 |
| TT2 | 2105 | 2320 | 1120 |
| TT3 | 2105 | 1060 | 1120 |
| TT4 | 2105 | 110 | 1120 |
| TT5 | 235 | 7200 | 80 |
| TT6 | 198 | 6330 | 868 |
| TT7 | 200 | 4600 | 860 |
| TT8 | 235 | 3310 | 74 |

| | | | |
|---|---|---|---|
| TT9 | 235 | 1030 | 80 |
| TTvent | 1725 | | 130 inside |
| Nozzle 45 | 180 | 4980 | 1120 |
| Nozzle 90 | 230 | 5000 | 1120 |
| Table | 250 | 4500 | 755 |
| outlets | 2055 | 0 | 1120 |

[a] to the centre

The uncertainly of the instrumentation is listed in Table 2. It's important to notice that measurements from all pressure transmitters and mass flow meter were recorded with a sample rate of 2 kHz and temperature measurements with a sample rate of 50Hz.

**Table 2. Instrumentation uncertainty.**

| Instrument | Uncertainty [%] |
|---|---|
| ESI Pressure transmitter | ±1% FSO BFSL[1] |
| GAMS Differential pressure transmitter | ±1% $FS_2$ |
| Mass flow | ±0.2% of flow rate |
| Thermocouples type K | ±0.75% |

[1] Full scale output Best Fir Straight Line
[2] Full scale

## Results and discussion

During the experiments, hydrogen was discharged from 350 bar and 700 bar, with 6 and 10 ACH. The nozzle directed 90° vertical downwards, was used in the first 2 experiments (700 bar with both ACH). For experiments 3-8 the nozzle was mounted 45° downwards and backwards (towards the ventilation wall). Table 3 presents: the parameters of the experiments; climatic conditions; initial pressure in the tank and initial mass flow rate and initital mass flow rateestimated with e-laboratory from Net-Tools [23] with under-expaded jet model [11], resulted from experimental initital tank pressure.

**Table 3. Parameters of jet fire experiments**

| Exp Nr | Nozzle angle [°] | Nozzle diameter [mm] | Air change per hour [1/h] | Ambient temp [°C] | Initial tank pressure [bar] | Initital mass flow rate [g/s] | Net-Tools Initital mass flow rate [g/s] | Blowdown duration [s] |
|---|---|---|---|---|---|---|---|---|
| 1 | 90 | 0.5 | 10 | 22 | 708 | 7.3 | 6.7 | 450 |
| 2 | 90 | 0.5 | 6 | 19 | 695 | 7.5 | 6.6 | 80 |
| 3 | 45 | 0.5 | 6 | 23 | 357 | 4.0 | 3.8 | 500 |
| 4 | 45 | 0.5 | 6 | 22 | 698 | 7.4 | 6.7 | 500 |
| 5 | 45 | 0.5 | 10 | 22 | 690 | 7.3 | 6.6 | 500 |
| 6 | 45 | 0.5 | 10 | 19 | 357 | 4.1 | 3.8 | 500 |
| 7 | 45 | 0.5 | 6 | 19 | 360 | 4.0 | 3.9 | 500 |
| 8 | 45 | 1.0 | 6 | 15 | 357 | 13 | 15.2 | 367 |

Experiments were recorded with Promon 500 high-speed camera from AOS technologies AG. Video frames from 4 different experiments showing hydrogen jet fires from both diameters, both initial

pressures, and both nozzle angles illustrate the flame development during the blowdown releases (Fig. 4). One layer with a fire-resistance plate was insufficient to protect the floor during experiments with 90° nozzle (the rest experiments had 3 layers). Due to cracks formed in the fire-resitance plates when exposed to the jet fire, the wooden floor beneath them caught fire. The visible fire from the burning floor can be seen after 300 s on Fig. 4, last row. The exp 2 had to be stopped after 80 s due to fire (floor and walls).

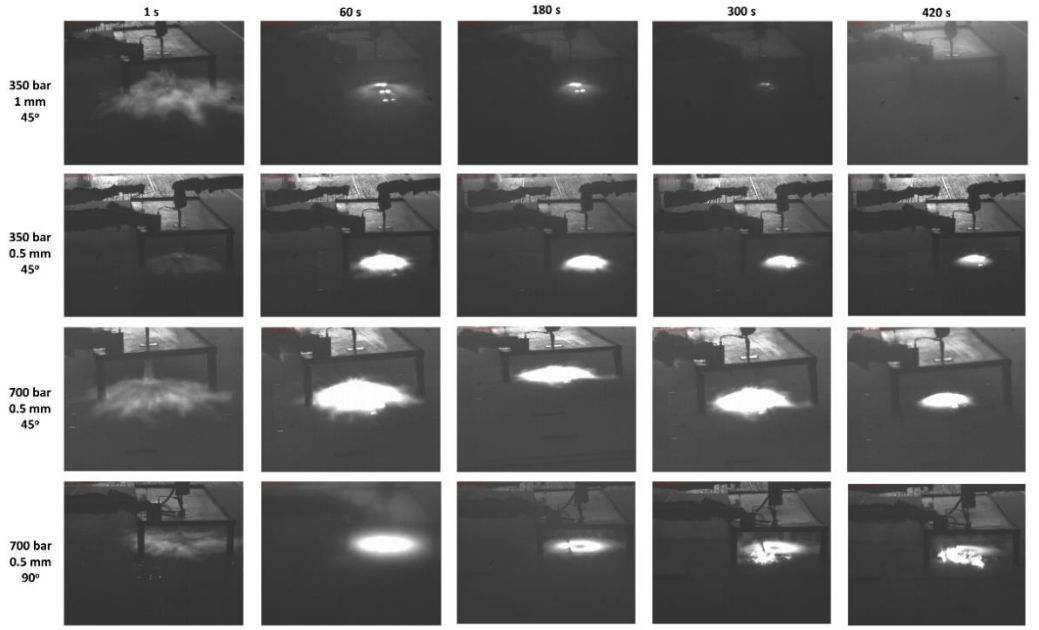


**Fig. 4.** Flame development from Exp.8 (top row), Exp.7 (second row), Exp.4 (third row), and Exp.1 (bottom row).

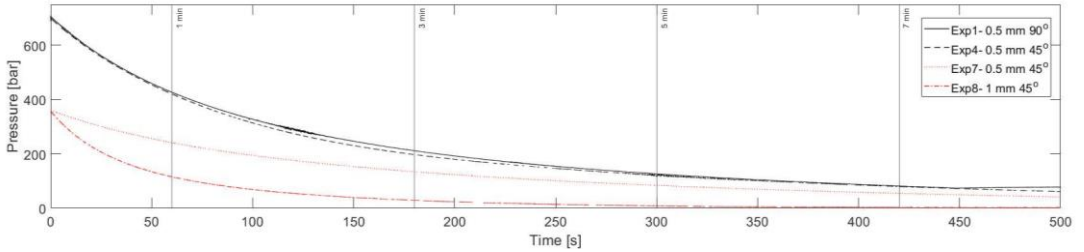


**Fig. 5.** Tank pressure during blowdown from Exp.1 (solid line), Exp.4 (dashed line), Exp.7 (dotted line), and Exp.8 (dot-dash line).

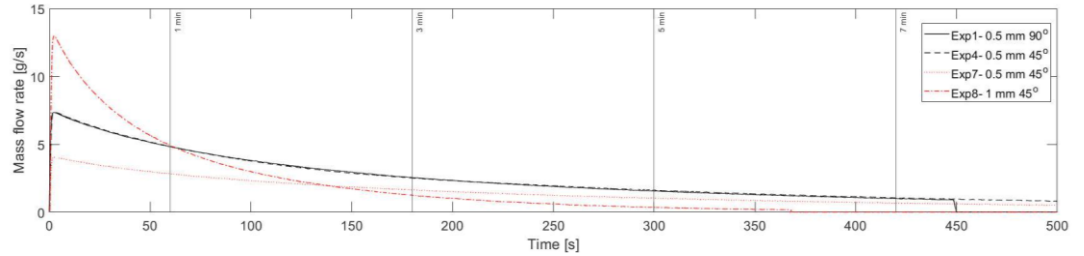


**Fig. 6.** Hydrogen mass flow rate during blowdown from Exp.1 (solid line), Exp.4 (dashed line), Exp.7 (dotted line), and Exp.8 (dot-dash line).

The hydrogen jet fire length is depending on the mass flow rate ($\dot{m}$) and nozzle diameter (D) [11,16]. That is why releases from 700 bar through 0.5 mm nozzle and 350 bar through 1 mm nozzle resulted in the largest impingement area. Higher mass flow rates due to higher initial tank pressure and larger nozzle diameter can be seen in Fig. 5 and Fig. 6. The novel dimensionless flame correlation [11] includes the $\dot{m} \propto D^2$ which means the mass flow rate from 350 bar through 1 mm nozzle should have ~16 g/s initial mass flow rate (not 13 g/s as was measured) compared to 4 g/s resulting during releases from 350 bar through 0.5 mm nozzle (conmfired with the resuts from e-Laboratory – Net-Tools Table 3). The pressure losses in the pipes can be the reason for this discrepancy. The experimental data showed that the variation in the tank pressure and mass flow rate dynamics during blowdown between experiments was low (about 15 bar and 0.09 g/s) for equal initial pressure and nozzle diameter. This can be seen in Fig. 5 and Fig. 6.

The hydrogen is released through higher TPRD diameters faster (Fig. 6) and hence bigger amount of energy is released in a shorter time. The smaller diameter (smaller TPRD diameter) will result in a lower mass flow rate and hence a lower energy rate released during combustion (comparing the same release time).

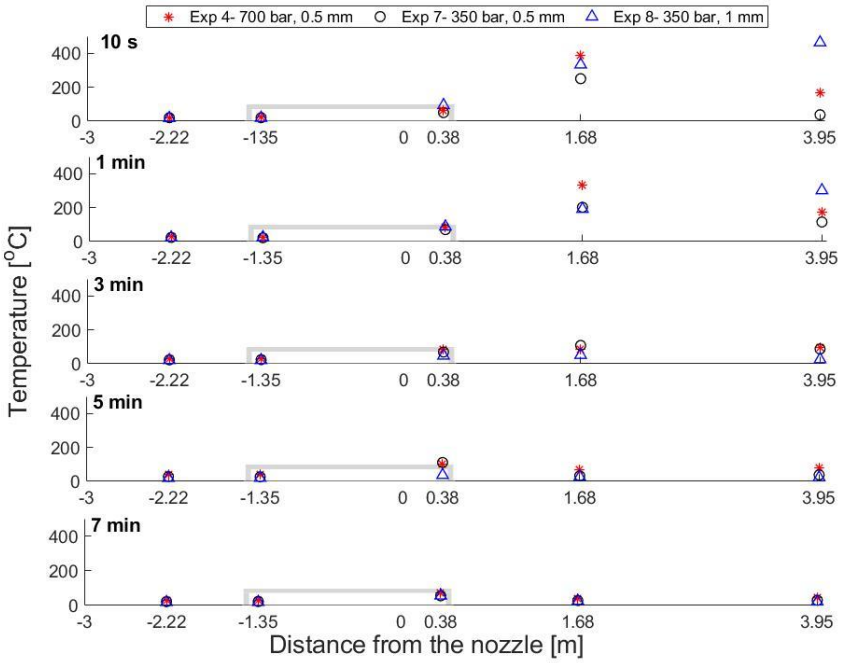


**Fig. 7.** Comparison of temperature resulted from different initial tank pressure and nozzle diameter (mass flow rates) at five longitudinal positions from the nozzle: TT5(-2.22 m), TT6(-1.35 m) TT7(0.38 m), TT8(1.68 m) and TT9(3.95 m).

The temperature resulted from the releases through 0.5 mm diameter nozzle from 700 bar and 350 bar initial tank pressure and through 1 mm diameter nozzle from 350 bar initial pressure (7.4 g/s- red star, 4.0 g/s- black circle, and 13 g/s- blue triangle respectively) are presented in Fig. 7. All three experiments were performed with the same airflow rate- 6 ACH. On the x-axis, the centre axis longitudinal distance from the nozzle is presented. The temperature at each position at different times is an average temperature in a 0.8 s period (+/- 0.4 s around the given time). Sensors TT6 and TT7, located under the car, in its corners have distances from the nozzle 1.35 m and 0.38 m respectively. The remaining three sensors presented in Fig. 7 were placed at the same height as TT6 and TT7 but on the container walls (inside). The hydrogen jet fire did not increase the temperature in front of the car. This can be seen in the plot of the temperature distribution in Fig 7. The maximum measured

temperature change was 3 ˚C decreased and 6 ˚C increased. The change is considered negligible. The temperature measured closest to the jet fire (TT7) was very similar for all three releases and did not exceed 110 ˚C. Since the hydrogen release during Exp.8 ended after 350 s (the tank was empty) the temperature after 5 min at the distance 0.38 m was lower than from two other experiments at the same time and position.

All those three experiments were performed with a nozzle angle of 45˚. That is why the highest temperature was measured behind the car (closer to the ventilation wall). The largest difference between experiments was also measured behind the car. As was expected, and observed from Fig. 4 the highest temperatures were measured for Exp.4 and Exp.8. What distinguishes thermal effects from these two experiments is the location where the highest temperature was measured. For the smaller TPRD diameter (0.5 mm) the highest temperature was measured closer to the car – 1.68 m from the release source and 1.18 from the car for the first 3 min. After that, the temperature measured 3.95 m from the car was close to the temperatures behind the car, and all of them were less than 105 °C. Nevertheless, at both locations, the temperature decreased to 26 degrees after 7 min (Exp.4 and Exp.7). Comparing temperatures measured at 1.68 m location to Exp.8 with releases through 1 mm TPRD diameter, after 10 s the temperature was 50 ˚C higher for Exp.4 than for Exp.8 but did not exceed 400 ˚C for any of the experiments. The temperature measured at 3.95 m from the release source was highest for Exp.8 (Fig. 8, TT9). After 10 s the temperature exceeds 450 ºC which is almost three times higher than for Exp.4 and 12 higher than Exp.7, at the same position. Nevertheless, the temperature decreased faster than the other two experiments and after 3 min it reached 50 ˚C and 25 ˚C at l.68 m and 3.95 m respectively.

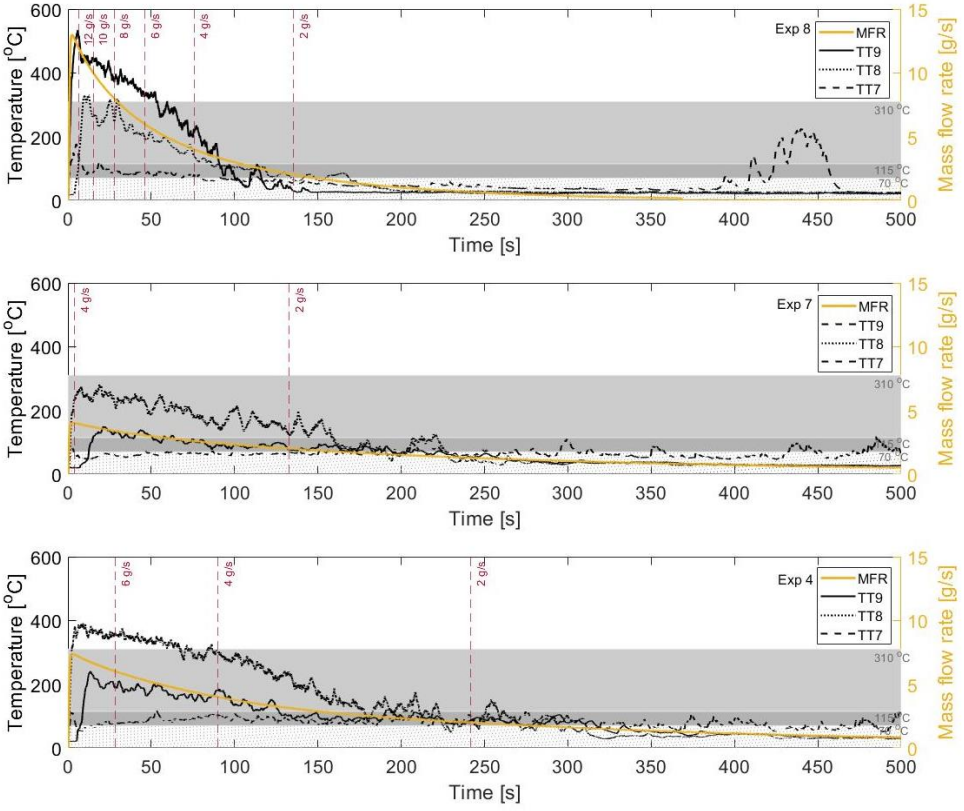


**Fig. 8.** Temperature behind the TPRD vs time,0.38 m. 1.68 m and 3.95 m behind the TPRD – TT7, TT8, and TT9 respectively.

The pain limits accordingly to several standards and guidelines [1–3] is 115 °C for no longer than 5 min exposure to convected heat. The 70 °C is considered as no harm limit [21], in other sources is less than 60 °C for 100% saturated air. After 4 min the temperatures presented in Fig. 8 did not exceed 115 °C. Fig. 8 shows that the temperature exceeded the 310 °C harm limit for both Exp.8 (1 min) and Exp.4 (2 min).

The heat transfer to the skin occurs faster in presence of water. While exposure to hot liquid water over 60 ˚C will cause 2nd-degree burns after 3 s and 3rd-degree burns in 5 s [24]. The tenability limits for hydrogen fire exposure should include the water saturation level in the air since the combustion product consists only of water. The humidity measurements are recommended for the next investigation stage and to be included in the analytical model for the heat transfer to human skin.

The temperature measurements under the ceiling (Fig. 9) showed that hot combustion products were ventilated from the container in both directions: through the vent with forced ventilation and the exit door. The temperature measured at the front and 1.855 m above the car (Fig. 9, TT1) did not differ from temperatures measured closer to the ventilation wall, behind the car (Fig. 9, TT2-TT4).

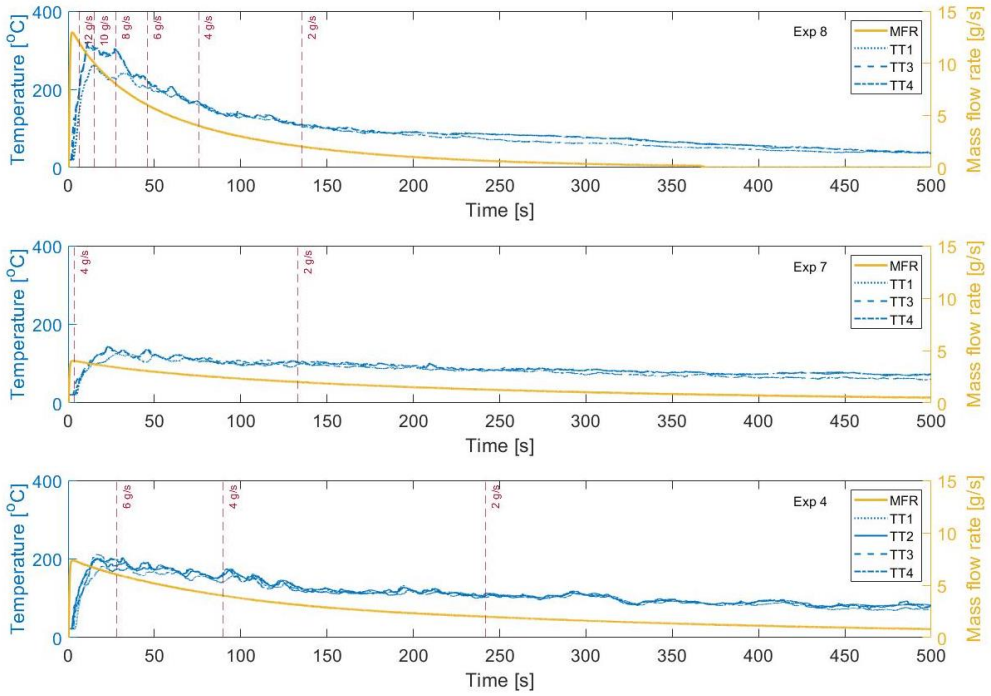


**Fig. 9.** The temperature under the ceiling vs time.

The temperature under the ceiling did not exceed 300 °C during experiments with 0.5 mm as the limit presented British and Dutch standards [9,10] but is important to notice that the presented temperatures are results from hydrogen jet fires only. The combustion products and their thermal effect from burning car and soundings are not included in the presented experiments.

The 6 and 10 ACH were investigated since they are the minimum requirements given by standards [9] together with the 300 °C maximum temperature in the ventilation criteria. In the BS 2013 the minimum ACH for car parks with natural and forced ventilation is 3 ACH which was considered too low for the geometry used in this work. The effect of forced ventilation is presented in Fig. 10.

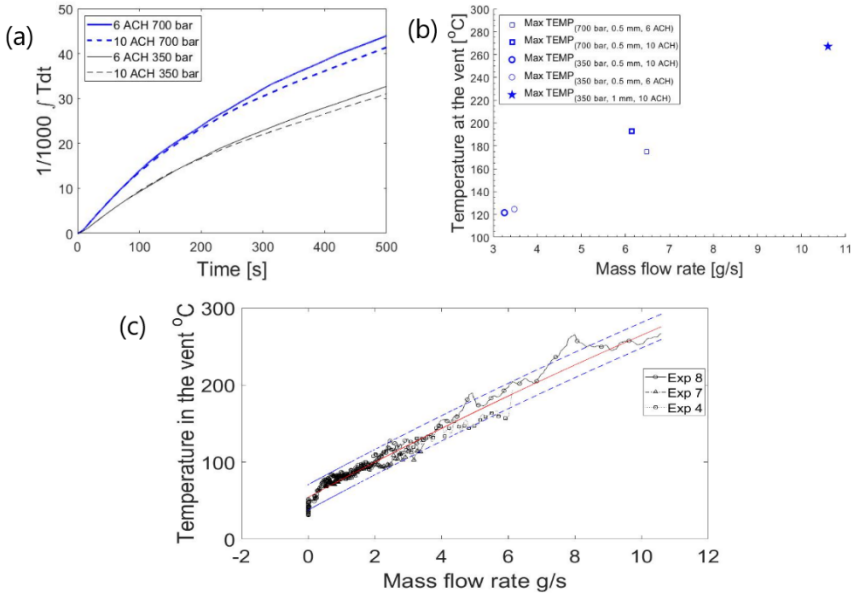


**Fig. 10.** Temperature effect in the ventilation pipe

Experiments with releases from 350 bar and 700 bar storage pressure (through 0.5 mm 45° nozzle) were used to compare the effect of a forced ventilation system on ventilating hot products through the ventilation pipe. Increasing the ventilation rate from 6 to 10 ACH decreased temperature inside the ventilation pipe by 3.3% and 6.9% for releases through 0.5 mm nozzle from 700 bar and 350 bar respectively (Fig. 10, a). The highest temperature measured in the ventilation pipe was for the experiments with the highest mass flow rate (Fig. 10, b). Which is the outcome of the conclusion that the higher the hydrogen mass flow rate higher the released energy from the combustion. Due to heat loss to the walls in the ventilation pipe, the measured temperatures were ~20 ˚C lower than temperatures measured under the ceiling (inside the container). That means the temperature in the ventilation pipe did not exceed the maximum requirements given in standards and can also be assumed equal to the temperature of hot products under the ceiling (too simplified calculation purposes). The temperature is depending on the hot products hence the hydrogen mass flow rate. The relation between mass flow rate to the temperature measured from Exp.4, Exp.7, and Exp.8 is presented in Fig. 10, c. Once again results showed the higher the mass flow rate, the higher the temperature. Temperature resulting from given mass flow rate was almost constant, little depended on starting conditions. This can be observed in Fig. 10,c, where the red line presents a first-degree polynomial fit and blue dash lines a 95% prediction interval.

## CONCLUSION

In this paper, the authors described the large scale experimental results conducted in June 2021 in Norway. The scenarios with ignited hydrogen releases from 1.0 mm and 0.5 mm TPRD diameter through 90° and 45° exhaust pipe were investigated. The hydrogen was released from the tank (initially 350 bar or 700 bar) into an enclosure imitating a carpark with two ventilation rates: 6 and 10 ACH. The obtained experimental data showed the relation between TPRD diameter and resulted temperature change inside the enclosure and ventilation pipe. The results show that the temperature in the ventilation system increases with the increase of hydrogen mass flow rate i.e. increase in TPRD diameter and/or storage pressure. Nevertheless, the temperature did not exceed 300 °C in the ventilation pipe during releases through both 1.0 mm and 0.5 mm nozzle diamter. The temperature limit under the ceiling was not exceeded during releases from 0.5 mm.

Most of the study focused on the 45° TPRD release. The temperature development around the car, showed a possible safe approach towards the front of the car. The biggest variation in temperature among the experiments was observed behind the car. The increase in TPRD diameter increased the measured temperature at the longest distance from the nozzle. Releases from higher storage pressure through the same TPRD diameter resulted in higher temperatures measured at the same location.

Decreasing the TPRD diameter results in a lower maximum temperature but a longer duration of blowdown. The consequence is an increase in the duration of high temperatures around the car which may cause 1st, 2nd and 3rd burn degrees. A solution concerning all possible consequences is needed in order to ensure safety around the hydrogen personal cars in case of unwanted hydrogen jet flames.

## ACKNOWLEDGMENTS

The authors wish to acknowledge funding from the Fuel Cells and Hydrogen 2 Joint Undertaking (JU) under grant agreement No 826193. The JU receives support from the European Union's Horizon 2020 research and innovation programme and United Kingdom. Germany. Greece. Denmark. Spain. Italy. Netherlands. Belgium. France. Norway. Switzerland.

This work was performed within MoZEES. a Norwegian Centre for Environment-friendly Energy Research (FME), co-sponsored by the Research Council of Norway (project number 257653) and 40 partners from research, industry, and the public sector.

## REFERENCES

[1] British Standard PD 7974-6:2004. Application of Fire Safety Engineering Principles to the Design of Buildings. Part 6: Human factors: Life safety strategies — Occupant evacuation, behaviour and condition (Sub-system 6) 2004.

[2] CFPA-E Guideline No 19:2009 F. Fire safety engineering concerning evacuation from buildings 2009.

[3] Molkov V. Fundamentals of Hydrogen Safety Engineering I. vol. 4. 2012. https://doi.org/10.1016/B978-0-08-087872-0.00418-2.

[4] ISO/TR 16576:2017. Fire safety engineering — Examples of fire safety objectives, functional requirements and safety criteria 2017.

[5] Christine Julie Andrews. Validating the relationship between burn temperature, duration of exposure and tissue injury severity for scald burns . The University of Queensland, 2017.

[6] Loo YL, Haider S, PY YL, Jeffery S. Predictor of the depth of burn injuries: A time and temperature relationship review. Int J MedicalScience Clin Invent 2018;5:4119–28. https://doi.org/10.18535/ijmsci/v5i11.01.

[7] Moritz AR, Henriques FC. Studies of Thermal Injury: II. The Relative Importance of Time and Surface Temperature in the Causation of Cutaneous Burns. Am J Pathol 1947;23.

[8] Gottuk, D. R Hall. John, Kazunori, H. Kuligowski, E. Puchovsky, M. Torero, J. Watts J.M. Wieczorek C. SFPE Handbook of Fire Protection Engineering. 5th ed. Springer; n.d.

[9] BSI Standards Publication BS 7346-7:2013. Components for smoke and heat control systems – Part 7: Code of practice on functional recommendations and calculation methods for smoke and heat control systems for covered car parks 2013.

[10] Nederlandse praktijkrichtlijn NPR 6095-1 (nl). Smoke and heat control systems - Part 1: Guidelines on design and installation of smoke and heat exhaust installations and smoke control systems in car parks 2012.

[11] Molkov V, Saffers J-B. Hydrogen jet flames. Int J Hydrogen Energy 2013;38:8141–58. https://doi.org/10.1016/J.IJHYDENE.2012.08.106.

[12] Middha P, Hansen OR. CFD simulation study to investigate the risk from hydrogen vehicles in tunnels.

Int J Hydrogen Energy 2009;34. https://doi.org/10.1016/j.ijhydene.2009.02.004.

[13] Palacios A, García W, Rengel B. Flame shapes and thermal fluxes for an extensive range of horizontal jet flames. Fuel 2020;279. https://doi.org/10.1016/j.fuel.2020.118328.

[14] Cirrone DMC, Makarov D, Molkov V. Simulation of thermal hazards from hydrogen under-expanded jet fire. Int J Hydrogen Energy 2019;44:8886–92. https://doi.org/10.1016/j.ijhydene.2018.08.106.

[15] BOUIX D, SAUZEDDE F, MANICARDI P, MARTIN M, FORERO-MORENO D., STUDER E, et al. FULL-SCALE TUNNEL EXPERIMENTS FOR FUEL CELL HYDROGEN VEHICLES: JET FIRE AND EXPLOSIONS. 9th Int. Conf. Hydrog. Saf., 2021, p. 1197–210.

[16] Schefer RW, Houf WG, Bourne B, Colton J. Spatial and radiative properties of an open-flame hydrogen plume. Int J Hydrogen Energy 2006;31. https://doi.org/10.1016/j.ijhydene.2005.11.020.

[17] Proust C, Jamois D, Studer E. High pressure hydrogen fires. Int J Hydrogen Energy 2011;36. https://doi.org/10.1016/j.ijhydene.2010.04.055.

[18] Willoughby DB, Royle M. The interaction of hydrogen jet releases with walls and barriers. Int J Hydrogen Energy 2011;36. https://doi.org/10.1016/j.ijhydene.2010.05.077.

[19] Schefer RW, Merilo EG, Groethe MA, Houf WG. Experimental investigation of hydrogen jet fire mitigation by barrier walls. Int J Hydrogen Energy 2011;36. https://doi.org/10.1016/j.ijhydene.2010.04.008.

[20] Hussein H, Brennan S, Molkov V. Dispersion of hydrogen release in a naturally ventilated covered car park. Int J Hydrogen Energy 2020;45:23882–97. https://doi.org/https://doi.org/10.1016/j.ijhydene.2020.06.194.

[21] Hussein H, Brennan S, Molkov V. Hydrogen Jet Fire from a Thermally Activated Pressure Relief Device (TPRD) from Onboard Storage in a Naturally Ventilated Covered Car Park. Hydrogen 2021;2. https://doi.org/10.3390/hydrogen2030018.

[22] Standard Norge NS 3940:2012. Areal- og volumberegninger av bygninger. Calculation of areas and volumes of buildings 2012.

[23] Karlsruher Institute of Technology (KIT). Net-Tools e-Laboratory jet parameters model. n.d. https://elab-prod.iket.kit.edu/integrated/jet_parameters/input.

[24] Antiscald. Burn Exposure Chart 2016. http://antiscald.com/index.php?route=information/information&information_id=15.

# A transient model for hydrogen pipe leak

**Welahettige P.[1],*, Gaathaug AV.[1] , Vaagsaether K.[1]**

[1] *University College of Southeast Norway, N-3901 Porsgrunn, Norway.*
**Corresponding author's email: prasanna.welahettige@usn.no*

## ABSTRACT

Early detection of hydrogen pipe leaks can avoid significant disaster situations. Beyond the available steady-state gas pipe leak model, a 1-D transient gas pipe leak model is developed in the study. The developed numerical model can be used for high-pressure gas pipe leak detection. A new source term is introduced for the pipe leak model based on the isentropic expansion and chocked flow model. When there is a leak, two pressure waves occur upstream and downstream. High-resolution numerical schemes are recommended to solve the model. In this study, the flux-limited-centered scheme is used for solving the advection term, and the source term is solved with Runge-Kutta 4th order explicit scheme with the source term splitting method. The developed model is validated with the experimental results: the expansion wave. The model results show that experimentally capturing the expansion wave with a small leak diameter is challenging. The pressure difference in the expansion wave to reference pressure is very small. The developed model can be used for early leak detection technology development.

**KEYWORDS:** Hydrogen leak, mathematical model, pipe flow, compressible flow, high-pressure gas distribution

## NOMENCLATURE

| | |
|---|---|
| $A$ | cross-sectional area ($m^2$) |
| $C_d$ | discharge coefficient |
| $c_P$ | constant pressure specific heat (J/(kg·K)) |
| $D$ | Pipe diameter |
| $e$ | energy ($J/m^3$) |
| $F$ | numerical flux |
| $H$ | heat transfer coefficient (J) |
| $i$ | cell identity |
| $L$ | pipe length (m) |
| Ma | Mach number |
| $\dot{m}$ | mass flow rate (kg/s) |
| $p$ | pressure (pa) |
| $S$ | source term |
| $T$ | temperature (K) |
| $t$ | time (s) |
| $U$ | conserved variable |
| $u$ | velocity (m/s) |
| $x$ | direction |
| $y$ | direction |

**Greek**

| | |
|---|---|
| $\gamma$ | heat capacity ratio |
| $\rho$ | density ($kg/m^3$) |
| $\mu$ | viscosity (Pa s) |

**Subscripts**

| | |
|---|---|
| $atm$ | atmospheric |
| $c$ | critical |
| $pipe$ | pipe |
| $leak$ | leak |

## INTRODUCTION

Hydrogen loss of containment in hydrogen distribution systems can harm infrastructure and life. It is vital to make early leak detection to mitigate possible hazards. The classical 'hole' and 'pipe' models are typically used for gas release applications and they usually assume steady-state in the in-containment states [1–4]. The hole-model assumes the pipe functioning as a tank where the hole diameter is much smaller than the pipe diameter. The gas pressure inside the pipe is assumed to be constant when the leak occurs. This assumption makes an overprediction of release rate in the hole model [1]. The hole model considers subsonic and supersonic flow based on the critical pressure in the leak hole[5]. If the pipe flow is subcritical, the flow can be either sonic or subsonic depending on the ratio of orifice diameter to pipe diameter [3]. The gas expansion through the hole is isentropic. The pipe model can be applied for the full-bore rupture of the pipe, and it cannot use for the small orifice leak. The pipe flow model is based on the continuity, momentum, energy, and equation of state. In the pipe model, the flow is assumed to be adiabatic, and the friction force is taken into account [3]. Combining the hole model and the pipe model can formulate the pipe leak model [1]. If the inlet pipe pressure is constant, the pipe flow condition reaches a steady-state condition after a while [6]. The numerical model based on the hole and pipe flow models has two parts. The first part is internal pipe flow from the pipe inlet to the leak point along the center of the pipe. The second part is gas release from the center of the pipe to the leak hole. Yuan et al. [2] has assumed a compressibility factor in the pipe. Our approach relaxed the constant compressibility factor assumption. The main flow stream bends toward the leak hole and accelerates through the leak hole. Rui et al. [7] use the Weymouth equation or the Pandhadle equation together with four experiments to identify to leak points (mass flow and locations) in the same pipe line. Acton et al. [8] have investigated full-bore hydrogen release in experimentally.

In this study, we developed a transient gas leak model. The advantage of using this model is that it can avoid the steady-state assumption. A high-resolution numerical scheme is used for solving the model. The model is validated with experimental and CFD simulation in the literature. The developed model is applied to a hydrogen pipe leak.

## TRANSIENT HYDROGEN PIPE LEAK MODEL

Figure 1 shows the discretized fluid domain for the pipe flow with a leak hole. The main flow direction is from left to right, $x$-direction. The leak occurs at the $i$th cell. The flow is assumed to be compressible.

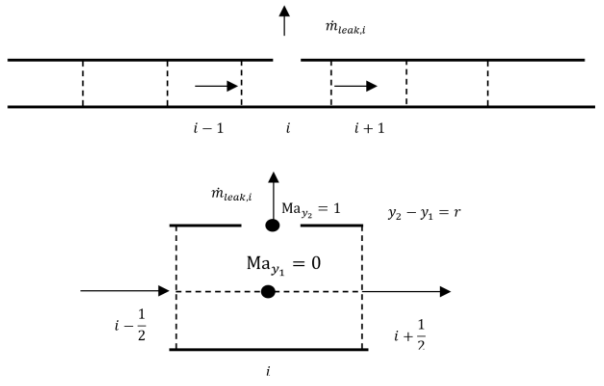


Figure 1. 1-D flow domain discretization: the Control volume at the leak cell

The leak rate from the control volume can correspond to the choked flow, where the control volume has higher pressure than the outside. The outside is in atmospheric condition. For sonic flow and subsonic flow, the choked flow rate is

$$\dot{m}_{leak} = \begin{cases} C_d A \sqrt{\gamma \rho_2 p_2 \left(\frac{2}{\gamma+1}\right)^{\frac{\gamma+1}{\gamma-1}}}, & p_{atm} < p_c \\ C_d p_2 A \sqrt{\frac{2}{RT}\frac{\gamma}{\gamma-1}\left(\left(\frac{p_{atm}}{p_2}\right)^{\frac{2}{\gamma}} - \left(\frac{p_{atm}}{p_2}\right)^{\frac{\gamma+1}{\gamma}}\right)}, & p_{atm} \geq p_c \end{cases}, \quad (1)$$

where,

$$p_c = p_2 \left(\frac{2}{\gamma+1}\right)^{\frac{\gamma}{\gamma-1}}. \quad (2)$$

The mass balance equation for the control volume with the leak gives,

$$\frac{d\rho}{dt} = -\frac{1}{\Delta x}\left((\rho u)_{i+\frac{1}{2}} - (\rho u)_{i-\frac{1}{2}}\right) - \frac{1}{A_p \Delta x}\dot{m}_{leak} \quad (3)$$

The momentum balance equation for the leaked control volume in $x$ direction, where $x$ direction is along the centerline,

$$\frac{d\rho u}{dt} = \frac{1}{\Delta x}\left((\rho u^2 + p)_{i-\frac{1}{2}} - (\rho u^2 + p)_{i+\frac{1}{2}}\right) - \frac{1}{A_{pipe}} f \frac{2}{D} \rho u^2 (\pi D \Delta x - A_{leak}) \quad (4)$$

Here, $f$ is the pipe wall friction factor from the Manning formula. It is assumed an isentropic expansion from center of pipe to the leak hole. The $y$-directional Mach number is assumed to be zero in the center of pipe, and it is equal to one at the leak hole due to sonic flow. The wall thickness is not considered. For the flow path $y_1$ to $y_2$, the isentropic expansion gives

$$\rho_{y_2} = \rho_i \left(\frac{2}{\gamma+1}\right)^{\frac{1}{\gamma-1}}. \quad (5)$$

The energy balance equation for the leak control volume gives,

$$\frac{de}{dt} + \frac{1}{\Delta x}\left(\left(\frac{1}{2}\rho u^3 + \rho u c_p T\right)_{i-\frac{1}{2}} - \left(\frac{1}{2}\rho u^3 + \rho u c_p T\right)_{i+\frac{1}{2}}\right) = -\frac{1}{A_p \Delta x}\left(\frac{1}{2}\dot{m}_{leak} u_{leak}^2 + \dot{m}_{leak} c_p T_{y_2}\right) \quad (6)$$

where,

$$c_p = c_1 + c_2 T_i + c_3 T_i^2 + c_4 T_i^3 + c_5 T_i^{-2}, \quad (7)$$

$$u_{leak} = \frac{\dot{m}_{leak}}{\rho_{y_2} A_{leak}}. \quad (8)$$

Here, $c_1$, $c_2$, $c_3$, $c_4$, and $c_5$ are constants parameters. For hydrogen, these parameters can be found from [9]. The model does not consider the heat transfer through the pipe wall. The equation (1), (2), and (3) can be presented in compact vector form with conservative variables,

$$\frac{\partial \mathbf{U}}{\partial t} = -\frac{1}{dx}\left(\mathbf{F}_{i+\frac{1}{2}} - \mathbf{F}_{i-\frac{1}{2}}\right) + \mathbf{S}_i \quad (9)$$

where,

$$\mathbf{U} = \begin{pmatrix} \rho \\ \rho u \\ e \end{pmatrix}, \qquad \mathbf{F}(\mathbf{U}) = \begin{pmatrix} \rho u \\ \rho u^2 + p \\ \frac{1}{2}\rho u^3 + \rho u c_p T \end{pmatrix}, \mathbf{S}(\mathbf{U}) = \begin{pmatrix} \frac{1}{A_p \Delta x}\dot{m}_{leak} \\ \frac{1}{A_p} f \frac{2}{D}\rho u^2(\pi D \Delta x - A_{leak}) \\ \frac{1}{A_p \Delta x}\left(\frac{1}{2}\dot{m}_{leak} u_{leak}^2 + \dot{m}_{leak} c_p T_{y_2}\right) \end{pmatrix}. \quad (10)$$

The source term contains the leak effect in the conservation laws. Equation (4) can be solved with high-resolution numerical schemes. In this study, the centered-TVD scheme is used for solving the advection term [10]. The numerical flux is calculated using the flux-limiter centered (FLIC) scheme. The SUPERBEE limiter function is used as the flux limiter. The limiter function is total energy-based. The source term is solved with the source term splitting method; the source term is solved with Runge-Kutta 4th order explicit scheme. Implementation of the FLIC scheme can be found in [11]. The time step is a variable function with flow velocity and speed of sound. The maximum absolute value of the eigenvalue of the Jacobian matrix gives the maximum velocity for time step calculation. The inlet boundary condition is fixed with constant pressure and velocity in the simulations. The outlet boundary is a zero-gradient condition.

## RESULTS AND DISCUSSION

### Model validation

The model validation is performed with experimental data from Yuan et al. [2]. The experiment was conducted for a methane pipe leak. The experimental parameters are: pipe diameter 50.8 mm; leak hole diameter 3.2 mm; pipe length 5 m; pipe inlet pressure 35 bar; inlet velocity 6.994 m/s; and horizontal pipe. The leak occurs in the middle of the pipe. In the experiment, the pressure sensor is located 3.5 m from the inlet. Figure 2 shows a comparison between simulated and experimental pressures that vary with time. Initial pipe inlet pressure is 35 bar when the leak starts at t=0. The pressure wave takes approximately 3 ms to reach the sensor location. The downstream pressure is slightly reduced after the leak begins. The simulation was stopped at 7 ms.

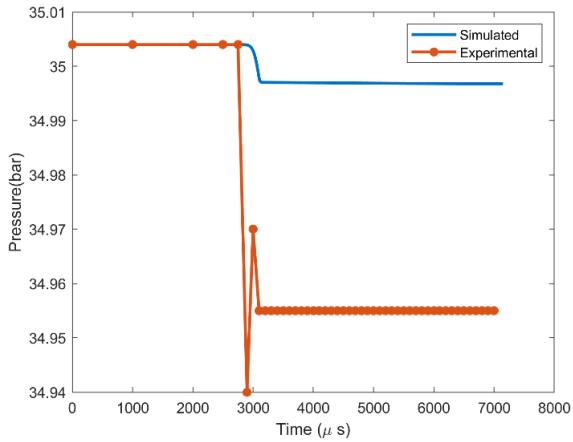


Figure 2. The model is validated with experimental results from Yuan et al. [2]. The pressure variation at 3.5 m is compared with the model predicted and the experimental results. In the experimental result, the average value is presented.

### Hydrogen pipe leak

The developed model is applied to a hydrogen distribution line. The pipe diameter is 50.8 mm. The leak hole is in the middle of the pipe. The leak hole diameter is 5 mm. The length of the pipe is 10 m. These parameters can be considered a typical example of hydrogen from storage to fuel cells. The pipe inlet hydrogen mass flow rate is 22.7 g/s and the inlet pressure is 10 bar. Figure 3 shows the

pressure variation inside the pipe after $t = 3$ ms. The leak starts at $t = 0$ s. The pipe inlet condition is constant throughout the simulation. A numerical discontinuity occurs at the leak hole control volume. At $t = 0$ s, the pipe rupture occurs. At the leak, the fluid inside the pipe is open to the atmosphere, and the high-pressure fluid moves out through the leak hole. Here it creates a sharp pressure drop in the pipe; This creates a numerical discontinuity in the leak control volume. A sharp density reduction occurs at the leak control volume. The density change in the other control volumes is small. By using the higher order numerical schemes, the spurious oscillation might be avoided. There are two expansion waves: one moves upstream, and the other moves downstream. The upstream wave speed is higher than the downstream wave speed; similar behavior has been observed from CFD simulation in [2].

The velocity profile shows a higher velocity on the left side of the leak hole and a lower velocity on the right side of the leak hole. The left expansion wave to the upstream has a higher pressure drop front than the right expansion wave: The gap between the left running head and the left running tail is higher than the right running head to the right running tail. Therefore, the velocity on the left side is higher than the velocity on the right side. The expansion waves accelerate fluid towards the leak hole.

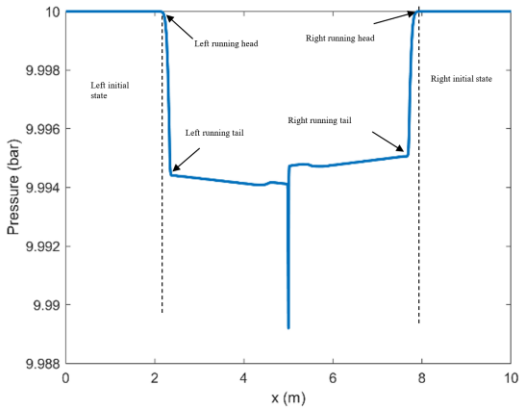


Figure 3. Pipe flow profile leak after 3ms, pipe diameter 50.8 mm, leak diameter 5 mm: Pressure

Figure 4 shows the $t - x$ plot for the pressure and velocity. Simulations are performed until 3 ms. According to the $t - x$ diagram, the wave propagation speed is $-u - a$ and $-u + a$. The speed of sound is $a = \sqrt{\gamma p/\rho}$ is not a constant; it is roughly ±l220 m/s for this case.

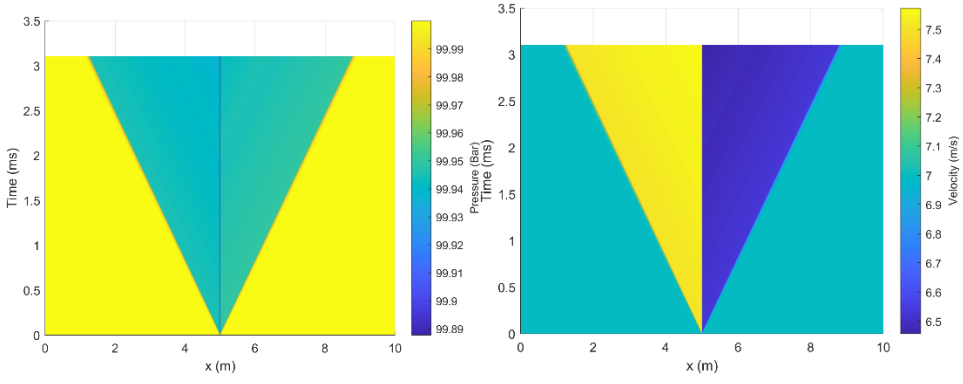


(a) (b)

Figure 4. Pipe flow profile variation with time: (a) Pressure, (b) Velocity

The hole diameter plays a significant role in the strength of the expansion waves propagating in the pipe. Figure 5 shows the pressure and velocity profiles for different leak hole diameters for the same pipe length. Simulation is shown for the leak diameters of 100 µm, 1 mm, and 5 mm for a pipe diameter of 50.8 mm. The average expansion wave scale is 2 Pa, 20 Pa, and 600 Pa for the reference pressure 1Mpa (10 bar). It is challenging to experimentally measure the tiny pressure reduction due to the small leak diameters because it needs a very sensitive pressure transducer to capture the expansion wave. The model is not suitable for very small leak diameters.

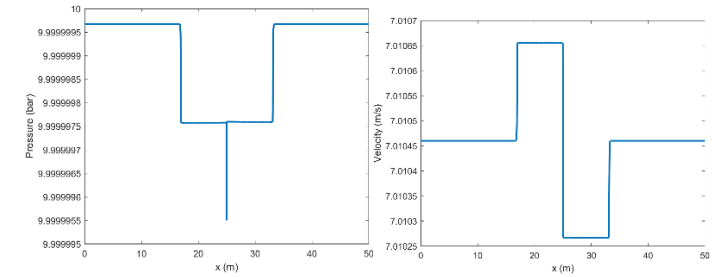


(a)

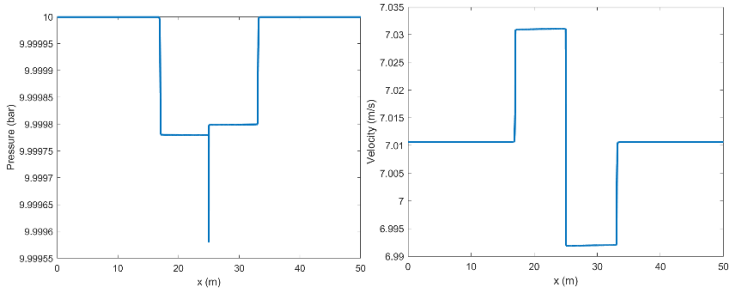


(b)

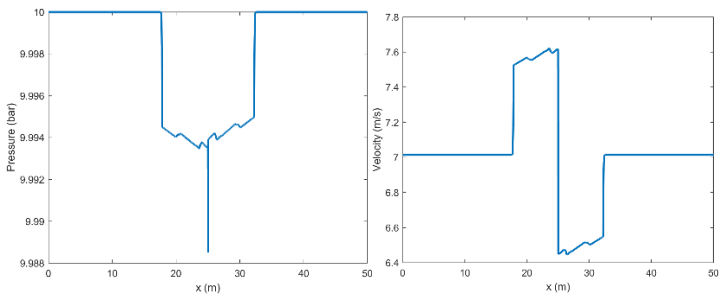


(c)

Figure 5. Pressure and velocity profile for different leak hole diameter. The pipe diameter is 50.8 mm. The simulated time is 5.9 ms to 6.6 ms. (a)$D_{leak}$ = 100 µm, $\frac{D_{leak}}{D_{pipe}}$ = 0.0019, (b)$D_{leak}$ = 1mm, $\frac{D_{leak}}{D_{pipe}}$ = 0.019, (c)$D_{leak}$ = 5 mm, $\frac{D_{leak}}{D_{pipe}}$ = 0.0984.

Figure 6 shows the pressure drop variation against the leak diameter. The pressure drop is calculated the maximum pressure at the expansion wave. The dimensionless correlation between pressure drop in the expansion wave and the pipe diameter is $\frac{dp}{p_{inlet}} = 0.068\left(\frac{D_{leak}}{D_{pipe}}\right)^2 - 0.00055\left(\frac{D_{leak}}{D_{pipe}}\right) - 3.2e^{-7}$. This correlation is import to decide the right pressure sensor to capture the expansion wave effect.

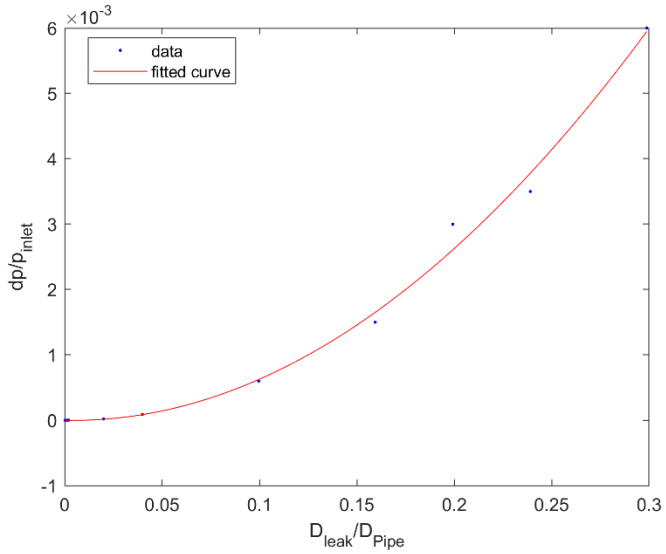


Figure 6. here shows the relation between the pressure drop due to the expansion wave in the pipe against leak diameter. The y -axis shows the ratio between the pressure drop and the pipe inlet pressure. The x-axis shows the ratio between leak diameter to the pipe diameter.

The developed model cannot identify the wave reflection from the bottom wall, as seen in Yuan [6].

The model is numerically stable for different flow rates, different inlet pressures, different pipe diameters and different hole diameters. The model works when $\frac{1}{200} < \frac{D_{leak}}{dx} < 1$. The model predicts the results for a known distance and diameter for a leak. The authors believe that the model can be used to develop a technology for early leak detection.

**Conclusion**

The study developed a transient pipe leak model. Based on the isentropic expansion and chocked flow model, a new source term was introduced. The flux-limited center scheme was applied to solve the advection term in the numerical model. The source term was solved with the source term splitting method. The model was validated with experimental results. Compared to the steady-state model in the literature, the presented model can capture the expansion wave in transient conditions. The strength of the expansion wave is a factor of leak hole diameter. It is required to have high accurate pressure transducers to capture expansion waves for small leak holes.

**Acknowledgment**

Economic support from the Research Council of Norway Project No. 327942 “Inline hydrogen loss of containment detection (HyLOCD)” is gratefully acknowledged. Collaboration work with H2NOR and Corvus Energy As are acknowledged.

**REFERENCES**

[1] Montiel H, Vílchez JA, Casal J, Arnaldos J. Mathematical modelling of accidental gas releases. Journal of Hazardous Materials 1998;59:211–33. https://doi.org/10.1016/S0304-3894(97)00149-0.

[2] Yuan F, Zeng Y, Luo R, Khoo BC. Numerical and experimental study on the generation and propagation of negative wave in high-pressure gas pipeline leakage. Journal of Loss Prevention in the Process Industries 2020;65:104129. https://doi.org/10.1016/j.jlp.2020.104129.

[3] Yuhua D, Huilin G, Jing'en Z, Yaorong F. Evaluation of gas release rate through holes in pipelines. Journal of Loss Prevention in the Process Industries 2002;15:423–8. https://doi.org/10.1016/S0950-4230(02)00041-4.
[4] Jo Y-D, Ahn BJ. A simple model for the release rate of hazardous gas from a hole on high-pressure pipelines. Journal of Hazardous Materials 2003;97:31–46. https://doi.org/10.1016/S0304-3894(02)00261-3.
[5] Chin DA. Fluid mechanics for engineers in SI units. Pearson; 2017.
[6] Yuan F, Zeng Y, Khoo BC. A new real-gas model to characterize and predict gas leakage for high-pressure gas pipeline. Journal of Loss Prevention in the Process Industries 2022;74:104650. https://doi.org/10.1016/j.jlp.2021.104650.
[7] Rui Z, Han G, Zhang H, Wang S, Pu H, Ling K. A new model to evaluate two leak points in a gas pipeline. Journal of Natural Gas Science and Engineering 2017;46:491–7. https://doi.org/10.1016/j.jngse.2017.08.025.
[8] Acton MR, Allason D, Creitz LW, Lowesmith BJ. Large Scale Experiments to Study Hydrogen Pipeline Fires. IPC2010, 2010 8th International Pipeline Conference, Volume 4: 2010, p. 593–602. https://doi.org/10.1115/IPC2010-31391.
[9] NIST. Isothermal properties for hydrogen n.d. https://webbook.nist.gov/cgi/inchi?ID=C1333740&Mask=1&Type=JANAFG&Table=on#JANAFG.
[10] Toro EF. Riemann solvers and numerical methods for fluid dynamics-A Practical Introduction. 3rd ed. Heidelberg: Springer Science & Business Media; 2009. https://doi.org/10.1007/b7976.
[11] Welahettige P. Transient drilling fluid flow in Venturi channels : comparing 3D and 1D models to experimental data 2019:1–234.

# Pressure limit of spontaneous ignition of cryogenic hydrogen in a T-shaped channel system

**Cirrone D.[1]*, Makarov D.[1], Molkov V.[1]**

*[1]Ulster University, HySAFER Centre, BT37 0QB, Newtownabbey, Northern Ireland, UK*
**Corresponding author's email: d.cirrone@ulster.ac.uk*

## ABSTRACT

Sudden releases of pressurised hydrogen may spontaneously ignite by the so-called "diffusion ignition" mechanism. Experimental and numerical studies have been performed on spontaneous ignition for compressed hydrogen at ambient temperature. There is a lack of knowledge of the phenomenon for compressed hydrogen stored at cryogenic temperatures. This study aims to close this knowledge gap by using a validated computational fluid dynamics (CFD) model to assess the effect of temperature decrease from ambient 300 K to cryogenic 80 K on the ignition dynamics. Previously used in our studies T-shaped channel system is selected as a configuration for the numerical analysis of cryogenic hydrogen ignition. The cryo-compressed hydrogen is initially separated from the air in the T-shaped channel system by an inertial burst disk (diaphragm). Simulations were carried out to determine the pressure limit leading to ignition in the configuration under investigation. It is found that the pressure limit for the cryo-compressed hydrogen at 80 K is 9.4 MPa, which is more than 3 times larger than for spontaneous ignition in the same setup for ambient temperature hydrogen (2.9 MPa).

**KEYWORDS:** "Diffusion ignition" mechanism, spontaneous ignition, cryo-compressed hydrogen, computational fluid dynamics.

## NOMENCLATURE

$b$ thickness of the diaphragm (m)
$d$ diameter of the diaphragm (m)
$k$ constant (0.92)
$P$ diaphragm burst pressure (Pa)
$t$ diaphragm opening time (s)

**Greek**

$\rho$ density of the diaphragm material (kg/m$^3$)

## INTRODUCTION

A sudden hydrogen release from a high-pressure vessel or equipment through the piping with air can be spontaneously ignited at comparatively low pressures of about 3 MPa (hydrogen at ambient temperature). This mechanism was postulated in 1973 by Wolanski and Wojcicki [1], following their observations on ignition occurrence when high-pressure hydrogen was admitted to a shock tube filled with air or oxygen. The authors suggested that ignition was caused by the high-temperature gradient at the contact surface where the oxygen heated by the primary shock wave, mixed and reacted with hydrogen due to diffusion. Experiments conducted by Bazhenova et al. [2] showed that an increase of the fuel initial temperature may cause an earlier ignition or ignition at lower pressures. Similar conclusions were reached by Golub et al. [3]. The authors investigated experimentally the effect of hydrogen pressure, temperature, and shock tube characteristics on the occurrence of spontaneous ignition. It was found that a shock tube diameter should be larger than 3 mm to obtain the ignition at hydrogen pressure below 40 MPa at ambient temperature. The authors observed a strong dependence of spontaneous ignition parameters on the initial temperature. For hydrogen pressure equal to 20 MPa, an increase of temperature from 300 K to 400 K caused a decrease in minimum shock tube diameter leading to ignition from 3 mm to 2 mm. Further experiments were conducted by Golub et al. in 2008 [4] to find the limit pressure for ignition in tubes of different lengths and cross-sectional shapes. The test on a tube with 5 mm diameter and 65 mm extension was selected by Bragin and Molkov [5] for

CFD modelling using a Large Eddy Simulation (LES) approach with Eddy Dissipation Concept (EDC) combustion sub-model with chemical kinetics. The minimum storage pressure leading to spontaneous ignition was found to be 2.04 MPa. In the following work [6], Bragin et al. simulated the experiments conducted by Golub et al. [7] on the sudden release of hydrogen from a high-pressure system into a T-shaped channel following the inertial flat burst disk rupture. Numerical simulations showed that the dynamics of the flat burst disk rupture process affects the potential for ignition and follow-up combustion, as a consequence of the difference between mixing processes of air with hydrogen for real inertial burst disk opening and idealistic instantaneous opening. Gong et al. [8] found that the shock pressure in a tube is a function of not only the storage to ambient pressures ratio, but depends also on the ratio of the characteristic shock propagation time to the burst disk (diaphragm) opening time. Overall, the mentioned experimental and numerical studies demonstrate that the pressure limit of hydrogen storage leading to spontaneous ignition depends on hydrogen temperature, the geometry of the system, the opening time of a rupture disk, etc. This work is not intended to give a comprehensive overview of spontaneous ignition studies but focuses on the effect of initial hydrogen temperature on the pressure limit for the ignition.

Hydrogen may be stored in cryo-compressed conditions, i.e. storage temperature below 120 K as generally considered for cryogenics [9] and pressures up to 35 MPa [10]. Cryo-compressed hydrogen (CcH2) storage at pressures below 20 MPa is considered to provide a better gain in gravimetric and volumetric capacities against the energy required for the compression and cooling down of the hydrogen gas [11]. Applications investigated in [12]–[14] involved insulated pressure vessels refuelled with cryogenic hydrogen at 80 K pressurised up to 30 MPa. Thus, the temperature of 80 K will be considered in the present study as representative for cryogenic releases. Following the trends observed in experimental studies on spontaneous ignition for hydrogen at temperatures higher than ambient [3], it would be expected that a decrease of temperature of compressed hydrogen to cryogenic values would require a higher pressure to obtain spontaneous ignition. However, the impact of increased density of cryogenic releases on the shock ignition process and the trade-off against the increased difficulty of igniting colder gas is unclear. A better understanding of this phenomenon is crucial for hydrogen safety engineering and the inherently safer deployment of CcH2 systems and infrastructure. To the best of the authors' knowledge, neither experimental nor numerical studies are available on the spontaneous ignition of CcH2. The present study aims to close this knowledge gap for the first time by using CFD modelling to assess the effect of temperature decrease from ambient to cryogenic 80 K on the pressure limit for spontaneous ignition and combustion dynamics. This numerical study is carried out for hydrogen releases in a T-shaped channel filled with air following an inertial flat burst disk rupture.

## PROBLEM FORMULATION AND NUMERICAL DETAILS

### Problem formulation

The case selected for the numerical analysis is the sudden release of hydrogen from a high-pressure system into a T-shaped channel following the inertial flat burst disk rupture. The geometry of the system is shown in Fig. 1a. It reproduces the experimental setup [7] and follows the previous numerical study at ambient temperature [6]. The high-pressure system is composed of a 210 mm long tube with 16 mm internal diameter (ID), connected to a 280 mm long tube with 10 mm ID. The flat burst disk is located at the end of the high-pressure tube and once ruptured releases hydrogen into the mock-up pressure relief device (PRD) open to the atmosphere. The PRD consists of an axial channel with a length of 48 mm and a diameter of 6.5 mm. The PRD has a flat end where two radial channels are located. These two radial channels vent hydrogen into the open atmosphere and have 6.25 mm length and 4 mm ID. A description of this hydrogen release system can be found in [6].

Simulations are performed for both ambient and cryogenic temperature to find the pressure limit leading to ignition. Table 1 shows the matrix of simulations. The resulting pressure limits for ambient temperature hydrogen are compared then to experimental and numerical tests performed in [7] and

[6] respectively. Light sensors were used in the experiments [7] to register the occurrence of spontaneous ignition. The authors [6] reported that no ignition was recorded for pressure 1.2 MPa, whereas the light was registered for tests at pressures in the range 2.43-2.90 MPa.

**Table 1. Storage pressure and temperature for selected scenarios.**

| Number of simulations | Storage temperature, K | Storage pressure, MPa |
|---|---|---|
| 6 | 300 | 1.35, 1.65, 2.43, 2.60, 2.80, 2.90 |
| 5 | 80 | 5.00, 7.50, 8.75, 9.40, 10.00 |

## CFD model and numerical details

The CFD model employed in the present study is based on the Large Eddy Simulation (LES) approach validated against tests on spontaneous ignition in different release geometries (see [4], [6]). The choice of the CFD sub-models was aimed to better represent the physical phenomenon independently from the specific features of the test geometry. In the present study, the approach was updated by using a different combustion sub-model. Simulations were carried out using ANSYS Fluent v.17.2 as a computational platform. The CFD model solved the conservation equations for mass, momentum, energy and species. The renormalization group (RNG) theory was used to model sub-grid scale turbulence, given its capability to reproduce turbulent, transitional and laminar flows [15]. The finite rate chemistry (FRC) model was used for combustion, which choice was justified by the small control volume size throughout the numerical grid. Hydrogen combustion in the air was simulated by a chemical kinetics mechanism that includes 37 elementary reactions and 18 species [16].

Figure 1a shows details of the numerical domain. A control volume (CV) size equal to 250 μm was employed at the burst bisk area whereas CV size 400 μm was maintained along the axial channel. An hexahedral mesh was employed in the axial channel, as in this portion of the TPRD it could be expected a reasonable alignment of the flow with the structured mesh. This choice was deemed to limit an eventual "numerical diffusion". CV size of 200 μm was used in the zone of intersection between the axial and radial channels. A tetrahedral mesh with smaller CV size was implemented at the intersection, as deemed to better represent the expected more complex structure of the flow and the shock in comparison to the axial channel. CV size was gradually increased to 10 mm in the far-field from the PRD. The total number of CVs was 417,685.

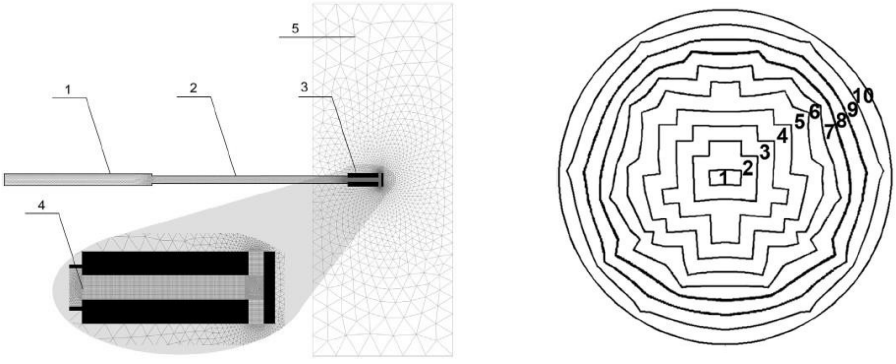


(a) (b)

**Fig. 1.** a) Central cross-section of the computational domain and numerical grid: 1 and 2 - high-pressure tubes, 3 - PRD, 4 - burst disk, 5 - external domain [6]; b) Sections of the burst disk used in the simulations to mimic its rupture process (opening in time): 1-10 are sections of the burst disk that open in series [6].

The external domain limit was modelled as non-reflecting pressure far-field boundary. Tube walls were modelled as non-slip isothermal surfaces for the case with ambient temperature hydrogen, whereas they were modelled as coupled walls made of steel for the case with cryogenic hydrogen. The specific heat at constant pressure for hydrogen at cryogenic temperatures was defined according to the NIST database [17], as a polynomial function of temperature: $c_{p,H2} = 6.97 \cdot 10^{-6}T^4 - 5.23 \cdot 10^{-3}T^3 + 1.31T^2 - 107T + 13300$. The initial air composition in the PRD (right from the burst disk) was composed of oxygen and nitrogen with mass fractions 0.23 and 0.77 respectively. At the initial moment, the ambient temperature and pressure were equal to 300 K and 101325 Pa respectively. The high-pressure tube was modelled as filled with hydrogen (mass fraction 1.0), and pressure and temperature as in [6]. An explicit method was used to solve the governing equations and a four-step Runge-Kutta algorithm was employed for the time advancement of simulations. The time step was determined from an imposed Courant Friedrichs Lewy (CFL) number of 0.3. A second-order upwind scheme with Advection Upstream Splitting Method (AUSM) was applied for flow discretisation. In the cases involving cryogenic hydrogen, it is considered that the air mixing with the expanding cold hydrogen within the TPRD will be highly heated by the shock wave at the considered pressures. Thus, the eventuality of the air components phase change was not taken into account in the present model.

Bragin et al. [6] highlighted the importance of modelling the inertial opening of the burst disk as it was found to generate more intense mixing between hydrogen and air and affect the temperature of the heated by shock air. The authors [6] simulated the non-instantaneous diaphragm opening by subdividing the flat burst disk area into 10 sections (see Fig. 1b) and by opening them in sequence. The same technique was employed in this study. The opening time, $t$, was calculated as [18]:

$$t = k\left(\frac{\rho b d}{P}\right)^{1/2}, \quad (1)$$

where $k$ is a constant equal to 0.92 (range 0.91-0.93), $\rho$ is the density of the diaphragm material, assumed to be annealed copper (8900 kg/m$^3$); $b$ and $d$ are the thickness and diameter of the diaphragm, equal to $5 \cdot 10^{-5}$ and $6.5 \cdot 10^{-3}$ m respectively; $P$ is the burst pressure (Pa). The diaphragm section opening time for each of the ten sections (for all 11 simulated burst pressure scenarios) is given in Table 2.

**Table 2. Opening times of ten burst disk sections (see Fig. 1b) for 11 simulated cases.**

| Burst disk section No. | 1 | 2 | 3 | 4 | 5 | 6 | 7 | 8 | 9 | 10 |
|---|---|---|---|---|---|---|---|---|---|---|
| Pressure, MPa | Opening times, μs | | | | | | | | | |
| 1.35 | 0 | 4.7 | 9.5 | 14.2 | 18.9 | 23.7 | 28.4 | 33.1 | 37.9 | 42.6 |
| 1.65 | 0 | 4.2 | 8.6 | 12.8 | 17.1 | 21.4 | 25.7 | 29.9 | 34.3 | 38.5 |
| 2.43 | 0 | 3.5 | 7.1 | 10.6 | 14.1 | 17.7 | 21.2 | 24.7 | 28.3 | 31.7 |
| 2.6 | 0 | 3.4 | 6.9 | 10.2 | 13.6 | 17.1 | 20.5 | 23.8 | 27.3 | 30.7 |
| 2.8 | 0 | 3.3 | 6.6 | 9.9 | 13.1 | 16.5 | 19.7 | 23.0 | 26.3 | 29.6 |
| 2.9 | 0 | 3.2 | 6.5 | 9.7 | 12.9 | 16.2 | 19.4 | 22.6 | 25.9 | 29.1 |
| 5.0 | 0 | 2.4 | 4.9 | 7.4 | 9.8 | 12.3 | 14.8 | 17.2 | 19.7 | 22.1 |
| 7.5 | 0 | 2.0 | 4.0 | 6.0 | 8.0 | 10.1 | 12.0 | 14.0 | 16.1 | 18.1 |
| 8.75 | 0 | 1.8 | 3.7 | 5.6 | 7.4 | 9.3 | 11.2 | 13.0 | 14.9 | 16.7 |
| 9.4 | 0 | 1.8 | 3.6 | 5.4 | 7.2 | 9.0 | 10.8 | 12.5 | 14.4 | 16.1 |
| 10.0 | 0 | 1.7 | 3.5 | 5.2 | 6.9 | 8.7 | 10.4 | 12.2 | 13.9 | 15.6 |

## RESULTS AND DISCUSSION

For hydrogen at ambient temperature, an initial storage pressure in the range 1.35 MPa - 2.9 MPa has been investigated. Pressure equal to 2.43 MPa is observed to not lead to the ignition. Temperature and hydroxyl (OH) mole fraction profiles are analysed to gain insights into the ignition dynamics. The mole fraction of OH is usually used as an indicator of the location of chemical reactions. Figure 2a shows the temperature profile across the symmetry plane of the axial channel. Maximum temperature reaches approximately 1500 K in the area of shock wave reflection where no hydrogen is present, see Fig. 2b. Temperatures in areas of hydrogen mixed with air are not sufficient to lead to the ignition. This is confirmed by the maximum hydroxyl mole fraction dynamics in time, which, as shown in Fig. 3, is rather negligible (horizontal line) during the entire process time when the ignition is expected (up to 90 μs). Results for storage pressures 1.35 MPa and 1.65 MPa are not shown as leading to similar results as 2.43 MPa. The absence of ignition for pressure 2.43 MPa somehow differs from the numerical study [6] where ignition was observed, even being rather weak and later self- extinguished. This non-critical difference could be associated with the difference in combustion models employed for the simulations, and the multiple modifications of the Fluent sub-models and schemes between versions v.6.3 and v.17.2. Experiments also confirmed the observations of the numerical study in [6], by recording ignition for this pressure [7].

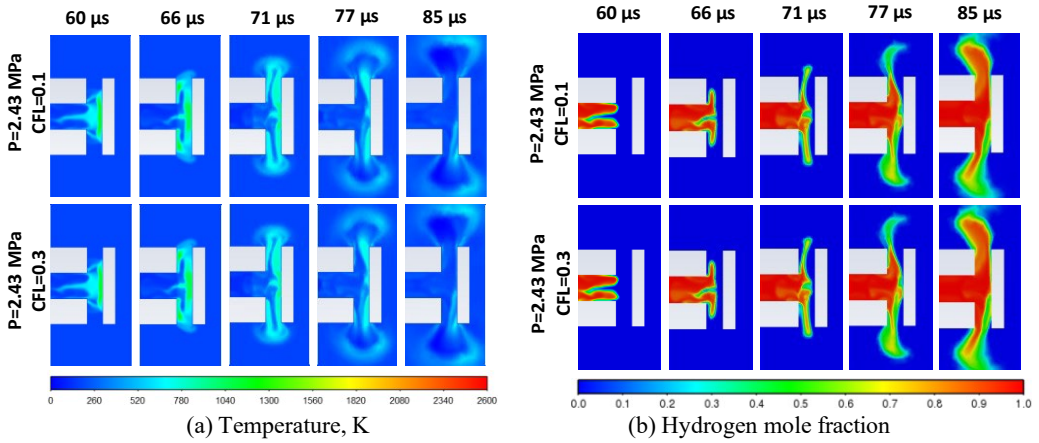


(a) Temperature, K (b) Hydrogen mole fraction

**Fig. 2.** Temperature (a) and hydrogen mole fraction (b) profiles on the symmetry plane for storage pressure of 2.43 MPa, CFL number equal to 0.1 and 0.3. The initial temperature of hydrogen is 300 K.

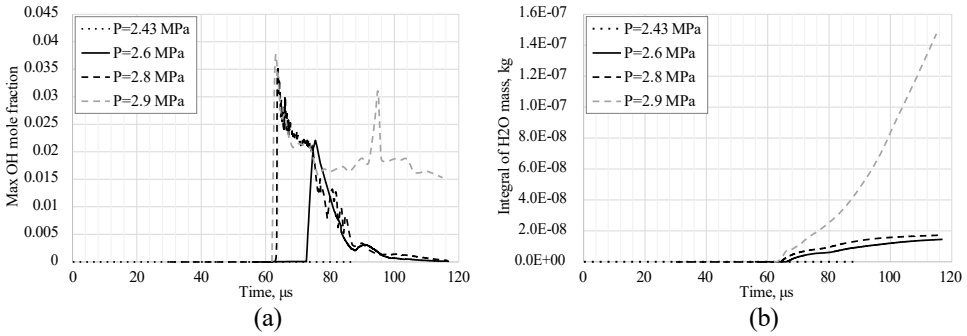


(a) (b)

**Fig. 3.** Dynamics in time across the computational domain: (a) maximum hydroxyl mole fraction, (b) integral of water vapour mass. The initial temperature of hydrogen is 300 K.

A simulation is performed for a CFL number decreased from 0.3 to 0.1 to assess time convergence of the simulation results. Figure 2 shows that the dynamics of temperature (a) and OH mole fraction (b) distributions for CFLs equal to 0.1 and 0.3 do not present any relevant and detectable difference, proving the time convergence of simulation results. Therefore, CFL=0.3 is used for the following simulations.

To find the pressure limit providing ignition, the hydrogen pressure is increased from 2.43 MPa to 2.6 MPa. Figure 4 shows the temperature and hydroxyl mole fraction in the time range 62-75 μs. Temperatures up to 2600 K are reached in the radial channels of the PRD. In the high-temperature zone, an OH mole fraction is starting to manifest local ignition at about 67 μs.

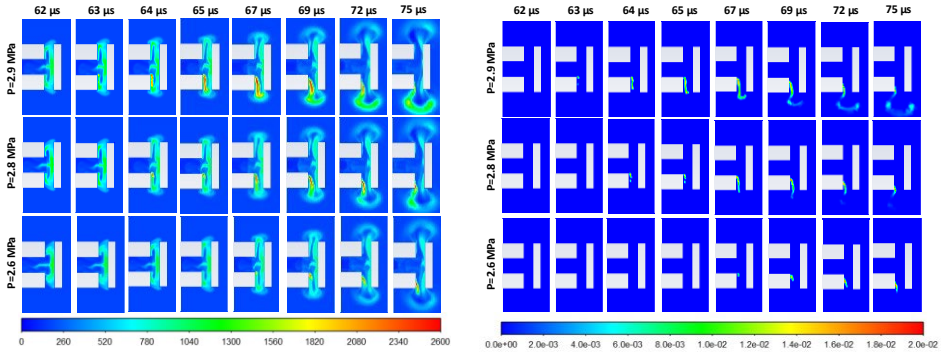


(a) Temperature, K (b) OH mole fraction

**Fig. 4.** Profiles on the symmetry plane for storage pressures 2.6, 2.8 and 2.9 MPa in time range 62-75 μs: (a) temperature, (b) hydroxyl mole fraction. The initial temperature of hydrogen is 300 K.

Figure 5 focuses on the combustion dynamics outside the PRD and shows how the OH mole fraction has completely disappeared from the symmetry plane by 90 μs for storage pressure 2.6 MPa.

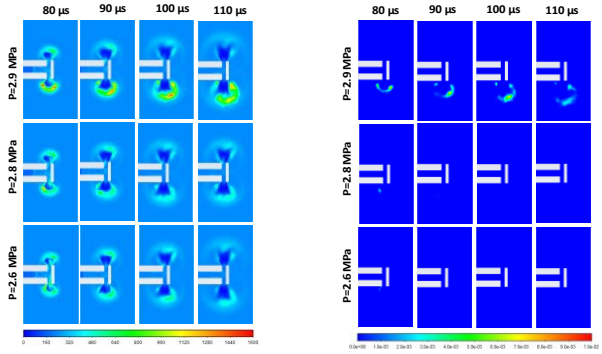


(a) Temperature, K (b) OH mole fraction

**Fig. 5**. Dynamics on the symmetry plane for storage pressures 2.6, 2.8 and 2.9 MPa in time range 80-110 μs: (a) temperature, (b) hydroxyl mole fraction. The initial temperature of hydrogen is 300 K.

Figure 6 provides a view of the reacting zone in the whole domain. It shows the volumetric distribution of OH mole fraction above the limit of 0.001, which is generally accepted as an indicator of a reacting zone in hydrogen-air flames [19]. This view gives insight into the location of any reacting zone beyond the symmetry plane. For storage pressure 2.6 MPa, at 90 μs combustion is present in a small zone just outside the bottom radial channel, and at 110 μs this has completely disappeared. This is fully in line with the maximum OH mole fraction recorded in the calculation domain and presented in Fig. 3a, which shows a peak at about 75 μs, to then decrease to zero within the following 20 μs except the case of 2.9 MPa.

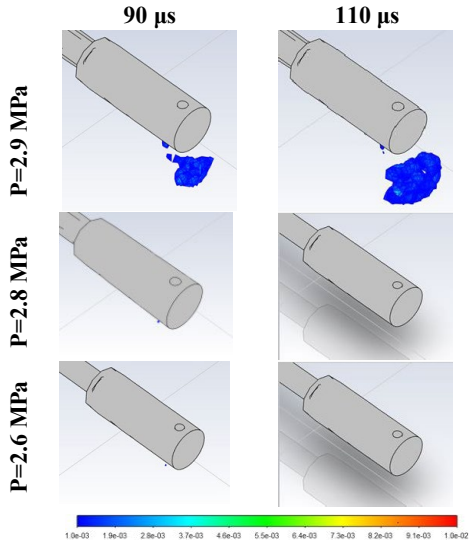


**Fig. 6.** Hydroxyl mole fraction 3D distribution for storage pressures 2.6, 2.8 and 2.9 MPa. The initial temperature of hydrogen is 300 K.

Therefore, numerical simulations demonstrate ignition at a pressure of 2.6 MPa, followed by self-extinction of reaction. The difference of 7% with the pressure limit for ignition of 2.43 MPa observed in experiments is considered of acceptable accuracy for complex engineering problems like this one. Numerical simulation for initial pressure equal to 2.8 MPa demonstrates a slightly larger and longer presence of ignition and combustion zones, but also in this case there is self-extinction of the reaction. For the initial storage pressure of 2.9 MPa, the combustion is initiated in the bottom radial channel of the PRD (see Figs. 4 and 6). A larger high-temperature zone can be observed for 2.9 MPa, with combustion initiated in a few localised spots as shown by the OH mole fraction in Fig. 4b. These mainly depend on the hydrogen concentration in the air in those locations, which is deemed to be closer to the stoichiometric concentration. Combustion develops with time into a cocoon outside the PRD, leading to sustained combustion and likely transition into a jet fire (see Fig. 5). Combustion is confirmed by the continuous presence of OH and the increase of water vapour mass in the domain (see Fig. 3). It can be observed that for all pressures in the range 2.6-2.9 MPa, the ignition process is asymmetrical and that the ignition spots are mainly concentrated in the lower radial channel. For a pressure of 2.9 MPa, external combustion is seen to be more enhanced towards the bottom side of the PRD. The asymmetry of the ignition and combustion process is deemed to be caused by the inertial and asymmetrical opening of the burst disk (see Fig. 1b). The simulation results well agree with the experimental evidence [7] and numerical study [6] demonstrating ignition and sustained reaction at initial storage pressure of 2.9 MPa.

The same procedure is applied to determine the pressure limit of spontaneous ignition for hydrogen stored at a cryogenic temperature of 80 K. The initial storage pressure was changed in the range 5-10 MPa. Figure 7 shows the temperature and hydroxyl profiles across the symmetry plane for pressures 7.5, 8.75 and 9.4 MPa, being the pressures closer to the determined pressure limit. Asymmetrical distribution of temperature at 55 µs reflects the stronger shock wave and effect of the inertial and not fully symmetrical opening of the burst disk. The higher shock wave pressure results in a higher temperature of the heated by shock air (over 2000 K). For storage pressures of 7.5 MPa and 8.75 MPa, triggering of ignition in the radial channel can be observed at 70 µs and 62 µs respectively. However, the further mixing of hot temperature air with the cryogenic temperature hydrogen leads to self-extinction of combustion by the time of 90 µs. This is confirmed by the absence of hydroxyl on the symmetry plane (Fig. 8) and in the 3D domain (Fig. 9). For a storage pressure of 9.4 MPa, ignition happens much earlier in the axial channel of the PRD. Larger high-temperature zones can be observed

in this case, as a consequence of the higher pressure of the shock wave and earlier development of combustion reactions. Figure 8 shows a combustion cocoon formed externally to the PRD. The reaction is enhanced outside the top radial channel, which is different to what was observed for atmospheric temperature hydrogen at pressure 2.9 MPa. The authours believe that this behaviour is a consequence of the different opening dynamics of the burst disk for the limiting pressures associated to the two hydrogen temperatures. The opening time for a pressure of 9.4 MPa (16.1 μs) is almost half of the time required for a pressure of 2.9 MPa (29.1 μs, see Table 2). This causes the interval of time between the opening of one burst disk section to another (see Fig. 1b) to be different by the same order of magnitude. Being the burst disk sections asymmetrical, they can easily induce an enhanced development of combustion towards the top channel for cryogenic hydrogen rather than towards the lower channel as observed for ambient temperature hydrogen. Comparing Figs. 4 and 7, it is possible to observe a larger combustion and high temperature zone for T=80 K and P=9.4 MPa (Fig. 7) in comparison to the case with ambient temperature hydrogen and P=2.9 MPa (Fig. 4). This is a direct consequence of the higher storage pressure, which does not only compansate but overcomes the decrease in combustion rate associated with the lower hydrogen temperature. The combined effect of higher pressure and lower temperature causes the hydrogen density to be up to 12 kg/m$^3$ for T=80 K. This value is similar to the density of the air compressed by the shock at the intersection of the TPRD in the ambient temperature case. Velocity of the flow is particularly enhanced for the cryogenic case, creating zones with flow velocity up to 2400 m/s at the exits from the radial channels of the TPRD.

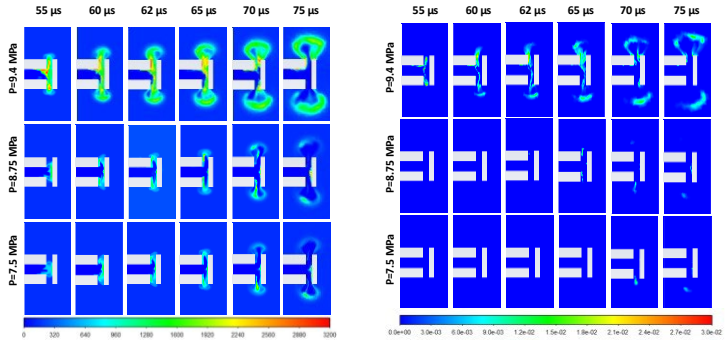


(a) Temperature, K (b) OH mole fraction

**Fig. 7.** Profiles for storage pressures of 7.5, 8.75 and 9.4 MPa in time range 55-75 μs: (a) temperature, (b) hydroxyl mole fraction. The initial temperature of hydrogen is 80 K.

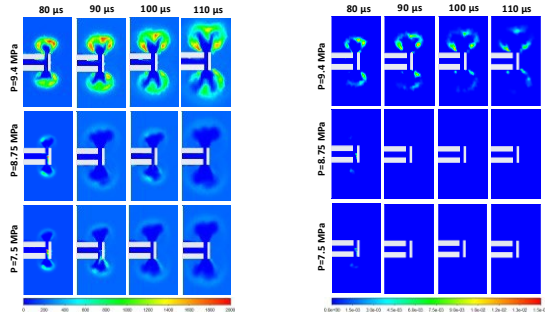


(a) Temperature, K (b) OH mole fraction

**Fig. 8.** Profiles for storage pressures of 7.5, 8.75 and 9.4 MPa in time range 80-110 μs: (a) temperature, (b) hydroxyl mole fraction. The initial temperature of hydrogen is 80 K.

Figure 9 shows the volumetric development of the reacting zone by the hydroxyl mole fraction distribution. It is concluded that pressure of 9.4 MPa leads to spontaneous ignition and likely leads to a transition into a hydrogen jet flame. It follows that for cryogenic hydrogen at 80 K, the pressure limit of spontaneous ignition is more than 3 times larger than for ambient temperature hydrogen for the considered system of the T-shaped channel. It should be underlined that these conclusions are

valid for the T-shaped channel with concrete burst disk. The storage pressure limit leading to spontaneous ignition strongly depends on the geometry and characteristics of the release system and burst disk. Furthermore, the potential for ignition occurrence at a certain pressure can be affected by the behaviour and timing of the burst disk opening, as it will affect the primary and reflected shock, and the shock-shock interactions ([20], [21], [22]). A faster rupturing rate can increase the likelihood of spontaneous ignition occurrence for a given pressure close to the limit.

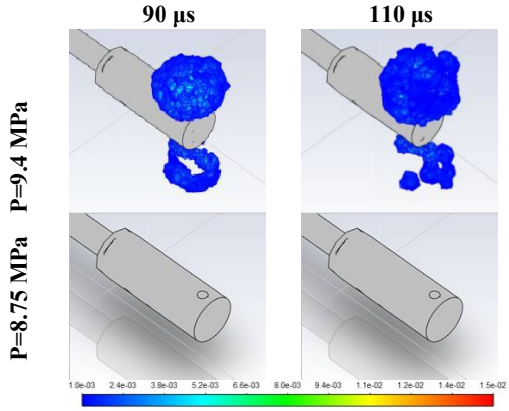


**Fig. 9.** Hydroxyl mole fraction 3D distribution for storage pressures of 8.75 MPa and 9.4 MPa. The initial temperature of hydrogen is 80 K.

## CONCLUSIONS

The originality of the research is given by the numerical investigation of the spontaneous ignition for cryo-compressed hydrogen in a T-shaped channel. Ignition and combustion dynamics were assessed in terms of temperature and hydroxyl mole fraction distributions. The significance of the research is given by the provision of a validated contemporary tool for hydrogen safety engineering to determine the pressure limits leading to spontaneous ignition for compressed hydrogen at both ambient and cryogenic temperatures. For ambient temperature hydrogen (300 K), it was found that a pressure of 2.9 MPa is required to obtain spontaneous ignition and likely transition into a jet fire outside the T-shaped channel. Pressure in the range 2.6-2.8 MPa was found to trigger ignition, later resulting in self-extinction. Simulations closely reproduce the experimentally observed pressure limit of 2.43 MPa which was sufficient to provide ignition, but not sustained jet flame. Validation of simulations against experiments established the rigour of the research. For cryogenic hydrogen (80 K), it was found that a pressure approximately 3 times larger than for warm hydrogen is required to trigger ignition and sustain combustion outside the T-shaped channel, which could likely lead to a hydrogen jet fire. The pressure limit of 9.4 MPa was found to lead to ignition and sustained jet fire in the considered setup. Simulation results showed that below this pressure, e.g. at 8.75 and 7.5 MPa, there was an ignition in the T-shaped channel which then self-extinguished, as demonstrated by the disappearance of high-temperature regions and hydroxyl species.

## ACKNOWLEDGEMENTS

This research has received funding from the Fuel Cells and Hydrogen 2 Joint Undertaking under grant agreement No 779613 (PRESLHY). The JU receives support from the European Union's Horizon 2020 research and innovation programme and the United Kingdom, Germany, Greece, Denmark, Spain, Italy, Netherlands, Belgium, France, Norway, Switzerland. The authors would like to acknowledge EPSRC for funding the project Kelvin-2 "Tier 2 High-Performance Computing Services", EP/T022175/1 and Innovate UK for funding the project "Northern Ireland Green Seas" (ID: 397841).

## REFERENCES


[1] P. Wolanski and S. Wojcicki, "Investigation into the Mechanism of Diffusion Ignition of a Combustible Gas Flowing into Oxidizing Atmosphere," in *Fourteenth Symposium (International) on Combustion*, 1973, pp. 1217–1223.

[2] T. Bazhenova, M. Bragin, V. Golub, and M. Ivanov, "Self-ignition of a fuel gas upon pulsed efflux into an oxidative medium," *Tech. Phys. Lett.*, vol. 32, no. 3, pp. 269–71, 2006.

[3] V. V. Golub *et al.*, "Shock-induced ignition of hydrogen gas during accidental or technical opening of high-pressure tanks," *J. Loss Prev. Process Ind.*, vol. 20, no. 4–6, pp. 439–446, 2007, doi: 10.1016/j.jlp.2007.03.014.

[4] V. V. Golub *et al.*, "Mechanisms of high-pressure hydrogen gas self-ignition in tubes," *J. Loss Prev. Process Ind.*, vol. 21, no. 2, pp. 185–198, 2008, doi: 10.1016/j.jlp.2007.06.012.

[5] M. V. Bragin and V. V. Molkov, "Physics of spontaneous ignition of high-pressure hydrogen release and transition to jet fire," *Int. J. Hydrogen Energy*, vol. 36, no. 3, pp. 2589–2596, 2011, doi: 10.1016/j.ijhydene.2010.04.128.

[6] M. V. Bragin, D. V. Makarov, and V. V. Molkov, "Pressure limit of hydrogen spontaneous ignition in a T-shaped channel," *Int. J. Hydrogen Energy*, vol. 38, no. 19, pp. 8039–8052, 2013, doi: 10.1016/j.ijhydene.2013.03.030.

[7] V. Golub, V. Volodin, D. Baklanov, S. Golovastov, and D. Lenkevich, "Experimental investigation of hydrogen ignition at the discharge into channel filled with air," *Phys. Extrem. states matter*, pp. 110–3, 2010.

[8] L. Gong, Q. Duan, J. Suna, and V. Molkov, "Similitude analysis and critical conditions for spontaneous ignition of hydrogen release into the atmosphere through a tube," *Fuel*, vol. 245, pp. 413–419, 2019.

[9] R. Radebaugh, "Cryogenics," *The MacMillan Encyclopedia Of Chemistry*. pp. 1–3, 2002.

[10] R. K. Ahluwalia, J.-K. Peng, and T. Q. Hua, "Cryo-compressed hydrogen storage," in *Compendium of Hydrogen Energy*, R. B. Gupta, A. Basile, and T. N. Veziroğlu, Eds. T.Q., 2016, pp. 119–145.

[11] N. T. Stetson, S. McWhorter, and C. C. Ahn, "Introduction to hydrogen storage," in *Compendium of Hydrogen Energy*, R. B. Gupta, A. Basile, and T. N. Veziroğlu, Eds. Woodhead Publishing, 2016, pp. 3–25.

[12] S. M. Aceves, G. D. Berry, and G. D. Rambach, "Insulated pressure vessels for hydrogen storage on vehicles," *Int. J. Hydrogen Energy*, vol. 23, no. 7, pp. 583–591, 1998, doi: 10.1016/s0360-3199(97)00079-7.

[13] G. Petitpas, P. Bénard, L. E. Klebanoff, J. Xiao, and S. Aceves, "A comparative analysis of the cryo-compression and cryo-adsorption hydrogen storage methods," *Int. J. Hydrogen Energy*, vol. 39, no. 20, pp. 10564–10584, 2014, doi: 10.1016/j.ijhydene.2014.04.200.

[14] T. Brunner, "BMW Hydrogen . Hydrogen Storage Workshop. Cryo-compressed Hydrogen Storage.," 2011.

[15] V. Yakhot and S. Orszag, "Renormalization group analysis of turbulence. I. Basic theory," *J. Sci. Comput.*, vol. 1, pp. 3–51, 1986.

[16] E. Gutheil, G. Balakrishnan, and F. Williams, "Structure and extinction of hydrogen-air diffusion flames.," in *Peters N, Rogg B, editors. Reduced kinetic mechanisms for applications in combustion systems.*, Springer-Verlag, Ed. New York, 1993, p. 179.

[17] I. H. Bell, J. Wronski, S. Quoilin, and V. Lemort, "Pure and Pseudo-pure Fluid Thermophysical Property Evaluation and the Open-Source Thermophysical Property Library CoolProp," *Ind. Eng. Chem. Res.*, vol. 53, no. 6, pp. 2498–2508, 2014.

[18] D. Spence and B. Woods, "A review of theoretical treatments of shock-tube attenuation," *J Fluid Mech*, vol. 19, pp. 161–174, 1964.

[19] E. M. Bulewicz and T. M. Sugden, "The recombination of hydrogen atoms and hydroxyl radicals in hydrogen flame gases," *Trans. Faraday Soc.*, pp. 1855–1860, 1958.

[20] F. L. Dryer, M. Chaos, Z. Zhao, J. N. Stein, J. Y. Alpert, and C. J. Homer, “Spontaneous ignition of pressurized releases of hydrogen and natural gas into air,” *Combust. Sci. Technol.*, vol. 179, no. 4, pp. 663–694, 2007, doi: 10.1080/00102200600713583.

[21] S. Golovastov and V. Bocharnikov, “The influence of diaphragm rupture rate on spontaneous self-ignition of pressurized hydrogen: Experimental investigation,” *Int. J. Hydrogen Energy*, vol. 37, no. 14, pp. 10956–10962, 2012, doi: 10.1016/j.ijhydene.2012.04.070.

[22] W. Kaneko and K. Ishii, “Effects of diaphragm rupturing conditions on self-ignition of high-pressure hydrogen,” *Int. J. Hydrogen Energy*, vol. 41, no. 25, pp. 10969–10975, 2016, doi: 10.1016/j.ijhydene.2016.04.211.

# Experimental Investigation of Impinging and Confined Hydrogen Jet Fires

**Meraner C.[1,*], Stølen R.[1], Li T. [1,*]**

[1] *RISE Fire Research AS, Trondheim, Norway.*
**Corresponding author's email: christoph.meraner@risefr.no, tian.li@risefr.no*

## ABSTRACT

Hydrogen is one of the most important energy carriers to replace hydrocarbon fuels. However, the specific properties of hydrogen, among others high flammability, need to be addressed to utilize hydrogen safely. A plausible fire scenario for hydrogen used in transportation is the opening of the thermal pressure relief device during a fire to prevent a rupture of the hydrogen tank. This would very likely result in an impinging and (semi-) confined hydrogen jet fire. Hydrogen jet flames have been studied extensively, and many experimental studies have documented the flame lengths and thermal radiation from horizontal and vertical hydrogen jet flames. However, data on the impact of impinging and confined hydrogen jet fires from large scale experiments are still missing. Therefore, twenty large scale hydrogen jet fire experiments and one large scale propane reference fire experiment have been conducted. From the selected experiments shown in this study, it was found that the main difference between an open impinging jet and an enclosed impinging jet fire is the extend of the high-temperature region in the steel target, while the hot spot at the impingement point is similar. Comparing the hydrogen to a propane jet fire with a comparable total chemical energy content, but constant release rate, showed that the propane jet fire led to a more uniform temperature increase in the steel target, without a local hot spot at the impingement region.

**KEYWORDS:** Confined, heat flux, hydrogen safety, impinging, jet fire.

## INTRODUCTION

When a hydrogen-powered vehicle is exposed to a fire, the content of the high-pressure hydrogen storage tank will be released via a thermal pressure relief device (TPRD) to prevent the tank from rupturing. The released hydrogen is likely to ignite and form a hydrogen jet fire. When this occurs in an enclosed environment, the hydrogen jet fire will impinge on the surrounding surfaces and may completely engulf a volume. Relevant cases for such scenarios can be all enclosures that hydrogen vehicles can enter, like tunnels, garages, bus terminals, ro-ro ships, etc. Enclosed fires have proved to be more severe than open fires in many cases because the heat from the fire can be maintained in the flame zone as the heat loss is limited by the compartment walls. These effects are observed in many different fire experiments where the increased enclosure of the fires leads to higher temperatures in the flame zone [1].

Hydrogen jet flames have been studied extensively, and many experimental studies have documented the flame lengths and thermal radiation from horizontal and vertical hydrogen jet flames. The radiative fraction of hydrogen jet fires is found to be in the 5–15% range of the total released heat and significantly lower than jet fires of hydrocarbon fuels due to the absence of $CO_2$ and soot in the combustion products of hydrogen fires [2–5].

The effect of barrier walls to mitigate the effects of hydrogen jet fires have been studied by Houf et al. [6] and by Willoughby and Royle [7]. The barrier walls were found to be effective in limiting the flame lengths, thermal exposure and overpressures on the unexposed side of the barrier. While these effects are desirable in cases where the jet fire can be shielded from people and other critical structures, the opposite effect can be seen on the fire-side of the barrier wall. This will be the case where a hydrogen jet is released in an enclosed space, and the flame is confined in the volume with other targets.

Hydrogen jet fires have also been released inside enclosures where the pressure peaking phenomenon has been studied. Experiments have been conducted by Xiao et al. in a 1 $m^3$ chamber [8] and by Lach and Gaathaug in a 14.9 $m^3$ chamber [9]. These experiments were made with small opening areas and generated potentially destructive overpressures inside the chambers with small hydrogen release rates.

Hydrogen release scenarios from fuel cell vehicles have been tested and described in the HyResponse project (hyresponse.eu) with a focus on safety for first responders to fires in hydrogen fuel cell systems. Accidental scenarios for fuel cell vehicles are tested in an open field to illustrate the hazards to first responders [10]. Proust et al. [11] characterized hydrogen flames (flame length, gas temperature and radiant fraction) released from a 900 bar reservoir through 1 mm, 2 mm and 3 mm orifices. These releases are transient blowdowns of the contents of the hydrogen tanks over a few minutes depending on the release opening diameter and tank volume, and pressure. The pressure decreases rapidly during the first stage of the release as the flow rate is higher when the tank pressure is higher.

Despite all the above-mentioned studies, to the best of the authors' knowledge, no experimental studies have been carried out concerning a realistic ignited hydrogen jet release from a fuel cell vehicle in an enclosed space. The following paper presents a series of hydrogen jet fire experiments that are designed to represent a full blowdown of the fuel from a hydrogen fuel cell vehicle inside an enclosed space where the focus is on how the impinging and enclosed transient hydrogen jet fire will expose the surrounding environment to heat. The thermal exposure of these surfaces is relevant for surfaces in spaces where hydrogen fuel cell vehicles are allowed and may cause an accidental release of its fuel in case of a fire.

## EXPERIMENTAL SETUP

### Enclosure construction and instrumentation

In order to quantify the severity of an enclosed hydrogen jet fire, the test setup was made to release a hydrogen jet fire onto steel panels representing varying degrees of enclosure and measure the thermal load to the exposed surfaces of the enclosure. The jet was ignited and directed horizontally or 45 ° down onto 3 m × 3 m panels with embedded temperature measurements. The exposed surfaces of the panels were made from 1.5 mm carbon steel, supported by a frame of 40 mm × 40 mm square steel. A total of 30 thermocouples were spot welded to the unexposed side of each steel panel in a grid with distances of 50 cm, as shown in Fig. 1 and Fig. 2. However, it should be noted that due to the limitation of the data logging system and the damage caused by the jet flame, not all the 30 thermocouples were recorded during the test for each panel. The unexposed surface is insulated with 25 mm AES wool with a density of 128 kg/$m^3$. According to the datasheet of the insulation manufacturer, the thermal conductivities measured according to the ASTM C201 method are 0.05, 0.08, 0.12, 0.18, 0.25 W/mK at 200, 400, 600, 800, 1000 °C, respectively [12].

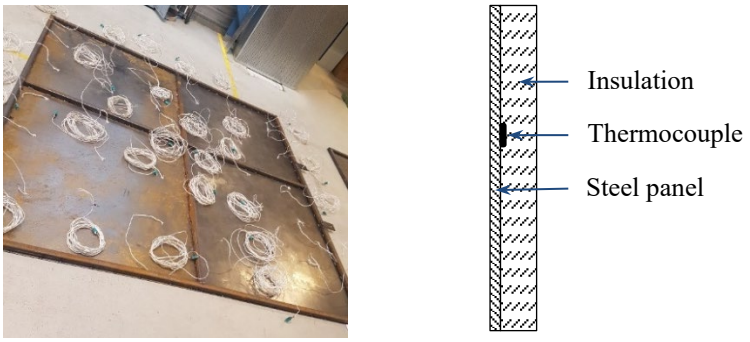


**Fig. 1.** Steel panel and thermocouples used in the test. The unexposed side prior to insulation (left). Schematic of the mounting location of the thermocouple (right).

Three different configurations were used in the test campaign: one panel on the ground, two panels (one on the ground and one rear wall), and five panels creating an enclosure with an open front. The five-panel and two-panel configurations are shown in Fig. 2. The 30 thermocouples were placed evenly on each panel used in the tests and shown in Fig. 2 (right) on the back panel. The test rig was also fully instrumented with a flow meter, a pressure transducer, and heat flux meters. In addition, visible light and infrared cameras were used to record the experiments. In total twenty-one experiments were conducted, denoted chronologically as T1 to T21, respectively. Seven of the experiments are shown in this study. The locations of the heat flux meters are listed in Table 1. Two types of flux meters were used at each location, an ellipsoidal radiometer and a total heat flux meter. All four flux meters were calibrated using a spherical black-body furnace.

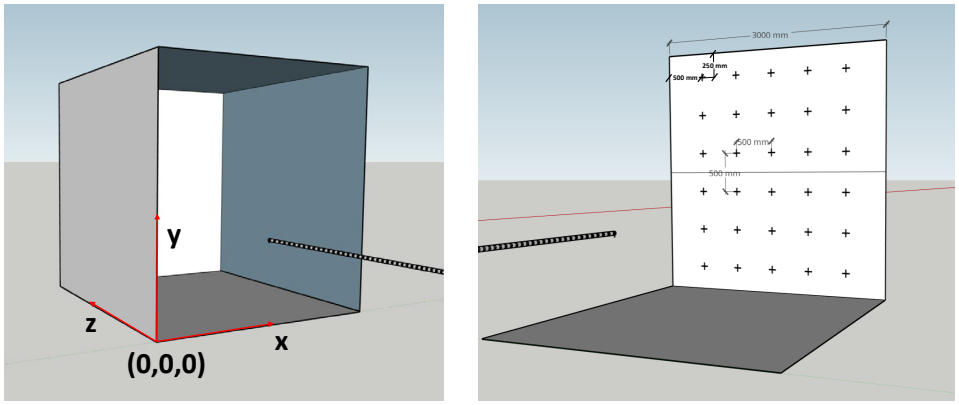


**Fig. 2.** Test setup with full open front box enclosure built with five panels (left) and open test setup with one vertical wall panel and a floor panel (right). X, Y and Z-axis are shown in red arrows.

**Table 1: Position of heat flux meters in T19 and T21. Distance in meters relative to the reference axis shown in Fig. 2. The side flux meters are mounted perpendicularly to the jet axis (facing the jet direction), and the jet flux meters are mounted parallel to the jet axis.**

| ID | Side flux meter | | | Jet flux meter | | |
|---|---|---|---|---|---|---|
| | x | y | z | x | y | z |
| T19 | 3 | 1 | 1.5 | 1.6 | 1 | 0 |
| T21 | 3 | 1 | 1.5 | 1.6 | 1 | 0 |

**Fuel supply, release, and ignition systems**

In each experiment, approximately 5 kg of hydrogen were released, which is comparable to the inventory in a passenger car where hydrogen is stored at 700 bar. However, the highest pressure available for the experiments was 300 bar. Therefore a blowdown scenario from 300 bar with a 6 mm nozzle was investigated in the experiments, comparable to hydrogen-powered passenger buses with a typical TPRD diameter of 5 mm and 350 bar reservoir pressure [13], although with a different tank volume. According to the UN ECE R134 [14], "[…] the hydrogen gas discharge from TPRD(s) of the storage system shall not be directed into enclosed or semi-enclosed spaces; into or towards any vehicle wheel housing; towards hydrogen gas containers; forward from the vehicle, or horizontally (parallel to the road) from the back or sides of the vehicle". It should be noted that "enclosed or semi-enclosed spaces" in UN ECE R134 [14] does not refer to the surroundings of cars (tunnels, garages, etc.) but to spacial volumes within the vehicle. Different vent angles and directions are possible according to these regulations. For example, in some cars, these vents are directed backwards and angled 45° down (based on personal communications with an automotive engineer), which was therefore also used as one of the release directions in the experimental campaign. In addition to the 45° release direction, a horizontal release direction was also investigated in the present study. Even though this release direction is prohibited by UN ECE R134 [14], it still can be applied for scenarios where a car is, for example, flipped after a collision. However, the main reason for a horizontal release is to compare to other experimental studies, where this direction is very common.

Hydrogen is supplied from 5 steel bottles containing 50 litres at a nominal initial pressure of 300 bar. Each bottle contains 12.3 $m^3$ hydrogen gas at standard conditions 20 °C and 1.013 bar. These bottles are connected using 4 meters long ¼″ hoses to a manifold made from 1″ branch T joints. The pressure is measured in one end of the manifold, and the gas is released towards the jet nozzle in the other end. The total volume of the manifold is approximately 0.3 litres. Following the manifold is a ball valve that is used to release the hydrogen at the test start. The ball valve is opened in approximately 0.1 seconds with ropes from a distance, estimated based on a 30 fps video footage from the experiment. A Coriolis mass flow meter with a ½″ flow tube measures the mass flow of the hydrogen. A 6 m long pipe with an internal diameter of 12 mm is connected to the mass flow meter and leads to the jet nozzle.

Two configurations of the manifold were used in the experiments (see Fig. 3). The ball valve is mounted before the pressure Coriolis mass flow meter in T1 to T16, whereas the ball valve is mounted after the flow meter in T17 to T20. Good reproducibility was obtained concerning the discharge rate and pressure in the manifold. No major differences in mass flow rates were found between tests with two different installation locations of the mass flow meter. In selected tests, a thermocouple, mounted inside the manifold, was used to monitor the temperature of the hydrogen supply system. The release history in T20 is presented as an example in Fig. 4, showing a peak release rate of 0.23 kg/s.

**Fig. 3.** Hydrogen manifold. From left to right are the pressure transducer, 5 hoses from hydrogen bottles, ball valve remotely operated by yellow ropes (left figure)/Coriolis mass flow meter (right figure), Coriolis mass flow meter (left figure)/ball valve remotely operated by yellow ropes (right figure), and the pipe leading to the jet nozzle.

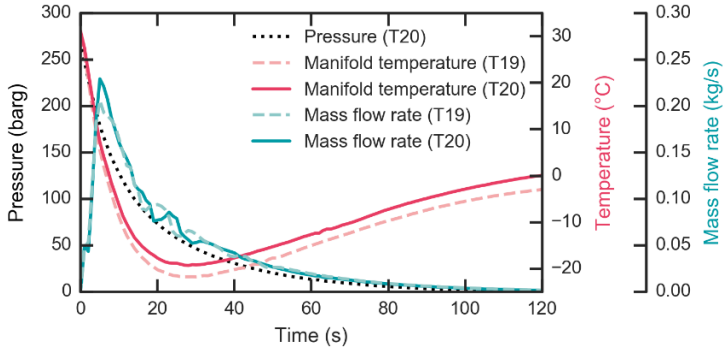


**Fig. 4.** Release mass flow rate, manifold pressure and temperature for T20.

Only one test was conducted using propane, in which the fuel delivery system is different. The ISO 22899-1 standard [15] was followed to set up the jet fire rig, resulting in a nominal flow rate of 0.3 kg/s. Note that the jet nozzle diameter is 17.8 mm, according to the standard. All experiments shown in this study were ignited using a propane gas burner mounted directly below the jet nozzle, as shown in Fig. 5. The flow of propane to the burner was stopped manually immediately after ignition. In all cases, the hydrogen jet was ignited immediately after the release.

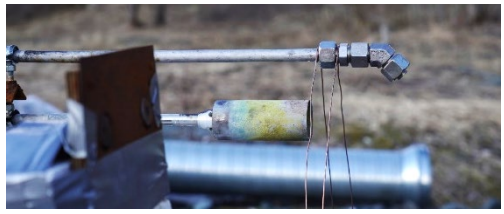

**Fig. 5.** The hydrogen supply pipe with a 45 ° angled nozzle and the propane burner.

### Experimental matrix

The experimental matrix and the corresponding weather conditions are shown in Table 2. Two release directions are included (J90: horizontal and J45: 45° down) based on the previously mentioned release scenarios. Comparisons are also made by using different enclosure configurations. It should be noted that T21 used propane as fuel.

**Table 2: Experimental matrix.**

| ID* | $T_{Ambient}$ (°C) | Relative humidity (%) | Wind speed (m/s) | Wind heading (from) | Jet direction (towards) | Jet position. x, y, z distance from origin (m) | Initial manifold pressure (barg) |
|---|---|---|---|---|---|---|---|
| T13 (J90-2p) | 10 | 60 | 0.8 | NE | N | 1.5, 1, 0 | 293 |
| T14 (J90-2p) | 9 | 66 | 1.4 | SW | N | 1.5, 1, 0 | 290 |
| T16 (J45-5p) | 10 | 81 | 0.6 | SE | N | 1.5, 1, 0 | 281 |
| T17 (J45-2p) | 5 | 62 | 0.6 | E | N | 1.5, 1, 0 | Not measured |
| T19 (J90-5p) | 22 | 45 | 0.8 | E/NE | N | 1.5, 1, 0 | Not measured |
| T20 (J45-5p) | 24 | 38 | 1.1 | NE | N | 1.5, 1, 0 | 305 |
| T21** (J90-5p) | 27 | 35 | 0.6 | E/NE | N | 1.5,1,0 | 8 |

* J*a*-*b*p, *a*: release directions in degree, *b*: numbers of panels. **Propane reference experiment.

## RESULTS AND DISCUSSION

The results are presented in the two following sections. The first section compares impinging hydrogen jet fires with confined hydrogen jet fires. The second section compares a horizontal hydrogen jet fire confined by 5 steel panels to a propane jet fire with the same configuration.

### Comparison between impinging and confined jet fires

The measured temperatures during T13, T14, and T19 are shown in Fig. 6, where the left-hand side shows the maximum steel temperature caused by a horizontal jet fire impinging onto the rear wall of a target consisting of two steel panels (T13 and T14) and a target consisting of five steel panels (T19). The time from release start to the maximum steel temperature is shown on the right-hand side of Fig. 6. Each of the "small" squares in the contour plots represents a single thermocouple measurement. Note, white squares represent locations that have not been logged. Furthermore, it can be seen that some of the measurements are apparently wrong, for example, the top left corner of the rear wall in T19. This is because some of the thermocouples lost contact with the backside of the steel panels after multiple experiments that caused the steel panels to buckle. The buckling of the steel panels was also the reason for changing the floor (i.e., bottom panel) with a new one after T16. Experiment T14 is a repetition of T13. It can be seen that the resulting steel temperatures for these two experiments are similar. Note, two thermocouples on the rear wall were broken after T13.

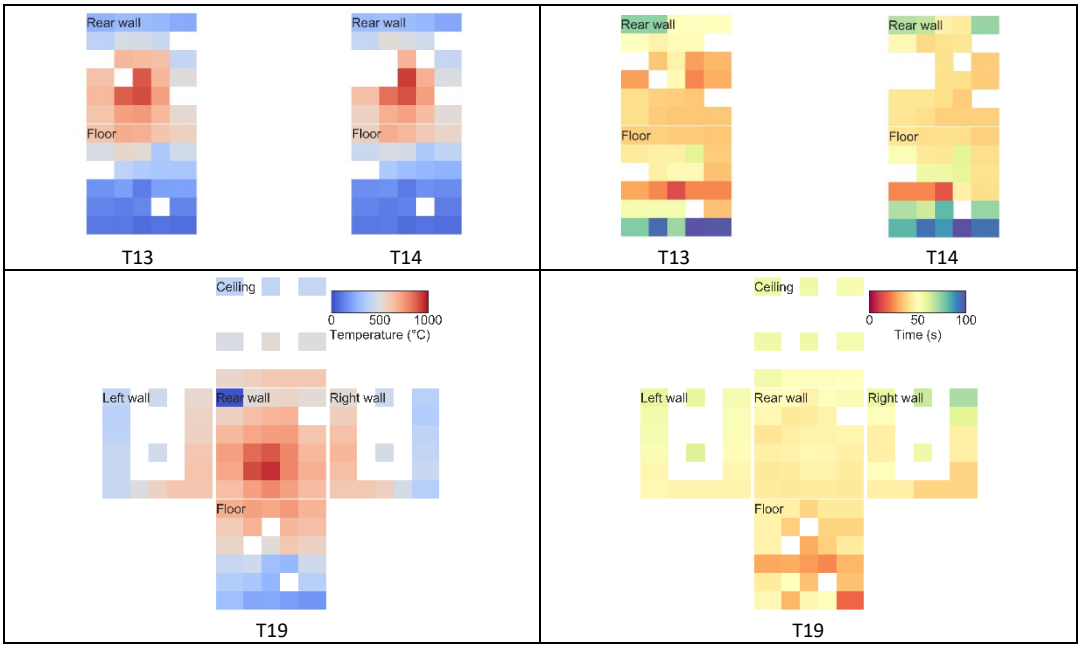


**Fig. 6.** Maximum temperature measured locally, each square representing one thermocouple, during the experiment (left). Time from the start of the release until the maximum temperature is measured (right). The experiments T13 (J90-2p), T14 (J90-2p) and T19 (J90-5p) are shown.

Both configurations, two panels and five panels, led to a similar maximum temperature of 900°C – 960°C, reached after 40–50 seconds at the rear wall. The main difference between the impinging in the confined jet fire is the extent of the high-temperature region. The entire rear wall as well as more than half of the bottom plate, exceed 500°C for the confined jet fire, while only approximately 1/3 of the bottom plate exceeds 500°C for the impinging jet fire. It can also be seen in T13 and T14 that it

takes around 75 seconds and more to reach the local maximum temperature in the regions furthest away from the impingement area, which indicates that this temperature increase is caused by the heat conduction within the steel panels, as the hydrogen mass flow rate is already significantly reduced at this point (see Fig. 4).

The lowest maximum temperatures measured for the confined jet fire (T19), around 200°C, are significantly higher compared to the impinging jet fire configuration (T13 and T14), which measured approximately 80 °C, showing the effect of the steel confinement.

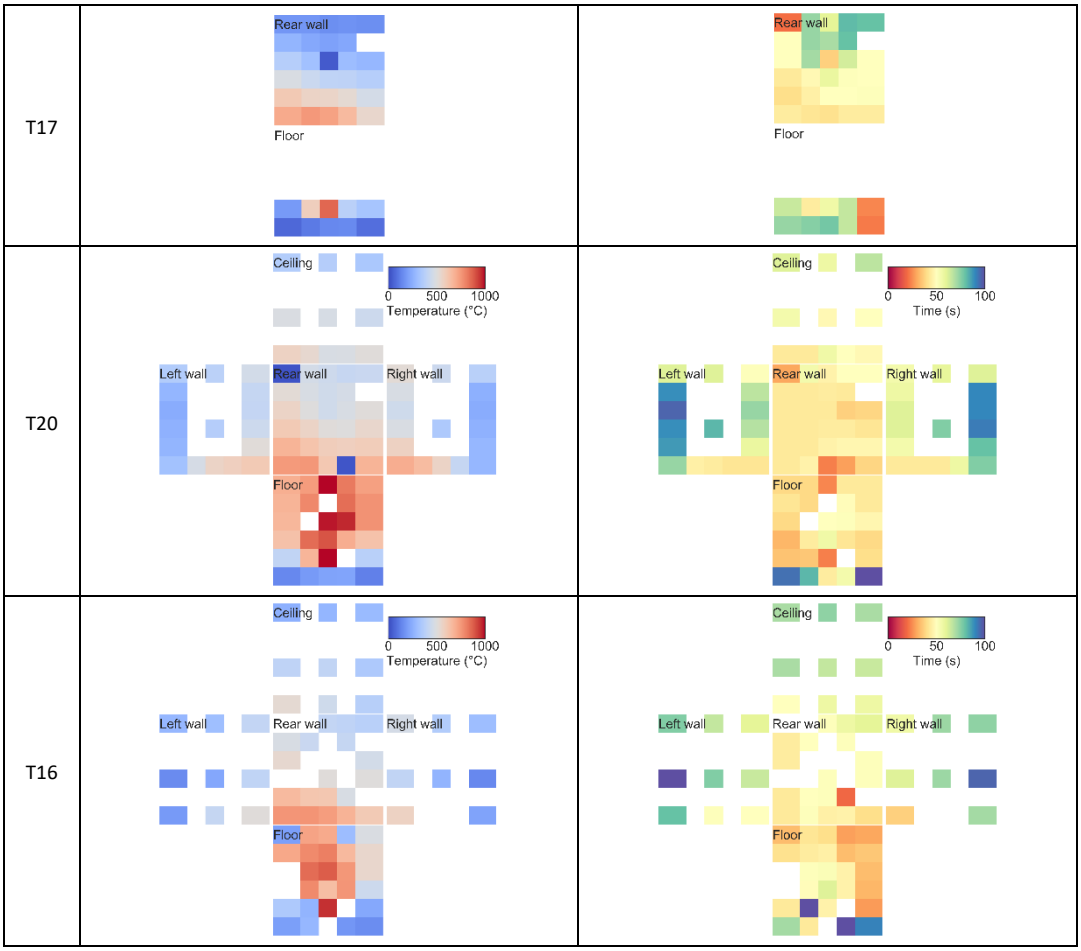


**Fig. 7.** Maximum temperature measured locally, each square representing one thermocouple, during the experiment (left). Time from the start of the release until the maximum temperature is measured (right). The experiments T17 (J45-2p), T20 (J45-5p) and T16 (J45-5p) are shown.

Fig. 7 shows the maximum temperature measured on the steel panels when the jet fire was impinging 45° downwards onto the floor panel of a target consisting of two panels (T17) and onto a target consisting of five panels (T20 and T16) on the left-hand side and the time until the local maximum is reached on the right-hand side. T20 is a repetition of T16. After T16 was conducted, the floor panel was replaced by a new one, several thermocouples have been repaired, and additional thermocouples, mainly on the side panels, were added. This could explain the larger difference between T16 and T20 compared to the difference between T13 and T14, which have been conducted right after each other on the same day.

Note that large parts of the floor panel temperature during the T17 experiment were not logged. However, the rear wall panel still provides a good comparison for the areas that are not directly impinged by the jet fire. Similar to the horizontal jet fire, it can be seen that the high-temperature region is smaller on the 2-panel target. Only the lower half of the rear wall reaches 500°C, compared to the 5-panel target.

**Comparison between hydrogen and propane jet fires**

Fig. 8 shows a comparison between a hydrogen jet fire and a propane jet fire. Both jet fires are impinging horizontally onto the rear wall of the 5-panel confinement. The top figures show the maximum local temperature (left) and time to reach the maximum for the hydrogen fire (right). The hydrogen fire is based on a blowdown scenario (see Fig. 4), while the propane jet fire is based on the ISO 22899-1 standard [15] jet fire with a constant propane mass flow rate of 0.3 kg/s. Hence, it is not possible to directly compare the two scenarios. However, the reference fire test with propane makes the 5-panel target used in this study comparable to well-known jet fire tests. Furthermore, it is possible to inspect some of the differences between the two different scenarios by selecting specific times during the propane experiment.

After 50 seconds, the chemical energy of the released propane is comparable to the total chemical energy stored in the hydrogen reservoir. A time of 50 seconds is furthermore comparable to the time when the local maximum temperatures in the hydrogen experiment are reached. The local maximum steel temperatures for T21 at this time are shown in Fig. 8. bottom left. Notably, the temperature distribution is comparable between the propane and hydrogen fire in most areas. However, the high-temperature region in the impinging zone that is visible for T19 is not present for T21.

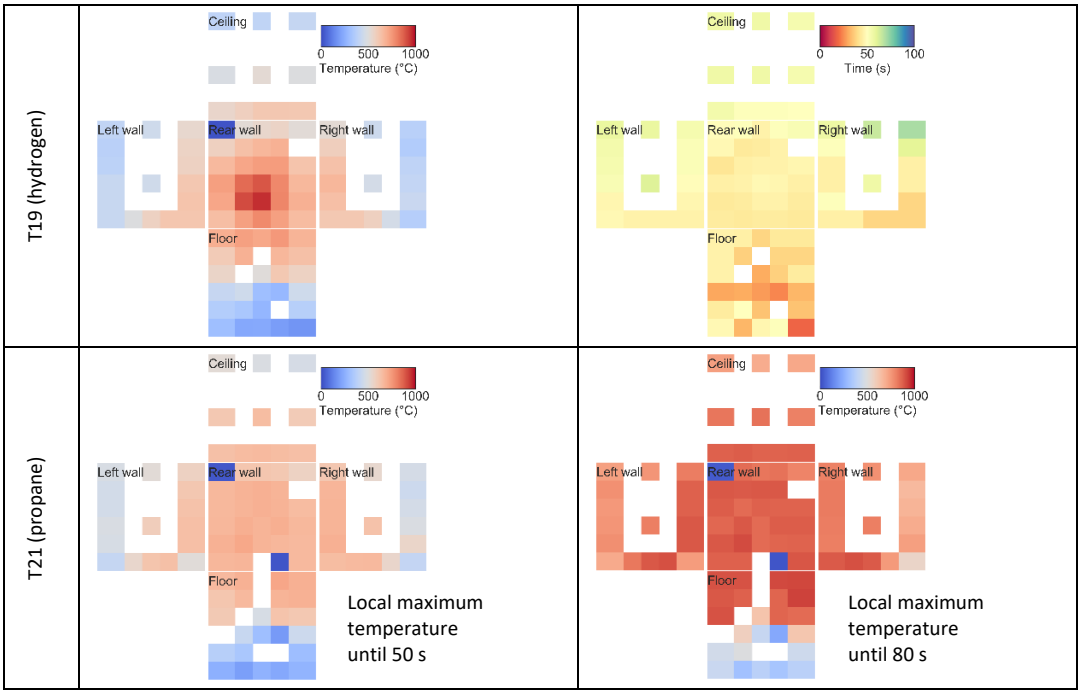


**Fig. 8.** Maximum temperature measured locally, each square representing one thermocouple, during T19 (upper left), T21 (until 50 s, lower left) and T21 (until 80 s, lower right). Time from the start of the release until the maximum temperature is measured during T19 (upper right).

After a release duration of approximately 80 seconds, the maximum steel temperature for T21 reaches similar values as the highest measured temperature in T19, which is around 960°C. The highest temperatures in the T21 experiment are interestingly first reached in the corner region of the floor panel and not around the impinging point at the rear wall. This could point to a locally underventilated fire. It was noted during the experiment that parts of the flames burned outside of the confinement. The thermal radiation between the different panels may also be a contributing factor.

Fig. 9 shows the total and radiative heat flux measured by heat flux meters facing in coaxial and heat flux meters facing perpendicular (90° to the right) direction relative to the jet release direction for the hydrogen (left) and the propane (right) jet fire. The hydrogen jet fire results immediately in a high heat flux exceeding the calibrated range of 200 kW/m$^2$ in the perpendicular direction. On the other hand, the propane experiment shows a much slower increase of the heat flux, which can be partially explained by a delay of ca. 10 seconds before the full propane flow rate is reached. The heat flux decreases following the decreasing release rate. Hence, the highest heat flux of 150 kW/m$^2$ and more, which is comparable to typical design heat fluxes used for hydrocarbon fuels, is limited to the first 20 seconds only. However, the total heat flux on the right wall is still above 20 kW/m$^2$ until 60 seconds, which can be critical in terms of fire spreading to some parts of adjacent vehicles [16].

More than half of the total heat flux to the side panel in T19 is contributed to convection at the beginning of the experiment and is considerably larger compared to the heat flux measured coaxial to the release direction. The heat fluxes decrease over time and reach a similar magnitude in both measurement locations after 20 seconds (for the radiation) to 60 seconds (for the total heat flux).

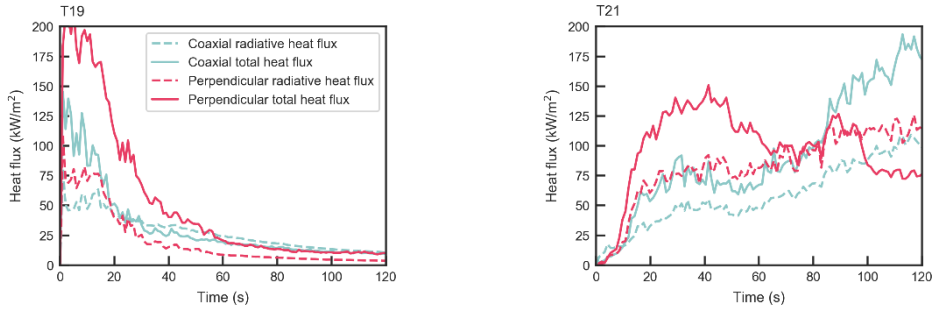


**Fig. 9.** Radiative and total heat flux measurements in coaxial (i.e., same as the jet release) and perpendicular (i.e., 90° to the right of the jet release) direction for a hydrogen jet fire (left) and a propane jet fire (right).

The radiative heat flux seen from the heat flux meter at the sidewall was larger before the 20-second mark than the heat flux measured at the release location. This is the opposite after the 20-second mark. The heat flux meter located on the sidewall sees a larger flame crosssection compared to the coaxially located flux meter, which sees more of the back wall. This means that when the radiative heat flux measured in the coaxial direction is larger than the heat flux at the sidewall, the thermal heat radiation from the hot back wall panel dominates the thermal radiation from the hydrogen flame. Note, this is a simplified view as all walls will exchange thermal radiation with each other, considering their individual viewing factors.

The measured heat flux for the propane experiment, on the other hand, is continuously increasing as the release rate is constant. This is with exception to the total heat flux measured perpendicular to the release at the right sidewall. The total heat flux and radiative heat flux are equal here, after approximately 60 seconds and the radiative heat flux is higher compared to the total heat flux after around 100 seconds. The cause for this is not known. However, it is believed the water cooling of the total heat flux meter might have been damaged during the experiment, which could have caused this behaviour. The experiments show that flame radiation seems to play a larger role in the propane jet

fire, which is in line with other studies reported in the literature. However, it should be noted that the hydrogen fire in T19 was not completely invisible and showed a yellow/orange colour, which could have been caused by contaminations in the air (e.g., particles entrained from the ground and panels).

## CONCLUSIONS

- Both configurations, two panels and five panels, led to a similar maximum temperature of 900 °C–960 °C, reached after 40–50 s. The main difference between the impinging and the confined hydrogen jet fire is the extent of the high-temperature region, which is smaller for the impinging (2-panel) configuration.
- The lowest maximum temperatures measured for the confined hydrogen jet fire (T19), around 200 °C, are significantly higher than the impinging jet fire configuration (T13 and T14), which measured approximately 80 °C.
- It appears that the heat radiation from the steel panels becomes the dominating source of thermal radiation for the hydrogen jet fire in T19 after ca. 20 seconds.
- Comparing a hydrogen jet fire with a decreasing release rate to a standard propane jet fire with a constant release rate showed a comparable temperature distribution in most areas. However, the high-temperature region in the impinging zone of the hydrogen jet fire was not visible for the propane jet fire. The comparison was conducted after 50 seconds with propane release, which gives a similar total chemical energy release as contained in the hydrogen reservoir.
- The highest temperatures in the propane experiment were first reached in the corner region of the floor panel and not around the impinging point at the rear wall, while the highest temperatures in the hydrogen experiments were measured around the impinging point.

## ACKNOWLEDGEMENT

This study is part of the $SH_2IFT$ (Safe hydrogen fuel handling and use for efficient implementation) project and the authors would like to acknowledge the financial support of the Research Council of Norway under the ENERGIX program (grant number:280964/E20).

## REFERENCES

[1] R. Stølen, A.W. Brandt, R. Wighus, Enclosure Fire Temperatures: Experimental Evidence and Standard Time-Temperature Curves, In: ISFEH19 Book of Proceedings, pp. 501–510, 2019.
[2] E.S. Fishburne, H.S. Pergament, The dynamics and radiant intensity of large hydrogen flames, Symp. Int. Combust. 17 (1979) 1063–1073.
[3] R.W. Schefer, W.G. Houf, T.C. Williams, B. Bourne, J. Colton, Characterization of high-pressure, underexpanded hydrogen-jet flames, Int. J. Hydrog. Energy 32 (2007) 2081–2093.
[4] R.W. Schefer, W.G. Houf, B. Bourne, J. Colton, Spatial and radiative properties of an open-flame hydrogen plume, Int. J. Hydrog. Energy 31 (2006) 1332–1340.
[5] A. Molina, R.W. Schefer, W.G. Houf, Radiative fraction and optical thickness in large-scale hydrogen-jet fires, Proc. Combust. Inst. 31 (2007) 2565–2572.
[6] W.G. Houf, R.W. Schefer, G. Evans, E. Merilo, M. Groethe, Evaluation of barrier walls for mitigation of unintended releases of hydrogen, Int. J. Hydrog. Energy 35 (2010) 4758 – 4775.
[7] D.B. Willoughby, M. Royle, The interaction of hydrogen jet releases with walls and barriers, Int. J. Hydrog. Energy 36 (2011) 2455–2461.

[8] J. Xiao, M. Kuznetsov, J.R. Travis, Experimental and numerical investigations of hydrogen jet fire in a vented compartment, Int. J. Hydrog. Energy 43 (2018) 10167–10184.
[9] A.W. Lach, A.V. Gaathaug, Large scale experiments and model validation of Pressure Peaking Phenomena-ignited hydrogen releases, Int. J. Hydrog. Energy 46 (2021) 8317–8328.
[10] V. Franck, A. Duclos, F. Laumann, S. Bertau, Detailed scenarios of typical accident for selected FCH systems and infrastructure, Report HyResponse D2.2, AREVA Energy Storage, 2015.
[11] C. Proust, D. Jamois, and E. Studer, High pressure hydrogen fires, Int. J. Hydrog. Energy, 36 (2011) 2367–2373.
[12] Thermal Ceramics, Data sheet FireMaster® Marine Plus blanket, 2018. https://www.morganthermalceramics.com/media/5143/fm-marine-plus-blanket-data-sheet-english.pdf, (accessed 10 January 2022).
[13] S. Brennan, D. Makarov, V. Molkov, Dynamics of flammable hydrogen–air mixture formation in an enclosure with a single vent, in Fire and Explosion Hazards, Proceedings of the Sixth International Seminar, pp. 493–503, 2011.
[14] Regulation No 134 of the Economic Commission for Europe of the United Nations (UN/ ECE) — Uniform provisions concerning the approval of motor vehicles and their components with regard to the safety-related performance of hydrogen-fuelled vehicles (HFCV) [2019/ 795]. Official Journal L 129 (2019) 43–89.
[15] ISO 22899-1:2007 Determination of the resistance to jet fires of passive fire protection materials. Part 1: General requirements. ISO Copyright office, 2007.
[16] Fire spread in car parks, Report BD2552, Building Research Establishment, 2010.

# Safety in human operation during bunkering of liquid hydrogen- Preliminary findings of CRIOP scenario analysis

**Lunde-Hanssen L.S.[1,] *, Ulleberg Ø.[2]**

[1] *Institute for Energy Technology, Control Room & Interaction Design, Halden, Norway.*
[2] *Institute for Energy Technology, Hydrogen Technology, Kjeller, Norway.*
**Corresponding author's email: linda-sofie.lunde-hanssen@ife.no*

## ABSTRACT

Hydrogen bunkering systems for ships is a relatively new concept and will lead to new challenges related to interaction between technology, people, and organization. Among key elements for safe and efficient operation is how well people involved in bunkering operations are supported in performing their tasks and making decisions. Institute for Energy Technology (IFE) is heading a national research project on the use of hydrogen in maritime applications (H2Maritime), with the goal to build new competence on the use of hydrogen and fuel cells in the maritime sector. One of the key objectives in H2Maritime project is to establish design criteria and operational philosophies for hydrogen bunkering and refuelling systems. A case study on bunkering of liquid hydrogen ($LH_2$) is currently being conducted using the crisis intervention and operability analysis (CRIOP) method, which is a human-centred approach to assess weak points and recommendations related to human factors. This paper evaluates the usefulness of this method as a tool to assess the human factors issues of human operation during bunkering and provides some initial findings from a use case involving a shore-based $LH_2$-bunkering facility for ships. The preliminary findings indicates that the method is an effective tool and has a potential for increasing the overall safety and performance of the total system by applying preventive measures with the knowledge of human factors.

**KEYWORDS:** Human factors, safety, liquid hydrogen, bunkering operations, maritime applications.

## INTRODUCTION

During the recent years, there has been a growing focus on using renewable energy and green energy carriers to reduce the carbon footprint. Hydrogen (H2) produced with zero emissions is considered a promising, environmentally friendly alternative to traditional fuel. However, several deficiencies have been identified regarding the knowledge about hydrogen, especially in terms of safety and safety barriers.

Most studies and publications related to hydrogen technology discuss safety related to the technical and physical aspects and barriers, such as performance of hydrogen technology, hydrogen behaviour, material behaviour and safety/risk zones. There are also numerous studies on technical and physical measures to mitigate the risks [1, 2, 3, 4].

In comparison, the human factors aspect of safety and the human-centred perspective in hydrogen systems is not well studied nor documented. There only exist a few papers that mention human/operator error and organisational weaknesses as possible or actual contributing factors in hydrogen accidents/incidents [5, 6, 7, 8], and even fewer recognise or discuss the importance of focusing on human factors to improve safety [9]. To our knowledge, no literature takes a human-centred approach and assess the human factors perspective to what safety barriers are needed to reduce the risks related to human operation during hydrogen bunkering. A human-centred approach that targets the human factor issues for assessing the safety barriers or measures needed to reduce the risks related to human operation during bunkering of hydrogen has not been found in any literature.

In many technological applications humans contribute in an essential way to maintain safety by controlling, supervising, monitoring, and/or intervening with the processes. This will also be the case in the operation of hydrogen bunkering systems for ships. New system concepts for hydrogen bunkering are likely to lead to new challenges related to interaction between technology, people, and

organization. Key elements for safe and efficient operation are how well people involved in bunkering operations are supported in performing their tasks and in making decisions, along with trust in automation, if automated bunkering systems are applied. Hence, to improve safety of operations it is important to assess the hazards related to human factors.

The main objective with this paper is to present a human-centred approach to assess weak points and provide recommendations related to human factors issues relevant for H2 safety in human operation of a bunkering system for ships. Institute for Energy Technology (IFE) is heading a national research project on the use of hydrogen in maritime applications (H2Maritime). One of the key objectives in the H2Maritime project is to establish design criteria and operational philosophies for hydrogen bunkering and refuelling systems. A case study on bunkering of liquid hydrogen ($LH_2$) is currently being conducted using a crisis intervention and operability analysis (CRIOP), a scenario analysis, developed by Johnsen et al. [10]. In this paper, we evaluate the usefulness of applying the CRIOP-method to assess the human factor issues related to the operation of an onshore-based $LH_2$-bunkering facility for ships (*use case*) and discuss some preliminary findings from the scenario analysis. Detailed descriptions and results that can reveal the owner of the *use case* is not included in this paper. Thus, the example of $LH_2$-bunkering facility for ships in Fig. 1 is therefore for illustration purposes only and is not use case specific.

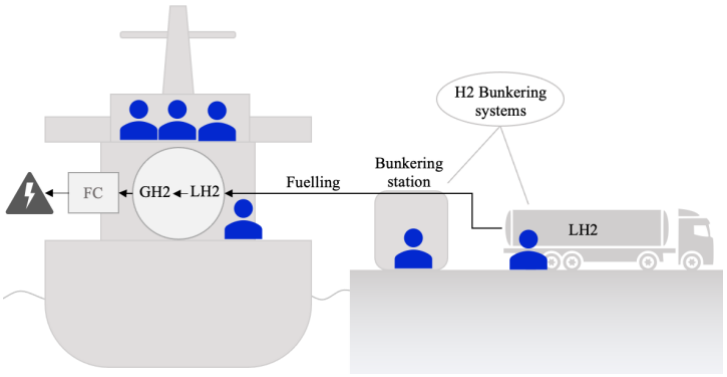


**Fig. 1.** Example of a LH2-bunkering facility for ships and possible roles in the bunkering operation team

## HUMAN-CENTRED APPROACH AND HUMAN FACTORS

A human-centred approach to design and development of safe systems concentrates on making usable and useful products for the users, with focus on their needs, and requirements, and by applying human factors considerations [11]. Solutions to problems are developed by involving the human perspective in all steps of the problem-solving process. The combination of humans and machines, or technology, in its organizational and environmental context, is considered as an overall system to be optimized [12].

The purpose of applying a human-centred approach is to improve effectiveness, efficiency, and human working conditions, and reduce possible negative effects on human health, safety, and performance [11].

Addressing human factors includes considerations about human behaviour, abilities, limitations, performance, and other human characteristics [13] as well as the complex interactions between humans, environment, tools/technology, and organisation. See the illustration in Fig. 2. The knowledge of the human factors, or the human aspect in interaction with a system in the work environment, is used to optimize the match between people and the systems in which they work - with the goal to improve safety and performance, aiming at eliminating or minimising the potential for human error [12].

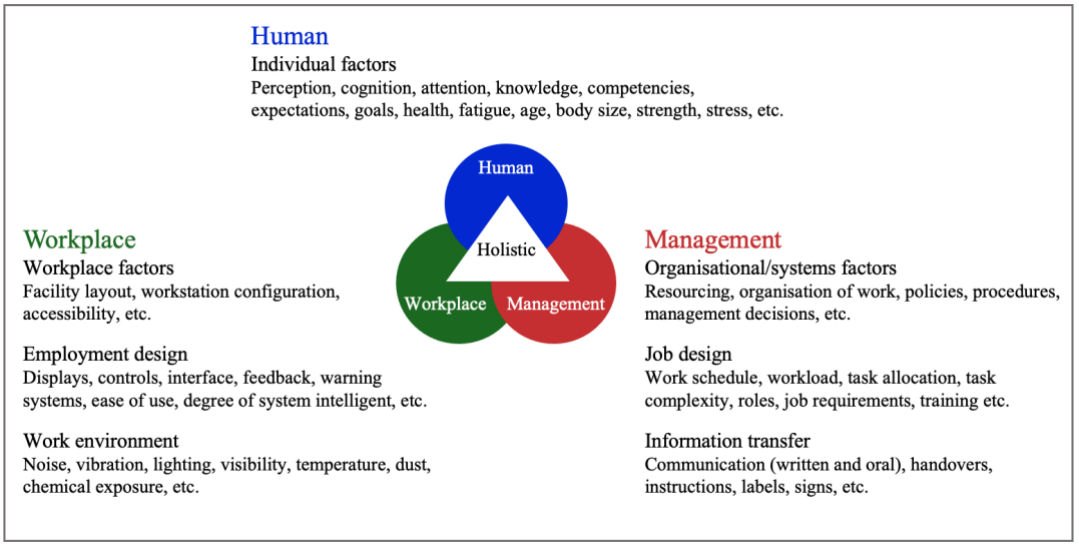


**Fig. 2**. The interaction of human factors (based on [11, 13, 18, 19])

## CHALLENGES AND POSSIBILITIES IN HYDROGEN

Hydrogen has been used for some time in the industry with highly controlled areas for storage and bunkering. Today, the use of hydrogen as a fuel is growing into the public sphere, such as commercial vehicle and maritime vessels. However, there are knowledge gaps that needs to be addressed concerning the use of hydrogen in maritime applications. This includes codes and standards, operational experience and training material, safe hydrogen bunkering, safety distances and hazardous zones [14], to name a few.

The use of hydrogen requires a sound technical design solution for bunkering and storage systems, and the right choice of components, materials, etc. due to the nature of hydrogen. Based on its safety-related properties, hydrogen can be considered a “challenging fuel”. Hydrogen is a small molecule and can easy leak through joints, seals, cracks, and even through intact materials, components, and systems. Leaks pose a risk of fire when mixed with air and has a wide flammability range [5]. In an enclosed or semi-open space, a hydrogen explosion could be a serious consequence from a hydrogen leak [14].

Hydrogen in the form of gas ($GH_2$) and liquid ($LH_2$) give different challenges. The storage of $GH_2$ requires high-pressure tanks, while the storage of liquid hydrogen requires cryogenic temperatures of -253°C to ensure that the hydrogen remains in liquid state [14]. The cryogenic temperature can pose a risk of severe frostbite when exposed to humans and damage to constructions, such as the ship hull [15]. Two key questions related to hydrogen safety from a human-centred perspective are:

1. *What are the challenges concerning human operation and performance in task execution?*
2. *What are the challenges that the personnel involved in hydrogen bunkering will face?*

Detection of hydrogen leakages and fires is a major challenge for human operation and performance during hydrogen operations. Hydrogen is a colourless and odourless gas, and clean hydrogen/air mixtures burn with an almost invisible flame [5, 14]. This implies that leakages and hydrogen-air fires are difficult to detect. The use of observation alone to assess the severity of leakages and hydrogen fires is therefore not a reliable technique. By comparison, natural gas is also odourless and colourless, but in the industry, the gas is usually added odorants to make it detectable by people. However, all known odorants contaminate fuel cells [16], which are often linked to hydrogen in power systems.

DNV (Det Norske Veritas) suggests sensor technology, such as gas detectors, acoustic leak detectors for detecting small leakages and optical sensors for detecting hydrogen fires [14].

Along with improved automation and sensor technology, more information becomes available. This creates some new challenges, including the following two key challenges: (1) How to avoid an unfortunate situation of "information overload" on the human, and (2) How to keep human "in-the loop" concerning automated actions. Hence, an appropriate level of information concerning the situation, automation actions and alarms must be provided to personnel involved in hydrogen bunkering.

There are some possibilities in technology that might be relevant for hydrogen bunkering. Remote operation and automation allow for the removal of personnel from the immediate sources of risk. Furthermore, VR (virtual reality), video surveillance, "intelligent" sensors and condition monitoring might compensate for the lack of proximity to the process during remote operation. To take advantage of the positive aspects of this, a human-centred approach would be appropriate.

## METHOD: CRIOP, SCENARIO ANALYSIS

The scenario analysis in the H2Maritime project applied the CRIOP method on a *use case* involving a shore-based $LH_2$-bunkering facility for ships. The focus of the CRIOP method is on the human aspects in terms of conditions for successful (safe and efficient) operation in control centres. The method can be applied to central control rooms, emergency control-rooms, and different types of cabins, such as the driving cabin of a train or the bridge of a boat [10].

CRIOP scenario analysis is used to validate aspects of human factors (HF) in a control room or cabin, to ensure that the control environment and required functions (support functions, equipment, rooms, etc.) enables the involved roles to operate a facility in a safe and efficient manner. The method can be applied in different stages a project, from preliminary work on different system concepts to more detailed design, final verification, and even after a period of system operation.

### Purpose of the scenario analysis

The purpose of using the scenario analysis in the *use case* of H2Maritime project was to obtain information as a basis for assessing whether the roles of the persons involved in the bunkering of hydrogen will be supported in maintaining adequate level of situational awareness and be able to make good decisions in case of challenging events, incidents, or accidents.

The objective of the scenario analysis is to assess today's design by:

- Describing demanding accident scenarios and then by
- Looking for human factors' weaknesses (problems and challenges) when performing the tasks required in the selected scenarios.

### The approach to scenario analysis

CRIOP offers a systematic analysis of scenarios. The activities involved are as follows:

3. Select scenarios
4. Develop scenarios
5. Sequentially Timed Events Plotting (STEP) diagram
6. Categorise according to the Simple Model of Cognition (SMoC)
7. Analyse tasks and identify weak points

### Scenario selection and development

In general, two or three scenarios need to be selected and described in advance of the workshop. The scenarios should contain realistic events that operators (human roles involved in bunkering) can recognize and that challenge the operations. This activity requires input from people experienced with the operations and facility. In the H2Maritime *use case* two scenarios were selected: (1) Small leak and (2) Large leak.

### STEP diagram

This activity involves describing the chosen scenarios by the means of a STEP diagram (see example in Fig. 3). The result of this activity is a stepwise description of the agents involved in the scenario and their actions. Agents include both human roles and other agents such as automation.

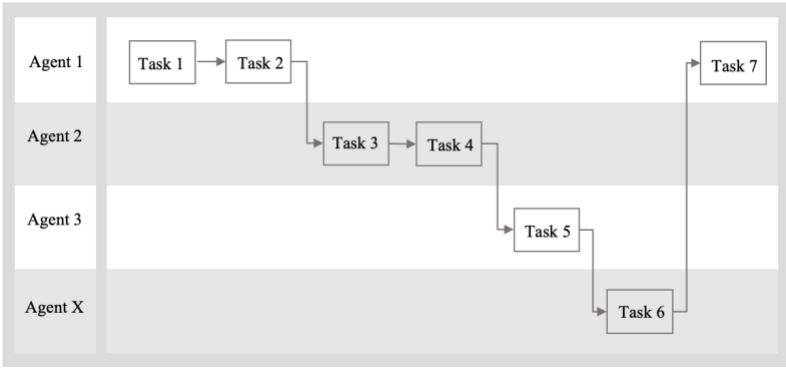


**Fig. 3.** STEP diagram example.

### Categorise according to SMoC model

To identify possible weak points, i.e., problems and challenges, that may affect the performance of tasks, the SMoC is used as a framework for the scenario analysis. Fig. 4 illustrates a modified version of SMoC from CRIOP method description [10], including a feedback loop according to Kirwan & Ainsworth [17]. This is also in line with the scenario checklist in CRIOP [10], used in the next activity of the method: Analysis of tasks and identify weak points.

Special emphasis needs to be placed on the operators' ability to observe and identify abnormal events, interpret the situation, make decisions, and perform necessary actions. Critical tasks were identified and each of these tasks were categorised according to the SMoC model (see Fig. 4).

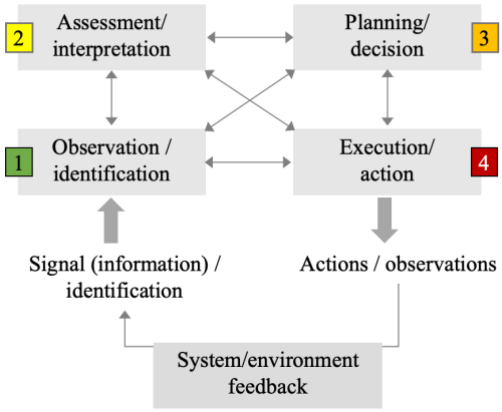


**Fig. 4.** SMoC, a simple model of human information processing.

The SMoC model illustrates four types of human information processing when handling tasks. Based on this model, a person (1) will observe and identify one or more visual or auditory signals/information, (2) interpret and organize the information that collectively provides situational awareness, (3) plan and determine what operation needs to be done after an assessment of alternative solutions, and finally (4) initiate and perform the planned action. Once the action is taken, a system or environment feedback is required to determine whether the action resulted in expected results. All four steps, from information being provided until action is taken, can affect human performance and can be a potential for errors. The type of information (e.g., sound, light, text), quality of the information provided (visible, readable, audible) can affect whether the operator sees/hears the information or not. What the information looks like, how understandable it is, in what order it is given and how reliable it is, are examples of what can affect the operator's interpretation and assessment of it, and finally the choice of any alternative decisions. Furthermore, the result can be affected by whether the execution is done at the wrong time (errors in sequence) or whether it is the correct execution on the wrong equipment or vice versa. The final step, the execution/action also addresses aspects such as motivation and the possibility to make short-cuts.

**Analysis of tasks and identify weak points**

Weak points, concerning the operators' ability to manage the scenarios can be discussed and described using the scenario checklist from the CRIOP method. This is a structured interview guide related to each step of the human information processing (see Fig. 4).

While discussing the questions in the scenario checklist, certain factors shall be considered: The focus of the scenario analysis is how roles involved in the scenario are supported regarding the factors outlined in Table 1.

**Table 1. Factors considered during scenario analysis[1] [10]**

| | |
|---|---|
| Task allocation | Time of day |
| Teamwork/ communication | Available time |
| Procedures/guidelines | Prioritisation / goal conflicts |
| Information | Competence and training |
| Human-system interface (HSI) | Work environment |
| Workload | Emergency response |

## PRELIMINARY FINDINGS

The preliminary findings include evaluation of CRIOP method as a tool to assess the human factors issues of human operation during $LH_2$-bunkering, and some initial findings from the *use case* chosen in the H2Maritime-project, involving a shore-based $LH_2$-bunkering facility for ships.

A CRIOP analysis is typically conducted in a workshop, where participants consist of a facilitator who leads the workshop, experienced persons with competence on the system and control environment to be reviewed, which for existing facilities consists of end-users (roles involved in using the facility/system for the operation) and system engineers/technical personnel from automation and instrument. A workshop with relevant participants were conducted to discuss the two chosen scenarios for bunkering operations.

The *use case* was a $LH_2$-bunkering facility under development; hence, there were no experienced end-users. The participants from the *use case* included a Captain and a Chief (in charge of the machinery onboard), who had not yet used or been trained in using the $LH_2$-bunkering system. The *use case* participants also included a Project Manager and a Project Engineer. Additionally, there was a representative with hydrogen systems expertise. The workshop was facilitated by a human factors and human-centred design specialist. More experience concerning the future facility, capabilities of the technology, and information needed might have resulted in more findings. On the other hand, postponing the scenario analysis until the end user have been properly trained and received practical experience with the operation of the $LH_2$-bunkering system would have posed other challenges. The potential for improvements is largest during the early phases of a development process and decreases as it matures.

Two scenarios were selected and described in advance of the workshop. The scenarios contained realistic events that operators (roles involved in bunkering) can recognize and that challenge operations during bunkering. One of the scenarios involved a small leakage in a $LH_2$-bunkering hose connection that develops and spreads. The main event in the other scenario involved a large leakage due to a rupture in a $LH_2$-bunkering hose.

The two scenarios [large and small hydrogen leakage] turned out to be quite similar when working with the STEP diagram. Hence, a STEP diagram was made for both scenarios, but only the small leakage scenario was analysed in detail. The major difference between the two scenarios is that the Emergency Shut Down (ESD) system is activated much earlier in the event of a large leakage. The

[1] Task allocation and communication is added to the method, as described in [10], as a result of experiences from using the method in other domains.

same operational tasks, including monitoring, inspections and troubleshooting applies for both. However, because of the condition for ESD activation, there is some difference in timing of inspection of the facility for the two scenarios.

A CRIOP scenario analysis is not a validation of the total system. The findings are related to the selected scenarios. Two scenarios including more variation of input and behaviours could have covered a broader spectrum of factors. The selection of scenarios is therefore crucial for the success of such analyses. However, a preliminary finding is that it is possible to derive some generic recommendations to the overall system design (as to interaction between human, technology, organisation, and environment) and that improvements can be given based on data material from the current use case scenario analysis. The method can for example be used to validate safe operation procedures and strengthen systems related to teamwork and allocation of responsibilities and tasks.

The collective work with the STEP diagram and discussions of topics in the scenario checklist resulted in a more detailed description of the scenarios, tasks, and responsibilities. As a result, some tasks were reallocated. Furthermore, some roles, responsibilities, and tasks, as described in the original scenarios, were altered during discussions when translating the scenario description to the STEP diagram, and further changed when discussing the topics in the scenario checklist. Questions related to whether the role is supported in performing the task (depending on available information from the intended roles´ work location and appropriate allocation of control functions) determined the need to reallocate a task. Using illustrations, pictures, drawings, and process diagrams of the $LH_2$-bunkering facility in addition to the STEP diagram was used when considering how well people involved in bunkering operations are supported in performing their tasks.

Technical functionalities related to situational awareness and prevention of unwanted actions were also discussed. However, in some cases the representatives from the owners of the *use case* were not certain whether the function would be implemented or not. The responsibilities and execution of actions during an emergency response situation were also discussed, which gave some new thoughts on the case. Two examples of some issues and questions that came up in the discussions are (1) What are the escape routes and who to evacuate when, depending on tasks that must be executed and expected severity of the situation? When is it reasonable/appropriate for the ship to leave the quay, considering risk for the ship and crew?

The scenario analysis was carried out as a group discussion of problems and possible solutions related to the events described in the scenarios. The participants were allowed to drift around other topics. In this way, the participants triggered each other to discussing important issues that were not directly related to the tasks in the scenarios. The participants were a group of professionals with different backgrounds, implying that different perspectives were brought to the discussions. The workshop also facilitated an arena for future end users to vent and get answers to concerns as well. Moreover, this was an arena for all parties to learn – about issues related to the facility and operation as well as about the different perspectives.

The participants from the use case stated that some topics discussed (findings) during the workshop had not been recognised during the HAZID and HAZOP reviews of the $LH_2$-bunkering system. They also commented that the CRIOP scenario analysis provided the opportunity for them to elevate themselves up from the technical details and evaluate the overall system, with a more holistic perspective on man, technology, organisation, and environment, and how the solution will work in practise. Thus, the method gave room for hydrogen safety discussions from a different perspective, raising new questions and giving focus to some unresolved issues.

Based on a preliminary evaluation of workshop results, it can be concluded that CRIOP is an effective tool to identify weak points and potential improvements related to safe operation of $LH_2$-bunkering systems. It is expected that the final analysis of the data collected for this case study will confirm this. Even though results from the scenario analysis have not been finalised, the preliminary findings indicates that the method can increase quality and mitigate important human factor issues.

## CONCLUSION

This paper presents a human-centred approach to assess weak points and provide recommendations related to human factors issues relevant for hydrogen safety in human operation of a $LH_2$-bunkering system for ships. Institute for Energy Technology (IFE) is heading a national research project on the use of hydrogen in maritime applications (H2Maritime). One of the key objectives in the H2Maritime project is to establish design criteria and operational philosophies for hydrogen bunkering and refuelling systems, and a case study on bunkering of $LH_2$ is currently being conducted using CRIOP scenario analysis.

In this paper, the CRIOP method is evaluated as a tool to assess the human factors issues of human operation during bunkering and provides some initial findings from a use case involving a shore-based $LH_2$-bunkering facility for ships.

The preliminary results suggest that successful integration of a hydrogen bunkering system for maritime applications should include end user representatives within system development, to bridge the gap between the requirements of the users, of other stakeholders and the system solution. The maturity of the hydrogen system and experience, both technical an operational, reflects the outcome of the method, the more competence on the total system, the more findings on weak or strong points. However, input from end users´ operational requirements and the human factors perspective is needed both early in design and iteratively throughout the design process as more knowledge is gained.

The CRIOP method appears to be a helpful tool. The workshop provided an opportunity for an interdisciplinary group, including end users, to discuss, learn and find weak points related to human factors that can influence safety. The method includes a holistic perspective on man, technology, organisation, and environment. This perspective gave the use case representatives a better understanding of how the solution will work in practise. Accordingly, the method allowed for safety discussions from a different perspective, raising new questions and giving focus to some unresolved issues.

Based on a preliminary evaluation of workshop results, CRIOP has been an effective tool to identify weak points and potential improvements. It is expected that the final analysis of workshop results will confirm this. The preliminary findings indicate that the method has a potential for increasing the overall safety and performance of the total system by applying preventive measures with the knowledge of human factors.

## ACKNOWLEDGMENTS

The work presented in this paper is a part of the H2Maritime research project, a knowledge-building project for industry (KPN project) funded by the Research Council of Norway and 5 industry partners. The authors would also like to acknowledge the useful data and information received from the owners of the liquid hydrogen bunkering facility used for the *use case* in this paper.

## REFERENCES

[1] E., Abohamzeh, F. Salehi, M. Sheikholeslami, R. Abbassi, F. Khan, Review of hydrogen safety during storage, transmission, and applications processes. Journal of Loss Prevention in the Process Industries 72 (2021) 104569

[2] F. Rigas, S. Sklavounos, Evaluation of hazards associated with hydrogen storage facilities, International Journal of Hydrogen Energy 30 (2005) 1501 – 1510

[3] Y. Feng, J. Cao, Y. Zhang, D. Jin, Safety Analysis and Risk Control of Shore-Based Bunkering Operations for Hydrogen Powered Ships. World Electric Vehicle Journal 12 (2021) 162.

[4] P. Xu, J. Zheng, P. Liu, R. Chen, F. Kai, L. Li, Risk identification and control of stationary high-pressure hydrogen storage vessel. Journal of Loss Prevention in the Process Industries 22 (2009) 950

[5] F. Yang, T. Wang, W. Deng, J. Dang, Z. Huang, S. Hu, Y. Li, Ouyang, M., Review on hydrogen safety issues: Incident statistics, hydrogen diffusion, and detonation process. International journal of hydrogen energy 46 (2021) 31467-31488.

[6] N.R. Mirza, S. Degenkolbe, W. Witt, Analysis of hydrogen incidents to support risk assessment. International Journal of Hydrogen Energy 36 (2011) 12068-12077

[7] Xu, P., Zheng, J. Liu, P., Chen, R., Kai, F., Li, L. Risk identification and control of stationary high-pressure hydrogen storage vessel. Journal of Loss Prevention in the Process Industries 22 (2009) 950–953.

[8] T. Skjold, D. Siccama, H. Hisken, A. Brambilla; P. Middha, K.M. Groth, A.C. LaFleur, 3d Risk Management For Hydrogen Installations (Hy3drm). https://h2tools.org/bibliography/3d-risk-management-hydrogen-installations-hy3drm (accessed 05.01.2022).

[9] F. Castiglia, M. Giardina, Analysis of operator human errors in hydrogen refuelling stations: Comparison between human rate assessment techniques, International Journal of Hydrogen Energy 38 (2013) 1166-1176.

[10] S.O.Johnsen, C. Bjørkli, T. Steiro, H. Fartum, H. Haukenes, J. Ramberg, J. Skriver, CRIOP: A scenario method for Crisis Intervention and Operability analysis, 2011. https://www.sintef.no/projectweb/criop/the-criop-methodology/ (accessed 12 January 2022)

[11] International Organisation for Standardization. Ergonomics of human–system interaction - Part 210: Human-centred design for interactive systems, ISO 9241-210:2010.

[12] International Organisation for Standardization. Ergonomic design of control centres – part 1: principles for the design of control centres, Geneva: ISO, first ed., 2000. ISO 11064-1.

[13] W. Karwowski, The discipline of human factors and ergonomics, in: G. Salvendy (Ed.) Handbook of human factors and ergonomics, fourth edition, John Wiley & Sons, Inc, New Jersey, 2012.

[14] DNV. Handbook for Hydrogen-Fuelled Vessels. https://www.iims.org.uk/wp-content/uploads/2021/07/Handbook_for_hydrogen-fuelled_vessels.pdf (accessed 3 September 2021)

[15] L. Van Hoecke, L. Laffineur, R. Campe, P. Perreault, S.W. Verbruggen, S. Lenaerts, Challenges in the use of hydrogen for maritime applications. Energy Environ. Sci., 14 (2021) 815-843.

[16] F. Rigas, P. Amyotte, Myths and Facts about Hydrogen Hazards, Chemical Engineering Transactions, 31 (2013) 913-918.

[17] B. Kirwan, L.K. Ainsworth (Eds.), A guide to task analysis, London, Taylor and Francis, 1992

[18] Work Safe BC. https://www.worksafebc.com/en/health-safety/hazards-exposures/ergonomics/human-factors (accessed 5 January 2022)

[19] S.J. Czaja, S.N. Nair, Human factors engineering and systems design, in: G. Salvendy (Ed.) Handbook of human factors and ergonomics, fourth edition, John Wiley & Sons, Inc, New Jersey, 2012.

# Influence of Sprinklers on the Thermal Exposure of a Tank Exposed to a Hydrogen Jet Flame

**Runefors, M.[1,*], McNamee, R.[1,2]**

*[1] Division of Fire Safety Engineering, Lund University, Lund, Sweden.*
*[2] Fire and Safety, Research Institutes of Sweden (RISE), Lund, Sweden.*
**Corresponding author's email: marcus.runefors@brand.lth.se*

## ABSTRACT

A high-pressure tank rupture is a challenging scenario requiring attention in most hydrogen applications. A common cause of rupture is an external fire heating the tank, causing increased internal pressure and/or reduction in the tensile strength of the tank material (with the relevance of each depending on tank material).

Most of the available methods for prevention of such ruptures have been developed, primarily, for buoyancy-driven flames from nearby combustible materials. However, in some applications, a rupture due to heating from a hydrogen jet, emanating from a leak on the system, also needs to be prevented. One method, that has been used in some sites in Sweden, is to use a deluge water spray system to cool the exposed tank. However, this approach has not yet been experimentally validated.

In this paper, a series of experiments are presented to assess the feasibility of such an approach. In the experiments a simulated tank is exposed to a small impinging hydrogen jet ($L_f \approx 1$ m) while simultaneously being cooled by a sprinkler system delivering water densities between 12.2 mm/min and 30.5 mm/min.

The results show that, although the temperature at most of the tank surface becomes significantly lower due to the sprinkler, temperatures can locally remain much higher ($\Delta T \approx$ 600-800K) which might still cause a rupture of a type-IV-tank. It is more likely that a sprinkler system can prevent rupture of a type-I-tank, but this has not been decisively proven.

**KEYWORDS:** Tank rupture; Jet fires; Plate-thermometers; Thermal exposure; Water film.

## INTRODUCTION

The high storage pressures needed to compensate for the low volumetric energy density of hydrogen leads to a large amount of stored mechanical energy which will be released in case of a tank rupture. This energy release is further reinforced by the feedback from the hydrogen combustion feeding into the pressure wave, which typically occurs for hydrogen [1]. Together, this leads to tank rupture potentially being a very destructive scenario which, in most situations, needs to be prevented.

There are a number of techniques available to mitigate the risk of a tank rupture, such as the installation of a temperature-activated pressure relief device (TPRD), but these need to be installed where they are directly affected by fire and, to the authors' knowledge, there are no products on the market that satisfy the pressure equipment directive for fixed installations. Alternative ways, such as Leak-Not-Burst-design [2] and intumescent painting of the tanks, has not yet been widely adopted.

All these methods have been developed primarily to prevent a rupture induced by a fire in nearby combustible material, but not for an impinging hydrogen jet flame which might in some situations be needed, at least for stationary application. One method, that has been used at some sites in Sweden, is to install a deluge water sprinkler system designed to 12.2 mm/min in water density. This density is based on the requirement in point 6.11.2.2 in NFPA 55-2020 [3], referring to Extra Hazard Group 1 according to NFPA 13 [4] for storage of flammable gases. This is used in combination with flow restriction in the hydrogen system that limits the size of potential jet flames. The underlying idea among the designers is that the water film formed on the tank surface provides enough cooling to prevent a potential impinging hydrogen jet from inducing a tank rupture.

However, a scientific underpinning of this approach is lacking. Indeed, to provide enough cooling of the tanks from hydrogen jets flames with a temperature of over 2000°C is certainly challenging. Also, the high storage pressures result in jets with potentially a very high momentum that might push the water film from the area of jet impingement.

In this paper, some experimental results are presented where a high-pressure hydrogen jet flame impinges on a metal cylinder constructed as a large plate thermometer equipped with a grid of 30 thermocouples. The influence of a deluge water sprinkler system, with different design densities, are investigated to assess whether it has a significant cooling effect on the temperatures at the area of jet impingement and if the effect is so substantial that it can affect the potential of a tank rupture.

## THEORY

### Hydrogen jet flames

Hydrogen jet flames have been extensively studied in the literature, and a broad range of correlations for flame length exist [5]. Also, there are several studies on thermal radiation emitted from such flames. However, few studies investigate the thermal structure of large-scale hydrogen diffusion flames, probably due to that this is generally less relevant for safety since the temperatures in the entire flame is high enough to provide a significant hazard for people and equipment.

Molkov [5] performed a literature review of axial temperature distribution based on three papers in the literature and found that the maximum axial temperature was 2180°C occurring at around 60-80% of the visible flame length. It can be noted that this value is very close to the theoretical upper limit, which is the adiabatic flame temperature at 2254°C. No study on the radial temperature distribution of a large-scale hydrogen diffusion flame has been identified.

Also, the literature on impinging hydrogen jets is scarce. There are some studies on the pressure effects of delayed jet ignition of impinging hydrogen jets [6], but few studies are concerned about the thermal impact of impinging jets on structures. A notable recent exception is the SH2IFT-project currently performed by SINTEF in Norway together with partners. They performed a series of impinging hydrogen jets and presented their results on a webinar on June 22nd, 2021. A scientific publication is currently underway according to direct communication with the authors. From the webinar, it can be noted that the maximum temperature measured on steel plate walls backed with ceramic wool (i.e. similar to the tank used in the current study), was approximately 1200°C and, for large jets/short distances, a cool spot were found around the stagnation zone due to impingement of unburned hydrogen. One study on the effect of sprinklers on impinging jets has been found and concluded that the sprinkler system had a moderate effect on gas temperatures, but a high effect on exposed structures [7].

### Temperature measurements using plate thermometers

The plate thermometer is a standardized measurement device used to regulate the thermal exposure during fire resistance testing in furnaces [8,9]. It is basically a 100 x 100 mm wide, and 0.7 mm thick, plate made of a nickel alloy. This plate is insulated with a 10 mm thick ceramic insulation on one side. In the centre of the metal plate, the hot junction of a type K thermocouple is attached by spot welding or screwing. During fire resistance testing, the metal side of the metal/insulation sandwich is pointing away from the test specimen, i.e. the temperature registered by the thermocouple is measuring an effective exposure temperature. As the size of the plate is 100 x 100 mm the convective heat transfer coefficient of the plate is similar to larger objects that are typically tested.

The plate thermometer concept for controlling the exposure in fire resistance furnaces was originally developed by Wickström [10]. The use of plate thermometers has then been extended and are used on a regular basis in the fire research area. In this context, concepts for using the plate thermometer for estimation of incident radiation [11] and a related methodology for heat transfer calculations based on the so-called "adiabatic surface temperature" have been developed [12,13].

## METHODS

The experiments were performed using a jet fire rig with a 0.6 mm nozzle connected to two 50 l bottles of hydrogen at approximately 176 bar pressure with a purity of above 99.9%. The jet was directed towards a simulated tank in the form of a cylinder made of 1.5 mm stainless steel with a diameter of 440 mm. The diameter was intended to simulate a Hexagon Type IV-tank with a volume of 76 l. The results are generally presented at 150 bar, 100 bar and 50 bar and, for those pressures, free-field flame length of approximately 1.1 m, 1.0 m and 0.8 m respectively can be expected based on the dimensionless flame length correlation developed by Molkov and Saffers [5]. The reservoir temperature for those calculations was estimated using adiabatic blowdown of the tanks, even if this can be expected to give too low temperatures, and therefore too long flame lengths, towards the end of the experiment since heat transfer can be expected to occur during the approximately 12 minutes of blowdown from 176 to 50 bar.

The cylinder was designed based on a plate thermometer design (see theory) with a backing of 25 mm ceramic insulation with a density of 80 kg/m$^3$. During all but one of the experiments, the cylinder was subjected to cooling with a sprinkler head delivering 12.2 to 30.5 mm/min. An overview of the experimental setup can be found in figure 1 below.

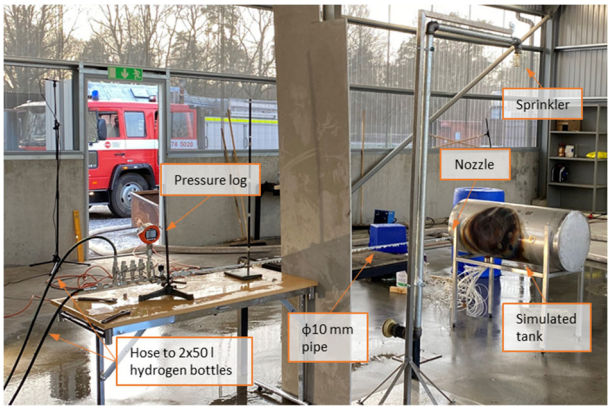


**Fig. 1.** Overview of the experimental setup.

In the simulated tank, 0.8 mm type KX ceramic fibre insulated thermocouples, with an accuracy of ±2.5°C up to 333°C and ±0.75% above that, were welded on the inside of the cylinder with a distance of 100 mm both in the horizontal direction and along the circumference. The positions are labelled so that "A0" was located at the central point of jet impingement and then the labelling was according to figure 2. In total, 30 thermocouples were used labelled from A-4 to A+5, B-4 to B+4, C-3 to C+3 and D-2 to D+2. Of these, A+2 and B-2 failed at an early stage of the experimental campaign and was therefore not included in the analysis. The temperatures were logged with a frequency of one second using a datalogger (dataTaker DT85). The distances used in the test can be found in figure 2 below.

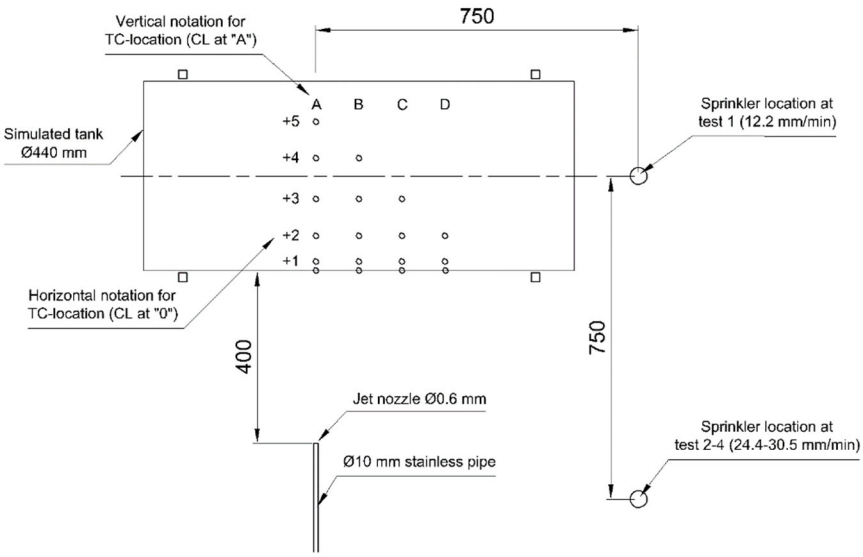


**Fig. 2.** Top-view of test setup with jet rig, simulated tank and sprinkler location.

As noted in figure 2, the sprinkler head was moved 750 mm after the first test to allow for a more direct impingement of the droplets on the most exposed location since it was found to be difficult for the sprinkler to affect that area. The sprinkler flow was based on nominal water densities in NFPA 13-2022 [4] ranging from 12.2 to 30.5 mm/min based on a 9 $m^2$ coverage area for Extra Hazard according to 10.2.4.2.1. The sprinkler system was fed from a fire truck and the flow was regulated using a needle valve and a magnetic-inductive flow meter (IFM Electronic SM9000). An overview of the test campaign and the actual densities at the point of jet impingement is found in the table below. The actual density was measured using a bucket test with a bucket of size 0.42x0.42 $m^2$ centred at the point of jet impingement and with a height of 0.6 m. The results can be found in table 1.

**Table 1. Sprinkler heads used in the different tests, nozzle pressure, nominal water density based on a 9 $m^2$ coverage area and actual density at the point of jet impingement.**

| **Test** | **Sprinkler head** | **Nozzle pressure** | **Nominal water density** (based on a 9 $m^2$ coverage area) | **Actual density at the location of jet impingement** |
|---|---|---|---|---|
| | | [bar] | [mm/min] | [mm/min] |
| 1 | Standard pendent K115 (V3406) | 0.91 | 12.2 | 6.3 |
| 2 & 3 | ESFR K-17[a] K240 (TY7226) | 0.83 | 24.4 | 13.0 |
| 4 | ESFR K-17[a] K240 (TY7226) | 1.31 | 30.5 | 17.6 |
| 5 | None | N/A | N/A | N/A |

[a] These sprinklers were intended to be standard pendent K160, but due to wrong delivery, noticed only after the experiments, an ESFR sprinkler was tested instead. This will cause the droplets to be slightly larger than intended, but the flow will be according to specification.

## RESULTS

First, some visual observations from the tests are presented, and, after that, quantitative results are shown.

### Visual observations

Snapshots of the tank at different times are given in table 2 below.

**Table 2. Snapshots of the tank mock-up at different pressure levels during the tests.**

| | 150 bar | 100 bar | 50 bar |
|---|---|---|---|
| | t = 68 s | t = 282 s | t = 688 s |
| No sprinkler | 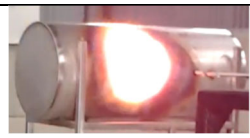 | 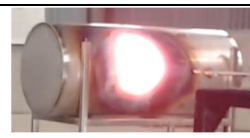 | 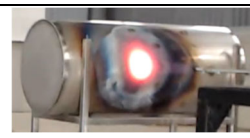 |
| 12.2 mm/min[a] | *N/A* |  | 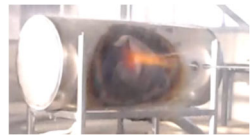 |
| 24.4 mm/min |  |  | 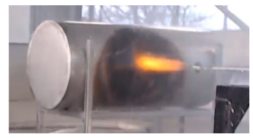 |
| 30.5 mm/min |  |  | 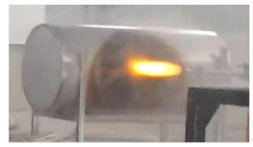 |

[a] Note that in this test, the sprinkler was placed along the tank centreline and not displaced by 750 mm as in the remaining tests.

A few things can be noted from the pictures above. At first, for the sprinkled cases at 150 bar, the point of highest temperature appear to be shifted downwards and left (i.e. away from the location of the sprinkler). Secondly, the flame length at 50 bar just barely reaches the tank, and, finally, it appears that the flame becomes more luminous as the sprinkler density increases.

### Temperature profile

The target temperature at the different locations is presented at three different pressures during the tank blowdown – 150 bar, 100 bar and 50 bar. This is complemented by the maximum temperature at each location throughout the experiment.

First, an overview of the temperature profile is given in table 3 through a visualization of the front view using ParaView. For increased readability, only the first of the two iterations at 24.4 mm/min sprinkler flow is presented. A comparison with the second iteration is presented in the discussion chapter. Parts of the tank that have colours different from the legend are not equipped with thermocouples (or the thermocouples were damaged during the experiments).

**Table 3. Overview of the temperature profiles of the tank at 150 bar, 100 bar and 50 bar as well as maximum temperature for the different tests**

| | Maximum | 150 bar | 100 bar | 50 bar |
|---|---|---|---|---|
| | | t ≈ 68 s | t ≈ 282 s | t ≈ 688 s |
| No sprinkler | 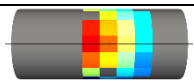 | 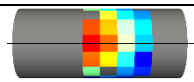 | 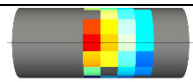 | 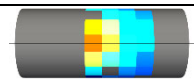 |
| 12.2 mm/min[a] | 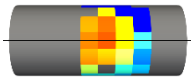 | 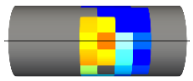 | 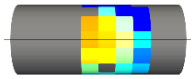 | 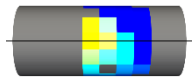 |
| 24.4 mm/min | 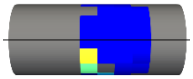 | 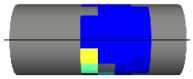 | 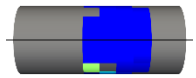 | 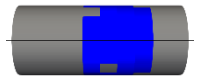 |
| 30.5 mm/min | 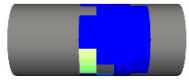 | 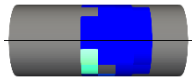 | 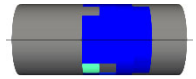 | 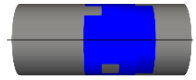 |



[a] Note that in this test, the sprinkler was placed along the tank centreline and not displaced by 750 mm as in the remaining tests.

While the profile above gives a reasonable overview of the results, the results are reiterated below in figure 3 to allow for a more quantitative comparison. The results shown are the temperatures in the vertical direction where "0" represent the point where the hydrogen jet impinges on the simulated tank.

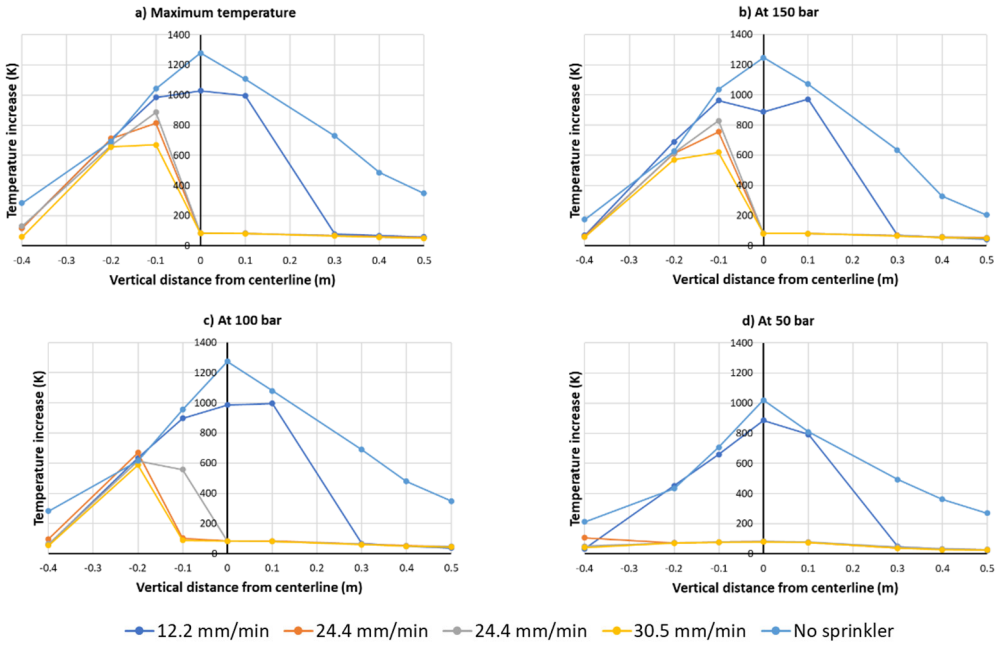


**Fig. 3.** Temperature increases along the vertical axis with zero at the point of jet impingement. Presented are maximum values for the entire experiment (a) and for three different pressures (b-d)

For the case without sprinklers, the temperature profile was quite axisymmetric, and the maximum temperature increase was 1278K which is roughly similar to the 1200K presented at the SINTEF-webinar mentioned in the theory section.

It can be noted that for the case with the lowest density (12.2 mm/min) and the sprinkler located along the centre axis of the tank, the influence on the temperature was quite high near the top of the cylinder, point 0.3-0.5, while the effect is smaller closer to the point of jet impingement. This is in line with observations during the experiment where it could be seen that the momentum from the jet acted to push away the water film formed on the tank.

For the remaining sprinkled cases, where the sprinkler was moved 750 mm to allow the droplets to more directly impinge on the front side of the tank, the effect is more substantial down to the point of jet impingement at 150 bar and slightly below at 100 bar. Below that point, the effect is neglectable at those pressures. For 50 bar, the temperature is quite low, which is likely to be due to the jet barely touching the tank and did no longer have the necessary momentum to push away the water film.

Figure 3 and table 3 show that either a measuring location is protected by a water film, causing the temperature to be approximately 100°C or below, or the sprinkler have very limited influence on the temperature. As noted above, it is also clear that pressure has an influence on the ability to form a water film. Therefore, it is of relevance to investigate the number of the 28 measuring locations that are protected by a water film (i.e. has a temperature below 100°C) as a function of pressure. This is presented in figure 4.

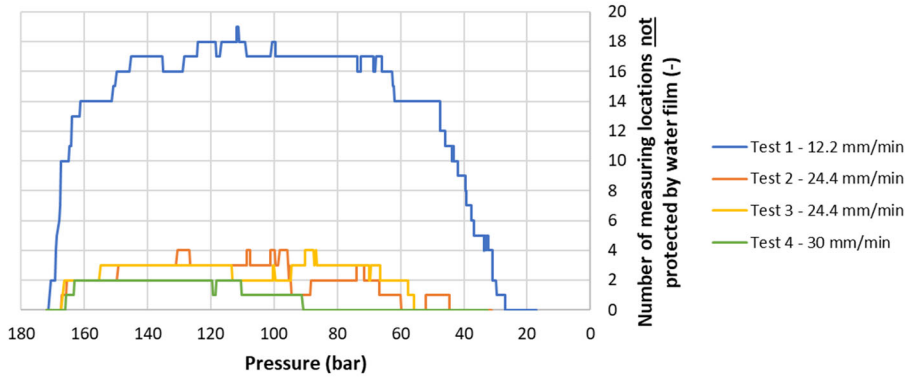


**Fig. 4.** Number of measuring locations (of 28) not protected by water film, as a function of pressure. Note the difference in sprinkler head location for test 1.

As can be seen from figure 4, more locations are being protected at the higher water densities and lower pressures since both these factors contribute to undisturbed water film formation.

## DISCUSSION

In this section, discussions on the usefulness of the approach and limitations of the study are provided.

### The influence of sprinklers on the thermal impact

The results show that a sprinkler system will provide some cooling of the tank, but locally the temperature can still increase 600-800K even for the rather small jet used in the current study. It is difficult to compare this value to bonfire tests performed according to ECE R134 since only the gas temperature are measured in that test and the flames are (more or less) engulfing the tank. However, since gas temperatures are higher compared to the tank temperature, a local failure of a Type-IV-tank

can probably be expected in less than 10 minutes when comparing to the results obtained in Makarov et al. [14]. Even if this is substantially longer than can be expected from the approximately 1300K increase in the unprotected tank, it is not likely to be acceptable in most designs. It could, however, possibly be used in combination with an emergency blowdown valve to increase the time allowed for blowdown. This has, however, not been studied in the current paper.

For a steel tank, a better performance can be expected since the sprinkler will provide a general cooling of the tanks and thereby reduce the risk of the internal pressure increase. The tank will, however, still be exposed to a hot spot. In the experiments, this temperature was in the order of 900 to 1100K which could affect the strength of the tank [15]. However, the difference between the simulated tank and a regular steel tank needs to be acknowledged. Firstly, in an actual steel tank, heat will be lost to the gas inside and redistributed, while, in the simulated tank, the inside was insulated with 25 mm ceramic wool. Secondly, the material in an actual steel tank is substantially thicker compared to the 1.5 mm steel that was used in the experiment allowing the locally high temperature to diffuse across the tank material. Because of this, it is possible that a rupture of a steel tank could be prevented by sprinkler cooling. However, more experiments are needed with, for example, different sizes of jet flames, different distances, and different sprinkler locations to confirm this.

**Repeatability**

In figure 5, a comparison between the results in the first and second test at 24.4 mm/min can be found. The comparison is for maximum temperature as well as the temperature at 150, 100 and 50 bar at all 28 locations resulting in 112 pointwise comparisons. The results from the two tests are generally in good agreement except for one substantial deviation and that is for location A-1 and 100 bar. This deviation is due to the fact that a water film was present at this location in test 2 and not in test 3. The physics of water film formation and breaking up is complex and sensitive to small perturbations in the initial conditions, and therefore, this was not unexpected. A deviation is also found at a few other locations (especially C-3 at 100 bar), but most other points, and all maximum values, showed a good agreement.

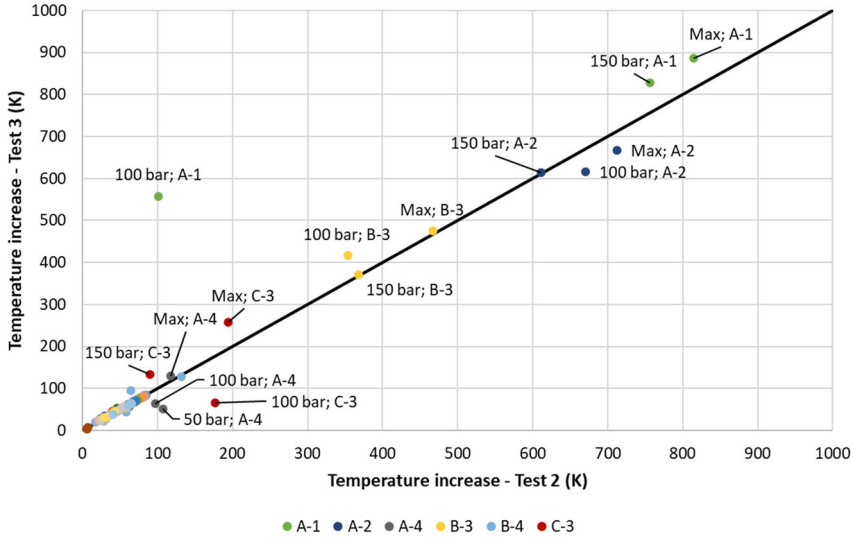


**Fig. 5.** Repeatability-diagram for the two repeats at 24.4 mm/min for maximum temperature and temperature at 150 bar, 100 bar and 50 bar for all 28 locations. Data series with all points below 100°C has been removed from legend to improve readability.

## Limitations

This current study is intended as a first test of the ability to use sprinklers to prevent tank rupture and is subject to several limitations.

One limitation is that measuring location was only placed in one direction from the point of jet impingement, this was due to an expectation of symmetry. However, since the water droplets came from one direction, the results were actually not exactly symmetric, which can be seen in figure 6 where a notable mark on the tank was visible slightly left of the A-1 measuring location. It is likely that the temperature at this location was higher which is also supported by observations presented in table 2. However, since the conclusion was that the design was generally not acceptable for type-IV-tanks and requiring more studies for type-I-tanks, the possibility of a higher temperature at this location will not affect the conclusion.

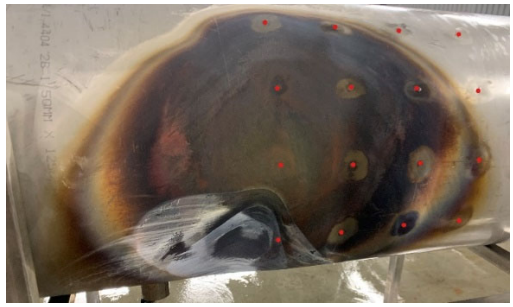

**Fig. 6.** Colour shift in the tank after the last test with sprinkler (test 4).
Measuring locations highlighted with red.

Another potential source of error was that the tank was deformed so that it buckled in approximately 1 cm near the point of jet impingement due to the expansion of the material when heated. However, this happened already during the first test, and no additional deformations were noted during the rest of the tests, so even if the deformation will lead to that the tank was not exactly cylindrical, it will still allow comparison between the different tests.

## CONCLUSIONS

When using a sprinkler system to protect a tank from a hydrogen jet fire, the primary protection mechanism is to create a water film on the tank. In the performed experimental study, the circumstances of the formation of such a film were investigated depending on the pressure of the release and the water density from the sprinkler system. In the experiments, the water film was found to cover most of the tank during the experiments, but could not form close to the point of jet impingement until the pressure of the release had been significantly reduced. This is likely due to the momentum of the jet pushing the water film. A higher water density was found to be linked to water film formation at slightly higher pressures.

The results show that, albeit a sprinkler system does provide some cooling of the tank, it cannot be expected to be able to prevent a tank rupture for a type-IV-tank even with high sprinkler densities (30.5 mm/min). It could potentially be used in tandem with an emergency blowdown valve to increase the allowable blowdown time, but this needs to be further investigated.

For type-I-tanks, sprinklers are expected be more beneficial since they will limit the pressure increase, but more studies are needed to investigate both the effect of jet flame size and if local temperature increases might induce a rupture due to reduction in tensile strength of the material.

Although not within the main scope of the current paper, it can be noted that there appears to be an increase in flame visibility with increasing water density. This might be due to impurities in the sprinkler water.

## ACKNOWLEDGEMENT

The financial support from the Swedish Civil Contingencies Agency, and the help of Carina Fredström during the experiments, is gratefully acknowledged.

## REFERENCES

[1] V. Molkov, S. Kashkarov, Blast wave from a high-pressure gas tank rupture in a fire: Stand-alone and under-vehicle hydrogen tanks, Int. J. Hydrogen Energy. 40 (2015) 12581–12603. https://doi.org/10.1016/j.ijhydene.2015.07.001.

[2] V. Molkov, D. Makarov, S. Kashkarov, Composite pressure vessel for hydrogen storage, WO 2018/149772 A1, 2018.

[3] NFPA, NFPA 55: Compressed Gases and Cryogenic Fluids Code, 2020 Edition, National Fire Protection Association, 2020.

[4] NFPA, NFPA 13: Standard for the Installation of Sprinkler Systems, 2022 Edition, National Fire Protection Association, 2022.

[5] V. Molkov, J.B. Saffers, Hydrogen jet flames, Int. J. Hydrogen Energy. 38 (2013) 8141–8158. https://doi.org/10.1016/j.ijhydene.2012.08.106.

[6] D.B. Willoughby, M. Royle, The Interaction of Hydrogen Jet Releases with Walls and Barriers, in: 3rd Int. Conf. Hydrog. Saf., 2009.

[7] T. Evanger, B. Grimsmo, V. B.E., C. Sesseng, R. Wighus, B.F. Magnussen, Large Scale Experimental and Computational Study of Fire Mitigating Effects of Water Droplet Spray Systems, in: Proc. Seventh Int. Semin. Fire Explos. Hazards, 2013.

[8] CEN, EN 1363-1:2020 Fire resistance tests - part 1: General requirements, 2020, (2020).

[9] ISO, ISO 834-1:1999 Fire-resistance tests - Elements of building construction - Part 1: General requirements, (1999).

[10] U. Wickström, A proposal regarding temperature measurments in fire resistance furnaces, SP Report 1986:17, Borås, Sweden, 1986.

[11] H. Ingason, U. Wickström, Measuring incident heat flux using the plate thermometer, Fire Saf. J. 42 (2007) 161–166.

[12] U. Wickström, R. Jansson, H. Tuovinen, Validation fire tests on using the adiabatic surface temperature for predicting heat transfer, SP Report 2009:19, Borås, Sweden, 2010.

[13] U. Wickström, Methods for Predicting Temperatures in Fire-Exposed Structures, in: M. Hurley, D. Gottuk, J.R. Hall Jr., K. Harada, E.D. Kuligowski, M. Puchovsky, J. Toreo, J.M. Watts, C. Wieczorek (Eds.), SFPE Handb. Fire Prot. Eng., Fifth, Society of Fire Protection Engineers, 2016.

[14] D. Makarov, Y. Kim, S. Kashkarov, V. Molkov, Thermal Protection and Fire Resistance of High-Pressure Hydrogen Storage, in: Proc. Eighth Int. Semin. Fire Explos. Hazards, 2016.

[15] The Engineering Toolbox, The influence of temperature on the strength of metals., (n.d.). https://www.engineeringtoolbox.com/metal-temperature-strength-d_1353.html (accessed January 27, 2022).

# CFD modelling of the entire fuelling process at a hydrogen refuelling station

**Hazhir Ebne-Abbasi[1,*], Dmitriy Makarov[1], Vladimir Molkov[1]**

*[1] HySAFER Centre, Ulster University, Newtownabbey, BT37 0QB, UK*
**Corresponding author's email: ebne_abbasi-h@ulster.ac.uk*

## ABSTRACT

Inherently safer refuelling protocols that account for heat and mass transfer in all components of fuelling line from high-pressure storage at hydrogen refuelling station through piping, pressure control valve, pre-cooler to onboard storage are of paramount importance for the deployment of hydrogen transport and infrastructure. This study aims at the development of a CFD model to simulate the hydrogen fuelling for the entire line which are currently not available. It is expected that the model will be ultimately able to simulate the fuelling of compressed gaseous hydrogen for arbitrary parameters and establish the numerical standard for the development of fuelling protocols. The CFD model is shown capable of accurately predicting hydrogen temperature and pressure through the entire hydrogen refuelling station line from the station's high-pressure tanks to onboard storage tanks. The CFD simulations accurately reproduced experimental data by Kuroki et al. (2021).

**KEYWORDS:** Hydrogen refuelling station, CFD model, compressed hydrogen, pressure control valve, pre-cooler, refuelling protocol

## INTRODUCTION

Safety is of paramount importance for the wider roll-out of hydrogen technologies including fuel cell electric vehicles (FCEV). SAE J2601 [1] specifies boundary conditions for onboard tank pressure and temperature during the fuelling process not to compromise tank integrity and to prevent its failure. Development of the fuelling protocol capable to provide fuelling time comparable with fossil fuel technologies and yet maintaining hydrogen pressure and temperature within the regulated boundaries is the challenging task the hydrogen stakeholders are currently facing.

Type IV tanks are usually made of carbon fibre reinforced polymer (CFRP) to bear the pressure load of compressed hydrogen, and hydrogen-tight plastic liner to limit permeation to the regulated level [2]. The integrity of these composite materials is endangered when they are exposed to high temperatures during fuelling due to the high compression ratio typically from 2 to 87.5 MPa for onboard storage and conversion of kinetic energy into internal energy [3]. For this reason, the fuelling protocols mentioned in SAE J2601 [1], SAE J2579 [4], ISO 15869 [5] and regulation GTR#13 [6], limit the allowable temperature inside the tank between -40°C and 85°C, and maximum fuelling pressure by 125% of the nominal working pressure (NWP) to prevent the state of charge (SOC) to exceed 100% to ensure the safety of tank while refuelling and its use afterwards. Crossing these limits may lead to hydrogen tank failure, including rupture, and unignited or ignited (fire) jets caused by hydrogen leaks [7], [8]. Hydrogen pre-cooling is typically used to keep the final hydrogen temperature in the tank below 85°C [9], [10]. The pre-cooling affects the fuelling station design, performance, reliability and cost [11].

The SAE J2601 [1] applies only to light-duty vehicles (LDV) with hydrogen capacity up to 10 kg and NWP up to 70 MPa. This protocol is limited to conditions at which experimental testing was carried out. It does not apply to the refuelling of heavy-duty vehicles (HDV). The situation with refuelling protocols becomes critical despite several projects carried out in this direction around the globe but without visible success. The underlying physical phenomena are yet to be understood and contemporary CFD models that imply important qualities compared to the reduced models, e.g.

control of real temperature deviation from the bulk temperature of 85°C due to temperature non-uniformity in onboard storage, yet to be developed and thoroughly validated.

To support inherently safer refuelling protocol development a model based on the fundamental laws is needed. So far most of the fuelling studies are focused on the state of hydrogen in onboard storage only. In many cases, due to high computational costs, simplified "integral" type reduced models are developed which have several disadvantages.

In 2012 Hosseini et al. [12] used a thermodynamic model to analyse tank filling based on energy and exergy analysis while adhering to a strong assumption of uniform temperature distribution inside the tank. Not only this model was not validated, but as a reduced model, it was unable to resolves temperature non-uniformity in tanks. In 2019 Molkov et al. [13] published and validated a physical model of onboard hydrogen storage tank thermal behaviour during fuelling. The model used pressure ramp and hydrogen temperature at tank inflow as input parameters. The model assumed direct connection between high pressure (HP) tank and the onboard tank therefore the effect of piping section on the fueling procedure was not taken into account. In 2021 Bai et al. [14] developed a thermodynamic model to analyze the dynamics of the onboard tank temperature and pressure while refuelling from a cascade-storage system of hydrogen fuelling station (HRS). Constant temperature and pressure in high-pressure tanks at HRS, uniform temperature and pressure inside the tanks, adiabatic hydrogen flow in pipes, and negligible pressure drop in pipes are among the simplifying assumptions used in this model. According to the authors [14], the model only follows the same trends as the reference experiment and it is "*relatively accurate*" due to the assumption. In 2021 Kuroki et al. [15] developed a reduced "*holistic mathematical model*" to simulate thermodynamic parameters of hydrogen from the high-pressure tank exit at HRS to the onboard storage tank. The model was used experimental temperature profiles for HP tanks as the input boundary and the HP tanks were not analysed. Besides, the reduced model couldn't resolve the onboard tank temperature distribution. In 2021, Charolais et al. [16] compared the different reduced models in the context of HDV refuelling in which they were not capable of resolving gas temperature non-uniformity inside the tanks.

Due to the need for challenging computational resources, previous CFD studies on refuelling were limited to simulations of the onboard tank only, see e.g. [11], [17]–[21]. However, the onboard tank is only a part of a more complex HRS system. These studies did not look at the crucial heat and mass transfer processes in the entire refuelling line [22]. Unlike reduced models, CFD models can provide three-dimensional distribution of parameters in the entire HRS geometry, which enables the optimisation of the HRS hardware and protocols, e.g. exclusion of hydrogen hot spots during refuelling or cold spots during emptying high-pressure HRS tanks [22]. Besides, a validated 3D model can be used to study the non-uniformity due to buoyancy inside tanks and/or investigate different complex piping configurations, all of which 2D models are incapable of.

This study aims at the development of a computationally affordable CFD model of refuelling accounting for the entire refuelling line, including pressure control valve and pre-cooler and comparison of simulations against experimental data by Kuroki et al. [15].

## VALIDATION EXPERIMENT

Figure 1 shows piping and instrumentation diagram (PID) of the experimental facility for hydrogen fuelling at the National Renewable Energy Laboratory's (NREL's) Hydrogen Infrastructure Research Facility (HITRF) used in the experimental study [15], which is employed here for the CFD model validation. The HP storage at the HRS consists of 6 equally sized 300 litres tanks at 88 MPa working in cascade mode, but only two of those tanks were involved in the experiment. The experiment started with emptying HP tank No.1 and then switched to tank No.2 when the pressure in tank No.1 reached approximately 63.5 MPa. The onboard storage includes three tanks of an equal volume of 36 litres. The specification of the onboard tanks is presented in Table 1. Specifications of each fuelling line component, i.e. pipelines geometry and thermal properties, valve flow coefficients, size and material of other parts, are given in the Appendix to the experimental paper by Kuroki et al. [15].

The experiment was carried out at the ambient temperature of 23°C, HP tank temperature reported as 17.5°C, initial onboard tank pressure 6.0 MPa, initial HP tank pressure 88 MPa, and the Average Pressure Ramp Rate (APRR) of 19.8 MPa/min. The location of pressure sensors (PT) and temperature sensors (TE) are shown in Fig. 1. The accuracy of temperature sensors was reported as ±1.5 K and of pressure sensors as ±1.0 MPa [15]. Though the temperature in the onboard tanks is reported as calculated based on measured pressure and settled density, i.e. density in the tank after the end of fuelling (reported to be more reliable than raw sensor data [23]), the experimental facility PID also shows temperature sensors (TE5) and (TE6) installed on two of three experimental tanks representing onboard storage. It is worth noting that in the experiment the mass flow rate was measured by recording the mass change in the tank. Also, the pressure measured at the tank inlet is assumed to be equal to the gas pressure inside the tank.

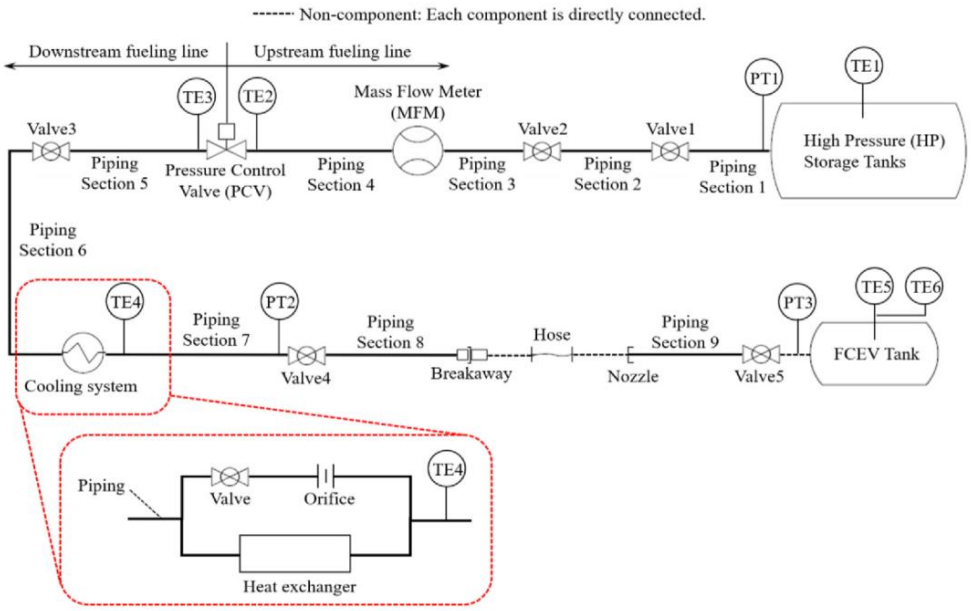


**Fig. 1.** Piping and instrumentation diagram (PID) of the experimental facility [15].

In the experiment, the pressure ramp was controlled using the pressure control valve (PCV) and pressure as a function of time is presented in the paper [15]. The pressure ramp rate was chosen in such a way that the temperature in the onboard tank stayed below the regulated limit of 85°C. The pressure ramp depends on the initial pressure, final pressure, fuelling time and boundary conditions, and was selected in the experiment according to SAE J2601 [1].

**Table 1. Onboard tanks specification [15]**

| Onboard tank specification | |
|---|---|
| *Volume [l]* | 36 |
| *Area [$m^2$]* | 0.65 |
| *Diameter [m]* | 0.25 |
| *Length [m]* | 0.85 |
| *CFRP tank wall* | |
| *Thickness δ [mm]* | 23.5 |
| *Thermal conductivity λ [W/(m.K)]* | 0.74 |
| *Specific heat C [J/(Kg.k)]* | 1120 |
| *Density ρ [Kg/$m^3$]* | 1494 |
| *Liner* | |

| | |
|---|---|
| *Thickness δ [mm]* | 3.8 |
| *Thermal conductivity λ [W/(m.K)]* | 0.50 |
| *Specific heat C [J/(Kg.k)]* | 2100 |
| *Density ρ [Kg/m³]* | 945 |

## CFD MODEL

### Calculation domain

The calculation domain included all components of the experimental facility [15] presented in Fig. 1 above. The HP tanks specification was not given in [15], so the design of a similar HP hydrogen storage tank was created and used in the simulations; the total wall thickness of this tank, including both CFRP and liner, was estimated as 33 mm. The three onboard 36 L storage tanks were modelled as a single 108 L tank with the same internal volume and internal surface area. Takano et al. [24] stated that the temperature dynamics inside the tanks is directly affected by the internal volume area to the internal volume of the tank. With the same logic, the internal volume and surface area of the 108L tank is similar to the experiment's three 36 litres tanks. Although the experimental onboard tanks are connected with different lines, the CFD model uses the mean piping length similar to how it was used in calculations [15]. The length and diameter of each pipeline were created based on the description of components in the Appendix to [15]. The entire piping section, excluding the valves, is 56.36 m long. Valves were modelled as parts of the piping section, each having length 0.1 m and internal diameters calculated based on their flow coefficient values available from [15].

The computational domain was meshed using 96,975 hexahedral control volumes (CV). The minimum mesh size in the tanks is 3 cm in the centreline of the tanks and grows with a growth rate of 1.1 towards the peripheral of the cylinder. The isometric view of the simulated HP tanks and the onboard storage tank along with the numerical mesh is presented in Fig. 2.

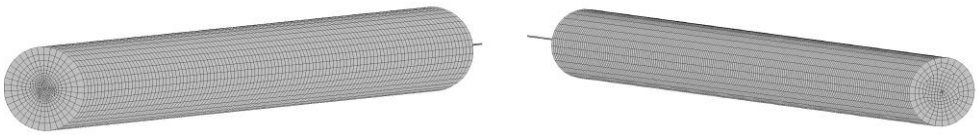

(a) (b)

**Fig. 2.** Isometric view and numerical mesh: (a) HP tank at HRS; (b) FCEV onboard tank.

### Governing equations

Governing equations include unsteady conservation equations for mass, momentum and energy:

$$\frac{\partial \bar{\rho}}{\partial t} + \frac{\partial}{\partial x_j}\left(\bar{\rho}\tilde{u}_j\right) = 0, \qquad (1)$$

$$\frac{\partial}{\partial t}\left(\overline{\rho}\tilde{u}_i\right) + \frac{\partial}{\partial x_j}\left(\overline{\rho}\tilde{u}_j\tilde{u}_i\right) = -\frac{\partial \overline{p}}{\partial x_i} + \frac{\partial}{\partial x_j}\left(\mu + \mu_t\right)\left(\frac{\partial \tilde{u}_i}{\partial x_j} + \frac{\partial \tilde{u}_j}{\partial x_i} - \frac{2}{3}\frac{\partial \tilde{u}_k}{\partial x_k}\delta_{ij}\right) + \bar{\rho}g_i, \qquad (2)$$

$$\frac{\partial}{\partial t}\left(\bar{\rho}\tilde{E}\right) + \frac{\partial}{\partial x_j}\left(\tilde{u}_j\left(\bar{\rho}\tilde{E} + \overline{p}\right)\right) = \frac{\partial}{\partial x_j}\left(\left(\lambda + \frac{\mu_t c_p}{Pr_t}\right)\frac{\partial \tilde{T}}{\partial x_j}\right). \qquad (3)$$

where $x_i$,$x_j$,$x_k$ are the Cartesian coordinates, $u_i$, $u_j$, $u_k$ are the velocity components, $t$ is the time, $p$ is the pressure, $\rho$ is the density, $g_i$ is the gravity acceleration in $i$-axis direction, $\mu$ and $\mu_t$ are the molecular and turbulent dynamic viscosity respectively, $\delta_{ij}$ is the Kronecker symbol, $E$ is the total energy, $T$ is the temperature, $c_p$ is the specific heat at constant pressure, $\lambda$ is the thermal conductivity, $Pr_t$ is the turbulent Prandtl number. Symbol "overbar" stands for Reynolds averaged parameters and "tilde" for Favre averaged parameters.

The model employs the NIST real gas model. Ansys fluent NIST real gas model uses the National Institute of Standards and Technology (NIST) Thermodynamic and Transport Properties of Refrigerants and Refrigerant Mixtures Database Version 7.0 (REFPROP v7.0) [25] to evaluate transport and thermodynamic properties of fluids. Flow turbulence was modelled using standard $k$-$\varepsilon$ turbulence model [26]:

$$\frac{\partial(\overline{\rho}\overline{k})}{\partial t}+\frac{\partial}{\partial x_j}\left(\overline{\rho}\tilde{u}_j\overline{k}\right)=\frac{\partial}{\partial x_j}\left(\left(\mu+\frac{\mu_t}{\sigma_k}\right)\frac{\partial\overline{k}}{\partial x_j}\right)+G_k+G_b-\overline{\rho\varepsilon}, \tag{6}$$

$$\frac{\partial(\overline{\rho}\overline{\varepsilon})}{\partial t}+\frac{\partial}{\partial x_j}\left(\overline{\rho}\tilde{u}_j\overline{\varepsilon}\right)=\frac{\partial}{\partial x_j}\left(\left(\mu+\frac{\mu_t}{\sigma_\varepsilon}\right)\frac{\partial\overline{\varepsilon}}{\partial x_j}\right)+C_{1\varepsilon}\frac{\overline{\varepsilon}}{k}(G_k+C_{3\varepsilon}G_b)-C_{2\varepsilon}\overline{\rho}\frac{\overline{\varepsilon}^2}{k}, \tag{7}$$

where $k$ is the turbulent kinetic energy, $\varepsilon$ is the dissipation rate of turbulent kinetic energy, $\mu_t=\bar{\rho}c_\mu\bar{k}^2/\bar{\varepsilon}$, $G_K=\mu_t S^2$, $G_b=-g_i(\mu_t/\bar{\rho}\,Pr_t)(\partial\bar{p}/\partial x_i)$, $c_m$=0.09, $\sigma_k$=1.0, $\sigma_\varepsilon$=1.3, $C_{1\varepsilon}$=1.44, $C_{2\varepsilon}$=1.92, $C_{3\varepsilon}=tanh\left|\tilde{u}_y/(\tilde{u}_x^2+\tilde{u}_z^2)^{0.5}\right|$, $S=\sqrt{2\bar{S}_{ij}\bar{S}_{ij}}$ is the mean rate of strain, $\bar{S}_{ij}=\frac{1}{2}\left(\frac{\partial\bar{u}_i}{\partial x_j}+\frac{\partial\bar{u}_j}{\partial x_i}\right)$.

**Numerical details**

Boundaries of all tanks, pipelines and valves were modelled as non-slip, impermeable walls. Initial conditions, including pressure inside the tank and temperatures, are those measured in the experiment [15]: pressure 88 MPa in HP storage tanks of HRS and pipes down to the PCV, pressure 6 MPa in pipes from PCV to FCEV onboard tank, initial temperature in the HP tank including tank wall 17.5°C, and temperature in the rest of the domain is 23°C. The boundary condition for the energy conservation equation was based on 3D conduction shell wall heat transfer model accounting for specified wall thickness and thermal properties of the material with convective heat transfer on the outer surface of the walls. Conduction heat transfer, which is governed by Fourier's law, is computed as below:

$$\frac{\partial(\rho C_p T)}{\partial t}=\nabla.(k\nabla T)+S \tag{8}$$

where $\rho$ is density, $C_p$ is specific heat, and $k$ is the thermal conductivity of the wall material. Using specified convective heat transfer coefficient at walls, ANSYS fluent computes heat flux to the walls as below:

$$q=h_{ext}(T_{ext}-T_w), \tag{9}$$

where $h_{ext}$ is external heat transfer coefficient and $T_{ext}$ is ambient temperature. Heat transfer coefficient 7 W/m$^2$/K was used in line with conclusions in [27] with the ambient temperature for HP tank set as 17°C and for the rest of the domain as 23°C.

The experimental procedure of switching HP tanks in the simulations was imitated by stopping the simulation at the specified pressure of 63.5 MPa (achieved at time 121.5 s) and re-initialising ("patching") the temperature and pressure inside the HP tank and HP tank wall temperature to the initial values.

The simulations using the CFD model were performed using ANSYS Fluent 2020R2 as a CFD engine [28]. The SIMPLE algorithm was applied for pressure-velocity coupling. Convective terms were discretised using a first-order upwind numerical scheme and a first-order implicit scheme was used for time marching.

**Modelling of the PCV**

To control the pressure in simulation to reproduce the experimental pressure ramp, the PCV in the CFD model was considered as a porous media. The porous media model adds a momentum sink term and a heat source term in the governing equations (2) and (3) respectively [29]. The momentum sink

term includes two parts: viscous (Darcy) loss term, i.e. the first term on RHS of Eq. (8), and an inertial loss term, i.e. the second term on RHS of the equation below:

$$S_i = -\left(\frac{\mu}{\alpha}u_i + C_2\frac{1}{2}\rho|u|u_i\right), \quad (10)$$

where $\mu$ is the laminar viscosity, $\alpha$ is the viscous resistance, $u$ is the velocity, $\rho$ is the density, and $C_2$ is the inertial resistance. The coefficients $\alpha$ and $C_2$ in this sink term provide the control of pressure drop at PCV and thus allow to define the needed pressure dynamics in the onboard tank, e.g. based on the prescribed APRR during the simulation of the experimental pressure for model validation or fuelling protocol development. The coefficients $\alpha$ and $C_2$ were introduced in simulations using the User Defined Function (UDF) capability of ANSYS Fluent. The UDF is programmed in a way that it first computes the average pressure in the onboard tank and compares its value with the experimental pressure profile. It has to be noted that the experimental pressure profile was approximated by a polynomial function as below:

$$p_{exp} = p_{initial} + 34999 \cdot t + 3736.3 \cdot t^2 - 15.21 \cdot t^3 + 0.018 \cdot t^4. \quad (11)$$

where $p_{initial}$ is the initial pressure in the onboard tank and $t$ is the actual fueling time. Then the normalised pressure difference is calculated as a measure of the departure of actual simulated pressure from the expected experimental pressure in the onboard tank:

$$dp_{norm} = 1 + \frac{p_{tank} - p_{exp}}{p_{exp}}. \quad (12)$$

where $p_{tank}$ is the volume average of the simulated onboard tank pressure while refueling. The porous media resistance coefficients are changed dynamically based on the normalised pressure difference to control the hydrogen flow rate in the PCV.

**Modelling of the heat exchanger**

Details of the cooling system heat exchanger were not described in the experimental paper [15]. Detailed modelling of the heat exchanger is out of the scope of this paper. For the modelling purposes in this study, the equivalent diameter, length of the pipe and flow coefficient of the heat exchanger were used as described in [15]. The temperature on the outer side of the heat exchanger pipe wall was dynamically changed to match the hydrogen temperature at the exit from the heat exchanger with the experimentally recorded temperature. The outer pipe wall temperature was changed using the UDF.

## SIMULATION RESULTS

The simulation results were compared against the experimental data [15]. Figure 2 compares temperature and pressure dynamics in the onboard tank. The location of thermocouples in the experiment is referred to as near the tank wall directly opposite the inlet [15]. As mentioned, the onboard tanks are modelled as a single tank, so, it is not possible to compare temperature at the location similar to the experiment and that is why its mass-averaged temperature is reported in Fig. 2a. The simulated temperature is in good agreement with experimental measurements by thermocouples TE5 and TE6 for the whole duration of the fueling process with a deviation of less than 5ºC. This ensures the CFD model's capability to accurately predict hydrogen temperature in the tank during the fuelling. The onboard storage experimental pressure is the input parameter of the refuelling protocol. The simulated pressure (Fig. 2b) reproduces the experimental one with a discrepancy of less than ±1% across the whole fuelling duration.

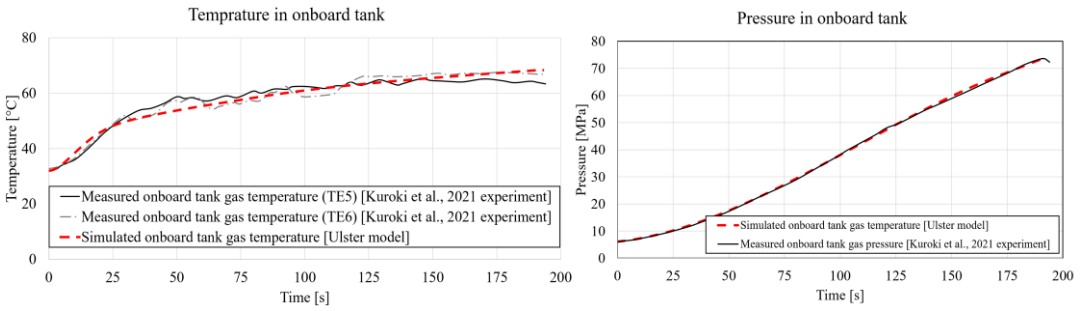


(a) (b)

**Fig. 2.** Comparison of experimentally measured and simulated parameters: (a) – the temperature in FCEV onboard tank; (b) – pressure in FCEV onboard tank.

Figure 3a compares the experimental and simulated temperature at the exit from the cooling system (measurement point TE4 in PID, Fig. 1). The simulated temperature at the exit from the heat exchanger is in good agreement with experimental data within acceptable engineering accuracy of ±5%. Figure 3b shows the comparison of the experimental and simulated mass flow rate across the PCV. The difference between measured and simulated mass flow rates may be explained by the fact that the experimental mass flow rate was obtained from measurements of the HP tank mass, which probably masked actual mass flow rate oscillations. Nevertheless, the simulated mass flow rate closely follows the experimental data.

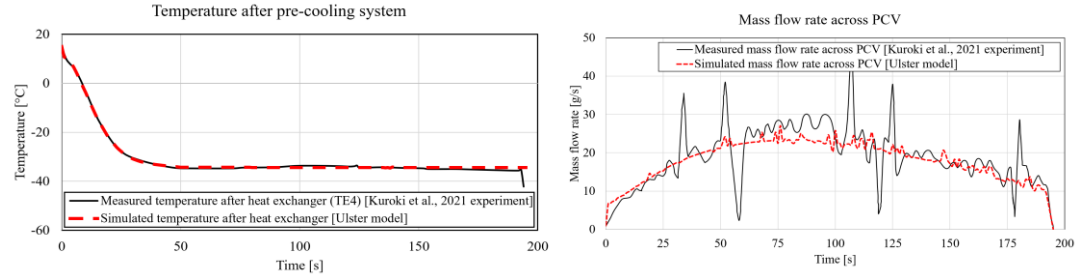


(a) (b)

**Fig. 3.** Comparison of experimentally measured and simulated parameters: (a) - temperature after the pre-cooler (TE4); (b) - mass flow rate at PCV location.

Figure 4a shows the comparison of experimental and simulated hydrogen temperature before and after the PCV. The temperature increase after passing the PCV is thought due to the Joule-Thomson effect: at the pressure and temperature of filling, hydrogen has a negative Joule-Thomson coefficient causing the temperature increase while its pressure decreases in the PCV [15]. The CFD model reproduces the experimentally observed temperature rise during passing the PCV well with a maximum deviation within ±5°C. Figure 4b shows the comparison of temperature and pressure inside the HP tanks. The simulation results for HP tank pressure and temperature follow the experimental results with a maximum deviation of less than 1%.

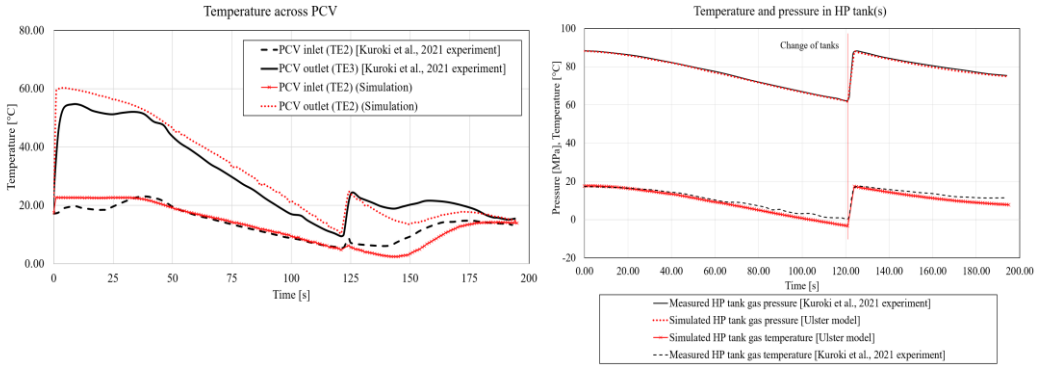


(a) (b)

**Fig. 4.** Comparison of experimentally measured and simulated parameters: (a) - hydrogen temperature before PCV (TE2) and after PCV (TE3); (b) - pressure and temperature inside HP tanks, including the switch of hydrogen supply from tank No.1 to tank No.2.

As stated, the geometry of the tanks in the current model is not exactly the same as the geometry of the tanks of the experiment, yet the model is capable to predict temperature non-uniformity inside the tanks. Although it is not possible to compare the non-uniformity of the current simulation with the reference experiment, but in future configurations, where new types of conformal tanks are to be studied, this feature could be an excellent tool to measure non-uniformities inside tanks.


Figure 5 - Capability of temperature non-uniformity prediction in the CFD model.

## CONCLUSIONS

The originality of this study is in the development for the first time of the CFD model able to simulate parameters of the entire refuelling process from a high-pressure storage tank at HRS through the key components such as the pressure control valve and the pre-cooler to the onboard storage tanks. The simulations are performed using the advanced modelling of main components of the refuelling process such as the pressure control valve, using the original porous media sub-model, and the pre-cooler, using heat exchange through the pipe wall sub-model.

The significance of the study is in the development of a computationally affordable contemporary tool for the design of fuelling protocols for the whole range of hydrogen-powered vehicles for road, rail, marine, and aeronautical applications. The CFD model is capable to provide insight into underlying physics without simplifications inherent for the reduced models and allows, for example, to develop innovative fuelling protocols that control the temperature non-uniformity inside high-pressure storage tanks to prevent their failure during refuelling.

The rigour of the work is in the thorough validation of the simulations against the available experimental data on refuelling at real scales. The simulated by the CFD model parameters agree with experimentally measured pressures and temperatures at different locations of the entire refuelling line

from the HRS storage tanks to onboard storage tanks. The experimentally observed increase of hydrogen temperature passing the PCV is well reproduced by the CFD model.

## ACKNOWLEDGMENTS

This research was funded by Fuel Cells and Hydrogen 2 Joint Undertaking (FCH2 JU) through the SH2APED project. The SH2APED project has received funding from the FCH2 JU under grant agreement No. 101007182. This Joint Undertaking receives support from the European Union's Horizon 2020 research and innovation programme, Hydrogen Europe and Hydrogen Europe Research. The authors are also grateful to the Engineering and Physical Sciences Research Council (EPSRC) of the UK for funding through the EPSRC Centre for Doctoral Training in Sustainable Hydrogen "SusHy" (Grant EP/S023909/1), and performing simulations using the Tier 2 High Performance Computing resources provided by the Northern Ireland High Performance Computing (NI-HPC) facility funded by the EPSRC (grant EP/T022175/1, https://www.ni-hpc.ac.uk/Kelvin2/).

## REFERENCES

[1] SAE International, SAE J2601, Rev 2020, Fueling Protocols for Light Duty Gaseous Hydrogen Surface Vehicles, SAE International (2020) 1–2.

[2] M. Dadashzadeh, S. Kashkarov, D. Makarov, V. Molkov, Risk assessment methodology for onboard hydrogen storage, International Journal of Hydrogen Energy 43 (2018) 6462–6475.

[3] N. De Miguel, B. Acosta, D. Baraldi, R. Melideo, R. Ortiz Cebolla, P. Moretto, The role of initial tank temperature on refuelling of on-board hydrogen tanks, International Journal of Hydrogen Energy 41 (2016) 8606–8615.

[4] J2579 ST. Technical information report for fuel systems in fuel cell and other hydrogen vehicles. 2008.

[5] ISO/TS 15869 Gaseous hydrogen and hydrogen blends — Land vehicle fuel tanks (2009).. https://www.iso.org/standard/52871.html (Accessed 07 January 2022).

[6] United Nations Economic Commission for Europe. Global Registry. Addendum 13: Global Technical Regulation No. 13., Global Technical Regulation on Hydrogen and Fuel Cell Vehicles, 2013.

[7] K. Sun , Z. Li, Development of emergency response strategies for typical accidents of hydrogen fuel cell electric vehicles, International Journal of Hydrogen Energy 56 (2021) 37679–37696.

[8] O. Lazarenko, V.-P. Parkhomenko, R. Sukach, B. Bilonozhko, A. Kuskovets, Design Features and Hazards of Hydrogen Fuel Cell Cars, Fire Safety 37 (2021) 52–57.

[9] J. Zheng, J. Guo, J. Yang, Y. Zhao, L. Zhao, X. Pan, J. Ma, L. Zhang, Experimental and numerical study on temperature rise within a 70 MPa type III cylinder during fast refueling, International Journal of Hydrogen Energy 38 (2013) 10956–10962.

[10] D. Melideo, D. Baraldi, M. C. Galassi, R. Ortiz Cebolla, B. Acosta Iborra, P. Moretto, CFD model performance benchmark of fast filling simulations of hydrogen tanks with pre-cooling, International Journal of Hydrogen Energy 39 (2014) 4389–4395.

[11] T. Bourgeois, T. Brachmann, F. Barth, F. Ammouri, D. Baraldi, D. Melideo, B. Acosta-Iborra, D. Zaepffel, D. Saury, D. Lemonnier, Optimization of hydrogen vehicle refuelling requirements, International Journal of Hydrogen Energy 42 (2017) 13789–13809.

[12] M. Hosseini, I. Dincer, G. F. Naterer, M. A. Rosen, Thermodynamic analysis of filling compressed gaseous hydrogen storage tanks, International Journal of Hydrogen Energy 37

(2012) 5063–5071.

[13] V. Molkov, M. Dadashzadeh, and D. Makarov, Physical model of onboard hydrogen storage tank thermal behaviour during fuelling, International Journal of Hydrogen Energy 44 (2019) 4374–4384.

[14] Y. Bai, C. Zhang, H. Duan, S. Jiang, Z. Zhou, D. Grouset, M. Zhang, X. Ye, Modeling and optimal control of fast filling process of hydrogen to fuel cell vehicle, Journal of Energy Storage 45 (2021) 102306.

[15] T. Kuroki, K. Nagasawa, M. Peters, D. Leighton, J. Kurtz, N. Sakoda, M. Monde, Y. Takata, Thermodynamic modeling of hydrogen fueling process from high-pressure storage tank to vehicle tank, International Journal of Hydrogen Energy 46 (2021), 22004–22017.

[16] A. Charolais, F. Ammouri, E. Vyazmina, Q. Nouvelot, T. Guewouo, M. Greisel, M. Gebhard, T. Kuroki, S. Mathison, protocol for heavy duty hydrogen refueling: a modeling benchmark, in ICHS, 2021, 1150–1160.

[17] D. Melideo, D. Baraldi, B. Acosta-Iborra, R. O. Cebolla, P. Moretto, CFD Investigation of Filling and Emptying of Hydrogen Tanks, Proceedings of International Conference on Hydrogen Safety (2015) 1–12.

[18] D. Melideo, D. Baraldi, M. C. Galassi, B. Acosta-Iborra, R. O. Cebolla, P. Moretto, Assessment of a CFD Model for the Simulation of Fast Filling of Hydrogen Tanks With Pre-Cooling, International Conference on Hydrogen Safety 1–11.

[19] P. Carrere, G. Lodiar, E. Vyazmina, F. Ammouri, A. Charolais, CFD simulations of the refueling of long horizontal H2 tanks, in International Conference on Hydrogen Safety (ICHS2021) 2021, 1175–1184.

[20] J. Zheng, J. Guo, J. Yang, Y. Zhao, L. Zhao, X. Pan, J. Ma, L. Zhang, Experimental and numerical study on temperature rise within a 70 MPa type III cylinder during fast refueling, International Journal of Hydrogen Energy 38 (2013) 10956–10962.

[21] V. Ramasamy, E. S. Richardson, Thermal response of high-aspect-ratio hydrogen cylinders undergoing fast-filling, International Journal of Heat and Mass Transfer 160 (2020) 120179.

[22] T. Bourgeois, F. Ammouri, D. Baraldi, P. Moretto, The temperature evolution in compressed gas filling processes: A review, International Journal of Hydrogen Energy 43 (2018) 2268–2292.

[23] J. Schneider, G. Meadows, S. R. Mathison, M. J. Veenstra, J. Shim, R. Immel, M. Wistoft-Ibsen, S. Quong, M. Greisel, T. McGuire, P. Potzel, Validation and Sensitivity Studies for SAE J2601, the Light Duty Vehicle Hydrogen Fueling Standard 3 (2014).

[24] T. Takano and M. Monde, Non-dimensional Parameters for Temperature Characteristic during Rapid Refueling or Discharging Hydrogen at a High Pressure, Journal of High Pressure Institute of Japan, vol. 46.3, (2008), 138–146.

[25] E. W. Lemmon, I. H. Bell, M. L. Huber, M. O. McLinden, NIST Standard Reference Database 23: Reference Fluid Thermodynamic and Transport Properties-REFPROP, Version 10.0, National Institute of Standards and Technology, Standard Reference Data Program, Gaithersburg, 2018.

[26] B. E. Launder and D. B. Spalding, The numerical computation of turbulent flows, Computer Methods in Applied Mechanics and Engineering, vol. 3, (1974), 269–289.

[27] I. Simonovski, D. Baraldi, D. Melideo, B. Acosta-Iborra, Thermal simulations of a hydrogen storage tank during fast filling, International Journal of Hydrogen Energy 40 (2015) 12560–12571.

[28] Ansys Inc, Ansys Fluent 2020 R2 User Manual. 2020. https://ansyshelp.ansys.com/account/secured?returnurl=/Views/Secured/corp/v202/en/flu_th/flu_th_sec_turb_realizke.html (Accessed 09 Jan 2022)

[29] Ansys Inc, ANSYS Fluent 2020 R2 user manual/ 7.2.3 Porous Media Conditions, (2020).

# Ignition likelihood of a sudden hydrogen release

**Proust C.[1],[2]**

*[1] INERIS, dept IDE-EMEX, Parc Techn. ALATA, PO box 2, 60550 Verneuil-en-Halatte, France.*
*[2] UTC, Alliance Sorbonne Univ., TIMR lab, Centre Pierre Guillaumat, 60200 Compiègne, France.*
**Corresponding author's email: christophe.proust@ineris.fr*

## ABSTRACT

Hydrogen is a widespread industrial product. It is currently being used in many sectors of the industry (electronics, metallurgy, chemistry,…) and its possible use as an energy carrier is envisioned. It is however recognised that this latter possibility would become a practical breakthrough only if safety issues are solved [2]. Very significant technical progresses have been made during the last decade but the implementation of robust methods to control the explosion risk would require a better understanding of the phenomena leading to an ignition of an hydrogen-air mixture. Various possibilities were recently surveyed by Asbury [1]. In this paper, a deeper analysis is proposed on the basis of recent experimental results and of the ignition theories. Sufficient evidence is found to claim that all ignition thresholds drop significantly when the pressure is increased. This facilicates ignition by very faint sources like corona discharges but also by weak mechanical sources : weak friction and impact of a single particle. The "diffused" ignition mechanism is also discussed but might not be the most plausible.

**KEYWORDS:** ignition, combustion,flame, hydrogen.

## INTRODUCTION

The worldwide consumption of hydrogen need is increasing, not only because of the spread of the demand of classical industries (chemistry, metallurgy,…) but also for environmental grounds through the development of new ways to convey and convert energies. Severe obstacles need however to be removed, one of the largest being to be able to master the safety of the storage of the required large quantities of hydrogen. Especially, using high pressure tanks (350 to 700 bar) appears as an industrial perspective. Explosions issues are usually addressed under the implicit assumption that ignition is « extremely probable » and even « spontaneous » so that nothing can be done in practise to avoid it. However, some authors [1, 2] indicate that even a massive leakage of hydrogen does not automatically ignites but that, when it does, the exact reason for igniting is often unclear. The same authors discuss some possible ignition mechanisms and conclude that static electricity resulting from high velocity flow of hydrogen could explain many "spontaneous" ignitions. Astbury [1] discarded that the Joule-Thomson effect could ignite hydrogen in case of a sudden expansion, at least in practical situations. He further mentions hot surface ignition, adiabatic compression and "diffusive" ignition.

This subject is regularly debated in the literature based on the newest findings. The present paper is on the same vein. In the following, a more theroetical approach is chosen in an attempt to highlight and link the most important parameters.

On the basis of the fundamental ignition modes of flammable atmospheres presented in the first section, various practical "spontaneous" ignition situations occuring when high pressure hydrogen is discharged in the open atmosphere are discussed in the second section..

## "FUNDAMENTAL" IGNITION MODES

Good monographs have been published during the last 50 years regarding the underlying physical mechanisms of flame development including ignition processes [3, 4, 5, 6]. In particular, the classical

"thermal explosion theory" [4] can be used to describe the phenomenology and show the links between the ignition processes and the combustion parameters. Most analytical developments rely on a highly simplified chemistry and, often, the heat release is represented by a one step chemical reaction following a global Arrhenius reaction rate: F (fuel) + O (oxidant as air) -> P (products) + heat.

The volumetric heat release rate, $Q_{comb}$ ($W/m^3$) in its simplest form reads:

$$\dot{Q}_{comb} = \rho \cdot A \cdot \Delta H_{comb} \cdot e^{-\frac{E_{act}}{R \cdot T}} \quad (1)$$

Where $\Delta H_{comb}$ is the specific heat release rate per unit mass of the mixture (J/kg), ρ the specific mass of the mixture ($kg/m^3$), A the preexponential factor of the Arrhenius law ($s^{-1}$), $E_{act}$ the energy of activation of the reaction (J/mole), R the perfect gas constant (8.314 J/mole/K) and T the temperature (K).

Note that $\Delta H_{comb}$ is a property of the mixture and is related to the maximum temperature of the combustion ($T_{ad}$) as measured in an adiabatic system. If $T_0$ is the initial temperature, $\rho_0$ the initial specific mass and Cp the specific heat capacity then (1) reads:

$$\dot{Q}_{comb} = \rho_0 \cdot A \cdot Cp \cdot (T_{ad} - T_0) \cdot \frac{T_0}{T} \cdot e^{-\frac{E_{act}}{R \cdot T}} \quad (2)$$

Because $E_{act}/R$ is typically on the order of 10000 K for most fuel-air mixtures, the evolution of (2) with T is largely dominated by the exponential term (as shown on Fig. 1 for instance). Note also that this equation is valid for T smaller or equal to $T_{ad}$. This expression does not include any limitation so that it may be inferred that combustion would occur at any temperature even without any ignition source. The speed of the combustion process would only depend on T. This might be true only if the process were perfectly adiabatic but not when heat losses are taken into account. Unless T is very large, gases exchange heat mainly by convection. Assuming a volume V ($m^3$) of the gas having a typical size D (in m, for instance $D = V^{1/3}$), then the volumetric heat lost by convection with the surrounding ($Q_{losses}$ in $W/m^3$) through the external area Aexchange ($m^2$) of V reads:

$$\dot{Q}_{losses} = h_{conv} \cdot \frac{A_{exchange}}{V} \cdot (T - T_0) \approx h_{conv} \cdot \frac{1}{D} \cdot (T - T_0) \quad (3)$$

where $h_{conv}$ is the exchange rate coefficient (unit of $W/m^2/K$), usually approximately constant for a given geometrical configuration and flowing conditions. It appears that, for a given size D, (3) varies linearly with T as shown on figure 1. Equations (2) and (3) then describe the behavior of a pocket of reactant raised at a given temperature T. Suppose an homogeneous and quiescent explosive atmosphere is prepared in the volume V. T is gradually increased. The combustion is active, but proceeds extremely slowly. As long as the heat losses (volumetric rate in $W/m^3$) are larger than the heat released by the combustion ($Q_{losses} > Q_{comb}$), the chemical reaction is dampened because T is forced to decrease. Because of the exponential temperature dependency of the reaction of combustion, there is a temperature for which the heat released by the combustion becomes larger than the linear heat losses ($Q_{losses} < Q_{comb}$). Above this temperature nothing prevents the runaway of the reaction and the explosion occurs (T increases up to $T_{ad}$).

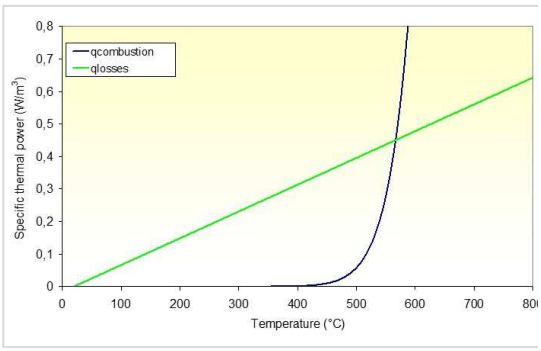


**Fig. 1:** volumetric heat release rate and losses in a volume V containing a homogeneous and quiescent stoichiometric hydrogen air mixture

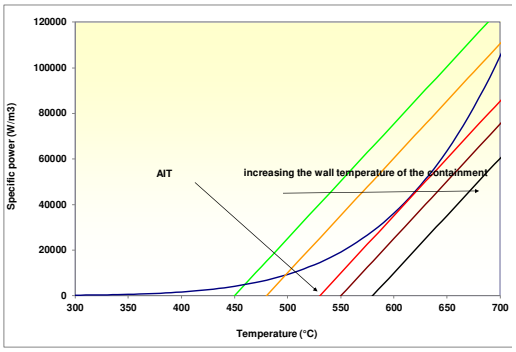


**Fig. 2:** fitting of the combustion parameters to retrieve the autoignition temperature of hydrogen-air mixtures

Although it is a very (even over) simplified theory, it is useful to investigate the various ignition modes (see [7] as an illustration). Such an approach is proposed below.

**Auto ignition mode (or volumetric combustion)**

A well-known application, particularly fitted to this modelling concept, is the autoignition problem. The temperature of the volume is progressively increased until the volumetric ignition/combustion regime is triggered. The latter occurs when the heat loss curve is tangent to the heat release curve. The mathematical solution for this situations reads :

$$\frac{2}{e} = \frac{E}{R \cdot AIT^2} \cdot \frac{V}{A_{exchange}} \cdot \frac{\rho_{AIT} \cdot \Delta H_{comb} \cdot A \cdot e^{-\frac{E_{act}}{R \cdot AIT}}}{h_{conv}} \qquad (4)$$

Knowing that the autoignition temperature (AIT) of hydrogen mixture is about 550°C, measured in a 50 mm size flask, this theory was applied to fit the combustion parameters (A and $E_{act}/R$). A good agreement (Fig. 2) is obtained with A= 1010 W/m$^3$ and $E_{act}/R$=10000 K. Note this value for $E_{act}/R$ is that recommended for hydrogen air mixtures [9].

Note that the slope of heat loss curves depends directly on the size of the vessel. Thus *AIT* is theoretically scale dependent (*D* in eq. (3)). The larger *D*, the smaller *AIT*. But $E_{act}$ is so large that this dependency with the size of the equipment remains small for *D* larger than a few centimeters, suggesting that *AIT* values measured on a lab scale are close to those for larger volumes, including process equipments.

The dependency with the pressure is potentially important. Because the chemical term increases with the initial pressure, via the dependency of $\rho_0$ in (1), *AIT* should decrease while increasing the initial pressure which is indeed observed [5, 8, 9] (Fig. 3). But also, due to the very specific chemistry of the combustion of hydrogen, *AIT* is known to decrease when the pressure drops below 0.5 bar.

The time required for the mixture to ignite once it has been heated up to a given temperature ("ignition delay") may be also be deduced, at least in principle, from this proposed simple theory. But experimental data are also available, obtained using the shock tube technique (Fig. 4).

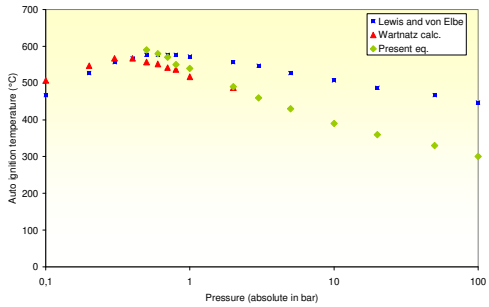


**Fig. 3:** estimated evolution of AIT as function of the pressure

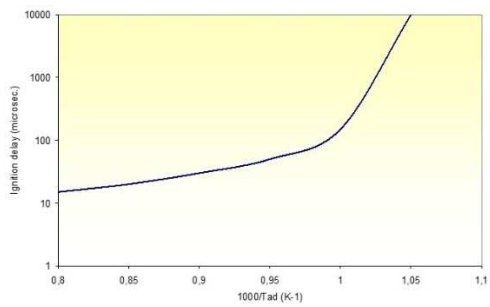


**Fig. 4:** ignition delays for hydrogen air mixtures (after [10])

The "volumetric" mode of ignition may appear rather theoretical (limited to adiabatic compression maybe). More readily only a pocket of the mixture will be heated by some mechanism while the rest of the volume will remain cold.

**Spark ignition**

In the spark gap, the heat of the ignition source, $E_{spark}$ (in J), is delivered punctually and instantaneously. At this point, D=0 and T are infinite, so that heat losses are infinite too and combustion cannot start. Some (small) amount of time is required for this initial "point" to spread out due to thermal conduction. Following, this initial amount of heat is spread by thermal conduction in the surrounding area but conserved if other thermal losses are ignored (heat radiation, thermal conduction to solid bodies). All along this "spreading" process", the spark energy is conserved according to the following expression (where D increases with time and Cp is the specific heat of the mixture in J/kg/K):

$$E_{spark} = \rho_0 \cdot Cp \cdot \frac{\pi}{6} \cdot D^3 \cdot (T - T_0) \qquad (5)$$

The heat loss curve formulated by equation (3) (with $h_{conv} \sim 2.\lambda/D$ where $\lambda$ is the thermal conductivity of the mixture at the spark temperature so approximately 0.1 W/mK) can now be computed using equation (5). For each spark kernel size, a temperature is calculated and a specific heat loss. This evolution is presented on Fig. 5 for various spark energies (curves labelled "spark"). The heat release represented by expression (2) can now be plotted using the values of $E_{act}/R$ and A found above. This curve stops at T=Tad with is the maximum combustion temperature. When Espark is too small ($E_{spark}$=0.015 mJ), the « spark heat loss » curve (line+triangles) never intercepts the heat release curve and, for any value of T, $Q_{losses}(T)>Q_{comb}(T)$ and the explosion cannot occur. When Espark is sufficiently large ($E_{spark}$=0.05 mJ), the « spark heat loss » curve (line+circles) intercepts the heat release curve and the explosion can occur since there is a domain where $Q_{losses}(T)<Q_{comb}(T)$ while $T<T_{ad}$.

The Minimum Ignition Energy (MIE) is thus obtained when the intercept occurs for $T=T_{ad}$, corresponding to the upper point of the heat release curve. This particular point corresponds to a specific size of the hot pocket of gas called the « minimum flame kernel », $D_{crit}$, which is then an intrinsic property of the mixture. It is the minimum size of a flame able to develop in a cold

environment. This definition is very close to that of the « minimum quenching distance »[1] ($D_{quench}$). Physically, both parameters can only be proportional.

The main outcome from this simplified theory are first that, at the MIE conditions, the temperature of the spark kernel is equal to $T_{ad}$ so that equation (5) can be used to calculate the MIE. Second, $T_{ad}$, $D_{crit}$ ($D_{quench}$) and MIE are interlinked. To find the relationship, equations (2) and (3) must be equated for $T=T_{ad}$ and $D=D_{crit}\sim D_{quench}$. ($T_{ad}-T_0$) should be replaced by a parameter proportional to $E_{spark}/D^3$ from equation (3). So the heat loss parameter is proportional to $E_{spark}/D^4$. The heat release parameter at $T_{ad}$, from equation (2), is proportional to the square of the laminar burning velocity $S_{lad}$ of the mixture [5]. It is known [3] that $D_{quench}$ and the $S_{lad}$ are linked :

$$Pe = \frac{Sl_{ad} \cdot D_{quench}}{a_{diff}} \approx 50 \qquad (6)$$

where $a_{diff}$ is the thermal diffusivity of the (cold) mixture (typically $2.10^{-5}$ $m^2/s$). So, the heat release parameter is proportional to $1/D^2$. Then the MIE should be proportional to the square of $D_{crit}\sim D_{quench}$. This very important relationship was discussed earlier by Lewis and von Elbe and is fully confirmed by available data (Fig. 6). On this graph, for hydrogen-air mixtures at ambient conditions, MIE=0.017 mJ and $D_{quench}$=0.7 mm. Following, the dependency of MIE with the temperature and with the pressure should largely be found in the variations of $D_{quench}$, and thus of $S_{lad}$ (and $a_{diff}$).

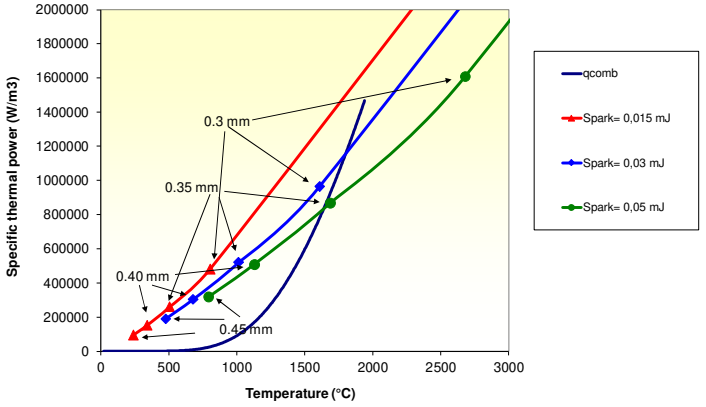


**Fig. 5:** simulated spark ignition of a hydrogen-air stoichiometric mixture for three different values of the initial spark energy (arrows and text refer to the hot pocket of gas size at different times)

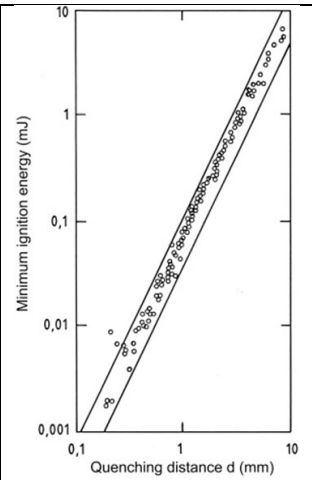


**Fig. 6:** relationship between MIE and $D_{quench}$ (from [11])

The laminar burning velocity of hydrogen air mixtures [4, 11] increases significantly with the temperature, approximately as $T^{1.3}$ according to [12], whereas the thermal diffusivity increases almost linearly with T. All in all, $D_{quench}$ should vary as $1/T^{0.3}$. Consequently, MIE should then vary

[1] the minimum quenching distance is the smallest gap between two cold parallel planes just allowing the flame to propagate steadily. If the distance is infinitesimally smaller, the flame is quenched.

proportionally to $1/T_0^{0.6}$. This point seems confirmed [13] and the variations of MIE with T seem rather moderate in the targeted situations.

The laminar burning velocity of hydrogen air mixtures [4, 12] increases very weakly with the pressure, approximately proportionally to $P^{0.25}$ according to [12], whereas the thermal diffusivity decreases almost linearly with P. All in all, $D_{quench}$ should vary as $1/P_0^{0.75}$. Consequently, MIE should then vary proportionally to $1/P_0^{1.5}$ which is potentially very consequent for the targeted applications. This important trend seems confirmed [14]. However, available experimental data is still very limited perhaps because the control of very small spark energies is extremely difficult. It seems that, qualitatively at least, pulsed laser ignition experiments can be used to this purpose [15]. Because of the various losses the measured minimum energy pulse (MPE) appears an order of magnitude larger than the traditional MIE. However, MPE is clearly decreasing while increasing the initial pressure following a linear trend. Since light absorption in the beam and heat radiation from the plasma should be proportional to the number of molecule per unit volume (i.e. pressure), energy losses should increase with pressure so that the part of the light pulse used to ignite the mixture should decrease even faster than linearly. This is in accordance with the present estimate.

**Hot surface ignition**

Ignition can also result from a prolonged exposure to a hot body. Again the ignition theory can be invoked knowing that V, the volume of the heated gas pocket, can be viewed as the thermal layer in contact with the hot surface [16]. The thickness of the layer (here parameter D) is typically comparable to the size of the heated body. This model was used in the past by Imperial College to interpret ignition experiments by laser illumination of targets immersed in a flammable atmosphere [17]. However this "static" view of the ignition problem is certainly too crude. Numerical modelling does not seem to provide a clear view either [18] but questions in particular the relative importance of the natural convection currents and of the details of the chemistry.

A more accurate description might be obtained using (a variation of) the auto ignition model developed by Frank Kamenestkii.

As soon as the temperature od the hot body is above the autoignition temperature, combustion occurs (necessary condition) in the thermal boundary. But "ignition" (of the surrounding atmosphere) can only occur if the flame is capable of propagating away. In the boundary layer, the heat flowing by conduction equals that transferred by convection to the surroundings :

$$\lambda \cdot \left(\frac{dT}{dx}\right)_p = h_{conv} \cdot \left(T_p - T_0\right) \qquad (7)$$

Where $T_p$ is the temperature of the hot surface and $h_{conv}$ the convective heat exchange coefficient. The latter incorporates to some extent the potential effect of the convection currents. It is assumed that $T_p$ is also the temperature of the burning atmosphere in contact with the hot surface at the moment of ignition.

Invoking the flame theory, this combustion zone will be able to escape from the boundary layer only if the conductive heat loss power is smaller than the heat release power. The limiting condition is obtained when both are equal reading :

$$\lambda \cdot \left(\frac{dT}{dx}\right)_p = h_{conv} \cdot \left(T_p - T_0\right) = \rho_0 \cdot Cp \cdot S_l \cdot \left(T_p - T_0\right) \qquad (8)$$

$S_l$ is the laminar burning velocity of the mixture at temperature $T_p$ and can be obtained using the expression for $S_{lad}$ where $T_{ad}$ is replaced by $T_p$ (Appendix). After some rearrangment, the following general solution can be obtained ($Nü=h_{conv}.D/\lambda$) :

$$e^{-\frac{E_{act}}{2\cdot R}\left(\frac{1}{T_p}-\frac{1}{T_{ad}}\right)} \cdot \frac{T_{ad}-T_0}{T_{ad}} \cdot \frac{T_p}{T_p-T_0} \cdot = \frac{h_{conv}}{\rho_0 \cdot Cp \cdot S_{lad}} = \frac{h_{conv}}{\lambda} \cdot \frac{\lambda}{\rho_0 \cdot Cp \cdot S_{lad}} = Nü \cdot \frac{D_{quench}}{Pe \cdot D} \qquad (9)$$

Because of its simplicity, this model is not meant to be quantitative but may help to illustrate the

relative influence of the various parameters. It was shown [18] that for an object larger that a few mm, the convection coefficient does not vary much (betwenn 35 and 65 $W/m^2K$) and that the critical ignition temperature does hardly vary (only by a few %). Experiments have shown that for large enough objects, Tp=860 K in hydrogen air mixtures at ambient temperature and pressure.

Using natural convection relationships (the heated object is supposed to be an horizontal cylinder with D=10 mm), it can be shown that increasing $T_0$ from 300 K to 600 K (below AIT) at $P_0$=1atm decreases the critical hot surface ignition temperature by about 100 K. Increasing $P_0$ from ambient pressure to 2 bar (absolute pressure) decreases the critical hot surface ignition temperature by about 100 K as well.

Note that when the size of the heated object reaches that of the quenching distance, this 1D approach cannot be valid anymore and the critical parameter is now the power delivered to the atmosphere by the source. The parametrisation can be approached by calculating the convective power of the source for $D=D_{quench}$. Experimentally a minimum power of $P_{min}$=0.15 W was measured for hydrogen air mixtures at ambient conditions [17]. Using the above theroretical approach, this power should be divided by 2 when either $T_0$ or $P_0$ are doubled.

In table 1 are presented these various ignition parameters as measured in the standard conditions ($P_{st}$=1atm and $T_{st}$=298K) and their estimated variations as function of $P_0$ and $T_0$.

**Table 1: ignition parameters of hydrogen air mixtures ( "~" means "proportional to")**

| Parameter | **Dquench** | **MIE** | **AIT** | **Tp** | **$P_{min}$** |
|---|---|---|---|---|---|
| Standard | 0.7 mm | 0.017 mJ | 833 K | 863 K | 0.15 W |
| Variations with $T_0$ | $\sim(T_0/T_{st})^{-0.3}$ | $\sim(T_0/T_{st})^{-0.6}$ | N.A | $\sim(T_0/T_{st})^{-0.25}$ | $\sim(T_0/T_{st})^{-1}$ |
| Variations with $P_0$ | $\sim(P_0/P_{st})^{-0.75}$ | $\sim(P_0/P_{st})^{-1.5}$ | $\sim(P_0/P_{st})^{-0.05}$ | $\sim(P_0/P_{st})^{-0.25}$ | $\sim(P_0/P_{st})^{-1}$ |

## "SPONTANEOUS" IGNITION OF HYDROGEN

The situation is that of a sudden release of hydrogen from a pressurized device. A practical situation is a rupture of a safety disc, or a valve… Today hydrogen may be used up to 100 MPa. It is known that "spontaneous" ignition might occur but the reasons for this are not clear yet. In the extreme situation of a sudden contact between that high pressure hydrogen and the ambient air a shock wave is propagating away inside air while a rarefaction wave is propagating upstream in hydrogen. In a 1D configuration, it is the well known "shock tube" problem. In table 2, estimates are given of the pressure, flow velocity and temperatures of the air and of the hydrogen between the shock and the rarefaction waves. Together with those specific flow conditions, small pieces of torn materials may be vibrated by the flow or projected away. In addition, tiny particles due to abrasion of valve seals for instance may be dispersed by the flow.

**Table 2: thermodynamic parameters in hydrogen and air between the shock and the rarefaction wave as function of the initial pressure of hydrogen (initial temperature=ambient, ideal gas approximation)**

| $P_{init}$ $H_2$ (MPa) | 100 | 70 | 50 | 20 | 10 | 5 | 2 |
|---|---|---|---|---|---|---|---|
| $P_{shock}$ (MPa) | 7 | 6 | 5 | 3.5 | 2.5 | 1.6 | 0.9 |
| Flow (m/s) | 2100 | 2000 | 1850 | 1500 | 1200 | 1000 | 720 |
| $T_{air}$ (K) | 3566 | 3128 | 2654 | 1943 | 1468 | 1004 | 707 |
| $T_{H2}$ (K) | 140 | 148 | 155 | 180 | 200 | 217 | 235 |

From this, several "spontaneous" ignition mechanisms may be thought about. Obviously, in the diffusive layer between the compressed air and hydrogen some thermal ignition mechanism may occur. This ignition mechanism is classically called "diffusive ignition". But because of the very low MIE, static electricity build up may be sufficient to trigger incendive discharge sparks especially when some particles are transported. The mechanical impact of tiny fragments could also be a source of ignition. Another possibility may exist when very small pieces of material are vibrated by the flow.

**Diffusive ignition**

The "diffusion-ignition" mechanism was first described by Wolanski [19] and further studied experimentally and theoretically in the last two decades [20, 21, 22, 23]. A excellent acount is given by Zhou et al. [24]. The ignition mechanism ressembles the autoignition process. From table 2, the temperature in the mixing layer corresponding to 10% $H_2$ in air was calculated because experiments have shown that the hot surface ignition process is optimum for this concentration and this conforms to the refined theoretical developments highlighting the role of the Lewis number [25]. Then an ignition delay can be deduced from the autoignition data (Fig. 4). In a 1D configuration (tube), if t is the time elapsed since the contact established between the high pressure hydrogen and air then the distance $L_s$ travelled by the shocked flow during this period of time (U=speed of the flow) is :

$$L_s = U \cdot t \qquad (10)$$

For each condition of table 2, the ignition delays were calculated together with the corresponding ignition distances ($L_s$). It appears clearly that diffusive ignition is improbable, in industrial situations (typically in m of pipe) when the driving pressure is below about 4 MPa. This seems in reasonable agreement with experimental results [24]. Considering that the minimum length to establish a shock-rarefaction complex could be the thickness of the wall of a ruptured element, typically some mms, diffusive ignition could occur above 10-20 MPa.

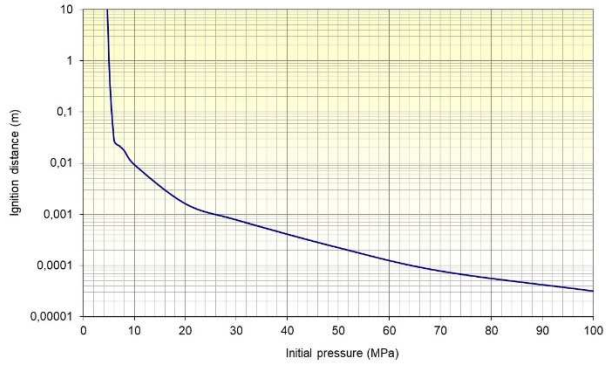


Figure 10: rough estimation of the "ignition distances" for the diffusion-ignition mechanism of hydrogen in contact with air

***Static electricity***

Astbury [1] mentions static electricity as a likely "ignition" source and suspects many accidents to result from a discharge of static electricity.

In industrial practise, static electricity is produced during the contact and subsequent separation of dissimilar materials. The work required to seperate the materials results in a deposit of electrical charges of opposite signs on the surfaces [26]. A typical situation is that of particles convected in a gaseous flow inside a duct. Particles frequently contact and separate with the surface wall, progressively charging ("triboelectic charging": [27]). If the charge conveyed by each particle is small, that accumulated on the confinment after multiple impacts (pipe) can be large. The accumulated

charges will produce an electricity field E in the surrounding which is linked to the surface charge density σ :

$$\sigma = \varepsilon_0 \cdot E \quad (11)$$

Where $\varepsilon_0$ is the electric field constant (8.85 $pC.V^{-1}.m^{-1}$). E cannot reach infinite value. This limit is the "breakdown": $E_{breakdown}$. When this limit is reached an ionised channel appears between the charged piece and the closest point of the uncharged item and all the accumulated electricity flows nearly instantaneously via this channel: this is a "spark". Since the surface charge density is limited due to the existence of the breakdown limit (eq 11), the amount of energy available depends on the geometry, hence on the "capacitance" C of the circuit. Hereafter, only a simplified approach is given in order to obtain orders of magnitudes. The reader is refered to the specific literature for further information ([28] for instance). If d is the distance between the discharge points ("electrodes"), then the energy delivered in the spark gap $Q_{spark}$ is on the order of :

$$Q_{spark} = \frac{1}{2} \cdot C \cdot (E_{breakdown} \cdot d)^2 \quad (11)$$

In ambient air, $E_{breakdown}$ is about 3 MV/m (about 2 MV/m in pure hydrogen) and varies as $(P_0/P_{st})^{-1}$ [29]. As recalled by Astbury d cannot be smaller than $D_{quench}$ otherwise the flame will not be able to escape from the spark gap. Since for ambient conditions $D_{quench}$ is 0.7 mm, the minimum charging voltage is only 2 kV which is quite small as far as electrostatic charging is concerned since charging up to 10-20 kV are readily possible [30]. Taking 10 kV as a representative value for triboelectric charging, a capacitance of 1 pF is required to release 20 µJ, the MIE of hydrogen-air at ambient conditions. Assuming a compact geometry (ex : sphere), a 1 pF capacitance would have a radius R of about 10 mm [31]:

$$C_{sphere} \approx 4 \cdot \pi \cdot \varepsilon_0 \cdot R \quad (12)$$

As mentioned by Glor [30], this is typically a screw… Considering now that the local pressure (and temperature) can be significantly above ambient, perhaps by a factor of 100 (table 2), during a sudden release of hydrogen, the MIE can virtually drop to a fraction of a microjoule according to the trends in table 1. A single particle of typically 100 µm would theoretically contain sufficient electrostatic energy to trigger an ignition. Such particles can easily be formed during a rupture or can be present in the device and lifted by the flow. According to [27], not more than a few tens of impacts are necessary to fully charge a particle and full charging is reached after typically 1 m of flow in a straight tube. Ignition can occur if the particle is properly discharged, e.g. in the mixing zone behind the shock wave. The probability for this mechanism may not be high because of the number of conditions required.

But there is another mechanism revealed by some surprising examples. Astbury reports one of them but another example is given by Wen [32]. Wen described an experiment in which a free vertical high pressure hydrogen jet "spontaneously" ignited close to a rod supporting a sampling line located at some distance from the outlet. A similar situation was encountered by the present author: while introducing hydrogen at high speed (sonic flow through a 1 m straight 14 mm inner diameter duct) inside a volume. « Spontaneous » ignitions were observed in a rather systematic way. It appeared that a piece of metal (2 cm size) was sitting in the jet at a a few cms from the nozzle. When this piece of metal was bounded with the duct (and earthed), ignition was prevented. Such examples confirms that static electricity was at work but, more precisely because of the distances between the "electrodes", that corona discharges were very probably responsible for the ignition. Corona discharge is a continuous process, not really a spark, but rather a persistant ionisation channel produced near a sharp edge pointing toward a charged plate [33, 34, 35]. The edge can be centimeters away from the plate and the voltage is lower than the breakdown limit. But near the edge the electrical field is locally distorted and the latter can be above the breakdown limit so that an ionised channel ("streamer") may appear locally, capable of igniting a flammable atmosphere provided the power released is large enough. If V is the voltage between the edge and the charged body, then the upper limit of the current I in the streamer is given by [34]:

$$I(\mu A) = \frac{4 \cdot V^2 (kV^2)}{d(mm)} \quad (13)$$

Setting V to 10 kV this gives I=40 µA for d=10 mm. The streamer will release about 0.4 W which is enough to ignite an hydrogen air mixture (table 1) but perhaps not other fuels as stated in the literature [4]. Such situations seems much more capable of igniting hydrogen air mixtures, typically in the free jet/plume in the open atmosphere. The remaining question is that of the charging mechanism of the "charged body", typically the containement. It is admitted that particles need to be conveyed by the gaseous flow for such charging to be possible. The particles charge themselves by triboelectric mechanisms and so will do the containement if properly insulated. For very dilute suspension, where particles could be considered as isolated, the charge to mass ratio $Q_m$ (C/kg) of the suspension is given by [28]:

$$Q_m = \frac{2.45 \cdot 10^{-5}}{\rho_p \cdot r_p^{1.3}} \quad (14)$$

Whre $r_p$ is the diameter of the particle and $\rho_p$ the specific mass of the material of the particle. For $r_p$ on the order of 1 µm and $\rho_p$ =1000 kg/m$^3$, $Q_m$ is about 0.1 C/kg. To produce a 10 µA current a particle flowrate of 0.1 g/s is then estimated. This is a very small quantity which may have accumulated in the piping over the time either as a consequence of some corrosion process or wear of moving parts.

***Friction, impacts and mechanical vibrations***

A sudden release could result from a fast opening of a valve connecting pressurized hydrogen to the atmosphere or from a failure. In this last situation, small pieces of material may be torn and protude into the flow, possibly vibrating, or be entrained by the flow and impact on solid surfaces. In each situation, the mechanical energy is transformed into heat and the ignition process is that of a hot surface or hot spot [36].

Friction and impacts are known to be efficient ignition sources. Some modelling was proposed in the past [36] and is used hereafter. During friction, the hot surface is generated in the rubbing zone and ignition occurs as soon as the rubbed zone is uncovered. The maximum temperature of the hot surface ($T_{frict}$) reads :

$$q_{frict} = f \cdot N \cdot U_f = \frac{4}{\pi} \cdot (\lambda_1 + \lambda_2) \cdot \frac{A}{R} \cdot \left(T_{frict} - T_0\right) \quad (15)$$

Where R is radius of contact area A, $\lambda_i$ the heat conductivity of body i in the rubbing zone, f the friction coefficient, N the normal load, $U_f$ the rubbing velocity and $q_{frict}$ the heat dissipated. Considering a valve for instance, connecting pressurized hydrogen to the atmosphere, N/A could be on the order of the overpressure inside the equipment, the heat conductivity of stainless steel is about 20 W/mK. Friction coefficients depend on many factors [37] including the nature of the rubbing material, surface roughness, presence of adsorbed liquid (water, oil, …). For unlubricated contacts, f could be set to 0.3 (VDI 2230). For a dry contact between steel components (f=0.3), R=0.005 m (A=π.R$^2$) $P_0$=100 MPa and $T_0$=20°C, $T_{frict}$ will surpass the critical hot surface temperature (590°C) as soon as $U_f$ > 0.2 m/s. One should not be surprised since it was shown possible to ignite hydrogen-air mixtures at rubbing velocities smaller than 1 m/s [38].

Fragments may also be projected by the flow and impact solid surface so that a localized hot spot appears. The hot spot is due to the short but intense friction of the impacting bodies during the contact period. In the present situation, the velocity at the impact could amount hundreds of m/s. It was shown experimentally [36] that the temperature in the contact zone can exceed 1000°C even at low impact velocity (40 m/s). It can be assumed then that the temperature at the spot $T_{imp}$ reaches the fusion point of the softest material. For stainless steel, this maximum is about 1500°C. It is well above $T_p$ but the size of the impact zone is usually very small and the relevant ignition parameter should be $P_{min}$. An estimate of the thermal power transferred to the atmosphere by the impact, $q_{impact}$, area reads :

$$q_{impact} = 2 \cdot \frac{\lambda_{atm}}{R_{impact}} \cdot \left(T_{impact} - T_0\right) \quad (16)$$

Where $R_{impact}$ is the radius of the impact zone and $\lambda_{atm}$ the heat conductivity of atmosphere surrounding the heated zone (in air, at the average temperature = 0.07 W/mK). $R_{impact}$ may be estimated using the well known Hertz theory:

$$R_{impact} = R \cdot \frac{3 \cdot \pi}{4} \cdot \Delta P_{impact} \cdot \left(\frac{1}{E_{young1}} + \frac{1}{E_{young2}}\right) \qquad \Delta P_{impact} = \frac{\rho_1 \cdot a_{sound1} \cdot \rho_2 \cdot a_{sound2}}{\rho_1 \cdot a_{sound1} + \rho_2 \cdot a_{sound2}} \cdot U_{impact} \quad (17)$$

Where $E_{youngi}$ is the Young modulus of material i involved in the impact, R the size of the projectile and $\Delta P_{impact}$ the pressure produced during the impact. The latter can be obtained by applying the wave theory at the interface [36]. Parameters $\rho_i$ and $a_{soundi}$ are respectively the specific mass and sound velocity in material i (Note that $E_{young}$ is close to $\rho.a_{sound}^2$). In case of a sudden release of pressurized hydrogen in air $U_{impact}$ may be close to the sound velocity in the flammable mixture so some hundreds of m/s. The specific mass of solids is typically between 1000 kg/m$^3$ and 8000 kg/m$^3$ and the sound velocity between 1500 and 5000 m/s. It can be shown then that $R_{impact}$ is about a tenth of R.

In atmospheric conditions and for $U_{impact}$=500 m/s, $P_{min}$ is reached for a projectile measuring about 1 mm. At 10 bar, a 0.1mm projectile might be large enough.

A further possibility, though somewhat theoretical, is the heating of a tiny protuding piece of metal by mechanical vibrations induced by a fast flow [39]. Again a hot spot ignition is expected. Consider a cylindrical pin (diameter D, length L), free to move at one extremity, protruding inside a flow (speed U). It is subjected to a pulsating drag forces due to the mechanism of "vortex shedding" [40] at a frequency F. If $F_{dyn}$ is the drag force applied on the length of the pin and $\delta$ the maximum displacement of the extremity of the pin (the displacement velocity is $\delta.2.\pi.F$ in a sinusoidal movement), then the order of magnitude of the mechanical power q communicated by the flow to the pin is:

$$q = F_{dyn} \cdot \delta \cdot 2 \cdot \pi \cdot F \qquad \text{where} \qquad F = 0.2 \cdot \frac{U}{D} \quad (18)$$

For a cylindrical pin, $F_{dyn} \sim \rho.U^2/2.L.D$ ($\rho$ is the specific mass of the gas) and $\delta = (F_{dyn}.L^3)/(8.\pi.E.D^4)$ where E is the Young modulus of the material of the pin. A rapid estimate shows that a steel pin of diameter D=1 mm, L=10 mm in a hydrogen flow with U=1000 m/s at ambient conditions would vibrate at 200 kHz and dissipate about 5 W. If it can be assumed that this energy is dissipated into heat (the vortex shedding frequency is above the natural longitudinal frequency of the object), it can be estimated that ignition by his mechanism is possible. Clearly further investigation is required.

## CONCLUSION

Following the work of Astbury, further analysis is proposed of some potential ignition mechanisms to account for "spontaneous ignition" following a sudden release of high pressure hydrogen. "Spontaneous ignition" covers ignition situations which result only from the leakage process and are notdue to external, independent ignition sources (like considered in ATEX rules).

A sudden release may result from an accident, such as a rupture of a component ,of a very fast opening of a valve for instance. In this paper, the possibility for fragments to be projected away and impact on nearby surfaces is considered as been part of "sudden release" scenarios. Friction on moving parts of a fast opening device too. It is also admitted that small amount of very fine dust might also be naturally present in the piping due to wear or corrosion for instance.

In the first part of this paper, the evolution of the relevant ignition parameters with pressure and temperature is presented partly based on a parametric analysis. It is shown that for hydrogen air mixtures, all ignition parameters drop when the pressure and the temperature increase. The influence of the pressure is impressive suggesting MIE could drop to a fraction of a microjoule when the pressure goes from atmosphere to 100 bar. The minimum igniting power of a hot spot may only be 1 mW while the autoignition temperature would only amount 400°C at 100 bar. Ignitability thus is

likely to increase strongly with the pressure favoring ignition by all potential processes releasing energy in the mixture. It might be justified to investigate such aspects more deeply in the future.

In the second part of this paper, the phenomena likely to produce sparks and hot surfaces during a sudden hydrogen release are tentatively analysed. Mainly four mechanisms are highlighted. The "diffusive" ignition mechanism is a possibility mostly at elevated pressure but special conditions are required to trigger this mechanism since a shock wave needs to be formed. The opening should be instantaneous like during a brittle rupture. Friction between moving parts seems likely to produce sufficient heat (temperature) at any pressure provided nevertheless that a flammable atmosphere can be formed in contact with the heated zone. Fragments being propulsed by the flow of the release can theoretically become charged due to impacts on solid surfaces (in a duct for instance). Provided the pressure is large enough (and MIE small enough) a single discharge spark from this fragment could be enough to trigger and ignition. But even if it is not the case, the heat produced during impact (due to the friction on the surface) might release enough power to ignite a pressurized hydrogen air mixture. Otherwise, in nearly all release circumstances, if fine deposits of dust are present inside the hydrogen containing equipment and can be raised by the outflow, tribocharging of some electricaly insulated object in the mixture is likely to ignite the mixture by corona discharge. A table is proposed to rank these potential ignition mechanisms as function of the release pressure P.

**Table 3 : potential ignition mechanisms as function of the pressure**

| P | Dust tribocharging | Friction | Fragment impact | Fragment tribocharging | Diffuse ignition |
|---|---|---|---|---|---|
| Over 10 MPa* | Yes | Yes | Yes | Yes | Yes |
| 1 – 10* MPa | Yes | Yes | Yes | No | No |
| Below 1 MPa | Yes | Yes | No | No | No |

*for characteristic "tube" lengths on the order of mms

## AKNOWLEGDMENT

The author would like to thank the European Union which sponsored this work under the project MULTHYFUEL.

## REFERENCES

[1] G. Astbury, S. Hawksworth, Spontaneous ignition of hydrogen leaks: a review of postulated mechanisms, Int. J. Hydrogen Energy. 32 (2007) 2178-2185.

[2] C. Proust, Fire and explosion safety in hydrogen containing processes : state of the art and outstanding questions, ISFEH09 symposium, Saint Peterburg, Russia, April 2019.

[3] I. Glasmann , Combustion, Academic Press, London, 1977.

[4] M. Hattwig, H. Steen, Handbook of Explosion Prevention and Protection, Wiley-VCH Verlag GmbH & Co. KGaA, ISBN 9783527307180, 2004.

[5] B. Lewis, G. Von Elbe (1987), Combustion, flames and explosions of gases : 3rd edition, Academic Press, London, ISBN 0-12-446751-2, 1987.

[6] F.A. Williams, Combustion theory : 2nd edition, Benjamin/Cummings publishing company Inc., Amsterdam, ISBN 0-8053-9801-5, 1985.

[7] J. Adler, F.B. Carleton, F.J. Weinberg, Ignition of flammable atmospheres by radiation heated fibrous agglomerates, Proc. R. Soc. Lond. A. 440 (1993) 443-460.

[8] Ü Mass, J. Wartnatz, Comb. And Flame. 74 (1987) 53-69.

[9] J. U. Steinle, E.U. Franck, High Pressure Combustion - Ignition Temperatures to 1000 bar, Act Bimsenges. Pllys. Chem. 99 (1995) 66- 73.

[10] T.P. Coffee, A.J. Kotlar, M.S. Miller, The Overall Reaction Concept in Premixed, Laminar, Steady-State Flames. I. Stoichiometries, Comb. and Flame. 54 (1983) 155-169.

[11] A.A. Konnov, Remaining uncertainties in the kinetic mechanism of hydrogen combustion, Comb. And Flame. 152 (2008) 507-528.

[12] M. Reyes, F. V. Tinaut, A. Horrillo, A. Lafuente, Experimental characterization of burning velocities of premixed methane-air and hydrogen-air mixtures in a constant volume combustion bomb at moderate pressure and temperature, Applied Thermal Engineering. 130 (2018) 684-697.

[13] R. M. Brokaw., M. Gerstein, Correlations of burning velocity, quenching distances, and minimum ignition energies for hydrocarbon-oxygen-nitrogen systems, Proc. Comb. Inst. 6 (1957) 66-74.

[14] E. Brandes, Safety characteristics at non-atmospheric conditions, SAFEKINEX meeting, PTB, Braunschweig, Germany, oct. 2006

[15] M. Weinrotter, H. Kopecek, E. Wintner, M. Lackner, F. Winter, Application of laser ignition to hydrogen-air mixtures at high pressures, Int. J. Hydrogen Energy. 30 (2005) 319-326.

[16] N. Laurendeau, N., Thermal ignition of methane-air mixtures by hot surfaces : a critical examination, Comb. and Flame. 46 (1982) 26-49.

[17] F. Carleton, H. Bothe, C. Proust, S. Hawksworth, Prenormative Research on the use of Optics in Potentially Explosive Atmospheres, Final report U.E contract SMT4-CT96/2104, 2000.

[18] C. Proust, Hot surface ignition in flowing streams of hydrogen air mixtures, ICHS symp. Adelaide, Australia, sept 2019.

[19] P. Wolanski, S. Wojcicki, Investigation into the mechanisms of the diffusion ignition of a combustible gas flowing into an oxidizing atmosphere, Comb. Inst. 14 (1973) 1217-1223.

[20] F.L. Dryer, M. Chaos, Z. Zhao, J.N. Stein, J.Y. Alpert, C. Homer, Spontaneous ignition of pressurized releases of hydrogen and natural gas into air, Comb. Science and Techn. 179 (2007) 663-694.

[21] V.V. Golub, D.I. Baklanov, S.V. Golovatsov, M.F. Ivanov, I.N. Laskin, A.S. Saveliev, N.V. Semin, V.V. Volodin, Mechanisms of high pressure hydrogen gas self-ignition in tubes, J. Loss Prev. Process Industries., 21 (2008) 185-198.

[22] T. Mogi, D. Kim, H. Shiina, S. Horiguchi, Self-ignition and explosion during discharge of high pressure hydrogen", J. Loss Prev. Process Industries. 21 (2008) 199-204.

[23] Z. Wang, X. Pan, Y. Jiang, Q. Wang, W. Yan, J. Xiao, T. Jordan, J Jiang, Experiment study on the pressure and flame characteristics induced by high-pressure hydrogen spontaneous ignition, Int. J. Hydrogen Energy. 45 (2020) 18040-18056.

[24] S. Zhou, Z. Luo, T. Wang, M. He, R. Li, B. Su, Research progress on the self-ignition of pressure hydrogen discharge : a review, Int. J. Hydrogen Energy, (2022) in press.

[25] E. Bourgin, M.M. Alves, C. Yang, F.F. Fachini, L. Bauwens, Effects of Lewis numbers and kinetics on spontaneous ignition of hydrogen jets, Proc. Comb. Inst. 36 (2017) 2833-2839.

[26] T. Matsuyama, M. Ogu, H. Yanamoto, J.C.M. Marijnissen, B. Scarlett, Impact charging with single particles of hundred micrometre size, Powder Techn. 135-136 (2003) 14-22.

[27] S. Matsusaka, H. Maruyama, T. Matsuyama, M. Ghadiri, Triboelectric charging of powders : a review, Chem. Eng. Sci. 65 (2010) 5781-5807.

[28] A.G. Bailey, Charging of solids and powders, J. of Electrosatics. 30 (1993) 167-180.

[29] R T Waters, Electrical breakdown at high pressures: a Paschen law function and compressible gas dynamics, J. of Physics D: Applied Physics. 52 (2018).

[30] M. Glor, Electrostatic hazrds in powder handling, ISBN 047192024X, Taylor & Francis Group

[31] L. Boyer, F. Houez, A. Tonck, J.L. Loubet, J.M. Georges, The influence of surface roughness on the capacitance between a sphere and a plane, J. Phys. D: Appl. Phys. 27 (1994) 1504-1508.

[32] J.X. Wen, Hydrogen Fires, First European Summer School on Hydrogen Safety, 2006.

[33] Z. Feng, Z. Long, Q. Chen, Voltage current characteristics of needle-plate system with different media on the collection plate, J. of Electrostatics 72 (2014) 129-135.

[34] M. Goldman, A. Goldman, R.S. Sigmond, The corona discharge, its properties and specific uses, Pure & Appi. Chem. 57 (1985) 1353-1362

[35] A. Jaworek, A. Krupa, Corona discharge from a multipoint electrode in flowing air, J. of Electrostatics 38 (1996) 187-197.

[36] C. Proust, S. Hawksworth, R. Rogers, M. Beyer, D. Lakic, D. raveau, P. Hervé, V. Pina, C. Petitfrere, X. Lefebvre, Developpement of a method for predicting the ignition of explosive atmospheres by mechanical friction and impacts (MECHEX), J. Loss Prev. Process Ind. 20 (2007) 349-365.

[37] I.V. Kragelskii, Friction and Wear, Butterworths, London, 1965.

[38] S. Hawksworth, R. Rogers, C. Proust, M. Beyer, S. Schenck, J. Gummer, D. Raveau, Ignition of explosive atmospheres by mechanical equipment, I.Chem. Symp. Series 150. 2005.

[39] K. Terao, T. Kuno, M. Mizuno, Heat treatment by ultrasonic heating, Bulletin of the JSME. 23 (1980) 1275-1282.

[40] T. Von Karmann, Aerodynamics, Mc Graw-Hill, New-York, ISBN-10, 1963.

## Appendix

Following Glassman [12], a flame is able to propagate if the thermal power transferred by conduction from the burning zone towards the reactant ahead of the ignition plane is smaller than the power released in the burning zone. The stable laminar burning velocity, $S_l$, is obtained when the two powers are equal. With a one-step zero order chemistry, the equations to solve are then :

$$\lambda \cdot \left(\frac{d^2T}{dx^2}\right)_{T:Tign \to Tb} = \rho_0 \cdot A \cdot \Delta H_{comb} \cdot \frac{T_0}{T} \cdot e^{-\frac{E_{act}}{R \cdot T}} \text{ and } \lambda \cdot \left(\frac{dT}{dx}\right)_{ign} \approx \rho_0 \cdot Cp \cdot S_l \cdot \left(T_{ign} - T_0\right)$$

Where :

- $S_l$ is the laminar burning velocity,
- $T_b$ is the temperature of the combustion gases,
- $T_{ign}$ is the ignition temperature of the reactants,
- $T_0$ is the initial temperature of the mixture,
- $E_{act}$ is activation energy of the global reaction,
- A is the preexponential coefficient of the global reaction,
- R is the perfect gas constant,
- $\rho_0$ is the specific mass of the mixture at $T_0$,
- Cp is the specific heat of the mixture (average between $T_0$ and $T_{ad}$),
- $\lambda$ is the heat conductivity of the mixture (at $T_{ad}$),
- $\Delta H_{comb}$ is the heat released by the combustion.

In the context of high asymptotics, when $E_{act}/R.T$ is large, $T_{ign}$ is always close to $T_b$. In the particular case of adiabatic flames, $T_b=T_{ad}$ the adiabatic combustion temperature and $S_l=S_{lad}$ such that :

$$S_{lad}{}^2 = 2 \cdot \frac{\lambda}{\rho_0 \cdot . Cp.} \cdot \frac{T_0}{T_{ad} - T_0} \cdot \frac{\Delta H_{comb}}{Cp \cdot (T_{ad} - T_0)} \cdot \frac{R \cdot T_{ad}}{E} \cdot A \cdot e^{-E_{act}/R.T_{ad}}$$

# Strength of Knowledge in Risk Assessments for Fuel-Air Explosions in Complex Geometries: Implications for Hydrogen Systems

**Skjold T.[1,*], Hisken H.[1,2], Derempouka E.[1], Lucas M.[1,3], Johnson, D.M.[4]**

[1] *University of Bergen, Department of Physics and Technology, Bergen, Norway.*
[2] *Gexcon Certification, Bergen, Norway.*
[3] *Gexcon, R&D Department, Bergen, Norway.*
[4] *DNV Spadeadam Research and Testing, Cumbria, UK.*
**Corresponding author's email: trygve.skjold@uib.no*

## ABSTRACT

This paper addresses one essential aspect of the strength of knowledge (SoK) in risk assessments for systems where fuel-air explosions in complex geometries represent a significant hazard: the understanding of physical phenomena and the ability of models and modellers to predict the consequences of accidental fuel-air explosions in industry and society. The main objective of this study is to highlight knowledge gaps and inherent sources of uncertainty in risk assessments that support decisions concerning the development, deployment and operation of emerging hydrogen technologies. The approach adopted entails a review of lessons learnt from selected large-scale experiments conducted over the last decades, covering various combinations of congestion, confinement, spatial scale and flammable fuel-air mixtures. The discussion elaborates on the inherent limitations in the predictive capabilities of model systems for hydrogen-air explosions in complex geometries, including brief discussions of the implications of weak knowledge from an ethical as well as a practical perspective. The suggestions for further work emphasise the importance of conducting further large-scale explosion experiments in test facilities that capture the complexity and spatial scale of the actual systems found in industry or society, in conjunction with blind-prediction benchmark studies for developers and users of advanced consequence models.

**KEYWORDS:** Strength of knowledge, Fuel-air explosion, Hydrogen safety, Ethical considerations.

## INTRODUCTION

### Risk assessments and strength of knowledge

The concept of *safety* implies control over *hazards* that can result in *losses*, and an *accident* is an unintended and sudden event that results in loss. In this context, *risk* is a measure of the expected losses for a specified system or activity. Figure 1 shows a general schematic of the activities involved in risk analysis, risk assessment and risk management. The primary purpose of the risk assessment is to support decision-making, in various contexts, by stakeholders such as policy makers, authorities, investors, insurance companies, employers, employees, customers and the public.

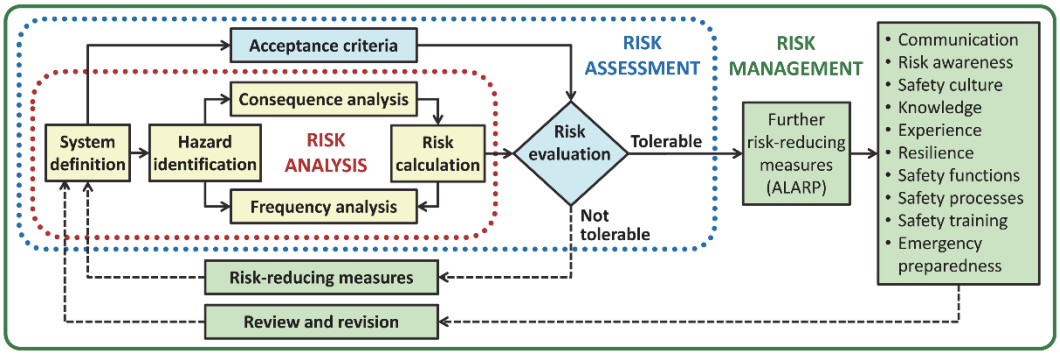


**Fig. 1.** General schematic for risk analysis, risk assessment and risk management.

A conventional quantitative risk assessment (QRA) entails the calculation of expectation values that combine event frequencies and consequences for the hazards identified for a specific system. There is, however, increasing awareness and recognition of the importance of reflecting knowledge and expressing uncertainty in the understanding, analysis, assessment, management and communication of risk [1-2], and various researchers have proposed methods for assessing the *strength of knowledge* (SoK) in risk assessments. One example is the crude direct grading approach described by Aven [3], where the SoK is considered *weak* if one or more of the conditions below are met:

1. The assumptions made represent strong simplifications.
2. Data are not available, or are unreliable.
3. There is lack of agreement/consensus among experts.
4. The phenomena involved are not well understood and/or models are non-existent or known/believed to give poor predictions.

On the other hand, the SoK is considered *strong* if all of the following conditions are met:

1. The assumptions made are seen as very reasonable.
2. Much reliable data are available.
3. There is broad agreement/consensus among experts.
4. The phenomena involved are well understood and the models used are known to give predictions with the required accuracy.

With this in mind, the present study addresses one essential aspect of the SoK in risk assessments for systems where fuel-air explosions in complex geometries represent a significant hazard: the understanding of physical phenomena and the ability of models and modellers to predict the consequences of accidental fuel-air explosions in industry and society.

## Consequence modelling for fuel-air explosions

Accidental fires and explosions cause severe losses in industry and society [4]. Figure 2 a shows the explosion pentagon, originally introduced for dust explosions [5]. However, by including both congestion and confinement, the concept applies equally well to fuel-air explosions with gaseous and liquid fuels. Figure 2 b shows a simplified event tree for accident scenarios where the initiating event is loss of containment of flammable material and lists several factors that influence the chain of events. This paper is primarily concerned with the ability of models and modellers to predict the consequences of deflagrations in complex geometries, with or without transition to detonation (DDT).

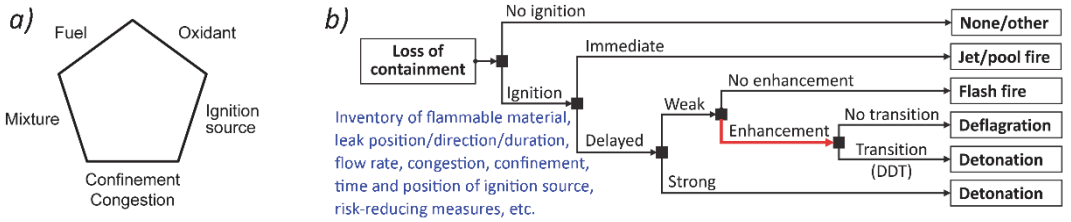


**Fig. 2.** The explosion pentagon (a) and a simplified event tree for scenarios involving loss of containment (b).

Tools for estimating the consequences of accidental fuel-air explosions range from empirical correlations and phenomenological models to advanced numerical model systems [6]. For large-scale complex geometries, it is common practice to use engineering models based on computational fluid dynamics (CFD) that rely on sub-grid models for capturing important physical phenomena.

## Hydrogen and hydrogen safety

Hydrogen and hydrogen-based fuels are expected to play a significant role in the global energy transition. Existing technologies can convert energy from renewable and non-renewable sources to hydrogen, hydrogen can be stored and transported in compressed, liquid or chemical form, and fuel cells, engines or turbines can convert hydrogen to electrical or mechanical energy and heat on demand. However, hydrogen is arguably the most reactive and easily ignitable of all energy carriers ever considered for widespread use in society. As such, it is not straightforward to achieve and document

the required level of safety for hydrogen systems. One example is the general requirements outlined in the international legislation for ships fuelled by low-flashpoint fuels, including hydrogen [7]:

*"The safety, reliability and dependability of the systems shall be equivalent to that achieved with new and comparable conventional oil-fuelled main and auxiliary machinery".*

Figure 3 shows the laminar burning velocity $S_L$ and the flammable concentration range for selected fuels [8]. Although $S_L$ provides a good indication of the relative reactivity of fuel-air mixtures, most accidental fuel-air explosions involve highly turbulent flow conditions, and it is also important to consider various hydrodynamic, thermo-diffusive and thermo-acoustic instabilities [9]. For hydrogen it is particularly important to account for the role of thermo-diffusive instabilities: cellular instabilities occur at sufficiently fuel-lean conditions (negative Markstein lengths) and pulsating instabilities occur at sufficiently fuel-rich conditions (positive Markstein lengths) [10]. Finally, the propensity of DDT in hydrogen-air mixtures has severe implications for explosion protection and risk assessments.

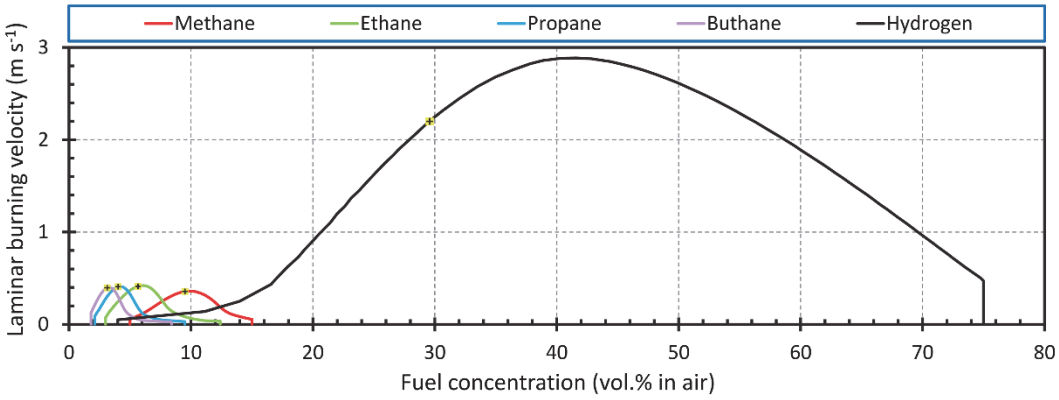


**Fig. 3.** Laminar burning velocities for selected fuels, where '+' indicates stochiometric concentrations.

The reactivity of the mixture has significant impact on fuel-air explosions in congested and partly confined geometries. Figure 4 summarises maximum overpressures measured in different experimental configurations with near stochiometric fuel-air mixtures:

a) Small-scale (1 m) and large-scale (10 m) wedge-shaped explosion vessels with obstacles [11-13].
b) A congested rig with dimensions 3m×3m×2m, placed 1.7 m from a wall, with ignition at the centre of the congestion, 0.5 m above ground [14]. The enhanced pressure outside the rig for pure hydrogen is caused by a transition to detonation as the flame exited the congested rig.

The results illustrate the strong effect of the reactivity of the fuel-air mixture, and the differences are enhanced for larger scales. With reference to Fig. 2 b, this implies that significant enhancement and DDT can occur for significantly smaller systems for hydrogen, compared to conventional fuels.

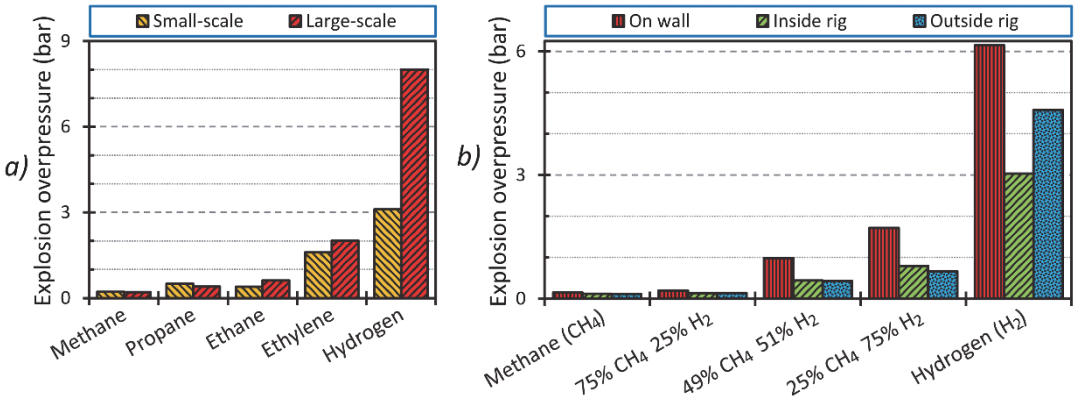


**Fig. 4.** Explosion pressures from experiments with near stoichiometric mixtures of various fuels in air.

## PHENOMENA AND MODELLING CAPABILITIES

This section summarises and discusses selected results and observations from various large-scale experiments and elaborates on the implications for the SoK in risk assessments for hydrogen systems.

### Case 1: A blind-prediction study for large-scale gas explosions

Figure 5 summarises results from two out of 27 tests with natural gas conducted as part of Phase 2 of the joint industry project (JIP) *Blast and Fire Engineering Project for Topside Structures* (BFETS) [15-16]. The experiments were conducted in a large-scale test rig representative of an offshore module with overall dimensions 25.6m×8m×8m. Figure 5 a shows unfiltered (+ and ×) and filtered (1.5 ms moving average and pressure peaks of duration 1 ms and 3 ms) overpressures measured for two experiments with end ignition and either low (Test 6) or high (Test 7) equipment density.

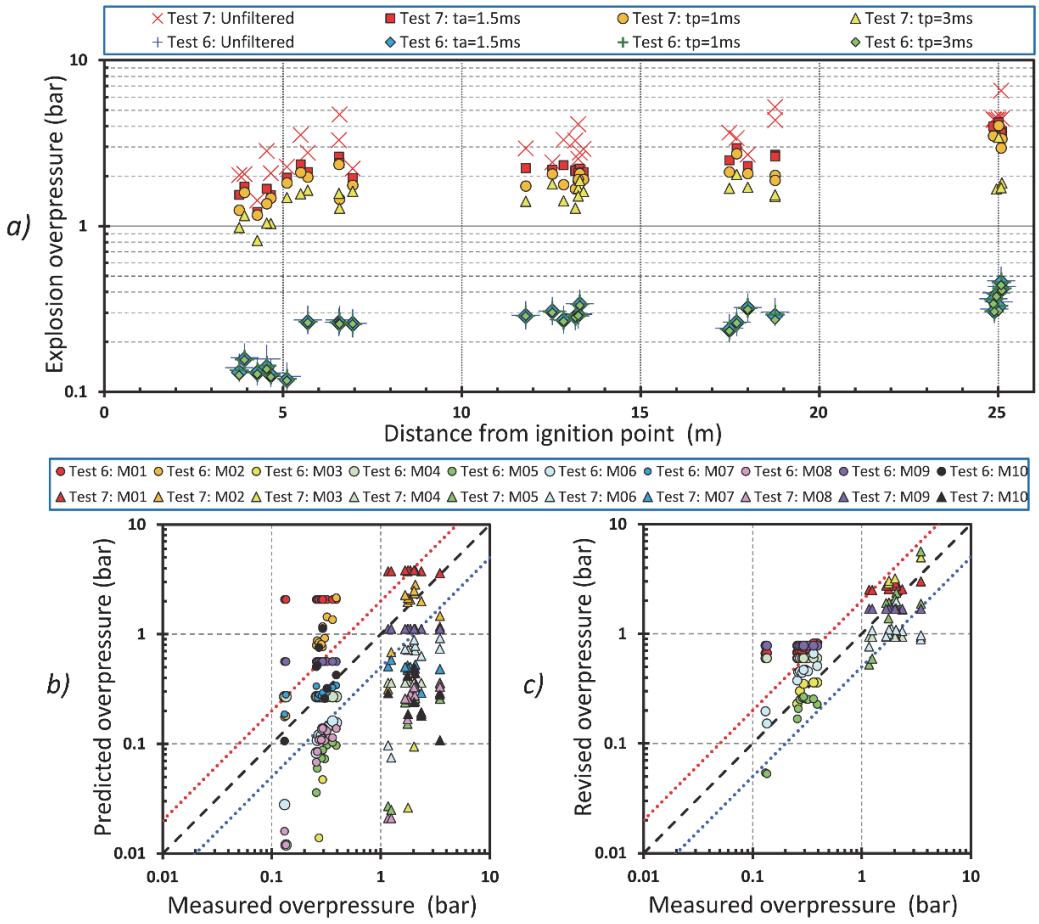


**Fig. 5.** Results from Test 6 and Test 7 from BFETS Phase 2.

Figure 5 b summarises the predictions for maximum explosion pressures measured in the same tests from a blind-prediction benchmark study involving ten models (M01-M10) [15]. After the evaluation of the blind-predictions, when the experimental results were known and some discrepancies between the digital model and the "as-built" geometry had been corrected, six of the ten modellers submitted the updated predictions summarised in Fig. 5 c. The considerable reduction in the scatter of the results from Fig. 5 b to Fig. 5c demonstrates the significant difference between blind-predictions, which arguably are most representative for risk assessments (the modellers received the same information for the blind prediction), and regular validation of models against known experimental results.

Observations concerning the SoK in risk assessments for fuel-air explosions:

- The level of congestion has significant effect on the severity of fuel-air explosions.
- The predictive capabilities of consequence models can only be assessed in blind-prediction benchmark studies involving large-scale experiments that resemble the actual systems.

**Case 2: Repeatability of large-scale gas explosions**

Figure 6 shows a representative geometry model from BFETS Phase 3A and a snapshot from an explosion during the experimental campaign (courtesy of DNV Spadeadam Research and Testing). Phase 3A included 45 experiments in a 28m×8m×12m test rig representative of an offshore module with relatively low degree of confinement. To investigate the repeatability of the experiments, the UK Health & Safety Executive (HSE) commissioned two additional test series: five repeated experiments with central ignition (Alpha), and six repeated experiments with end ignition (Beta) [17]. The two series involved different levels of congestion, and the experiments were performed with mixtures of natural gas and air for equivalence ratios in the range 1.05-1.14.

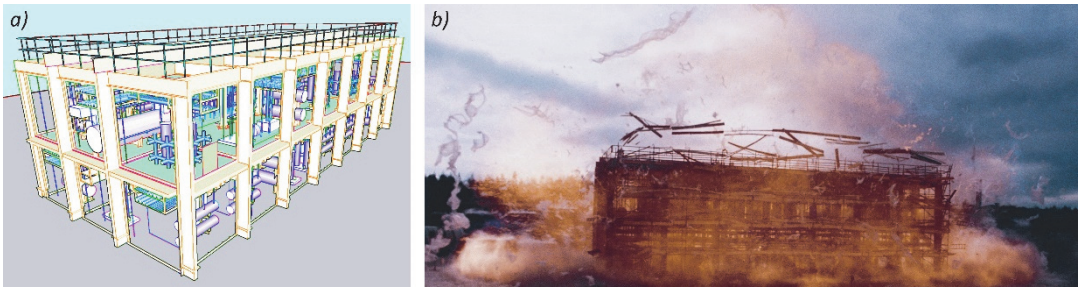


**Fig. 6.** Geometry model for the test rig (a) and an explosion in the same rig.

Figure 7 a shows unfiltered (+ and ×) and filtered (◊ and ○, 1.5 ms moving average) overpressures as a function of distance from the ignition point. The vertical dashed lines indicate the maximum travel distance for the flame front within the rectangular module. Some of the highest explosion pressures measured near the exit of the rig, especially for end ignition, are likely caused by DDT events [18]. To get an impression of the inherent variation between repeated tests, Figs. 7 b and c show absolute pressures normalised by the average value of the filtered absolute pressures for each pressure sensor, for Alpha and Beta, respectively. Near the exit of the rig, the normalised overpressures show a scatter of a factor 2 (indicated by the dotted blue and red lines in Figs. 7 b and c).

Since the blind-prediction study mentioned in Case 1, commercial consequence models developed for fuel-air explosions with natural gas in offshore facilities have been extensively validated against the experiments conducted as part of BFETS. The model predictions are often satisfactory, provided the modellers adhere to the guidelines provided by the model developers [19]. It is, however, important to keep in mind that engineering models for industrial fuel-air explosions in complex geometries cannot resolve all relevant physical phenomena on the computational grid, and therefore rely heavily on sub-grid models tuned and optimised based on results from specific experiments. This implies that the uncertainty in the model predictions is likely to increase for configurations that deviate significantly from the original experiments. The results are also sensitive to how the simulations are set up, including the resolution of the computational mesh. As such, modellers with experience from validation against large-scale experiments that resemble the actual system under consideration are likely to produce more accurate results compared to less experienced users.

Observations concerning the SoK in risk assessments for fuel-air explosions:

- Repeated large-scale experiments are crucial for assessing the inherent limitations in the predictive capabilities that can be achieved with state-of-the-art consequence models.
- The spread in the normalised explosion pressures for repeated experiments increases with the distance from the ignition point, as the flames accelerate through the congested rig.
- It is important to limit the maximum travel distance for flames in congested geometries.

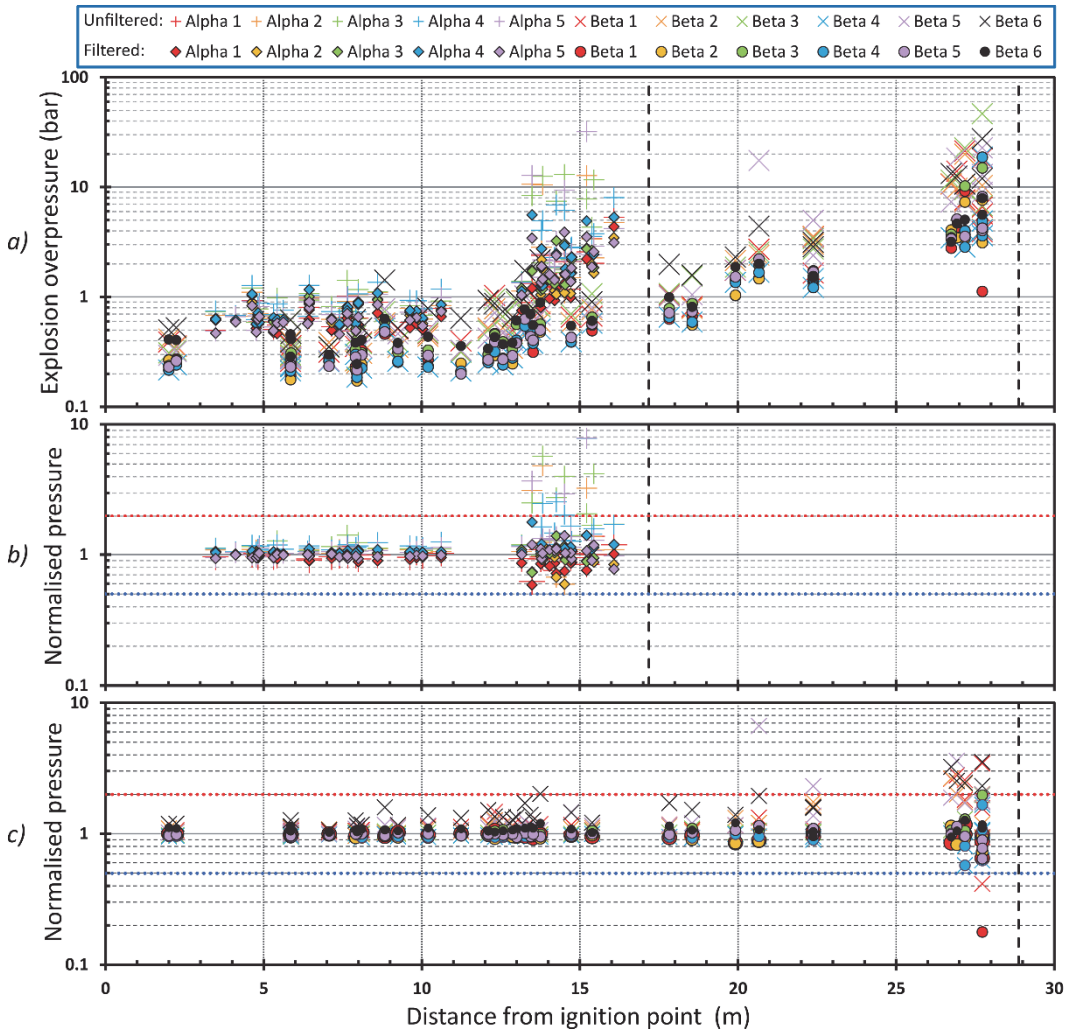


**Fig. 7.** Maximum internal overpressures from the Alpha and the Beta series.

## Case 3: Effect of initial flow field for gas explosions

Whereas the experiments described above entailed explosions in homogeneous and initially quiescent fuel-air mixtures, pressurised releases typically result in inhomogeneous gas clouds with pre-ignition turbulence and non-zero mean flow speeds. To limit the computational cost of simulating multiple release and dispersion scenarios, it is common practice in probabilistic explosion studies to represent the realistic non-homogenous fuel-air clouds with equivalent homogeneous clouds that can be placed and ignited in various positions. Although several researchers have proposed and investigated methods for defining equivalent gas clouds, there is limited consensus concerning the validity, accuracy and level of conservatism associated with the various concepts [20-22].

Figure 8 summarises model predictions and experimental results from the JIP *Assessing the Influence of Real Releases on Explosions* (AIRRE). The project was motivated by literature studies and CFD simulations that indicated significant differences in the explosion pressures obtained from ignited jet releases pointing into congested regions of varying congestion density and the corresponding pressures obtained with the equivalent homogeneous gas cloud method Q9 [23-24]. The shaded areas in Fig. 8 indicate model predictions with the CFD tool FLACS for ignited jet releases with mass flows 1, 10 and 100 kg $s^{-1}$ (blue) and the corresponding predictions using the Q9 approach (red).

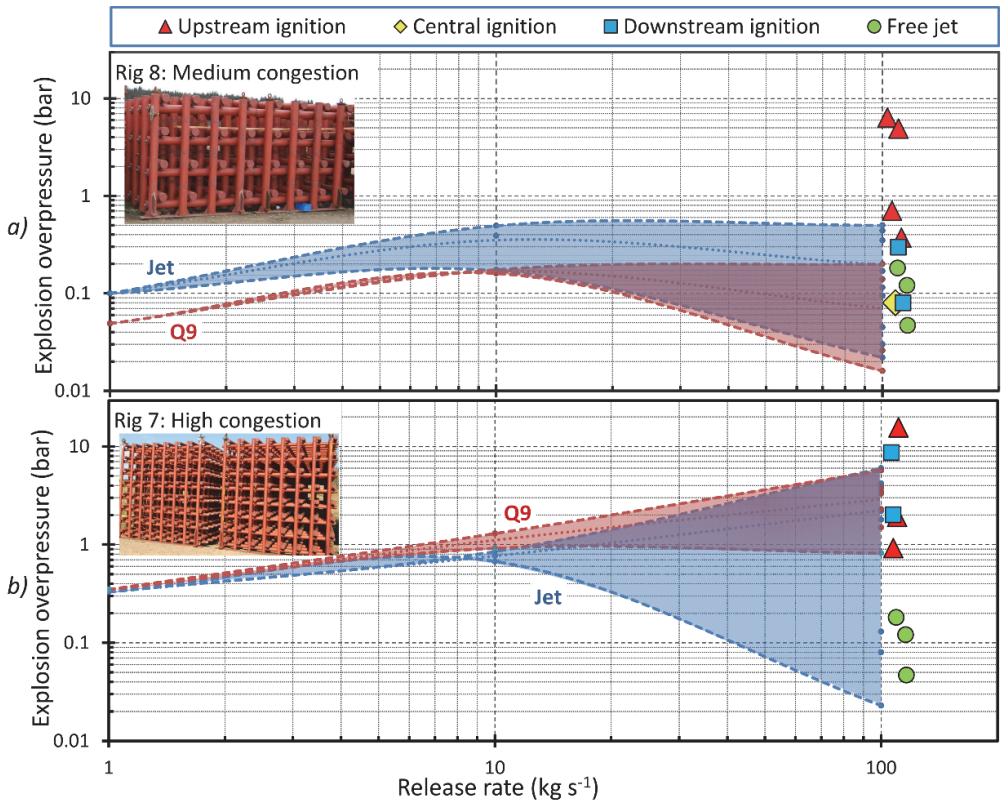


**Fig. 8.** Predicted and experimental maximum overpressures for ignited releases of natural gas [25].

The AIRRE project included 16 experiments with delayed ignition of natural gas jets with mass flows in excess of 100 kg $s^{-1}$, including free jets and jets directed into congested regions with medium or high level of congestion (Fig. 8). The position of the ignition points varied relative to the position of the release and the congested rig [24].

Observations concerning the SoK in risk assessments for fuel-air explosions:

- The initial flow field, level of congestion and location of the ignition source relative to the origin of the jet release can have significant impact on the consequences of fuel-air explosions.
- It is important to continuously challenge the established consequence models by conducting large-scale experiments involving scenarios that have not been thoroughly investigated in the past, and that explore phenomena that are relevant for actual accident scenarios in industry.

**Case 4: Explosions in interconnected vessel systems**

As part of the EU-funded project *Dust Explosion Simulation Code* (DESC), the UK Health & Safety Laboratory (HSL) conducted a total of 34 dust explosion experiments in the interconnected vented vessel system illustrated in Fig. 9 a [26-27]. Dust-air suspensions were ignited in one of three locations in the larger vessel after a pre-set ignition delay time of 0.5 s measured from the activation of the valves controlling the dust dispersion system. The experimental program included 34 tests with various dusts and different vessel configurations. Of these, only Test 13 with coal dust produced significant pressure enhancement in the secondary vessel.

Figure 10 summarises the maximum explosion pressures measured in the two vessels and the connecting pipe for three tests with coal dust ($K_{St}$ 143 bar m $s^{-1}$ and $P_{max}$ 7.4 bar), nominal dust concentration 500 g $m^{-3}$, and ignition positions 1-3 indicated in Fig. 9a. The same figure includes results from three CFD simulations that explored the effect of modest variation in the location of the ignition point (± 0.6 m in Y-direction) for Test 13 [28-29].

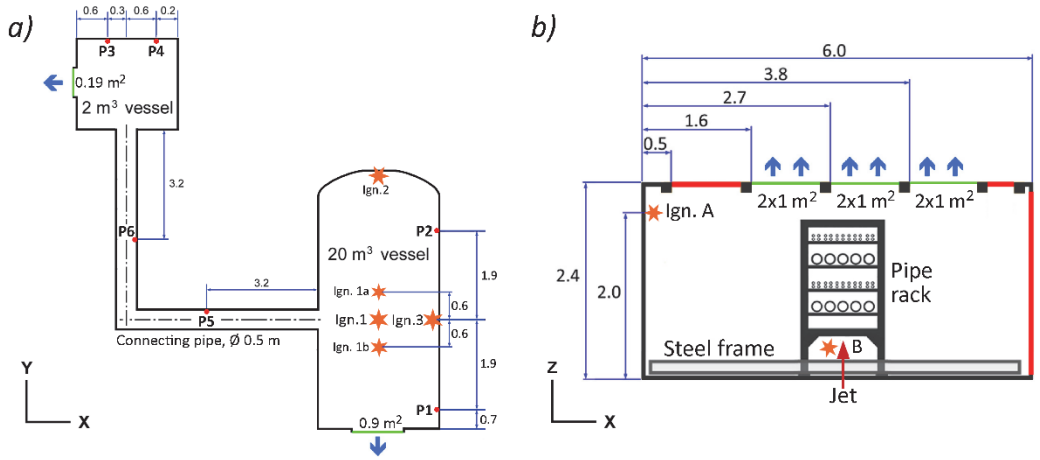


**Fig. 9.** Cross-sections of the interconnected vessel system (a) and a vented 20-foot container with pipe rack (b).

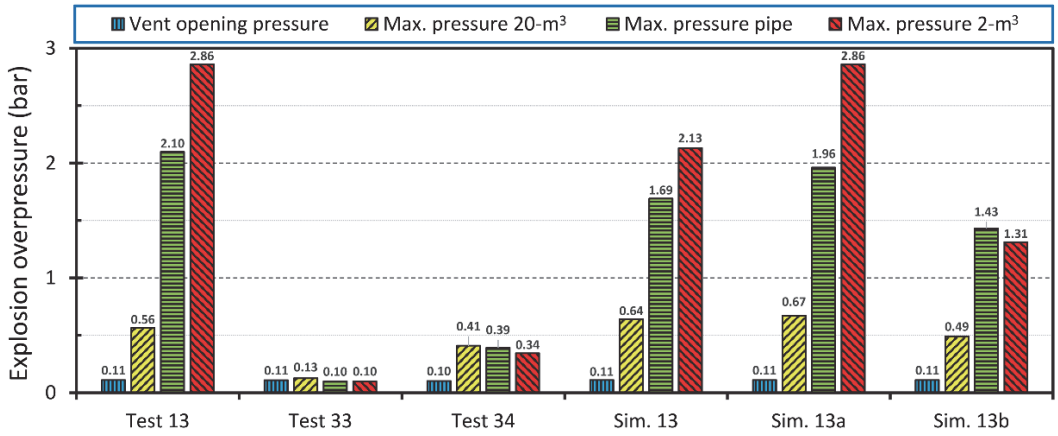


**Fig. 10.** Summary of results from experiments and simulations for coal dust explosions.

Observations concerning the SoK in risk assessments for fuel-air explosions:

- Fuel-air explosions in complex confined geometries can be very sensitive to modest variations in the initial and boundary conditions.
- It is not straightforward to validate consequence models for fuel-air explosions from large-scale experiments that are not repeated.

### Case 5: Vented hydrogen deflagrations

As part of the EU-funded project *Improving Hydrogen Safety for Energy Applications through pre-normative research on vented deflagrations* (HySEA), Gexcon conducted 66 vented hydrogen deflagration tests in 20-foot shipping containers. This included 42 tests with initially quiescent and homogeneous mixtures and 24 tests with inhomogeneous mixtures created by jet or diffusive releases near the ground [30]. Figure 9 b shows a vertical cross-section of a container with six 1-m$^2$ vent openings in the ceiling and a pipe rack fixed to a steel frame in centre position (configuration 'P2').

Figure 11 a summarises the results from 15 vented deflagration tests, with either the pipe rack ('P2') or only the steel frame on the floor ('FO'). The symbol '*' indicates tests where the container was damaged beyond repair. The six vent openings were covered with either plastic film ('Open') or commercial vent panels ('Panels'). In the tests with jet releases ('Jet'), the ignition source was located near the ceiling ('A'). In the tests with initially quiescent homogeneous mixtures ('Q'), the ignition source was located on the floor ('B'). Tests 71 and 72 included significantly higher level of congestion ('HC') inside the container [30].

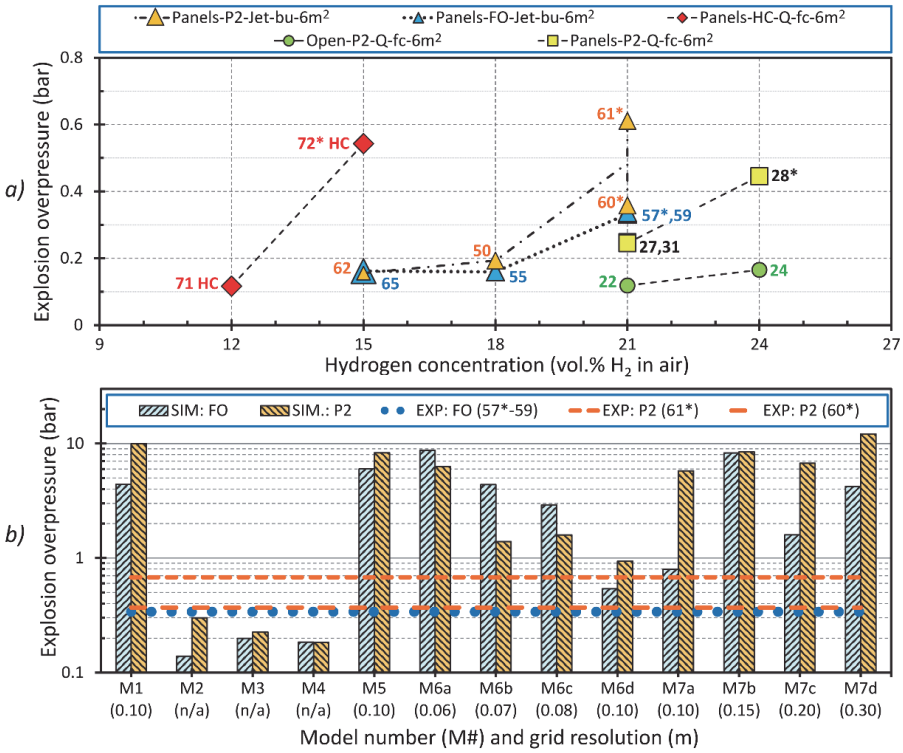


**Fig. 11.** Experimental results (a) and model predictions (b) for vented hydrogen deflagrations in containers.

Figure 11 b summarises the experimental results and model prediction from one of the blind-prediction benchmark studies conducted as part of the HySEA project [31]. The scenarios involved vented deflagrations in inhomogeneous hydrogen-air mixtures resulting from continuous stratification of hydrogen during vertical jet releases, either with (tests 60 and 61) or without (tests 57 and 59) the pipe rack. Seven participants (M1-M7) submitted model predictions, including two contributions that included predictions for four different grid resolutions (M6a-d and M7a-d). Apart from submissions M2, M3 and M4, all modellers used the same commercial CFD tool.

Figure 11 b shows that spread in the model predictions covers almost two orders of magnitude. There is also significant spread in the predictions by modellers using the same commercial CFD tool. The modellers that set up the dispersion scenarios correctly in the commercial CFD tool predicted the stratification of hydrogen inside the container prior to ignition quite well but overestimated the explosion pressures significantly. Given the significant difference in the measured pressures for the two tests with pipe rack (tests 60 and 61), it cannot be ruled out that additional repetitions might have resulted in higher explosion pressures.

Observations concerning the SoK in risk assessments for fuel-air explosions:

- Congestion and buoyancy-driven stratification in confined geometries can result in violent explosions, even for relatively low (nominal) concentrations of hydrogen in air.
- There can be significant variations in model predictions from different users of the same model.

## ETHICAL CONSIDERATIONS

The following example, quoted from the paper *The Ethics of Belief* delivered by William Kingdon Clifford at the monthly meeting of the Metaphysical Society in London on 11 April 1876 [32], highlights selected aspects concerning engineering ethics and the strength of knowledge in risk assessments for systems with a significant potential for loss:

*A shipowner was about to send to sea an emigrant-ship. He knew that she was old, and not overwell built at the first; that she had seen many seas and climes, and often had needed repairs. Doubts had been suggested to him that possibly she was not seaworthy. These doubts preyed upon his mind, and made him unhappy; he thought that perhaps he ought to have her thoroughly overhauled and refitted, even though this should put him at great expense. Before the ship sailed, however, he succeeded in overcoming these melancholy reflections. He said to himself that she had gone safely through so many voyages and weathered so many storms that it was idle to suppose she would not come safely home from this trip also. He would put his trust in Providence, which could hardly fail to protect all these unhappy families that were leaving their fatherland to seek for better times elsewhere. He would dismiss from his mind all ungenerous suspicions about the honesty of builders and contractors. In such ways he acquired a sincere and comfortable conviction that his vessel was thoroughly safe and seaworthy; he watched her departure with a light heart, and benevolent wishes for the success of the exiles in their strange new home that was to be; and he got his insurance-money when she went down in mid-ocean and told no tales.*

*What shall we say of him? Surely this, that he was verily guilty of the death of those men. It is admitted that he did sincerely believe in the soundness of his ship; but the sincerity of his conviction can in no wise help him, because he had no right to believe on such evidence as was before him. He had acquired his belief not by honestly earning it in patient investigation, but by stifling his doubts. And although in the end he may have felt so sure about it that he could not think otherwise, yet inasmuch as he had knowingly and willingly worked himself into that frame of mind, he must be held responsible for it.*

*Let us alter the case a little, and suppose that the ship was not unsound after all; that she made her voyage safely, and many others after it. Will that diminish the guilt of her owner? Not one jot. When an action is once done, it is right or wrong for ever; no accidental failure of its good or evil fruits can possibly alter that. The man would not have been innocent, he would only have been not found out. The question of right or wrong has to do with the origin of his belief, not the matter of it; not what it was, but how he got it; not whether it turned out to be true or false, but whether he had a right to believe on such evidence as was before him. […] To sum up: it is wrong always, everywhere, and for anyone, to believe anything upon insufficient evidence.*

Clifford does not provide a clear definition of 'sufficient evidence', and it can be argued that his summary statement is itself an expression of belief, and hence not objectively verifiable [33]. Nevertheless, from an ethical perspective it seems pertinent to critically assess the SoK in risk assessments for hydrogen systems. Widespread deployment of hydrogen technologies in society will require massive investments, and the prospects of severe accidents represent a significant risk to all stakeholders. There have been several serious accidents involving hydrogen in recent years, and the stakes with respect to the potential for severe losses will increase dramatically as the use of hydrogen shifts from controlled environments in industrial facilities to the public domain, and applications extending from passenger cars to buses, trains, ferries and airplanes.

## OVERALL DISCUSSION AND CONCLUSIONS

The purpose of a risk assessment is to increase the knowledge about a system, and support decisions that may entail difficult economic, ethical or political deliberations. The inherent lack of relevant data that can support probabilistic risk assessments for the emerging hydrogen technologies implies increased focus on inherently safe or robust design. To this end, critical assessment of the inherent uncertainty in model predictions for relevant accident scenarios represents a crucial first step towards increased SoK in risk assessments for hydrogen systems. This can be achieved by conducting repeated large-scale explosion experiments in test facilities that capture the complexity and spatial scale of the actual systems found in industry or society, in conjunction with blind-prediction benchmark studies for developers and users of advanced consequence models. Hence, the predictive capabilities of both models and modellers can be assessed, documented and improved through an iterative process involving planning and specifications, announcements, modelling, submission of blind-predictions,

completion of experimental campaigns, data analysis, retrospective workshops, submission of revised predictions, identification of knowledge gaps, reporting, and improvements to model systems.

The extensive research conducted in the aftermath of the Buncefield explosion in 2005 has resulted in increased knowledge and awareness of DDT and detonations in accidental fuel-air explosions [34-35]. Given the extreme reactivity of hydrogen-air mixtures, compared to the conventional fuels for which most consequence models have been developed and validated, it is essential to develop models and methods for incorporating detonation scenarios in safety engineering and risk assessments for hydrogen systems [18]. A framework for specifying the SoK concerning the predictive capabilities of consequence models should assess whether a given model reproduces important trends observed in experiments, whether the model is likely to overpredict or underpredict consequences, to what extend the model can estimate the probability of DDT, as well as the level of accuracy that can be expected for different categories of scenarios: ±20%, within a factor 2, within an order of magnitude, etc.

In addition to the uncertainty concerning physical phenomena and the predictive capabilities of models and modellers, it is important to explore other aspects of the SoK in risk assessment for hydrogen systems. The agreement/consensus among experts can for instance be assessed in expert workshops and benchmark studies involving comparative risk assessments for hypothetical systems.

## ACKNOWLEDGEMENTS

The authors gratefully acknowledge the financial contribution from the Research Council of Norway (RCN) to the projects *Safe Hydrogen Implementation: Pre-normative research for Ships* ($SH_2$IPS, grant agreement number 326281) and *Safe Hydrogen Fuel Handling and Use for Efficient Implementation 2* ($SH_2$IFT-2, grant agreement number 327009).

## REFERENCES

[1] R. Flage, T. Aven, Expressing and Communicating Uncertainty in Relation to Quantitative Risk Analysis, Reliab.: Theory Appl. 4 (2009) 9-18.

[2] T. Aven, Misconceptions of Risk, Wiley, Chichester, 2010.

[3] T. Aven, Practical Implications of the New Risk Perspectives, Reliab. Eng. Syst. 115 (2013) 136-145.

[4] Marsh JLT Specialty, 100 Largest Losses in the Hydrocarbon Industry 1974-2019, Marsh, 2020.

[5] C.W. Kauffman, Agricultural Dust Explosions in Grain Handling Facilities, In: Lee, J.H.S. and Guirao, C.M. (Eds.), Proceedings of the International Conference on Fuel-Air Explosions, pp. 305-347, 1982.

[6] T. Skjold, C. Souprayen, S. Dorofeev, Fires and explosions, Prog. Energy Combust. Sci. 64 (2018) 2-3.

[7] IMO, IGF Code – International Code of Safety for Ships Using Gases or Other Low-flashpoint Fuels, International Maritime Organisation (IMO), London, 2016.

[8] A.A. Konnov, A. Mohammad, V.R. Kishore, N.I. Kim, C. Prathap, S. Kumar, A Comprehensive Review of Measurements and Data Analysis of Laminar Burning Velocities for Various Fuel+Air Mixtures, Prog. Energy Combust. Sci. 68 (2018) 197–267.

[9] P. Clavin, G. Searby, Combustion Waves and Fronts in Flows. Cambridge University Press, Cambridge, 2016.

[10] A.L. Sánchez, F.A. Williams, F.A., Recent Advances in Understanding of Flammability Characteristics of Hydrogen, Prog. Energy Combust. Sci. 41 (2014) 1–55.

[11] M. Bjørkhaug, Investigation of Turbulent Explosion Properties for Hydrogen-Air and Some Hydrocarbon-Air Mixtures, Report Chr. Michelsen Institute (CMI), CMI-875110-2, Bergen, 1988.

[12] M. Bjørkhaug, Large-scale Investigation of Turbulent Explosion Properties for Hydrogen-Air and Some Hydrocarbon-Air Mixtures, Report Chr. Michelsen Institute (CMI), CMI-25110-2, Bergen, 1988.

[13] D. Bjerketvedt, J.R. Bakke, K. van Wingerden, Gas Explosion Handbook, J. Hazard. Mater. 52 (1997) 1-150.

[14] L.C. Shirvill, T.A. Roberts, M. Royle, D.B. Willoughby, P. Sathiah, Experimental Study of Hydrogen Explosion in Repeated Pipe Congestion – Part 2: Effects of Increase in Hydrogen Concentration in Hydrogen-Methane-Air Mixture, Int. J. Hydrog. Energy 44 (2019) 3264-3276.

[15] C.A. Selby, B.A. Burgan, Blast and Fire Engineering for Topside Structures – Phase 2: Final Summary Report, Report No. SCI-P-253, ISBN 1-85942-078-8, The Steel Construction Institute, 1998.

[16] D.M. Johnson, G.A. Shale, B.J. Lowesmith, D. Campbell, Blast and Fire Engineering Project for Topside Structures Phase 2: Final Report on the Explosion Test Programme, Report No. R1579, BG Research and Technology, 1997.

[17] J.A. Evans, R. Exon, D.M. Johnson, The Repeatability of Large Scale Explosion Experiments, Offshore Technology Report – OTO 1999 042, Health & Safety Executive (HSE), October 1999.

[18] O.R. Hansen, D.M. Johnsen, Improved Far-field Blast Predictions from Fast Deflagrations, DDTs and Detonations of Vapour Clouds Using FLACS CFD, J. Loss Prev. Process Ind. 35 (2015) 293–306.

[19] T. Skjold, H.H. Pedersen, L. Bernard, P. Middha, V.D. Narasimhamurthy, T. Landvik, T. Lea, L. Pesch, A Matter of Life and Death: Validating, Qualifying and Documenting Models for Simulating Flow-related Accident Scenarios in the Process Industry, Chem. Eng. Trans. 31 (2013) 187-192.

[20] V. Tam, M. Wang, C.N. Savvides, E. Tunc, S. Ferraris, J.X. Wen, Simplified Flammable Gas Volume Methods for Gas Explosion Modelling from Pressurized Gas Releases: A Comparison with Large-Scale Experimental Data, IChemE Symposium Series, 154 (2008) 858-868.

[21] O.R. Hansen, F. Gavelli, S.G. Davis, P. Middha, Equivalent Cloud Methods Used for Explosion Risk and Consequence Studies, J. Loss Prev. Process Ind. 26 (2013) 511–527.

[22] J. Stewart, S. Gant, A Review of the Q9 Equivalent Cloud Method for Explosion Modelling, FABIG Newsletter, Issue 75, March 2019, 16–25.

[23] T. Skjold, H. Hisken, L. Mauri, G. Atanga, L. Bernard, K. van Wingerden, A. Foissac, P. Quillatre, V. Blanchetière, A. Dutertre, D. Kostopoulos, A. Pekalski, D. Allason, M. Johnson, L. Jenney, E. Leprette, D. Jamois, Assessing the Influence of Real Releases on Explosions: Motivation and Previous Work, Proceedings Twelfth International Symposium on Hazards, Prevention and Mitigation of Industrial Explosions, Kansas City, 12-17 August 2018, pp. 695-718.

[24] H. Hisken, L. Mauri, G. Atanga, M. Lucas, K. van Wingerden, T. Skjold, P. Quillatre, A. Dutertre, T. Marteau, A. Pekalski, L. Jenney, D. Allason, M. Johnson, E. Leprette, D. Jamois, J. Hébrard, C. Proust, Assessing the Influence of Real Releases on Explosions: Selected Results from Large-Scale Experiments, J. Loss Prev. Process Ind. 72 (2021) 104561.

[25] T. Skjold, L. Mauri, P. Quillatre, A. Foissac, V. Blanchetière, A. Dutertre, T. Marteau, A. Pekalski, D. Allason, M. Johnson, L. Jenney, J. Hebrard, D. Jamois, E. Leprette, H. Hisken, G. Atanga, M. Lucas, D. Muthusamy, K. van Wingerden, Assessing the Influence of Real Releases on Explosions (AIRRE): Background and Selected Results, FABIG, 98th UK Technical Meeting, 27-28 March 2019.

[26] P. Holbrow, DESC: Interconnected Vented Explosion Tests, Report EC/04/30, Health & Safety Laboratory (HSL), Buxton, 2004.

[27] P. Holbrow, DESC: Phase 2 Interconnected Vented Explosion Tests, Report EC/04/72, Health & Safety Laboratory (HSL), Buxton, 2005.

[28] T. Skjold, Review of the DESC Project, J. Loss Prev. Process Ind. 20 (2007) 291-302.

[29] T. Skjold, Flame Propagation in Dust Clouds: Challenges for Model Validation, Proceedings Eighth International Symposium on Hazards, Prevention and Mitigation of Industrial Explosions, Yokohama, 5-10 September 2010: 11 pp.

[30] T. Skjold, H. Hisken, S. Lakshmipathy, G. Atanga, M. van Wingerden, K.L. Olsen, M.N. Holme, N.M. Turøy, M. Mykleby, K. van Wingerden, Vented Hydrogen Deflagrations in Containers: Effect of Congestion for Homogeneous and Inhomogeneous Mixtures, Int. J. Hydrog. Energy 44 (2019) 8819-8832.

[31] T. Skjold, H. Hisken, L. Bernard, L. Mauri, G. Atanga, S. Lakshmipathy, M. Lucas, M. Carcassi, M. Schiavetti, V.C.M Rao, A. Sinha, I.C. Tolias, S.G. Giannissi, A.G. Venetsanos, J.R. Stewart, O.R. Hansen, C. Kumar, L. Krumenacker, F. Laviron, R. Jambut, A. Huser, Blind-prediction: Estimating the Consequences of Vented Hydrogen Deflagrations for Inhomogeneous Mixtures in 20-Foot ISO Containers. J. Loss Prev. Process Ind. 61 (2019) 220-236.

[32] W.K. Clifford, The Ethics of Belief, Contemporary Review 29 (1877) 289-307.

[33] N. Levin (Ed.), Philosophy of Western Religions: An Open Educational Resource. N.G.E. Far Press, 2019.

[34] D.M. Johnson, G.B. Tomlin, D.G. Walker, Detonations and Vapor Cloud Explosions: Why it Matters, J. Loss Prev. Process Ind. 36 (2015) 358-364.

[35] E.S. Oran, G. Chamberlain, A. Pekalski, Mechanisms and Occurrence of Detonations in Vapor Cloud Explosions, Prog. Energy Combust. Sci. 77 (2020) 100804.

# Battery Safety

# A comparative study on the suppression capacity and the environmental impact of different extinguishing agents of lithium-ion battery fires

**Ubaldi S.[1], Di Bari C.[2] , De Rosa A.[3], Quinterno M.[3], Mazzaro M.[3] , Ferrigno G.[4] , Arrighi F.[4], Secci D.[4], Russo P.[1,*]**

*[1] Sapienza University of Rome, Department of Chemical Engineering Materials Environment, Rome, Italy;*
*[2] ENEA, TERIN-PSU-STMS, CR Casaccia, Rome, Italy;*
*[3] National Fire Brigade, Central Directorate for Prevention and Technical Safety, Rome, Italy;*
*[4] Sapienza University of Rome, Department of Chemistry and Pharmaceutical Technologies, Rome, Italy;*
**Corresponding author's email: paola.russo@uniroma1.it*

## ABSTRACT

Lithium-ion batteries (LIBs) represent the technology currently used in laptops, smartphones, electrical vehicles (EVs), plug-in hybrid electric vehicles (PHEVs), and energy storage system (ESS). The choice over LIBs is due to their low weight, high energy density and charging capacity. However, the increase in use has shown the limits of these devices, especially if subjected to electrical, mechanical, or thermal abuse. Moreover, news on fires involving LIBs is increasingly frequent. Fire suppression and rapid cooling methods would help to mitigate or even eliminate the battery fire hazards. In order to identify an efficient suppression system for LIBs fire, tests on NMC Kokam lithium-ion pouch cells, with different capacity (25Ah and 40Ah), were conducted using different extinguishing agents, such as water mist, water with F500 additive and $CO_2$. By combining the cell temperature measurements and videos recorded by camera it was possible to obtain information on timing of the main events and the effect of extinguishing agents. Furthermore, at the end of the fire tests, the solid and liquid residues were sampled to evaluate their composition through Gas-Chromatography (GC) and Inductively Coupled Plasma-Optical Emission Spectrometry (ICP-OES) to determine the Volatile Organic Compounds (VOCs) and metals trace. This information is also useful to identify the environmental impact of different extinguishing agents and for post-fire soil management in the case of large-scale accidents.

**KEYWORDS:** Extinguishing agent; Fire test; Lithium-ion batteries; Thermal runaway.

## INTRODUCTION

Lithium-ion batteries (LIBs) are a source of electrical energy generated by the conversion of chemical energy. The geometry and the chemical composition of cells depend on the producer and the final application, such as smartphone, laptop, electrical vehicles (EVs), plug-in hybrid electrical vehicles (PHEVs) and energy storage system (ESS) [1]. Li-ion cells are cylindrical, button, prismatic, and pouch in shape and consist of four components: anode, cathode, separator, and electrolytic solution, with variable chemical composition. The anode consists of a Cu collector covered with graphite while the positive electrode, cathode, consists of a layer of transition metal oxides deposited on Al collector. Between the two electrodes there is a porous polymer separator, made of polyethylene or polypropylene, which allows both electrical insulation and the passage of lithium ions. The electrodes are immersed in an electrolytic solution of various organic carbonates, such as ethylene carbonate ($C_3H_4O_3$) and diethyl carbonate ($C_5H_{10}O_3$) in which a lithium salt is dissolved, generally lithium hexafluorophosphate ($LiPF_6$) [2].

Due to these properties, LIBs provide greater energy and power densities than traditional batteries, but recurrent fires highlight the LIBs risks. They are mainly due to the presence of organic electrolytes, flammable liquids and with a high content of oxygen which makes them intrinsically prone to runaway reactions [3].

Depending on the composition and the voltage, the LIBs must operate within the so-called "safety window", which is delimited by the cell temperature (0-80°C) and by the voltage (2-4V): operating outside this window will result in a rapid attenuation of the battery performance which causes safety problems [4, 5]. The high temperatures favour the degradation of internal materials, from the melting of the polymer separator (90-120°C) to highly exothermic reactions (150-200°C) with the production of oxygen [6]. The production of heat and combustible vapours/gases inside the cell leads to an increase in pressure which is compensated by the opening of the safe valve, present on one pole of the cylindrical cell, or the opening of an area between the two terminals which have a lower resistance seal, for pouch cell. If the heating continues (210-300°C) the thermal runaway occurs [7]. The thermal runaway is a chemical phenomenon during which a chain of exothermic reactions occurs violently inside the battery, releasing a large amount of heat that increase the battery temperature and internal pressure, resulting in fire and/or explosion with the projection of fragments and the emission of toxic gases and vapours [8]. Even low temperatures lead to a degradation of LIBs with effects on their performance and safety, in fact below 0°C the lithium metal is deposited, in the form of dendrites, on the surface of the graphite negative electrode, reducing the cycle life of batteries [9].

Currently, literature studies have investigated the thermal stability and fire hazards of battery materials by focusing on the electrochemical reactions that occur within the battery. Tests are usually conducted on cells or small-scale LIBs in a cone calorimeter or in the room corner test facility, with the aim of studying the influence of parameters, such as chemical composition, state of charge (SOC), and environmental conditions on the fire risks associate with LIBs [10–12]. In particular, the onset temperatures of the thermal runaway vary depending on LIBs chemical and physical characteristics and the relative SOC. The higher the SOC, the higher the level of stored energy, leading to more explosive and faster reactions with thermal runaway occurring earlier.

On the contrary very few studies focus on the extinguishment of battery fires. To fight LIBs fire events, an extinguishing agent with some fundamental properties is required: high heat capacity, high wettability, low viscosity, low electrical conductivity, and a positive environmental impact [13]. Extinguishing agents are classified as water-based, gaseous, dry powders and aerosol based on their physical state [14]. The main agents studied are water, micro-encapsulation technology called F500, dry powders, Novec and $CO_2$ [13–17]. Water is the most used and cheapest way to fight fire, and in the case of water mist, the small droplets allow to cool a large surface by absorbing thermal energy more quickly. The encapsulating agent F-500 is a surfactant and consists of molecules with a polar, hydrophilic, and a nonpolar, hydrophobic, part that leads to the formation of micelles capable of encapsulating a variety of liquid, gaseous and solid substances by intensive mixing and are not flammable in the long term [17]. Dry powders are mainly divided into ABC powder, D powder and BC powder, according to the fire class of fire, with a different composition. Due to the small particle size, the powders have a total flooding fire extinguishing ability, filling the entire space but only under specific conditions. Novec is a new, environmentally friendly agent which, thanks to its low boiling point, 49.2°C, can be effectively vapourised in a wide range of temperatures. Studies in the literature show that the cooling efficiency is limited compared to other extinguishing agents but has a better efficacy in reducing the CO emitted. The $CO_2$ extinguisher is ideal for fires of electrical equipment. However, the extinguishing effect is limited because $CO_2$ decreases the surface temperature but not the internal one, causing a new rise in temperatures in a short time. From the results of literature, it emerges that water has a good cooling effect, proportional to the agent's dosage. $CO_2$ has the problem of the non-total suppressive effect due to the presence of the flame even after use and a new rise in temperature. F500 features high efficiency in fire extinguishing and explosion prevention.

Information on the environmental impact of the residues of LIBs after the application of extinguishing agents, to our knowledge, is not available in the literature, but it is of considerable interest especially for the post-fire soil management in the event of major accidents. To fill this gap, fire tests were conducted on Kokam lithium-ion pouch cells with different capacities (25Ah and 40Ah). The temperature of the cell and the main events occurring during the tests were recorded and then the efficiency of the three different extinguishing agents, water mist, F500 and $CO_2$, was evaluated. In

addition, solid and liquid residues were collected at the end of each test for subsequent analysis (i.e., gas chromatography coupled by photoionization detector (GC-PID), gas chromatography coupled by mass spectrometry (GC-MS), and Inductively Coupled Plasma-Optical Emission Spectrometry (ICP-OES)) to characterize the composition in terms of VOCs and metal traces. The final aim is to compare the efficiency, in terms of cooling rate and hazardous compounds in the residues, of the three extinguishing agents investigated.

## MATERIALS AND METHODS

### Materials

Kokam lithium- ion pouch (Li-Po) battery Superior Lithium Polymer Battery (SLPB) have been used, and the Tab. 1 lists the technical specifications. From the Material Safety Data Sheet [18], it follows that the cathode formula is a combination of transition metals oxides, lithium cobalt manganese nickel oxides ($LiMnNiCoO_2$) (NMC) (20-50%w/w), while the anode consists of carbon (15-35%w/w). Aluminum foil (3-12%w/w) is used as the cathode current collector and copper foil (3-12%w/w) as the anode current collector. The electrodes are immersed in an electrolytic solution (10-20%w/w) of lithium hexafluorophosphate ($LiPF_6$) in a mixture of organic solvents: ethylene carbonate (EC) ($C_3H_4O_3$) and ethyl methyl carbonate (EMC) ($C_4H_8O_3$).

**Table 1. Kokam SLPB technical specifications.**

| Cell id | Chemical composition | Capacity [Ah] | Voltage [V] | Weight [g] | Width [mm] | Length [mm] | Thickness [mm] |
|---|---|---|---|---|---|---|---|
| Kokam 25Ah | NMC | 25 | 3.7 | 555 | 226 | 227 | 6.0 |
| Kokam 40Ah | NMC | 40 | 3.7 | 835 | 226 | 227 | 9.1 |

Before being tested, the cells were loaded using a PS 8000 2U Laboratory Power Supply from Elektro-Automatik. The cells were charged at Constant Current (CC) with a maximum voltage limit of 3.7V, corresponding to the 100% of State of Charge (SOC).

### Fire tests

The fire tests were carried out in open space surrounded by perimeter walls and a protective mesh as a ceiling to minimize the risk of projection of solid fragments, and by following the subsequent steps: (i) the cell was positioned in the middle of the grid above the burner, (ii) two thermocouples were fixed to the ends of the cell, (iii) propane flame was lit, and (iv) extinguishing agent was applied after thermal runaway occurred, for about 10 s. Two water-based, water mist and F500, and one gaseous, $CO_2$, extinguishing agents were tested. Test conditions are listed in Tab. 2.

**Table 2. Experimental test conditions.**

| Test id | Li- ion cell | Burner | Extinguishing agent |
|---|---|---|---|
| K25-P-A | Kokam 25 | Propane | Water mist |
| K25-P-F5 | Kokam 25 | Propane | F500 |
| K25-P-$CO_2$ | Kokam 25 | Propane | $CO_2$ |
| K40-P-A | Kokam 40 | Propane | Water mist |
| K40-P-F5 | Kokam 40 | Propane | F500 |
| K40-P-$CO_2$ | Kokam 40 | Propane | $CO_2$ |

The temperature on the surface of the cell were obtained by the thermocouples located on the cell, while the ignition, venting, flame appearance, thermal runaway, extinguishment time, were obtained by the video, recorded by the camera.

**GC-PID method**

The analysis on liquid sample was carried out by gas chromatography coupled to photoionization detector (GC-PID), according to the EPA method 8015D [19].

A Perkin Elmer Clarus 500 GC with autosampler and coupled with a Photo Ionization Detector (PID) was used for the analyses. The detector was coupled to a PG Plus (Vici DBS) hydrogen generator. The column used was a StabilWax-DA – Restek (30m x 0.25mm i.d. x 0.25µm). Perkin Elmer Turbochrom workstation software was used to set instrument parameters, acquire, process and report data.

For each test 1 mL of liquid residue was aliquoted in 1.5 mL vials, without pre-treatment. BTEX, a standard solution which contains 200µg/mL of the following compounds: benzene, toluene, ethylbenzene, m-xylene, p-xylene, and o-xylene in methanol (Restek), was used as standard to obtain the retention time ($t_R$) of each compound, the calibration line, and the limits of quantification (LOQ) and detection (LOD).

The GC-PID analysis method was performed with helium as the carrier gas with a flow rate of 1 mL/min. The injector was set at 200°C and 1.0 µL of sample was injected with a split ratio of 70:1. The analysis involves a programmed temperature: from 100°C (2.5 min) up to 200°C (10 min) with a heating rate of 30°C/min, for a total run of 16 min. The detector was set at a temperature of 270°C.

**SPME-GC-MS method**

In the case of solid and liquid residues, the VOC analysis was carried out by gas chromatography coupled to mass spectroscopy (GC-MS) according to the EPA 8260D method [20]. For this analysis the samples do not require a pre-treatment process and are extracted by solid phase microextraction (SPME) prior to injection into the GC, according to the EPA 5012A method [21].

An Agilent Technologies 7890B GC System was used for analysis, with an EST (Flex) analytical autosampler and coupled to an Agilent 5977B GC/MSD. The column used was a HP-5MS (Agilent Technologies Inc.) (30m x 0.25mm i.d. x 0.25µm). The extraction technique was based on SPME using a 100µm polydimethylsiloxane (PDMS) fiber (Supelco). Agilent Chem Station software was used to set instrument parameters, while Agilent MassHunter Workstation Software was used to process and report data. The mass spectra were compared with those of the NIST mass spectral library.

For each test 10 mL of liquid residue and 5 g of solid residue were aliquoted in separate 20 mL vials. In addition, an internal standard (ISTD) was added to all samples prior to analysis, specifically 3µL for the solid sample and 10 µL for the liquid sample. BTEX was used as an ISTD; it contains 200µg/mL of the following compounds: benzene, toluene, ethylbenzene, m-xylene, p-xylene, and o-xylene in methanol (Restek). The extraction method was based on SPME, using a 100µm PDMS fiber (Supelco), which allows adsorption of non-polar compounds.

At the beginning of each analysis session the PDMS fiber was conditioned for 30 min at 200°C. Before the analysis in GC-MS, the sample was subjected to heating in a heated oven maintained at a temperature of 75°C for 15 min and subjected to stirring. The fiber was then exposed in the headspace of the sample for 15 min at 75°C. The operating conditions of the gas chromatograph were the transfer line at 250°C and helium as the carrier gas. The analysis involves a programmed temperature: from 45°C (3 min) to 250°C (10 min) with a heating rate of 15°C/min, for a total run of 27 min. The mass spectrometry works in electronic impact (EI) mode at 70eV and the source was maintained at a temperature of 230°C. The mass spectra were acquired in scan mode, with m/z between 40 and 400.

### ICP-OES method

The metal traces were determinate by Inductively Coupled Plasma-Optical Emission Spectrometry (ICP-OES) with a methodology that involves a pre-treatment, an acid digestion with a mixture of nitric and hydrochloric acids, according to the EPA 200.8-1 method [22].

A Thermo Fisher Scientific iCAP 7200 ICP-OES Duo was used for the analyses in axial and radial mode. The ICP-OES used uses an echelle lattice spectrometer and a high-performance CID detector. The sample introduction system consists of a concentric glass pneumatic nebulizer coupled to a cyclonic nebulization chamber, also made of glass. The temperature of the ICP-OES was kept constant at 20°C by a Neslab ThermoFlex900 chiller (Thermo Fischer Scientific). Thermo Fisher Scientific Qtegra Intelligent Scientific Data Solution (ISDS) software was used to create LabBooks for sample analysis and to acquire, process and report data. An ASX-560 autosampler (Teledyne Cetac Technologies) was used for positioning the samples.

The standard solutions were made by subsequent dilutions starting from "Certipur® ICP multi-element standard solution XVI" (Merck KGaA) containing the following elements at a concentration of 100 mg/L and diluted in nitric acid: As, Be, Ca, Cd, Co, Cr, Cu, Fe, Li, Mg, Mn, Mo, Ni, Pb, Sb, Se, Sr, Ti, Tl, V, Zn, and "Elemental Impurities according to ICH Q3D oral Standard 2" containing the following elements at concentration of 100 mg/L and diluted in hydrochloric acid: Au, Ir, Os, Pd, Pt, Rh, Ru. (Sigma-Aldrich). The dilutions were carried out using a 4% solution of $HNO_3$ and HCl, prepared with: Suprapur® Hydrochloric acid 36% (Merk KGaA), Suprapur® Nitric acid 69% (Merck KGaA), Ultrapure water (18.2 MΩ · cm) obtained by the Direct-Q® 3 UV Millipore purification system, using Merck's ultra-dry. The 4% acid solution was used as an analytical blank and as a washing solution. Hydrochloric acid and nitric acid were used to produce reverse aqua regia used during the digestion. It was produced using concentrated acid solutions according to the ratio: 3 parts of concentrated $HNO_3$ and one part of concentrated HCl. Standard solutions were prepared at the following concentrations: 50ppm, 10ppm, 1ppm and 0.1ppm. Argon 5.0 (purity> 99.999% mol), Nippon Gases (Rivoira) was used [23-24]. The extraction method was optimized from the existing procedure: EPA 200.8-1 method [21]. The samples were previously homogenized using a laboratory porcelain mortar and then weighed about 0.150 g on an analytical balance, transferred to glass flasks and 10 mL of reverse aqua regia was added. Digestion was performed at room temperature (20°C), all samples were shaken using "Mini Rocker-Shaker mr-1" for 3 h. At the end of the digestion, the samples were transferred to a falcon and diluted with ultrapure water to a final volume of 50 ml, then filtered. To remove any residual carbon still present in the form of $CO_2$, all samples were placed inside a sonicator for 15 min and centrifuged for 5 min at 7500 rpm. A 10 mL aliquot of the supernatant was taken and placed in a 10 mL conical-bottom Falcon tube.

## RESULTS

### Fire tests

The main events of the fire test on the Kokam cell were reported in Fig. 1. After positioning the cell with thermocouples on the grid, the propane flame was lit, Fig. 1a. Under continuous heating the internal pressure of the LIB increases, leading to the opening of the area with a lower resistance seal, and the venting of the gas/vapour, Fig. 1b. The venting phase is characterized by the swelling, Fig. 1c, of the cell followed by a hissing explosion and the spray of a large quantity of white aerosol mainly consisting of the electrolytic solution, which ignited instantly with the formation of a flame jet. Due to the exothermic reaction, the temperature has risen becoming more dramatic and involving the whole system, triggering the so-called "thermal runaway" (TR), Fig. 1d. At this point the amount of smoke emitted and the flames have decreased, and the system has extinguished, Fig. 1e and Fig. 1f.

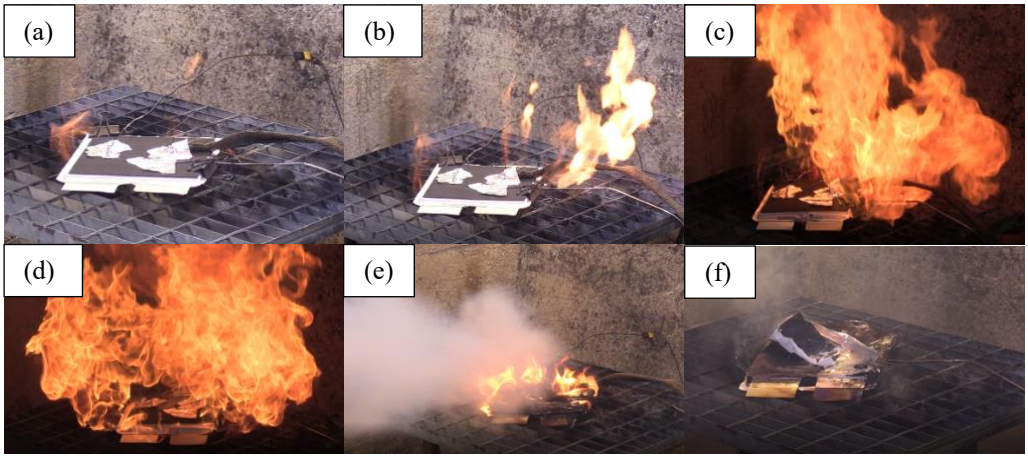


**Fig. 1.** K40-P-$CO_2$ test: (a) ignition, 0s; (b) venting, 10s; (c) swelling, 15s; (d) thermal runaway, 60s; (e) extinction, 65s; (f) post extinction, 75s.

At the end of each test both solid and liquid residues were collected in glass and plastic containers, for subsequent laboratory analysis. The time (s) and temperature (°C) of the major events observed in tests with different extinguishing agents are shown in Tab. 3.

**Table 3. Major events with relative time, t, [s] and temperature, T, [°C] for K25 and K40.**

| | K25-P-A | | K25-P-$CO_2$ | | K25-P-F5 | | K40-P-A | | K40-P-$CO_2$ | | K40-P-F5 | |
|---|---|---|---|---|---|---|---|---|---|---|---|---|
| | t [s] | T [°C] | t [s] | T [°C] | t [s] | T [°C] | t [s] | T [°C] | t [s] | T [°C] | t [s] | T [°C] |
| Start | 0 | 25 | 0 | 29 | 0 | 26 | 0 | 25 | 0 | 26 | 0 | 26 |
| Venting | 45 | 150 | 10 | 35 | 40 | 89 | 90 | 132 | 10 | 31 | 40 | 100 |
| Thermal runaway | 65 | 419 | 40 | 406 | 55 | 396 | 100 | 379 | 60 | 406 | 85 | 475 |
| StartExt | 65 | 419 | 40 | 406 | 55 | 396 | 110 | 370 | 65 | 512 | 90 | 459 |
| EndExt | 75 | 78 | 50 | 195 | 65 | 80 | 120 | 98 | 75 | 319 | 100 | 45 |
| StartExt | - | - | 115 | 345 | - | - | - | - | 295 | 289 | - | - |
| EndExt | - | - | 125 | 295 | - | - | - | - | 305 | 187 | - | - |
| StartExt | - | - | 175 | 300 | - | - | - | - | 500 | 207 | - | - |
| EndExt | - | - | 185 | 91 | - | - | - | - | 510 | 101 | - | - |

It is important to underline that in the tests conducted with $CO_2$ as an extinguishing agent, three extinguishing steps were necessary: the first two with $CO_2$ and third one at the end with water mist to definitively cool the system.

From the data it is possible to calculate the rate of temperature increase that leads to the venting $v_v$, Eq. (1), and the cooling rate $v_c$, Eq. (2) for each extinguishing agent. The values (°C/min) of $v_c$ for the different application phases are reported in Tab. 4.

$$v_v = \left(T_{venting} - T_{start}\right) / \left(t_{venting} - t_{start}\right) \quad (1)$$

$$v_c = \left|\left(T_{end\ extinction} - T_{start\ extinction}\right) / \left(t_{end\ extinction} - t_{start\ extinction}\right)\right| \quad (2)$$

**Table 4. Values of the cooling rate ($v_c$) (°C/s) for the different phases of extinguishing agent application.**

| Sample id | $v_c'$ | $v_c''$ | $v_c'''$ |
|---|---|---|---|
| K25-P-A | 34 | - | - |
| K25-P-$CO_2$ | 21 | 5 | 21 |
| K25-P-F5 | 32 | - | - |
| K40-P-A | 27 | - | - |
| K40-P-$CO_2$ | 19 | 10 | 10 |
| K40-P-F5 | 41 | - | - |

The average of the $v_v$ values for the K25 and K40, 1.6 ± 1.1°C/s and 1.2 ± 0.7°C/s respectively, allowed to exclude a significant difference in the response due to the capacity value. On the contrary, significant differences were observed in the cooling rate, in fact by varying the agents the rate changed from 36°C/s for F500, and 31°C/s for water mist to a lower value of 20°C/s for $CO_2$ at the first extinguishing phase. These values highlight the greater efficiency of water-based agents compared to gaseous agents.

**BTEX analysis**

Liquid residues were analysed by GC-PID. The quantification of BTEX were obtained by interpolating the areas with the calibration lines of the standards. From the analysis of the standards the retention time, $t_R$ expressed in minutes, of the compounds were found to be: 4.380 for benzene, 6.081 for toluene, 7.544 for ethylbenzene, 7.712 for p-xylene, 7.817 for m-xylene and 8.551 o-xylene.

In all samples the analyte concentrations are below the detection limit (LOD), 200 ppb for benzene and 10 ppm for the other compounds, except in the sample K40-P-F5 which has a benzene concentration of 500 ppb.

**Hydrocarbon compounds analysis**

Solid and liquid residues were analysed by SPME-GC-MS, and in Tab. 5 and Tab. 6 are listed the compounds identified, with the respective $t_R$, expressed in minutes.

**Table 5. Compounds identified in the solid residues and correspondent $t_R$ (min) by SPME-GC-MS.**

| Compounds | K25-P-A | K40-P-A | K25-P-F5 | K40-P-F5 | K25-P-$CO_2$ | K40-P-$CO_2$ |
|---|---|---|---|---|---|---|
| 1-butanol | - | - | - | - | 2.24 | - |
| 2,4-dimethyl-1-heptene | - | - | - | - | 4.91 | - |
| 1,3-propanediamine | 7.15 | 7.15 | - | - | - | - |
| undecane, 2,2-dimethyl | - | - | - | - | 7.15 | - |
| 1-hexanol, 2-ethyl | - | - | 7.64 | 7.62 | - | - |
| tetradecane | - | - | 9.56 | 9.55 | - | - |
| decane, 3-bromo | - | 9.56 | - | - | - | 9.56 |
| tridecane | - | - | 10.55 | 10.54 | - | - |
| biphenyl | - | - | 11.40 | - | - | - |
| octadecane | - | - | 11.46 | 11.46 | - | - |
| undecane, 4,7-dimethyl | - | - | - | - | - | 11.46 |
| diphenyl-ether | 11.59 | 11.60 | - | - | - | - |

| | | | | | | |
|---|---|---|---|---|---|---|
| 5-octadecene | - | - | 13.06 | - | - | - |
| 1,4-butanediol | 13.12 | - | - | - | - | - |
| hexane, 3,3-dimethyl | - | - | - | - | - | 13.12 |
| hexadecane | - | - | 13.12 | 13.12 | - | - |
| undecane, 5,7-dimethyl | - | 13.17 | - | - | - | - |
| heptadecane | - | - | 13.83 | - | - | - |
| isophthalic acid | 14.93 | 14.93 | - | 14.93 | - | - |
| terephthalic acid | - | 16.58 | - | - | 16.58 | 16.58 |

- : below the detection limit

-

**Table 6. Compounds identified in the liquid residues and correspondent $t_R$ (min) by SPME-GC-MS.**

| **Compound** | K25-P-A | K40-P-A | K25-P-F5 | K40-P-F5 | K25-P-$CO_2$ | K40-P-$CO_2$ |
|---|---|---|---|---|---|---|
| octanal | 7.32 | - | - | - | - | - |
| 1-hexanol, 2-ethyl | 7.64 | 7.64 | - | - | 7.64 | 7.63 |
| 1-octanol | 8.14 | 8.15 | 8.11 | 8.11 | - | - |
| nonanal | 8.55 | 8.55 | - | - | 8.55 | 8.55 |
| hexanoic acid, 2-ethyl | 8.62 | 8.62 | - | - | - | - |
| decanal | 9.64 | 9.64 | - | - | - | - |
| 1-decanol | 10.28 | 10.28 | 10.22 | 10.34 | 10.29 | 10.29 |
| undecanal | 10.63 | 10.63 | - | - | - | - |
| diphenyl | 11.40 | 11.40 | 11.35 | 11.41 | 11.40 | - |
| tetradecane | 11.46 | 11.45 | - | 11.46 | - | - |
| diphenyl ether | 11.59 | 11.60 | - | - | - | - |
| acenaphthylene | 12.07 | - | - | - | - | - |
| 1-heptadecene | - | - | 12.24 | - | - | - |
| hexadecane | - | 13.12 | - | - | - | - |
| 3-heptadecene | - | - | 13.83 | - | - | - |
| phenanthrene | 14.71 | - | - | - | 14.71 | 14.71 |
| 1-octadecanol | - | - | 14.56 | - | - | - |
| hexadecanal | - | - | 14.75 | 14.75 | - | - |

- : below the detection limit

Based on the analysed matrices and the extinguishing agent used, significant differences were found in the class of compounds identified, such as petroleum distillate compounds for F500 or alcohols for water mist.

**Metals analysis**

Solid and liquid residues were analysed by ICP-OES and in Tab. 7 are listed the metal concentrations, in ppm, for liquid (L), internal electrode material (I), and external metallic coating (E) of the cell residues from fire tests. Metals have been grouped to make the following table easier to read.

- Group 1 (concentration <0.1ppm): As, Au, Be, Cd, Os, Pb, Pd, Rh, Ru, Sb, Se, Tl and V.
- Group 2 (concentration >50ppm): Ca, Co, Fe, Li, Mg, Mn, Ni, Sr and Zn.

**Table 7. Metals concentrations (ppm) in liquid (L), internal (I) and external (E) solid residues by ICP.**

| Sample id | Group 1 | Group 2 | Cu | | | Cr | | | Ti | | |
|---|---|---|---|---|---|---|---|---|---|---|---|
| | L - I - E | L - I - E | L | I | E | L | I | E | L | I | E |
| K25-P-A | <0.1 | >50 | >50 | >50 | >50 | >50 | <0.1 | <0.1 | <0.1 | <0.1 | <0.1 |
| K25-P-$CO_2$ | <0.1 | >50 | 21 | >50 | >50 | 21 | 11 | <0.1 | <0.1 | <0.1 | >50 |
| K25-P-F5 | <0.1 | >50 | >50 | >50 | >50 | >50 | 5 | <0.1 | <0.1 | <0.1 | >50 |
| K40-P-A | <0.1 | >50 | >50 | >50 | >50 | >50 | <0.1 | 20 | <0.1 | <0.1 | <0.1 |
| K40-P-$CO_2$ | <0.1 | >50 | - | >50 | >50 | - | <0.1 | 12 | - | <0.1 | <0.1 |
| K40-P-F5 | <0.1 | >50 | >50 | >50 | >50 | >50 | 12 | <0.1 | <0.1 | <0.1 | <0.1 |

It is possible to highlight a common trend of the concentrations of metals. Group 2 has higher concentration (>50ppm) as it contains all the metals that are part of the initial chemical composition of the cells under examination, NMC Kokam. Cu is found in liquid (L), internal electrode material (I), and external metallic coating (E) except for $CO_2$ tests where the amount in liquid is less than 20 ppm. Also for Cr which is found mainly in liquid residues (>50ppm), the amount for $CO_2$ tests is less than 20 ppm.

## DISCUSSION

From the results obtained it emerges that the use of different extinguishing agents leads to significant differences both in terms of cooling rate, Eq. 2, and chemical composition of solid and liquid residues.

Regarding to the temperatures, Fig. 2 compares the temperature profile of the cell surface in the following tests: K40-P-$CO_2$, K25-P-$CO_2$, K25-P-A, and K40-P-F5.

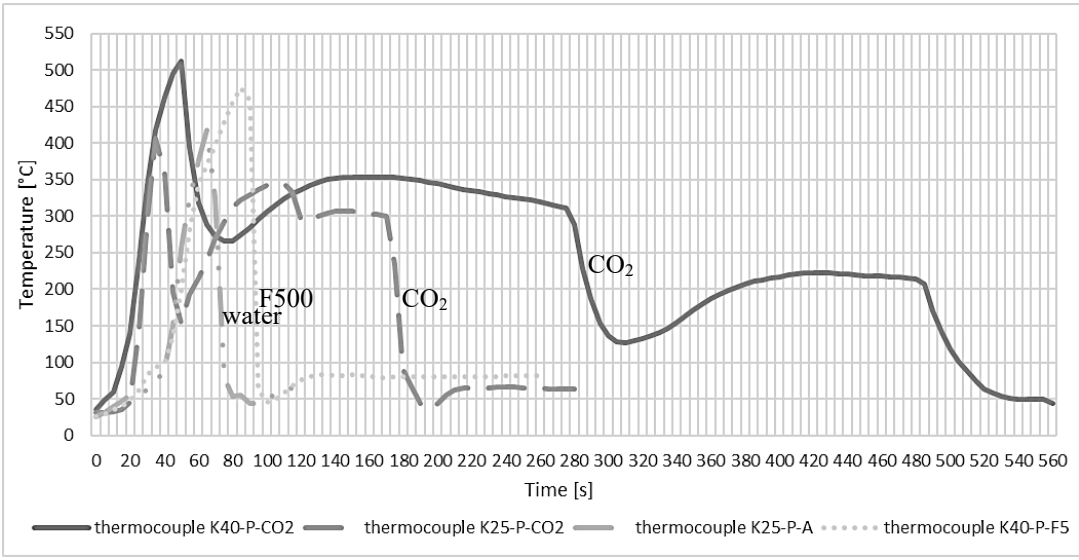


**Fig. 2.** Temperature profile of the cell surface: K40-P-$CO_2$ (line), K25-P-$CO_2$ (dashed line), K25-P-A (line dots), K40-P-F5 (dots)

Comparing the tests with the same extinguishing agent, such as $CO_2$, it is observed that the cell capacity (25Ah and 40Ah) does not significantly influence the heating rate during the ignition phase and the cooling rate during the application of the extinguishing agent. On the contrary, a different behaviour was observed depending on the extinguishing agent applied. In fact, in the case of water

mist and F500, only one application was sufficient to cool the device at temperatures below 100°C, while using $CO_2$ even after the second application, temperatures above 300°C were recorded. Only the final application of water mist has definitively shut down the thermal runaway.

Differences are observed between the extinguishing agents not only in terms of temperature but also in the compounds identified both in solid and liquid residues by GC-PID, GC-MS, and ICP-OES. By varying the matrices and the extinguishing agents, different compounds were detected. For example, the solid residues from extinguishment with F500 for both cells present compounds of the petroleum distillate, such as tetradecane, tridecane, octadecane, hexadecane, while the liquid residues collected after water mist extinguishment contain alcohols and phenyl, such as 1-octanol, 1-decanal, diphenyl, and diphenyl ether. The concentrations of BTEX were also different in the samples, in fact benzene is less than 200 ppb while toluene, ethylbenzene and xylene isomers are less than 10 ppm in all liquids, except for a sample containing 500 ppb of benzene. The concentration values relating to metals do not show significant differences as the solid or liquid matrix varies. The measured concentrations, less than 0.1 ppm for As, Au, Be, Cd, Os, Pb, Pd, Rh, Ru, Sb, Se, Tl and V and greater than 50 ppm for Ca, Co, Fe, Li, Mg, Mn, Ni, Sr and Zn, are due to the initial chemical composition of the Kokam lithium-ion pouch cell with lithium-nickel-manganese-cobalt-oxides cathode.

## CONCLUSION

The increased use of LIBs poses new challenges in the field of safety and fire management. A relevant issue is certainly the evaluation of extinguishing agents to identify the most suitable and efficient one. Tests were conducted on commercial NMC pouch cells subjected to thermal abuse to establish the efficiency of the extinguishing agents and the chemical composition of the residues, solid and liquid.

From the monitoring of the various fire/extinguishing tests it emerged that:

1. Different cell capacities (25Ah and 40Ah) do not significantly affect the rate of temperature rise leading to the venting and thermal runaway.
2. The water-based extinguishing agents, water mist and F500, show a greater efficiency than gaseous one, $CO_2$, after the first application. Water-based have a faster and more effective cooling effect, with temperatures below 100°C with one application.

The instrumental analyses of the residues showed the following trends:

- in all liquid residues the concentrations of BTEX are below the limit of detection (LOD), except for a sample with 500 ppb of benzene from test with F500;
- with the same analysed matrix and extinguishing agent, it is possible to identify compounds characteristic for each extinguishing agent, such as alcohols in the samples from tests with water mist or hydrocarbons in those from tests with F500 application;
- there are no differences between liquid and solid residues, in terms of metal concentration (ppm), as the extinguishing agent used varies. The difference in the detected concentrations is due to the starting cathodic composition of the batteries, such as lithium, nickel, cobalt, and manganese.

## REFERENCES

[1] J.-M. Tarascon, M. Armand, Issues and challenges facing rechargeable lithium batteries., Nature 414 (2001), 359–367.

[2] J. Garche, Electrochemical power sources: fundamentals, systems, and applications li-battery safety, Elsevier, Amsterdam, Netherlands, Oxford, Cambridge, MA, 2019.

[3] M. Ghiji, S. Edmonds, K. Moinuddin, A Review of Experimental and Numerical Studies of Lithium Ion Battery Fires, Applied Sciences 11, (2021) 1247.

[4] D. Ouyang, M. Chen, Q. Huang, J. Weng, Z. Wang, J. Wang, A Review on the Thermal Hazards of the Lithium-Ion Battery and the Corresponding Countermeasures, Applied Sciences 9, (2019) 2483.

[5] R. Zhang, B. Xia, B. Li, L. Cao, Y. Lai, W. Zheng, H. Wang, W. Wang, State of the Art of Lithium-Ion Battery SOC Estimation for Electrical Vehicles, Energies 11, (2018) 1820.

[6] A. Bacaloni, S. Insogna, C. Di Bari, N. Andreucci, M. Mazzaro, M.A. Navarra, Characterization of Li-ion batteries for safety and health protection, Italian Journal of Occupational and Environmental Hygiene 10 (2019) 1-52.

[7] L. Lu, X. Han, J. Li, J. Hua, M. Ouyang, A review on the key issues for lithium-ion battery management in electric vehicles, Journal of Power Sources 226, (2013) 272–288.

[8] Q. Wang, P. Ping, X. Zhao, G. Chu, J. Sun, C. Chen, Thermal runaway caused fire and explosion of lithium ion battery, Journal of Power Sources 208, (2012) 210–224.

[9] L.A. Selis, J.M. Seminario, Dendrite formation in Li-metal anodes: an atomistic molecular dynamics study, RSC Adv. 9, (2019) 27835–27848.

[10] J. Zhao, F. Xue, Y. Fu, Y. Cheng, H. Yang, S. Lu, A comparative study on the thermal runaway inhibition of 18650 lithium-ion batteries by different fire extinguishing agents, iScience. 24, (2021) 102854.

[11] B. Mao, H. Chen, L. Jiang, C. Zhao, J. Sun, Q. Wang, Refined study on lithium ion battery combustion in open space and a combustion chamber, Process Safety and Environmental Protection. 139, (2020) 133–146.

[12] Z. Huang, C. Zhao, H. Li, W. Peng, Z. Zhang, Q. Wang, Experimental study on thermal runaway and its propagation in the large format lithium ion battery module with two electrical connection modes, Energy, 205, (2020) 117906.

[13] S. Yuan, C. Chang, S. Yan, P. Zhou, X. Qian, M. Yuan, K. Liu, A review of fire-extinguishing agent on suppressing lithium-ion batteries fire, Journal of Energy Chemistry, 62, (2021) 262- 280.

[14] M. Ghiji, V. Novozhilov, K. Moinuddin, P. Joseph, I. Burch, B. Suendermann, G. Gamble, A Review of Lithium-Ion Battery Fire Suppression, Energies, 13, (2020) 5117.

[15] W. Luo, S. Zhu, J. Gong, Z. Zhou, Research and Development of Fire Extinguishing Technology for Power Lithium Batteries, Procedia Engineering, 211, (2018) 531–537.

[16] P. Russo, C. Di Bari, M. Mazzaro, A. De Rosa, I. Morriello, Effective fire extinguishing systems for lithium-ion battery, Chemical Engineering Transactions. 67, (2018) 727–732.

[17] F-500 Encapsulator Technology, https://www.f-500.it/, accessed 12 May 2021.

[18] Kokam: Kokam SLPB Material SAfety Data Sheet, accessed 27 Septmeber 2013.

[19] U.S. EPA: Method 8015D: Nonhalogenated Organics usign GC/FIP, (2003)

[20] U.S. EPA: Method 8260D: Voaltile Organic Compounds by Gas Chromatography/mass Spectrometry, (2018)

[21] U.S. EPA: Method 5021A: Volatile Organic Compounds in Various Sample Matrices Using Equilibrium Headspace Analysis, (2014)

[22] U.S. EPA: Method 200.8: Determination of Trace Elements in water and Wastes by Inductively Coupled Plasma-Mass Spectrometry, (1994)

[23] F.C. Pinheiro, A.I. Barros, J.A. Nóbrega, Microwave-assisted sample preparation of medicines for determination of elemental impurities in compliance with United States Pharmacopeia: How simple can it be?, Analytica Chimica Acta. 1065, (2019) 1–11.

[24] C. Støving, H. Jensen, B. Gammelgaard, S. Stürup, Development and validation of an ICP-OES method for quantitation of elemental impurities in tablets according to coming US pharmacopeia chapters, Journal of Pharmaceutical and Biomedical Analysis. 84, (2013) 209–214.

# The suppression effect of heptafluoropropane released at different times on lithium-ion battery fires

**Jiajia Xu, Lin Zhang, Yujun Liu, Qingsong Wang***

*State Key Laboratory of Fire Science, University of Science and Technology of China, Hefei China.*

**Corresponding author's email: pinew@ustc.edu.cn*

## ABSTRACT

The complexity of Lithium-ion battery (LIB) fire makes the effective method to extinguish the fire crucial. In this work, a series of experiment are conducted on large-scale LFP LIB with 243 Ah to investigate the impact of the heptafluoropropane (HFC-227ea) released at different times on suppressing LIB fires. The results show that the development process of LIB fire can be divided into four stages. The earlier the HFC-227ea is released, the easier the fire will be extinguished. Furthermore, the best time to release the HFC-227ea is in stage II, when the flame is smaller and the cooling efficiency is the highest. And the maximum cooling efficiency is 28.4%. Besides, once the cell occurred thermal runaway (TR), the fire is difficult to extinguish and requires increased flow rate to effectively extinguish, e.g. from 8.5 g/s to 11.1 g/s. These results may provide ideas for fire protection design of large-scale $LiFePO_4$ LIBs.

**KEYWORDS:** Lithium ion battery, heptafluoropropane, fire suppressing, release time.

## NOMENCLATURE

| | |
|---|---|
| $c$ | specific heat of the cell (kJ/kg·K) |
| $C$ | orifice flow meter calibration constant (-) |
| $m$ | mass of the cell (g) |
| $\Delta p$ | differential pressure (Pa) |
| $q$ | heat release rate (kW) |
| $Q_c$ | heat generation of the cell (J) |
| $Q_f$ | THR of the cell combustion (J) |
| $t$ | extinguishing time (s) |
| $T_e$ | temperature of the gas (K) |
| $T_p$ | peak temperature of the cell (K) |
| $T_s$ | temperature of the cell at safety venting (K) |
| $\Delta T$ | temperature difference during the release of the HFC-227ea (K) |
| $\mathrm{d}T/\mathrm{d}t$ | temperature rise rate during spraying (J/(kg·K)) |
| $X_{O_2}$ | oxygen concentration (-) |

**Greek**

| | |
|---|---|
| $\eta$ | cooling efficiency (%) |

## INTRODUCTION

The pollution caused by fossil energy and energy shortage make the new energy attractive for people. As of December 2020, Lithium-ion batteries (LIBs) with a total capacity of more than 16 GWh had used in energy storage. LIBs have become the prime resource of the new energy because of their high work voltage, long cycle life, high energy density and no environmental pollution [1]. Nevertheless, the accidents with lithium-ion batteries still occur frequently, which pose a challenge to battery safety. These accidents, caused by thermal runaway (TR), often led to fires [2, 3]. To guard against accidents and reduce fire damage, a proper extinguishing method is necessary to suppress the battery fires.

In recent years, many researchers have done some experiments to study fire suppression technology of lithium ion batteries [4-10]. Si et al. [11] compared the suppressing effect of heptafluoropropane (HFC-227ea) and carbon dioxide ($CO_2$) on LIBs fires. The results showed that both HFC-227ea and $CO_2$ can extinguish LIBs fire, cool the battery and reduce the hazard of the explosion. Moreover, $CO_2$

had better cooling effect than HFC-227ea. Liu et al. [12] investigated the efficiency of dodecafluoro-2-methlpentan-3-one ($C_6F_{12}O$) with different doses on suppressing LIBs fire. They found that $C_6F_{12}O$ has good inhibitory on LIBs fire. However, the battery still remained high temperature after spraying $C_6F_{12}O$. Meng et al. [7] found that dry power could suppress LIBs fire. But suppressing and cooling effects depended on the spraying distance and time. In all these studies, the time to extinguish the fire was after the battery was triggered into TR, when battery often generated violent jet fire and high temperature. This made it more difficult to extinguish the battery fire and lower the temperature. Hence, it is vital to understand the TR mechanism of the battery and find the right time to spraying the extinguish agent.

Hence, many studies on TR mechanism have been conducted to provide the basis for design of battery safety [13-16]. Feng et al. [13] investigated the thermal runaway mechanism of the battery. The results showed that TR was caused by chain reactions. Before TR, the battery temperature rose gently. Liu et al. [16] studied the TR and fire behaviors of LIB under overheated conditions. Three stages of TR were found in experiments. After safety venting, the battery can be ignited by external fire and burned steadily. As the TR occurs, the flame became jet fire as a result of a large amount of flammable gas generated caused by exothermic reactions inside the battery. Therefore, the battery is often accompanied by violent jet fire and high temperature during TR, which increases the difficulty of extinguishing fire and cooling the battery. In order to ensure the effect of extinguishing fire, it is important to choose appropriate fire extinguishing parameters, such as time to spray extinguishing agent, extinguishing agent dose.

According to present research results, some extinguishing agents can extinguish LIBs fire, but high temperature remains after spraying. Moreover, the LIBs fire become violent when TR occurs, which is not conducive to extinguish the fire. Therefore, existing fire suppressing strategies are inadequate. Meanwhile, most studies released extinguishing agent after TR, which is the most difficult time to extinguish the fire. Additionally, researches on releasing extinguishing agent before TR are limited. The battery flame is relatively gentle before TR. At this time, releasing fire extinguishing agent is more likely to suppressing the flame, and even inhibit the occurrence of TR.

In this work. a series of experiments are conducted on the battery to investigate the impact of the HFC-227ea released at different times on lithium-ion battery fires. The extinguishing process, temperature, voltage, mass loss, heat release rate, heat generation and cooling efficiency are analyzed and compared to determine the best time to extinguish the fire. Moreover, the test with large flow nozzle is also performed to study the effect of flow rate.

## EXPERIMENTAL

### Battery Samples

A kind of large-scale prismatic commercial LIB (LFP/Graphite) with 243 Ah was used in this study. The nominal voltage of the cell is 3.2 V and its size is 170 mm × 70 mm × 200 mm. The mass of the cell is 5.3 kg. Before the test, each battery was cycled three times and eventually charged to 100% state of charge (SOC).

### Experimental Apparatus

A schematic diagram of the experimental apparatus is shown in Fig. 1, which consists of fire test platform, support frame, nozzle, agent store tank, battery, scale, camera, gas analyzer, HRR analyzer and computer. The size of the fire test platform was 1.8 m × 1.8 m × 1.68 m. The battery was placed on the scale to measure the mass loss of the battery during tests. Meanwhile, the nozzle fixed on a support frame directly faced the safety valve of the battery. To ensure the fire extinguishing effect and avoid the nozzle being damaged by flame, the distance between the nozzle and safety valve was 30 cm and the spray angle was 45°. The fire extinguishing agent was stored in agent store tank and sprayed from the nozzle. The gas generated in the tests was exhausted through overhead pipe. During this process, the gas analyzer extracted the gas to monitor its composition and concentration.

Meanwhile, the HRR analyzer monitored the oxygen concentration to obtain the HRR, which is calculated by oxygen consumption principle. A sony camera recorded the whole experiments through the view window. As for the battery, it was clamped by two steel plate to simulate the situation of a single battery in the module. A heating plate with 500 W of the same size as the battery was attached to the battery, heating the battery until the fire extinguishing agent sprays on the cell. In order to prevent heat loss, two aluminosilicate fiberboards were arranged on the inside of the steel plate. The data of the temperature and voltage are recorded by datalogger.

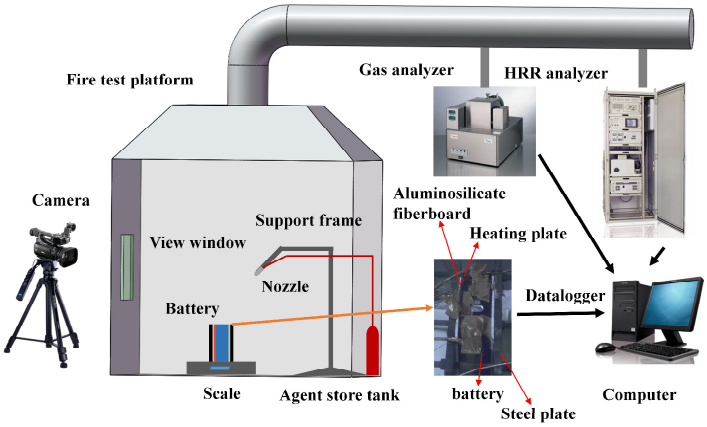


**Fig. 1.** Schematic diagram of the experimental apparatus

Figure 2 shows the distribution of thermocouples in the experiments. Eight K-type thermcouples (TC) with an accuracy of 1 °C were fixed on the surface and above the battery to measure the battery temperature. The surface of the cell close to the heating plate was measured by TC0, and the surface furthest from the heating plate were measured by TC1-3. TC4 was used to measure the temperature on the side of the cell. Meanwhile, the temperature of the upper surface of the cell was measured by TC5-6, and TC6 was fixed near the safety valve. Additionally, the flame temperature and the hot smoke temperature were measured by TC7, which was fixed at 10 cm above the battery.

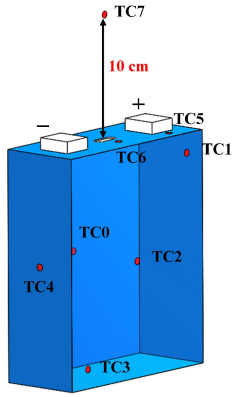


**Fig. 2.** Distribution of thermocouples in the experiments

Five tests were conducted and the experimental conditions of these tests were listed in Table 1. The extinguishing agent used in tests were HFC-227ea, which is currently the most used fire extinguishing agent in the field of LIB. The pressure was 2.5 MPa. Case 1 used no extinguishing agent and was set as control group. To investigate the effects of releasing extinguishing agent at different times, cases 2-4 were designed. Further, the fire started at safety venting, then developed and eventually reached

its maximum during TR. Hence, three releasing time nodes during this period were respectively applied to cases 2-4. Meanwhile, cases 4-5 were designed to compare the effect of the extinguishing agent with different mass flow rate. Before the test, the battery was arranged and placed on the scale. Then, the heating plate was turned on to heat the battery. When the battery occurred safety venting, a large amount of combustible gases were ejected from the safety valve. A lighter was used to ignite these gases. Once the specified time node was reached, the heating plate was turned off and HFC-227ea was released to extinguish the LIB fire.

**Table 1. The detail of experimental conditions**

| Item | Extinguishing agent | Pressure (MPa) | Releasing time node | Spraying time (s) | Mass flow rate (g/s) |
|---|---|---|---|---|---|
| Case 1 | – | – | – | – | – |
| Case 2 | HFC-227ea | 2.5 MPa | Safety venting | 120 | 8.5 |
| Case 3 | HFC-227ea | 2.5 MPa | 3 minutes after venting | 120 | 8.5 |
| Case 4 | HFC-227ea | 2.5 MPa | Thermal runaway | 120 | 8.5 |
| Case 5 | HFC-227ea | 2.5 MPa | Thermal runaway | 120 | 11.1 |

## RESULTS AND DISCUSSION

### Experimental Phenomena

Figure 3 shows the thermal runaway process of the LIB without extinguishing agents. Five distinct events can be detected. They are safety venting (S), Ignition (I), development (D), thermal runaway (T) and after thermal runaway (A). When the heating plate started heating, the time is recorded as 0 s. At 2367 s, the safety valve was ruptured due to the increased internal pressure inside the cell, accompanying by the ejection of a large amount of combustible gases [17-19]. Subsequently, the gases were ignited by a lighter. Two seconds later, the flame began to stabilize. As the gases burned, the internal pressure of the cell decreased, and the rate of gas production decreased, which is related to the size of the fire. Additionally, the internal reaction of the battery is relatively moderated at this time. Hence, the flame gradually become smaller, as shown in Fig. 3(e). Then, the flame maintained. With constant heating, the cell temperature gradually increased, and the internal reactions started to become violent, leading to an increase in the flame. At 2766 s, the cell was triggered into TR and the flame reached its maximum. Then, the flame gradually decreased until it went out after TR. It can be found that in whole process, the flame went through four stages, (I) from large to small, (II) stable combustion, (III) from small to large, and (IV) from large to small until it went out. To further describe the TR process of the LIB without extinguishing agents, the mass loss and mass loss rate are analyzed, as shown in Fig. 4. The mass of the cell did not change before the safety venting, while it sharply increased the moment the safety venting, which is due to the recoil force caused by the ejection of the gases. Subsequently, because of the loss of the gases and electrolyte, the mass of the cell started to decrease. And the mass loss rate of the cell dropped from 137.0 g/s to 0.6 g/s. As a result, the flame went smaller, which is the stage I. Then mass of the cell began to decline at a constant rate of about 0.36 g/s, and the battery entered into stable combustion stage. Subsequently, the mass loss rate of the cell increased gradually and reached the maximum value of 5.9 g/s, indicating the cell was being triggered into TR. This is the stage III. In stage IV (as well the end of TR), the mass loss rate of the cell gradually decreased to 0. Furthermore, the mass of the cell only lost 323 g before TR (stages I and II), while 814 g was lost during TR (stages III and IV), which indicates the intensity of the LIB fire during TR.


**Fig. 3.** Thermal runaway process of the LIB without extinguishing agents

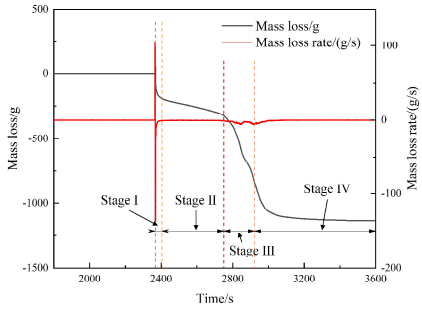


**Fig. 4.** Mass loss and mass loss rate of the LIB without extinguishing agents

The extinguishing process of the LIB at different extinguishing time nodes in cases 2-5 is shown in Fig. 5. Note that (b) represents the moment of releasing the HFC-227ea, while (a) represents the moment before releasing. Moreover, three extinguishing time nodes are in stage I, II and IV, respectively. In case 2, the fire was extinguished in less than 1 s. In this time, the fire was getting small, which made it easy to extinguish. Additionally, the similar situation occurred in case 3, the fire in stage II was the smallest in the test. Therefore, the fire was also extinguished as soon as the HFC-227ea was released. In cases 2-3, the battery still vented a small amount of gases after the fire was extinguished. Unlike previous results, the fire in case 4 was not extinguished, which may be caused by two reasons. One is that the fire was getting more intense during TR. The other is the increase in gas production rate, making it more difficult for extinguishing agent to enter the battery. Hence, the fire in case 4 was just blown sideways during the release of the extinguishing agent and not extinguished. To extinguishing the LIB fire during TR, the nozzle with bigger flow rate was used in case 5. The fire was also extinguished in less than 1 s. However, the battery still vented large amounts of gases generated by TR. Hence, it can be indicated that the best time to extinguish the LIB fire is before TR, especially in stage II, when the fire is minimal. Once the cell is triggered into TR, the difficulty of extinguishing the fire will be increased because the extinguishing agent cannot enter the battery to suppress the reactions. At this point, it is necessary to change the extinguishing conditions to put out LIB fire, such as using a high-flow nozzle.

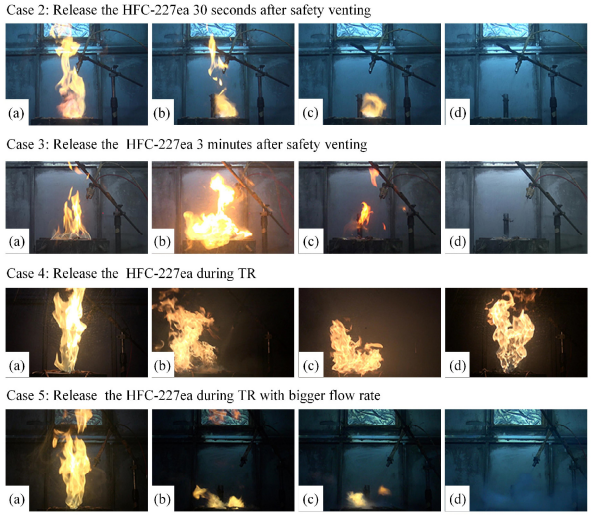


**Fig. 5.** Extinguishing process of the LIB at different extinguishing time nodes in cases 2–5

## Temperature and Voltage Responses of the Cell

The temperature and voltage of the cell are the important parameters to reflect the process of TR. The temperature and voltage responses of the cell without extinguishing agents are shown in Fig. 6. After the heating plate was turned on, the temperature of the cell slowly increased. At 2367 s, the safety valve ruptured, accompanying by a large amount of combustible gases and electrolyte ejected. Due to the ejected gases taken away some heat, the cell temperature dropped by up to 22 °C. Subsequently, the cell was ignited and the cell temperature rose faster, which mainly because of the exothermic reactions inside the cell. And the temperature rise rate was about 0.14 °C/s. As T5 was close to the fire, T5 fluctuated wildly after ignition. At 2766 s, the cell temperature started to rise sharply, reaching a peak of 525 °C in a short time. Meanwhile, the voltage of the cell dropped. The cell was triggered into TR. As the TR expanded, the voltage of the cell dropped to about 0 v and the battery completely failed at 2928 s. And the surface temperature of the cell farthest from the heating plate (T1-T3) began to rise sharply. After TR, the cell temperature decreased gradually. Fig. 6(b) shows the fire temperature above the safety valve. Since T6 was located in the inner flame, the temperature was lower than T7 located in the outer flame. The maximum flame temperature was 896 °C, and it appeared during TR. Hence, the cell occurred TR often caused extremely high battery temperature and violent flames, which increase the difficulty of extinguishing fire.

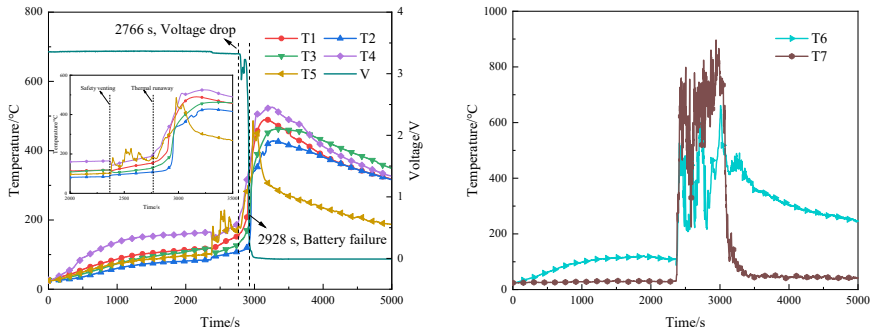


**Fig. 6.** Temperature and voltage responses of the cell without extinguishing agents, (a) voltage and temperature of the cell surface; (b) fire temperature above the safety valve.

Figure 7 shows the temperature and voltage responses of the cell with HFC-227ea sprayed after safety venting. The cell was immediately ignited by a lighter after safety venting. To stabilize the combustion, the HFC-227ea was released after 30 seconds of ignition. T5 dropped from 140 °C to 64 °C rapidly as soon as the HFC-227ea sprayed. This was mainly due to the extinguishing of the flame and the cooling effect of HFC-227ea. Meanwhile, the cell temperature stopped rising during the releasing of HFC-227ea. Once the spray was over, the cell temperature decreased gradually, while T5 was bounded slightly due to the high temperature inside the cell. The cell was not triggered into TR during the whole test. Moreover, the voltage of the cell had been maintained at 3.3 V during the test. In terms of the fire temperature, T6 and T7 rose sharply when the cell was ignited. The peak temperature was 711 °C at T7, which was 21% less than that of T7 in case 1. Then, the fire temperature dropped below 10 °C during the release of HFC-227ea. T6 was also bounded slightly after spraying, which was because of the high temperature gases escaping from the safety valve. Therefore, releasing the HFC-227ea after safety venting can suppress the increase of the cell temperature to prevent the occurrence of TR.

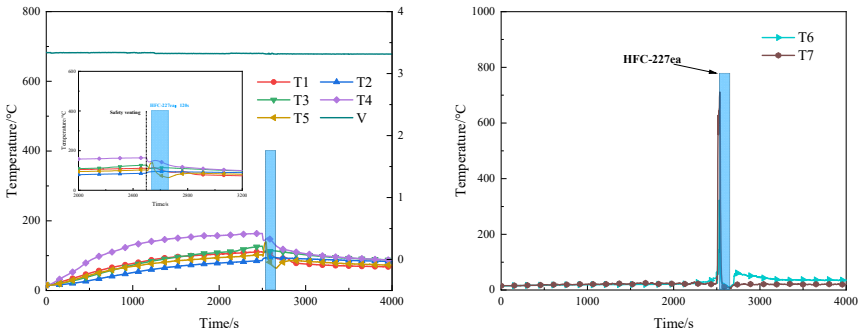


**Fig. 7.** Temperature and voltage responses of the cell with HFC-227ea sprayed after safety venting, (a) voltage and temperature of the cell surface; (b) fire temperature above the safety valve.

To compare the difference in extinguishing timing, the temperature response of the cell surface (T2) in cases 1-5 were analyzed, as shown in Fig. 8. Once the cell occurred TR, HFC-227ea could not inhibited TR, only alleviate it. However, releasing the HFC-227ea before the TR could prevent TR. The critical parameters of the cell in cases 1-5 were listed in Table 2. It can be seen that the earlier the release of HFC-227ea, the lower the battery temperature. In cases 2-3, when the HFC-227ea was released before TR, the cell temperature would be decreased due to HFC-227ea, and the cooling rate was about 0.2-0.3 °C/s. Whereas, once the cell was triggered into TR, HFC-227ea can hardly restrain the temperature rise of the cell. But it can alleviate the temperature rise rate. And the inhibition effect was more significant when the nozzle with high flow rate was used. For example, the temperature rise rate during spraying was 0.6 °C/s in case 4, while it was 0.1 °C/s in case 5. Additionally, releasing the HFC-227ea after TR may not extinguish the fire. However, increasing the flow rate of the HFC-227ea could extinguishing the fire. This was mainly because the bigger flow rate made the HFC-227ea enter into the cell to extinguish the fire and cool the cell.

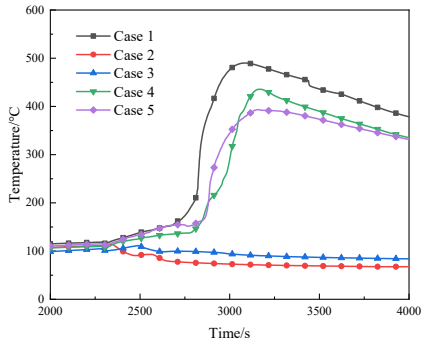


**Fig. 8.** Temperature response of the cell surface (T2) in cases 1-6.

**Table 2. Critical parameters of the cell in cases 1-5**

| Item | Case 1 | Case 2 | Case 3 | Case 4 | Case 5 |
|---|---|---|---|---|---|
| Peak temperature (°C) | 490 | 114 | 111 | 436 | 393 |
| Temperature rise rate during spraying $dT/dt$ (°C/s) | 1.1 | -0.2 | -0.3 | 0.6 | 0.1 |
| Extinguishing fire | - | Yes | Yes | No | Yes |
| Extinguishing time $t$ (s) | - | 1 | 1 | - | 1 |

## Heat Release Rate and Heat Generation of the Cell

The heat release rate (HRR) based on oxygen consumption principle reflects the risk of battery combustion, and the heat generation can indicate the high temperature hazard of the cell. Fig. 9 shows the HRR of the cell in cases 1 and 2. In case 1, three peaks were observed in Fig. 9(a). The first one was 36.6 kW and occurred after safety venting, which was due to ignition. Then, the flame became smaller and the HRR dropped to about 5 kW. Once the cell was triggered into TR, the second and third peaks appeared one after another. The value of them were 78.3 kW and 88.6 kW, respectively. It can be inferred that the battery had two jelly rolls. With the continuous expansion of TR, two jelly rolls occurred TR in turn, which can also be verified by two peaks of mass loss rate shown in Fig. 4. Unlike case 1, case 2 had only one peak after safety venting, whose value was 29.7 kW. Because the fire was extinguished by HFC-227ea, the HRR dropped to 0. Additionally, the cell was not triggered into TR.

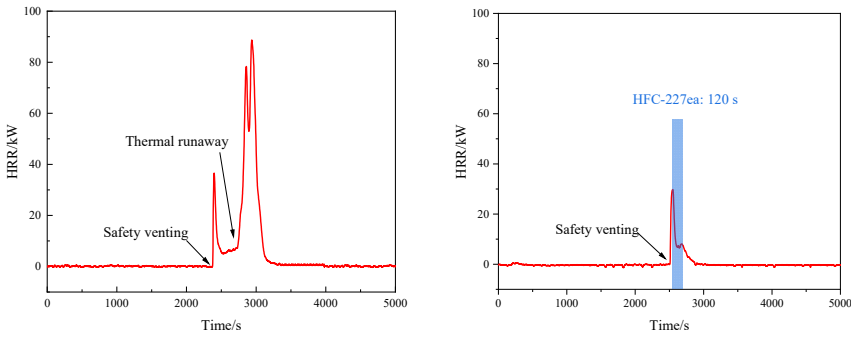


**Fig. 9.** The heat release rate (HRR) of the cell in cases 1 and 2, (a) without extinguishing agents in case 1; (b) with HFC-227ea sprayed after safety venting in case 2.

To further investigate the fire hazard of the cell, the total heat release (THR) of the cell combustion was analyzed, which can be calculated according to Eq (1) [20-22], which was 20772 kJ in case 1.

$$Q_f = \int q \mathrm{d}t \tag{1}$$

$$q = (13.1\times10^3)\times1.1\times C\sqrt{\frac{\Delta p}{T_e}}\times\frac{0.2095 - X_{O_2}}{1.105 - 1.5X_{O_2}} \tag{2}$$

where $Q_f$ is the THR of the cell combustion, $q$ is the HRR (kW), $t$ is the time, $C$=1.362 is the orifice flow meter calibration constant, $\Delta p = 17$ Pa is the differential pressure, $T_e$ is the temperature of the gas and $X_{O_2}$ is the oxygen concentration. Because the reactions inside the battery reacts violently during TR, the cell generated a lot of heat, which can be reflected by the cell temperature. Hence, the heat generation of the cell can be obtained from the following equation:

$$Q_c = cm(T_p - T_s) \tag{3}$$

where $Q_c$ is the heat generation of the cell, $c = 1.1$ kJ/kg·K is the specific heat of the cell [15], $m$ is the mass of the cell, $T_p$ is the peak temperature of the cell and $T_s$ is the temperature of the cell at safety venting. Thus, $Q_c$ was about 1746.5 kJ in case 1.

In cases 2-5, the HFC-227ea was used to suppress the LIB fire. Due to the releasing time was different, the cell temperature was different. To compare the cooling effect of the HFC-227ea in cases 2-5, herein we defined the cooling efficiency ($\eta$), which can be expressed as Eq. (4).

$$\eta = \frac{\Delta T}{T_p} \tag{4}$$

where $\Delta T$ is the temperature difference during the release of the HFC-227ea. Note that $\Delta T$ is the temperature difference between the peak temperature in case 4 or 5 and the peak temperature in case 1, if the cell occurred TR. Hence, the total heat release, heat generation of the cell and cooling efficiency for all cases were listed in Table 2. With the delay of the extinguishing time node, the larger the THR and the more heat generated by the battery itself. In case 4, $Q_f$ was higher than that in case 1, which was because the fire was not extinguished and the release of HFC-227ea diluted the concentration of oxygen in the pipe. In case 5, due to the increase in flow, the flame was quickly extinguished and the THR was about 78% lower than the THR in case 4. From the aspect of cooling efficiency, releasing the HFC-227ea before TR can improve cooling efficiency, especially in stage II. The $\eta$ in case 2 was lower than that in case 3. This was mainly because in the initial stage of safety venting, the gas flow rate was fast, so that the HFC-227ea cannot enter into cell.

**Table 3 THR, heat generation of the cell and cooling efficiency in cases 1-5.**

| Item | Case 1 | Case 2 | Case 3 | Case 4 | Case 5 |
|---|---|---|---|---|---|
| $Q_f$ (kJ) | 20638 | 837 | 2330 | 23144 | 5061 |
| $Q_c$ (kJ) | 1746.5 | 40.8 | 128.3 | 1515.4 | 1293.6 |
| $\eta$ (%) | - | 19.1 | 28.4 | 11.2 | 19.8 |

## CONCLUSIONS

In this work, the extinguishment and cooling effect of the HFC-227ea sprayed at different extinguishing time on large-scale prismatic commercial LIB (LFP/Graphite) with 243 Ah were investigated. Furthermore, the tests with different flow rate after TR were carried out. The conclusions obtained from this work are as follows.

(1) The LIB fire went through four stages after safety venting. When the battery occurred TR, not only the temperature rose rapidly, but also some events occurred. For example, the flame became violent and the mass loss accelerated. The peak temperature of the cell and fire were 525 °C and 896 °C, respectively. And the mass loss rate during TR peaked at 5.9 g/s.

(2) When the flow rate of the HFC-227ea was 8.5 g/s, the LIB fire was extinguished in less than 1 s before TR. Once the cell occurred TR, the flow rate was required to 11.1 g/s to extinguished the fire. Hence, the earlier the HFC-227ea is released, the easier the fire would be extinguished and the lower the temperature.

(3) As the release time of the HFC-227ea advanced, the total heat release and heat generation of the cell decreased significantly. Additionally, the maximum cooling efficiency of the HFC-227ea was 28.4 % in case 3. These conclusions indicated that it is better to release the extinguishing agent before TR, especially in stage II. And it may provide ideas for fire protection design of large-scale $LiFePO_4$ LIBs.

## ACKNOWLEDGMENTS

This work is supported by the Key Research and Development Plan of Anhui Province (No. 202104a07020003), the University Synergy Innovation Program of Anhui Province (No.GXXT-2020-079). Dr. Q.S Wang is supported by Youth Innovation Promotion Association CAS (No.Y201768).

## REFERENCES

[1] P. Ping, Q. Wang, P. Huang, K. Li, J. Sun, D. Kong, C. Chen, Study of the fire behavior of high-energy lithium-ion batteries with full-scale burning test, Journal of Power Sources, 285 (2015) 80-89.

[2] D. Ouyang, M. Chen, Q. Huang, J. Weng, Z. Wang, J. Wang, A review on the thermal hazards of the lithium-ion battery and the corresponding countermeasures, Applied Sciences, 9 (2019) 2483.

[3] Q. Wang, P. Ping, X. Zhao, G. Chu, J. Sun, C. Chen, Thermal runaway caused fire and explosion of lithium ion battery, Journal of Power Sources, 208 (2012) 210-224.

[4] Y. Liu, Q. Duan, J. Xu, H. Li, J. Sun, Q. Wang, Experimental study on a novel safety strategy of lithium-ion battery integrating fire suppression and rapid cooling, Journal of Energy Storage, 28 (2020) 101185.

[5] W.-t. Luo, S.-b. Zhu, J.-h. Gong, Z. Zhou, Research and Development of Fire Extinguishing Technology for Power Lithium Batteries, Procedia Engineering, 211 (2018) 531-537.

[6] B.K. Mandal, A.K. Padhi, Z. Shi, S. Chakraborty, R. Filler, Thermal runaway inhibitors for lithium battery electrolytes, Journal of Power Sources, 161 (2006) 1341-1345.

[7] X. Meng, K. Yang, M. Zhang, F. Gao, Y. Liu, Q. Duan, Q. Wang, Experimental study on combustion behavior and fire extinguishing of lithium iron phosphate battery, Journal of Energy Storage, 30 (2020) 101532.

[8] E. Meyer, Spacecraft Fire Safety Research: Combustion of Lithium-ion Batteries to Predict Fire Scenarios, Honors Research Projects. 694 (2018).

[9] T. Liu, C. Tao, X. Wang, Cooling control effect of water mist on thermal runaway propagation in lithium ion battery modules, Applied Energy, 267 (2020) 115087.

[10] Q. Wang, K. Li, Y. Wang, H. Chen, Q. Duan, J. Sun, The efficiency of dodecafluoro-2-methylpentan-3-one on suppressing the lithium ion battery fire, Journal of Electrochemical Energy Conversion Storage, (2018) 694.

[11] R.J. Si, D.Q. Liu, S.Q. Xue, Experimental Study on Fire and Explosion Suppression of Self-ignition of Lithium Ion Battery, Procedia Engineering, 211 (2018) 629-634.

[12] Y. Liu, Q. Duan, J. Xu, H. Chen, W. Lu, Q. Wang, Experimental study on the efficiency of dodecafluoro-2-methylpentan-3-one on suppressing lithium-ion battery fires, RSC Advances, 8 (2018) 42223-42232.

[13] X. Feng, M. Ouyang, X. Liu, L. Lu, Y. Xia, X. He, Thermal runaway mechanism of lithium ion battery for electric vehicles: A review, Energy Storage Materials, 10 (2018) 246-267.

[14] Z. Huang, C. Zhao, H. Li, W. Peng, Z. Zhang, Q. Wang, Experimental study on thermal runaway and its propagation in the large format lithium ion battery module with two electrical connection modes, Energy, (2020) 117906.

[15] H. Li, Q. Duan, C. Zhao, Z. Huang, Q. Wang, Experimental investigation on the thermal runaway and its propagation in the large format battery module with Li (Ni1/3Co1/3Mn1/3) O2 as cathode, Journal of Hazardous Materials, 375 (2019) 241-254.

[16] P. Liu, C. Liu, K. Yang, M. Zhang, F. Gao, B. Mao, H. Li, Q. Duan, Q. Wang, Thermal runaway and fire behaviors of lithium iron phosphate battery induced by over heating, Journal of Energy Storage, 31 (2020) 101714.

[17] A.W. Golubkov, D. Fuchs, J. Wagner, H. Wiltsche, C. Stangl, G. Fauler, G. Voitic, A. Thaler, V. Hacker, Thermal-runaway experiments on consumer Li-ion batteries with metal-oxide and olivin-type cathodes, Rsc Advances, 4 (2014) 3633-3642.

[18] F. Larsson, P. Andersson, P. Blomqvist, B.E. Mellander, Toxic fluoride gas emissions from lithium-ion battery fires, Scientific Reports, 7 (2017) 10018.

[19] J. Sun, J. Li, T. Zhou, K. Yang, S. Wei, N. Tang, N. Dang, H. Li, X. Qiu, L. Chen, Toxicity, a serious concern of thermal runaway from commercial Li-ion battery, Nano Energy, 27 (2016) 313-319.

[20] M. Chen, D. Zhou, X. Chen, W. Zhang, J. Liu, R. Yuen, J. Wang, Investigation on the thermal hazards of 18650 lithium ion batteries by fire calorimeter, Journal of Thermal Analysis and Calorimetry, 122 (2015) 755-763.

[21] C. Tao, Q. Ye, C. Wang, Y. Qian, C. Wang, T. Zhou, Z. Tang, An experimental investigation on the burning behaviors of lithium ion batteries after different immersion times, Journal of Cleaner Production, 242 (2020) 118539.

[22] L. Zhang, Y. Li, Q. Duan, M. Chen, J. Xu, C. Zhao, J. Sun, Q. Wang, Experimental study on the synergistic effect of gas extinguishing agents and water mist on suppressing lithium-ion battery fires, Journal of Energy Storage, 32 (2020) 101801.

# Fire Dynamics

# A Comparative Study on the Effect of Natural and Forced Convection Correlations on the CFD Simulation Results of Liquid Pool Fires

**Hong M. C.[1], Merci B.[1], Beji T.[1]***

[1] *Ghent University, Dept. of Structural Engineering and Building Materials, Ghent, Belgium.*
**Corresponding author's email: tarek.beji@ugent.be*

## ABSTRACT

The paper presents a detailed analysis of predictive numerical simulations of liquid pool fires, i.e., a 1 m – diameter methanol pool fire and a 0.7 m × 0.8 m ethanol pool fire. The burning rate is predicted using the 'film' model, including empirical correlations for heat and mass transfer. Although the forced convection approach (used for instance in the Fire Dynamics Simulator, FDS) yields relatively good results in terms of fuel evaporation rate, it is shown that its suitability for the cases at hand is somewhat questionable from a fundamental standpoint. Therefore, the natural convection approach has been implemented in FDS. The predicted burning rates are similar to the forced convection approach. However, the liquid surface temperature is higher (and closer to the boiling point of 64.8°C for methanol) using natural convection, with deviations (from forced convection) that exceeded 20°C near the burner wall. Based on the extensive analysis carried out for the methanol pool fire, a single simulation has been conducted for the ethanol test case with satisfactory results for the peak Heat Release Rate (HRR) and the burning time. The overall transient behavior remains difficult to capture, but the predicted surface temperature is much closer to the boiling point.

**KEYWORDS:** Liquid pool fires, CFD, forced convection, natural convection.

## INTRODUCTION

Liquid pool fires are driven by a very complex interaction between several physical and chemical phenomena that occur at the level of both the gas and the liquid phase. Despite the strong advances in combustion and fire science, there are currently no fully predictive and reliable models of liquid pool fires, mainly due to the strong coupling at the liquid – gas interface.

The most common approach to estimate the burning rate of a liquid pool fire and the subsequent hazards (*e.g.*, the thermal radiation to the surroundings) is to use semi-empirical correlations such as the correlation of Babrauskas [1] and the correlation of Ditch et al. [2]. Furthermore, a more adavanced global model has been developed in [3] where 'the mass flux of burning fuel […] depends on the heat feedback from the flame to the fuel surface'. These models can be coupled to the correlation of Peatross and Beyler [4] to account for the reduction of the burning rate as a function of the oxygen concentration. Nevertheless, relying on a more advanced technique such as Computational Fluid Dynamics (CFD) is an interesting alternative, given the potential to solve accurately the fire driven flow (at the level of the gas phase) and the interaction with the liquid phase.

Most of the CFD model developments have been focused so far on the gas phase and, relatively speaking, less effort has been devoted to the coupling with the liquid phase. In [5], a predictive iterative algorithm has been proposed with the aim to 'maintain an equilibrium fuel vapor pressure in the first gas-phase cell above the liquid boundary'. The main drawback of this approach is the high sensitivity to the spatial resolution [5]. In [6], the burning rate in a mechanically ventilated enclosure is predicted based on the heat flux at the liquid surface (divided by the heat of gasification) and the local oxygen concentration (using the correlation of Peatross and Beyler) in the 'vicinity of the flame'. One of the drawbacks of such approach is the difficulty to define, from a CFD perspective, the 'vicinity of the flame'[7]. Currently, the most 'popular' approach to predict the burning rate of a pool

fire using CFD is based on the so-called 'film' model where the local fuel evaporation rate is 'governed by Stefan diffusion' [5]. In this approach, an empirical correlation is used to estimate the convective mass transfer coefficient. More specifically, in [5], the choice has been to use the correlation for forced convection in the turbulent regime, which remains the option used in the Fire Dynamics Simulator (FDS) [8]. In [9], it has been argued based on a simplified in-house model (without solving the flow field) that the correlation for natural convection in the laminar regime might be more appropriate. In this paper, we elaborate this work further by implementing the natural convection correlations in FDS 6.7.5 and assessing the CFD predictions against available data for large-scale methanol and ethanol pool fires.

## HEAT AND MASS TRANSFER MODELLING

The general modelling framework used in this work is based on the description provided in [5] and [8]. In the following section, we will recall the main elements given therein as well as the new features implemented in FDS in the context of this work, *i.e.*, the natural convection approach (see Natural Convection Approach).

### Liquid Evaporation Model

The local evaporation rate of the liquid fuel is governed by Stefan diffusion [5]:

$$\dot{m}'' = h_m \frac{\overline{p}_m MW_F}{RT_g} \ln\left(\frac{X_{F,g}-1}{X_{F,\ell}-1}\right) \tag{1}$$

where $h_m$ is the mass transfer coefficient, $\overline{p}_m$ is the background pressure of the $m^{th}$ pressure zone (see [8] for more details), $MW_F$ is the molecular weight of the fuel gas, $R$ is the universal gas constant, $T_g$ and $X_{F,g}$ are respectively the gas temperature and the volume fraction of fuel vapor in the center of the first gas phase cell above the liquid, and $X_{F,\ell}$ is the volume fraction of the liquid vapor at the surface. The latter is calculated using the integrated Clausius–Clapeyron equation:

$$X_{F,\ell} = \exp\left[-\frac{L_v MW_F}{R}\left(\frac{1}{T_s}-\frac{1}{T_b}\right)\right] \tag{2}$$

where $L_v$ is the heat of vaporization, $T_s$ is the surface temperature of the fuel, and $T_b$ is the boiling temperature of the fuel. The mass transfer coefficient $h_m$ is defined as:

$$h_m = \frac{\mathrm{Sh}\, D_{\ell,g}}{L} \tag{3}$$

where Sh is the Sherwood number, $D_{\ell,g}$ is the diffusivity of the liquid species in the gas phase, and $L$ is the length scale of the liquid surface, which is also used for the convective heat transfer calculation.

The key questions that open up at this stage (and which are thoroughly examined in this paper) are how to calculate Sh and $L$ in Eq. (3), in order to calculate $h_m$. This will be addressed in the sections of Forced Convection Approach and Natural Convection Approach. But first, we will give an overview of the heat transfer modelling in which the approach to calculate the convective heat transfer coefficient, $h$, is analogous to the calculation of $h_m$.

### Heat Transfer Within the Fuel

The liquid fuel is treated as a thermally thick solid, *i.e.*, the convective motion within the solid is not directly solved. One-dimensional heat transfer is considered. Fourier's equation in the following form is solved:

$$\rho_\ell c_\ell \frac{\partial T_\ell(x,t)}{\partial t} = \frac{\partial}{\partial x}\left( k_\ell \frac{\partial T_\ell(x,t)}{\partial x} \right) + \dot{q}_r'''$$ (4)

where $t$ is the time, $x$ is the distance from the liquid surface, $\rho_\ell$, $c_\ell$, and $k_\ell$ are the density, specific heat, and thermal conductivity of the fuel and $\dot{q}_r'''$ is the radiative exchange term (see [5] for more details).

The thermal boundary condition on the liquid surface reads:

$$-k_\ell \frac{\partial T_\ell}{\partial x}(0,t) = \dot{q}_c'' + \dot{q}_r'' - L_v \dot{m}''$$ (5)

where $\dot{q}_c''$ is the convective heat flux and $\dot{q}_r''$ is the radiative heat flux. The convective heat flux at the liquid surface is calculated as:

$$\dot{q}_c'' = h\left(T_g - T_s\right)$$ (6)

Similarly to Eq. (3), the convective heat transfer coefficient $h$ is calculated as:

$$h = \frac{\mathrm{Nu}\ k_g}{L}$$ (7)

where $k_g$ is the thermal conductivity of the surrounding gas and Nu is the Nusselt number.

**Forced Convection Approach**

The empirical correlations for the Sherwood number in the case of a flow parallel to a flat plate, and considering the Chilton-Colburn analogy (*i.e.*, Sh = Nu), read [10]:

$$\mathrm{Sh} = 0.664\,\mathrm{Re}^{1/2}\,\mathrm{Sc}^{1/3} \quad \text{if} \quad \mathrm{Re} < 3\times10^5$$ (8a)

$$\mathrm{Sh} = 0.037\,\mathrm{Re}^{4/5}\,\mathrm{Sc}^{1/3} \quad \text{if} \quad 3\times10^5 < \mathrm{Re} < 10^8$$ (8b)

where Re is the Reynolds number and Sc is the Schmidt number (taken here as Sc = 0.6). Equations (8a) and (8b) correspond to a laminar and a turbulent regime, respectively. The Reynolds number is calculated as:

$$\mathrm{Re} = \frac{\rho_g\, u\, L}{\mu_g}$$ (9)

where $\rho_g$ and $\mu_g$ are the density and the dynamic viscosity of gas at the arithmetic mean (film) temperature of the thermal boundary layer between the surface and the surrounding gas [10], $u$ is the velocity of the cross flow and $L$ is the length of the plate across which the flow is developing.

It is important to recall here that our fire scenario of interest is a pool fire in open atmosphere and under quiescent conditions. Therefore, in the absence of any cross flow (*e.g.*, induced by a wind) at the edge of the liquid pool, a fundamentally different definition of the velocity, $u$, is made. It is taken in [5] as the flow velocity in the gas phase cell adjacent to the liquid surface. Furthermore, the initial condition for the velocity in Eq. (9) $u$ = 0 m/s. If there is an artificial background noise, Eq. (9) will yield a very low Re. In fact, theoretically speaking, the Sherwood number must be higher than 1 and thus, Eq. (8a) gives a minimum Reynolds number, $\mathrm{Re}_{min}$ = 76. The approach adopted in [5] consists of setting $\mathrm{Re}_{min}$ = 5 x $10^5$ in Eq. (9) and using Eq. (8b) for the turbulent regime, which corresponds to Sh = 1031 and a minimum evaporation mass flux. The implications of this approach on the transient profile of the burning rate will be discussed later in the paper. The empirical correlations for the Nusselt number for respectively the laminar and the turbulent regime read [10]:

$$\mathrm{Nu} = 0.664\,\mathrm{Re}^{1/2}\,\mathrm{Pr}^{1/3} \quad \text{if} \quad \mathrm{Re} < 3\times10^{5} \tag{10a}$$

$$\mathrm{Nu} = 0.037\,\mathrm{Re}^{4/5}\,\mathrm{Pr}^{1/3} \quad \text{if} \quad 3\times10^{5} < \mathrm{Re} < 10^{8} \tag{10b}$$

where Pr is the Prandtl number (taken here as Pr = 0.7).

**Natural Convection Approach**

As discussed in the previous section, the forced convection configuration may not be representative of a liquid pool fire in a quiescent environment, primarily because there is no forced flow parallel to the liquid surface. Rather, it is believed that the flow at the gas-liquid interface is driven by the combustion-generated buoyancy. Therefore, instead of using a Reynolds number, it is suggested to rely on the local Grashof number, Gr, which takes into account the buoyancy force and is defined as:

$$\mathrm{Gr} = \frac{g\,L^{3}}{\nu_{air}^{2}}\frac{\left|\rho_{air}-\rho_{g}\right|}{\rho_{g}} \tag{11}$$

where $g$ is the gravitational acceleration, $\nu_{air}$ and $\rho_{air}$ are respectively the kinematic viscosity and density of the surrounding gas (taken here as air at 20°C and thus $\nu_{air} = 1.53\times10^{-5}$ m$^2$/s and $\rho_{air} = 1.20$ kg/m$^3$) and $\rho_g$ is the gas density in the gas phase cell adjacent to the liquid surface. The length scale $L$ for natural convection over a plate is taken as [10]:

$$L = A/P \tag{12}$$

where $A$ and $P$ are respectively the area and the perimeter of the plate (assumed to be equivalent to the liquid surface in pool fires).

The empirical correlations for the Nusselt number for respectively the laminar and the turbulent regime in the natural convection correlation read [10]:

$$\mathrm{Nu} = 0.54\left(\mathrm{Gr.Pr}\right)^{1/4} \quad \text{if} \quad 10^{4} < \mathrm{Gr.Pr} < 10^{7} \tag{13a}$$

$$\mathrm{Nu} = 0.15\left(\mathrm{Gr.Pr}\right)^{1/3} \quad \text{if} \quad 10^{7} < \mathrm{Gr.Pr} < 10^{11} \tag{13b}$$

For the sake of completeness, it is noted that in FDS, $h$ is calculated as [8]:

$$h = \max\left[C\left|T_g - T_s\right|^{1/3}, \frac{\mathrm{Nu}\;k}{L}\right] \tag{14}$$

where $C$ is the coefficient of empirical natural convection models (taken $C = 1.52$ for a horizontal planar surface). Given that Nu is calculated in FDS using the forced convection expression, Eq. (14) becomes somewhat inconsistent because the first expression therein is based on natural convection whereas the second one is based on forced convection. Nevertheless, for the cases at hand in this paper, it is found that the first expression is not used in the calculations.

By analogy to Eqs. (13), the expressions for the Sherwood number read:

$$\mathrm{Sh} = 0.54\left(\mathrm{Gr.Sc}\right)^{1/4} \quad \text{if} \quad 10^{4} < \mathrm{Gr.Sc} < 10^{7} \tag{15a}$$

$$\mathrm{Sh} = 0.15\left(\mathrm{Gr.Sc}\right)^{1/3} \quad \text{if} \quad 10^{7} < \mathrm{Gr.Sc} < 10^{11} \tag{15b}$$

where Sc is the Schmidt number (here, Sc = Pr = 0.7). It is quite interesting to note at this stage that considering the cubic dependence of the Gr on the length scale $L$ (see Eq. (11)) in conjunction with Eq. (15b) for natural convection in the turbulent regime, the Sherwood number, Sh, is directly proportional to $L$. Consequently, the mass transfer coefficient, $h_m$, becomes independent of the $L$ (see Eq. (3)) and so is then the liquid evaporation rate (see Eq. (1)). This observation renders Eq. (15b)

particularly attractive for CFD simulations of liquid pool fires, where the calculations are performed on a 'cell basis' and thus, as pointed out in [5], it is typically not very appropriate to rely on a global geometrical parameter such as $L$. We note that the forced convection correlation in the turbulent regime, Eq. (8b), used in [5] yields $\dot{m}'' \sim L^{-1/5}$ if Eq. (3) is used or $\dot{m}'' \sim L^{-1}$ if the constant minimum Reynolds number, $Re_{min}$ = 5 x $10^5$, is used. Therefore, as pointed out in [5], $L$ becomes a model parameter rather than a true geometrical parameter.

## TURBULENCE, COMBUSTION AND THERMAL RADIATION MODELLING

The default FDS settings are used in this work (see [8]), unless specified otherwise. This means that Large Eddy Simulation (LES) is used for the treatment of turbulence, including the modified Deardorff model for the sub-grid scale viscosity. Infinitely fast chemistry is computed within the Eddy Dissipation Model (EDM) framework for turbulent combustion. The Radiative Transport Equation (RTE) is solved using the Finite Volume Method (FVM). Additionally, a radiative fraction, $\chi_r$, is prescribed in order to make sure that a minimum fraction from the heat generated by combustion is lost to the surroundings by thermal radiation. This is particularly important for under-resolved flows. It should be mentioned as well that the default number of radiation angles has been increased from 100 to 500 as suggested in [11].

## EXPERIMENTAL CONFIGURATIONS AND NUMERICAL SETTINGS AND TESTS

### Experimental settings for the 1 m – diameter methanol pool fire

The first experimental study considered in this work [12] consists of 'a series of measurements […] to characterize the structure of a 1 m diameter methanol ($CH_3OH$) pool fire steadily burning with a constant lip height in a quiescent environment'. The burner (which was water-cooled at its bottom) is a circular steel pan with an inner diameter of 1.00 m, a depth of 0.15 m, and a wall thickness of 1.6 mm. The lip height is maintained at 10 mm and the burner is mounted on cider blocks, 0.3 m above the floor. The measured steady-state burning rate is 12.8 ± 0.9 g/s, which corresponds to a burning rate per unit area of 16.3 ± 1.2 g/m$^2$/s. Gas phase temperature measurements at the axis of the fire plume and heat flux measurements in the surroundings of the flame are also provided. The radiative heat feedback to the liquid surface was found to represent 79% of the total heat feedback.

### Experimental settings for the large – scale ethanol pool fire

The second test case considered in this work is a 0.70 m × 0.81 m × 0.05 m ethanol pool fire examined experimentally in [13]. The initial fuel liquid layer thickness is 9 mm and the initial lip height is about 4.1 cm. The Heat Release Rate (HRR) in open atmosphere and quiescent conditions has been measured by putting the burner under a hood.

It is important to mention at this stage that the 'bulk' of the numerical simulations discussed in this paper are devoted to the first test case, *i.e.*, the 1 m – diameter methanol pool fire. By the end of this comprehensive set of simulations, we carried out one single simulation for the ethanol pool fire in order to examine the level of accuracy of the predictions without carrying out any further sensitivity analysis on numerical or physical parameters and models.

### Numerical settings and test cases for the 1 m – diameter methanol pool fire

Given that FDS solves the flow in a Cartesian system of coordinates, a square burner has been prescribed in the numerical simulations with a side length, $L_{burner}$ = 0.88 m, which corresponds to an area $A_{burner}$ = 0.7744 m$^2$ (1.4 % lower than the actual area). Simulations (not shown here) demonstrate that the difference in the results between a square and a round burner (set-up using the 'stair stepping' method) is marginal. The fuel depth specified in the calculation is the same as in the experiments, *i.e.*, 0.15 m. The prescribed lip height in the simulations is 1 cm.

The liquid fuel properties used in this work are displayed in Table 1. For methanol, the properties are taken from the FDS input file in GitHub [11]. For ethanol, they are taken from [5]. Soot and CO are not considered in this work, given that we are dealing with alcohols.

The computational domain has been set to $1.36 \times 1.36 \times 2.64$ m$^3$. The height of the domain has been chosen to make sure that the flame (combustion region) does not extend beyond the top boundary. A wider domain (larger horizontal dimensions) did not yield different results (simulations not shown here). The six sides of the computational domain have been set to 'OPEN', which means that the fluid flow in or out of the computational domain depends on the local pressure gradient. The bottom boundary is set as 'OPEN' because the burner was elevated in the experiments.

**Table 1. Liquid fuel properties.**

| Fuel | Methanol | Ethanol |
|---|---|---|
| $\rho$ (kg/m$^3$) | 792 | 794 |
| $c$ (kJ/kg.K) | 2.53 | 2.44 |
| $k$ (W/m.K) | 0.20 | 0.17 |
| $L_v$ (kJ/kg) | 1098.3 | 837 |
| $\Delta H_c$ (kJ/kg) | 20934 | 27474 |
| $\chi_r$ (-) | 0.21 | 0.25 |
| $T_b$ (℃) | 64.6 | 78.5 |

**Table 2. List of numerical simulations for the methanol pool fire.**

| Sim. ID | Forced Vs. Natural[c] | Laminar Vs. Turbulent[c] | $Re_{min}$ | $L$ | Cell size (cm) |
|---|---|---|---|---|---|
| FT8 | Forced | Turbulent | $5 \times 10^5$ | $L_{burner}$ | 8 |
| FT4 | Forced | Turbulent | $5 \times 10^5$ | $L_{burner}$ | 4 |
| FT2 | Forced | Turbulent | $5 \times 10^5$ | $L_{burner}$ | 2 |
| FT1 | Forced | Turbulent | $5 \times 10^5$ | $L_{burner}$ | 1 |
| FL2[a] | Forced | Laminar | 0 | $L_{burner}$ | 2 |
| NL2 | Natural | Laminar | NA | $A_{burner} / P_{burner}$ | 2 |
| NT2 | Natural | Turbulent | NA | $A_{burner} / P_{burner}$ | 2 |
| NT8 | Natural | Turbulent | NA | $A_{burner} / P_{burner}$ | 8 |
| NT4 | Natural | Turbulent | NA | $A_{burner} / P_{burner}$ | 4 |
| NT1 | Natural | Turbulent | NA | $A_{burner} / P_{burner}$ | 1 |
| NT2_Prime[b] | Natural | Turbulent | NA | $A_{burner} / P_{burner}$ | 2 |

[a]Numerical instabilities were encountered in this simulation before reaching the prescribed 500s simulation time.

[b]This simulation is similar to NT2, except that the coefficient 0.15 in Eq. (15b) has been lowered to 0.05.

[c]Equations (8) and (10) are used for forced convection approach, and Eqs. (13) and (15) are for the natural convection approach.

The main numerical simulations carried out in this work for the methanol pool fire are listed in Table 2. The nomenclature is as follows: the first letter is either F or N (Forced Vs Natural convection), the second letter is T or L (Turbulent Vs Laminar regime), and the number denotes the cell size in cm.

The first simulations that will be analyzed in this paper are based on the model choices described in [5], *i.e.*, forced convection in the turbulent regime with $Re_{min} = 5 \times 10^5$. The first choice to be discussed here (besides the cell size, see simulations FT8 to FT1) is with respect to the flow regime. In other words, bearing in mind that the flow velocities at the liquid surface in case of a pool fire are typically 'low', the Re numbers are expected to be low, which would rather correspond to a laminar regime and make the choice of $Re_{min} = 5 \times 10^5$ not consistent with the actual flow conditions. Therefore, after simulations FT8 to FT1, FL2 is carried out based on the implementation of Eq. (10a) (for forced convection in the laminar regime) in FDS and without setting any predefined $Re_{min}$.

The second series of simulations (*i.e.*, simulations NL2 to NT1, see Table 2) is focused on natural convection (by implementing Eqs. (13) and (15) in FDS), arguing (as already discussed above) that this is more representative of the actual conditions than forced convection. The specific choice of using the turbulent instead of the laminar regime in simulations NT2 to NT1 is based on simulations of NL2 and NT2, where the Rayleigh number is found to fall in the turbulent regime. More details will be given in the section 'Results and discussions'.

It is important to bear in mind that no sensitivity analysis on the length scale $L$ is carried out here, because the latter parameter is considered in this study as a 'true geometrical parameter', rather than a 'model parameter', as advocated in [5]. Therefore, differences between the forced and natural convection approaches do not stem only from the different expressions of Sh but also from the definition of the length scale.

The simulation time has been set to 500 s and the quasi-steady state parameters are averaged over the last 200 s.

**Numerical settings for the large – scale ethanol pool fire**

As mentioned earlier, the simulation settings for this test case are based on the outcome of the methanol pool fire simulations. That means that the cell size is set to 2 cm (because the pool size is similar to the methanol case). Furthermore, regarding heat and mass transfer modelling, the natural convection approach in the turbulent regime is used and compared to the forced convection approach, as described in [5].

## RESULTS AND DISCUSSIONS

### Methanol pool fire – forced convection approach

Prior to the analysis of the numerical results of the first 4 simulations (see Table 2), it is believed to be of interest to perform a simplified hand calculation based on the prescribed $Re_{min} = 5 \times 10^5$ and the initial conditions for the gas, $T_g$ = 293 K. By taking Sc = 0.6 and using Eq. (8b), one obtains a minimum Sherwood number, $Sh_{min}$ = 1130.91. The binary diffusion of methanol vapor in air (using kinetic theory) is estimated as $D_{\ell,v} = 1.48 \times 10^{-5}$ m$^2$/s. Therefore, based on the latter two values and a length scale $L_{burner}$ = 0.88 m, Eq. (3) gives a mass transfer coefficient, $h_m$ = 0.019 m/s. Furthermore, the initial molar concentration of methanol vapor at the liquid vapor can be taken as $X_{F,\ell} = 0.149$ by using Eq. (2) and assuming $T_s$ = 293 K. The initial molar concentration of methanol vapor is the gas phase cell adjacent to the liquid is taken as $X_{F,g} = 0$. Finally, using all the above information to estimate a minimum mass loss rate per unit area based on $Re_{min} = 5 \times 10^5$ and Eq. (1) gives $\dot{m}''_{\min} \simeq 4$ g/m$^2$/s. This value is in a relatively good agreement with the value calculated by FDS after the first time step of 0.04 s and which is $\dot{m}''_{\min} \simeq 5.5$ g/m$^2$/s. Interestingly, this value appears to be in the range of critical mass flux values, *i.e.*, 3 to 6 g/m$^2$/s, for ignition of PMMA under various conditions as reported by [14]. Furthermore, as mentioned in [5], in order to circumvent the need to model an ignition source in the simulations, the auto-ignition temperature is set to 0 K. This allows the mixture methanol vapor – air above the liquid surface to ignite almost instantaneously at the start of the simulation, generating

(thanks to the minimum $\dot{m}''_{\min} \simeq 4$ g/m$^2$/s ) enough heat to raise continuously the surface temperature and yield a quasi-steady burning rate of about 22 g/m$^2$/s when a cell size of 2 cm is used (see **Fig. 1a**).

The cell sensitivity analysis displayed in **Fig. 1a** shows that, strictly speaking, convergence is not reached. Nevertheless, the difference between 1 cm and 2 cm simulations is sufficiently small to carry out the next simulations using the latter cell size. We note as well that from 8 cm down to 2 cm, the predicted fuel burning rate is increasing. However, the 1 cm–simulation result is slightly lower than the 2 cm–simulation result, which remains to be explained.

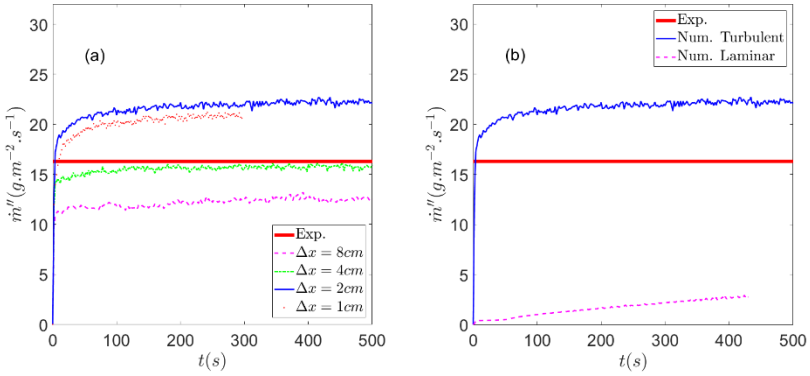


**Fig. 1**. Burning rate profiles for the forced convection simulations. (a) Cell sensitivity analysis using the turbulent regime correlation. (b) Comparison Turbulent Vs Laminar regime, using a 2 cm cell size.

Despite the physical basis behind the concept of a critical mass flux for ignition, the basis of the calculation, which is $Re_{min} = 5 \times 10^5$ is 'questionable'. In fact, the Reynolds number, Re, in the cell adjacent to the liquid surface has been calculated in the 'FT2' simulation and is found to be in the range [500 – 2500], which is two orders of magnitude lower than the prescribed $Re_{min} = 5 \times 10^5$, indicating that the flow is laminar rather than turbulent. This has led us to run the simulation FL2 (see Table 2), where the laminar regime is considered and no minimum Re is prescribed. The latter setting implies that the Reynolds number used in the calculation is solely based on the flow velocity, $u$, which is the result of the combustion-generated buoyancy. The profiles displayed in **Fig. 1b** show that the burning becomes in this case very slow in comparison to the simulation FT2 and no steady-state is reached within the 500 s simulation time.

**Methanol pool fire – natural convection approach**

Before discussing the profiles for the natural convection approach, it is important to recall here that Eq. (11) for Gr, in conjunction with Eqs. (15), does not give a minimum Sherwood number (which would correspond to a minimum fuel mass flux), yet the burning rate in the natural convection approach increases quite rapidly. In fact, from the start of the simulation, combustion occurs (because the auto-ignition temperature has been set to 0 K) and yields a high gas temperature in the gas phase cell adjacent to the liquid. By virtue of the ideal gas law, such temperature corresponds to a relatively low gas density in the very same cell (see **Fig. 2a**), which will generate, early in the simulation, relatively high Grashof and Rayleigh (= Gr.Pr) numbers (see **Fig. 2b**). Based on the above results, an advantage of the natural convection approach over the forced convection approach is that the liquid evaporation rate is not dependent on the flow field at the interface liquid – gas, but only on the gas temperature (and thus density). Nevertheless, a further analysis of simulation NL2 shows that the Rayleigh number, Ra = Gr.Pr, at quasi-steady state is between $2 \times 10^8$ and $3 \times 10^8$ (see **Fig. 2b**), which corresponds to a turbulent regime rather than a laminar one. That is why the simulations carried out after NL2 were based on the correlation for the turbulent regime.

**Fig. 3a** shows that the predicted burning rate using the laminar regime correlation is lower than for the turbulent regime. The cell size sensitivity analysis displayed in **Fig. 3b** gives qualitatively the

same trend as for the forced turbulent approach. Nevertheless, the difference between the 1 cm and the 2 cm results appears to be slightly higher.

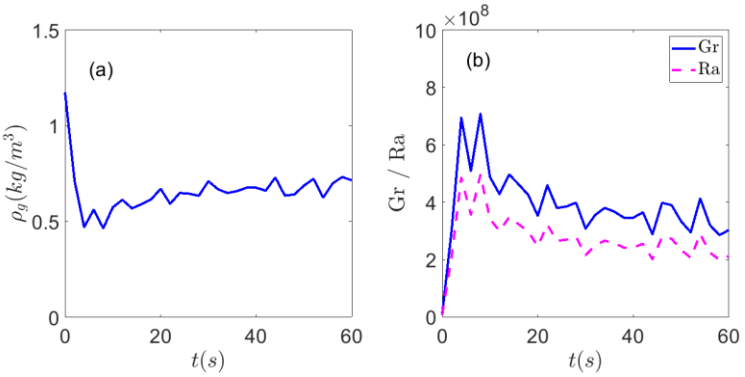


**Fig. 2.** Temporal profile of the (a) gas density near the liquid surface and (b) Gr and Ra for the first 60 s of simulation NL2 (see Table 2) in the center of the pool.

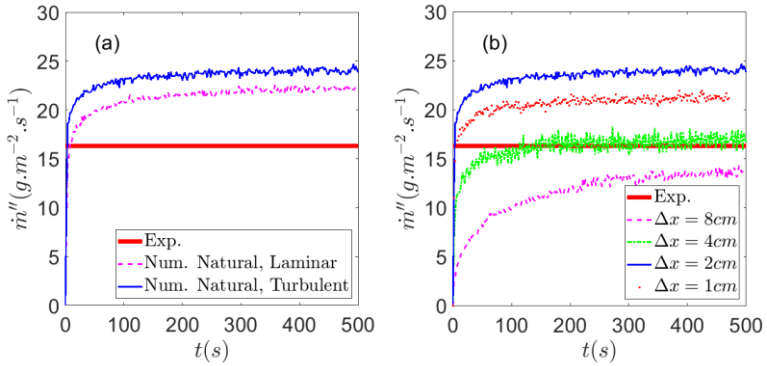


**Fig. 3.** Burning rate profiles for the natural convection simulations. (a) Comparison Turbulent Vs Laminar regime, using a 2 cm cell size. (b) Cell sensitivity analysis using the turbulent regime correlation.

### Further analysis of the methanol pool fire results

**Fig. 4** shows that the burning rate predictions with a forced or natural convection approach are quite similar, yielding both an overestimation of about 37 and 50 %, respectively. Besides several potential reasons linked to the gas phase, it is believed that an adjustment of coefficients used in the heat and mass transfer correlations of interest might help improving the agreement with the experimental data. Obviously, for the time being, this can be seen as a mere calibration exercise. Nevertheless, if the work carried out in this paper is to be extended to a much wider range of experimental conditions, mostly in terms of fuel type and burner diameter, the need to propose another set of coefficients might be better justified. For the time being, the simulation Natural (modified) in **Fig. 4** has been carried out by prescribing the same settings as NT2, except that the coefficient 0.15 in Eq. (15b) has been lowered to 0.05, see simulation NT2_Prime in Table 2. More particularly, it is shown that the surface temperature is closer to the boiling point when using the natural convection approach. The deviations are particularly substantial near the burner wall. Unfortunately, there are currently no measurements available for the surface temperature. Nevertheless, it seems quite plausible that the natural convection approach results are closer to reality.

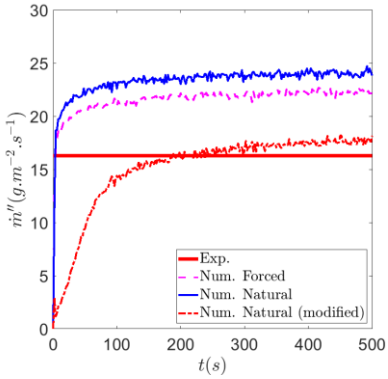


**Fig. 4.** Burning rate profiles using the forced, the natural and the modified natural convection approach.

The results are further analyzed in **Fig. 5**, which gives the radial distribution of the total heat flux and the surface temperature for simulations FT2, NT2 and NT2_Prime.

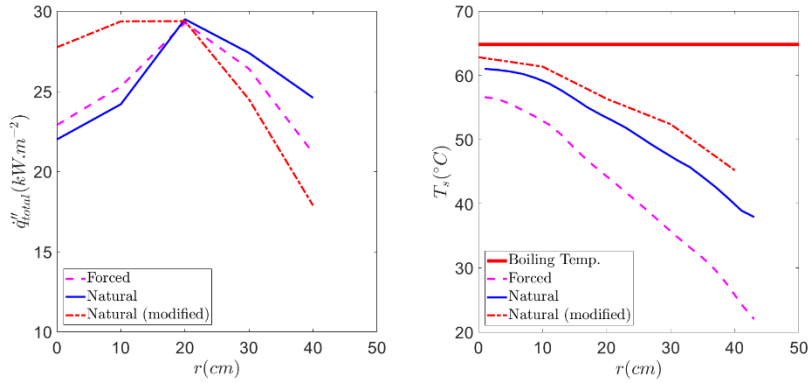


**Fig. 5.** Radial distribution of the total heat flux (left) and the liquid surface temperature (right) for the forced, natural and natural modified (where the coefficient 0.15 in Eq. (15b) is lowered to 0.05) approaches.

**Table 3. Average heat fluxes at the liquid surface for the forced, natural and natural modified approaches.**

| Heat Flux | Forced | Natural | Natural (modified) |
|---|---|---|---|
| $\dot{q}''_{total}$ (kW/m$^2$) | 24.8 | 27.4 | 20.8 |
| $\dot{q}''_{r}$ (kW/m$^2$) | 17.5 (71%) | 16.7 (61%) | 16.4 (79%) |
| $\dot{q}''_{c}$ (kW/m$^2$) | 7.3 (29%) | 10.7 (39%) | 4.4 (21%) |

The total heat flux values displayed in Table 3 are consistent with the predicted burning rates shown in **Fig. 4**, in that the higher the heat flux the higher the burning rate. Additionally, it is shown that with the modified natural approach, the radiative heat feedback to the liquid surface accounts for 79% of the total feedback, which is the value reported experimentally in 12[12].

**Ethanol pool fire**

**Fig. 6 (left)** shows that the transient behavior of the HRR is not well captured by the simulations. However, the peak values are in a good agreement. It is noted that the modified natural approach gives a slight improvement regarding the transient stage in that the quasi-steady stage is not reached (too)

quickly as the forced convection approach. This is believed to be important in the predictions of the surface temperature displayed in **Fig. 6 (right)**. In fact, it is argued that a sudden increase in the burning (evaporation) rate, as in the forced approach, causes a substantial evaporative cooling (see the third term on the right-hand side of Eq. (5)) that prevents the liquid surface temperature from rising to sufficiently high levels. Experimental measurements are not available, but it is believed that the surface temperature should approach the boiling point of $T_b$ = 78.5°C for ethanol, where the modified natural approach predicts a temperature closer to the boiling point than the forced convection approach.

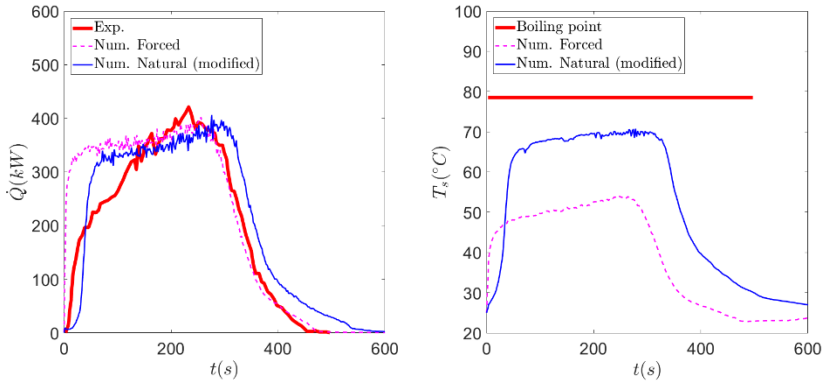


**Fig. 6.** Predictions of the HRR profile (left) and the mean liquid surface temperature evolution (right) for the ethanol pool fire using the forced and the natural (modified) approach.

## CONCLUSIONS

In this work, natural convection correlations are implemented in the Fire Dynamics Simulator (FDS) for heat and mass transfer in predictive simulations of liquid pool fires (a 1 m – diameter methanol pool fire and a 0.7 m × 0.8 m ethanol pool fire). It is shown indeed, based on qualitative and quantitative arguments, that the natural convection approach is more relevant than the forced convection approach currently used in FDS, especially in the absence of a cross flow, from a wind for example. Additionally, the flow regime is shown to be turbulent at the liquid–gas interface by post-processing the Rayleigh number in the natural convection approach. In terms of burning rate predictions, the deviations between the forced and the natural approaches is not significant though. However, the predicted liquid surface temperature is significantly closer to the boiling point and this is believed to be more representative of reality. Finally, an adjustment of the natural convection correlation is proposed in this paper in order to improve the predictions for the two pool fires of interest. More test cases, in terms of fuel type and burner diameter, will be carried out in the future in order to further assess the natural convection approach.

## ACKNOWLEDGMENTS

This work was supported by Bel V [Scientific Research Agreement A18/TT/0674, Amendment N°1, Reference A19/TT/1632]. The authors would also like to thank the support from the FDS team, especially to Randall McDermott, Marcos Vanella, and Glenn P. Forney, for sharing their experience in modifying and compiling the source code of FDS.

## REFERENCES

[1] V. Babrauskas, Estimating large pool fire burning rates, Fire Technology 19 (1983) 251-261.

[2] B.D. Ditch, J.L. de Ris, T.K. Blanchat, M. Chaos, R.G. Bill, S.B. Dorofeev, Pool fires – An empirical correlation, Combust. Flame 160 (2013) 2964-2974.

[3] A. Hamins, J.C. Yang, T. Kashiwagi, A global model for predicting the burning rates of liquid pool fires, Report No. NISTIR 6383, National Institute of Standards and Technology, Gaithersburg, Maryland, USA, 1999.

[4] M. Peatross, C. Beyler, Ventilation Effects On Compartment Fire Characterization, Fire Safety Science 5 (1997) 403-414.

[5] T. Sikanen, S. Hostikka, Modeling and simulation of liquid pool fires with in-depth radiation absorption and heat transfer, Fire Saf. J. 80 (2016) 95-109.

[6] S. Suard, M. Forestier, S. Vaux, Toward predictive simulations of pool fires in mechanically ventilated compartments, Fire Saf. J. 61 (2013) 64.

[7] J. F. P. Segovia, T. Beji, B. Merci, CFD simulations of pool fires in a confined and ventilated enclosure using the Peatross – Beyler correlation to calculate the mass loss rate, Fire Technology 53 (4) (2017) 1669 – 1703.

[8] National Institute of Standards and Technology, Gaithersburg, Maryland, USA, and VTT Technical Research Centre of Finland, Espoo, Finland. Fire Dynamics Simulator, Technical Reference Guide, 6th ed., March 2020. Vol.1: Mathematical Model; Vol.2: Verification Guide; Vol.3: Validation Guide; Vol.4: Configuration Management Plan.

[9] T. Beji, B. Merci, Development of a numerical model for liquid pool evaporation, Fire Safety Journal 102 (2018) 48-58.

[10] P. Incropera, D.P. de Witt, Introduction to Heat Transfer, Wiley, New York, United States, 1996.

[11] FDS input file on GitHub. https://github.com/firemodels/fds/tree/master/Validation/NIST_Pool_Fires/FDS_Input_Files, (Accessed 11 June 2021)

[12] K. Sung, J. Chen, M. Bundy, A. Hamins, The characteristics of a 1 m methanol pool fire, Fire Safety Journal. 120 (2020), 103121.

[13] I. R. Thomas, K. A. M. Moinuddin, I. D. Bennetts, The effect of fuel quantity and location on small enclosure fires, J. Fire Protect. Eng. Vol. 17 (2007), 85–102.

[14] D. J. Rasbash, D. D. Drysdale, D. Deepak, Critical Heat and Mass Transfer at Pilot Ignition and Extinction of a Material, Fire Safety Journal 10(1986) 1-10.

# Improvement of Flow Field Characterization in case of Fire Scenario in a Ventilated Compartment with PIV Technique

**Zaidaoui H.[1], Pretrel H.[1,*], Varrall K.[2], Vauquelin O.[2]**

*[1]Institut de Radioprotection et de Sûreté Nucléaire (IRSN) - PSN-RES/SA2I/LEF - Centre de Cadarache - 13115 Saint Paul Lez Durance – France*
*[2]Institut Universitaire des Systèmes Thermiques Industriels (IUSTI), UMR CNRS 7343, Aix Marseille Université, Technopôle de Château-Gombert, 13453 Marseille, France*
**Corresponding author's email*: hugues.pretrel@irsn.fr

## ABSTRACT

For the risk assessment of fire scenario in nuclear facilities, smoke movement is identified as a key phenomenon. A detailed experimental description of smoke flow is necessary to accurately validate CFD numerical predictions, which are increasingly used for fire risk evaluations. The present work deals with an experimental analysis of the flow inside a mechanically ventilated reduced-scale fire enclosure, named STYX. Velocity flow fields are characterized using the particle Image Velocimetry (PIV) technique in case of a fire event. Five fields of view, barely investigated experimentally, were considered for a given fire scenario. The capability of the PIV technique to describe the multi-dimensional characteristics of smoke flow measured inside a fire compartment were pointed up. The present study adds a valuable contribution and new informations to the previous experimental studies dealing with smoke flow behavior in a fire compartment.

**KEYWORDS:** PIV technique, Compartment fires, smoke dynamics, Mechanical ventilation.

## NOMENCLATURE

| | |
|---|---|
| Q | Flow rate ($m^3/h$) |
| $T$ | Temperature (°C) |
| $t$ | Time (s) |
| $X$ | Radial axis (m) |
| $Y$ | Longitudinal axis (m) |
| Z | Height (m) |
| $f$ | Frequency (Hz) |
| P | Electric power (W) |
| D | Diameter (m) |

**Abbreviation**

| | |
|---|---|
| PIV | Particle Image Velocitmetry |
| FDS | Fire Dynamics Software |
| CCD | Charged-Coupled Device |
| Vel Mag | Velocity Magnitude (m/s) |
| HRR | Heat Release Rate |

**Greek**

| | |
|---|---|
| $\rho$ | Density ($kg/m^3$) |
| $\lambda$ | Conductivity (W/m.K) |

## INTRODUCTION

Fire compartments represent a major interest since they can be responsible of fatal accidents. Fire smoke can affect key safety equipment because it is a vector for spreading heat, chemicals and soot particles. Nowadays, there is a strong development of numerical tools as CFD or zone-codes to assess the behavior of flow field during a fire event. In parallel to this numerical activity, there is consequently an important need of detailed experimental data base to perform the necessary process of verification and validation of numerical tools as well as to improve the physical understanding of the flow field. However, experimental databases including velocity field remain limited due to the difficulty of implementing advanced measurement techniques on large-scale experiments involving fire. For fires in confined and ventilated environments, hostile environments, containment and the presence of soot are added. Under these conditions, obtaining experimental multidirectionnal velocity field data remains a challenge. Optical techniques such as particle imaging (e.g. PIV) are rarely exploited for fire even though they offer a global measurement of two-dimensional velocity fields or

tridimensional velocity fields in case of stereo-PIV technique (SPIV). The PIV technique consists in following the displacement of tracer particles injected in the flow to determine the instantaneous velocity field of the flow. The injected particles are illuminated using a thin laser sheet. The displacement of the particle tracers in the flow is then determined by analyzing a sequence of successive flow images recorded using digital CCD camera(s). Knowing the spatial distance travelled by a group of particles, in a specific area of the flow, during the time interval separating two successive images, the instantaneous velocity of the flow at this area is measured subsequently. An overall measure of two (our case) or three (in case of SPIV) instantaneous velocity components in the field of view can be obtained using specific image processing algorithms.

The first attempts at medium-scale PIV measurements were conducted in 1996 during the study of air entrainment in a pool fire of diameter D = 15 and 30 cm [1]. It was found that PIV measurements of the fire-induced flow field can be used to obtain the entrainment rates of pool fires. Recently, SPIV measurements of large-scale velocity fields of smoke flow at a doorway, in the specific case of a natural ventilated room corner test ISO9705, were performed by Bryant [2,3]. The experimental data presented were for average velocity quantities for a 1.7m x 2.3m (width x height) viewing area. PIV measurements were compared to conventional measurements (bidirectional velocity probes). The results yielded a wide range of discrepancies between the velocity data, especially at the flow interface where the flow velocity is low. The velocity inferred from the bi-directional velocity probe measurements was found to be on average 10% and 7% greater than the SPIV measurements. Based on Bryant's work, Koched et al. [4,5] conducted a study on the smoke flow at a doorway induced by a fire source in a medium-scale compartment (NYX). The average velocity fields measured at the doorway cross-section were used to identify and separate the counter-flows. Analysis was primarily based on flow velocity fluctuation measurements, such as turbulent intensities and turbulent kinetic energy and large flow structures identified by contour analysis of the Reynolds stress tensor. This study provided valuable experimental informations thanks to SPIV technique applied to fire-induced flow. Varrall et al. [6,7] investigated the mixed convection exchange flow through a horizontal vent with SPIV. The results showed that the evolution of the dimensionless average velocity changes for natural convection, depending on whether the flow has the same direction as the ventilation or an opposite direction, from a square root to a convex curve with increasing ventilation rate. Subsequently, there was the study of Becerra et al. [8] which confirmed these results and showed that the flow has a geometric instationarity in the organization of the rising and falling fluids, but they tend on average to be distinctly organized. The upward and downward flow analysis show a substantial similarity between the natural and forced convection flows in the bi-directional regime. However, the flow inside a fire compartment has never been studied in detail in the literature, hence the interest of this study. PIV technique was also applied in tunnel ceiling-jet configuration for fire research. Oka et al. [9] performed a series of experiments on the quasi-steady state fire-driven ceiling-jet running along the center of the ceiling in a flat ceilinged horizontal tunnel with natural ventilation. The experimental results showed that the ceiling-jet thickness gradually grows with an increase in the distance from the fire source and maintains a constant value after reaching a distance of more than twice the height of the tunnel. A theoretical correlation and empirical formulas to represent the velocity and temperature rise distributions within the ceiling-jet in a direction perpendicular to the tunnel ceiling were developed. Recently, Betting et al. [10, 11] conducted experimental and numerical investigations of the flow characteristics in compartment fires. Experimental facility composed of a maritime container and FDS software based on the LES approach for numerical simulations were used. Velocity profiles were compared for fire heat release rate up to 200 kW. The position of the stagnation plane, the main location of mixing, can be seen to be relatively insensitive to the heat release rate evolution. A good agreement was observed for both ventilated and confined configurations.

As compartment fires are multi-physical and multi-scale problems, there is a need of improving the understanding of the flow field. This may help in challenging the results obtained with CFD

calculations strongly dependent on turbulence models considered, as well as the results provided by zone-code approach inherently global without enough local descriptions. The present study aims to push the analysis a few steps forward, using the PIV technique, to depict in detail bi-dimensional features of velocity field in case of a fire inside a confined compartment. The measurements were carried out on the reduced-scale experimental facility STYX of the Institut de Radioprotection et de Sureté Nucléaire (IRSN). First, the experimental setup and the typical description of the flow are presented. Then temperature profiles and mean velocity fields obtained by the PIV technique are illustrated. Several areas of interest are defined to analyze the overall flow fields (cf. Fig. 1).

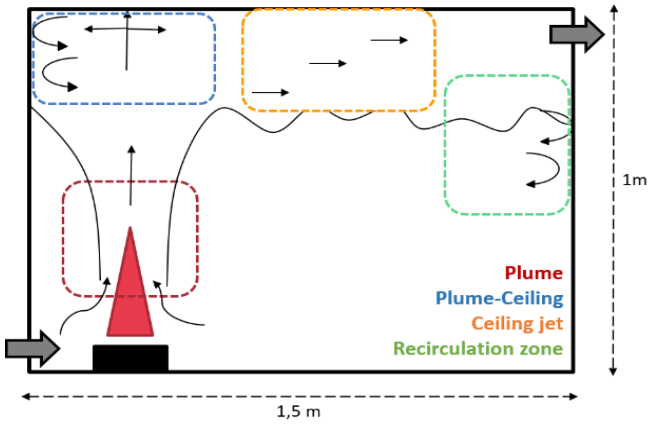


**Fig. 1.** Zones of interest for PIV measurements

## EXPERIMENTAL METHODS

### Experimental set-up

The experiments are carried out in a medium-scale device named STYX, consisting of a compartment formed by four walls, a floor and a roof. This volume (1.5 m x 1 m x 1 m) is confined and ventilated mechanically (cf. Fig. 2). The enclosure is manufactured by assembling plates of Monalite® (calcium silicate) with = 970 kg/m3, $\lambda$ = 0.26 W/m.K at 600 °C and able to withstand a maximum gas temperature of 1000°C. The Monalite® plates used have a thickness of 38mm for the floor and ceiling and 25mm for the walls. A silicone gasket is used when assembling the different Monalite® plates to ensure the tightness of the enclosure. In addition, the enclosure is equipped with two transparent perpendicular walls allowing the laser sheet application as well as the camera's optical access for the visualization of PIV measurements. The entire enclosure is mounted on a removable metal frame.

The fire source is simulated by an electrical resistor of about 2 kW ±200 W of convective heat, producing a thermal plume. This electrical resistor makes it possible to reach a thermal steady state in the compartment, and to generate, without mass inlet, a plume with no soot, which eases the optical access during PIV measurements. The electrical resistor is positioned on the side of the compartment as illustrated in Fig. 2. It allows to study both the flows under ceiling (ceiling-jet) and the near wall induced-flows.

The enclosure is mechanically ventilated with an inlet line and an exhaust line connected to a fan. This ventilation is provided in the compartment where air combined with seeding particles are supplied by two openings on the lower left side of the enclosure and exhausted by two openings on the upper right side, as illustrated in Fig. 2. All the ventilation openings are 0.06 m x 0.12 m.

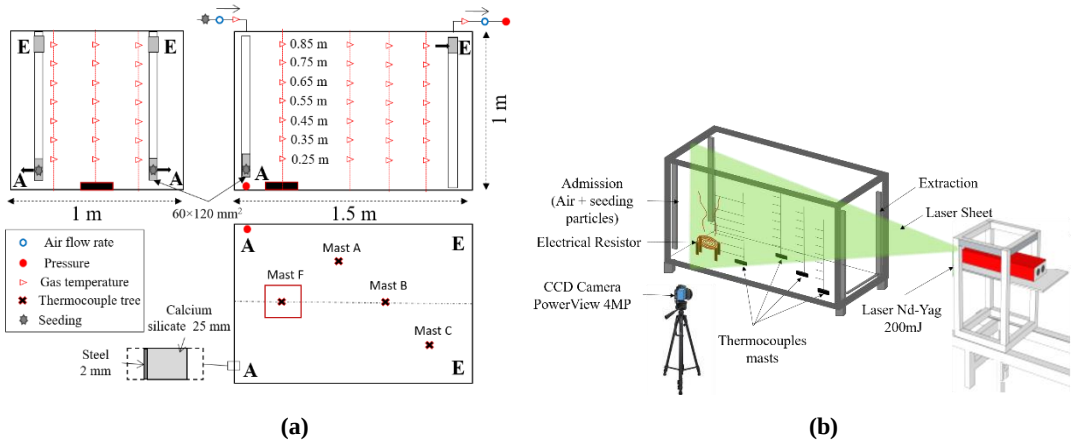


**(a)** **(b)**

**Fig. 2**. (a) Schematic configuration of the experimental apparatus STYX (b) PIV system

## Conventional measurement techniques

The temperature measurements were carried out with type K thermocouples (TC) of 1 mm diameter. The thermocouples, 28 in number, are distributed on four masts: one mast (F) at the level of the heating source (electrical resistor) and three masts (A, B and C) are distributed diagonally in the enclosure, as shown in Fig. 2. Each mast assembles 7 TCs, spaced 10mm apart. The lowest TCs are placed at 25mm from the floor of the enclosure. The temperature measurements serve as a reference for the qualification of the thermal stratification of the enclosure on the one hand and as a basis for analytical calculations of the flow velocity profile at the doorway on the other hand. The steady-state is reached after approximately 45 minutes of heating.

The mechanical ventilation flow rates are measured via an EMERSON Rosemount 3051 CD pressure transmitter connected to a Rosemount 1195 integral orifice primary element, ensuring an error of less than 2 %. All sensors (thermocouples and pressure transmitters) are connected to a NI CompactDAQ Ethernet chassis, and the signals are recorded at a sampling rate of 2 Hz via NI SignalExpress software.

## PIV system

Measurements of the mean velocity fields of the flow are performed by the PIV technique, a non-intrusive optical technique for measuring the velocity of a tracer present in the flow. The principle of this technique is described in the works [12] and [13]. The PIV acquisition chain comprises a laser source, a particle source (tracer), a CCD camera to record the displacement of the tracer, a synchronizer between the cameras and the laser, and a software to control the whole chain and to process the recorded images.

The tracer used is olive oil pulverized into fine particles using a pneumatic particle generator, supplied with compressed air at a pressure of 4 bar. The PIV measurements are performed after several renewals of the compartment volume in order to ensure that the whole flow is homogeneously seeded with particles and that the injection location (through the inlet ventilation line) does not affect the measurements. The light source used is a pulsed Nd-YAG laser with a power of 200 mJ/pulse clocked at a maximum frequency of 15 Hz. It allows the generation of two laser pulses separated by a lapse of time (dt) fixed by the operator according to the velocity of the flow. A CCD camera with a 4 MP resolution allows recording the displacement of the particles in time. It allows to record one pair of images per second at full resolution. The acquisition of the images is synchronized to the laser pulses using a synchronizer box. The Insight4G® software is used to control the entire system. The cameras are calibrated using a test pattern. For the velocity measurements, the configuration chosen is shown in Fig. 2(b). The recorded fields vary between 200mm x 200mm and 330mm x 330mm with a

resolution of 2048pixels x 2048pixels. The magnification factor, spatial resolution and number of vectors are relatively different for each field measured. Each image is subdivided into square interrogation areas (IAs) of various sizes ranging from 128pixels x 128pixels to 32pixels x 32pixels. A spatial overlap of 50 % is taken into account between the respective IAs of the same pair of images. Table 1 summarizes the different characteristics of the PIV system. However, both systematic and random PIV error sources are minimized by recent developments in processing algorithms but can be further reduced by optimizing the experimental setup and calibration. However, quantifying the remaining measurement uncertainties for all experimental and processing parameters such as seeding density, interrogation window size, out-of plane-motion, has remained a significant challenge.

**Table 1**. PIV system characteristics

| **Laser Nd:Yag, New Wave Solo 200 XT** | | **Cameras 630091 PowerView™ 4MP-HS** | |
|---|---|---|---|
| - Laser energy (mJ/pulse)<br>- Wave length (nm)<br>- Pulse duration (ns)<br>- Thickness of the laser sheet (mm) | 200<br>532<br>5<br>< 4 | - CCD resolution ($px^2$)<br>- Focal length (mm) | 2048 × 2048<br>50 |
| **Oil Droplet generator Model 9307-6** | | **Software parameters** | |
| - Particle material<br>- Particle size dp (µm) | Olive oil<br>$0.5 \leq dp \leq 3$ | - Adaptive interrogation area size (px2)<br>- Overlap (%)<br>- Number of snapshots N<br>- Field size ($cm^2$)<br>- Calibration factor (µm/px)<br>- t (µs) | 128 to 32<br>50<br>50<br>20x20 - 33x33<br>98.8 - 163.2<br>500-800 |

## RESULTS

### Study conditions

The ventilation rate is fixed throughout the entire study (Q ~ 30 $m^3/h$). It ensures to reach rapidly a quasi-steady flow with significant thermal stratification. Instantaneous and mean temperature measurements of the various TC masts are shown in the figures below (Fig. 3 (a) and (b)). The steady-state is reached after approximately 30-45 minutes of heating.

The average vertical temperature profiles computed on the quasi-steady period for A, B, and C masts show that the temperature inside the enclosure is relatively homogeneous in the horizontal plan and that the regime is stationary (cf. Fig. 3 (c)). The extreme temperatures recorded reach 43°C in the lower part of the chamber and 200 °C in the upper part. Repeatability tests have shown that the fluctuations of the mean temperature values do not exceed 5 %. The PIV measurements are conducted during the quasi-steady period, as shown in Fig. 3 (a).

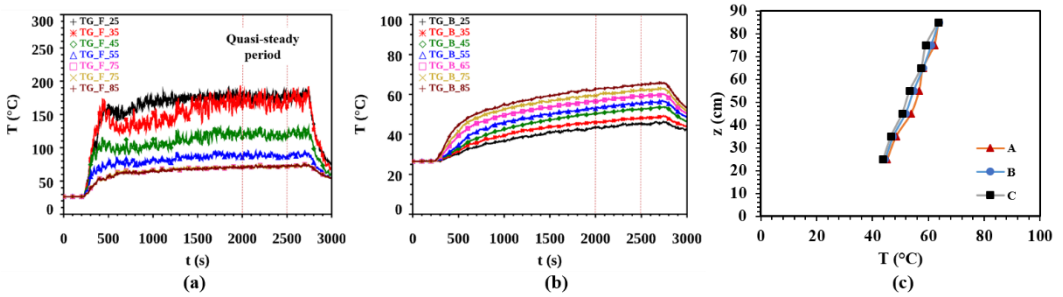


**Fig. 3.** Temperature profiles ; (a) time variation of the gas temperature of the mast F; (b) time variation of the gas temperature of the mast B; (c) temperature stratification at steady-state regime (mast A, B, and C).

## Mean velocity fields

In this section, the flow dynamics are studied from the average and fluctuating magnitudes of the velocity measurements performed inside the enclosure using the PIV technique at different zones of interest. A parametric study was conducted to evaluate the effect of the number of images pairs used to extract the mean velocity fields. As shown in Fig. 4, a given area near the right side wall is chosen for this convergence study. The velocity profiles are plotted for various number of images pairs from 50 to 1000. The results show that the total number of 50 images chosen in this paper can be considered as representative. This conclusion has been checked for different areas in the compartment.

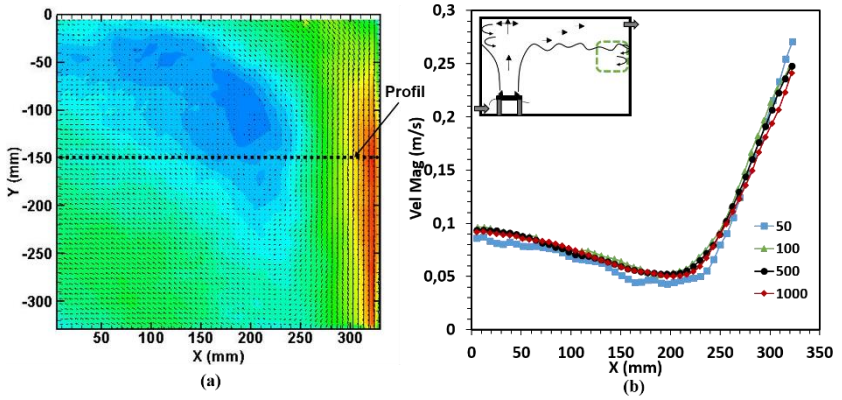


**Fig. 4.** Evolution of the mean velocity profiles along the radial axis at Y = -150mm for four different numbers of image snapshots.

The study focuses on five different flow fields, illustrated in Fig. 1, identified as key areas of transfer phenomena in case of a fire in the ventilated compartment. These areas of interests have been selected in order to highlight the capability of PIV technique for flows of different features. The first one is the plume area in which the process of air entrainment induced by buoyancy governs the amount of smoke filling the upper part of the room. Then the plume-ceiling interaction is an area of interest in order to characterize the input conditions of the induced ceiling jet flow that propagates radially under the ceiling. Flows in the vicinity of the side wall have also been identified as important due to the process of recirculation and downward flow barely studied and which explains the smoke spreading in the lower part of the compartment.

Three repeatability tests are performed for each field.

## Plume area

Mean flow field velocity contour and streamlines of the plume directly above the electrical resistor are illustrated in Fig. 5 (a) and (b). The velocity profile extracted at the dotted line is reported in Fig. 5 (c). A slight inclination of the plume and a strong entrainment generated by fresh air were observed. This tilt is mainly related to the position of the electric resistor near the side wall inducing low pressure area between the left side wall and the plume. The low-velocity amplitudes in the center of the lower part of the plume are related to the specific circular shape of the electrical resistance coil, whose center is hollow. The velocity reaches its maximum (1.2 m/s) in the plume center at ~20 cm above the electrical resistor. However, the higher fraction of the heat released by a heat source is transferred by convection to the plume in an upward motion driven by buoyancy [14]. The iso-contours velocity show clearly the direction of the air entrained within the plume. This results demonstrate the capability of PIV to thoroughly detail the velocity fields within the air entrainment region.

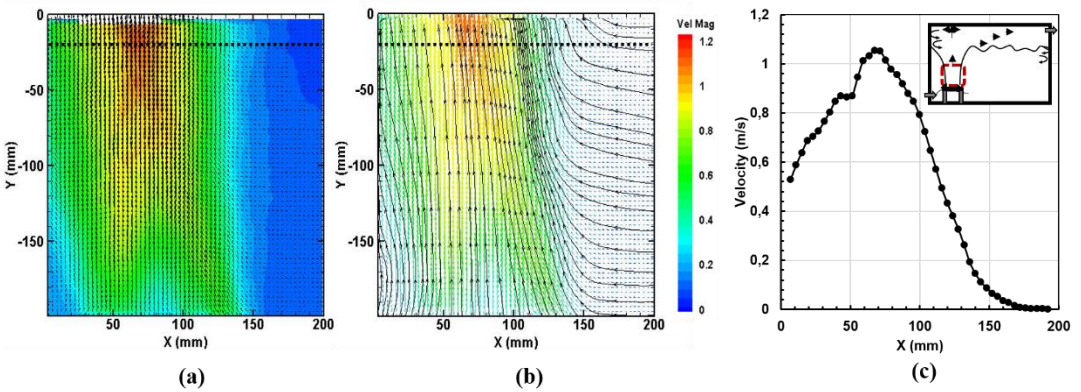


**Fig. 5**. Plume mean velocity fields in m/s; (a) contour and vectors (b) flow streamlines (c) velocity profile of the vertical component along the dotted line.

### Plume-ceiling interaction

A second area of interest is the plume-ceiling interaction whom an example of result is presented in Fig. 6.

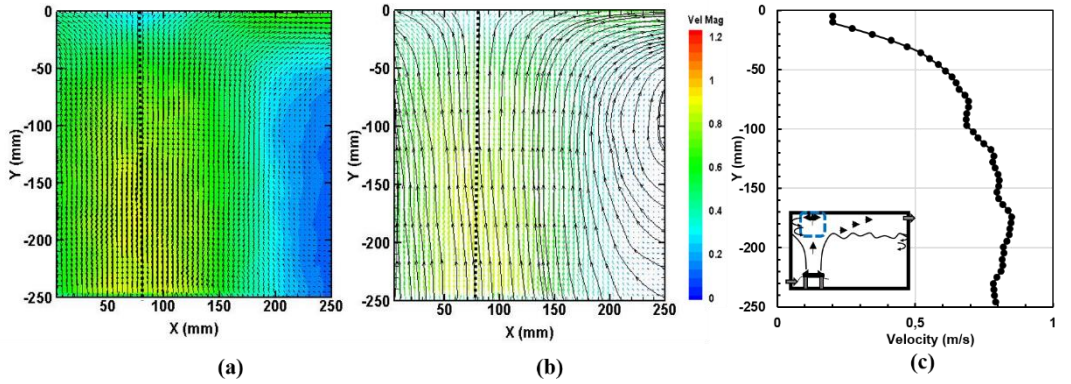


**Fig. 6.** Plume/ceiling interaction mean velocity fields in m/s; (a) contour and vectors (b) streamlines (c) velocity profile of the horizontal component along the dotted line.

As expected, we observe the presence of a dead spot in the center of the plume contact area with the ceiling. The first stage of the ceiling jet formation and the generation of a small vortex are observed. It is important to note that the plume velocity and fresh gases entrainment play an important role in ceiling jet stabilization and thickness. Fig. 6 (c) shows the velocity profile extracted at the dotted line, velocity diminution and dead area under ceiling are depicted. This result points out the capability of the PIV to quantify the boundary conditions of the ceiling jet onset.

### Ceiling jet

The radial ceiling jet has also been investigated. Mean velocity field contours and streamlines and velocity profile extracted at the dotted line is presented in Fig. 7.

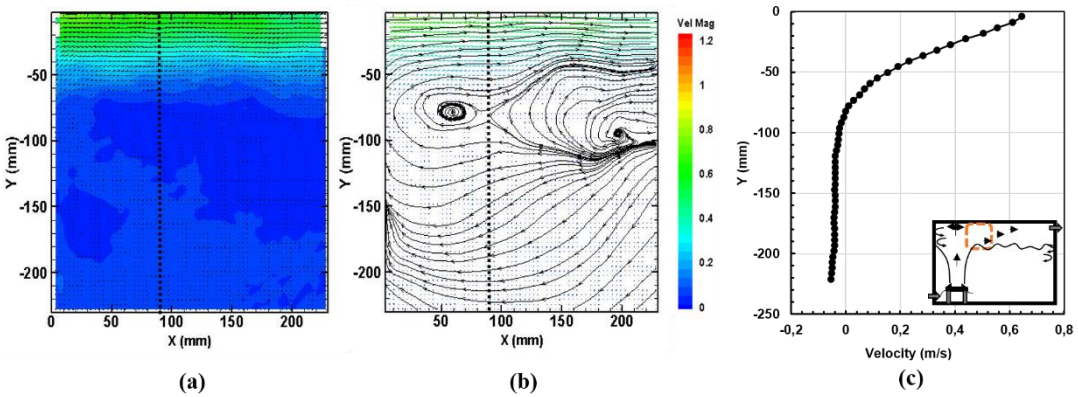


**Fig. 7.** Ceiling-jet mean velocity fields in m/s; (a) contour and vectors (b) streamlines (c) velocity profile of the horizontal component along the dotted line.

The ceiling jet is characterized as a horizontal flow with iso-velocity line parallel to the ceiling plan. As mentioned before, the fresh gas entrainment affects the ceiling jet movement. As expected, the velocity is greater near the ceiling area. An interesting result is the slow flow field below the ceiling jet. Vortices generation is reported below the layer of ceiling jet, which are responsible for maintaining a smooth movement of the plume throughout the ceiling. The streamlines show clearly how these vortices are generated through shear layers motion occurring between the hot and cold gases (cf. Fig. 7 (b)).

**Plume, ceiling and left wall interaction**

Another complex flow field is the one in the upper left corner of the compartment in which there is a strong interaction between the plume and the walls. In this way, Fig. 8 shows the correspondent mean velocity fields and the velocity profile extracted at the dotted line. A strong recirculation zone induced by the ceiling jet trajectory is created. The distance traveled vertically by the plume to create the vortex at the left wall of STYX is strongly related to the position of the heat source, the velocity of the plume and the temperature of and around the plume. The vortex also induces a downward flow along the sidewall that is clearly reported in Fig. 8 (c). This result show that the occurrence of vortex favors a downward motion of smoke along sidewall toward the lower part of the enclosure. This flow participates to the mechanism of smoke filling within the compartment.

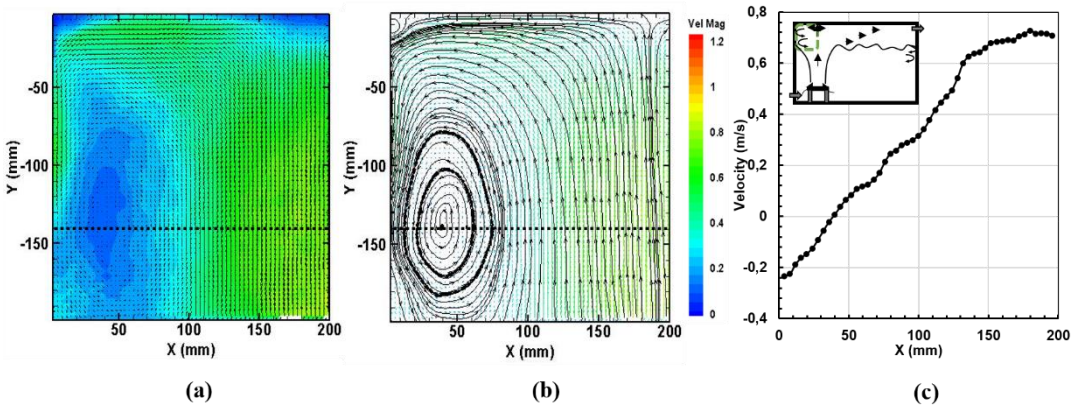


**Fig. 8.** Plume recirculation (left side) mean velocity fields in m/s; (a) contour and vectors (b) streamlines (c) velocity profile of the vertical component along the dotted line.

### Downward flow on right sidewall

The last flow field investigated is identified near the sidewall opposite to the heat source position. Results are presented in Fig. 9. The velocity profile clearly shows a vertical downward flow that accelerates along the vertical sidewall which is pointed out in Fig. 9 (c). This flow results from the interaction of the ceiling-jet against the right wall. Then due to heat exchange with the wall, the smoke cools down and then stabilize at a position where the temperature is similar to the temperature of the lower part of the compartment. An interesting feature is then the re-entrainment of this smoke leading to a large vortex.

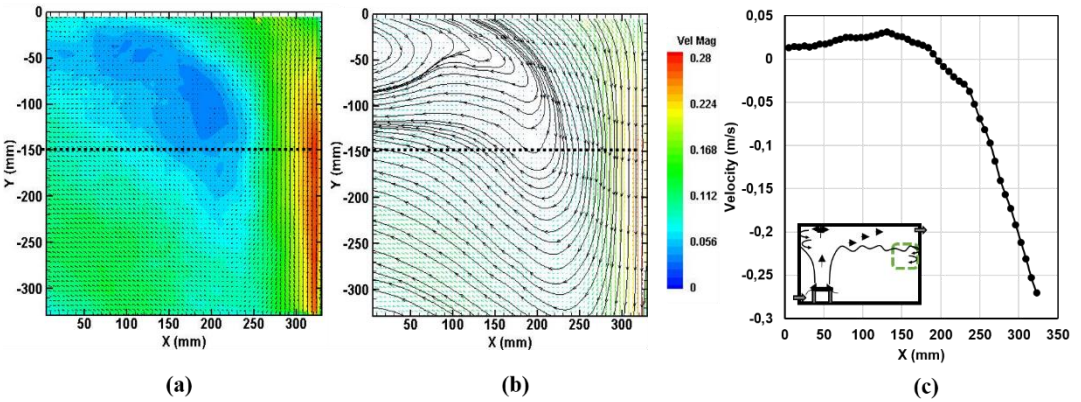


**Fig. 9.** Plume recirculation (right side) mean velocity fields in m/s; (a) contour and vectors (b) streamlines (c) velocity profile of the vertical component along the dotted line.

This result shows the mechanism of recirculation along vertical sidewall that contributes to re-entrained smoke within the upper part of the room. These measurements detail the process of smoke layer generation with a horizontal ceiling jet that propagates under the ceiling and a process of recirculation and re-entrainment induced by the sidewall that forms then the smoke layer.

### Global view of the flow field within the compartment

A reconstruction of the flow field is depicted in Fig. 10. This illustration shows the tilted shape of the thermal plume because of the sidewall vicinity. Then the radial ceiling jet is reported. The mechanism of flow interaction with both vertical sidewall is observed explaining the process of the downward velocity at the vertical walls and re-entrainment of smoke within the upper layer. Indeed, PIV technique offers a detailed description of the smoke flow within the compartment.

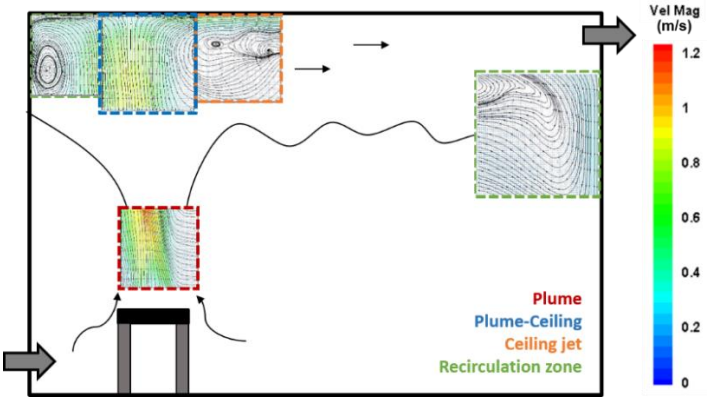


**Fig. 10.** Flow field reconstruction

## CONCLUSION

Experimental data for temperature evolution and bi-dimensional mean velocity fields in a reduced-scale fire compartment were recorded and analyzed. The capability of PIV technique to investigate flow fields in case of fire event in a confined and ventilated enclosure was highlighted. The fire source is simulated by an electrical resistor. Five flow fields of interest were identified for this study. It was shown that fire compartment filling is controlled by horizontal shear layers and vortices generation. Plume, ceiling-jet, and plume-ceiling interaction flows were described. This work improves the understanding of the fire compartment flows and offers relevant new informations on fire smoke flows trajectories and local velocities, for the validation of the simulation models dealing with mechanically ventilated confined fire. The study also highlights the potential of advanced optical measurement techniques for flows encountered in fire scenarios. The very promising results of this technical feasibility study give us the prospect of carrying out tests on real fire using a propane gas burner and a pool fire. Moreover, the spatial resolution of PIV measurements remains an asset for the comparison with numerical simulations.

## REFERENCES

[1] X.C. Hou, Jayavant P. Gore, Howard R. Baum, Measurements and Prediction of Air Entrainment Rates of Pool Fires, Proc. Combust. Inst. 26, (1996) 1453–1459.

[2] R. A. Bryant, Particle Image Velocimetry Measurements of Buoyancy Induced Flow Through a Doorway, NISTIR7252, 2005.

[3] R. A. Bryant, The Application of Stereoscopic PIV to Measure the Flow of Air into an Enclosure Containing a Fire, Experiments in Fluids, 47 (2009) 295–308.

[4] A. Koched, H. Pretrel, O. Vauquelin, L. Audouin, Experimental Determination of the Discharge Coefficient at a Doorway for Fire Induced Flow in Natural and Mixed Convection. Fire Mater. 40 (2014) 114–128.

[5] A. Koched, H. Pretrel, O. Vauquelin, L. Audouin, Measurement of Turbulence Statistics in Compartment Fire using Stereoscopic PIV, 18th Int. Symp.on the App of Laser and Imag Tech to Fluid Mech (2016).

[6] K. Varrall, H. Pretrel, S. Vaux, O. Vauquelin, Stereoscopic Particle Image Velocimetry Investigation of the Bidirectional Natural Convection Flow through a Horizontal Vent. Fire Technol, 52 (2016) 2027–2041

[7] K. Varrall, H. Pretrel, S. Vaux, O. Vauquelin, Stereoscopic Particle Image Velocimetry Investigations of the Mixed Convection Exchange Flow through a Horizontal Vent, Exp Fluids 58 (2017) 151.

[8] P. B. Barrios, H. Pretrel, S. Vaux, O. Vauquelin Flow Behaviour of the Exchange Flow through a Ceiling Vent in Natural Convection: A Numerical Approach using CALIF3S-ISIS CFD software, 3rd European Symposium on Fire Safety Science, 2018

[9] Y. Oka, H. Oka, O. Imazeki, Ceiling-jet Thickness and Vertical Distribution along Flat-Ceilinged Horizontal Tunnel with Natural Ventilation, Tunnelling and Underground Space Technology,53 (2016) 68-77.

[10] B. Betting, E. Varea, C. Gobin, G. Godard, B. Lecordier, B. Patte-Rouland, Experimental and Numerical Investigations of the Flow Characteristics in Confined fires, 3rd European Symposium on Fire Safety Science, 2018.

[11] B. Betting, E. Varea, C. Gobin, G. Godard, B. Lecordier, B. Patte-Rouland, Experimental and numerical Studies of Smoke Dynamics in a Compartment Fire, Fire Safety Journal 108 (2019) 102855.

[12] M. Raffel, C. Willer, D. Wereley, J. Kompenhans, Particle Image Velocimetry, a practical guide, 2nd ed., Springer, New York, 2007.

[13] R. J. Adrian, Particle-Imaging Techniques for Experimental Fluid-Mechanics, Annual Review of Fluid Mechanics 304 (1991) 23–261.

[14] B. Merci and T. Beji, Fluid Mechanics Aspects of Fire and Smoke Dynamics in Enclosures, CRC press, 2016.

# Influence of source elevation on a pool fire in a forced-ventilated enclosure.

**GEORGES E.[1,*], PRETREL H.[1], VARRALL K.[2], VAUQUELIN O.[2]**

*[1] Institut de Radioprotection et de Sûreté Nucléaire (IRSN), PSN-RES/SA2I, Centre de Cadarache, Saint Paul lez Durance, France*
*[2] Laboratoire IUSTI, UMR 7343, Aix Marseille Université, Marseille, FRANCE*
**Corresponding author's email: emeline.georges@irsn.fr*

## ABSTRACT

In nuclear facilities, fires can spread until reaching the upper part of a closed and mechanically-ventilated compartment. In this area of the room, the fire sources are under-oxygenated, but lie in an environment with significant radiative heat flux. Previous studies dealt with elevated fires, and results showed that fire pan elevation affects two phenomena: the combustion process and the flows inside the room. The present study aims to understand the effects of elevation on fire dynamics in a special ventilation configuration: air inlet in the lower part of the compartment, and vitiated air exhaust in the upper part. A series of tests was carried out in a reduced-scale apparatus, with a 0.09 m diameter pan filled with dodecane liquid fuel and placed at various heights. Two aspects were analyzed: the mass loss rate (MLR) and the gas temperature inside the room. First of all, the experimental results confirm the coupled and antagonistic effects of decreasing oxygen concentration and increasing temperature on the mass loss rate that were already highlighted in the literature. In addition, these results also show the role played by the flame height on the change in the combustion regime. Finally, vertical temperature stratification is much more pronounced when the fire is elevated until a certain height. Beyond this limit, stratification starts to disappear.

**KEYWORDS:** Burning rate, compartments, elevated fires, pool fires.

## INTRODUCTION

In nuclear power plants, facilities often consist of closed, but mechanically-ventilated compartments. If a fire occurs, it can spread to the upper part of the room (e.g. cable tray fires). The fire is then evolving in an environment with a low oxygen concentration since smoke pollutes this area, and a high temperature, due to the radiation heat fluxes from smoke and the nearby ceiling. However, the increase in radiative heat flux contributes to the rise in fire power, while the decrease in oxygen concentration has the opposite effect. These two physical phenomena therefore have both combined and antagonistic effects. In this context, they compete with each other, and according to their respective contributions, combustion is driven by either under-oxygenation or external heat flux. Understanding elevated fire dynamics is thus of great interest in the field of nuclear safety.

In numerous research articles, elevated fires are only one series of tests among others, designed to study fairly broad topics, such as fires in mechanically-ventilated compartments for Backovsky *et al*. [1] and Cetegen [2], or are only a means of achieving specific combustion regimes such as ghosting flames in Yang *et al*. [3] and Sugawa *et al*. [4]. More recently, studies have started to consider elevated fires as an issue in its own right.

When dealing with this issue, studies addressing this subject consider various ventilation configurations, depending on the applications intended for the work. Thus, the articles of Tiwari *et al.* [5], Polukhina [6], Mounaud [7], Coutin *et al*. [8],[9] and Zhang *et al.* [10] dealt with elevated fires in a naturally-ventilated compartment, the works of Wang *et al.* [11] and Zhang *et al.* [12],[13] a closed compartment and Pretrel a closed and mechanically-ventilated compartment [14]. The conditions of each study differ substantially. Some use a gas fire source (propane) [7],[8],[9], others liquids with various hydrocarbons, ranging from heptane [6],[10],[11],[12],[13] to diesel [5] and

dodecane [14]. Some tests were carried out at a large scale, and others at a reduced one, with compartments of various sizes organized in different ways, especially for openings in naturally-ventilated compartments. There can be door openings of different dimensions located in the side walls of the compartment [5],[6],[7], as well as ceiling vents [10].

These various configurations lead to different results, especially for the mass loss rate (MLR). Figure 1 combines the results of the various articles on this subject, and presents a dimensionless mass loss rate, noted MLR*, which corresponds to the ratio between the mean MLR and the mean MLR at ground level, as a function of z*, the non-dimensional elevation (ratio between the pan elevation and the compartment height). Mean MLR was calculated for tests with a quasi-steady phase and computed over this period, which may vary from one test to another. Results show two opposite trends: an increase in MLR* with pan elevation for closed compartments, and a decrease in MLR* with elevation for naturally- and mechanically-ventilated rooms. These two trends illustrate the combined effects of under-oxygenation, which reduces elevated fire power, and the increase in radiative heat flux, which, on the contrary, enhances pyrolysis. These results therefore show that, under specific surrounding conditions, either radiative heat flux or oxygen concentration is predominant and drives the combustion process. However, the specific surrounding conditions for each regime are currently fairly misunderstood, and the relationship between burning rate, radiative heat fluxes and oxygen concentration is not yet exactly determined. It is interesting to note that closed compartments seem to generate an environment in which radiative heat flux prevails. Similarly, mechanically- and naturally-ventilated boxes create environmental conditions for which oxygen concentration drives combustion. Thus, the geometry of the device, as well as the ventilation configuration (type, positions, directions, flow rates and speeds) influence the emergence of these regime and are therefore crucial when studying elevated fires.

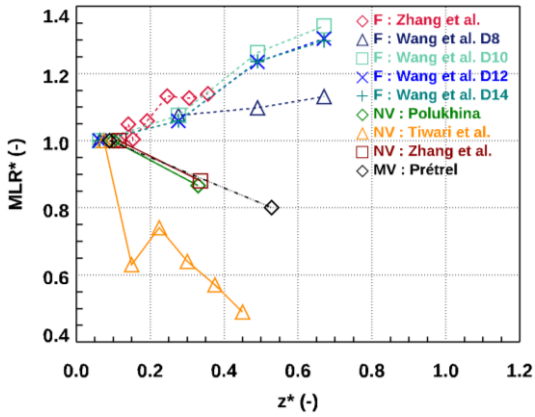


**Fig. 1.** MLR* as a function of the dimensionless elevation z*.

In an attempt to explain these trends, the authors study combustion efficiency and combustion regimes. The results show that the pan elevation affects combustion quality: the higher the fire, the worse the combustion rate. Indeed, in a polluted atmosphere, the fire can access less oxygen and the combustion reaction is consequently less efficient. Moreover, elevated fire tests can sometimes be divided into two groups: those for which the flame does not impinge on the ceiling and the MLR has a quasi-steady phase, and those for which the flame impinges on the ceiling and the MLR is largely unsteady. We can infer that flame height is involved in combustion regime changes. The fire elevation therefore affects combustion, but results illustrate that it likewise has an effect on flows within the compartment, i.e. everything related to the room filling process by smoke, thermal stratification or concentration fields. The results indeed show that the interface between smoke and fresh air does not go down to the floor as it would for a ground test, but stops at the pan level. The lower part of the compartment will then continue to be filled through wall jets. After some time, the smoke accumulates

on the ground and rises up until it fills the whole compartment. Finally, the results illustrate a more pronounced smoke stratification for elevated fires than for ground-level fires. We can infer a hot upper layer and a cold lower one. Moreover, the higher the fire, the more significant the break between these two layers.

Despite a growing interest in recent years, the understanding of elevated fires is still relatively limited. The present study aims to understand the effects of elevation on fire dynamics in a specific configuration with natural air inlet in the lower part of the room and mechanical vitiated air exhaust in the upper part. This configuration has not been investigated in the literature yet. The analysis is based on a series of reduced-scale tests, performed in the NYX facility of the Institut de Radioprotection et de Sûreté Nucléaire (IRSN). Two aspects are investigated: the burning rate and gas temperature in the compartment.

## TOOLS AND METHODOLOGY

### Experimental setup

The experimental device NYX has already been used for previous studies [15], [16], [17]. This fire test apparatus is a 1:4 reproduction of one room of IRSN's large scale DIVA facility, and therefore has the following dimensions: L = 1.5 m (length), W = 1.25 m (width) and H = 1 m (height) for a total volume of 1,875 $m^3$. Its walls are made of a double layer: the first one is a 2 mm thick steel plate ($\rho$ = 7817 $kg/m^3$, k = 51.9 W/K/m, $C_p$ = 446 J/kg/K, with $\rho$ the density, k the conductivity and $C_p$ the specific heat) and the second one is a 25 mm thick calcium silicate layer ($\rho$ = 2700 $kg/m^3$, k = 0.22 W/K/m, $C_p$ = 920 J/kg/K). In order to see inside the compartment with cameras placed outside, one of the double-layer walls is replaced by a glass plate. Since the chosen ventilation configuration for this work comprises a natural fresh air inlet and a mechanical exhaust, openings are milled in the lower part, on the longest sides of the compartment. These openings are 0.75 m long, 0.10 m high and are centered. Smoke is extracted through two vents located in the upper part of the compartment. A picture and a brief description of NYX are given in Fig. 2.

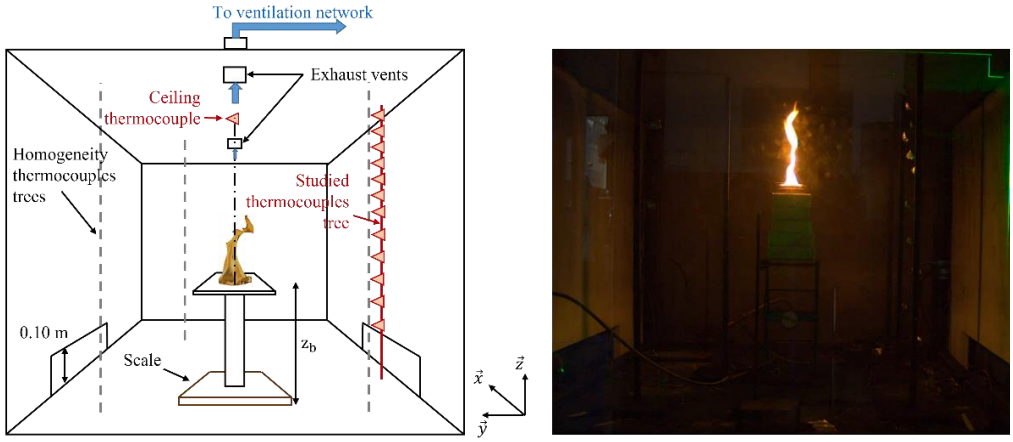


**Fig. 2.** A lateral view of the NYX apparatus is shown on the left. The triangles represent the thermocouples. The righthand image shows an example of a test for $z_b/H$ = 0.62.

The weighing system used to measure fuel mass loss all along the test is a SARTORIUS scale with a precision of 0.01 g. The burning rate is then computed using the time derivative of the mass loss. K-type thermocouples with a diameter of 0.5 mm are used to measure gas temperature in order to study thermal stratification. These thermocouples evaluate the temperature up to 1300 °C with a precision of 3 °C. They are distributed over 4 vertical trees located outside the plume region. Three lateral trees

are placed in the compartment corners with 4 thermocouples. They are used to assess compartment gas temperature homogeneity. The fourth tree (x = -0.15 m , y = -0.35 m with the pan center as the origin) is composed of 12 thermocouples distributed every 0.1 m between 0.165 m and 0.665 m, and then every 0.05 m from 0.665 m to 0.965 m to improve discretization near the ceiling and catch the steep gradient. This mast will provide the data used for the analysis. Finally, a thermocouple is placed over the center of the pan, near the ceiling, at 0.95 m from the floor. Bidirectional probes placed in the exhaust ventilation ducts measure flow rates between 0 $m^3/h$ and 130 $m^3/h$ with an error not exceeding 4% of the reading data. All measurements are recorded by a National Instrument (NI) system at a frequency of 1 Hz.

**Fire source**

In order to simplify the study, the chosen fire source is a hydrocarbon pool fire, and more precisely dodecane ($\Delta H$ = 42 MJ/kg and $T_b$ = 210 °C with $\Delta H$ the combustion enthalpy and $T_b$ the boiling temperature). A volume of 0.134 L of fuel is poured into a borosilicate pan with an inner diameter of 0.09 m and a height of 0.028 m. This volume, poured for all tests, corresponds to an average fuel mass of 101.72 g ± 1.5 g.

Since the tests are carried out in a compartment, a reference in the open atmosphere is needed. Correlations are commonly used such as Babrauskas' [18], or Heskestad's [19]. However, they are only partially or not validated at all for such a small pan size. For this reason, the 0.09 m diameter pan was characterized in an open atmosphere in terms of flame height and MLR using a weighing system and a camera. With the mass loss, a mean burning rate of 0.06 g/s ± 6% was determined. In order to evaluate the flame height in a free atmosphere, image processing was based on a method from Audouin *et al.*[20]. All the pictures are digitized: a threshold at which the flame is considered to be present in a pixel was chosen, which allowed each pixel to be assigned a value of 0 (flame is absent) or 1 (flame is present). The pictures were then computed with an arithmetic mean: the mean image obtained corresponds to the flame probability. Two heights are calculated for this image: a first one corresponding to a flame probability of 95% and the other a probability of 5%. The flame height is finally defined as the mean of these two values, with a correcting coefficient of 0.8. This method leads to a value of 0.167 m ± 2%.

**Methodology**

Eleven tests were carried out with the 0.09 m diameter pan. The initial extraction flow rate was set to 50 $m^3/h$. This high value was chosen in a first approach in order to get rid of the smoke interface effect on the fire. The pan is then placed in the center of the compartment at a height $z_b$. The different configuration settings are described in Table 1. The fuel is manually poured into the pan, and the fire is manually ignited with a propane burner. Finally, the glass wall is closed a few seconds after ignition. The mass loss, gas temperature, but also the flow rate which may slightly change after ignition, are measured throughout the test.

| $z_b/H$ | 0.06 | 0.15 | 0.20 | 0.31 | 0.39 | 0.51 | 0.62 | 0.72 | 0.77 | 0.81 | 0.87 |
|---|---|---|---|---|---|---|---|---|---|---|---|
| Initial fuel mass (g) | 100.2 | 102.2 | 101.2 | 101.5 | 101.8 | 101.8 | 101.4 | 102.1 | 102.3 | 100.9 | 101.6 |

**Table 1. Test settings**

**RESULTS**

**Elevation effects on the mass loss rate**

The first variable of interest is the MLR. Variation in burning rate over time is given for various elevations in Fig. 3: for illustration purposes not all elevations are plotted on this graph. The curves are divided into two groups. Figure 3 a shows tests with a slightly decreasing MLR with pan elevation

(group I), and Fig. 3 b tests with an increasing burning rate with elevation (group II). Moreover, the open atmosphere MLR for a 0.09 m diameter pan is added to each graph to facilitate comparison.

The group I graph shows three significant points. First, all the curves share the same behavior. During the ignition period, the increase in MLR is similar for all tests whether confined or not. Around 150 s, elevated fires carried out in NYX start to dissociate from the one performed in an open atmosphere and at ground level. Their burning rates decrease until reaching a quasi-steady phase. This phase is never completely steady because of the apparatus thermal inertia and the fixed fuel volume used. The MLR then increases slightly because of the borosilicate pan. At the end of the fire, only a small volume of fuel indeed remains: this small quantity is strongly heated by the pan and the flame. This is a common phenomenon for pool fires with variable fuel height during the combustion process. The last phase is the fire extinction by lack of fuel for all the tests performed. Secondly, fire duration increases with pan elevation: from around 2090 s for the ground-level fire to 3160 s for $z_b/H = 0.62$. Since the fuel mass is constant for the whole campaign, fire duration quantifies the heat release rate of a fire, i.e. if the fire duration increases, it implies that the burning rate falls. Thirdly, the ground fire MLR is similar to the fire in a free atmosphere, whereas elevated fire burning rates are lower than for the ground-level test.

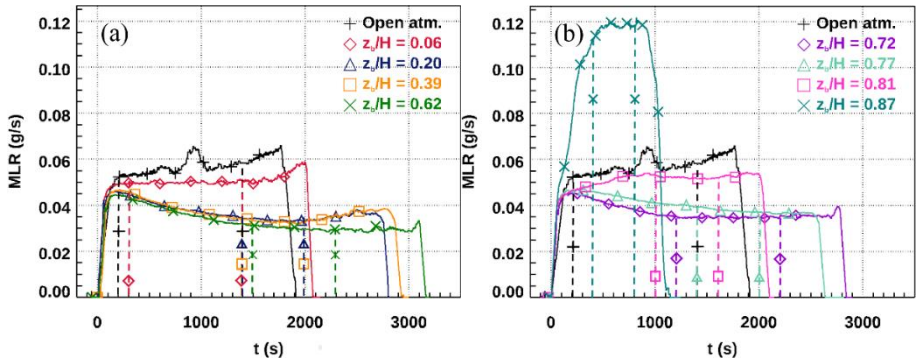


**Fig. 3.** MLR as a function of time for various elevations. (a): decreasing burning rate with elevation tests (group I); (b) increasing MLR with pan elevation tests (group II).

Group II fire tests show contrasting results. The ignition and dissociation period are similar for all tests as previously described. From $z_b/H = 0.72$, the steady value of the MLR is slightly greater than the value observed for group I. Beyond $z_b/H = 0.72$, MLR keeps climbing until reaching almost twice the open atmosphere burning rate for the highest fire ($z_b/H = 0.87$). Consequently, fire duration only reduces with pan elevation from 2840 s for $z_b/H = 0.72$ to 1150 s for the highest test.

These two graphs clearly illustrate that elevation affects the MLR and fire duration. Furthermore, this effect is much more significant for group II fire tests. In order to focus on the effects of elevation on the fire, Fig. 4 shows the ratio between the mean MLR for tests carried out in NYX and mean MLR for the open atmosphere fire as a function of non-dimensional pan elevation. The mean mass loss rates are computed over the quasi-steady period defined by dashed lines for each test as shown in Fig. 3.

In Fig. 4, regions A and B combine tests from group I, and region C shows tests from group II. The ground-level test MLR is, as explained before, almost the same as in a free atmosphere. Then, between the floor and the first elevation ($z_b/H = 0.15$), the burning rate shows a drastic decrease of around 40%. Actually, the inlet openings are located between these two elevations, i.e. the fire test performed below $z_a$ (a value representing the opening upper limit) is in front of the air inlet. This position can explain the similar MLRs for open-atmosphere and ground-level tests.

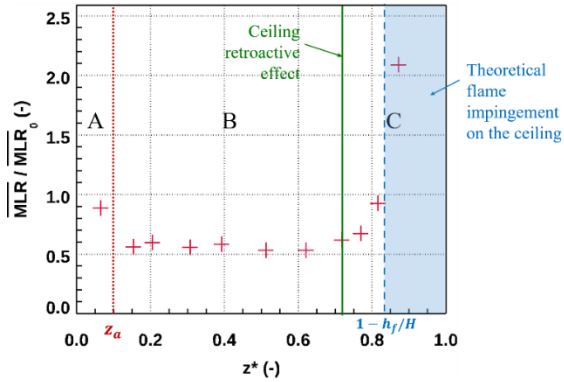


**Fig. 4.** Ratio between mean MLR and mean open atmosphere MLR as a function of non-dimensional pan elevation.

In region B, mean MLR ratio decreases slightly. Elevation does not have a significant influence. However, from a height $z_b/H = 0.72$, a distinct behavior appears: in region C, the effect of elevation is much more visible with a rapidly-increasing mean MLR ratio.

This graph highlights two phenomena. First of all, the results underline a change in combustion regimes between regions B and C, symbolized by a continuous green line. From the height of $z_b/H = 0.72$, the flame begins to impinge on the ceiling. The Fig. 5 displays flame pictures for region B and C tests. For $z_b/H = 0.62$, the flame does not impinge on the ceiling, whereas for $z_b/H = 0.72$, some parts of the flame start touching it. For $z_b/H = 0.81$, the flame starts spreading over the ceiling and finally, for $z_b/H = 0.87$, the flame impinges continuously on and spreads over the ceiling. When the flame reaches the ceiling, it is heated up as shown by the graph in Fig. 6. It displays the value of the nearby ceiling thermocouple as a function of non-dimensional pan elevation. At $z_b/H = 0.72$, the temperature near the ceiling is greater than 300 °C. Beyond this elevation, this temperature is even above 600 °C, i.e. for these tests, the thermocouple close to the ceiling is inside the flame [21]. Since the ceiling is heated up, it produces additional heat fluxes which come back to the fuel surface. The flame, which spreads along the ceiling, also generates more radiative heat fluxes compared to a classical vertical flame (e. g. $z_b/H = 0.62$). Radiative heat fluxes back to the fuel surface are therefore not only composed by vertical flame fluxes, but also retroactive fluxes from the ceiling and the spreading flame. This phenomenon enhances fuel pyrolysis, which is directly linked to heat fluxes received by the fuel surface. Since beyond $z_b/H = 0.72$, the higher the fire, the flatter the flame, this change of shape explains the significant increase in the MLR at the greater elevation.

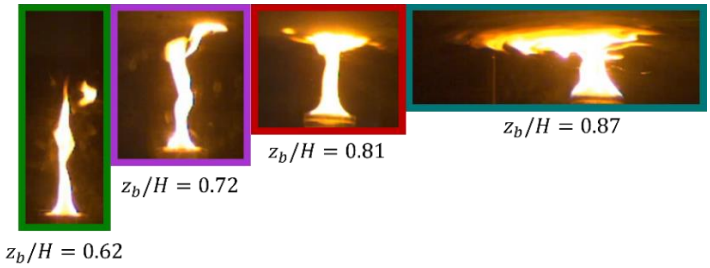


**Fig. 5.** Qualitative analysis of flame behavior for different pan elevations.

In Fig. 4, the dashed blue line represents the region where the 0.09 m diameter pan flame should theoretically impinge on the ceiling. This limit position is based on the open atmosphere flame height. The results show that the ceiling feedback begins earlier than this limit (near $z_b/H = 0.72$): the ceiling

effect is thus non-negligible even if the flame does not touch the ceiling continuously. Nevertheless, flame height seems to play a role in the change in combustion regime.

The second phenomenon highlighted by Fig. 4 is the competition between the decrease in oxygen concentration and the increase in radiative heat fluxes for the mass loss rate. In region B, the mean MLR ratio falls lightly. At these elevations, external heat fluxes have only a weak impact on the MLR, in which case, oxygen concentration drives the combustion process. On the contrary, in region C, radiative heat fluxes prevail and lead the combustion. This explains why the mass loss rate increases sharply beyond $z_b/H = 0.72$. In the literature, these two tendencies were not obtained in the same configuration except for Polukhina, who only achieved results for two different heights.

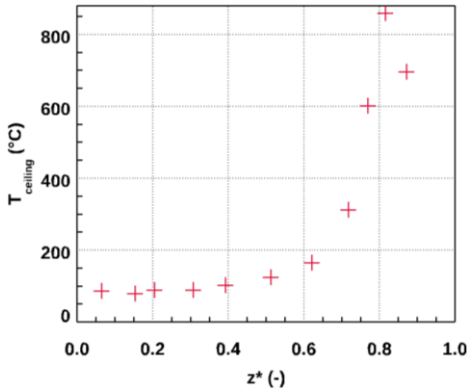


**Fig. 6.** Temperature at a height of 0.95 m, centered on the fuel pan as a function of non-dimensional elevation.

**Elevation effects on gas temperature**

Figure 7 displays variation in temperature over time for tests at various heights. A typical temperature profile generally follows the same trends as the MLR. Thus, they all show a first stage with a rapid temperature increase, then for the group I test ($z_b/H = 0.31$), temperatures decrease until a quasi-steady period. For group II pool fires, gas temperatures keep increasing slowly for $z_b/H = 0.72$, and quickly for $z_b/H = 0.87$. Despite these differences, all the curves presents a quasi-steady phase. Mean values can be defined over this period.

In a stratified compartment, temperature profiles are combined into two distinct groups: one group of thermocouples in the warm and dense smoke, where high temperatures are measured, and one group of thermocouples outside the smoke, where lower temperatures are measured. For $z_b/H = 0.06$, no group of thermocouples is visible: thermal stratification is very weak. For $z_b/H = 0.31$, two groups are discernible: the first with the two highest thermocouples, and the second with the other 4 thermocouples. However, the break between these two groups is not clear since the cold layer has temperatures ranging from 20 °C to 40 °C. For $z_b/H = 0.72$, all thermocouples except the one at a height of 0.965 m measure rather cold temperatures. The temperature differences between these two groups are quite significant. The same stratification type is visible for $z_b/H = 0.87$, but the colder thermocouple group shows larger temperature amplitudes: the stratification begins to disappear. This variation in temperature over time can also be used to compare compartment thermal trends for tests with seemingly similar MLRs. For example, the ratios between mean MLR and mean open atmosphere MLR for $z_b/H = 0.31$ and $z_b/H = 0.72$ are almost similar, but their temperature profiles show different thermal structures. For $z_b/H = 0.31$, temperatures decrease just after the ignition phase until stabilization, while for $z_b/H = 0.72$ they only increase. Thermal stratification is also much more pronounced for $z_b/H = 0.72$: the top layer is warmer and the bottom one colder with very clustered thermocouples, which means that the break between them is largely pronouced.

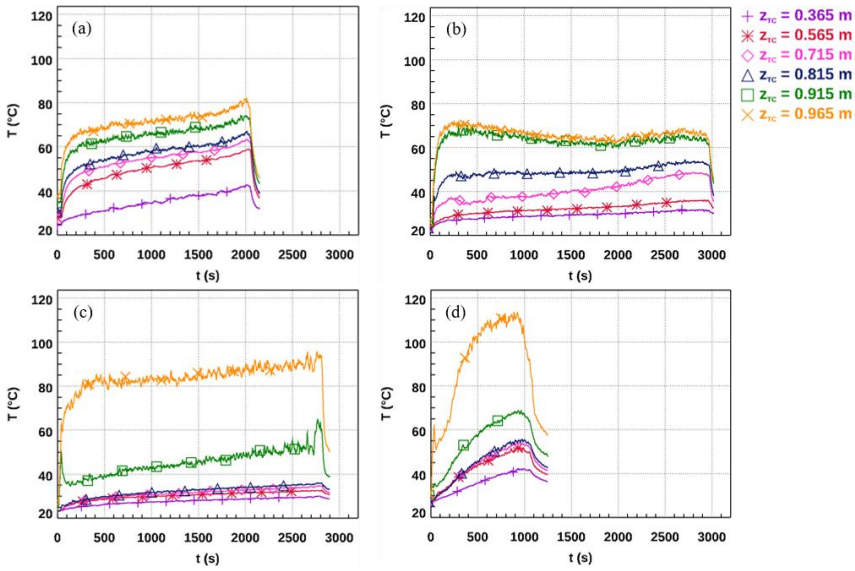


**Fig. 7.** Variation in temperature over time. (a): $z_b/H = 0.06$ ; (b): $z_b/H = 0.31$ ; (c): $z_b/H = 0.72$ ; (d): $z_b/H = 0.87$.

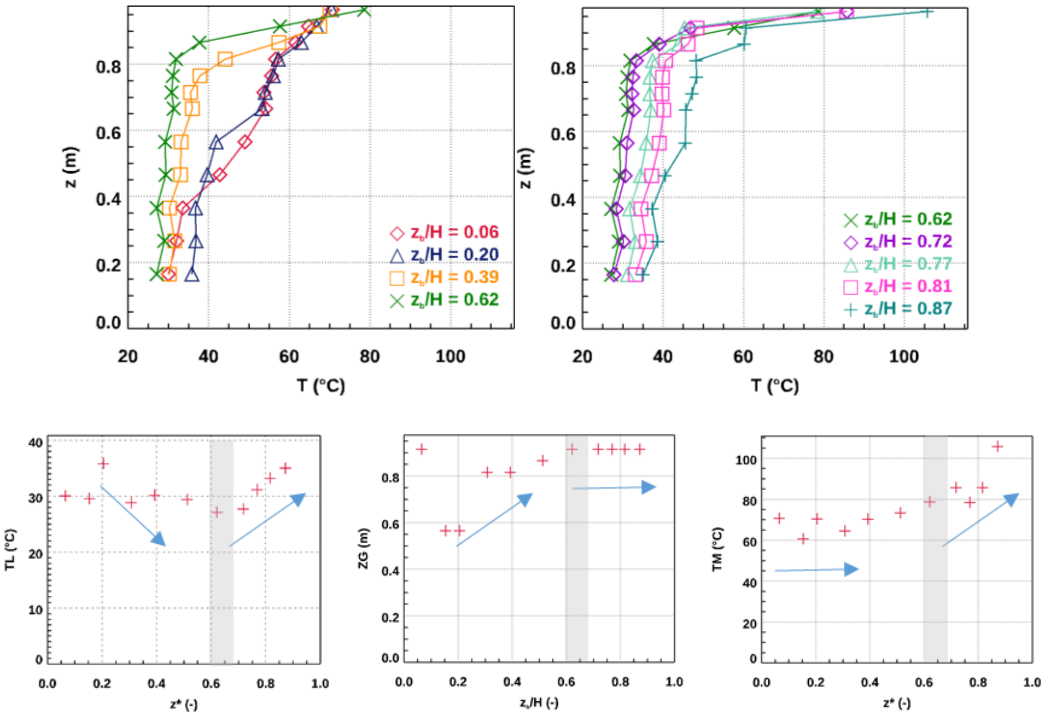


**Fig. 8.** On the top, the mean vertical temperature profiles for various elevations. On the bottom, from left to right, the lowest temperature, the maximum gradient position and the maximum temperature extracted from the temperature profiles.

Figure 8 shows the average vertical temperature profiles (computed on the quasi-steady phase) for tests at different elevations. Since all the thermocouple trees show homogeneous results, data come from the one with the most thermocouples. In order to interpret the variation in thermal stratification,

three quantities are considered : the lowest temperature (TL), the location of the highest gradient ZG (that can be considered as a possible interface between two layers) and the maximum temperature (TM). The lower and upper layers can be considered to be below and beyond the vertical position of the maximum gradient respectively. The variation in the three quantities versus the pool elevation (provided in Fig. 8) shows two typical regimes, one for low elevations and one for high elevations. For the first regime for low fire elevations, the lowest temperature decreases with elevation due to the fact that the heating of the lower layer by flame radiation decreases as the fire is elevated. The maximum temperature does not increase significantly and follows the same trend as the MLR that remains constant for low elevations. The location of the interface climbs due to the increase in fire elevation. The second regime, for high elevations, shows different vertical temperature profiles. The lowest and the maximum temperatures increase because the MLR increases and the flame impinges on the ceiling. In addition, the interface position does not change substantially because it has already reached a high position close to the ceiling. The critical position that distinguishes the two regimes is located around 0.6-0.7 (in grey in Fig. 8).

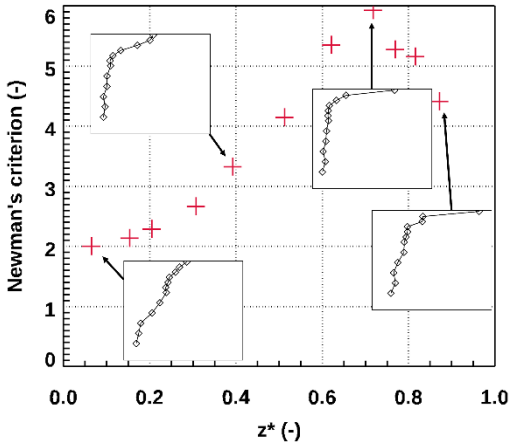


**Fig. 9.** Newman's criterion and temperature profile shapes for various elevations.

In order to quantify the thermal stratification in a tunnel, Newman [22] proposed a criterion, defined as follows:

$$NC = \frac{\Delta T_{cf}}{\Delta T_{av}} = \frac{T_{ceiling} - T_{floor}}{T_{mean} - T_{floor}} \quad (1)$$

where NC is the Newman's criterion, $T_{ceiling}$ the gas temperature near the ceiling, $T_{floor}$ the gas temperature near the floor, and $T_{mean}$ the mean temperature in the region of interest. Even though the configuration studied is not a tunnel, this criterion can be a relevant indicator for variation in stratification with fire elevation. This criterion is plotted in Fig. 9 as a function of the non-dimensional height. It supports the findings explained earlier: the value of the criterion increases with elevation until a maximum at the height $z_b/H = 0.72$, and then decreases. That is to say stratification is indeed clearer when the fire is elevated, but until a limit beyond which it starts to vanish. This limit seems to be related to flame impingement.

## CONCLUSION

This work aims to study the effects of elevation on fire dynamics by focusing on the mass loss rate and gas temperature. The chosen ventilation configuration consists of natural air inlet in the lower part and vitiated air exhaust in the upper one. The analysis is based on a series of small-scale dodecane

pool fire tests in an apparatus with a weighing system, to determine the mass loss rate, and thermocouples for measuring gas temperature. The results show that elevation affects the MLR in two ways. In a first range of heights, the influence of elevation is quite small, the mass loss rate decreases rather slowly: the reduction of available oxygen explains this decrease. In a second range, when the flame begins to impinge on the ceiling, the effects of elevation are more pronounced, and the MLR increases sharply until being well above its open atmosphere value. Since the pool fire is close to the ceiling and smoke, it lies in an environment with great radiative heat fluxes, which control the combustion and hence the increase in mass loss rate. The results also confirm the link between flame height and changes in the combustion regime for elevated fires. Finally, the study of the gas temperature in the compartment shows that stratification actually increases with pan elevation, but up to a maximum value, and then decreases. These findings, obtained in an original ventilation configuration, support and complete previous studies on elevated fires.

## ACKNOWLEDGMENTS

The authors would like to acknowledge Électricité de France (EDF) which supported this work.

## REFERENCES

[1] J. Backovsky, K. L. Foote, N. J. Alvares, Temperature Profiles in Forced-Ventilation Enclosure Fires, In: Wakamatsu, T. (Ed.), Fire Safety Science–Proceedings of the Second International Symposium, pp, 315–324, 1989.

[2] B. M. Cetegen, Entrainment and Flame Geometry of Fire Plumes, PhD thesis, California Institute of Technology, Pasadena, USA, 1982.

[3] Z. Yang *et al*., Studies on ghosting fire from pool fire in closed compartments, J. Univ. Sci. Technol. China 40 (2010) 751–756.

[4] O. Sugawa *et al*., Burning Behavior in a poorly-ventilated compartment fire -Ghosting Fire-, Fire Sci. Technol. 9 (1989) 5–14.

[5] M. K. Tiwari *et al*., "Effects of elevated pool fire in a naturally ventilated compartment," J. Therm. Anal. Calorim. 146 (2021) 341-353.

[6] K. Polukhina, Elevated Fires, Master thesis, Lund University, Lund, Sweden, 2016.

[7] L. G. Mounaud, A Parametric Study of the Effect of Fire Source Elevation in a Compartment, Master thesis, Virginia Polytechnic Institute and State University, Blacksburg, Virginia, USA, 2004.

[8] M. Coutin, J. M. Most, Aerodynamic characterization of a compartment fire as a function of its behavior, In: Evans, D. (Ed.), Fire Safety Science–Proceedings of the Seventh International Symposium, pp, 407–418, 2002.

[9] M. Coutin *et al*., Behavior of the combustion of a fuel material in the vitiated upper zone of an open compartment, Third International Seminar on Fire and Explosion Hazards, 2000.

[10] J. Zhang *et al*., Experimental study on elevated fires in a ceiling vented compartment, J. Therm. Sci. 22 (2013) 377–382.

[11] J. Wang *et al*. Early Stage of Elevated Fires in an Aircraft Cargo Compartment: A Full Scale Experimental Investigation. Fire Technol. 51 (2015) 1129–1147.

[12] J. Zhang *et al*., Impacts of elevation on pool fire behavior in a closed compartment: A study based upon a distinct stratification phenomenon, J. Fire Sci. 31 (2012) 178–193.

[13] J. Zhang *et al*., Smoke filling in closed compartments with elevated fire sources, Fire Saf. J. 54 (2012) 14–23.

[14] S. Suard, P. Zavaleta, H. Pretrel, Overview of the OECD PRISME 3 Project, 16th SMIRT Post-Conference Seminar on Fire Safety in Nuclear Power Plants and Installations,Ottawa, ONT, Canada, 2019.

[15] H. Prétrel, L. Bouaza, and S. Suard, Multi-scale analysis of the under-ventilated combustion regime for the case of a fire event in a confined and mechanically ventilated compartment, Fire Saf. J. 120 (2021) 103069.

[16] M. Mense *et al*., Experimental and numerical study on low-frequency oscillating behaviour of liquid pool fires in a small-scale mechanically-ventilated compartment, Fire Saf. J. 108 (2019) 102824.

[17] J. Li *et al*., Experimental study on the effect of mechanical ventilation conditions and fire dynamics on the pressure evolution in an air-tight compartment, Fire Saf. J.125 (2021) 103426.

[18] V. Babrauskas, Estimating large pool fire burning rates, Fire Technol. 19 (1983) 251–261.

[19] G. Heskestad, Luminous heights of turbulent diffusion flames, Fire Saf. J. 5 (1983) 103–108.

[20] L. Audouin et al., Average centreline temperatures of a buoyant pool fire obtained by image processing of video recordings, Fire Saf. J. 24 (1995) 167–187.

[21] S. C. P. Cheung, G. H. Yeoh, A fully-coupled simulation of vortical structures in a large-scale buoyant pool fire, Int. J. Therm. Sci. 48 (2009) 2187–2202.

[22] J. S. Newman, Experimental evaluation of fire-induced stratification, Combust. Flame 57(1984) 33–39.

# The assessment of the laminar smoke point soot modeling concept for diluted laminar diffusion flames

**Motaghian S.[1],*, Beji T.[1]**

[1] *Ghent University, Department of Structural Engineering and Building Materials, Ghent, Belgium.*
**Corresponding author's email: shahrooz.motaghian@ugent.be*

## ABSTRACT

Laminar smoke point (LSP)-based soot models for ethylene laminar diffusion flames diluted by nitrogen are assessed by performing CFD simulations using OpenFOAM. More specifically, the treatment of soot oxidation is investigated using either a Constant Soot Oxidation (CSO) or an Oxygen Dependent Soot Oxidation (ODSO) model. Furthermore, the Lindestedt and Moss-Brooks two-equation soot models are also considered to evaluate the relative accuracy of the LSP-based soot models. The results show that the maximum soot volume fraction in the computational domain and on the centerline has been best predicted by the Lindestedt model, whereas significant over-predictions have been observed using the LSP models and even more so the Moss-Brooks model. The shift in the peak soot concentration from the flame's axis to its wings when the fuel volume fraction increases could not be captured by any of the three models. In the LSP approach, as expected, the ODSO has produced more qualitatively consistent estimations of soot volume fraction and soot oxidation rate distributions in comparison to CSO. Furthermore, a modification is proposed to estimate the pre-exponential factor in the soot formation, taking into account the dilution effect.

**KEYWORDS:** Laminar smoke point, soot modeling, CFD, diluted laminar flames, OpenFOAM.

## INTRODUCTION

The soot produced in fires has negative effects on health and, in the shorter term, visibility, and evacuation and rescue efforts. Moreover, soot is the main contributor to thermal radiation, the dominant heat transfer in fires. Computational Fluid Dynamics (CFD) has been used to predict soot production and transport in fire-driven flows. Given the relatively large domains over which a fire spans (as opposed, for example, to combustion engine applications), a 'suitable' soot modeling approach in fire simulations should not be computationally expensive. Therefore, models based on detailed chemical mechanisms are not very appropriate, let alone the fact that many fuels involved in fires are complex and sometimes, not readily known.

The Laminar Smoke Point (LSP) height has been considered as a reliable measure of the level of sootiness of fuels; the LSP height of many fuels and combustibles is indeed available in the literature. Therefore, several LSP-based semi-empirical models have been developed to predict soot concentrations (and the subsequent thermal radiation) in diffusion flames. Delichatsios [1] developed an analytical formulation for soot formation rate on the centerline of laminar diffusion flames, assuming that gas-phase reactions (inception) are dominant in the soot formation process. A mixture fraction threshold has been set to determine the onset of the soot inception. Beji et al. [2,3] extended the model proposed by Delichatsios [1] and implemented it in CFD simulations. 'Critical' mixture fraction values have been defined for the initiation of soot formation and soot oxidation processes. Furthermore, in [2,3], a power-law temperature dependence has been incorporated into the soot formation expression originally proposed in [1]. These modifications allowed to improve the accuracy of the predictions in the lower part of the laminar diffusion flames and to capture the high soot concentration at the 'wings'. The soot oxidation rate, set as constant in [3], has been improved by Yao et al. [4] by using an oxygen concentration dependence model. The constant parameters of these soot

models were generalized for various fuels by using their respective LSP heights as the only fuel-dependent factor involved in these models. Lautenburger et al. [5] also developed a model based on the same concept. They assumed that each of the soot formation and oxidation rates is a product of two polynomial functions, one dependent on mixture fraction and the other on the temperature. The constants used in the polynomials and the critical mixture fractions were determined by numerical calibration.

The LSP-based soot models mentioned above are commonly used for sufficiently ventilated normal laminar and turbulent diffusion flames. However, the potential presence of diluent agents (*e.g.* nitrogen, carbon dioxide and water vapor) influences the flame dynamics (*e.g.*, in terms of height, temperature field and location of peak soot concentration as a function of the dilution level) due to thermal [6], transport [7], and chemical [8] effects. Thus, an evaluation and extension of the LSP-soot models to such scenarios is highly relevant. The current study aims to assess the accuracy and capability of these models in simulating the diluted laminar ethylene flames investigated experimentally in [9–11].

Several studies have investigated the soot processes in the diluted flames numerically using the detailed sectional soot approach [12,13]. For example, McEnally et al. [11] used such an approach but were not able though to predict the peak soot concentration on the axis and not the wings. Smooke et al. [10] numerically investigated the same flame as in [11] using the same approach, except that they modified the kinetic mechanism proposed by Sun et al. [14] to increase the predicted concentration of benzene by a factor of two. The maximum soot volume fraction was well predicted on the axis for the fuel volume fraction of 32% but not 40%. Following the two studies discussed above, Smooke et al. [9] proposed a soot aging modification to [10] by cutting off surface growth of the soot particles beyond a certain size (25nm), but larger particles were allowed to be formed by coalescence and aggregation. Their numerical results showed improvement to their previous results [10] in terms of transition of maximum soot volume fraction from the axis of the flame to the wings for the fuel volume fraction of 40% and higher. The substantial computational cost and the dependence on complex kinetic mechanisms make sectional and in general, detailed models 'unattractive' for fire simulations. Nmira et al. [15] assessed the LSP soot modeling concept (Models developed by Lautenberger et al. [5] and Yao et al. [4]) for various laminar diffusion flames including two acetylene diluted flame (in normal and zero-gravity conditions) that were experimentally studied by Konsur et al. [16]. They found out that the LSP-based soot models could accurately locate the position of maximum soot concentration in different levels above the burner but underestimated the magnitudes. The effect of dilution has not been investigated in [15]. Furthermore, a complex kinetic mechanism for ethylene has been used. Assessing LSP-based soot models when a simple global reaction for the fuel is applied is more relevant for practical fire simulations.

It is intended in the current study to carry out a comprehensive assessment of the LSP-based soot models proposed in [3] and [4] by simulating the diluted flames examined experimentally in [9–11]. Furthermore, the two-equation soot models proposed by Leung et al. [17] and Brooks and Moss [18] are used as additional modelling references.

## FLAME SETUP

The flame studied here is a normal diffusion laminar flame (NDF) having concentric circular inlets (Fig. 1). In the inner inlet, the fuel is diluted with nitrogen and injected with a fully developed parabolic velocity profile at the exit of the burner. An air co-flow is injected at the outer inlet following a plug flow profile. The average velocity of both the diluted fuel and the air inlets is 35 cm/s. The

temperature of cold fuel and air is considered to be 300 K. This flame is investigated experimentally and numerically by Smooke et al. [8–10].

## NUMERICAL METHODOLOGY

The flame is simulated using an axisymmetric computational domain and a grid sensitivity analysis has been carried out. The density of the grid is higher in the centeral region of the domain (0.2 mm cell size) and larger cells of ~0.4 mm are used near the open boundaries. Conservation equations of continuity, momentum, sensible enthalpy, species mass fraction, and soot mass fraction (and another transport equations in [17] and [18]) are solved using OpenFOAM [19] and, more specifcally, FireFOAM [20], a solver designed to numerically simulate fire scenarios.

A single-step reaction of ethylene, assuming infinitely fast chemistry, is used to model the oxidization of the diluted fuel when LSP-based soot models are applied. GRI-III [21] mechanism and finite-rate chemistry modeling are also used for ethylene combustion and soot chemistry modeling to resolve the concentration of important species required in the two-equation soot models [17] and [18]. Models associated with the soot modeling of the diluted flames are implemented into the OpenFOAM source code. In the next section, details about soot models used in the current study are presented.

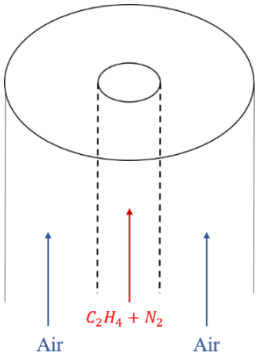


**Fig. 1**. Schematic of the burner configuration

### Soot modeling approaches

LSP-based models introduced in the previous section are known as semi-empirical models. The two-equation models are also considered semi-empirical soot models. In this section, the mathematical details of LSP-based soot models applied in the current study are provided and then, the two-equation models used in the simulations are discussed briefly.

Delichatsios [1] developed a theoretical description of axisymmetric laminar diffusion flames and formulated an estimate of soot formation rate on the centerline of the flame using a mixture fraction parameter. He assumed that heterogeneous formation reactions are dominant in soot formation over the heterogeneous surface growth mechanism in diffusion flames. Beji et al. [3] added a temperature power-law dependence to the soot formation rate formulation as the following:

$$\dot{\omega}'''_{s,f} = A\rho^2 Y_F T^{\lambda} \exp\left(\frac{T}{-T_a}\right) \qquad \text{where} \qquad Z_{s,ox} \leq Z < Z_{s,f} \tag{1}$$

where $A$ is the pre-exponential factor (calibrated numerically to be $4 \times 10^{-5}$ m$^3$/(kg.K$^{\lambda}$.s) for ethylene), $\dot{\omega}'''_{s,f}$ is the soot formation rate, $\lambda$ is the temperature exponent proposed to be 2.25. $T_a$ is the activation temperature assumed to be 2000 K. Beji et al. [3] introduced two critical mixture fractions that corresponded to soot formation ($Z_{s,f}$) and soot oxidation ($Z_{s,ox}$) processes. $Z_{s,ox}$ is reported in

[22] for fuels based on their C/O ratio and $Z_{s,f}$ is found by numerical calibration. A constant soot oxidation rate ($\dot{\omega}'''_{s,ox}$) is assumed in [3]:

$$\dot{\omega}'''_{s,ox} = -1 \quad \text{kg/m}^3\text{/s} \qquad \text{where} \qquad Z \le Z_{s,ox} \quad \text{and} \quad T \ge 1300\ K \tag{2}$$

The temperature constraint (i.e., T > 1300 K) accounts for "*freezing of soot burnout*" as soot oxidation stops at lower temperatures.

The soot mass fraction equation is introduced for CFD applications as:

$$\frac{\partial \rho Y_s}{\partial t} + \frac{\partial \rho u_j Y_s}{\partial x_j} = \frac{\partial}{\partial x_j}\left(0.556 Y_s \frac{\mu}{T}\frac{\partial T}{\partial x_j}\right) + \dot{\omega}'''_s \tag{3}$$

where $\rho$ refers to gas-phase density and $\mu$ is the molecular dynamic viscosity of the gas-phase. The first term on the right-hand side of Eq. (3) refers to the thermophoretic force caused by the temperature gradient. The source term of Eq. (3) is treated as the sum of the contributions of soot formation and soot oxidation processes.

$$\dot{\omega}'''_s = \dot{\omega}'''_{s,f} - \dot{\omega}'''_{s,ox} \tag{4}$$

Yao et al. [4] used a similar approach to Beji et al. [3] for soot formation rate and in terms of soot oxidation modeling, they applied the model initially proposed by Lee et al. [23] and modified by Leung et al. [17]. This model assumes that $O_2$ is the main and only oxidizing agent. The soot oxidation rate is estimated as:

$$\dot{\omega}''_{s,ox} = A_{ox}[O_2]T^{1/2}\exp\left(\frac{-E_{a,ox}}{RT}\right) \quad \text{kg/m}^2\text{s} \ \text{ where } T \ge 1300\ K \tag{5}$$

In Eq. (5), $A_{ox}$ is a pre-exponential factor taken as 120 kg.m/(mol.K$^{0.5}$.s), $[O_2]$ is the molar concentration of oxygen, and $E_{a,ox}$ is the activation energy taken as $163{,}540$ J/mol. The oxidization freezing temperature of 1300 K is also taken into account. The soot particulate surface area ($A_s$) is assumed constant, $A_s$ =160 m$^2$/g, after calibration for different fuels. Thus, the source term of Eq. (3) can be written as:

$$\dot{\omega}'''_s = \begin{cases} \dot{\omega}'''_{s,f} - \dot{\omega}''_{s,ox}\rho Y_s A_s & \text{for} \quad Z_{s,ox} \le Z < Z_{s,f} \\ -\dot{\omega}''_{s,ox}\rho Y_s A_s & \text{for} \quad Z \le Z_{s,ox} \end{cases} \tag{6}$$

The models proposed by Beji et al. [3] (Constant Soot Oxidation (CSO) model) and Yao et al. [4] (Oxygen Dependent Soot Oxidation (ODSO) model) are assessed in the current work. The soot modeling parameters associated with the LSP soot modeling concept are directly correlated with the level of dilution. The stoichiometric mixture fraction ($Z_{st}$) is determined by:

$$Z_{st} = \frac{Y_{o_2,0}}{sY_{F,0} + Y_{o_2,0}} \tag{7}$$

where $Y_{o_2,0}$ and $Y_{F,0}$ are the mass fraction of oxygen and fuel in the oxidizer and fuel streams, respectively and $s$ is the stoichiometric air-fuel ratio. With the increasing level of dilution, $Y_{F,0}$ decreases and $Z_{st}$ increases. LSP length of many fuels is available in the literature. Li and Sunderland [24] assumed that the LSP length of diluting agents is infinity and thus the LSP height of the diluted fuel is estimated as:

$$\text{LSP}_{l,f,d} = \frac{\text{LSP}_{l,f}}{Y_{F,0}} \tag{8}$$

where $\text{LSP}_{l,f}$ is the LSP height of the pure fuel and $\text{LSP}_{l,f,d}$ is the LSP height of the diluted fuel. The pre-exponential factor of soot formation equation for the diluted fuel, $A_{f,d}$, is determined as in [3]:

$$\frac{A_{f,d}}{A_f} = \frac{\mathrm{LSP}_{l,f}}{\mathrm{LSP}_{l,f,d}} \tag{9}$$

Critical mixture fractions for soot formation and oxidation are functions of the stoichiometric mixture fraction as in [3]:

$$Z_{s,f} = 2.5 Z_{st} \tag{10}$$

$$Z_{s,ox} = 1.25 Z_{st} \tag{11}$$

The fuel diluted levels and their corresponding LSP parameters are listed in Table 1.

**Table 1. LSP soot modeling-related parameters for different dilution levels.**

| Fuel volume fraction (%) | $Z_{st}$ | $\mathrm{LSP}_{l,d}$ (m) | $A_d$ ($m^3/(kg.s.K^{2.25})$) | $Z_{s,f}$ | $Z_{s,ox}$ |
|---|---|---|---|---|---|
| 32 | 0.17 | 0.33 | 1.28e-5 | 0.43 | 0.21 |
| 40 | 0.14 | 0.26 | 1.6e-5 | 0.36 | 0.18 |
| 60 | 0.10 | 0.17 | 2.4e-5 | 0.25 | 0.12 |
| 80 | 0.07 | 0.13 | 3.2e-5 | 0.19 | 0.09 |

The other models used in the simulations are the two-equation models proposed by Leung and Linstedt [17] (Linstedt model) and Brooks and Moss [18] (Moss-Brooks model). The mathematical description of Linstedt and Moss-Brooks and models constants for ethylene can be found in [17,25] and [26], respectively. The main differences between two-equation models and the LSP-based soot models are (a) they have expressions for soot surface growth and coagulation mechanisms and (b) complex kinetic mechanisms are required to be applied to predict the concentration of important species involved in soot evolution mechanisms (e.g. acetylene, OH, and O). The computational cost of these models is much higher than the LSP model, mainly because of using much larger kinetic mechanisms for combustion and soot chemistries and solving for another transport equation (the soot number density or the soot nuclei concentration). It is worth mentioning that it is possible to develop correlations between the fuel concentration (or mixture fraction) and involved species concentrations using complex mechanisms. This approach helps to avoid solving directly for the species mass fractions directly during simulation, which requires complex kinetic mechanisms. Mentioned correlations should be developed for different fuels separately via calibration [27].

The framework of the two-equation soot models applied in the current study is quite similar. Besides the two transfer equations being solved, the Linstedt and Moss-Brooks models use Arrhenius type expressions for soot inception and surface growth mechanisms considering acetylene as the most important intermittent species. Linstedt model solves the soot particles number density equation and in Moss-Brooks model, the transport equation of the soot nuclei concentration (which is a function of soot particles number density) is solved. Similar to LSP, Lindstedt and Moss-Brooks also solve for the soot mass fraction. Lindstedt model assumes the smallest soot particles have the mass of 700 carbon atoms and in Moss-Brooks model the mass of the incipient soot particles is set to 12 carbon atoms. Lindstedt model takes $O_2$, OH, and O species as the soot oxidizing agents, and $O_2$ and OH are the species involved in the soot oxidation mechanism in Moss-Brooks model. It is worth mentioning that these models recommend different model constants for the closure of their respective soot sub-models.

**Radiation modeling**

Radiation heat transfer is modeled in the current study by using the P1 method to solve for Radiative Transfer Equation (RTE). While most studies have used Discrete Ordinate Method (DOM), P1 could give results completely identical to the results of DOM in axisymmetric domains with a lower computational cost. The radiative properties of species are calculated by RADCAL coefficients. The radiative contribution of soot particles are accounted for by adding the soot absorption coefficient to that of the gas phase:

$$\kappa_{tot} = \kappa_g + \kappa_s \tag{12}$$

and the soot absorption coefficient is treated as:

$$\kappa_s = C_{\kappa,s} f_v T \tag{13}$$

where $C_{\kappa,s}$ is a constant with a value of 1226 $(mK)^{-1}$.

## RESULTS AND DISCUSSION

### The effect of soot oxidation treatment

The distributions of soot volume fraction captured by CSO and ODSO models in the LSP approach are compared in Fig. 2 while similar soot formation model presented by Eq. (1) is applied with both soot oxidation models. Both models find the maximum soot volume fraction in the regions near the wings for all cases. For all dilution levels, soot is oxidized sooner using CSO and thus, lower soot concentrations are predicted higher in the flame. At low dilution levels (60% and 80% fuel mass fraction), the soot volume fraction distribution predicted by ODSO model is qualitatively more consistent with the experimentally obtained distribution (see [9]) in the regions near the flame's tip (marked in Fig. 2 for lightly diluted flames). Furthermore, Smooke et al. [9] found out that the soot particles move downstream on streamlines near the centerline in a similar way to the numerical results of ODSO model.

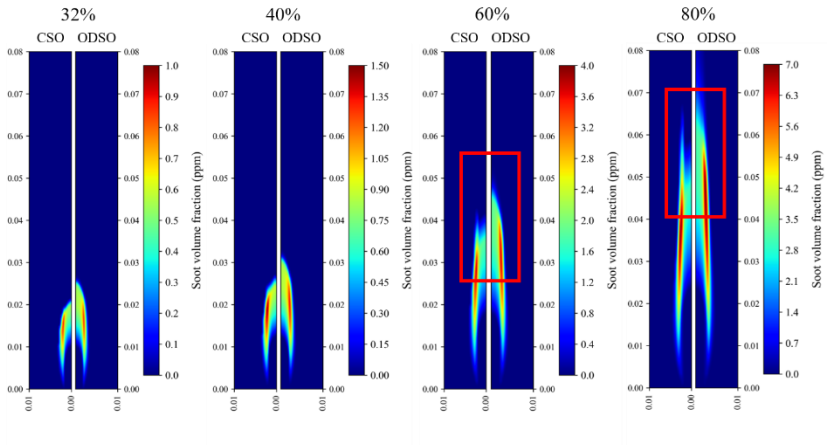


**Fig. 2**. Soot volume fraction distribution obtained by CSO and ODSO models for different fuel volume fractions

Fig. 3 shows the difference between the two models applied in the current study in terms of their soot oxidation treatment. CSO model starts oxidizing soot in lower levels for all fuel volume fractions. Oxygen cannot penetrate the flame sheet (due to the infinitely fast chemistry assumption) thus, ODSO model gives the soot particles more time to travel. It is also observable that the soot oxidation approaches used in CSO and ODSO models have not affected the soot distributions obtained in the region covering from the burner to the middle of the flame. The main reason is that in LSP-based models developed to this date, the formation and oxidation regions are completely decoupled as the soot formation occurs in the rich part of the flame. CSO model explicitly separates formation and oxidation regions by defining mixture fraction ranges for both processes and there is no oxygen in the formation regions for ODSO model to oxidize the soot particles. The soot oxidization rate distribution obtained by ODSO model is more consistent with the numerical results of Smooke et al.[9] since it

finds the maximum soot oxidation rate on the centerline for the heavily diluted cases and in the wings as the fuel volume fraction increases.

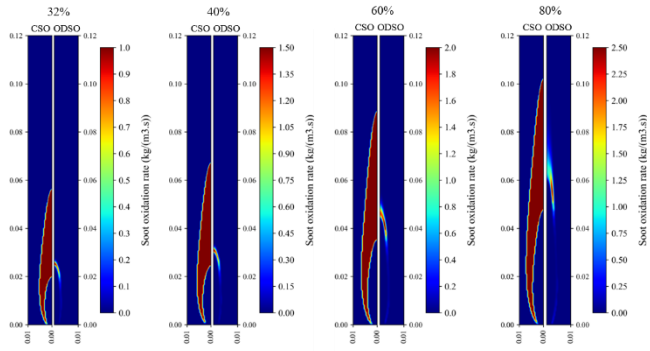


**Fig. 3**. Soot oxidation rate distribution obtained by CSO and ODSO models for different fuel volume fraction

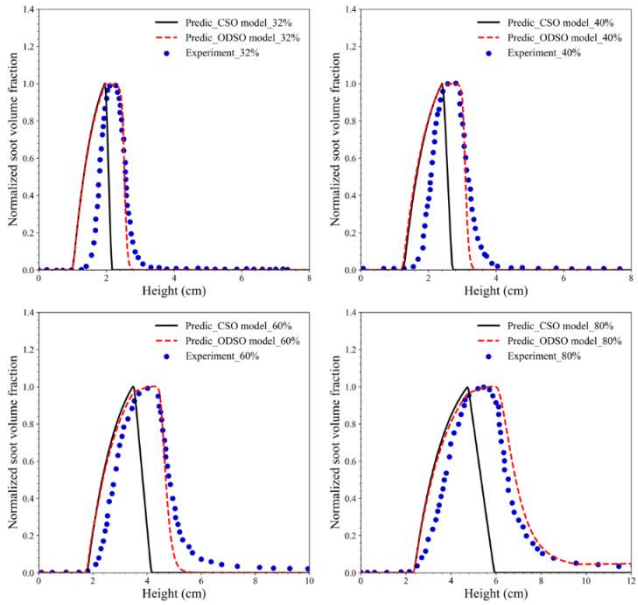


**Fig. 4**. Normalized soot volume fraction profile against height on the centerline obtained by CSO and ODSO models compared with experimental measurements.

The effect of soot oxidation treatment on the axial soot volume fraction distribution is also observable in Fig. 4. The ODSO model has produced more consistent results with the experimental data in terms of height at which the soot volume fraction starts to decay (under the effect of oxidation).

**The effect of dilution**

The results obtained on the peak soot volume fraction are presented and discussed in this section. To properly interpret the numerical results obtained by CSO and ODSO models, two indexes are defined; the first index presents the relative difference between predicted and measured values of maximum volume soot fraction in the domain and on the centerline:

$$E_{f_{v,max}} = \frac{(f_{v,max})_{Pred} - (f_{v,max})_{Exp}}{(f_{v,max})_{Exp}} \tag{14}$$

The second index evaluates the accuracy of the simulations in predicting the migration of soot from the tip of the flame to the wings as the fuel volume fraction increases.

$$P_{f_v} = \frac{(f_{v,max})_{Centerline}}{(f_{v,max})_{Domain}} \tag{15}$$

Fig. 5 displays the accuracy of numerical results based on the indexes defined above. Both models have significantly overestimated maximum soot volume fraction in the whole domain and on the burner's axis. The simulations are considerably more accurate at predicting the peak soot volume fraction on the centerline. The accuracy of both models significantly improves where the fuel volume fraction increases. Furthermore, both models (CSO and ODSO) have not been able to capture the migration of maximum soot volume fraction from the tip of the flame to the wings as the fuel volume fraction increases although, they correctly estimated the decrease of $P_{f_v}$. The effect of using higher values for $A_s$ (up to 270 m$^2$/g) is found to be negligble, which is consistent with the results of Yao et al.[4] for $A_s > 160$ m$^2$/g.

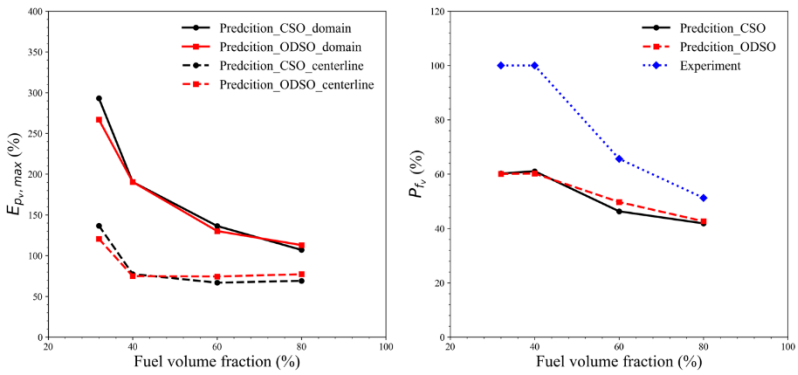


**Fig. 5**. Evaluation of predicted maximum soot volume fraction by CSO and ODSO models based on $E_{f_{v,max}}$ and $P_{f_v}$ indexes

Fig. 6 shows that the centreline temperature predictions using the ODSO model agree well with the experimental data for fuel volume fractions of 32% and 40% [10]. However, at lower dilution levels, the flame height is under-predicted, yielding underestimated temperatures at high elevations above the burner. This is due to the overestimated soot concentrations (see Fig. 5) and the subsequent thermal radiation. For high dilution levels this effect is less pronounced because of the significantly lower soot concentrations and the reduced impact on temperature prediction. The high temperatures recorded in the experiments near the burner (heights < 1cm) are reported to be due to limitations associated with thermocouple measurements and large temperature gradients [10]. The results also show the decrease in soot radiative contribution from 44% for the least diluted flame to 15% in the most diluted flame as the flame becomes less sooty with the increase of dilution level.

The significant overestimations displayed in Fig. 5 (right) are assumed to stem from a limitation of Eq. (9) to address the dilution effect. Here, it is assumed that the pre-exponential factor is also a function of the level of dilution:

$$\frac{A_{f,d}}{A_f} = g(Y_{F,0}) \frac{\mathrm{LSP}_{l,f}}{\mathrm{LSP}_{l,f,d}} \tag{16}$$

A simple function $g(Y_{F,0}) = Y_F$ is assumed to incorporate the effects of dilution. The results of simulations using the functions of Eq. (16) **Error! Reference source not found.** and Eq. (9) ($g(Y_{F,0}) = 1.0$) are presented and compared in Fig. 7. The accuracy of results is significantly improved for all fuel volume fractions especially for 32%, 40%, and 60%. However, modifying Eq. (9) did not lead to capturing the shift of soot concentration peak from the axis of the flame to the wings as the dilution level decreases. Further studies on diluted flames with different fuels are essential to evaluate the generality of Eq. (16).

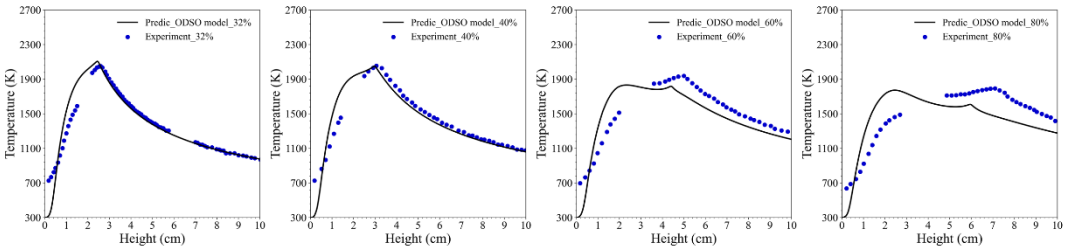


**Fig. 6**. Temperature profile on the centerline obtained ODSO model compared with experimental measurements for different levels of dilution. [10].

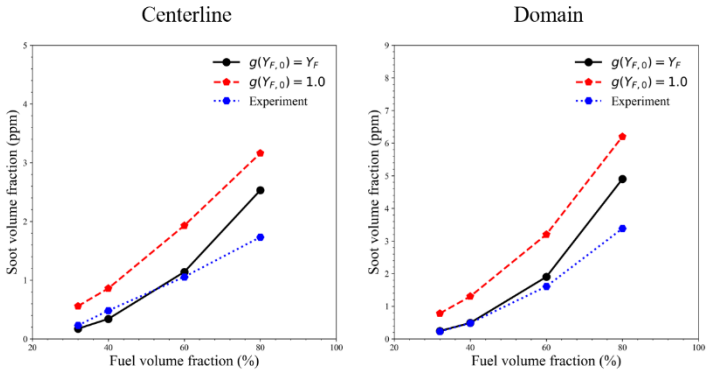


**Fig. 7**. Peak soot volume fraction obtained by numerical simulations using $g(Y_{F,0}) = Y_F$ and $g(Y_{F,0}) = 1.0$ compared with experimental measurements [9]

## Effect of the soot modeling strategy

In this section, the maximum soot volume fraction in the domain and on the centerline is estimated using Lindstedt and Moss-Brooks two-equation models. The predictions mentioned models are compared with the ones from LSP (ODSO) model in Fig. 8. The results of Eq. (9) are used in the discussions here. The Lindstedt model predicts the peak soot volume fraction significantly more accurately for all fuel volume fractions, in particular for highly diluted flames and on the centreline. However, it is not able to capture the shift of maximum soot concentration from the flame's tip to the wings when the level of dilution decreases (Fig. 9). On the other hand, Moss-Brooks models predictions are shown to be inaccurate since most of the soot particles are accumulated in the flame's wings in all dilution levels. The difference between the two models stems from their respective predictions of soot nucleation and surface growth, using different model constants for ethylene yielding different soot formation distributions as illustrated in Fig. 10.

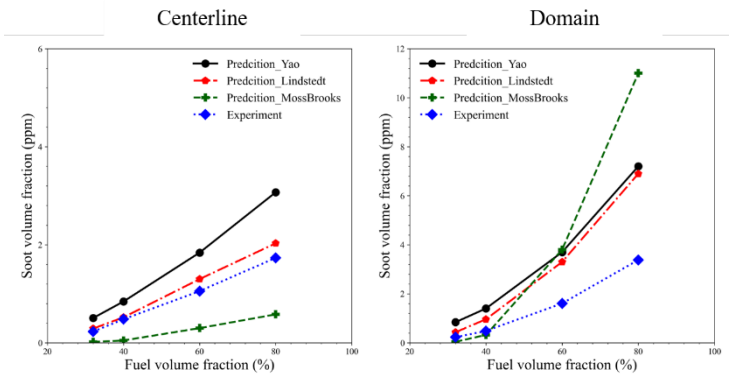


**Fig. 8**. Peak soot volume fraction obtained by ODSO, Lindstedt, and Moss-Brooks models compared with experimental measurements [9]

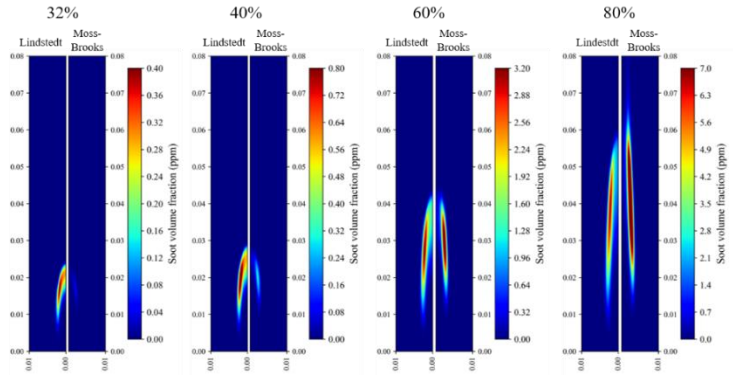


**Fig. 9**. Soot volume fraction distribution obtained by Lindstedt, and Moss-Brooks models for different fuel volume fractions

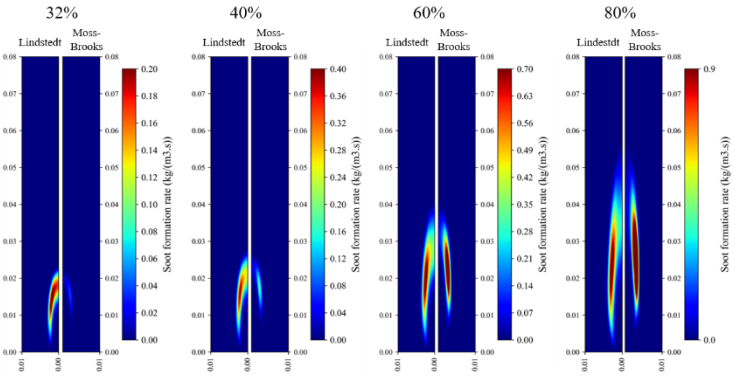


**Fig. 10**. Soot formation rate distribution obtained by Lindstedt and Moss-Brooks models for different fuel volume fractions

The LSP (ODSO) gives a lower level of agreement in comparison to the Lindstedt model but appears to perform better than the Moss-Brooks model for the simulation of the flames investigated here. Therefore, it has been shown that applying soot models in which a more comprehensive chemistry modeling is done via using detailed kinetic mechanisms doesn't necessarily result in more accurate predictions. Based on the results shown here, the ODSO model offers a good balance between computational efficiency and accuracy.

## CONCLUSION

In this paper, the accuracy of two LSP-based soot models for diluted combustion is evaluated by simulating the flames investigated by Smooke et al. [9–11]. Both models treat soot formation similarly and one of them uses a constant soot oxidation rate (Constant Soot Oxidation (CSO) model proposed by Beji et al. [3]) and the other model uses an oxygen concentration-dependent expression (Oxygen Dependent Soot Oxidation (ODSO) model studied by [4]) for soot oxidation modeling. Moreover, two other semi-empirical models proposed by Leung et al. [17] (Lindestedt model) and Brooks and Moss [18] (Moss-Brooks) are used in the simulations of the diluted flames using GRI-III mechanism to see the effect of accounting for more details of soot evolution on the accuracy of results. These models are implemented in FireFOAM.

ODSO and CSO models have presented quite similar predictions in terms of peak soot found in the domain and on the centerline. However, it has been shown that using the ODSO model results in more qualitatively consistent predictions with experimental measurements. Furthermore, an improvement in the results has been obtained by considering the dependence of the pre-exponential factor in the soot formation rate on the fuel volume fraction at the inlet. Comparing the results of ODSO model with the prediction of Lindestedt and Moss-Brooks models has shown that Lindestedt model's results are more agreeing with experimental reports between all models and Moss-Brooks model's have been the least accurate one. Thus, using more detailed soot models does not necessarily lead to more accurate results. None of the models evaluated in the current study could reproduce the shift in location of the peak soot concentration from the flame's tip to its wings when the level dilution increases.

## REFERENCES

[1] M.A. Delichatsios, A Phenomenological Model for Smoke-Point and Soot Formation in Laminar Flames, Combust. Sci. Technol. 100 (1994) 283–298.

[2] T. Beji, J.P. Zhang, M. Delichatsios, Determination of soot formation rate from Laminar smoke point measurements, Combust. Sci. Technol. 180 (2008) 927–940.

[3] T. Beji, J.P. Zhang, W. Yao, M. Delichatsios, A novel soot model for fires: Validation in a laminar non-premixed flame, Combust. Flame. 158 (2011) 281–290. http://dx.doi.org/10.1016/j.combustflame.2010.08.017.

[4] W. Yao, J. Zhang, A. Nadjai, T. Beji, M.A. Delichatsios, A global soot model developed for fires: Validation in laminar flames and application in turbulent pool fires, Fire Saf. J. 46 (2011) 371–387. http://dx.doi.org/10.1016/j.firesaf.2011.06.004.

[5] C.W. Lautenberger, J.L. De Ris, N.A. Dembsey, J.R. Barnett, H.R. Baum, A simplified model for soot formation and oxidation in CFD simulation of non-premixed hydrocarbon flames, Fire Saf. J. 40 (2005) 141–176.

[6] H. Guo, F. Liu, G.J. Smallwood, Soot and NO formation in counterflow ethylene/oxygen/nitrogen diffusion flames, Combust. Theory Model. 8 (2004) 475–489.

[7] H. Guo, F. Liu, G.J. Smallwood, Ö.L. Gülder, A numerical study of the influence of transport properties of inert diluents on soot formation in a coflow laminar ethylene/air diffusion flame, Proc. Combust. Inst. 29 (2002) 2359–2365.

[8] F. Liu, H. Guo, G.J. Smallwood, Ö.L. Gülder, The chemical effects of carbon dioxide as an additive in an ethylene diffusion flame: Implications for soot and NOx formation, Combust. Flame. 125 (2001) 778–787.

[9] M.D. Smooke, M.B. Long, B.C. Connelly, M.B. Colket, R.J. Hall, Soot formation in laminar diffusion flames, Combust. Flame. 143 (2005) 613–628.

[10] M.D. Smooke, R.J. Hall, M.B. Colket, J. Fielding, M.B. Long, C.S. McEnally, L.D. Pfefferle, Investigation of the transition from lightly sooting towards heavily sooting co-flow ethylene diffusion flames, Combust. Theory Model. 8 (2004) 593–606.

[11] M.D. Smooke, C.S. McEnally, L.D. Pfefferle, R.J. Hall, M.B. Colket, Computational and experimental study of soot formation in a coflow, laminar diffusion flame, Combust. Flame. 117 (1999) 117–139.

[12] S.H. Park, S.N. Rogak, W.K. Bushe, J.Z. Wen, M.J. Thomson, An aerosol model to predict size and structure of soot particles, Combust. Theory Model. 9 (2005) 499–513.

[13] S.H. Park, S.N. Rogak, A novel fixed-sectional model for the formation and growth of aerosol agglomerates, J. Aerosol Sci. 35 (2004) 1385–1404.

[14] C.J. Sun, C.J. Sung, H. Wang, C.K. Law, On the structure of nonsooting counterflow ethylene and acetylene diffusion flames, Combust. Flame. 107 (1996) 321–335.

[15] F. Nmira, J.L. Consalvi, R. Demarco, L. Gay, Assessment of semi-empirical soot production models in C1-C3 axisymmetric laminar diffusion flames, Fire Saf. J. 73 (2015) 76–90.

[16] B. Konsur, C.M. Megaridis, D.W. Griffin, Fuel preheat effects on soot-field structure in laminar gas jet diffusion flames burning in 0-g and 1-g, Combust. Flame. 116 (1999) 334–347.

[17] K.M. Leung, R.P. Lindstedt, W.P. Jones, A simplified reaction mechanism for soot formation in nonpremixed flames, Combust. Flame. 87 (1991) 289–305.

[18] S.J. Brookes, J.B. Moss, Predictions of soot and thermal radiation properties in confined turbulent jet diffusion flames, Combust. Flame. 116 (1999) 486–503.

[19] OpenFOAM, (2021). https://www.openfoam.com/ (accessed September 14, 2021).

[20] Fire Modeling, Simulation and Research – FM Global, (2021). https://www.fmglobal.com/research-and-resources/research-and-testing/theoretical-computational-and-experimental-research/open-source-fire-modeling (accessed September 14, 2021).

[21] GRI-Mech 3.0, (2021). http://combustion.berkeley.edu/gri-mech/version30/text30.html (accessed October 8, 2021).

[22] B.M. Kumfer, S.A. Skeen, R. Chen, R.L. Axelbaum, Measurement and analysis of soot inception limits of oxygen-enriched coflow flames, Combust. Flame. 147 (2006) 233–242.

[23] K.B. Lee, M.W. Thring, J.M. Beér, On the rate of combustion of soot in a laminar soot flame, Combust. Flame. 6 (1962) 137–145.

[24] L. Li, P.B. Sunderland, An improved method of smoke point normalization, Combust. Sci. Technol. 184 (2012) 829–841.

[25] M.R.J. Charest, C.P.T. Groth, Ö.L. Gülder, A computational framework for predicting laminar reactive flows with soot formation, Combust. Theory Model. 14 (2010) 793–825.

[26] S. V. Cowart, G. Krishnamoorthy, On the relative contributions of soot to radiative heat transfer at different oxygen indices in ethylene – O2/CO2 laminar diffusion flames, Fuel. 285 (2021) 119269. https://doi.org/10.1016/j.fuel.2020.119269.

[27] A. Snegirev, E. Markus, E. Kuznetsov, J. Harris, T. Wu, On soot and radiation modeling in buoyant turbulent diffusion flames, Heat Mass Transf. Und Stoffuebertragung. 54 (2018) 2275–2293.

# A Two-Step Combustion Scheme for Predicting CO in Under-Ventilated Compartment Fires

**Kevin McGrattan[1,*], Randall McDermott[1], and Jason Floyd[2]**

[1]National Institute of Standards and Technology, Gaithersburg, Maryland, USA
[2]UL Fire Safety Research Institute, Columbia, Maryland, USA
[*]Corresponding author's email: kevin.mcgrattan@nist.gov

## ABSTRACT

A two-step combustion model is proposed for predicting carbon monoxide in under-ventilated compartment fire simulations. The scheme consists of a relatively fast first step that converts most of the carbon in the fuel molecule to CO with the remainder going to soot precursors, and a relatively slow second step in which the CO and soot are oxidized to form $CO_2$. Both steps are mixing-controlled and performed serially rather than in parallel to account for the difference in reaction rate. Validation calculations are described, ranging from a laminar diffusion flame to full-scale under-ventilated compartment fires.

**KEYWORDS:** Fire chemistry, modeling, compartment fires, computational fluid dynamics

## MODEL DESCRIPTION

There are several challenges in computational fluid dynamics (CFD) modeling of under-ventilated fires. First, there is the issue of grid resolution. A typical large-scale fire simulation is performed on a numerical grid with cells on the order of 10 cm or greater, and the resolved temperature field is too coarse to allow detailed kinetic modeling of products of incomplete combustion. Second, in a real fire event the fuel gas is a complex mixture of many different species for which little information is available as input to a fire model.

A partial solution to these problems is to exploit empirical sub-models that are relatively insensitive to temperature and fuel type. Such is the case for a single-step, mixing controlled combustion model, where the user specifies post-flame yields of CO and soot in lieu of predicting their creation and oxidation within the flame envelop. In the Fire Dynamics Simulator (FDS), the consumption rate of fuel gas, $\dot{m}'''_F$, is modeled using the Eddy Dissipation Concept (EDC) of Magnussen and Hjertager [1, 2]:

$$\dot{m}'''_F = -\rho \frac{\min(Y_F, Y_A/s)}{\tau_{mix}} \tag{1}$$

where $\rho$ is the gas density, $Y_F$ and $Y_A$ are the cell mean mass fractions of fuel and air, respectively, and $s$ is the mass stoichiometric coefficient for air. The mixing time, $\tau_{mix}$, is taken as the fastest of the three physical processes of diffusion, $\tau_d$, subgrid-scale advection, $\tau_u$, and buoyant acceleration, $\tau_g$, which scale differently with the filter width, $\Delta$, as shown in Fig. 1 [3]. The upper bound of the mixing time, $\tau_{flame}$, is the inverse of the fundamental or "puffing" frequency of the fire. The lower bound, $\tau_{chem}$, is the actual chemical reaction time.

The default mixing-controlled, single-step combustion model in FDS works well for well-ventilated fires where the objective is to predict the transport of smoke and hot gases, but it is not appropriate for under-ventilated compartment fires or near-field radiation emission, extinction, and other detailed fire phenomena. The most logical extension of the single-step model is a two-step model suggested by Westbrook and Dryer [4] in which CO is produced in a relatively fast first step, and then oxidized to

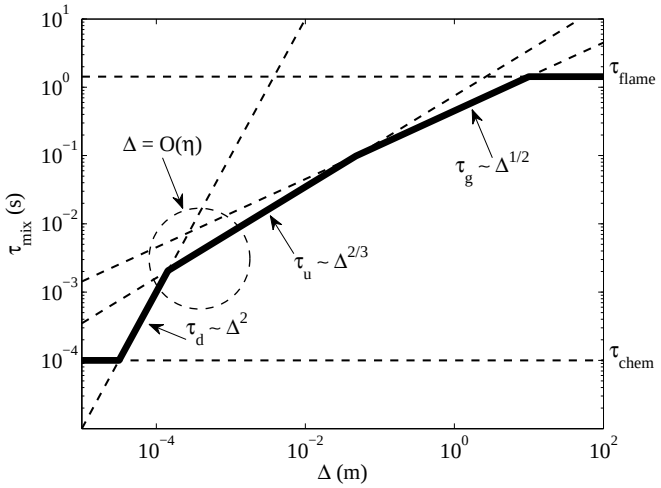


Fig. 1. Reaction time scale model. The symbols $\tau_d$, $\tau_u$, and $\tau_g$ are the mixing time scales associated with diffusion, advection, and buoyancy, respectively. The filter width is denoted by $\Delta$. The Kolmogorov scale, $\eta$, denotes the length scale of the smallest turbulent eddies [3].

$CO_2$ in a slower second step. Using simple stoichiometry to illustrate the idea, propane could undergo the following two-step reaction:

$$C_3H_8 + 2\,O_2 \longrightarrow 2\,CO + C + 2\,H_2 + 2\,H_2O \tag{2}$$

$$2\,CO + C + 2\,H_2 + 3\,O_2 \longrightarrow 3\,CO_2 + 2\,H_2O \tag{3}$$

The stoichiometric coefficients 2 for CO and 1 for C in the first step are chosen simply to demonstrate the basic idea; they do depend on the fuel type. A discussion of this dependency is at the end of this section. The carbon, C, and hydrogen $H_2$ included in the first step represent all the intermediate species other than CO and water vapor that are formed early in the process. In a typical fire simulation the exact stoichiometry of the fuel molecule is unknown and taken as an effective mixture of the principal combustibles. The two reactions are assumed to be mixing-controlled and temperature-independent. To account for the fact that the first reaction is relatively fast compared to the second, the reactions occur serially. That is, in a given discrete time step, the available oxygen first reacts with any fuel present, forming soot precursors, CO, and water vapor. If any oxygen remains, it is free to oxidize the soot, CO, and $H_2$. It is the availability of oxygen and rate of mixing that determine the progression of the reaction, not temperature. Under well-ventilated conditions, these multiple reactions typically occur within a single time step, which is essentially the one-step, mixing-controlled model. However, in under-ventilated conditions, some soot, CO, and $H_2$ remain when there is not enough oxygen present.

There are two obvious questions. First, how are the fuel's carbon and hydrogen atoms distributed in the first step, and second, are soot, CO, and $H_2$ created and oxidized at the same rate, as the simple scheme suggests? Measurements made by Falkenstein et al. [5], discussed below, indicate that near the base of lightly sooting pool fires of acetone, ethanol, and propane, the mass ratio of CO to soot ranges from about 50 to 100, while measurements by Köylü and Faeth [6] indicate that this ratio drops to approximately 0.4 beyond the flame envelop. Neither of these measurements can be predicted using this simple two-step scheme. Instead, the ratio of CO to soot must be specified at the start and end of

the combustion cycle. In practice, this leads to the generalized scheme:

$$\mathrm{C_xH_yO_zN_v} + \nu_{\mathrm{O_2},1}\,\mathrm{O_2} \longrightarrow \underbrace{\nu_{\mathrm{H_2},1}\,\mathrm{H_2} + \nu_{\mathrm{H_2O},1}\,\mathrm{H_2O} + \nu_{\mathrm{CO},1}\,\mathrm{CO} + \nu_{\mathrm{S},1}\,\mathrm{Soot} + \nu_{\mathrm{N_2},1}\,\mathrm{N_2}}_{\text{Int. Prod.}} \tag{4}$$

$$\text{Int. Prod.} + \nu_{\mathrm{O_2},2}\,\mathrm{O_2} \longrightarrow \nu_{\mathrm{CO_2}}\,\mathrm{CO_2} + \nu_{\mathrm{H_2O},2}\,\mathrm{H_2O} + \nu_{\mathrm{CO},2}\,\mathrm{CO} + \nu_{\mathrm{S},2}\,\mathrm{Soot} + \nu_{\mathrm{N_2},2}\,\mathrm{N_2} \tag{5}$$

It is assumed in the model that most of the fuel's carbon atoms are converted to CO in the first step, depending on the fuel's propensity to soot, as indicated by its smoke point, soot yield, or radiative fraction, all of which are correlated [7]. Based on the limited experimental measurements discussed below, the fraction of carbon atoms in the fuel molecule that form CO in the first step is assumed to be in the range of 0.9 to 1.0 for "clean" fuels like methane, methanol, and ethanol; 0.8 to 0.9 for lightly sooting fuels like acetone, 0.7 to 0.8 for moderately sooting fuels like propane, and 0.6 to 0.7 for "dirty" fuels like toluene and heavy hydrocarbons. As will be seen from the validation studies below, the predictions are far from perfect, but at least they hold the promise of providing some way to model CO in under-ventilated fire scenarios where the precise fuel stoichiometry is not known, but there is some information about the smoke production rate, which is usually high in a real fire burning modern synthetic furnishings.

Because this scheme is limited to two steps to reduce computing time, the handling of soot is very crude. Soot and CO are not generated, transported, and oxidized together as suggested by Eq. (3). Rather, soot precursors are formed relatively early and undergo a far more complex process to form solid particulate. Nevertheless, soot is crudely represented as the carbon, C, that eventually forms soot and does not participate in forming CO. As will be shown in the examples below, the concentration of CO in an under-ventilated compartment fire is limited by the supply of oxygen, not carbon; thus, the exact distribution of the carbon atoms in the fuel is not a critical input parameter for compartment fire simulations.

## VALIDATION CASES

Even though the objective of this simple two-step combustion model is to predict the CO concentration in large-scale, under-ventilated compartment fires, it is still worthwhile to compare model predictions against measurements made in simple laboratory burner experiments. In the FDS Validation Guide [8], there are a variety of case studies that employ the two-step model, ranging from a laminar diffusion flame simulation performed as a direct numerical simulation (DNS) (resolution on the order of 1 mm) to full-scale simulations of flashed-over compartments (10 cm resolution). The over-ventilated cases are important for two reasons. First, real fires are well-ventilated at the start, and it is important to demonstrate that the two-step reaction scheme essentially acts like the single-step scheme when adequate oxygen is present. Second, one can consider the region within the flame envelop to be an oxygen-limited environment where one can readily observe the creation and oxidation of CO and soot.

Note that in the figures below, the character string above the plot identifies the version of the FDS source code.

### Smyth Slot Burner Experiments

Smyth et al. [9, 10] conducted diffusion flame experiments at NIST using a methane/air Wolfhard-Parker slot burner, which consists of an 8 mm wide central slot flowing fuel surrounded by two 16 mm wide slots flowing dry air with 1 mm separations between the slots. The slots are 41 mm in length. Measurements were made of all major species and a number of minor species along with temperature and velocity.

Two-dimensional simulations of this experiment are performed using two different combustion models at two different grid resolutions, 0.250 mm and 0.125 mm. The first model is a modified version of the two-step mechanism by Andersen et al. [11] where the first reaction is assumed to be infinitely fast followed by a reversible CO to $CO_2$ reaction modeled with Arrhenius kinetics. As discussed by Westbrook and Dryer [4], the kinetic constants for the reduced CO mechanism may be model dependent. Here, the Arrhenius constant for the forward CO to $CO_2$ reaction is tuned to match the Smyth experimental data.

A second set of simulations is run at the same two spatial resolutions, using the two-step reaction scheme described above, where only CO and no soot is generated in the first reaction step. Of interest here is that the time step size for the finer grid simulation is comparable to the chemical time scale which is on the order of $\delta/s_L$, the flame thickness divided by the laminar flame speed. This means that the use of "fast chemistry" at these time and length scales becomes questionable. Nevertheless, the results of the simple two-step scheme are encouraging, as shown in Fig 2. The fact that the CO concentration is predicted reasonably well by both the finite rate and infinite rate reaction schemes means that there is promise that the two-step fast chemistry model can work over a wide range of length scales.

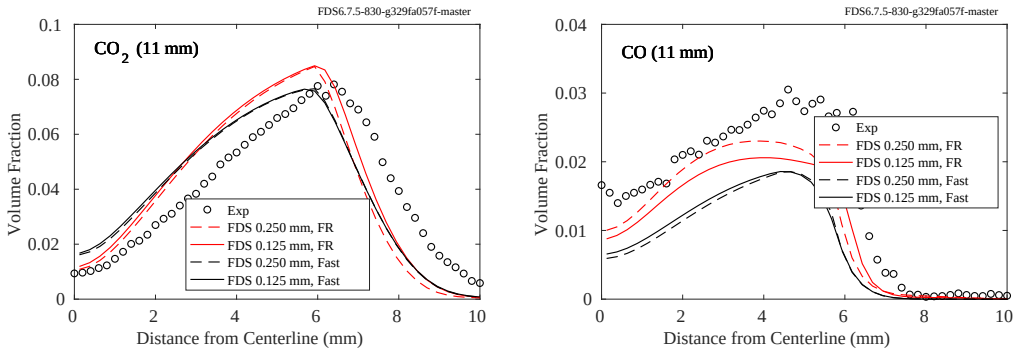


Fig. 2. Predicted and measured $CO_2$ and CO 11 mm above a Wolfhard-Parker methane-air slot burner. Predictions are shown for two different grid resolutions (0.25 mm and 0.125 mm) and two different reaction schemes (Finite Rate [11] and Fast chemistry) .

### NIST Pool Fire Species Measurements

Falkenstein-Smith et al. [5] measured the time-averaged centerline species concentrations within the flaming region of 30 cm pool fires of acetone, ethanol, methane and propane. The measurements were made using a gas chromatograph/mass spectrometer system (GC/MSD). The volume fraction of each species was calculated via the number of moles identified by the GC/MSD at each centerline point. Soot mass fractions were measured during the gas sampling process.

The numerical simulations are conducted at three different grid resolutions—2 cm, 1 cm, and 0.5 cm. For all cases, it is assumed, without any theoretical justification, that 50 % of the hydrogen atoms in the fuel are converted to $H_2$ in the first step, and the remainder form $H_2O$. It is also assumed that 95 % of the carbon atoms in the methane fuel molecule form CO in the first reaction step, 95 % for ethanol, 75 % for propane, and 80 % for acetone. Figure 3 displays comparisons of mean centerline profiles of CO and soot for the four fuels.

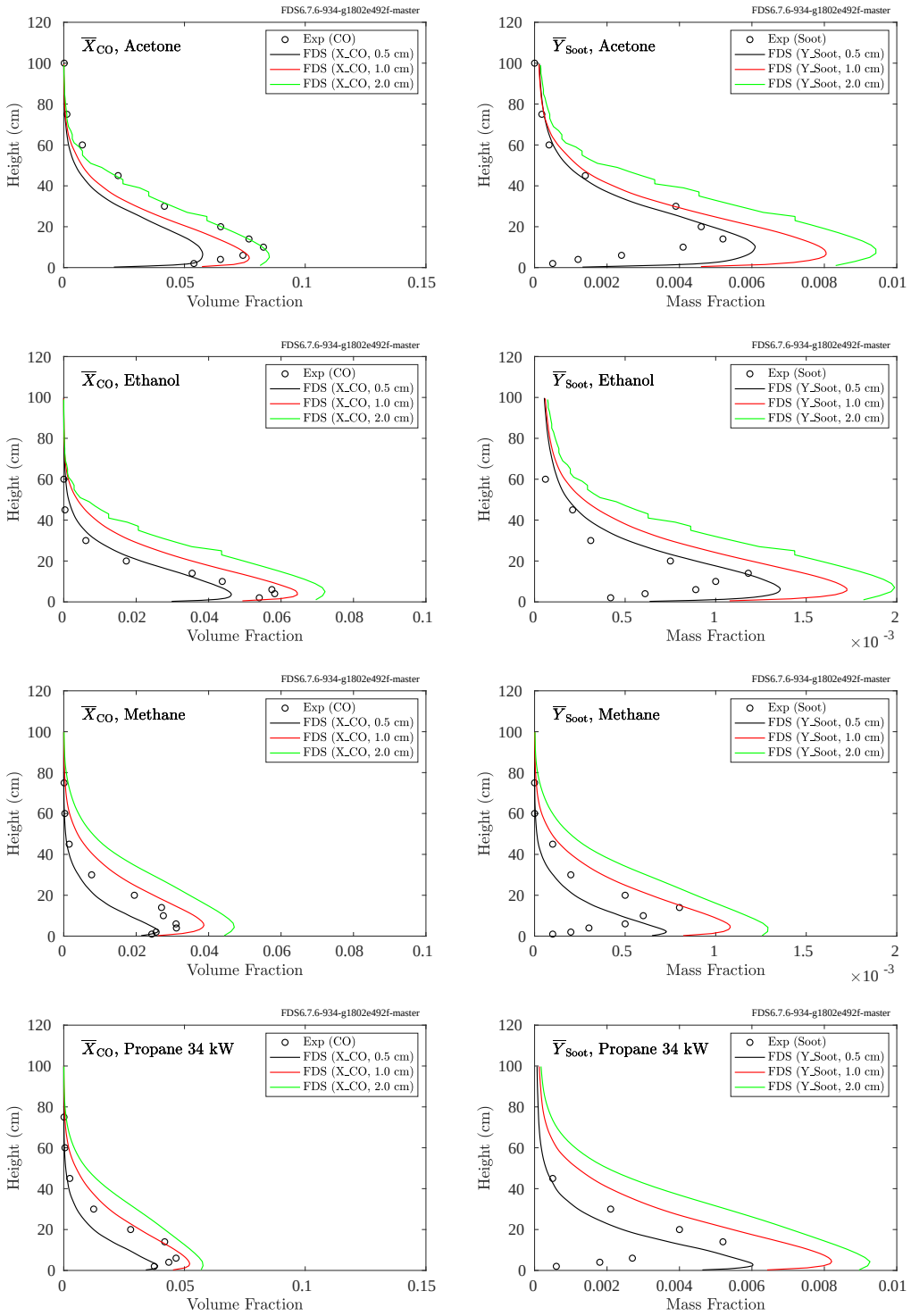


Fig. 3. Centerline CO and soot profiles for acetone, ethanol, methane and propane for three grid resolutions, 0.5 cm, 1 cm, and 2 cm.

### University of Maryland Line Burner Experiments

Experiments have been performed at the University of Maryland (UMD) by White et al. [12] using a burner consisting of a 50 cm by 5 cm fuel slot surrounded by a co-flowing air stream. Controlled suppression of the flame is achieved via the gradual introduction of nitrogen into the co-flowing air stream.

Simulations of the experiments are performed at three grid resolutions: 12.5 mm, 6.25 mm, and 3.125 mm, using 24, 164, and 204 meshes respectively. A snapshot of the fine resolution simulation is shown in Fig. 4. For both the methane and propane fires, it is assumed that 2 moles of CO are produced for every mole of C (soot). The choice does have an affect on the predicted radiative fraction of the fire and the heat flux to the radiometer because the more soot generated in the first step, the greater the radiative fraction.

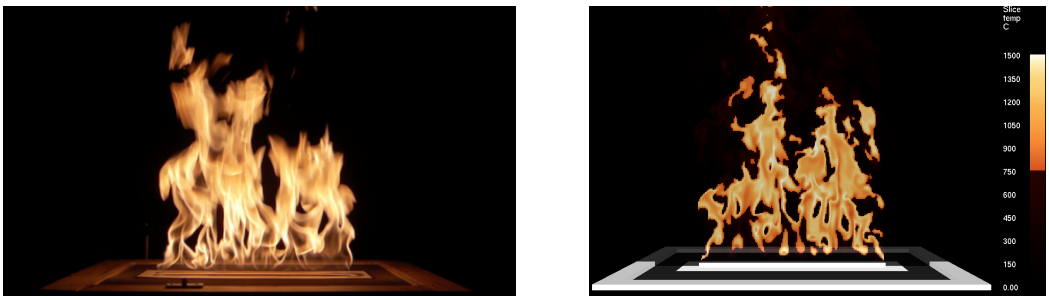


Fig. 4. Photograph of the University of Maryland Line Burner Experiment [12] (left) and the corresponding FDS simulation (right).

Extinction of the fire is achieved using the *critical flame temperature* concept, which is the default extinction model in FDS. The CFT is 1507 °C for methane and 1447 °C for propane [13]. In addition, combustion is suppressed below the auto-ignition temperatures of 540 °C and 450 °C for methane and propane, respectively, except in a small volume just above the burner where the fuel is allowed to burn on contact with oxygen. This is a simple way to simulate the effect of a spark igniter. A plot of combustion efficiency versus oxygen concentration in the oxidizer stream is shown in Fig. 5.

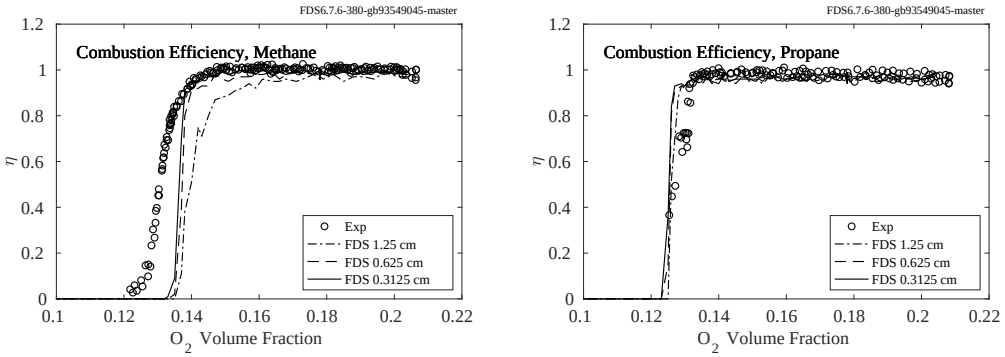


Fig. 5. UMD Line Burner combustion efficiency, $\eta$, as a function of oxygen concentration in the oxidizer stream. The simulations were performed at three grid resolutions, 1.25 cm, 0.625 cm, and 0.3125 cm.

In the experiments discussed here, soot and CO were not measured. However, the heat flux to a distant radiometer was used to estimate the radiative fraction. In the FDS simulations, the radiative fraction is not specified but rather predicted based on the computed flame temperature and gray gas radiation model, RadCal. As seen in Fig. 6, the radiative fraction decreases with decreasing oxygen concentration in the oxidizer stream. This is a remarkable result because the simple two-step reaction scheme is able to predict the decrease of soot and CO within the flame envelop as the oxygen stream is diluted. In the experiment, as the co-flow was diluted with more and more nitrogen, the flame color changed from yellow to blue as the in-flame soot volume fraction apparently decreased. A next step will be to try to reduce the grid-dependence of the simulations. Even though the two-step combustion scheme is temperature-independent, the predicted radiation emission is not.

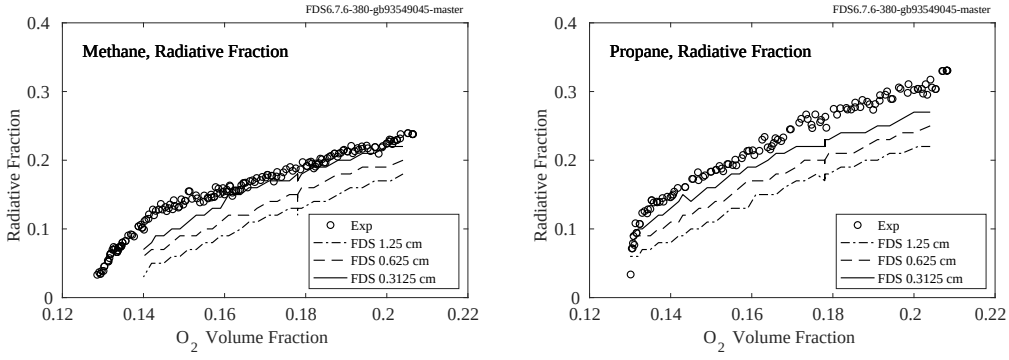


Fig. 6. A comparison of the measured and predicted radiative fraction of the flame in the University of Maryland line burner experiments.

### NIST Reduced Scale Enclosure Experiments, 1994

The NIST Reduced Scale Enclosure (RSE) was a 40 % scale version of the ISO 9705 compartment [14]. It measured 0.98 m wide by 1.46 m deep by 0.98 m tall. A door, centered on the smaller wall, was 0.48 m wide by 0.81 m tall. A 15 cm diameter natural gas burner was positioned in the center of the compartment. The fires ranged from 50 kW to 600 kW. Species measurements, including CO concentration, were made near the ceiling in the front and back of the compartment.

Figure 7 shows the measured and predicted CO concentrations. The measurements were made 10 cm below the ceiling and 30 cm from the left side wall. The front position was 10 cm from the wall with the door; the back position was 30 cm from the rear wall. The simulations are run at three resolutions, for which the "resolution index" (RI), $D^*/\delta x$, is 5, 10, and 20. In all cases, it is assumed that 2 moles of CO are produced in the first reaction step for every 1 mole of C (soot).

### NIST Full Scale Enclosure Experiments, 2008

The NIST Full Scale Enclosure Experiments were conducted in an ISO 9705 compartment [15]. The compartment was 2.4 m wide by 3.6 m long by 2.4 m high with a 2 m high door at one end. The door width varied between 0.1 m and 0.8 m. The experiments were designed to study the effects of fuel type, fuel distribution, and vent size in under-ventilated compartment fires. Twenty-seven experiments have been simulated, which include 7 different fuels (natural gas, heptane, toluene, nylon, propanol, propylene, and styrene) and 4 ventilation openings. Peak heat release rates range from approximately 100 kW to 2.5 MW. Species concentrations and temperature measurements were made at the front and rear of the compartment.

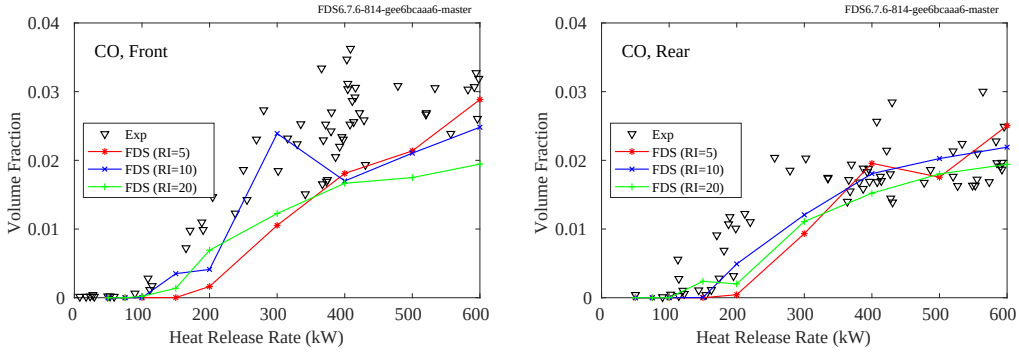


Fig. 7. Comparison of measured and predicted CO concentration, NIST RSE experiments.

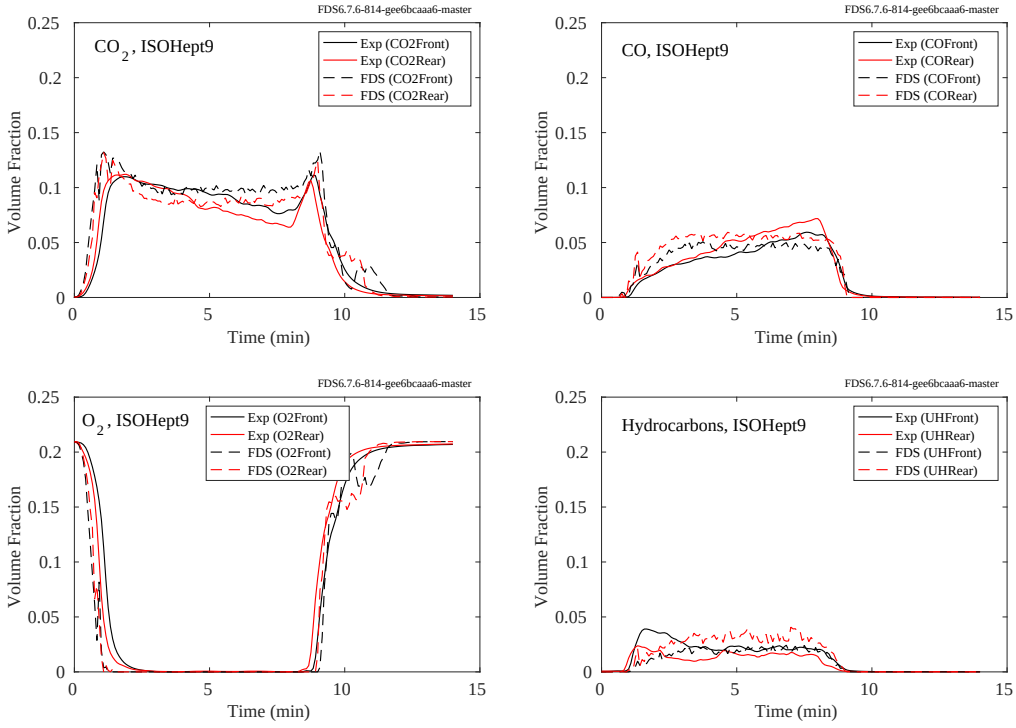


Fig. 8. Summary NIST Full-Scale Enclosure Experiment, Test 9, heptane fuel.

In all simulations, it is assumed that 2 moles of CO are produced in the first reaction step for every 1 mole of C (soot). The simulations are all run with 10 cm resolution. Figure 8 shows the results from one experiment. Notice that the concentrations of CO and unburned hydrocarbons (UHC) increase substantially just as the oxygen concentration decreases to zero. The simple two-step model mimics this behavior because these relatively high concentrations of CO and UHC are the consequence of lack of oxygen. A more detailed model might predict, for example, the gradual increase in CO over the course of the 8 min period of under-ventilation which the simple two-step model does not capture.

Figure 9 compares the measured and predicted peak CO concentration in the NIST reduced and full-scale compartment fire experiments. The fuels in these experiments ranged from “clean” natural gas to “dirty” toluene.

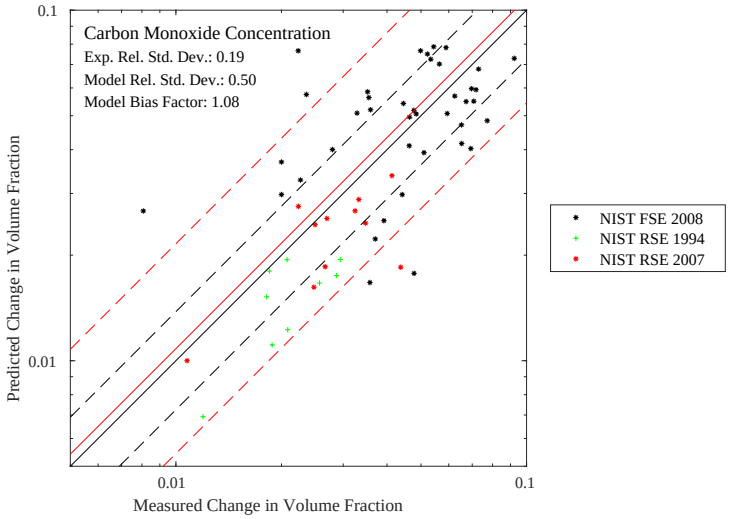


Fig. 9. Measured vs. predicted CO concentration for compartment fires. Note that NIST RSE 2007 refer to experiments very similar to the NIST RSE 1994 experiments, but with a variety of fuels other than natural gas.

## CONCLUSION

A relatively simple two-step combustion model has been proposed for practical, large-scale fire simulations. The scheme is designed to predict the increased CO concentration in under-ventilated compartment fires for which the exact stoichiometry of the fuel molecule is unknown, the numerical grid is potentially tens of centimeters, and flame temperatures and local strain rates are unresolved. The simulations described in this paper are performed on numerical grids ranging from 0.125 mm to 10 cm, nearly three orders of magnitude.

There are certainly limitations of this approach, most notably the fact that CO and soot follow considerably different paths from creation to oxidation. However, in most cases, the aim of the fire simulation is to identify conditions under which the fire becomes starved of oxygen and generates increased amounts of these by-products. Full-scale compartment experiments have demonstrated that the two-step model can identify when under-ventilation sets in, and can predict to some extent the increased CO concentration within the enclosed space. The uncertainty in the model prediction is commensurate with the uncertainty in the composition of the fuel gas species.

## ACKNOWLEDGMENTS

The work presented in this paper is part of the Fire Risk Reduction in Buildings Program at NIST.

## REFERENCES


[1] B.F. Magnussen and B.H. Hjertager. On Mathematical Modeling of Turbulent Combustion with Special Emphasis on Soot Formation and Combustion. In *Proceedings of the Sixteenth Symposium (International) on Combustion*, pages 719–729. Combustion Institute, Pittsburgh, Pennsylvania, 1977.

[2] T. Poinsot and D. Veynante. *Theoretical and Numerical Combustion*. R.T. Edwards, Inc., Philadelphia, Pennsylvania, 2nd edition, 2005.

[3] R. McDermott, K. McGrattan, and J. Floyd. A simple reaction time scale for under-resolved fire dynamics. In *Fire Safety Science – Proceedings of the 10th International Symposium*, pages 809–820, University of Maryland, College Park, Maryland, USA, 2011.

[4] C.K. Westbrook and F.L. Dryer. Simplified Reaction Mechanisms for the Oxidation of Hydrocarbon Fuels in Flames. *Combustion Science and Technology*, 27:31–43, 1981.

[5] R. Falkenstein-Smith, A. Hamins, K. Sung, and J. Chen. Mapping the Chemical Structure of Centerline Profiles in Medium-Scale Pool Fires. NIST Technical Note in preparation, National Institute of Standards and Technology, Gaithersburg, Maryland, October 2019.

[6] Ü.Ö. Köylü and G.M. Faeth. Carbon Monoxide and Soot Emissions from Liquid-Fueled Buoyant Turbulent Diffusion Flames. *Combustion and Flame*, 87:61–76, 1991.

[7] J. de Ris and X.F. Cheng. The Role of Smoke-Point in Material Flammability Testing. In *Fire Safety Science – Proceedings of the Fourth International Symposium*, pages 301–312. International Association for Fire Safety Science, 1994.

[8] K. McGrattan, S. Hostikka, R. McDermott, J. Floyd, C. Weinschenk, and K. Overholt. *Fire Dynamics Simulator, Technical Reference Guide, Volume 3: Validation*. National Institute of Standards and Technology, Gaithersburg, Maryland, USA, and VTT Technical Research Centre of Finland, Espoo, Finland, sixth edition, September 2013.

[9] T.S. Norton, K.C. Smyth, J.H. Miller, and M.D. Smooke. Comparison of Experimental and Computed Species Concentration and Temperature Profiles in Laminar, Two-Dimensional Methane/Air Diffusion Flames. *Combustion Science and Technology*, 90:1–34, 1993.

[10] K.C. Smyth. NO Production and Destruction in a Methane/Air Diffusion Flame. *Combustion Science and Technology*, 115:151–176, 1996.

[11] J. Andersen, C.L. Rasmussen, T. Giselsson, and P. Glarborg. Global Combustion Mechanisms for Use in CFD Modeling Under Oxy-Fuel Conditions. *Energy & Fuels*, 23(3):1379–1389, 2009.

[12] J. P. White, E. D. Link, A. C. Trouvé, P. B. Sunderland, A. W. Marshall, J. A. Sheffel, M. L. Corn, M. B. Colket, M. Chaos, and H.-Z. Yu. Radiative emissions measurements from a buoyant, turbulent line flame under oxidizer-dilution quenching conditions. *Fire Safety Journal*, 76:74–84, 2015.

[13] C. Beyler. *SFPE Handbook of Fire Protection Engineering*, chapter Flammability Limits of Premixed and Diffusion Flames. Springer, New York, 5th edition, 2016.

[14] N. Bryner, E. Johnsson, and W. Pitts. Carbon Monoxide Production in Compartment Fires - Reduced-Scale Test Facility. NISTIR 5568, National Institute of Standards and Technology, Gaithersburg, MD, 1994.

[15] A. Lock, M. Bundy, E.L. Johnsson, A. Hamins, G.H. Ko, C. Hwang, P. Fuss, and R. Harris. Experimental Study of the Effects of Fuel Type, Fuel Distribution, and Vent Size on Full-Scale Underventilated Compartment Fires in an ISO 9705 Room . NIST Technical Note 1603, National Institute of Standards and Technology, Gaithersburg, Maryland, 2008.

# Observations on the delay time of backdraught in the absence of a pilot source

**Wu C.L.[1], Carvel R.[2,*]**

*[1] Chang Jung Christian University, Department of Fire Safety Science, Tainan, Taiwan.*
*[2] University of Edinburgh, School of Engineering, Edinburgh, UK.*
**Corresponding author's email: Ricky.Carvel@ed.ac.uk*

## ABSTRACT

Most backdraught studies to date have used gaseous fuels and piloted ignition scenarios. In such circumstances the delay between the opening of the compartment door and the onset of backdraught is entirely dependent on the time taken for the gravity current to extend from the open doorway to the location of the ignition source, typically on the opposite wall in experimental studies. Few studies have investigated backdraught in the absence of a pilot source. A series of reduced scale backdraught tests have been carried out using solid polypropylene and polyethylene fuel sources, without a pilot source being present. The observed backdraught delay times are considerably longer than the times suggested in the literature, based on the velocity of the gravity current. The delay times are shorter at higher temperatures, but vary with the chemistry of the fuel as well as the temperature and geometry of the compartment. A simple theory of auto-ignition chemistry is presented to explain the observations.

**KEYWORDS:** compartment fires, backdraught, underventilated fires, ignition.

## INTRODUCTION

Despite being feared by fire-fighters for many decades, and brought to popular attention by Ron Howard's motion picture "Backdraft" in the 1990s, backdraught remains one of the unresolved issues in the field of fire science. Research has so far explained the mechanisms involved in backdraught, as will be discussed, but rigorous definitions of instances where backdraught can occur, and detailed definitions of backdraught dynamics remain elusive.

Backdraught generally occurs in conditions where a compartment containing a fire has a very limited fresh air supply, and the fire becomes considerably ventilation-controlled or is extinguished. If there is a sudden supply of fresh air, e.g. due to a window or door opening or breaking, possibly due to the fire, or sometimes due to the intervention of fire-fighters, a backdraught may occur. Backdraught has led directly to fire-fighter injuries and fatalities; thus, it is essential to study backdraught in order to mitigate or avoid its effects in future fire-fighting interventions.

Fundamental research into backdraught has been ongoing sporadically since the early 1990s. Fleischmann et al. [1,2,3] originally conducted a series of experiments using a reduced-scale compartment with a methane burner as the fuel supply. They observed the propagating flame of backdraught, defined the primary mechanisms of the phenomenon, and identified experimentally what fire-fighters had previously observed anecdotally, that there is always a delay between the time the compartment door is opened and the onset of backdraught. To explain this delay time, Fleischmann et al. observed, studied and quantified the "gravity current" phenomenon using compartment fire experiments [1] and salt water modelling techniques [4]. Subsequently, a number of studies investigating the gravity current have been carried out, using full scale fire experiments [5], reduced scale apparatuses [6], salt water modelling [7] and computational fluid dynamics models [8]. The consensus among this literature is that the delay time of backdraught is dependent on the velocity of the gravity current, which itself is dependent on the density difference between the hot compartment gases and the cooler inflowing air.

In general, the velocity of the gravity current is:

$$v_{GC} = v^* \sqrt{\frac{\Delta\rho}{\rho} gH} \quad (1)$$

where $H$ is the height of the compartment, $g$ is the acceleration due to gravity, $\rho$ is the density of the gases in the compartment, $\Delta\rho$ is the density difference between the compartment gases and the inflowing air, and $v^*$ is the non-dimensional velocity; this varies with compartment opening geometry and was quantified by Fleischmann et al. [4] as 0.44 for a full side opening, 0.35 for a door, 0.32 for a slot opening and 0.22 for a window.

Most studies assume, and some have shown, that the delay time of backdraught is the time taken for the gravity current to travel from the compartment opening to the rear wall of the compartment. This has generally been observed because most backdraught studies have had a pilot source in the compartment, positioned on the rear wall of the compartment, directly opposite the opening.

However, it has also been shown that backdraught does not require the presence of a pilot spark [9]. The present study was carried out to experimentally measure the delay time of backdraught in a compartment when no pilot source is present. This scenario may be more representative of real backdraught conditions than situations with a pilot spark present.

## EXPERIMENTAL

A small scale fire compartment (0.8m × 0.4m × 0.4m) was designed and built for backdraught research, see Figs. 1 and 2. It was instrumented with 24 K type thermocouples distributed across 7 thermocouple trees. The configuration of these is detailed in [9] and need not be repeated here. The fuel was contained in a steel tray, which is 0.2m × 0.2m × 0.05 m, and was positioned 100 mm from the rear wall. The compartment was constructed out of two-layers of expanded insulating vermiculate boards, for which the maximum working temperature is 1,100 °C.

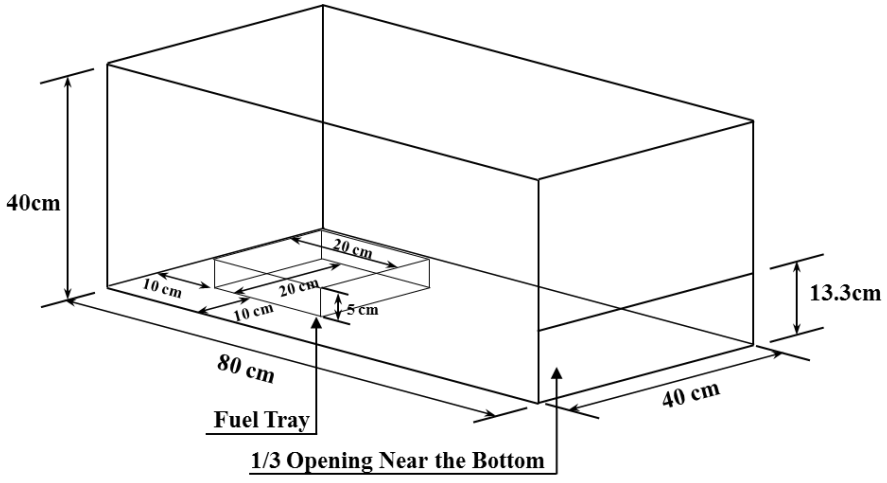


**Fig. 1.** Schematic of the test compartment


**Fig. 2.** Photographs of the test compartment

There were three removable baffles which could be positioned across the opening of the compartment, to investigate the effects of opening size. In all the experiments described here, the upper two baffles were kept in place, such that the opening was fixed at 0.13m × 0.4m wide. Experiments where the opening size was varied have been published elsewhere [10]. A sliding outer door is used to seal and open the compartment, this ensures that the experimenter is safely to the side of the compartment when the door is opened, and is well out of the way of any ejected flames.

In order to generate realistic backdraught phenomena, solid fuels were used as the fire source. For most of the experiments described here, this was Polypropylene (PP) in the form of pellets (approx. 3 mm diameter). A short series of tests using High Density Polyethylene (HDPE) in the form of thin strips (20 mm × 100 mm × 2 mm) is also presented. To aid ignition and repeatability, a small quantity of n-Heptane ($C_7H_{16}$) was used as accelerant to start and establish the burning process. Initial tests were carried out to identify the optimum fuel load for these experiments. It was determined that 300 g of PP with 150 mL of n-Heptane was sufficient to achieve flashover conditions in the compartment, and that most of the liquid accelerant was consumed in the first 5 minutes of burning. About 7 to 12 minutes after ignition, the heat release rate of the fire is quasi-steady and the temperature in the compartment rises in a steady and highly repeatable manner. The fire transitioned to flashover after about 13 minutes. With 300 g of HDPE fuel the fire growth was slightly slower, with the steady growth phase lasting from 13 to 18 minutes after ignition, and reaching flashover after about 20 minutes. The primary focus of this research concerns what happens when the door is closed during the steady growth or post-flashover time frames, is kept closed for a variable period of time, and is then opened again.

It has previously been shown that backdraught behaviour correlates better using the maximum recorded temperature in the compartment at the time of door closure or opening, rather than the average temperature [9]. The highest temperature in the compartment was consistently observed directly above the fuel tray, and it is this temperature value which will be used as the characteristic compartment temperature in the discussion that follows.

## RESULTS

Results show that when the door is closed, the fire self-extinguishes within seconds, and the overall temperature in the compartment begins to diminish (although the temperature at low level increases in the first few seconds). Due to the insulating nature of the compartment construction, the temperatures take hundreds of seconds to diminish to ambient. Fig. 3. Shows the temperature variation in the compartment after the door was closed at 12 minutes after ignition of a PP fire, and the door was kept closed. In Fig. 3 the red line represents the maximum temperature in the compartment, near the ceiling at the rear, and the grey line represents a thermocouple near the floor and near the door.

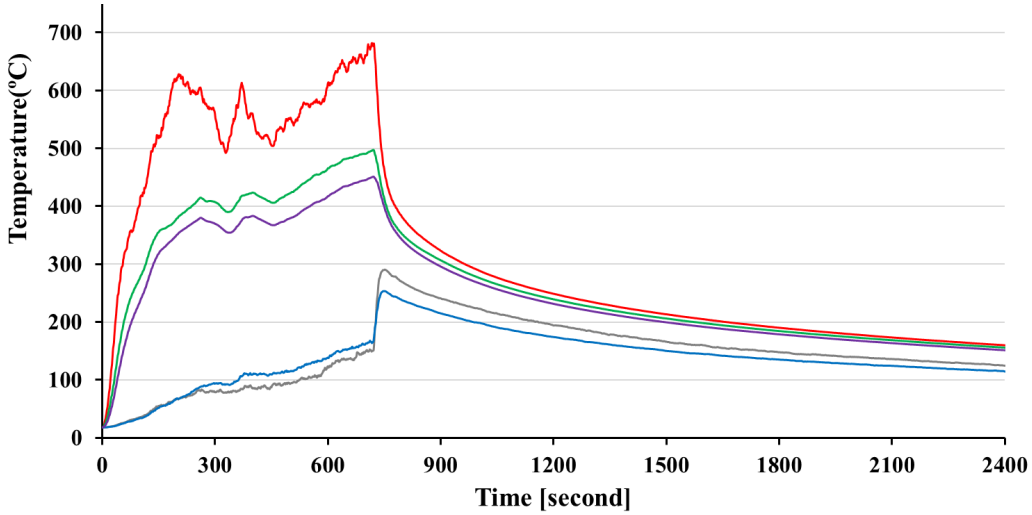


**Fig. 3.** Selected temperatures in the compartment when the door is kept closed.

When the temperatures in the compartment are high, the fuel will continue to pyrolyse, but the evolved gases cannot burn as there is insufficient oxygen present. If/when the temperature drops below the pyrolysis temperature, no further gaseous fuel will be produced and the compartment will enter a phase entirely dominated by cooling. The compartment is reasonably well sealed when closed, so when the door is closed the proportion of fuel in the gas phase will not diminish significantly unless condensation occurs.

Attempts were made to quantify the rate of production of the pyrolysis gases and the duration of the pyrolysis phase, using mass-loss measurements; placing the fuel tray on a platform on a spindle which passed through the floor of the compartment, and which was attached to a loadcell below. Unfortunately, the small variations in mass following the closure of the door were almost completely masked by errors and noise in the data due to the experimental configuration. So far, it has not been possible to quantify the duration of the pyrolysis phase or distinguish it from the cooling phase. The most reliable data obtained so far, for door closures made at around flashover for both fuels, show that the PP fuel tray lost 28.8 g in mass during a 257 s door closure, and the HDPE fuel tray lost 65.4 g during a 446 s closure. This shows a higher average mass loss rate per second for HDPE compared to PP, approximately 0.15 g/s compared to 0.11 g/s, respectively. It should be noted that as the temperature in the compartment is gradually diminishing when the door is closed, it is assumed that the pyrolysis rate will also diminish across this time, so it is unwise to infer anything from average mass loss rates, particularly when comparing tests with different door closure times.

In this test series two parameters were varied to affect the compartment conditions at the time of door opening: the pre-burn duration and the duration of door closure. Varying the pre-burn time controls the temperature in the compartment at the start of the pyrolysis phase (and hence the length of the pyrolysis phase), and varying the door closure time controls the temperature of the compartment at the time of door opening.

Results from a series of 21 tests using PP fuel and 6 tests using HDPE fuel are presented in Fig. 4. Tests using PP are indicated using triangles, tests with HDPE are indicated using circles. The trendlines have been added to the data for clarity. The data are plotted as maximum temperature in the compartment at the time of door opening, versus the observed backdraught delay time.

It is clear from the data that there are reasonably well defined trends in behaviour; at higher temperatures the delay times are short, but at lower temperatures the delays can be much longer. Previous research has shown that backdraught will not occur for PP in the absence of a pilot flame at temperatures below about 340°C and below about 320°C for HDPE [11,12].

It is also clear from the data that there are two distinct trends for the different fuels, so the delay time is seen to be clearly dependent on the chemistry of the fuel, not merely the temperature of the compartment.

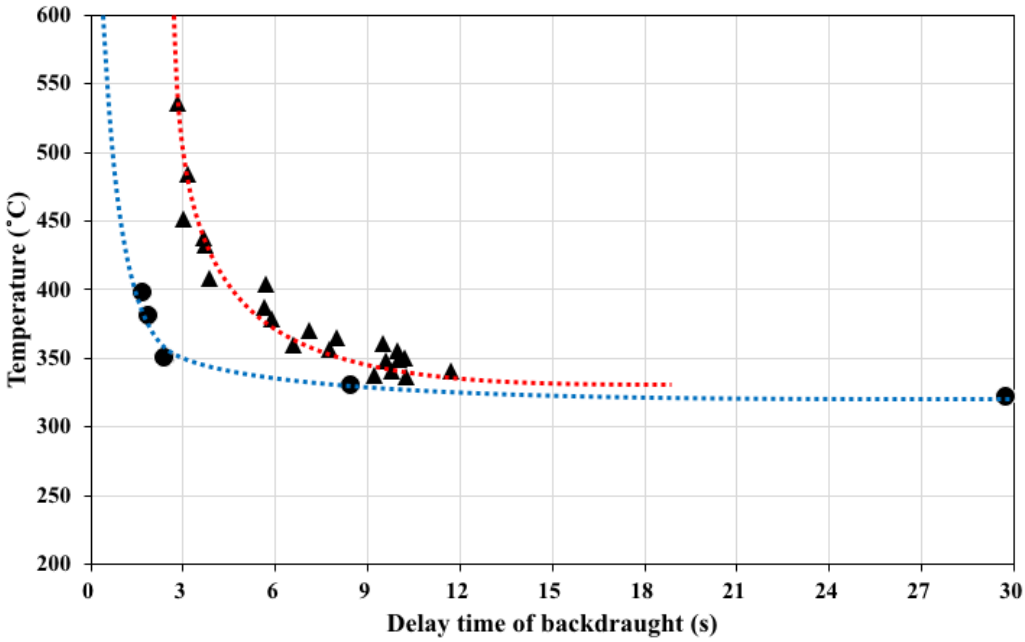


**Fig. 4.** Backdraught delay time vs. maximum temperature in the compartment at the time of door opening. (Note there are two HDPE data points at 350°C which are almost exactly the same.)

## DISCUSSION

At first glance, the data for these non-piloted experiments appears to be consistent with the theory of backdraught delay time established in the literature using piloted experiments. Superficially, the trends are the same, with shorter delays at high temperatures and longer delays at lower temperatures. However, the delays shown in Fig. 4 do not correspond to the gravity current travel time. Using Equn. (1) it can be shown that for the small compartment used here, at temperatures around 350°C, the gravity current will reach the rear wall of the compartment in less than two seconds. Even when it is acknowledged that, due to thermal stratification, the temperatures near the floor of the compartment may be up to 100°C lower than the characteristic maximum temperature plotted here, the corresponding slower gravity current time is still less than 2.2 s. This is notably shorter than the observed delay times for HDPE fuel, and considerably shorter than the delay time for PP fuel. It is clear that something other than the transit of the gravity current to the back of the compartment determines the backdraught delay.

Results for piloted backdraught experiments, carried out in the same apparatus, have been published previously [9,10,11,12]. The observed backdraught delay in these experiments is broadly consistent with the theory of backdraught delay due to gravity current transit. Something else is determining the backdraught delay time when no pilot source is provided.

Analysis of the pyrolysis products from PP and HDPE samples in low oxygen conditions have shown that the dominant pyrolysis species for PP are from the pentane family, while PE pyrolyses to members of the hexane family (identified by FTIR spectrometry) [11,12]. Auto ignition of pentane requires generally higher temperatures than those for hexane.

For mixtures above the auto-ignition temperature for both fuels, for any given initial temperature, more mixing with the inflowing air is required for pentane to auto-ignite than for hexane. This is perhaps best explained using a flammability diagram, see Fig. 5. Suppose the initial fuel mixture in the closed compartment, which is above the upper flammability limit (UFL), is 300°C. In order to reach a flammable mixture which is above the auto-ignition limit, a pentane mixture requires more air, and more mixing time with the air, to form an auto-ignitable flammable mixture than a hexane mixture. This is best visualised by following the arrow on Fig. 5, the conditions for auto-ignition of a hexane mixture would clearly be reached before those for a pentane mixture. Of course, the pyrolysis products present here are not pure pentane or hexane, the mixtures are far more complex than that, but the general trends will be the same.

This explains the two clearly distinct trends in the data. All other factors being equal, the pyrolysis products from PP fuel need more mixing time, and to reach a mixture closer to stoichiometric than with the products from PE pyrolysis. If a pilot source is present, the different auto-ignition properties of the fuels make no difference, as the zone for piloted ignition is considerably larger, as shown. In such instances the chemistry of the fuel has less of an influence on the backdraught delay.

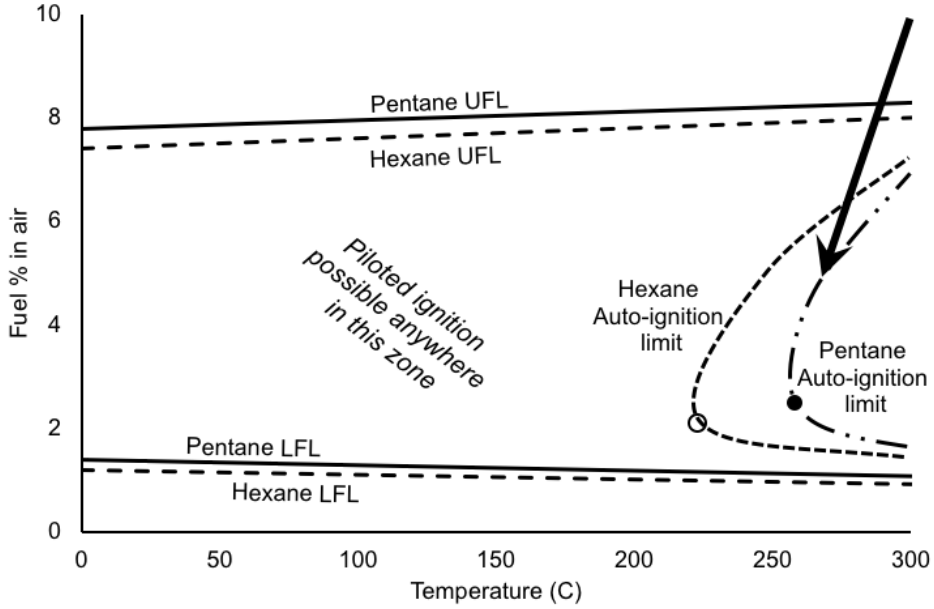


**Fig. 5.** Approximate representation of flammability limits and auto-ignition limits for Pentane and Hexane fuels in air. Based on data from Zabetakis [13].

## CONCLUSIONS

Backdraught experiments, using polypropylene and polyethylene solid fuels, in a reduced scale apparatus, with no pilot source present, have clearly shown that the backdraught delay time is not directly related to the gravity current velocity, as in piloted ignition scenarios, but varies with the chemistry of the pyrolysis products, and gas mixing.

## ACKNOWLEDGEMENTS

Thanks to all the fire research team at the University of Edinburgh, especially Michal Krajcovic and Agustin Majdalani. Special thanks to professors Dougal Drysdale and Albert Simeoni for their

guidance and advice from the outset of this project. This research project was supported by the Ministry of Education, Taiwan.

## REFERENCES

1 C.M. Fleischmann, P.J. Pagni, R.B. Williamson, Preliminary Backdraft Experiments, in: 12th Jt. Panel Meet. UJNR Panel Fire Res. Safety. (1992) pp. 208–215.

2 C.M. Fleischmann, P.J. Pagni, R.B. Williamson, Exploratory backdraft experiments, Fire Technol. 29 (1993) 298–316. doi:10.1007/BF01052526.

3 C.M. Fleischmann, P.J. Pagni, R.B. Williamson, Quantitative Backdraft Experiments, in: 4th Int. Symp. Fire Saf. Sci., (1994) pp. 337–348.

4 C. Fleischmann, P. Pagni, R. Williamson, Salt Water Modeling Of Fire Compartment Gravity Currents, Fire Saf. Sci. 4 (1994) 253–264. doi:10.3801/IAFSS.FSS.4-253.

5 D. Gojkovic, Initial Backdraft Experiments, Report 3121, Department of Fire Safety Engineering, Lund, Sweden, 2000.

6 G. Guigay, A CFD and Experimental Investigation of Under-Ventilated Compartment Fires, University of Iceland, 2008.

7 X. Yao, A.W. Marshall, Quantitative salt-water modeling of fire-induced flow, Fire Saf. J. 41 (2006) 497–508. doi:10.1016/j.firesaf.2006.06.003.

8 W.G. Weng, W.C. Fan, Y. Hasemi, Prediction of the formation of backdraft in a compartment based on large eddy simulation, Eng. Comput. 22 (2005) 376–392. doi:10.1108/02644400510598732.

9 Wu, C.L. & Carvel, R. (2017) An experimental study on backdraught: the dependence on temperature. Fire Safety Journal, Volume 91 (2017), Pages 320-326. doi:10.1016/j.firesaf.2017.04.003

10 Wu & Carvel “Influence of Compartment Geometry on the Occurrence of Backdraught” Proceedings of the 15th International Fire Science & Engineering Conference, Interflam 2019, London, 1-3 July 2019, pp. 553-559

11 C.L. Wu “An experimental study of Backdraught using solid fuels” PhD Thesis, University of Edinburgh, 2019.

12 C.L. Wu, S. Santamaria & R. Carvel “Critical Factors Determining the Onset of Backdraft Using Solid Fuels”. Fire Technol 56, 937–957 (2020). doi:10.1007/s10694-019-00914-9

13 M.G. Zabetakis “Flammability Characteristics of Combustible Gases and Vapors” US Bureau of Mines, Bulletin 627, 1965.

# Fully-involved fire dynamics in ceiling-vented Compartments

**Lawson C.[1], Loggie I.[1], Majdalani A.[2], Carvel R.[1,*]**

[1] *University of Edinburgh, School of Engineering, Edinburgh, UK.*
[2] *Cosmos Investments, United Kingdom & Argentina.*
**Corresponding author's email: Ricky.Carvel@ed.ac.uk*

## ABSTRACT

Side-vented compartment fires are well described in the literature. Compartment fires with only a ceiling-vent are poorly understood in comparison. A series of 29 experiments in a reduced-scale, ceiling-vented compartment have been carried out to observe and characterise the four expected modes of burning. Ghosting flames and pool fire behaviour are both observed when the compartment temperatures are above 500°C, the former occurring at lower fuel loadings, the latter at higher fuel loadings. Pulsing behaviour is less common and exists at lower temperatures as a transition between other modes of burning. Asymmetric flow patterns can also occur with asymmetric arrangements of fuel or with very large ceiling vents.

**KEYWORDS:** compartment fires, post-flashover, underventilated fires, ceiling vents.

## INTRODUCTION

Fire conditions in compartments with vertical side openings have been extensively researched, with significant theoretical analysis and multiple experimental studies. The fire behaviour is relatively well understood and flow through the opening has two distinct regions consisting of hot gases being exhausted from the upper segment, and cold air being entrained below. Various correlations and relationships have been derived based on this flow exchange and currently form the foundation of compartment design for fire safety [1,2].

The same cannot be said with regard to fire behaviour in compartments with only a horizontal opening in the roof. This is a more complex situation that has not been adequately explored in previous research. Due to the location of the vent, the flow exchange is complicated by buoyancy effects and the inflowing and outflowing gases compete for all parts of the vent.

Although this is a relatively immature area of research, ceiling vented compartments represent a number of real scenarios including basements and fires in the holds of ships. Subsequently, there is a need for research into fire behaviour under such conditions, to ultimately offer advice to Fire Safety Engineers for design, and to offer practical guidance to fire brigades in approaching and fighting such fires.

## LITERATURE REVIEW

The SFPE Handbook has a chapter on "Vent Flows" (authored by Emmons in the 1st to 4th editions of the book, and expanded by Tanaka for the 5th edition) [3,4] which briefly addresses the question of flow through horizontal vents. This treats the issue of vent flows from a purely fluid dynamics perspective, and questions of fire dynamics are not addressed.

The earliest work systematically investigating flow through horizontal openings was carried out by Epstein [5] using the salt-water modelling technique. In these experiments there was a density difference across the opening, but no pressure or temperature differences. Epstein identified four regimes of flow which varied with the dimensions of the opening (and hence with the Froude number); these were: (i) oscillatory exchange flow, (ii) Bernoulli flow, (iii) turbulent diffusion with Bernoulli flow, and (iv) turbulent diffusion flow. Epstein & Kenton [6] advanced the study with the addition of

pressure as well as buoyancy effects, they defined the conditions under which pressure overcomes the density effects to give a unidirectional flow.

In parallel to these experimental studies, Emmons [3] derived a theoretical 'standard vent model' from first principles. This was critiqued and refined by Cooper [7,8], resulting in the VENTCF2 algorithm which was incorporated into fire 'zone' models in the 1990s.

Jaluria and Tan [9] also used salt-water experiments to study flow under combined pressure and buoyancy effects, and concluded that the impact on flow velocity resulting from a unidirectional pressure-driven flow is much greater than the effect of a bi-directional, buoyancy-governed regime. They defined the buoyancy parameter, B, as a means of distinguishing between unidirectional flow and bidirectional flows. This parameter essentially represents the ratio of density difference to pressure difference, and continues to be used in more recent research, including the work of Chow and Gao [10].

Satoh *et al.* [11] conducted early research into airflow oscillation across a horizontal vent by using a thermal heat source in a top (and bottom) vented compartment. In observing temperature oscillation representative of vent flow behaviour, a relationship between the frequency of oscillation and thermal power was empirically derived. Kerrison *et al.* [12] later conducted a two-dimensional numerical analysis of the same concept and derived an expression that showed a good agreement with that identified by Satoh.

Building on this previous research, Chow and Gao [10] presented a more comprehensive theoretical analysis of the oscillation of airflow across a ceiling vent. They identified the transient flow oscillation to consist of three distinct phases: (i) linear growth, (ii) non-linear growth and (iii) stable. Whilst the equations derived appear to show some level of correlation to previous experiments using a thermal power source, it is important to note that there is still insufficient data to confirm their accuracy or even applicability when applied to vent flows for a real fire.

Takeda [13] and Tu [14] conducted some of the earliest experimental research into compartments with horizontal vent openings and real fires. In both cases, the horizontal opening and the fuel load were positioned symmetrically in the middle of the compartment.

In a series of compartment fire experiments using polymethylmethacrylate (PMMA) slabs as fuel, Takeda [13] observed two significant effects arising from the presence of a top opening. Given the position of the vent, a hot upper layer was not able to form as generally observed in a side-vented compartment, this significantly reduced the fire growth rate. Furthermore, results indicated the inflow of air was reduced to around 30-50% of the value expected for a similarly sized, side-vented compartment fire. This reduced airflow led to a reduced mass-burning rate. In those experiments where an approximately steady-state mass loss rate was achieved, a transformation in the burning mode became apparent, with evidence of a pale blue flame that detached from the fuel surface and appeared to "float" within the compartment. This burning behaviour is similar to the "ghost" flame observed by Sugawa *et al.* [15] in a side-vented compartment with restricted ventilation.

Tu [14] used a replenishing ethanol fuel system as a fire source. By varying the vent opening, three different burning scenarios were identified: (i) choked and then extinguished, (ii) erratic pulsating pool fire, and (iii) strong steady-state pool fire. Increasing vent size led to a greater mass loss rate, which tended towards a constant value for each opening size. That is, the steady burning rate is generally limited by the ventilation flow, not by the fuel properties.

Quintiere [2] comments on the inefficiency of horizontal vents at supplying air for a fire to consume, he notes that the flow through a horizontal vent modelled using Epstein's [5] empirical relationship is approximately $1/10^{th}$ that of a vertical opening of the same size. This inefficiency suggests that top-vented compartment fires may be broadly analogous to aspects of underventilated compartment fires, such as those studied by Sugawa *et al.* [15] and Utiskul *et al.* [16].

The influence of vent opening size on temperature rise was recently studied by Li et al. [17] using a heptane fuel source in a full size compartment (3m × 3m × 1.95m) with an asymmetrically located ceiling opening. In agreement with the findings of Takeda [13], this research indicated that the temperature variation in the compartment increased gradually over its height, with no clear thermal stratification layers, indicating that the gases within the compartment were relatively well mixed. This profile is notably different to the pre-flashover, side-vented compartment fire, which generally exhibits well defined hot upper and cool lower layers.

Li et al. observed that when the fire is growing, it is the fire size and not the opening size which is the most significant factor governing the maximum gas temperature in the compartment and rate of temperature rise. It is acknowledged that this study focused on a pre-flashover fire, in the early stages of fire growth, and the behaviour is thus still controlled by the fuel characteristics, and largely independent of the ventilation. The influence of varying the vent size on a fully developed regime with established compartment temperatures might be expected to yield different results, but this remains to be investigated.

Chen *et al.* [18], using the same apparatus as Li *et al.* [17], investigated the relationship between the rate of gas temperature rise in the compartment and the mass loss rate of the fuel. The study demonstrated a strong correlation between the two variables and a resulting relationship was derived between the average rate of non-dimensional temperature rise and the mass loss rate. This study, therefore, provides a valuable method of estimating the mass loss rate of a fuel based on the transient temperature profile. This is one of the first relationships that may have a practical application in predicting the fire dynamics in a top vented compartment.

Zhang et al. [19] also investigated the relationship between the rate of gas temperature rise and the heat release rate. Their theoretical analysis derived a correlation using Epstein's vent flow equation [5] considering the energy balance within the compartment. A series of experimental tests were then conducted and the results used to provide constants for the theoretical equation. They concluded that the average gas temperature rise in a ceiling vented compartment was proportional to the heat release rate to the power ⅔.

During the research conducted by Zhang *et al.* [19] and Chen *et al.* [18] experimental results have generally evidenced a uniform temperature across any horizontal plane throughout the compartment. This agrees with previous research conducted by Chen [20] and indicates that hot gases are well mixed within the compartment.

The majority of existing experimental studies focus on consistent test parameters, with little variation in the physical conditions. However, the influence of vent position has been investigated by Zhang *et al.* [21] by comparing the results obtained from an opening in the corner of the ceiling with results for the centrally positioned opening. Using a fire source of 100 kW it was evident that whilst gas temperatures for the corner opening were greater, the pressure difference and mass loss rate across the centrally positioned opening were more significant. On the basis of the observed conditions, conclusions were reached that a 'more dangerous' fire was apparent for the central opening position due to the increased pressure difference and the ejection of flames from the compartment observed.

Rodriguez [22] has identified correlations between the mass loss rate and the experimental configuration, as part of an unpublished Masters' thesis at the University of Edinburgh. Unlike other studies, Rodriguez focused on fully developed fire behaviour using wooden cribs in addition to polypropylene pellets. A correlation between the mass loss rate and the opening size was identified for both fuel types with an increase in the ventilation area proportional to an increase in the mass loss rate. The influence of varying the experimental conditions was also studied and analysis indicated that a centrally positioned fire provided a higher mass loss rate than a fire positioned in a corner or beside a wall. The limitations of this study were part of the motivation for the present study.

Finally, Chitty and Fraser-Mitchell [23] carried out three full-scale ceiling-vented compartment fire tests in 2015. The compartment was 3.6 × 3.6 × 2.4 m high, constructed of concrete blocks, and

insulated with ceramic blankets. The three tests had the same fuel loading of wooden cribs, but varied in the size of the ceiling vent. There was a sealed door on one compartment wall, but results suggest it was not airtight through the experimental test campaign. The ceiling-vents were nominally 1 × 2 m, 1 × 1.5 m, and 1 × 1 m, but due to the construction of the compartment, there was a beam (wrapped in ceramic insulation) bisecting the opening in the longer dimension, which slightly reduced the opening area, splitting it into two rectangles. Temperature data and gas concentrations ($O_2$, CO, $CO_2$) were recorded, and some limited visual observations were made. In the two tests with the larger openings, the fires grew from ignition to fully involved fires, with external flaming through the ceiling vents after 23 minutes and 30 minutes, respectively. The test with the 1 $m^2$ opening did not exhibit external flaming. Temperatures reached a steady-state 'plateau' up to about 1000°C in the first test, about 700°C in the second test and about 600°C in the last. However, the temperature data show considerable temperature gradients between the 'front' of the compartment and the 'rear' suggesting that the 'front' door leakage played a role in the fire dynamics. The lack of visual observations of the mode(s) of burning in these tests was the other motivation for the present study

## OBJECTIVES AND METHODOLOGY

Based on the literature review, above, it is apparent that different modes of burning may occur in a fully established ceiling vented compartment fire, depending on the thermal conditions in the compartment, the nature and location of the fuel, and the size and location of the opening. The aim of the experiments described here was to observe the various modes of burning and quantify the conditions under which they occur.

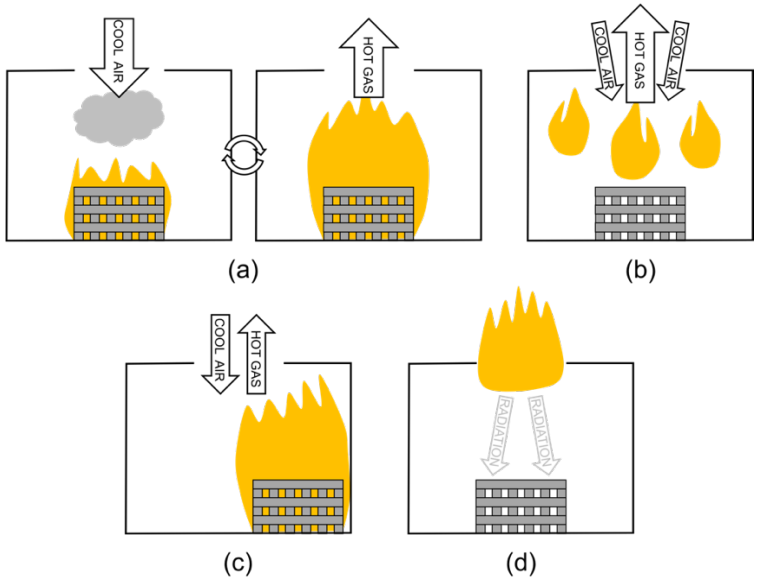


**Fig. 1.** Burning modes: (a) pulsating flame, (b) detached ghost flame, (c) asymmetric burning, and (d) pool fire.

The four expected modes of burning are shown schematically in Fig. 1. These are:

a) The *pulsing mode* or *pulsing diffusion flame*. This describes a burning behaviour with an oscillation between a reduced fire with an entrainment of air inward, and a period of large flames with an outward flow of hot gases.

b) The *ghost flame* or *ghosting mode.* This was expected to occur under restricted ventilation, which results in a detached flame circulating around the compartment.

c) The *asymmetric burning mode*. This was anticipated to occur under larger openings where, contrary to the other modes, there is a clear segregation between the hot outflow gases and cooler air inflow.

d) The *'pool fire' mode*. This was expected to occur at high temperatures, with high fuel loads. Under these conditions, the flames detach from the fuel and move to the opening, where there is a plentiful supply of oxygen, but radiate down to the fuel in the compartment at a sufficient intensity to maintain a supply of pyrolysis gases.

To observe and characterize these modes of burning, a test compartment was constructed with inner dimensions of 600 mm × 600 mm × 400 mm high. (This is essentially a $1/6^{th}$ scale replica of the compartment used by Chitty & Fraser-Mitchell [23].) The housing was constructed from 25 mm thick ceramic fibreboard, with all joints sealed using fire cement and taped externally to minimise air leakage. The compartment also contained a 180 mm × 275 mm glass viewing panel to allow for observation during testing.

The compartment was fitted with an adjustable vertical opening on one sidewall to permit conventional side-vented flashover conditions to be achieved within the enclosure, as will be discussed below. The roof consisted of a six-hatch-system that enabled the horizontal opening area and position to be varied. Each hatch measured 200 mm × 100 mm allowing the area to be varied from 0.02 $m^2$ to 0.12 $m^2$. The apparatus is shown in Fig. 2.

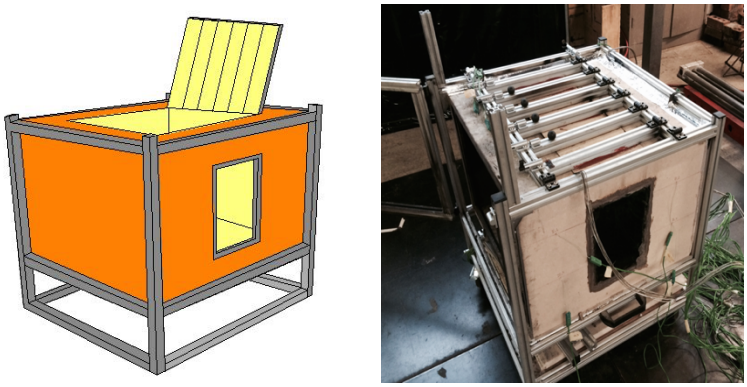

**Fig. 2.** Schematic and photograph of the test apparatus.

A wooden crib of Scandinavian Spruce was used in all experiments. For most experiments, the crib was constructed of 8 layers, each consisting of 4 sticks measuring 225 mm × 32 mm × 16 mm. To ensure repeatability of the tests, the wood was oven dried at 103°C for a period of 24 hours before being used. In each test small quantities of heptane soaked into rolls of tissue paper were used to ignite the cribs.

Temperatures were recorded in the compartment using four thermocouple trees each with eight semi-rigid K type thermocouples spaced equally over the height of the compartment. The trees were placed towards the corners of the compartment at positions approximately 100 mm from the adjacent walls, as shown in Fig. 3. In some tests bi-directional probes were positioned across the opening to quantify the flow, and various thin-skin calorimeters were positioned on the walls of the compartment to quantify heat flux. Results from these will not be discussed in this paper.

As the aim of this study was to observe and quantify fully-involved, post flashover fire dynamics, and does not concern the mechanism or likelihood of a ceiling vented compartment actually attaining such conditions, the fire was generally allowed to grow to 'conventional' (i.e. side-vented) flashover conditions by igniting the crib with all the ceiling vents closed, and one side of the compartment was raised to give a rectangular opening of 600 mm × 150 mm high. After about 4 minutes of burning, the

compartment reached flashover conditions (that is, external flaming was established), after this, the ceiling vents were opened in the desired configuration and the side wall lowered into place.

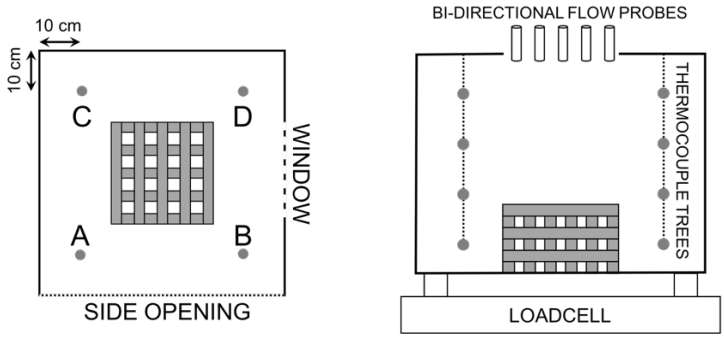


**Fig. 3.** Plan and side view of the compartment showing the location of the thermocouple trees

## RESULTS

A total of 29 experiments were carried out as summarised in Table 1. It is not necessary to present all the data here. Fuel load, fuel position, and the number and arrangement of open ceiling vents were varied between tests. All four modes of burning were observed in the test series, some tests exhibited transitions between modes of burning as the temperatures in the compartment changed and/or the fuel began to deplete. All tests were allowed to burn to extinction, but the quantity of wood/char remaining at the end of a test varied considerably between tests. In some tests the fire self-extinguished then violently reignited after a period of 10s of seconds or sometimes minutes, these instances are denoted 'reignition' in Table 1.

Temperature and heat release rate (HRR) data from Test 17, a reasonably typical test, are shown in Fig. 4 (note: The temperature data come from Tree A, with TC1A being the thermocouple closest the ceiling and TC8A being the thermocouple closest to the floor). In this test, flashover occurred at about 240 s, after which the central two ceiling vents were opened, creating a 100 × 100 mm centrally located opening, and the side vent was closed.

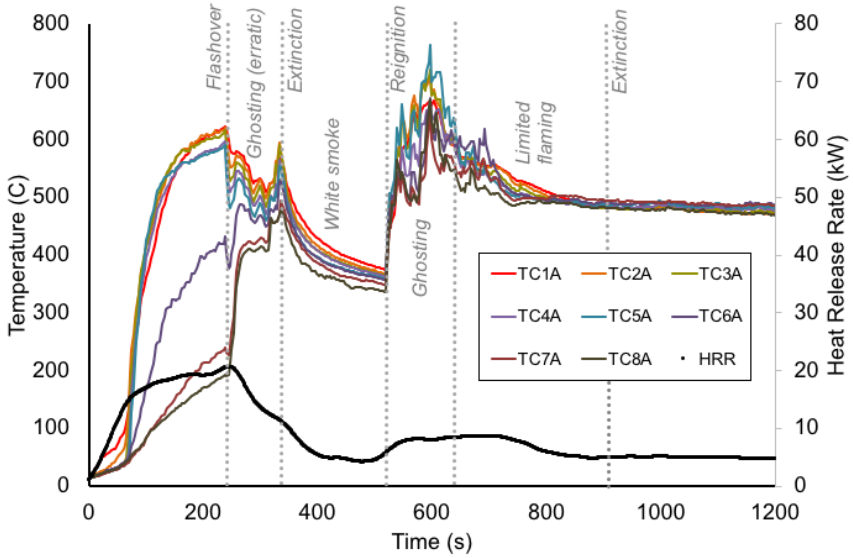


**Fig. 4.** Temperature and HRR data from Test 17 (double opening), with some observations.

**Table 1.** Summary of experiments

| Test Number[†] | Number of vent openings[‡] | Number of sticks in crib[#] | Pulsing | Ghosting | Asymmetric | Pool | Other observations |
|---|---|---|---|---|---|---|---|
| 9 | 2 | 64 | X | X | | X | |
| 10 | 2 | 32 | | X | | | Reignition |
| 11 | 2 | 32 | | X | | | |
| 12 | 2 | 32 (side) | | | X | | |
| 13 | 2 (side) | 32 (side) | | X | | | Erratic |
| 14 | 2 | 32 (corner) | | X | | | |
| 15 | 2 | 32 | | X | | | |
| 16 | 2 | 32 | | | | | No flashover |
| 17 | 2 | 32 | | X | | | Reignition |
| 18 | 2 | 32 (side) | | X | | | |
| 19 | 4 | 32 | | | X | | |
| 20 | 3 (offset) | 32 | | X | | | |
| 21 | 1 (offset) | 32 | X | | | | Reignition |
| 22 | 3 (offset) | 32 (side) | | | X | | |
| 23 | 2 | 32 (bigger sticks) | | X | | X | |
| 24 | 2 | 32 | X | X | | | |
| 25 | Varied 2 to 4 | 32 | | X | X | | Reignition |
| 26 | Varied 2 to 4 | 32 (side) | | X | X | | |
| 27 | Varied 4 to 2 | 32 | | X | X | | Erratic |
| 28 | Varied 3 to 4 | 32 | | X | X | | |
| 29 | Varied 3 to 1 | 32 | | X | | | Erratic |

[†] Tests 1 to 8 were exploratory in nature, varying number of openings and fuel configurations during tests; detailed records and observations were not kept, so these tests are not included here.

[‡] Openings positioned symmetrically on the compartment, except where noted.

[#] Fire positioned centrally in the compartment, except where noted.

After this, as can be seen in Fig. 4, the heat release rate and temperature in the compartment both began to diminish, with ghosting flames being observed in the compartment over a period of about 90 s. These are designated 'erratic' ghost flames as there was some rapid but not periodic fluctuation between reduced flaming and intensified flaming, but with the flames clearly detached from the wooden crib, so this was not the pulsing behaviour expected from the literature review. While the overall temperature of the compartment diminished in this period, it should be noted that the temperature at low levels in the compartment increased until there was less than a 100°C temperature gradient across the compartment height.

Following this period of ghosting, there was a brief surge in flaming followed by flame extinction, and a column of white smoke emerged from the opening, with no obvious inflow of air into the compartment. This lasted for about 3 minutes. Without warning, this was followed by a backdraught-like smoke explosion, a rapid increase of temperature inside the compartment and a return to the ghosting flame behaviour (less erratic) over a period of about two minutes. After this, the fuel was much depleted and the flames localised around the base of the crib until final extinction.

Tests 10, 11 and 15 were carried out with the same test parameters as Test 17, resulting in similar observations, with the ghosting flame behaviour being observed within the same temperature range.

Test 24 was slightly different from Test 17, in that the ceiling vents were opened, and the side vent closed, at an earlier stage in fire development, before the compartment had attained flashover. The data from Test 24 are shown in Fig. 5.

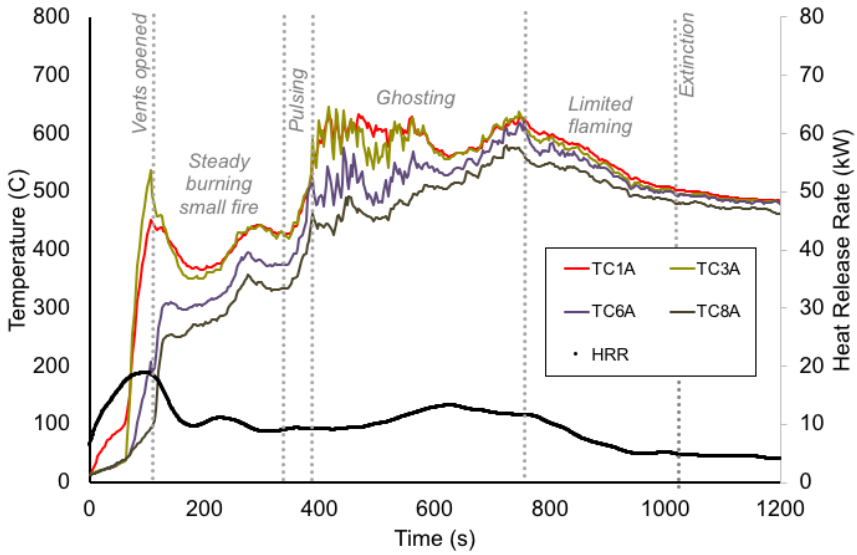


**Fig. 5.** Temperature and HRR data from Test 24 (double opening), with some observations.

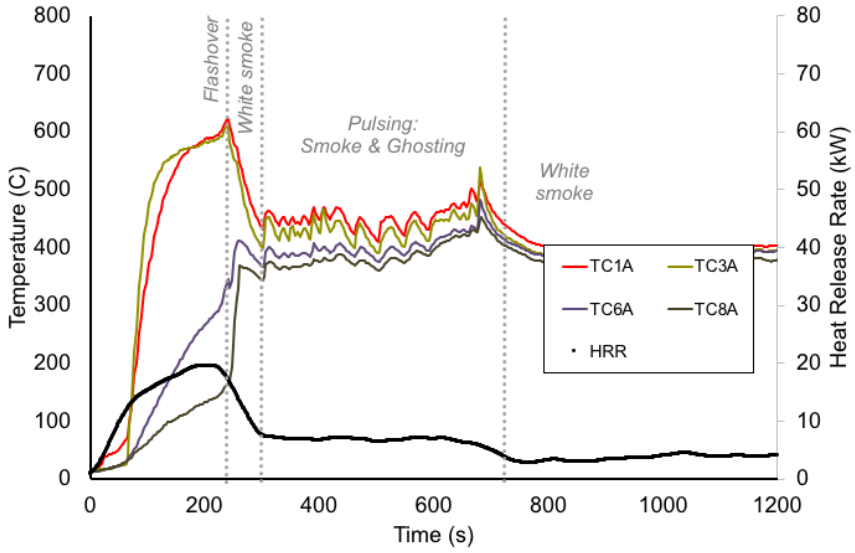


**Fig. 6.** Temperature and HRR data from Test 21 (single opening), with some observations.

This was one of the three tests where the pulsing regime was clearly evident. However, the pulsing period only lasted for about 30 seconds, transitioning to the ghosting regime once the compartment temperatures were in the 500 to 600°C range. The pulsing mode served to rapidly elevate the temperatures in the compartment much faster than the localised burning did. It would appear that the pulsing mode exists as a transitional mode in between localised burning and generalised burning in the form of ghosting; in some ways it may be analogous to flashover in side-vented compartments.

When smaller ventilation openings were used (i.e. when only one ceiling vent was open as in Tests 21 and 29), the pulsing mode was observed again, but in these instances the pulsing varied (somewhat erratically) between a brief outflow of white smoke with no flaming evident, and short periods of reignition followed by ghosting. In Test 21, data for which can be seen in Fig. 6, this pulsing behaviour

was observed over an extended period of over 6 minutes. Consistent with the observations from Test 24, above, the temperatures in the compartment were in the 400 to 500°C range during the pulsing regime. In this instance it seems that the small ventilation opening prevented the temperature rise necessary to sustain 'steady' ghosting behaviour.

The 'pool fire' regime was only observed in the two tests with a very high fuel load, Tests 9 and 23. Data for Test 23 are presented in Fig.7. Here, there was a brief period of pulsing after the ceiling vents had been opened and the side vent closed. Once the temperatures in the compartment had stabilised, the flames moved to the opening and persisted there for over 5 minutes, with flames emerging from the opening, and no apparent inflow of air into the compartment. During this time the temperature inside the compartment increased steadily, while there was a slight diminishing of the heat release rate.

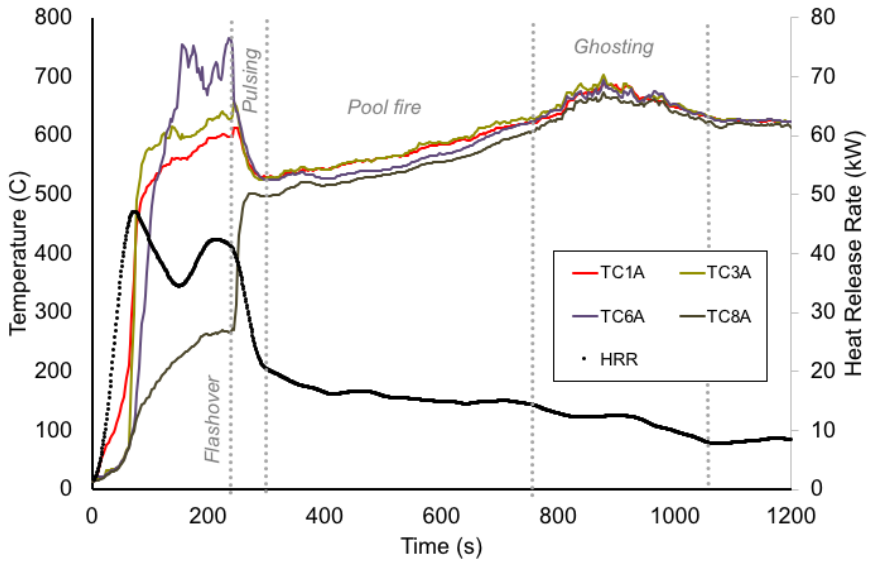


**Fig. 7.** Temperature and HRR data from Test 23 (double opening, larger fuel source), with some observations

At about 750 s after ignition, the rate of production of pyrolysis gases must have dropped below the critical level to sustain the pool fire mode, and the compartment transitioned to the ghosting mode until the fuel became depleted.

As expected, in fire tests where the fuel or openings were positioned asymmetrically, the asymmetrical burning mode was observed. It is of interest to note that in Test 13, where the fire was positioned under the opening, but at the side (not centrally in the compartment), asymmetric burning was not observed, and the test observations were largely similar to Test 17.

Asymmetric burning was also observed in tests with very large ceiling vents (i.e. 4 vents open), even when the fuel was positioned centrally under the opening. In these instances, the opening was considerably larger than the area (in plan) of the wood crib, so it is easy to visualise the configuration permitting inflow at the ends of the large opening and outflow at the centre of the vent. The rectangular form of the opening (as opposed to square) may promote this, but this cannot be confirmed without further testing.

## DISCUSSION

A common rule of thumb for the onset of flashover in a conventional, side-vented compartment fire is when the temperature at the ceiling reaches about 600°C [1]. This temperature would seem to be critical in ceiling vented compartment fire scenarios as well. When the temperatures (at all heights)

in the compartment were about 500 to 600°C, the compartment could sustain 'fully involved' ghosting fire behaviour for periods of several minutes. This scenario appears to be analogous to post-flashover conditions in conventional compartments, where temperatures are high and the rate of burning is dependent on the inflow of air through the vent. However, unlike side-vented compartments, this mode of burning is not characterised by a rapid increase in heat release rate or the onset of external flaming, rather this mode of burning is characterised by a largely steady HRR, in some instances even a slight reduction in HRR.

When more fuel is present, the temperatures are about 500 to 600°C (and possibly higher), and the pyrolysis rate/HRR is slightly larger, the fully involved fire can exhibit a 'pool fire' behaviour, where external flames are formed at the opening, and are sustained by the mass flow of pyrolysis gases from the fuel and the plentiful supply of air outside the compartment. The observations in these tests are consistent with the results of the first two tests by Chitty and Fraser-Mitchell [23].

It is clear across all tests that 'fully involved' fire behaviour in a ceiling-vented compartment only occurs when the temperatures in the compartment exceed 500°C. Below this limit the fire may simply self-extinguish, or may exhibit pulsing behaviour. Self-extinction may occur while there is a significant concentration of pyrolysis products in the gas phase, this will also be followed by an increase in airflow into the compartment as it cools, which may result in a flammable mixture being formed in the compartment some seconds or minutes after the extinction event. If this occurs while the compartment remains hot enough [24] or if there is a pilot source or residual smouldering present, a smoke explosion could occur. Fire-fighters, in particular, need to be aware of this possibility.

At the outset of this study, it was expected that the pulsing fire behaviour would be observed regularly. However, this is not the case, with the pulsing behaviour only being observed occasionally, for brief moments, and as a transition between other modes of burning. The pulsing mode appears to function as a mechanism for rapidly raising the temperature of the compartment fire, and it may be an indicator of a flashover-like transition from localised burning to the generalised burning behaviours of ghosting and the pool fire mode.

These experiments were carried out at reduced scale. At this scale, the ghosting mode was evident while the HRR was about 10 kW, and the pool fire mode was evident while the HRR was about 15 kW. Assuming these phenomena scale according to conservation of the Froude number [2], the HRR will vary with the compartment scale to the power $^5/_2$. While HRR data were not recorded for the full scale tests of Chitty & Fraser-Mitchell [23], this would suggest that the HRR in those cases was about $6^{5}/_{2} = 88$ times larger than here, so perhaps above 1.3 MW in the cases where external burning was observed, and perhaps below about 880 kW in the third instance, where external burning was not observed. Further testing needs to be carried out to confirm the scalability of these observations.

## CONCLUSIONS

Fully-involved, ceiling-vented compartment fire behaviour has been studied in a reduced scale laboratory compartment. When temperatures are above 500°C, such compartments may exhibit sustained periods of either ghosting flames, when pyrolysis rates are lower, or pool fire behaviour when pyrolysis rates are higher. At temperatures below this a pulsing mode may also exist, but only as a short transient period between other burning modes. An asymmetric burning pattern is only observed with very large ceiling vents or when there is asymmetry between the fuel and the vent.

## ACKNOWLEDGEMENTS

The authors would like to thank the Fire Service Research and Training Trust (FSRTT) for funding of Dr Majdalani. Thanks also to Debbie Smith, Richard Chitty and Sebastian Ukleja, all formerly of BRE Global, for help, advice, access to data and useful discussions. Credit to Prof Albert Simeoni at

WPI for getting this whole project going. Thanks, as always, to Michal Krajcovic for enabling everything that happens in the lab.

## REFERENCES


1 Drysdale, D., (2011), An Introduction to Fire Dynamics (3rd Ed.), John Wiley and Sons

2 Quintiere, J. (2006), Fundamentals of Fire Phenomena, John Wiley and Sons

3 Emmons, H., Vent Flows, Sect. l/Chapter 8, SFPE Handbook of Fire Protection Engineering (1st Edition), SFPE, Boston, pp. 130-138, 1988.

4 Tanaka, T. (2016) Vent flows, Chapter 15 in M.J. Hurley (ed.) SFPE Handbook of Fire Protection Engineering, 5th Edition, DOI: 10.1007/978-1-4939-2565-0_15

5 Epstein, H., (1988), Buoyancy-Driven Exchange Flow Through Small Openings In Horizontal Partitions, Journal of Heat Transfer, 100, pp. 885-893

6 Epstein, M. and Kenton, M., (1989), Combined Natural Convection and Forced Flow through Small Openings in Horizontal Partitions with Special Reference to Flows in Multi-Compartment Enclosures, Journal of Heat Transfer, 111, pp. 980-987.

7 Cooper, L., (1989), Calculation of the Flow Through a Horizontal Ceiling/Floor Vent, Gaithersburg, MD: National Institute of Standards and Technology.

8 Cooper, L., (1994), VENTCF2: An Algorithm and Associated Fortran 77 Subroutine for Calculating Flow Through a Horizontal Ceiling/ Floor Vent in a Zone-Type Compartment Fire Model, Gaithersburg, MD: National Institute of Standards and Technology.

9 Jaluria, Y., and Tan, Q., (1992), Flow Through Horizontal Vents as Related to Compartment Fire Environments, Gaithersburg, MD: National Institute of Standards and Technology.

10 Chow, K., and Gao, Y., (2009), Oscillating Behaviour of Fire-Induced Air Flow Through A Ceiling Vent, Applied Thermal Engineering, 29, pp. 3289-3298.

11 Satoh, K., Lloyd, J. and Yang, K., (1984), Flow and Temperature Oscillations of Fire in a Cubic Enclosure with a Ceiling and Floor Vent, Part III, Report of Fire Research, Tokyo, Japan: Institute of Japan, No. 57.

12 Kerrison, L., Galea, M. and Patel, M., (1998) A Two-Dimensional Numerical Investigation of the Oscillatory Flow Behaviour in Rectangular Fire Compartments with a Single Horizontal Ceiling Vent, Fire Safety Journal 30, pp. 357-382.

13 Takeda, H., (1989), Model Experiments of Ship Fire, 22nd Symposium (International on Combustion), The Combustion Institute, pp. 1311-1317.

14 Tu, K. (1991), An Experimental Study of Top Vented Compartment Fires, Gaithersburg, MD: National Institute of Standards and Technology.

15 Sugawa, O., Kawagoe, K., Oka, Y. and Ogahara, I., (1989), Burning Behaviour in a Poorly-Ventilated Compartment Fire-Ghosting Fire, Fire Science and Technology, 9(2), pp. 5-14.

16 Utiskul, Y., Quintiere, J., Rangwala, A., Ringwleksi, B, Wakatsuki, K. and Naruse, T., (2005), Compartment Fire Phenomena Under Limited Ventilation, Fire Safety Journal 40, pp. 367-390.

17 Li, Q., Zhang, J., and Lu, S, (2013), Influence of Roof Opening on Gas Temperature Rise in an Enclosure, Procedia Engineering, 62, pp. 194-201.

18 Chen, R., Lu, S., Zhang, B., Li, C., and Lo, S., (2014), Correlation of Rate of Gas Temperature Rise with Mass Loss Rate in a Ceiling Vented Compartment, Heidelberg, Berlin: Science China Press and Springer, 59(33), pp. 4559-4567.

19 Zhang, J., Lu, S., Li, C. and Li, Q., (2014a), Fire-Induced Temperature Correlations in Ceiling Vented Compartments, New York: Springer Science.

20 Chen, B., Lu, S., Li, C. and Yuan, M., (2013), Analysis of Compartment Fires with a Ceiling Vent, Procedia Engineering, 62, pp. 258-265.

21 Zhang, J., Lu, S., Li, C. and Yuen, R., (2014b), Vent Location Impacts on Building Compartment Fire under Natural Roof Ventilation, APCBEE Procedia, 9, pp. 360-364.

22 Rodriguez, D., (2012), Fire Dynamics in a Compartment with only a Ceiling Opening, MSc Thesis, Edinburgh: University of Edinburgh.

23 Chitty, R. & Fraser-Mitchell, J. (2015) Compartment sizes, resistance to fire and fire safety project; Final Work Stream Report BD2887 for Work Stream 4 - Fire protection of basements and basement car parks. BRE Report 286858 (D26V1), 24th February 2015. Published by DCLG. https://assets.publishing.service.gov.uk/government/uploads/system/uploads/attachment_data/file/783477/WS_4_DCLG_BD_2887__D26V1__286858_Final_work_stream_4_report.pdf [Accessed September 2019]

24 Wu, C.L. & Carvel, R. (2017) An experimental study on backdraught: the dependence on temperature. Fire Safety Journal, Volume 91, July 2017, Pages 320-326. doi:10.1016/j.firesaf.2017.04.003

# Numerical investigation of the effect of ventilation conditions of Externally Venting Flames on curvilienar geometries.

**Warrier A.[1,2,*], Khan K.[2], Nasriani H.R.[2], Ndlovu S.[2], A. Chamchine[2], Graham T.L.[2], Asimakopoulou E.[2]**

*[1] International College of Engineering and Management, 111 Seeb St, Seeb, Oman.*
*[2] University of Central Lancashire, School of Engineering, Preston PR1 2HE, Lancashire, UK*
**Corresponding author's email: anoop@icem.edu.om*

## ABSTRACT

Façade fires have become increasingly common and when occuring in high rise buildings they are characterized by rapid fire spread. Most of the studies on externally venting flames (EVF) characteristics and testing guidelines concern orthogonal geometries. The aim of the current work is to progress the current state of the art by investigating EVF characteristics and development in non-orthogonal geometries e.g., curvilinear or free form. A numerical investigation is conducted in a curvilinear geometry using a heptane liquid pool fire to investigate the EVF characteristics and factors influencing its development. A parametric study was conducted by altering the ventilation conditions and heat release rate. Six different fire scenarios in curvilinear geometries have been considered to investigate the accuracy of currently available empirical correlations in predicting EVF characteristics. For the considered fire scenarios, velocity, temperature and oxygen concentration spatial distributions are also predicted both in the interior and exterior of the fire compartment. Predicted values enable assessing EVF development and the results indicate that both ventilation conditions and fire load may adversely affect the fire characteristics and impact on the facade.

**KEYWORDS:** Externally venting flames, façade, fire spread, curvilinear geometry, computational fluid dynamics.

## INTRODUCTION

Modern day aesthetics and green building initiatives demand the use of different façade materials and systems, including materials with combustible characteristics, which has resulted in the occurrence of an increased number of façade fires around the world [1, 2]. Those types of fires, also referred to as "Externally Venting Flames" (EVF), are essentially flames and hot combustion products ejecting through compartment openings, aided by bouyancy, when the compartment fire is either in under or well ventilated condition [3]. EVF increase the risk of external flame spread and have a great impact on the fire spread through the building envelope to different storeys but also to adjacent buildings, especially for high-rise buildings [4]. New engineering technologies and advanced manufacturing techniques have enabled the construction of new façade systems, e.g., curved glass façade systems. Further, non-orthogonal, curvilinear or "free-form" geometries are widely used in building façade designs and they pose a significant challenge for the fire safety design of the building as the emphasis on aesthetics many a times results in the use of non conventional building materials which aggravates and enhances the fire spread in such constructions [4]. Though there has been multitude of studies on facade fires in orthogonal buildings, the influence of geometry in the context of non orthogonal geometry upon the spread of fire is least studied. A database of façade fire incidents has been developed as a part of this research to showcase the research need on façade fires. The developed registry capitalized on the previous database developed by Boner et.al., covering fire incidents from 1990-2019 [2, 5]. That registry was further developed to include recent incidents from 2019-2021 that has happened around the globe, based on authenticated data/information received through reliable resources. The analysis of the data has been completed using Microsoft Excel. Based on this data analysis, fire incidents are categorized as per different types of geometries and are presented in Table 1.

**Table 1. Fires classified based on geometry of building involved.**

| No | Geometry of the building | Number of façade fire incidents | % Incidents |
|---|---|---|---|
| 1 | Rectilinear | 48 | 58 % |
| 2 | Curvilinear | 21 | 25 % |
| 3 | Non Orthogonal | 14 | 17 % |

Data analysis indicates that most of the façade fires engulfed multiple stories and that there is a need for increased legal and design regulations, especially in developing countries [4]. Modern architecture and the current construction trend is to build non orthogonal buildings rather than traditionally built rectilinear. From the above fire incident data base, it can be observed that at least 42 % of the buildings involved in high rise building fires were either curvilinear, 25%, or non- orthogonal buildings, 17%. This breakdown came from a total of 83 fires analyzed (1990-2021) [5]. Very limited studies exist for such complex geometries and considering that these buildings account for nearly half the fire statistics, the impact of EVF and fire spread in these geometries warrants further research and study. Fire safety regulations currently being used, do not address the risks associated with the dynamic characteristics of EVF in non-orthogonal geometries [6, 7]. To bridge this knowledge gap, this study aims at investigating the burning behavior of liquid fuel pool fires in curvilinear geometries to help identify the key factors influencing EVF development and their impact on the façade.

## EVF DESIGN METHODOLOGIES

Since the 60's, a significant amount of research has been conducted on EVF geometrical and thermal characteristics initially by Yokoi [8] followed by Webster and Seigel [9]. Based on the above studies Thomas and Law reexamined the experimental data and developed a correlation for EVF height [10]. Further, Law developed a design methodology to assess fire safety of external structural elements based on EVF characteristics, which has been adopted in Eurocode 1 (EC1) [12] considering two distinct ventilation modes, namely No Forced Draught (NoFD) and Forced Draught (FD) [11,12]. If the fire compartment has openings on opposite sides or if additional air is being supplied using other sources, EC1 calculations shall be based on the FD condition and otherwise with the NoFD ventilation condition [12]. Later on, Klopic and Turan studied the effect of ventilation and wind on EVF and its impact on the heat flux at the façade wall focusing on window breakage and suggested the risk of secondary fires [13]. Asimakopoulou et al. investigated various design correlations and concluded that many of them were non-conservative and highlighted the need to improve EVF design methodologies [14]. Most widely used correlations to estimate EVF thermal and geometrical characteristics are presented in Table 2.

**Table 2. Empirical correlations for EVF shape and centreline temperature.**

| EVF | | NoFD | FD | Ref |
|---|---|---|---|---|
| Height | $L_L = \max\left[0; h_{eq}\left[2.37\left[\frac{Q}{A_v\rho_g\left(h_{eq}g\right)^{\frac{1}{2}}}\right]^{\frac{2}{3}} - 1\right]\right]$ | ✓ | | [12] |
| | $L_L = \left[1.366\left(\frac{1}{u}\right)^{0.43}\frac{Q}{A_v^{\frac{1}{2}}}\right] - h_{eq}$ | | ✓ | [12] |
| | $L_L = D_v\left[-1.02 + 0.23\frac{Q^{\frac{2}{3}}}{D_v}\right]$ | ✓ | | [15] |
| Projection | $L_H = \frac{h_{eq}}{3}$ if $h_{eq} \leq 1.25w_t$<br>$L_H = 0.3h_{eq}\left(\frac{h_{eq}}{w_t}\right)^{0.54}$ if $h_{eq} > 1.25w_t$ and window distance$> 4w_t$ | ✓ | | [12] |

| | | | | |
|---|---|---|---|---|
| | $L_H = 0.454 h_{eq} \left(\frac{h_{eq}}{2w_t}\right)^{0.54}$ in any other cases | | | |
| | $L_H = 0.605 \left(\frac{u^2}{h_{eq}}\right)^{0.22} \left(L_L + h_{eq}\right)$ | | ✓ | [12] |
| | $0.13 L_L$ | ✓ | | [8] |
| Width | $w_t$ | ✓ | | [12] |
| | $w_t + L_H$ | | ✓ | [12] |
| Cenerline Temerature | $T_Z = (T_w - T_o)\left\{1 - \left[0.4725 \left(\frac{L_x W_t}{Q}\right)\right]\right\} + T_o$ where $\frac{L_x w_t}{Q} < 1$ | ✓ | | [12] |
| | $T_z = (T_w - T_o)\left\{1 - \left[0.3325 \left(\frac{L_x \sqrt{A_v}}{Q}\right)\right]\right\} + T_o$ where $\frac{L_x \sqrt{A_v}}{Q} < 1$ | | ✓ | [12] |
| | $T_Z = \left\{\left[1 - 0.0027 \left(\frac{lw}{\dot{m}}\right)\right][T_o - T_a]\right\} + T_a$ | ✓ | | [11] |
| | $T_Z = \left\{\left[1 - 0.019 A_w^{\frac{1}{2}} \left(\frac{l}{\dot{m}}\right)\right][T_o - T_a]\right\} + T_a$ | | ✓ | [11] |

EC1 design methodology, based on the work of Law [10], indicates that EVF flame height depends on the Heat Release Rate, HRR, ($Q$), area of all vertical openings ($A_V$), weighted average of the opening height and the external wind speed [12]. Wind speed is an influencing parameter only for FD conditions. Heskestad has not considered FD conditions for the calculation of flame height [15]. EVF projection is considered as distance measured from façade to the flame centreline [12]. The EC1 methodology for calculating the NoFD conditions mainly depends on the opening geometry [12]. However, during FD conditions, flame height and external wind speed are also contributing factors [12]. In Yokoi's correlation, based on open pool fire experiment, flame projection depends only on the flame height [8].

## NUMERICAL SIMULATION

### Description of the geometry

The current study is conducted considering a curvilinear fire compartment made of steel and its schematic is depicted in Fig. 1. The fire compartment has a semi cylindrical shape with 4.4 m length, 4 m wide (at grade level) and maximum height of 3 m. The fire compartment comprises of two equal sized openings on either side of the wall with a 1.1 m width and 2 m height. In order to replicate NoFD and FD conditions, two ventilations modes are simulated. Fig. 1 (right) is a top view the fire compartment with two equal sized openings on opposite walls of the compartment which will facilitate FD conditions, namely Door 1 and Door 2. However, to simulate NoFD conditions, Door 2 remains closed and thus the compartment has only a single opening.

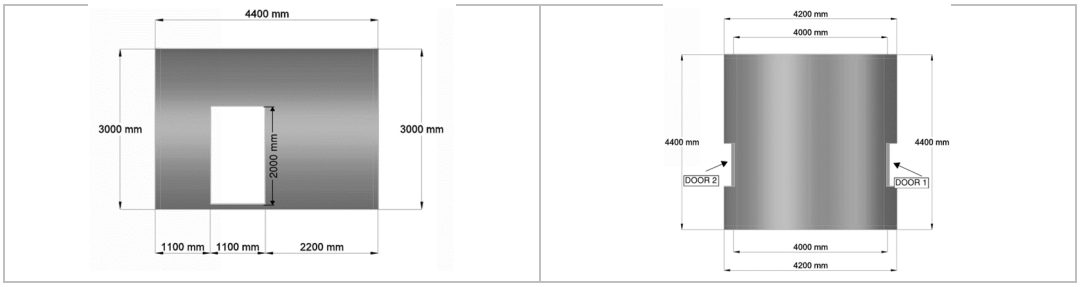


**Fig. 1.** Geometrical configuration of the fire compartment front (left ) and top (right) view.

### Description of the numerical code

The Fire Dynamic Simulator (FDS, Version 6.7.0) is used for the current study to perform the Computational Fluid Dynamics (CFD) simulations [17]. The FDS code, developed by NIST, is a CFD tool capable of studying fundamental fire dynamics and combustion, aimed at solving practical fire

problems in fire protection engineering. A form of the Navier-Stokes equations, appropriate for low-speed, thermally driven flows, emphasizing on smoke production and heat transfer from fires, are numerically solved, using a three-dimensional, Cartesian grid. The core algorithm is a semi-implicit (explicit in velocity and implicit in pressure) predictor corrector scheme that is second order accurate in space and time, by using central differences. The time step is dynamically adjusted in order to satisfy the CFL criterion. Turbulence is modelled using the Large Eddy Simulation (LES) approach for length scales smaller than those that are explicitly resolved on the numerical grid. Thermal radiation is simulated using the finite volume methodology on the same grid as the flow solver. Conjugate heat transfer in solid bodies immersed in the computational domain are simulated by solving an 1-D heat transfer equation in the direction normal to the solid surface; a dedicated non-uniform mesh, independent of the CFD computational mesh, is used for the respective simulations. Multi-layered wall assemblies can be simulated by utilizing detailed thermo-physical properties (e.g. density, thermal conductivity, specific heat) for each material. Solid reactions (e.g. pyrolysis) can be modelled by using appropriate chemical kinetics models. Predictions of the FDS code have been extensively validated [18].

**Computational domain**

As previous studies have revealed [16] the computational domain shall extend at least one hydraulic diameter for such studies. The calculated hydraulic diameter is 1.4 m. However, to capture the geometric and thermal characteristics of the flame more accurately, an increased domain dimension is considered (from the edge of the opening) as depicted in the Fig. 2 below. The domain was extended 2.5 meters in positive and negative X axis for FD Condition from edge of the respective openings on the opposite side of the compartment and 2.5 meters in +ve for No FD, 1.5 meters in +ve and –ve Y Axis for FD and NoFD and 5 meters in +ve Z Axis for FD and NoFD Conditions.

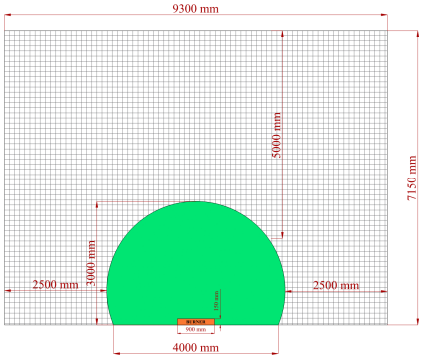


**Fig. 2.** Extended Computational domain

The non-dimensional expression $D^*/dx$ is a measure of how well the flow field is resolved in the simulation of buoyant plumes. Where $dx$ is the size of cells and $D^*$ is the characteristic fire diameter (D*) [17]. The $D^*/dx$ ratio indicates the adequacy of the grid resolution. A higher $D^*/dx$ would mean a better resolution for the simulation of fire, as FDS uses a structured mesh. A grid sensitivity analysis for three different $D^*/dx$ values namely 4 (coarse mesh), 10 (moderate mesh), 16 (fine mesh) was conducted and results for the temporal evolution at 1.8 m height at the centreline of Door 1 are depicted in Fig. 3. The $D^*/dx$ ratio of 16 was found to be the most optimal with a corresponding cell size of 0.07 m. These values enables adequate resolution of plume dynamics and other geometric characterisitcs of the model [17]. The total computational grid consist of 716,958 cubic cells for NoFD and a 963,186 cubic cells for FD conditons. The numerical investigation for both models assumed ambient conditions and an ambient temperature of 40° C.

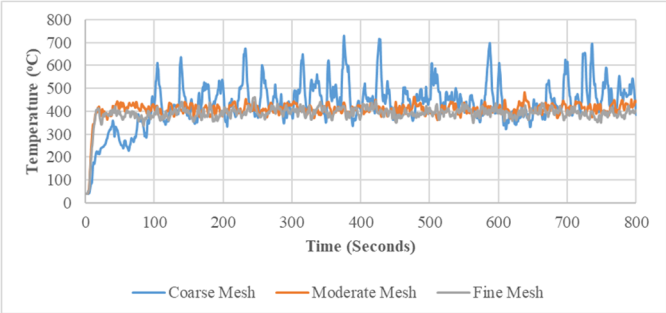


**Fig. 3.** Temporal evolution of the temperature at the centreline of Door 1, 1.8 m height from the ground for the different meshes used.

**Simulation details**

Aiming to investigate the effect of ventilation conditions and fuel load on the development of an EVF from a curvilinear fire compartment, a set of relevant numerical test cases have been chosen. As indicated in Table 3, both NoFD and FD conditions were investigated and a parametric study has been conducting by varying the HRR using 1.5 MW,2 MW and 4 MW fires. A burner size of 0.9 m x 0.9 m x 0.15 m (high) is used at the center of the compartment as depicted in the Fig. 2. All solid surfaces, including walls and floors, are provided with boundary condition with following material properties corresponding to steel, e.g. 7850 kg/m$^3$ density, 0.46 kJ/(kg·K) specific heat, 0.02 m thickness, and emissivity of 0.95. The soot yield, which represents the fraction of heptane fuel mass converted to smoke particulates, is set equal to 0.015 kg/kg and the corresponding CO yield was set equal to 0.006 kg/kg. Six different simulation cases are considered as detailed in the Table 3.

**Table 3. Examined test cases.**

| Simulation Case | Ventilation Mode | Door 1 | Door 2 | HRR (MW) |
|---|---|---|---|---|
| NoFD-1.5 | NoFD | ✓ | N/A | 1.5 |
| NoFD-2.0 | | ✓ | N/A | 2.0 |
| NoFD-4.0 | | ✓ | N/A | 4.0 |
| FD-1.5 | FD | ✓ | ✓ | 1.5 |
| FD-2.0 | | ✓ | ✓ | 2.0 |
| FD-4.0 | | ✓ | ✓ | 4.0 |

**General configuration and measuring locations**

Measuring devices are set up in the numerical model to measure temperature, heat flux on the curvilinear sides of the compartment, to analyze the impact of EVF on the exterior of the compartment. The location of the thermocouples, heat flux meter and velocity devices for this analysis are indicated in Fig. 4.

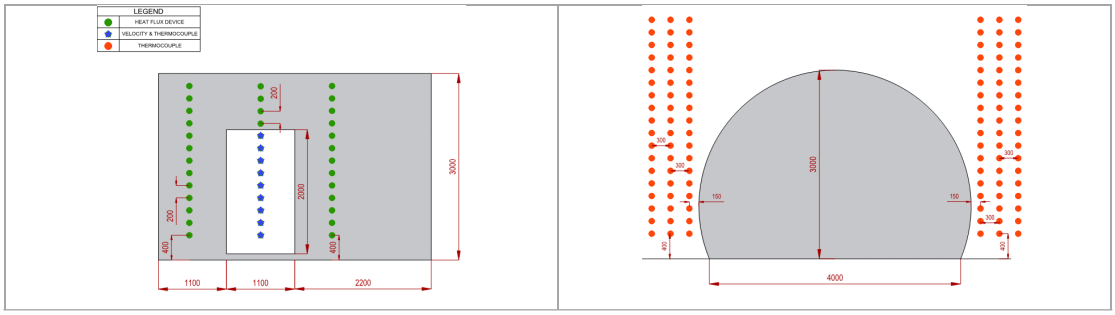


**Fig. 4.** Measuring locations side (left) and front (right) view; dimensions in mm.

## RESULT AND DISCUSSION

### Velocity Flow field

For any fire in a compartment, during its growth phase, the plume developed will impinge on the ceiling and the hot gases including the flame spread out radially through the ceiling and flow out through the available opening(s). However, in compartments with curvilinear geometry smoke movement/flow can be a complex fire dynamic process due to the interaction of turbulence, combustion, radiation etc. with the geometry of the compartment [19]. Similar studies has been conducted in the past with semi cylindrical ceiling in geometries like tunnels, atriums, etc. to understand the smoke flow movement. L Kaihua et.al studied the smoke flow movement in a curvilinear tunnel with various curvatures and revealed that due to the bending wall effect in curved tunnels, the smoke movement is impacted which results in the inconsistency of temperature profile [20].

In this study, ceiling is of curvilienar shape and the fire is seated at the center of the compartment with a constant heat release rate of 1.5 MW, 2 MW and 4 MW, as shown in Fig. 5. As in the case of a rectangular compartment fire, the mass flow entrainment through the bottom half of the opening causes a recirculation zone inside the compartment. However, in the case of FD conditions, a more rigorous and intense mixing of cold air from both side of the compartment opening occurs and results in the formation of two recirculation zones inside the compartment (from both sides) ensuing a more turbulent flow which owes to the higher velocity and high reynolds number of the incoming flow.

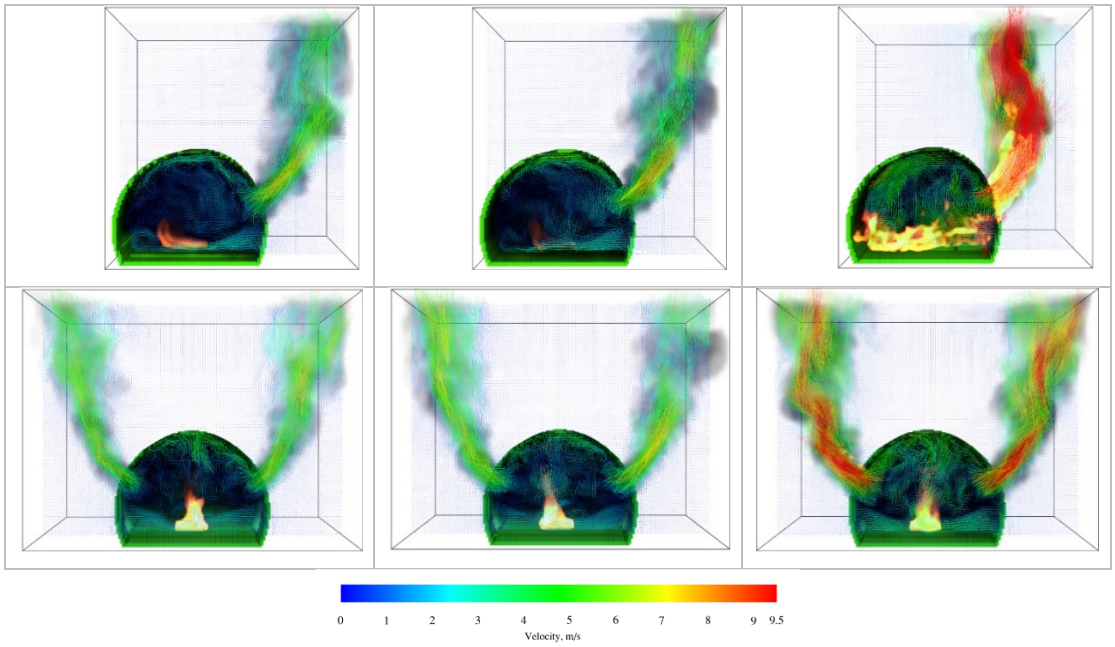


**Fig. 5.** Gas mixture velocity and flame locations predictions for FD-1.5 (bottom left), NoFD-1.5 (top left) FD-2.0 (top middle), NoFD-2.0(bottom middle), FD-4.0 (top right) and NoFD-4.0 (top right) 500 s after fire intiation.

Under NoFD conditons, the plume including the flame can be seen tilting sideways (X direction as seen in Fig. 5, top right) due to the incoming flow of air. However, in the FD conditions the incoming flow from both sides induces a backward tilt of the flame (Y direction as seen in Fig. 5, bottom right). Under NoFD condition a circular flow pattern is visible inside the compartment which is due to the curvilinear ceiling shape and as the incoming flow is from one side.

The maximum velocity recorded in the EVF is 9.5 m/s under NoFD condition. Further to this, it is noticed that due to the curvilinear geometry there are additional recirculation zones formed outside the compartment, next to the opening, pushing the plume outward causing further projection of external plume. At the initial stage of EVF flow, an orderly laminar flow projects out from the opening and continues with a high velocity, outside the opening. External combustion exists as the EVF progresses outside the opening since the reaction is supported by the availability of air. As the flow progresses further up, turbulence starts to develop and once the reaction is completed (this can be analyzed through the oxygen concentration spatial distribution as seen in Fig. 7) the laminar jet turns to a buyancy driven flow.

**Temperature field**

Maximum temperatures were observed at the centreline of the opening approximately at a height of 1.8 m from the floor level and EVF temperature gradually decreased with increasing height and distance from the opening. The temperature increases with respect to height at the interior of the compartment and higher temperature values exist in the ceiling due to the upward flow movement and an increased temperature in the range of 790° C is observed for the cases of higher HRR (4 MW).

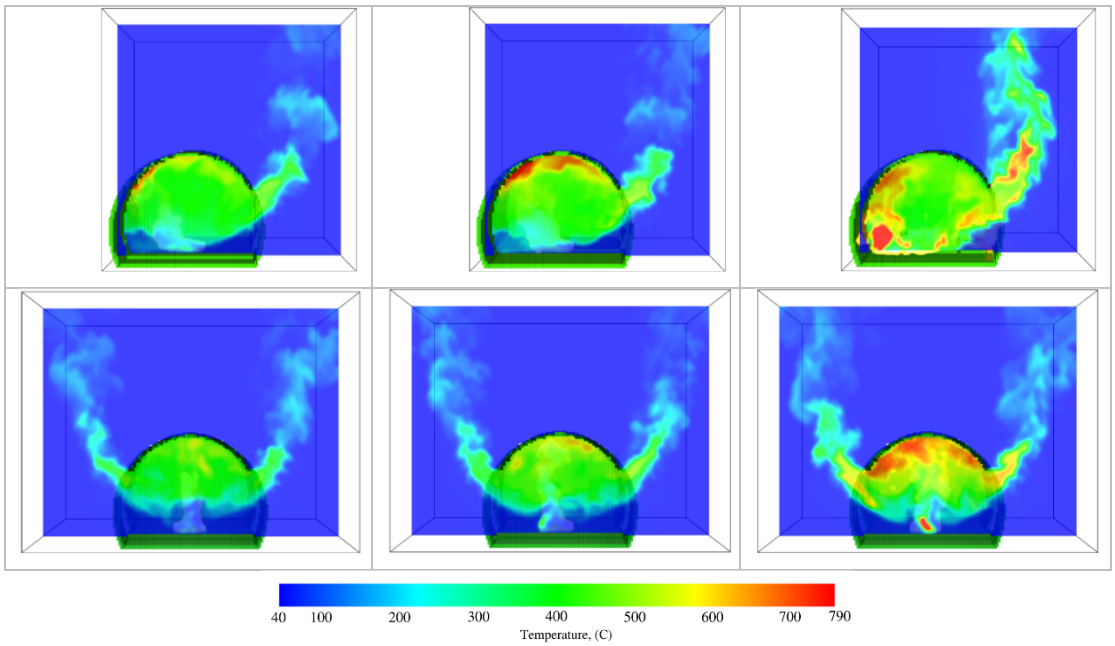


**Fig. 6.** Spatial distribution of gaseous temperature 500 s after fire initiation for FD-1.5MW (bottom left), No FD-1.5MW (top left) FD-2.0 MW (bottom middle), NoFD-2.0MW(top middle) and FD-4.0 MW (bottom right), NoFD-4.0MW (top right).

The maximum temperature distribution is observed under NoFD conditions with 4 MW fire (Fig. 6, top right), after 10 seconds of fire intiation, where a clear stratification of hot and cold layer inside the compartment and a transient increase in temperature with respect to height. Following this, an increase in the volume of hot upper layer and larger volume of unburned gas flows out in the exterior domain forming larger EVF and a stronger buoyant plume. It is important to note that as the plume further goes up, the EVF temperature decreases with respect to the height. At 500 s after the fire initiation, a clear division of hot and cold layer can be seen at the interior of the compartment for the case of FD condition whereas the separation of hot and cold layer are no longer visible in NoFD where a well mixed layers of hot gases is sustained. Under NoFD conditions higher temperature ranges are observed.

### Oxygen Concentration

Figure 7 depicts the spatial distribution of oxygen concentration inside the compartment 500 s after fire initiation. A lesser concentration of oxygen is observed during NoFD conditions compared to FD conditions. As stated above, similar to the temperature field, there is a clear distinction of hot and cold zone in FD conditons which is attributed to the incoming flow of cold air from both openings.

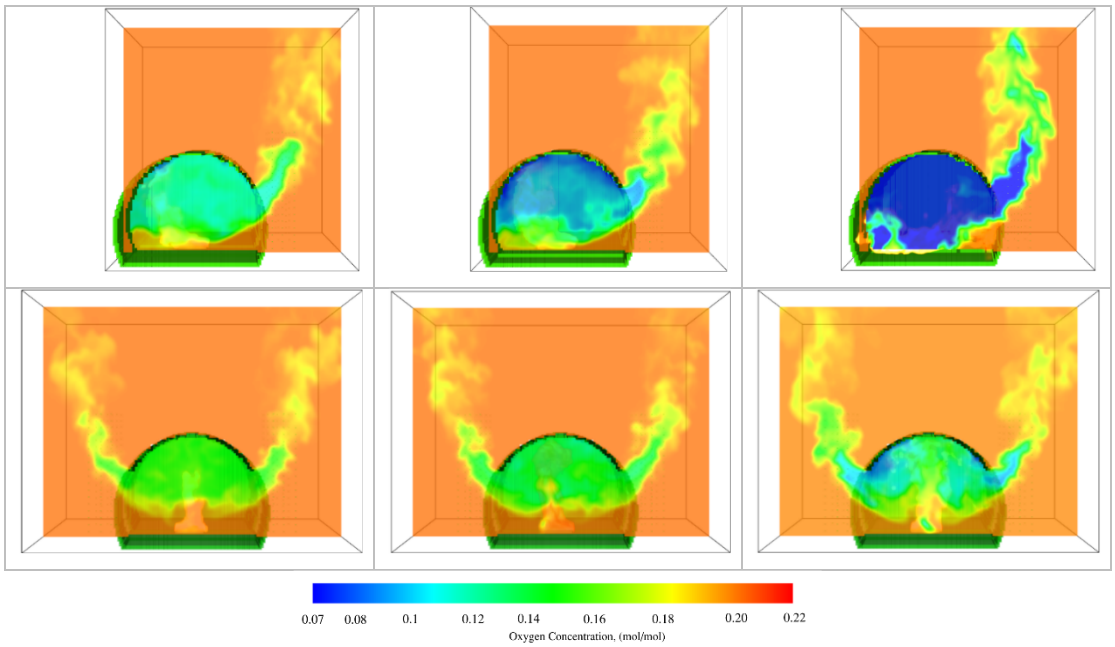


**Fig. 7.** Spatial distribution of oxygen concentration 500 s after fire initiation for FD-1.5MW (bottom left), No FD-1.5MW (top left) FD-2.0 MW (bottom middle), NoFD-2.0MW(top middle) and FD-4.0 MW (bottom right), NoFD-4.0MW (top right).

### Validation of Numerical Result with Engineering Correlation.

Table 4 below depicts the calculated values based on the correlations as illustrated in Table 2. Note that the calculation methodologies for FD conditions are based on a wind speed of 0.1 m/s. EVF centerline temperature is calculated with an axis length from window, $L_x$ equal to 1.5 m and this applicable to all cases. Under FD conditions with higher HRR values (2 MW and 4 MW) EC1 design methodology falls beyond the range of applicability for the calculation of centerline temperature. This is mainly because centre line temperature equation specified in EC1 for FD condition is not in the range of applicability, $\frac{L_x\sqrt{A_v}}{Q} < 1$ for HRR of 2 MW and 4 MW, as the calculated value is more than 1.The EVF flame height for No FD Conditions showed varying values for different HRR. For NoFD condition with 1.5 MW EC1 values were in agreement with numerical results whereas in 2 MW, EVF was showing fluctuating/pulsating results in the numericla simulations. While considering the mean flame height, an approximate value of 1 m is observed and this is consistent in correspondence to the EC1 value of 0.81 m. However, the maximum flame height is in the range of 3 m for this case. For 4 MW, EC1 value of 2.9 m was an underprediction compared to the consistent flame height of 6 m appeared on FDS.

Under FD conditions, in all three cases, EC1 values overestimated the numerical results. Under 4 MW numerical cases, the flame height which appeared on both sides of the opening corresponded to 3 m compared to an EC1 value of 5 m. Comparing numerical results with Heskestaad correlation, it can be generally seen that Heskestaad values were also on the increased side compared to the FDS results, except in NoFD with 4 MW fire where the values are found to be in good agreement. The analysis of EVF Width

in NoFD indicates that 1.5 MW and 2 MW shows good agreement between FDS values and EC1 which corresponds to the actual door width of 1.1m. However, the 4 MW fire shows an increased flame width. In FD condition EC1 values were on a increased side compared to the FDS results. Finally, the EVF Projection analysis demonstrates that for all cases, including FD and NoFD ventilation conditions, FDS predicts higher values than the engineering correlations of EC1 and Yokoi.

**Table 4. EVF geometrical characteristics according to empirical correlations.**

| Cases | Height (m) | | Projection (m) | | Width (m) | Centr. Temperature (K) | |
|---|---|---|---|---|---|---|---|
| | EC1[12] | Heskestad[15] | EC1[12] | Yokoi[8] | EC[12] | EC1[12] | FDS [c.work] |
| NoFD-1.5MW | 0.32 | 3.16 | 0.86 | 0.04 | 1.10 | 593.80 | 515.25 |
| NoFD-2.0MW | 0.81 | 3.68 | 0.86 | 0.10 | 1.10 | 714.80 | 540.40 |
| NoFD-4.0MW | 2.91 | 5.22 | 0.86 | 0.37 | 1.10 | 986.10 | 900.20 |
| FD-1.5MW | 0.62 | 2.04 | 0.50 | 0.08 | 2.56 | 534.00 | 543.45 |
| FD-2.0MW | 1.50 | 2.56 | 0.66 | 0.20 | 2.84 | NR | 553.34 |
| FD-4.0MW | 5.00 | 4.10 | 1.32 | 0.65 | 3.52 | NR | 663.42 |

*NR – Not in Range.

## EVF TEMPERATURE ANALYSIS

The gas mixture temperature formed outside the compartment was measured during the fully developed phase of the fire, the vertical distribution of the temperatures of the final 100 s of the simulations are shown on Fig. 8. The total simulation run time for both ventilation mode cases was 900 s, which was chosen to ensure the fire is fully evolved in the compartment and reached relatively steady state. A comparative analysis is only possible for FD conditions for 1.5 MW fire, which indicates that the EC1 methodology and numerical results have similar patterns. The EC1 design methodology results at lower heights have increased values that gradually decrease as the height increases. It is important to note that comparison is not possible for other FD cases with higher HRR (2 MW and 4 MW) as the EC1 design methodology falls beyond the range of applicability of the engineering correlation for centerline temperature. However, under NoFD condition all three cases were compared which indicates that EC1 values predict an increased temperature when compared to the numerical results as depicted in Fig. 8 (right). This necessitates further validation using experimental analysis.

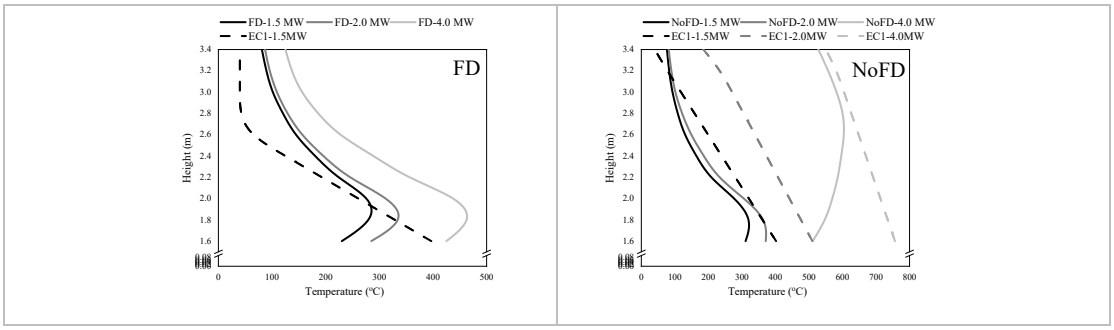


**Fig. 8.** Vertical distribution of averaged temperature at the exterior of the fire copmartment; effect of oventilation conditions FD (left) and NoFD (right).

## CONCLUSION.

EVF thermal and geometric characteristics in curvilinear geometry are analysed in the current study and comparisons are made with available engineering design correlations. Engineering correlations used to calculate EVF geometrical characteristics for FD conditions such as flame height and width were found to be on the conservative side when compared with numerical results. However, under NoFD cases with higher HRR EVF design methodologies tend to under predict the flame height values. For increased

HRRs, EC1 correlations are not in the range of applicability and thus comparison is not possible. Similarly, EVF centerline temperatures were also found to be on the conservative side for all ventilation conditions with varying HRR when compared with numerical results. It is identified that, further validation is necessary to substantiate this study. Authors plan to perform large scale experiments with well documented conditions to deepen the understanding of façade fire development in curvilinear geometries and further validate the presented numerical results.

## REFERENCES


[1] E. Asimakopoulou, D. Kolaitis, M. Founti, Performance of a ventilated-façade system under fire conditions: An experimental investigation, Fire Mater. 44(6) (2020) 776-792.

[2] M. Bonner, W. Wegrzynski, B. Papis, G. Rein, KRESNIK: A top-down, statistical approach to understand the fire performance of building facades using standard test data, Building Environ 169 (2020) 106540.

[3] L. Hu, Z. Qiu, K. Lu, F. Tang, Window ejected flame width and depth evolution along façade from under-ventilated enclosure fires, Fire Safety J. 76 (2015) 44-53.

[4] N. White, M. Delichatsios, Fire hazards of exterior wall assemblies containing combustible components, first ed., Springer Briefs in Fire, Springer, New York, 2014.

[5] M. Bonner, G. Rein, List of Facade Fires 1990-2020, 2020.

[6] E. Asimakopoulou, K. Chotzoglou, D. Kolaitis, J. Zhang, M. Delichatsios. Numerical investigation of externally venting flame characteristics in a corridor-façade configuration, Fire Safety J. 110 (2019) 102912.

[7] D. Kolaitis, E. Asimakopoulou, M. Founti, Fire behaviour of gypsum plasterboard wall assemblies: CFD simulation of a full-scale residential building, Case Studies in Fire Safety 7 (2017) 23-35.

[8] S. Yokoi, Study on the prevention of fire-spread caused by hot upward current, BRI Report 34.,1960.

[9] L. Seigel, The projection of flames from burning buildings. Fire Technol, 5(1) (1969) 43-51.

[10] P. Thomas, M. Law, The projection of flames from burning buildings. Fire Research Station., 1972.

[11] M. Law, T. O'Brien, Fire safety of bare external structural steel, The Steel Construction Institute, SCI Publication 009, 1989.

[12] EN 1991-1-2, Eurocode 1: Actions on Structures, Part 1-2 – General Actions – Actions on Structures Exposed to Fire, European Committee for Standardization, Brussels, Belgium, 2002.

[13] S. Klopovic, O. Turan, A comprehensive study of externally venting flames—: Part II: Plume envelope and centre-line temperature comparisons, secondary fires, wind effects and smoke management system. Fire Safety J, 36(2), (2001) 135-172.

[14] E. Asimakopoulou, D. Kolaitis, M. Founti, Assessment of fire engineering design correlations used to describe the geometry and thermal characteristics of Externally Venting Flames. Fire technol 53 (2017) 709-739.

[15] G. Heskestad, Virtual origins of fire plume. Fire Safety J 5(2) (1983) 109–114.

[16] X. Zhang, M. Yang, J. Wang, Y. He, Effects of computational domain on numerical simulation of building fires, J Fire Prot Eng 20 (2010) 225-250.

[17] K. McGrattan, S.Hostikka, J. Floyd, R. Mcdermott, M. Vanella, Fire Dynamics Simulator User's Guide, 6th Edition, National Institute of Standards and Technology, 2020.

[18] K. McGrattan, S. Hostikka, J. Floyd, R. Mcdermott, M. Vanella, M., Fire Dynamics Simulator Technical Reference Guide Volume 2: Verification, NIST Special Publication 1018-2, 6th Edition, National Institute of Standards and Technology, 2020.

[19] W. Feng, W. Mingnian, C. Ricky, W. Yu., Numerical study on fire smoke movement and control in curved road tunnels. Tunn Undergr Space Technol 67 (2017) 1-7.

[20] L. Kaihua, X. Kaihua, S. Congling, Y. Manjiang, W. Jie, D. Yanming., Investigation On The Tunnel Curvature Effect Upon The Ceiling Temperature Of Tunnel Fires: A Numerical Simulation. Fire technol 57 (2021) 2839-2858.

# Blow-off of Fuel Jet Flames in the Atmosphere

**Adriana Palacios[1], Derek Bradley[2], Longhua Hu[3,*]**

[1]*Universidad de las Americas, Puebla, Department of Chemical, Food and Environmental Engineering, Puebla, Mexico.*

[2]*University of Leeds, School of Mechanical Engineering, Leeds, UK.*

[3]*State Key Laboratory of Fire Science, University of Science and Technology of China.*
**Corresponding author's email: hlh@ustc.edu.cn*

## ABSTRACT

Further data from experiments with the atmospheric burning of jet fuels, particularly their blow-off and flame quenching characteristics, have been collected and interpreted. These are characterised in terms of both their dimensionless Flow Number and Flame Thickness. Regimes of Lifted Flames, Flame Blow-off, Choked Flow and Flame Quench have been defined by these Dimensionless Groups. New data are presented for a variety of hydrocarbon and ammonia-hydrogen fuels. New techniques are required for the assessment of the latter, including derivation of their acoustic velocities and the characterisation of their laminar flames, including burning velocity and flame thickness. It is possible to create $NH_3$+$H_2$ jet flow blends with burning rates and blow-off velocities closer to those of hydrocarbons than of $H_2$. The properties of individual fuels are displayed in terms of the fuel velocities at which blow-off occurs for different pipe diameters. The properties of individual fuels displayed in this way show a greater diversity than is evident from the dimensionless groups. Similarities are drawn between premixed and jet flow flame quenching. Blow-off velocities from a pipe of 3 mm diameter display an approximate correlation with the heat release rates of the flames just prior to blow-off.

**KEYWORDS:** Blow-off; Jet flames; Hydrogen-ammonia; Hydrocarbons.

## NOMENCLATURE

$a$ acoustic velocity at pipe exit plane (m/s)
$C_p$ specific heat at constant pressure (kJ/kmole·°C), at $T$ or (J/kg·K), at $T^v$
$Cv$ specific heat at constant volume (kJ/kmole·°C), at $T$
$D$ pipe diameter (m) or (mm)
$k$ thermal conductivity (W/m·K) at $T^v$
$M$ Mach number at pipe exit plane, ($u_i/a_j$)
$MW$ Molecular weight (kg/kmol)
$P_a$ atmospheric pressure (Pa)
$P_i$ initial stagnation pressure (Pa)
$R$ mass specific gas constant equal to the Universal Gas constant of 8314 J/kmol·K
$S_L$ maximum laminar burning velocity of the fuel air mixture at ambient atmosphere (m/s)
$T$ ambient temperature (K)
$T^v$ temperature at inner layer of laminar flame (K)
$u$ fuel flow velocity at exit plane of burning jet fuels supply pipe (m/s)
$U^*$ dimensionless Flow Number for choked and unchoked flow, $(u_i/S_L)\ (\delta_k/D)^{0.4}(P_i/P_a)$
$U_b^*$ $U^*$ value at blow-off
$X$ molar fraction
$X_a$ ammonia fuel molar fraction in the fuel mixture

**Greek**

$\delta_k$ flame thickness, $(k/C_p)_{To}/\rho_u S_L$ (m), Eq. (1)
$\gamma$ ratio of specific heats
$\rho$ density (kg/m$^3$)

**Subscripts**

$a$ ambient conditions
$b$ blow-off conditions
$i$ initial stagnation conditions
$u$ unburned gas
$1$ gas 1
$2$ gas 2

## INTRODUCTION

The paper deals with the blow-off of atmospheric jet flames from the end of fuel pipes, usually of circular cross-section. The origins of the work are the culmination of both lengthy mathematical

modelling of fuel flame blow-off, and compilations of the experimental data of the phenomena. In [1] a dimensionless flow number, $U^*$, is introduced, with which jet flame heights and lift-off distances have been correlated. The fuel blow-off velocity, $u$, is that of the gaseous fuel at the exit plane of the pipe, ahead of the flame. A dimensionless Flow Number, $U^*$, was defined by:

$$U^* = (u/S_L)\ (\delta_k/D)^{0.4}(P_i/P_a). \quad (1)$$

Fuel properties are expressed through its maximum laminar burning velocity with air, $S_L$, and its laminar flame thickness, $\delta_k$, normalised by the pipe diameter, $D$. Hydrogen and hydrocarbon thermo-physical and isentropic expansion data were obtained from the GasEq Code [2].

The inclusion of $S_L$ arose as a consequence of the computations showing that after fuel/air mixing in the fuel jet, reaction was predominantly in the most reactive zone, where the mixture had a laminar burning velocity, close to its maximum value [1]. For the avoidance of flame quenching, the ratio, $\delta_k/D$, must be sufficiently small. The approach of Göttgens et al. [3] was employed, in the derivation of $\delta_k$. This involved identifying an inner layer temperature, $T^o$, below which, no reaction occurs.

In the expression for $U^*$ the initial stagnation to exhaust pressure ratio, $(P_i/P_a)$, arising from the exit plane fuel velocity, $u$, is given by:

$$(Pi/P_a) = [(M^2(\gamma - 1) + 2)/2]]^{\gamma/(\gamma - 1)}. \quad (2)$$

In the case of mixed fuels, the physico-chemical parameters are those of the fuel blend. The filled black filled circular symbols in Fig. 1 are of $CH_4$+$H_2$ blends. In a study of hydrogenation of natural gas burners $S_L$ values of such blends were obtained experimentally [4].

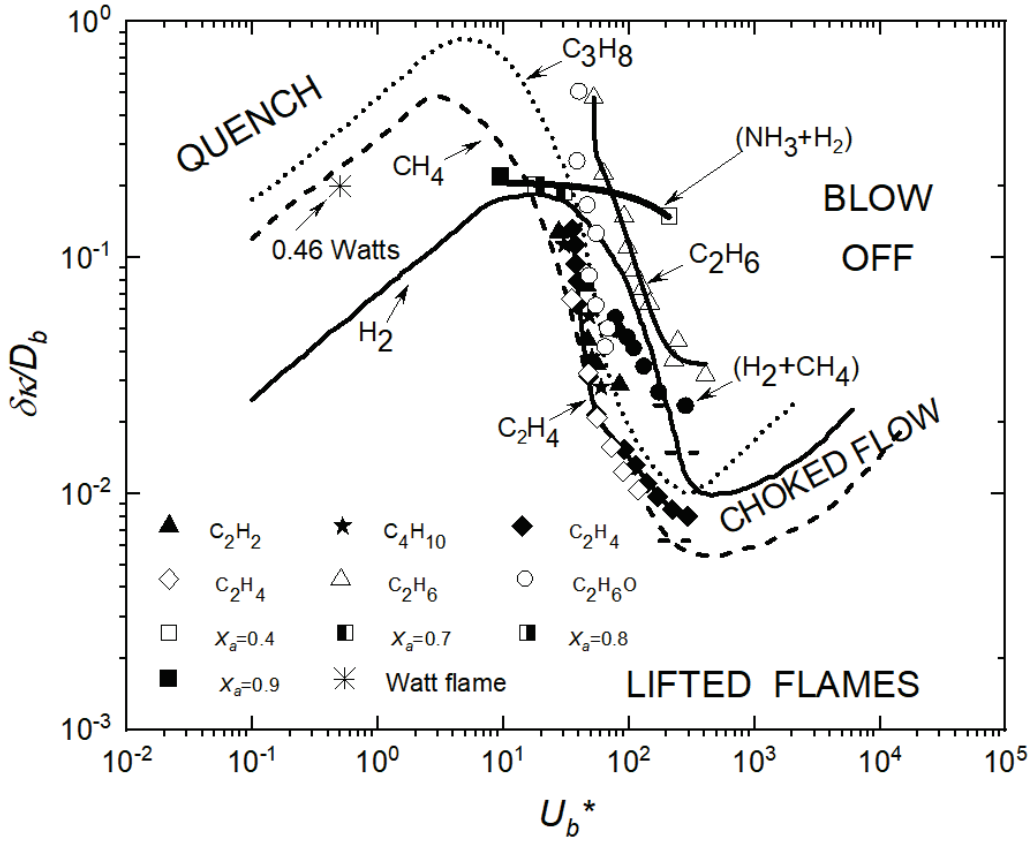


**Fig. 1.** Regimes of jet flame combustion of different fuels. The new data points are indicated by open symbols and, for $NH_3$+$H_2$, with variably filled squares.

In [5] a general correlation of flame Blow-off and Quench, is expressed in terms of $U^*$ and $\delta_k/D$. This is demonstrated by the past and present experimental results in Fig. 1. A sufficiently high fuel velocity will lift the flame well clear of the burner, and it will then blow-off. This upper regime of Flame Blow-off is indicated, as also can be the lower one of Lifted Flames. The Blow-off boundary is indicated by the value, $U_b^*$, which separates the regimes. Sonic fuel velocities can arise at the exit plane.

On the upper left of the diagram is another regime, of significantly lower fuel velocities. This is bounded by a solid surface, at which Flame Quenching can occur. This arises when an excessive proportion of the heat release rate is lost to the pipe. This loss increases with a diminution in pipe diameter, $D$, with the result that, with increasing $\delta_k/D$, flame quenching eventually occurs. However the Quench boundary is not as well defined as the Blow-off boundary. The Quench and Blow-off Boundary curves for $C_3H_8$, $CH_4$, and $H_2$, all form a continuum, tracing the transition from the onset of quenching to the development of Blow-off. It will be shown that heat release rates, measured at blow-off show an almost 10-fold variation, depending upon the propensity of the flame to extinction. This was found to be similar to that occurring for similar flames under premixed conditions [6].

## NEW DATA

The present paper introduces new data from the additional fuels into Fig. 1. Experimental data points, from a variety of sources, have been correlated in the course of the present study, and the ranges of results appear in Table 1, as well as in Fig. 1. These new data points for the new fuels are indicated by the open symbols, and by variably filled squares for ammonia/$H_2$. Ethane [7], propane [5] and hydrogen [5] data yielded somewhat higher values of $U_b^*$, while those for ethylene [7], and dimethyl ether [7] are somewhat lower. New burner diameters range between 0.1 and 14 mm. The ammonia-hydrogen mixtures [8] had $NH_3$ fuel mole fractions, $X_a$, of 0.4, 0.7, 0.8, 0.9. These are indicated by square symbols. If the ammonia proportion is rather low, the square is empty, if it is moderately low the left half is black, if moderately high the right half is black and if it is very high, it is completely black. Table 1 shows the ranges of the different new measurements.

**Table 1. New experimental data for the derivation of values of $U^*$ and $\delta_k/D$.**

| Author (Year) [Reference] | Fuel | Pipe Diameter ($D$), mm | Blow-Off Velocity ($u$), m/s |
|---|---|---|---|
| Um et al. (2013) [8] | Ammonia-Hydrogen | 2.7 | 15 – 125 |
| Stamps and Tieszen (2014) [7] | Ethane | 1 – 14 | 29 – 329 |
| Stamps and Tieszen (2014) [7] | Ethylene | 1 – 6 | 75 – 310 |
| Stamps and Tieszen (2014) [7] | Dimethyl Ether | 1 – 12 | 23 – 95 |

## TREATMENT OF (NH3+H2) MIXTURES

As a fuel, $NH_3$ has poor flammability, with a maximum atmospheric laminar burning velocity of only about 0.06 m/s, which compares with a value of about 2.9 m/s for hydrogen. However, $NH_3$ is very effective as a liquefying agent for hydrogen. The stored energy density capabilities of liquified $NH_3$+$H_2$ are higher than those of, both batteries and hydrogen, alone [9]. With 40% $NH_3$ as a fuel with $H_2$, the laminar burning velocity has a more practical value of 0.8 m/s.

Um et al. [8] have measured the lift-off and blow-off jet velocities, $u$, of ($NH_3$+$H_2$) blends, for different $NH_3$ fuel fractions, $X_a$, in the range between 0 and 1, from a pipe of 2.7 mm diameter, $D$.

The necessary maximum laminar burning velocities of the fuel mixture, $S_L$, were obtained from the computed laminar burning velocities of Lhuillier et al. [10], again for different fractions of $NH_3$ in ($NH_3$+$H_2$) mixtures, at the different equivalence ratios. Flame thicknesses, in the absence of any guidance from [3], were taken from the generalised values collated by Lee et al. in [11]. Here, some computed values of the flame thickness are presented as a function of equivalence ratio and the stoichiometric fraction of the ammonia. It was necessary to extrapolate the given data to the present conditions. As the ammonia fraction in ($NH_3$+$H_2$), increased from 0.4 to 0.9, the laminar flame thickness, $\delta_k$, increased from 0.4 to 0.6 mm. Rather tentative, values enabled the ($NH_3$+$H_2$) blow-off data of Um et al. [8] to be plotted in Fig. 1. More blow-off data over wider ranges of $NH_3$/$H_2$ blends and jet diameters are required to make this plot more definitive.

Evaluation of $P_i/P_a$, from Eq. (2), requires appropriate values of acoustic velocities, $a$, for the different ammonia-hydrogen concentrations, in order to determine the Mach number in the equation. Here the procedures followed those of Dixon and Greenwood [12]. For a single specie, the acoustic velocity is found from:

$$a = (\gamma RT)^{0.5}, \quad (3)$$

with a value of $R$ given by 8314 J/kmol·K, divided by the average molecular weight of the $NH_3$+$H_2$ mixture. The value of $\gamma$, the ratio of specific heats, is obtained for the mixtures of gases from the expression in [11]:

$$\gamma_{mixture} = \frac{Cp_1 \cdot X_1 + Cp_2 \cdot X_2}{Cv_1 \cdot X_1 + Cv_2 \cdot X_2}. \quad (4)$$

Here $C_p$ and $C_v$ are the specific heats at constant pressure and volume (J/kg·K), respectively, of the gases 1 and 2. Values of $Cp$ and $Cv$ were calculated at 25°C and 1 atm, for pure $H_2$ and pure $NH_3$, using the software, following Aspen-Hysys V10® [13]. These results, together with other data used for the calculation of $a$, through Eqs. (3-4), are shown in Table 2. These values were substituted into Eq. (4) to yield $\gamma$ values for the $NH_3$+$H_2$ mixtures, for the different $NH_3$ and $H_2$ molar fractions, $X_{NH3}$ and $X_{H2}$ in the experiments.

**Table 2. Data used in Eqs. (3)-(4), obtained from the software Aspen-Hysys V10®** [13].

| **Fuel** | ***Cv*** **(kJ/kmole·°C)** | ***Cp*** **(kJ/kmole·°C)** | $\gamma$ | ***MW*** **(kg/kmol)** | ***a*** **(m/s)** |
|---|---|---|---|---|---|
| Ammonia | 27.41 | 35.69 | 1.3 | 17.03 | 437 |
| Hydrogen | 20.11 | 28.42 | 1.4 | 2.016 | 1314 |

The low ammonia concentration acoustic velocity for a particular $NH_3$+$H_2$ mixture, was found from Eq. (3). The calculated value of $\gamma$ for the particular mixture was substituted into Eq. (3), together with the ambient temperature, $T$ = 298.15 K, together with the value of $R$, which was then divided by the average molecular weight of the $NH_3$+$H_2$ blend. The highest ammonia blended fuel velocities were with $X_a$=0.4, with the maximum proportion of $H_2$. This gave a maximum value of $P_i/P_a$ value of 1.03. With maximum $NH_3$, at $X_a$=0.9, and $P_i/P_a$=1.0006.

## BLOW-OFF VELOCITIES FOR DIFFERENT FUELS AT DIFFERENT PIPE DIAMETERS

Much detailed information concerning the blow-off of different fuels is concisely embodied within the dimensionless Blow-off relationships of Fig. 1. To demonstrate some of the marked practical differences between fuels with regard to blow-off, the blow-off velocities at different pipe diameters were accessed. Each specie retains its thermophysical properties. Values of $U^*$ on the generalised

curve and the corresponding values of $\delta_k/D$ are noted. From the appropriate physico-chemical properties, $S_L$, $\delta_k$, and $a$, the selected pairs of dimensionless groups yielded the fuel blow-off velocities, $u$, at the different values of pipe diameter for blow-off, $D$. Figure 2 shows the plots of the values of $u$ against $D$ for $H_2$, and also for three values of ($NH_3$+$H_2$), for different fractions of ammonia in the ($H_2$+$NH_3$) fuel mix.

Striking aspects are the high blow-off velocities that are attained with $H_2$. These contrast with the much lower values with the $NH_3$+$H_2$ mixture. Hydrogen flames can be sustained on exceptionally small diameter burners, whilst being able to operate with high velocities on higher diameter burners.

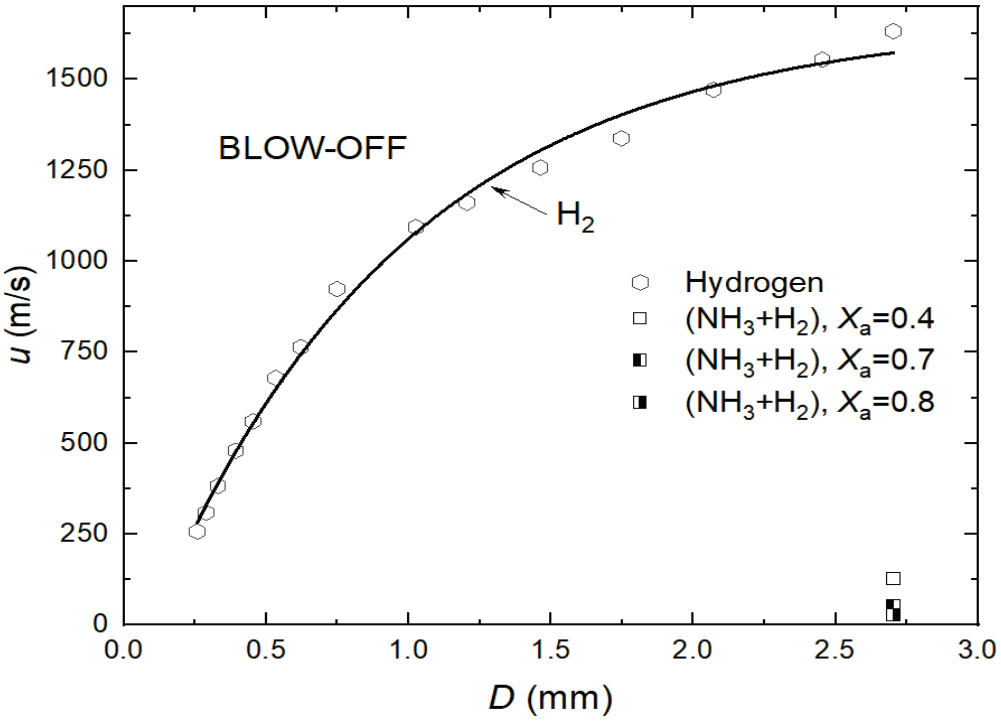


**Fig. 2.** Blow-off velocities and pipe diameters for $NH_3$+$H_2$ ($X_a$ = 0.4-0.8) and hydrogen jet flames.

It can be seen from Fig. 3 that ethane and ethylene require higher diameter burners to sustain blow-off velocities, in both instances, of up to 300 m/s. Interestingly, in the case of ethane, at the lower values of $D$, the ($NH_3$+$H_2$) blends can attain similar jet velocities. With the relatively high proportion of $H_2$ at $X_a$=0.4, the blow-off velocity is relatively high and closer to that of ethylene than the ethane values. With the higher $NH_3$ content of $X_a$=0.7, the blow-off velocity is reduced, but is still close to that of ethane in Fig. 3, and might remain at larger values of $D$. The $NH_3$+$H_2$ blend, although limited experimentally in the present study, by just a single-valued $D$, has a greater affinity with the two hydrocarbons than with $H_2$, see Fig. 3.

The performance of the two paraffins, $CH_4$ and $C_3H_8$, shown in Fig. 4, might be regarded as robust, even down to moderately small pipe diameters. This trend continues with the butane characteristics, shown in Fig. 5, but the more complex molecular structure of Di-methyl ether leads to a smaller fuel velocity, that requires a greater pipe diameter.

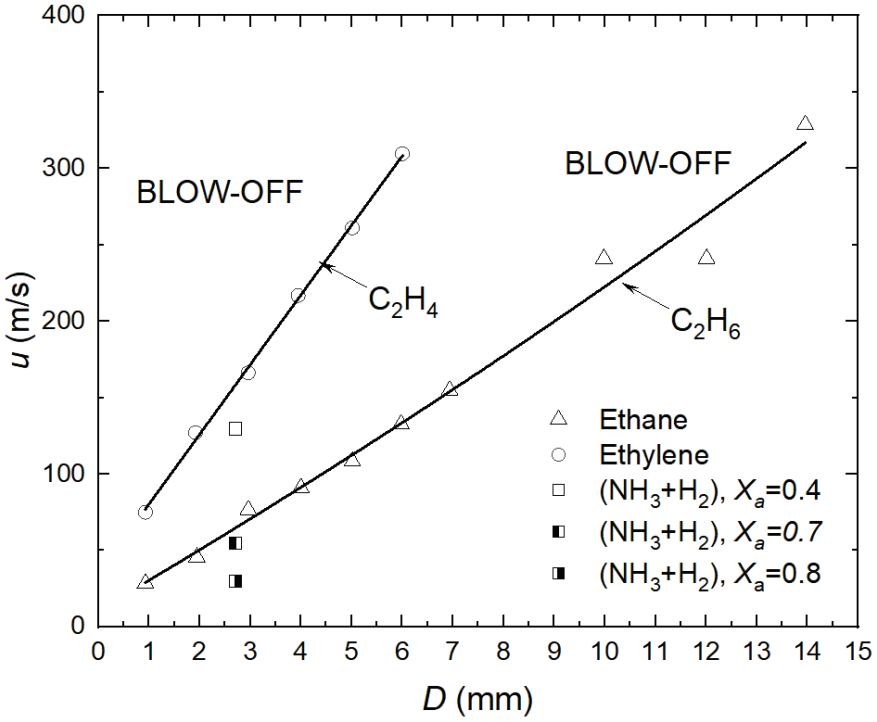


**Fig. 3.** Fuel jet flame Blow-off velocities, at different pipe diameters, for ethane, ethylene, and ($NH_3$+$H_2$) blends.

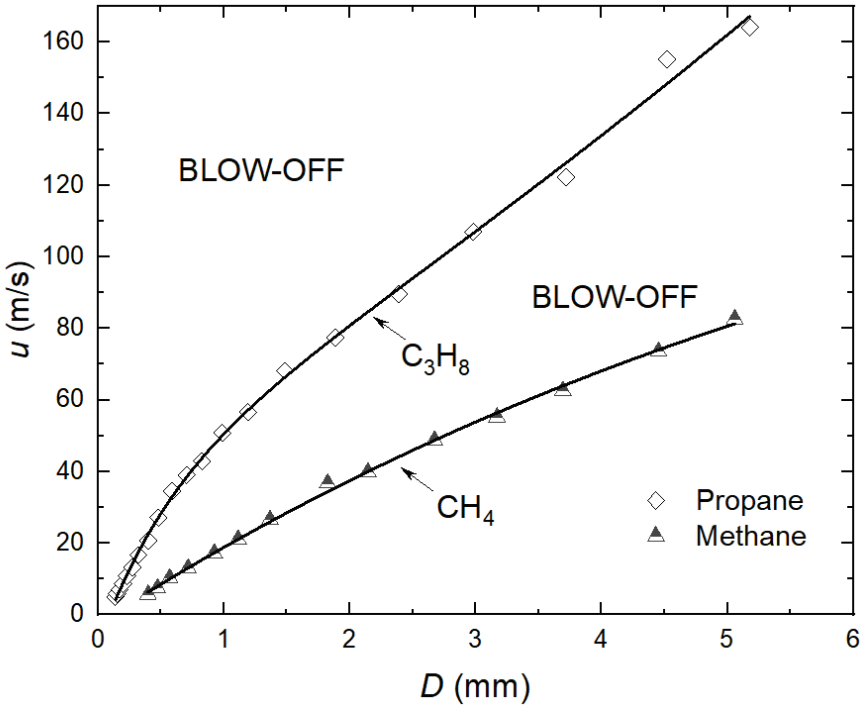


**Fig. 4.** Fuel jet flame Blow-off velocities at different pipe diameters for methane and propane jet flames.

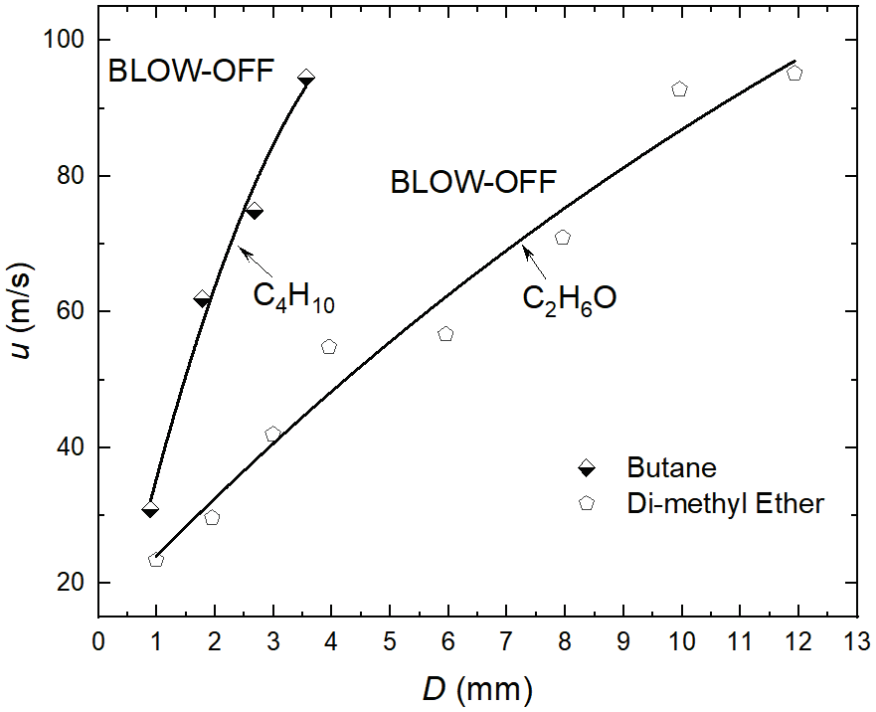


**Fig. 5.** Fuel jet flame Blow-off velocities at different pipe diameters for butane and Di-methyl ether jet flames.

## DISCUSSION

### Differences between Fuels

Figures 2 to 5 display a greater diversity in the different fuel characteristics than is apparent from Fig. 1. This is confirmed by Table 3, which, from these data collates seven of the blow-off velocities, *u*. All are from a pipe of 3 mm diameter, and present the associated jet flame heat release rate, just prior to blow-off. Such jet flames can arise in a variety of circumstances, on burners, engines and flares. There is almost a hundred-fold range in heat release rates in Table 3. It is of interest that blow-off velocities from a 3 mm diameter pipe give an indication of practical heat release rates of different fuels. The lower values tend to be associated with the larger, more complex, molecules, and the highest values are with hydrogen.

**Table 3. Velocities of different fuels just prior to blow-off, and the power at blow-off, from a 3 mm diameter pipe.**

| Fuels | *u*, m/s | Blow-off Heat Release Rate, kW |
|---|---|---|
| Hydrogen | 1,600 | 1,455 |
| Ethylene | 160 | 65 |
| Propane | 108 | 200 |
| Butane | 86 | 171 |
| Ethane | 77 | 38 |
| Methane | 58 | 15 |
| Di-methyl Ether | 41 | 16 |

Hydrogen has many contrasting, unique, properties. At the lower velocities it is disadvantaged because of a specific energy that is lower than that of methane, an aspect relevant to the conversion

from natural gas to $H_2$ [4]. This can result in reduced heat release rates in hob burners. $H_2$ heat release rates can range from a few watts in a single flame of a hob burner, to 7 MW, as in a projected large flare, that might arise when flare-burning of vented hydrogen from an overheated nuclear reactor [14]. At such higher flow rates, $H_2$ benefits, not only from its high burning velocity, but also from its high acoustic velocities, which make these available whilst maintaining subsonic flows.

**Low burn rates and Flame Quench**

The highest energy release rate of a fuel is not necessarily optimal practically, and the use of ammonia to "slow down" reaction can be just as valuable. The flame quenching mechanism associated with blow-off is very similar to that associated with the flame quenching associated with premixed flames. The two mechanisms, together with reaction zone dissipation and measurement of the probabilities of flame survivals, have been studied in detail, using swinging laser sheet experimental techniques, in [6]. There, it is shown that flame extinction at jet flame blow-off is closely related to the flame extinctions observed in the single kernel quenching of premixed flames. As a consequence, $U^*$, has similarities with the Karlovitz number employed in correlations with premixtures. Also, just as normalised jet burner diameters, $D/\delta_k$, change with $U^*$, in a similar fashion similarly normalised kernel diameters change with the Karlovitz number in premixed flames.

This joint applicability to both types of flame is demonstrated by Fig. 8 in [6]. A unifying aspect is not only flame quenching, but also its obverse, namely, flame initiation from an initial hot kernel of reacting gas. The descending order of the fuels in Table 3 is one of declining chemical activity and fuel velocity, and of more sharply declining heat release rate. The value of $D$ has a dominant role on quench, dominant role of $D$ on quench. Where it is small, in Fig. 1 at the top of the diagram, quenching is more probable. Where it is large, at the bottom of the diagram, there can be large, lifted, stable flames. Relative to most hydrocarbons, $H_2$ acts like a larger diameter flame, through its low flame thickness and low $\delta_k/D$ value. Although $C_3H_8$ is prone to leakages at small diameter holes. Significantly smaller leakages are possible with $H_2$, because of its high diffusivity and reactivity, with a, uniquely small $\delta_k$. Its flame is scarcely visible, making detection difficult. Possibly the weakest flame that has been subjected to analysis is the 0.46 watt $H_2$ leakage type flame, with a flow rate of 3.9 μg/s [15] on a 0.152 mm diameter hypodermic needle. In Fig. 1 its heat release rate and location is shown, with coordinates of approximately $U^*$=0.5, and $\delta_k/D$=0.2. An increase in flow rate might eventually lead to blow-off.

**($NH_3$+$H_2$) Flames**

The contrasting locations of the ($NH_3$+$H_2$) points in the plots of Figs. 2 and 3 are noteworthy. In the former, the ($NH_3$+$H_2$) blow-off points are far removed from those of $H_2$. In contrast, in Fig. 3 the $NH_3$+$H_2$ points are much more closely related to the hydrocarbon points. The $NH_3$+$H_2$ blend has similar burning characteristics to a hydrocarbon, avoiding both the slow burning characteristics of $NH_3$ and the fast burning $H_2$.

There is clearly a potential for practical ($NH_3$+$H_2$) and ($NH_3$+$CH_4$) gas turbine power generation. Developed powers of between 18.4 and 44.4 kW are reported in [16]. With $NH_3$+air, combustion efficiencies that ranged from 89% to 96%. Supportive data on $CH_4$+$NH_3$ laminar burning velocities are available in [17].

In combination with Eq. (2), to evaluate ($Pi/P_a$), with the appropriate value of $\delta_k/D$, a horizontal line drawn in Fig. 2 can represent an increasing fuel velocity, which is less than that for blow-off, and the velocity can be calculated up to that existing at blow-off.

**CONCLUSIONS**

1. The $U^*$-$\delta_k/D$ Blow-off diagram has been strengthened by the introduction of further data from new fuels, and further sampling of existing fuels.

2. Operational understanding of the practical behaviour of blended fuels, through experience with methane-hydrogen and ammonia-hydrogen blends has improved.

3. Ammonia has become a successful fuel, when combined with hydrogen. Such blends can have similar heat release rates properties to conventional hydrocarbon fuels.

4. There is, however, a dearth of information on the $NH_3$-$H_2$ blends, particularly of different blow-off diameters. More data over a range of $NH_3/H_2$ blends are required, to make this plot more definitive.

5. Although energetically, there are advantages in hydrogen-ammonia as a fuel, their jet flames can blow-off at very low heat release rates.

6. There are large variations in the heat release rates of different fuels just prior to blow-off.

7. The less reactive fuels blow-off more easily. The the blow-off velocity can be indicative of the heat release rate of the fuel.

8. Flame extinction at jet flame blow-off is closely related to that observed for premixed turbulent flame kernels. As a consequence, $U^*$, has similarities with the Karlovitz number employed with premixtures.

## REFERENCES

[1] D. Bradley, P.H. Gaskell, X.J. Gu, A. Palacios, Jet Flame Heights, Lift-Off Distances, and Mean Flame Surface Density for Extensive Ranges of Fuels and Flow Rates. Combust. Flame. 164 (2016) 400–409.

[2] C. Morley, GasEq. A chemical equilibrium program for windows (2005). htpp://www.gaseq.co.uk.

[3] J. Göttgens, F. Mauss, N. Peters, Analytic Approximations of Burning Velocities and Flame Thicknesses of Lean Hydrogen, Methane, Ethylene, Ethane, Acetylene and Propane flames, Proc. Combust. Inst. 24 (1992) 129–135.

[4] A. Palacios, D. Bradley, Conversion of Natural Gas Jet Flame Burners to Hydrogen. Int. Jour. Hydrog. Energy. 46 (2021) 17051–17059.

[5] A. Palacios, D. Bradley, Generalised Correlations of Blow-off and Flame Quenching for Sub-sonic and Choked Jet Flames. Combust. Flame. 185 (2017) 309–318.

[6] D. Bradley, M. Shehata, M. Lawes, P. Ahmed, Flame Extinctions: Critical Stretch Rates and Sizes, Combust. Flame. 212 (2020) 459–468.

[7] D. Stamps, S. Tieszen, Blowout of Turbulent Jet Diffusion Flames, Fuel. 118 (2014) 113–122.

[8] D.H. Um, J.M. Joo, S. Lee, O.C. Kwon, Combustion Stability Limits and $NO_x$ Emissions of Nonpremixed Ammonia-Substituted Hydrogen-Air Flames, Int. J. Hydrog. Energy. 38 (2013) 14854–14865.

[9] H. Kobayashi, A. Hayakawa, K.D. Kunkuma, A.Somarathne, E.C. Okafor, Science and Technology of Ammonia Combustion, Proc. Combust. Inst. 37 (2019)109–133.

[10] C. Lhuillier, P. Brequignya, N. Lamoureuxd, F. Continoe, C. Mounaim-Roussellea, Experimental Investigation on Laminar Burning Velocities of Ammonia-Hydrogen/Air Mixtures at Elevated Temperatures, Fuel. 263 (2020) 116653.

[11] J.H. Lee, S.I. Lee, O.C. Kwon, Effects of Ammonia Substitution on Hydrogen/Air Flame Propagation and Emissions, Int. J. Hydrog. Energy. 35 (2010) 11332–11341.

[12] H.B. Dixon, G. Greenwood, On the Velocity of Sound in Mixtures of Gases, Proc. R. Soc. A. 109 (1925) 561–569.

[13] Aspen-Hysys V10®, 2021 Aspen Technology Inc. https:/-Home.aspentech.com/products/pages/new-in-aspen-plus.

[14] A. Palacios, D. Bradley, Hydrogen Generation, and Its Venting from Nuclear Reactors, Fire Saf. J. 113 (2020) 102968.

[15] M.S. Butler, C.W. Moran, P.B. Sunderland, R.L. Axelbaum, Limits for Hydrogen Leaks that Can Support Stable Flame, Int. Jour. Hydrog. Energy. 34 (2009) 5174–5182.

[16] Osamu Kurata, Norihiko Iki, Takayuki Matsunuma, Takahiro Inoue, Taku Tsujimura, Hirohide Furutani, Hideaki Kobayashi, Akihiro Hayakawa, Performances and Emission Characteristics of $NH_3$–Air and $NH_3$–$CH_4$–Air Combustion Gas-Turbine Power Generations, Proc. Combust. Inst. 36 (2017) 3351–3359.

[17] C. Okafor, Y. Naito, S. Colson, A. Ichikawa, T. Kudo, A. Hayakawa, H. Kobayashi, Experimental and Numerical Study of the Laminar Burning Velocity of $CH_4$-$NH_3$-Air Premixed Flames, Combust. Flame. 187 (2018) 185–198.

# Analysis of Sensitivity of Vertical Corner Flame Spread Dynamics to Uncertainties in the Model Input

**Chaudhari D.M.[1,2*] and Stoliarov S.I.[2]**

*[1] Fire Safety Research Institute (FSRI), Columbia, Maryland, U.S.A.*
*[2] University of Maryland, Department of Fire Protection Engineering, College Park, Maryland, U.S.A.*
**Corresponding author's email: dushyant.chaudhari@ul.org*

## ABSTRACT

A semi-empirical model combining a first-principal pyrolysis sub-model with an empirical representation of flame heat feedback was developed to simulate flame spread in a vertical corner scenario similar to that of the standard Single Burning Item test. This model was applied to a range of materials including poly (methyl methacrylate) (PMMA), polyisocyanurate (PIR) foam, and oriented strand board (OSB). Overall, the model captured the flame spread dynamics with a reasonable degree of success, but it also had some notable deviations from the experimental data. To better understand the reasons for the observed deviations, the sensitivity of the model predictions to various input parameters was examined in this work. Each input parameter was varied (one at a time) by its estimated uncertainty and a sensitivity coefficient was calculated as the change in predicted HRR error normalized by the fractional change in the input parameter. The activation energy was found to have the highest magnitude (absolute value) of the sensitivity coefficient, followed by flame heat flux. Absorption coefficient had the lowest magnitude of the sensitivity coefficient. Based on the sensitivity analysis results, flame heat flux parameter uncertainty was estimated to have the largest impact on model predictions. The average HRR error for PMMA reduced from 33% to 11% after decreasing flame heat flux by its uncertainty (10%). For OSB, the simulations with increased flame heat flux, a consequence of a more radiative flame for OSB than PMMA, still underpredicted peak HRR. The discrepancy in OSB predictions were attributed to limitation of using the flame heat feedback model which was calibrated on PMMA data. This limitation could be overcome by calibrating the empirical flame heat feedback model for materials with different radiative fractions.

**KEYWORDS:** Single Burning Item; pyrolysis; flame heat flux; ThermaKin.

## INTRODUCTION

Fire hazard of materials used in the built environment are usually quantified via standardized reaction-to-fire tests and the final use of the material is dependent on the relative ranking derived using these tests. However, such testing can be prohibitively expensive and with increasing use of synthesized polymers, a cost-effective, viable alternative to testing is modelling of material flammability [1].

One test of importance for research and material classification is Single Burning Item (SBI) test which subjects two 1.5 m tall panels mounted in a corner geometry to a triangular propane sandbox burner flame [2,3]. The corner scenario allows for studying both vertical (concurrent) and lateral (creeping/opposed flow) flame spread. Recently, the IAFSS working group on Measurement and Computation of Fire Phenomena (MaCFP) highlighted the need to collect detailed data in such standardized scenarios to function as a target for advanced fire models [4].

Several studies have sought to measure parameters that define flame spread in the SBI scenario. Zeinali et. al. [5,6] performed one of the most comprehensive measurements in an SBI setup using calcium silicate board and medium density fibreboard (MDF) as panel materials. However, the flame heat flux, a key parameter governing flame spread, was measured only at three locations. In our previous study, we [7] measured flame heat flux at 28 locations for flame spreading over poly(methyl methacrylate) (PMMA) in a corner configuration similar to the SBI setup. The flame heat flux data were correlated with the HRR measurements to obtain an empirical flame feedback model. This empirical model was then coupled with a comprehensive pyrolysis solver, ThermaKin [8–10], to

establish a flame spread modelling framework [7]. The flame spread model was used to predict heat release rate dynamics during flame spread over PMMA and later was successfully applied to polyisocyanurate (PIR) foam [11].

The application of the flame spread model to PMMA and PIR foam indicated that the largest errors in HRR prediction were observed for PMMA, with maximum average HRR error of over 40%. Although that study highlighted the effect of changing specific heat capacity (a pyrolysis parameter with largest impact on gasification test results) [12,13] on the modelling results, the sensitivity of HRR to all input parameters was not investigated. Zeinali et al. [14] also simulated the SBI test over MDF in FireFoam and found that the uncertainty in the density of MDF affected the HRR evolution, with errors in peak HRR errors ranging from 4% to 16%. Computational fluid dynamic (CFD) based models applied for predicting large fire scenarios, are also sensitive to accuracy of the sub-models [15], grid size [16], unresolved length scales near the flame front [16], and uncertainties in pyrolysis properties [14]. Thus, quantifying the sensitivity of the flame spread model to the input parameters could provide an insight into parameters that have the most impact on the large-scale modelling results.

The present study aims to apply our previously developed flame spread modelling framework to an important wall-lining material, Oriented Strand Board (OSB). The second objective is to quantify sensitivity of the modelling results to the input parameters by performing a sensitivity analysis of the flame spread model for flame spread over three materials: PMMA, PIR foam, and OSB. Finally, the impact of input parameter uncertainty on the modelling results was explored. First, large-scale experiments were performed over OSB in the developed corner configuration, followed by the sensitivity analysis of the flame spread model.

## EXPERIMENTAL SETUP OVERVIEW

A previously built corner configuration was based on the Single Burning Item test setup [2], with a triangular propane sandbox burner having an equivalent HRR of 30 kW used as the ignition source. In these experiments, simultaneous oxygen consumption calorimetry, measurements of flame heat flux and radiation intensity at 900±10 nm wavelength were performed. Flame heat flux was measured for flame spreading on PMMA at 28 locations in the experiments using water-cooled Schmidt Boelter heat flux gauges, and radiation intensity using a modified DSLR camera setup. Seven experiments were performed on PMMA, two on PIR foam, and three on OSB. None of the studied materials exhibited significant deformation or delamination during the data collection periods of these experiments. Additional information and details of the experimental setup can be found in Ref. [7].

## MODELLING FRAMEWORK

ThermaKin, a comprehensive pyrolysis solver, solves unsteady mass and energy conservation equations for a material in the condensed phase which may undergo chemical or physical changes in response to user-defined external boundary conditions. Each material is defined as a mixture of components, where each component can degrade via Arrhenius-type reaction kinetics. Flexible boundary conditions implemented in ThermaKin enable simulation of a wide range of fire scenarios. In this work, ThermaKin was coupled with an empirical flame feedback model as detailed in a later subsection. Additional details and validation of ThermaKin can be found elsewhere [8–10].

### Pyrolysis model parameterization

Comprehensive pyrolysis models of the three materials used in this work were developed and validated in separate studies by inverse analyses of a series of milligram- and gram-scale tests [12,17]. For brevity, the development of the pyrolysis models is not discussed here, but can be found in Ref. [11,12,18,19].

Thermal degradation of black cast PMMA in inert TGA-DSC atmosphere was represented using two first-order reactions in series [12], of PIR foam using seven first-order reactions in series while accounting for the contribution from its flammable blowing agent component [11], and of OSB using five first-order reactions in series [18,19]. The pyrolysis property set for each material was validated by predicting mass loss rate in radiation-driven gasification tests [20] and heat release in cone calorimetry tests.

**Flame spread modelling**

Flame spread modelling was performed with a target to predict heat release rate during flame spread in the corner configuration over the three materials. In the flame spread model, each panel used in the experiments was first discretized in 28 rectangular elements, as shown in Fig. 1. The elements were decided such that the heat flux gauges (used in the PMMA experiments) were approximately at the geometric centre of the element. The empirical flame heat feedback model consisted of a functional correlation developed between the flame heat flux and the heat release rate for each element. Using this flame heat feedback model, a time-dependent heating boundary condition for each element was produced for an arbitrary instantaneous input HRR profile.

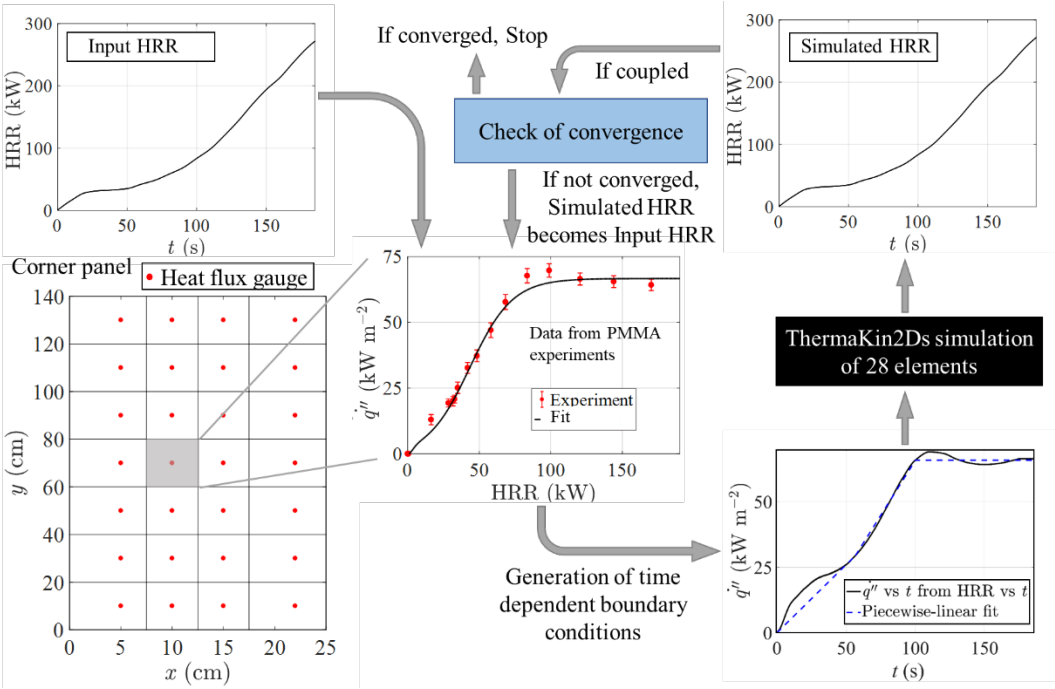


**Fig. 1.** Schematic of flame spread modelling framework

The instantaneous heat flux profile was described using a three piece-wise linear fit to prescribe it as a time-dependent heating condition for each element. One-dimensional pyrolysis simulations were performed for each element subjected to this heating boundary condition in ThermaKin2Ds module of ThermaKin. The heat release rate was then predicted using Eq. (1), which includes the contribution to HRR from the combustion of gaseous pyrolyzates emanating from individual elements and the propane burner contribution. Heat transfer through the calcium silicate board, which was the backing material for each flammable substrate used in this study, was computed by ThermaKin2Ds using thermal properties of Marinite I obtained from the manufacturer [21].

$$\text{Simulated HRR}(t) = \text{HRR}_{\text{b}}(t) + 2\sum_{j=1}^{28} A_j\left[\sum_{i=1}^{Ng} \dot{m}''_{ij}(t)\Delta H_c^i\right] \quad (1)$$

In Eq. (1), the index $i$ is used for summation of $Ng$ pyrolyzates, index $j$ is used for summation of contribution from 28 elements, each having the front surface area of $A_j$, $\dot{m}''_{ij}$ is the instantaneous mass flux predicted by ThermaKin2Ds of pyrolyzate gas $i$ from element $j$, $\Delta H_c^i$ is the heat of combustion of a pyrolyzate gas $i$, and $\mathrm{HRR_b}(t)$ is the contribution from the propane burner which is simulated as a linear rise to a plateau of 30 kW in 10 s. The initial input HRR profile was assumed to be twice that of the magnitude of simulated propane burner HRR profile, i.e., a linear rise to 60 kW in 10 s. Here, t = 0 s corresponds to ignition of the propane burner. The simulated HRR was then subsequently used as the input HRR for further simulations until the convergence criterion, CR, given by Eq. (2), was calculated to be below 5 kW for any time, $t_l$, between 1 s and the end of simulation time, $t_e$.

$$CR = \frac{1}{t_l}\int_0^{t_l} |\text{Input HRR}(t') - \text{Simulated HRR}(t')|dt' \tag{2}$$

The simulations were conducted for the duration of the experiments: $t_e$ = 185 s for PMMA, 600 s for PIR foam, and 300 s for OSB. All simulations were performed in an automated MATLAB script which post-processed the ThermaKin2Ds output, generated the boundary conditions, and called ThermaKin2Ds as a subroutine. The simulations were conducted at a time step of 0.01 s and spatial discretization within the condensed phase solid of 5 × $10^{-5}$ m. Increasing or decreasing these integration parameters by a factor of two did not alter the results, indicating convergence. It is important to note that the simulations were also independent of the initial input HRR profile.

Model predictions of HRR evolution were compared quantitatively with experimental HRR using Eq. (3), which calculates the $\mathrm{HRR_{error}}$. It is important to note that this error is normalized by the maximum peak HRR of a particular material so that the error is not dominated by portions of the experiment where HRR was low.

$$\mathrm{HRR_{error}} = \frac{1}{t_e}\int_0^{t_e} \frac{\text{Simulated HRR} - \text{Experimental HRR}}{\text{Peak Experimental HRR}} dt' \tag{3}$$

## SENSITIVITY ANALYSIS APPROACH

Sensitivity analysis was performed by individually changing one input parameter by its uncertainty. The input parameters considered were all pyrolysis properties and the external heat flux boundary condition. All parameters were increased by its uncertainty, which are listed in Table 1. The uncertainty values used here for $\alpha$, $\varepsilon$, $\Delta H_c$ were measured in other studies, values for $\rho$, $\dot{q}''$ were measured for experiments conducted with PMMA [7], and values for all other parameters were calculated from sensitivity analysis of inverse analysis techniques used to calculate the parameters. For materials having multiple decomposition mechanisms and multiple solid-phase components where each component had respective thermo-physical properties, the sensitivity analysis was performed by changing respective values for all solid-phase components.

**Table 1. Uncertainties in input parameters used in the sensitivity analysis**

| *Type* | *Parameter* | *Variable* | *Uncertainty* | *Reference* |
|---|---|---|---|---|
| *Reaction kinetics and thermodynamics* | Pre-exponential factor | $A$ | 40% | [22] |
| | Activation energy | $E$ | 2% | [22] |
| | Heat of decomposition | $\Delta H_r$ | 5% | [22,23] |
| *Thermo-physical* | Specific heat capacity | $C_p$ | 10% | [12,22,23] |
| | Thermal conductivity | k | 10% | [24] |
| | Density | $\rho$ | 5% | [12,24] |
| *Optical* | Absorption coefficient | $\alpha$ | 30% | [25] |
| | Emissivity | $\varepsilon$ | 2% | [25] |

| *Type* | *Parameter* | *Variable* | *Uncertainty* | *Reference* |
|---|---|---|---|---|
| *Gas-phase combustion* | Heat of combustion | $\Delta H_c$ | 5% | [7,26] |
| *Heat feedback* | Heat flux | $\dot{q}''$ | 10% | [7] |

The impact of change of a specific parameter on the HRR evolution was evaluated by calculating the sensitivity coefficient, $S_{HRR}$, using the following expressions,

$$S_{HRR} = \frac{\Delta \mathrm{HRR}_{\mathrm{error}}}{\delta P} \tag{4}$$

$$\Delta \mathrm{HRR}_{\mathrm{error}} = HRR_{error}^{P+\delta P} - HRR_{error}^{P} \tag{5}$$

where, $\delta P$ is the fractional change in an input parameter, $HRR_{error}^{P+\delta P}$ is the $HRR_{error}$ evaluated for simulation with one parameter increased by $\delta P$, and $HRR_{error}^{P}$ represent base-case $HRR_{error}$. Thus, the parameter $S_{HRR}$ provides a quantiative value for the change in $HRR_{error}$ for a fractional change in the parameter value. For example, a 0.01 fractional increase in a parameter having a sensitivity coefficient of –0.5 would decrease the $HRR_{error}^{P}$ by a magnitude of 0.005 (or 0.5%).

## MODELLING RESULTS

Simulation results presented here for PMMA and OSB were obtained by using hybrid and radiation heat flux model and that for PIR foam were conducted using radiation heat flux model only. In the radiation heat flux model, the heat flux boundary condition was modelled as purely radiative. Due to the non-monotonous nature of heat flux profile for PIR foam, only radiation heat flux model was used for PIR foam to facilitate implementation in ThermaKin2Ds. In the hybrid heat flux model, the heat flux boundary condition was represented by a convective expression ($h\Delta T$, where $\Delta T$ is the difference between the flame temperature, assumed as 1500 K, and the surface temperature computed by ThermaKin) below a 30 kW m$^{-2}$ threshold followed by a transition to radiation above this threshold. This threshold represents 2.5 times the contribution of convection to total heat flux, as estimated in previous study [7], and provides a conservative estimate for transition from convection to radiation dominated heat flux. A small contribution from background radiation (equivalent to gauge cooling water temperature of 291 K) added to flame heat flux profiles was set to be incident on the surface.

The final converged simulations are shown in Fig. 2 for PMMA, OSB, and PIR foam compared with their experimental data, from the time of propane burner ignition. The error bars shown here represent an average uncertainty of 10% in experimental measurements, calculated as two standard deviation of the mean [7]. The biggest fire size, indicated by the peak HRR, was PMMA (~280 kW), followed by OSB (~130 kW), and PIR foam (~80 kW). For PMMA, after ignition of the panels at 45 s, the HRR initially increased exponentially and then linearly. OSB HRR increased linearly to the peak after panel ignition, while PIR foam HRR peaked almost instantly after propane burner ignition and then decayed to a steady value to primarily propane contribution (~30 kW) after 120 s.

As seen in Fig. 2, the predictions are different for simulations which use radiation heat flux model and those which use the hybrid heat flux model. For PMMA and OSB, the $\mathrm{HRR}_{error}$ for simulations using radiation heat flux model was 48% and –18%, which changed to 33% and –28% respectively for simulations using hybrid heat flux model. The reduction in the $\mathrm{HRR}_{error}$ for PMMA from the use of radiation to hybrid heat flux model highlight the importance of accurate knowledge of contribution of convection and radiation to the total heat flux. The increase in $\mathrm{HRR}_{error}$ magnitude for OSB was due to reduction in total net heat flux because of the use of the convection expression for the hybrid heat flux model. The model provided excellent HRR predictions for PIR foam, with 2% of the experimental HRR.

The strong feedback between flame heat flux and the HRR in the simulations was more evident for larger fire growth (higher HRR). A slight overprediction (or underprediction) at an earlier iteration resulted in larger overprediction (or underprediction) in HRR in subsequent iterations due to the strong interaction. Thus, the excellent predictions for the PIR foam could be attributed to lack of significant flame spread that tends to amplify modelling errors. The model provides good predictions of HRR during the growth phase for OSB, but underpredicts the peak HRR by about 25%.

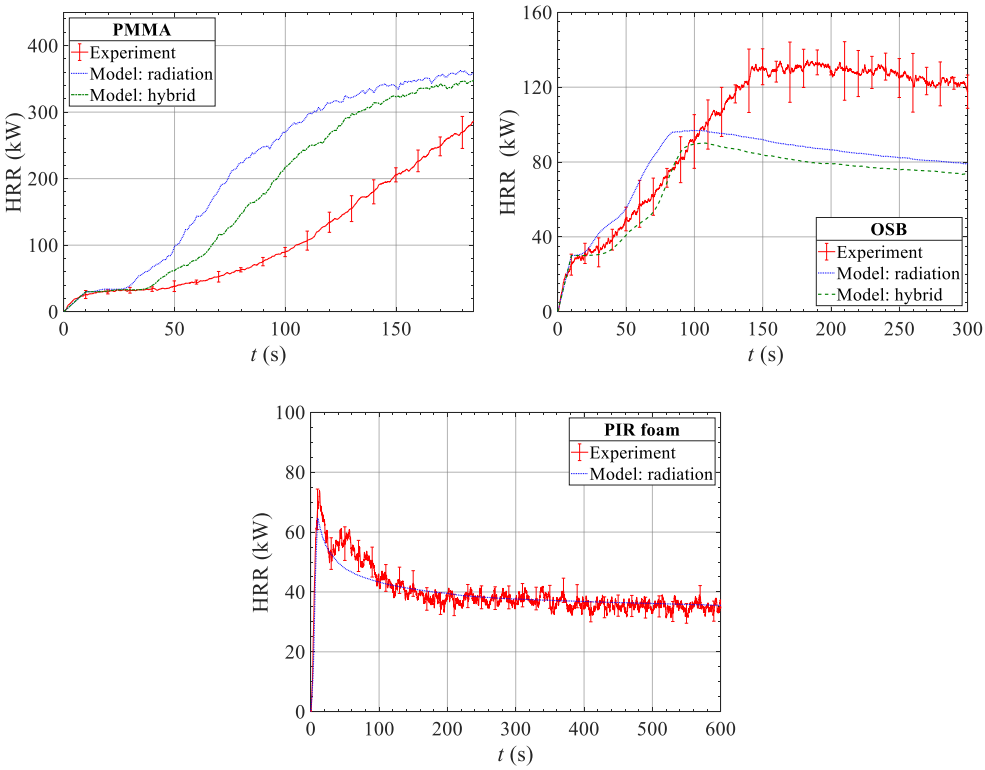


**Fig. 2.** Comparison of experimental HRR with flame spread model predictions for PMMA, OSB, and PIR foam.

## SENSITIVITY ANALYSIS RESULTS

The results of sensitivity analysis, performed to quantify the impact of changing input parameters on HRR predictions, are shown in Fig. 3 for simulations using both the radiation and hybrid heat flux model. The base case for PMMA and OSB were the converged simulations conducted with original parameters using either hybrid or radiative heat flux model (separate values calculated for both heat flux models), while that for PIR foam were converged simulations conducted with original parameters using only the radiation heat flux model. This figure shows the $S_{HRR}$ values for simulations when the input parameters were increased individually.

The parameters with smallest and highest magnitude (absolute value) of $S_{HRR}$ are $\alpha$ and $E$ respectively. The second largest magnitude of $S_{HRR}$ is calculated for the flame heat flux parameter. The order of these three parameters, from lowest to highest magnitude of $S_{HRR}$, is the same for all the three materials studied and is independent of the type of the heat flux model used. The order of other parameters is different depending on the material and the utilized heat flux model. For example, $C_p$ has the third highest magnitude of $S_{HRR}$ for PMMA when hybrid heat flux model is used but for the radiation heat flux model, it has the fourth highest magnitude (emissivity having third highest magnitude). Emissivity has higher magnitude of $S_{HRR}$ than $C_p$ for OSB for both heat flux models.

The $S_{HRR}$ for $E$, $C_p$, $\varepsilon$, $\dot{q}''$,$\Delta H_r$, $\rho$ showed a linear correlation with peak HRR (80, 130, and 280 kW for PIR foam, OSB, and PMMA respectively) with a coefficient of determination higher than 0.95. However, such linear proportionality was not observed for $A$, $k$, $\alpha$, $\Delta H_c$. $S_{HRR}$ did not correlate linearly for the fire growth rate index (kW $s^{-1}$), calculated as the ratio of difference between the peak HRR and the propane burner contribution (30 kW) and the time to peak HRR from propane burner ignition (185 s, 145 s, and 13 s for PMMA, OSB, and PIR foam respectively). Thus, it can be inferred that the input parameters have different sensitivity coefficient values for fires of different peak HRR. This aligns with the earlier observation that uncertainties introduced early amplify in scenarios involving significant heat release.

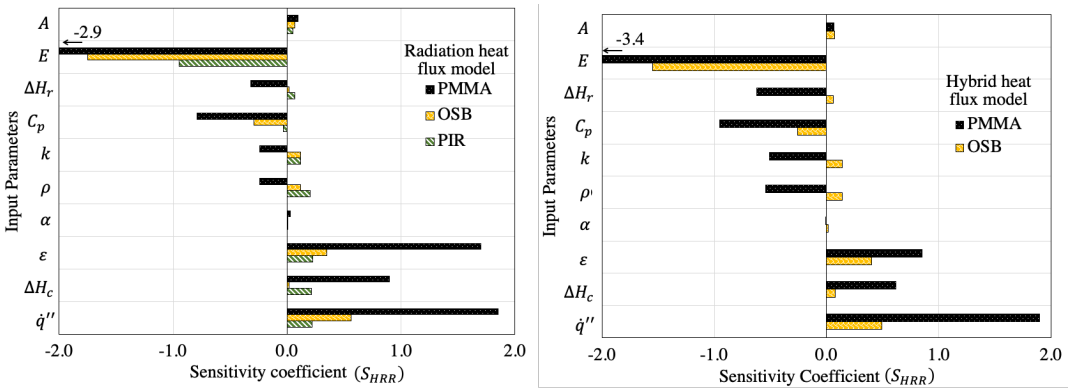


**Fig. 3.** Sensitivity coefficients ($S_{HRR}$) for input parameters for simulations conducted using the radiation heat flux model and the hybrid heat flux model

It is important to note that the impact of a parameter uncertainty on the model results (change in $HRR_{error}$) can be estimated by multiplying $S_{HRR}$ with the respective parameter uncertainty. From Fig. 2, the differences between model predictions and the experimental HRR are significant for PMMA and OSB. Therefore, further analysis was performed to understand which parameter uncertainty had the most effect on the modelling results.

For both PMMA and OSB, this was done for simulations using hybrid heat flux model since this model better represented the heat flux that would be observed during the fire growth. Expected $HRR_{error}$ change was calculated by multiplying each $S_{HRR}$ with respective parameter uncertainties (Table 1). The value of this product was calculated for all parameters to find the most impactful parameter. The parameter with maximum expected change was flame heat flux for both, PMMA and OSB. So, the impact of uncertainty in the flame heat flux parameter to the modelling results was further quantified. In addition to the flame heat flux parameter, only the parameters for which the total $HRR_{error}$ change normalized by the maximum expected total $HRR_{error}$ change (for flame heat flux) was greater than 50% were regarded as the parameters that would potentially have significant effect on the modelling results. The parameters which satisfied this criterion, along with the flame heat flux, were the heat capacity parameter for PMMA, and heat capacity and activation energy for OSB. The result of changing these parameter values by their uncertainty on the model prediction are discussed below, first for PMMA, and then for OSB.

For PMMA, since the model overpredicted HRR, decreasing the flame heat flux was expected to reduce the magnitude of $HRR_{error}$ (positive value of $S_{HRR}$ for $\dot{q}''$ also suggest the impact of change in this direction). Similarly, increasing heat capacity is expected to reduce the $HRR_{error}$ magnitude for PMMA. Thus, simulations performed using heat flux profile decreased by 10% (its uncertainty) and heat capacity increased by 10% (its uncertainty) were performed separately and the results are shown in Fig. 4. The simulation with decreased heat flux had an $HRR_{error}$ of 11% for PMMA while the

simulation with increased heat capacity had an error of 24%. These $HRR_{error}$ are lower than the 33% error for the original simulation performed using hybrid heat flux model. Model predictions when other parameters were changed are not shown in this figure because they did not improve the predictions more than the presented two cases, as expected from the result of multiplication of sensitivity coefficient and the respective parameter uncertainty. From these results, it can be concluded that reducing errors in the modelled flame heat flux and pyrolysis parameters (heat capacity in this case) is important for improving model predictions. The discrepancy in model predictions and the experimental data for simulations conducted with original parameters can be partially attributed to the relative inaccuracy of knowing contribution of convection and radiation to the total heat flux. The discrepancy could also be because of relatively coarse discretization of panel for modelling flame heat fluxes (28 elements) than what could be possible with a CFD based model. It would be beneficial to simulate this experiment with a CFD based model to better understand how the accuracy of gas-phase modelling affects the predictions of fire dynamics during the flame spread.

For OSB, since the model underpredicted the HRR, increasing $\dot{q}''$, decreasing $E$ and decreasing $C_p$ (other two parameters which are estimated to have significant impact on modelling results) was expected to reduce the magnitude of $HRR_{error}$. Simulations performed by increasing $\dot{q}''$ by 10%, decreasing $E$ by 2% for all reactions, and decreasing $C_p$ by 10% for all solid-phase components were performed separately and the results are also shown in Fig. 4. These results suggest that the $HRR_{error}$ for all these simulations is approximately –20%. Although the errors for these simulations are lower than those with the original simulation with the hybrid heat flux model ($HRR_{error}$ = –25%), none of these simulations capture the peak HRR. This could be because the empirical flame heat feedback model which is calibrated with the PMMA data was applied directly to OSB. From the data collected during experiments with OSB, the radiation intensities derived from the DSLR camera images (captured at 900±10 nm) were higher for the OSB flame than for the PMMA flame. The radiation intensity profiles at same HRR between OSB and PMMA also indicated a different flame structure, with a wider flame observed for OSB than PMMA near the propane burner flame region. The flame heat flux (acquired using water-cooled Schmidt-Boelter heat flux gauges) also indicated a faster rise with HRR for OSB than that observed for PMMA at same locations. Thus, the correction of flame heat flux for OSB by 10% may not be representative of the actual difference arising from difference in the flame structure.

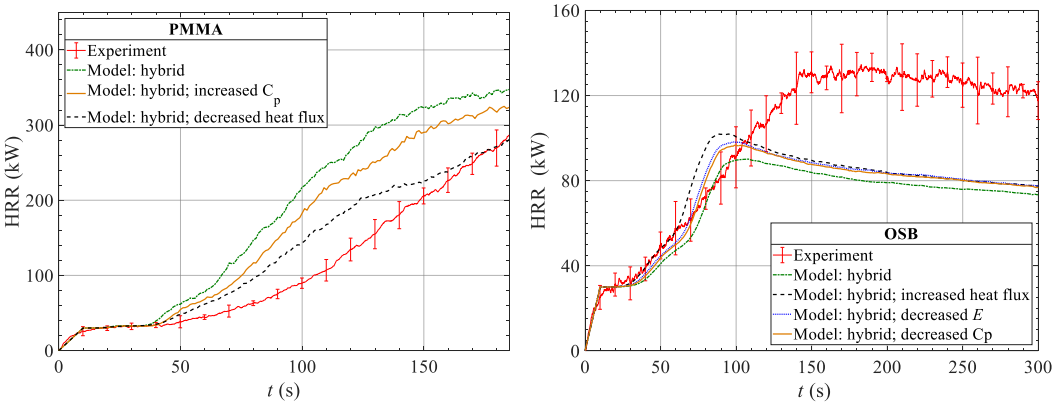


**Fig. 4.** Comparison of experimental HRR and model predictions of flame spread simulations performed for PMMA and OSB to understand the impact of input parameter uncertainty.

## CONCLUSION

The ability of a previously developed semi-empirical flame spread model to predict fire dynamics during flame spread over three materials (PMMA, OSB, and PIR foam) in a corner configuration was

investigated. This flame spread model was based on coupling of comprehensive pyrolysis model developed and validated for each material and empirical flame heat feedback model developed based on experimental data obtained during the flame spread over PMMA. The model provided excellent predictions of HRR evolution for PIR foam, but the average HRR error for PMMA and OSB were found to be sensitive to the representation of flame heat flux. Simulations which assumed purely radiative heat flux had an average HRR error of 48% (PMMA) and –18% (OSB), and these errors changed to 33% (PMMA) and –25% (OSB) for the simulations where the flame heat flux profile was represented using combination of convection expression and radiation. Thus, the accurate knowledge of contribution of convection and radiation to the total heat flux is important.

Sensitivity analysis was performed by changing one input parameter at a time and quantifying the sensitivity coefficient, defined as the change in the HRR error from the base-case per fractional change in the input parameter. Activation energy was determined to have the highest magnitude (absolute value) of sensitivity coefficient, followed by the flame heat flux. Absorption coefficient had the lowest magnitude of the sensitivity coefficient. Based on the sensitivity analysis, flame heat flux uncertainty was estimated to have the largest impact on model predictions. Simulations conducted by decreasing flame heat flux by 10% (its uncertainty) decreased the average HRR error for PMMA to 11% while increasing the heat flux by 10% for OSB improved the error to –20%. Thus, while the heat flux variation for PMMA represents a realistic estimate for its uncertainty, the actual difference for OSB is likely to be larger since this variation does not include the impact of observed differences in the flame structure (higher radiation intensity and wider flame for OSB). The flame heat feedback model can potentially be improved by accounting for the differences in the radiative heat feedback for the fuels with different radiative fractions, which can be estimated from separate bench-scale tests.

Two additional important conclusions from this study are: (1) the sensitivity to uncertainties increases significantly for the materials like PMMA that support fast fire growth and exhibit a strong coupling between the processes in the condensed and gas phases, which amplifies the uncertainties; (2) for the materials that exhibit fast fire growth, even moderate uncertainties in the measured parameters (consistent with the state of the art for such measurements) can translate into poor fire growth predictions. These uncertainties will have to be reduced substantially to deliver fire growth predictions comparable in accuracy to the corresponding measurements.

## REFERENCES

[1] R.G. Bill, P.A. Croce, The International FORUM of Fire Research Directors: A position paper on small-scale measurements for next generation standards, Fire Saf. J. 41 (2006) 536–538.

[2] EN-13823 - Reaction to fire tests for building products - Building products excluding floorings exposed to the thermal attack by a single burning item, (2004).

[3] R. Van Mierlo, B. Sette, The Single Burning Item (SBI) test method - A decade of development and plans for the near future, Heron. 50 (2005) 191–207.

[4] A. Brown, M. Bruns, M. Gollner, J. Hewson, G. Maragkos, A. Marshall, R. Mcdermott, B. Merci, T. Rogaume, S. Stoliarov, J. Torero, A. Trouvé, Y. Wang, E. Weckman, Proceedings of the first workshop organized by the IAFSS Working Group on Measurement and Computation of Fire Phenomena ( MaCFP ), Fire Saf. J. 101 (2018) 1–17.

[5] D. Zeinali, S. Verstockt, T. Beji, G. Maragkos, J. Degroote, B. Merci, Experimental study of corner fires — Part I : Inert panel tests, Combust. Flame. 189 (2018) 472–490.

[6] D. Zeinali, S. Verstockt, T. Beji, G. Maragkos, J. Degroote, B. Merci, Experimental study of corner fires — Part II : Flame spread over MDF panels, Combust. Flame. 189 (2018) 491–505.

[7] D.M. Chaudhari, G.J. Fiola, S.I. Stoliarov, Experimental analysis and modeling of Buoyancy-driven flame spread on cast poly(methyl methacrylate) in corner configuration, Polym. Degrad. Stab. 183 (2021) 109433.

[8] S.I. Stoliarov, R.E. Lyon, Thermo-kinetic model of burning for pyrolyzing materials, Fire Saf. Sci. 9

(2008) 1141–1152.

[9] S.I. Stoliarov, I.T. Leventon, R.E. Lyon, Two-dimensional model of burning for pyrolyzable solids, Fire Mater. 38 (2014) 391–408.

[10] J.D. Swann, Y. Ding, S.I. Stoliarov, Characterization of pyrolysis and combustion of rigid poly(vinyl chloride) using two-dimensional modeling, Int. J. Heat Mass Transf. 132 (2019) 347–361.

[11] D.M. Chaudhari, S.I. Stoliarov, M.W. Beach, K.A. Suryadevara, Polyisocyanurate foam pyrolysis and flame spread modeling, Appl. Sci. 11 (2021).

[12] G.J. Fiola, D.M. Chaudhari, S.I. Stoliarov, Comparison of Pyrolysis Properties of Extruded and Cast Poly(methyl methacrylate), Fire Saf. J. 120 (2021) 103083.

[13] D.M. Chaudhari, Experiments and Semi-Empirical Modeling of Buoyancy-Driven, Turbulent Flame Spread over Combustible Solids in a Corner Configuration, Ph.D. Thesis, University of Maryland, College Park, (2021).

[14] D. Zeinali, A. Gupta, G. Maragkos, G. Agarwal, T. Beji, M. Chaos, Y. Wang, J. Degroote, B. Merci, Study of the importance of non-uniform mass density in numerical simulations of fire spread over MDF panels in a corner configuration, Combust. Flame. 200 (2019) 303–315.

[15] J. Zhang, M. Delichatsios, M. Colobert, Assessment of Fire Dynamics Simulator for Heat Flux and Flame Heights Predictions from Fires in SBI Tests, Fire Technol. 46 (2010) 291–306.

[16] M. Hjohlman, P. Andersson, P. van Hees, Flame spread modelling of complex textile materials, Fire Technol. 47 (2011) 85–106.

[17] M.B. McKinnon, S.I. Stoliarov, Pyrolysis model development for a multilayer floor covering, Materials (Basel). 8 (2015) 6117–6153.

[18] J. Gong, H. Zhu, H. Zhou, S.I. Stoliarov, Development of a pyrolysis model for oriented strand board. Part I: Kinetics and thermodynamics of the thermal decomposition, Orig. Artic. J. Fire Sci. 39 (2021) 190–204.

[19] J. Gong, H. Zhou, H. Zhu, C.G. McCoy, S.I. Stoliarov, Development of a pyrolysis model for oriented strand board: Part II—Thermal transport parameterization and bench-scale validation, Https://Doi.Org/10.1177/07349041211036651. 1 (2021).

[20] J.D. Swann, Y. Ding, M.B. McKinnon, S.I. Stoliarov, Controlled atmosphere pyrolysis apparatus II (CAPA II): A new tool for analysis of pyrolysis of charring and intumescent polymers, Fire Saf. J. 91 (2017) 130–139.

[21] Marinite I - Refractory product datasheet,. https://www.bnzmaterials.com/wp-content/uploads/2013/03/Mar-I.pdf (accessed June 15, 2019).

[22] J. Li, S.I. Stoliarov, Measurement of kinetics and thermodynamics of the thermal degradation for non-charring polymers, Combust. Flame. 160 (2013) 1287–1297.

[23] J. Li, S.I. Stoliarov, Measurement of kinetics and thermodynamics of the thermal degradation for charring polymers, Polym. Degrad. Stab. 106 (2014) 2–15.

[24] J. Li, J. Gong, S.I. Stoliarov, Gasification experiments for pyrolysis model parameterization and validation, Int. J. Heat Mass Transf. 77 (2014) 738–744.

[25] G. Linteris, M. Zammarano, B. Wilthan, L. Hanssen, Absorption and reflection of infrared radiation by polymers in fire-like environments, Fire Mater. 36 (2012) 537–553.

[26] R.N. Walters, S.M. Hackett, R.E. Lyon, Heats of combustion of high temperature polymers, Fire Mater. 24 (2000) 245–252.

# Characterization of the geometrical and radiative properties of small heptane pool fires

Bouaza LAFDAL[1,2]*, Pascal BOULET [1], Rabah MEHADDI[1], ElMehdi KOUTAIBA [2], Tarek BEJI [3], Gilles PARENT [1]

[1] Université de Lorraine, CNRS, LEMTA, F-54000, Nancy, France
[2] Université Paris-Est, Centre Scientifique et Technique du Bâtiment (CSTB), 84 avenue Jean Jaurès, Champs-sur-marne, 77447, Marne-la-Vallée, France
[3] Department of Structural Engineering and Building Materials, Ghent University, Sint-Pietersnieuwstraat 41, 9000 Ghent, Belgium.

## ABSTRACT

This work aimed to investigate experimentally the radiative and geometrical characteristics of small heptane pool fires in open atmosphere. Six series of tests were conducted considering small circular pools with diameters of 5, 8, 9, 11, 13 and 15 cm. The mass loss rate can be summarized in four phases: the growth phase (first 450 s), steady burning, boiling and decay phase. The temporal profiles of the flame geometrical characteristics, i.e., height and surface, were determined using an image processing technique. The experimental flame height was compared to the commonly used correlations. Two different behaviors were observed. In the first instants, during the growth and the steady burning phases, for all pool diameters the predicted and experimental flame height show a good agreement. In the second phase (t > 450 s) and for pools larger than 9 cm, the calculation over-estimates the flame height, especially before flame extinction. Finally, the flame radiative fractions were estimated using a Monte Carlo method combined with an image processing method and compared to the usual "point source model". Results from both methods showed a good agreement with a maximum deviation of 9%.

**Keywords:** Pool fires, radiative fraction, ray tracing, image processing

## NOMENCLATURE

| | |
|---|---|
| $\Delta H_c$ | Heat of combustion ($kJ/kg$) |
| $\dot{m}''_{f,\infty}$ | Limiting burning rate per unit area ($kg/(m^2 s)$) |
| $\dot{m}''_1$ | Mass loss rate per unit area ($kg/(m^2 s)$) |
| $\dot{m}_f$ | Mass Loss Rate ($kg/s$) |
| $\dot{Q}$ | Heat release rate ($kW$) |
| $D$ | Pool diameter ($m$) |
| $F$ | View Factor |
| $H$ | Flame height ($m$) |
| $k$ | Absorption-extinction coefficient ($m^{-1}$) |
| $q''$ | Radiative heat flux ($W/m^2$) |
| $S$ | Flame surface ($m^2$) |

**Greek**

| | |
|---|---|
| $x$ | Combustion efficiency |
| $x_{rad}$ | Radiative fraction |

**Subscripts**

| | |
|---|---|
| $f$ | Fire |

**Superscripts**

| | |
|---|---|
| $''$ | Per unit area |

## INTRODUCTION

Hydrocarbon pools are one of the most used fire sources in fire safety research. These pool fires have been the subject of numerous studies. For instance, Babrauskas [1] studied experimentally the Heat Release Rate of a pool for various pool diameters and fuel types. Based on these experiments, he proposed a correlation between the pool diameter, the fuel type and the mass loss rate per unit area. Hiroshi and Taro [2] conducted an experimental study on the air entrainment and the radiative properties of heptane pool fires. These authors analysed five pool diameters (0.3, 0.6, 1, 2 and 6 m). The comparison of their results with the correlation established by Babrauskas [1] shows a good agreement. Hiroshi [3] reported a series of experiments for pool diameters ranging from 3 m to 50 m. Here again, different fuel types such as gasoline, kerosene, heptane were considered. The results of this study highlighted the relation between the fuel mass loss rate and the tank diameter.

An important characteristic of liquid pool fires is the radiative fraction of the resulting flame. [2] and [3] have shown that the radiative fraction is a function of the pool diameter. For pool fires with diameters lower than 2 m, these authors found

that the flame radiative fraction ranged between 0.3 and 0.5. For diameters larger than 2 m, the radiative fraction decreases as the pool diameter increases. This fraction varies between 0.3 and 0.04. This variation was explained by the blockage created by thick smoke and the subsequent reduction in combustion efficiency. Hamins et al [4] carried out an experimental study to investigate the radiative fraction of pool fires with respect to the fuel type. They found that for a fixed pool fire diameter (0.3 m), the radiative fraction varies as a function of the fuel type. Recently, Muñoz et al [5] performed a set of outdoor large scale pool fires (1.5, 3, 4, 5 and 6 m diameter). To estimate the radiative heat flux distribution, these authors used an infrared camera. By evaluating the radiation emitted by each pixel of an image of the flame, the total radiative flux is then determined.

As it can be noticed, a considerable work has been done in order to characterize the radiative properties of large pool fires. However, fewer studies investigated small-scale pool fires ($D < 0.3\ m$) even though those pools are frequently used as a fire source [6, 7, 8, 9, 10]. The radiative fractions of eight fuels burned in two small pools (4.6 and 7.1 cm) were evaluated by Gore et al [11]. More recently, Liu and Zhou [12] analysed the radiative fraction of small-scale pool heptane fires (4, 6, 8, 10 cm) under various pressure conditions. Under atmospheric pressure, the radiative fraction varied between 0.27 and 0.37.

The view factor (which is also called shape or form factor) is an important parameter which should also be taken into account in the evaluation of the radiative heat transfer. In the case of simple geometries this factor can be easily calculated analytically, some of these factors are gathered in tables [13]. For complex geometries other methods are used like direct integration, contour integral, Monte Carlo and other algebraic methods. For this study, a ray tracing method (or Monte Carlo method) was used to evaluate the view factor between the flame and the heat flux sensor. The Monte Carlo method is a statistical method based on random path of energy quanta. In other words, randomly chosen energy quanta emitted from the flame are transported randomly in space. Knowing the new position of the energy quanta, we can calculate the number of particles that reached the target (heat flux sensor). Finally, the ratio between the number of received particles and the number of emitted particles gives us the view factor. This method has been proven to show a good agreement with analytical results [14] [15]. The reliability of this method has also been confirmed experimentally by Erez [16].

Another important characteristic of pool fires is the flame height. In order to estimate this variable, a number of correlations were established. For instance, Thomas [17] provided a relation between the flame height ($H$), the fire diameter ($D$) and the mass loss rate per unit area. This correlation is expressed as

$$\frac{H}{D} = 42 \times \left( \frac{\dot{m}''}{\rho_a \sqrt{gD}} \right)^{0.61}, \tag{1}$$

where $\dot{m}''\ (kg/m^2/s)$ is the mass loss rate per unit area, $g\ (m/s^2)$ is the gravitational acceleration and $\rho_a\ (kg/m^3)$ is the air density.

Heskestad [18] introduced one of the most used correlations, in which the flame height was expressed as a function of the heat release rate and the pool diameter. This correlation was obtained by analyzing a large range of experimental data involving different types of fuels. The flame height is then given by:

$$\frac{H}{D} = 3.7 \times \dot{Q}^{*2/5} - 1.02, \tag{2}$$

where $H$ is flame height ($m$), $D$ is the fire source diameter ($m$), and $\dot{Q}^*$ is a dimensionless heat release rate, defined as:

$$\dot{Q}^* = \frac{\dot{Q}}{\rho_a C_p T_0 \sqrt{g} D^{5/2}}, \tag{3}$$

This dimensionless heat release rate is known as the Zukoski number [19] and it represents the ratio between the heat release rate of the fire and the advected enthalpy rate [20].

The results of this literature review raise many questions. For instance, concerning the correlation by Babrauskas, it has been established in the steady state of the fire combustion and for large pool fire diameters. It can then be asked how this correlation varies in time and if it remains valid for small pool fire diameters. The same question can be asked for the geometrical characteristics of the pool fire flames such as their heights and their surfaces. Concerning the radiative properties of the flames, again, the values in the literature are valid in the case of the steady state fires. It would be interesting to measure this fraction as a function of time. Moreover, the experimental method used by the majority of authors to determine these radiative fractions is the so-called “point source” method. It appears therefore interesting to confirm this method with another method.

The main purpose of this article is to characterize experimentally small pool fires over time. This will allow us to answer some of these questions. The following article is organized as follows: first, the experimental apparatus and the experimental method are presented. Then, the experimental results of geometrical characteristics of the fire plume and radiative properties of the flame are reported and discussed. Finally, we draw our conclusions.

## EXPERIMENTAL SETUP

The experiments were conducted in open atmosphere using small circular steel pans. Various diameters ranging from 5 cm to 15 cm were considered, the depth and the thickness of the pans were fixed at 4 cm and 0.4 cm respectively. During this study heptane was used as fuel, filling completely the pan. The fuel mass loss rate was measured using a high precision electronic weighing scale, isolated from the pan with a 1.2 cm thick Fermacell plate ($\rho$ = 1150 $(kg/m^3)$, $k$ = 0.32 $(W/m/K)$, $c$ = 1200 $(J/kg/K)$). Flame geometric properties were determined using two visible Lumenera cameras (1376 × 1032 $pX^2$). Fig. 1 gives an overview of the experimental setup.

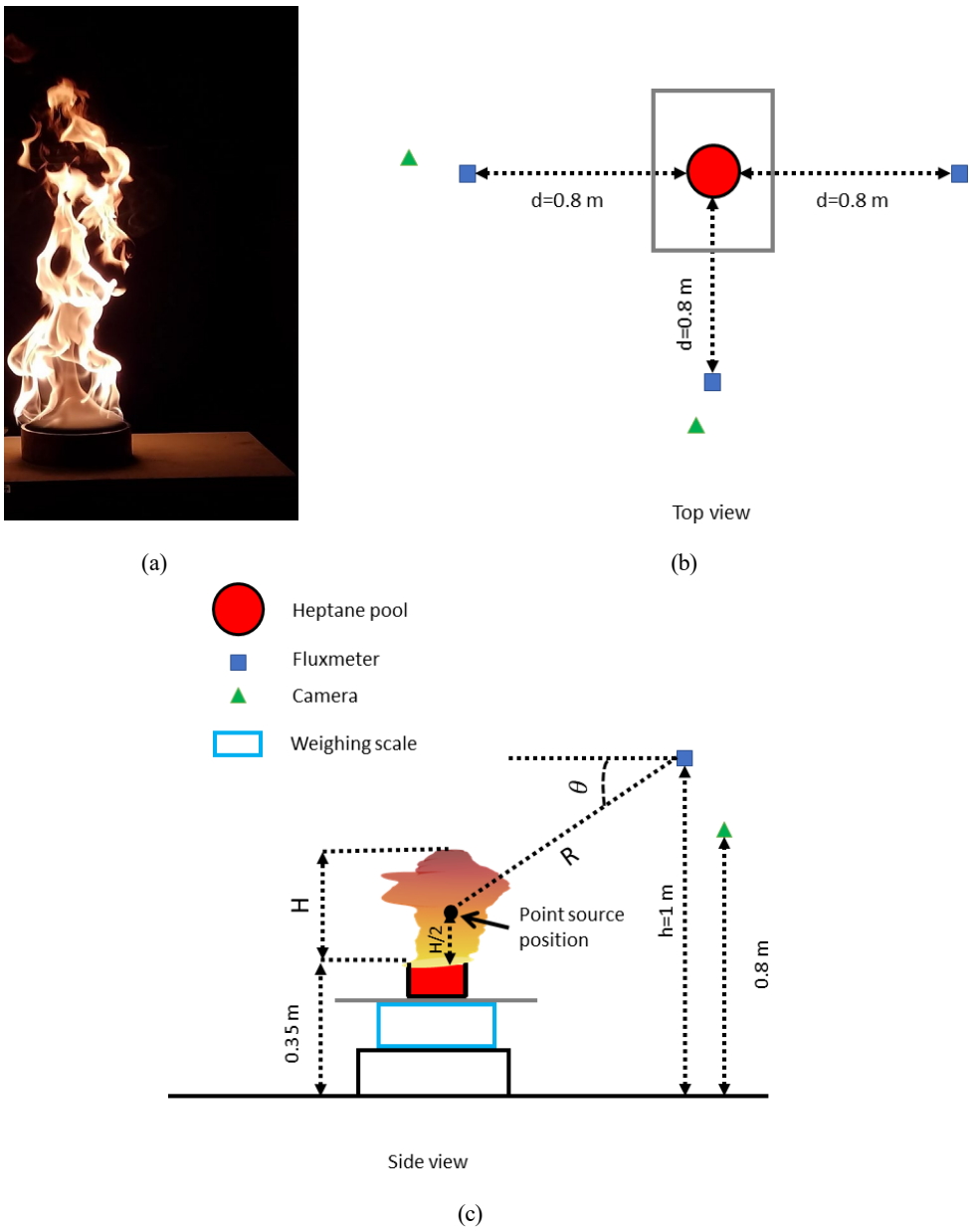


Figure 1: (a) photography taken during a pool fire experiment, (b) and (c) show a schematic representation of the experimental setup with all the dimensions and positions of the sensors, red circle represents the heptane pool, blue squares represent the radiative heat flux sensors, the green triangles represent the cameras.

## RESULTS AND DISCUSSION

### Mass Loss Rate

By taking into account the heat of combustion of heptane ($\Delta H_c$), the heat release rate (HRR) can be expressed as

$$\dot{Q} = x \times \dot{m}_f \times \Delta H_c, \quad (4)$$

where $\dot{m}_f$ is the fuel mass loss rate, $x$ is the combustion efficiency. Following[21], the values of $x$ and $\Delta H_c$ for Heptane fuel are respectively set to 0.93 and 44.6 ($kJ/kg$).

Figure 2a illustrates the evolution of the mass loss rate per unit area (MLRPUA) for different pool diameters. As can be noticed, the variation of MLRPUA for the different pans can be described in four stages. The growth phase, where the flame spreads all over the pool surface. This phase is very short for a heptane pool fire. The second phase is characterized with a steady burning. For pans larger than or equal to 11 cm, a third stage with a very rapid increase in the MLRPUA is observed. It is due to the fast evaporation of the thin layer of fuel remaining in the pool. Finally, the MLRPUA decreases until extinction. In order to estimate the mass loss rate, Babrauskas[1] presented a predictive relationship. This formula is based on the pool

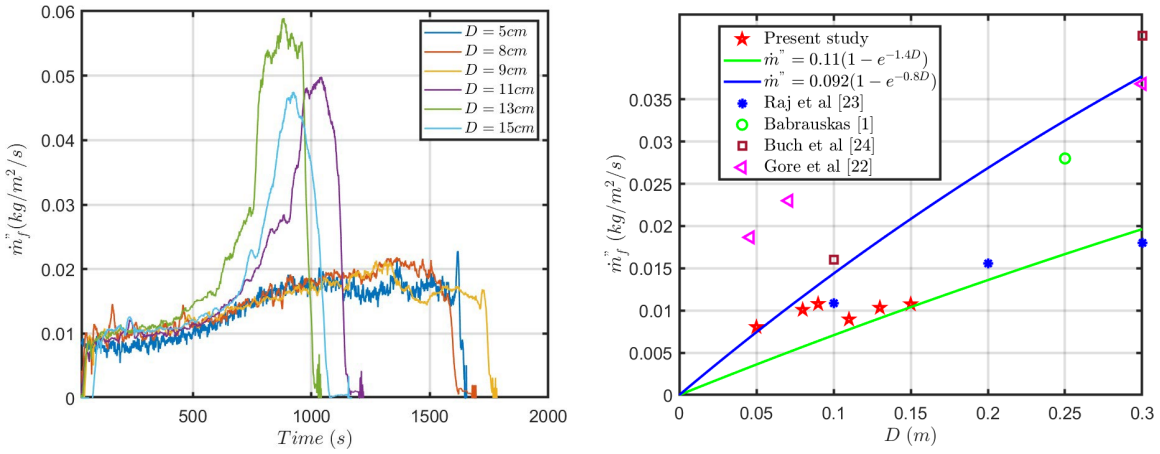


(a) (b)

Figure 2: (a) Temporal evolution of the mass loss rate per unit area for the different pool diameter, (b) evolution of the mean mass loss rate during the steady burning (the first 450 s in our case) for small heptane pool fires [1, 22, 23, 24] in comparison with relationship of Babrauskas.

diameter $D$, the absorption-extinction coefficient $k$ and $\beta$ the mean beam-length corrector. This relation is given by

$$\dot{m}'' = \dot{m}''_{f,\infty}\,[1 - exp(-k\beta D)]\,, \tag{5}$$

where $\dot{m}''$ and $\dot{m}''_{f,\infty}$ are respectively the mass loss rate per unit area and the limiting burning rate per unit area. For heptane $\dot{m}''_{f,\infty} = 0.101(\pm 0.009)\ (kg/m^2/s)$ and $k\beta = 1.1(\pm 0.3)\ (m^{-1})$ [21] [1].

Figure 2b shows a comparison between Babrauskas's and some experimental results, including results from the present study. For a small pool diameter the Babrauskas' relationship relationship predicts a quasi linear increase of $\dot{m}''_f$ with the pan diameter, whereas the experimental results show a quasi constant $\dot{m}''_f$. This behavior is thus quite different from what is predicted by Brabrauskas. In fact, the relation presented by Babrauskas was established for pans with a diameter higher than 0.2 m, in such a case the heat transfer is dominated by the flame radiative heat feedback into the fuel surface. However, for small pools, the fuel evaporation is controlled mainly by the convective heat flux which is rather constant with the pool diameter. Which explain the constant behavior observed here[1].

**Flame Geometrical Characteristics**

The geometrical characteristics of the flame were obtained by analyzing the images taken during each test using the visible camera. The most important steps in image processing are: First of all, the choice of the equipment and its settings should be adapted to the studied phenomenon. We believe that the most important camera setting is the integrating or exposure time. If that one is chosen such as the image is not overexposed or too much underexposed, then the flame shape will be unchanged using Otsu [25] threshold. In some cases the image may need some enhancement and filtering (e.g. remove of noise) so that it will be suitable for further analysis. This step depends on the filter and it can be highly dependent on the user's perception of a good image. The next step is the segmentation which consist on isolating the different components of an image. The most common method is thresholding which consist on separating the different pixels based on their RGB levels (e.g. transform the image to a white/dark image). The last step is the extraction of the desired information. Note that each step is sensitive and must be handled with great precaution like any type of measurement. A Matlab algorithm was used to process the pictures. The original images were transformed to binary images, where the white pixels represent the flame and the dark pixels represent the rest of the image. To make this distinction the background was removed by defining a threshold luminosity. In other words, if the pixel luminosity is larger than the threshold luminosity, the pixel is considered as white, otherwise, it is not taken into account and set to dark. To prevent bias due to the user, the threshold is estimated using Otsu's [25] method based on the variance calculation also known as the maximum interclass variance method. An example of the result of this process is

shown in Fig. 3. The second step is to delimit the flame contour, for this a matlab function"bwboundaries" was used, this latter returns the coordinates of the pixels at the interface white/dark as it is shown in Fig. 3 (red curve). The contour coordinates (pixels) is then converted to real coordinates in meters and extracted. Then these coordinates served in the calculation of the flame height, this latter was defined as the greatest difference in ordinates between two points of same abscissa along the flame contour.

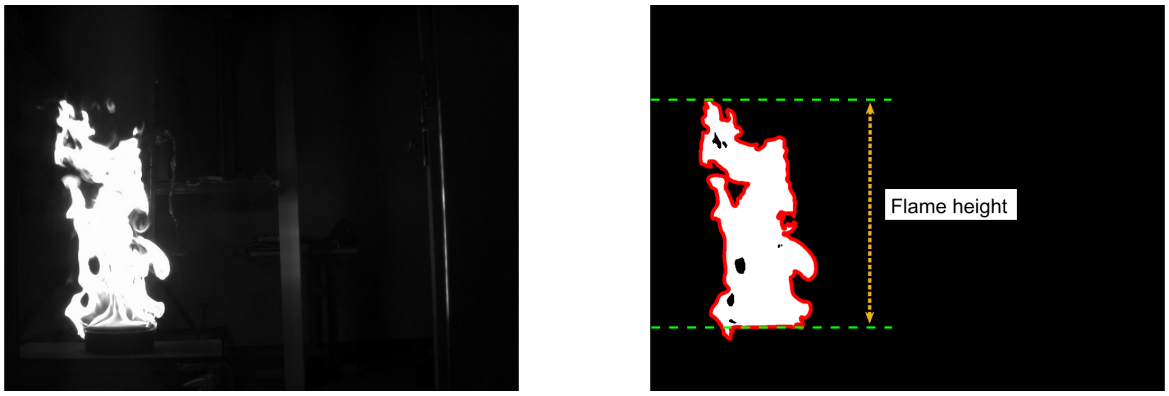


Figure 3: Illustration of the process of delimiting the contour of a flame and determining its height.

The temporal variations of the flame height for the different pool diameters are represented in Fig. 4. As can be noticed, the flame height and the mass loss rate variation have similar trends. Here also we can distinguish two behaviors, for the pans with diameters of 5, 8, 9 cm the flame height is quasi-stationary. For the pools of 11, 13, 15 cm, the flame height temporal profile can be decomposed into two phases, the first one is characterized by a steady flame height, then second stage where the flame height increase as the MLR increases.

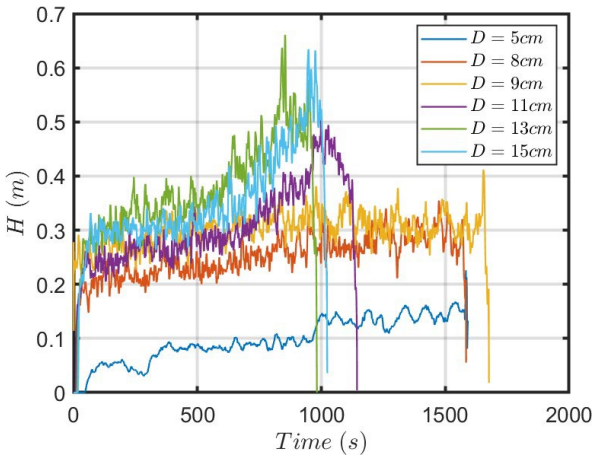


Figure 4: Temporal evolution of the flame height for different pool diameters

Figure 5 represents a comparison between the experimental flame height and the correlations mentioned above (Eq. (1) and Eq. (2)). For the quasi-steady part (t<450 s), Heskestad's correlation gives a good estimation of the flame height. However, for the rest of the experiment, we observe that this correlation over estimates the flame height especially for the large diameters ( 11, 13, 15 cm), this can be explained by the rapid and important rise in the heat release rate observed in this phase, this increase is also observed in the flame height however it is less pronounced. A similar behavior is noted while comparing the experimental flame height to Thomas' correlation. This latter slightly underestimates the flame height, yet it remains acceptable considering that this relationship was initially established for wood crib fires.

## RADIATIVE HEAT FLUX

### Point Source Method

Three radiative heat flux sensors were installed around the flame at a distance of 0.8 m from the fire source. This distance corresponds more than five times the pool diameter as recommended by A. T. Modak [26] and corroborated by Hamins et al

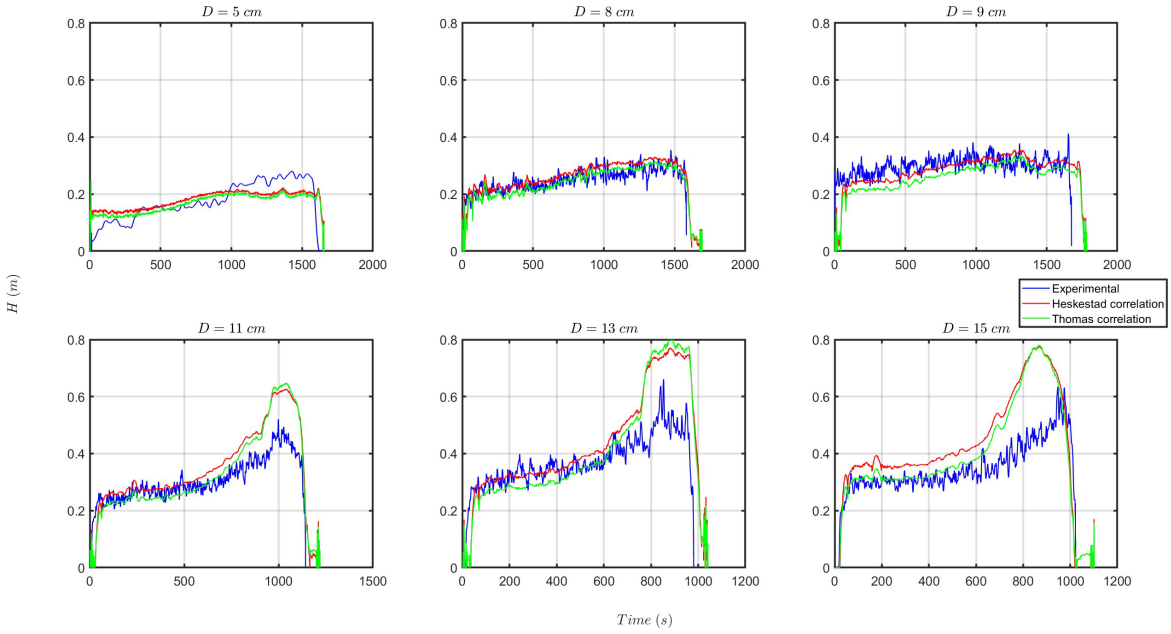


Figure 5: Comparison between the experimental flame height, Thomas's correlation, and Heskestad's correlation

[27]. Taking into account the previous recommendation and under the assumption of isotropy, the radiative heat release rate can be obtained with a single location measurement and can be estimated as follows

$$Q_r = \frac{4\pi R^2 q''}{cos(\theta)}, \tag{6}$$

In equation 6, a $1/cos(\theta)$ factor has been added compared to the usual formula, because the sensor was vertical, and located above the point source, so the $\theta$ angle between the normal of the sensor and the direction of radiation coming from the point source (see Fig. 1c) is not zero nor even negligible. $q''(W/m^2)$ is the measured radiative heat flux, $\theta$ is the angle between the normal to the sensor and the line of sight from the target to the point source location and $R$ is the distance between the heat flux sensor and the mid-height point of the flame [12] [28] given by

$$R = \sqrt{d^2 + (h - 0.35 - H/2)^2} \tag{7}$$

where $d$ is the horizontal distance between the pool and the radiative heat sensor (in our case 0.8 m), $H$ the flame height and $h$ the sensor height. The radiative fraction can then be estimated as the ratio between the radiative heat release rate and the total heat release rate

$$x_{rad} = \frac{Q_r}{Q}, \tag{8}$$

This method known as the "point source" method and is largely used in the literature. In order to challenge this method for small pool fires, a second method is described in the following section.

**Monte Carlo Method**

To calculate the radiative heat release rate, a second approach consists in considering the radiation phenomena as a volume phenomena rather than treating it as coming from a point source. At the scale considered in this work, the flame is optically thin, so that the radiation emitted by hot gases and soot in the flame is not significantly absorbed along its path between emission and the flame external surface. From the two flame images taken along two perpendicular directions, see Fig. 1b, the flame surface is reconstructed assuming an elliptical cross-section (which is the best that can be done with the available information). An example of a 3D flame surface is shown in Fig. 6 below. The flame volume is the inner volume defined by this surface.

Based on this second approach, the radiative heat release rate can be expressed as

$$Q_r = \frac{S \times q''}{F}, \tag{9}$$

where $S$ is the sensor surface ($9 \times 10^{-4}\ m^2$), $F$ is the view factor between the flame and the sensor. It corresponds to the fraction of radiation emitted by the flame that reaches the sensor. Since the flame shape is irregular, it is impossible to

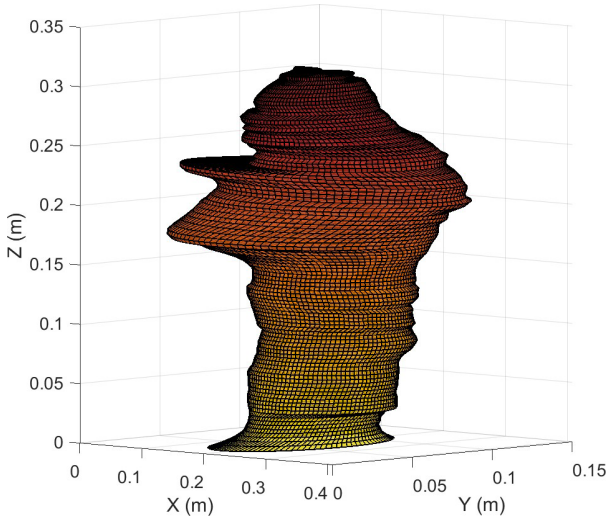


Figure 6: Illustration of the 3D flame reconstruction based on the front and side images

calculate analytically this factor, thus a Monte Carlo method was adopted. It is considered that quanta are emitted homogeneously in the flame volume and because the flame is optically thin their probability to be absorbed inside the flame is negligible. Quanta are tossed isotropically in a solid angle $\Delta\Omega$ defined such as quanta propagating in this solid angle have a chance to reach the sensor. It is indeed useless to launch quanta in directions for which there is no chance for them to hit the sensor. A great amount of calculation time is spared this way. The total number of quanta considered to calculate F is thus equal to the number of quanta actually tossed multiplied by the ratio $4\pi/\Delta\Omega$ that corresponds to the ratio of quanta propagating in all directions ($4\pi$ sr) and quanta propagating only in the $\Delta\Omega$ solid angle. Eventually, F is the ratio of quanta that reached the sensor by the total number of quanta assuming emission in the $4\pi$ sr solid angle. Since this method is based on statistical convergence, it is important to consider a sufficiently large number of quanta. Fig. 7 shows the variation of the view factor as a function of the number of quanta as well as the associated uncertainty. Indeed one of the big strength of the Monte Carlo method is its ability to provide the standard deviation $\sigma$ corresponding to the calculated quantity. We can see that this uncertainty is only 4.5% when $10^6$ quanta are used (uncertainty with a 68% confidence level associated to a $1\sigma$ interval. A 95% confidence level would be obtained considering a $2\sigma$ interval).

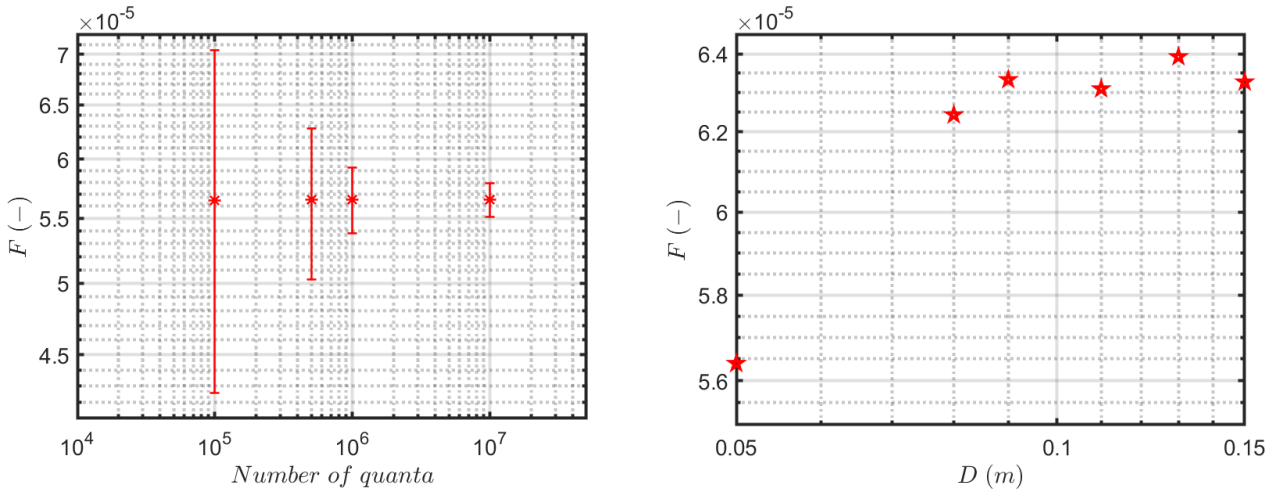


Figure 7: (a) Variation of the view factor as a function of the number of quanta considered in the decretization of the flame surface (for a 5 cm pool), (b) evolution of the view factor for different pool diameters

The evolution of the radiated heat release rate is represented in Fig. 8, as one may notice, the variation of the radiative heat release rate have the same trend as the heat release rate since both are almost proportional. Figure 9 shows the variation of the radiative fraction ($\chi_{rad} = Q_r/Q$) as a function of the pool diameter. The results from the current study are presented side by side with the available results from previous studies. According to the experimental results the radiative fraction for the used pans (5, 8, 9, 11, 13 and 15) varies between 28% and 39%. These results are consistent with the prediction of Hiroshi

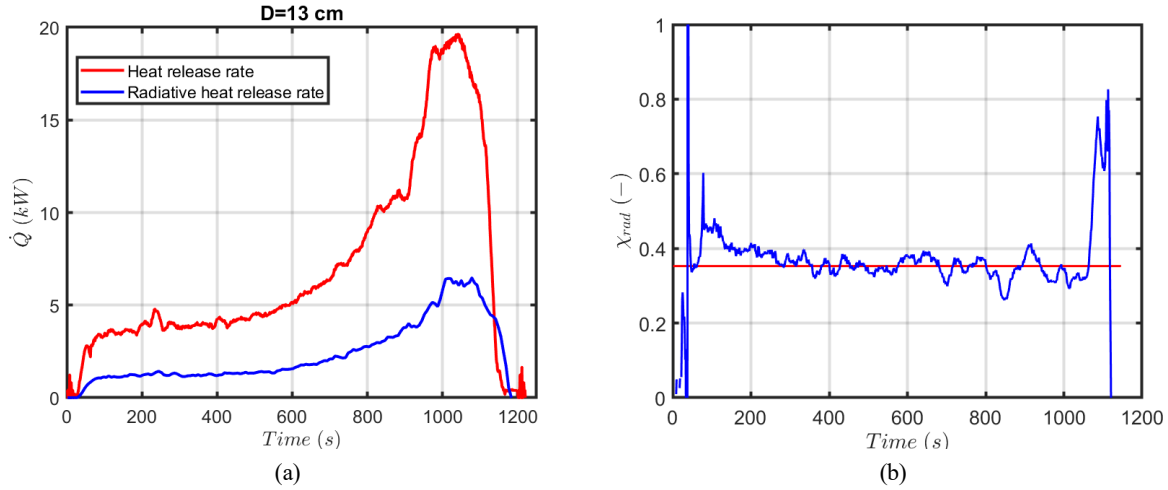


(a) (b)

Figure 8: (a) Temporal evolution of the total heat release rate in red and the radiative heat release rate in blue, (b) temporal evolution of the radiative fraction

and Taro [2], Hiroshi [3].

Knowing the view factor (F), the surface of the sensor (S) and taking into account the measured heat flux, the radiative heat release rate can be calculated using Eq. (9). Figure 9 shows the variation of the radiative fraction , method 1 and method 2 refers respectively to Eq. (6) and Eq. (9) used to determine the radiative heat release rate.

The comparison between the results from the two methods shows a good agreement, as the deviation is between 1% and 9%. The main difference between the two methods lays on the assumption regarding the flame shape, in the point source model a generic flame shape was adopted to establish the relation between the measured heat flux and the radiative heat release rate, however for Monte-Carlo method the visible flame shape was considered as a radiant volume. Despite these differences and taking into account the errors (13%) reported by Hamins et al [27], the point source method gives good estimation of the radiative fraction.

It is worth noting that the S/F ratio calculated by the Monte Carlo Method is here equal to 14.52 $m^2$, for the 8 cm diameter pan, that can be compared to the $4\pi R^2/cos(\theta) = 13,\ 20\ m^2$ factor involved by the Point source method with position of the point source as calculated by equation (6) i.e. at mid-height of the flame. That is explained because the base of the flame is generally larger than its apex, so more radiation comes from the lower part of the flame for which R is larger and $cos(\theta)$ is smaller, resulting to a view factor smaller than the one predicted by the point source method when this one is located at the mid-height of the flame. Using the position of the barycenter of flame volume as the position of the point source instead, it is found a 14.37 $m^2$ factor, which is very close to the factor obtained by the Monte Carlo Method.

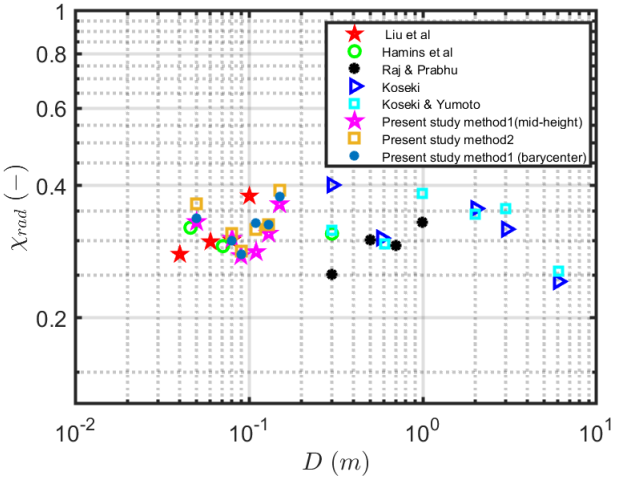


Figure 9: Variation of the radiative fraction as a function of the pool diameter (adapted from [12])

**CONCLUSION**

An experimental investigation of heptane pool fires in open atmosphere was conducted. Six pool diameters (5, 8, 9, 11, 13, 15) were tested. This work allowed us to determine the geometrical properties (height, surface) of flames resulting from a heptane pool combustion. These properties were then compared to the existing correlations. Heskestad [18] and Thomas [17] correlations gave a good estimation of the flame height. In the second part of this study, the radiative fraction was estimated using two methods, the first one is the commonly used point source model based on Eq. (6). The radiative fraction ranged between 28% and 39%. In order to take into account the flame shape in the radiative fraction estimation, a second method based on a Monte-Carlo approach coupled with image processing was implemented. The image processing served to obtain the flame shape, then the Monte-Carlo method was used to determine the view factor between the flame and the heat flux sensor. Once these quantities were estimated Eq. (9) was used to calculate the radiative heat flux. It was observed that the radiative fraction estimated using this method varies between 28% and 39%. This method confirms the results obtained previously with the point source approximation with a maximum deviation of 9% and 5% using the barycenter. The Monte-Carlo method combined with flame reconstruction method represent a more general method for calculating the radiative heat release rate especially when the distance between the flame and the radiative heat sensor is not large enough to consider a point source emission or to calculate radiative heat fluxes received by walls located near a flame.

# References


[1] Vytenis Babrauskas. Estimating large pool fire burning rates. *Fire Technol*, 19(4):251–261, November 1983.

[2] Koseki Hiroshi and Yumoto Taro. Air entrainment and thermal radiation from heptane pool fires. *Fire Technol*, 24(1):33–47, February 1988.

[3] Hiroshi Koseki. Combustion properties of large liquid pool fires. *Fire Technol*, 25(3):241–255, August 1989.

[4] A. Hamins, S. J. Fischer, T. Kashiwagi, M. E. Klassen, and J. P. Gore. Heat Feedback to the Fuel Surface in Pool Fires. *null*, 97(1-3):37–62, April 1994. Publisher: Taylor & Francis.

[5] M Munoz, J Arnaldos, J Casal, and E Planas. Analysis of the geometric and radiative characteristics of hydrocarbon pool fires. *Combust. Flame*, 139(3):263–277, November 2004.

[6] Hisahiro Takeda and Kazuo Akita. Critical phenomenon in compartment fires with liquid fuels. *Proc. Combust. Inst*, 18(1):519–527, 1981.

[7] A Tewarson. Some Observations on Experimental Fires in Enclosures, Part II - Ethyl Alcohol and Paraffin Oil.pdf. *Combust. Flame*, 19(3):363–371, 1972.

[8] Kwang Ill. Kim, Hideo Ohtani, and Yoichi Uehara. Experimental study on oscillating behaviour in a small-scale compartment fire. *Fire Saf. J*, 20(4):377–384, January 1993.

[9] Yunyong Utiskul, James G. Quintiere, Ali S. Rangwala, Brian A. Ringwelski, Kaoru Wakatsuki, and Tomohiro Naruse. Compartment fire phenomena under limited ventilation. *Fire Saf. J*, 40(4):367–390, June 2005.

[10] Maxime Mense, Yannick Pizzo, Hugues Prétrel, Christine Lallemand, and Bernard Porterie. Experimental and numerical study on low-frequency oscillating behaviour of liquid pool fires in a small-scale mechanically-ventilated compartment. *Fire Saf. J*, 108:102824, September 2019.

[11] J. Gore, M. Klassen, A. Hamins, and T. Kashiwagi. Fuel Property Effects On Burning Rate And Radiative Transfer From Liquid Pool Flames. *Fire Safety Science–Proceedings of the Third International Symposium*, 3:395–404, 1991.

[12] Jiahao Liu and Zhihui Zhou. Examination of radiative fraction of small-scale pool fires at reduced pressure environments. *Fire Saf. J*, 110:102894, December 2019.

[13] John R Howell. A Catalog Of Radiation Heat Transfer Configuration Factors.

[14] Fei He, Jiashun Shi, Li Zhou, Wu Li, and Xiaolong Li. Monte Carlo calculation of view factors between some complex surfaces: Rectangular plane and parallel cylinder, rectangular plane and torus, especially cold-rolled strip and W-shaped radiant tube in continuous annealing furnace. *Int. J. Therm. Sci.*, 134:465–474, December 2018.

[15] M. Mirhosseini and A. Saboonchi. View factor calculation using the Monte Carlo method for a 3D strip element to circular cylinder. *Int. Commun. Heat Mass Transf*, 38(6):821–826, July 2011.

[16] Giacomo Erez. Modélisation du terme source d'incendie: montée en échelle à partir d'essais de comportement au feu vers l'échelle réelle: approche "modèle", "numérique" et "expérimentale". *PhD thesis, Université de Lorraine, France, 2019*.

[17] P H Thomas. The Size of Flames from Natural Fires. *Proc. Combust. Inst*, pages 844–859.

[18] Gunnar Heskestad. Fire Plumes, Flame Height, and Air Entrainment. In *SFPE Handbook of Fire Protection Engineering,Section 2, Chapter 2–2*. Quincy, MA, USA, 1995.

[19] E. Zukoski. Fluid Dynamic Aspects Of Room Fires. *Fire Safety Science*, 1:1–30, 1986.

[20] James G. Quintiere. *Fundamentals of fire phenomena*. Wiley, Chichester, 2006. OCLC: 254253146.

[21] National Fire Protection Association and Society of Fire Protection Engineers, editors. *SFPE handbook of fire protection engineering*. National Fire Protection Association ; Society of Fire Protection Engineers, Quincy, Mass. : Bethesda, Md, 3rd ed edition, 2002.

[22] J. Gore, M. Klassen, A. Hamins, and T. Kashiwagi. Fuel Property Effects On Burning Rate And Radiative Transfer From Liquid Pool Flames. *Fire Saf. Sci.*, 3:395–404, 1991.

[23] Vinay C. Raj and S.V. Prabhu. Measurement of geometric and radiative properties of heptane pool fires. *Fire Saf. J*, 96:13–26, March 2018.

[24] R. Buch, A. Hamins, K. Konishi, D. Mattingly, and T. Kashiwagi. Radiative emission fraction of pool fires burning silicone fluids. *Combust. Flame*, 108(1-2):118–126, January 1997.

[25] Nobuyuki Otsu. A threshold selection method from gray-level histograms. *IEEE Trans Syst Man Cybern. SMC- 9 (1979) 62–66*.

[26] Ashok T. Modak. Thermal radiation from pool fires. *Combust. Flame*, 29:177–192, January 1977.

[27] A. Hamins, M. Klassen, J. Gore, and T. Kashiwagi. Estimate of flame radiance via a single location measurement in liquid pool fires. *Combust. Flame*, 86(3):223–228, August 1991.

[28] Longhua Hu, Qiang Wang, Michael Delichatsios, Shouxiang Lu, and Fei Tang. Flame radiation fraction behaviors of sooty buoyant turbulent jet diffusion flames in reduced- and normal atmospheric pressures and a global correlation with Reynolds number. *Fuel*, 116:781–786, January 2014.

# Experimental Study of the Fire Dynamics in a Non-combustible Parallel Wall setup

**Mendez J.[1],*, Lange D.[1], Hidalgo J.P.[1], McLaggan M.S.[2]**

[1] *University of Queensland, School of Civil Engineering, St. Lucia, QLD, Australia.*
[2] *University of Sheffield, Department of Civil and Structural Engineering, Sheffield, SY, UK.*
**Corresponding author's email: j.mendez@uq.edu.au*

## ABSTRACT

Narrow gaps and cavities present in modern construction systems have been deemed to be one of the key elements that enable fire spread after an initial fire event. A parametric experimental study was performed to characterise the fire dynamics in a cavity using a medium-scale (1.8m high) non-combustible parallel wall testing rig. Three different cavity widths, three different heat release rates and two air entrainment conditions at the base of the setup (i.e., closed, with no air entrainment at the base; open, with unrestricted air entrainment at the bottom) were studied, resulting in a total of approximately 36 experiments. Measurements of the flame height and the total external heat flux on the cavity walls were performed. It has been shown that both the heat fluxes and the flame heights increased as the cavity width was reduced. Correlations were sought to quantify the maximum heat exposure of a cavity as a function of the geometry of the system, the size of the fire and the ventilation condition. The results obtained in this study can be used for assessing the risks associated with ventilated façade systems, and as a benchmark future studies which will introduce combustible materials to the experimental setup.

**KEYWORDS:** Cavity, flame height, parallel wall, ventilated facades.

## NOMENCLATURE

| | |
|---|---|
| $C$ | correction factor for thin-skin calorimeter (-) |
| $c_P$ | constant pressure specific heat (J/(kg·K)) |
| $g$ | gravitational constant (m/(s$^2$)) |
| $h$ | heat transfer coefficient (kW/(m$^2$·K)) |
| $k$ | thermal conductivity (W/(m·K)) |
| $K$ | bidirectional probe correction factor (-) |
| $L_b$ | length of the burner (m) |
| $L_f$ | flame height (m) |
| $L_C$ | characteristic length (m) |
| $Nu$ | Nusselt number (-) |
| $q''$ | heat flux (W/m$^2$) |
| $Q'$ | heat release rate per unit length (kW/m) |
| $Ra$ | Rayleigh (-) |
| Re | Reynolds number (-) |
| $T$ | temperature (K) |
| $t$ | time (s) |
| $U$ | outflow velocity (m/s) |
| $V$ | voltage output (V) |
| $W$ | cavity width (m) |
| $z$ | height (m) |

**Greek**

| | |
|---|---|
| $\alpha$ | absorptivity (-) |
| $\delta$ | thickness (M) |
| $\Delta P$ | differential pressure (Pa) |
| $\varepsilon$ | emissivity (-) |
| $\rho$ | density (kg/m$^3$) |
| $\sigma$ | Stefan-Boltzmann constant (kW/(m$^2$·K$^4$)) |
| $\nu$ | viscosity (m$^2$/s) |

**Subscripts**

| | |
|---|---|
| $c$ | convective |
| $NC$ | natural convection |
| $FC$ | forced convection |
| $g$ | gas |
| $r$ | radiative |
| $TSC$ | thin-skin calorimeter |

## INTRODUCTION

Ventilated facades in buildings are a common type of exterior envelope which introduce an air cavity to improve ventilation flow, drain excess moisture, and reduce building energy consumption [1]. Although the cavity is normally designed according to local construction regulations, these cavities can allow the fire to spread causing a chimney effect and the resulting fire can spread to the interior surfaces of the cavities. Recent façade fire events, such as the Lacrosse building fire (Melbourne) and the Grenfell tower fire (London), have raised international concern about these fires and our ability to assess them. These systems represent a hazard even when non-combustible materials are used. To deliver a reliable testing framework, it is necessary to understand the effects of the system components on the fire physics.

### Previous research

The presence of surfaces near a flame restricts air entrainment across the plume. Extensive research has been made on the effect of the presence of a wall on the flame height [2-3] and the heat transfer to the surfaces involved [4]. Further experimental studies have been conducted to characterise the flame height and the heat transfer to non-combustible cavity walls exposed to a flame. Foley and Drysdale measured the distribution of total external heat flux on a wall exposed to a line burner. Different configurations were tested in which the distance to a parallel wall were varied. Correlations were obtained by the authors but it was recommended to conduct studies in a wider range of the variables of interest to extend the application of said correlations [5]. Another study on a single wall and parallel wall setup was conducted by Livkiss *et al* [6]. The results from the study indicated that no significant change was observed for the flame heights when the HRR per unit length of a line burner to cavity width ratio was lower than 300 kW/m$^2$. De Ris and Orloff measured flame heights and flame heat-flux distributions for a wide range of fuels burning between two parallel plates and obtained a model for the heat transferred to the cavity walls [7]. Also, a semiquantitative study of the heat transfer was conducted. Besides, Livkiss et. al simulated a fire driven flow between two parallel vertical walls. The flame heights and heat exposure to the walls of the cavity were determined using FDS and compared with experimental results. The authors highlighted that the Nu number calculation might not be ideal for cavity scenarios and that it should be used with caution [8].

### Research significance

The characterisation of the flame height and the incident heat flux from an external flame is essential to establish the boundary condition for both the ignition and flame spread over combustible linings. The present study aims to characterise the effect of the cavity width, the size of the fire and the ventilation condition on the fire dynamics of the system. This characterisation will be used to establish the basis for understanding the contribution of the cavity to the fire dynamics through the development of a robust mid-scale testing framework.

## METHODOLOGY

A prototype parallel wall system was built in order to execute a parametric study that sheds light on the dynamics of a fire confined by a cavity. The testing apparatus was built in order to quantify the effect of the size of the cavity, the heat release rate from the energy source and the air entrainment on the incident heat flux and the flame heights of different cavity fires. Flame height and total external heat flux on the cavity walls were used as the outputs for the characterisation of the fire dynamics of the system.

## Experimental setup

The experimental setup consisted of two 600 mm wide, 1800 mm high, 25 mm thick, vermiculite walls (Skamol V-1100 (375), see Table 1 for thermal properties). These walls were placed in a parallel configuration separated by an air gap, and mounted on an aluminium frame (see Fig. 1 (a)). One of the walls was mounted on movable elements that allowed simple and rapid modification of the cavity air width for different experiments. The non-combustible walls were replaced between the experiments after signs of deterioration were detected, e.g. cracks. One of the walls was instrumented with 15 thin-skin calorimeters (TSCs, comprised by a metallic Inconel disc and a vermiculite core) and 15 gas-phase thermocouples (TCs) (see Fig. 1 (b), (c)). These were installed to measure the evolution of the temperature of the wall (solid phase) and the gas phase temperature at vicinity of the solid surface, respectively (see Fig. 1(c)). No cooling system was used for the TSCs.

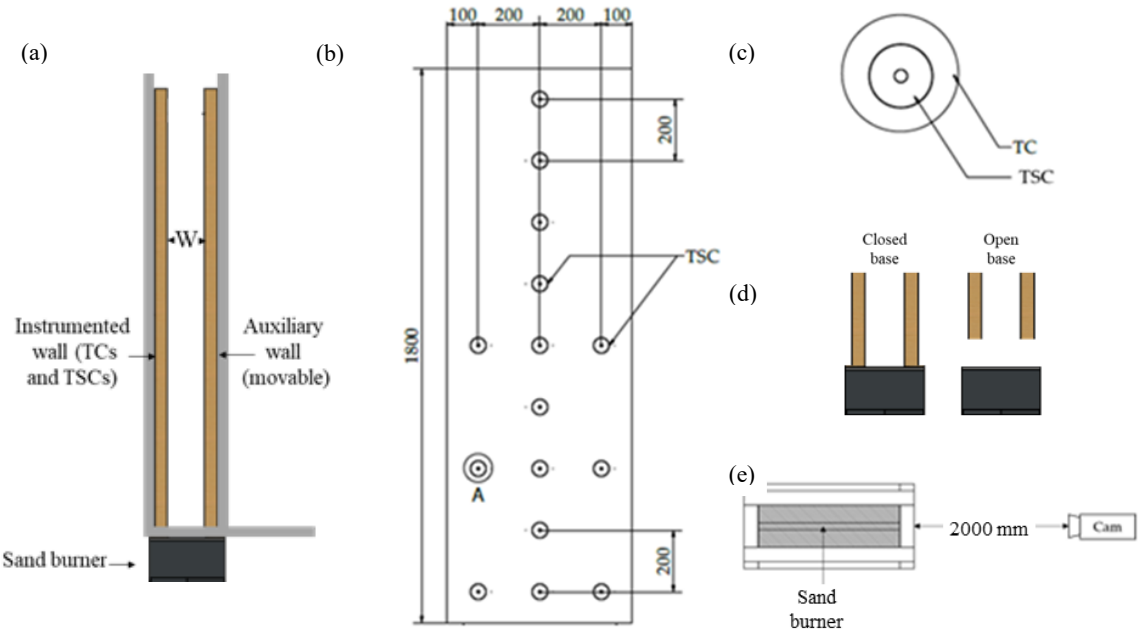


**Fig. 1.** (a) Lateral view of the experimental setup. (b) Instrumented wall (dimensions in mm). (c) detail of the TSCs and TCs location. (d) Closed and open base configuration. (e) Top view of the setup and camera location

A sand methane burner was placed at the base of the parallel walls to generate fires with different heat release rates per unit length (Q'). The burner heat release rate was calculated as the product of the mass flow rate of the natural gas and its effective heat of combustion (approximately $52.5 \cdot 10^3$ kJ/kg). The heat released was controlled by using a mass flow controller. It should be noted that methane has a lower radiative fraction if compared to other gaseous fuels, as noted by deRis and Orloff [7]. The width of the burner was modified by partially covering the upper surface with a non-combustible material to obtain the desired width to match the cavity width. This ensured that the flame impinged both cavity walls instead of a single lining. The length of the burner was kept constant at 480 mm. It was designed to be shorter than the wall width to ensure that flames would not escape the cavity. Bidirectional McCaffrey probes with a 0.015 m diameter. The three velocity probes were located in the centreline of the wall and in an equidistant point between the walls. The probes were located 450, 1050 and 1550 mm above the burner.

**Table 1. Temperature dependant thermo-physical properties of the non-combustible boards and TSC materials**

| Material | Thermal conductivity (W/(m·K)) | Density ($kg/m^3$) | Specific heat capacity (J/kg·K) | Emissivity (-) |
|---|---|---|---|---|
| Vermiculite (SKAMOL V-1100 (375)) | 0.12 @ 200°C<br>0.15 @ 400°C<br>0.16 @ 600°C<br>0.19 @ 800°C | 375 @ 20°C | 0.94 | Not used |
| Inconel | 15 @ 200°C<br>18 @ 400°C | 7800 @ 20<T< 1000 °C | $450 + 0.28T - 2.91\cdot10^{-4}T^2 + 1.34\cdot10^{-7}T^3$ @ 20<T< 1000 °C | 0.44 to 0.36 @ 216<T< 490°C |

To study the effect of the air entrainment on the behaviour of the cavity fire, two arrangements were tested. In one of them, the vermiculite boards were located in contact with the burner to prevent the air entrainment at the base, this configuration was denoted "closed base" (see Fig. 1 (d)). In the other arrangement, the experimental rig was lifted up 80 mm from the position in the closed base configuration in order to allow air entrainment from the bottom of the walls, this configuration is denoted as "open base". The investigated experimental configurations are presented in Table 2.

**Table 2. Experimental conditions**

| Test | Cavity width (m) | $Q'$ (Nominal) (kW/m) | $Q'$ (Real) (kW/m) | Base configuration |
|---|---|---|---|---|
| C1 | 0.05 | 20, 35, 50 | 20.80, 36.40, 51.56 | Closed |
| C2 | 0.05 | 20, 35, 50 | 20.80, 36.40, 52.03 | Closed |
| C3 | 0.10 | 20, 35, 50 | 20.80, 36.40, 52.03 | Closed |
| C4 | 0.10 | 20, 35, 50 | 20.80, 36.40, 52.06 | Closed |
| C5 | 0.15 | 35, 50, 74 | 36.41, 52.06, 79.73 | Closed |
| C6 | 0.15 | 35, 50, 74 | 36.46, 52.06, 77.37 | Closed |
| O1 | 0.05 | 20, 35, 50 | 20.80, 36.50, 52.06 | Open |
| O2 | 0.05 | 20, 35, 50 | 20.80, 36.60, 52.03 | Open |
| O3 | 0.10 | 20, 35, 50 | 20.80, 36.60, 52.12 | Open |
| O4 | 0.10 | 20, 35, 50 | 20.80, 36.50, 52.08 | Open |
| O5 | 0.15 | 35, 50, 74 | 36.44, 52.05, 77.25 | Open |
| O6 | 0.15 | 35, 50, 74 | 36.44,52.05, 78.32 | Open |

For each cavity width, three burner heat release rates were tested sequentially one after another within the same experiment (see Table 2). Every test was carried out twice in order to account for the variability in the experimental procedure. For each heat release rate, the test was run until a quasi-steady state was achieved as measured by thermocouples, which took a minimum of 10 minutes and

up to 15 minutes. The data was then extracted from a 90 s window where a steady state was reached, and those are the results presented in this manuscript.

**Quasi-steady state determination**

The quasi-steady state criteria for the experiment was set as a function of the evolution of the temperature in the solid phase. It was required that the temperature did not vary more than 2.5 °C per second and that the difference between the first and last temperatures measured in the span were not higher than 20 °C (see Eq. (1)).

$$T_s(t) - T_s(t+1) \leq 2.5; T_s(t=90) - T_s(t=0) \leq 20 \quad (1)$$

where $T_s$ is the solid-phase temperature, measured using the TSCs.

**Flame height determination**

Flame heights were measured as the tip of the continuous flame from 2250 photos corresponding to all the frames of a 90 s span of the previously defined quasi-steady state. A height reference was incorporated in the walls of the setup in order to calibrate the height of the flame.

An algorithm was developed to determine the flame height, defined as the solid flame tip. An alternative algorithm was developed which estimates the flame height considering the intermittency of the continuous flame but it is not discussed in this study. Two image manipulation tools were used to reduce the computational resources required. First, a colour threshold image filter was created to separate the flame from the background of the video. This filter consisted of an RGB threshold and was manually calibrated in the Color Threshold built-in application in MATLAB2019b ®.

**Table 3.** RGB threshold filter inputs

| Channel | Minimum Threshold | Maximum Threshold |
|---|---|---|
| Red | 240 | 255 |
| Green | 183 | 255 |
| Blue | 125 | 255 |

The reported values were determined based on visual observation of the effect of the threshold in the image, considering that the flame was isolated from the background. Second, the frames of the video were cropped into the area of interest to eliminate the extra pixels that were not relevant for the flame height. The original image was converted into a binary image and all the regions of the image with a flame were then identified, as depicted in Fig. 2 (a), and their corresponding area was measured. The largest area could be generally identified as the persistent flame but could also correspond to the intermittent flame. A pulsating flame was considered to be present if the second largest area was at least 20% the size of the largest area. In order to avoid this problem, the areas for the two largest objects were compared and the persistent flame was assigned as the object located closest to the bottom of the picture, i.e., closest to the burner.

Once the solid flame was identified, it was then converted into a contour and its dimensions were then recorded (see contours in Fig 2 (c)). The flame height for that individual frame was determined as the largest vertical distance of the contour. As this distance was measured in pixels, it was then transformed into metres using the pixels to height calibration mentioned above. Finally, the average flame height was determined as the mean of the individual measurements and then corrected to account for the view angle for the camera.

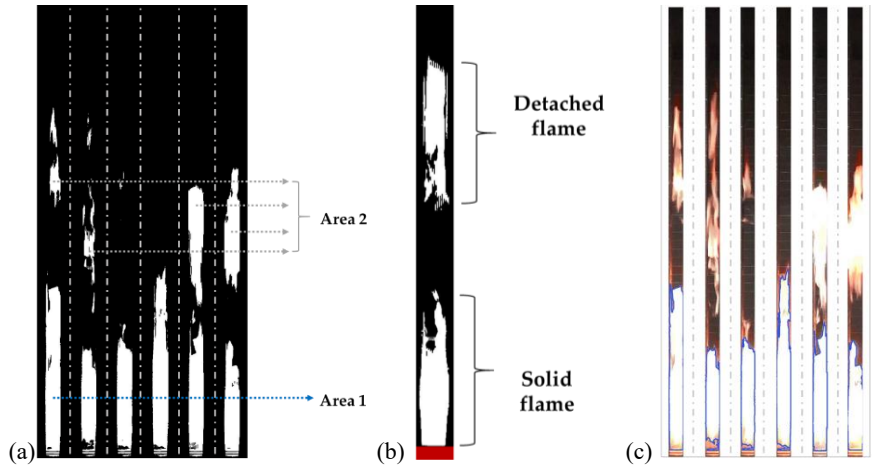


**Fig. 2.** (a) Flame areas in the binary image. *(*b) Solid or attached and intermittent flame. (c) Solid flame delimited by a contour

**Total external heat flux calculation**

Heat transfer from flames is mainly attained by radiation and convection. The total external heat flux (Eq. 2) on the wall was defined as the sum of a radiative (Eq. (3) and a convective (Eq. (4)) component, after the work of Hidalgo *et al* [9]).

$$q'' = q_r'' + q_c'', \tag{2}$$

$$q_r'' = \left[1/(\alpha_{TSC}(1-C)\right] \bullet \left[\rho_{TSC} C_{P_{TSC}} \delta_{TSC} dT_S / dt + \varepsilon_{TSC} \sigma T_s^4 + h_c (T_s - T_g)\right], \tag{3}$$

$$q_c'' = h_c (T_s - T_g), \tag{4}$$

where $\alpha_{TSC}$ is the absorptivity of the TSC metal disc, C is a correction factor for the heat transfer by conduction, $\rho_{TSC}$ is the density of the TSC metal disc, $\delta_{TSC}$ is the thickness of the disc, $C_{P_{TSC}}$ is the specific heat capacity of the disc, $\varepsilon_{TSC}$ is the emissivity of the disc, $\sigma$ is the Stefan-Boltzmann constant, $T_s$ is the solid-phase temperature measured by the TSC, and $T_g$ is the gas phase temperature, measured by the gas-phase TCs. The convective heat transfer coefficient ( $h_c$ ) in Eq. (3) and Eq (4) was calculated using Eq.(5). The results are compared in the results section.

$$h_c = Nu(k_g / L_C), \tag{5}$$

The Nusselt number ( $Nu$ ) was calculated using two different approximations. One for the natural convection regime ( $Nu_{NC}$ , see Eq.(6)) [10,11] and for the forced convection regime ( $Nu_{FC}$ , see Eq.(7)) [12].

$$Nu_{NC} = 0.68 + (0.67 Ra^{1/4}) / (1 + (0.492 / Pr)^{9/16})^{4/9}, \tag{6}$$

$$Nu_{FC} = 0.037 Re^{4/5} Pr^{1/3}, \tag{7}$$

Where the Reynolds number ( Re ) was calculated using the velocities obtained using bidirectional velocity probes described in the experimental section. The outflow velocity of the gases, $(U)$, was calculated using Eq. (8) [13].

$$U = K(2\Delta P / (\rho g))^{0.5}, \quad (8)$$

The correction factor, $(K)$, was calculated according to the corresponding model of the differential pressure transducers, following the an adaptation of the model proposed by Gupta *et al* [14].

$$K = 0.0649 \ln V + 0.8486, \quad (9)$$

## RESULTS AND DISCUSSION

### Flame height

The flame height as a function of the HRRPUA of the burner is presented in Fig. 3. The error bars correspond to the minimum and maximum measurement for a test corresponding to a repetition in a specific configuration. It is clear that for both open and closed based configurations, the flame height dramatically increases with narrower cavity widths and large HRRs. A significant difference is observed between the open and closed base configurations when the narrowest cavity and the two highest heat release rates were combined (Q'/W>700 kW/m$^2$). For those combinations, the open base configuration led to higher flames.

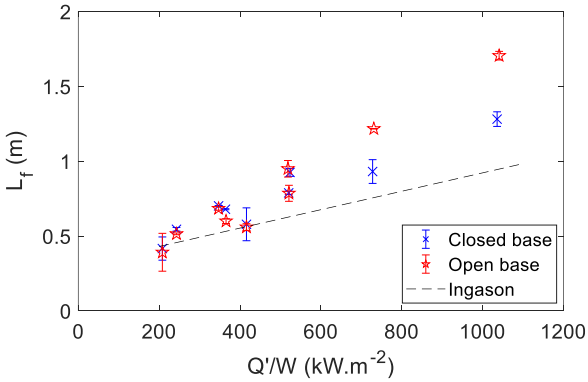


**Fig. 3.** Experimental flame heights vs heat release rate per unit area

This might indicate that air entrainment from the base helps push the flame towards the centre of the cavity, away from the walls. The influence of air entrainment on the elongation of the flame seems not to be significant for the rest of the configurations. The results are compared to the model proposed by Ingason [15] for flames constrained by storage racks. It can be observed that the flames for the parallel wall are higher for larger HRRPUA. This can be explained by the presence of extra gaps in the storage rack setup that allow the entrainment of cool air that generates a decrease on the buoyancy of the plume and to lower flame elongations. Further comparison against available models for flame height as a function of the nondimensional HRR is required and will be performed at later stages of this research.

### Heat transfer

*Outflow gas velocities*

The average outflow velocities are displayed in Fig. 4 for all the experiments. Closed and open base configurations lead to different behaviours in the outflow velocity profiles. No clear trends for the cavity size are observed whereas a higher outflow velocity is observed for a larger HRR as it would be expected.

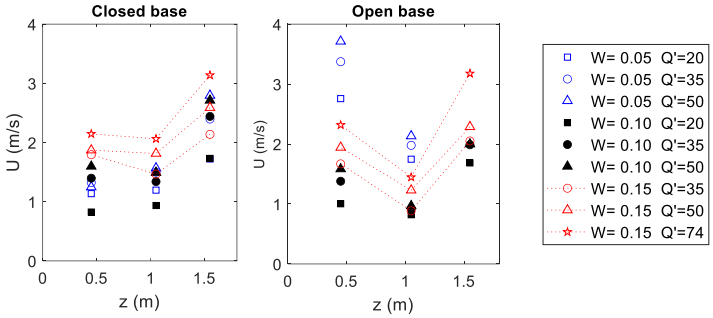


**Fig. 4.** Gas outflow velocities vs height above the burner

Higher outflow velocities at the probe located closer to the burner for the narrowest cavity width for the closed base configuration, compared to the open base one. This could be explained by the extra inflow of air from the bottom of the setup. These velocities were used to estimate the Nusselt number for forced convection ( $Nu_{FC}$ ).

*Convective heat transfer coefficient*

The magnitude of the convective heat transfer coefficient for the natural convection and forced convection approximation are presented in Fig. 5 The error bars represent the maximum and minimum value of the coefficient for the whole experiment.

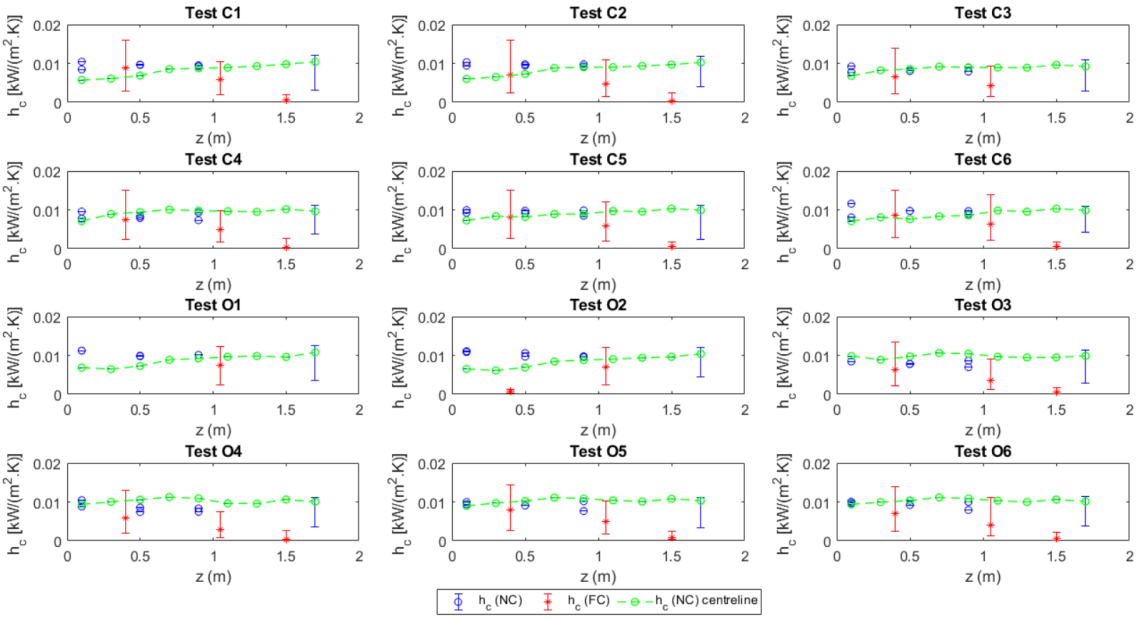


**Fig. 5.** Convective heat transfer coefficient for the different experimental approaches

It can be observed that for most of the measurements for the natural convection approach $h_c$ is larger away from the centreline than at the centreline for all the closed base configurations (C1-C6) and for

the narrowest cavity with the open base (O1-O2). The behavior reverses for the rest of the open base configuration tests (O3-O6).This indicates a change in the flow dynamics of the system and in the heat transfer as a result of a change in the air entrainment condition. It was estimated that using either of the approximations would lead to a deviation not higher than 1 kW/m$^2$ in the convective heat flux component, which is negligible considering the order of magnitude of the incident radiant heat flux (see Eq. (2)). Hence, the natural convection approximation was used, since it provided a greater number of locations for the characterisation of the convective and total convective heat flux.

*Heat flux vs height*

The total external heat flux (refer to Eq. (4) as a function of height is presented in Figure 6. Error bars correspond to the 20th and 80th percentile of the measurements for the steady state span. As with the flame heights, there are clear distinctions for different burner HRR, with higher HRR consistently giving higher total external heat flux across the height of the wall.

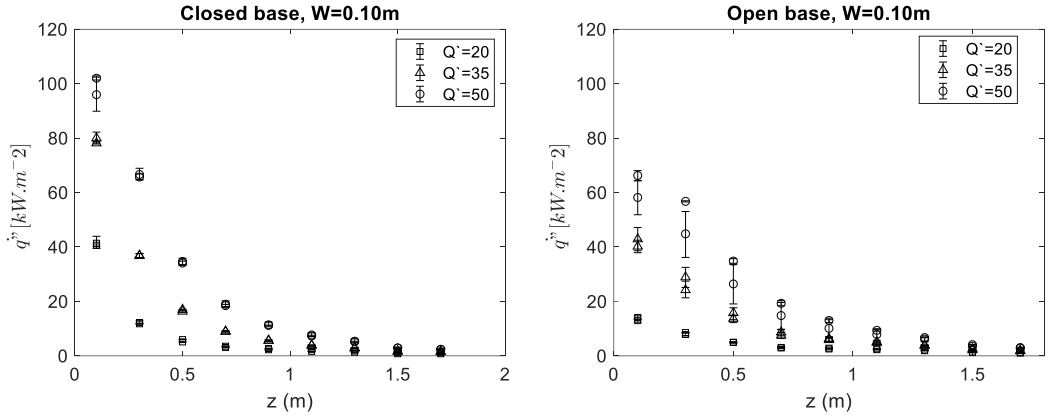


**Fig. 6.** Centreline total external heat flux

A comparison of closed base (left) and open base (right) also shows that a higher external heat flux is registered in the wall for the closed base scenario compared to the open scenario condition, and the highest incident heat flux is close to the burner. The difference observed between the closed and open scenarios is because the flame fills the whole cavity impinging both walls for the closed base. When the base is open, cool air flows upwards from the base and comes between the flame and the walls, preventing direct flame impingement and reducing the total external heat flux. Flame impingement increases the temperature of both walls and generates a larger radiative exchange between the two surfaces. This thermal exchange was enhanced as the cavity width decreased for both open and closed base configurations. It is possible to observe that although the flame heights are similar for both base configurations, the behaviour of the total external heat flux is different. A deeper study considering the influence of the system variables on the heat flux spatial distribution was conducted to explore the mechanisms underlying the discrepancies between the two base configurations.

*Heat flux spatial distribution*

The TSCs located distant from the centreline were used to quantify the spatial variation of the total heat flux over the wall. A subset of the results is presented in Fig. 7. It is evident that for both open and closed based configurations, the flame tip is present close to the centreline, where the highest heat

flux value is present. A decay of the heat flux towards the edges of the wall can be noticed. This can be explained by the change in the view factor and by the air entrainment from the open sides of the setup. The view factor at the lateral edges is lower than at the centreline of the wall, which implies a lower radiative heat transfer. As for the air entrainment, this process could only happen laterally, via the cavity when the base was closed. The entrainment decreased as the cavity width was reduced. This causes the flame to be pushed towards the centreline of the walls by the incoming air. Conversely, when the base is open, air is entrained both vertically from the bottom of the burner and horizontally through the cavity between the walls. Also, it was observed during the experiments that for the closed base, the flame behaved as a uniform sheet filling the entire cavity, whereas for the open scenario, the flame impinged the walls for a shorter distance.

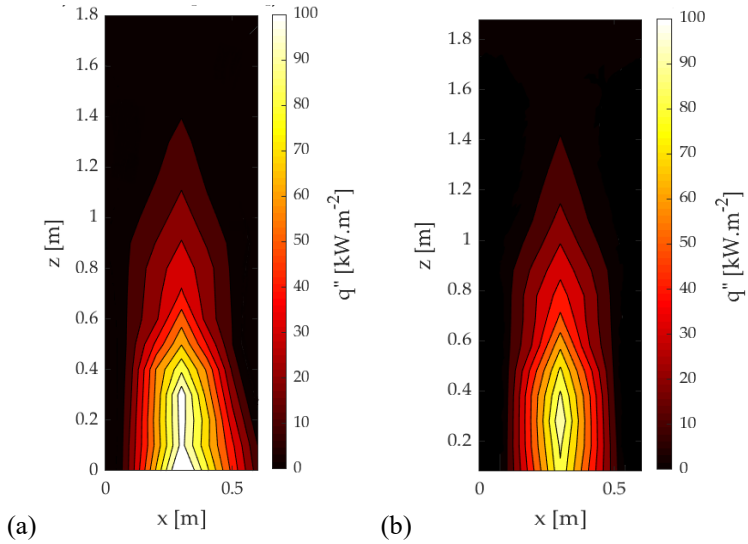


**Fig.7.** Heat flux spatial distribution (a) HRR = 35kW/m, W = 0.05m, closed base (b) HRR = 35 kW/m, W = 0.05m, open base

The exposure of combustible linings to these external heat fluxes could lead to their ignition and to the flame spread across said materials. Correlations were sought between the HRRPUA of the burner - defined as the ratio of the HRR per unit length of the burner and the cavity width - and the maximum external heat flux on the cavity.

*Maximum heat flux vs Q'/W*

The maximum heat flux for each base type, cavity width and heat release rate combination is presented in Fig. 8. Filled markers represent the closed base configurations and the hollow ones represent the experiments with an open base. The maximum heat flux was obtained as a proxy for the heat exposure of the walls. The maximum incident heat flux increases as the HRRPUA increases until certain value ($Q'/W < 500$ kW/m$^2$ for the closed base and $Q'/W < 700$ kW/m$^2$ for the open base configuration). Beside said critical value the value for the maximum external heat flux seems to stay constant around 105-110 kW/m$^2$.

The correlations obtained for the peak external heat flux and the HRRPUA are presented in Eq. (10) and Eq. (11). The presence of two outliers (closed, 0.15m, 74kW; open, 0.05m, 20kW) might indicate

that the trend for the external heat flux could be different and additional experiments should be executed to validate the model or generate a more accurate one.

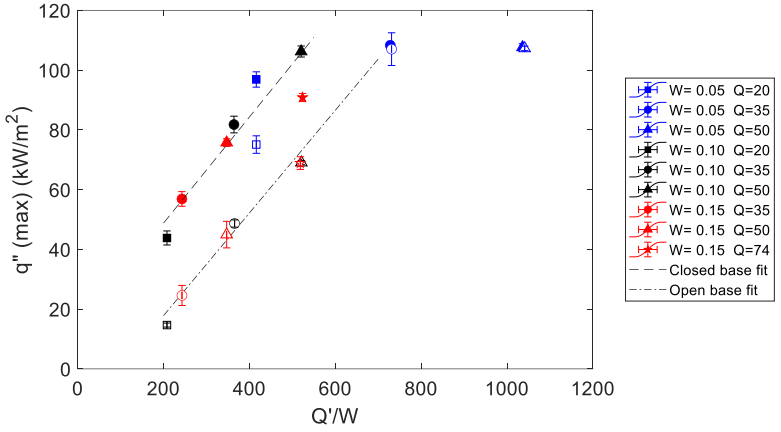


**Fig 8.** Maximum external heat flux vs Q'/W

*Open base:*

$$q'' = 0.18Q'/W + 13.28, \qquad 200 \le Q'/W \le 750, \tag{10}$$

*Closed base:*

$$q'' = 0.17Q'/W + 16.54, \qquad 200 \le Q'/W \le 450, \tag{11}$$

It is evident that a higher heat flux is obtained for the closed base scenario in most of the tried configurations due to the factors previously discussed in this paper. This indicates that allowing the entrainment of cool air on this kind of setups might present potential advantages in terms of lowering the heat exposure of the walls and could lower the risk for unintended ignition of combustible linings.

## CONCLUSIONS AND FUTURE WORK

A parametric experimental study to characterise the effect of different variables on the dynamics of a cavity fire been conducted. An experimental non-combustible parallel plate setup has been used to characterise the effect of the cavity width and the air entrainment at the base of the system to the flame height and the heat exposure of the walls of the system. It has been found that a smaller cavity width leads to more elongated flames. Also, it has been shown that the air entrainment at the bottom of the setup only has a significant effect on the flame height for HRRPUA values above 700 kW/m$^2$. This could be used as a design criterion knowing the maximum heat that could be released into the cavity and using the cavity width as a design parameter to set a maximum allowable flame impingement distance.

The trends for the outflow velocities are not certain and a higher number of instruments should be included to shed light on the flow dynamics behaviour within the cavity. It is recommended that an initial estimate of the outflow velocities is made previously with another instrument to select the appropriate kind of probe and differential pressure transducer for the application. Additionally, it is recommended that additional probes are located at the base of the setup and along the cavity in an in-plane orientation to quantify the air entrained to the plume and correlate it to the physics of the system. As for the heat transfer, preventing the air entrainment at the base of the setup lead to higher total external heat fluxes for almost all the configurations. The inflow of air from the base decreases the

flame impingement, leading to a lower heat exposure. However, this conclusion might not be appluicable if combustible linings form part of the cavity walls. The presence of a cavity at the base of the wall might help the fire spread and ince the material ignites, reradiation within the walls can increase heat fluxes as noted by Alpert [16]. It was also shown that the heat transferred to a wall increases as the cavity width decreases and also when the heat release rate from the fire source increases. The influence of the restriction of air entrainment can also be observed in the spatial heat transfer distribution. The peak external total flux seems to not exceed a value of 105-110 $kW/m^2$ for the tested conditions. Additionally, correlations were obtained for the maximum expected external heat flux on the wall as a function of the Q'/W ratio, that can be used as a design tool if a maximum allowable heat transfer exposure is set as a design criterion.

The results of this work have direct relevance to problems of ignition and upward flame spread in confined spaces which have inward-facing combustible surfaces. These results will be compared with previous research on similar setups in order to obtain a more detailed and theoretically sound characterisation of the fire dynamics of the system.

## REFERENCES

[1] A. B. Besir, E. Cuce, Green roofs and facades: A comprehensive review, Renewable and Sustainable Energy Reviews. 82 (2018) 915-939.
[2] Y. Hasemi and T. Tokunaga, Some experimental aspects of turbulent diffusion flames and buoyant plumes from fire sources against a wall and in a corner of walls, Combust. Sci. and Technol., 40 (1984) 1–17.
[3] W. Takahashi, H. Tanaka, O. Sugawa and M. Ohtake, Flame and plume behaviour in and near a corner of walls, Fire Safety Science. 5 (1997) 261–271.
[4] G. Back, C.L. Beyler, P. DiNenno, P. Tatem, Wall incident heat flux distributions resulting from an adjacent fire, Fire Safety Science, 4 (1994) 241-252.
[5] M. Foley and D. D. Drysdale, Heat transfer from flames between vertical parallel walls, Fire Saf. J. 24 (1995) 53–73.
[6] K. Livkiss, S. Svensson, B. Husted, and P. van Hees, Flame Heights and Heat Transfer in Façade System Ventilation Cavities, Fire Technol. 54 (2018) 689–713.
[7] J. L. de Ris, L. Orloff, Flame Heat Transfer between Parallel Panels, Fire Safety Science–Proceedings of the Eigth International Symposium, pp, 999–1010, 2005.
[8] K. Livkiss, B. P. Husted, T. Beji, and P. van Hees, Numerical study of a fire-driven flow in a narrow cavity, Fire Saf. J. 108 (2019) 102834.
[9] J. P. Hidalgo, C. Maluk, A. Cowlard, C. Abecassis-Empis, M. Krajcovic, and J. L. Torero, A Thin Skin Calorimeter (TSC) for quantifying irradiation during large-scale fire testing, Int. J. Therm. Sci., 112 (2017) 383–394.
[10] F.P. Incropera, D. DeWitt , T.L. Bergman, A.S. Lavine , Principles of heat and mass transfer, seventh ed., John Wiley & Sons, Inc., 2011.
[11] R.B. Bird, W. E. Stwewart, and E.N. Lightfoot, Transport Phenomena, second ed., John Wiley & Sons, Inc., 2002.
[12] S.W., Churchill, H.H.S., Chu, Correlating equations for laminar and turbulent free convection from a vertical plate. Int J Heat Mass Transf. 18 (1975) 1323-13299.
[13] B.J. McCaffrey, G. Heskestad, A robust bidirectional low-velocity probe for flame and fire application, Combust. Flame. 26 (1976) 125–127.
[14] V. Gupta, C. Maluk, J.L. Torero, and J.P. Hidalgo, Analysis of Convective Heat Losses in a Full-scale Compartment Fire Experiment, in 9th International Seminar on Fire and Explosion Hazards.(2019) 490–501.
[15] H. Ingason, Fire experiments in a two dimensional rack storage, BRANDFORSK-project 701-917, 1993.
[16] R. L. Alpert, Evaluation of the Hazard of Fire Resistant Materials Using Measurements from Laboratory and Parallel Panel Tests, Fire Safety Science–Proceedings of the Seventh International Symposium, pp, 41–57, 2003.

# An Experimental Investigation on the Impact of Burner Height and Location on the Characteristics of Under-ventilated Compartment Fires

**Dionysios I. Kolaitis*, Andrianos E. Koklas**

*Fire Engineering Unit, Laboratory of Heterogeneous Mixtures and Combustion Systems,*
*School of Mechanical Engineering, National Technical University of Athens,*
*Heroon Polytechneiou St. 9, Polytechneioupoli Zografou, Athens 15780, Greece*
** Corresponding author, e-mail:* dkol@central.ntua.gr

## ABSTRACT

Fire sources in compartment fires exhibit a predominantly uneven spatial distribution. In this context, the impact of the height and location of the fire source on the developed thermal and flow field is investigated by performing 33 fire tests in a ¼ scale compartment-façade experimental setup. A broad variety of measuring sensors is employed to characterise the conditions developing inside the compartment. A parametric study is performed, aiming to evaluate the impact of three different fire power levels, four different burner height values and three different burner locations. The obtained gas temperature measurements are used to assess the prediction accuracy of several fire engineering design correlations; in certain cases, the correlations are found to produce non-conservative results, while their prediction accuracy is significantly affected by the burner location and height.

**KEYWORDS:** compartment fires, burner height, burner location, fire engineering

## 1. INTRODUCTION

Even though it is well known that the fire sources in "real" compartment fires exhibit a predominantly uneven spatial distribution, the large majority of relevant compartment fire experimental studies employ an artificial fire source, usually in the form of a gas burner, located at the geometrical centre of the compartment. As a result, there are scarce reports in the literature on the effects of burner location and height on the characteristics of the developing fire. Tofilo et al. [1] tested the effect of the burner position in two locations (centre and rear corner) and concluded that the temperature and the heat flux inside the compartment are larger when the burner is located at the rear corner. Hwang et al. [2], using a large-scale compartment, found that the temperature inside the compartment is larger when the burner is located at the back of the compartment. Backovsky et al. [3] investigated the effect of burner height (ranging between 7% and 40% of the total height of the compartment) and concluded that increasing the burner height results in increasing gas temperatures. Finally, Ji et al. [4] observed that increasing the burner height, results in increasing the upper layer temperatures.

In this context, the main scope of this work is to investigate the effects of the burner height and location on the characteristics of the thermal and flow fields developing inside the compartment, in the case of under-ventilated fires. A thorough analysis of the experimental data allows to determine the impact of these parameters on the compartment (indoor) temperatures, the compartment wall temperatures and the gas velocities (both incoming and outgoing through the opening). In addition, several fire engineering design correlations, aimed at estimating the compartment gas temperatures, are evaluated by employing the obtained measurements.

## 2. EXPERIMENTAL SETUP

The fire compartment dimensions corresponded to a ¼ scale of the ISO 9705 standard compartment, representing a typical room [5, 6, 7]. The internal dimensions of the model compartment were 900

mm (length) x 600 mm (width) x 600 mm (height); the door-type opening's dimensions were 200 mm (width) x 500 mm (height). Two layers of standard fire-resistant gypsum plasterboards were used for the construction of the test compartment. The model compartment is shown in Fig. 1 (left). The inverse opening factor ($O_{inv}$) is calculated using Eq. 1 [8], where $A_t$, $A_f$ and $A_o$ are the total area of the compartment, the floor area and the area of the opening, respectively, whereas $h_o$ is the opening height. Using Eq. 1, the inverse opening factor of the experimental compartment was calculated to be equal to 31.67 $m^{-1/2}$; since its value is higher than 8 $m^{-1/2}$, a ventilation-controlled (under-ventilated) fire is expected to be developed [8].

**Fig. 1.** Fire compartment (left) and porous burner (right).

$$O_{inv} = \frac{A_t - A_f - A_o}{A_o\sqrt{h_o}} \tag{1}$$

A porous burner, made of aluminium oxide was used as the fire source. The burner dimensions were 125 mm (length) x 175 mm (width) x 55 mm (height) and the hole diameter was 1 mm (Fig. 1, right). The burner was fed with 99.95 % pure methane ($CH_4$).

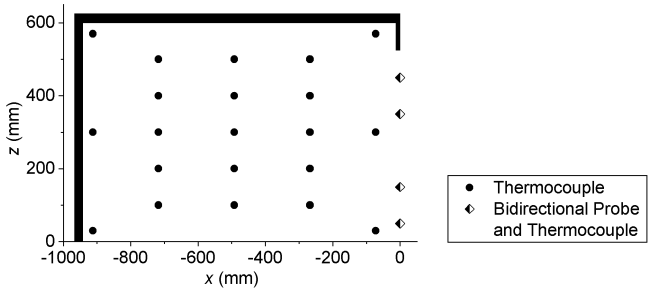


**Fig. 2**. Spatial distribution of measurement sensors for a typical fire test.

A broad sensor network was installed both inside the compartment to determine the main characteristics of the developing flow and thermal fields. Overall, 25 K-type thermocouples, 4 bi-directional velocity probes, 1 continuous gas analyser, 3 digital flow meters and 2 optical cameras were used. The spatial distribution of the measurement sensors is depicted in Fig. 2. The origin of the coordinate system used is located at the centre of the door, at floor level; all sensors were installed along the symmetry axis of the compartment ($y$ = 0 mm).

### 2.1 Parametric Study

A total of 33 test cases were performed examining the effect of the burner's thermal power, location and height. Three fire power levels, i.e. 90 kW, 120 kW and 144 kW, were tested. For all the investigated thermal power levels, under-ventilated conditions were established. Three burner locations were examined, i.e. Front (F), Center (C) and Back (B), located, respectively, 267.5 mm, 492.5 mm and 717.5 mm away from the compartment opening, which corresponds to the 25%, 50% and 75% of the total compartment length, respectively. Also, four burner heights were examined, i.e. 150 mm, 200 mm, 300 mm and 400 mm above the compartment floor which correspond to the 25%, 33%, 50% and 66% of the total compartment height, respectively. Table 1 summarizes the main characteristics of every test.

**Table 1.** Main characteristics of all the investigated test cases.

| No. | Fire Test | Fire power level $Q$ (kW) | Distance from the opening $x_B$ (mm) | Height above the floor $z_B$ (mm) |
|---|---|---|---|---|
| 1 | Q090-F150 | 90 | -267.5 | 150 |
| 2 | Q120-F150 | 120 | -267.5 | 150 |
| 3 | Q144-F150 | 144 | -267.5 | 150 |
| 4 | Q090-F200 | 90 | -267.5 | 200 |
| 5 | Q120-F200 | 120 | -267.5 | 200 |
| 6 | Q144-F200 | 144 | -267.5 | 200 |
| 7 | Q090-F300 | 90 | -267.5 | 300 |
| 8 | Q120-F300 | 120 | -267.5 | 300 |
| 9 | Q144-F300 | 144 | -267.5 | 300 |
| 10 | Q090-F400 | 90 | -267.5 | 400 |
| 11 | Q120-F400 | 120 | -267.5 | 400 |
| 12 | Q144-F400 | 144 | -267.5 | 400 |
| 13 | Q090-C150 | 90 | -492.5 | 150 |
| 14 | Q120-C150 | 120 | -492.5 | 150 |
| 15 | Q144-C150 | 144 | -492.5 | 150 |
| 16 | Q090-C300 | 90 | -492.5 | 300 |
| 17 | Q120-C300 | 120 | -492.5 | 300 |
| 18 | Q144-C300 | 144 | -492.5 | 300 |
| 19 | Q090-C400 | 90 | -492.5 | 400 |
| 20 | Q120-C400 | 120 | -492.5 | 400 |
| 21 | Q144-C400 | 144 | -492.5 | 400 |
| 22 | Q090-B150 | 90 | -717.5 | 150 |
| 23 | Q120-B150 | 120 | -717.5 | 150 |
| 24 | Q144-B150 | 144 | -717.5 | 150 |
| 25 | Q090-B200 | 90 | -717.5 | 200 |
| 26 | Q120-B200 | 120 | -717.5 | 200 |
| 27 | Q144-B200 | 144 | -717.5 | 200 |
| 28 | Q090-B300 | 90 | -717.5 | 300 |
| 29 | Q120-B300 | 120 | -717.5 | 300 |
| 30 | Q144-B300 | 144 | -717.5 | 300 |
| 31 | Q090-B400 | 90 | -717.5 | 400 |
| 32 | Q120-B400 | 120 | -717.5 | 400 |
| 33 | Q144-B400 | 144 | -717.5 | 400 |

## 2.2 Scaling Effects

Due to the increased difficulties and hazards of a full-scale fire experiment, it is common practice to perform fire tests in small scale compartments, aiming to identify phenomena that are still valid for full-scale compartments. In order to achieve this, the Buckingham Pi method [9] is used. The Heat Release Rate (HRR) is one of the most important factors affecting a compartment fire. In order for a fire in a small scale compartment to have the same characteristics with a fire in the full scale

compartment, the characteristic dimensionless number $\Pi_2$ (Eq. 2) should remain constant, where $Q_l$* or $\Pi_2$ is the dimensionless heat release rate, $Q$ (kW) is the heat release rate, $\rho_\infty$ (kg/m$^3$) is the ambient density, $T_\infty$ (K) is the ambient temperature, $g$ (m/s$^2$) is the gravitational acceleration and $l$ (m) is the characteristic length. The temperature is independent of the scaling of the compartment ($T \sim l^0$).

$$Q_l^* \equiv \Pi_2 = \frac{\dot{Q}}{\rho_\infty c_p T_\infty \sqrt{g} l^{5/2}} \tag{2}$$

Table 2 summarizes the dimensions and the fire power levels of the small-scale compartment used in the fire tests, as well as the respective values for the corresponding full-scale compartment.

**Table 2**. Dimensions and burner thermal power for the small- and the full-scale compartmnent.

| Parameter | Small-scale compartment | Full-scale compartment |
|---|---|---|
| Length (mm) | 900 | 3600 |
| Width (mm) | 600 | 2400 |
| Height (mm) | 600 | 2400 |
| Burner HRR (kW) | 89.70 | 2870.40 |
| | 119.60 | 3827.20 |
| | 143.51 | 4592.32 |

## 3. MEASUREMENT UNCERTAINTIES

In order to estimate the uncertainty of the measurements the ASME methodology [10] was used. The total measurement uncertainty, $U_t$, was estimated by using Eq. 3, where $B_t$ is the systematic uncertainty and $S_t$ is the random uncertainty. A coverage factor value of $K = 2$ was used to achieve a 95% confidence interval ($2\sigma$) for the total uncertainty [10].

$$U_t = \pm K \left[ \left( B_T / 2 \right)^2 + \left( S_T \right)^2 \right]^{1/2} \tag{3}$$

The gas temperatures were measured using K-type thermocouples connected to the signal acquisition system via extension wires. The systematic uncertainties of the thermocouples were a standard calibration uncertainty of ±2.2ºC or ±0.75% of the measured value (the largest value is taken into account) for a 99% confidence interval ($3\sigma$), an uncertainty due to the wires and their extension of ±2.2ºC and a conversion uncertainty of ±0.5%. The opening velocities were measured using bi-directional velocity probes. In terms of the systematic uncertainties, the bi-directional velocity probes exhibited a flow approaching uncertainty of ±10% [11], a conversion uncertainty of ±1% of the maximum pressure of the pressure sensor (10 Pa). For both the thermocouples and the bi-directional velocity probes and for 95% confidence interval, the random uncertainty is estimated using Eq. 4.

$$S_1 = S_T = 2\sigma_X \tag{4}$$

### 3.1 Indoor gas temperature corrections

In the interior of a fire compartment, the measured temperatures obtained using bare bead thermocouples might not be fully representative of the actual temperature. This is because of a variety of physical phenomena, with the radiative heat transfer having the dominant influence. A “correction” methodology, proposed by Welch et al. (2007) [12], is used in order to estimate the actual gas temperature ($T_{gas}$). The correction methodology is based on the solution of the heat balance equation for the thermocouple bead, which results in Eq. 5 where $\varepsilon_{TC}$ is the emissivity of the thermocouple, $\sigma$

($W/m^2K^4$) is the Stefan–Boltzmann constant, $h_{TC}$ ($W/m^2K$) is the heat transfer coefficient (Eq. 6), $k$ ($W/m{\cdot}K$) is thermal conductivity, Nu (-) is the Nusselt number, $d_{TC}$ ($m$) is the diameter of the thermocouple, $T_{TC}$ ($K$) is the measured temperature and $T_S$ ($K$) is the effective temperature of the surroundings. $T_S$ is estimated using Eq. 7; the weighting factor ($w_i$) is depended on the relative position of the thermocouples and $N$ is the total number of the thermocouples inside the compartment.

$$T_{gas} = \frac{\varepsilon_{TC}\sigma}{h_{TC}}\left(T_{TC}^4 - T_S^4\right) + T_{TC} \tag{5}$$

$$h_{TC} = \frac{kNu}{d_{TC}} \tag{6}$$

$$T_S = \left(\sum_{i=1}^{N} w_i T_{gas,i}^4\right)^{\frac{1}{4}} \tag{7}$$

The relative error of the gas temperature measurements, expressed as $(T_{gas} - T_{TC})/T_{TC}$, is shown in Fig. 3, for two characteristic test cases. Generally, the "corrected" gas temperature values are higher than the corresponding measured values in the upper layer ($z > 300$ mm) and lower when $z < 300$ mm.

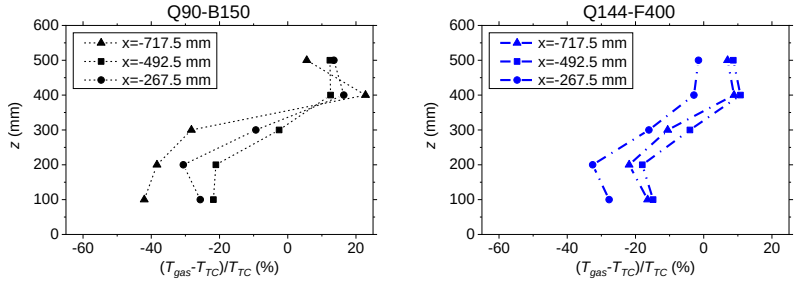


**Fig 3**. Relative error of gas temperature measurements for test cases Q090-B150 (left), and Q144-F400 (right).

## 4. EXPERIMENTAL RESULTS

All experimental data presented henceforth correspond to time-averaged values over a period of 180 s; data recording was commenced only after steady-state conditions (determined by means of temporal gradient limiting values) were established in each fire test.

### 4.1 Indoor gas temperatures

The effects of the burner HRR ($Q$), height ($z_B$) and location ($x_B$) on the compartment's average temperature and the compartment's upper layer temperature are illustrated in Fig. 4. As expected, increasing the burner's HRR results in an increase of the average compartment temperature and the average upper layer (ceiling jet) temperature. Increasing the distance between the opening and the burner ($x_B$), both the average compartment temperature and the average upper layer temperature increase, thus corroborating similar findings reported in the literature [1, 2]. Also, increasing the burner height ($z_B$) results in decreasing average compartment temperatures; this trend has also been reported in previous works by Backovsky et al. [3] and Ji et al. [4].

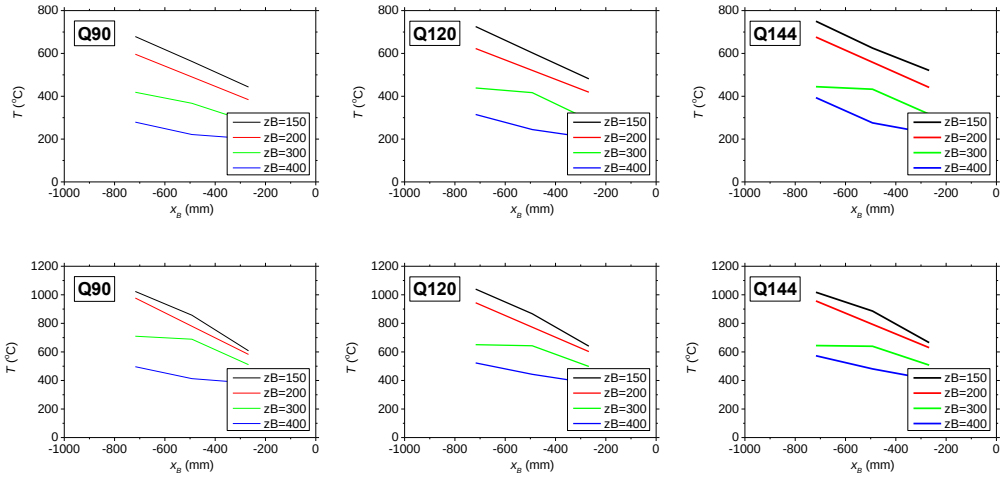


**Fig. 4**. Effects of burner HRR, height and location on the average compartment temperature (top) and the average upper layer temperature (bottom) for a fire power of 90 kW (left), 120 kW (center) and 144 kW (right).

## 4.2 Opening Temperatures

The vertical distribution of gas temperatures at the opening, for some characteristic test cases, is depicted in Figs. 5-7. In general, increasing the burner HRR and the burner distance from the opening results in a slight increase of the opening temperatures; however, increasing the burner height results in decreasing opening temperatures at all heights.

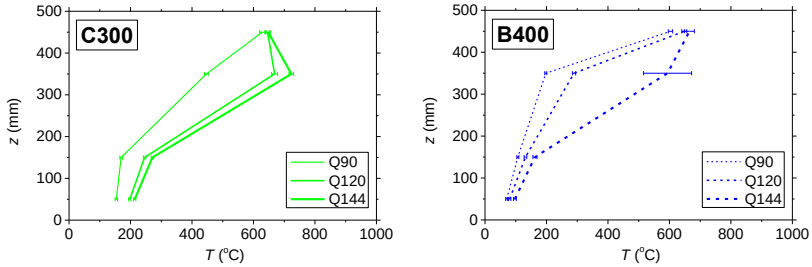


**Fig. 5.** Effect of burner HRR on the opening temperatures for the cases C300 (left) and B400 (right).

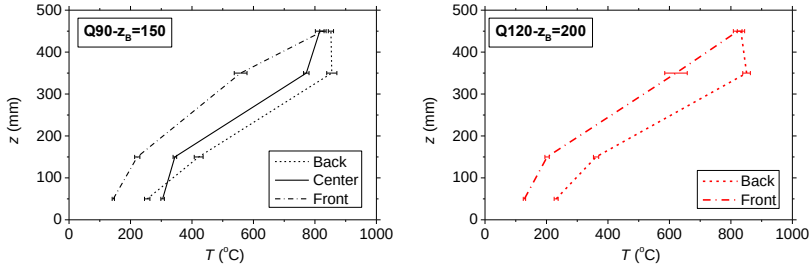


**Fig. 6**. Effect of burner location on the opening temperatures for cases Q90-$z_B$=150 mm (left) and Q120-$z_B$=200 mm (right).

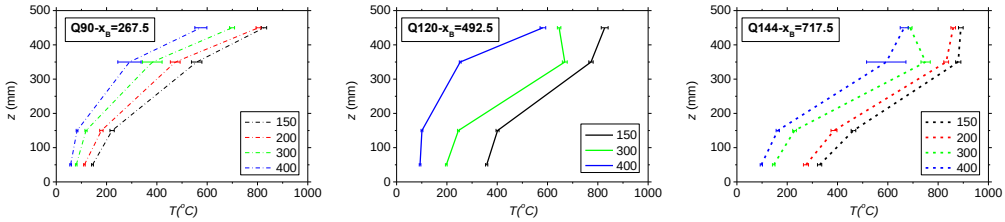


**Fig. 7**. Effect of burner height on the opening temperatures for cases Q90-Front (left), Q120-Center (center) and Q144-Back (right).

Figure 8 illustrates the impact of the burner location (left to right) and the burner height (top to bottom) on the spatial gas temperature distribution inside the test compartment, for a constant HRR (144 kW).

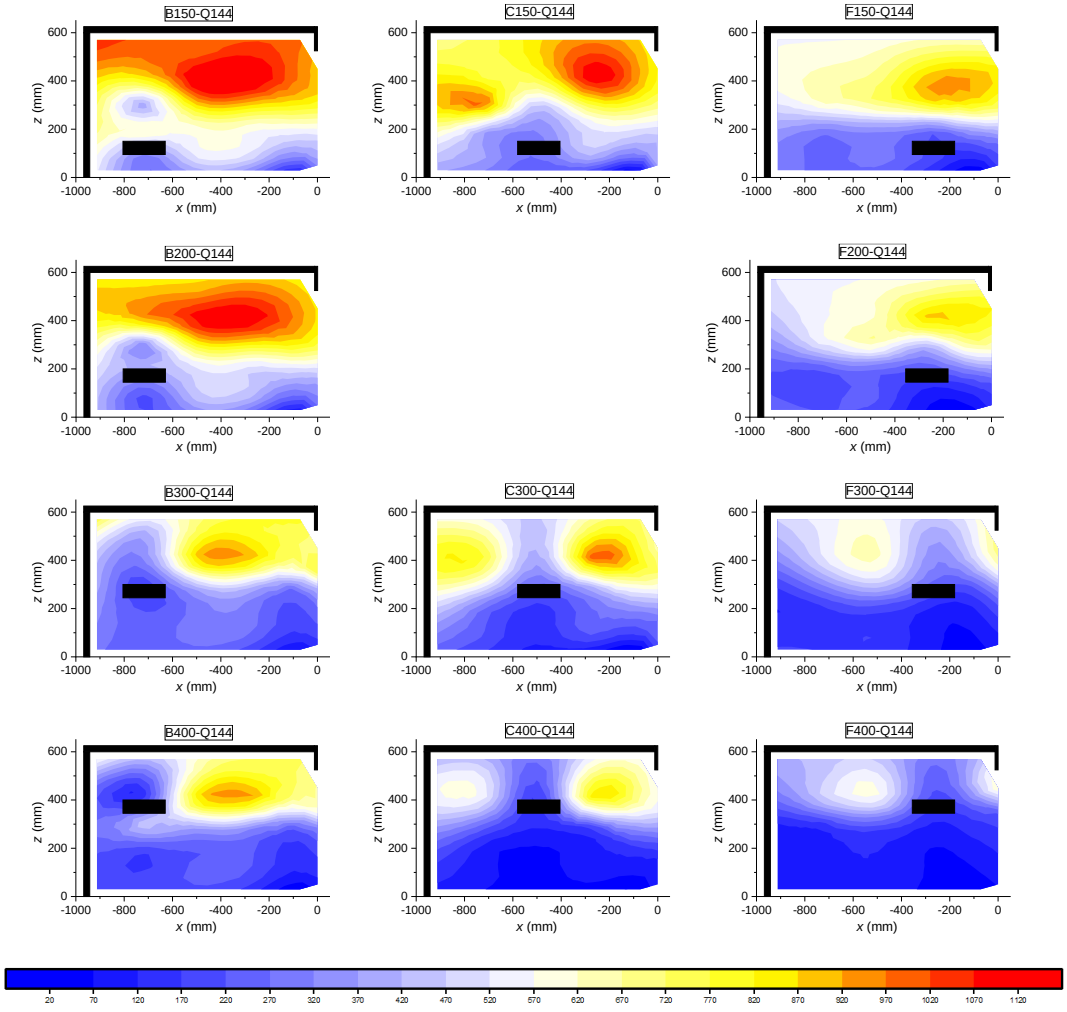


**Fig. 8**. Effects of burner location (left to right) and burner height (top to bottom) for $Q$ = 144 kW.

### 4.3 Opening Velocities

The vertical distribution of horizontal velocities ($u$) at the opening is depicted in Figs. 9-11 for some representative test cases. Positive velocities correspond to exhaust gases exiting through the opening, whereas negative velocities indicate ambient air entering into the compartment.

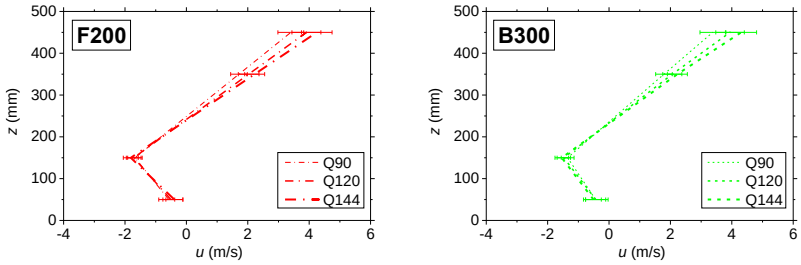


**Fig. 9**. Effect of burner HRR on the opening horizontal velocity for test cases F200 (left) and B300 (right).

The burner's HRR and location do not significantly affect the velocity of the incoming ambient air, whereas the outgoing exhaust gas velocity is increased with increasing HRR and distance between the burner and the opening. Increasing the burner height results in decreasing exhaust gas and increasing ambient air velocities.

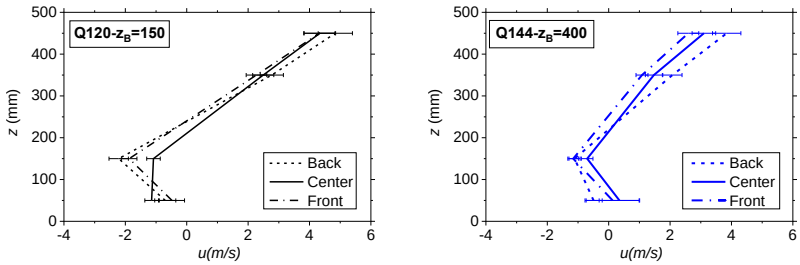


**Fig. 10**. Effect of burner location on the opening horizontal velocity for test cases Q120-$z_B$=150 mm (left), and Q144-$z_B$=400 mm (right).

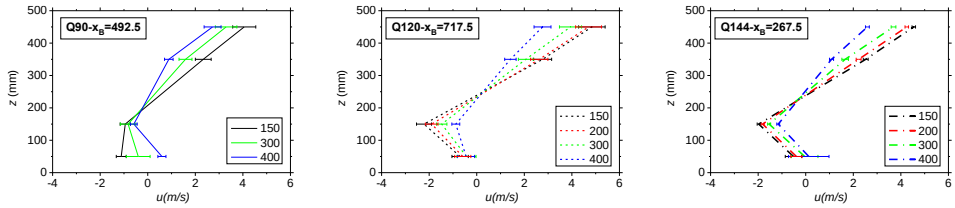


**Fig. 11**. Effect of burner height on the opening horizontal velocity for test cases Q90-Center (left), Q120-Back (center) and Q144-Front (right).

## 5. CRITICAL EVALUATION OF ENGINEERING CORRELATIONS

In order to estimate the gas temperature of the fire, a set of engineering correlations is given in the SFPE Handbook of Fire Protection Engineering [13] for the compartment upper layer gas temperature and in Eurocode 1991-1-2 [14] for the opening temperature. Aiming to evaluate and assess the

accuracy of these correlations, their predictions are compared against the experimentally determined values.

### 5.1 Upper layer gas temperatures

The method of Babrauskas (Eq. 8) [13] can be used to determine the upper layer gas temperature, where $T_\infty$ ($K$) is the ambient temperature, $T^*$ is an empirical constant equal to 1725 K and $\theta_i$ are specific factors; their values, calculated for each of the investigated HRR levels, are given in Table 3.

$$T_g = T_\infty + (T^* - T_\infty) \cdot \theta_1 \cdot \theta_2 \cdot \theta_3 \cdot \theta_4 \cdot \theta_5 \tag{8}$$

**Table 3**. Estimated values of $\theta$ factors for Eq. 8.

| Factor | Description | Values | | |
|---|---|---|---|---|
| | | Q90 | Q120 | Q144 |
| $\theta_1$ | Burning rate stoichiometry factor | 0.9313 | 0.9978 | 0.9919 |
| $\theta_2$ | Wall steady-state losses factor | 1.0000 | 1.0000 | 1.0000 |
| $\theta_3$ | Wall transient losses factor | 1.0000 | 1.0000 | 1.0000 |
| $\theta_4$ | Opening height effect factor | 0.7476 | 0.7476 | 0.7476 |
| $\theta_5$ | Combustion efficiency factor | 0.8884 | 0.8884 | 0.8884 |

Alternatively, based on the MQH [15] method, the compartment's upper layer gas temperature can be estimated using Eq. 9, where $Q$ (kW) is the HRR, $c_p$ (kJ/kg·K) is the specific heat of air, $\rho_\infty$ ($kg/m^3$) and $T_\infty$ ($K$) are the ambient density and temperature, respectively, $A$ (m$^2$) is the area of the window, $H$ ($m$) is the window height, $A_T$ ($m^2$) is the total area of the enclosure and $h_k$ (W/m$^2$K) is the heat transfer coefficient which, for steady state conditions, is calculated using Eq. 10, where $k_W$ (W/m·K) is the thermal conductivity of the wall and $\delta$ ($m$) is the wall thickness.

$$T_g = 480 \times \left( \frac{\dot{Q}}{\sqrt{g} c_p \rho_\infty T_\infty A \sqrt{H}} \right)^{2/3} \times \left( \frac{h_K A_T}{\sqrt{g} c_p \rho_\infty T_\infty A \sqrt{H}} \right)^{-1/3} + T_\infty \tag{9}$$

$$h_K = \frac{k_W}{\delta} \tag{10}$$

In Fig. 12, the experimentally determined upper layer gas temperatures are compared against the respective predictions. In most cases, both correlations are found to over-predict the measured temperature values. The observed discrepancies are mainly attributed to the fact that the employed correlations are appropriate for a full-scale compartment and not a small-scale compartment.

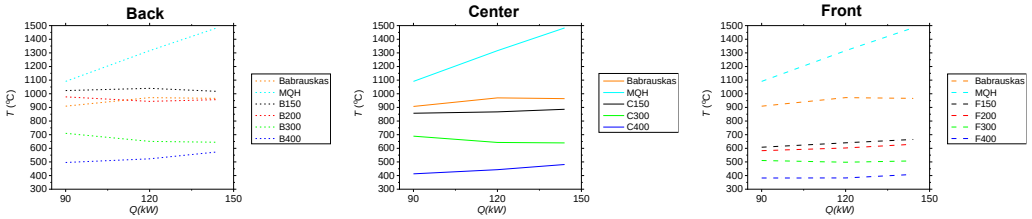


**Fig. 12**. Comparison between experimental and predicted upper layer gas temperature values.

Figure 13 depicts the relative deviation (%) between the experimental and the predicted upper layer gas temperature values for all the 33 test cases considered here. Predictions of the Babrauskas correlation lie closer to the measured temperatures, although there are some cases where the predicted values are not conservative (e.g. B150). On the other hand, the MQH methodology is found to always produce conservative results, exhibiting, however, larger errors. For both correlations, as the burner height increases or the distance between the burner and the opening is decreased, the observed discrepancies between the measured and the calculated temperature values increase. Babrauskas' method is not affected from the increase of the burner HRR, while the MQH method performs better at lower HRR levels. In general, the prediction accuracy of both correlations is found to increase with increasing burner distance from the opening and decreasing burner height.

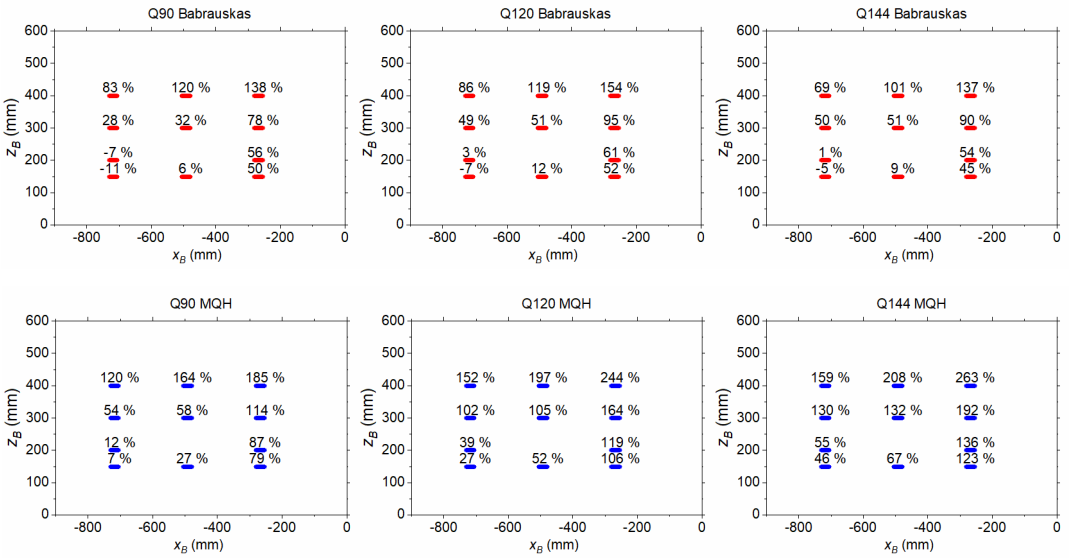


**Fig. 13.** Relative errors of the Babrauskas (top) and MQH (bottom) correlations for test cases Q90 (left), Q120 (center) and Q144 (right).

### 5.2 Opening temperatures

Equation 11 is proposed in Eurocode EN 1991-1-2 [14], to determine the gas temperature at the opening; $T_0$ (K) is the initial temperature (here considered equal to 293 K), $Q$ (kW) is the HRR, $L_f$ (m) is the flame length along the centreline axis and $w_t$ (m) is the opening width. The geometrical characteristics of the flame were obtained using the images recorded using the optical cameras.

$$T_w = T_0 + \frac{520}{1 - 0.4725\left(\frac{L_f w_t}{\dot{Q}}\right)} \tag{11}$$

In Table 4, the measured average exiting gas temperatures at the opening are compared against the respective Eurocode correlation predictions; the latter, generally under-predict the measured values, resulting in potentially non-conservative results for fire safety engineering design calculations.

**Table 4**. Comparison of measured opening gas temperatures and respective Eurocode predictions.

| Test Case | Experimental values (ºC) | Eurocode predictions (ºC) | Deviation (%) |
|---|---|---|---|
| Q090-F150 | 692.15 | 540.59 | -21.90 |
| Q120-F150 | 798.85 | 540.62 | -32.33 |
| Q144-F150 | 832.24 | 540.61 | -35.04 |
| Q090-F200 | 638.42 | 540.56 | -15.33 |
| Q120-F200 | 721.72 | 540.58 | -25.10 |
| Q144-F200 | 777.97 | 540.59 | -30.51 |
| Q090-F300 | 540.33 | 540.50 | + 0.03 |
| Q120-F300 | 535.78 | 540.49 | + 0.88 |
| Q144-F300 | 634.31 | 540.52 | -14.79 |
| Q090-F400 | 432.93 | 540.44 | + 24.83 |
| Q120-F400 | 384.13 | 540.40 | + 40.68 |
| Q144-F400 | 426.58 | 540.42 | + 26.69 |
| Q090-C150 | 793.71 | 540.64 | -31.88 |
| Q120-C150 | 800.08 | 540.62 | -32.43 |
| Q144-C150 | 794.87 | 540.61 | -31.99 |
| Q090-C300 | 537.74 | 540.51 | + 0.51 |
| Q120-C300 | 657.34 | 540.55 | -17.77 |
| Q144-C300 | 685.52 | 540.55 | -21.15 |
| Q090-C400 | 396.12 | 540.42 | + 36.43 |
| Q120-C400 | 417.29 | 540.42 | + 29.51 |
| Q144-C400 | 546.82 | 540.48 | -1.16 |
| Q090-B150 | 853.45 | 540.67 | -36.65 |
| Q120-B150 | 873.79 | 540.68 | -38.12 |
| Q144-B150 | 885.06 | 540.66 | -38.91 |
| Q090-B200 | 812.17 | 540.65 | -33.43 |
| Q120-B200 | 841.85 | 540.67 | -35.78 |
| Q144-B200 | 846.00 | 540.64 | -36.09 |
| Q090-B300 | 573.60 | 540.53 | -5.77 |
| Q120-B300 | 659.12 | 540.56 | -17.99 |
| Q144-B300 | 719.56 | 540.56 | -24.88 |
| Q090-B400 | 400.53 | 540.43 | + 34.93 |
| Q120-B400 | 468.92 | 540.45 | + 15.25 |
| Q144-B400 | 629.47 | 540.51 | -14.13 |
| | | **Average deviation** | **-11.62** |

## 6. CONCLUSIONS

In this work, the effects of the burner power, height and location on the characteristics of the flow and thermal fields developing in a compartment fire were investigated experimentally, by using a medium scale compartment in under-ventilated conditions. The main trends that have been observed by analysing the obtained experimental data are presented in Table 5; an “upwards” arrow corresponds to an increase of the respective measured quantity and vice-versa for a “downwards” arrow.

**Table 5**. Summary of the observed effects when the burner HRR, height and location are modified.

| Measured Quantity | Increasing burner HRR | Increasing burner height | Increasing distance between opening and burner |
|---|---|---|---|
| Average temperature | ↑ | ↓ | ↑ |
| Upper layer average temperature | ↑ | ↓ | ↑ |
| Opening temperature | ↑ | ↓ | ↑ |
| Exhaust gas velocity | ↑ | ↓ | ↑ |
| Incoming ambient air velocity | - | ↓ | - |

In general, increasing the burner height results in decreasing temperatures inside the compartment, as well as decreasing velocities of the two main flows exiting and entering the compartment through the opening. This behaviour may be attributed to the reduced combustion efficiency and the restricted exhaust gas flow observed when the burner height approaches the ceiling of the compartment. On the other hand, increasing the distance between the burner and the opening results in generally higher compartment temperatures, leading to higher exhaust gas velocities.

In addition, a detailed comparison of the experimentally obtained quantities against the respective predictions of several fire engineering design correlations, proposed in the SFPE Handbook of Fire Protection Engineering [13] and the Eurocode EN 1991-1-2 [14], allowed a critical assessment of the latter's prediction accuracy and the impact of varying the burner location and height.

## ACKNOWLEDGEMENTS

The assistance of Mr. Charalambos Mavrakis and of Dipl. Eng. Christos Kontis and Christoforos Tsichlas during the testing phase of this work is gratefully acknowledged.

## REFERENCES

[1] Tofilo P., Delichatsios M.A., Silcock G.W.H., Shields T.J. (2004) Wall Heat Fluxes in Enclosure Fires, Proceedings of the 6th Asia-Oceania Symposium on Fire Science & Technology.

[2] Hwang C.H., Lock A., Bundy M., Johnsson E., Ko G.H., Effects of Fuel Location and Distribution on Full-Scale Underventilated Compartment Fires, Journal Fire Sciences 29 (2011) 21-52

[3] Backovsky J., Foote K.L., Alvares N.J., Temperature Profiles in Forced-Ventilation Enclosure Fires, Fire Safety Science 2 (1989) 315-324.

[4] Ji J., Fu Y., Li K., Sun J., Fan C., Shi W., Experimental study on behavior of sidewall fires at varying height in a corridor-like structure, Proc. Combust. Inst. 35 (2015) 2639-2646.

[5] Asimakopoulou E.K., Kolaitis D.I., Founti M.A., Thermal Characteristics of Externally Venting Flames and their Effect on the Exposed Façade Surface, Fire Safety Journal 91 (2017) 451-460

[6] Asimakopoulou E.K., Chotzoglou K., Kolaitis D.I., Founti M.A., Characteristics of externally venting flames and their effect on the façade: A detailed experimental study, Fire Technology 52 (6) (2016) 2043-2069

[7] ISO 9705:1993 Fire tests - Full-scale room test for surface products, ISO, Geneva (1993).

[8] P.H. Thomas, A.J.M. Heselden, Fully Developed Fires in Single Compartments, Fire Research Station, London, UK, 1972.

[9] Quintiere J. 2006, Fundamentals of Fire Phenomena. Wiley, West Sussex, England.

[10] Nakos J.T. Uncertainty analysis of thermocouple measurements used in normal and abnormal thermal environment experiments at Sandia's Radiant Heat Facility and Furnace Canyon Burn Site, 2004.

[11] Kim S.C, Kim J.Y., The Effect of Flow Approaching Angle on the Velocity Measurement Using Bi-directional Velocity Probe, Procedia Engineering 62 (2013) 797-803.

[12] Welch S., Jowsey A., Deeny S., Morgan R., Torero J.L., BRE large compartment fire tests—Characterising post-flashover fires for model validation, Fire Safety Journal 42 (8) (2007) 548-567.

[13] Hurley M.J., Gottuk D.T., Hall, J.R., Harada, K., Kuligowski, E.D., Puchovsky, M., Torero, J.L., Watts, J.M., Wieczorek, C. (2016), SFPE Handbook of Fire Protection Engineering, 5th Edition.

[14] EN 1991-1-2:2002, Eurocode 1. Actions on structures. General actions. Actions on structures exposed to fire, CEN, Brussels (2002)

[15] McCaffrey, B.J., Quintiere, J.G., Harkleroad, M.F., Estimating room temperatures and the likelihood of flashover using fire test data correlations, Fire Technology 17 (1981) 98-119.

# Impact of Sloped Terrain, Fuel Moisture Content and Fuel Load on Fuel Litter Fires: An Experimental Study

**Kolaitis D.*, Pallikarakis C., Founti M.**

*National Technical Universtiy of Athens, School of Mechanical Engineering,*
*Heterogeneous Mixtures & Combustion Systems, Fire Engineering Unit,*
*Heroon Polytechniou 9, Athens 15772, Attica, Greece.*
**Corresponding author's email: dkol@central.ntua.gr*

## ABSTRACT

An experimental investigation of small-scale wildland fires was conducted, using an inclinable combustion table. A continuous fuel bed of "Pinus Halepensis" needles was ignited, and various geometric and thermal properties of the propagating flame front were dynamically recorded. An in-house image processing algorithm was developed to identify the geometrical characteristics of the flame envelope (height, angle and front position), thus allowing the estimation of the flame's rate of spreading. In addition, the fire's instantaneous Heat Release Rate (HRR) was estimated by means of oxygen calorimetry; heat flux measurements at the downstream end of the fuel bed were also obtained. Ten fire tests were performed in total, by varying different parameters, such as the slope angle, the fuel load and the fuel moisture content (FMC); these tests constituted both a repeatability and a parametric study, aimed at investigating the influence of the main parameters in the dynamics of the flame front. Increasing the slope angle or the fuel load resulted in increasing rate of spreading, HRR and heat flux of the flame; the same trends were observed when the FMC was decreased.

**KEYWORDS:** wildland fires, experiment, slope, rate of spread, HRR

## 1. INTRODUCTION

Wildland fire is a natural phenomenon which, due to both its importance to the natural flora (and fauna) equilibrium and its implications to the human society, has attracted attention from multiple fields of science and engineering. The main purpose of research activities in wildland fire dynamics is the identification of the most important multi-scale, interacting, physical phenomena that characterise wildland fires, aiming to understand, predict and, ultimately, control them.

Large-scale wildland fires are the subject of great interest, since they are associated with the most important hazards, since their successful and timely extinction is, usually, a nearly impossible task. It is obvious, that comprehensive field experimentation at these scales is not possible. Therefore, relevant scientific knowledge is commonly acquired by means of experimentation in small-scale laboratory test rigs. Laboratory experimentation on small-scale wildland fires allows the study of the respective physical phenomena in their most fundamental form, using a controllable environment. Laboratory fires of dead fuel litter have been on the spotlight since the 1960s [1], since they offer a rather simple experimental layout (which can be modelled as a solid porous material); also, they may have a large impact, especially at the early stages of a wildfire event. In general, the behaviour of wildland fires is mainly affected by a plethora of parameters, corresponding to the fuel, the local geomorphology and the prevailing weather conditions. The effects of the first two parameters have been studied in the past, using fuel beds in inclinable tables, by recording the visual [2-7], thermal [4-7] and flow properties [6,7] of the propagating fire front.

In this context, a laboratory-scale experimental study on fuel litter fires is presented in this work, aiming to evaluate the impact of three important parameters, namely the slope angle, the fuel load and the Fuel Moisture Content (FMC) on various geometrical and thermal properties of the propagating flame.

## 2. EXPERIMENTAL METHDODOLOGY

### 2.1 Experimental Apparatus

The experimental study presented in this work consists of a series of ten laboratory experiments of propagating wildland fire on pine needle fuel beds resting on an inclinable table. A sketch of the inclinable table is given in Fig. 1 (left). The table has a ceramic area of 2 m x 2 m, that is capable of rotating to change its slope from 0º to 30º. Two cameras are positioned to record the side-view and the back-view of the propagating flame; they can be seen in Fig. 1 (right).

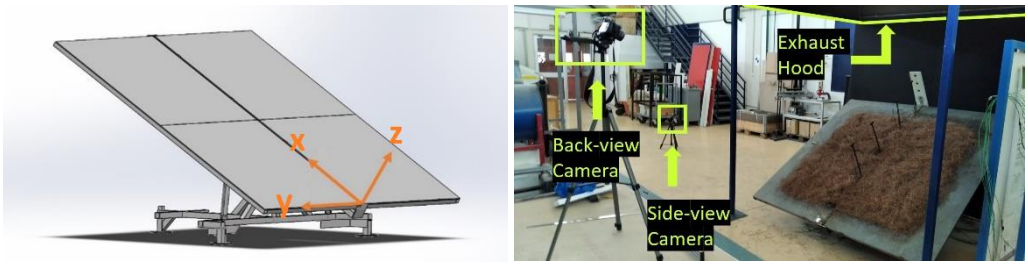


**Fig. 1.** Model representation of the inclinable table (left) and photo of the actual test rig before ignition (right).

The inclinable table is equipped with several measuring sensors in order to record various thermal and flow quantities of interest. A grid of 86 K-type thermocouples is used; 70 of them are laid close to the centreline of the table (on the plane $y$ = 70 mm), while the other 16 thermocouples are located perpendicular to the fire propagation axis. For the flow velocity measurements, four bi-directional Pitot tubes are positioned along the centreline of the table ($y$ = 0 mm) at a constant height ($z$ = 400 mm), oriented to measure the velocity along the fire propagation ($x$) direction. Furthermore, three heat flux sensors are placed at the downstream end of the inclinable table at various heights, on the plane of symmetry ($y$ = 0 mm). The positions of the aforementioned sensors are depicted in Fig. 2, following the world coordinate origin, defined in Fig. 1 (left). The inclinable table is located under an exhaust hood that collects the gas combustion products (Fig. 1, right); a gas sample is then fed to a continuous gas analyser, measuring $O_2$, $CO_2$ and CO levels, thus allowing the estimation of the fire's instantaneous HRR value by means of oxygen calorimetry. The hood is additionally equipped with a thermocouple and an averaging Pitot tube to determine the mass flow rate of the combustion products. The signal from all the instrumentation (excluding the cameras) is recorded through a digital signal acquisition device, using a 0.8 Hz sampling rate.

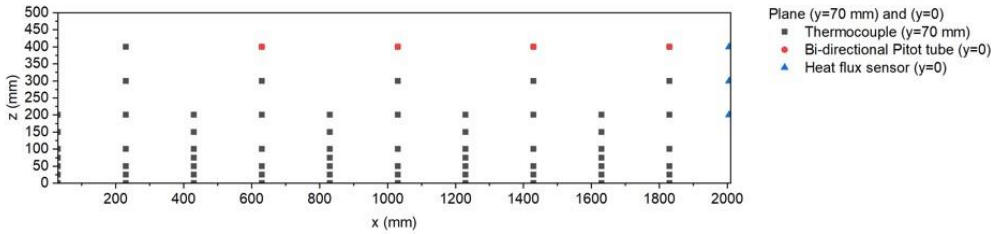


**Fig. 2.** Locations of thermocouples, bi-directional Pitot tubes and heat flux sensors along the propagation axis (x), at the y=70 mm plane.

### 2.2 Fuel bed characteristics

The fuel beds tested comprised of dead needles of "Pinus Halepensis" trees that have been gathered outdoors. In order to study the effect of fuel moisture content, part of the fuel was oven treated at

105ºC for 24 hours [8]. Both the treated and the untreated fuels were stored in airtight barrels. The untreated fuel remained in the barrels (before experimental use) for a period of at least 1 week, which was deemed sufficient for the fuel's FMC to be uniform. The fuel moisture was measured through a moisture analyser and was estimated to be approximately 8% for the untreated fuel and 1% for the treated fuel (in wet basis). A sample from the fuel was characterized to estimate important fuel properties, such as needle density $\rho_p$ (kg/m$^3$), surface-to volume-ratio $\sigma$ (m$^{-1}$) and heat content $h_u$ (MJ/kg). For the estimation of $\rho_p$ and $\sigma$ the needle shape was assumed to be cylindrical; these parameters were determined by averaging the measurements of the length, mean diameter and mass of 100 individual needles. The heat content was measured via bomb calorimetry. The calculated values of the needle density ($\rho_p$), surface to volume ratio ($\sigma$) and heat content ($h_u$) are 827 kg/m$^3$, 7447 m$^{-1}$ and 19.17 MJ/kg, respectively. It is noted that $\rho_b$ and $\sigma$ refer to the untreated needles, while the heat content refers to the treated ones.

The fuel bed dimension was roughly 1.7 m x 1.7 m. The (wet basis) fuel load was either 0.5 kg/m$^2$ or 1.0 kg/m$^2$. The fire ignition was performed with the help of a handheld $C_4H_{10}$ igniter that initiated a point ignition at the middle of the fuel bed ($x$ = 150 mm, $y$ = 0 mm, $z$ = 0 mm).

### 2.3 Visual identification of the flame envelope

Identification of the flame front properties using the side view camera footage was based on an image processing algorithm. This process aims to determine the dynamic shape of the fire front; due to the point ignition pattern as well as due to the lateral air entrainment at the sides of the fuel bed, a U-shaped flame front was established in all test cases (Fig. 3, left). As a result, at each time instant, the flame front at the symmetry plane ($y$ = 0 mm) advances further than all its side planes; therefore, it is assumed that the flame edge that is visible from the side-view camera corresponds to the fire front at $y$ = 0 mm.

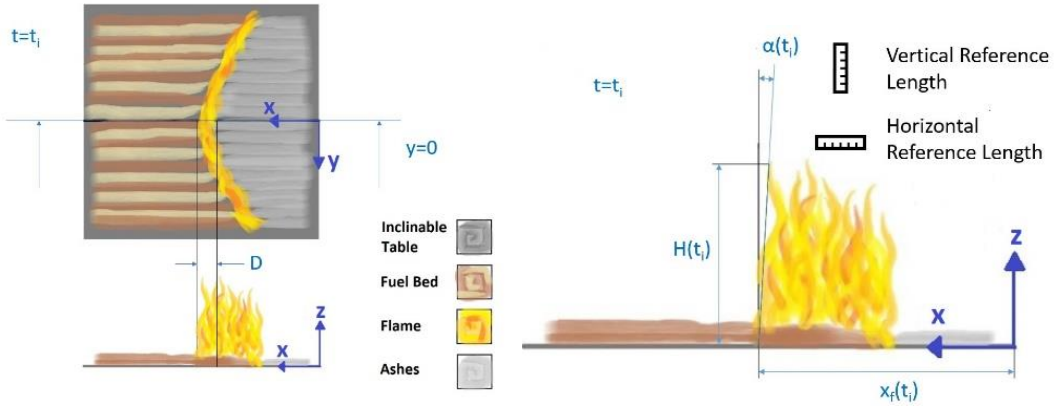


**Fig. 3.** Model representation of the propagating fire front at an arbitrary time $t_i$ (left) and definition of the main geometrical properties of the flame envelope, i.e. flame height, angle and horizontal position (right).

The image processing algorithm allows the determination of three geometrical properties from the video generated by the side-view camera, namely the flame height $H$ (mm), the flame angle $\alpha$ (degrees) between the flame front and the vertical axis and the flame front horizontal position $x_f$ (mm); these three quantities are depicted in Fig. 3 (right). After the recorded video is converted to an image sequence, each snapshot is processed using six steps: image cropping and "chromatic" processing, flame identification, transformation from image pixel coordinates to real world coordinates, extraction of the geometrical flame properties from the identified flame front and, finally, post processing of the resulting signals as a function of time.

The 25 frames per second video is converted to an image sequence of 5 frames per second, corresponding to a time step of 0.2 s between two sequential images. The image corresponding to the beginning of time ($t$ = 0 s) is the image where the point ignition takes place. The final image that was used is each fire test is the image where the flame front at the middle of the fuel bed width reached the end of the fuel bed length; the latter instance was identified by using the video of the back-view camera.

Processing of each sequential image initiates with its cropping, aiming to include only the flame and the black background (whenever possible), as well as a "chromatic" processing to facilitate the upcoming flame identification. The "chromatic" processing consists of the application of a median filter, the maximizing of the image saturation and the colour change of orange-to-blue. The identification of the flame in the resulting image is performed using a chromatic criterion (commonly utilized in flame identification applications) based on the $Y'C_bC_r$ colour model [9]. More specifically, an algorithmic scan of each image pixel checks whether the luma Y' of the pixel is greater or equal than the pixel's blue chrominance $C_{b,}$ in which case the pixel is deemed as a flame containing pixel. The process result is a binary black-and-white image where the two colours represent the absence and the presence of the flame, respectively. A coordinate transformation from the image pixel coordinates to the real-world coordinates is then performed with the help of a reference length scale (c.f. Fig. 3, right). Then, the flame front is scanned and identified; to exclude possible artefacts, originating from isolated flame "tufts" (c.f. Fig. 4), an empirical method was used to essentially "isolate" the flame front.

**Fig. 4.** Flame front identification steps (from left to right): Cropped image, "chromatically" processed image, binary black-and-white image, flame front identification.

The flame height, angle and "front" position are defined by the height, angle and the lowest point of the final line segment. The flame front length is geometrically calculated through the flame height and angle, using the assumption of a small flame depth, $D$ (m) (corresponding to the thickness of the propagating flame sheet, Fig. 3, left, estimated at the level of the fuel bed) relative to the flame height. The fire's Rate Of Spread (ROS) is calculated through the difference of the flame front position from two sequential images divided by the time step of the sequence (0.2 s). The temporal evolution of each parameter is constructed using all the images of the sequence. The final step of the method includes the smoothing of the signal via the application of a Gaussian filter.

### 2.4 Estimation of Heat Release Rate

Estimation of the fire's Heat Release Rate (HRR) is performed by employing the gas combustion products composition and mass flow rate, using the oxygen calorimetry methodology. The latter is founded upon the fact that for most organic substances, a relatively constant amount of net heat is released per unit mass of oxygen consumed [10]. The method was later expanded to increase its precision by including the concentration of the gas products $CO_2$ and CO [11]. In the present work, the method including the concentration of the consumed $O_2$ and the produced $CO_2$ and CO is utilized.

## 3. RESULTS AND DISCUSSION

Six different test cases were investigated, in order to determine the impact slope angle, (wet) fuel load and fuel moisture content (FMC) on the rate of fire spreading, as well as on the geometrical and thermal properties of the fire front. The main characteristics of the six test cases are presented in Table

1. To test the repeatability of the test rig, three identical fire tests were performed for two specific test cases (i.e. test cases 3 and 5); as a result, ten fire tests were performed in total.

The measured properties were the Heat Release Rate, the heat flux at the downstream end of the table and the spatio-temporal temperature distribution; in addition, the main geometrical characteristics of the flame envelope, namely the flame height, angle and position, as well as the estimated rate of spread were determined. In some of the following graphs, experimental results are shown as a function of a "dimensionless" time ($\tau$), which corresponds to the ratio of the "actual" time to the time it took for the respective fire front to propagate up to the downstream end of the fuel bed.

**Table 1**. Summary of the investigated test cases

| Case | FMC | Slope | Fuel load | Repetition |
|---|---|---|---|---|
| **1** | 8% (Untreated) | 0° | 0.5 kg/m$^2$ | x 1 |
| **2** | | 10° | | x 1 |
| **3** | | 20° | | x 3 |
| **4** | | 30° | | x 1 |
| **5** | 1% (Oven-treated) | 0° | | x 3 |
| **6** | | 0° | 1 kg/m$^2$ | x 1 |

### 3.1 Repeatability study

Aiming to assess the repeatability of the experimental setup, the temporal evolution of heat flux levels at the downstream end of the combustion table, at three different heights, is shown in Fig. 5 for the three fire tests performed using the conditions of test case 5. The depicted error bars correspond to the estimated measurement uncertainties. The heat flux levels converge sufficiently to infer adequate levels of repeatability. In addition, the temporal evolution of the estimated ROS and the main geometrical characteristics of the flame envelope for the same three tests are presented in Fig. 6. Larger discrepancies are observed in the temporal evolution of the flame front's geometrical properties, compared to the heat flux level measurements. This observation is mainly attributed to the inherently turbulent nature of the flame front that results in intense flame fluctuations; however, the corresponding time-averaged values for each fire test are quite similar, thus suggesting that adequate levels of repeatability are indeed achieved. Similar observations are made for the three fire tests performed using the conditions of test case 3.

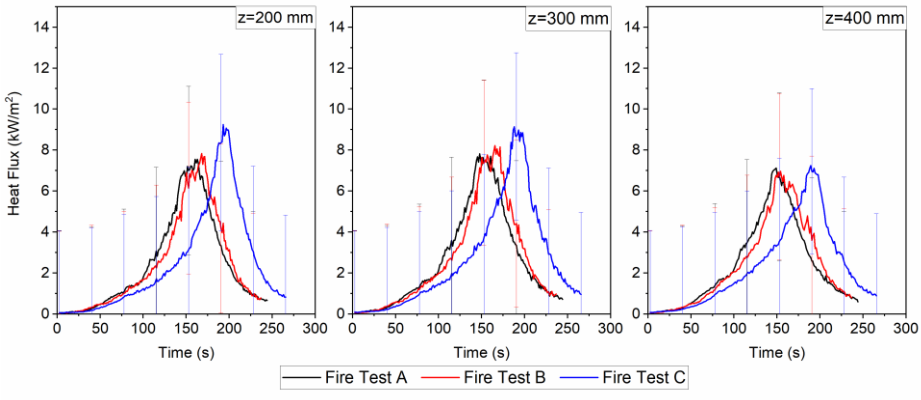


**Fig. 5.** Temporal evolution of heat flux at a height of 200 mm (left), 300 mm (middle) and 400 mm (right), for the three fire tests performed using the conditions of test case 5.

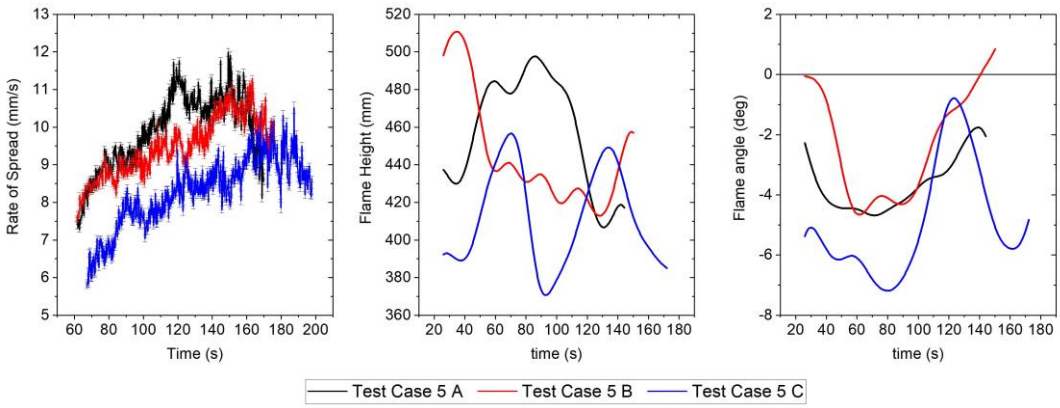


**Fig. 6.** Temporal evolution of fire spreading rate (left), flame height (middle) and flame angle (right) for the three fire tests performed using the conditions of test case 5.

### 3.2 Flame envelope geometrical characteristics and rate of spread

The temporal evolution of the fire's ROS, the flame height, angle and length is depicted in Fig. 7 for all the six different test cases considered here (c.f. Table 1).

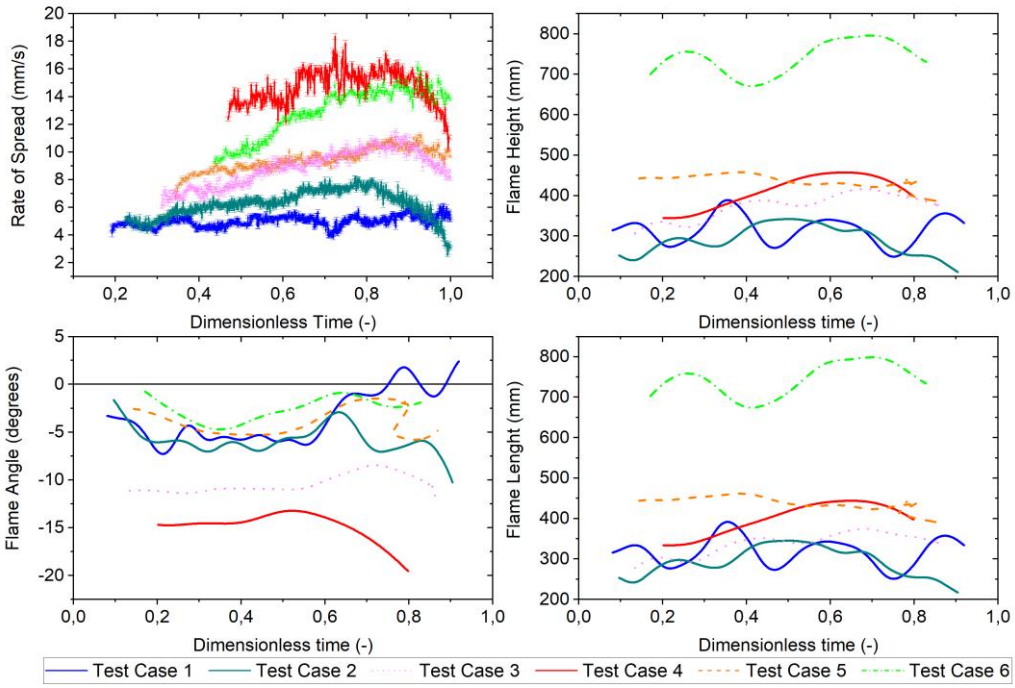


**Fig. 7.** Temporal evolution (dimensionless time) of ROS (top, left), flame height (top, right), flame angle (bottom, left) and flame length (bottom, right) for the 6 test cases considered.

It is evident that varying the slope, fuel load and FMC may induce significant changes in both the geometrical characteristics of the flame envelope and the rate of fire spread. Regarding the slope angle, an increase of the slope from 0 to 10 degrees induces an apparent increase in ROS, while the

flame height and angle appear to be unaffected. A further increase from 10 to 20 degrees results in a further increase of the ROS, as well as a slight increase of the flame height and a decrease of the flame angle. Finally, increasing the slope from 20 to 30 degrees dramatically increases the ROS, whereas the trend for increasing flame height and decreasing flame angle is continued.

When the fuel load is doubled, while keeping the FMC the same (test case 5 vs. test case 6), an increase in both the ROS and the flame height is observed, while the flame angle seems to remain unaffected. The same observations are made when the FMC is decreased, while keeping the dry fuel load roughly the same (test case 1 vs. test case 5).

### 3.3 Heat release rate

In Fig. 8, the temporal evolution of the estimated HRR is shown for all the considered test cases. It is evident that the HRR increases with increasing slope, a trend similar to that observed for the ROS. Moreover, doubling the fuel load results in roughly doubling of the HRR, which is expected, due to the increase of the combustible matter mass. As expected, when the FMC is reduced, a higher Heat Release Rate is observed; in fact, reducing the FMC form 8% to 1%, results in an increase of the peak HRR value of approximately 65%.

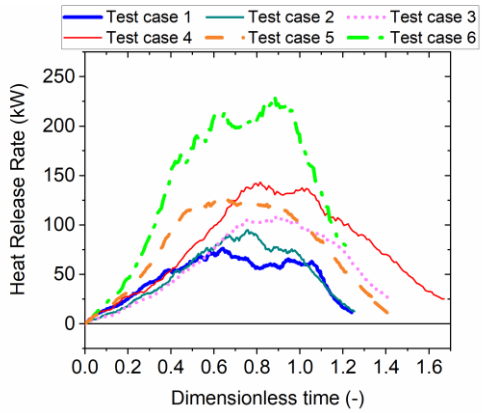


**Fig. 8.** Temporal evolution (dimensionless time) of HRR for the 6 test cases considered.

### 3.4 Heat flux

The temporal evolution of the measured heat flux at the downstream end of combustion table, at three different height levels, is shown in Fig. 9 for all the considered test cases. Similar to the observed trends for the HRR, increasing the slope results in increasing heat flux levels, an observation that is attributed to the gradual decrease of the angle between the flame front and the table; the latter quantity is different than the geometrically defined “flame angle”. It is interesting to note that the heat flux is almost doubled when the fuel load is doubled, a fact that is mainly attributed to the significant increase of the flame height. Finally, it is noted that the measured heat flux levels at three different height levels, namely 200 mm, 300 mm and 400 mm above the fuel bed, do not exhibit notable differences.

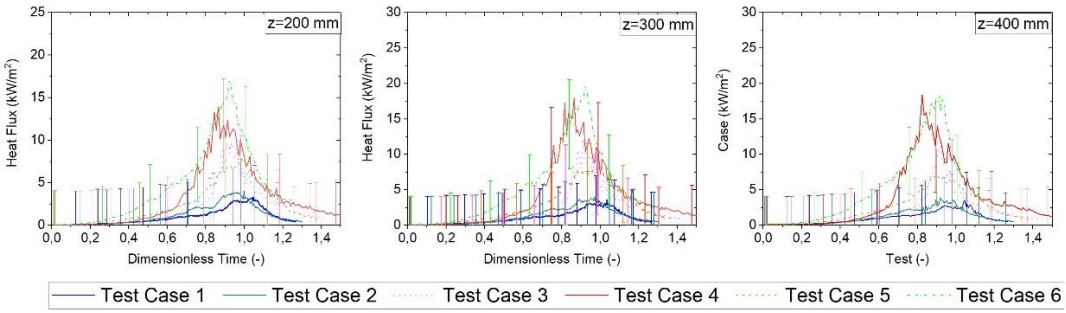


**Fig. 9.** Temporal evolution (dimensionless time) of heat flux measurements, at a height of 200 mm (left), 300 mm (middle) and 400 mm (right), for the 6 test cases considered.

### 3.5 Temperature profiles

Figures 10 to 12 depict the spatial distribution of gas temperatures across the centre plane of the combustion table, for three dimensionless time instances, namely 25%, 50% and 75%, respectively.

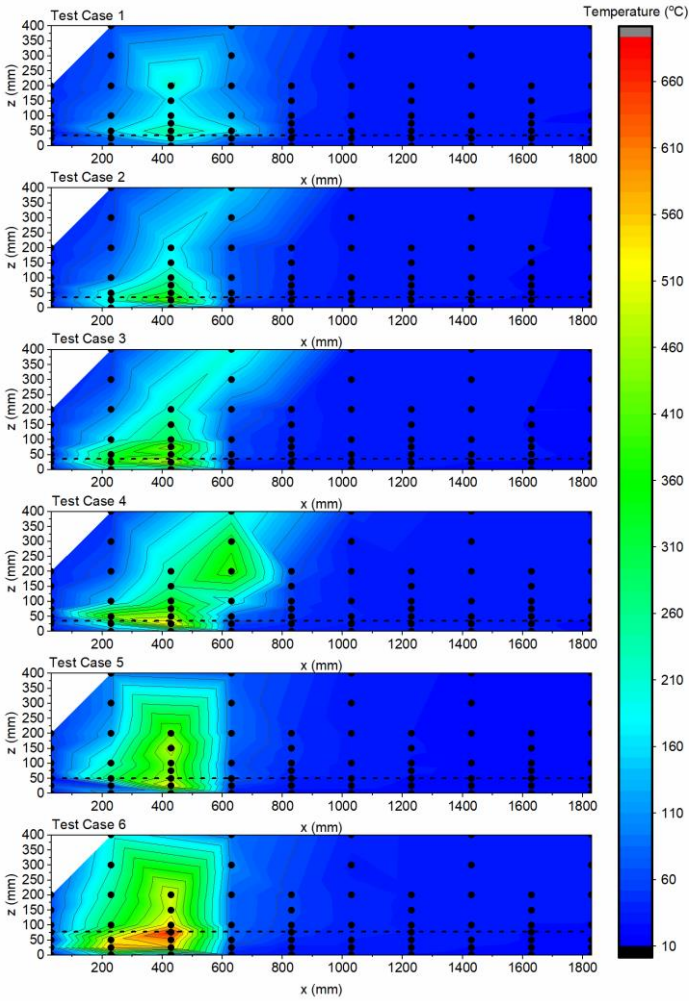


**Fig. 10**. Temperature field at dimensionless time $\tau = 0.25$ for all test cases.

The developing temperature fields inside and above the fuel bed (the horizontal dashed line corresponds to the initial thickness of the pine needle layer in each test case), are depicted; the point ignition is located at $x = 0$ mm and the flame front progresses from left to right.

It is interesting to note that in the non-sloped terrain cases (test cases 1 and 5) the temperatures that are developing during the burning of the untreated fuel (test case 1) are lower than the temperatures of the treated fuel, which exhibits a lower FMC (test case 5). This is since the moisture content acts as a heat sink. When the slope is increased (test cases 2-4), the mean temperatures seem to increase as well. It is also interesting to note that as the slope increases and the flame propagates (faster), the "trail" of high temperatures behind the flame front appears to be longer. The latter indicates either the existence of secondary flames following the the "main" flame front or heat generated via ember combustion. In any case, the higher temperatures induce a stronger buoyant plume; naturally the thermal buoyancy is further intensified when the fuel load is increased.

It is evident that increase gas temperature levels are associated with higher temperatures "inside" the pine needle layer; in fact, the region where the highest temperature is observed in test case 6 is located under the fuel bed surface.

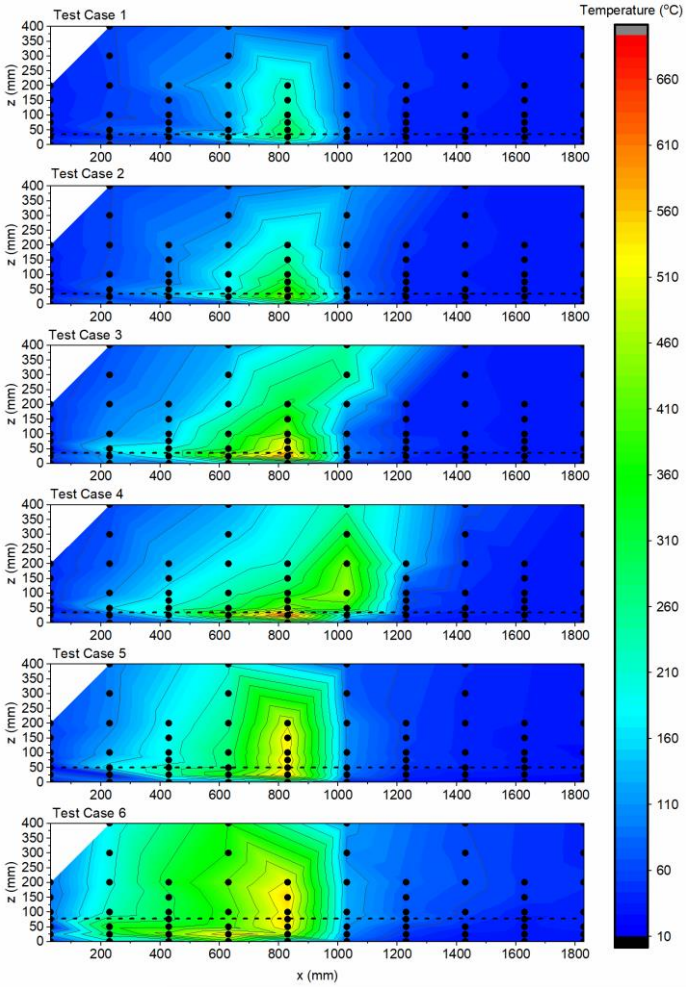


**Fig. 11**. Temperature field at dimensionless time $\tau = 0.50$ for all test cases.

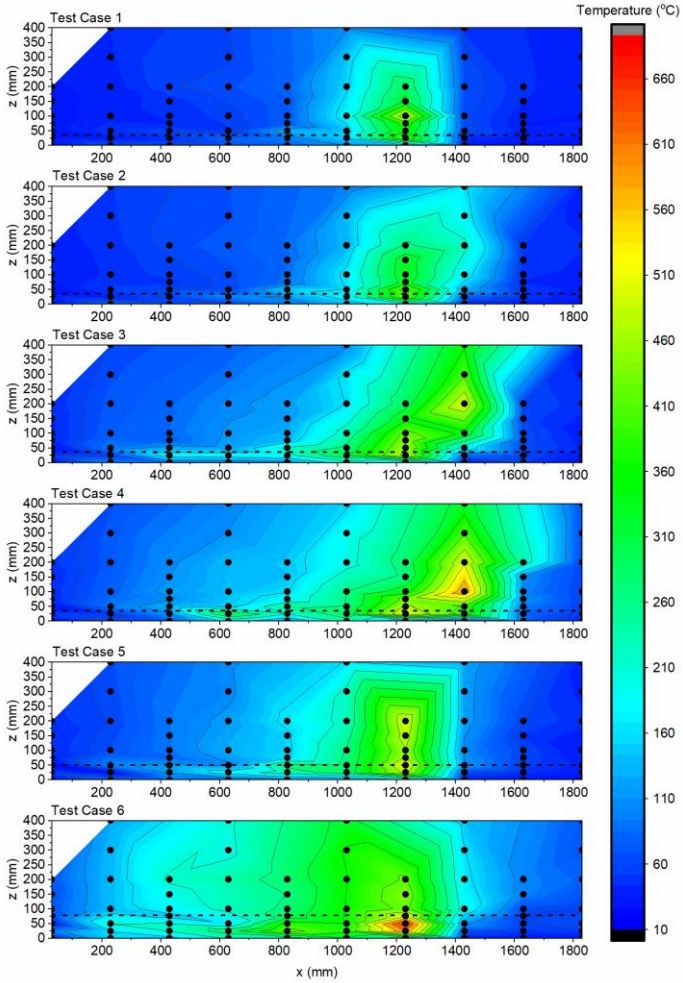


**Fig. 12**. Temperature field at dimensionless time $\tau = 0.75$ for all test cases.

## 4. CONCLUSIONS

The laboratory experimental investigation of a fire propagating on a pine needle litter fuel bed verified that the main fire characteristics are affected by changes in slope, fuel load and Fuel Moisture Content (FMC). Increasing the slope results in higher fire rate of spreading (ROS), more intense combustion (HRR) and higher heat lux levels. Doubling the fuel load resulted in significant increases in the rate of spread, flame height, Heat Release Rate and radiative heat flux. Lastly, a decrease in the fuel moisture (with a simultaneous slight decrease of the net fuel load) resulted, once more, to a noticeable increase of all the above quantities.

## REFERENCES

[1] R. C. Rothermel, H. E. Anderson, Fire Spread Characteristics determined in the laboratory, U.S. Forest Service Research Paper INT-30., 1966.

[2] D. X. Viegas, L. P. Pita, Fire spread in canyons, Int. J. Wildland Fire 13 (2004) 253-274.

[3] J. R. Martines-de Dios, J. C. Andre, J. C. Goncalves, B. Ch. Arrue, A. Ollero, D. X. Viegas, Laboratory fire spread analysis using visual and infrared images, Int. J. Wildland Fire 15 (2006) 179-186.

[4] J.-L. Dupuy, J. Marechal, D. Portier, J.-C. Valette, The effects of slope and fuel bed width on laboratory fire behavior, Int. J. Wildland Fire 20 (2011) 272-288.

[5] F. Morandini, Y. Perez-Ramirez, V. Tihay, P.-A. Santoni, T. Barboni, Radiative, convective and heat release characterization of vegetation fire, Int. J. Therm. Sci. 70 (2013) 83-91.

[6] X. Silvani, F. Morandini, J.L. Dupuy, A. Susset, R. Vernet, O. Lambert, Measuring velocity field and heat transfer during natural fire spread over large incinable bench, Exp. Therm. Fluid Sci. 92 (2018) 184-201.

[7] Z. Campbell-Lochrie, C. Walker-Ravena, M. Gallagher, N. Skowroski, E. V. Mueller, R. M. Hadden, Investigation of the role of bulk properties and in-bed structure in the flow regime of buoyancy-dominated flame spread in porous fuel beds, Fire Safety J. 120 (2021) 103035.

[8] S. Matthews, Effect of drying temperature on fuel moisture content measurements, Int. J. Wildland Fire 19 (2010) 800-802.

[9] T. Celik, H. Demirel, H. Ozkaramanli, M. Uyguroglu, Fire detection using statistical color model in video sequences, J. Vis. Commun. Image R. 18 (2) (2007) 176-185.

[10] W.M. Thornton, The Relation of Oxygen to the Heat of Combustion of Organic Compounds, The London, Edinburg and Dublin Philosophical Magazine and Journal of Science 33:194 (1917) 196-203.

[11] M. L. Janssens, Measuring Rate of Heat Release by Oxygen Consumption, Fire Technol. 27 (1991) 234-249.

[12] A. L. Buck, New Equations for Computing Vapor Pressure and Enhancement Factor, J. Appl. Meteorol. 20 (1981) 1527-1532.

[13] D. X. Viegas, On the existence of a steady state regime for slope and wind driven fires, Int. J. Wildland Fire 13 (2004) 101-117.

# Experimental Study on the Effect of Mechanical Ventilation on the Fire Behavior in a Reduce-scale Room of the Castle of Chambord

**Abdulrahman S.A.[1], Chetehouna K.[1,*], Cablé A.[2], Abdlgwad A.[1], Gascoin N.[1], Kadoche M.[2]**

[1] *INSA Centre Val de Loire, Université d'Orléans, PRISME, EA 4229, Bourges, Cher, France*
[2] *EXEC SAS, Goussainville, Val d'Oise, France.*
**Corresponding author's email: khaled.chetehouna@insa-cvl.fr*

## ABSTRACT

An experimental study was conducted to investigate the effect of ventilation on the burning behaviour of a pool fire in a reduced scaled cultural heritage room. For this purpose, a reduced scale ($1/8^{th}$) test bench of a room of the Château of Chambord (France) was built based on onsite 3D scans and scaling laws. Room fire behaviour investigations were then carried out using an heptane pool fire of 8 cm diameter corresponding to a Heat Release Rate (HRR) of 2.5kW and located at the center of the room. The applied ventilation flow ranged from 0 to 1.79, 4.04 and 6.06 Air Change per Hour (ACH). The influence of the ventilation rate on several parameters: flame morphology, flame height, flame temperature, temperature distribution, heat flux, extinction time, and gas composition ($O_2$ and $CO_2$ levels) was then analysed. Notably, it was observed that the maximum heat flux was greatly by the ventilation conditions in the compartment and varied increasingly with the studied air renewal rate for the four test cases. This preliminary study aims to obtain a better understanding of the behaviour of fires in cultural heritage rooms, with the subsequent objective of studying innovative fire suppression systems and strategies suited for the built cultural heritage.

**KEYWORDS:** pool fire, heritage building, reduced-scale, ventilation, heat release rate.

## NOMENCLATURE

| | |
|---|---|
| ACH | Air Change per Hour (Vol/h) |
| $A_{Pan}$ | Area of the pan ($m^2$) |
| HRR | Heat Release Rate (kW) |
| $\Delta h$ | Hat of combustion of the fuel (MJ/kg) |
| $k$ | Extinction coefficient |
| $\dot{m}''$ | Burning rate per unit area ($kg/m^2$ s) |
| $\dot{m}''_{\infty}$ | Max. burning rate per unit area ($kg/m^2$ s) |
| $\dot{Q}$ | Heat release rate (kW) |
| $\dot{Q}_c$ | Fire convective heat release rate (kW) |
| $T$ | Temperature (K) |
| $t$ | Time (s) |
| $U$ | ventilation velocity (m/s) |
| $\dot{V}$ | Volume flow ($m^3/s$) |

**Greek**

| | |
|---|---|
| $\beta$ | Mean Beam length correction |
| $\chi$ | combustion efficiency |

**Subscripts**

| | |
|---|---|
| $F$ | Full-scale |
| $M$ | Model-scale |

## INTRODUCTION

Cultural heritage monuments are symbolic piece of art and pride of the nations and their people. These building are rare and delicate (mostly combustible) properties which are irredeemable in case of accidental loss to fire. They are ancient (some are over 800 years old) and their protection by conventional automatic fire suppression systems is rendered difficult. In fact, some cannot support safely any additional load (for instance in the case of wet sprinkler systems) and architectural and aesthetic integration remains a challenge. Moreover, most heritage buildings are situated at remote

locations and may be completely engulfed by fire before the arrival of firemen. Hence, it appears crucial to *(i)* better understand how fire behave in cultural heritage buildings, which the present work is devoted to, and *(ii)* to develop new fire suppression systems and strategies suited for such buildings. In this context, data from 3D measurements of the castle of Chambord (Loire Valley, France) [1] were taken into consideration for a case study of cultural heritage fire. The château de Chambord is one of the most famous castles in the world as it is an emblem of French Renaissance architecture. It was built at the beginning of the 16th century and has been part of the UNESCO World Heritage list since 1981. One of the major driving phenomenon of fire in cultural heritage buildings (for instance castles or cathedrals) is ventilation. In fact, large rooms connected by corridors, and the presence of numerous chimneys can be responsible for an increased supply of oxygen and rapid development of fire. A fire can be referred to as under-ventilated when the availability of air is limited, in which case it can be said to ventilation controlled, and can lead to pre-flash over and flash over development stage. On the other hand, a fire which burns at its maximum potential according to the limit of the amount of the available fuel is referred to as a fuel-controlled fire. Several studies on underventilated fires [2] [3] or fuel-controlled fires [4] [5] are available in the litterature. It is worthy to note that given the different configuration of experimental setups, there is yet no widely acceptable general correlations for the influence of the under-ventilated fire condition and production of gaseous species. Furthemore, no studies are available to the best knowledge of the author regarding the specific context and geometries of cultural heritage. Hence, the present study aims to assess experimentally the influence of ventilation on a pool fire behaviour in a reduced-scale room model of the castle of Chambord. Reduced-scale studies are easier to carry out than full scale studies, but require the use of suitable scaling laws. Such laws have been previously proposed for compartment fires by Quintiere [5], Emori [6] or Heskestad [7]. Hekestad's scaling correlations were applied in this work, essentially for the study of heat loss properties and for the dimensions of the enclosure.

## MATERIAL AND METHODS

### Scaling Techniques

The relationship between full scale and reduced scale of the experimental setup was achieved following a 1/8 scale down of the castle's room geometry, which was 12m long by 8.32 large by 6.4 m high, having an opening (door) of 2 m by 0.8 m at the east side of the room. The 1/8th model room used in the experiments was based on scaling laws proposed by Heskestad [7] aiming at producing the same average gas temperature in the upper part of the room as the full-scale test, see Table 1. The latter rely upon the preservation of the conservation of the Froude number ($Fr=v/\sqrt{gL}$) , assuming that temperature remains unchanged in the scaling process The scaling factor for the geometrical length scales is 1/8. The new lengths of the enclosure geometry are thus 1.5m x 1.04m x 0.80m. The resulting free volume of the enclosure (internal volume of the chimney deduced) is 1.218 $m^3$.

**Table 1. Summary of Scaling correlations**

| Characteristic relationship | scaling model[a] |
|---|---|
| Heat release Rate (kW) | $\dot{Q}_F = \dot{Q}_M \left(L_F / L_M\right)^{5/2}$ |
| Convective heat release rate | $\dot{Q}_{C,F} = \dot{Q}_{C,M} \left(L_F / L_M\right)^{5/2}$ |
| Ventilation Rate (m/s) | $U_{F=} U_M \left(L_F / L_M\right)^{1/2}$ |
| Temperature | $T_F = T_M$ |

[a]L is the length scale. Index F refers to the full-scale and M is the model scale (in the current study, $L_F = 8$ and $L_M = 1$).

## Experimental set-up and Instrumentation

The reduced-scale compartment, representative of a typical room of a cultural heritage building, is depicted in Fig 1. Notable typical features of such buildings which are represented here are : large room dimensions (100 $m^2$), high ceiling height (6.4 m), presence of large wooden beams covering the entire ceiling area, and the presence of a large chimney, located at the corner of the room which is acting as an air exhaust. All these features have a potentially high impact on the airflow and fumes distribution (in particular concerning convective and ceiling jet flows), and consequently on the fire development in the room. For the model, the walls and top slab were made of 10 cm thick concrete bricks, while a glass doors (100 cm x 50 cm, and 50 cm x 50 cm, respectively) were located on the front and sides of the compartment to facilitate the observations of the metrology during the tests. The air inlet is represented by a door connected to a 100 mm inlet duct, while the outlet is located at the lower section of the enclosure and is represented by the entrance of the chimney, which is later connected to a 160mm outlet duct. Forced ventilation was achieved by an exhaust fan connected to the outlet, while fresh air was flowing inside of the enclosure from the inlet.

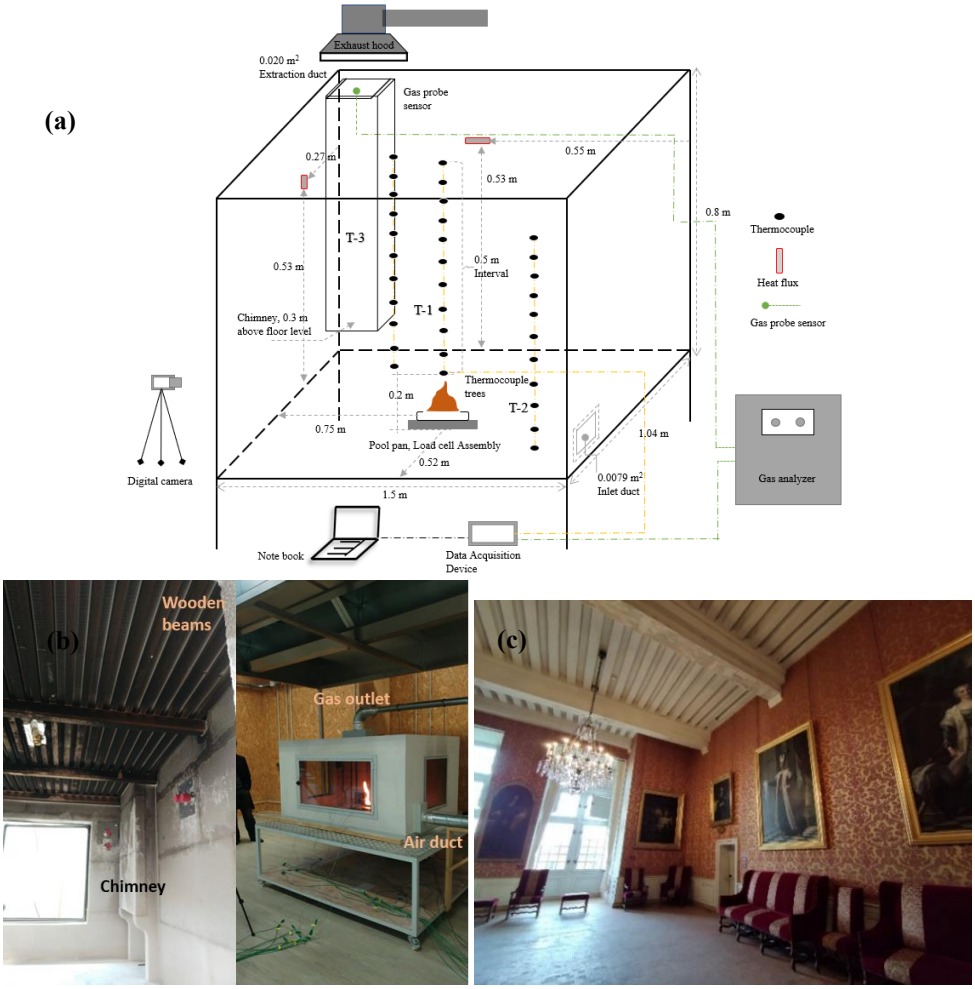


**Fig. 1.** (a) Schematic diagram of the experimental rig, (b) View of the inside and outside reduced-scale experimental rig, (c) View of a typical room of the Castle of Chambord

A heptane pool was used as fuel for all of the conducted tests. The measured variables, metrology and corresponding uncertainty are listed in Table 2. A PXI data acquisition device was used to centralize

the data acquisition from all devices. Flame morphology and flame height were obtained based on Digital Image Processing Technology for different cases and configurations of the tests.

**Table 2. Measuring devices used for experimental tests**

| Characteristics | Device | Uncertainty |
|---|---|---|
| Temperature | K-thermocouples: Arrays of 3 TC trees | ± 2.5 $^{O}$C |
| Heat flux | Total heat flux meter | ± 20 W/m$^2$ |
| Fuel mass loss | Load cell | ± 0.001g |
| [$O_2$] and [CO] | Gas Analyser | ±2% |
| Inlet air flow rate | Pitot tube | 0.10-2.00 l/min |
| Flame morphology/extinction time | Digital camera | ±1s |

## Heptane Pool Fire Source

n-heptane pool fires were used to control the HRR, consisting in an 8 cm diameter and 2 cm deep stainless steel pan, supported by on a load cell (weighing balance). The initial fuel mass of heptane was selected as 25 grams, equivalent to a 0.007 m fuel depth. The corresponding HRR was estimated by equations (1) and (2) [7]:

$$\dot{Q} = \chi \dot{m}'' A_{pan} \Delta h \tag{1}$$

$$\dot{m}'' = \dot{m}''_{\infty} \left[1 - \exp\left(k\beta D\right)\right] \tag{2}$$

Where $\dot{Q}$ is the heat release rate, $\chi$ is the combustion efficiency, $\dot{m}''$ is the burning rate per unit area, $A_{pan}$ is the area of pan, $\Delta h$ is the heat of combustion of the fuel, $\dot{m}''_{\infty}$ is the maximum burning rate per unit area, $k$ is the extinction coefficient and $\beta$ is the mean beam length correction. $D$ represents the diameter of the pool pan. For heptane, $\chi$ is 0.924, $\Delta h$ is 44.6 MJ/kg, $\dot{m}''_{\infty}$ is 0.101 kg/m$^2$ and $k\ \beta$ is 1.1 m$^{-1}$. Hence, the corresponding HRR conditions are approximately 2.5 kW.

## Test Procedure

Pool fire experimental tests were conducted with different ventilation regimes. Test configurations were as follows: Test 1 - with inlet and outlet duct closed. Test 2 - inlet and outlet open, natural ventilation. Test 3 and Test 4 - inlet and outlet open, varied forced ventilation applied. In Tests 2, 3 and 4, ventilation was forced by a fan through the exhaust. Each test configurations was repeated twice, to ensure the reproducibility of the obtained test results, in particular in terms of fire extinguishment time. In particular, the temperature and heat flux profiles looked similar for the reproducibility tests. One set of results was kept and is presented in this study.

The air-flow total and dynamic pressures converted to air velocity v, was measured by the pitot tube in the air inlet duct, and converted into mass flow rate using Eq. (3)[8][9],

$$\dot{m}_a = \rho_\infty A_d v \quad (3)$$

where ρ, density of air at ambient temperature (1.225 kg/m3) and $A_d$ is the area of the air-inlet duct, 0.0078 m2. At the time of extinction, the measured air velocity values are 1.48 m/s for Test 3 and 2.9 m/s for Test 4. The values of ventilation parameters and global equivalent ratios are presented in Table 3. The combustion process depends strongly on the equivalence ratio [3][4], an equivalence ratio less than 1 can be regarded as complete combustion while an equivalence ratio larger than 1 corresponds to a combustion process disturbed by lack of oxygen [10]. It can be seen that global equivalence ratio decreases with increasing mass loss rate, and this is consistent throughout the tests despite the elevated HRR at test 3.

**Table 3. Summary of ventilation parameter for the test configurations**

| Vent type | Ventilation parameter $\dot{m}_{air}/A_{fuel}$ (g/m$^2$s) | Fuel mass loss rate $\dot{m}_{fuel}/A_{fuel}$ (g/m$^2$s) | Global equivalence ratio $\phi = 3.521\ \dot{m}_{fuel}/\dot{m}_{air}$ |
|---|---|---|---|
| Test 1: closed compartment | - | 10.90 | - |
| Test 2: Zero ventilation | 0.153 | 10.96 | 0.252 |
| Test 3: forced ventilation | 0.275 | 15.90 | 0.203 |
| Test 4: forced ventilation | 0.519 | 12.15 | 0.083 |

## RESULTS AND DISCUSSION

Varied ventilation conditions were applied; test 1 corresponded to 0 ACH, 1.79 ACH for test 2, 4.04 ACH for test 3 and 6.06 ACH for test 4. The video captured frames of the oscillating heptane pool flame in a sequence of images of 1/30 s are depicted in Fig. 2. Generally, 4 distinct regimes can be observed from the frames of the flame mopology in this study. (a) and (b) A rapidly growing fire at an initial 20 s to 30 s after ignition of the fuel, the fuel pan and heptane liquid being rapidly heated, consequence of the availability of fuel and oxygen. (c) an intermittent oscillating flame followed by a short steady burning, occuring between 120 to 240 s of burning, flame height remaining unchanged but gradually increasing in width. This is followed by the boiling stage and flageration of the flame observed as a result of the interaction of the buoyant plume and the gradually decreasing oxygen. Boiling of the fuel also occur at this point while flame tries to reach its peak height, which was observed in frame (d), 240 – 300s, which also coincides with the period of "steady state" burning of fuel. The fourth regime, frame (e) and (f), occurs after 300s of ignition. It is rather short and indicates the decay stage of the flame, where extinction occurs for lack of fuel rather than depletion of oxygen. This stage is also accompanied by rampant ghosting flames, this refers to flames which lift-of from the fuel surface and floats away burning in undefined direction.

For test 1 (0 ACH), the flame rose steadily for close to 1 minute, reaching half of its total height. The growth stage was followed by turbulent burning as the flame fuel began to boil. No tilting of the flame occurred, since there was no impact of ventilation flows. Frames (a) (b) indicate an oscillating flame gradually increasing evidently for availablity of fuel and oxygen and lack of interaction with outside air. One would expect the flame temperature to be within 500 – 600 $^oC$, however at flame extinction 457 s, the centreline plume temperature revealed a maximum value of 800 $^oC$, with an heat flux of 400 w/m$^2$. Maximum oxygen vitiation and $CO_2$ yield were respectively 14.5% and 1.75%, as a result of the complete combustion, and CO yield was insignificant for all test cases. For test 2 (1.79ACH), a somewhat reluctant burning was noticed for the first 30 s of flame development.

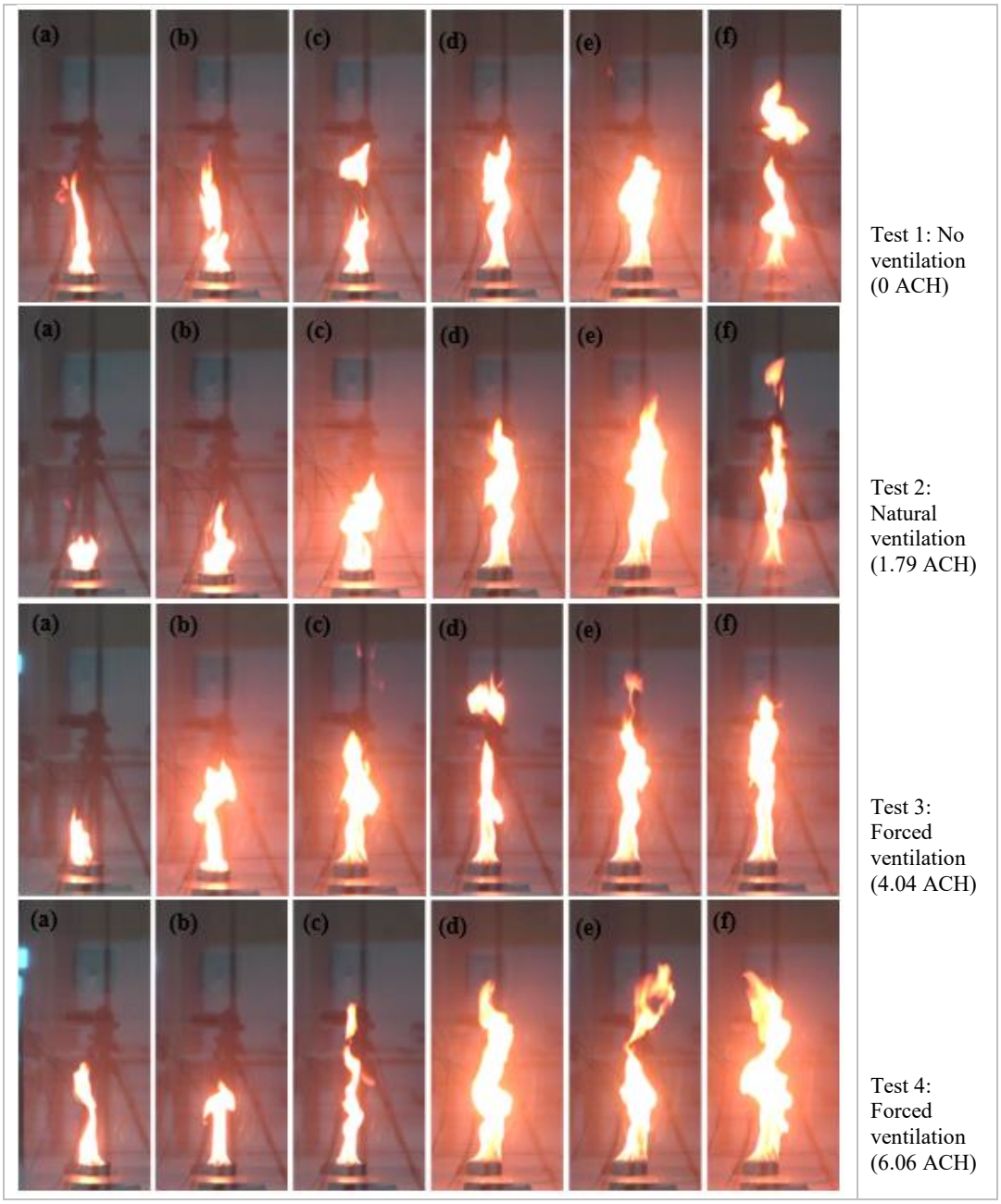


**Fig. 2.** Influence of ventilation captured at 3 s and further 30 s interval (L-R), revealing gradual changes of flame height and combustion regime at HRR value of 2.5kW.

Tilting of the flame was noticed slightly in (c) (d) (e), with a tilt angle towards the inlet duct at the lower of part of the compartment appeared to be greater than all other cases. The fuel burned clearly and steadily, the influence of the ceiling vent and the inlet vent flows respectively prescribed a glowing flame as indicated by frames (a)(b). The flow of gases in and out of the compartment was driven by buoyant forces, and this increased the burning regime while causing an abrupt boiling of the fuel. Flame extinction for test 2 occured at 443 s, with a maximum flame temperature of 650 $^{o}$C which indicates a sharp decrease from test 1, and an heat flux of 900 w/m$^2$. Maximum $CO_2$ production

was 1% and (the lowest obtained for all tests), while peak value of oxygen concentration for test 2 and test 3 were 16.5%. For test 3 (4.04ACH), with the increase of ventilation flow rate, a flame development similar to test 2 was observed. However, rampant gosting flames were observed for the entire burning regime, as well as an extended burning. The trends of the flames are similar with test 2. The third frame (c) indicates a flame influenced by the applied ventilation, buoyant gas acting against the incoming air. $CO_2$ yield is 1.4%, with the highest flux rate measured of 1480 w/$m_2$ was when the flame temperature ranges from 600-700 ºC for both test 3 and test 4. Typical fuel controlled combustion process is displayed in this case. For test 4 (6.06ACH), the flame appearred steady for nearly 200 s, with a minimal oscillation of the flame noticable as turbulent burning started as compared to test 3. As observed in frame (a), 30s after ignition of the fuel, flame oscillates at violently and appears to maintains the hieghest point of the all cases. The flame appears to bend towards the area of the inlet vent as indicated in frame (b) as a result of the increased ventilation. Frames (c) and (d) depict boiling of the fuel that was not able to achieve steady flame before extinction occurs at 409 s. Even though, this is a fuel controlled combustion, the magnitude of flame tilt was observed very much in (d) (e). The burning rate is similar to test 1 and the fuel consumption rate is similar to test 2. heat flux was obtained as 1300 w/$m^2$, with a peak oxygen concentration of 17.5%, highest of all the test cases. Average mass loss rate ranged between 10.9-12.15 g/s. In Fig 3, the variation of heat flux and gas temperature distribution as a function of room are depicted. The graphs in this figure illustrate that the fire development and the sequence of events inside the compartment can be observed and readily distinguished for all tests, but they occur at different times after ignition. Two zone can be distinguished from the temperature histories, and an increase of the maximum heat flux in the compartment can be observed in correlation with the increasing ventilation. It has been shown by Quintiere and Rangwala [5] that at the point of extinction, limiting oxygen concentration depends on local temperature and heat flux to the fuel surface. Thermal stratification shows similar trends for test 3 and test 4. However, higher temperature gradient is displayed in test 3 indicating a stronger influence of the higher ventilation (6.06 ACH) on the burning regime, and varied between 0.0605-0.0611 (g/s). This is in line with previous findings from the literature indicating that the burning rate depends strongly on the ventilation parameters (ventilation rate, size and shape of ventilation openings) [11] and that the burning rate is decreasing under low ventilation conditions [9].

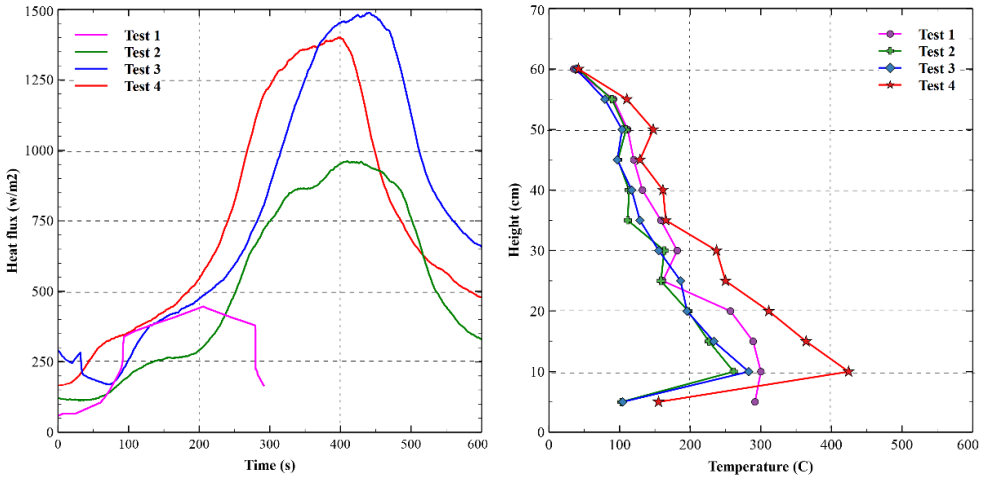


**Fig. 3.** (Left) Comparison of total heat flux values for different ventilation conditions, (Right) temperature distribution with room height at t= 240 s for different ventilation conditions.

The temperatures measured by the thermocouple located at the plume centerline region (see Fig. 4) are important as well, as they represent the temperature in the lower layer of gas which feeds the flame [5]. At 0 ACH, the flame appears to be steady at 50% of the initial burning stage and gradually grows to its maximum height and remain in that position before decaying and extinction. Similarly, for the

other tests cases, this indicates a reduction of combustible gas in the compartment after the fuel boils violently, so that the air to fuel equivalence ratio near the inlet duct is much lower than 1. This also means that oxygen concentration is lower at the base of the fuel pan and at the opening. Hot gases at stratified layer height above fuel pan are responsible for heating of the fuel and sudden burst of ghosting flame. This experiment defines the flame behavior when there is no influence of external air and provide refrence for the study of other cases with ventilation applied. The temperature profile of test 4 are similar to the natural ventilation conditions of test 1, however its burning duration being faster resulted in a stronger plume and higher temperature within the first 200 s.

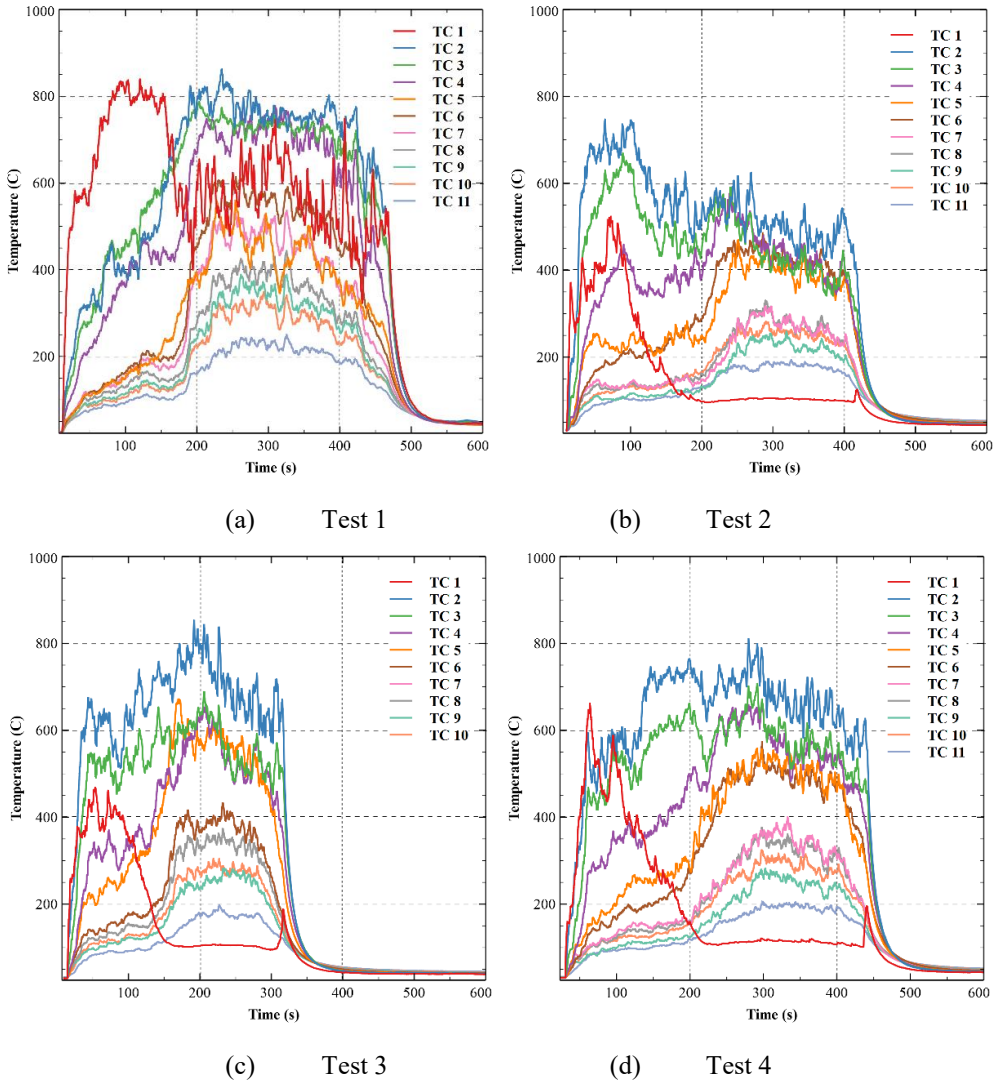


**Fig. 4.** Variation of temperature measurement along plume centerline above fuel pan.

Fig. 5 presents the changes in oxygen concentrations and $CO_2$ yield measured at the exhaust duct. At intial minutes of the burning, no significant change was observed as the air in the compartment has not yet been vitiated. Then, the oxygen concentration within the enclosure deceases gradually up to 14.5% for zero ventilation, a consequence of the combustion and accompanied with the production of carbon dioxide and soot [12]. Similar trends was observed for burning regime in test 2 to 4 and average oxygen concentration across the ventilation applied experiments is 16.5-17.5%. The overall trend is that oxygen concentration increases as the ventilation increases. Two situations of flame

extinction was observed: a steady flame was achieved for test 2 and 3 until minimum oxygen concentration (MOC=11.5%) of pool was reached. A steady flame was however not achieved in the case of test 1 and 4 as extinction was abrupt (due to fuel burnt out) after occurance of ghosting flames reaching height and extending beyond 2 cm. an increase of the oxygen concentration takes place at shortly before flame extinction at 167 – 177 s for all cases, and stops a few seconds before the flame dies. The time for sudden increase in oxygen concentration (Fig 5) coincides nearly with the time of peak gas temperature distribution as shown in Fig 3. CO2 concentration shows a smooth trend during the fully developed fire and levels reached are fairly similar with peak values occur shortly after 120 s. Small scale fire tests have shown a linear evolution of CO2 concentration as a function of O2 concentration [13]. Comparison of the species concentration at flame extinction are presented in Table 4. In all cases of burning regime, flame extinction occurs due to fuel burn out. HRR value is slightly higher than the theoritical value in the case of test 3 and test 4 because of the reduced extinction time, however its response to ventilation flow is indicated by a higher $CO_2$ production.

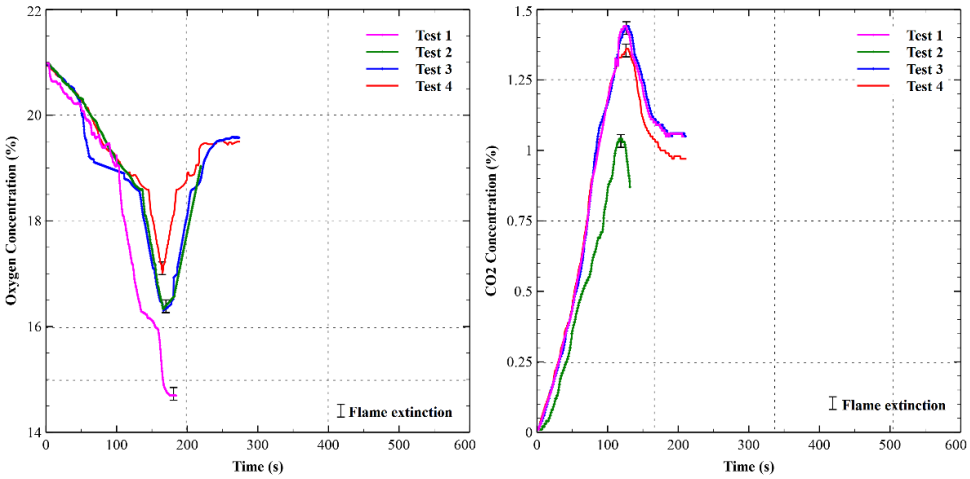


**Fig. 5.** (Left) Oxygen concentration and (Right) Carbon dioxide concentration at exhaust.

**Table 4. Comparison of the species concentration at flame extinction for 0.005 m$^2$ heptane pool area**

| Parameters | Test 1 | Test 2 | Test 3 | Test 4 |
|---|---|---|---|---|
| HRR (kW) | 2.44 | 2.45 | 2.70 | 2.73 |
| [O2] (% vol.) | 14.5 | 16.5 | 16.5 | 17.5 |
| [CO2] (% vol.) | 1.45 | 1.0 | 1.45 | 1.35 |

## CONCLUSIONS

A 1/8th reduced-scale compartment of a room of the Castle of Chambord was built in order to study the effect of ventilation conditions on the burning behaviour of heptane pool fires in the scope of a cultural heritage geometry. Complete confinement, natural ventilation, and two levels of mechanical ventilations were studied. The results of this investigation indicated that the temperature distribution above the flame, as well as the heat flux values at the walls were greately influenced by the ventilation level and increased alongside the ACH. This can be attributed to the increase in mass loss rate resulting from the increased supply of $O_2$ along with the ventilation. For all cases, carbon dioxide concentration was also found to increase linearly with the decrease of oxygen concentration. Gas temperature reached up to more than 800 $^0$C for all cases of ventilation flows, with rampant ghosting flames close to extinction. However, the temperature near the floor was found to be higher for the case with 0 ACH, indicating that cross-flow ventilation can both contribute to enhance the fire and

mass loss rate at higher ACH, but can also lead to a reduction of local temperature by convective exchanges. This reduced scaled experimental study has offered important results in terms of flame morphology, thermal parameters and species concentration in the scope of a cultural heritage room. On the basis of this premiminary study, further experimental works will be carried out to test and define efficient fire suppression strategies ms suited to the protection of historic buildings.

## ACKNOWLEDGMENTS

The authors gratefully acknowledge the support and funding from the Centre-Val de Loire Region and the French National Agency for Research (ANR), in the scope of the APR-IR EPIC and ANR LabCom GreenSprink projects, as well as the Petroleum Trust Development Fund (PTDF-2019), Nigeria, in the scope of the PhD sponsorship of the first author. Xavier Brunetaud, who has provided the 3D scans of the Château of Chambord generated in the APR-IR VALMOD project is gratefully acknowledged.

## REFERENCES

[1] X. Brunetaud, L.D. Luca, S. Janvier-Badosa, S.K. Beck, M. Al-Mukhtar, Application of digital techniques in monument preservation, European Journal of Environmental and Civil Engineering, 16(5), (2012), 543-556.

[2] J.C. Lassus, L.J. Garo, E. Studer, P. Jourda, P. Aine, Ventilation effects in confined and mechanically ventilated fires, International Journal of Thermal Sciences, (2014) 75, 87-94.

[3] Si-Xian, A., Loo, A. Coppallea and A. Philippe, Flame extinction in a ventilation-controlled compartment, Procedia Engineering, 62 ( 2013 ) 301 – 308.

[4] V. Babrauskas, Estimating large pool fire burning rates. Fire Technol., (1983), 19, 251–261.

[5] J.G. Quintiere, A.S. Rangwala, A theory for flame extinction based on flame temperature. Fire Mater., (2004), 28, 387–402.

[6] R.I. Emori, K. Saito, k. Sekimoto, Scale Models in Engineering, Mokei no Riron to Ohvou, 3rd edn Gihodo. Tokyo (2000).

[7] G. Heskestad, Scaling the Interaction of Water Sprays and Flames, Fire Safety Journal, (2002) 37, 535–548.

[8] D. Gottuk, D. White, Liquid Fuel Fires: The SFPE Handbook of Fire Protection Engineering, 4th edition ed., Quincy: Society of Fire Protection Engineers, Quincy, 2008, pp. 2-350.

[9] Y. Utiskul, J.G. Quintiere, A.S. Rangwala, B.A. Ringwelski, K.. Wakatsuki, T. Naruse, Compartment Fire Phenomena under Limited Ventilation, Fire Safety Journal, (2005), 40, 367-390.

[10] Drysdale D. Introduction to fire dynamics. New York: Willy; 1997.

[11] L.L. Martins, A.S. Ribeiro, J. Alves e Sousa, Measurement uncertainty of discharge air velocity by graphical integration in closed conduits using Pitot tubes. Journal of Physics: Conference Series, (2018), 1-4.

[12] H. Pretrel, L. Bouaza, S. Suard, Multi-scale analysis of the under-ventilated combustion regime for the case of a fire event in a confined and mechanically ventilated compartment. Fire Safety Journal (2021) 120, 1-9.

[13] A.J. Wang, B. Manescau, K. Chetehouna, C. De Izarra, S. Rudz, Experimental investigation of the confinement effect on a flame impinging a ceiling in an enclosure, Fire Safety Journal (2021) 122, 1-9.

# Material behavior in Fires

# Fibre optic cables exposed to fire – Using data transfer as damage criteria

**Åström J.[1*], Lindahl S.[1], Van Hees P.[1]**

[1] *Lund university, Division of Fire safety engineering, Lund, Skåne, Sweden.*
**Corresponding author's email: joakim.astrom@brand.lth.se*

## ABSTRACT

For safety systems it is important that signals and data transfer still work, even during a fire. Therefore, the ability of a cable or system to function during a fire or the so-called functional performance is of high importance for critical communication and control systems. The aim of this study was to analyse whether it is possible to use fibre optic cables in high reliability facilities for critical safety features such as nuclear power or particle accelerator plants. The functionality has been quantified by the data packages transferred through the cable. Looking at both how these packages are affected and the risk that the data signal becomes corrupted or lost due to fire conditions was investigated. It was examined if the failure criteria could be tied to a critical radiation or temperature such as for metal conductor cables. The testing set-up consisted of a special sample holder which was constructed to fit under the cone heater from the ISO 5660-1 cone calorimeter. The cone heater was used to expose the cables to a varying heat flux. The results from the tests were analysed looking at data loss, temperature, and functionality. Lastly, a statistical analysis was conducted. This analysis did not show a strong correlation between data loss and temperature. However, it did show a strong correlation between temperature and bend diameter. Meaning that as the temperature of the cable rise, it is more likely to bend in such a way that it will break.

**KEYWORDS:** Data transfer, fibre optic cables, functional criteria, risk.

## INTRODUCTION

In buildings such as nuclear power and particle accelerator plants, there is a need to be able to control some or all safety features from a distance. This is done by sending data back and forth through cables, leading to a need for cables to be able to function as intended even under challenging conditions such as fires. The browns Ferry Nuclear Power Plant accident in March 1975 highlighted the importance of cable functionality [1]. A fire in one of the cable distributions rooms damaged 1600 cables and 600 of these were cables that monitored and controlled safety equipment. Due to the damage by the fire several safety systems stopped working, some systems were put in motion by themselves, and some instruments on the control panel showed misleading indications [1]. This accident lead to more stringent requirement for functional performance of cables in nuclear facilities.

Previously electrical cables made of copper have been tested to great extent in many large cable test series for example in work by Andersson and van Hees [2], but less has been done on fibre optic cables. Andersson and van Hees [2] looked at critical temperatures of copper cables and found that they went into short circuit at specific critical temperatures. However, these results are not applicable to fibre optics as the functional criteria was short circuits which is not a phenomenon that occurs in an optical fibre in a similar manner. This knowledge gap was first identified by the European Spallation Source (ESS) and as a result, a bachelor thesis was written [3]. In the thesis, Rosenqvist [3] concluded that there was no way to translate his measurement of light attenuation into data loss. Consequently, there is a need to further study fibre optic cables functionality.

In a recent master thesis conducted at Lund University, Åström and Lindahl [4] performed an experimental study in order to bridge the knowledge gap identified by Rosenqvist [3]. The aim of the thesis by Åström and Lindahl [4] was to further analyse whether it is possible to use fibre optic cables

in high reliability facilities for critical safety features and whether the data transfer is affected by a fire. This paper is based on the master thesis work presented by Åström and Lindahl [4].

## FIBRE OPTICS

Fibre optics refer to the mode of transportation in the cable, in this case an optical signal, light, transferred along a fibre over a distance [5]. The optical signal is created by a transmitter that sends photons corresponding to an electrical current [5]. The fibre guides the photons to the receiver where it is translated back to an electrical signal [5]. The fibre itself is usually made of glass [7], polymer fibres do exist [8] but they are rarely used for data transfer. To keep the light inside the fibre it makes use of different refractive indices. In the centre of the fibre there is a core with a high refractive index allowing light to travel through it [6]. Surrounding the core is a cladding with a lower refractive index. A difference in refractive properties means that more light is reflected into the core as the light hits the cladding [6]. As a result of the refractive index quotient, the so-called critical angle can be calculated. If the light hits the cladding at a steeper angle than the critical angel it will be refracted out the core, into the cladding [6]. However, if the light hits the cladding at a greater angle than the critical it will be internally reflected [6].

### Light loss

If too much light is lost along the fibre the signal cannot be interpreted by the receiver. A central parameter for the distance the light can travel through a fibre is attenuation [9] which represents the decrease of light intensity along the fibre due to three material properties [9]. The first being, absorption of the light into the molecules of the fibre core [5], [9]. Second, scattering of the light as the it hits impurities within in the core or the larger silicon dioxide molecules themselves [5], [9]. Third and last there is leakage (also called radiation loss) of light out of the core and into the cladding [5], [9]. Leakage is commonly accounting for the least of the attenuation. However, attenuation as a result of leakage increases drastically with wrongful handling and installation of the fibre cable because of micro- and macro bending [9]. Micro bending comes from irregularities from the manufacturing process [9]. Macro bending is an effect from bending the cable more than what is recommended by the manufacturer. One source specifies that loss due to macro bending occurs as the fibre is bent to a diameter less than 30 mm [9].

### Physical properties

As previously stated, the fibres are most commonly made from glass, more precise silicon dioxide with the molecules in an amorphous structure [7]. These thin strains of glass have some important physical properties related to heating, some of which were deemed important in this study. One of the most important properties is the tensile strength of a single fibre. Silicon dioxide fibres has a theoretical tensile strength of about 14 to 20 GPa [5], [7]. However, due to impurities in the glass structure these values are unattainable. In reality the tensile strength of a single fibre is around 0,35 GPa [7]. The tensile strength of the fibre is also affected by temperature as shown by Tu & Tu [10]. In their study they subjected fibres to increased temperatures, both using an oven and using a process of annealing. Tu & Tu [10] concluded that the reduced tensile strength likely are due to small cracks and impurities that grow with the increase in temperature.

Further, related to heating are expansion and melting point. According to Zeng, et al. [11] expansion is difficult to predict due to the amorphous structure of the molecules. The melting point of the fibre is quite high, according to Ringdalen & Tangstad [12] pure silicon dioxide melts around 1790 – 1900 ºC.

## DATA TRANSFER

In order to conduct this study, there was a need to understand the basic concepts of how data is transferred over a network. The signal is interpreted as on or off, which becomes data as ones and

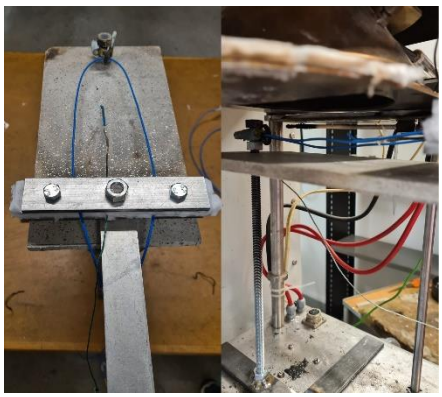

**Fig. 1.** Sample holder set-up and placement under the cone heater [4]. Also note the thermocouple placed in the centre and at the small ring.

## Sample cables and network settings

The cables used contained as little additional protection for temperature as possible, i.e., the cables were not fire resistant for a certain temperature. The outer jacket was made from a halogen free flame

retardant polyolefin [16]. Inside this jacket, there was an optical fibre alongside an aramid fibre strength member [16]. The optic fibre and the strength member were free to move inside the jacket [16], see figure 2. No effort was made to remove neither the jacket nor the strength member in the cable [4]. The reason for this was that in previous work both by Rosenqvist [3] and by Ritz et al. [17] concluded that other materials could put additional strain on the fibre during the test.

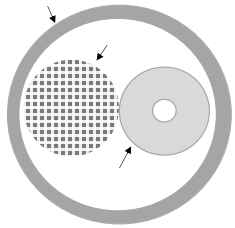

**Fig. 2.** Cable cross section.

The cables were tested at a data rate of 1 Gbit/s, because this was the maximum output of the created network [4]. To minimize disturbances from other sources a LAN was built using two computers and two switches. UDP packages with a size of 65 353 bites were sent over the network and data loss was measured at 10 Hz [4].

## Fire conditions

For the fire conditions, a cone heater from an ISO 5660-1:2019 [18] cone calorimeter was utilized. This choice was made to create a representative and repeatable fire exposure on the cable [4]. During the tests, the cables was exposed to a stepwise increasing heat flux based on the work of Rosenqvist [3]. The tests were initiated with a heat flux of 15 kW/m$^2$, with every 10 minutes it was increased first to 25 kW/m$^2$, then 35 kW/m$^2$, and finally 50 kW/m$^2$ [4]. After these initial 30 minutes of ramp up the heat flux was kept constant at 50 kW/m$^2$. The test ended after a complete cable break or a maximum of 90 minutes [4]. This was based on standards for other tests, such as the IEC 60331-25:1999 [15] and the assumption that after 90 minutes, a steady state would have been reached in the 2 mm cable.

Besides the tests in the cone calorimeter one test was done using a propane flame. This was done to investigate the difference in impact between the conical heater and a flame on the cable [4]. For the propane test, the sample holder had to be reverted to the initial design, see figure 3, as the gas burner was placed underneath the bend of the cable.

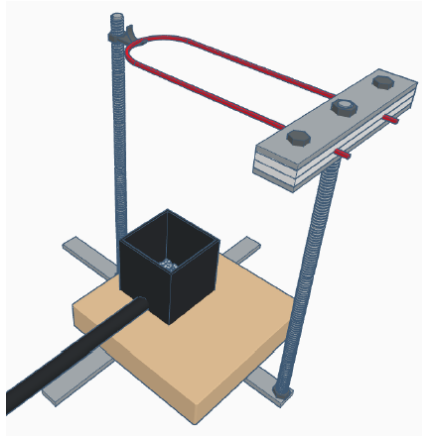

**Fig. 3.** Set-up with the propane burner [4].

| Test nr. | Initial bend diameter [mm] | Heat flux |
|---|---|---|
| 1-2 | 60 | Gradually Increasing |
| 3-4 | 60 | 50 kW/m$^2$ |
| 5-6 | 60 | Gradually Increasing |
| 7-21 | 60 | Gradually Increasing |
| 22 | 60 | 50 kW/m$^2$ |
| 23 | 40 | Gradually Increasing |
| 24 | 30 | Gradually Increasing |
| 25 | 30 | 50 kW/m$^2$ |
| 26 | 20 | Gradually Increasing |
| Propane | 60 | - |

## RESULTS AND DISCUSSION

The results and discussion presented in this section are derived from the result by Åström & Lindahl [4] and for more detailed presentation of results see the full thesis. However, this section is written to be understandable without the thesis.

### Data transfer

The experiment was developed from previous studies on fibre optic cables and the physical properties of optical fibre. The aim of the study was based on the findings by Rosenqvist [3], that a bent fibre led to higher attenuation, which was further supported by the physical aspects of macro bending as previously discussed. However, none of the conducted tests showed that data was lost nor corrupted before the cable broke [4].

One exception to the results is Test 7, where a momentary data loss of around 80 % was seen [4]. This proved to be related to the measurements being done in the so-called user space [4]. In Test 8 some data was lost leading up to the break of the cable, which was expected after the literature study. However, this effect was not seen again in any of the following tests and can therefore not be expected when fibre optic cables are affected by fire [4].

As described above some additional tests were conducted. These tests were based on the weaknesses identified in the literature study. It was found that cables bent to a smaller diameter than 30 mm would lead to a lot of attenuation from macro bending. Therefore, three of the additional tests were mounted with a bend diameter of less than or equal to 30 mm [4]. Even with this narrow initial bend, no data loss could be measured before complete break [4].

Lastly, one test was conducted over a propane flame. This was done to see if there were clear differences to the tests performed under the cone heater [4]. The result from this test was in line with the other tests and no loss was measured before complete break [4].

**Temperature**

Measuring the temperature of a fibre about the size of a strain of hair was a challenge in the study. To resolve this the temperature was based on two independent nodes [4]. One node was a thermocouple placed inside a piece of the cable jacket in the centre of the test sample. This was done to get a sense of the temperature effect the jacket had on the fibre. In some tests the jacket charred and fell off early, leaving the fibre exposed. In others the plastic charred and stayed on the fibre for the remainder of the test, resulting in a heat protection of the fibre [4]. To capture these variations, the measurements from each test were gathered to create a temperature interval within which the fibre would be affected.

The second node was a thermocouple in contact with the small ring that supported the bend of the cable. At this node, the fibre would first be separated from the ring but as the jacket would melt and disappear, the fibre would come in direct contact with the ring [4]. Thus, it is assumed that the ring would represent the temperature of the thin fibre when the jacket had melted. However, this is at the time only a hypothesis due to the uncertainty in the temperature of the fibre, which was very thin in relation to the bead size of the thermocouple. The same principle as for the centre measurement was applied in the presentation of the temperature at the small ring, meaning an interval of all the conducted tests. Figure 4 shows the temperature intervals at the centre and at the small ring.

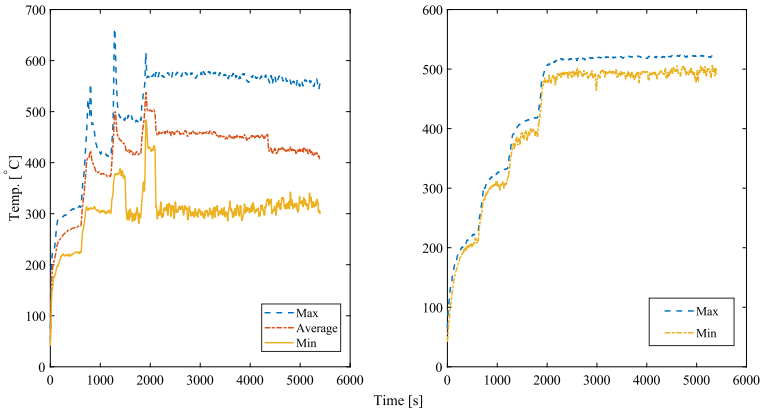


**Fig. 4.** Temperature measurements at centre (left) and at the small ring (right) [4].

Most of the cables broke when the heat flux was increased from 35 to 50 kW/m$^2$ [4]. The last increase was as previously mentioned after 30 minutes from start of test. For the exact break times the reader is referred to the full Master thesis report [4]. It was also around this time that the remaining plastic casing would start to glow, which led to an increase in temperature of the fibre. In most of the tests, the break occurred where the plastic started glowing [4].

Therefore, it could be said that the temperature alone was not enough to break the fibre. From the literature it was found that the tensile strength decreased with an increase in temperature [10]. A similar effect could be what was observed in this study. The cables always broke around the place where the narrowest bend had occurred, in one case this was along the initial straight of the cable where it twisted more than usual, see figure 5. By measuring the smallest diameter after each test, it was shown that for the main tests the bend of the cables that broke had a diameter smaller than 45 mm. Another observation by Tu & Tu [10] is confirmed in this study: the cables that did not break during the test, would always break either while removing the sample holder from the cone heater, which resulted in an increase of mechanical strain, or during cooling of the sample [4]. The latter could be compared to the annealing experiment made by Tu & Tu [10].

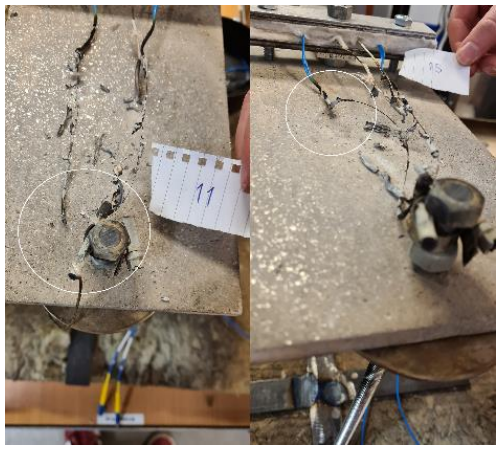

**Fig. 5.** Cables post-test with the breaking points highlighted [4].

## Damage criteria

This study also attempted to describe a damage criterion, meaning a level of strain leading to data loss or signal disturbance, severe enough to corrupt the data. From the results of the study, this would be a combination of temperature and bend diameter [4]. Since all the cables in the main tests were mounted with a bend in accordance with the manufacturers installation criteria it was deemed as a credible worst case. This means that the effects seen during the tests, such as the change in bend diameter, and melting and glowing of the cable would also occur with a properly installed cable affected by a fire. With this assumption of the test setup a statistical analysis of the data was made.

In the analysis, data of temperature and time of break was combined to create a probabilistic distribution of critical temperature [4]. The analysis was made with the cables that broke in the main tests, meaning that the four cables that broke during cooling are removed from this analysis. As discussed above in the section on temperature it was difficult to exactly measure the temperature of the fibre itself, therefore the measurements were divided into maximum, average and minimum. The same principle was used for the statistical analysis and three distributions were created [4]. Using a parametric bootstrap with 1000 resamples the best fit was evaluated using Anderson-Darling statistics. All three showed a better fit with the normal distribution compared to the gamma-, lognormal- and Weibull distributions [4]. Table 2 shows the confidence interval n (μ) n the standard deviation (σ) for the three distributions.

**Table 2. Confidence intervals for the parameters of the three normal distributions.**

| Parameter | Mean [ºC] | 95 % lower [ºC] | 95 % upper [ºC] | Conf. Interval width [ºC] |
|---|---|---|---|---|
| $\mu_{min}$ | 403 | 378 | 429 | 51 |
| $\sigma_{min}$ | 41 | 23 | 60 | 37 |
| $\mu_{average}$ | 477 | 460 | 493 | 33 |
| $\sigma_{average}$ | 26 | 15 | 39 | 24 |
| $\mu_{mac}$ | 526 | 510 | 542 | 32 |
| $\sigma_{max}$ | 25 | 15 | 38 | 23 |

Figure 6 shows the fit comparison for the minimum distribution.

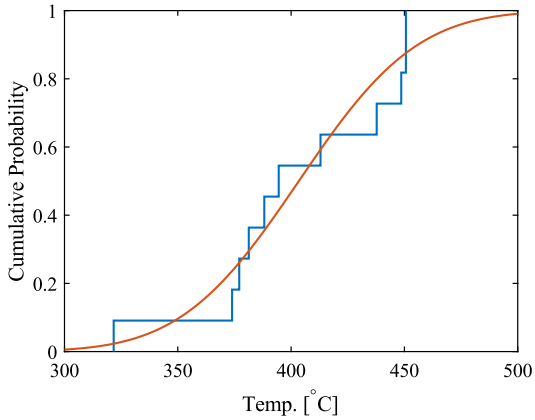


**Fig. 6.** Fit comparison for the Min distribution [4].

Lastly, the 5th percentile for each of the fits were calculated and presented in table 3.

**Table 3. 5th percentile for each fitted distribution, and lowest measured during tests.**

| Distribution | 5th percentile [ºC] | Lowest measured [ºC] |
|---|---|---|
| Minimum | 366 | 322 |
| Average | 433 | 411 |
| Maximum | 483 | 466 |

The statistical analysis is based on a small sample size and the result should be used conservatively in probabilistic analysis until a larger sample is analysed. From the discussion on temperature, it is concluded that the temperature reaches local maximums at the point of break but as the measurements in the study was averaged this is not quantified. Therefore, it seems possible that further studies on the relationship between bend diameter and temperature for optical fibres would indicate that they survive even higher temperatures.

## CONCLUSIONS

This study shows a high level of signal endurance in fibre optic cables that are affected by fire. A bigger study of different types of data packages and bandwidth could provide further insight to the resilience of the signal during heating. Further, from the study a temperature of 336 ºC was derived as a 5th percentile value of the minimum distribution. With a temperature distribution and critical values, it is possible to apply previously developed models for other types of cables like the FDS integrated THIEF model [19]. However, this was not the focus in this study. Lastly, an important note is that even correctly installed cables can bend during heating in such a way that the cable breaks. This emphasize the need for careful installation and as far as possible narrow bends and twists of the cable should be avoided when used for critical systems.

## ACKNOWLEDGEMENT

The authors are grateful to Dr. Stefan Höst, LTH, for sharing some of his knowledge on fibre optic networking. Also, a special thank you to Johannes Josefsson at Nexans AB, for helping us choose and for supplying the cables necessary for this study, and Gunnar Knutsson at Network Infrastructure, LU, for supplying the switches necessary to create the test network.

## REFERENCES


[1] A. Åslund, Säkerhetsrelaterade systemkomponenters felmoder vid brand på kärnkraftverk, Report No. T-SIP PM 00/06, SwedPower AB, 2000.

[2] P. Andersson, P. Van Hees, Performance of Cables Subjected to Elevated Temperatures, Fire Safety Science–Proceedings of the Eighth International Symposium, pp, 1121–1132, 2005.

[3] J. Rosenqvist, Fiber optics communication failure modes, Bachelor thesis, department of fire safety engineering, Lund University, Lund, Sweden, 2014.

[4] J. Åström, S. Lindahl, Damage Criteria for Fibre Optic Cables Exposed to Fire – Using data transfer as functional criterium, Master thesis, Division of Fire Safety Engineering, LTH, Lund University, Lund, Sweden, 2021.

[5] J. Hecht, Understanding Fibre Optics, LaserLight Press, Auburndale, Massachusetts, 2006.

[6] E. Wright, D. Bailey, Practical Fiber Optics, Newnes, 2003.

[7] F. Mitschke, Fiber Optics – Physics and Technology, Springer, Berlin, 2016.

[8] S. Abrate, Plastic Optical Fibers for Data Communications, In: DeCusatis, Handbook of Fibre Optic Data Communication, Academic Press Inc., San Diego, California, 2013, pp. 37-54.

[9] R. Hui, Fiber optic measurement techniques, Academic Press, San Diego, California, 2009.

[10] Y. Tu, S. Tu, Tensile strength of silica optical fibers for high-temperature sensing applications, In: L. Ye, Recent Advances in Structural Integrity Analysis – Proceedings of the International Congress, Woodhead Publishing, pp. 158-162, 2014.

[11] H. Zeng, F. Ye, X. Li, L. Wang, B. Yang, J. Chen, X. Zhang, L. Sun, Calculation of thermal expansion coefficient of glasses based on topological constraint theory, Chemical Physics Letter 662, pp. 268 – 272, 2016.

[12] E. Ringdalen, M. Tangstad, softening and Melting of SiO2, an Important Parameter for Reactions with Quartz in Si Production, In: R. Reddy, P. Chaubal, P. Pistorius, U. Pal, Advances in Molten Slags, Fluxes and Salts – Proceedings of the 10th International Conference on Molten Slags Fluxes and Salts, Springer International Publishers, Switzerland, pp. 43-51, 2016.

[13] P. Loshin, TCP/IP clearly explained, Morgan Kaufmann Publisher Inc., San Francisco, California, 2003.

[14] CENELEC, SS-EN 50200:2006 – Method of test for resistance to fire of unprotected small cables for use in emergency circuits, Svensk Elstandard, Stockholm, 2006.

[15] IEC, IEC 60331-25:199 – Tests for electric cables under fire conditions – Circuit integrity – Part 25: procedures and requirements – Optical fibre cables, International Electrotechnical Commission, Geneva, 1999.

[16] Nexans, Korskopplingskablage 1xSM G.652D/G.657A LC/UPC-LC/UPC, https://www.nexans.se/sv/, (accessed 3 oktober 2020)

[17] P. Ritz, P. Kupilik, M. Pinkerová, O. Veselý, Changes of Transmission Parameters of Various Types of Cables During Fire, IWCS., Providence, Rhode Island.

[18] ISO, SS-ISO 5660-1:2019 – Reaction-to fire tests – Heat release, smoke production and mass loss rate – Part 1: Heat release rate (cone calorimeter method) and smoke production rate (dynamic measurement) (ISO 5660-1:2015, IDT), Swedish Standards Institute, Stockholm, 2019.

[19] K. McGrattan, Cable Response to Live Fire (CAROLFIRE) Volume 3: Thermally-Induced Electrical Failure (THIEF) Model, National Institute of Standards and Technology, Gaithersburg, Maryland, 2008.

# Measurement of the surface temperature of a wood sample with a thermo-phosphorescent powder

**Chaudary A.[1], Godard G.[1,], Coppalle A.*[1]**

[1] *UMR 6614 CORIA, INSA Rouen, St Etienne Rouvray France.*
**Corresponding author's email: alexis.coppalle@coria.fr*

## ABSTRACT

The thermo-phosphorescence property of a rare earth powder has been used in order to measure the surface temperature of a wood sample. The method needs an exitation laser pulse in the UV spectrum and an optical detection system of the phosphor signal at a red wavelenght. The measure of the lifetime of the exponetional decay of the signal allows to determine the temperature, using a calibration on a steel plate. The wood sample was heated on one face and the method applied on the other face, by coating with the powder a small strip at the center. The experimental setup allows to determine the surface temperature from ambiant to 400°C. Comparison with the results obtained with two infrared cameras, working in two different spectral ranges, makes it possible to calculate the wood emissivity factor at these wavelenghts and in the observed temperature range. Analysis will show that the agreement is good if a suitable emissivity factor is used.

**KEYWORDS:** Surface temperature, wood, fire, thermophosphorescence.

## INTRODUCTION

The measurement of the surface temperature of a solid which is heated is an important issue. In fires, the solid may degrade under the effect of a heat source, and in a many studies, one want to know the temperature values at the surface in order to understand the different processes occuring during degradation, the vaporisation of water, the onset of the pyrolysis... A low temperature, close to ambiant, several types of temperature sensors can be used, which need a contact with the surface sample, Platinum resistance thermometers (Pt 100), Thermistors (CTN), Thermoelectric couples (type K, J, N, T etc.). However some questions remains, and precautions have to be taken.

Three effects may influence the surface temperature measurements, they are due to the contact between the sensor and the sample, the macro-constriction, the contact resistance and the fin effect [1-2]. They can be briefly described as follow: The effect of macro-constriction is the thermal conductance due to the application of the thermometer on the surface which promotes heat flow by conduction inside the material. The contact resistance is a thermal resistance due to cavities created during contact. The surfaces facing each other have a certain roughness which contains air. Local thermal resistance limits heat exchanges. The fin effect: thermal conductance also called the "radiator" effect due to the increase in the heat exchange surface along the thermometer sheath.

As a non-contact method, infrared (IR) pyrometry and thermometry can be used to measure the surface temperature of solids. However, accurate emissivity values, in the wavelenght range of detection, have to be known. At ambient or low temperatures, values have been determined and they are well known for a large variety of materials.

At high temperature, only thermocouples and IR thermometry can be used. However, the same problems described above remain, but more acutely. It is generally difficult to have a good contact between the thermocouple and the solid surface, with a low thermal resistance. The extreme difficulty to measure the surface emissivity during fire tests implies that in most of the studies values are presumed. This knowledge of surface emissivity is the major drawback for using of IR technique to determine temperature.

So it is interesting to develop a method for the surfaces at high temperatures. It must be able to circumvent the biases stated above. Since several years, studies [3-4] have demonstrated that phosphor thermometry has appeared to be an interesting technique for remote-temperature measurements in extreme conditions. It has been demonstrated the abability in using the thermophosphore powders deposited on a surface and excited by a laser in order to determine the temperature. Two categories of implementation are commonly used: the lifetime approach and the spectral technique. They will be described hereinafter. Phosphor thermometry has been used in several applications for surface temperature measurements, e.g. diesel engines, in manufacturing processes, in cylinders [5-7].

The aim of the present study is to analyze the feasability and the limits of phosphor thermometry with lifetime method for surface temperature measurement of a wood sample. First the theory and the signal processing are described, then the optical setup and the calibration porcedure, and finally results obtained on a wood sample heated by a burner are presented, discussed and compared to the ones obtained with IR cameras.

## THEORY AND SIGNAL PROCESSING

### Principles of the phosphorescence

Figure 1 summarises the principle of electron transfer leading to the phosphorescence signal [8]. First an electron increases its energy by absorbing an U.V. photon, provided by an intense light source like a laser for exemple. It losses partially this energy by collisional transfer, afterward it goes to its fundamental state by emitting a photon, most of the time in the red wavelength range. The number of photons N2 emitted from the level 2 is controlled by two processes, as shown by equation 1,

$$\frac{dN_2}{dt} = - \left(W_{2-1}^{rad} + W_{2-1}^{coll}\right) N_2 \quad (1)$$

where the first term at the right representes the efficiency of the radiative transfer and the second one the efficiency of the collisional transfer from excited level 2 to the fundamental 1. With a short laser pulse, the decay of N2 is exponential and the lifetime $\tau$ of the phosphorescence signal is

$$\tau = 1/ \left(W_{2-1}^{rad} + W_{2-1}^{coll}\right) \quad (2)$$

These two efficiencies are temperature dependant so the phosphorescence signal decay is also function of the temperature.

The radiative transfer between levels 2 and 1 is not occuring at one wavelenght. Due to the collisional effects, the posphorescence signal is broadened in a small wavelenght range around the fundamental.

### Signal processing for the temperature measurement

The two main methods of signal analysis to determine the temperature are based on measuring the lifetime [4-9] or the intensity ratio at two wavelengths [10]. The former benefits from a higher accuracy, precision and, as compared to the spectral method when used with Mg4FGeO5,6:Mn thermographic phosphor [11], it is also suitable for probing static samples with long thermal characteristic timescales [12]. The intensity ratio method, although delicate to implement, is interesting for making 2D imagery.

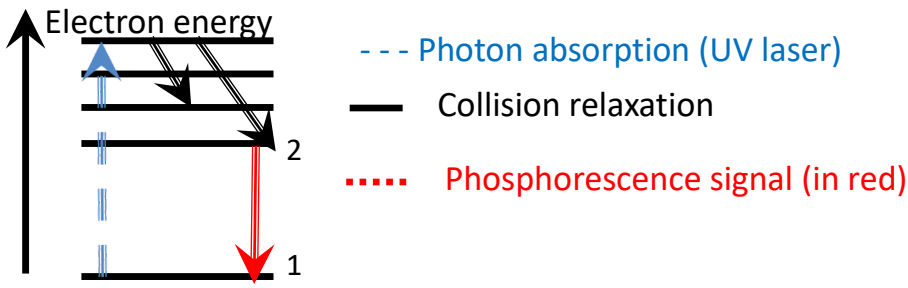


**Fig. 1.** Principle of the electron energy transfer leading to a phosphorescence signal.

In this work, the lifetime method has been chosen due to its simplicity of implementation and its accuracy. So only point measurements will be presented. A large number of phosphors are available today, covering a wide range of temperatures [13]. In this study, the thermographic phosphor powder used is Mg4FGeO5,6:Mn which is well suited for the 20-500°C range. It consists of ceramic host material Mg4FGeO5,6 doped with rare-earth Mn activator in concentrations between 1 to 10 percent. Therefore in this study, the commercial powder Mg4 FGeO5,6:Mn (Osram SV067) was chosen.

## EXPERIMENTAL SETUP

### Optical setup

It is shown on fig. 2. The 3rd harmonic of a Nd:YAG laser (pulse duration ~4-6ns at 355 nm) operating at a repetition rate of 10Hz is used as the excitation source. Dielectric attenuators are connected in series to adjust the laser energy to 6 mJ per pulse, preventing from thermal damage of the phosphor coating. The luminescence of the phosphorescence signal is collected on a 60 mm diameter PDA probe (DANTEC Dynamics). Dimensions of the collected surface on the samples are 0.12 mm width and 0.2 mm height. The luminescence signal is passed to the optical instrumentation using a fiber. A 550 nm optical high-pass filter is used to remove interferences from the laser excitation while phosphorescence is extracted with an optical band-pass filter at 642±10 nm. After this one, there is a photomultiplier tube connected to a current-to-voltage converter and a digital oscilloscope (YOKOGAWA DLM 2024).

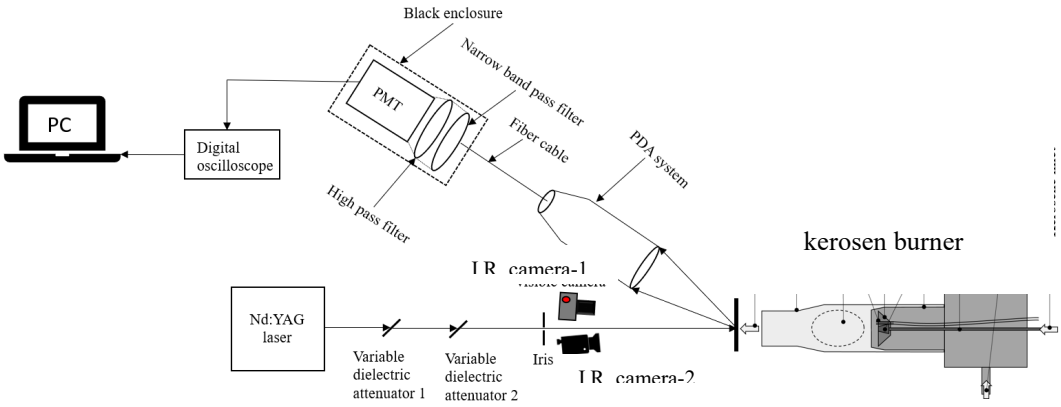


**Fig. 2.** Schematic of the experimental setup using a kerosene burner as well as the phosphor thermometry (PT) optical bench.

**Phosphor coating on wood samples**

The phosphor powder is mixed with a water-based ceramic binder (Zyp coatings Inc., HPC), with a phosphor mass concentration of 5%. Several techniques exist for deposition of phosphor coating, However, they requires controlled atmosphere and special equipments for application. In the present study, a simple method was used. The phosphor-binder mixture is sprayed using an airbrush (SOTAR 2020).

## CALIBRATION

The calibration is an important step of the method. The goal is to determine the relationship betwen the lifetime $\tau$ and the phosphor temperature when the powder is deposed on a solid surface. It is performed with a thin stainless-steel plate while keeping the spatial arrangement and the optical setup identical. On the backside of the stainless-steel plate, a K-type thermocouple is welded and a phosphor layer is coated on it. On the front side, a butane torch lighter is used to heat the sample. By changing the distance between the torch and the steel plate, the temperature at the TC is varied. Phosphorescence signals are collected for different temperatures. For each temperature, between 20 to 50 individual waveforms are recorded, with an acquisition rate equal to 25khz, and averaged to estimate $\tau$. Figure 3 shows the steel plate with thermocouple welded on it.

Upon a laser excitation (~4-6ns), the phosphorescence signal decays exponentially and can be

modeled as

$$I\,(t) = I_0 e^{\left(\frac{-t}{\tau}\right)} + B \tag{3}$$

where $I_0$ is the initial intensity, $t$ is the time, $\tau$ is the decay lifetime and $B$ is the base line. The influence of the coating thickness is investigated by varying the number of passes with the airbrush. Two pass coating thickness is about 10$\mu$m. Figure 4 shows the normalized intensity of phosphorescence decays measured at different temperatures. At higher temperature, lifetime becomes shorter.

The calibration curve is shown in Fig 5. The important issue is that the two calibration curves, 2 and 4 passes, are well superimposed, and so the temperature measurement will not be sensitive to the thickness of the coating. Results shown in Figs. 4 and 5 are in good agreement with the literature results [14,15].

**Fig 3**. Steel plate with the thermocouple welded on it

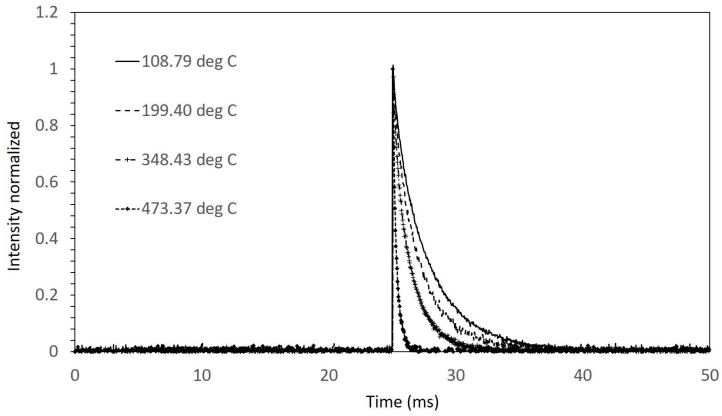


**Fig 4.** Normalized phosphorescence signals at different temperatures for 2 pass coating

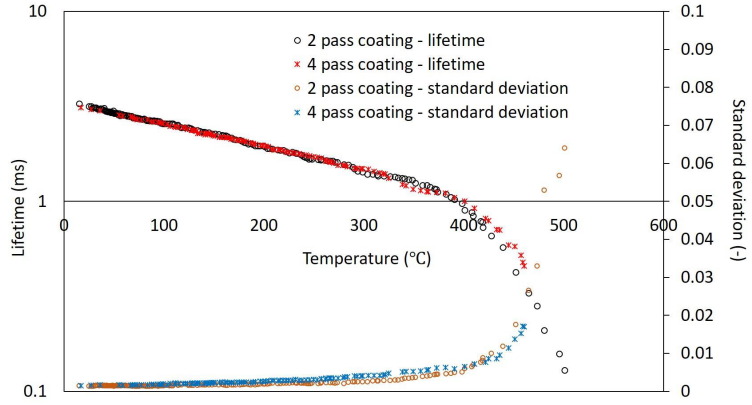


**Fig 5.** Calibration curve of Mg4FGeO5,6:Mn. Phosphorescence lifetime/temperature relation

## APPLICATION TO THE MEASUREMENT OF SURFACE TEMPERATURE OF A WOODEN SAMPLE

The wood sample is made of plywood with 12mm thickness.

### wood sample heating

The sample has been placed in front of the flame of a kerosene burner. This last one is included in a test bench designed to analyse the fire reaction of materials at laboratory scale, and more details can be found in [16]. The test bench is shown in Fig. 6. The burner is fueled with a kerosene mass flow rate of 0.3 g/s. Air flow rate is set to 5 g/s to obtain a fuel to air ratio equal to 0.85 of the stoichiometric value, in order to obtain flame temperature equals to 980°C and heat flux equals to 113 kW/m2.


**Fig. 6.** View of the kerosen-burner test bench

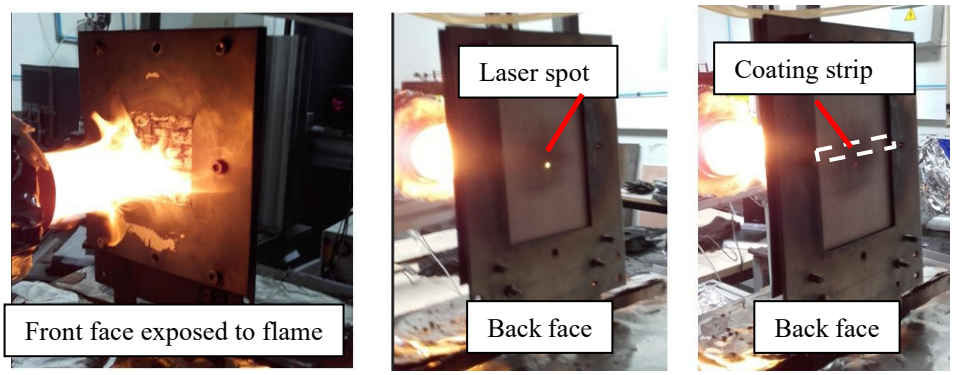


**Fig. 7.** Views of the wood sample and its holder

The test bench is equipped of two infrared cameras, focused at the back face, as shown in Fig. 2. The first one (FLIR A6750) is sensitive in the 2-5 µm wavelength range and the second one (FLIR ThermaCam) in the 7-15 µm range. In order to be able to compare values given by the two cameras observed during the heating phase of the wood sample, the ranges 80 230°C and 80-400°C have been chosen for the A6750 and ThermaCam cameras respectivelly.

**Results**

Figure 8 presents examples of the temperature mappings obtained with the two cameras, using the same emissivity equal to 0,92, value recommended in [17] for temperature close to ambient (up to 60°C). For the test-1, the temperature gradients at the center of the sample are low, and at this location the surface temperatures are homogeneous. The laser spot for the thermophosphor thermometry being in the center of the coating strip, the infrared results have been also analysed at the same location. A more quantitative analysis is done below by comparing the variation of the temperature as a function of time at the center of the thermophosphor coating strip. In order to look at the influence of the coating on the surface temperature, another point just above the strip has been also used for the FLIR A6750 camera.

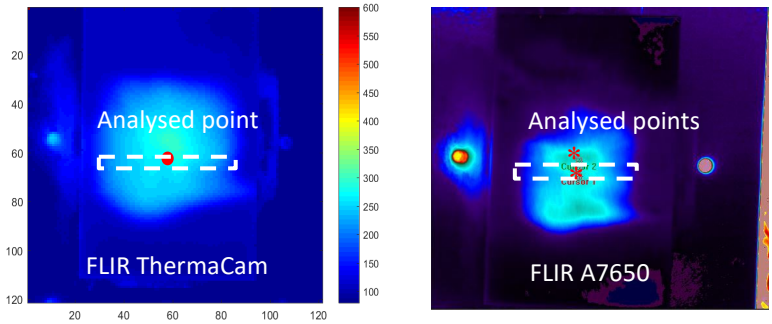


**Fig. 8.** Exemple of temperature mappings obtained with the two cameras. Red marks are for the positions of the analysed points of the IR cameras.

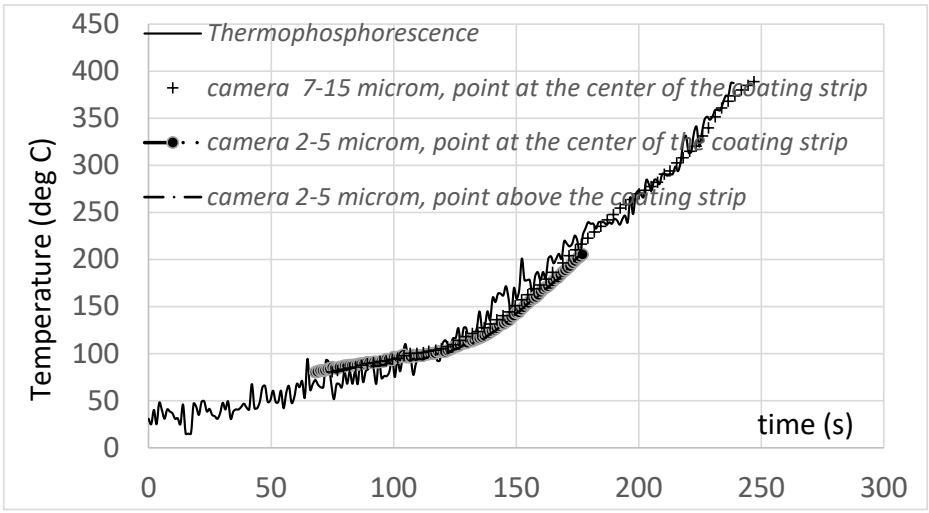


**Fig. 9.** Test-1, Comparison of the temperatures measured at the center with the two IR cameras and the thermophosphorescence method. The temperature at a location just above the coating strip is also show.

In the temperature range of the A6750 camera, all temperature results can be compared. For the temperature calculations, the same and constant emissivity 0.92 has been used for both IR cameras. There is a good agreement between the results provided by the two IR cameras, which are not sensitive in the same spectral range (see above). So it seems that there is no variation of the emissivity of the wood between 2-5 µm and 7-15 µm, but also that it doesn't change between 80 and 230°C.

We can observed that there is also a good agreement between the thermo-phosphorescence results and the ones of the ThermaCam camera up to 300°C. This reinforces the previous point on the emissivity, i.e. the value for wood doesn't vary between 80 and 300°C.

At last, one can seen on fig. 9 that there is a good superposition of temperature results given by the A6750 IR camera at the center and just above the phosphor coating strip. That means the deposit layer has no influence on heat transfers, its small tickness (10µm) do not act as a thermal barrier with respect to the exchange of the back surface of wood with ambiant air.

Two other tests have been carried out. Figure 10 presents examples of the temperature mappings obtained with the A6750 camera. The ThermaCam camera mapping are not shown since they are vey similar. Compared to test-1 (fig. 8), the temperature is less homogeneous in middle of the sample, certainly due to different char formations on the exposed surface. This process has a great influence on the heat transfer through the thickness.

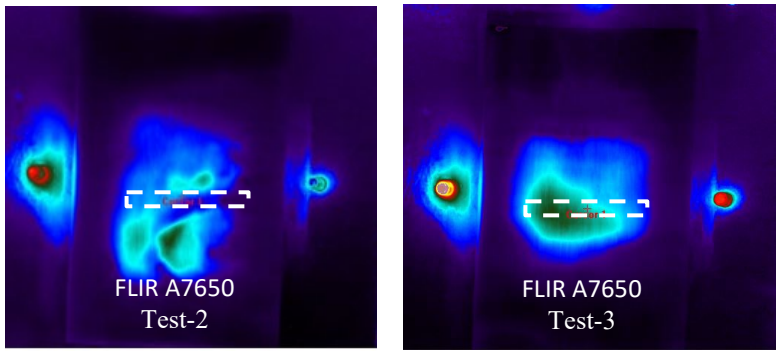


**Fig. 10.** Exemple of temperature mappings obtained with the camera A6750 for test-2 and test-3.

The temperature results at the center of the coating strip are reported on fig. 11.

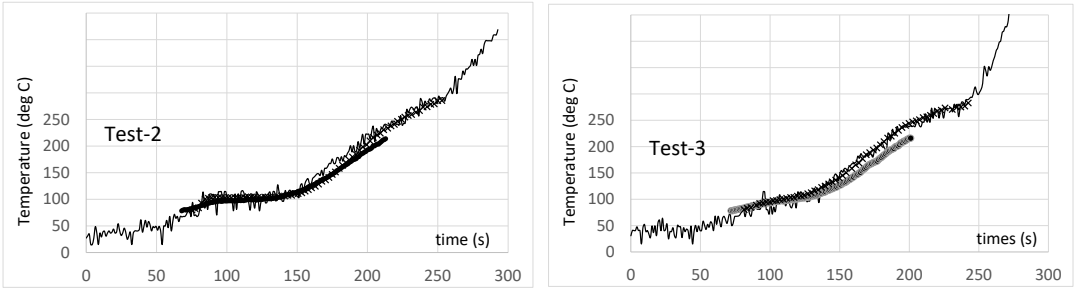


**Fig. 11.** Test-2 and Test-3, comparison of the temperatures measured at the center with the two IR cameras and the thermophosphorescence method.

As for the test 1, two comparisons are important. First there is a satisfactory overall agreement between the two IR camera results, exept in the 150-230 °C range for the test-3. No clear explanation has been found for this last case. It is possible that they occured a slight misalignement of the two cameras, so that the temperature was not measured at the same place and was different, as suggested by the temperature mapping shown on fig. 10. The globally satisfactory agreement between the two IR camera suggests again that there is no variation in the emissivity of the wood between 2-5 µm and 7-15 µm.

We can also observed that there is a good agreement between the thermo-phosphorescence results and the ThermaCam camera ones up to 300°C. This reinforces the previous point on the emissivity, i.e. the wood value doesn't vary between 80 and 300°C. However, greater than 300°C, there is a discrepancy between the two measurement methods. This temperature correspond more or less to the onset of the back surface degradation, with a beginning of smoke emission. Further studies are necessary to confirm if these process may influence the measurements.

However it is interesting to note that water vapor exchange through the wood surface do not influence the phosphorescence signal emsission, since a temperature plateau is observed at 100°C with this méthod. This is particularlly visible for test-2.

## CONCLUSION

In this work, The thermosphorescence optical method has been applied to measure the temperature surface of wood sample heated up to 400°C. A simple methode of calibration has been developped up to 500°C. It uses a thermocouple welded on a thin steel plate with thermophosphor powder deposited on it, and heated at the back face with a small flame torch.

Detection of the thermophosphorescence signal on a small spot on the back surface of the wood sample allows to follow the temperature increase up to 400°C, and monitoring the heating periode before the drying of the surface, the temperature plateau at 100°C, and then the increase of temperature up to 400°C.

The camparison with two IR cameras, working in different spectral ranges (2-5 and 7-15 mm), allows to estimate the emissivity of wood for these wavelengths. The same value equal to 0.92 has been been found, and no variation has been observed as a function of the temperature.

The thermophosphorescence optical method is applicable for measuring the surface temperature of wood, with several adventages compared to other methods. It avoid the issue of the quality of the contact when using thermocouple, and it does not need to know the emissivity of the material as it is the case in the IR thermography.

However in this study, the thermophosphorescence method was applied and analysed for temperatures which does not reach the thermal decomposition of the surface. Further works are necessary to look if it remains applicable during this process.

## REFERENCES

[1] B.Cassagne, G.Kirsch, J-P.Bardon, Theoretical analysis of errors related to parasitic heat transfers during the measurement of a surface temperature by direct contact, Int. J. Heat Mass Transfer 23 (1980) 1207-1217.

[2] Z. Zhang, B. Tsai, G. Machin, Radiometric Temperature Measurements, first ed., Academic Press 2009

[3] Khalid, A.H. and Kontis, K., Thermographic phosphors for high temperature measurements: principles, current state of the art and recent applications. Sensors, 8 (2008.) 5673-5744.

[4] Allison, S.W. and Gillies, G.T., Remote thermometry with thermographic phosphors: Instrumentation and applications. Review of Scientific Instruments, 68(1997), 2615-2650.

[5] Binder, C., Feuk, H. and Richter, M., Phosphor thermometry for in-cylinder surface temperature measurements in diesel engines. Journal of Luminescence, 226 (2020) 117-415.

[6] Ojo, A.O., McCallum, F., Andreu, A. and Heyes, A.L., On the use of phosphor thermometry for temperature monitoring in manufacturing processes. In 1st International Conference on Phosphor Thermometry (2018) 111-114.

[7] Ervin, J., Murawski, C., MacArthur, C., Chyu, M. and Bizzak, D.,. Temperatur measurement of a curved surface using thermographic phosphors. Experimental thermal and fluid science, 11(1995), 387-394.

[8] Brübach, J., Pflitsch, C., Dreizler, A. and Atakan, B., On surface temperature measurements with thermographic phosphors: a review. Progress in Energy and Combustion Science, 39 (2013).37-60.

[9] Fuhrmann, N., Baum, E., Brübach, J. and Dreizler, A., High-speed phosphorthermometry. Review of Scientific Instruments, 82 (2011)

[10] Kusama, H., Sovers, O.J. and Yoshioka, T., Line shift method for phosphor temperature measurements. Japanese Journal of Applied Physics, 15 (1976)

[11] Fuhrmann, N., Brübach, J. and Dreizler, A., Phosphor thermometry: A comparison of the luminescence lifetime and the intensity ratio approach. Proceedings of the Combustion

Institute, 34 (2013) 3611-3618.

[12] Brübach, J., Pflitsch, C., Dreizler, A. and Atakan, B., On surface temperature measurements with thermographic phosphors: a review. Progress in Energy and Combustion Science, 39 (2013) 37-60.

[13] Aldén, M., Omrane, A., Richter, M. and Särner, G., Thermographic phosphors for thermometry: a survey of combustion applications. Progress in energy and combustion science, 37 (2011) 422-461.

[14] Omrane, A., Ossler, F., Aldén, M., Gtoransson, U. and Holmstedt, G., Surface temperature measurement of flame spread using thermographic phosphors. Fire Safety Science, 7 (2003), pp.141-152.

[15] Meyer, C.W., Meier, D.C., Montgomery, C.B. and Semancik, S., Temperature measurements of microhotplates using fluorescence thermometry. Sensors and Actuators A: Physical, 127(2006) 235-240.

[16] Schuhler, E., Chaudhary, A., Vieille, B. and Coppalle, A., Fire behaviour of composite materials using kerosene burner tests at small-scales. Fire Safety Journal, (2021) p.103290.

[17] Lopez, G., Basterra, L. A., Acuna, L., et al., Determination of the emissivity of wood for inspection by infrared thermography. Journal of nondestructive evaluation, 32 (2013) 172-176.

# Analysis of the load bearing capacity of concrete semi-confined spaces exposed to the combustion of two cars at the Wildland-Urban Interface

**Vacca P.[1], Pastor E.[1,*], Planas E.[1]**

*[1] Department of Chemical Engineering, Centre for Technological Risk Studies, Universitat Politècnica de Catalunya·BarcelonaTech, Edurad Maristany 10-14, E-08019 Barcelona, Catalonia, Spain*

**Corresponding author's email: elsa.pastor@upc.edu*

## ABSTRACT

The issue of artificial fuels stored in concrete semi-confined spaces at the Wildland-Urban Interface (WUI) microscale is analysed in a quantitative way. Sub-system hazard testing by following a Performance-Based Design (PBD) approach is presented for these types of scenarios with the goal of quantifying the damage inflicted to the structure by the combustion of artificial fuels. The proposed methodology consists of a three-step approach: (1) the adiabatic surface temperature of the walls of the semi-confined space is obtained by using the Computational Fluid Dynamics (CFD) modelling software FDS (Fire Dynamics Simulator), which simulates the fire scenario that is to be examined, (2) the temperature profile through the analysed cross-section of the wall is identified by using a finite difference method, and finally (3) the load bearing capacity over time of the cross-section is analysed according to Eurocode 2. A simple example of the used methodology is presented in this paper, which consists of the combustion of two cars in a garage-like concrete semi-confined space. Results show that the load bearing capacity of the analysed cross-section will drop to 74% when the thickness of the wall is 10 cm, while for bigger thicknesses it will stay above this value.

**KEYWORDS:** Fire Dynamics Simulator, Performance-Based Design, Wildland-Urban Interface fires.

## INTRODUCTION

Investigation of past Wildland-Urban Interface (WUI) fires has highlighted the issue of fuels located in the surroundings of a building. This area, defined as the WUI microscale, is characterized by the presence of all sorts of combustible elements that may jeopardize the integrity of the main structure: ornamental vegetation, ground fuels, fences, stored material, outbuildings (e.g., garages, garden or storage sheds) or even adjacent structures [1]. These fuels very often lack any type of management [2], and in case of their ignition, and provided significant flame duration and intensity is achieved, consequences might have a severe impact [3]. Secondary structures such as garages, sheds, or even spaces below porches and decks, are sometimes used as storage areas, resulting in the accumulation of all types of artificial fuels in these confined or semi-confined (i.e. open on at least one side) spaces. Artificial fuels have the potential to burn for long periods of time, and they are the ones that can create the most damage during the post-frontal combustion fire phase, which consists of the sustained burning of the items present on a property once the main wildfire front has passed. Should they be ignited when stored in semi-confined spaces, the consequent great heat build-up created by the fire in such spaces could cause substantial damage to the structure as well as contribute to fire spread on the property [1]. If these semi-confined spaces are adjacent to the main building on a property, then the heat accumulation could also cause structural damage to the building's envelope. An example of the damage caused during past fires by the ignition of fuels in semi-confined spaces is given in Fig. 1.

**Fig. 1.** Greatly damaged semi-confined space in the Mati fire (Greece, 2018) [4]

The hazard posed by these type of scenarios, along with other WUI microscale scenarios, can be evaluated following a Performance Based Design (PBD) approach, through which the degree of safety that meets the objectives of property protection and life safety can be assessed in a quantitative way [1]. A methodology for sub-system hazard testing is here presented for concrete semi-confined spaces scenarios. This specific WUI microscale PBD approach can also be implemented for the vulnerability assessment of a whole building and property, in which different sub-systems (e.g. glazing systems, semi-confined spaces, LPG tanks) can be analysed simultaneously.

The objective of this work is to identify the wall thickness at which structural survivability of semi-confined spaces built in concrete is achieved in case of combustion of typical WUI artificial fuel packs. The methodology focuses on concrete walls, since it is one of the most common building materials at the Mediterranean WUI.

## METHODOLOGY

The analysis for the identification of the vulnerability of semi-confined spaces is performed with a three step approach: (1) the adiabatic surface temperature of the concrete walls of the semi-confined space is obtained by using the Computational Fluid Dynamics (CFD) modelling software FDS (Fire Dynamics Simulator) [5], which simulates the fire scenario that is to be examined, (2) the temperature profile through the wall is identified by using a finite difference method, and (3) the load bearing capacity over time of the analysed wall cross-section is calculated according to Eurocode 2 (EN 1992-1-1 [6] and EN 1992-1-2 [7]). The analysis is performed on concrete walls, which must be designed and constructed in such a way that they maintain their load bearing capacity function (criterion R) during the required time of exposure to a fire [7], which, in this methodology, is the complete duration (i.e. including the decay phase) of the combustion of artificial elements commonly present at the WUI microscale.

### FDS scenario buildup

FDS [5] has been validated in multiple fire engineering applications and it is nowadays the most popular CFD modelling tool for PBD evaluations of complex building fire scenarios. This tool can also be used for WUI microscale scenarios, because it allows to model with great flexibility the many variables and thus scenarios that WUI fire problems present, including the definition of different configurations, materials and fire loads, which is otherwise very difficult to achieve in experimental tests. With the proper characterization of the fire source and of the building features, FDS can provide information on key variables for WUI risk management. This tool allows for the analysis of a large number of scenarios and can cover the diverse fire safety needs of the WUI microscale. Results from simulations can then be compared to previously set performance criteria, in order to obtain relevant

and solid conclusions [1]. This way the same tool can be used to analyse simultaneously all the different sub-systems of a building, making the analysis time and cost effective.

For the simulations of fuels or fuel packs in semi-confined spaces, knowledge is needed on the geometry of the space, the type of materials that compose it (e.g. physical and thermal properties), and finally on the fire characteristics of the ignited fuels. The latter information can be found in specific PBD codes and standards, or from small- and real-scale tests (i.e. [8], [9]). In FDS, the needed fire inputs include the surface of the fire, its Heat Release Rate Per Unit Area (HRRPUA), its spread rate or an assigned Heat Release Rate (HRR) curve.

The needed output from fire simulations is the adiabatic surface temperature of the analysed member [10], which can be used as a simple boundary condition input for finite element thermal/structural models [11]. The adiabatic surface temperature represents an effective exposure temperature that can be passed on to a more detailed model of the solid object, and it provides the gas phase thermal boundary condition in a single quantity, which is not affected by the uncertainty associated with the solid phase heat conduction model within FDS. Additionally, there is no need to specify the convective heat transfer coefficient, which is computed by FDS. The objective in passing information to a more detailed model is to get a better prediction of the solid temperature (and ultimately its mechanical response) than FDS can provide [12]. This output can be obtained with a boundary file, which also gives a visual on the distribution of the adiabatic surface temperature along a surface, or by placing devices at different locations on the surface of the member that will then be analysed.

**Temperature profile and load bearing capacity**

Once the adiabatic surface temperature is obtained, it is used as a boundary condition on the heated side for the computing of the heat flux as given in Eq. (1) [11], where $\dot{q}''_{tot}$ (W/m$^2$) is the total net heat flux to the surface, $\varepsilon$ is the emissivity, $\sigma$ ($5.67 \cdot 10^{-8}$ W·m$^{-2}$K$^{-4}$) is the Stefan-Boltzmann constant, $T_{AST}$ and $T_s$ (K) are respectively the adiabatic surface temperature and the object surface temperature, and $h_{conv}$ (W·m$^{-2}$·K$^{-1}$) is the convective heat transfer coefficient. The value of $\varepsilon$ is 0.7, while the one for $h_{conv}$ is 25 W·m$^{-2}$·K$^{-1}$ [7], which is a conservative value.

$$\dot{q}''_{tot} = \varepsilon\sigma(T_{AST}^4 - T_s^4) + h_{conv}(T_{AST} - T_s) \quad (1)$$

The temperature distribution in the cross-section of the wall is obtained through an explicit finite difference method that solves the one dimensional partial differential equation of heat conductivity, as given in Eq. (2), Eq. (3) and Eq. (4), where $\rho$ is the density of the material (kg/m$^3$), $c_p$ is the specific heat (J·kg$^{-1}$·K$^{-1}$), $\lambda$ is the thermal conductivity (W·m$^{-1}$·K$^{-1}$), $\theta$ is the temperature (°C), $L$ is the thickness of the wall (m), and $\dot{q}''_{loss}$ indicates the heat losses on the non-exposed side of the wall (W/m$^2$). The values of the thermal properties of the concrete change depending on the temperature, and the specific heat capacity is modelled as a constant value of 2020 J·kg$^{-1}$·K$^{-1}$ for a moisture content of 3%, according to EN 1992-1-2 [7].

$$\dot{q}''_{tot} = -\lambda \frac{\delta\theta}{\delta x}\Big|_{x=0} \text{ for } x = 0 \quad (2)$$

$$\rho c_p \frac{\partial\theta}{\partial t} = \frac{\partial}{\partial x}\left(\lambda \frac{\delta\theta}{\delta x}\right) \text{ for } 0 < x < L \quad (3)$$

$$-\lambda \frac{\delta\theta}{\delta x}\Big|_{x=L} = \dot{q}''_{loss} \text{ for } x = L \quad (4)$$

Once the temperature profile through the wall is calculated, the load bearing capacity can be found according to the Eurocode 2. An ad-hoc code has been developed to analyse the structural survivability of concrete walls during the duration of the previously simulated fire, which uses the temperature profile through the wall as input, and outputs a curve of the load bearing capacity of the wall over time.

As the temperature rises, concrete loses its compressive and tensile strengths, impacting the stress-strain relationship. The total strain at any point of the cross section is calculated with Eq. (5), while

the mechanical strain for each point is calculated according to Eq. (6), where $\varepsilon_0$ is the average strain, $\chi$ is the curvature ($m^{-1}$), $y$ is the point's coordinate from the center of the cross-section (m), and $\varepsilon_{therm}$ is thermal elongation defined by the Eurocode [7].

$$\varepsilon_{tot} = \varepsilon_0 + \chi\, y \tag{5}$$

$$\varepsilon_{mech} = \varepsilon_{tot} - \varepsilon_{therm} \tag{6}$$

Then the stress at any point ($\sigma$) is calculated using the mechanical strain and stress-strain diagrams of concrete at elevated temperature [7].

The axial force and the moment are calculated for every point in time for any combination average strain value and the curvature according to Eq. (7) and Eq. (8) respectively [6], where $\sigma$ is the stress and $A$ is the area of each slice. For each value of the average strain, the code finds the value of the curvature so that the moment around the center of the cross-section is equal to zero.

$$N = \sum \sigma\ A \tag{7}$$

$$M = \sum \sigma\ y\, A \tag{8}$$

The maximum value of the axial force is then chosen as the capacity for that point in time ($N^t$) and the reduction factor ($\eta_{fi}^t$) can be identified at every time step by dividing it with the ambient capacity ($N_{amb}$), as given in Eq. (9).

$$\eta_{fi}^t = \frac{N^t}{N_{amb}} \tag{9}$$

Using the design method presented in EN 1992-1-2 [7], it can be assumed that the effects of actions on the structural member in case of fire can be obtained by multiplying the effects of actions for normal temperature with the factor ranging from 74% to 33% (i.e. the reduction factor ranges between these two values for all combinations of live/dead load ratio). Under the assumption that the member was designed with 100% utilization, it can be concluded that if the reduction factor from Eq. (9) is higher than 74% the wall will not fail and that if it falls below 33%, then collapse of the structure is guaranteed.

## WORKED EXAMPLE

An example of the described methodology is here shown. A concrete semi-confined space that is assumed to share its left wall with a house is here analysed. This wall must be designed so that the performance criterion of load bearing capacity remains above 74%. Intitally, the analysis is performed with a wall thickness of 10 cm. After analysing the combustion of different fuel packs typical of the WUI (e.g. [9], [13]), a worst case scenario was chosen, which consists of the combustion of two cars.

The scenario is simulated in FDS, as shown in Fig. 2. The dimensions of the semi-confined space are 5.8 x 5.8 x 2.5 $m^3$, with a front opening of 4.6 x 2 $m^2$. The mesh that includes the semi-confined space is divided into 10 cm cubes, while the areas outside of this spaces are simulated with a cell size of 20 cm. The fire inputs are given according to the Belgian standard NBN S 21-208-2 [14]: the area of the fire is 25 $m^2$ and its assigned Heat Release Rate (HRR) curve is given in Fig. 3, which reaches a peak of 8 MW. The fire duration is 75 minutes, while the simulation was run for approximately 8 more minutes (i.e. up to 5000 s).

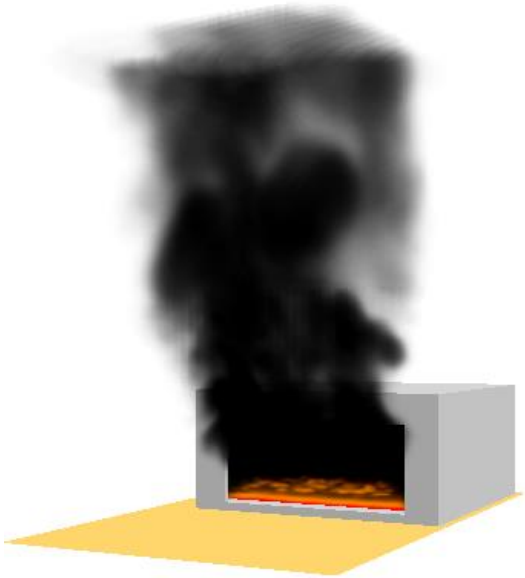

**Fig. 2.** Simulated semi-confined space at 20 minutes

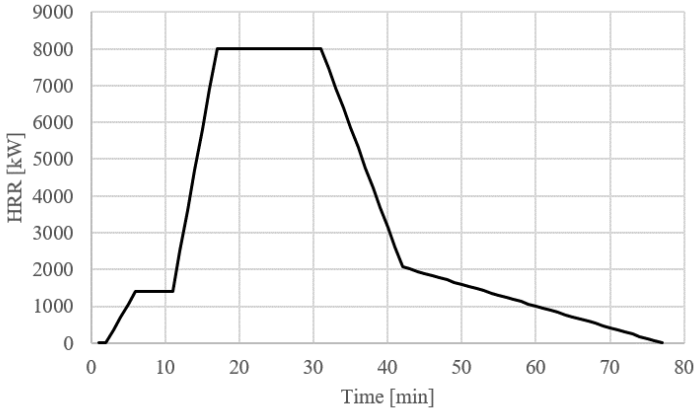


**Fig. 3.** HRR curves for the combustion of two cars [14]

The adiabatic surface temperature is measured on this wall by devices located at different heights (about every 0.5 m) and locations along the wall, at a distance of respectively 0.1 m, 0.6 m, 1.1 m and 1.6 m from the back wall. A boundary file was also inserted to measure the adiabatic surface temperature on all surfaces, which indicates that the highest adiabatic surface temperatures are those on the back wall as well as on the parts of the side walls close to the back corners, as shown in Fig. 4.

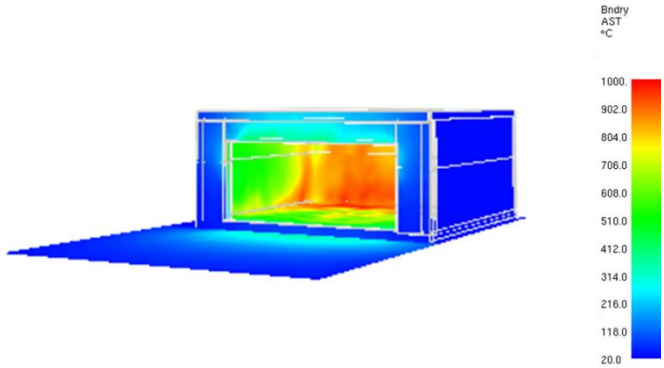


**Fig. 4**. Adiabatic surface temperature at 30 minutes

The devices located along the left wall at a distance of 0.6 m from the back wall are those which recorded the highest temperatures. The temperatures at this location are given in Fig. 5 for the different heights along the wall, and the devices which indicated the highest temperatures overall are those located at a height of 0.1 m and 0.5 m.

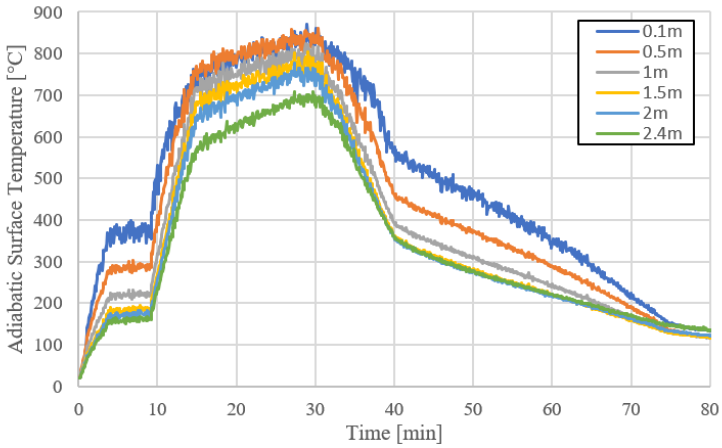


**Fig. 5**. Adiabatic surface temperature for the duration of the fire measured by the devices placed at different heights

The load bearing capacity will therefore be analysed for the cross section that shows the highest adiabatic surface temperature (i.e. at 0.1 m). The calculated temperature profile through the thicknesses at different times is given in Fig. 6a. The highest temperature reached by the surface of the cross-section reaches approximately 720°C at 30 minutes, and it drops significantly until a depth of 6 cm, after which it remains constant. The longer the duration of the fire, the more the temperature has time to rise also deeper within the wall. This can be seen from the curves at 45, 60 and 75 minutes. At 75 minutes (at the end of the combustion of the two cars) it can also be seen that the temperature at the surface is lower than the tempertaure at a depth of 2 cm. This shows the importance of analysing the whole duration of the fire, and even the cool down phase of the wall once the fire is extinguished. It can also be seen that the temperature at the back is rising from the time of 30 minutes up to the end of the simulation, going from the ambient temperature 20°C to reaching its peak of 100°C at 75 minutes.

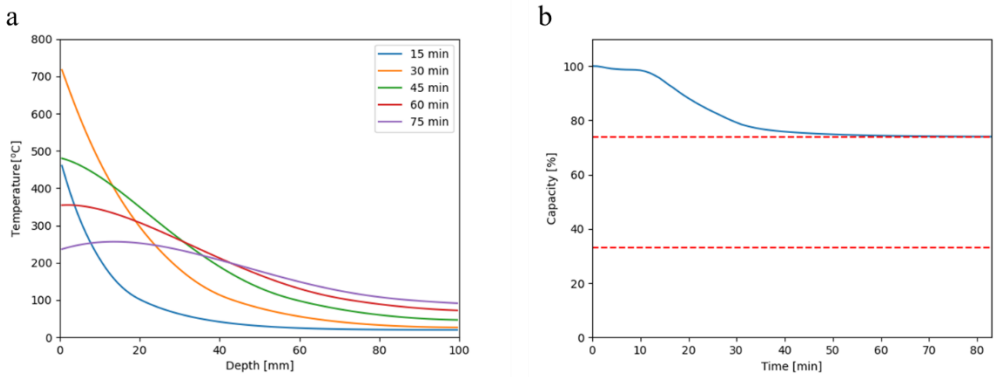


**Fig. 6**. (a) Temperature profile through the analysed cross-section of 10 cm; (b) load bearing capacity of the analysed cross-section

The load bearing capacity of the analysed cross section for the whole duration of the FDS simulation is given in Fig. 6b. For the analysed thickness, the load bearing capacity drops below the performance criterion of 74% after about 60 minutes fron the start of the fire.

Given that the performance criterion is not met for the design of a wall thickness of 10 cm, another anaylsis is performed for a wall thickness of 15 cm. The results are given in Fig.7.

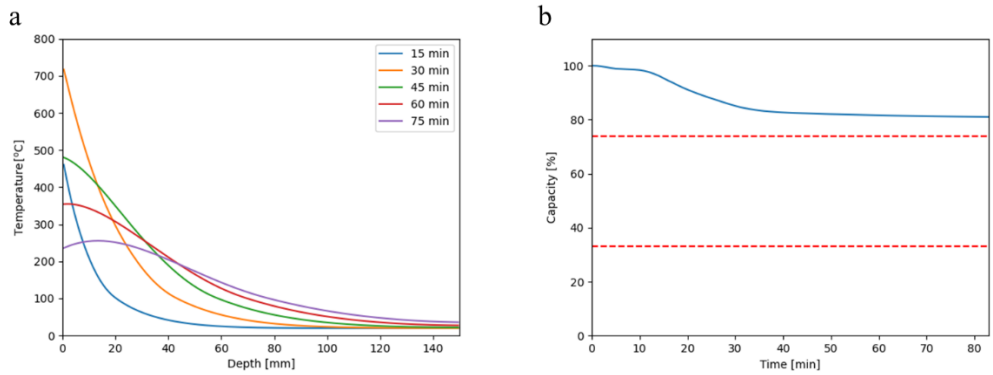


**Fig. 7**. a) Temperature profile through the analysed cross-section of 15 cm; (b) load bearing capacity of the analysed cross-section

As shown in Fig. 7a, for a wall thickness of 15 cm, the temperatures at the back of the wall remain below 100°C for all given times (the peak temperature at the back is 40°C at 75 minutes). Fig. 7b shows that the load bearing capacity of the analysed cross section does not drop below the performance criterion of 74% for a wall thickness of 15 cm.

A wall thickness of at least 15 cm, which is the minimum recommended thickness for concrete walls in many countries, can therefore be deemed safe for a scenario that considers the combustion of two cars inside the analysed semi-confined space. It can also be assumed that the combustion of fuels and fuel packs with a shorter burning time and a lower HRR curve will not cause structural damage to the a wall with the same characteristics as those anaylsed.

## CONCLUSIONS

A PBD methodology for the analysis of the load bearing capacity of concrete walls of semi-confined spaces at the WUI microscale exposed to the combustion of fuels is presented. The methodology comprises three steps. Firstly, the combustion of the fuels is simulated in FDS, which outputs the

adiabatic surface temperature of the analysed wall; this is a parameter that can be used as an intermediary between the fire and the structural models [11]. The temperature profile through the cross section of the analysed wall is then calculated with a finite difference method, and finally this output is used for the analysis of the load bearing capacity according to Eurocode 2. A worked example shows the steps of this methodology, which shows that concrete walls with a thicnkess of at least 15 cm can maintain their load bearing capacity even when the combustion of fuels contained in these spaces reaches high HRR peaks such as 8 MW.

Further work for the identification of the vulnerability of semi-confined spaces in WUI microscale fire scenarios should include the analysis of other construction materials, as well as the insertion of weak building elements such as glazing systems, which could cause fire spread to the enterior of the main building, in case the semi-confined space is adjacent to it.

## ACKNOWLEDGEMENTS

This work has been partially performed under the European research project WUIVIEW, and projects CTQ2017-85990-R funded by MCIN/ AEI /10.13039/501100011033/ FEDER “Una manera de hacer Europa” and PID2020-114766RB-100 funded by MCIN/ AEI /10.13039/501100011033.

## REFERENCES

[1] P. Vacca, D. Caballero, E. Pastor, E. Planas, WUI fire risk mitigation in Europe: A performance-based design approach at home-owner level, J. Saf. Sci. Resil. 1 (2020) 97–105. https://doi.org/10.1016/j.jnlssr.2020.08.001.

[2] D.M. Molina-Terrén, G. Xanthopoulos, M. Diakakis, L. Ribeiro, D. Caballero, G.M. Delogu, D.X. Viegas, C.A. Silva, A. Cardil, Analysis of forest fire fatalities in Southern Europe: Spain, Portugal, Greece and Sardinia (Italy), Int. J. Wildl. Fire. 28 (2019) 85–98. https://doi.org/10.1071/WF18004.

[3] E. Pastor, Direct Flame Contact, Encycl. Wildfires Wildland-Urban Interface Fires. (2019) 1–7. https://doi.org/10.1007/978-3-319-51727-8_64-1.

[4] D. Caballero, J. Sjöström, Deliverable D5.1 - Inventory of pattern scenarios, 2019. https://www.wuiview.org/download/WUIVIEW_D5.1_F.pdf.

[5] NIST, Fire Dynamics Simulator, (2020). https://www.nist.gov/services-resources/software/fds-and-smokeview.

[6] European Committee for Standardization, EN 1992-1-1: Eurocode 2: Design of concrete structures - Part 1-1: General rules and rules for buildings, 2004.

[7] EN 1992-1-2: Eurocode 2: Design of concrete structures - Part 1-2: General rules - Structural fire design, 2004.

[8] National Fire Research Laboratory, Fire Calorimetry Database (FCD), (2020). https://doi.org/https://doi.org/10.18434/mds2-2314.

[9] P. Vacca, E. Planas, C. Mata, J.A. Muñoz, F. Heymes, E. Pastor, Experimental analysis of real-scale burning tests of artificial fuel packs at the Wildland-Urban Interface, Saf. Sci. 146 (2022). https://doi.org/10.1016/j.ssci.2021.105568.

[10] U. Wickstrom, D. Duthinh, K. Mcgrattan, Adiabatic Surface Temperature for Calculating Heat Transfer To Fire Introduction, in: Proc. Elev. Int. Interflam Conf. Intersci. Commun., London, 2007. https://www.nist.gov/publications/adiabatic-surface-temperature-calculating-heat-transfer-fire-exposed-structures.

[11] U. Wickström, A. Robbins, G. Baker, The use of adiabatic surface temperature to design

structures for fire exposure, J. Struct. Fire Eng. 2 (2011) 21–28. https://doi.org/10.1260/2040-2317.2.1.21.

[12] K. McGrattan, S. Hostikka, R. McDermott, J. Floyd, C. Weinschenk, K. Overhold, Sixth Edition Fire Dynamics Simulator User's Guide (FDS), NIST Spec. Publ. 1019. Sixth Edit (2020).

[13] V. Babrauskas, Heat Release Rates, in: M.J. Hurley, D.T. Gottuk, J.J.R. Hall, K. Harada, E. Kuligowski, M. Puchovsky, J.L. Torero, J.J.M. Watts, C. Wieczorek (Eds.), SFPE Handb. Fire Prot. Eng., Fifth edit, Springer US, 2016: pp. 799–904.

[14] Belgische normcommissie, NBN S 21-208-2: Fire protection in buildings - Design of smoke and heat exhaust ventilation systems (SHEV) for enclosed car park, 2014.

# Fire Performance of Residential Shipping Containers Designed with a Shaft Wall System

**Àgueda A.[1], Vacca P.[1], Marimon F.[2], Pastor E.[1], Planas E. [1,*]**

*[1] Universitat Politècnica de Catalunya - BarcelonaTech, Centre d'Estudis del Risc Tenològic (CERTEC), Barcelona, Catalunya, Spain.*
*[2] Universitat Politècnica de Catalunya - BarcelonaTech, Departament de Resistència de Materials i Estructures a l'Enginyeria, Barcelona, Catalunya, Spain.*
**Corresponding author's email: eulalia.planas@upc.edu*

## ABSTRACT

A seven story building made of shipping containers is planned to be built in Barcelona, Spain. This study mainly aimed to evaluate the fire performance of one of these residential shipping containers whose walls and ceiling will have a shaft wall system installed.

The default assembly consisted of three fire resistant gypsum boards for vertical panels and a mineral wool layer within the framing system. This work aimed to assess if system variants (e.g. less gypsum boards, no mineral wool layer) could still be adequate considering fire resistance purposes.

To determine if steel temperatures would attain a predetermined temperature of 300-350ºC (a temperature value above which mechanical properties of steel start to change significantly) the temperature evolution within the shaft wall system and the corrugated steel profile of the container was analysed under different fire conditions.

Diamonds simulator (v. 2020; Buildsoft) was used to perform the heat transfer analysis from the inside surface of the container (where the fire source was present) and within the shaft wall and the corrugated profile. To do so gas temperatures near the walls and the ceiling were required, so these temperatures were obtained from two sources: (1) The standard fire curve ISO834; (2) CFD simulations performed using the Fire Dynamics Simulator (FDS). Post-flashover fire scenarios were modelled in FDS taking into account the type of fuel present in residential buildings according to international standards.

The results obtained indicate that temperatures lower than 350ºC were attained on the ribbed steel sheet under all the tested heat exposure conditions. When changing the assembly by removing the mineral wool layer, fire resistance was found to still be adequate. Therefore, under the tested conditions, the structural response of the containers would comply with fire protection standards, even in the case where insulation was reduced.

**KEYWORDS:** Diamonds software, Fire Dynamics Simulator (FDS), Sea container, Story building

## INTRODUCTION

Modular buildings are attracting significant attention from the construction industry. They are becoming alternative solutions basically because construction methods are faster than conventional ones [1,2]. The structural performance of modular integrated constructions has been extensively explored [3,4,5]. However, although steel columns and steel load-bearing walls cladded with different fire-resistant panels (such as gypsum boards with or without mineral wool) have been studied experimentally and numerically over the last years (e.g. [6,7]), few studies have focused specifically on the fire performance of these elements in modular buildings [8,9]. More specifically, for housing or service buildings made of shipping containers (e.g. [10,11]) there are very limited available studies that evaluate their fire performance. Therefore, this paper provides insight into the fire performance of this type of buildings by reporting the thermal response of a shaft wall system and the corrugated steel when a complete shipping container is exposed to a fire. The originality of this work lies in the

fact the fire curve has been obtained from numerical simulations, instead of using exclusively the standard fire curve ISO 834.

Shipping containers are originally designed for the transport of indeterminate products. Once the products are loaded inside it, the container is securely locked and, during transport, it behaves as a compact box with no openings. The reuse of sea containers for residential purposes, which is becoming a popular practice, implies lower loads of use than the original ones, but it obliges to consider the negative effect of the opening of the container and the removal of the access door. This is associated with a loss of monolithism and rigidity. Safety in case of fire must be guaranteed for these structures.

Wall assembly configurations for a story building planned to be built in Barcelona (Spain) made of shipping containers were evaluated in order to find the configuration that would meet established fire safety criteria. Therefore, the objective of this study was to conveniently evaluate the effect of the temperature increase of corrugated steel profiles in case of fire.

On the contrary, we did not aim at performing a specific structural analysis at ambient temperature, nor at studying the evolution of the structure of the containers up to the collapse in case of an accidental fire situation. Steel temperature evolution was obtained by means of a non-linear thermal simulation of the problem in a transient regime.

Single and double containers are both planned to be used in the building, nevertheless this study focuses on the double container only because it has two different types of walls, as shown in Fig. 1. TYPE 1 (single) walls would be affected by the fire on one side only, while TYPE 2 (double) walls could be affected on both sides.

The default shaft wall system defined for walls and ceiling of the container consists of three fire resistance gypsum fiberboards of 15 mm thickness and a mineral wool layer of 50 mm thickness within the galvanised cold-formed steel profile system. We aimed to assess if system variants (e.g. less gypsum boards, no mineral wool layer) could still be adequate considering fire resistance purposes.

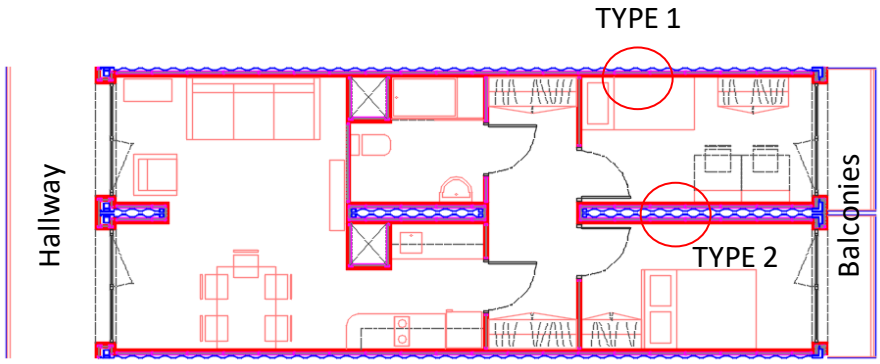


**Fig. 1.** Generic double module (hallway on the left side; balconies on the right side). Types of divisions: TYPE 1 (simpe wall); TYPE 2 (double wall).

The Eurocode 3 standard, in its part 1.3 EN 1993-1-2:2005 [12], evaluates the loss of the mechanical properties of steel as a function of temperature (Table 3.1 in [12]). According to these data, it seems reasonable to assume that up to a temperature of 300°C there will be no significant effect on the mechanical properties of steel. Specifically, there is an almost null decrease of the effective yield strength (i.e. $k_{y,\theta} = 1.0$) and, on the other hand, the longitudinal elastic modulus is only reduced by a factor $k_{E,\theta} = 0.8$.

Another relevant reference is found in EN 1993-1-2:2005 Eurocode [12] for thin profiles, also called Class 4 sections, which are the main structural elements of the container since they have a thickness between 1.5 and 4 mm (e.g. rectangular tubes, shaped profiles and corrugated profile). In section 4.2.3.6, it is stated that for members with Class 4 cross-sections other than tension members, it may be assumed that the load-bearing function of a steel member shall be maintained if at time *t* the steel temperature at all cross-sections is not more than a critical temperature of 350ºC [12]. So, if steel temperature is below 300-350°C during the evolution of the fire, the structural evaluation performed at ambient temperature will continue to be valid in the accidental fire situation.

To analyse the transient behaviour of steel temperature under a fire scenario taking place inside a modified sea container, two approaches were followed to measure gas temperature evolution near the wall. We used conventional ISO834 curve and, alternatively, we also estimated this temperature using a Computational Fluid Dynamics (CFD) simulator, i.e. Fire Dynamics Simulator (FDS) [13]. In the first section of this work, FDS simulations that were performed are described. Then we present and discuss steel temperature results obtained from heat transfer simulations performed with Diamonds software [14] using different insulation configurations.

## FIRE SIMULATION

Several fire scenarios were simulated using FDS. The software Pyrosim [15] was used for the definition of the geometrical model because its graphical interface facilitates the creation of geometries and allows exporting the generated work to FDS code. Smokeview [13] was used to visualize the obtained results. The main output variable of interest for these simulations was the gas temperature near the walls of the container. More specifically, gas temperature at the ceiling, where the highest temperatures were expected.

### Fire Curve Definition

To define the fire curve, we assumed a worst case scenario where a post-flashover would take place. Smoke layer (upper layer; UL) temperatures ($T_{UL}$) would be higher than 500°C, all fuel available would eventually burn, and fire extinguishing mechanisms would not be activated.

To define the fire curve the next methodology was followed, based on the New Zealand performance standard code [16]:

1. A simulation was run with a pre-flashover fire curve, whose characteristics were extracted from the European standard EN 1991-1-2002 [17]. It was assumed that the fire growth was at a moderate rate set by the $t^2$ model until the flashover was reached, or until the Heat Release Rate (HRR) reached the maximum value, or until it had limited ventilation.

2. According to the results of the first simulation, the 5 cases reported in section 2.3.3. of the New Zealand performance standard code [16] were checked to determine which one would apply and the final simulation was performed by adjusting the HRR curve according to the corresponding action specified in that table. In our scenarios, Case 3 was applied in all simulations (i.e. $T_{UL}$=500ºC before HRR reached the peak and fires were not ventilation limited; so at $T_{UL}$=500ºC the HRR was increased up to the peak over a period of 15 s).

To specifically set the fire curve (Fig. 2a), an average fire density value ($q$) of 780 MJ/m$^2$ was used, as recommended for dwellings by the EN 1991-1-2002 standard [17]. The HRR peak that could be achieved was extracted from the HRR per unit area (HRRPUA) value reported in the same standard, which is 250 kW/m$^2$. The value recommended in the New Zealand standard was considered too conservative (500 - 1000 kW/m$^2$). The fire growth rate was considered to be $\alpha$ = 0.011 kW/s$^2$, as recommended by the EN 1991-1-2002 standard. In general, values proposed by the New Zealand standard are equivalent to those proposed by the EN 1991-1-2002 standard for library buildings; therefore, they are much more conservative.

The decay phase of the fire was also defined following the indications of the EN 1991-1-2002 standard [17], according to which a linear decay could be assumed, starting when 70% of the fire load was consumed and ending when all the fire load was consumed. The surface area of the dwelling occupied by the fuel was considered equal to 50 $m^2$ for the double module.

**Scenarios**

The geometry of the container was defined so that household furniture within the container (e.g. bed, table, sofa, kitchen furniture) was not included as rectangular obstructions in the model. However, their presence was taken into account through the fire density value associated to the type of building.

The domain set for the simulations included the container where the fire was generated, the balconies and a hallway where there were glazing systems, and an identical container on top of the one under study (Fig. 2b). Also, in order to have a complete view of the movement of the smoke and the flames when they emerged to the exterior, the domain was set beyond the balcony and the hallway (Fig. 2b).

The characteristic length of the fire ($D^*$) (Eq. 1) is a useful length scale when the flow is dominated by the heat release rate of the fire. It characterizes the source term driving the fluid flow, and it is not necessarily any physical length. Therefore, we used this length and the values normally assigned for fine, medium and coarse meshes (Table 1) to stablish the spatial resolution in our domain.

$$D^* = \left(\frac{\dot{Q}}{\rho_\infty c_p T_\infty \sqrt{g}}\right)^{2/5} \tag{1}$$

**Table 1. Values normally assigned to establish the number of cells available in the characteristic length of the fire ($D^*$) and type of mesh resolution. $dx$ refers to cell size.**

| $D^*/dx$ | Type of mesh resolution |
|---|---|
| 16 | Fine |
| 10 | Medium |
| 4 | Coarse |

In this work, since $\dot{Q}_{max} \sim 12000\ kW$, a characteristic length of 2.58 m was calculated and a cell size of 10 cm would be enough to obtain a fine resolution for the mesh. However, the size of the cells was 0.05 m around the central TYPE 2 wall to get results with a better resolution, and 0.10 m in the other parts of the container. Several rectangular meshes had to be prescribed to handle the whole domain (Fig. 3). Differences in meshes distribution between scenarios were due to computational requirements.

The walls of the container were defined in FDS considering the following simplifications: (1) The galvanised cold-formed steel profile of the shaft wall system were not simulated; (2) The steel sheet was considered plain, not ribbed. Consequently, the air gap between the ribbed steel sheet of the container and the mineral wool layer was not simulated either. Regarding the insulation material, FDS simulations where performed considering only one gypsum board for vertical cladding and the mineral wool layer.

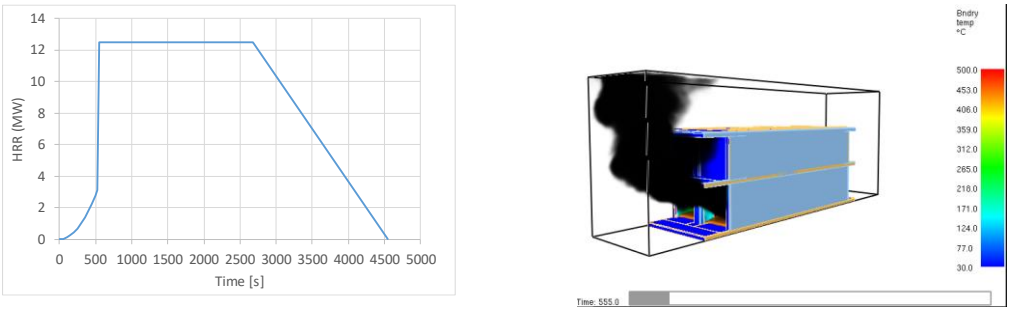


(a) (b)

**Fig. 2.** a) HRR curve; b) View of the simulation domain. Boundary temperatures, and smoke and flames view a few seconds after the complete breakage of the left window in simulation #1.

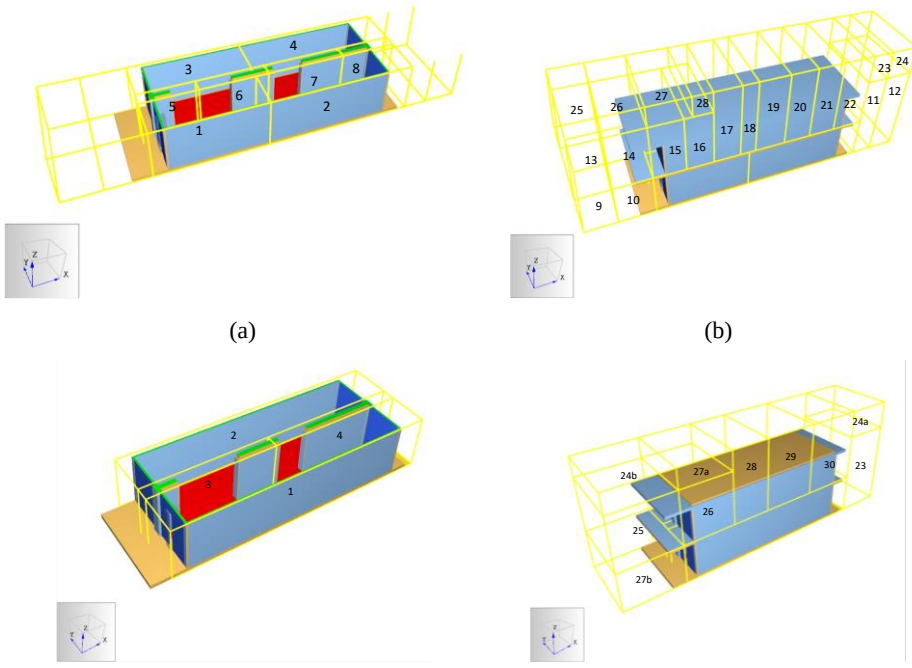

(a) (b)

(c) (d)

**Fig. 3.** Geometry considered: (a) Inside the container for simulation #1 (meshes 1-4 had a cell size of 0.10 m and meshes 5-8 of 0.05 m); (b) Outside the container for simulation #1 (meshes with a cell size of 0.10 m); (c) Inside the container for simulations #2-3 (meshes 1-2 had a cell size of 0.10 m and 3-4 of 0.05 m); (d) Outside the container for simulations #2-3 (meshes with a cell size of 0.10 m). Red area represents fire surface.

Three simulations were performed (Table 2). Differences between these three simulations were due to the initial openings configuration and the breakage control of the glazing systems.

A large initial opening was set, so that numerical instabilities associated with a completely airtight compartment were avoided and the fire was able to follow the desired HRR curve. Finally, our openings configuration was based on some preliminary results obtained using different opening areas. Two situations were simulated:

- The inhabitants of the module leave the living room door (hallway) partially open (0.42 m x 2.2 m). This was considered in simulations #1 and #3. The glass door of the bedroom (balcony) is left closed.
- The inhabitants of the module leave both doors of the bedroom (balcony) and the living room (hallway) partially open (0.21 m x 2.2 m). This was considered in simulation #2.

A function to control glazing systems breakage was also defined. A limiting value for glass breakage of 500ºC [16] was set. In simulations #2-3, the glass breakage control was set only on the hallway side, so that it was assumed that the glass of the balconies would not break during the evolution of the fire. This was done because it represents a more conservative case since the fire would still be controlled by the fuel but would have a lower air intake and therefore temperatures inside the container would be higher. However, for simulation #1 the breakage control was set at both sides of the container (see Table 2). Gas temperatures at all solid obstructions were recorded.

**Table 2. Scenarios simulated with FDS for the double container**

| Simulation ID | #1 | #2 | #3 |
|---|---|---|---|
| Initial openings | 1, hallway | 2, hallway and balconies | 1, hallway |
| Dimensions of the initial openings | 0.42 m x 2.2 m | 0.21 m x 2.2 m each one | 0.42 m x 2.2 m |
| Breakage control of the glazing systems | Both sides | Hallway side only | Hallway side only |

The ambient conditions used were the default FDS conditions, where the initial temperature is 20˚C and there is no wind.

## FDS Results

The initial opening defined on the container and the time of glass breakage (Table 3) determined the behaviour of the fire. In simulation #1, on the left (hallway) half of the container (i.e. where the initial opening was located), peak gas temperatures at the ceiling were observed at the beginning of the fire, reaching values of 1000ºC. Just after glass breakage on the balconies side, at around 880-890 s, the temperature decreased sharply due to the increase in ventilation until stabilization (Fig. 4a). This behaviour was not observed on the right (balconies) half of the container (i.e. where there was no initial opening); here a smooth increase for the ceiling gas temperature was observed for the development phase of the fire (Fig. 4b).

**Table 3. Breakage time (min) for windows on the hallway and the balconies. Two times are included to indicate breakage time of the two windows present on each side**

| Simulation | Hallway | Balconies |
|---|---|---|
| #1 | 7.6 and 9.0 | 14.7 and 15.0 |
| #2 | 8.1 and 8.2 | - |
| #3 | 7.1 and 9.0 | - |

In simulations #2 and #3, since the glass on the right side of the double module was not broken, peak temperatures were maintained for approximately the entire duration of the growth phase of the fire and exceeded slightly 1000°C (Fig. 4c and d). These curves indicated that this situation would be much more unfavourable than the previously simulated scenario (#1).

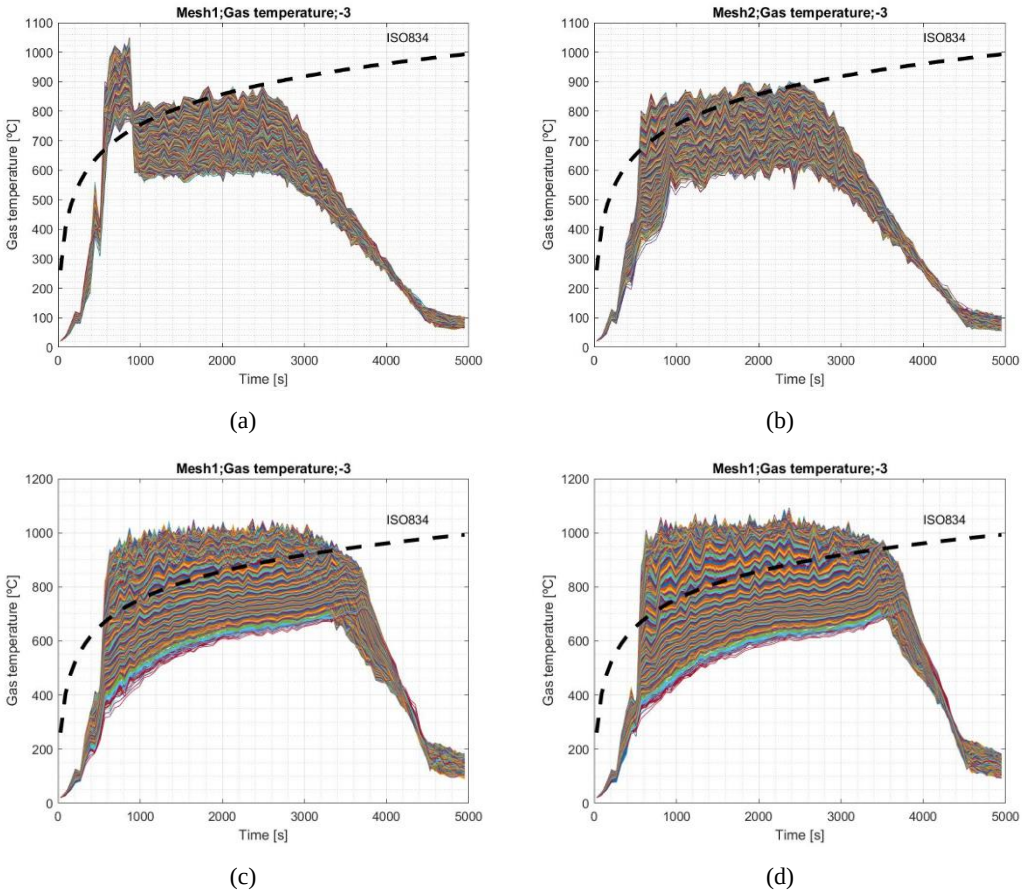


**Fig. 4.** Gas temperature evolution near the ceiling (-3 indicates that cells facing in the negative z direction of the boundary, the ceiling, are considered). Temperature series (T(t)) shown are associated to a particular mesh of the domain, i.e. (a) mesh 1 in simulation #1; (b) mesh 2 in simulation #1; (c) mesh 1 in simulation #2; (d) mesh 1 in simulation #3. ISO 834 curve is also included for comparison purposes. Each T(t) series corresponds a cell of the boundary.

## HEAT TRANSFER SIMULATION

### Scenarios

In order to carry out the thermal simulations, the structural calculation program Diamonds (version 2020; [14]) was used. Several insulation configurations were considered, i.e. only 15+15 mm gypsum boards, 15+15 mm gypsum boards and 50 mm mineral wool, in combination with exposure to the standardized fire curve ISO834 and the most unfavourable fire curve obtained from the FDS study reported previously (Fig. 5).

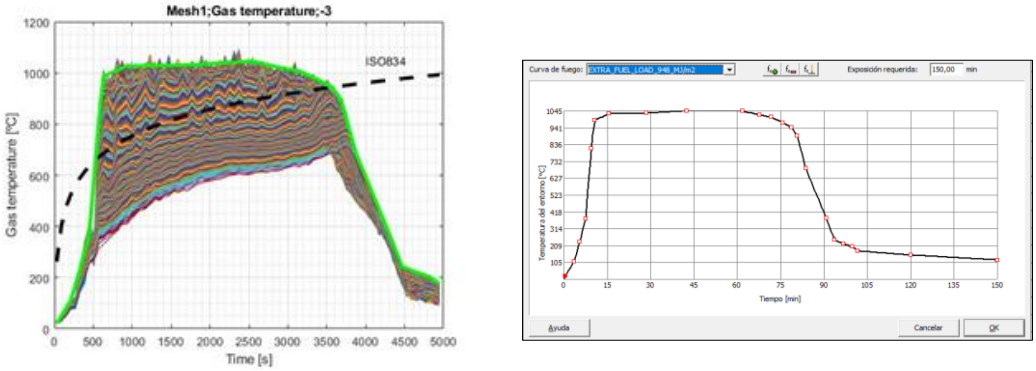


**Fig. 5.** Most unfavourable fire curve from FDS simulations (scenario #3) transferred to Diamonds software using discrete gas temperature data.

The geometry of the shaft wall system was modelled with Diamonds (Fig. 6) considering the single wall configuration and also the double wall one, i.e. TYPE 1 and TYPE 2 divisions according to Fig. 1. By imposing adiabatic boundary conditions, it was possible to analyse only a complete wave of the corrugated profile.

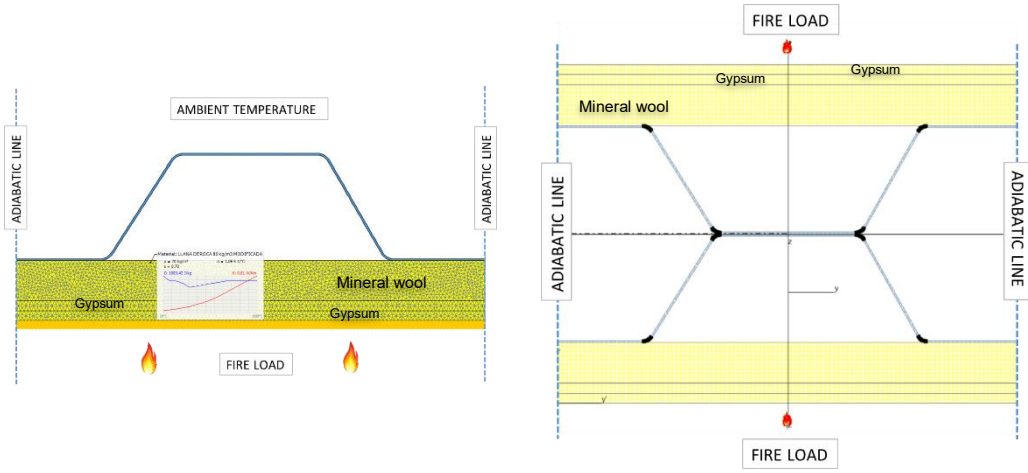


(a) (b)

**Fig. 6.** Geometry and boundary conditions (adiabatic, ambient, fire) considered for: (a) TYPE 1 wall, with mesh details; (b) TYPE 2 walls. Wall defined here consists of two fire resistance gypsum fiberboards of 15 mm thickness and a mineral wool layer of 50 mm thickness within the galvanised cold-formed steel profile system.

## Mineral Wool Properties

The thermal properties for mineral wool insulation were obtained from the literature. Fig. 7 shows the variation of thermal conductivity [W/mK] and specific heat [J/kgK] as a function of temperature. These properties correspond to those of a standard product, i.e. with low density (80 kg/m$^3$) and without special requirements.

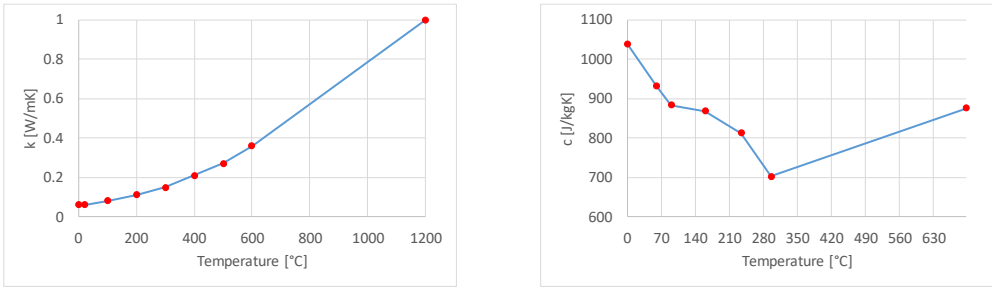


(a) (b)

**Fig. 7.** Thermal conductivity [$W \cdot m^{-1} \cdot K^{-1}$] (a) and specific heat [$J \cdot kg^{-1} \cdot K^{-1}$] (b) variability as a function of temperature for mineral wool with a density of 80 kg/m$^3$.

## Validation of the Properties of 15+15 mm Gypsum Boards

Before analysing temperature evolution on steel under different fire scenarios and configurations, we performed an exercise to validate the physical properties of the gypsum boards, which depend on temperature (Fig. 8). This was implemented by using experimental data from the manufacturer, who supplied the readings of the thermocouples installed on the cold side of its 15+15 mm system under standard curve ISO834 exposure according EN 1364-1:2015 [18]. A clear correlation was observed between the results obtained in the laboratory and those obtained through a numerical simulation using Diamonds (Fig. 9), confirming the effect of temperature on thermal conductivity and specific heat of gypsum boards. We also verified that the results obtained were similar to those available in the literature [19]. An emissivity value of $\varepsilon = 0.8$ was considered, as reported in [19]. Finally, the density of the gypsum material was considered to be 800 kg/m$^3$ according to a technical document from the manufacturer of this gypsum fibreboards.

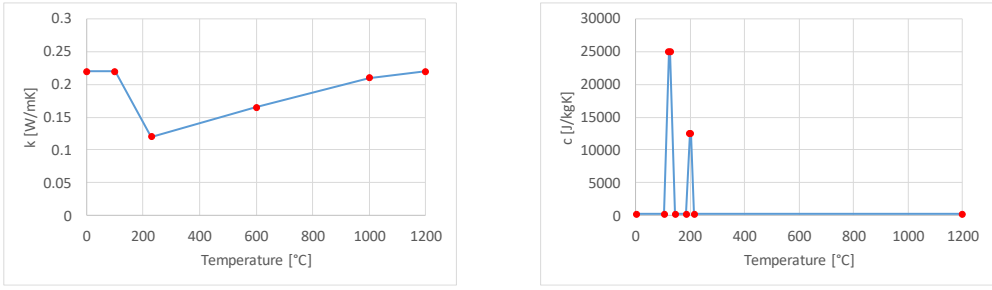


(a) (b)

**Fig. 8.** Thermal conductivity [$W \cdot m^{-1} \cdot K^{-1}$] (a) and specific heat [$J \cdot kg^{-1} \cdot K^{-1}$] (b) variability as a function of temperature for gypsum boards.

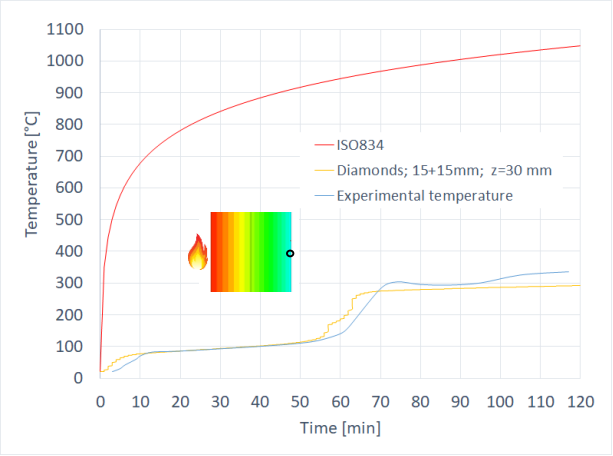


**Fig. 9.** Temperature evolution for the validation of properties of 15+15 mm gypsum boards. ISO834 fire curve (red); experimental data from an ISO834 curve according EN 1364-1:2015 [18] for a vertical 15+15 mm gypsum boards system (blue); numerical simulation results obtained from Diamonds for an ISO834 test on a 15+15 mm gypsum boards system at a distance of 30 mm from the fire source (yellow).

## RESULTS

Maximum temperature values obtained on steel for the different case studies are shown in Table 4. Peak values were observed for TYPE 2 walls, as expected since the heat source would be placed at both sides of the steel sheet.

**Table 4. Maximum temperature on steel for different case studies**

| Case | Geometry | Fire curve | Steel maximum temperature (time[a]) |
|---|---|---|---|
| CASE 1 | Simple wall, Gypsum boards 15+15 mm | ISO834 | 263 ºC (90 min.) |
| CASE 2 | Simple wall, Gypsum boards 15+15 mm, and 50 mm mineral wool | ISO834 | 128 ºC (90 min.) |
| CASE 3 | Simple wall, Gypsum boards 15+15 mm | FDS | 196 ºC |
| CASE 4 | Simple wall, Gypsum boards 15+15 mm, and 50 mm mineral wool | FDS | 83 ºC |
| CASE 5 | Double wall, Gypsum boards 15+15 mm | ISO834 | 301 ºC (90 min.) |
| CASE 6 | Double wall, Gypsum boards 15+15 mm, and 50 mm mineral wool | ISO834 | 152 ºC (90 min.) |
| CASE 7 | Double wall, Gypsum boards 15+15 mm | FDS | 220 ºC |
| CASE 8 | Double wall, Gypsum boards 15+15 mm, and 50 mm mineral wool | FDS | 83 ºC |
| CASE 9[b] | Double wall, Gypsum boards 15+15 mm, Fire load = 948 MJ/m$^2$ | FDS | 318 ºC |

[a]Time included only if peak temperature is observed at the end of the simulation.
[b]Extreme hypotheses.

The most unfavourable cases are CASE 1 (Fig. 10a) and especially CASES 5 (Fig. 10b) and 7 (Fig. 10c). These cases correspond to a double ribbed sheet metal wall with only two 15+15 mm gypsum boards, without considering the existence of the mineral wool insulation, and exposed to the fire on both sides. This very unfavourable situation considers the real possibility that mineral wool does not exist locally, for example because this space is occupied by service installations. It is also the situation of some structural profiles of the container that for some assembly reason are only covered exclusively with two 15+15 mm gypsum boards.

CASE 5 corresponds to the situation where there is exposure to the ISO834 standardized curve for 90 minutes. A maximum temperature of 301°C is reached. So, we can assure the fulfilment of an R90 requirement. The R90 resistance value is usually required for a residential building with a height less than 28 m, according the Spanish Technical Code [20].

CASE 7 corresponds to exposure to the fire curve obtained from the FDS study. Here the maximum temperature does not exceed 220 °C, which corresponds to 70 minutes of fire development. This is the maximum temperature reached during the entire duration of this fire until its decay.

With mineral wool actually installed in the system, lower temperatures than those mentioned above were obtained under exposure to ISO834 and also to FDS curves for the other considered cases.

CASE 9 deserves special consideration because it represents an extreme fire scenario where the fire load was increased to a value of 948 MJ/m$^2$. This higher value refers to the 80th percentile according to Eurocode 1 [17]. If this value is considered, the total duration of the fire increases, as shown in Fig. 10d. In this case an estimation has been made on how maximum temperatures at the wall would change if the fire load were 948 MJ/m$^2$ and how this increase could affect transitory steel temperatures. Through CASE 9, it has been estimated that temperatures of approximately 318°C at 83 min could be reached. This means that even in an extreme scenario, both in terms of geometry and heat transfer, the mechanical properties of steel are not affected during this extreme fire. In other words, the structure would resist the full-time duration of the fire until its decay.

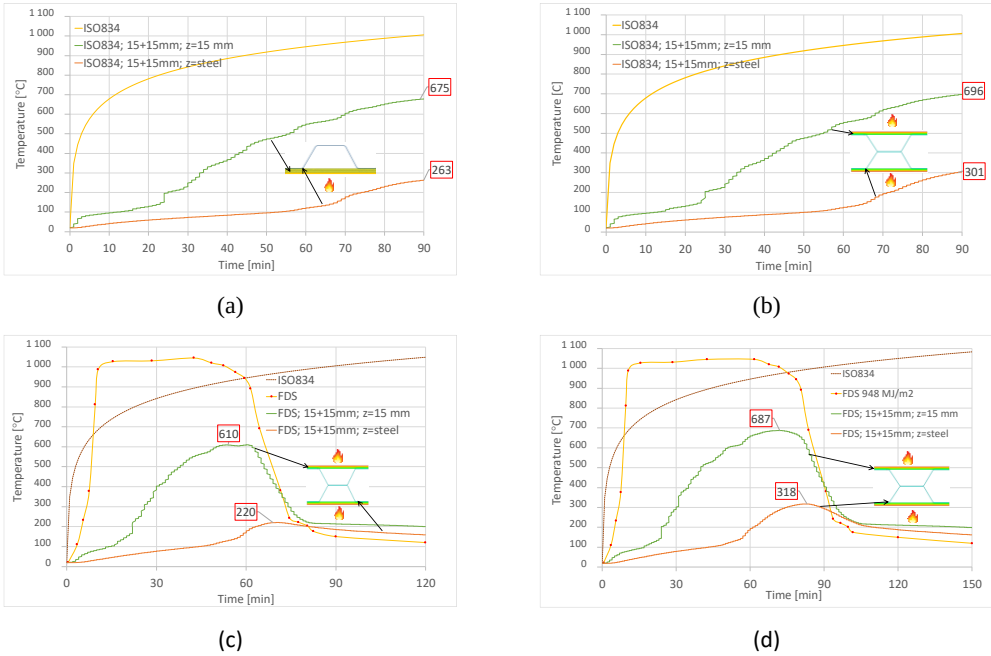


**Fig. 10.** Temperature evolution for the most unfavourable cases according to maximum temperatures in steel reported in Table 4: (a) CASE 1; (b) CASE 5; (c) CASE 7; (d) CASE 9 (fire load 948 MJ/m$^2$). z variable refers

to the depth of interest; i.e. z = 15 mm means temperature at a depth equal to 15 mm from the surface of the wall, z = steel means temperature at a depth equal to first steel location.

## CONCLUSIONS

Two approaches were followed to set gas temperature evolution near the wall in case of fire inside the container; i.e. conventional ISO834 curve and gas temperature curve obtained from FDS simulations. According to the thermomechanical study developed for the corrugated profile of a container under the analysed fire scenarios, it can be concluded that the effect on the properties of steel would be minimal since expected temperatures are below 300-350 °C. Within this temperature range the yield strength, $f_y$, and the elastic modulus, E, of steel are minimally reduced.

## ACKNOWLEDGEMENTS

This work has been partially done under Project PID2020-114766RB-100 funded by MCIN/ AEI /10.13039/501100011033 and a project funded by Ajuntament de Barcelona.

## REFERENCES

[1] W. Ferdous, Y. Bai, T.D. Ngo, A. Manalo, P. Mendis, New advancements, challenges and opportunities of multi-storey modular buildings – A state-of-the-art review, Eng. Struct. 183 (2019) 883-893

[2] S. Navaratnam, T. Ngo, T. Gunawardena, D. Henderson, Performance review of prefabricated building systems and future research in Australia, Buildings 9(2) (2019) 38

[3] S. Abdelmageed, T Zayed, A study of literature in modular integrated construction – Critical review and future directions, J. Cle. Prod. 277 (2020) 1240044

[4] R.G. Zafra, J.R.M. Mayo, P.J.M. Villareal, V.M.N. De Padua, Ma.H.T. Castillo, M.B. Sundo, M.S. Madlangbayan, Structural and thermal performance assessment of shipping container as post-disaster housing in tropical climates, Civil Eng. J. 7(8) (2021)

[5] Z. Ye, K. Giriunas, H. Sezen, G. Wu, D-C. Feng, State-of-the-art review and investigation of structural stability in multi-story modular buildings, J. Build. Eng. 33 (2021)

[6] W. Chen, J. Ye, Y. Bai, X-L. Zhao, Improved fire resistant performance of load bearing cold-formed steel interior and exterior wall systems, Thin-Walled Struct. 73 (2013) 145-157

[7] W. Chen, J. Ye, X. Li, Thermal behaviour of gypsum-sheathed cold-formed steel composite assemblies under fire conditions, J. Construct. Steel Res. 149 (2018) 165-179

[8] D. Perera, K. Poologanathan, P. Gatheeshgar, I.R. Upasiri, P. Sherlock, H. Rajanayagam, B. Nagaratnam, Fire performance of modular wall panels: Numerical analysis, Structures 34 (2021) 1048-1067

[9] Y. Yu, P. Tian, M. Man, Z. Chen, L. Jiang, B. Wei, Experimental and numerical studies on the fire-resistance behaviors of critical walls and columns in modular steel buildings. J. Build. Eng. 44 (2021)

[10] L.A. Pereira-de-Oliveira, L.F.A. Bernardo, A.R.A. Marques, Architectural building design with refurbished shipping containers: A typological and modular approach, J. Eng. Res. 10(1A) (2022)

[11] C.S. Tan, P.C.H. Ling, Shipping container as shelter provision solution for post-disaster reconstruction, International Conference on Civil and Environment Engineering, E3S Web of Conferences 65, 08007 (2018)

[12] EN 1993-1-2:2005. Eurocode 3: Design of steel structures. General rules - Structural fire design. CEN - European Committee for Standardization. Brussels, 2005.

[13] NIST. Fire Dynamics Simulator (FDS). https://pages.nist.gov/fds-smv/ (accessed 25 October 2021).

[14] Diamonds (version 2020). Buildsoft company. Hundelgemsesteenweg 244/1B-9820 Merelbeke. https://www.buildsoft.eu/en (accessed 25 October 2021).

[15] Thunderhead Engineering. Pyrosim v3.3.0. https://www.thunderheadeng.com/pyrosim (accessed 25 October 2021).

[16] Ministry of Business, Innovation & Employment. C/VM2 Verification Method: Framework for Fire Safety Design. For New Zealand Building Code Clauses C1-C6 Protection from Fire. Building Code, 2013.

[17] EN 1991-1-2:2002. Eurocode 1: Actions on structures - Part 1-2: General actions - Actions on structures exposed to fire. CEN - European Committee for Standardization. Brussels, 2002. Incorporating corrigendum March 2009.

[18] EN 1364-1:2015. Fire resistance tests for non-load bearing elements. Part 1: walls. CEN - European Committee for Standardization. Brussels, 2015.

[19] I. Rahmanian. Thermal and mechanical properties of gypsum boards and their influences on fire resistance of gypsum board based systems, PhD Thesis, Manchester University, Manchester, UK, 2011. https://www.escholar.manchester.ac.uk/api/datastream?publicationPid=uk-ac-man-scw:137521&datastreamId=FULL-TEXT.PDF (accessed 22 November 2021)

[20] Spanish Building Technical Code. CTE Código Técnico de Edificación. Documento Básico DB-SI Seguridad en caso de incendio. Ministerio de la Vivienda. Madrid, 2010.

# Thermal Characterization of a Green-Poxy Resin-Based Bio-Composite Reinforced with Banana Leaf Fibres for Transportation Applications

**Melati A.[1.2*], Settar A.[1], Chetehouna, K.[1], Foucault L. [1], Sahli M.[3]**

*[1] INSA Centre Val de Loire, Université Orléans, PRISME EA 4229, F-18020 Bourges, France*
*[2] Physics Department, UIN Sunan Kalijaga Yogyakarta, Indonesia.*
*[3] Ceramics Laboratory, Univ des Frères Mentouri Constantine 1, Algeria*
**Corresponding author's email: asih.melati@insa-cvl.fr*

## ABSTRACT

Currently, green bio-composites have great potential in many aspects of life: transportation, industry sports, buildings etc.The use of GBC is due to its inexpensive cost of production as well as the fact that it is renewable, sustainable and eco friendly. In the present work, thermal degradation of green-poxy resin-based GBC reinforced with banana leaf fibres is investigated. GBC plates of 50×50 cm² with 5.4 mm of thickness are first manufactured using Vacuum Bag Resin Transfer Moulding (VBRTM) process. Thirty percent (30%) of fire retardant (FR) based on ammonium polyphosphate and boric acid (Halogen free) is applied at the sample surface to evaluate the GBC ability to withstand fire and improve its flammability (noted GBC+FR). To investigate the thermal behaviour of GBC and GBC+FR materials, TGA was carried out with three different heating rates under an inert atmosphere. Mass loss and conversion rate results show that only one pyrolysis reaction is occur during the samples degradation. Moreover, FR as mixing for GBC increases char residue by 3 - 8% and improves the thermal stability during thermal degradation.

**KEYWORDS:** Green-Bio-Composites, banana leaf fibre, thermal degradation, TG Analysis.

## INTRODUCTION

Nowadays, bio-based composites reinforced with natural fibres composites have seen significant development in many applications of daily life. They have attracted growing interest for the following four reasons: very good ecological properties, encouragement of the growth of sustainable agriculture, promotion of economic development, and enhancement of smallholder participation in the value chain. Natural fibres can be derived from animals, plants, and minerals. They are reinforced by chemical or natural matrix, composites. For a natural-based matrix it is called Green Bio-Composites (GBC). Due to their wide applications in transportation [1]–[3], several researchers have been conducted on many types of GBC materials reinforced by flax [4], [5], sisal [6], hemp [7], water hyacinth [8], jute [9], coir [10], bamboo [11], banana [12], [13], abaca [14] and so on. Plant natural fibres contain cellulose, hemi-cellulose, and lignin. Cellulose has an effect on mechanical properties. Hemicellulose has an effect on moisture absorption, heat capacity, biodegradation, and flammability, while lignin has an effect on char formation [15]. Inrecent decades, the use of Banana Leaves Fibres (BLF) as reinforcement on GBC is attracting more and more attention, especially for GBC products where the ability to withstand fire is required. A chemical compound of raw banana leaf fibre is 82.44% yield, 19.82% hemicellulose, 22.37 % lignin [16], and biochemical analysis of banana leaves after thermal exposition TGA shows Cellulose 43.34%, hemicellulose 34.34%, lignin 15% and extractives 7.32% [17]. It contains 44.01±0.22 of C, 6.10±0.03 H, 1.360±0.007 O, and 38.84±0.1 N respectively [18]. BLF mechanical properties of BLF are given in Table 1.

**Table 1. Physical and mechanical properties of banana leaf** [3].

| Properties | Value |
|---|---|
| Density | 950-750 Kg/m $^3$ |
| Water absorption | 60% |
| Tensile strength | 180 – 430 MPa |
| Young Modulus (E) | 23 GPa |

In the literature, reinforced GBC containing BLF is hybridised with other natural fibres such as cassava starch [19], kenaf [20], sisal/roselle [21], glass [22], and sisal/coconut sheath [23]. Concerning the applications in the transportation domain, BLF are promising fibres not only for interior but also exterior transportation applications. Samal et al. reported that banana is applied in underfloor protection passenger cars [24]. However, their thermal and flammability behaviour are still questionable. In addition, even though there are studies reporting on using banana leaf fibres in composites, none were found on the utilisation of BLF as thermal protection, especially its combination with biodegradable resin. To improve the GBC ability to withstand fire, several types of Fire Retardant (FR) can be applied even on the GBC surface or as a mixture during the manufacture of GBC materials.

From that perspective, the present work deals with a thermal degradation analysis of GBC materials mixed or not with FR based on ammonium polyphosphate and boric acid (halogen-free). GBC plates are first manufactured using the Vacuum Bag Resin Transfer Moulding process (VBRTM). To study and compare thermal degradation, a TGA test was conducted on the GBC and FR mixed GBC. As a result, a good protective effect and thermal decomposition of the used FR are reached.

## MATERIALS & METHODS

### Natural fibre and matrix selection

In the present work, BLF long fibres have been selected among numerous natural fibres used as reinforcement on GBC materials. Several criteria were applied to select the most appropriate reinforcement. Regarding the final use of the GBC material, which is intended to be used for a particular sector. The selection was based on the mechanical, thermal, and chemical behaviours of such natural fibres. In addition, particular attention was given to their thermal behaviour and ability to withstand fire.BLF fibres have interesting properties: high ash content when exposed to flame and low water absorption because of the hemicellulose higher it contains.

For the matrix, biobased epoxy was used to manufacture the material. A combination of Green-poxy SR 56 with SD 8823 hardener by Sicomin France was chosen in this work. This choice is made in order to reduce the non-degradable proportion of the final product. In fact, Green-poxy contains a higher bio-based carbon content, approximately 56 – 60 %. It is also suitable with resin transfer moulding, either injection or infusion process, which facilitates the bio-composite manufacture. In addition, this resin has good viscosity even in hot process fabrication.

### Vacuum Bag Resin Transfer Moulding experimental bench

The Vacuum Bag Transfer Moulding (VBRTM) process was chosen to manufacture the GBC materials used during the thermal characterization. Figure 1 shows the schematic view of the VBRTM experimental bench used to manufacture GBC material (Fig. 1 a). The VBRTM bench is composed of three distinguished parts: (1) moulding section; (2) resin mixture section, and (3) vacuum section. Firstly, the glass table is polished using wax liquid to avoid the adherence of the GBC material after curing. The moulding section is composed of 4 different layers, which are set successively as follows: (1) 17 BLF layers of 50×50 cm² with 5.4 mm of thickness and 315 g mass; (2) one peel ply layer of 60×60 cm²; and (3)) an injection mesh layer of 60×60 cm². All the layers are then covered by a vacuum

bag sealed with the glass table in order to avoid air leaks during the vacuum application, as shown in Fig. 1 b. Secondly, the resin mixture is prepared as described above. A ratio of 100 (Green-Poxy SR 56): 26 (SD 8823 hardener) is considered based on Sicomin recommendations. The mixture is first stirred in the resin mixture section for approximately 15 minutes to have a good homogeneity as well as to avoid air bubble presence within the mixture. It is important to note that the moulding section is equipped with spiral tubes throughout the periphery of the moulding section. It allows a regular infusion front through BLF layers. Finally, the vacuum section is constituted by the vacuum pump, followed by a vacuum chamber preventing the resin mixture from reaching the pump suction.

After mixing the resin, the whole system was vacuumed under a pressure of -0.92 bar at ambient temperature. Before starting the infusion process, a leak test was conducted. The setup is maintained under the desired pressure for 30 minutes which corresponds to three times the infusion duration which takes approximately 10 minutes from opening the connection between the resin mixture and moulding sections. The final GBC plate with a thickness of 6.6 mm is shown in Figure 1 c. It was obtained after a curing duration of 24 hours before demoulding and post cured for 48 hours in an isothermal oven (24 hours at 24°C + 24 hours at 40°C) to complete the GBC polymerization process.

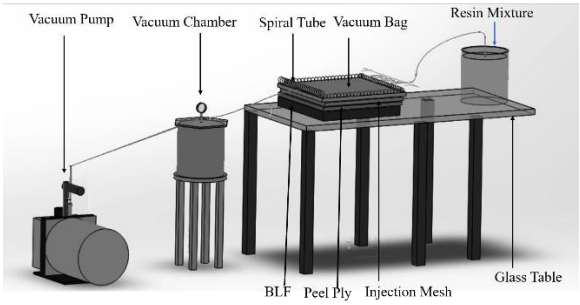


(a)

(b)

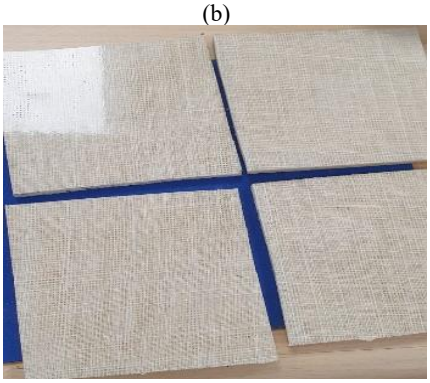

(c)

**Fig. 1.** VBRTM experimental bench details: (a) Schematic view; (b) moulding section; (c) final GBC material.

## Sample preparation and thermal characterisation

In this section, sample preparation and thermal characterisation methods are detailed. Based on the GBC plate obtained after curing, 30 small samples of 5×5×6 $mm^3$ were prepared as shown in Fig. 2 a to be used for thermogravimetric analysis (TGA). Samples have been divided into 2 categories. The first one is used as virgin GBC which is used for comparison purposes (Fig. 2 a), while the second is mixed at the cube surface by Fire Retardant, referenced as GBC+FR (Fig.2 b). In the literature, many

FR have been used to protect such GBC materials. In this work, a mixture of 29% Exolit IFR 36 powder FR by Clariant Switzerland, which is based on ammonium polyphosphate, and 1% Boric Acid powder by Sicomin France is considered. The FR mixture is mixed with 70% resin used to manufacture the GBC plate. The BLF weight percentage ratio in GBC is 28%, while the BLF percentage in GBC+FR is 15%. On GBC+FR, the weight ratios of APP, BA, resin (green-poxy + hardener), and natural fibre BLF were 29,1,55, and 15, respectively. These resin and hardener ratio methods were based on the datasheet from Sicomin [25], and the ratio of FR was based on our team's previous experiment[26]

This FR can extinguish the fire by releasing carbon foams on the material coated surface, which leads to a reduction in further oxygen access through the GBC material. Boric Acid FR tends to slow the spread of flames, although it can also encourage smouldering (glowing) of the material. On the other hand, during combustion in the pyrolysis process, boric acid has stronger catalytic dehydration. While Exolit APP has low water solubility even in powder form. Concerning the preparation of the FR mixture, electrical steering is used to ensure that Boric Acid and Exolit IFR 36 powder are well incorporated within the resin. Thereafter, a coating layer of 1 mm is applied at each face of the mixed sample (please see Fig. 2 b). To ensure the homogeneous distribution of FR coating on sample surfaces, a mean density coating is calculated. Only samples with 1.144 mg/mm² of density were selected. As done for the GBC plate, GBC+FR samples are post cured for 48 hours in an isothermal oven at the same temperatures as for the GBC plate. Finally, GBC and GBC+FR samples are crushed into powder form to conduct TGA tests, as shown in Fig.2.c and Fig.2.d, respectively. The sample was crushed into powder form because on a matter scale, the powder size produces homogeneous microstructures of recrystallization with low volume fractions and random spatial inclusion distribution.

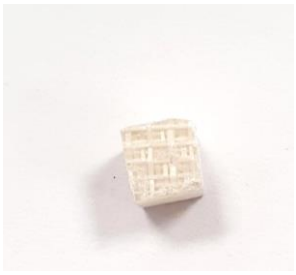

(a) GBC

(c) Powdered GBC

(b) GBC+FR

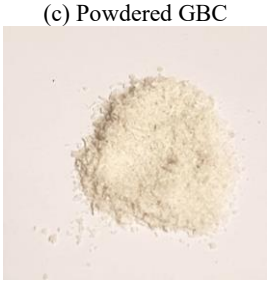

(d) Powdered GBC+FR

**Fig. 2.** Pictures on the GBC and GBC+FR samples were used for thermal characterisation.

Themys One TGA machine by Setaram France was used to explore the mass loss as a function of time and temperature of GBC and GBC+FR samples under an inert (helium) atmosphere. Samples were heated at three controlled heating rates (5 °C/min, 10 °C/min, and 15 °C/min) from a temperature of 30 °C until 870 °C. As noted above, the purpose of this thermal characterisation is to explore the protective effect of FR coated on GBC materials. To ensure accurate measurements, TGA tests have been repeated twice for repeatability purposes . However, the MLR curve and conversion rate were analysed

by completing the standard deviation, as a result of calculating the mean of two repeatability data for each heating rate. Table 2 recapitulates the initial mass of the samples used during TGA tests.

**Table 2. The initial mass of samples used for TGA tests**

| Samples | Heating Rate (°C/min) | Initial mass 1 (mg) | Initial mass 2 | Mean initial mass |
|---|---|---|---|---|
| GBC | 15 | 15.74 | 15.08 | 15.41 |
| | 10 | 15.09 | 15.65 | 15.27 |
| | 5 | 15.45 | 15.15 | 15.30 |
| GBC +FR | 15 | 15.79 | 15.58 | 15.65 |
| | 10 | 15.60 | 15.60 | 15.60 |
| | 5 | 15.74 | 15.74 | 15.74 |

The mass loss is determined on based on the conversion degree parameter noted α, which is obtained by Eq. (1):

$$\alpha = \frac{m_t - m_0}{m_f - m_0} \times 100 \quad (1)$$

Where indices 0, f, and to denote the initial, final and at time masses, respectively.

To compare the mass loss of GBC and GBC+FR samples, the mass Loss Rate (MLR), also named the conversion rate, is evaluated as given by Eq. (2):

$$MLR = \frac{dm_t}{dt} \quad (2)$$

where $dm_t$ and $dt$ denote the mass variation between instants $t$ and instant $t-1$, and the time variation, respectively.

To determine the char amount obtained for GBC and GBC+FR, the residual mass ratio *R* is calculated. This allows to highlight the effect of FR coating on GBC material. The R ratio is expressed by Eq. (3) as follows:

$$R = \frac{m_f}{m_i} \times 100 \quad (3)$$

## RESULTS AND DISCUSSIONS

### TGA Test on GBC

The TGA result performs the mean of two pyrolysis experiments and shows the standard deviation value for both experiments. Figure 3 represents the mass loss rate (MLR) (Fig. 3 a) and the conversion rate (Fig. 3 b) as a function of temperature evolution. In Fig. 3 a, the GBC mass loss begins at the temperature of approximately 257°C (at a heating rate of 5°C/min) and - 274°C (at a heating rate of 15°C/min), which indicates the onset temperature for GBC and depicts the degradation process. After this temperature, a sharp decrease in terms of mass loss is observed until 405°C, where 74.734% Of GBC mass is transformed. Beyond that, the mass is still decreasing slightly until the end of the test. In addition, Figure 3.a shows the approximate thermal stability at a temperature of 240°C before the

degradation process occurs Fig.3 is also equipped with a standard deviation value to determine the minimum and maximum data values for each heating rate. The largest standard deviation values for each heating rate 5, 10 and 15°C/min were 4.26, 7.94 and 2.02%, respectively. Data on the heating rate of 10 °C/min has the largest standard deviation. In an inert atmosphere, only one reaction is then observed as shown by the peak in Fig. 3 b. cellulose lignin and hemicellulose. In the BLF combustion process, the first degraded is hemicellulose, followed by lignin and finally cellulose. In the temperature range of 200°C, lignin started to decompose, while cellulose was depolymerized and dehydrated at 200 - 280°C. . On the other hand, from the datasheet, resin green-poxy reached an exothermic peak at 250°C and was thermally stable at this temperature. The resin green-poxy contributes to the strengthening of the compatibility of fibre and increases thermal decomposition Moreover, if the heating rate is high, the flammability will be higher.

From Fig. 3 b, one notes that there are three peaks which are located at 328.2 °C, 331 °C, and 338 °C for 5°C/min, 10°C/min and 15°C/min, respectively. The percentages of char residue left were 15.5%, 12.48% and 10.90 %, respectively. The thermal properties of GBC are listed in Table 3. A higher heating rate gives the most important GBC mass loss until 10.9%. While for a low heating rate (5 °C/min), the mass loss is only 15.5%. A higher heating rate provides a higher temperature peak and smaller mass residue.

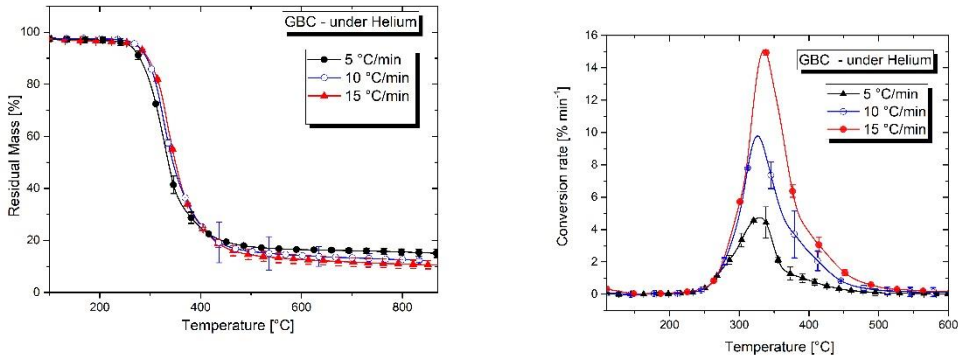


(a) (b)

**Fig. 3.** GBC thermal decomposition as function of temperature under inert atmosphere: (a) Mass loss rate (MLR); (b) Conversion rate

## TGA Test on GBC Coating FRs

For the GBC sample, Fig. 4 represents the mass loss (Fig. 4 a) and the conversion rate (Fig. 4 b) as a function of temperature evolution. GBC+FR thermal decomposition occurs at267 C, 279°C, and 287 °C for 5 °C/min, 10 °C/min and 15 °C/min, respectively. the In fact, as seen in Fig 4.a GBC+FR material has achieved thermal stability at 260 °C, and over that temperature the degradation process has begun. The Powder size distribution on GBC+FR has a strong effect on matter level because using narrow distributions, it will show better statistics (i.e.,homogeneous recrystallization), thus increasing the amount of oxygen content.

Moreover, from the literature mentioned, FR Borid Acid loses all its water and transforms to boron oxide (B2O3) above 150°C and becomes borax at 200°C, while FR Exolit decomposes above 240°C. Figure 4.b also provides a standard deviation value, it can be seen that the largest standard deviation value at heating rates of 15 °C/min is 11.3%. This is characterized by the role of FR, which has slowed the degradation process and provided protection against the spread of fire. It means that the FR used plays a protective role regardless of the heating rate applied to the sample.

Fig. 4 b one notes that there are three peaks of the conversion rate, which are located at 308.6°C, 321°C, and 324.2°C for 5°C/min, 10 °C/min and 15°C/min, respectively. In addition, one remarks that the maximum mass loss is almost 18% for the three heating rates (Fig. 4 a). This means approximately 72.008% mass transformed. This fact confirms the protective aspect of the presence of FR mixed on the GBC sample . According to the Material Safety Data Sheet (MSDS) of Exolit IFR36 given by Clariant, the FR is effective at temperatures below 580°C, while the boric acid effectiveness remains significant below 500 °C . It can be concluded that the present FR is appropriate for GBC materials reinforced by BLF.

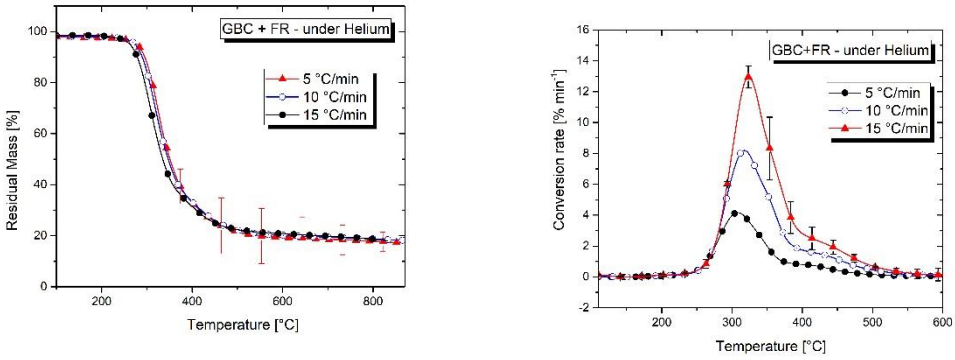


(a) (b)

**Fig. 4.** GBC+FR thermal decomposition as function of temperature under inert atmosphere: (a) Mass loss; Rate (MLR) (b) Conversion Rate

**GBC vs. GBC+FR**

To complete the analysis conducted above on GBC and GBC+FR, a comparison study is realized. Table 3 resumes the most important parameters leading to highlight the effect of FR mixing. This confirms that only one reaction occurs for both materials. In addition, the reaction peaks occur at the same temperature. However, from the overall point of view, GBC+FR presents higher thermal degradation than GBC. Thermal stability before the decomposition process is reached by GBC mixed FR at 260°C, while GBC without FR at 240°C. The key parameter of this delayed degradation of GBC+FR was the formation of hard glassy fire protective coating of borophospate compound which appeared from FR (Exolit APP and Borid Acid. The decrease in the temperature at which the thermal decomposition stopped due to the fire retardancy was 10°C ± 4°C. We can also note that the residual mass is different between the compared materials.For example, for 15°C/min, 3% of the difference is noticed. Thus, GBC+FR produces more char residue than GBC. Finally, thermal decomposition shows that GBC decomposed more prior than GBC+FR.

In addition, for the post degradation process, the thermal stability obtained on GBC and GBC+FR, GBC+FR had higher thermally-stable than GBC. A descreapancy is noticed in the GBC materialAfter the decomposition process, where the temperature ranged from 525°C to 625 °C, there was still a far-ranging decline in the mass of the sample. While for GBC+FR thermal stability at constant temperature (570°C) is obtained due to the presence of FR.

**Table 3. Comparison of GBC and GBC+FR thermal and mass parameters**.

| Materials | Heating Rate (°C/min) | Final mass Loss (mg) | Residual mass (mg) | $T_{onset}$ (°C) | T Inclination (°C) | Thermal stability (°C) before degradation | Thermal stability (°C) post degradation |
|---|---|---|---|---|---|---|---|
| GBC | 15 | 13.77 | 1.98 | 274 | 332.7 | 240 | 516 |
| | 15 | 13.51 | 1.57 | 274 | 333.24 | 240 | 515 |
| | 10 | 13.23 | 1.87 | 265 | 331.667 | 238 | 593 |
| | 10 | 13.75 | 1.90 | 266 | 329.83 | 238 | 556 |
| | 5 | 13.13 | 2.33 | 257 | 328.19 | 235 | 525 |
| | 5 | 13.12 | 1.89 | 259 | 328.29 | 236 | 517 |
| GBC+FR | 15 | 13.08 | 3.18 | 287 | 324.15 | 260 | 570 |
| | 15 | 12.4 | 3.18 | 281 | 323.23 | 260 | 570 |
| | 10 | 12.80 | 2.80 | 279 | 321.37 | 260 | 570 |
| | 10 | 12.80 | 2.80 | 279 | 321.37 | 260 | 570 |
| | 5 | 12.90 | 3.65 | 267 | 308.60 | 260 | 570 |
| | 5 | 12.90 | 3.65 | 267 | 308.60 | 260 | 570 |

Figure 5 gives a comparison between GBC and GBC+FR on t mass loss rate and conversion rate.. From the pictures it is clearly seen that the FR provides a good thermal protection for GBC especially on the part delay decomposition process and increase residual mass In fact,a high constant residual ratio (around 8%) was obtained. This is due to the thermal stability of such mixed material with FR, regardless of heating rate used. After knowing these GBC thermal properties, the opportunity for the application of this material in the underfloor protection passenger car and another particular sector is more widely open.

## CONCLUSIONS

In this paper, thermal degradation analysis of GBC materials mixed or not with a fire retardant is conducted. GBC plates are first manufactured using the Vacuum Bag Resin Transfer Moulding process (VBRTM). To study and compare thermal degradation, TGA tests were conducted on the GBC and mixed GBC. In the inert atmosphere, both compared samples have only a one-step reaction and a higher heating rate gives higher thermal degradation. The FR (Exolit IFR36 and boric acid) provides able to slow down the decomposition process than the sample without FR. Furthermore, FR supports higher thermal stability before the degradation process than without FR , and increases char residue amount by 8 % under an inert atmosphere. Banana leaf fibres (BLF) as green bio-composites reinforced by biodegradable resin and of FR- mixed have great potential in a particular sector

In future works, thermal analysis tests on GBC and GBC+FR under an oxidative atmosphere will be conducted to comprehensively bring scientific contributions related to the thermal behaviour of these two materials In addition, the improvement of the effectiveness and combinations of intumescent FR on GBC thermal behaviour is also challenging to maintain the weakness of GBC flammability.

## REFERENCES


[1] M. Rashid, K. Chetehouna, A. Cablé, and N. Gascoin, *Analysing Flammability Characteristics of Green Biocomposites: An Overview*, vol. 57, no. 1. Springer US, 2021. doi: 10.1007/s10694-020-01001-0.

[2] R. A. Kurien, D. P. Selvaraj, M. Sekar, and C. P. Koshy, "Green composite materials for green technology in the automotive industry," *IOP Conference Series: Materials Science and Engineering*, vol. 872, no. 1, 2020, doi: 10.1088/1757-899X/872/1/012064.

[3] D. Verma and I. Senal, *Natural fiber-reinforced polymer composites*. Elsevier Ltd, 2019. doi: 10.1016/B978-0-08-102426-3.00006-0.

[4] T. H. Panzera *et al.*, "Static, fatigue and impact behaviour of an autoclaved flax fibre reinforced composite for aerospace engineering," *Composites Part B: Engineering*, vol. 197, p. 108049, 2020, doi: 10.1016/j.compositesb.2020.108049.

[5] S. Selmi, M. Habibi, L. Laperrière, and S. Kelouwani, "Characterisation of Natural Flax Fibers Honeycomb: Compression Damage Analysis Using Acoustic Emission," *Journal of Natural Fibers*, vol. 00, no. 00, pp. 1–10, 2020, doi: 10.1080/15440478.2020.1789531.

[6] J. Naveen, M. Jawaid, P. Amuthakkannan, and M. Chandrasekar, *Mechanical and physical properties of sisal and hybrid sisal fiber-reinforced polymer composites*. Elsevier Ltd, 2018. doi: 10.1016/B978-0-08-102292-4.00021-7.

[7] S. Krishnasamy *et al.*, "Effects of stacking sequences on static, dynamic mechanical and thermal properties of completely biodegradable green epoxy hybrid composites," *Materials Research Express*, vol. 6, no. 10, 2019, doi: 10.1088/2053-1591/ab3ec7.

[8] N. Sumrith and R. Dangtungee, "Mechanical properties of water hyacinth fiber reinforced bio-based epoxy composite," *Key Engineering Materials*, vol. 818 KEM, pp. 7–11, 2019, doi: 10.4028/www.scientific.net/KEM.818.7.

[9] S. Dixit, V. Verma, and G. Dixit, "Performance and emission analysis of OilJFWPB recovered by the oxidative thermal degradation of the mixture of waste polyethylene and Jute," *Alexandria engineering journal*. Elsevier, 2018.

[10] K. R. Sumesh and K. Kanthavel, "The influence of reinforcement, alkali treatment, compression pressure and temperature in fabrication of sisal/coir/epoxy composites: GRA and ANN prediction," *Polymer Bulletin*, vol. 77, no. 9, pp. 4609–4629, 2020, doi: 10.1007/s00289-019-02988-5.

[11] I. Pope, J. P. Hidalgo, A. Osorio, C. Maluk, and J. L. Torero, "Thermal behaviour of laminated bamboo structures under fire conditions," *Fire and Materials*, vol. 45, no. 3, pp. 321–330, 2021, doi: 10.1002/fam.2791.

[12] U. K. Komal, M. K. Lila, and I. Singh, *PLA/banana fiber based sustainable biocomposites: A manufacturing perspective*, vol. 180. Elsevier Ltd, 2020. doi: 10.1016/j.compositesb.2019.107535.

[13] T. Saxena and V. K. Chawla, "Banana leaf fiber-based green composite: An explicit review report," *Materials Today: Proceedings*, vol. 46, no. xxxx, pp. 6618–6624, 2020, doi: 10.1016/j.matpr.2021.04.099.

[14] R. R. Niranjan, S. Junaid Kokan, R. Sathya Narayanan, S. Rajesh, V. M. Manickavasagam, and B. V. Ramnath, "Fabrication and testing of abaca fibre reinforced epoxy composites for automotive applications," *Advanced Materials Research*, vol. 718–720, pp. 63–68, 2013, doi: 10.4028/www.scientific.net/AMR.718-720.63.

[15] A. U. R. Shah, M. N. Prabhakar, and J. Il Song, "Current advances in the fire retardancy of natural fiber and bio-based composites – A review," *International Journal of Precision Engineering and Manufacturing - Green Technology*, vol. 4, no. 2, pp. 247–262, 2017, doi: 10.1007/s40684-017-0030-1.

[16] Q. Tarrés, E. Espinosa, J. Domínguez-Robles, A. Rodríguez, P. Mutjé, and M. Delgado-Aguilar, "The suitability of banana leaf residue as raw material for the production of high lignin

content micro/nano fibers: From residue to value-added products," *Industrial Crops and Products*, vol. 99, pp. 27–33, 2017, doi: 10.1016/j.indcrop.2017.01.021.

[17] R. K. Singh, D. Pandey, T. Patil, and A. N. Sawarkar, "Pyrolysis of banana leaves biomass: Physico-chemical characterization, thermal decomposition behavior, kinetic and thermodynamic analyses," *Bioresource Technology*, vol. 310, p. 123464, Aug. 2020, doi: 10.1016/j.biortech.2020.123464.

[18] K. Bilba, M. A. Arsene, and A. Ouensanga, "Study of banana and coconut fibers. Botanical composition, thermal ddegradation,and textural observations," *Bioresource Technology*, vol. 98, no. 1, pp. 58–68, 2007, doi: 10.1016/j.biortech.2005.11.030.

[19] R. Jumaidin, N. A. Diah, R. A. Ilyas, R. H. Alamjuri, and F. A. M. Yusof, "Processing and characterisation of banana leaf fibre reinforced thermoplastic cassava starch composites," *Polymers*, vol. 13, no. 9, 2021, doi: 10.3390/polym13091420.

[20] A. Alavudeen, N. Rajini, S. Karthikeyan, M. Thiruchitrambalam, and N. Venkateshwaren, "Mechanical properties of banana/kenaf fiber-reinforced hybrid polyester composites: Effect of woven fabric and random orientation," *Materials and Design*, vol. 66, no. PA, pp. 246–257, 2015, doi: 10.1016/j.matdes.2014.10.067.

[21] D. Chandramohan and J. Bharanichandar, "Natural fiber reinforced polymer composites for automobile accessories," *American Journal of Environmental Sciences*, vol. 9, no. 6, pp. 494–504, 2014, doi: 10.3844/ajessp.2013.494.504.

[22] L. A. Pothan, C. N. George, M. J. John, and ..., "Dynamic mechanical and dielectric behavior of banana-glass hybrid fiber reinforced polyester composites," *Journal of Reinforced …*, 2010.

[23] K. Senthilkumar, I. Siva, N. Rajini, J. T. W. Jappes, and S. Siengchin, *Mechanical characteristics of tri-layer eco-friendly polymer composites for interior parts of aerospace application*. Elsevier Ltd, 2018. doi: 10.1016/B978-0-08-102131-6.00003-7.

[24] S. K. Samal, S. Mohanty, and S. K. Nayak, "Banana/Glass Fiber-Reinforced Polypropylene Hybrid Composites: Fabrication and Performance Evaluation," *Polymer-Plastics Technology and Engineering*, vol. 48, no. 4, pp. 397–414, Apr. 2009, doi: 10.1080/03602550902725407.

[25] "greenpoxy 56 Sicomin.pdf. https://greenpoxy.org/products/#29"

[26] M. Rashid, K. Chetehouna, L. Lemée, C. Roudaut, and N. Gascoin, "Study of flame retardancy effect on the thermal degradation of a new green biocomposite and estimation of lower flammability limits of the gaseous emissions," *J Therm Anal Calorim*, Feb. 2022, doi: 10.1007/s10973-022-11233-7.

# New Approach to Cable Tray Fire Modelling Through a FLASH-CAT Modification

**Lázaro D.[1,*], Lázaro M.[1], Jimenez, M.A.[2], Alvear D.[3]**

*[1] GIDAI Group. University of Cantabria, Spain.*
*[2] Consejo de Seguridad Nuclear, CSN, Spain*
*[3] Dirección General de Industria, Energía y Minas, Gobierno de Cantabria, Spain.*
**Corresponding author's email: lazarod@unican.es*

## ABSTRACT

As part of the structures, systems or components (SSCs) in nuclear power plants, the understanding of cable fire propagation can be crutial in their safety. The study of the fire propagation in cable trays is one of the key points in the study and modeling of fire behaviour in confined and ventilated rooms.

The model referred as FLASH-CAT (Flame Spread over Horizontal Cable Trays) consists of a relatively simple model for predicting the growth and spread of a fire within a vertical stack of horizontal cable trays. The model was validated by comparing the prediction of the model with a total of 26 Multiple Tray Experiments performed in in NUREG/CR 7010. Nevertheless, some limitations were found in the applicability of the FLASH-CAT model. Some of those limitations comes from the fact that the experiments used to validate the model consider cables that burn in an open space; this is, they are away from walls and well below the ceiling, additionally the model only considers two kinds of cables, thermoplastic or thermoset, and recommend the same properties for all the cables in each of these groups.

In order to try to deal with these limitations of the model, a modification of the FLASH-CAT model is proposed. With this modification the model is able to predict the HRR in a confined and ventilated room considering the thermal behaviour properties of the cables that the model tries to simulate. To validate this modification, the proposed model is compared to several experimental test performed under the PRISME 2 Programme. Results show the validity of the model to predict the HRR of the cable trays in the studies cases.

**KEYWORDS:** cable tray fire, enclosure, flame spread, FLASH-CAT.

## INTRODUCTION

During the last years different models have tried to predict the growth and spread of a fire within cable trays. The prediction of cable fire spread is as difficult as important. Cable fires can compromise, for example, nuclear power plants (NPP) safety, as occurred in the incidents of Browns Ferry NPP by a fire in the cable spreading room [1], of the Armenia NPP where the fire was initiated by a short in the power circuits inside cable galleries, and propagated rapidly until it became a large fire [2], or of the Beloyarsk NPP where the fire started in the turbine building due to a break in the oil system, and it propagated to cables and from there into the control building [2]. Such is the importance of the fire safety that the European Nuclear Safety Regulators Group has selected the fire protection in nuclear installations as the topic for the second Topical Peer Review (TPR) under the Nuclear Safety Directive [3], which will take place between 2023 and 2024, and it will focus on the fire protection.

Nevertheless, the study and prediction of cable fire propagation is a very complex issue. The physical and chemical solid and gas-phase phenomena involved in cable fire spread are extraordinarily complicated so all approximations to represent them demand a certain level of simplification. Moreover, just the definition of the input parameters for modeling fire propagation tends to be open to the modeler criteria which are highly likely to affect the final results [4] [5]. This can be caused by the uncertainty in the model input parameters considered by each user, but also due to the methodology selected by the user. To facilitate and unify the modeller definitions, the Nuclear Regulatory Commission of United States (U. S. NRC) published the NUREG 1934 "Nuclear Power

Plant Fire Modeling Analysis Guidelines" [6]. Nevertheless, such an essential aspect in nuclear power plants like cable fire propagation was not addressed in this work, as it is not already fully validated in fire models.

In fact, cable fire modelling is a key priority to be solved as it is noted in the last research activities FY 2018-2020 defined by the U. S. NRC [7]. The Best Practice Guidelines of NEA/CSNI/R(2014)11 [8] recommend the use of benchmark exercises to assess the capabilities of fire models for nuclear power plants applications. The Benchmark Exercise No. 3 [9] which involves horizontal and vertical cable trays, and modify the ventilation conditions, is of special interest for NPP. These experimental tests were used in [10] and [11] to evaluate the fire computer model FDS [12]. Another experimental program developed to quantify the mass and energy released from burning electrical cables was the Cable Heat Release, Ignition, and Spread in Tray Installations during Fire (CHRISTIFIRE) [13] [14]. Additionally, the International Collaborative Project to Evaluate Fire Models for Nuclear Power Plant Applications (ICFMP) conducted a series of five Benchmark Exercises used for evaluating and validating current fire models from around the world [15]. Finally, part of the PRISME program (PRopagation d'un Incendie pour des Scénarios Multilocaux Elémentaires –Propagation of fire for elementary multi-room scenarios) [16] [17], has studied experimentally the cables trays fire propagation under oxygen-starved conditions (confined and ventilated rooms).

All these tests are used to define, calibrate and validate new models to predict cable fire propagation. Nevertheless, understanding thermal solid phase degradation and gas phase combustion is not an easy task. Therefore, computational modelling of cable fire behaviour is a major challenge and one of the trending topics in fire science due to the complexity of the involved phenomena. Such is the complexity of phenomena involved that even widely used and validated softwares for computational modelling includes simplified methods to predict the fire behaviour of cables in their user guide [12].

Some of these simplified models are usually founded on the results of a finite number of experimental tests to define the reaction and propagation of fires in cable trays, as is the case of FLASH-CAT model [13]. FLASH-CAT (Flame Spread over Horizontal Cable Trays) model allows predicting the growth and spread of a fire within a vertical stack of horizontal cable trays. Nevertheless, FLASH-CAT model makes some assumptions as that the cable trays are horizontal and stacked vertically with a spacing of less than 0.45 m, the cables burn in the open air, the cables are only exposed to the ignition source below, it only considers the cables as either thermoplastic or thermoset, it does not take into account the effect of the heat release by the ignition source in the ignition time of the lower cable tray, etc. FLASH-CAT model considers as input parameters the horizontal spread rate (S), the vertical spread rate (defined by the time of ignition of each cable tray), the vertical propagation angle ($\theta$), the heat release rate per unit area (HRRPUA) of the cables, the heat of combustion ($\Delta H_c$), the vertical distance between the two trays ($h_i$), the number of cables per tray, the mass fraction of non-metallic material, the char yield, the mass per unit length of cable and the width of the tray. The NUREG/CR 7010 [13] recommends certain parameter values for the global definition of the model, like for S and HRRPUA, just considering if cables are thermoset or thermoplastics. Nevertheless, some studies [18] [19] [20] obtain some FLASH-CAT model input parameters from video fire analyses of tests. These studies show different values from the recommended by the NUREG/CR 7010 [13], and also, show variation of the horizontal spread rate in the different cable trays. The use of the new measured parameters increased the accuracy of the model for the analyzed experimental tests.

In [19], FLASH-CAT is applied to obtain the HRR of the cable trays in open conditions of PRISME experimental test with horizontal stacked trays, nevertheless they do not consider any modification in FLASH-CAT to predict cable fire propagation in confined rooms. In order to extend the applicability of the FLASH-CAT model to confined and ventilated rooms, in [21] it is presented a model derived from the FLASH-CAT. The implemented model differs from FLASH-CAT in the expressions of the flame spread velocity along cables and fuel heat release rate for which a correction is applied to take into account the effect of the oxygen depletion in the fire room on the fire heat release rate. These equations take into account the oxygen concentration in the air surrounding the cable trays during the fire. This can be performed with a computational model which allows to include these equations in

the simulation and recalculate those values during simulation, as the two-zone model ISIS does. Nevertheless, this is not possible in other extensively used computational models as FDS or CFAST. They conclude that additional compartment fire experiments are required for the improvement and the full validation of the model, given the multitude of parameters involved in the definition of the cable tray fire source. The development of such a semi-empirical model is a common practice in fire safety engineering concerned with complex combustibles. It opens the way to parametric studies.

Although these simplified methods can obtain considerably good results in certain types of scenarios, their extrapolation to other more complex scenarios is limited or even non-existent. Greater degree of details are to be used in the fire computational models that enable users to define cables in a more complex way, and to study their behaviour in a greater number of scenarios. There are different methods to define cable fuel properties. One way of dealing with horizontal cable trays may be imposing the mass loss rate (MLR) obtained experimentally by a bench-scale calorimetry and allowing horizontal propagation by prescribing a radial propagation speed [22]. Another simplified way to approximate the fire behaviour of cables is to consider an ignition temperature and a HRRPUA upon reaching this temperature [12] [23] [24], or by means of the burning rate [25]. In [26], the definition of the cables by using ignition temperature and a HRRPUA derived from a simplification of cone calorimeter tests was performed to model the scenario CFSS1 from PRISME.

Finally, another more complex approach to model fire spread in cables is based on the study of the kinetics of the decomposition reactions of the different cable components. This approach requires the definition of the decomposition scheme and the kinetic parameters of the reactions, such as the activation energy, the pre-exponential factor and the reaction order. These kinetic parameters have been used to model cable fires in small scale [27]. It has been also used in [28], where good representation for the cone calorimeter tests were obtained, but not for the horizontal cable tray tests. In [29], the inverse modelling with computational models and cone calorimetric tests is used to model the cable tray test defined in CHRISTIFIRE Phase 1 [13]. In this work, great differences were shown in the modelling of the cable trays due to the different FDS versions (FDS 6.5.3 and FDS 6.3.2). In [30] [31], McGrattan defines the cables as a solid plate with the width of the cable tray and obtains the activation energy and the pre-exponential factor to adjust mass loss rate in a temperature close to ignition temperature.

Although these approaches can obtain good aproximation to the experimental results, their complexity to define the input parameters and the variability in the cable fire spread phenomenon explain that these methods are not completely validated, and in certain occasions the results of its application show large deviations from experimental results.

In order to try to deal with these limitations, the present work includes some modifications of several equations used in FLASH-CAT and some recommendation in the definition of the HRRPUA input parameter. These variations try to predict the HRR in a confined and ventilated room considering the thermal behaviour properties of the specific cables that the model tries to simulate. The modified FLASH-CAT version has been validated with some experimental test obtained from PRISME 2 program. This new approach allows to obtain the fire propagation in horizontal cable trays the HRR of the cable trays, which can be used as input in computational models as FDS or CFAST. Nevertheless, more work is required to validate the proposed model with more experimental tests by using different types of cables and under different ventilation conditions.

## METHODOLOGY

In the present paper, we propose a modified version of FLASH-CAT and a methodology to define some of the required input parameters to represent horizontal cable tray fire propagation. This modified version will allow to analyse enclosure fire scenarios, which was not possible in the original FLASH-CAT [13]. The considerations made in the model to include the calculation of fire spread in enclosure fire scenarios are included below.

**Enclosure fires**

There are some previous works that consider the effect of the oxygen availability in ventilation controlled scenarios on the combustion, spetially on the heat release. An example of this is the work carried out by the IRSN in which they extend the applicability of the FLASH-CAT model to ventilated enclosures. In [21] a model derived from FLASH-CAT is presented. It introduces modifications in the expressions of the horizontal spread rate (Eq. (1)) and the heat release rate ($\dot{Q}(t)$) (Eq. (2)).

$$S(t) = \frac{4\left(\dot{q}''_{f,\infty} x(O_2)\right)^2 \delta_c}{\pi(k\rho c_p)\left(T_{ign} - T_{amb}(t)\right)^2} \quad (1)$$

$$\dot{Q}(t) = 0.45 \dot{q}''_{bs} x(O_2) \frac{\Delta H_c}{\Delta H_{c,\infty}} \sum_i^n S_i(t) \quad (2)$$

where $\dot{q}''_{f,\infty}$ is the incident heat flux from flames to the fuel surface in well ventilated conditions [kW m$^{-2}$], $x(O_2)$ is a correction factor dependent of the $O_2$ with a value between 0 y 1, $\delta_c$ heated fuel distance [m], k is the conductivity [W m$^{-1}$ K$^{-1}$], $\rho$ is the density [kg m$^{-3}$], $c_p$ is the specific heat [J kg$^{-1}$ K$^{-1}$], $T_{ign}$ the ignition temperature, $T_{amb}$ ambient temperature, $\dot{q}''_{bs}$ cone calorimeter HRR, $S_i$ area, $\Delta H_c$ effective heat of combustion, and $\Delta H_{c,\infty}$ effective heat of combustion under *well-ventilated* conditions.

In these two expressions, a correction is incorporated to consider the effect of oxygen depletion in the vicinity of the cable trays ($x(O_2)$). The incorporation of these equations in the computational fire model ISIS allows to adapt the horizontal spread rate and the HRRPUA in real time throughout the simulation. Nevertheless, this cannot be used without using ISIS. That is why, we decided to analyse the global conditions of ventilation and oxygen availability in the fire enclosure, and its effect on the combustion of the cables.

More examples of the use of reduction of the HRR with the oxygen concentration decrease are found in the SFPE Handbook. In chapter 88 of the SFPE handbook [32], the authors indicate that the maximum theoretical (ventilationcontrolled) HRR may be estimated using the well known correlation between HRR and the mass of oxygen consumed in a longitudinal ventilation flow:

$$\dot{Q} = (0.21 - \eta_{O_2}) \cdot V \cdot \rho \cdot \Delta H_{c,ox} \quad (3)$$

Where $\eta_{O_2}$ is the depleted oxygen level on the downstream side, V is the volumetric airflow, $\rho$ is density of the inflowing airflow and $\Delta H_{c,ox}$ is the heat of combustion for oxygen.
Also in the SFPE handbook, in the chapter 36 [33], authors present an equation based on an experimental campaign to correlate the ratio of ventilation-controlled chemical heat of combustion ($(\Delta H_{ch})_{vc}$) to well-ventilated chemical heat of combustion ($(\Delta H_{ch})_{wv}$) versus equivalence ratio ($\phi$):

$$\frac{(\Delta H_{ch})_{vc}}{(\Delta H_{ch})_{wv}} = 1 - \frac{0.97}{exp\left[\left(\frac{\phi}{2.15}\right)^{-1.2}\right]} \quad (4)$$

The heat released during the combustion, as well as the flame temperature, are controlled by the thermodynamics of energy conversion between reactants and products. The dependence of these two parameters, heat and temperature, on the fuel / air ratio is shown in Fig. 1 [34]. This figure shows that the heat released when burning the fuel, which would be equivalent to the HRR, is constant for the lean mixtures (excess oxidant). This is because all the fuel released in the pyrolysis is consumed. However, this heat decreases for rich mixtures (excess fuel), since there is not enough $O_2$ to burn all the released fuel. The flame temperature has a maximum under stoichiometric conditions (*st*) (fuel-oxygen ratio for complete combustion) and decreases for mixtures with excess air (more air to heat) and mixtures with air deficiency (less fuel burned).

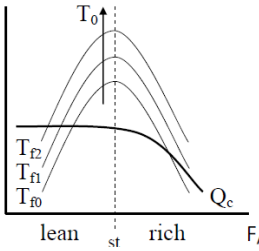


**Fig. 1.** Dependence of heat release ($Q_c$) and flame temperature ($T_0$) versus fuel/air ratio (F/A) [34].

A way to determine the relationship between fuel and air is the equivalence ratio, which determines the instantaneous relationship between fuel flow, oxygen flow and the stoichiometric coefficient for the analysed fuel. This equivalence ratio is widely used in gas combustion efficiency studies, in which the fuel / oxygen mixture is easily controllable, however, in the case of solid fuels and in the study of fires this relationship is difficult to calculate. That is why the concept of the global equivalence ratio (GER) has appeared. The GER can be used to express the total ventilation of a control volume, such as a fire enclosure. However, due to the complex interaction between the plume and the upper and lower layers, as well as the possible spread of fire, there is no single definition for GER. The GER can be calculated with the Eq. (5). It requires to introduce the mass of the fuel (integral of the HRR curve over the heat of combustion($\Delta H_c$)), the mass of oxygen entering the room (integral of the air mass flow ($\dot{m}_{air}$) introduced by the ventilation system in the enclosure multiplied by the density of the air ($\rho_{air}$)) and the $O_2$ concentration in the air ($Y_{O2,Air}$).

$$GER = \frac{1}{r_{O_2}} \times \frac{m_f}{m_{O_2}} = \left(\frac{1}{\phi_{C_xH_y,st} \times Y_{O2,Air}}\right) \times \frac{\int_{t_0}^{t_f} \left(HRR(t)/\Delta H_c\right) dt}{\rho_{air}\left(\int_{t_0}^{t_f} \dot{m}_{air}(t) dt\right)} \quad (5)$$

As it can be seen in the previous equation, it is necessary to know the HRR released in the combustion to calculate the GER. However, in our case this HRR is the value that we intend to calculate with our model. For this reason, it is considered the HRR calculated for an open enclosure. That is the HRR obtained by applying original FLASH-CAT for the same cable trays. The application of the original FLASH-CAT model will consider same input parameters (time to ignition, HRRPUA, horizontal spread rate) but without considering their reduction caused by the lack of oxygen for combustion. Then, this HRR is divided by the heat of combustion to estimate the total fuel gases released, despite the fact that in the new enclosure some fuel gases may not contribute to combustion.

Finally, GER value is used to define the HRRPUA released by the cables and the horizontal spread rate. A distinction has been made between fires with under-ventilated conditions (GER greater than 1), and well ventilated (GER less than 1). In the case of a well-ventilated scenario, the same HRR released will be maintained as the gases generated in the pyrolysis have enough oxygen to burn. However, the temperature of the flame decreases, and as a large quantity of air has to be heated, a decrease in the horizontal spread rate in the cable trays will be considered. To do so, model employs the following equation:

$$S = S_0 \cdot GER^2 \quad (6)$$

where $S_0$ is the horizontal spread rate under stoichiometric conditions [m/h]. This equation is based on the equation used by the IRSN in [21] to adjust the horizontal spread rate with the squared $O_2$ concentration. When an under-ventilated scenario is analysed, some pyrolysis gases produced may not have enough $O_2$ for combustion. In this case, the HRR will decrease, and thus, the horizontal spread rate will be reduced. The following equations, based on those described by the IRSN in [21], allow to estimate the HRRPUA and the horizontal spread rate for under-ventilated conditions.

$$HRRPUA = HRRPUA_0/GER \quad (7)$$

$$S = S_0/GER^{1/2} \quad (8)$$

Note that in the adaptation of these equations with respect to those described in [21] the factor $x(O_2)$ used in these equations is less than 1, while in the present case the GER is greater than 1.

Fig. 2 shows a comparison of the proposed equation (7) to consider the decrement of the HRRPUA associated with the decreasing of the O2 available for combustion (GER increasing) versus the experimental results provided in the SFPE Handbook [33]. Proposed equation shows a good approach to the experimental data. Note that the ratio of ventilation-controlled to well-ventilated chemical heat of combustion defined in [33] is equivalent to the ratio of ventilation-controlled to well-ventilated HRRPUA.

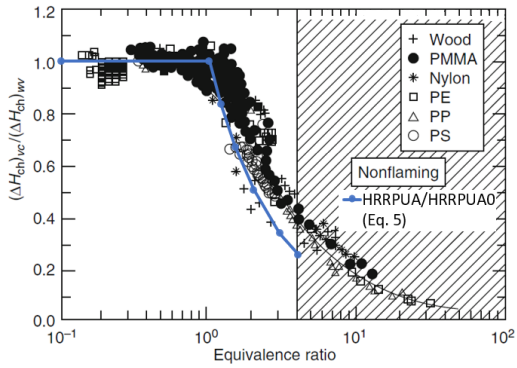


**Fig. 2.** Comparison of the experimental ratio of ventilation-controlled to well-ventilated chemical heat of combustion versus equivalence ratio taken from [33] with the equation (5) proposed. (Fig. modified from [33])

## Horizontal fire spread

The definition of the horizontal propagation of the fire in each cable tray was carried out in one direction, and in two senses through symmetry (Fig. 3). It should be noted that the original FLASH-CAT methodology was validated and calibrated considering this type of one-dimensional horizontal propagation, and considering that the ignition source affects the entire width of the cable tray, as it is done in the current modified version.

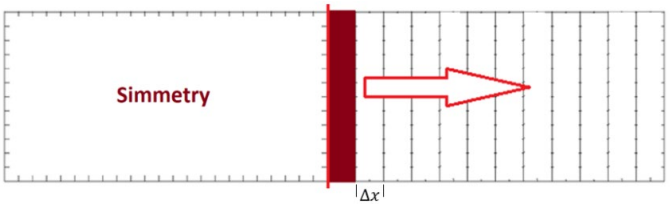


**Fig. 3.** Fire spread calculation in FLASH-CAT model.

Each ignited layer of cell (red cell in Fig. 3) will affect the adjacent cell. It is considered in the proposed model that the adjacent cells will ignite when the necessary time passes for the spread rate to make the propagation length reach the size of a cell (spatial step $\Delta x$), counting from the moment when the initial cell ignited. This will take place in time t, calculated with the Eq. (9):

$$t = t_{ign} + \frac{s}{\Delta x} \tag{9}$$

where $t_{ign}$ is the time to ignition of the adjacent cell. From time *t*, the new cell will ignite, releasing the HRRPUA imposed on the model and beginning to affect the neighboring cell through the spread rate. The method defines a parameter called normalized horizontal propagation distance (HPD), which indicates the time steps necessary for a cell to ignite and it is calculated using the following equation:

$$HPD = \frac{s \cdot \Delta t}{\Delta x} \tag{10}$$

Where $\Delta t$ is the time step. The inverse of this parameter indicates the number of "time steps" for a cell to ignite. HPD is therefore an indication of the proportion of the cell affected in a time step by another cell.

**Heat release rate**

In the NUREG/CR 7010 [13], where the original FLASH-CAT is described, it is recommended the use of the HRRPUA values of 150 kW/m$^2$ for the thermoset cables, and 250 kW/m$^2$ for the thermoplastic cables. This recommendation is based on the calibration and validation performed of the model, nevertheless thermokinetic properties of the cables and boundary conditions durning fire can highly influence the heat release by the cables. It is recommended in the present methodology to employ cone calorimeter to obtain the HRRPUA curve of the specific cables to be included in the model. This will give a better approximation of the behaviour of the specific cables.

According to the large amount of heat generally released in a cable tray fire scenario, it is proposed to perform the cone calorimeter test under a heat flux of 100 kW/m$^2$. In case cone calorimeter results are available under lower heat flux only, it can be applied a methodology as defined in FDS [12] to extrapolate burning rate data collected from a cone calorimeter or similar device to a different heat flux. This model proportionally scales time and the HRRPUA values of the experimental HRRPUA curve. Those parameters are adjusted by the ratio of the experimental cone heat flux to the desired incident flux.

Although the use of cone calorimeter can improve the aproximation of the model to the real behaviour of the cables, intrinsic characteristics of the cone calorimeter tests can affect the results. Cone calorimeter tests are performed using a sample of 100 mm x 100 mm located in a sample holder insulated in the back side. Nevertheless, this insulation can accumulate heat and provoque a second peak in the HRRPUA [35]. This second peak is typically found in the cone calorimeter tests of cables [36], nevertheless is not found in large scale tests. That is why we propose to not consider the second cone calorimeter HRRPUA peak.

## RESULTS AND DISCUSSIONS

In order to validate the proposed FLASH-CAT modification, two experimental test from PRISME 2 have been selected [16] [17] [21]. PRISME-2 Cable Fire Spreading (PR2-CFS) campaign investigates fire spread on complex fire sources, like horizontal cable trays or electrical cabinet, and fire consequences in a confined and ventilated multi-rooms facility. Cases PR2-CFS-1 and PR2-CFS-3 were selected, as they consider horizontal cable trays in an enclosure with ventilation. Fig. 4, taken from [21], represents the scheme of the experimental setup of the CFS tests.

Both the PR2-CFS-1 and PR2-CFS-3 fire tests involved a fire source composed of 5 horizontal cable trays. Two rooms of the DIVA facility (the fire and adjacent rooms) were involved in these fire tests and were connected by a doorway (see Fig. 4). PR2-CFS-1 fire test contain halogenated flame retardant (HFR) cables [37], while PR2-CFS-4 fire test employs a halogen free flame retardant (HFFR) cable [38]. Both PR2-CFS-1 and PR2-CFS-3 fire tests involved ventilation renewal rates (VRR) of 4 h$^{-1}$.

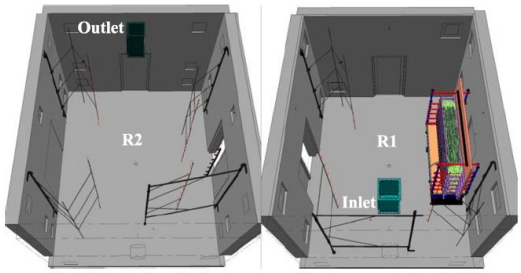


**Fig. 4.** Scheme of the experimental setup of the CFS tests [21].

**PRISME PR2-CFS-1**

Table 1 includes the input parameters to define the modified FLASH-CAT model of the PR2-CFS-1 fire tests. The spread rate considered in the model is the recommended in the NUREG/CR 7010 for the thermoset cables (1.1 m/h). The time to ignition of the different trays was obtained from [20], where same cables where used in an open configuration. The time to ignition of the different cable trays are very close to each other, considering values of 40 s, 58 s, 66 s, 72 s and 86 s for the trays 1 to 5, respectively.

**Table 1. Input parameters to define the modified FLASH-CAT model of the PR2-CFS-1 fire tests**

| Cable Type | Nº Cables per tray | Nº Trays | Tray Spacing [m] | Tray Length [m] |
|---|---|---|---|---|
| HFR cables | 49 (13mm) | 5 | 0.3 | 2.4 |
| Tray Width [m] | HRRPUA [kW/m$^2$] | Heat of Combustion [kJ/kg] | Spread Rate [m/h] | Vertical propagation angle [º] |
| 0.45 | Modified cone for 100 kW/m$^2$ | 22 [21] | 1.1 | 32 |

The HRRPUA considered for the cables is represented in the Fig. 5, with the original cone calorimeter test result for the cable under a heat flux of 50 kW/m$^2$ [37] (black solid line), and it modifications to remove the second peak (grey solidline). The extrapolation of the cone calorimeter HRRPUA to the heat flux of 100 kW/m$^2$ is represented by the grey dashed line.

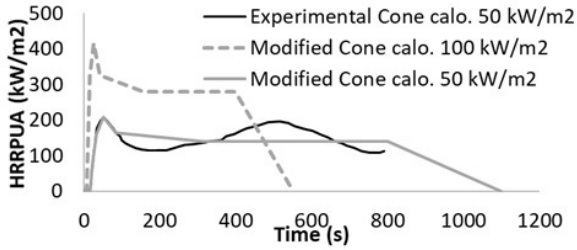


**Fig. 5.** Cone calorimeter HRRPUA modification for the FFR cables.

Using these input parameters in the modified FLASH-CAT model, we found the total HRR shown in the Fig. 6, where it is compared with the CFS1 experimental test results [21]. As it can be seen in the figure, although the proposed model predicts a higher initial peak, the global behaviour and the total heat release is estimated properly. Both, experimental and simulated, have a quick growth, until the fully developed phase is reached. Predictions extend the fully developed phase for around 500 s, while the experimental fully developed step is of around 330 s. Then, the HRR decreases in both cases. It is also included in the Fig. 6 the application of the FLASH-CAT modification without considering the reduction of the horizontal spread rate in the cable trays (grey curve). As it can be seen low influence in the results is found in this scenario.

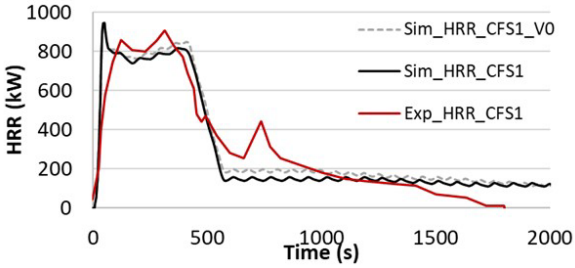

**Fig. 6.** Experimental and simulated CFS1 HRR curve.

## PRISME PR2-CFS-3

Table 2 includes the input parameters to define the modified FLASH-CAT model of the PR2-CFS-3 fire tests. The spread rate considered in the model is the recommended in the NUREG/CR 7010 for the thermoset cables (1.1 m/h). The time to ignition of the different trays was obtained from [20], where same HFFR cables where used in an open configuration. Values of 264 s, 396 s, 603 s, 741 s and 834 s where used for the ignition of the trays 1 to 5 respectively. The comparison of these values versus those employed in the PR2-CFS-1 fire scenario shows the relevance of the cable composition in the definition of the input parameters.

**Table 2. Input parameters to define the modified FLASH-CAT model of the PR2-CFS-3 fire tests**

| Cable Type (%) | Nº Cables per tray | Nº Trays | Tray Spacing [m] | Tray Length [m] |
|---|---|---|---|---|
| HFFR cable | 32 (20 mm) | 5 | 0.3 | 2.4 |
| Tray Width [m] | HRRPUA [kW/m2] | Heat of Combustion [kJ/kg] | Spread Rate [m/h] | Vertical propagation angle [º] |
| 0.45 | Modified cone for 100 kW/m$^2$ | 27 [21] | 1.1 | 32 |

The HRRPUA considered for the cables is represented in the Fig. 7, with the original cone calorimeter test result for the cable under a heat flux of 80 kW/m$^2$ [38] (black dashed line), and it modifications to remove the second peak (grey solid line). The grey dashed line represents the HRRPUA curve extrapolated for a cone calorimeter under a heat flux of 100 kW/m$^2$.

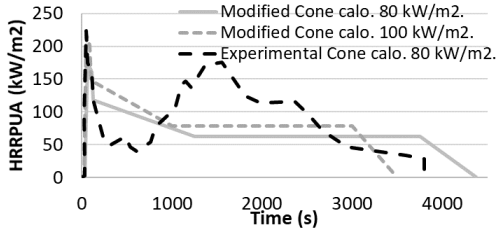


**Fig. 7.** Cone calorimeter HRRPUA modification for the HFFR cables.

Using these input parameters in the modified FLASH-CAT model, we found the comparison of the total HRR shown in the Fig. 8, where it is compared with the CFS3 experimental test results [21]. As it can be seen, the proposed model predicts the initial increase of the HRR, and then, the predicted HRR stay in a fully developed fire with a HRR of around 300 kW until its final decrease. As in the previous fire scenario, the total amount of heat release is similar between the experimental and the prediction. It is also included in the Fig. 8 the application of the FLASH-CAT modification without considering the reduction of the horizontal spread rate in the cable trays (grey curve). It has a lot of influence in the HRR peak as more amount of cables are burning at the same time. As it can be seen, although it differs more from the experimental test results, it is in the side of safety.

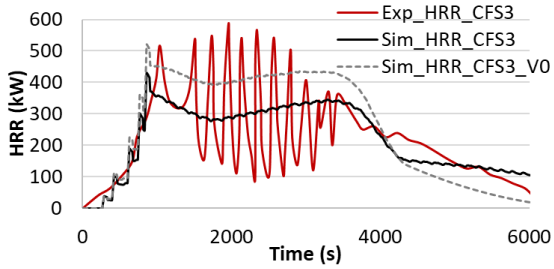


**Fig. 8.** Experimental and simulated CFS3 HRR curve.

## CONCLUSIONS

A modified FLASH-CAT model is proposed to predict horizontal cable tray fires in a mechanically ventilated enclosure. This model allows to evaluate the effect of oxygen in the fire development and the heat release by the cable trays. Additional considerations are defined to employ in the model the HRRPUA release by the actual cables. To do so, it is defined a methodology to consider the HRRPUA measured in the cone calorimeter test. It is evaluated the hypothesis that, due to the large amount of heat typically released in these scenarios, a HRRPUA curve for the cables obtained from a cone calorimeter test performed under a heat flux of 100 kW/m$^2$ will produce a more realistic representation of the HRR released by the cables.

Proposed model has been validated versus two experimental tests obtained from PRISME-2 Cable Fire Spreading campaign that investigates fire spread on horizontal cable trays in a confined and ventilated multi-rooms facility. PR2-CFS-1 and PR2-CFS-3 fire tests were considered. Both cases contain a fire source composed of 5 horizontal cable trays. PR2-CFS-1 fire test contain halogenated flame-retardant cables, while PR2-CFS-4 fire test employs halogen-free flame-retardant cables. Both PR2-CFS-1 and PR2-CFS-3 fire tests involved ventilation renewal rates (VRR) of 4 h$^{-1}$.

Model predicts the total HRR released by the analysed cable trays under the defined ventilation conditions. Model HRR results show a good approach to the experimental test results, obtaining similar tendency in the curves, and also, the total heat release by the cable trays in both analysed fire scenarios. Nevertheless, more work is required to validate the proposed model with more experimental tests by using different types of cables and under different ventilation conditions.

## ACKNOWLEDGES

The authors would like to thank the Consejo de Seguridad Nuclear for the cooperation and co-financing the project “Metodologías avanzadas de análisis y simulación de escenarios de incendios en centrales nucleares”.

## REFERENCES

[1] «U.S.NRC The Browns Ferry Nuclear Plant Fire of 1975 and the History of NRC Fire Regulations,» 2009.

[2] «NUIREG/CR-6738, SAND2001-1676P, Risk Methods Insights Gained From Fire Incidents, Sandia National Laboratories, U.S. NRC,» 2001.

[3] «CSN,» [En línea]. Available: https://www.csn.es/en/-/el-plenario-de-ensreg-selecciona-la-proteccion-contra-incendios-en-centrales-nucleares-como-tema-para-el-segundo-ejercicio-de-revision-tematica.

[4] G. Rein, J. L. Torero, W. Jahn, J. Stern-Gottfried, N. L. Ryder, S. Desanghere, M. Lázaro, F. Mowrer, A. Coles, D. Joyeux, D. Alvear, J. Capote, A. Jowsey, C. Abecassis-Empis y P. Reszka,

«Round-Robin Study of a priori Modelling Predictions of The Dalmarnock Fire Test One,» Fire Safety Journal, vol. 44 (4), nº doi:10.1016/j.firesaf.2008.12.008, pp. 590-602, 2009.

[5] W. Jahn, G. Rein y J. L. Torero, «The Effect of Model Parameters on the Simulation of Fire Dynamics,» de Fire safety science–proceedings of the ninth international symposium, 2008.

[6] «EPRI 1023259 NUREG 1934 Nuclear Power Plant Fire Modeling Analysis Guidelines (NPP FIRE MAG), U. S. NRC, EPRI,» 2010.

[7] «NUREG-1925, Rev. 4, Research Activities FY 2018-2020, U. S. NRC,» Washington, D.C. , March 2018.

[8] «Nuclear Safety NEA/CSNI/R(2014)11, Best Practice Guidelines for the Use of CFD in Nuclear Reactor Safety Applications – Revision,» OECD, NEA, February 2015.

[9] «NUREG-6905: Report of Experimental Results for the International Fire Model Benchmarking and Validation Exercise # 3,» United States Nuclear Regulatory Commission (U.S. NRC), Washington, DC, USA, 2006.

[10] M. K. Dey, «Evaluation of Fire Models for Nuclear Plant Fire Safety and Risk Analysis, Deytec Tec hnic al Report No. 2009-05,» 2009.

[11] K. McGrattan, «NISTIR 7338 Evaluation of Fire Models for Nuclear Power Plant Applications Benchmark Exercise #3 International Panel Report,» 2007.

[12] K. McGrattan, S. Hostikka, J. Floyd, R. McDermott y M. Vanella, «NIST Special Publication 1019, Sixth Edition, Fire Dynamics Simulator User's Guide,» NIST, VTT, Maryland, USA, 2019.

[13] «NUREG/CR-7010 Cable Heat Release, Ignition, and Spread in Tray Installations During Fire (CHRISTIFIRE), Phase 1: Horizontal Trays,» 2012.

[14] «NUREG/CR-7010 Cable Heat Release, Ignition, and Spread in Tray Installations During Fire (CHRISTIFIRE), Phase 2: Vertical Shafts and Corridors,» 2013.

[15] M. Röwekamp, J. Dreisbach, W. Klein-Heßling, K. McGrattan, S. Miles, M. Plys y O. Riese, «International Collaborative Fire Modeling Project (ICFMP): Summary of Benchmark Exercises No. 1 to 5 ICFMP Summary Report,» September 2008.

[16] «NEA/CSNI/R(2017)14, Investigating Heat and Smoke Propagation Mechanisms in Multi-Compartment Fire Scenarios. Final Report of the PRISME Project, OECD, NEA,» January 2018.

[17] S. Suard, P. Van Hees, M. Roewekamp, S. Tsuchino y R. Gonzalez, «Fire development in multi‐compartment facilities: PRISME 2 project,» Fire and Materials, vol. 43, nº DOI: 10.1002/fam.2754, p. 433‒435, 2019.

[18] T. Beji, S. Verstockt, P. Zavaleta y B. Merci, «Flame Spread Monitoring and Estimation of the Heat Release Rate from a Cable Tray Fire Using Video Fire Analysis (VFA),» Fire Technol. , vol. 52 , p. 611–621, 2016.

[19] S. Bascou, P. Zavaleta y F. Babik, «Cable tray FIRE test simulations in open atmosphere and in confined and mechanically ventilated compartments with the CALIF3S/ISIS CFD software,» Fire and Materials, nº DOI:10.1002/fam.2680, pp. 1-18, 2018.

[20] P. Zavaleta y T. Beji, «Improved Assessment of fire spread over horizontal cable tray supported by video fire analysis,» Fire technology, vol. 55, pp. 233-255, 2019.

[21] W. Plumecocq, L. Audoin y P. Zavaleta, «Horizontal cable tray fire in a well-confined and mechanically ventilated enclosure using a two-zone model,» Fire and Material, nº DOI:10.1002/fam.2698, pp. 1-13, 2019.

[22] J. Spille, O. Riese y J. ZehfuB, «Experimental and numerical investigations of the influence of cable arrangements on cable trays concerning mass loss rate and fire propagation,» de SMIRT 24. 15 th International Seminar on fire safety in nuclear power plants and Installations, Bruges, Belgium, 2017.

[23] «NUREG-1934. Nuclear Power Plant Fire Modeling Analysis Guidelines (NPP FIRE MAG),» 2012.

[24] K. Liang, X. Hao, W. An, Y. Tang y Y. Cong, «Study on cable fire spread and smoke temperature distribution in T-shaped utility tunnel,» Case studies in thermal engineering, vol. 14, nº DOI:10.1016/j.csite.2019.100433, 2019.

[25] J. Hietaniemi, S. Hostikka y J. Vaari, «FDS simulation of fire spread-comparison of model results with experimental data,» VTT Building and Transport, 2004.

[26] T. Beji y B. Merci, «Numerical simulations of a full‐scale cable tray fire using small‐scale test data,» Fire and Materials. , nº DOI: 10.1002/fam.2687, p. 1–11, 2018.

[27] S.-Y. Mun y C.-H. Hwang, «Experimental and Numerical Studies on Major Pyrolysis Properties of Flame Retardant PVC Cables Composed of Multiple Materials,» Materials, vol. 13, nº DOI:10.3390/ma13071712, 2020.

[28] T. Hehnen, L. Arnold y S. La Mendola, «Numerical Fire Spread Simulation Based on Material Pyrolysis—An Application to the CHRISTIFIRE Phase 1 Horizontal Cable Tray Tests,» Fire, Vols. %1 de %23, 33, nº doi:10.3390/fire3030033, 2020.

[29] T. Hehnen, L. Arnold, P. van Hees y S. La Mendola, «Simulation of fire propagation in cable tray installations for particle accelerator facility tunnels,» de 8th International symposium on tunnel safety and security, Boras, Sweden, 2018.

[30] «GRS-124. Evaluation of fire models for nuclear power plant applications. Benchmark exercise No. 5: Flame spread in cable tray fires,» ISBN 978-3-931995-81-2, 2006.

[31] M. Röwekamp, W. Klein-HeBling, O. Riese y H. P. Berg, «Cable tray fires - Experiments and results of fire simulation codes,» Journal of Konbin, nº DOI: 10.2478/v10040-008-0057-z, 2008.

[32] R. Carvel y H. Ingason, «Chapter 88 Fires in Vehicle Tunnels,» de SFPE Handbook of Fire Protection Engineering Fifth Edition, Springer, 2016.

[33] M. Khan, A. Tewarson y M. Chaos, «Chapter 36 Combustion Characteristics of Materials and Generation of Fire Products,» de SFPE Handbook of Fire Protection Engineering Fifth Edition, Springer, 2016.

[34] C. Fernández-Pello, «On Fire Ignition,» de Fire Safety Science-Proceedings of the Tenth International Symposium, DOI: 10.3801/IAFSS.FSS.10-25, 2011.

[35] G. Zhao, T. Beji, B. Merci y D. Zeinali, «Numerical study on the influence of in-depth radiation in the pyrolysis of medium density fibreboard,» de Proceedings of the Fire and Materials 2017 Conference, 2017.

[36] S. Grayson, P. Van Hees, U. Vercellotti, H. Breulet y A. Green, «Fire Performance of Electrical Cables- new methods and measurement techniques. Final report on the European Commision SMT Programme Sponsored Research Project SMT4-CT96-2059,» ISBN 0 953212 5 9, 2000.

[37] J. Mangs y S. Hostikka, «VTT-R-06873-12. Experimental characterization of the MCMK cable for fire safety assessment,» 2013.

[38] R. Meiniera, R. Sonniera, P. Zavaleta, S. Suard y L. Ferry, «Fire behavior of halogen-free flame retardant electrical cables withthe cone calorimeter,» Journal of Hazardous Materials, vol. 342, p. 306–316, 2018.

# Fire Behavior of Aluminium Composite Panel Material using a Small Scale Test Method

**Sirait V.[1] , Nugroho R. A.[1], Nugroho Y.S.[1,*]**

*[1]Fire Safety Engineering Research Group, Department of Mechanical Engineering, Universitas Indonesia, Kampus UI Depok 16424, Indonesia*
**Corresponding author's email: yulianto.nugroho@ui.ac.id*

## ABSTRACT

The human need for high-rise buildings increases along with the increase of the human population. At the same time, the amount of available land tends to remain constant. Research supporting high-rise buildings construction that can accommodate these needs is always carried out to increase building safety. The use of facades in building construction for energy-saving and aesthetic reasons has also begun to be massively applied. It offers thermal load efficiency since the façade will block the sunlight directed to the high-rise building surface. However, apart from the advantages provided by installing facades in buildings, there are several consequences on the safety side caused by the façade (i.e., Aluminium Composite Panel-ACP) material itself. This study aims to support the wealth of knowledge in realizing the safety of a building with a facade, especially in a fire building. In this work, a newly developed test facility was introduced. This research facility enables the measurement of the mass-loss rate of the materials and direct measurement of the surface temperatures of the sample. In particular, this work studies the effect of the initial flame contact point with the façade materials. This study found that the mass loss rate of the ACP sample due to the dripping of the insulation material increased as the pilot flame directly impinged the core material made of high-density polyethylene.

**KEYWORDS:** Facade, Aluminium Composite Panel, Building fire.

## INTRODUCTION

The facade is the outermost layer of a building in architectural and ornamental envelopes **[1]**. In a hot climate area, façade installation will affect the building thermal load for cooling energy-saving purposes by blocking the sunlight directed to the building **[2]** and affect thermal loss for heating energy saving purposes by blocking the heat coming from inside the building [**3].** However, the facade of the building needs to be considered carefully. One of the hazards caused by installing a facade is the potential for flame to spread through the air gaps in the façade.

The flame spread phenomenon in a building fire caused by cladding has occurred several times in the whole of the world. One of the well-known cases is the Grenfell tower fire in England on June 14$^{th,}$ 2017, with 72 people were perished in the incident. The building used aluminium composite panel cladding, and the fire spread through the cladding from its source, which was a kitchen of a flat. **[8].** Apart from the flame spreading through the façade, the flame also spread from the falling material of the façade **[8]**, which was an aluminium composite panel. Another case that happened is a dwelling building in Jecheon, South Korea **[6].** The fire was initiated firstly from a car in an underground park and propagated through the cladding made from the aluminium composite panel. Twenty-nine people died in this case.

Butler, in 2009, tried to analyze the behavior of thermoplastics as its concern to flame spread in a building fire **[7]**. Through the research, Butler explained the model of melting and dripping thermoplastic objects in fire. Huang, in 2018, tried to analyze the dripping phenomenon of wire coated with Polyethylene **[4]**.

Referring from the existing research, this research tries to analyze the behavior of aluminium composite panels as building façade material in a building fire through the small-scale test method.

The result in this paper shows us that the bigger flame directly impinged the core material of the aluminium composite panel is, thus the more substantial possibility of fire spread through material drip happened.

## METHODOLOGY

The lab-scale experimental setup is used in this research. The setup is made to enable capturing ACP's behavior in building fire phenomena. This experiment tries to examine the character of the aluminium composite panel in fire, especially about the fire spread through the material caused by dripping material. These experiments map the possibilities of the dripping fire phenomenon based on the location of flame impingement at the aluminium composite panel. The specimen's mass and surface temperature are being logged during the testing time to define the specimen's response to the flame ejected. The duration of the flame ejection is decided to be seven minutes. It is calculated from the empirical pre-experiment trial considering the safety aspect of the experiments and the ability of the setup to handle the growth of the fire that occurred in the experiment.

The specimen that is being tested is a commonly sold aluminium composite panel in Indonesia. The Fourier transform infrared spectroscopy (FTIR) test for analyzing the core material of the aluminium composite panel was done in the Center for Materials and Processing Failure Analysis (CMPFA) Fakultas Teknik Universitas Indonesia.

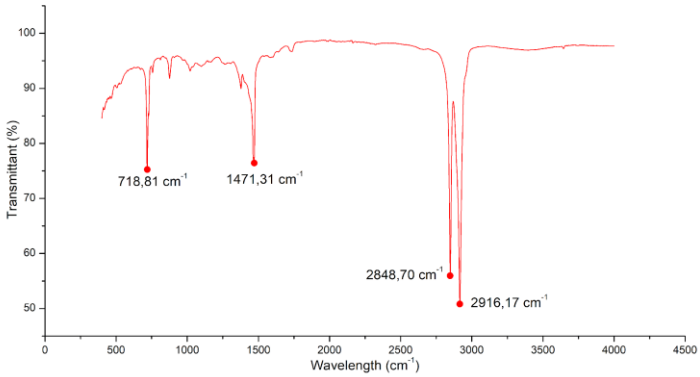


**Fig. 1.** FTIR Test Result

The **Fig.1**. FTIR test result graph shows us absorbance bands at wavelength 2916.17 $cm^{-1}$, 2848.70 $cm^{-1}$, 1471.31 $cm^{-1}$, and 718.81 $cm^{-1}$. The characteristic of polyethylene material absorbance bands are located at 2914 $cm^{-1}$, 2847 $cm^{-1}$, 1470 $cm^{-1}$and 718 $cm^{-1}$ **[5]**. Based on the comparison of the test result and the paper, the core material is identified as polyethylene.

### Experimental setup and procedure

These experiments assume that the specimen is the building façade and the flame source is the fire source that occurred in the building. Since the façade in the building is installed with an air gap between the building surface and the cladding, we also try to make a gap between the specimen and the flame source. The flame in this experiment represents a building fire spread out through a building window from its source located inside the building. The flame in this experiment will directly impinge

the specimen that does not being painted since the painted side one will face directly to the environment due to its aesthetics in the real installation. Referring to Butler's study in 2009, we benchmarked and modified the experiment setup to gather the mass measurements as contributions to this.

The experiment uses an aluminium profile as the testing frame structure material to support devices and the research specimens' placement. The flame torch is used to represent the building fire. The thermal camera is used to measure the surface temperature that is not being painted.

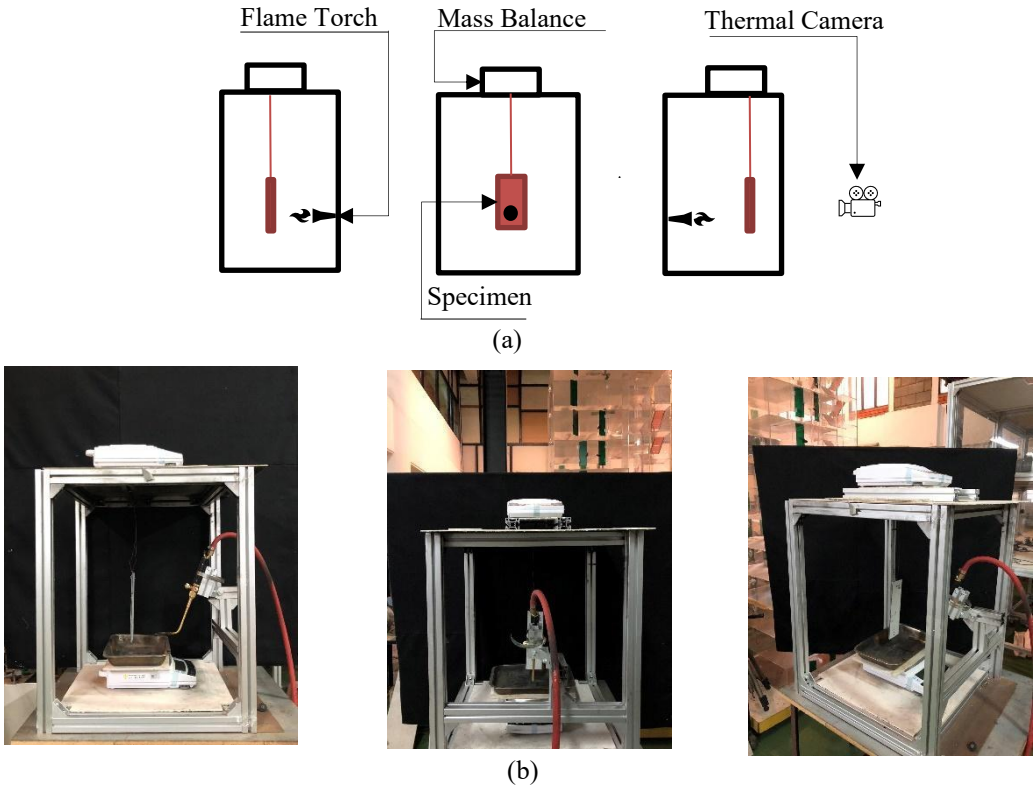


**Fig. 2.** Experimental setup (a) Schematic; (b) Real setup

**Table 1. Experiment Setup Type Numbering**

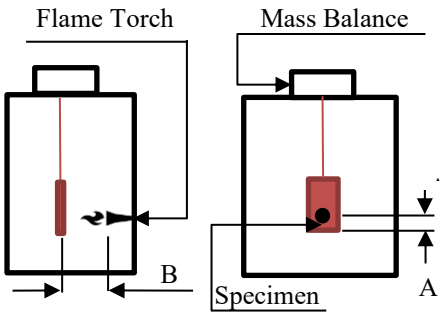


| Type | A(cm) | B(cm) |
|---|---|---|
| 1 | 1 | 4 |
| 2 | 3 | 4 |
| 3 | 5 | 4 |
| 4 | 1 | 6 |
| 5 | 3 | 6 |
| 6 | 5 | 6 |

There are six setup variations with two adjustable variables. Those two variables are the distance between the flame and the specimen, and the following variable is the distance of the flame impingement point measured from the base of the specimen. The details of variation is described inside **Table 1** with the additional variable information image beside the table.

This research uses liquefied petroleum gas (LPG) as the fuel for the flame. LPG was chosen because of its simplicity in the marketplace in the area where the research took place. The diffusion flame mechanism is also chosen in this experiment to represent the building fire phenomenon that happens in the environment realistically. The flame in all experiments remains in the same amount while it is quantified by measuring its heat flux. The measurement setup uses the experiment setup as shown in **Fig.2.** When the LPG flame impinges the heat flux sensor surface, the measurement value could reach up to 120 kW/m$^2$ .

**Table 2. Measurement Equipment Information**

| Mass balance | | Thermal Camera | |
|---|---|---|---|
| Capacity | 4200g | Thermal sensitivity/NETD | <0.05°C @ +30°C (+86°F) / 50mK |
| Sensitivity Stability against temperature range | ± 3 ppm/°C (10 to 30°C) | Object Temperature Range | –25 to +100°C (–13 to 212°F) –40 to +550°C (–40 to +1022°F |
| Pan size | Approx. 170 x 180 mm | | |
| Surface Thermocouple | | | |
| Type | Type K | Accuracy | ±5% or ± 5°C of reading |
| Heat Flux Transducer | | Fluke Thermogun | |
| Type | heat flux model no. 64-10sb-20 | Infrared temperature range | -40°C to 800°C (-40°F to 1472°F) |
| Output Signal | linear output, 10 millivolts | Infrared accuracy | < 0°C (32°F): ±(1.0°C (±2.0°F) + 0.1°/1°C or°F); |
| Maximum Allowable Operating Body Temperature | 400°F | | > 0°C (32°F): ±1% or ±1.0°C (±2.0°F), whichever is greater |

The specimen size for this experiment is 10 x 25 cm$^2$, using 4mm-thick aluminium composite panel. It is formed with two layers of 0.21mm-thick aluminium in the front and the back and 3.38mm-thick polyethylene in the middle of those layers. It will be hung to be able to measure the mass while there is a flame ejection on the surface. The specimen is hung on a piece of wire as a connector to a mass balance in a steady position, so it will not give much error on mass measurement because of its movement. The thermal camera was placed on the backside of the experiment frame to capture the surface temperature of the specimen. It was done by using a spirit level to make sure the device was well-laid on the top of the experiment structure. The experiment started with turning on the stopwatch to ensure the time frame and the measurement unit were being turned in sequence.

## RESULT AND DISCUSSION

There are three times repetitions for every type of setup experiment. As a result, six types of setup of experiments is classified into two different phenomena. The first phenomenon, so-called the growing

flame, occurs when the flame touches the insulation layer so that the insulation material experiences intense heating and burns. Meanwhile, the second phenomena occurs when the heat source cannot heat up the insulation materials to their ignition temperature, so-called the non-growing flame. The growing flame happened in the type 1 and type 4 experiment setup. Meanwhile, the non-growing flame results are shown in types 2, 3, 5, and 6 experiments. Type 1 and 4 experiment setup results show a considerable amount of mass loss reaching the peak mass loss rate at around 400s, close to the end time of flame ejection at 420s. The growing flame in type 1 and type 4 experiments setup was caused by direct contact between the flame and the insulation material of the aluminium composite panel core. The growing flame phenomenon caused significant mass loss. **Fig. 3** shows the mass loss percentage and mass loss rate percentage of type 1 and type 2, respectively. The non-growing flame phenomena were identified in all six types of the experiment setup.

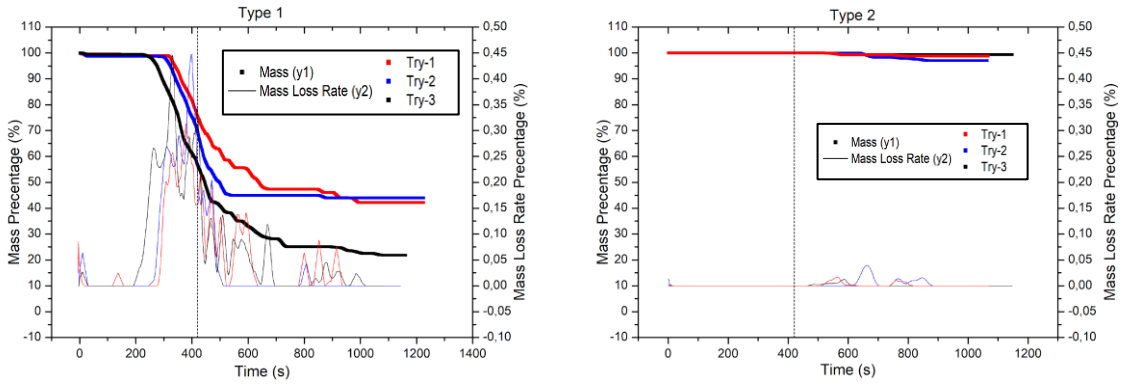


(a) (b)

**Fig. 3.** Mass loss and mass loss rate of experiments. (a) Type 1; (b) Type 2

The growing flame phenomenon was caused by the polyethylene that became an extra fuel for the flame ejected from the flame torch. The flame size gets bigger upon the time as shown in **Fig.4.a**. It could be possible since type 1 and 4 setup experiments located the flame impingement point only 1cm from the base of the specimen, where it is the nearest distance between the impingement point and the uncovered part of the core material, polyethylene, compared to another experiment setup. The growing flame phenomenon will start with burning the lowermost side of the aluminium composite panel, and it will last until the insulation burns out. However, the experiment results also show that the air supply to the burning insulation material plays a role. The amount of air decreased by time since the space for air entering the burning space (polyethylene between the aluminium layer) got smaller because at upper location of the polyethylene, that will be burned later, is further to the lowermost sides of the specimen. The farther the location of the polyethylene core from the initial contact point with the impinging flame, the less air supply because it will only get air supply from the specimen side.

There is no growing flame in type 2, 3, 5, and 6 setups since there is no direct contact between the flame ejected and the aluminium composite panel core material. The flame kept impinging the aluminium layer during seven minutes of flame ejection and it didn't cause any additional flames beside the flame ejected from the torch, as shown in **Fig.4.b.**

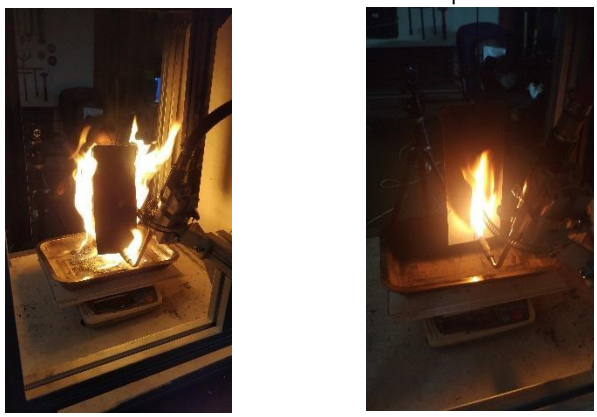

(a) (b)

**Fig. 4.** 2 Phenomenons (a) Growing flame (b) Non-Growing Flame

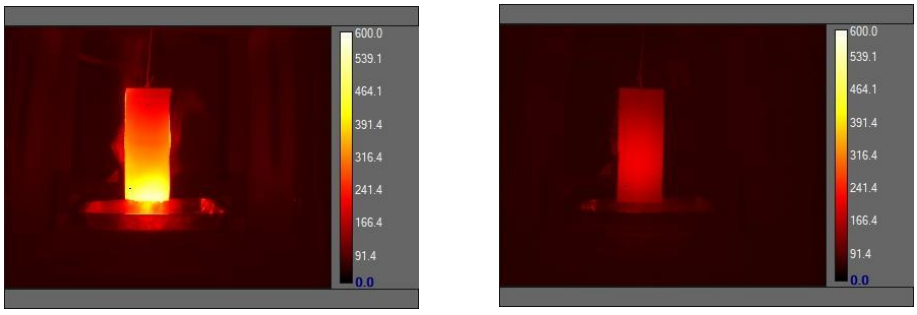


(a) (b)

**Fig. 5.** Surface Temperature Profile at 420s. (a) Type 1; (b) Type 2;

The surface temperature of the specimen captured by the thermal camera is shown in **Fig.5**. The figures were captured at 420s, the time the flame torch is just being turned off. The growing flame phenomenon figure shows a higher value of its peak temperature as shown in **Fig 5.a**. It was caused by the presence of flame grown (**Fig.4.a**) by the polyethylene as its extra fuel. This growing flame phenomenon also causes the dripping fire phenomenon. It is captured in **Fig. 5.a** that there are small dots as a dripping fire image.

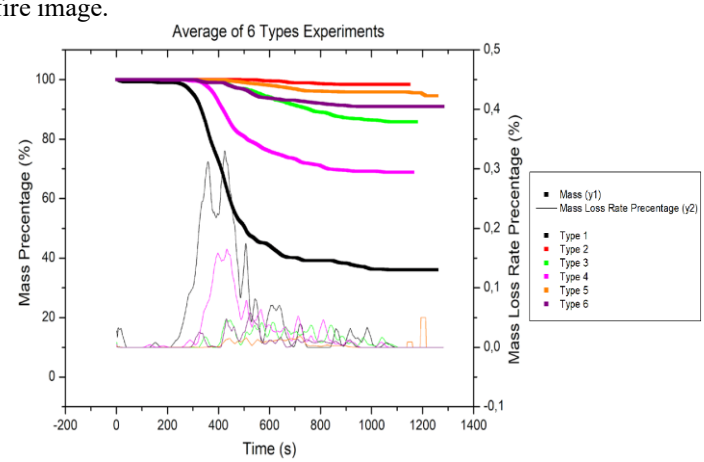


**Fig. 6.** Result comparison graph between 6 types of experiment setup

As result, **Fig. 6**. shows the comparison of those six types of experiments setup. It can be seen that type 1 and type 4 lose the mass specimen the most compared to others. It is caused by burned polyethylene. Burning polyethylene will slowly drip and leaving the specimen to fall down. When the burning polyethylene falls down, the material also carries the flame, so there will be new flame spots after the polyethylene falls.

It is also can be seen that type 1 loses more amount of mass than type 4. It is caused by the different amount of heat flux received to burn the specimen since the flame torch in type 1 is located nearer than in type 4. We also tried to measure the mass of dripping materials that happened in type 1 and type 4. Fig.7. shows that the dripping phenomenon in type 1 happened faster compared to type 4 caused by the greater heat flux received. There is also total mass loss measured in the dripping phenomenon. It is caused by a material that is volatile during the burning specimen phenomenon. There are some burned materials that could not be measured in the mass balance under the specimen.

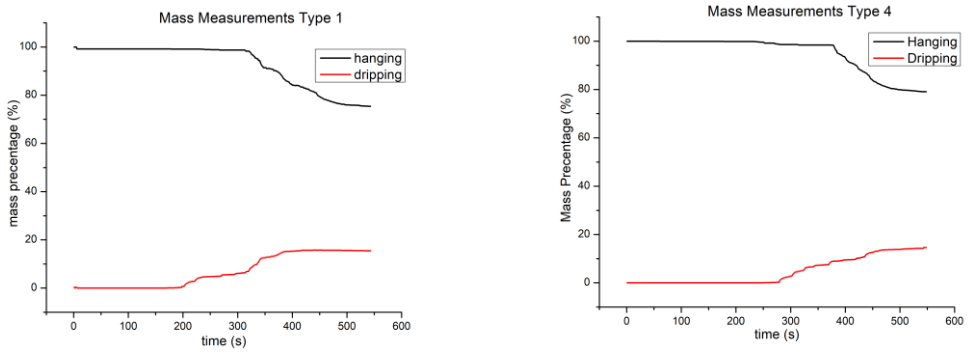


(a) (b)

**Fig. 7.** Mass of dripping materials (a) Type 1; (b) Type 4

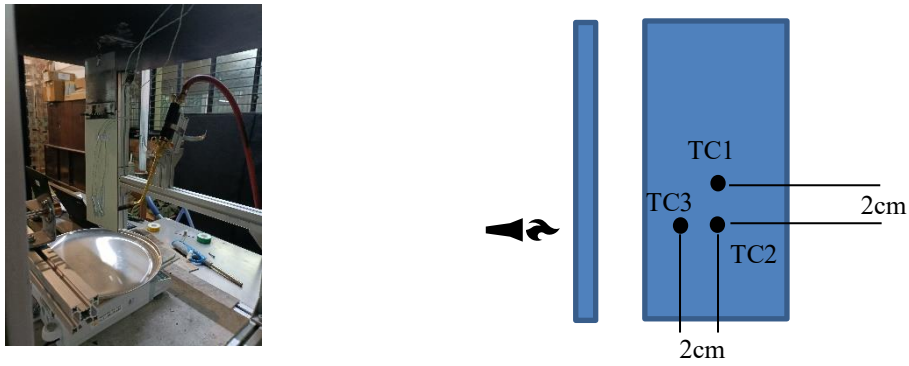


(a) (b)

**Fig.8.** Temperature measurement setup (a) real ; (b) schematic diagram.

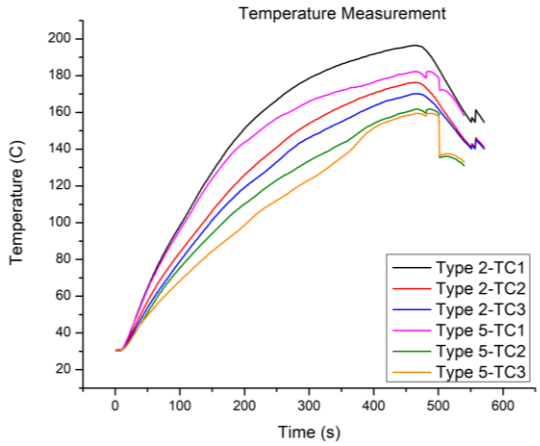


**Fig. 9.** Back surface temperature measurements

**Fig.9**. shows the temperature measurement of the type 2 experiment setup. This research tried to analyze the temperature more detailly on the heated surface and the back surface of the specimen. Using an infrared thermal gun, the temperature measurements on the heated surface could reached 350ºC (for non flame impingement case). The surface thermocouples are used for measuring the temperature of the back surface of the specimen, as shown in **Fig.8**. The temperature measured on the back surface is lower than on the heated surface. It is caused by the thermal conductivity of both aluminium and polyethylene material.

## CONCLUSION

All the trials of 6 types setup experiments concluded that the temperature profile in the specimen surface is affected by the distance between the flame source and the specimen. The growing flame phenomenon in type 1 and type 4, two setup experiments with the nearest flame impingement point distance from the specimen's base, is caused by direct contact between the flame and the core material of aluminium composite panel. The specimens in those setups also significantly lost their mass during the experiment. The dripping material phenomenon from the core material of the aluminium composite panel is also proven in this research. Apart from being an extra fuel for the flame growth, polyethylene adds more risk of fire spread through dripping material since the burning polyethylene fell, also bringing the flame together with the drip. The amount of heat flux received by the specimen, varied by adjusting the distance between the flame source and specimen, showed a positive correlation with the amount and dripping rate of the dripped polyethylene. The possibility of the dripping material phenomenon becomes bigger when the flame directly contacts the polyethylene as the core material of the aluminium composite panel.

## ACKNOWLEDGMENT

The authors would like to thank Universitas Indonesia for all the financial and facilities support for finishing this research, and to the Ministry of Education, Culture, Research and Technology of Republic Indonesia for supporting Mr. Viliasio Sirait education through the Beasiswa Unggulan Scholarship since the third semester in 2018 until the graduation in 2021.

**REFERENCES**

[1] C. Manton Harris, Dictionary of Architecture and Construction. McGraw-Hill Education, New York, 2000.

[2] Cheuk Lun Chow, Spread of Smoke and Heat along Narrow Air Cavity in Double-skin Façade Fires. Thermal Science Vol. 18 (2014) 405–416.

[3] Yongqiang Luo, Ling Zhang, Zhongbing Liu, Lei Xie, Xiliang Wang, Jing Wu,. Experimental study and performance evaluation of a PV-blind embedded double skin Facade in winter season. Energy (2018) 326-342.

[4] Xinyan Huang, Critical Drip Size and Blue FlameShedding of Dripping Ignition in Fire, Sci Rep 8, 2018.

[5] Ronald P. D'Amelia, Samantha Gentile, William F. Nirode, Ling Huang, Quantitative Analysis of Copolymers and Blends of Polyvinyl Acetate (PVAc) Using Fourier Transform Infrared Spectroscopy (FTIR) and Elemental Analysis (EA). World Journal of Chemical Education Vol.4. No.2 (2016) 25-31.

[6] Eric Guillaume, Talal Fateh, Renaud Schillinger, Roman Chiva, Sebastian Ukleja, Study of Fire Behaviour of Facade Mock-Ups equipped with Aluminium Composite Material-based Claddings, using Intermediate-scale Test Method, Fire and Materials (2018) 1–17.

[7] Kathryn M. Butler, A Model of Melting and Dripping Thermoplastics Objects in Fire, Conference Proceedings - Fire and Materials 2009, 11th International Conference and Exhibition.

[8] Jose L. Torero, Greenfell tower: Phase 1 Report, Torero, Abecassis Empis and Cowlard, 2018

# Fire Safety Engineering

# Experimental study on the thermal behavior of a tank during burning of leaking contents

**Wang J.[1,2], Wang M.[1], Yu X.[1], Zong R.[1,2]*, Lu S. [1,]***

[1] *State Key Laboratory of Fire Science, University of Science and Technology of China, Hefei, Anhui, China.*
[2] *Suzhou Key Laboratory of Urban Public Safety, Suzhou Institute for Advanced Research, University of Science and Technology of China, Suzhou, Jiangsu, China.*
**Corresponding author's email:zongrw@ustc.edu.cn, sxlu@ustc.edu.cn*

## ABSTRACT

The study on the thermal behavior of a tank during burning of leaking contents is of great significance to the emergency response for tank fire incidents. To investigate the thermal behavior of the tank, experiments were carried out on a 50 L tank with initial leakage hole, and the tank was filled to 10% capacity with n-heptane. The liquid leaked from the tank to form three types of fires heating up the tank, including spill fire, pool fire and jet fire. The tank internal pressure and temperature profiles, and the flame morphology throughout the burning process were presented and discussed in conjunction with the experimental variables investigated, which included tank leakage diameter, spillage height and the effect induced by tank tilting. The results indicated that the pressure rose fastest when the leaking liquid was boiling and burning. The peak pressure increased with increasing leak diameter and spillage height, and the peak pressure rose significantly when the tank was tilted. Changes of leakage hole had a greater impact on the wall temperature as the height increased. A hazard analysis showed that the probability of tank failure decreased with increasing leak diameter, but the threat posed by the pool fire to the surroundings increased with increasing leak diameter. These results will provide scientific support for emergency response teams to control similar tank fire incidents.

**KEYWORDS:** Burning of leaking contents, Tank pressure response, Temperature response

## 1. INTRODUCTION

Over the past decades, significant efforts have been devoted to investigating the fire or explosion hazard in tanks under external thermal aggression [1-5]. When the tank is heated, the wall temperature and the internal pressure rise due to heat transfer. The mechanical strength of the tank wall starts to decrease as the wall temperature exceeds a certain value. The internal pressure increases as the temperature of liquid and vapor rises. If the stress caused by the internal pressure is greater than the mechanical strength of the tank wall, a fissure will form and the tank will eventually fail [6]. If the failure mode is catastrophic, a boiling liquid expanding vapor explosion (BLEVE) will occur, which results from the rapid depressurization of the hot and saturated liquid [7]. Birk [8] and Lin et al. [9] found that the increase in the degree of liquid stratification reduced the liquid energy and thus reduced the chance of a BLEVE. In addition, the tank wall thickness and PRV (pressure relief valve) set pressure had an important effect on the occurrence of the BLEVE [10].

Previous research has focused on tanks that are intact in the early stage of the fire. However, in some cases, the tank might have initial cracks due to human factors (such as in a road tanker involved in a traffic accident) and can release some liquid in the early stage of the fire. For example, the Zarzalico accident [11] occurred with an initial crack on a common LNG road tanker. The released methane was suddenly ignited as a fire, further heating up the tanker. Finally, an explosion occurred and the resulting fireball produced large radiant heat fluxes to the surroundings, leading to catastrophic consequences. In traffic accidents involving road tankers, leakage holes are easily formed on the tank wall due to the collision. Recently, Wang et al. [12] have carried out some experiments to study the fire behavior of the tank during burning of leaking contents. However, previous studies still lack experiments to investigate the effects of spillage height or other factors on the fire behavior. What is

lacking in the previous studies is what this paper investigates. The results can provide a fundamental basis for the control of similar tank fire incidents.

## 2. EXPERIMENTAL SETUP AND METHOD

As can be seen from Fig. 1, a threaded hole was placed at the bottom of the tank used in the tests. Screw bolts with different leak holes were installed in the larger hole to investigate the effects of leak diameter on the experimental results. A square pan (60 cm×60 cm×5 cm) collected the released liquid to form pool fire under the tank. The tank was made of stainless steel with a thickness of 1.5 cm. The length of the tank was 86 cm, the outer diameter 32 cm, the volume 50 L and the mass 135 kg.

If the tank is filled with more n-heptane, such as 20 L, 25 L, the tank may explode due to overpressure during the burning process, causing the huge damage to the experimental staffs. It is important to stress that the objective of this paper is to investigate the fire behavior of a tank during burning of leaking contents, and a near empty tank could meet the experimental requirements. To ensure the safety of experimental staffs, the tank was filled with 5 L of n-heptane, which was ignited after leaking was allowed for 2 s. The filling level of the tank was 10 %, and it did not represent the worst-case conditions. Besides, the initial liquid level was 4.75 cm, and it decreased with the leakage of n-heptane.

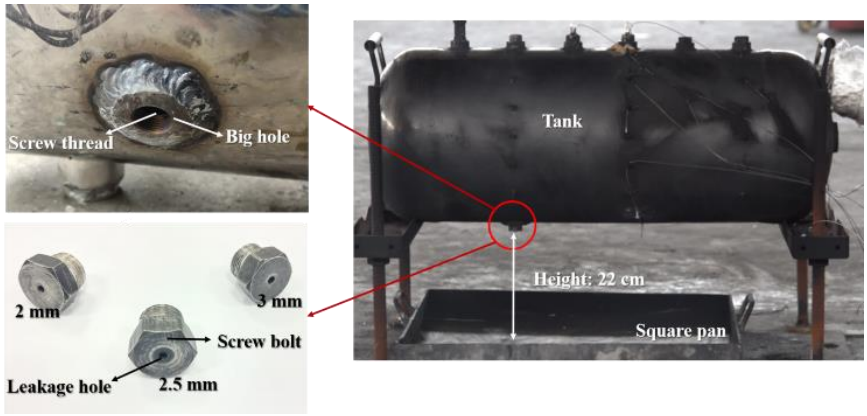


**Fig. 1.** Experimental apparatus configuration.

Fig. 2 is a schematic diagram of Fig. 1 showing some details of the experimental apparatus. Thermocouples T1 and T2 are attached to the outer wall of the tank to monitor the wall temperature. T3 is in the liquid inside the tank and close to the leakage hole to monitor the temperature of the leaking liquid. T4 is in the vapor space inside the tank to monitor the gas temperature. A pressure sensor with measuring range of 0-1 MPa is used to obtain the gauge pressure in the tank.

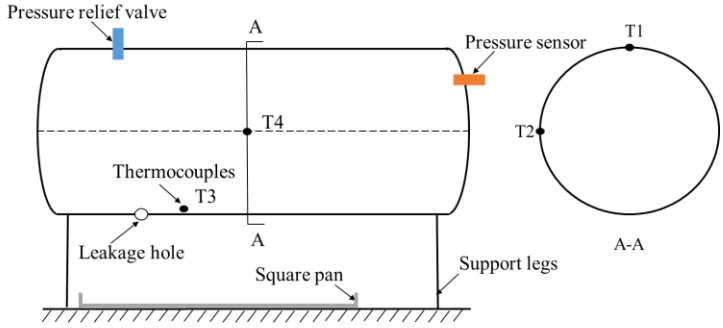


**Fig. 2.** Schematic diagram of experiment facility

The height of the leakage hole ($H$) impacts the flame volume below the tank, thereby affecting the heat fluxes received by the tank. The leak diameter ($D$) determines the leakage flow, and, ultimately, the heat release rate of the external fire. These two factors greatly affect the thermal behavior of the tank, and one objective of this paper is to quantify the effects of $H$ and $D$ on the thermal behavior. Tests were performed for the six conditions listed in Table 1.

**Table 1. Experimental parameters of all tests**

| $H$ / cm | $D$ / mm | Test number |
|---|---|---|
| | 2 | A1 |
| 22 | 2.5 | A2 |
| | 3 | A3 |
| | 2 | B1 |
| 32 | 2.5 | B2 |
| | 3 | B3 |

## 3. RESULTS AND DISCUSSION

### 3.1 Fire characteristics of a tank during burning of leaking contents

Fig. 3 shows a typical test result where the internal pressure first increases to a peak and then decreases to the initial value. Based on the behavior of internal pressure and flame characteristics, the fire is characterized by four stages, including initial stage (I), developing stage (II), fully developed stage (III) and decay stage (IV). Test A1 is used to explain the regimes of these four stages in detail.

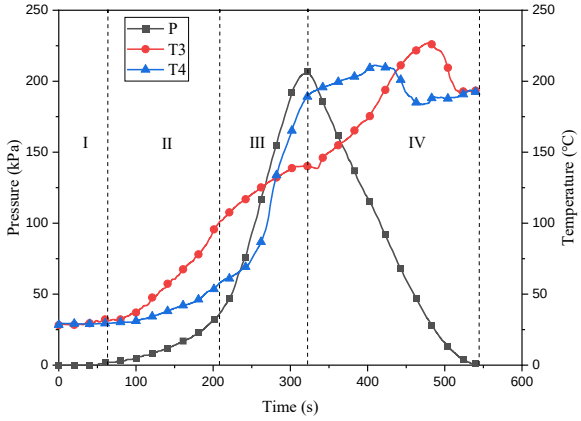


**Fig. 3.** Thermal response in test A1.

In Fig. 4 a, the flammable liquid leaks from the tank and is ignited, forming a spill fire which heats the tank. A stable white stream (indicated by the blue arrow) is formed as the liquid drops from the leakage hole into the square pan. The developing stage is also called steady burning stage, where n-heptane has spread to the entire pan, forming steady pool fire, as shown in Fig. 4 b. The tank is fully engulfed by fire and the wall temperature is rising rapidly. In Fig. 3, the pressure increases rapidly during the developing stage due to the increase in vapor pressure. The indication of the start of the fully developed stage is that the rate of pressure rise suddenly increases, as shown in Fig. 3. In this stage, the internal liquid temperature exceeds the boiling point of n-heptane (98.6 °C). Once the liquid leaks from the tank, it immediately boils and burns with a cracking sound. In Fig. 4 c, the stable white

stream no longer exists because the liquid at the leakage outlet splashes around. The splashing liquid increases air entrainment towards the leakage hole, forming air vortexes, further strengthening air entrainment during this stage. At the end of stage III, the liquid leaks out completely and the pressure reaches the maximum. Indication of the onset of the decay stage is that pressure starts to decrease rapidly, as shown in Fig. 3. The high temperature fuel vapor has been ejected from a leakage hole and burns, forming downward jet flame impinging on the pan with whistling sound. Once the high concentration fuel vapor hits the pan, it spreads out and burns along the pan. In conclusion, the flammable liquid leaks from the tank and starts a fire to heat up the tank, causing elevation of the liquid temperature and of the internal pressure. The increase in internal pressure promotes the increase in the leakage rate and further aggravates the external heat release rate, resulting in a greater increase in the internal pressure. This forms a positive feedback loop, which ultimately leads to tank failure if the thermal insult lasts for a sufficiently long time.

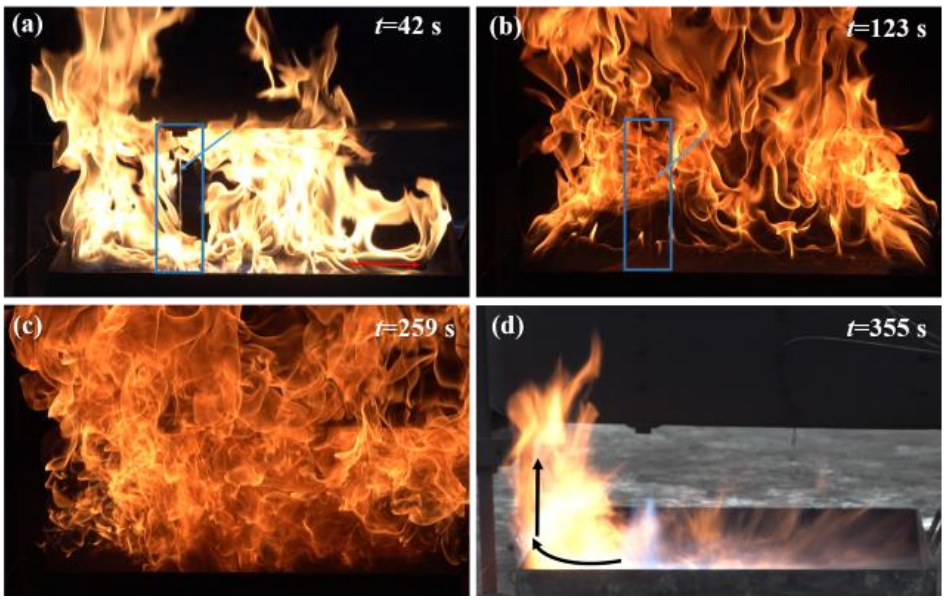


**Fig. 4** Flame morphology in test A1. (a) Stage I; (b) Stage II; (c) Stage III; (d) Stage IV.

In similar tank fire incidents, if the tank is at low filling level (a near empty tank), it will be most likely to explode in the fully developed stage due to the sharp increase in pressure, posing the greatest threat to the surroundings. Firefighters need to know when the fully developed stage starts. According to the cracking sound caused by boiling burning (see Fig. 4 c), it can be inferred that fire has entered the fully developed stage and the internal pressure will rise sharply. After this, the tank failure may occur at any time, and safety distance must be extended immediately. If firefighters choose to continue to extinguish the fire, they must be prepared and upgrade safety protection, otherwise they must keep a safe distance from the burning tank.

### 3.2 Thermal response

In Fig. 5, the time to reach peak pressure is shown to decrease with increasing *D*, indicating that the time required for the liquid to leak out completely decreases with increasing *D*. Regardless of the height *H*, the peak pressure decreases with increasing *D*. Although the liquid leaks out completely from the tank with larger leakage hole, there is still a large amount of liquid remaining in the tank with the smaller leakage hole and the temperature of the liquid continues to rise. As a result, the vapor pressure increases as the temperature of the liquid increases. Fig. 6 depicts the internal gas temperature measured by T4, the dotted lines represent the moment when the liquid has leaked out completely. When the tank with a larger leakage hole starts to release fuel vapor due to the completion of liquid

leakage, the rise in gas temperature does not promote a rise in pressure, because the volume expansion due to heat transfer to the gas inside the tank does not exceed the relief provided by the outflow. With a smaller leakage hole, the temperature of the gas inside the tank will continue to increase, and this increase will promote a rise in pressure, for as long as the gas in the tank cannot be released because of the remaining leaking liquid. The resulting effect is to cause the peak pressure to increase as $D$ decreases.

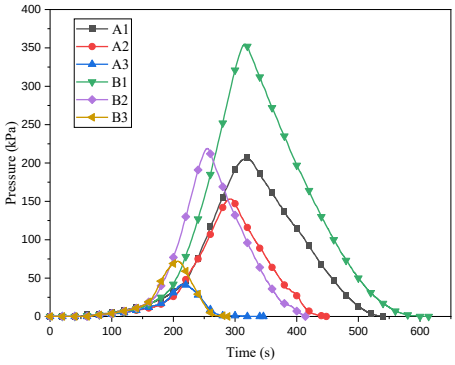


**Fig. 5.** The pressure response in six tests

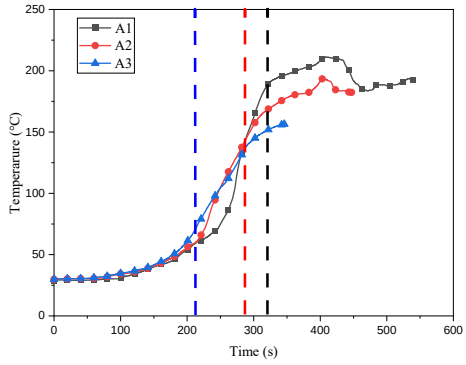


**Fig. 6.** The internal gas temperature

As shown in Fig. 5, when $D$ is held constant, the peak pressure increases with increasing $H$. This is attributable to the elevation of the flame size below the tank. The peak pressure is reached under continuous heating in stage III. At this stage, the liquid leaking from the tank boils and splashes. The splashed fuel entrains more air towards the bottom of the tank. It can be seen from Fig. 7 that the strongest flame is concentrated below the bottom of the tank, and most of the heat received by the tank comes from the flame below the tank. A larger of $H$ leads to an increase in the flame volume below the tank (see red rectangle in Fig. 7). As a result, the heat fluxes received by the tank rise, resulting in an increase in the peak pressure.

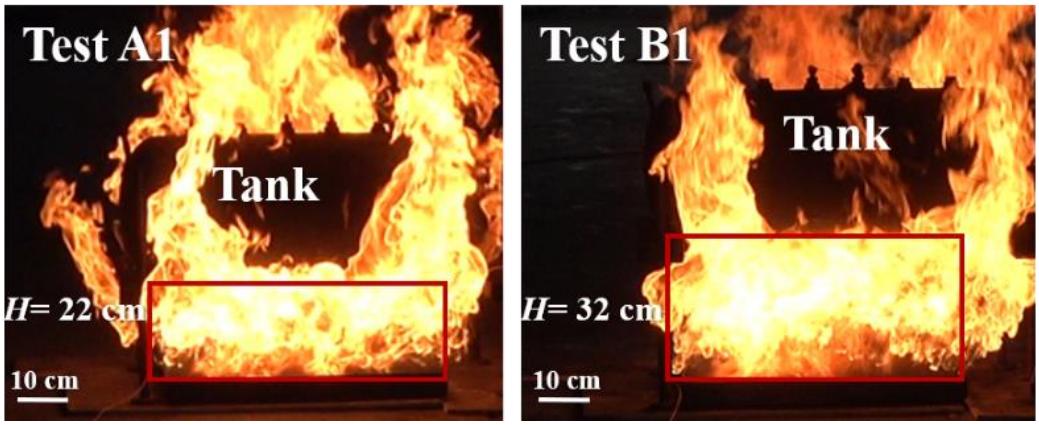


**Fig. 7.** Comparison of flame between test A1 and test B1 in stage III

Once the liquid spillage is over, the evolved fuel gas starts to eject from the leakage hole. With continuous decline in driving pressure, the jet velocity is also decreasing. Fig. 8 shows the transition process of the jet flame due to the decline in pressure. The momentum of the jet, which is downward, is in the opposite direction of buoyancy. At 322 s, the jet is violently impinging on the floor with the flame spreading to the entire pan. From 322 to 426 s, the lift-off height of jet flame gradually increases (see white rectangle in Fig. 8). From 426 to 518 s, the blue flame still stays inside the pan, so the lift-

off height reaches the maximum and almost keeps constant. This phenomenon also appears in test A1, but the maximum lift-off height in test A1 is lower than that in test B1 because of the difference of *H*. Suddenly at 520 s, the blue flame rises towards the leakage hole, so the lift-off height decreases, presumably because of a drop in the exit velocity of the jet. At the same time, the jet flame expands within the pan and forms a wide range of yellow flames at 520 s, but the fire size at *t*=520 s is much smaller than that at *t*=322 s due to the sharp drop in amount of fuel in the pan. After 581 s, there is no lift off of the flame, because the fuel discharge rate has decreased below a limit known as the lift-off stability limit.

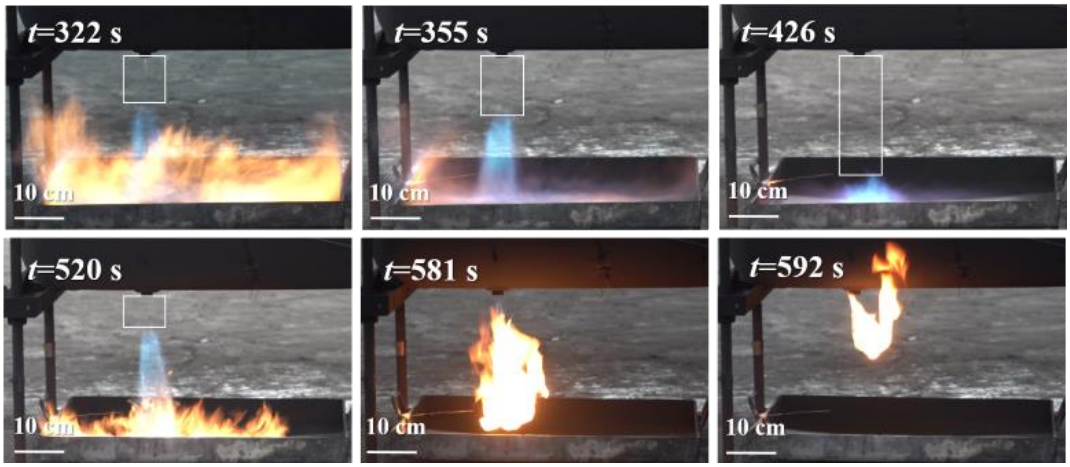


**Fig. 8.** The jet flame in test B1

The temperatures measured by T1 and T2 are averaged to represent an approximate average wall temperature, as shown in Fig. 9. It should be noted that the average temperature is only used to compare the difference in tank wall temperature among different tests. Compared to Fig. 9 a, there is a larger difference between the curves in Fig. 9 b. The enhanced turbulence of the flame due to greater height results in larger wall temperature differences between different leakage holes. Wall temperature increases may promote material degradation of the wall, leading to a sudden failure [8]. The maximum wall temperature appears to be about the same for all *D*, so the degree of material degradation does not change with *D*.

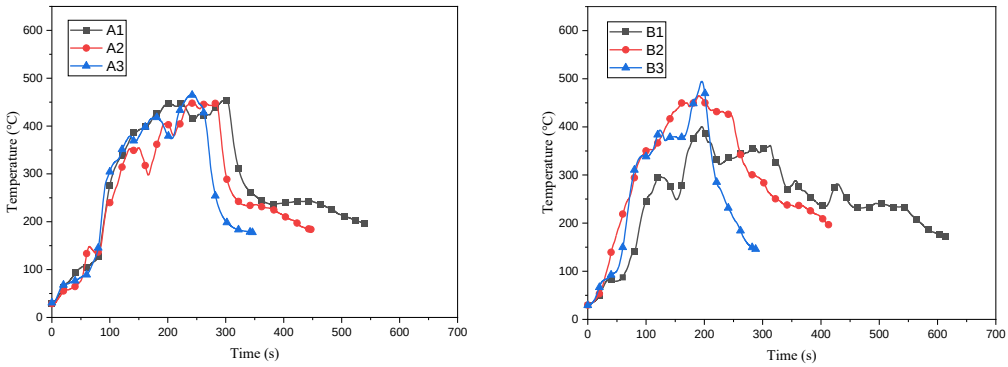


(a) (b)

**Fig. 9.** Average wall temperature. (a) *H*=22 cm; (b) *H*=32 cm.

### 3.3 Fire behavior with a tilted tank

After burning for 78 s, the tank was tilted, but was still held above the pan and the fire fed by the fuel leakage through the coupling went on, as shown in Fig. 10. The other experimental condition of this test is the same as that of test A3. In Fig. 10 a, a white stream is formed (see blue arrow), no longer vertically downward this time, but tilted. This means that the leaking liquid has a certain initial momentum, which can overcome the influence of gravity and tilt with the tank. Fig. 10 b displays the buoyancy-controlled jet fire due to low jet velocity caused by low pressure, indicating the leakage-burning coupling process is coming to an end.


(a) (b)

**Fig. 10.** Fire of the tilted tank. (a) $t$=104 s; (b) $t$=663 s;

At the initial stage of tilting, a portion of the liquid is still above the leakage hole (Fig. 11 a), and continues to leak. When the liquid no longer covers the leakage hole, the liquid distribution in the tank is shown in Fig. 11 b. Therefore, the leakage mode changes from liquid leakage to vapor leakage.

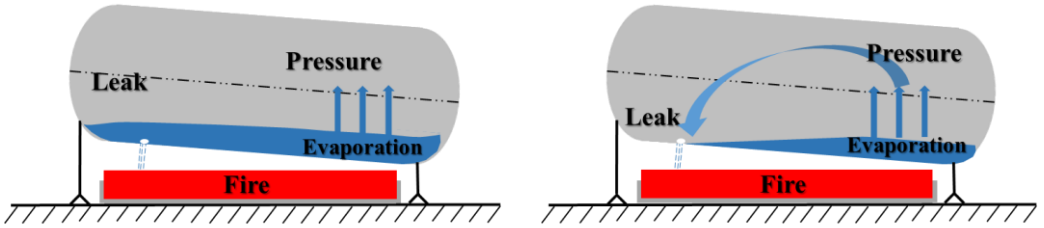


(a) (b)

**Fig. 11.** The leak mechanism in the tilted tank. (a) liquid leakage; (b) vapor leakage.

The released fuel vapor forms a jet fire that further heats the tank, and the liquid in the tank continues to be heated and vaporizes strongly. Although some fuel vapor leaks from the tank, the pressure is still increasing rapidly from 380 s to 560 s (Fig. 12 a), indicating that the vapor pressure is increasing. This means more gas is produced by vaporization than is released. Since there is more liquid accumulated at the right bottom in the tank, it takes longer time for the liquid to vaporizes completely. Therefore, the duration of the leakage-burning coupling process is longer as the tank is tilted, as shown in Fig. 12 b. Longer heating time causes the gas temperature to rise, which eventually far exceeds the values observed inside the undisturbed tank.

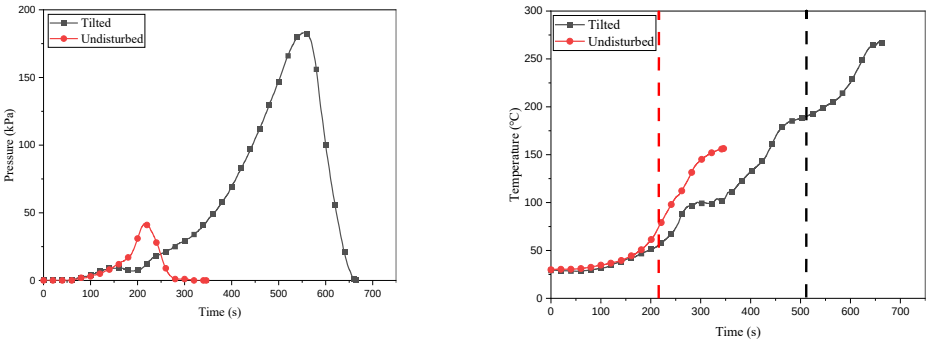


(a) (b)

**Fig. 12.** Comparison of results between two tanks. (a) Pressure; (b) Gas temperature.

The dotted lines in Fig. 12 b represent the moment when the pressure reaches the maximum or liquid in the tank completely disappears. Although there is no liquid to vaporize in the undisturbed tank, there is still liquid to vaporize in the tilted tank, leading to the observed pressure increase. The greater amount of fuel vapors and the higher gas temperature together cause the peak pressure in the tilted tank to be greater than that of the undisturbed tank, as shown in Fig. 12 a. For the tilted tank, if the liquid accumulates away from the leakage hole, the pressure will also increase sharply. As a result, the probability of tank failure also rises significantly, and firefighters need to upgrade their safety protection or extinguish the fire remotely.

### 3.4 Hazard analysis

The peak pressure decreases with increasing *D*, indicating that the peak stress induced by the internal pressure in the tank wall decreases with increasing *D*. The degree of material degradation does not change with *D*, suggesting that the ultimate strength of the wall does not change with *D*. If the stress induced in the wall is greater than the ultimate strength of the wall, the tank will deform and fail [6]. It can be concluded that for the tank during burning of leaking contents, the probability of tank failure decreases with increasing *D*. However, one cannot conclude that the hazards of similar tank fires decrease with increasing *D*. This is because the hazards of the fires include not only the tank failure but also the pool fire formed by the leaking liquid. Fig. 13 shows the typical flame shapes of pool fires in stage II and III under different leak diameters. In stage II, the flame size of test B1 is almost the same as that of test B3, meaning that the radiative heat fluxes emitted to the surroundings by these two cases are almost same. However, in stage III, the flame size in test B3 is much larger than that in test B1, implying a corresponding increase in the radiative heat fluxes emitted to the surroundings. In addition, due to the greater thermal radiation in test B3, the iron exhaust hood above the flame made detectable deformation noise, while no such phenomenon was observed in test B1. Therefore, we can conclude that the pool fire poses a greater threat to the surroundings as *D* increases.

For test B1, the small leak diameter leads to small leakage flow so that there is only a small amount of liquid in the pan in stage III. Therefore, the fire in stage III is mainly formed by the leaking liquid. The leaking liquid boils and splashes, entraining air towards the bottom of the tank and forming vortexes. The formation of vortexes leads to a reduction in flame height or flame size. For test B3, the leakage flow is larger due to the larger leak diameter, so there is liquid left in the pan in stage III. In stage III, because the liquid leakage flow increases, there is too much liquid in the pan. This causes the fuel vapor to expand to the right, approximately 30 cm (see black arrow). Therefore, the pool size increases significantly, spreading beyond the diameter of pan, leading to an increase in flame height and flame size.

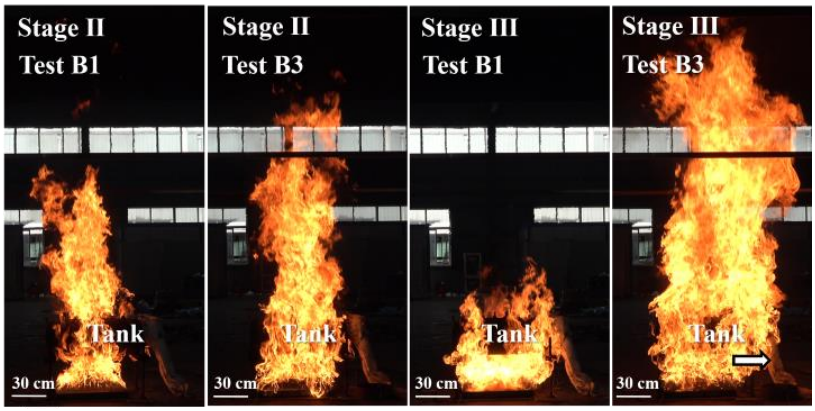


**Fig. 13.** The typical flame morphology of pool fire in stage II and III

In order to assess the hazards of similar fires, both pool fire and tank failure are required to be taken into consideration. In this study, due to the high design pressure of the tank and shorter heating time, tank failure did not occur. If one can be assured that the tank will not fail, the fire with a larger leakage hole is more dangerous because the thermal radiation emitted to the surroundings is greater. However, if the design pressure is smaller and the tank is exposed to fire for longer time, the tank may suffer failure. If there is uncertainty about the tank failure, the tank fire with a smaller leakage hole is more dangerous due to greater probability of failure. Once the tank fails, it will explode and produce a fireball and fragments. The hazards of explosion are far greater than the hazards of pool fire.

## 4. CONCLUSIONS

This work focused on the thermal behavior of a tank during burning of leaking contents. Experimental data collected in the tests showed that this fire was characterized by four stages, including initial stage, developing stage, fully developed stage and decay stage. The pressure rose fastest during the fully developed stage and reached a maximum. After this, the fire entered the decay stage, where a downward jet flame impinged on the floor with fast depressurization. The following comments highlight the results of these tests with low filling level:

1) The peak pressure decreases with increasing leak diameter, but the degree of material degradation does not change with the leak diameter. Thus, the probability of tank failure decreases with increasing leak diameter

2) The larger leak diameter leads to greater leakage flow, causing more liquid to flow into the pan. This encourages the fuel vapor to expand around, so the pool diameter increases, resulting in an increase in flame size. Thus, the pool fire poses a greater threat to the surroundings as the leak diameter increases.

3) According to the cracking sound caused by burning when the leaking liquid is boiling, one can realize that the fire has entered the fully developed stage and the pressure will rise sharply. In addition, if the tank is tilted and the liquid accumulated away from the leakage hole, the pressure will also increase sharply. Sharp rise in pressure may lead to tank failure, so one must keep a safe distance from the burning tank.

More investigations would be required to provide more solid insights on the similar fires. Since the mass of the tank used in this study was too large for us to measure the mass loss using an electronic balance, we were able to calculate the key parameters such as the heat release rate. In the future, we will carry out some tests on a smaller tank with higher filling level. An electronic balance will be used to record the mass loss rate of the fuel for calculating the heat release rate. The future work will help us make more comprehensive conclusions.

## REFERENCES

[1] J. Stawczyk, Experimental Evaluation of LPG Tank Explosion Hazards, Journal of Hazardous Materials. B96 (2003) 189-200.

[2] A.M. Birk, D. Poirier, C. Davison, On the Response of 500gal Propane Tanks to a 25% Engulfing Fire, Journal of Loss Prevention in the Process Industries. 19 (2006) 527-541.

[3] C.C. Manu, A.M. Birk, I.Y. Kim, Stress Rupture Predictions of Pressure Vessels Exposed to Fully Engulfing and Local Impingement Accidental Fire Heat Loads, Engineering Failure Analysis. 16 (2009) 1141-1152.

[4] R. Tschirschwitz, D. Krentel, M. Kluge, E. Askar, K. Habib, H. Kohlhoff, S. Krüger, P.P. Neumann, S.U. Storm, M. Rudolph, A. Schoppa, M. Szczepaniak, Experimental Investigation of Consequences of LPG Vehicle Tank Failure under Fire Conditions, Journal of Loss Prevention in the Process Industries. 56 (2018) 278-288.

[5] S. Ruban, L. Heudier, D. Jamois, C. Proust, L. Bustamante-Valencia, S. Jallais, K. Kremer-Knobloch, C. Maugy, S. Villalonga, Fire Risk on High-pressure Full Composite Cylinders for Automotive Applications, International Journal of Hydrogen Energy. 37 (2012) 17630-17638.

[6] R. Bubbico, B. Mazzarotta, Dynamic Response of a Tank Containing Liquefied Gas under Pressure Exposed to a Fire: A Simplified Model, Process Safety and Environmental Protection. 113 (2018) 242-254.

[7] R.C. Reid, Possible Mechanism for Pressurized-Liquid Tank Explosions or BLEVE's, Science. 203 (1979) 1263-1265.

[8] A.M. Birk, Scale Effects with Fire Exposure of Pressure-liquefied Gas Tanks, Journal of Loss Prevention in the Process Industries. 8 (1995) 275-290.

[9] W. Lin, Y. Gong, T. Gao, A. Gu, X. Lu, Experimental Studies on the Thermal Stratification and Its Influence on BLEVEs, Experimental Thermal and Fluid Science. 34 (2010) 972-978.

[10] A.M. Birk, M.H. Cunningham, The Boiling Liquid Expanding Vapour Explosion, Journal of Loss Prevention in the Process Industries. 7 (1994) 474-480.

[11] E. Planas, E. Pastor, J. Casal, J.M. Bonilla, Analysis of the Boiling Liquid Expanding Vapor Explosion (BLEVE) of a Liquefied Natural Gas Road Tanker: The Zarzalico Accident, Journal of Loss Prevention in the Process Industries. 34 (2015) 127-138.

[12] J. Wang, M. Wang, X. Yu, R. Zong, S. Lu, Experimental and Numerical Study of the Fire Behavior of a Tank with Oil Leaking and Burning, Process Safety and Environmental Protection. 159 (2022) 1203-1214.

# Upward Flame Spreading and Surface Smouldering over Thin Material with Varied Sample Thickness and Oxygen Concentration Diluted with Carbon Dioxide

**Wenlong Wang[1], Jun Fang[1,*], Yongming Zhang[1]**

*[1] State Key Laboratory of Fire Science, University of Science and Technology of China, Hefei, Anhui 230026, P. R. China.*
**Corresponding author's email: fangjun@ustc.edu.cn*

## ABSTRACT

As a clean, high-efficiency and low-cost extinguisher, carbon dioxide has been widely used in many fire scenarios. An investigation was carried out to elucidate the dynamics of flame spreading and surface smouldering at a high carbon dioxide concentration like the fire scene after the application of extinguishing agents. Three regimes can be divided by the flame spread rate depending on the ambient oxygen concentration. The extinction regime corresponds to the combustion below the lean oxygen limit characterized by the non-existence of flame. With the increase of oxygen concentration, in the linear regime, only a steady single-sided flame can survive eventually after the ignition of double-sided flames symmetrically and simultaneously, and the flame spread rate increases with the oxygen concentration linearly. Furthermore, in the convergence regime, both the two-sided flames can exist with stronger burning intensity and longer flame length, however, the flame spread rate maintains at a constant level with the oxygen concentration due to the limited maximum fuel vapour released. The flame spread rate is inversely proportional to the sample thickness for thinner paper, nevertheless, the effect of the temperature gradient in the depth direction for the thicker paper must be considered when the paper thickness reaches 0.57mm in this work. Unique partial smouldering phenomenon such as periodic holes was found. The vertical approaching stage, fusion stage and horizontal separation stage of two adjacent arc-like smouldering zones are analyzed, associated with total smouldering time with oxygen concentration. The long-lasting smouldering process on the sample surface raises the danger of the transformation to flaming, and should be highly valued in fire control practice.

**KEYWORDS:** single-sided flame, periodic holes, secondary fire hazards, thermal thin

## INTRODUCTION

As an important stage in fire development, flame spreading can be regarded as continuous ignition and extinguishment process, and has attracted extensive attention and research in the past half-century [1-7]. According to the relationship between the orientation of flame spread and external ventilation, flame spreading can be roughly divided into concurrent-flow or opposed-flow types. In particular, in a natural convection scenario, the flame-induced buoyant flow spreads vertically, opposite to the direction of gravitational acceleration. Therefore, upward flame spreading is regarded as a typical concurrent-flow paradigm, which is one of the most common fire forms. The hypothesis of thermal-thin material can be adopted if the temperature gradient can be omitted in the thickness dimension of the solid phase, that is, the heat penetration depth greatly exceeds the physical thickness of the sample. Thermal-thin materials tend to spread at a relatively faster rate, which means there is a greater potential to ignite the surrounding fresh unburned combustibles, and a higher fire hazard. However, due to the self-accelerating and unsteady characteristic of most of the upward flame spreading over thermal-thin material, it has brought difficulties and challenges to the research work. Therefore, its dynamic mechanism has not been fully understood, and further research and analysis are urgently needed.

Carbon dioxide fire extinguishers are clean, high-efficiency, and low-cost. They extinguish the flame by absorbing heat during the gasification process of compressed liquid carbon dioxide and isolating

the fuel from the air by enveloping the reaction region. They are widely used in initial fires in libraries, archives, valuable equipment, and precision instruments. In addition, the active ingredients of foam fire extinguishers and dry powder fire extinguishers are also carbon dioxide. After spraying the extinguishing agent above mentioned, the fire scene will be surrounded by a high carbon dioxide atmosphere. Since World War II, the relatively peaceful international environment has provided good conditions for the development of the national economy of many countries. The massive use and consumption of fossil energy have led to a sharp increase of the $CO_2$ concentration in the atmosphere, and global warming and rising sea levels have brought new crises and challenges to human production and life. Syukuro Manabe [8] revealed that doubling the present $CO_2$ concentration will raise the global average temperature about 3.5℃ by the use of a simplified three-dimensional general circulation model, and he was awarded the 2021 Nobel Prize in Physics for this work. Hence, it's particularly important to figure out the underlying combustion characteristics and evaluate the fire risk of materials under the environment of high or enhanced $CO_2$ concentration.

In the study, the $CO_2$ concentration is varied to simulate the fire scene after the $CO_2$ extinguishing agent is injected, and an attempt is made to reveal the fire dynamics mechanism of upward spreading over thermal-thin materials, which is deemed to the worst fire scenario for its drastic reaction intensity, providing guidance for fire rescue practice, and reference for analyzing the impact of the global climate change on fire safety situation.

## 1 Experimental setup

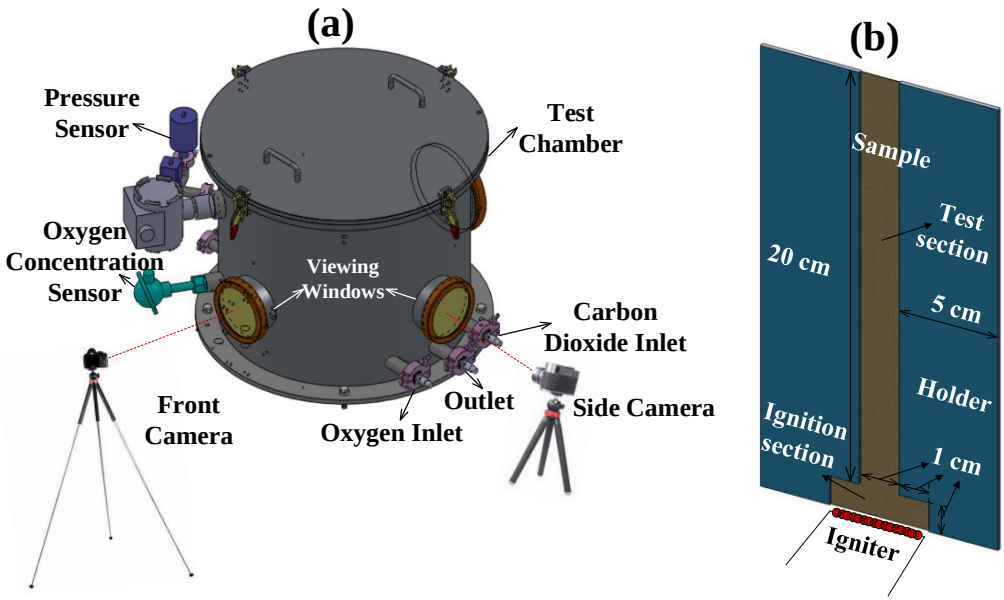


Fig. 1 Schematic diagram of the experimental setup. (a) enclosed test chamber and image acquisition arrangement; (b) sample holders and ignition device.

In this study, four kinds of homogeneous charring printing papers with different thicknesses (0.1mm, 0.17mm, 0.33mm and 0.57mm) and corresponding area densities (70g/m$^2$, 120g/m$^2$, 230g/m$^2$ and 400g/m$^2$) produced by Xiangzhiyuan® Co. Ltd are selected as experimental materials. All samples are placed in an electric oven and dried at a constant temperature of 105℃ for 12 hours to eliminate the influence of sample moisture content on experimental results. Then, the dried test samples are stored in an airtight vessel with silica gel desiccant until being used. As shown in Fig. 1b, the test sample is fixed between two stainless steel holders with 1mm thickness. The test section is 20cm long and 1cm wide, at this width, flame spreading can maintain at a stable rate by the balance between the heat generation from the reaction zone and heat loss and momentum loss to the holders on both sides[5,

9]. The ignition section is located at the bottom region of the sample with 1cm high and a wider width of about 3cm, so that the test section can be ignited evenly. The nickel-chromium coiled wire with a diameter of 4mm and a length of 3cm is positioned just underneath the centerline of the bottom open edge of the sample, so that both sides of the sample can be piloted simultaneously and symmetrically. The sample, holders and igniter are all put into an enclosed cylindrical test chamber with a diameter of 50cm and a height of 40cm before each test, as shown in Fig. 1a. Then the chamber is sealed and evacuated to 0.3kPa through the vacuum pump connected to the outlet. Pure oxygen and carbon dioxide gases at a predetermined ratio are injected into the chamber controlled by the Alicat mass flowmeters connected to the oxygen inlet and the carbon dioxide inlet respectively. The oxygen mass concentration varies from 17% to 25%, and the carbon dioxide mass concentration varies from 83% to 75% correspondingly. The inlet valves are closed once the total pressure of the chamber reaches 100kPa, that is, 1atm. The pressure sensor and oxygen concentration sensor embedded in the chamber are used for real-time monitoring and control of total pressure and oxygen concentration. A fan prepositioned in the chamber is turned on for at least 5 minutes until the readings from the oxygen concentration sensor attain stability to make sure the gases mixed uniformly. Then 5 minutes of stillness is required to remove the flow field disturbance induced by the fan. The constant current source jointed with the nickel-chromium coil is initiated at 3A and shut down immediately after ignition. Two digital cameras with a frame rate of 29.97 frame/s are placed at proper positions to record the front and side view images respectively. The test conditions and results of the steady-state in this study are shown in Table 1. For the convenience of elaboration, one-sided and two-sided are used to describe the ignition methods, while single-sided and double-sided are used to describe the flame state. For instance, two-sided ignition means two sides of the paper sample are ignited synchronously, and then, double-sided flames are obtained. During the tests, the variation range of chamber pressure is less than 1kPa, and the oxygen concentration less than 0.5%, which are monitored and verified by corresponding sensors, so they all can be considered as constant. For each condition, at least 3~5 tests are conducted to ensure the reliability and universality of the experimental results, and their average values are used for subsequent analysis and discussion.

## 2 Results and discussion

### 2.1 Effect of the ambience

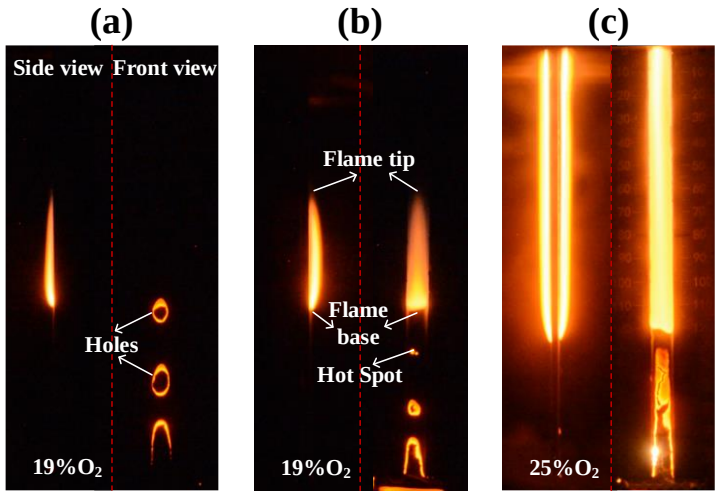


**Fig. 2** Flame spreading images over charring paper of 0.33mm width with varied $O_2$ and $CO_2$ concentration at 1atm. The left part of each image separated by the red dashed line is obtained from the side view camera, and the right part from the front view camera. (a) Only the back(left) branch of the flame survived and periodic holes occur at the sample surface after the front branch(right) blows off at 19% $O_2$ and 81% $CO_2$. (b) Only the front(right) branch of the flame survived and holes occur at the sample surface after the back(left) branch blows off at 19% $O_2$ and 81% $CO_2$. (c) Strong symmetrical double-sided flames at 25% $O_2$ and 75% $CO_2$.

**Table 1 Test conditions and results of the steady-state in this study.**

| Oxygen Mass Concentration / % | Sample Thickness / mm | Ignition Method | Steady State | |
|---|---|---|---|---|
| | | | Linear Regime | Convergence Regime |
| 17-25 | 0.10 | One-sided | Single-sided flame | Double-sided flames |
| | 0.10, 0.17, 0.33, 0.57 | Two-sided | Single-sided flame | Double-sided flames |

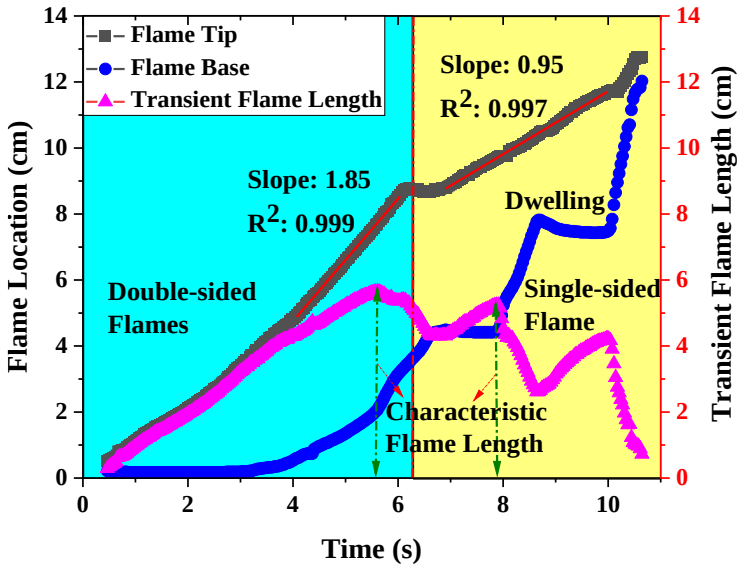


Fig. 3 Flame location (tip & base) and transient flame length with time of the remaining branch flame over 0.33mm sample at 1atm, 19% $O_2$ and 81% $CO_2$.

When the oxygen concentration is below 17%, the double-sided flames ignited symmetrically can't be self-sustained in the test section and blow off successively. When the oxygen concentration is 19%, as shown in Fig. 2, one branch of the double-sided flames will blow off affected by the self-induced buoyant flow, while which branch extinguishes eventually is random [10-12]. Fig. 2a shows the right side (front side) flame blows off, however, Fig. 2b shows the left side (backside) flame. The other flame will survive and discrete hot spots appear on the sample surface as a sign of partial solid-phase smouldering. These hot spots will evolve into holes with a circular outline until the smouldering front reaches the leading edge of the holders. When the oxygen concentration is 25%, both sides of the flames can be maintained stably with rapid spreading rates and longer flame lengths, and at the same time, the entire glowing surface of the burned area is left behind.

As shown in Fig. 2b, the flame tip and flame base are marked by the white solid lines with an arrow. The colour experimental image will be converted to a grayscale image, and then to a binary image further at an adaptive threshold by an independently developed Matlab code, so as to track the positions of the flame tip and flame base. Then the transient flame length can be obtained by subtracting the location data of the flame base from that of the flame tip. Fig. 3 shows the corresponding processing results of flame location (tip & base) and transient flame length. There are periodical speed-up and dwelling behaviours corresponding to the periodic holes for the flame base, thereby variable flame length, while the flame tip spreads at a relatively steady rate. Therefore, for the double-sided and single-sided flames, the maximum flame lengths are selected as the characteristic flame lengths, and the flame spread rates are obtained by fitting the curve of the steady flame tip location with time linearly using the least square method. The spread rate is 1.85cm/s with a variance of 0.999 for the former, while 0.95cm/s with a variance of 0.997 for the latter respectively.

Although the flame spread rate is traditionally defined as the rate of advancement of the pyrolysis front, the movement of the flame tip is supposed to be coincident with that of the pyrolysis front considering thin materials burn out quickly in this study. The sample surface smouldering time is the total time lapses from the occurrence to the complete extinction of the smouldering on the sample surface.

For the comparison of the effect of $CO_2$ and $N_2$, we supplement several experiments conducted over 0.1mm paper sample at 1atm and normal air. The double-sided flames achieve a steady state and maintain a symmetrical structure shortly after the two-sided ignition. The flame tip and base spread at a steady rate of 5.49cm/s without blow-off and periodic holes observed.

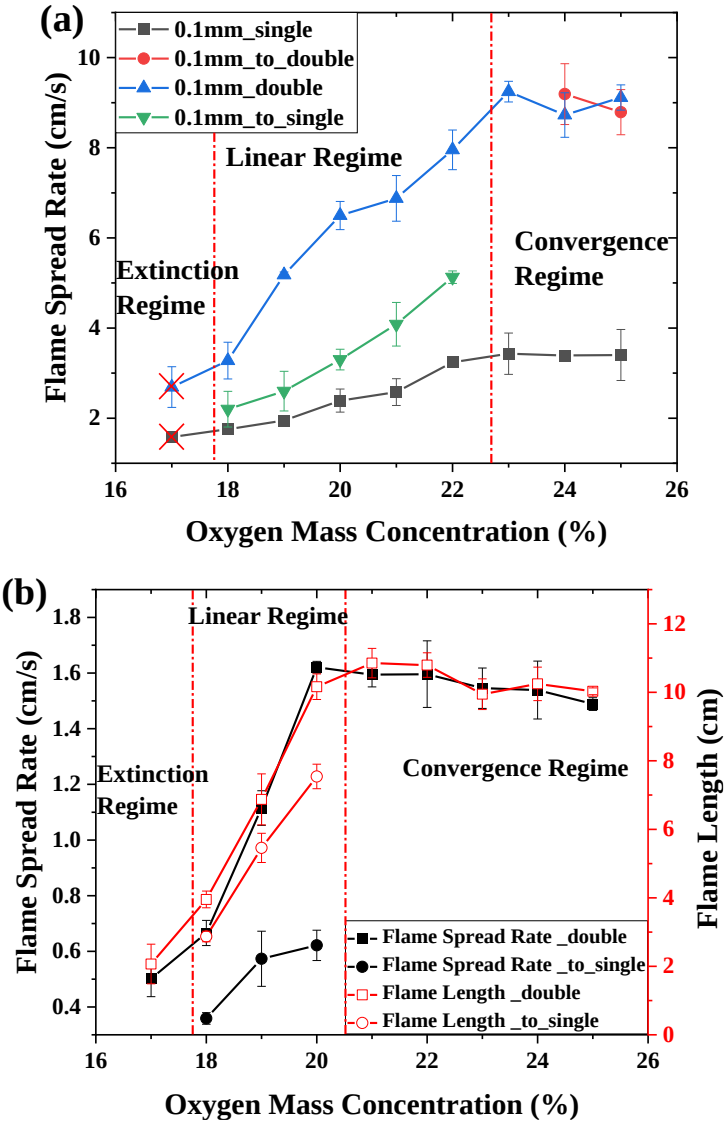


Fig. 4 Flame spread rate or flame length vs. oxygen mass concentration. (a) 0.1mm sample; (b)0.57mm sample. "_single" and "_double" in the legends signify the initial single-sided and double-sided flames after one-sided and two-sided ignition respectively. In addition, "_to_double" and "_to_single" signify the finally steady double-sided and single-sided flames.

As shown in Fig. 4b, three regimes can be divided by the flame spread rate depending on the ambient oxygen concentration: extinction regime, linear regime and convergence regime. Furthermore, Fig. 4b also shows the variation of flame length with oxygen mass concentration, which is consistent with the trend of the spread rate. The corresponding oxygen concentration in the extinction regime is lower than the lean oxygen limit, and the flame is completely extinguished. In the linear regime, the flame spread rate and length decrease linearly with the oxygen mass concentration. One branch of the double-sided flames blows off, and the remaining branch flame survives at about half of the spread rate before unilateral extinction for the lack of the heat flux transferred from the other branch flame (or in other words, the nearly doubled pyrolysis depth), accompanied by a partial smouldering process on the solid surface. While the maximum flame length for the single-sided flame shrinks only 20~30%, which is comparatively less than the attenuation ratio of the spread rate. In the convergence regime, the oxygen concentration is high enough to support stable and strong symmetrical double-sided flames, and an intense smouldering process among the entire surface follows closely, however, the flame spread rate converges to a constant value subjected to the limited mass loss flux of the sample surface. In the linear regime, In order to clarify the mechanism of the linear regime stabilized with single-sided flame and the convergence regime with double-sided flames, a one-sided ignition experiment for the 0.1mm thick sample is conducted through a horizontally placed stainless steel plate on the back to extinguish the back flame, which means only the front flame can survive in the test section. As shown in Fig. 4a, both one-sided ignition and two-sided ignition results can be divided into three regimes as mentioned above. In the two-sided ignition experiment, the flames will transform into a single-sided flame in the linear regime, and the converted flame spreads more rapid than the flame in the one-sided ignition experiment, which is probably attributed to the effect of the two-sided ignition in the preheating of the fuel ahead of the flame making it easier to reach the pyrolysis temperature and therefore resulting in faster spreading flames. In the one-sided ignition experiment, the flame will transform into a double-sided flame in the convergence regime, and the converted flames spread almost at the same rate compared with the flame in the two-sided ignition experiment.

### 2.2 Effect of sample thickness

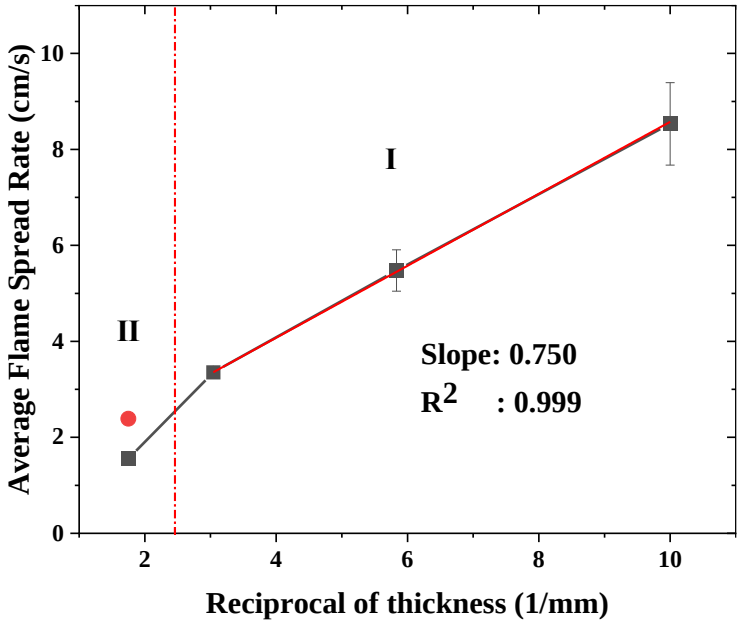


Fig. 5 Average flame spread rate in the steady-state vs. the reciprocal of sample thickness. The red dot represents the predicted flame spread rate at 0.57mm thick sample extrapolated from the linear fitting curve symbolized by a red solid line.

To simplify the analysis, the expression of the flame spread rate can be obtained just by establishing the balance between the net heat flux transferred from the flame to the solid sample and the energy required for raising the sample temperature from the ambient level to the pyrolysis temperature [3, 13, 14], as shown in Eq.1:

$$V_f \sim \frac{\dot{q}''_{net} L_f}{\rho c_p \tau \left(T_{ig} - T_\infty\right)} , \tag{1}$$

Where $V_f$ represents the flame spread rate. $\dot{q}''_{net}=\dot{q}''_{cond}+\dot{q}''_{conv}+\dot{q}''_{rad}-\dot{q}''_{re-rad}$ represents the net heat flux from the flame to the solid surface, which equals the sum of conductive heat flux $\dot{q}''_{cond}$, convective heat flux $\dot{q}''_{conv}$ and radiative heat flux $\dot{q}''_{rad}$ from flame to solid surface minus the re-radiative heat flux $\dot{q}''_{re-rad}$ emitted from the solid surface. In this study, the variation of $\dot{q}''_{net}$ with oxygen can be considered small, which is accordant with the conclusion in chapter 2.3. $L_f$ represents the flame length, which is proportional to the pyrolysis length $L_p$ with a constant coefficient of about 1.54 for paper samples used in this study same as that in Zhao [7]. $\rho$ represents the sample density. $c_p$ represents the specific heat capacity of the paper. $\tau$ represents the sample thickness. $T_{ig}$ represents the sample pyrolysis temperature. $T_\infty$ represents the initial temperature of the sample, namely the ambient temperature.

As shown in Fig. 4, in the convergence regime, the flame spread rate hardly varies with the increase of oxygen concentration and remains constant basically. Therefore, they can be addressed to obtain the average flame spread rate and used to investigate the effect of sample thickness on the flame spread. As shown in Fig. 5, at a smaller sample thickness, the average flame spread rate is proportional to the reciprocal of the sample thickness, which verifies Eq. 1. However, when the sample thickness reaches 0.57mm, the actual flame spread rate is only 65% of the predicted value given by the red fitting curve, indicating that the temperature gradient in the thickness direction of the sample becomes significant, and the isothermal distribution model based on the thermal-thin hypothesis is no longer fully applicable. The enhanced in-depth heat loss in the thickness direction of the sample results in a smaller flame spread rate. Therefore, the two regimes can be divided in Fig. 5. In the I regime, The hypothesis of thermal thin is fully applicable, however, the influence of thickness effect needs to be considered in the II regime. Colomba Di Blasi [15] conducted a numerical simulation to study the effects of solid thickness on the concurrent flame spread over charring materials and concluded that in the thermally thin regime, the spread rates decrease as the solid thickness is increased, however, in the thermally thick regime, much lower and constant spread rates is acquired, which is consistent with our results.

### 2.3 Dimensionless Flame length

The flame length reflects the stretching effect of the buoyant flow on the gas-phase flame. The elongated flame enhances the heat transfer to the unburned region, expands the pyrolysis zone, and promotes the flame spread downstream [3, 13]. In the convergence regime, the ambient oxygen concentration is high enough to maintain the stable existence of the double-sided flame, and the flame length is relatively constant. In the linear regime, flame length varies significantly with the transformation from the double flame to a single flame and the local smouldering process on the sample surface, so the corresponding maximum flame length is selected as the characteristic flame length, as shown in Fig. 3. Then the flame length is dimensionalized with sample thickness as the reference size. As shown in Fig. 6, whether it is a single-sided flame or a double-sided flame, the flame spread rate decreases with the dimensionless flame length. However, there is a larger slope for most of the double-sided flames compared with the single-sided ones, which owes to the larger heat flux from the double-sided flame to pyrolysis front, as indicated in Eq. 1.

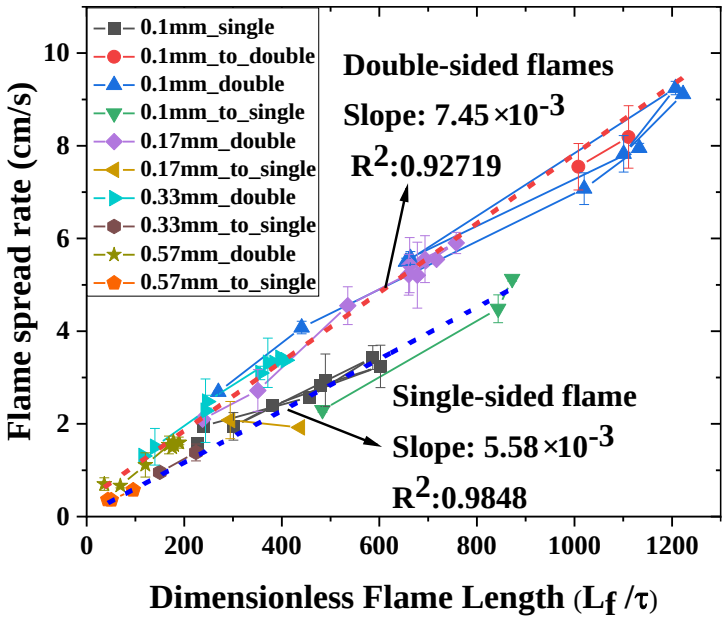


Fig. 6 Flame spread rate vs. dimensionless flame length.

### 2.4 Solid surface smouldering

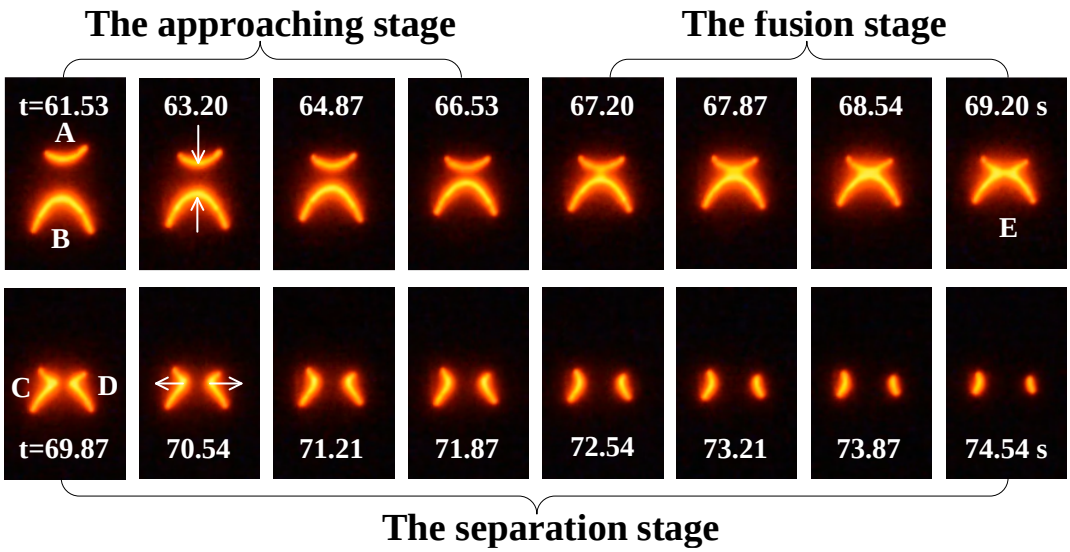


Fig. 7 The fusion and extinction process of the surface smouldering over 0.33mm thick sample at 20% $O_2$, 80% $CO_2$ and 100.20kPa. The moment when the sample is just ignited is selected as the timing origin. Five uppercase letters are used to mark different branches of the smouldering zone. 'A' represents the lower branch of the upper hole. 'B' represents the upper branch of the lower hole. 'C' and 'D' represent the left and right branches of the smouldering zone at the horizontal separation stage respectively. 'E' represents the crown-like fusion smouldering zone. The white arrow lines symbolize the spread orientations of the four individual smouldering zones towards the unburned char layer respectively, leaving the ash layer behind.

As shown in Fig.2, in the linear regime, the ambient oxygen concentration is too low to sustain the stable double-sided flame. Therefore, when the flame length (thus flame volume and self-induced buoyant flow) of a certain flame reaches a critical size, the flame base continues to accelerate downstream under the enhanced buoyancy, and eventually surpass the flame tip to extinguish the flame [11]. After the unilateral extinguishment, the heat flux obtained in the pyrolysis zone is halved, so that the flame spread rate on the remaining side is reduced to about half of the original. At the same time, due to the sudden disappearance of the flame on the opposite side, the pyrolysis thickness corresponding to the remaining side flame increases. The halved flame spread rate and the increased pyrolysis thickness means that there is a longer residence time for the gas-phase flame to continuously heat the pyrolysis zone on the sample surface. Then the local zone of the sample surface, especially the region adjacent to the flame base with fierce burning intensity, reaches and even exceeds the secondary pyrolysis temperature, so that the smouldering process begins and red hot spot forms when the hot char layer is first exposed to the fresh oxygen just after the gas phase flame leaves, as shown in Fig. 4b. Subsequently, the hot spot will expand itself towards the surrounding unburned char layer at an approximate radial speed, while the internal char layer is completely consumed, leaving a gloomy non-flammable ash layer. The ring-like smouldering zone named as a hole forms between the smouldering front and the solid-phase burnout front. The hole continues to enlarge until the diameter is close to the sample width of 1cm. The transverse conduction heat loss and momentum loss of the smouldering front to the stainless steel holders on both sides become significant and even exceeds the heat generated from the reaction zone, resulting in the leftmost and rightmost (closest to the sample holder) of the smouldering front extinguished first as the weak position. The continuous annular smouldering zone is split into upper and lower branches, which will continue to spread downstream and upstream on the sample surface respectively.

Fig. 7 shows the vertical approaching stage (61.53~66.53s), fusion stage (67.20~69.20s), and horizontal separation stage(69.87~74.54s) of two adjacent holes after the rupture. In the vertical approaching stage, both the smouldering fronts of the branch ‘A’ and ‘B’ present a convex profile that bends toward the unburned char layer in the middle region, which is consistent with the boundary layer caused by the heat loss to the holders on both sides. The spread orientation of the branch ‘B’ is the same as the self-induced buoyant flow, that is, the forward smouldering process. Fresh oxygen is entrained around the solid surface, and heat is brought into the unburned char layer downstream by convection, thereby enhancing the spread rate and burning intensity of the arc-like smouldering zone with brighter glowing. The regions near the edge of the sample and holders spread at a lower rate for large lateral heat loss, while the region along the centerline of the sample is hardly affected by the holders, and spreads at a higher rate for the enhancement effect of the buoyant flow, resulting in greater convexity and curvature of the smouldering front in branch ‘B’. The spread orientation of the branch ‘A’ is opposite to buoyant flow, that is, the opposed smouldering process. While the buoyant flow brings fresh oxygen to the reaction zone, it also takes away the heat generated by the smouldering through the convection effect. Consequently, a relative slow smouldering process is established with a nearly flat front. In the fusion stage, the tips of the branch ‘A’ and ‘B’ merge at the moment they contact each other, and then the fusion zone expands from the middle to both edges of the sample on the transverse. For the combined heating effect of the branch ‘A’ and ‘B’ aforementioned, the fusion zone have a continually enhanced burning intensity and brighter glowing until the fracture occurs at the middle of the sample due to the burnout of the char layer therein. Two independent branches of the smouldering region marked as ‘C’ and ‘D’ are obtained again, and spread towards the holders on both sides at almost the same rate. Meanwhile, the burning intensity weakens, and the scale of the smouldering zone shrinks. Eventually, the entire smouldering region quenches absolutely by the heat loss to side holders.

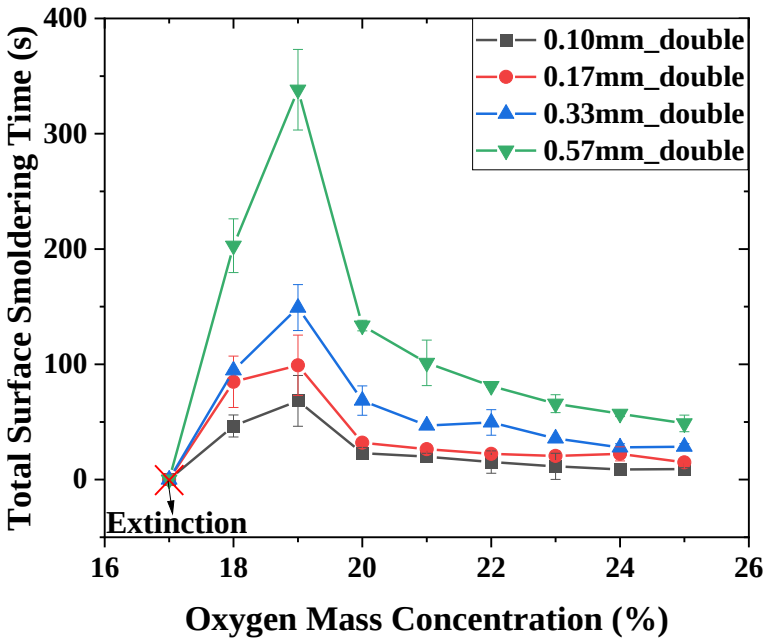


Fig. 8 Total smouldering time over sample surface vs. oxygen mass concentration.

The smouldering process is almost conducted at a rather slow rate in a quiescent environment after the gas-phase flame leaves, in other words, much time is needed for the char layer to be burnout completely. As shown in Fig. 8, below the lean oxygen limit, no flame can survive after the piloted ignition, and the solid phase is too cold to initiate a smouldering process. As the oxygen concentration increases, the gas-phase flame intensity and temperature increase, and accordingly, the heat flux transferred to the solid-phase pyrolysis zone increases, so that a local region of the sample surface can reach the pyrolysis temperature of the char layer. Then periodic holes appear after the gas-phase flame leaves. The smouldering front is stabilized by the radiative heat flux from the carbon dioxide gas for its absorption and re-emission characteristics at the infrared spectrum, without quenching due to excessive surface re-radiative heat loss [16]. The long-lasting smouldering zone on the solid surface has brought new dangers to the fire site, and the transition from smouldering to flaming is likely to occur once the ventilation conditions are improved, leading to a second fire accident. Therefore, in fire protection engineering, it is extremely important to extinguish the potential smouldering process in the fire scene after eliminating the gas phase flame. As the oxygen concentration continues to increase, the range, burning intensity and spread rate of the smouldering zone on the sample surface increase a lot, which leads to a decrease in the overall smouldering time, converging to a stable value under high oxygen concentration ultimately. In addition, the smouldering time of the sample surface increases with the sample thickness, that is because more fuel is stored in a thicker sample and more time is required to burn them out. In general, under high oxygen concentration, although the smouldering time of the sample surface is short, the destructive power is huge for the violently burning flame with a rapid rate of spread. At lower oxygen concentration above the lean oxygen limit, although the gas-phase flame is relatively weak, the slow local smouldering process on the sample surface brings a long-lasting safety hazard to the fire site, which should not be underestimated. Therefore, in the fire fighting and rescue practice, in addition to eliminating gas-phase flames, the investigation of the solid-phase smouldering process should also be much accounted of, in order to thoroughly eradicate fire hazards and ensure the safety of personnel and property. Furthermore, with the massive emissions of fossil fuel products, the carbon dioxide concentration in normal air increases a lot and the global temperature grows to warm, which indicates the increasing smouldering time for charring fuel and much severe fire prevention situation in wildland fires.

## 3 Conclusions

In this study, upward flame spread and surface smouldering process over thin charring paper were investigated. The major findings are summarized as follows.

(a) Three regimes can be obtained as the ambient oxygen concentration increases, stabilizing with 0-sided, 1-sided and 2-sided flames respectively. In the extinction regime, no flame can exist independently. In the linear regime, the flame spread rate is linearly proportional to the oxygen concentration. In the convergence regime, there is no apparent change in the rate of spread with oxygen concentration.

(b) The flame spread rate is inversely proportional to the sample thickness. For thin papers lower than 0.33mm, the hypothesis of thermal-thin profile can be applied perfectly. However, for a paper of 0.57mm, the impact of sample thickness must be considered.

(c) There is a linear relationship of the flame spread rate over the dimensionless flame length. The slope of the fitting curve for double-sided flames is bigger than that of the single-sided flame for the almost doubled heat flux transferred to the pyrolysis front.

(d) In the linear regime, the partial smouldering process characterized by periodic holes on the sample surface appears due to the continuous heating from the remaining branch flame of halved spread rate after unilateral blow-off. Furthermore, the sample surface smouldering time increases with sample thickness. The long-lasting existence of smouldering raises the potency of the transition to flaming, thereby the secondary fire issue, which should also be considered in fire fighting practice.

## Acknowledgements

This work was supported by the National Natural Science Foundation of China (No. 51636008, and 52076201), the Key Research Program of the Chinese Academy of Sciences (No. QYZDB-SSW-JSC029), Fundamental Research Funds for the Central Universities (No. WK2320000051).

## References

[1] A.C. Fernandez-Pello, S.R. Ray, I. Glassman, Flame Spread in an Opposed Forced Flow: the Effect of Ambient Oxygen Concentration, Proc. Combust. Inst. 18 (1981) 579-589.

[2] X. Zhao, Y.T. Liao, M.C. Johnston, S. James, P.V. Ferkul et al., Concurrent Flame Growth, Spread, and Quenching over Composite Fabric Samples in Low Speed Purely Forced Flow in Microgravity, Proc. Combust. Inst. 36(2017) 2971-2978.

[3] J. De Ris, Spread of a Laminar Diffusion Flame, Proc. Combust. Inst. 12 (1969) 241-252.

[4] I.I. Feier, H.Y. Shih, K.R. Sacksteder et al., Upward Flame Spread over Thin Solids in Partial Gravity, Proc. Combust. Inst. 29 (2002) 2569-2577.

[5] L.K. Honda, P.D. Ronney, Mechanisms of Concurrent-flow Flame Spread over Solid Fuel Beds, Proc. Combust. Inst. 28 (2000) 2793-2801.

[6] J. Fang, X. He, K. Li, J. Wang, Y. Zhang, Transition Condition and Control Mechanism of Subatmospheric Flame Spread Rate over Horizontal Thin Paper Sample, Combust. Flame 188 (2018) 90-93.

[7] L. Zhao, J. Fang, S. Tao, J. Wang, Y. Zhang, Effects of Ambient Parameters and Sample Width on Upward Flame Spread over Thermally Thin Solids, Fire Technol. 57 (2020) 145-161.

[8] S. Manabe, R.T. Wetherald, The Effects of Doubling the $CO_2$ Concentration on the Climate of a General Circulation Model, J. Atm. Sci. 32 (1975) 3-15.

[9] Y. Pizzo, J.L. Consalvi, P. Querre, M. Coutin, B. Porterie, Width Effects on the Early Stage of Upward Flame Spread over PMMA Slabs: Experimental Observations, Fire Saf. J. 44 (2009) 407-414.

[10] J. Kleinhenz, P. Ferkul, R. Pettegrew, K.R. Sacksteder, J.S. T'Ien, One-sided Flame Spread Phenomena of a Thermally Thin Composite Cotton/fiberglass Fabric, Fire Mater. 29 (2005) 27-37.

[11] M.C. Johnston, J.S. T'Ien, D.E. Muff, X. Zhao, S.L. Olson, P.V. Ferkul, Self Induced Buoyant Blow Off in Upward Flame Spread on Thin Solid Fuels, Fire Saf. J. 71 (2015) 279-286.

[12] C. Li, Y.T. Liao, Numerical Investigation of Flame Splitting Phenomenon in Upward Flame Spread over Solids with a Two-stage Pyrolysis Model, Combust. Sci. Technol. 190 (2018) 2082-2096.

[13] A.C. Fernandez-Pello, T. Hirano, Controlling Mechanisms of Flame Spread, Combust. Sci. Technol. 32 (1983) 1-31.

[14] G. Cox, D. Drysdale, Combustion Fundamentals of Fire, Academic Press, London, 1995.

[15] C. D. Blasi, Influences of Sample Thickness on the Early Transient Stages of Concurrent Flame Spread and Solid Burning, Fire Saf. J. 25 (1995) 287-304.

[16] P.E. Martin, E.F. Barker, The Infrared Absorption Spectrum of Carbon Dioxide, Phys. Rev. 41 (1932) 291.

# WATER SPRAYS COOLING OF A HOT METALLIC PLATE

**Acem* Z.[1], Mehaddi R.[1], Dréan V.[2], Laumesfeld J.[2], Parent G.[1], Collin A.[1], Proal N.[2], and Wilhelm A.[2]**

*[1] Université de Lorraine, CNRS, LEMTA, F-54000 Nancy, France*
*[2] EFECTIS, France.*
**Corresponding author's email: zoubir.acem@univ-lorraine.fr*

## ABSTRACT

In the present work, experiments were performed in order to assess the spray cooling efficiency of a hot steel plate for three different nozzles. For this purpose, special cares were taken for both the measurement of the surface temperatures and the characterization of the sprays. Firstly, the surface temperatures were measured thanks to K-type thermocouple wires directly welded onto the surfaces of the plate in a separated contact. This technique provides an accurate measurement of the surface temperature during the cooling. Secondly, the spray characteristics of each nozzle were also thoroughly investigated. It was found that droplets size and velocity distributions of each nozzle follow a lognormal law. Corresponding Sauter Mean diameter (SMD) and Mean velocity range respectively from 170 to 230 µm and from 5.6 to 22.4 $m.s^{-1}$. Spray cooling started after heating the plate between 500 – 600 °C by means of a radiative panel. The cooling rate were very high and time to reach 20 °C varied from 4 s to 1 minute according the used nozzle. Heat Flux (Q) and Heat Transfer Coefficient (HTC) were calculated from temperature data. It was found that high level of critical heat flux (CHF), around 3 $MW.m^{-2}$, were achieved for two of the three nozzles studied. With regards to the water consumption, the most efficient nozzle was the one with the lowest flow rate of only 1.6 $l.min^{-1}$. Finally, the results obtained in this study may constitute valuable experimental data which can help for the validation of numerical codes (FDS, FIREFOAM) commonly used in fire safety engineering.

**KEYWORDS:** Spray cooling, Critical heat flux, Heat transfer coefficient, Spray characteristics,

## INTRODUCTION

Spray cooling systems were studied since more than 60 years, especially in the metal industry and the electronics field [1,2]. G. Liang and I. Mudawar [3,4] provided an exhaustive review in two parts adressing all regimes experienced by the fluid during the spray cooling, from the film boiling regime at high temperature to the single phase liquid regime at relatively low temperature. They also pointed out some needs of further experimental research to help understanding some remaining locks, mainly concerning surface temperature spatial gradients assessment, surface to nozzle distance, fluid types and operating conditions. In the field of fire safety, the use of water-based suppression systems to improve fire suppression [5], extinguishment [6], equipment and people protection [7,8] have been also widely addressed over years. Their efficiency is no longer in question but progress are needed in the CFD modelling of such complex systems, involving several physical phenomena. The present work proposes to investigate the water spray cooling of a hot steel plate by different types of nozzles to provide accurate data for CFD validation purposes. The experimental setup is first described. It involves a one square meter steel plate, which can be oriented vertically or horizontally, a radiative panel for the heat source and three types of nozzles. The surface temperatures of the plate were measured with K-type thermocouples. The selected nozzles achieved different spray patterns, mass flux, droplet sizes and velocities. All these parameters, determined in a separate study, are then presented. Finally, the results of spray cooling experiments are presented and discussed. In particular, surface temperatures evolutions during cooling allow to calculate the heat flux Q and the Heat Transfer coefficient (HTC). Results are analysed with regards to the sprays characteristics of each nozzle.

## EXPERIMENTAL SETUP

The experimental setup is presented in Fig. 1. It includes a steel plate (oriented horizontally or vertically) , a radiative panel and water spray and mist systems. The steel plate has a one square meter surface with 2 mm depth and is coated with a high temperature resistant matt black painting. The 1 m x 1 m x 0.002 m plate is equipped on both sides by 20 K-type thermocouple wires with 1 mm diameter. Chromel and alumel wires are 0.5 mm spaced and directly welded on the plate surface. Thus, the electrical contact between the wires is ensured by the steel plate, providing a mean temperature of the plate over the wires spacing (separated contact). The choice of the separate contact makes it possible to overcome problems associated either with direct radiation on the thermocouple, or with a thermocouple junction embedded in a drop of water. This technique provides an accurate and direct measurement of the surface temperature, while it is often extrapolated from sheated thermocouples embedded inside the plate or placed in the back side [1, 9-13]. The side facing the radiative panel ("Heated side") and the side facing the nozzle ("Cooled side") were respectively fitted with 5 and 15 thermocouples. The 50 x 50 cm radiative panel is propane fueled. It delivers a total power of 50 kW with a radiative part estimate to 25 kW, representative of a radiative heat flux close to 100 kW/m². The radiative heat flux received by the plate was controlled by setting the panel/plate distance, thus modifying the view factor. In the present work, the distance between the plate and the radiative panel was 20 cm. The received radiative heat flux, measured in the center of the plate with a radiative heat flux sensor, was estimated to 54 kW/m$^2$. In horizontal configuration, the total heat flux was measuredat 88 kW/m$^2$ correponding to an additional convective contribution about 24 kW/m$^2$.

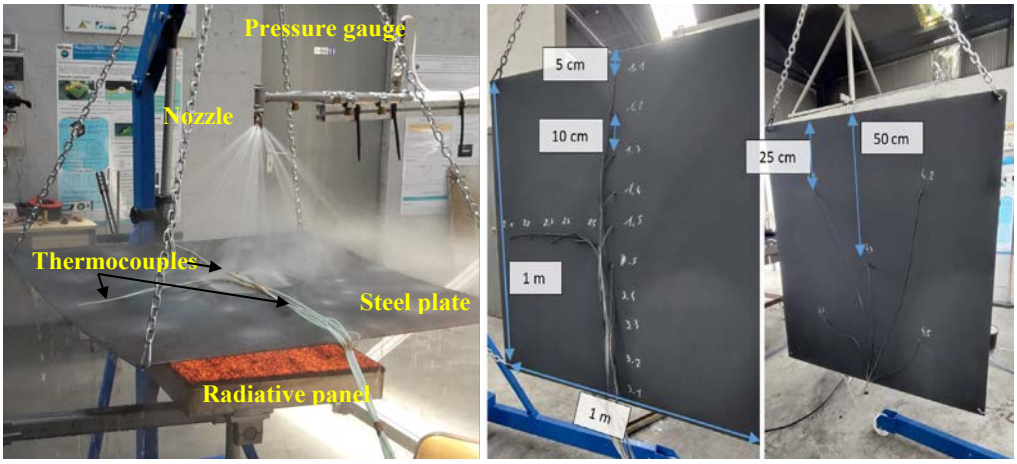


(a) (b)

**Fig. 1.** (a) Experimental setup in horizontal configuration; (b) Thermocouples positions.

## SPRAYS CHARACTERISTICS

Prior to the spray cooling experiments, a separate study was carried out to characterize the droplet size and velocity distributions of the different used nozzles.

Three types of nozzle covering large droplet size and velocity domains were used and are presented in Fig. 2. :

- A Protectospray D3 nozzle from Tyco® (Fig 2 a.):

The nozzle has a 5.16 mm orifice diameter, a deflection angle of 65° and a flow rate number of 17.3 l.min$^{-1}$.bar$^{-1/2}$. The resultant cone is uniformly filled with water droplets, when operating from 1.4 to 4 bars. In fact, as it can be seen in Fig 2 a., the spray pattern is more like an hollow star shaped cone with alternately low and high volume fraction arches.

- An assembly of four flat jet nozzle TPU400067 from Spraying Systems® (Fig 2 b.):

This nozzle produces a quasi flat spray with an elliptic transversal section with a flow rate number of 0.15 $l.min^{-1}.bar^{-1/2}$. According to manufacturer data, the angle according to the large axis is in the range 24° at 1.5 bars to 60° at 15 bars.

- A SU42 conical jet nozzle from Spaying Systems® (Fig 2 c.):

Both compressed water and compressed air are supplied to the nozzle to produces a water mist. Compressed water and air are internaly mixed to produce a fully atomized conical spray.

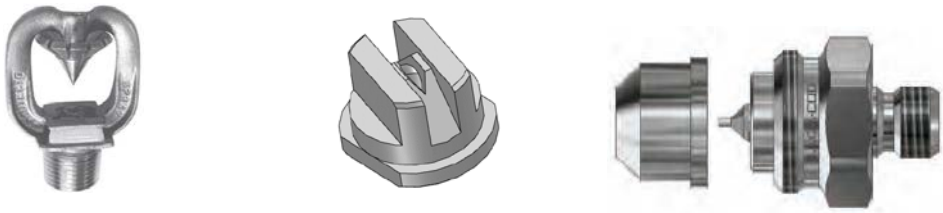

a) b)

**Fig. 2.** Studied nozzle (a) Protectospray D3; (b) TPU400067; (c) SU42.

The sprays characteristics were measured at 50 cm from the nozzle, since it was the distance set between the nozzle and the steel plate for the experiments. The SpraySpy® device from AOM systems, presented in Fig 3., was used to determine the size and the velocity of the droplets. It is based on the time-shift method [14] which exploits the light scattered of a laser beam crossed by a droplet. Depending on the order of the refraction, the back scattered signals asynchronously reach the detectors resulting in a time-shift which is directly correlated to the size and the velocity of the droplet.

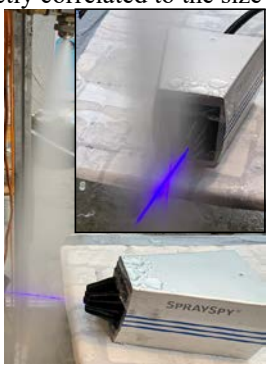


**Fig. 3.** Characterization of the SU42 spray with the SpraySpy system.

The size and velocity distributions for each nozzle are gathered hereafter in figure 4. The measurements were performed at 50 cm height in the centers of the spray pattern for the SU42 and the TPU 400067 nozzles and in the two arches of the Protectospray D3 nozzle. Statistics correspond to a sampling of 20 thousand droplets. Flow rates and water and air pressures are the same as for cooling experiments and are presented in Table 1.

**Table 1. Flow rates and water and air pressures**

| | **SU42** | **TPU 400067** | **Protectospray D3** |
|---|---|---|---|
| **Flow rates ($l.min^{-1}$)** | 4.6 | *0.38* | 34.5 |
| **Water pressure (bar)** | *6.2* | 6 | *4* |
| **Air pressure (bar)** | *4.5* | - | - |

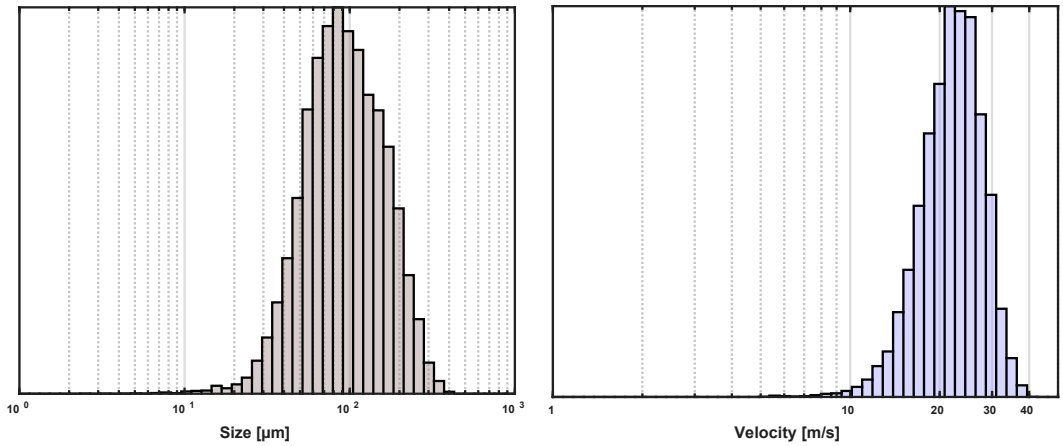


**a) SU42 nozzle :**

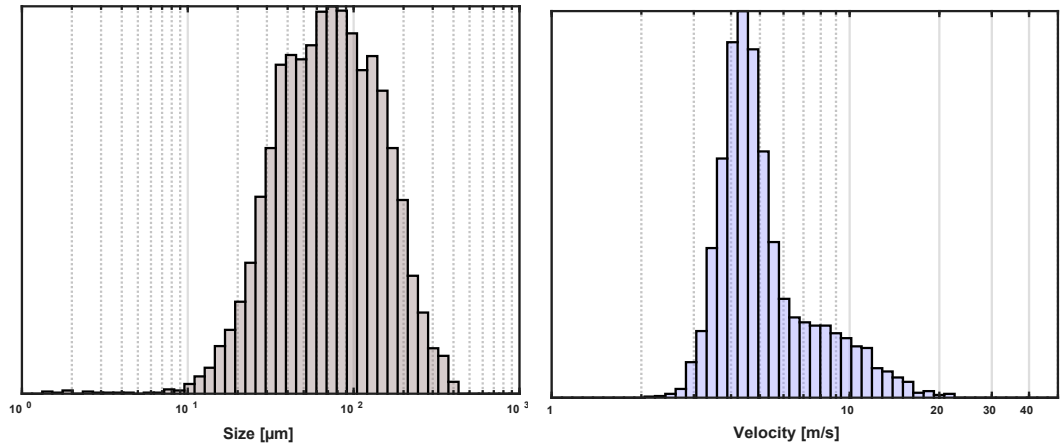


**b) TPU 400067 nozzle :**

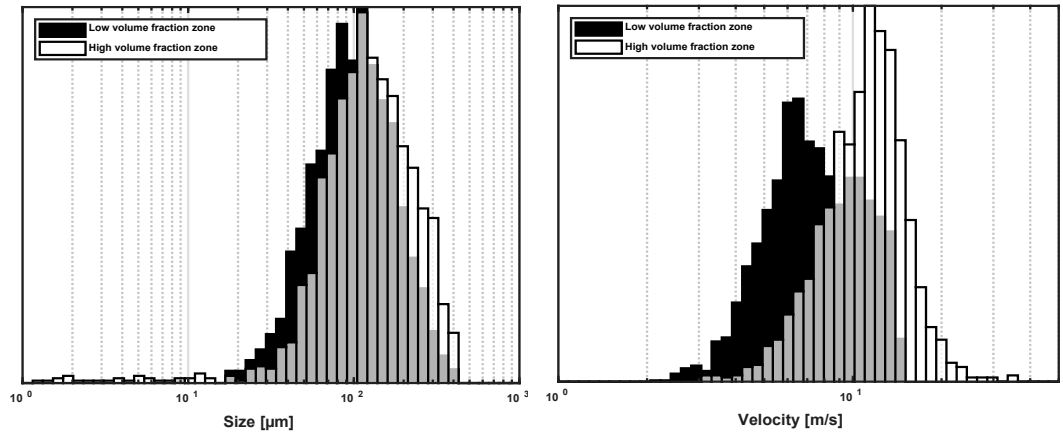


**c) Protectospray D3 nozzle :**

**Fig. 4.** Particule size and velocity distributions at 50 cm heigth:

For each nozzle, it apppears that the size and the velocity of the droplet follow a lognormal distribution, except for the TPU 400067 velocity distribution. For the SU42 nozzle, the droplets size and velocity are distributed around a mean size and velocity close to 80 µm and 22 m/s respectively. Distributions of the TPU 400067 are a little bit wider and are also dispersed around 80 µm for the size and around 5 m/s for the velocity. As mentionned before (see Fig 1a.), the Protectopsray D3 spray pattern is like an hollow star cone composed by alternatively low and high volume fraction zone. It appears that the size distribution of the two zone are slightly the same around 100 µm. The major difference is in the velocity distributions, which are centered around 6 and 11 m/s respectively for the low and the high volume fraction zones. Averaged values, like the Sauter Mean Diameter (SMD) and the Mean Velocity ($v_m$), the droplet Weber number and mass flux were also calculated for each nozzle and are listed in Table 2.

**Table 2. Sauter Mean Diameter (µm) and mean velocity (m/s)**

| | Sauter Mean Diameter (µm) | Mean Velocity (m/s) | Weber number (-) | Mass flux G (kg/m²/s) |
|---|---|---|---|---|
| SU42 | 171 | 22.4 | 1175 | 3.14 |
| TPU 400067 | 182 | 5.6 | 78 | 0.22 |
| Protectospray D3 - Low | 192 | 7.8 | 160 | 9.90 |
| Protectospray D3 - High | 230 | 11.4 | 409 | |

* with ρ and σ refer to respectively the density and the surface tension of water

Based on the mass flux limit (0.7 kg/m²/s) between light and dense sprays established by Yoshida *et al.* [13], it appears that the SU42 and the Protectospray D3 nozzles can be considered as dense sprays and the TPU 400067 nozzle as a diluted spray. The droplet Weber number $We_d$, calculated by using the Sauter diameter and the mean velocity is given by Eq. (1) :

$$We_d = \frac{\rho * SMD * v_m^2}{\sigma} \quad (1)$$

with ρ and σ refer to respectively the density and the surface tension of water

It compares the relative importance of inertia and surface tension forces. The studied configurations cover a large range of droplet $We_d$ number, between 80 and 1200. For the TPU 400067, the $We_d$ is close to 80, the limit where the droplets will rebound from the surface in the film boiling regime established by Yoshida *et al.* [13]. As the $We_d$ increases, the rebound will be followed by desintegration in fine droplets which is the case for the SU42 and the Protectospray D3 nozzles.

## SPRAY COOLING EXPERIMENTS

Spray cooling of a hot metallic plate, both in vertical and horizontal orientations, was performed in order to investigate the efficiency of different sprays provided by each nozzle. The nozzles were centered above the plate at a distance of 50 cm. Experiments with the TPU 400067 nozzle were performed with an assembly of 4 nozzles in order to achieve an 1.6 l.min$^{-1}$ flow rate. The nozzles were uniformely positioned around the center of the plate in order to avoid spray interactions. For each configuration, the plate is heated with the radiative panel until reaching a quasi-steady state. Then, the spray is activated and the radiative panel is turned off at the same time. The temperature recorded at the center of the "cooled side" and the "heated side" of the plate are plotted in Fig. 5.a and Fig. 5.b for respectively vertical and horizontal configuration.

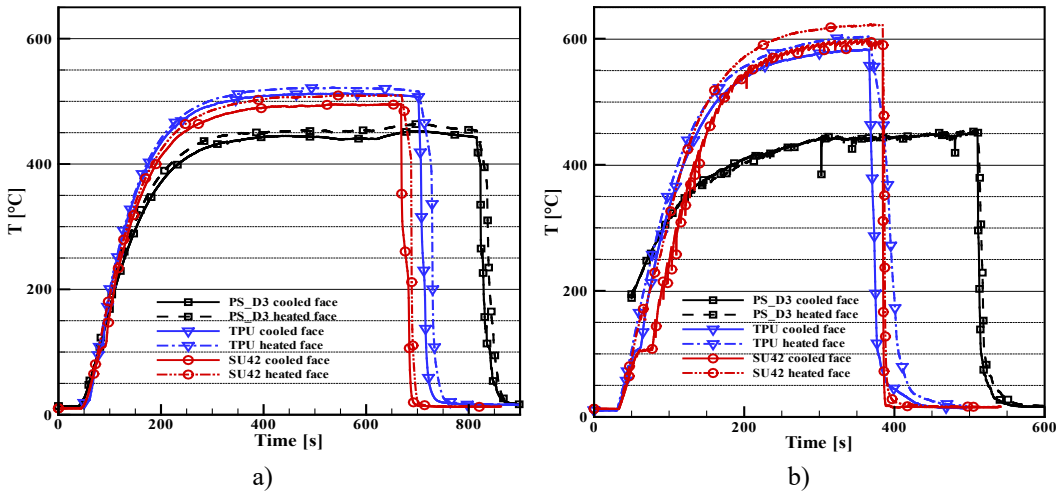


**Fig. 5.** Temperature evolutions at the center of both sides of the plate: (a) vertical orientation; (b) horizontal orientation.

As it can be seen, the cooling rates are very high for each side of the plate. The time for the "cooled side" to reach the ambient temperature of 20°C ranges from 4 s (nozzle: SU42; plate: horizontal) to 66 s (nozzle: TPU 400067; plate: horizontal). The cooling rates of the "heated side" are also very high and the times to reach 20°C are slightly delayed from 5 s to 35 s according the used nozzle and the configuration. The most important delay of 35 s was recorded with the TPU 400067 nozzle and the plate oriented horizontally.These high cooling rates imply high levels of heat flux (Q) and Heat Transfer Coefficient (HTC). Following the same approach of [10], Q and HTC in the center of the plate were calculated as follow :

The heat flux Q ($W.m^{-2}$) is calculated from Eq. (2) by considering the Fourier conduction in the center of plate where a one-dimensional heat transfer is assumed.

$$\mathbf{Q}= \lambda \frac{\Delta T}{e} \tag{2}$$

Where λ is the thermal conductivity of the plate, e the thickness of the plate and $\Delta T=T_{CS}-T_{HS,}$ the temperature difference between the "Cooled side" and the "Heated side" in the center of the plate. The Heat Transfer Coefficie nt ($W.m^{-2}.K^{-1}$) can be then calculated thanks to Eq.(3):

$$\mathbf{HTC}= \frac{Q}{(T_{CS}-T_{im})}= \frac{Q}{\Delta T_{CS}} \tag{3}$$

where $\Delta T=T_{CS}-T_{im}$, the temperature difference between the "Cooled side" and the impinging water temperature $T_{im}$.

Heat fluxes (Q) and Heat transfer coefficients (HTC) were calculated for each studied case and represented in Fig. 6. We retrieve the shape of the well-known boiling curve with the different phase experienced by the fluid during the cooling of the plate. At high $\Delta T_{CS}$, in the film boiling regime, a vapor film is created between the water and the surface of the plate. This film vapor contributes to isolate the plate from the water and induces a rather low heat exchange. As $\Delta T_{CS}$ decreases, below the Leidenfrost temperature, the vapor film tends to break up and the heat transfer increases until reaching the Critical Heat Flux (C.H.F.). This regime is known as the transition boiling regime which is followed by the nucleate boiling regime, where the vaporization of water leads mainly to isolated bubbles. The heat flux starts then to decrease until the natural convection regime with a liquid film.

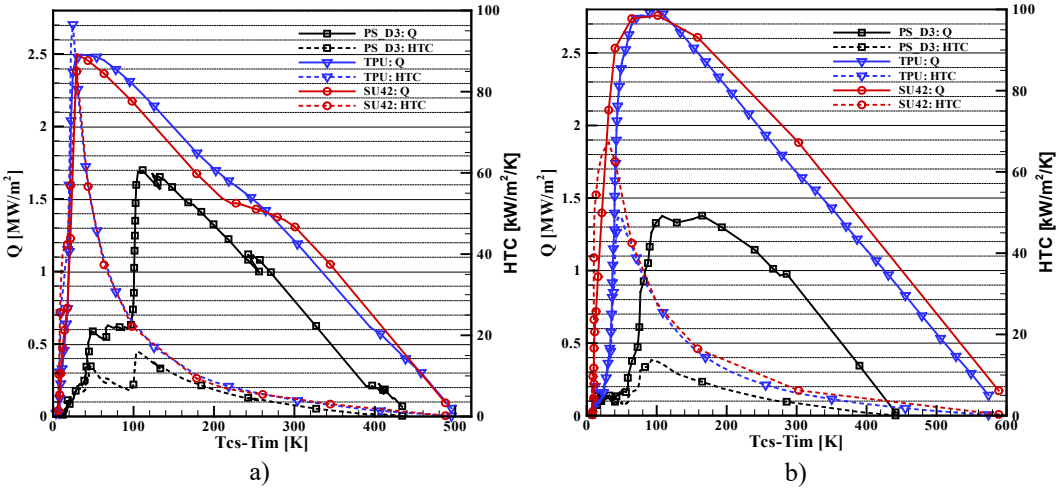


**Fig. 6.** Q and HTC obtained for each nozzle once the spray is activated depending on whether the plate is positioned: (a) vertically or (b) horizontally.

Given the level of $\Delta T_{CS}$, it appears that the film boiling regime was never achieved in our experiments. This is quite understandable when the plate is vertically positioned. Buoyancy and gravity contribute both to naturally drive away the vapor. In the horizontal configuration, it is rather due to the high velocities of the droplets which enable them to go through the vapor film and break it up. So, the cooling starts directely in the transition boiling regime until reaching the CHF. The CHF obtained for each experiment are gathered in Table 3 with respect to the corresponding flow rates .

**Table 3. Critical Heat Flux and Flow Rates.**

| Nozzle | Orientation | Flow rates ($l.min^{-1}$) | C.H.F. ($MW.m^{-2}$) |
|---|---|---|---|
| Protectospray D3 | Vertical | 34.5 | 1.67 |
| Protectospray D3 | Horizontal | 34.5 | 1.37 |
| TPU 400067 | Vertical | 1.6 | 2.49 |
| TPU 400067 | Horizontal | 1.6 | 2.8 |
| SU 42 | Vertical | 4.6 | 2.49 |
| SU 42 | Horizontal | 4.6 | 2.76 |

Whatever the orientation of the plate, results in Fig. 6. show that very high Q and HTC are achieved with the TPU 400067 and the SU42 nozzles. Variations are very similar for the two nozzles, with C.H.F around 2.8 $MW.m^{-2}$ in horizontal configuration and around 2.5 $MW.m^{-2}$ in vertical configuration. This is also the case for the HTC with maximum values reached around 100 $kW.m^{-2}.K^{-1}$ in vertical position. The HTC slightly decreases in horizontal position but maximum values are still high around 70 $kW.m^{-2}.K^{-1}$. Even if the cooling time is faster with the SU42 than with the TPU40067 nozzles (4 s and 24 s versus 66 s and 43 s resp. in horizontal and vertical configuration), the fluid consumption must also be considered to assess the overall cooling efficiency. In this case, the relative low flow rate of the TPU 400067 could be very attractive for achieving very high cooling efficiency while saving water consumption. Especially since the TPU400067 nozzle does not need a compressed air supply like the SU42.

Results for the Protectospray D3 are significantly lower than the two other nozzles but they are still consistent with those obtained by Dou *et al.*[9], who have mainly performed experiments in horizontal position with comparable flow rates and mass flux. The higher flow rate (34.5 $l.min^{-1}$) and the slightly larger droplet size contribute to shorten the transition boiling regime. The nucleate boiling regime is then reached for a higher $\Delta T_{CS}$ resulting in a lower heat transfer.

## CONCLUSION

In the present work, spray cooling experiments of a hot plate were performed in order to assess the cooling efficicency of three nozzles. A specific setup was built involving a radiative panel as the heat source, water and air compressed supplies and a metallic hot plate. In particular, the surface of the plate was carefully fitted with K-type thermocouple wires. The wires were welded separately on the surface so that the electrical contact between the wires is ensured by the plate. It provides a direct and very accurate surface temperature measurement during the cooling, which is no longer the case with classical thermocouples when the junction is embedded in a drop of water.

Prior to the experiments, a separate study was carried out to characterize the droplet size and velocity distributions of the different nozzles. It was found that the distributions follow a lognormal law with mean Sauter diameter ranging from 170 µm to 230 µm and mean velocities between 5 $m.s^{-1}$ and 22 $m.s^{-1}$. These parameters were very useful for the determination of the Weber number and for understanding the behavior of the different sprays.

Regarding the spray cooling experiments, it appeared that for all the tested configurations the cooling starts directly in the transition boiling regime. The results showed that the SU42 and the TPU 400067 nozzles presented the best cooling efficiency with very high C.H.F. (2.5 and 2.8 $MW.m^{-2}$ resp. in vertical and horizontal configuration) and HTC. The behavior of the two nozzles were very similar whereas their sprays parameters are quite different in terms of velocity, mass flux and flow rate. With the lowest flow rate, the TPU 400067 nozzles achieved the best cooling performance with a more rational use of water. Conversely, with cooling time comparable to the TPU 400067 (~ 1 min), the performance of the Protectospray D3 nozzle was less efficient. This sprinkler like nozzle appears to be more adapted to fire control or mitigation rather than spray cooling of facades or structures.

Finally, the sprays characteristics as well as all the surface temperatures investigated in this study constitute also a relevant set of data entry for numerical modeling of spray cooling structures in fire safety engineering using FDS or FIREFOAM codes for instance.

## REFERENCES

[1] L.I. Urbanovich, V.A. Goryainov, V.V. Sevost'yanov, Yu. G. Boev, V. M. Niskovskikh, A. V. Grachev, A. V. Sevost'yanov, V. S. Gur'ev, Investigation of heat exchange in the water-spray cooling of high-temperature metal surfaces. Journal of Engineering Physics 39, (1980), 900–905.

[2] M. Trela, An approximate calculation of heat transfer during flow of an air-water mist along a heated flat plate, International Journal of Heat and Mass Transfer, Volume 24, Issue 4, (1981), 749-755.

[3] G. Liang, I. Mudawar, Review of spray cooling – Part 1: Single-phase and nucleate boiling regimes, and critical heat flux, International Journal of Heat and Mass Transfer, Volume 115, Part A, (2017), 1174-1205.

[4] G. Liang, I. Mudawar, Review of spray cooling – Part 2: High temperature boiling regimes and quenching applications, International Journal of Heat and Mass Transfer, Volume 115, Part A, (2017), 1206-1222.

[5] G. Grant, J. Brenton, D. Drysdale, Fire suppression by water sprays, Progress in Energy and Combustion Science, Volume 26, Issue 2, (2000), 79-130.

[6] Y.F Li, W.K. Chow, Study of Water Droplet Behavior in Hot Air Layer in Fire Extinguishment, Fire Technol 44 (2008), 351–381.

[7] S. Lechêne, Z. Acem, G. Parent, G. Jeandel, P. Boulet, Upward vs downward injection of droplets for the optimization of a radiative shield, International Journal of Heat and Mass Transfer, Volume 54, Issues 9–10, (2011), 1689-1697,

[8] R. Mehaddi, A. Collin, P. Boulet, Z. Acem, J. Telassamou, S. Becker, F. Demeurie, J.-Y. Morel, Use of a water mist for smoke confinement and radiation shielding in case of fire during tunnel construction, International Journal of Thermal Sciences, Volume 148, (2020), 106156.

[9] R. Dou, Z. Wen, G. Zhou, Heat transfer characteristics of water spray impinging on high temperature stainless steel plate with finite thickness, International Journal of Heat and Mass Transfer, Volume 90, (2015), 376-387.

[10] W.-L. Cheng, F.-Y. Han, Q.-N. Liu, H.-L. Fan, Spray characteristics and spray cooling heat transfer in the non-boiling regime, Energy, Volume 36, Issue 5, (2011), 3399-3405.

[11] W. Jia, H.-H. Qiu, Experimental investigation of droplet dynamics and heat transfer in spray cooling, Experimental Thermal and Fluid Science, Volume 27, Issue 7, (2003), 829-838.

[12] A. Cebo-Rudnicka, Z. Malinowski, Identification of heat flux and heat transfer coefficient during water spray cooling of horizontal copper plate, International Journal of Thermal Sciences, Volume 145, (2019), 106038.

[13] K.-i. Yoshida, Y. Abe, T. Oka, Y. Mori, A. Nagashima, Spray cooling under reduced gravity condition, J. Heat Transfer – Trans. ASME 123 (2001) 309–318.

[14] W. Schäfer and C. Tropea, Time-shift technique for simultaneous measurement of size, velocity, and relative refractive index of transparent droplets or particles in a flow, Appl. Opt. 53, (2014), 588-597.

# Combustion properties of the $C_3H_6$/air

**Mousse-Rayaleh A.*, Abid S., M. idir, de Persis S., Comandini A., Chaumeix N.**

*ICARE, CNRS-INSIS, 1C Avenue de la Recherche Scientifique,45071 Orléans Cedex 2, France.*
**Corresponding author's email: ayan.mousse-rayaleh@cnrs-orleans.fr*

## ABSTRACT

Propene ($C_3H_6$) is an important intermediate species in the combustion of heavy hydrocarbons. In this paper, the results of a comprehensive study on the fundamental parameters of premixed flames $C_3H_6$/air are presented. The expanding spherical flames were studied in a spherical bomb over a wide range of equivalence ratio for two temperatures 298 and 373K at an initial pressure of 100kPa. From these experiments, the laminar flame speed $S_L°$, the Markstein length Lu unburned gases, the thickness flame $\delta_{gradT}$, the overall activation energy, were determined. These parameters have also been simulated using COSILAB to verify the validity of the San Diego kinetic mechanism 2016. Other combustion properties were also calculated as the Zel'dovich number β and the effective lewis number.

**KEYWORDS:** Combustion parameters, Laminar flame, Propene, Spherically propagating flame.

## NOMENCLATURE

$E_a$ activation energy (J/mol)
$c_P$ constant pressure specific heat (J.kg$^{-1}$.K$^{-1}$))
ER or $\varphi$ equivalence ratio (-)
$Le_{eff}$ effective lewis number (-)
$S^0_{L,exp}$ experimental unstretched laminar flame speed (cm.s$^{-1}$)
$R_f$ flame radius (mm)
$T_f$ flame temperature (K)
$P_{ini}$ initial pression (kPa)
$T_{ini}$ initial temperature (K)
$L_e$ Lewis number
$L_b$ Markstein length burned gases (mm)
$L_u$ Markstein length unburned gases (mm)
$S^0_{L,RCSF}$ radiation-corrected flame speed (cm.s$^{-1}$)
$k$ stretch (s$^{-1}$)
$t$ time (s)
$V_S$ stretched spatial flame speed (cm.s$^{-1}$)
$S^0_L$ unstretched laminar flame speed (cm.s$^{-1}$)
$V^0_S$ unstretched spatial flame speed (cm.s$^{-1}$)

**Greek**

$\rho_b$ burned gases density (kg.m$^{-3}$)
$\sigma$ expansion ratio (-)
$\delta_{therm}$ flame thickness based on the thermal diffusivity (mm)
$\delta_{gradT}$ flame thickness based on the simulated temperature profile (mm)
$\lambda$ thermal conductivity (W.m$^{-1}$.K$^{-1}$)
$\rho_u$ unburned gases density (kg.m$^{-3}$)
β Zel'dovich number (-)

## INTRODUCTION

Propene ($C_3H_6$) is an important component of liquefied petroleum gas (LPG) and due to the shale gas abundance there may be excess LPG available as an alternative energy source [1]. It is also a key intermediate in the combustion of higher alkanes such as propane, butane, heptane and iso-octane [2]. These compounds constitute a significant part of real hydrocarbon fuels. Therefore, it is important to understand the combustion properties of propene. The abstraction of a hydrogen H atom from propene can also be involved in the formation of aromatic and polyaromatic hydrocarbons which are the main precursors of soot particle emissions. In the context of the mitigation of the formation of pollutants

from advanced combustion systems, it is mandotory to understand the oxidation chemistry of alkenes such as propene.

Several experimental and numerical studies have examined the pyrolysis and oxidation of propene over temperature and pressure ranges. Burcat and Radhakrishnan [3] studied the ignition delay of propene-oxygen-argon mixture in a shock tube over a temperature ranging form 1274 to 1840K for post-shock pressures of 2.19 to 7.04 atm. The concentrations were varied from 0.6 to 1.6% of propene and from 2.7 to 14.4% of oxygen diluted in argon. Qin et al. [4] also studied the ignition delay of the mixture [0.8-3.2%] propene and [3.6-15.1%] oxygen diluted in argon behind reflected shock waves at post-shock temperatures ranging from 1270 at 1820 K with pressures from 0.95 to 4.7 atm. The measurements carried out in Qin et al. study were observed to be shorter than those in Burcat and Radhakrishan's study under similar conditions; however, Qin et al. did not identify possible sources of the disagreement. The thermal decomposition of propene behind reflected shock waves over a temperature range of 1200-1800 K has been investigated by Hidaka et al. [5] by measuring the profiles of $C_3H_6$, $C_2H_2$, $C_4H_6$, $C_3H_4$ and $C_6H_6$ using IR laser kinetic absorption spectroscopy coupled with gas chromatography. There are several mechanisms in the literature that can be used to simulate the combustion of propene. Westbrook and Pitz [6] have developed a detailed chemical kinetic mechanism to describe the oxidation and pyrolysis of propane and propene. The mechanism consists of 163 elementary reactions for 41 chemical species. The mechanism is tested and compared with the experimental results of shock tubes and turbulent flow reactor for pressures of 1 to 15 atm and temperatures of 1000 to 1700K. Dagaut et al. [7] proprosed a kinetic chemical reaction mechanism capable of reproducing their speciation results based on previous studies [6]. They presented additional rate constants for the reactions of propenes with the hydroxyl and hydroperoxyl radicals of Baldwin and Walker [8]. Wilk et al. [9] have developed a mechanism capable of simulating static reactor data at low temperature (530-740 K), equivalence ratios of 0.8 to 2.0 and a pressure of 600 Torr. It is one of the few mechanisms developed in the literature to simulate the low temperature oxidation of propene. In this study, a slight CNT region is observed near a temperature of 620 K in the calculation, however the behavior measured experimentally is not clear. The authors said they "were unsure whether the slight deviations in the experimental data are real indications of NTC's behavior or whether it is data scattering." Simonyan and Mantashyan [10] also report conflicting evidence for the presence of NTC. The presence of NTC for propene is inconclusive.

There have been some experimental studies of propene laminar flames. Law and colleagues [6,11] reported laminar flame speed measurements for propene in two studies. Davis et al. [11] reported laminar flame speed for propene/air mixtures at room temperature and atmospheric pressure performed using the countercurrent twin flame configuration. Jomaas et al. [12] studied the laminar flame speed of C2-C3 hydrocarbons, including propene, from a spherical flame in a constant pressure chamber at pressures of 1, 2 and 5 atm. The laminar flame speed reported by Jomaas et al. [12] at ER = 1.0 is ≈ 3 cm/s slower than that reported by Davis et al. [11], Saaed and Stone [13].

A comprehensive and unprecedented study into the oxidation of propene is being carried out by several different groups using a wide range of experimental facilities and techniques, with an emphasis on ignition delays and ignition speeds. laminar flame [14].

Despite these numerous data in the literature, the uncertainty that are reported do not allow a proper determination of fundamental parameters that relies only on detailed kinetic simulations such as the Zeldovich number and the effective Lewis number. Indeed,these properties are based on detailed kinetic simulations which inturns relies on precise flame speeds with very low uncertainties. The focus of the present study is the to accurately determined the fundamental combustion properties of propene/air mixture over wide range of equivalence ratio and at two initials temperatures 298 and 373K and 100kPa through the investigation of laminar expanding spherical flames.

## MATERIAL AND METHOD

### Experimental set-up

Laminar flame speed were determined using a stainless steel bomb with an internal volume of 56 L and an internal diameter of 474 mm (Fig. 1a). It consists of two concentric spheres allowing the circulation of a heat transfer fluid in order to heat the device to the desired temperature. It has been sized in order to ensure that it is able to withstand combustion reactions at the respective temperature and pressure conditions of 473K and 50 bar. The temperature is measured using a thermocouple inside the bomb. A high frequency piezoelectric pressure transducer (Kistler 601A) is mounted on the inner wall of the vessel to monitor pressure during combustion. Two tungsten electrodes located along the diameter of the sphere are connected to a high voltage source to generat spark leading to ignition of the mixture. The spark simultaneously triggers oscilloscope that record pressure, voltage, current and the camera via a TTL generator. The spherical bomb is equipped with two opposing quartz windows (optical diameter 97 mm, thickness 50 mm). The flame propagation is observed using a Z-shaped Schlieren device (Fig. 1.b) and a high-speed camera (PHANTOM V1611) up to 25000 fps to record the Schlieren images of the growing flame (Fig. 2a). A continuous white lamp is used to illuminate the flame through two lenses and two concave spherical mirrors. The frame resolution has been set at 768 x 768 pixels². Before the mixture was introduced, the facility and the lines were evacuated through two primary pumps. All gases were supplied by Air Liquide. Air is composed of 20.9%$O_2$ + 79.1%$N_2$ with a purity of purity> 99.9999%. The purity of propene is greater than 99.5%. The mixtures were prepared directly at the facility using the partial pressure method. Partial pressures and total pressure were measured using two Baratron capacitive pressure sensors (MKS-631) of 0-100 Torr (13.3 kPa) and 0-1000 Torr (133.3 kPa). The mixtures were allowed to rest for 5 min after the filling process to eliminate any turbulence [15]. The initial temperature was reported prior to the ignition of the mixture. The experiments were carried out at an initial pressure of 100 kPa and initial temperatures of 298 and 373K.

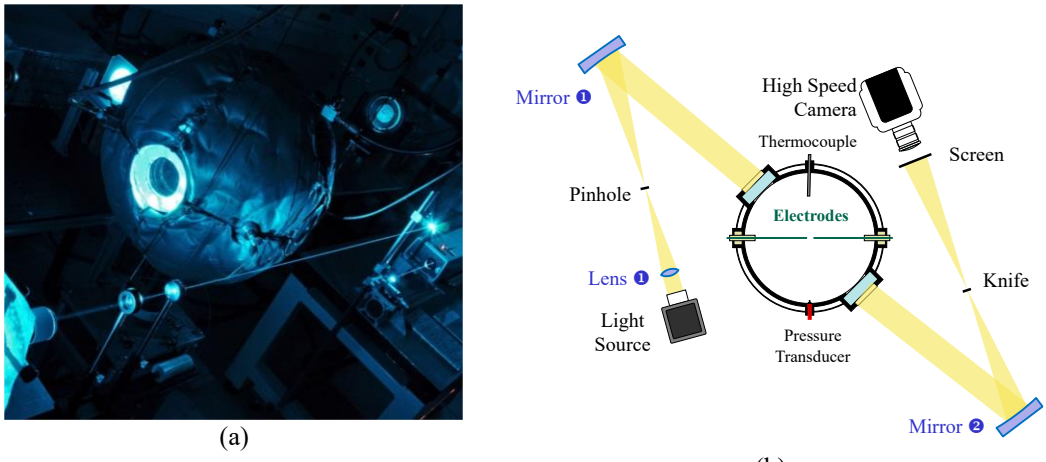


**Fig. 1.** (a) Spherical bomb picture ; (b) Schlieren configuration

### Experimental conditions

The experiments were carried out with mixtures of $C_3H_6$/air for an initial pressure of 100 kPa and temperatures of 298 and 373K. To obtain very precise results, the experiments were carried out with initial pressure, $P_{ini}$ = ± 0.1 kPa, initial temperature, $T_{ini}$ = ± 1 K and with the composition of the mixture, ER = ± 0.1 %. Particular attention has been paid to the placement of the electrodes (alignment, distance between the tips, diameters) in order to reduce flame-electrode interactions.

## Methodology

Schlieren images of the growing flame (Fig. 2a) were processed using a code developed in the laboratory using Matlab libraries to obtain the flame radius $R_f$ as a function of time. A propagation speed is derived from the evolution of the flame radius as a function of time, $V_S$ (Eq. (1)). As the flame expands from the point of ignition, the rate of stretch seen by the flame decreases according to Eq. (2). The unstretched speed $V_S°$ is determined by considering a nonlinear variation the flame speed with the stretch rate. Several relations can be used [16, 17]. In the present study, the nonlinear equation proposed by Ronney and Sivashinsky [18] and later modified by Kelley and Law [19] (noted NQ for Quasi-steady Nonlinear model in [17]) was used. The laminar burning speed $V_S°$ and the Markstein length are derived from the solution of Eq. (3) [15,19]:

$$V_S = \frac{dR_f}{dt} \tag{1}$$

$$k = 2\left(\frac{V_S}{R_f}\right) \tag{2}$$

$$\left(\frac{V_S}{V_S^0}\right)^2 . \ln\left(\frac{V_S}{V_S^0}\right)^2 = \frac{2L_b.k}{V_S^0} \tag{3}$$

An example of unstretched speed extraction is given in Fig. 2b. The experimental radius range used in this data processing was from 10 to 46 mm. The minimum radius was set to eliminate the effect of ignition energy while the maximum radius was was chosen to avoid the effect of pressure on the laminar flame [20] (Fig. 2d). Since the pressure remains constant during the observation time, the laminar flame speed, $S_L°$ is determined according to Eq. (4). The densities of unburnt and burnt gases are calculated using the COSILAB equilibrium code [21] with the assumption of a constant pressure combustion.

$$S_L^0 = \frac{V_S^0}{\sigma} \tag{4}$$

$$\sigma = \frac{\rho_u}{\rho_b} \tag{5}$$

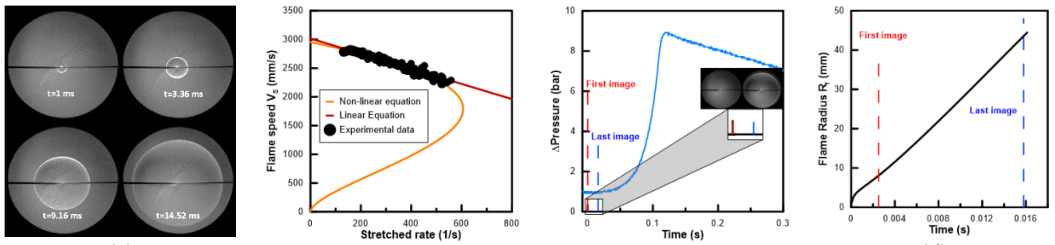


(a) (b) (c) (d)

**Fig. 2.** Examples of results for a $C_3H_6$/air flame at ER=0.9, Tini= 300 K and Pini= 100 kPa: (a) flame images, (b) flame speed versus stretch rate, (c) pressure profile, (d) flame radius

According to Santner et al. [22], radiative heat loss can be a great source of experimental uncertainty in flame speed measurements using the outward-propagating spherical flame method. Equation 6 is used to verify the influence of radiative loss in our flames [23]. The results are shown in Fig. 3. As one can see the differences between the laminar flame speed obtained experimentally and the flame speed corrected for the radiation vary from 0.48 to 0.68 cm/s : the radiation is minimal for an equivalence ratio between 0.85 and 1.35. It is only for very lean and very rich mixture that the ratio correction is aboved 0.5 cm/s at 298K. Increasing the initial temperature leads to a increase of correction to be applied.

$$S_{L,RCSF}^0 = S_{L,exp}^0 + 0.82\,.\,S_{L,exp}^0\,.\left(\frac{S_{L,exp}^0}{S_0}\right)^{-1.14}.\left(\frac{T_{ini}}{T_0}\right).\left(\frac{P_{ini}}{P_0}\right)^{-0.3} \tag{6}$$

Where $S_0$ = 1 cm.s$^{-1}$ , $T_0$ = 298K and $P_0$ = 1atm

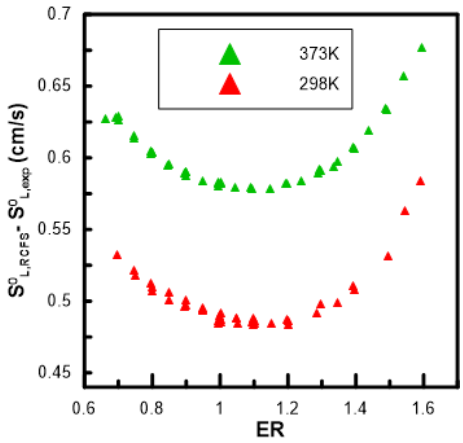


**Fig. 3.** Evaluation of the radiation-corrected speed according to [22].

### Combustion parameters fundamentals

From the 1D-simulation of the laminar flame speed using COSILAB [21], a set of fundamental combustion parameters: flame thickness, activation energy, Zel'dovich number, effective lewis number were estimated of the $C_3H_6$/air mixture (Fig. 8 and Fig. 9). These parameters are necessary to establish the flame acceleration criterion. To calculate them, a detailed kinetic mechanism must be used with the ability to reproduce experimental results for $C_3H_6$/air mixtures over a wide range of initial conditions. For this study, the UCSD 2016 mechanism [24] was used.

## RESULTS AND DISCUSSION

### Laminar flame speed

Laminar flame speed is more precisely defined as the speed at which unburned gases move in the normal direction with respect to the flame front. As mentioned previously, different relationships can be used to extract the unstretched speed $V_S$ ° using the spherically expanding flame method [17]. The four extrapolations methods: linear model based on stretching (LS), linear model based on curvature (LC), non-linear model with 3 parameters (N3P), non-linear model in the form of expansion (NE) and the quasi-stationary non-linear (NQ) model were used to verify that the present data are not impacted. The results obtained with these models are shown in Fig. 4a. As one can see, there is a perfect agreement between the extrapolation models exemplifying that the flames obtained in the present spherical vessel are large enough so that the stretch rate can be considered as weak [16]. This also verifyed via the calculation of the parameter $\{Ma_{linear}.Ka_{middle}\}$, the Markstein number is obtained using the LS model and Karlovitz number is calculated at the middle radius for each experiment. According to Wu et al. [17] , this parameter must be between -0.05 and 0.15 in order for the solution of equation 3 to be independent from the extrapolation method (Fig. 4b). As one can see that ony few experiments in very lean and very rich conditions are not within this range. Their respective unstretched laminar flame speed and Markstein lengths are then dependent on the chosen processing method.

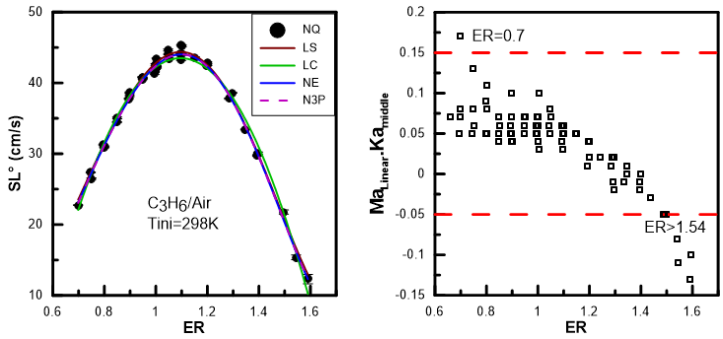


**Fig. 4.** Extrapolation models on $S_L°$ (a) $C_3H_6$/Air mixtures at Tini=298K and Pini=100kPa; and (b) $Ma_{linear}.Ka_{middle}$ parameter for all experimental results at 298 and 373K

Figure 5 shows the measured laminar flame speed, $S_L°$ for propene ($C_3H_6$) measured in this study and from the literature at 298K and 100kPa, according to the experimental method used:

- the spherically propagated flames method by Princeton [14], TAMU, [14] Jomaas et al. [12] and Saeed and Stone[13],
- the heat flux burners method by VUB (a), Lund and Nancy [14],
- and finally counter-current flames method by Davis & Law [11].

In each case, the maximum laminar flame speed is obtained for equivalence ratio around 1.1.

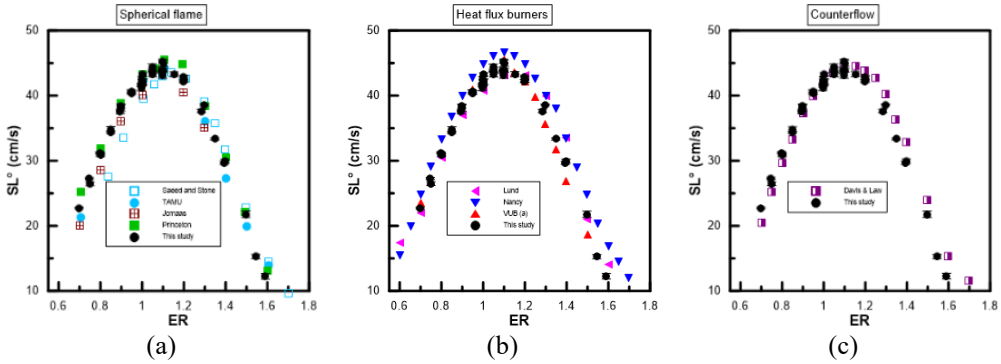


**Fig. 5.** $S_L°$ $C_3H_6$/Air at 100kPa and 298K: (a) Spherical flame ; (b) This study compared with heat flux burners ; (c) This study compared with counterflow

Figure 5a represents the laminar flame speeds obtained by the spherical bomb method at 298K and 100 kPa. As one can see, on the lean side, a very good agreement is found between all the different sets at the exception of the data of Saeed and Stone which are significantly lower. On the rich side of the curve, the discrepancy between the different authors is larger and the present work agrees fairly well with the data of TAMU and Princeton groups. In the case of the heat-flux burner (Fig. 5b), our data agrees very well with the data of VUB, while bth Lund and Nancy data are significantly higher than VUB data (same method). Finally, in the case of the counterflow flame burner (Fig. 5c), a very good agreement is found with the data of Davis and Law on the lean side while their data are systematically higher on the rich side. It is noteworthy to point that the largest scaterring in the data is observed near the stoechiometry and for rich conditions.

The Markstein length of fresh gases is determined using equation 7 and the results are report in Fig. 6 as a function of the equivalence ratio for two initial temperatures.

$$L_u = \frac{L_b}{\sigma} \quad (7)$$

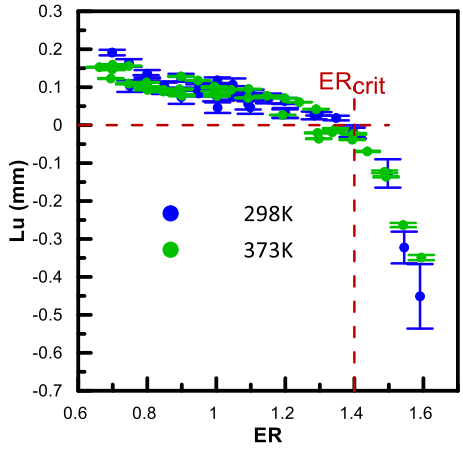


**Fig. 6.** Markstein length of $C_3H_6$/Air at 100kPa for 298 and 373K

As one can be seen on Fig. 6, Lu becomes negative for a critical equivalence ratio of $ER_{crit} = 1.4$ for $C_3H_6$/air mixtures for both temperatures, Lu <0 corresponds to thermo-diffusive instabilities. Increasing the initial tempertaure does no change the value of the Markstein length.

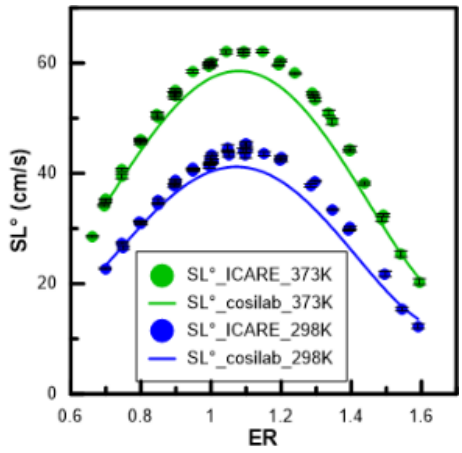


**Fig. 7.** Laminar flame speed $S_L°$ of $C_3H_6$/Air at 100kPa: the symbols correspond to experimental results and the line COSILAB results [21], at Tini=298 and 373K

Figure 7 represents the experimental and simulated laminar flame speeds, for two temperatures 298K (blue color) and 373K (green color) at 100kPa. The symbols are the experimental results and the line corresponds to the simulation. As expected, the speed of the flame increases with increasing initial temperature. Overall, a good agreement is obtained between experimental and simulated results using the UCSD 2016 mechanism [24] for lean and rich mixtures. However, the model understimate the laminar flame speed for an equivalence ratio ranging from 1 to 1.3.

As mentioned earlier, combustion parameters for safety analyzes are derived from laminar flame speed such as laminar flame, thickness, effective Lewis number, activation energy Ea and hence the number of Zel'dovich β.

**Fundamental premixed flame properties**

Because of the many theories that exist on the propagation of laminar flames (thermal, diffusion and global), there are also several ways to define the thickness of a laminar flame. However, the most widely used definition remains that established by Zel'dovich [25]. The latter is based on the theory of Mallard and Le Châtelier which breaks down the flame front into two parts: a preheating zone and a reaction zone. The thickness of the preheating zone $\delta_{therm}$ results in a balance between thermal diffusion and species diffusion Eq. (8).

$$\delta_{therm} = \frac{\lambda}{C_p \rho_u S_L^\circ} \tag{8}$$

These parameters $\lambda$, $\rho_u$, $C_p$ can be deduced from thermodynamic equilibrium calculations performed using the COSILAB [21] "Equilibrium" code.

The other method is based on the temperature profile of the flame front according to equation 9 which is obtained when simulating laminar flame speed using the code "one dimensional freely propagating flame".

$$\delta_{gradT} = \frac{T_f - T_{ini}}{\left(\frac{dT}{dx}\right)max} \tag{9}$$

Figure 8a reports the flame thickness versus the equivalence ratio based on the gradient of temperature ($\delta_{gradT}$) for the mixtures considered in the present study for $C_3H_6$/air at 298 and 373K. As expected, increasing the initial temperature from 298 to 373K, leads to a decrease in the flame thickness.

**Effective lewis and Zel'dovich number**

Figure 8b reports the values of the effective Lewis numbers Eq. (10) for the mixtures considered in the present study. $Le_{eff}$ is between the calculated Lewis number of $C_3H_6$ and $O_2$. The Lewis numbers of the reactants ($C_3H_6$ and $O_2$) are also given in order to illustrate that the $Le_{eff}$ of the mixture is driven by Le $C_3H_6$ under lean conditions and by Le $O_2$ under rich conditions. As one can see, Leeff Following the trend of Lu (Fig. 6), it has to be noted that the studied flames are stable ($Le_{eff} > 1$). The increase in temperature causes a decrease in the number of lewis and consequently $Le_{eff}$.

$$Le_{eff} = 1 + \frac{(Le_{Excess} - 1) + (Le_{Deficiant} - 1) \cdot A}{1 + A} \tag{10}$$

With $A = 1 + \beta(\varphi - 1)$ (11)

$\varphi = ER$ ; $ER \geq 1$ (12)

$\varphi = 1/ER$ ; $ER < 1$ (13)

The Zeldovich number β represents the activation energy normalized by temperature according to the following equation:

$$\beta = \frac{E_a \cdot (T_f - T_{ini})}{R \cdot T_f^2} \tag{14}$$

The evolution overall activation energy and β with the equivalence ratio is presented in Fig. 9b. In each case, the minimum β is obtained at the equivalence ration for which the laminar flame speed is the highest one. As it could be intuitively predicted, the reactivity of the mixtures of interest increases with the temperature. The decrease of β with the initial temperature increase. With the appearance of thermo-diffusives from the equivalence ratio of 1.4, is very unstable. The activation energy is deduced from the slope of the Eq. (15). As one can see in Fig 9a, trends are very well reproduced for overall activation energy.

$$2.\ln \rho_u S_L^0 = \mathrm{f}\left(\frac{1}{T_f}\right) \tag{15}$$

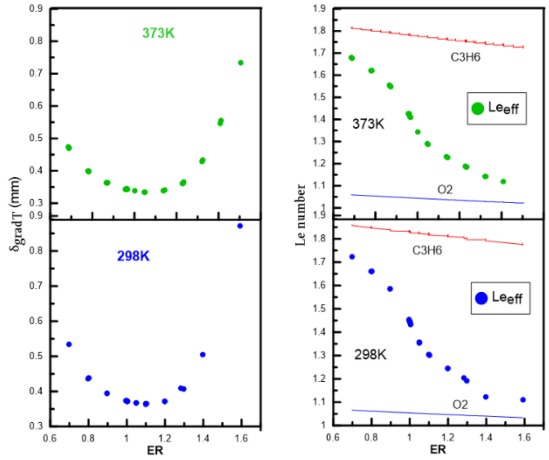


**Fig. 8.** $C_3H_6$/Air at 100kPa at 298 and 373K : (a) Thickness flame and ; (b) Lewis number and effective for $C_3H_6$ and $O_2$

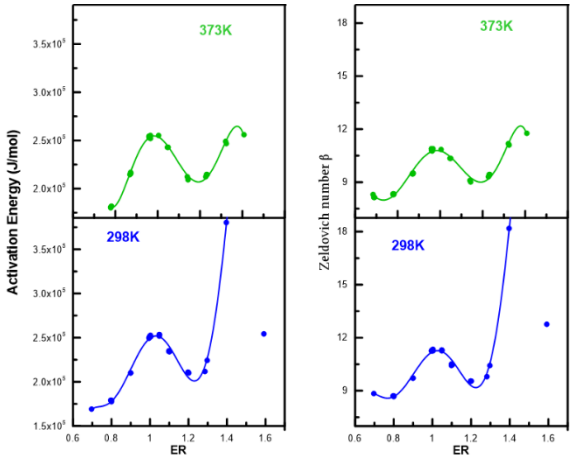


**Fig. 9.** $C_3H_6$/Air at 100kPa at 298 and 373K : (a) Overvall activation energy ; (b) Zeldovich number

## CONCLUSION

In the present work, laminar flame speed of $C_3H_6$/air mixture have been studied for two initial temperatures (298 and 373K) and 100kPa on the spherical bomb method. From these $S_L°$ and Lu have been determined. The UCSD 2016 chemical kinetic model was used in order to simulate laminar flame speeds in the same initial conditions. An overall good agreement was found except from equivalence ratio 1 to 1.3. This validation demonstrates that this model can be improve for $C_3H_6$/air to simulate premixed flame properties. The model was subsequently used to perform calculations of the following parameters: thickness flame $\delta_{gradT}$, effective Lewis number $Le_{eff}$ , Zel'dovich number β and overall activation energy Ea.

## ACKOWLEDGEMENT

A. Mousse-Rayaleh acknowledges the financial support from the Frecnh Ministery of Higher Education and Research (MESRI PhD grant).

## REFERENCES

[1] K.J. Morganti, T.M. Foong, M.J. Brear, G. da Silva, Y. Yang, F.L. Dryer, Fuel 108 (2013) 797–811.
[2] S.G. Davis, C.K. Law, H. Wang, Combust. Flame 119 (1999) 375–399.

[3] A. Burcat, K. Radhakrishnan, Combust. Flame 60 (1985) 157–169.

[4] Z. Qin, H. Yang, W. C. Gardiner, Combust. Flame 124 (2001) 246–254.

[5] Y. Hidaka, T. Nakamura, H. Tanaka, A. Jinno, H. Kawano, T. Higashihara, Int. J. Chem. Kinet. 24 (1992) 761–780.

[6] C.K. Westbrook, W.J. Pitz, Combust. Sci. Technol. 37 (1984) 117–152.
[7] P. Dagaut, M. Cathonnet, J.C. Boettner, J. Phys. Chem. 92 (1988) 661–671.
[8] R. Baldwin, R. Walker, Proc. Combust. Inst. 18 (1981) 819–829.
[9] R. Wilk, N. Cernansky, W. Pitz, C. Westbrook, Combust. Flame 77 (1989)
145–170.
[10] T.R. Simonyan, A.A. Mantashyan, React. Kinet. Catal. L 17 (1981) 319–322.
[11] S.G. Davis, C.K. Law, H. Wang, Combust. Flame 119 (1999) 375–399.
[12] G. Jomaas, X.L. Zheng, D.L. Zhu, C.K. Law, Proc. Combust. Inst. 30 (2005) 193–200.
[13] K. Saeed, R. Stone, J. Energy Inst. 80 (2007) 73–82.
[14] S.M. Burke, W.K. Metcalfe, O. Herbinet, F. Battin-Leclerc, F.M. Haas, J. Santner, F.L.sDryer, H.J. Curran, Combust. Flame (2014) accepted.

[15] D. Nativel , M. Pelucchi , A. Frassoldati , A. Coman- dini , A. Cuoci , E. Ranzi , *Combust. Flame* 166 (2016) 1–18 .
[16] Z. Chen , *Combust. Flame* 158 (2011) 291–300 .
[17] F. Wu , W. Liang , Z. Chen , Y. Ju , C.K. Law , *Proc. Combust. Inst* 35 (2015) 663-670 .
[18] P. Ronney , G. Sivashinsky , *J. Appl. Math.* 49 (4) (1989) 1029–1046 .
[19] A. Kelley , C.K. Law , *Combust. Flame* 156 (2009) 1844–1851 .
[20] M. Burke , Z. Chen , Y. Ju , F. Dryer , *Combust. Flame* 156 (2009) 771–779 .
[21] COSILAB, *The Combustion Simulation Laboratory* , Rotexo GmbH & Co. KG, Haan, Germany, 2009 Version 4.3.2 http://www.SoftPredict.com .
[22] J. Santner , F. Haas , Y. Ju , F. Dryer , *Combust. Flame* 161 (2014) 147–153.
[23] H. Yu , W. Han , J. Santner , et al. , *Combust. Flame* 161 (2014) 2815–2824.
[24] http://web.eng.ucsd.edu/mae/groups/combustion/mechanism.html
[25] I. Glassman, *Combustion*, 3rd edition, Academic Press, San Diego, California, 1997.

# Fire Suppression and Mitigation

# Effects of Seawater on the Performance of Aqueous Film-Forming Foam Based on Anionic, Nonionic and Amphoteric Surfactants

**Yu X.Y.[1,2], Miao X.Y. [1], Yu X.[1,2], Li H.[1], Qiu K.[1], Lu S.X. [1,*], Zong R.W. [1,2,*]**

*[1] State Key Laboratory of Fire Science, University of Science and Technology of China, Hefei 230026, China*

*[2] Suzhou Key Laboratory of Urban Public Safety, Suzhou Research Institute, University of Science and Technology of China, Suzhou, Jiangsu, 215123, China*

**Corresponding author's email: zongrw@ustc.edu.cn*

## ABSTRACT

In this study, six aqueous film-forming foam (AFFF) concentrates based on anionic (SDS), nonionic (APG) and amphoteric (CAB) surfactants were prepared by using deionized water and seawater, respectively. The interfacial properties, foaming ability, foam stability and fire-fighting performance of AFFF formulations were in detail studied. It is found that the $AFFF_{APG}$ and $AFFF_{CAB}$ can resist the negative influence of inorganic salts in seawater. In contrast, the presence of seawater leads to a decrease in equilibrium surface tension and foaming ability of the AFFF sample containing the SDS, compared to the deionized water cases. Salts in the seawater have different effects on the foaming ability. The addition of $Na^+$ is beneficial to enhancing the foaming ability of the $AFFF_{SDS}$ samples, while $K^+$, $Mg^{2+}$ and $Ca^{2+}$ can weaken the foaming ability of the solution. For the stand-alone foams without oil, the foam stabilizing effect of seawater is not observed by detecting the change of foam height with time. Instead, the $AFFF_{SDS}$ sample diluted by seawater has the lowest foam stability in the presence of n-heptane, which leads to poor oil sealing performance. Foams made from seawater exhibit longer fire extinction times and shorter burn-back times than seawater-free cases. $AFFF_{APG}$ exhibits the best fire extinguishing and burn-back performance among all formulations, though its spreading coefficient is not very high, indicating that it is insufficient to evaluate the fire-fighting performance by considering the spreading coefficient. The effect of seawater on fire-fighting performance is closely related to foam properties, especially for foam stability in the presence of oil.

**KEYWORDS:** Salt, surfactant, aqueous film-forming foam, foam properties, fire-fighting performance.

## 1. INTRODUCTION

Foam has been used in many industrial fields such as firefighting, mineral flotation, food processing, foam fractionation, processing of textiles, personal care products, enhanced oil recovery and so forth in the past few decades [1-3]. Foam stability refers to the ability of the bubble to resist collapse, which is one of the most basic properties of foams [4]. Generally, foam ageing is controlled by three basic processes including the drainage induced by gravity, the coalescence of adjacent bubbles due to the rupture of inter-bubble lamellae, and the coarsening caused by inter-bubble gas diffusion [5].

Aqueous film-forming foam (AFFF) is a type of high-efficient fire extinguishing agent used to fight liquid fuel fire [6]. The high efficiency of fire extinguishment is provided by an aqueous film layer and foam blanket formed on the surface of liquid fuel in application [7]. AFFF concentrates consist of fluorocarbon surfactants, hydrocarbon surfactants, stabilizers, organic solvents, water and so on. AFFF has been widely used in ships, warships and marine oil platforms for Class B fire-fighting during the past few decades [8], and their concentrates are inevitably diluted by seawater once applied in these sites [9]. The performance of AFFF is more or less affected by a number of inorganic salts in seawater [9]. Thus, it is worth exploring the influence of seawater on the performance of AFFF.

Up to now, some studies have been conducted on the effect of salts on the foam properties of the surfactant solution. Dlugogorski et al. combined the observations from fire experiments with the computer ionisation modelling of fluorocarbon surfactants to explain the compatibility of fluorocarbon surfactants with seawater [10]. Angarska et al. investigated the effects of bivalent

electrolytes on film stability, and they reported that the foam films containing $Mg^{2+}$ are more stable than those containing $Na^{+}$ at low surfactant concentration [11]. Akram showed that the counterions exert a strong influence on the critical micelle concentration (CMC), aggregation number and size and shape of aggregates of ionic surfactant systems [12]. The seawater consists of a large amount of NaCl and divalent metal cations, including $Mg^{2+}$ and $Ca^{2+}$ which can combine with negatively charged groups of ionic surfactants to generate precipitations [13]. The surfactant precipitations have great effects on the interfacial properties and can reduce the adsorption kinetics of surfactants [11-13]. The effects of salt on foam stability are complex, and recently it has been reported the two opposite effects of salts (defoaming [14] and stabilizing effect [15,16]) on foam stability which is closely related to the type and concentration of salts and surfactants. On the one hand, salts can stabilize foam by electrostatic shielding and reducing the surface tension [14]. On the other hand, the addition of salts can promote the surfactant to fall into the precipitation domain to behave the defoaming effect by bridging mechanism [15,16]. Until now, which effect dominates the foam performance of AFFF solution is unclear, and the current works on the relationship between the interfacial properties, foam stability and fire extinguishing performance affected by seawater are still insufficient.

In the present work, six AFFF concentrates based on anionic surfactant (SDS), nonionic surfactant (APG) and amphoteric surfactant (CAB) were prepared. The deionized water and seawater were used to dilute concentrates and obtain the AFFF formulations. Then, the surface activity, foaming ability, foam stability, fire extinguishing and burn-back performance of AFFF formulations were deeply studied. The results in this study are helpful to the theoretical guidance in the field of ocean firefighting.

## 2. EXPERIMENTAL SECTION

### 2.1. Materials

The AFFF concentrates utilized in this work consist of 3 wt.% fluorocarbon surfactant, 3~18 wt.% hydrocarbon surfactants, 13 wt.% organic solvent, 3 wt.% foam stabilizer, and deionized water. The amphiprotic fluorocarbon surfactant is short-chain (Capstone® FS-50, 27.0 %), with six carbon atoms in its perfluorinated radical, purchased from Dupont. The adding concentration of FS-50 in AFFF concentrates is about 237 times its critical micellization concentration (CMC) which is about 0.0126 wt.%. We used three typical hydrocarbon surfactants: sodium dodecyl sulfate (SDS, 99.0 %, anionic), alkyl polyglycoside (APG, 50.0%, nonionic), and cocoamidopropyl betaine (CAB, 35.0%, amphoteric), which were purchased from Aladdin, Shanghai Fine Chemical Co. LTD, and Shandong Usolf Chemical Technology Co. LTD, respectively. The contents of the three surfactants in the AFFF concentrates are as follows: SDS-5 wt.%, APG-18 wt.% and CAB-3 wt.%. Xanthan gum (molecular weight=2000 kDa) is a water-soluble polymer used as the foam stabilizer, purchased from Sigma-Aldrich.

The AFFF concentrates were diluted by deionized water or seawater, at a volume ratio of 3:97. The artificial seawater [17] composes of 24.5 g/L NaCl (420 mM), 5.2 g/L $MgCl_2$ (55 mM), 1.2 g/L $CaCl_2$ (11 mM), 0.7 g/L KCl (9 mM), 3.3 g/L $MgSO_4$ (27 mM), and 0.2 g/L $NaHCO_3$ (2 mM). All salts used in this work were purchased from Sinopharm Chemical Reagent (Shanghai, China). The resulting AFFF samples were denoted as $AFFF_{SDS}$, $AFFF_{SDS}$ (seawater), $AFFF_{APG}$, $AFFF_{APG}$ (seawater), $AFFF_{CAB}$, and $AFFF_{CAB}$ (seawater). Besides, we also prepared the AFFF solutions by using the water containing different salts separately to study the effects of various salts in seawater on the foam properties. The fuel used in the fire extinguishing and burn-back tests is n-heptane (98%), provided by Macklin. All of the materials were used as received.

### 2.2. Measurements of aqueous solution properties of AFFF

The surface and interfacial tension were measured at 25°C using a tension meter (QBZY-3, Shanghai Fangrui Instrument Co. LTD). The dynamic viscosity of foam solutions was measured with a DV-1 digital viscometer.

The film-forming property is an important parameter of the AFFF solution, which can be characterized by the spreading coefficient ($S$). Theoretically, if $S>0$, an upper liquid can form a film on the surface of the lower liquid. The spreading coefficient ($S$) is defined as follows [18]:

$$S = \gamma_L - \gamma_U - \gamma_{LU} \quad (1)$$

Here $S$ is the spreading coefficient, $\gamma_L$ is the surface tension of the lower liquid, $\gamma_U$ is the surface tension of the upper liquid, and $\gamma_{LU}$ is the interfacial tension between the two liquid surfaces. For AFFF, the upper liquid is AFFF aqueous solution and the lower liquid is n-heptane. When $S$ is positive, the AFFF solution can spread instantly over the surface of the lower n-heptane. This also means that the upper AFFF foam can form an aqueous film over the n-heptane surface.

### 2.3. Foaming ability measurements

Ross-Miles technique [19] is a standard method for measuring foaming ability. The apparatus has been introduced briefly in the previous work [20]. The stream of the tested foam solution in a container (250 mL) broke up into drops, which impinged on the surface of the same solution in the reservoir (50 mL). The distance between the upper container and the lower reservoir is 1 m. Air entrainment occurred as drops of the solution hit the clean air-solution surface. The height of foam continued to increase until the flow from the reservoir ceased. The initial foam height ($h_0$) was immediately measured as the characterization of the foaming ability.

### 2.4. Foam generation

The foam generation method may affect the foam properties. In our study, the foams were produced by using the same procedure. The developed compressed-air foam generation system comprises two compressed air cylinders, a pressure vessel containing foam solution, gas and fluid flowmeters, a mixing chamber, valves and foam conveying pipes, as shown in Fig. 1. The compressed-air foam was made by injecting compressed air into the AFFF solution at a pressure of 0.35 ± 0.03 MPa in the pressure vessel. The blue flow directional arrows illustrate that the compressed air was used to force the foam solution out of the pressure vessel. Subsequently, the foam solution was combined with compressed air in a mixing chamber, thereby producing uniform foams. On the whole, the foams used in this article were produced by mixing compressed air with the foam solution. A similar experimental method was described in detail elsewhere [21].

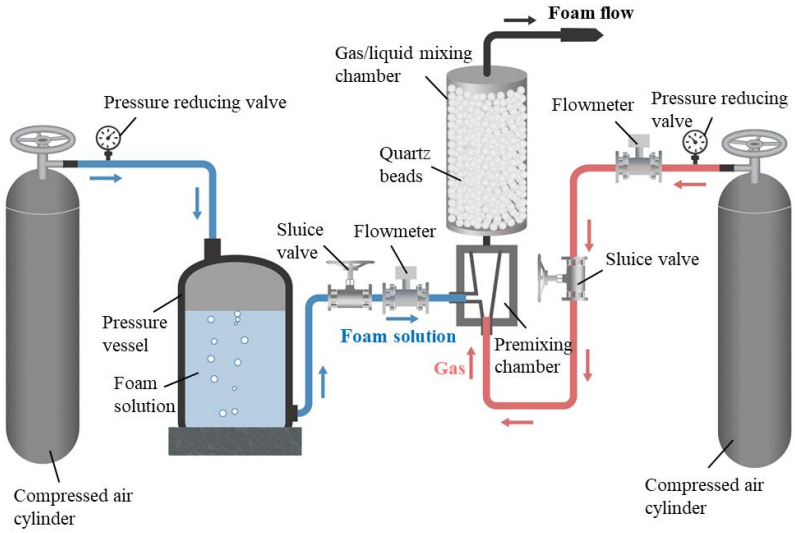


**Fig. 1** Experimental apparatus for foam generation.

### 2.5. Liquid drainage and foam stability tests

The experimental setup of foam drainage is presented in Fig. 2. It was established based on the mechanism of a communicating vessel to record the instantaneous mass of the liquid drained from foams. The foam solution was added into the communicating vessel before the experiment to obtain

the same height of liquid level at both ends of the communicating vessel. Moreover, the surface of the foam solution at the right end of the communicating vessel just touched the highest point of the outlet nozzle without liquid coming out.

During the experiment, the foams provided by the foam-generating apparatus continuously fell into the foam container from above its center. Small quartz beads were added to the left end of the connected vessel effectively to reduce the impact of foam flow on the liquid surface. The gas flow rate was 75 L/h, and the liquid flow rate was 15 L/h. The foam was collected by foam container for 90 s with a fixed flow rate. Due to the presence of the communicating vessel, the incremental mass of the beaker was exact representative of the liquid drained from foam. The data were recorded by an electronic balance and simultaneously transferred to a laptop once per second.

Part of the foam (200 mL) was also injected into the measuring cylinder (diameter: 55 mm) containing 50 ml n-heptane to detect foam stability. Foam evolution was tracked using a Sony camera (FDR AX-700). The foam height versus time was determined by using a MATLAB program and was used as the characterization of the foam stability.

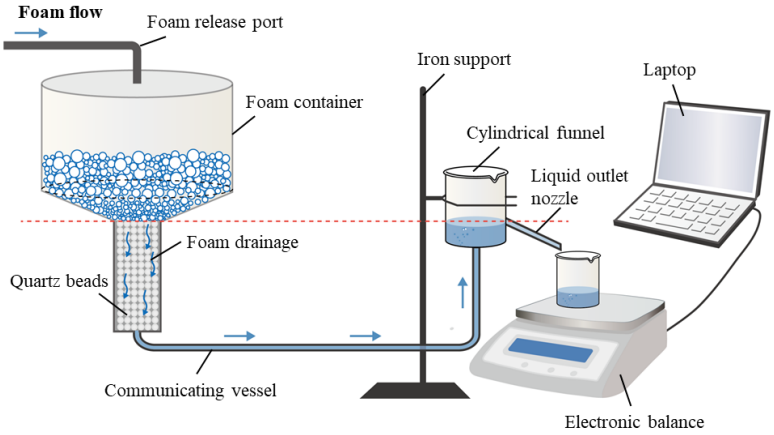


**Fig. 2** Experimental apparatus for liquid drainage tests.

### 2.6. Fire extinguishing and burn-back tests

According to the Chinese standard GB15308-2006 [22], the experimental steps are as follows: 9 L n-heptane in the fire tray was ignited firstly, and the ignition time was recorded as 0 s. After 60 s of pre-burning, the AFFF foam was applied to the fire tray (diameter: 596 mm, depth: 150 mm) from the center at a mass rate of 750 g/min. The time when the flame height decreased to 0.3-0.4 m was defined as 90 % control time [22], and the time when the flame was completely extinguished was recorded as the fire extinguishing time. The foam application was stopped after 180 s. In the burn-back test, 1 L n-heptane in the burn-back pot (diameter: 120 mm, depth: 80 mm) was ignited at 240 s. The flame radiation from the burning n-heptane in the burn-back pot results in the degradation of foam in the fire tray. The height of the burn-back pot was dynamically adjusted to ensure that the pot lip was at the same level as the foam surface. The duration from the time of igniting the burn-back pot to the moment when the n-heptane in the fire tray was fully ignited again was recorded as the burn-back time.

## 3. RESULTS AND DISCUSSION

### 3.1. Effect of seawater on the properties of AFFF solutions

Table 1 shows the comparison of aqueous solution properties for different AFFF formulations. It can be seen that the surface tension of the AFFF solution sample containing CAB diluted by deionized water (16.32 mN/m) is smaller than that of $AFFF_{SDS}$ and $AFFF_{APG}$ samples. Besides, the addition of seawater has little effect on the surface tension of $AFFF_{APG}$ and $AFFF_{CAB}$ samples and the solution sample containing only FS-50. This is is predictable because APG does not contain any ionized groups.

In addition, CAB and FS-50 exist as a zwitterion with cationic and anionic (betaine) centres and does not form surfactant crystal (precipitation) in seawater.

It is clearly seen that seawater has a great effect on the surface activity of the AFFF sample containing SDS. The spreading coefficient of AFFF solutions was calculated based on Eq (1), where the surface tension of n-heptane is 20.35 mN/m. $AFFF_{SDS}$ solution prepared by seawater has lower surface tension and higher interfacial tension than that of the $AFFF_{SDS}$ solution prepared by deionized water. $Mg^{2+}$, $Ca^{2+}$ and $K^{+}$ in seawater can combine with the negatively charged groups of SDS to generate the surfactant precipitation which has a Krafft point higher than the room temperature [13]. Instead, $Na^{+}$ is often beneficial to reduce the surface tension of the solution containing SDS through electrostatic shielding effects [11]. The addition of polyvalent cations consumes the hydrocarbon surfactant SDS in the solution. Therefore, for the seawater cases, the adsorption of SDS molecules at the air-liquid interface is expected to decrease due to the consumption of SDS molecules, and the surface tension lowering effects is mainly dominated by the fluorocarbon surfactant FS-50. Due to the oleophobicity of fluorocarbon chains, the solution-oil interfacial tension of fluorocarbon surfactants is normally higher than that of hydrocarbon surfactants with analogous structures. This explains the increase in the solution-oil interfacial tension for $AFFF_{SDS}$ solution after adding seawater.

The spreading coefficient of the $AFFF_{SDS}$ solution in seawater is slightly higher than the $AFFF_{SDS}$ solution in deionized water. A larger *S* means that it is more conducive for the surfactant solution to form an aqueous film on the n-heptane surface in thermodynamics. For the AFFF solution based on CAB and APG, no significant change in the spreading coefficient is observed after adding seawater. In addition, the viscosity of the AFFF samples is hardly changed by adding seawater into the solution systems.

**Table 1** Results of the aqueous solution properties of different AFFF samples.

| Formulation | Viscosity (mPa·s) | Surface tension (mN/m) | Interfacial tension-heptane* (mN/m) | *S* (mN/m) |
|---|---|---|---|---|
| 0.1% FS-50 | 9.72 | 15.12 | 5.51 | -0.28 |
| 0.1%FS-50 (seawater) | 9.64 | 15.09 | 5.48 | -0.22 |
| $AFFF_{SDS}$ | 1.62 | 17.53 | 1.12 | 1.70 |
| $AFFF_{SDS}$ (seawater) | 1.53 | 16.88 | 1.41 | 2.06 |
| $AFFF_{APG}$ | 1.52 | 17.54 | 1.27 | 1.54 |
| $AFFF_{APG}$ (seawater) | 1.51 | 17.43 | 1.23 | 1.69 |
| $AFFF_{CAB}$ | 1.34 | 16.32 | 1.63 | 2.40 |
| $AFFF_{CAB}$ (seawater) | 1.41 | 16.18 | 1.71 | 2.46 |

* $\gamma_{n\text{-heptane}}$ = 20.35 mN/m

### 3.2. Effect of seawater on the foam properties of AFFF formulations

#### 3.2.1. Foaming ability

Fig. 3a illustrates the foaming ability of different AFFF solution samples. Apparently, the $h_0$ of the AFFF sample containing SDS diluted by seawater (~85 mm) is much lower than that of $AFFF_{SDS}$ diluted by deionized water (~230 mm), which means the seawater can greatly weaken the foaming ability of the AFFF sample containing SDS. The effects of seawater on foaming ability is not significant for $AFFF_{APG}$ and $AFFF_{CAB}$ samples. Fig. 3b isolates the effects of various salts in seawater on the foaming ability of $AFFF_{SDS}$. The type of salts has a great influence on foaming ability. Ions are classed as strongly (kosmotrope) or weakly (chaotrope) hydrated, and the matched ions form ion pairs more readily. $Na^{+}$ is a kosmotrope, while $K^{+}$ is a chaotrope. For SDS, the sulfate head group is chaotropic and prefers to combine with $K^{+}$ rather than $Na^{+}$. The foaming ability has the following orders: $AFFF_{SDS}/CaCl_2$<$AFFF_{SDS}/MgSO_4$<$AFFF_{SDS}/MgCl_2$<$AFFF_{SDS}/KCl$<$AFFF_{SDS}/NaCl$. $Na^{+}$ can slightly enhance the foaming ability, while $K^{+}$ and $Ca^{2+}$ and $Mg^{2+}$ can dramatically weaken the foaming ability of the solution containing SDS due to the formation of KDS, $Mg(DS)_2$ and $Ca(DS)_2$ precipitations that can reduce the adsorption kinetics of surfactants [15,16]. Note that the content of $K^{+}$ is relatively small in the seawater, therefore it is $Ca^{2+}$ and $Mg^{2+}$ in seawater that affects the foamability greatly.

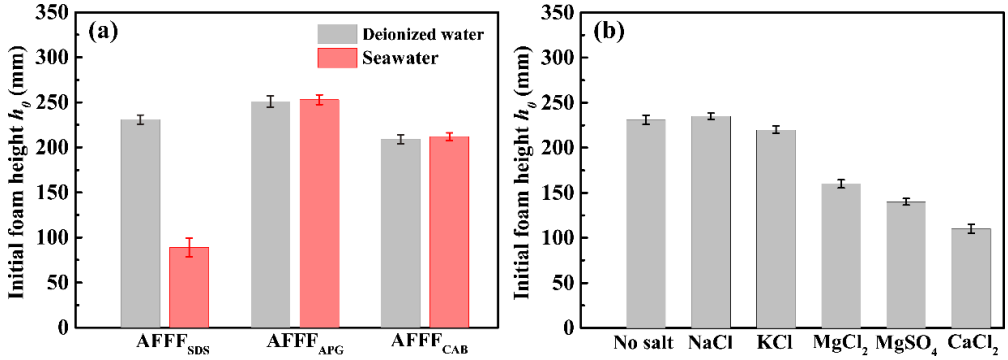


**Fig. 3** (a) Foaming ability of different AFFF solution samples in the presence of seawater and deionized water. (b) Foaming ability of AFFF$_{SDS}$ samples in the presence of different salts (24.5 g/L NaCl (420 mM), 5.2 g/L $MgCl_2$ (55 mM), 1.2 g/L $CaCl_2$ (11 mM), 0.7 g/L KCl (9 mM), 3.3 g/L $MgSO_4$ (27 mM)).

### 3.2.2. Foam stability and liquid drainage

Fig. 4 shows the change in normalized foam height over time for different foam in contact with the n-heptane layer. For the oil-free cases (Fig. 4a), the incorporation of seawater can slightly weaken the stability of AFFF$_{SDS}$. The height evolution of other foams shows little difference at the time scale of our observations. For the cases in Fig. 4b, one can see the expansion of the foam, which is witnessed by the increase in foam height over time. It has been reported that foam expansion for fluorinated foams is originated from the transportation of oil vapour among the foam films [23]. AFFF$_{SDS}$ (seawater) degrades rapidly after 6 hours because the rate of foam degradation is faster than that of foam expansion. In addition, it was reported that a small amount of surfactant precipitation can produce a defoaming effect because precipitation/particles can be incorporated into the surfactant monolayers resulting in a decrease in the maximum of the disjoining pressure curve and therefore producing less stable thin films [14]. On the other hand, it should be noted that excessive surfactant precipitation by salts may generate a foam stabilization effect [15,16]. In recent research, Zhang et al. carried out a systematic study to link the formation of surfactant precipitation to foam performance [15,16], and they observed that the bubble surface can be protected with the excessive surfactant precipitation KDS which strongly arrests the foam ageing. In our study, no obvious foam stabilizing effect is observed, because the stabilization effect of salt can only occur at both relatively high surfactant concentration and high salt concentration (one needs adequate surfactant precipitation to stabilize foam) [16]. The foam stability of AFFF$_{APG}$ and AFFF$_{CAB}$ is insignificantly affected by seawater. In addition, one can observe that different liquid foams have different foam expansion rates. The quantitative relationship between foam expansion in the presence of oil and foam stability is not fully understood. The difference in the expansion rate of foam may be associated with the difference in coarsening and coalescence rate of the bubbles at the foam-oil interface [23].

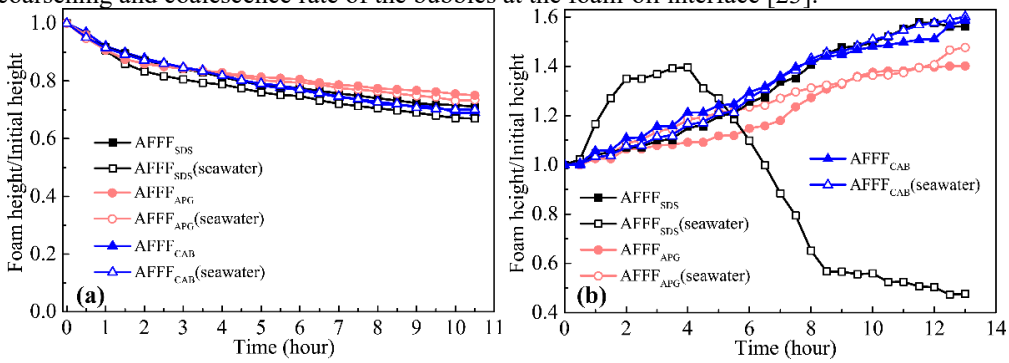


**Fig. 4** Foam stability of different samples. (a) The stand-alone foam without oil as the control group. (b) Foam in contact with n-heptane.

The dimensionless liquid mass curves of foam drainage for different AFFF samples are shown in Fig. 5. For the AFFF samples diluted by deionized water, the foam drainage rates give the following order: $AFFF_{APG}$<$AFFF_{SDS}$<$AFFF_{CAB}$. The slower foam drainage rate means that the liquid is not easy to flow out from the foam structure, which can help foams to stay wet and maintain good foam stability. $AFFF_{APG}$ shows the lowest liquid drainage rate than the AFFF samples containing the other two surfactants (SDS and CAB). The difference in liquid drainage rate may come from the difference in initial bubble size distribution which is related to the foaming ability. Not all gases are incorporated into the $AFFF_{SDS}$ (seawater) during foaming due to low foaming ability. For the AFFF samples diluted by seawater, the foam drainage rate of $AFFF_{SDS}$ (seawater) increases dramatically, leading to extremely poor foam stability. Besides, the addition of seawater slightly increases the foam drainage rate of $AFFF_{APG}$ (seawater) and $AFFF_{CAB}$ (seawater) samples. A fast liquid drainage rate does not contribute to enhancing the fire-fighting performance of foam, because dry foam has a thinner liquid film than wet foam and is more prone to be destroyed by thermal radiation and oil vapour.

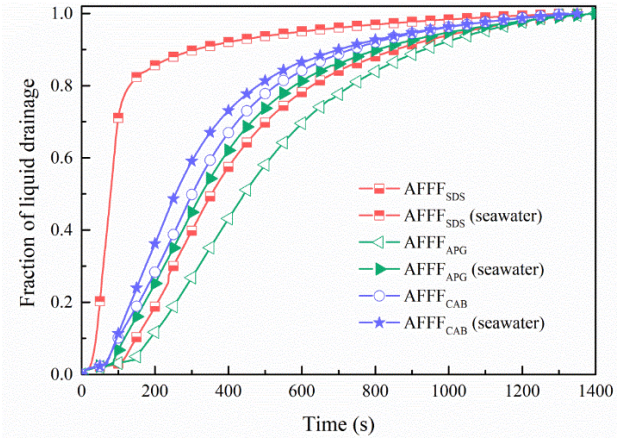


**Fig. 5** Fraction of liquid drainage over time for different foam formulations.

### 3.3. Fire extinguishing and burn-back performance of AFFF formulations

#### 3.3.1. Fire extinguishing test

As shown in Fig. 6, the images of the fire extinguishing process of $AFFF_{SDS}$, $AFFF_{APG}$ and $AFFF_{CAB}$ samples are used to describe the interaction between flame and foams during the test. Clearly, the process of the fire extinguishing test can be roughly divided into three stages: (1) pre-burning stage, (2) foam spreading stage and (3) flame extinguishing stage. The detailed descriptions are as follows:

(1) After igniting the n-heptane in the fire tray (Fig. 6a), the flame spreads rapidly on the surface of n-heptane and gradually reaches a steady-state (Fig. 6b);

(2) After a 60 s pre-burning stage, the AFFF foams begin to be released from above the center of the fire tray. Then, the foams spread until the whole surface of the n-heptane is completely covered. At the same time, the flame intensity is gradually weakened (Fig. 6c);

(3) With the release of the foams, the thickness of the foam blanket increases. Thus, the inhibition of the foam blanket on the n-heptane vapour enhances. The flame height gradually decreases to 0.3-0.4 m, and this moment is considered as the 90 % control time [22]. In the end, the flame is completely extinguished (Fig. 6e).

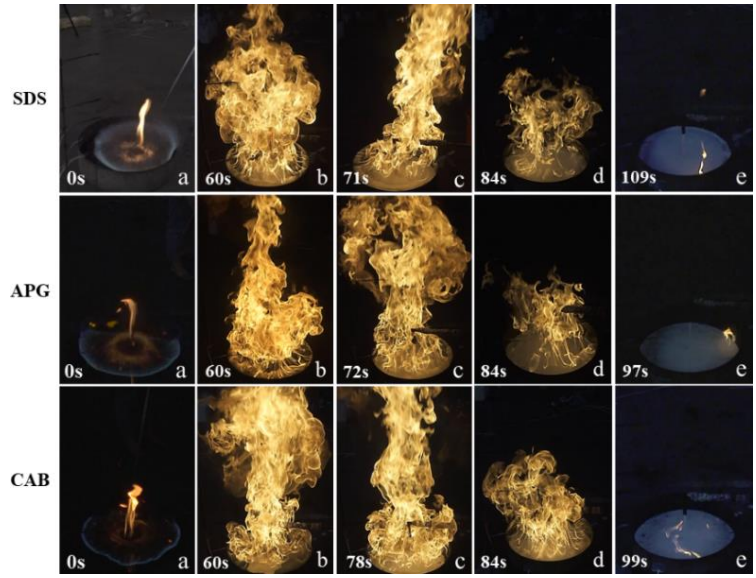


**Fig. 6** Interaction between flame and foam during the fire extinguishment tests of $AFFF_{SDS}$, $AFFF_{APG}$, $AFFF_{CAB}$ formulations. Foams were prepared with deionized water.

Table 2 shows the foam spreading time on the n-heptane surface, 90 % control time and fire extinguishing time of different AFFF formulations. The fire extinguishing time is longer than the foam spreading time because a foam blanket with sufficient thickness is needed to extinguish the flame. In our experiments, no strong correlation between spreading coefficient and foam spread time was observed. The 90 % control time of the three AFFF samples is almost the same, whereas the fire extinguishing time increases in the order: $AFFF_{APG} < AFFF_{CAB} < AFFF_{SDS}$. For the AFFF samples diluted by seawater, the foam spreading time and 90 % control time of the three AFFF samples rise slightly. The addition of seawater significantly increases the fire extinguishing time of the AFFF sample containing SDS while the seawater does not strongly affect the fire extinguishing time of $AFFF_{APG}$ (seawater) and $AFFF_{CAB}$ (seawater) samples.

**Table 2** Comparison of the fire extinguishing test results for different AFFF formulations.

| Formulation | Foam spreading time (s) | 90 % fire control time (s) | Fire extinguishing time (s) |
|---|---|---|---|
| $AFFF_{SDS}$ | 13±0.7 | 24±1.6 | 49±2.5 |
| $AFFF_{SDS}$ (seawater) | 10±1.0 | 26±1.5 | 175±9.5 |
| $AFFF_{APG}$ | 15±0.9 | 24±1.7 | 37±2.0 |
| $AFFF_{APG}$ (seawater) | 13±1.1 | 28±1.3 | 41±1.8 |
| $AFFF_{CAB}$ | 14±1.2 | 24±1.5 | 39±1.7 |
| $AFFF_{CAB}$ (seawater) | 12±1.1 | 30±1.7 | 42±1.6 |

The foam spreading time and 90 % control time of $AFFF_{SDS}$ and $AFFF_{SDS}$ (seawater) are almost the same, but the fire extinguishing time of the latter is much longer than the former. Due to the action of the inorganic salts in seawater, the foaming ability, foam stability and sealability of the AFFF sample containing the anionic surfactant (SDS) are greatly weakened. The fast foam spreading rate promotes a decrease in 90 % control time, but the flame is continuously jumped from the edge of the fire tray extending the fire extinguishing time due to the fast drainage rate and insufficient oil sealing performance.

Although the addition of seawater can reduce the surface tension and slightly improve the spreading coefficient $S$ of the solution, the $AFFF_{SDS}$ containing seawater still has the lowest fire extinguishing performance. Recent studies have shown that there is no inevitable relationship between fire

extinguishing time and film-forming ability (the spreading coefficient) [24,25]. This view is also confirmed in this work where the foam formulation with a higher spreading coefficient does not have a better fire extinguishing performance. It is observed that, for the seawater cases, the foam with higher foam stability in the presence of oil has a better extinguishing time. The stability of foam in the presence of oil may be the key parameter to decide fire-fighting capacity. In addition, the stability of the liquid film in contact with oil dominated by disjoining pressure [26] may also play an important role in the fire-fighting performance.

### 3.3.2. Burn-back test

Fig. 7 shows the images of the burn-back tests of $AFFF_{SDS}$, $AFFF_{SDS}$ (seawater), $AFFF_{APG}$, $AFFF_{CAB}$ samples. It can be observed that the burn-back process can be divided into three stages, namely (1) foam expansion stage, (2) foam blanket decay stage and (3) fire tray re-ignition stage. The detailed descriptions of the three stages are as follows:

(1) After igniting the n-heptane in the burn-back pot (Fig. 7a), the foam blanket expands due to the continuous heating. The height of the foam blanket gradually increases, and then stops expanding after reaching the maximum height (Fig. 7b);

(2) Due to the evaporation and drainage processes of the foams, the thickness of the foam blanket is becoming thinner and the foam stability is getting worse. Meanwhile, the n-heptane vapour continues to diffuse upward and further erodes the foam blanket above. The foams on the top of the blanket are quickly destroyed because they are directly exposed to the flame in the burn-back pot. As time goes on, some holes are appearing around the burn-back pot. In consequence, the n-heptane vapour below spills out of the holes and the flashover occurs (Fig. 7c).

(3) With the further heat radiation of the burn-back pot, a great number of holes gradually appear on the surface of the foam blanket. Thus, a large amount of n-heptane vapour escapes above the foam blanket, and then the flame starts to spread over the surface of the fire tray (Fig. 7d). Finally, the foam blanket is completely destroyed, and the fire tray is fully re-ignited (Fig. 7e).

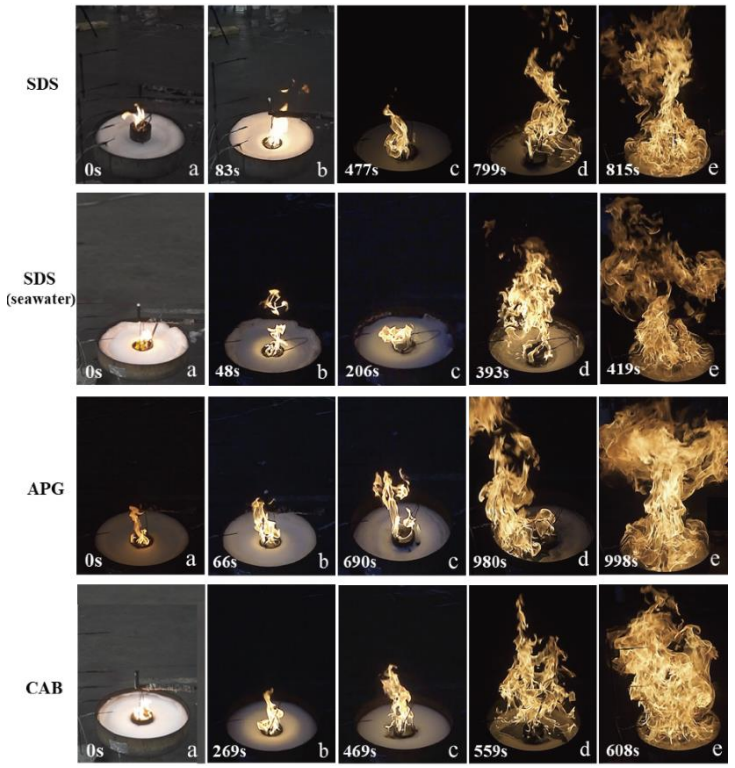

**Fig. 7** Interaction between flame and foam during burn-back tests of $AFFF_{SDS}$, $AFFF_{SDS}$ (seawater), $AFFF_{APG}$, $AFFF_{CAB}$ formulations.

The comparison of burn-back test results for different AFFF formulations is shown in Table 3. For the three AFFF samples diluted by deionized water, the total burn-back time decreases in the order: $AFFF_{APG}$>$AFFF_{SDS}$>$AFFF_{CAB}$. The burn-back tests show that AFFF foam containing APG has a better ability to inhibit fuel vapour compared to the AFFF foam based on SDS and CAB, which may explain the lower rate of foam expansion of $AFFF_{APG}$. If we use seawater to dilute the AFFF concentrates, the order of the total burn-back time is changed into $AFFF_{APG}$>$AFFF_{CAB}$>>$AFFF_{SDS}$. This result is consistent with the foam stability data as shown in section 3.2.2 rather than the spreading coefficient results. The addition of seawater has adverse effects on the burn-back performance of $AFFF_{SDS}$ (seawater) sample by affecting the foam stability and foaming ability, whereas the burn-back performance of $AFFF_{APG}$ (seawater) and $AFFF_{CAB}$ (seawater) samples is not affected significantly. Notably, the burn-back time of $AFFF_{SDS}$ (seawater) is less than 10 min, which no longer meets the requirements of GB15308-2006 (600 s) [22]. Although the foam layer looks intact, one can see the flame occurs on the foam blanket of $AFFF_{SDS}$ (seawater) at t=393 s in Fig. 7 due to the poor sealing performance of the foam. Compared with other cases, $AFFF_{SDS}$ (seawater) has the fastest liquid drainage rate, which means that $AFFF_{SDS}$ (seawater) is easier to become dry and has thinner liquid films and can not prevent fuel vapour from penetrating the liquid bubble film.

**Table 3** Comparison of burn-back test results for different AFFF formulations.

| Formulation | Burn-back time (s) |
|---|---|
| $AFFF_{SDS}$ | 815±18 |
| $AFFF_{SDS}$ (seawater) | 419±43 |
| $AFFF_{APG}$ | 998±29 |
| $AFFF_{APG}$ (seawater) | 768±31 |
| $AFFF_{CAB}$ | 608±23 |
| $AFFF_{CAB}$ (seawater) | 606±27 |

## 4. CONCLUSIONS

In this work, the interfacial properties, foam performances and fire-fighting capacity of six AFFF formulations diluted by seawater and deionized water were experimentally investigated. The conclusions are summarized as follows:

(1) The AFFF samples based on the nonionic surfactant (APG) or amphoteric surfactant (CAB) can resist the negative influence of inorganic salts in seawater. In contrast, the presence of seawater leads to a decrease in equilibrium surface tension and foaming ability of the AFFF sample containing the anionic surfactant (SDS), compared to the deionized water cases. The result comes from the combination of $DS^-$ and metal cations of seawater solution, generating the surfactant precipitation which has a Krafft point higher than the room temperature. It is found that different salts in the seawater have different effects on the foaming ability of $AFFF_{SDS}$ samples which has the following orders: $AFFF_{SDS}/CaCl_2$<$AFFF_{SDS}/MgSO_4$<$AFFF_{SDS}/MgCl_2$<$AFFF_{SDS}/KCl$< $AFFF_{SDS}/NaCl$.

(2) For the stand-alone foams without oil, the foam stabilizing effect of seawater is not observed by detecting the change of foam height with time. Among the six AFFF formulations, the $AFFF_{SDS}$ sample diluted by seawater has the lowest foam stability in the presence of n-heptane. In contrast, the foam stability of $AFFF_{APG}$ and $AFFF_{CAB}$ is insignificantly affected by seawater, and one can observe the expansion of foam rather than fast degradation. Besides, the addition of seawater remarkably accelerates the liquid drainage rate of $AFFF_{SDS}$ and slightly increases the foam drainage rate of $AFFF_{APG}$ (seawater) and $AFFF_{CAB}$ (seawater) samples.

(3) Foams made from seawater exhibit longer fire extinction times and shorter burn-back times than seawater-free cases. Except for $AFFF_{SDS}$ (seawater), the fire-fighting performances of the other five formulations all meet the requirements of AFFF provided by GB15308-2006. $AFFF_{APG}$ shows the best fire extinguishing and burn-back performance, though its spreading coefficient is not very high. This means that it is not sufficient to evaluate the fire-fighting performance by spreading

coefficient. The effect of seawater on fire-fighting performance is more closely related to the foam stability in the presence of oil which is controlled by drainage, coarsening and coalescence. In addition, the stability of liquid film in contact with oil for fire-fighting foam is perhaps an important parameter affecting the foam stability and fire-fighting performance, which involves the measurement of the disjoining pressure and needs to be considered in future works.

## ACKNOWLEDGEMENTS

The work in this study was financially supported by the Anhui Key Research and Development Plan Project (No. 1804a0802202) and the Opening Fund of State Key Laboratory of Fire Science (No. HZ2019-KF03). The authors sincerely appreciate the support.

## REFERENCES

[1] X.Y. Yu, Y.R. Lin, F. Li, X. Yu, H. Li, R.W. Zong, S.X. Lu, Highly stable fluorine-free foam by synergistically combining hydrolyzed rice protein and ferrous sulfate, *Chem. Eng. Sci. 2*50 (2022) 117378.

[2] S.A. Magrabi, B.Z. Dlugogorski, G.J. Jameson, A comparative study of drainage characteristics in AFFF and FFFP compressed-air fire-fighting foams, *Fire Saf. J.* 37 (2002) 21-52.

[3] X.Y. Yu, F. Li, X.Y. Miao, N. Jiang, R.W. Zong, S.X. Lu, C.H. Li, Experimental investigation on the spread of aqueous foam over ethanol surface, *Chin. J. Chem. Eng.* 28 (2020) 2946-2954.

[4] N.D. Denkov, Mechanisms of foam destruction by oil-based antifoams. *Langmuir* 20 (2004) 9463-9505.

[5] Z. Briceño-Ahumda, D. Langevin, On the influence of surfactant on the coarsening of aqueous foams, *Adv. Colloid Interface Sci.* 244(2017) 124-131.

[6] K.M. Hinnant, S.L. Giles, A.W. Snow, J.P. Farley, J.W. Fleming, R. Ananth, An analytically defined fire suppressing foam formulation for evaluation of fluorosurfactant replacement, *J. Surfactants Deterg.* 21 (2018) 711-722.

[7] B.Z. Dlugogorski, S. Phiyanalinmat, E.M. Kennedy, Dynamic surface and interfacial tension of AFFF and fluorine-free class B foam solutions, *Fire Safety Science-Proceedings of the 8th International Symposium* (2005) 719-730.

[8] X.Y. Yu, N. Jiang, X.Y. Miao, F. Li, J.Y. Wang, R.W. Zong, S.X. Lu, Comparative studies on foam stability, oil-film interaction and fire extinguishing performance for fluorine-free and fluorinated foams, *Process Saf. Environ. Prot.* 133 (2020) 201-215.

[9] J. Rakowska, Best practices for selection and application of firefighting foam, *MATEC Web of Conferences* 247 (2018) 00014.

[10] B.Z. Dlugogorski, T.H. Schaefer, Compatibility of aqueous film-forming foams (AFFF) with sea water, *Fire Saf. J.* 120 (2021) 103228

[11] J.K. Angarska, K.D. Tachev, I.B. Ivanov, A. Mehreteab, G. Brose, Effect of magnesium ions on the properties of foam films stabilized with sodium dodecyl sulphate, *J. Colloid Interface Sci.* 195 (1997) 316-328

[12] M. Akram, S. Yousuf, T. Sarwar, Kabir-ud-Din, Micellization and interfacial behavior of 16-E2-16 in presence of inorganic and organic salt counterions, *Colloids Surf., A* 441 (2014) 281-290.

[13] I. Kr.znaric, J. Bozic, N. Kallay, Association and precipitation of alkaline earth dodecyl sulphate in aqueous media, *Croat. Chem. Acta* 52 (1979) 183-189.

[14] H. Zhang, C.A. Miller, P.R. Garrett, K.H. Raney, Mechanism for defoaming by oils and calcium soap in aqueous systems, *J. Colloid Interface Sci.* 263(2003) 633-644.

[15] L. Zhang, H. Wang, B. Zheng, H. Du, A. Salonen, Surfactant crystals as stimulable foam stabilizers: Tuning stability with counterions, *J. Surfactants Deterg.* 22 (2019) 1237-1245.

[16] L. Zhang, L.L. Tian, H.L. Du,`S. Rouzie, N. Wang, A. Salonen. Foams stabilized by surfactant precipitates: criteria for ultrastability, *Langmuir* 33(2017) 7305-7311.

[17] ASTM D1141-1998, Standard Practice for Preparation of Substitute Ocean Water.

[18] W. D. Harkins, A. Feldman, Films. the spreading of liquids and the spreading coefficient, *J. Am. Chem. Soc.* 44 (1922) 2665-2685.

[19] J. Ross, D.G. Miles, An apparatus for comparison of foaming properties of soaps and detergents. *Oil Soap* 18 (1941) 99-102.

[20] M.J. Rosen, Surfactants and Interfacial Phenomena, John Wiley & Sons, Inc., 2004.

[21] Y.J. Sheng, N. Jiang, X.X. Sun, S.X. Lu, C.H. Li, Experimental Study on Effect of Foam Stabilizers on Aqueous Film-forming Foam, *Fire Technol.* 2 (2017) 1-18.

[22] Foam Extinguishing Agent, GB15308-2006, Chinese Standard (2006).

[23] K.M. Hinnant, M.W. Conroy, R. Ananth, Influence of Fuel on Foam Degradation for Fluorinated and Fluorine-free Foams. *Colloids Surf., A* 522 (2017) 1-17.

[24] K.M. Hinnant, S.L.Giles, E.P. Smith, A.W.Snow, R. Ananth, Characterizing the Role of Fluorocarbon and Hydrocarbon Surfactants in Firefighting-Foam Formulations for Fire-Suppression, *Fire Technol.* 56 (2020) 1413-14411.

[25] K.M. Hinnant, M. Button, S. Giles, A.W.Snow, R. Ananth, Fuel effects on aqueous film formation and foam degradation and their impact on fire suppression by foams containing fluorosurfactants, *Fire Mater.* 45 (2021) 833-841.

[26] P.R. Garrett, The mode of action of antifoams, Marcel Dekker, Inc., 1993.

# Computational Fluid Dynamics Simulations of Water Spray Interaction with a Fire-Driven Flow in a Confined and a Mechanically Ventilated Enclosure

**Beji T.[1,*], Prétrel H.[2]**

[1] *Ghent University, Department of Structural Engineering and Building Materials, 9000, Ghent, Belgium.*
[2] *Institut de Radioprotection et de Sûreté Nucléaire (IRSN), Centre de Cadarache, 13115, St Paul Lez Durance, France.*
**Corresponding author's email: Tarek.Beji@UGent.be*

## ABSTRACT

The paper presents a detailed numerical study on the interaction between two water sprays and a fire-driven flow in a confined and mechanically ventilated enclosure of 4.9 m × 8.7 m × 3.9 m (height). The fire source is a 1.2 m × 1.2 m × 0.3 m propane burner, which is positioned in a corner and generates a well-controlled heat source of about 290 kW. The mechanical ventilation consists mainly of an inlet and an extraction duct delivering each a flow rate of about 2500 $m^3$/h. The two nozzles are mounted at 0.9 m below the ceiling and deliver a total flow rate of 107 l/min with a volume-median droplet diameter of about 470 µm. The CFD simulations carried out with the Fire Dynamics Simulator (FDS, 6.7.0) show a good agreement with the experimentally measured room pressure profile. More particularly, the under-pressure peak which occurs upon activation of the water spray system is well-predicted (*i.e.*, -993 Pa in the experiments Vs -832 Pa in the simulations) provided that a sufficiently computational droplet injection rate is prescribed ($N_p$ = 80,000 droplets per second). As observed in the experiments, the CFD simulations show that the water sprays cause a relatively uniform species and temperature distribution from floor to ceiling. Thermal stratification is sustained though, especially in the region between the nozzles and the ceiling. Finally, an energy balance analysis shows that the experimentally estimated fraction of heat absorbed by the water (*i.e.*, 65%) is higher than the one calculated in CFD (*i.e.*, 40%).

**KEYWORDS:** Compartment fire, mechanical ventilation, water spray, CFD.

## INTRODUCTION

The interaction of mechanical ventilation with a fire-driven flow in a confined room has been thoroughly investigated in the last decade [1–16]. This fire scenario is, indeed, highly relevant to several practical applications such as nuclear installations [1–5, 7–9, 16] or 'passive houses' [6, 10]. In the nuclear industry, the mechanical ventilation network is designed to create, in normal operating conditions, a so-called 'pressure-cascade' which allows to prevent the potential release of radioactive material to the surrounding ambient environment. However, in the event of fire, the induced pressure yields a hazardous situations which requires mitigation procedures, *e.g.*, Inlet Valve Closure (IVC) [1]. In 'passive houses', the air-tightness combined with the insulation of the walls and ceiling allow for energy savings. However, in the event of a fire, the thermal expansion of the gases may yield pressure levels that are sufficiently high (in the order of 100 Pa) to prevent inward opening of doors and subsequently hinder evacuation in the early stages of a fire [6, 10]. It has been reported as well that, at a more developed stage of the fire, the pressure could be sufficiently high to cause structural damage, *e.g.*, window frame expelled out of the fire room.

It is shown therefore that, regardless of the context, the fire-induced pressure in an air-tight compartment is a fundamental problem that requires in-depth analysis and detailed comprehensive studies. The general picture that emerges from several experimental studies, *e.g.*, [13–15] is that the pressure increases during the fire growth stage. When (if) the fire reaches steady-state, the pressure is

at its peak and starts to decrease asymptotically towards a steady-state value (which is, obviously, higher than the value prior to the fire). The mechanical ventilation flow rates vary as a function of pressure, following a qualitatively similar pattern. The pressure 'signature' at extinction consists typically in an under-pressure peak controlled by the mechanical ventilation as well as the heat losses to the boundaries. More qualitative and quantitative details are given in [13–15].

The available experimental data *e.g.*, [2, 8, 13–15] is key in fostering the development of numerical tools, which will be used for design purposes as well as to further deepen the current level of understanding of the fire scenarios of interest. For example, simplified engineering models based on the well-mixed approach [5] or the two-zone approach [9] can be used for 'screening' purposes prior to a more detailed approach where CFD can provide more insights onto the fire dynamics, *e.g.*, [4, 11–12, 16].

In the configuration of interest in this paper, an additional component is added to the problem and which is the activation of a water spray system. Obviously, it is of prime interest (as in other configurations involving water sprays) to estimate the cooling effect of water. But, a more specific objective in the scenario at hand, is to examine the effect of water on the room pressure and the subsequent ventilation flow rates. In the fire tests carried out in [8], the under-pressure that occurs upon the activation of the water spray system is about -1000 Pa, which is (in absolute values) higher than the peak over-pressure of about 600 Pa reached by the end of the fire growth stage (and prior to the activation of the water spray system). After reaching the under-pressure peak, and during steady-state water spray activation, the pressure increases asymptotically to higher steady-state value. Shutting down the water spray system yields an increase in the pressure. All these general features have been relatively well reproduced in [9] where the two-zone approach is used. The experimental work carried out in [8] provides as well insights onto the effects of sprays on thermal and chemical stratification.

The work described in this paper aims to provide an assessment of the Fire Dynamics Simulator (FDS, 6.7.0) [17–18] based on the experimental work described in [8]. Regarding the numerical parameters, in addition to the cell sensitivity analysis, a particular attention will be given to the number of injected computational droplets per second, $N_p$. The analysis of the results is first focused on the general overall behavior in terms of pressure and mechanical ventilation profiles. Then, the effect of water sprays on thermal and chemical stratification is examined. The CFD analysis of these aspects will be complementary to the experimental data in that more details of complex flow features are visualized. Finally, the energy balance obtained with FDS will be compared to the experimental estimates in order to identify elements in the modelling or in the experimental design that need to be further looked at and refined in order to reach a good level of accuracy.

## DESCRIPTION OF THE FIRE TEST

The description provided here is based on [8] for the general settings as well as the specific test case A2a in Table 1 of [8], which is the test case of interest here.

### Enclosure and fire source

The compartment is a room in IRSN's DIVA facility with the following dimensions: 4.88 m × 8.67 m x 3.90 m (height), see Fig. 1. The walls, floor and ceiling are made of concrete and the ceiling is covered with calcium silicate panels to protect it from thermal degradation. The fire source is a propane gas fire, which generates a constant and well-controlled heat source of about 290 kW over a period of around 900 s. The temporal Heat Release Rate (HRR) profile is provided in Fig. 2 (left). The latter profile includes a 42 s–pre-ignition period, which allows to have stabilized flow conditions with respect to the mechanical ventilation, prior to the fire. The fire source is located in the north-west corner of the room (see Fig. 1) to prevent (partial) extinction by direct interaction of the water sprays with the flame. The study is thus focused on the interaction of the water sprays with the smoke layer.

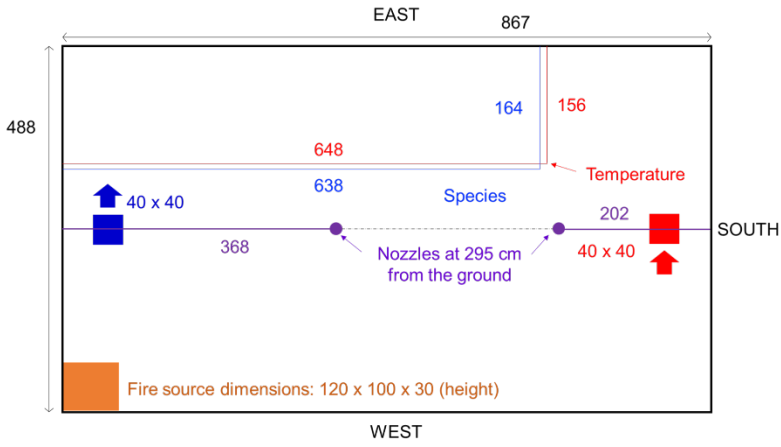


**Fig. 1.** Top view sketch of the enclosure, including the positioning of the measurements.

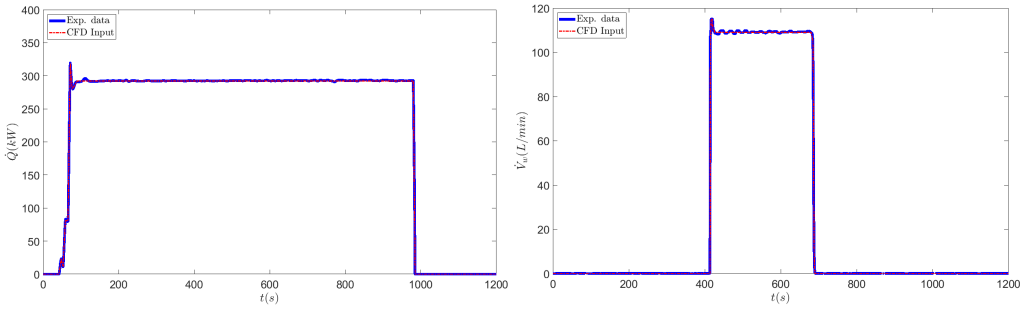


**Fig. 2.** Experimental and numerical profiles of the fire HRR (left) and the water volume flow rate (right).

### Mechanical ventilation system

The ventilation system consists of an inlet and an exhaust duct (see Fig. 1), each connected to the upper part of the room about 0.85 m from the ceiling. The ventilation area is 30 cm × 60 cm. The ventilation ducts are connected to a complex ventilation network and an industrial system equipped with blower and exhaust fans, which are positioned far from the fire room. A full description of the ventilation network is provided in [9].

### Water spray system

The water spray system is made of two nozzles located 2.97 m from the ground and about 0.85 m from the ceiling. The water spray is activated and shut off manually using a valve on the water pipe system. The 6.35 mm–diameter nozzle is a Deluge type, Protectospray® D3, HV nozzle with K-coefficient of 26 l/min/bar$^{1/2}$. The two nozzles produce a total water flow rate of 107 l/min at an operating pressure of 421 kPa. At a flow rate of 124 l/ min, the maximum spray half-angle (*i.e.*, angle between the vertical axis and the outer boundary of the spray) is about 45°. Phase Doppler Anemometer (PDA) tests carried out at IRSN's CALIST facility show that the droplet size distribution fits a log-normal distribution with a mean mass median diameter (MMD) of about 590 µm and a geometric standard deviation of 1.5 at 100 kPa. Increasing the nozzle pressure causes a reduction in the MMD to 450 µm at 568kPa. As shown in Fig. 2 (right), the water spray system is activated at 414 s and shut off at 690 s.

### Measurements

Several measurements have been carried out in [8]. We recall here the main measurements used in this paper for CFD assessment purposes.

The ventilation flow rate is measured with Pitot tube devices, connected to pressure transducers and located in the inlet vent and exhaust ventilation ducts. The gas pressures in the room and in the ventilation network are also measured with pressure transducers.

The gas temperatures are measured with 1.5 mm K-type thermocouples fixed on five vertical trees. In this paper, we are focusing on the measurements carried out in the SE position, see Fig. 1. The thermocouple tree is equipped with 8 K-type thermocouples located 0.55 m, 1.05 m, 1.55 m, 2.05 m, 2.55 m, 3.05 m, 3.55 m and 3.90 m from the ground. Each thermocouple is equipped with metal protective caps to prevent droplets coming into contact with its tip.

Oxygen and carbon dioxide concentrations are measured in the SE (see Fig. 1) at two vertical positions named 'low' and 'upper'. Each sample point is connected to a sampling system and gas analyzers for oxygen and carbon dioxide. The sampling system controls the pressure and the flow rate and dries the gas sample. The molar fractions, presented here, are based on the dry sample. The time delay due to the sampling process is corrected.

## NUMERICAL MODELLING

Computational Fluid Dynamics (CFD) simulations have been carried out with the Fire Dynamics Simulator (FDS, 6.7.0). For several numerical and physical aspects, the default settings have been prescribed unless specified otherwise. The most important aspects are provided hereafter.

### Fire source and thermal boundary conditions

The default turbulent combustion modelling based on infinitely fast chemistry and Eddy Dissipation Modelling (EDM) has been used in this work. The prescribed soot and CO yields are respectively, $y_s$ = 0.024 and $y_{CO}$ = 0.005. The Radiative Transport Equation (RTE) is solved using the default numerical and physical parameters in conjunction with a prescribed radiative fraction of $\chi_r = 0.286$.

The temporal HRR profile is prescribed in FDS using a 'ramp' function in order to 'follow' very closely the experimental profile (see Fig. 2, left). This is because it has been shown in [15] that the fire growth stage strongly influences the pressure development.

The walls are made of concrete and are 35 cm-thick. The floor is made of concrete and is 30 cm-thick. The ceiling is made of a 30-cm concrete layer, followed by a 10 cm-thick gap of air, followed by a 1 cm fiber wool layer and then, a 1.27 cm-thick calcium silicate layer (starting from the inside of the room). The above information has been prescribed in the CFD calculations in order to solve 1D Fourier's equation for heat transfer by conduction using the thermal properties displayed in Table 1.

**Table 1. Thermal properties of the boundaries**

| | Concrete | Calcium Silicate | Fiber Wool | Air |
|---|---|---|---|---|
| Density (kg/m$^3$) | 2200 | 970 | 360 | 1.276 |
| Thermal conductivity (W/m.K) | 1.30 | 0.25 | 0.07 | 0.024 |
| Specific heat (kJ/kg.K) | 0.88 | 0.97 | 1.00 | 1.00 |

### Mechanical ventilation

In the simulations carried out in this work, the complex mechanical ventilation network (as described in [9]) has been simplified to one inlet duct and one exhaust duct. An approximate length of 30 m has been prescribed to each duct. The cross-section area of each duct has been set to 0.4 m × 0.4 m = 0.16 $m^2$. In the simplified approach, the variation of the mechanical ventilation flow rates with pressure is evaluated *a posteriori* by plotting the pressure difference between the outside (*i.e.*, ambient pressure) and the inside (*i.e.*, room pressure) as a function of the flow rates, see Fig. 3. The latter figure shows a quadratic behavior for the inlet, but a more complex behavior for the outlet. Thus, instead of prescribing quadratic fan curves, a 'ramp' is used, as highlighted in Fig. 3 with the solid red line. This makes the calculation with respect to ventilation not fully predictive as in [3]. However, this is deemed acceptable because the focus of the paper is on the water spray effect.

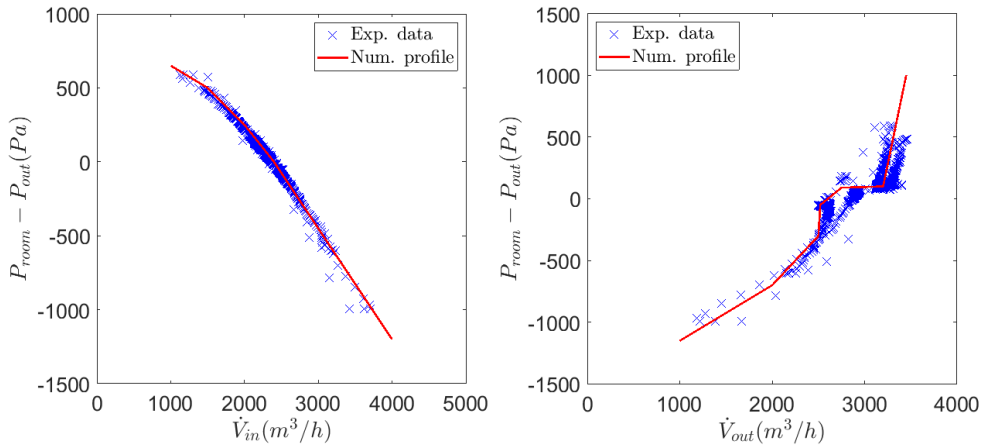


**Fig. 3.** Experimental and numerical data for the room pressure difference as a function of the volume flow rates at the inlet (left) and the extrcation (right).

### Water spray modelling

The nozzle parameters described above have been prescribed in the simulations, *i.e.*, a spray half-angle of 45°C, an orifice diameter of 6.35 mm and a water flow rate profile equally divided between the two nozzles and following the experimental data, as shown in Fig. 2 (right). Additionally, an atomization length of 20 cm has been prescribed. Thus, computational droplets are injected into the domain at 20 cm from the nozzle in order to be tracked in a Lagrangian way. A uniform angular distribution of the water flow rate has been prescribed at the water injection boundary. Note that the droplet size distribution has not been measured at the operating pressure of 421 kPa, but at two other pressures of 100 kPa and 568 kPa. Therefore, an estimate of droplet the volume-median diameter (VMD) has been calculated based on the -1/3 dependence of the VMD on the pressure [18], which gives a value of VMD = 470 µm. The prescribed standard deviation is 1.5.

### Measurements

The measurements carried out in the simulations have been set to mimic the experimental measurements, including details such as the thermocouple bead diameter of 1.5 mm and the species measurements carried out on a dry basis. Additionally, slice files have been prescribed in order to have an overview of the fire dynamics inside the enclosure.

### Simulation tests

A structured uniform mesh has been used in this work. The sensitivity analysis carried out here has been solely focused on two numerical parameters which are the cell size, $\Delta x$, and the injected number

of particles per second, $N_p$. After selection of $\Delta x$ and $N_p$, the discussion of the results will be based on one simulation.

## RESULTS AND DISCUSSION

### Sensitivity analysis on $\Delta x$ and $N_p$

Figure 4 (left) shows that refining the mesh from a 20 cm cell size to a 10 cm cell size, does not yield significant differences in the predicted overall pressure profile. This is in agreement with the work reported in [11–12] where a relatively coarse mesh appears to suffice in order to predict global parameters such as the pressure or the mechanical ventilation profiles. Figure 4 (right) shows as well that the gas temperature near the ceiling does not vary strongly with the cell size. Therefore, a cell size of 20 cm has been selected for the remainder of the simulations.

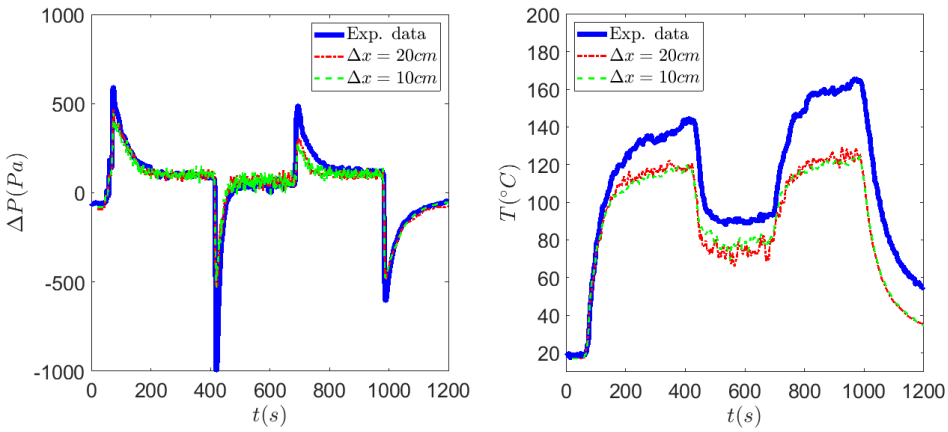


**Fig. 4.** Influence of the cell size, $\Delta x$, on the room pressure profile (left) and gas tempertaure profile near the ceiling in the SE position.

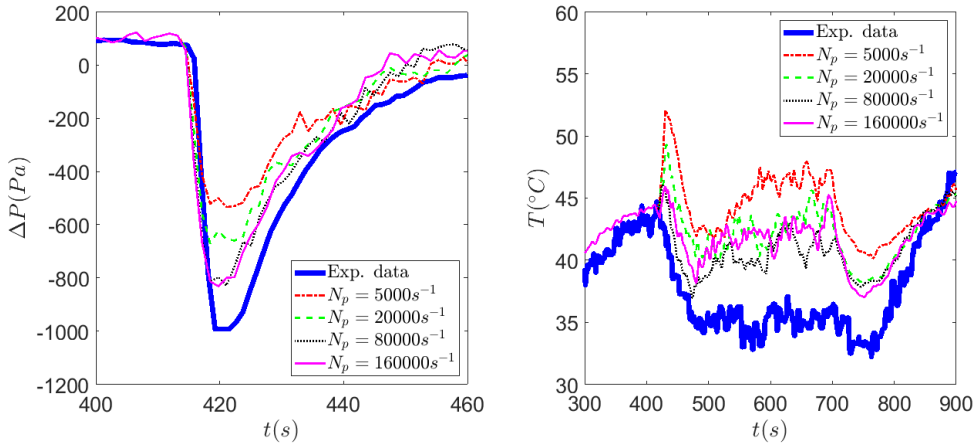


**Fig. 5.** Influence of the number of particles per second, $N_p$, on the room pressure profile (left) and gas tempertaure in the lower layer in the SE position.

As demonstrated in [19], the injected number of particles per second can have a significant effect on water spray simulations in a Lagrangian – Eulerian framework. This is confirmed for the scenario at hand. Figure 5 (left) shows that using the default number of particles per second, *i.e.*, $N_p$ = 5,000

particles per second, results in a significant underestimation of about 50% in the under-pressure peak observed upon activation of the water spray system. This is due to the fact that statistical convergence has not been reached with respect to the heat absorbed by the droplets per unit time. Figure 5 (left) shows that convergence is reached at a rate of $N_p$ = 80,000 particles per second, which gives results that are similar to $N_p$ = 160,000 particles per second. The need to increase the value of $N_p$ is confirmed for the gas temperature at the lower layer (see Fig. 5, right) where the increase in temperature after water spray activation appears to be an 'artifact' of a low $N_p$ value.

**Pressure and ventilation flow rates**

The pressure and ventilation flow rates predicted with $\Delta x$ = 20 cm and $N_p$ = 160,000 particles per second show a relatively good agreement with the experimental data, as displayed in Figs. 6 and 7.

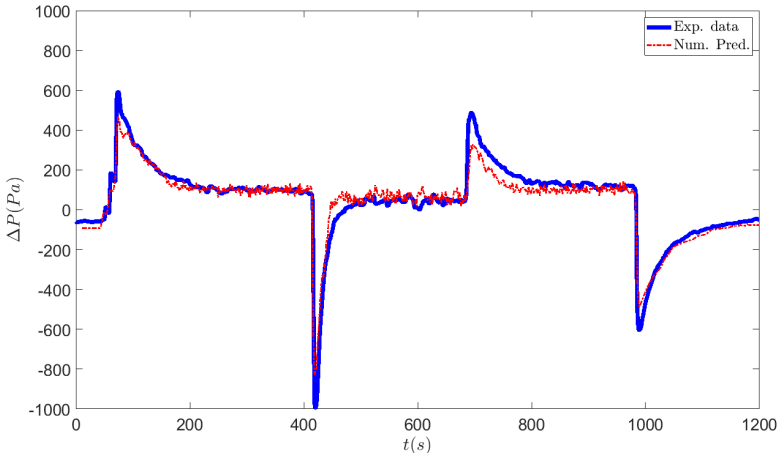


**Fig. 6.** Comparison of the experimental and numerical profiles of the pressure.

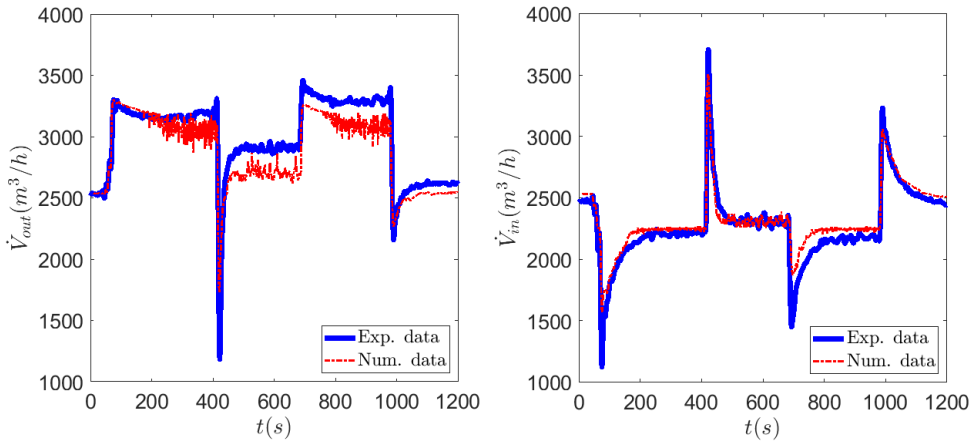


**Fig. 7.** Comparison of the experimental and numerical profiles of extraction rates (left) and inflow rates (right).

**Thermal and chemical stratification**

Figure 8 shows that gas temperature reduction by about 50°C near the ceiling (at $z$ = 390 cm) upon water spray activation is relatively well captured by the simulations. Nevertheless, prior to water activation, there is a discrepancy of about 20°C which might be due to the convective heat transfer

calculation. At the lower position, *i.e.*, $z$ = 55 cm, the cooling, already moderate in the experiments (about 10°C reduction), is less pronounced in the simulations (about 5 to 2°C reduction).

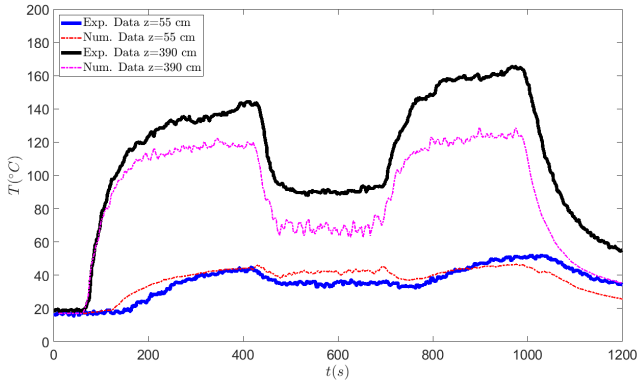


**Fig. 8.** Comparison between experimental and numerical data for the gas temperature at two different heights (*i.e.*, 55 and 390 cm) in the SE position.

Figure 9 gives a more complete overview (than Fig. 8) on the thermal field prior to water activation between 300 and 400 s (left) and during water activation between 550 and 650 s (right). Figure 9 clearly shows the overall reduction in gas temperature, although near the inlet ventilation duct (on the left of the compartment) peak temperatures of about 120°C remain, highlighting the localized effect of water. The water spray 'pattern' in Fig. 9 (right) can be easily visualized. One can clearly see that, near the sprays, the temperature is almost uniform across the height (about 40°C). Nevertheless, above the nozzles, higher gas temperatures of about 70°C are recorded, indicating that a certain level of thermal stratification is sustained probably because the nozzles are not mounted flush to the ceiling.

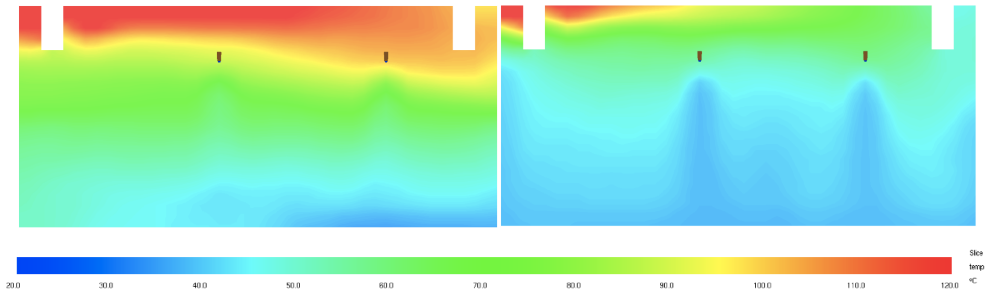


**Fig. 9.** Slice file visualization of the time-averaged temperature field in the center of the room prior to water spray activation between 300 and 400 s (left) and after spray activation between 550 and 650 s (right).

Figure 10 shows the temporal profiles of carbon dioxide (left) and oxygen (right) concentrations at two heights (labeled as 'low' and 'up'). One can clearly see that upon the activation of the water sprays, pronounced mixing takes place, which yields similar concentrations at the two positions. This behavior is observed experimentally as well as numerically. The largest discrepancies between the simulations and the experiments occurred after shutting off the water and at the level of the upper position. No clear explanations are available at this moment.

Figure 11 shows that after activation of the water, relatively uniform concentrations of carbon dioxide and oxygen are predicted near the water sprays, although slightly higher $CO_2$ concentrations are recorded near the ceiling. Additionally, the specific 'pattern' observed near the inlet duct (the duct positioned at the left) when the water spray system is active is indicative of the injection of fresh air which reaches the bottom of the compartment and ensures a relatively high level of oxygen and a relatively low level of $CO_2$.

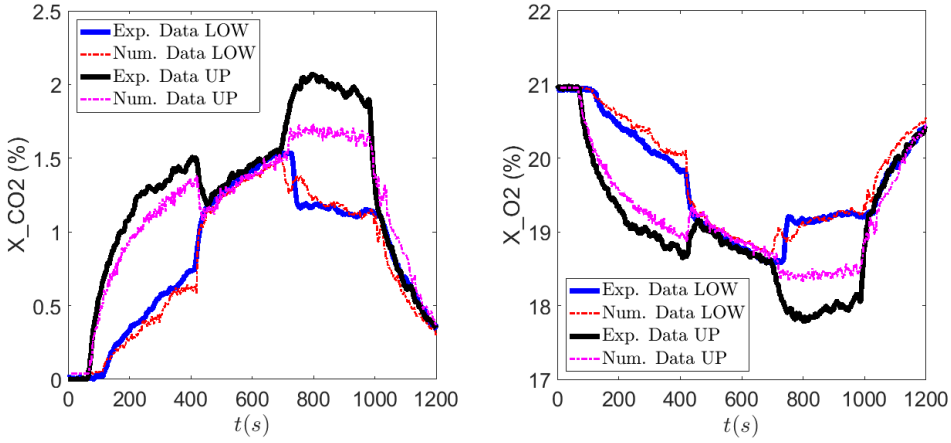


**Fig. 10.** Comparison between the experimental and the numerical temporal profiles $CO_2$ (left) and $O_2$ (right) at two heights (labeled as 'up' and 'low') in the SE position.

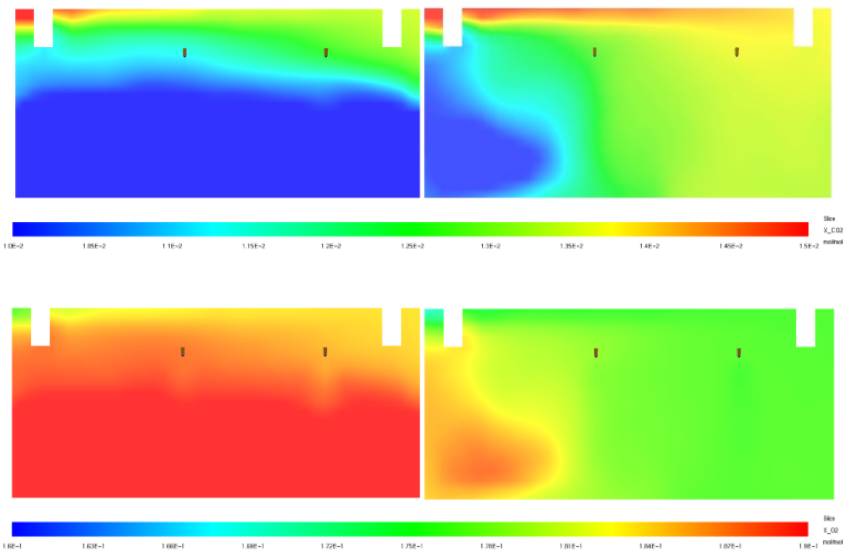

**Fig. 11.** Slice file visualization of the time-averaged concentration of $CO_2$ (top) and $O_2$ (bottom) in the centre of the room prior to water spray activation between 300 and 400 s (left) and after spray activation between 550 and 650 s (right).

## Energy balance

At quasi-steady state, according to [8], the energy balance reads:

$$\dot{Q}_{fire} = \dot{Q}_{vent.} + \dot{Q}_{walls} + \dot{Q}_{water}, \quad (1)$$

where $\dot{Q}_{fire}$ is the fire HRR, $\dot{Q}_{vent.}$ is the 'net energy extracted by the ventilation', $\dot{Q}_{walls}$ is the heat loss through the walls, and $\dot{Q}_{water}$ is the heat absorbed by the water droplets.

The net energy extracted by the ventilation can be calculated as:

$$\dot{Q}_{vent.} = \dot{m}_{ext}\, c_p \left(T_{ext} - T_{amb}\right) = \frac{\rho_{amb} T_{amb}}{T_{ext}} \dot{V}_{out} c_p \left(T_{ext} - T_{amb}\right). \quad (2)$$

The flow rate $\dot{V}_{out}$ and the temperature of the gas $T_{ext}$ at the extraction are post-processed. The ambient temperature and density are known. Therefore, assuming a constant specific heat of the gas, *i.e.*, $c_p$ = 1 kJ/(kg.K), one can make an estimate of net energy extracted by the ventilation. It is noteworthy to mention that, for the scenario at hand, the temperature of the gas at the inlet remained at ambient condition (*i.e.*, there is no reverse flow in the inlet duct) and thus, the inlet is not considered in Eq. (2). A second important note is that in the overall energy budget displayed automatically by FDS at the end of each numerical simulation, Q_CONV is provided as 'the flow of sensible enthalpy *into* the computational domain'. For the scenario at hand, it has been verified that, at quasi-steady state) $\dot{Q}_{vent.}$ = Q_CONV within a relative deviation of less than 6%.

The heat loss through the walls is estimated solely on the basis of the overall energy budget displayed automatically by FDS. More specifically, this is done by taking:

$$\dot{Q}_{walls} = \text{Q\_RAD} + \text{Q\_COND}, \quad (3)$$

where, according to the FDS user guide [17], Q_RADI denotes 'the thermal radiation *into* the domain from the exterior boundary' and Q_COND denotes 'the convective heat flux *into* the computational domain' and, more particularly, 'the heat convected from the gas to a surface'. The latter two quantities are interpreted in this analysis as the heat received by the walls by radiation and convection, respectively, and subsequently transferred / lost by conduction through the walls.

The heat absorbed by the water droplets is (similarly to the heat loss through the walls) estimated based on the overall energy budget displayed automatically by FDS by taking:

$$\dot{Q}_{water} = \text{Q\_PART}, \quad (4)$$

which is believed to be essentially dominated by the energy transferred via convection from the gas to the water droplets and not by the absorbed radiation (by the water droplets) and the energy transferred from hot solid surfaces (typically, the walls and floor in this case).

**Table 2. Energy balance**

| | $\dot{Q}_{vent.}$ (kW) | | $\dot{Q}_{walls}$ (kW) | | $\dot{Q}_{water}$ (kW) | |
|---|---|---|---|---|---|---|
| | Exp. | Num. | Exp. | Num. | Exp. | Num. |
| Before water activation | (35 %) | 73.9 (25.3 %) | (65 %) | 213.9 (73.4) | 0 | 0 |
| During water activation | (10 %) | 24.3 (8.3 %) | (25 %) | 150.9 (51.7 %) | (65 %) | 115.3 (39.5 %) |

Table 2 shows that, prior to the activation of the water spray system, the estimated 'net energy extracted by the ventilation' (resp. the heat loss to the walls) is underestimated (resp. overestimated) in the numerical simulation in comparison to the experimental data by about 28% (resp. 13%). This is in accordance with the under-estimations of the gas temperature reported earlier in Fig. 8, which is indicative of overestimated heat losses to the walls and causes an underestimation of 'net energy extracted by the ventilation' because of the underestimation of $T_{ext}$, see Eq. (2). As shown in Fig. 7,

the extraction rate is well predicted (*i.e.*, -4 % deviation) in the period [300 s – 400 s] and thus, this is less likely to be the reason for the deviations in the energy balance prior to water activation.

After activation of the water spray system, deviations in the energy balance concerning $\dot{Q}_{vent.}$ and $\dot{Q}_{walls}$ remain with the same qualitative trend. Additionally, part of the heat will be absorbed by the water. As shown in Table 2, relatively less heat is absorbed by the water in comparison to the experimental estimate, which is to some extent linked to the underestimation of the gas temperature, but requires further investigation.

## CONCLUSION

In this paper, the Fire Dynamics Simulator (FDS, 6.7.0) is assessed against a well-documented set of experimental data for the interaction of two water sprays with a fire-driven flow in a confined and mechanically ventilated enclosure.

A preliminary set of simulations shows that a relatively coarse mesh with a cell size of 20 cm suffices to capture well the global fire dynamics in the enclosure, especially in terms of pressure and mechanical ventilation profiles. Nevertheless, upon activation of the water spray system, it has been shown that observed under-pressure peak of about -1000 Pa can only be captured if the number of injected particles per second, $N_p$, is raised from the default value of 5,000 to a value of 80,000 in order to reach statistical convergence.

With respect to thermal stratification, similarly to the experiments, it appears that the mixing (and the subsequent loss of stratification) is more pronounced for the chemical species than for the temperature. However, it must be noted that the water nozzles were not mounted flush to the ceiling, which causes the temperature to remain at a relatively high level in-between.

Finally, with respect to the energy balance, it appears that the heat losses to the walls is overestimated in the simulations, which causes the net energy extracted by the ventilation to be under-predicted because of the lower gas temperatures. The latter causes the heat absorbed by the water droplets to be under-estimated in the numerical simulations when the water spray system is activated.

The obtained results are quite encouraging. Nevertheless, a further analysis will be carried out to better point out the sources of 'error' and improve the agreement.

## REFERENCES

[1] H. Prétrel, J.M. Such, Effect of ventilation procedures on the behavior of a fire compartment scenario, Nucl. Eng. Des. 235 (2005) 2155–2169.

[2] H. Prétrel, W. Le Saux, L. Audouin, Pressure variations induced by a pool fire in a well confined and force-ventilated compartment, Fire Safety J. 52 (2012) 11–24.

[3] J. Wahlqvist, P. Van Hees, Validation of FDS for large-scale well-confined mechanically ventilated fire scenarios with emphasis on predicting ventilation system behavior, Fire Safety J. 62 (2013) 102–114.

[4] H. Prétrel, S. Suard, L. Audouin, Experimental and numerical study of low frequency oscillatory behavior of a large-scale hydrocarbon pool fire in a mechanically ventilated compartment, Fire Safety J. 83 (2016) 38–53.

[5] T. Beji, B. Merci, Assessment of the burning rate of liquid fuels in confined and mechanically-ventilated compartments using a well-stirred reactor approach, Fire Technol. 52 (2) (2016) 469–488.

[6] R.K. Janardhan, S. Hostikka, Experiments and Numerical Simulations of Pressure Effects in Apartment Fires, Fire Technol. 53 (3) 2016.

[7] T. Sikanen, S. Hostikka, Predicting the heat release rates of liquid pool fires in mechanically ventilated compartments, Fire Safety J. 91 (2017) 266–275.

[8] H. Prétrel, Interaction between water spray and smoke in a fire event in a confined and mechanically ventilated enclosure, Fire Safety J. 91 (2017) 336–346.

[9] W. Plumecocq, L. Audouin, J.P. Joret, H. Prétrel, Numerical method for determining water droplets size distributions of spray nozzles using a two-zone model, Nucl. Eng. Des. 324 (2017) 67–77.

[10] S. Hostikka, R.K. Janardhan, U. Riaz, T. Sikanen, Fire-induced, pressure and smoke spreading in mechanically ventilated buildings with air-tight envelopes, Fire Safety J. 91 (2017) 380–388.

[11] J. Li, T. Beji, S. Brohez, B. Merci, CFD study of fire-induced pressure variation in a mechanically-ventilated air-tight compartment, Fire Safety J. 115 (2020) 103012.

[12] J. Li, T. Beji, S. Brohez, B. Merci, Experimental and numerical study of pool fire dynamics in an air-tight compartment focusing on pressure variation, Fire Safety J. 120 (2021) 103128.

[13] J. Li, H. Prétrel, S. Suard, T. Beji, B. Merci, Energy balance equation for pressure in air-tight compartment fires: detailed discussion and experimental validation, Fire Safety J. 122 (2021) 103362.

[14] J. Li, H. Prétrel, S. Suard, T. Beji, B. Merci, Experimental study on the effect of mechanical ventilation conditions and fire dynamics on the pressure evolution in an air-tight compartment, Fire Safety J. 125 (2021) 103426.

[15] J. Li, H. Prétrel, T. Beji, B. Merci, Influence of fire heat release rate (HRR) evolutions on fire-induced pressure variations in air-tight compartments, Fire Safety J. 126 (2021) 103450.

[16] O. Ukairo, S. Dembele, A. Heidari, H. Prétrel, J. Wen, Investigation of fires in a mechanically ventilated compartment using the CFD code FireFOAM, Nucl. Eng. Des. 384 (2021) 111515.

[17] K. McGrattan, S. Hostikka, J. Floyd, R. McDermott, M. Vanella, Fire Dynamics Simulator User's Guide, NIST Special Publication 1019, Sixth Edition, 2021.

[18] K. McGrattan, S. Hostikka, J. Floyd, R. McDermott, M. Vanella, Fire Dynamics Simulator Technical Reference Guide Volume 1: Mathematical Model, NIST Special Publication 1018-1, Sixth Edition, 2021.

[19] T. Beji, S.E. Zadeh, G. Maragkos, B. Merci, Influence of the particle injection rate, droplet size distribution and volume, flux angular distribution on the results and computational time of water spray CFD simulations, Fire Safety J. 91 (2017) 586–595.

# Numerical investigations on water mist fire extinguishing performance: physical and sensitivity analysis

**Robinet A.[1], Chetehouna K.[1,*], Cablé A.[2], Florentin E.[3], Oger A.[4]**

*[1] INSA Centre-Val de Loire, Université d'Orléans, PRISME, EA 4229, Bourges, Cher, France.*
*[2] EXEC SAS, Goussainville, Val d'Oise, France.*
*[3] INSA Centre-Val de Loire, Université d'Orléans, LaMé, EA 7494, Bourges, Cher, France.*
*[4] DGA Techniques Terrestres, Bourges, Cher, France.*
**Corresponding author's email: antonin.robinet@insa-cvl.fr*

## ABSTRACT

More and more buildings are constructed to sustain the global population and economic growth. Combined with the ongoing climate change, fire safety actors face the challenge of finding effective and environmentally friendly alternatives to existing and past fire suppression technologies such as fire sprinklers and halon-based systems. Water mists are one of the promising candidates. In this context, the smaller droplets of water mist sprays compared to those produced by traditional sprinklers induce new fire suppression mechanisms which need to be studied and better understood. Furthermore, there is a need for reliable numerical tools to conduct scientific studies regarding fire safety and to dispose of quantitative information regarding fire suppression by water mist. In the present original numerical study, the capabilities of the CFD code FDS to accurately reproduce an experimental scenario of pool fire water mist suppression are investigated. In addition, a global sensitivity analysis method is presented based on the factorial design. It is then applied to provide quantitative insights regarding the parameters which play the most important role in the performance of water mist fire suppression. Results show a correct reproduction of temperature levels and gas concentrations, while the sensitivity analysis highlights the importance of the flow rate, discharge duration and total volume of water for the performance of water mists.

**KEYWORDS:** Water mist, fire suppression, CFD, FDS, sensitivity analysis.

## NOMENCLATURE

$D$ droplet diameter (m)
$D_{v,0.5}$ median droplet diameter (m)
$f_b$ drag force (N)
$h_s$ sensible enthalpy (J)
$H$ stagnation energy per unit of mass (J/kg)
$\dot{m}'''_\alpha$ production rate of species $\alpha$ (kg/(s.m$^2$))
$\dot{m}'''_{b,\alpha}$ production rate by evaporation (kg/(s.m$^2$))
$\dot{q}''$ heat flux (W/m$^2$)
$\dot{q}'''$ heat release rate per unit of volume (W/m$^3$)
$\dot{q}'''_b$ energy transferred to droplets (W/m$^3$)
$Q$ water flow rate (L/min)
$Z_\alpha$ mass fraction of species $\alpha$ (-)

**Greek**

θ spray cone angle (deg)
ρ density (kg/m$^3$)
τ viscous stress (Pa)
$\tau_d$ water discharge duration (s)

## INTRODUCTION

Fire remains an actual and important threat to humans and their infrastructure. It is estimated that 5000 fires ignite each day in the European Union, generating a yearly loss of 126 billion of euros [1]. Many systems exist to protect against indoor fires, most of them relying on a nozzle to deliver a fluid onto the fire, be it water, inhibiting gas or foam. In this context, halon based extinguishing agents such as Halon 1301 have been used extensively in the past due to their efficiency to suppress fires, but their role in the destruction of the ozone layer have led to their ban by the Montreal Protocol in 1989 [2]. Since then, research on fire safety has focused on finding efficient and environment-friendly alternatives.

Water is a prime candidate as a clean extinguishing agent as it is an abundant, inexpensive, and non-dangerous product, with fire sprinklers being already a mature and common way to protect indoor infrastructures. In fact, today, 96% of fires in sprinkler-protected buildings are controlled or extinguished by the system in the premises [3]. However, this technology is ineffective against oil and electrical fires and is not suitable to protect water sensitive infrastructure such as a data centers because the droplets diameter is too large and would cause further damage to the equipment. Water mists are a promising technology is this regard. They are defined by the NFPA 750 (National Fire Protection Association) standard as a spray whose 99% of the flow-weighted cumulative volumetric distribution of water droplets have a diameter inferior to 1000µm [4]. While traditional sprinklers suppress the fire by cooling the reaction surface, water mists have different suppression mechanisms. They first have a cooling effect by extracting heat from the flame. This heat turns the droplets to steam which expands, smothering the fire by oxygen displacement. Finally, the numerous and fine droplets form an opaque mist which blocks the radiative effect of the fire. Cui and Liu detail the research progress on suppression rules of water mists on different types of fires [5]. Detailed reviews of fire suppression by sprinklers and water mists also exist in the literature [6] [7].

Numerical studies have been conducted by fire safety engineers and researchers as both a cost-effective alternative to experiments and a way to explore new configurations on the fly. In their review, Shen et al. [8] detail many applications of CFD (Computational Fluid Dynamics) codes ranging from enclosure, jet and pool fires, gas dispersion and different types of explosions. In the last decade, a lot of research has been done to explore water mist suppression for various configurations. CFD codes have been used to highlight water mist fire suppression mechanisms through the study of the influence of droplet size [9] [10] [11]. The effects of confined space on water mist performance [12] [13] as well as room geometry [14], ventilation conditions [15], presence of objects shielding the fire [16], type of burning material [17] or fire offset relative to the nozzle [18] have been studied. Most of these studies highlight the mechanisms involved in water mist suppression by conducting parametric studies, but none has provided a mathematical model that could take the involved parameters' interactions into account. Being able to measure these interactions could give a finer interpretation and better understanding of the physics of fire suppression by water mist. In particular, quantitative insights can be obtained using a sensitivity analysis. This technique has already been used to determine model sensitivity of fire scenarios [19] [20] but not for a fire suppression one.

In this work, CFD capabilities to model a simple water mist geometry is studied by reproducing the experimental conditions obtained by Yinshui et al. [21]. The CFD code FDS (Fire Dynamics Simulator) developed by the NIST (National Institute of Standards and Technology) in its version 6.7.6 is used [23]. It is a well-tested and recognized Large Eddy Simulation code in the fire safety domain and used for fire suppression assessment. Then, a global sensitivity analysis based on a full factorial design is conducted to identify the most important parameters when it comes to water mists performances and to demonstrate the potential of this method in the field of fire suppression.

## NUMERICAL MODELLING

### Computational domain & conditions

Figure 1 shows the computational domain considered in the present work, based on Yinshui et al. [21]. It consists of a 1m x 1m x 2m compartment with acrylic [22] walls. On the floor lies a 314cm$^2$ dodecane pool fire with a heat release rate of 516kW.m$^{-2}$. A high-pressure water mist nozzle is positioned 1.80m above the fire. A thermocouple is located 0.45m above the fire, and gas probes monitoring the $O_2$, $CO_2$ and CO concentrations are situated at 1.30m near the wall. A 0.20m diameter exhaust vent is located at 1.80m from the ground. To compensate for the loss, air leaks entering the domain are modelled using the edges of the 0.80m x 0.80m door of the compartment. Free burning is allowed for 60 seconds before the activation of the water mist nozzle. A mesh sensitivity analysis was performed according to the NUREG-1824 [24]. The results are presented below.

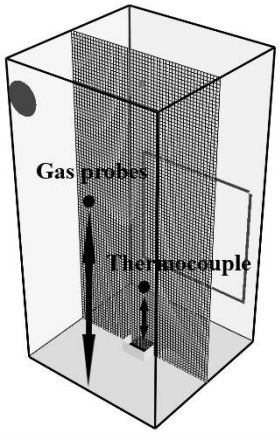


**Fig. 1.** Domain studied in the present work and slice of the calculation grid

### Governing equations

FDS solves a form of the Navier-Stokes equations of conservation of species, mass, momentum and energy appropriate for low-speed, thermally-driven flow with an emphasis on smoke and heat transport from fires. Turbulence is treated by means of Large Eddy Simulation (LES) [25]. FDS uses the concept of "lumped species" where a mixture of gas species for the air transport and react together. For example, air is a lumped species that consists of nitrogen, oxygen, and trace amounts of water vapor and carbon dioxide. The lumped species mass fractions Z are linearly related to the primitive species mass fractions Y using a matrix multiplication. From there all conservation equations can be derived [26]. Here is the transport equation for a lumped species $\alpha$ :

$$\frac{\partial}{\partial t}\left(\rho Z_\alpha\right)+\nabla\cdot\left(\rho Z_\alpha u\right)=\nabla\cdot\left(\rho D_\alpha \nabla Z_\alpha\right)+\dot{m}'''_\alpha+\dot{m}'''_{b,\alpha} \tag{1}$$

The summation of Eq. (1) over all species gives the mass conservation equation:

$$\frac{\partial\rho}{\partial t}+\nabla\cdot\left(\rho u\right)=\dot{m}'''_b \tag{2}$$

Because of the low Mach number approximation, the internal energy and enthalpy may be related. The energy conservation equation can then be written in terms of the sensible enthalpy:

$$\frac{\partial}{\partial t}\left(\rho h_s\right)+\nabla\cdot\left(\rho h_s u\right)=\frac{D\bar{p}}{Dt}+\dot{q}'''+\dot{q}_b'''-\nabla\cdot\dot{q}'' \tag{3}$$

Finally, the momentum conservation equation can be written as:

$$\frac{\partial u}{\partial t}-u\times\omega+\nabla H-\bar{p}\nabla\left(1/\rho\right)=\frac{1}{\rho}\left[\left(\rho-\rho_0\right)g+f_b+\nabla\cdot\tau\right] \tag{4}$$

Liquid droplets associated with water mist systems are modelled within the Lagrangian formalism [27]. Drag and drag reduction phenomenon are accounted as well. The liquid droplets diameter is represented by a combination of log-normal and Rosin-Rammler distributions using the cumulative volume diameter $D_v$ :

$$F(D\le D_{v,0.5})=\frac{1}{\sqrt{2\pi}}\int_0^{D_{v,0.5}}\frac{1}{\sigma D}\exp\left(\frac{\left[\ln(D/D_{v,0.5})\right]^2}{2\sigma^2}\right)dD \tag{5}$$

$$F(D\ge D_{v,0.5})=1-\exp\left(-0.693\left(\frac{D}{D_{v,0.5}}\right)^{\gamma}\right) \tag{6}$$

For the diesel pool fire, no indication of heat release rate (HRR) or mass loss was given by Yinshui et al. [21]. The standard t-squared model for the fire growth was therefore used. Dodecane was used as a surrogate as it has close molecular formulation and is already implemented in FDS. Fire growth rate for the dodecane is 0.047kW.s$^{-2}$ [28]. The rise to a full-grown fire was achieved after 19 seconds. For the HRR decrease following water mist activation however, no predicting model was found and a simple correlation with the extinguishing time was used.

**Mesh sensitivity analysis**

In any CFD case, it is important to choose the correct mesh resolution. It usually is the best compromise between precision and computation time. The FDS User Guide recommends an optimal mesh size defined by the non-dimensional number $D^*/\partial x$, with $\partial x$ being the cell size in the x direction (m) and $D^*$ the characteristic fire diameter (m), determined using the following expression:

$$D^*=\left(\frac{\dot{Q}}{\rho_\infty c_p T_\infty\sqrt{g}}\right)^{2/5} \tag{7}$$

with $\dot{Q}$ the heat release rate of the fire (kW), $\rho_\infty$ the density of the air, $c_p$ the specific heat (J/K), $T_\infty$ the temperature of the far field air (K) and $g$ the acceleration of gravity (m/s$^2$). In the NUREG-1824 [24], the United States Nuclear Regulatory Commission prescribed that $4\le D^*/\partial x\le 16$, which gives the range of mesh sizes [1.15cm ; 4.61cm] should be used. In the present work, the test case from Yinshui et al. which provided the best results in terms of fire suppression time was selected as the reference case. Five meshes were chosen for the mesh sensitivity analysis. Using an equal cell dimension for all directions (x, y, z), the mesh size of 4.0cm producing a total of 31 250 total cells into the domain was first chosen. The latter was then multiplied by 1.5, 2, 6 and 8 reaching the respective mesh sizes of 3.3cm, 3.1cm, 2.2cm and 2.0cm. Finer meshes were not considered as the

computational time of multiple days becomes prohibitive for very little benefits in the scope of the current study. The resulting comparisons of temperature profiles between the experimental result and the different meshes are presented in Fig. 2. The absolute error computed between the experimental and the numerical average temperature decreases as the mesh size increases, ranging from 40.3% to 2.0%. The calculation time ranges from 2.1h to 26.3h. Between 2.2cm and 2cm, the absolute error is divided by 13, from 26.9% to 2.0% whereas the computation time is only multiplied by 1.5, from 17.6h to 26.3h. Therefore, the mesh size of 2cm was selected as reference for the validation case. As for the time step, no analysis is performed as FDS handles it automatically using adaptive CFL (Courant–Friedrichs–Lewy) condition, ensuring convergence by adjusting the timestep according to local velocity and cell dimensions.

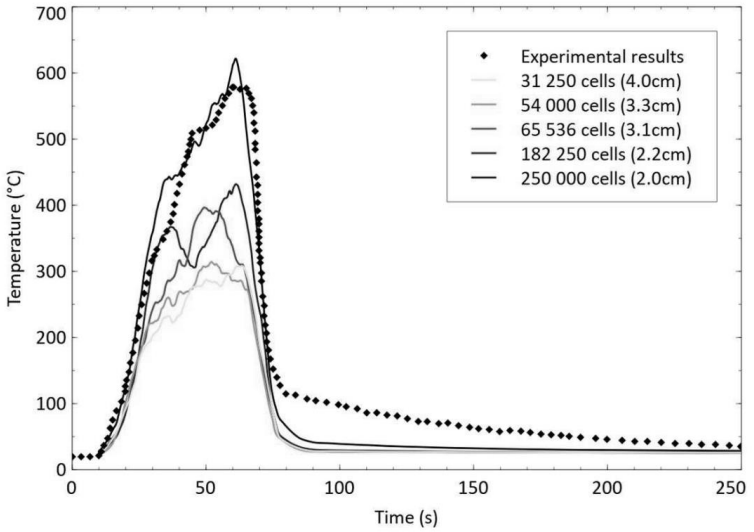


**Fig. 2.** Mesh sensitivity analysis comparison with experimental data

## Validation case

FDS capabilities to model the mechanisms involved in fire suppression by water mist are discussed here. Efforts are focused on reproducing the results of the first test conducted by Yinshui et al. [21] whose conditions are summarized in Table 1. This case has one of the best extinguishing time and both its temperature and $O_2$, $CO_2$, and CO gas concentrations are given. Figure 2 presents the evolution of the temperature inside the compartment for timesteps of 10 seconds (fire development), 45 seconds (fully developed fire), 62 seconds (on-going fire suppression) and 70 seconds (extinguished fire) using a slice centered on the fire. It can be seen that the exhaust ventilation has an effect on the water mist droplets spatial distribution inside the volume. Instead of being centered on the fire, the spray cone highlighted in red is tilted from its nominal axis under the influence of the exhaust air flow. Temperature and gas species quantities have also been monitored over time from the sensors positions described above and are compiled in Fig. 4. The temperature profile is presented on Fig. 4a. and is accurately modelled from 0 to 60 seconds. The peak of temperature is superior in the simulation (563°C) than in the experiment (530°C). The decrease in temperature following the water mist activation is sharper in the simulation than observed experimental results. The difference can be attributed to the lack of model for the decrease of the heat release rate by water aspersion or the precision of experimental measurements. The gas concentrations presented in Fig. 4b, Fig. 4c and Fig. 4d are well modelled by the FDS simulations.

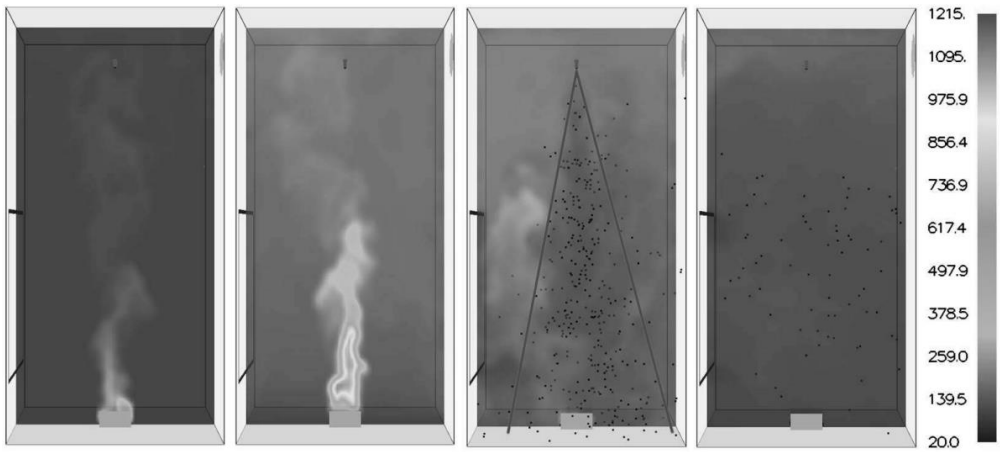


**Fig. 3.** Temperature slices centered on the fire at 10, 45, 62 and 70 seconds

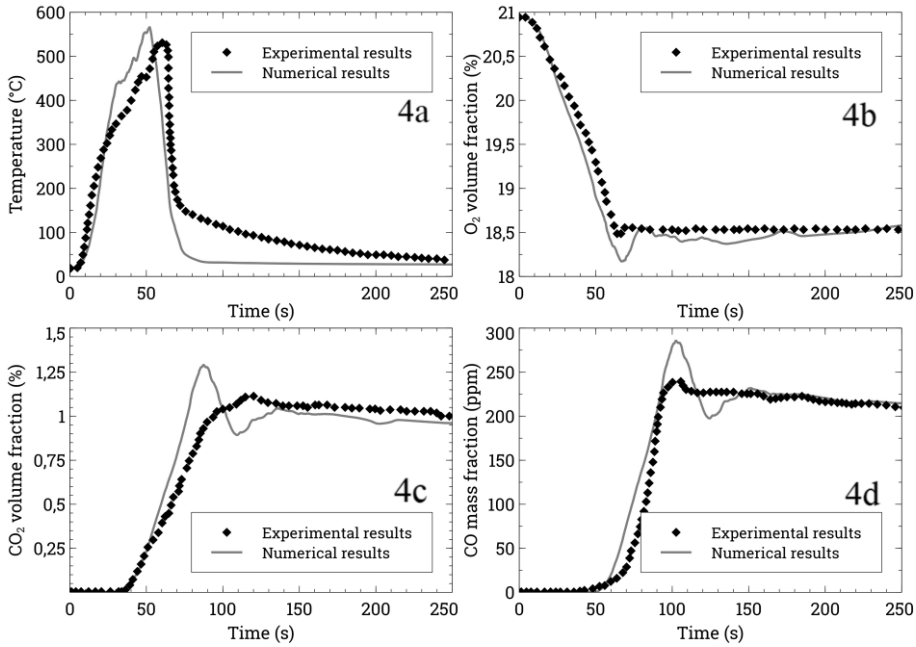


**Fig. 4.** Temperature and gas concentrations profiles between experimental and numerical results

The dioxygen concentration decreases linearly as the fire burns. It reaches a constant value of 18.5% after the fire suppression. This behaviour highlights the dioxygen displacement because no more dioxygen is consumed by the fire after suppression. The carbon dioxide concentration rise becomes noticeable after 40 seconds of free burn and continues to rise after the fire suppression up until 100 seconds. After this time, it also reaches a constant value of 1.0%. The rise of carbon monoxide concentration is also slow with a slightly sharper rise in the simulation. As for the carbon dioxide, the concentration rises after the fire suppression that happen at 60 seconds. The final value of concentration is around 215ppm. For Fig. 4c and Fig. 4d, a transitional period following the nozzle activation is observed. This could be the influence of the high-pressure nozzle that induces higher displacement of those species compare to what happens experimentally. This behaviour could also explain the sharper temperature decrease in Fig. 4a.

## PARAMETER SENSITIVITY ANALYSIS APPROACH

### Sensitivity analysis

The performance of a water mist system depends on many parameters such as the water flow rate, the spray cone angle, the nominal pressure, the droplets size distribution, the presence of a ventilation or obstacles, etc. However, it is difficult to conduct experimental studies by varying all these parameters at the same time, not considering that some of them can be hard to measure for large ranges of values. It is therefore important to know in advance which parameters are of importance and which one can be fixed to a nominal value because they have little impact on the experience output. In the present work, a sensitivity analysis based on the factorial design was conducted. Each of the three input parameters of the model considered in this study, *ie.* water mist flow rate ( $Q$ ), spray cone angle ( $\theta$ ) and discharge duration ( $\tau_d$ ) was evaluated at two normalized levels ( $\pm 1$ ) around a nominal value, one 10% higher and the other 10% lower. A fourth parameter, the median droplet diameter was also taken into account. It follows that $2^3 = 8$ simulations must be performed for the three parameters factorial design and $2^4 = 16$ simulations for the four parameters factorial design.

Table 1 presents the values of the input parameters of the first experimental test conducted by Yinshui et al. which is set as nominal values, as well as their respective variations (minimum and maximum) used for the sensitivity analysis. The outputs of the FDS model are the mean temperature ( $T$ ) in degree Celsius, the final volume fraction of $O_2$ ( $X_{O_2}$ ) and $CO_2$ ( $X_{CO_2}$ ) in addition to the final mass fraction of CO ( $Y_{CO}$ ) in ppm.

**Table 1. Range of input parameters for the full factorial design**

| Input parameter | Unit | Minimum | Nominal [Yinshui et al] | Maximum |
|---|---|---|---|---|
| Water flow rate $Q$ | L/min | 1.8 | 2 | 2.2 |
| Spray cone angle $\theta$ | deg | 54 | 60 | 66 |
| Discharge duration $\tau_d$ | s | 2.43 | 2.7 | 2.97 |
| Droplet diameter | µm | 72 | 80 | 88 |

### Approximation of the FDS model

Generally, any output quantity $\xi$ is expressed as a function of the *n* input parameters $x_i$ :

$$\xi = f(x_1,\ldots,x_n) = f_{k,0} + \sum_{i=1}^{n} f_{k,i}(x_i) + \sum_{i,j=1/i\neq j}^{n} f_{k,ij}(x_i,x_j) + \cdots + f_{12\ldots n}(x_1,\ldots,x_n) \tag{8}$$

Using the factorial design method, an approximation of the system must first be chosen. A simple linear model is chosen in the absence of a previous study highlighting the behavior of our input parameters. The *m* output quantities studied are then expressed as:

$$\forall k \in [1,m], \xi_k(x_1,\ldots,x_n) = \alpha_{k,0} + \sum_{i=1}^{n} \alpha_{k,i} x_i + \sum_{i,j=1/i\neq j}^{n} \alpha_{k,ij} x_i x_j + \ldots + \alpha_{k,\,1,n} \prod_{i=1}^{n} x_i \tag{9}$$

Or in a more condensed and accurate way:

$$\forall k \in [1,m], \xi_k(X) = \alpha_{k,0} + \sum_{k=1}^{n} \sum_{\substack{I \subset 1,n \\ card(I)=k}} \alpha_{k,I} \prod_{i \in I} x_i \tag{10}$$

Each $\xi_k$ can then be rewritten with the matrix form $\vec{\xi}_k = X\vec{\alpha}_k$ which can then be used to extract the vector of coefficients $\vec{\alpha}_k$ from $\vec{\alpha}_k = X^{-1}\vec{\xi}_k$ (direct inversion of the matrix).

**Sensitivity analysis results**

The sensitivity analysis techniques described above were then applied to the numerical predictions from the CFD model which was studied in the validation case. The early work with three parameters has been extended with a four parameters study. There is no uncertainty related to the factorial design of this model as FDS simulations are deterministic. In turn, it means that any discrepancy can be traced to the motivations behind the construction of the numerical model under FDS. In order to obtain a visual representation of the significance of each parameter and their interactions, all the results are presented below in the form of Pareto charts (Fig. 5 & Fig. 6), where parameters are displayed in decreasing order of normalized effect. An effect close to zero means that the concerned parameter has no influence whereas an effect closer to one suggests that the parameter has the most influence. Independent parameters are highlighted in grey while all interactions are displayed in black.

Figure 5 depicts the effects of the input parameters on the different output quantities. Fig. 5a presents such effects for the temperature. It can be observed that the discharge duration $\tau_d$ is the most significant parameter with a coefficient of 0.30, closely followed by the interaction $Q\theta\tau_d$ at 0.25 and $\theta\tau_d$ at 0.15. For the $O_2$ volume fraction in Fig. 5b, the most important parameters are $Q$, $Q\theta\tau_d$, $\tau_d$ and $Q\tau_d$ almost tied with respective coefficients of 0.21, 0.21, 0.19 and 0.19. For the $CO_2$ volume in Fig. 5c and the CO mass fraction in Fig. 5d, the most important parameters are again $Q$, $Q\tau_d$, $Q\theta\tau_d$ with respective coefficients 0.29, 0.26 and 0.18.

From all four sub-figures the importance of the discharge duration $\tau_d$ for the variation of the output quantities is apparent. This trend can be explained as a fire is a chemical phenomenon with a lot of inertia which remains thermally active long after actions have been taken to suppress it and can even reignite if the suppression is not long enough to reach extinction. It is therefore understandable that the discharge duration is an important parameter for the temperature decrease. The interactions of the input parameters all have a coefficient around 0.05. These interactions are not easily interpreted but it is intuitive that $Q$ and $\tau_d$ condition the total mass of water entering the domain whereas $Q$ and $\theta$ influence the local values of the water mass fraction. $Q\theta$ (L.rad/min) can then be thought as the water spatial density, $Q\tau_d$ (L) the total water volume and $\theta\tau_d$ (rad.s) the potential water reaching the fire, be it spatial or temporal.

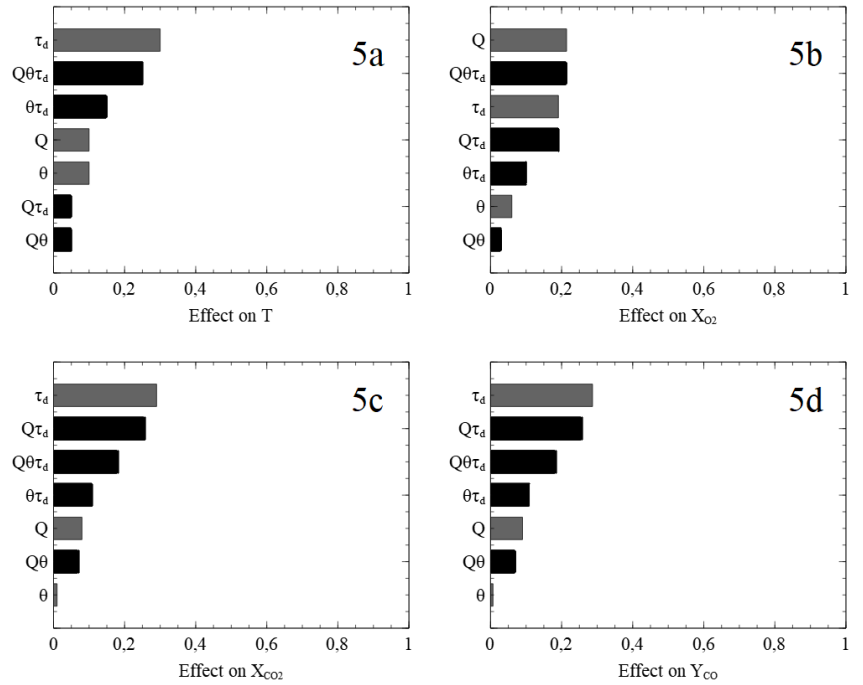


**Fig. 5.** Results of the three parameters full factorial design

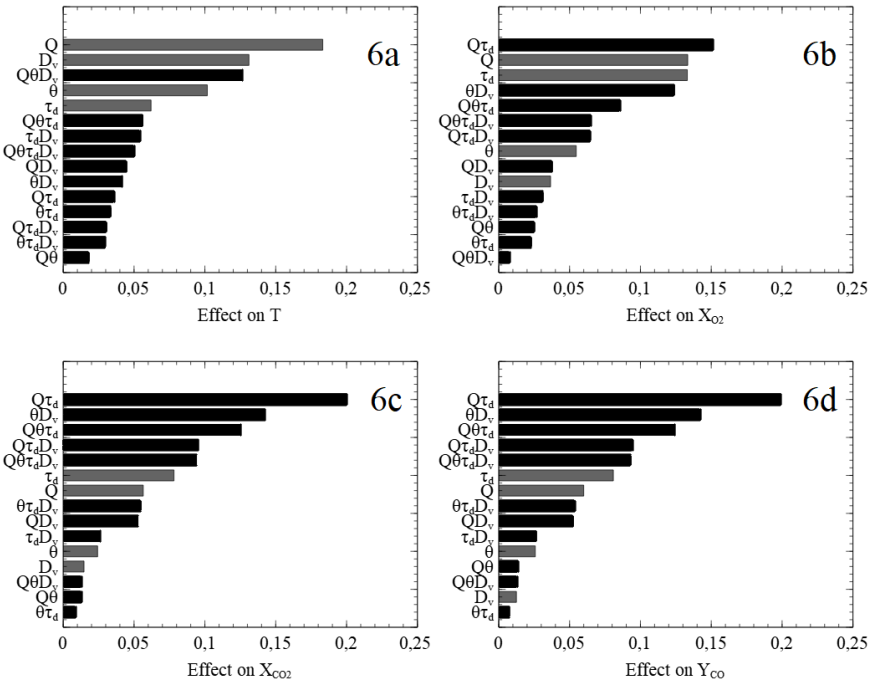


**Fig. 6.** Results of the four parameters full factorial design

Fig. 6 depicts the results of the same factorial design when the droplet diameter $D_v$ is taken into account. The effects are shown from 0 to 0.25 to better visualize the results. Fig. 6a presents the effects for the temperature. The most significant parameter is the flow rate $Q$ with an effect of 0.18. Then we have the droplet diameter $D_v$ at 0.13, followed by the interaction $Q\theta D_v$.

For the $O_2$ volume fraction in Fig. 6b, the most important parameters are $Q\tau_d$ at 0.15 followed by $Q$ and $\tau_d$ with effects at 0.13. For the $CO_2$ volume in Fig. 6c and the CO mass fraction in Fig. 6d, the most important parameters are interactions, the main one being $Q\tau_d$ at 0.20.

With the four parameters full factorial design, it is now apparent that the total volume of water sprayed $Q\tau_d$ and the flow rate $Q$ are the most influencial parameters. It follows that the discharge duration still plays a role in the suppression mechanism, as highlighted by the previous three parameters full factorial design. In particular for the temperature, we see that the median droplet diameter $D_v$ is second in terms of importance. This is in line with previous experimental observations, where the superiority of water mist systems over traditional sprinklers is attributed to the greater surface area of exchange of smaller droplets.

## CONCLUSION

The suppression of a diesel compartment fire by a water mist system based on experimental results produced by Yinshui et al. [21] was numerically investigated using the CFD code FDS and a heat release rate (HRR) approach. After conducting a mesh sensitivity analysis, a validation case was performed. The gas concentrations of $O_2$, $CO_2$ and CO were correctly reproduced from start to finish. The predicted temperature decrease was overestimated which may be due to the lack of a heat release rate decrease model under water mist aspersion. This model could be improved using empirical data or numerical techniques such as described by Jenft et al. [9]. In their work they relate the pyrolysis rate and the temperature of each fuel cell on the free burning phase. When water impinges a fuel cell, the computed temperature is used to force the corresponding pyrolysis rate. Another solution to further improve the numerical predictions would be to use a model based on the diesel characteristics and volume available rather than on the heat release rate.

A sensitivity analysis was then conducted using a full factorial design. Previous work focused on the three parameters from the validation case ($Q$, $\theta$, $\tau_d$), while new findings take the median droplet diameter $D_v$ into account. Comparing the results from Fig. 5 and Fig. 6, the flow rate $Q$, the discharge duration $\tau_d$ and the interaction $Q\tau_d$ which is the total volume of water sprayed are highlighted as major parameters. For the temperature in particular, the droplet diameter $D_v$ is shown to play an important role, as observed experimentally. The two methods showcased the great potential of sensitivity analysis to improve the efficiency of experimentations. They were able to confirm the observations and interpretations of the literature on the fire suppression mechanisms through the years. Therefore, this method could be used to explore configurations and parameters not easily accessible through experiments. These factorial designs could be extended with the number of parameters or ranges. Other sensitivity analysis techniques based on the variance decomposition (ANOVA) are currently investigated for a four parameters study.

## REFERENCES


[1] European Fire Safety Strategy advocacy, https://firesafeeurope.eu/european-fire-safety-strategy-needed/, (accessed 6 October 2021).

[2] Office of Environmental Quality's abstract of The Montreal Protocol on Substances That Deplete the Ozone Layer, https://www.state.gov/key-topics-office-of-environmental-quality-and-transboundary-issues/the-montreal-protocol-on-substances-that-deplete-the-ozone-layer/, (accessed 24 November 2021).

[3] The EU Fire Safety Guide, https://www.modernbuildingalliance.eu/EU-fire-safety-guide, (accessed 25 October 2021).

[4] Technical Committee on Water Mist Fire Suppression Systems, NFPA 750 Standard on Water Mist Fire Protection Systems, 2019 Edition, 2018.

[5] Y. Cui, J. Liu, Research progress of water mist fire extinguishing technology and its application in battery fires, Process Safety and Environmental Protection 149 (2021) 559-574.

[6] Z. Liu, A.K. Kim, A Review of Water Mist Fire Suppression Systems – Fundamental Studies, Journal of Fire Protection Engineering 10 (1999) 32-50.

[7] S.A. Adbulrahman, K. Chetehouna, A. Cablé, Ø. Skreiberg, M. Kadoche, A review on fire suppression by fire sprinklers, Journal of Fire Sciences (2021) 39(6), 512-551.

[8] R. Shen, Z. Jiao, T. Parker, Y. Sun, Q. Wang, Recent application of Computational Fluid Dynamics (CFD) in process safety and loss prevention: A review, Journal of Loss Prevention in the Process Industries 67 (2020) 104252.

[9] A. Jenft, A. Collin, P. Boulet, G. Pianet, A. Breton, A. Muller, Experimental and numerical study of pool fire suppression using water mist, Fire Safety Journal 67 (2014) 1-12.

[10] Z. Wang, W. Wang, Q. Wang, Optimization of water mist droplet size by using CFD modeling for fire suppressions, Journal of Loss Prevention in the Process Industries 44 (2016) 626-632.

[11] H. Liu, C. Wang, I. M. C. Cordeiro, A. C. Y. Yuen, Q. Chen, Q. N. Chan, S. Kook, G. H. Yeoh, Critical assessment on operating water droplet sizes for fire sprinkler and water mist systems, Journal of Building Engineering 28 (2020) 100999.

[12] J. Lee, Numerical analysis on the rapid fire suppression using a water mist nozzle in a fire compartment with a door opening, Nuclear Engineering and Technology 51 (2019) 410-423.

[13] T.-s. Liang, Z.-l. Liu, X.-k. Xiao, S.-m. Luo, G.-x. Liao, W. Zhong, Experimental and Numerical Study of Fire Suppression Performance of Ultra-Fine Water Mist in a Confined Space, Procedia Engineering 52 (2013) 208-213.

[14] P. Zhang, X. Tang, X. Tian, C. Liu, M. Zhong, Experimental study on the interaction between fire and water mist in long and narrow space, Applied Thermal Engineering 94 (2016) 706-714.

[15] J. Lee, Numerical analysis of how ventilation conditions impact compartment fire suppression by water mist, Annals of Nuclear Energy 136 (2020) 107021.

[16] Y. Liu, X. Wang, T. Liu, J. Ma, G. Li, Z. Zhao, Preliminary study on extinguishing shielded fire with water mist, Process Safety and Environmental Protection 141 (2020) 344-354.

[17] F. Pancawardani, D. Arini, R. P. Yunindar, M. L. Ramadhan, F. A. Imran, Y. S. Nugroho, Analysis of Water Mist Fire Suppression System Applied on Cellulose Fire, Procedia Engineering 170 (2017) 344-351.

[18] J. Lee, J. Moon, Numerical analysis of the effect of horizontal distance between a water mist nozzle and ignition source on reduction in heat release rate, Annals of Nuclear Energy144 (2020) 107560.

[19] A.J. Wang, B. Manescau, Q. Serra, K. Chetehouna, E. Florentin, C. De Izarra, Numerical simulations of outdoor wind effects on smoke spreading along a corridor: Physical and sensitivity analysis, International Journal of Thermal Sciences 142 (2019) 332-347.

[20] N. Hamamousse, A. Kaiss, F. Giroud, N. Bozabalian, J.-P. Clerc, N. Zekri, Small World Network Model Validation. Case Study of Suartone Historical Fire in Corsica, Combustion Science and Technology (available online 11 May 2021).

[21] L. Yinshui, J. Zhuo, W. Dan, L. Xiaohui, Experimental research on the water mist fire suppression performance in an enclosed space by changing the characteristics of nozzles, Experimental Thermal and Fluid Science 52 (2014) 174-181.

[22] Thermal Properties of Plastic Materials (acrylic), https://www.professionalplastics.com/professionalplastics/ThermalPropertiesofPlasticMaterials.pdf, (accessed 25 October 2021).

[23] FDS 6.7.6 and Smokeview 6.7.16 GitHub page, https://github.com/firemodels/fds/releases/tag/FDS6.7.6, (accessed 10 October 2021).

[24] United States Nuclear Regulatory Comission, Verification and Validation of Selected Fire Models for Nuclear Power Plant Applications, 2007.

[25] National Institute of Standards and Technology, Fire Dynamics Simulator User's Guide, NIST Special Publication 1019 Sixth Edition, 2021, p. 3.

[26] National Institute of Standards and Technology, Fire Dynamics Simulator Technical Reference Guide Volume 1: Mathematical Model, NIST Special Publication 1018-1 Sixth Edition, 2021, pp. 7-10.

[27] National Institute of Standards and Technology, Fire Dynamics Simulator Technical Reference Guide Volume 1: Mathematical Model, NIST Special Publication 1018-1 Sixth Edition, 2021, pp. 100-101.

[28] B. Karlsson, J. G. Quintere, Enclosure Fire Dynamics, CRC Press, 2000, p. 54.

# A case study into inhibition limits of Novec in Stoichiometric Propane-Air mixture

**Nagaraju S.[1]*, Abid S.[1,2], Comandini A. [1], Chaumeix N. [1]**

[1] *Institut de Combustion, Aérothermique, Réactivité et Environnement, CNRS Orleans, France.*
[2]*University of Orleans, France*
**Corresponding author's email: sharath.nagaraju@cnrs-orleans.fr*

## ABSTRACT

Inhibition capability of Novec-1230, $C_6F_{12}O$, was experimentally studied in stoichiometric propane/air mixture at an initial temperature and pressure of 300 K and 1 bar, respectively. For this, the propane/air flammability limits were experimentally measured at the same conditions. In the inhibition studies, $C_6F_{12}O$ concentration was varied from 6 % - 10.4 % and pressure inside the ignition chamber was monitored with two pressure sensors. The flames were visualised and recorded using a high speed camera to understand its behavior near the limiting conditions. From the inhibition experiments, the inerting point where $C_6F_{12}O$ inhibits combustion, was found to be $9.3\pm0.4_{mol}$%. The observed overpressure near the limiting conditions are reported as well. To complement the experimental results and to understand the behavior of $C_6F_{12}O$ in propane/air mixture, we have carried out numerical studies over a wide range of equivalence ratios and temperatures. The calculated laminar flame speeds with 1% $C_6F_{12}O$ in the propane/air mixture at an equivalence ratio of 0.6 is nearly 20% higher than that of the no inhibitor case, at the same conditions. Equilibrium calculations shows that at 8.5% $C_6F_{12}O$ in stoichiometric propane-air mixture, the observed pressure values are 0.6% of $P_{AICC}$. The adiabatic flame temperatures at an equivalence ratio of 0.6 is higher in propane-air-inhibitor mixture than the neat propane-air mixture for a range of $C_6F_{12}O$ concentrations.

**KEYWORDS:** Novec, $C_6F_{12}O$, flammabity limits, propane flames, Inhibition

## INTRODUCTION

1,1,1,2,2,4,5,5,5-nonafluoro-4-(trifluoromethyl)-3-pentanone (Novec 1230), with the global formula $C_6F_{12}O$ is widely considered as a replacement for existing halons as it can be used in various fire suppression application, for example: fire in Lithium-ion batteries due to thermal runaways [1], electrical systems [2], streaming applications [3], hush houses (noise suppressing engine facilities) [4], and aircraft hangers [5]. Being a low environmental impact agent, it also has an additional advantage over current fire supressing agents [6,7]. A comparison of environmental impact of three fire suppresants, Novec 1230, Halon 1211, Halotron I is given in Ref. 7 (See Table 2 in Ref. 7).

As explained in previous literatures $C_6F_{12}O$, Novec-1230, has been proposed as a replacement for the existing Halons as the Montreal Protocol restricts its further production [7]. Halons are currently being used in supressing fire in aircraft and needs to be phased out. To be a replacement in fire suppressing applications in aircrafts, a series of tests laid down by the FAA were carried out with the proposed inhibitor, $C_6F_{12}O$ [7]. The results of the study, compiled in the report by Jeremy Casey, illustrates the fire suppression capability of $C_6F_{12}O$ in various situations. Tests in which $C_6F_{12}O$, Novec 1230, showed a complete fire supressing capabilities are in the engine fire test, three dimensional inclined plane test, 16 feet pan fire test and wheel brake fire test. In spite of these positive results that are reported in the literature and usage of the above-said agent in various applications, $C_6F_{12}O$ is still not used to suppress fires in aircraft cargo bay as it was found to produce a greater overpressure compared to no inhibitor case [8]. This indicates that $C_6F_{12}O$ participates in the combustion rather than inhibiting it.

In order to understand occurence of these overpressures, several works have ben carried out [9-13] and the majority of them have been summerised in the report authored by Linteris [14]. The

participation of inhibitor in combustion resulting in overpressures greater than no inhibitor were seen in lean mixture, especially for a range of equivalence ratios, 0.63-0.68 [13]. Although this observed overpressure is not desired, it not completely surpising as several other fluorinated hydrocarbons were seen to exhibit similar behavior in previous studies [13, 15,16]. In fact, not just the fluorinated carbons, HBr has been observed to promote the flame at lean equivalence ratios[17]. Numerical studies carried out by Pagliaro et. al [18], showed that $C_6F_{12}O$ in propane-water vapor mixture at equivalence ratio of 0.6, acted as a promoter or supressor of combustion depending on the ratio of fluorine to hydrogen, [F]/[H], in the mixture. Higher the hydrogen concentration, better the inhibition ability of $C_6F_{12}O$ in proane-air-water vapor mixture i.e. one can expect $C_6F_{12}O$ being a promoter of the combustion at higher $C_6F_{12}O$ concentrations. Also, numerical studies of pure $C_6F_{12}O$ combustion in air carried out at 400 K resulted in a burning velocity of 0.37 cm/s[19]. This indicates that the experimentally non-observable neat $C_6F_{12}O$ flame can however have exothermic reaction that can act as a promoter of combustion for several hydrocarbon fuels. The above-mentioned works points out to a fact that $C_6F_{12}O$, like other fluorinated fire suppressor, is involved in combustion in lean fuel/air mixture. However, it is a capable inhibitor and can be used in various fire suppresant appplications.

The goal of this study is to fill the voids in the literature on the inhibition studies of $C_6F_{12}O$. It is known that both the $T_{adia}$ and $S_L^0$, are the highest at stoichiometric conditions and hence require higher inhibition agent to reduce them to a level where ignition could not occur. Hence, the inhibition limit of the $C_6F_{12}O$ in stoichiometric propane/air conditions has been obtained. To complement the experiments, we have also carried out numerical studies to obtain various thermodynamic parameters at the inhibition limits. As the studies are being done to understand the safety aspects of $C_6F_{12}O$ in the aircraft application, the current numerical work was carried out at a range of temperature experienced in real flight conditions. Although temperature and pressure vary during the flight, here, we have carried out only temperature parametrization on the mechanism.

## EXPERIMENTAL DETAILS

The experimental facility is shown in Fig. 1. It consists of an ignition chamber, NC2V, encompassed by a classical Z-type schlieren system with Phantom V-12 high speed camera. The ignition chamber is hollow SS-304 cylinder of volume 4.3 liters has a wall thickness of 30 mm and an internal diameter of 130 mm. Two pressure transducers, one from PCB (113B26) and the other from Kistler (603B) are used to obtain the pressure profile inside the chamber from the combustion of propane/air(/$C_6F_{12}O$) mixture. The ignition of the fuel was done through spark created between two electrodes at the center of the cylinder. The discharge voltage was measured with Tektronix P6015A voltage probe while the current was measured with Bergoz Current Transformer CT-D1.0-B current probe. In the case of $C_6F_{12}O$ studies, the products in the chamber after the combustion was purged with nitrogen through a CLEANSORB Model Number: CS025LS column for nearly 40 minute to trap HF and other fluorinated compounds formed during the combustion process.

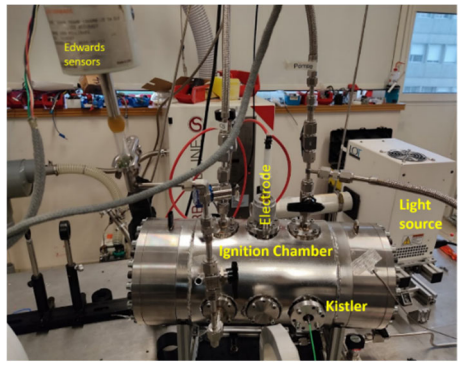


**Fig. 1.** A photograph of the facility used in the present work

## Gases, Chemicals and Preparation of mixture

Air alphagaz-2, with a purity of 99,9999% and, consiting of 79.1% N2 and 20.9% O2, ≥99.5% purity Propane (N25), and FK-5-1-12 ($C_6F_{12}O$), supplied by Air-Liquide were used in the present experiments. Apart from the ignition chamber shown in the photograph two glass vessels, a hollow sphere with an internal volume of 10 litre and a hollow cylinder with a 1 litre internal volume, were used as mixing tank and $C_6F_{12}O$ reservoir, respectively. Internally, the mixing tank was also equipped with a magnetic stirrer that was used to ensure a uniform mixture of $C_6F_{12}O$ /propane/air. To better understand the facility and the connections between the mixing vessels and the ignition chamber, a schematic of the facility with gas lines is shown in Fig. 2 a. and the connections from experimental facility to the data acquisition system is shown in Fig. 2 b. The uncertainty in the present work is primarily in the mixture preparation. The accuracy propane concentration in propane-air mixture is 0.01% while for $C_6F_{12}O$ in propane-air-$C_6F_{12}O$ mixture is 0.1%. In the present settings, the resolution of the measured overpressure from the combition of PCB and Kistler sensors is 0.01 bar.

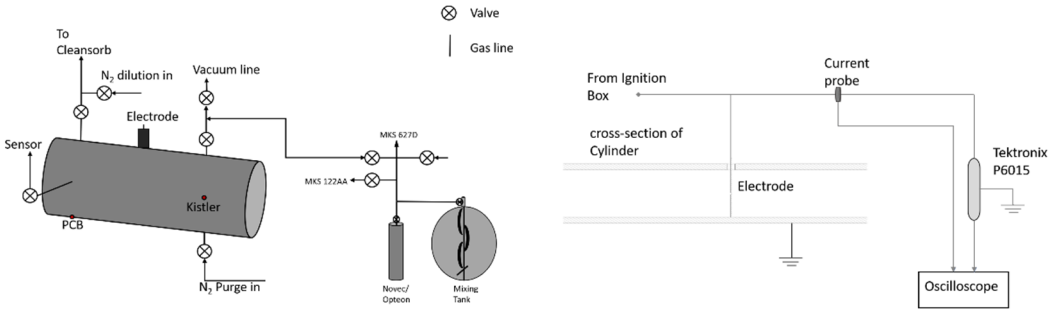


**Fig. 2.** (a) A schematic of the chamber showint connections between various componens of the system (left) and (b) cross-sectional schematics showing the electrode and measuring devices in the system.

Initially, the $C_6F_{12}O$ reservoir was dipped inside a liquid nitrogen bath and evacuated to remove air. The vessel was retrieved-allowed to liquify-submerged again in the liquid nitrogen bath and the process was repeated for a total of three times. Once this was done the bottle was sealed with a high vacuum valve with three O-rings. The 10-liter mix-tank was evacuated before each run to a pressure lower than $10^{-2}$ mbar, followed by introduction of desired vapor pressure of $C_6F_{12}O$ and then preparing a stoichiometric mixture of propane/air in it. In the mixing tank, two pressure sensors, MKS 122AA-01000-100 and MKS-627D 14TBC1B 06517521, were used to record the filling pressures of all three, inhibitor, propane and air. After complete mixing, the mixture was introduced into the evacuated ignition chamber until a pressure of 1 bar is reached in it. The pressure in the ignition chamber was recorded using Edwards 600AB3028716 sensor.

Only the recorded pressure traces could be used from the initial experiments as the recorded time resolution in the oscilloscope was not enough to obtain the ignition energy. Later, the experiments were repeated near the inhibition limit to obtain the mean ignition energy.

## Choice of electrode distance

A custom made discharge box has been used in the present work to create the spark across the electrode. Energy dissipation of the system used across the electrodes should be optimized to maximize the energy deposition to the fuel/oxidizer mixture. For this, a set of 100 discharges in air were done for three distinct electrode distances, 3.5 mm, 4.8 mm and 6.2 mm. The mean for the above-mentioned distances were 164 mJ, 168 mJ and 190 mJ, respectively. A typical scatter of the ignition energies for an electrode distance of 6.2 mm along with the voltage and current signals are shown in

Fig. 3. Similar scatter was obtained for 3.5 and 4.8 mm as well. Since the deposited energy and the spark gap was more than the other two cases, further experiments were carried out at 6.2 mm electrode gap.

## RESULTS AND DISCUSSION

### Propane Flammability Limits

Both the higher and lower flammability limits of Propane/air mixture was determined to understand thermodynamic parameters at which extinction event could be seen. The mean ignition energies at the lower and higher limits of the propane were 169 mJ and 249 mJ, respectively. The standard deviation were 26.07 mJ and 28.43 mJ, respectively for lower and higher limits.

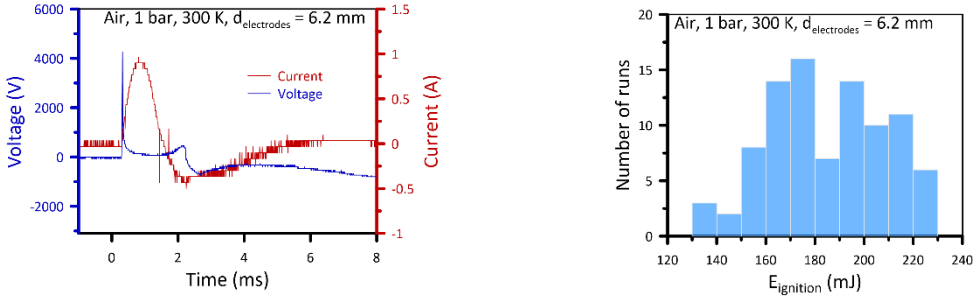


**Fig. 3. (a)** Typical voltage and current signal obtained in the experiments **(b)**. Distribution of deposited energies in air when electrodes separated by a distance 6.2 mm.

The molar percentage of propane in air was varied from 2.0% to 10.3% keeping the ignition pressure constant at 1 bar. Here, the flammability is defined as the ability of the flame/combustion to increase the pressure by 2% of the initial value. Since all the experiments were conducted at 1.0 bar, experiments in which a 0.02 bar overpressure was observed were considered to be flammable. A logistic function was used to fit the ignition probability data and to obtain the flammability limits. Using the fit, shown in Fig. 4 a. for lower flammability limits and Fig. 4 b. for the higher flammbility limits, we obtained values of the lower and upper limiting points, and are 2.12±0.08 % and 10.18±0.09 %, respectively. Similar values were seen when the limits were defined based on the visual analysis of the flame. Here, the successful ignition is defined as the ability of the flame to successfully spread in the chamber without getting extinguished after the ignition at the spark gap. The shape of the flame at various propane concentrations near the limiting conditions is given in Fig. 5.

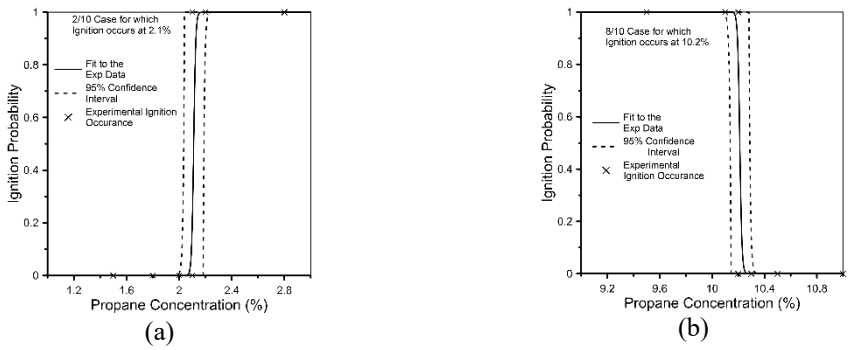


**Fig. 4.** Logistic distribution function for propane flammability limit. (a) Lower flammability limit (Left) and (b) higher flammability limit (Right).

The localised flames in Fig. 5, seen at $10.3_{mol}$% propane content, are due to the high deposited energies from the ignition box. They eventualy fades off near the wall. They neither fully propagate nor cause any pressure rise in the combustion chamber.

### $C_6F_{12}O$ (Novec-1230) inhibition experimental determination

The inhibition capabilities of $C_6F_{12}O$ was measured in stoichiometric propane/air mixture. The stoichiometric mixture was chosen as the reference as the concentration of inhibitor required to reach inflammable condition will be high compared to both the rich and lean mixture. Here, the $C_6F_{12}O$ molar percentage was varied from 5.9% to 10.4%. From the initial numerical studies, based on the values ($T_{adiab}$ and Laminar flame speeds) at which propane inhibitions were observed, $C_6F_{12}O$ was expected to inhibit the flame for stoichiometric propane/air mixture are 6% itself. Hence, the starting molar percent of novec was chosen at 5.9%. However, on observing a completely developed flame, resulting in an overpressure value grated than 0.2 bar, the concentration of $C_6F_{12}O$ was steadily increased until an inerting point was found. Authors, would like to inform here that the initial pressure for the 5.9% experiment was 0.9 bar while the rest of the experiments were carried out at 1bar. The measured overpressure values as a function of $C_6F_{12}O$ molar percentage in stoichiometric propane/air mixture is plotted in Fig. 6. In the present wok, we have used measured overpressure at novec concentration of 7.5% to normalise the pressure value in order to define the flammability limits of the mixture. In the literature $P_x/P_{max}$ was used to normalise the pressure values[20]. Since in the present work, experiments were carried out onwards of 7.5% Novec concentration, it becomes necessary to specify the concetration at which overpressure is being used as a normalising factor. For novec, the value of $P_x/P_{7.5}$ corresponding to 2% overpressure is 0.16. i.e. if the the ratio of $P_x/P_{7.5}$ is lower than 0.16 in any chamber, the limitting point is said to be reached. The variation of normalised pressure ratio is also given in Figure 6.

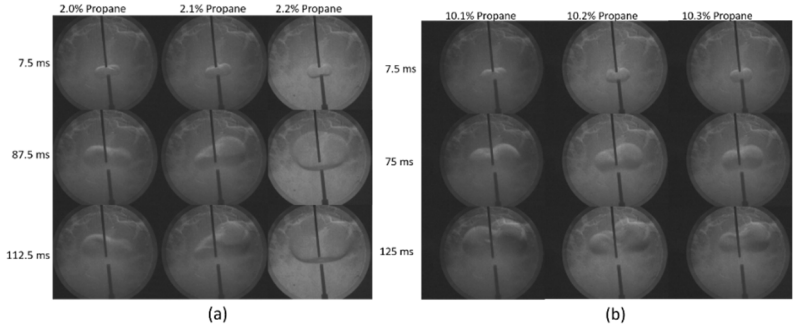


**Fig. 5.** Schlieren images of the propane/air flame at three distinct intervals for (a) lower flammability limit (Left) and (b) higher flammability limit (Right), respectively.

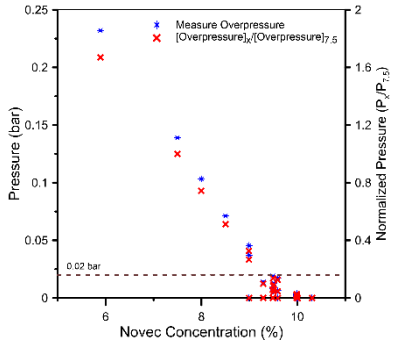


**Fig. 6.** Measured overpressure for different C6F12O concentration along with the normalized pressure value. Px is the overpressure value measured at Novec concentration, x, and $P_{7.5}$ is the pressure at 7.5% of $C_6F_{12}O$ concentration in stoichiometric propane/air mixture.

In this set of experiments, the mean energy deposited is 296 mJ with a standard deviation of 69 mJ. As seen from the Fig. 6, if the definition of the flammability is changed to a case at which an overpressure of 0.05 bar is observed, the inflammable point will be at 9%. Also, only one in ten runs resulted in a flame that increased the pressure by 0.21 bar i.e 2.1% of the initial value. Even at 9.5% and 10% there were flame that had nearly no considerable increase in the pressure values, however sustainable. Considering practical applications where inhibitor can have a small variation in the concentration we wanted to get to a point where the flame is not sustainable and was not acting as a pilot flame. The $C_6F_{12}O$ molar percent at which no flame existed in stoichiometric propane/air mixture was 10%. Similar to propane, a logistic fit was done to the ignition probability to obtain the inerting point and is shown in Fig. 7 a. At the above mentioned ignition energy distribution, 9.3±0.4% of $C_6F_{12}O$ was required to reach an inflammable case for the stoichiometric propane/air mixture. Also, in Fig. 7 b. visualized flames at three distinct time intervals for three different concentrations are given. It can be seen that at 9.5 % of the $C_6F_{12}O$ concentration, the flame is quite weak and at 10% the flame is completely extinguished.

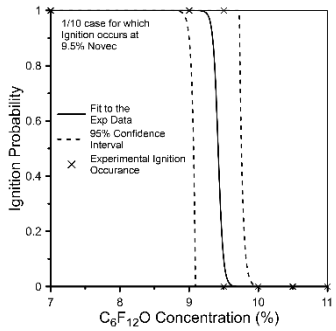


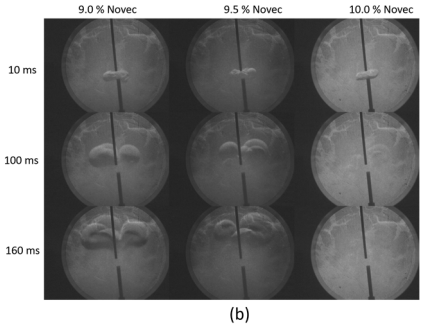


**Fig. 7. (a)** Logistic distribution function for $C_6F_{12}O$ flammability limit in Propane/Air stoichiometric mixture. (Left) and (b) Schliren images of the flame for three concentrations of C6F12O near innertin point (Right).

To illustrate the variation in measured pressure values for the same $C_6F_{12}O$ concentration, a plot showing the pressure history for thirteen experiment at 9.5% $C_6F_{12}O$ concentration is given in Fig. 8. As one can see in the figure, pressure value in only one case is close to flammability level and when it is corrected for the negative baseline observed before the flame, the magnitude crosses the threshold for the definition of combustion.

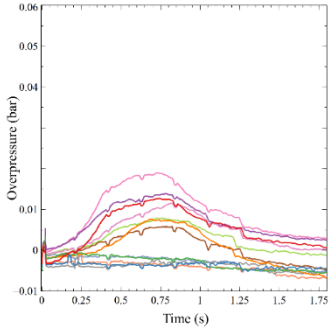


**Fig. 8.** Recorded pressure profiles from the 9.5% C6F12O in stoichiometric propane/air mixture.

## NUMERICAL STUDIES

Numerical studies for $C_6F_{12}O$ (Novec) in propane/air mixture was carried out in Cosilab [21] using a mechanism available in the literature. Overall, the mechanism used here has 181 species and 1513 reversible reactions. The mechanism used in the present study consists of

- San Diego mechanism for oxidation of hydrogen, CO, and C1 to C4 hydrocarbons [22],
- C1 and C2 hydro-fluorocarbon sub-mechanism [10,23], C3 Fluro-carbon sub mechanisms [24].
- The $C_6F_{12}O$ reactions from mechanism given by Linteris[11].

The transport and thermodynamic data was taken from Linteris et al. [11]. Since the primary reason for studying the $C_6F_{12}O$ was for inhibition of flames in the aircrafts, the simulations were carried out for various initial temperatures that can be seen in practical situations during the flight, ranging from 233 K to 300 K. The study carried out at various temperatures are the first and it will give an insight into the dependency of various parameters on the initial temperature

As mentioned in the previous section, from the numerical studies of propane/air mixture, at the flammability limit, the 1D-simulation gives a flame speed of about 5 cm/s. Thus, we carried out simulations to find out laminar speeds of propane/air mixture at various Novec 1230 concentrations. The obtained results are plotted in Fig. 9 a. The burning velocities from the similar conditions are given in Fig. 9 b. From Fig. 9 a and 9 b., it can be seen that at the lower $C_6F_{12}O$ concentrations, the difference in the calculated velocities greatly vary with the initial temperature. For example, the laminar flame speed at 300 K for stoichiometric propane/air mixture is 39.81 cm/s while for the same mixture at 223 K is 25.7 cm/s. However, when the $C_6F_{12}O$ molar percent reaches 6%, the observed velocities in propane/air mixture are independent of the initial temperature.

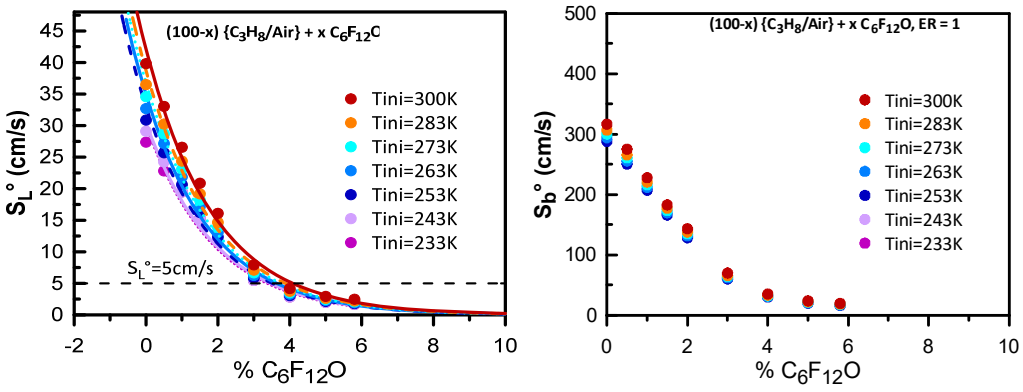


**Fig. 9.** Calculated laminar flame speed at different termperatures for various C6F12O (Novec-1230) concentration (Left) . Calculated burning speed as a function of C6F12O concentration at different initial temperature.

As in the previous reported works [12–14], the Novec-1230's contribution to combustion is clearly seen for lean fuel/air mixture, shown in Fig. 10 a. The laminar speed at 300 K for propane/air mixture at an equivalence ratio of 0.6 is 11.9 cm/s and it increase to 14.2%, 14.6% for 0.5% and 1% of $C_6F_{12}O$ in the propane/air mixture, respectively. This effects slowly fades at 2% $C_6F_{12}O$, where the calculated laminar flame speed is 11.74 cm/s. The effect of $C_6F_{12}O$ addition into propane/air mixture for a wide range of equivalence ratio is plotted in Fig. 10 b. Here, it can be seen that contribution of $C_6F_{12}O$ to propane/air combustion is not present for fuel rich mixture.

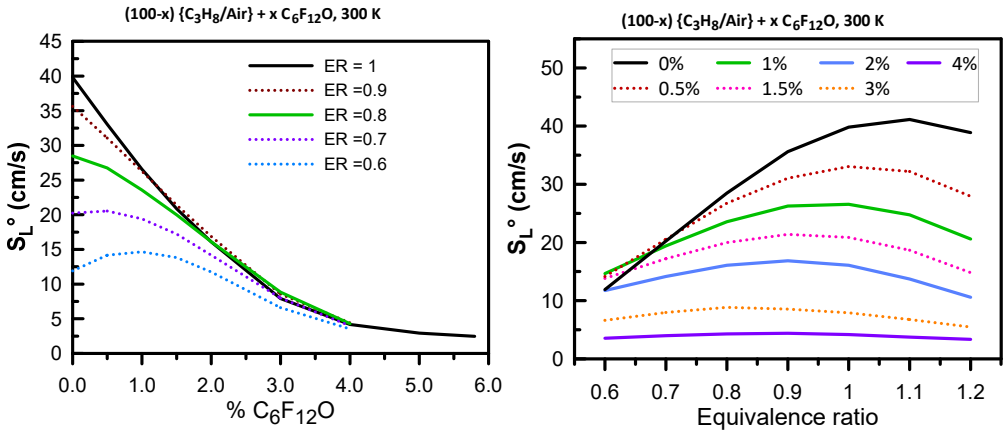


(a) (b)

**Fig. 10.** Calculated laminar flame speed as function of $C_6F_{12}O$ at different equivalence ratios (Left). Calculated burning speed as a function of equivalence ratio at different $C_6F_{12}O$ contents.

We have also carried out equillibrium calculations to obtain maximum pressure obtained at adiabatic isochoric complete combustion ($P_{AICC}$) condition and flame temperature.

The experimental peak pressure values are compared with the numerically calculated pressure assuming ($P_{AICC}$) in Fig. 11 a. As seen in the figure, even at 7.5 % of $C_6F_{12}O$, the experimental pressure is 1.6% of the $P_{AICC}$ indicating a slower, incomplete combustion. The difference in $P_{Exp}$ and $P_{AICC}$ increases to two orders of magnitude when the $C_6F_{12}O$ content is increased to 8.5%. The temperature profiles obtained from the simulation at the three different $C_6F_{12}O$ molar percent in stoichiometric propane/air mixture at an initial temperature of 300 K are given in Fig. 11 b. As seen in the figure, the rise in temperature for the with 6% $C_6F_{12}O$ is slower than that of the 2% $C_6F_{12}O$ case, indicating a slower combustion at former case.

The adiabatic flame temperature as a function of equivalence ratio for various concentrations of $C_6F_{12}O$, are given in Fig. 12. As seen from the figure, the location at which the temperature reaches peak value of 2258 K, shifts to leaner side on addition of $C_6F_{12}O$ (from ER=1.05 for 0% $C_6F_{12}O$ case to 0.90 for 1% $C_6F_{12}O$ case). For 2-7% of the $C_6F_{12}O$ in propane/air mixture, the calculated value reaches similar value, irrespective of $C_6F_{12}O$ content, near the higher flammability value of propane/air mixture ($\phi$=2.44). On the leaner side a considerable increase in the temperature could be seen for the above-mentioned range of $C_6F_{12}O$ molar percent. For 8-10% $C_6F_{12}O$ a uniform decrease in the temperature was observed over considered equivalence ratios of propane/air mixtures.

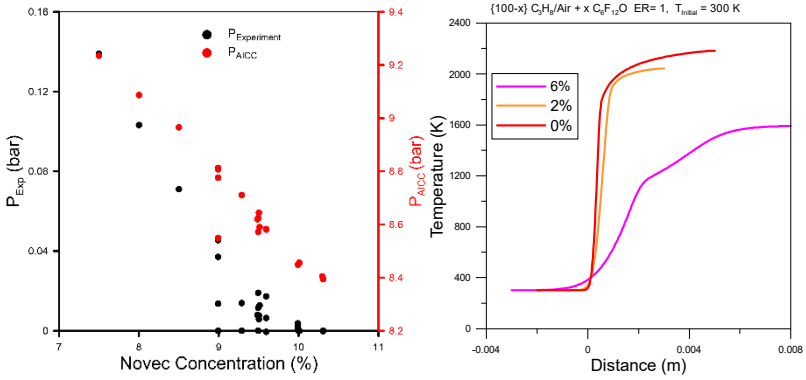


**Fig. 11.** Comparison of calculated and measure peak pressures for C6F12O in the stoichiometric/air mixture (Left). Evolution of temperature as a function of distance for three C6F12O concentrations

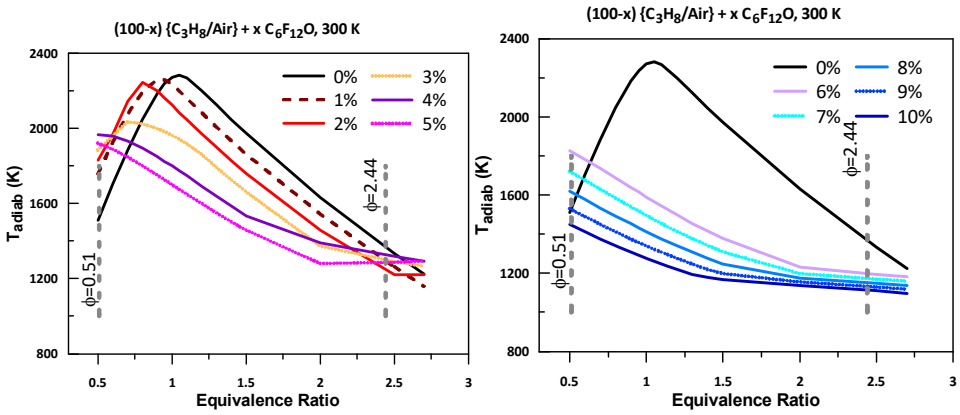


**Fig. 12.** Calculated adiabatic flame temperatures as a function of equivalence ratio for different C6F12O concentration. Equivalence ratio (ϕ) marked in the plots corresponds to lower and higher flammability values of propane/air mixture.

## CONCLUSION

An experimental investigation into the inhibition capability of $C_6F_{12}O$, Novec, was carried out by adding it to the stoichiometric propane/air mixture in an enclosed cylinder, NC2V. It was found that more than 9.3% of $C_6F_{12}O$ is required to completely inhibit the flame at initial pressure and temperature of 1 bar and 300 K. The measured maximum pressure values are given in the paper which indicates that at 9% the overpressure reduces below 5% of the initial value.

Numerical studies were carried out to understand the behaviour of the inhibitor, $C_6F_{12}O$, in propane/air flame over a wide range of equivalence ratios (0.6 to 2). The results indicates that for leaner propane/air mixture and at lower $C_6F_{12}O$ content, the inhibitor participates in the combustion process, as seen in the laminar flame speeds and adiabatic flame temperature calculations. $P_{AICC}$ calculations showed that the experimental pressures at 8.5% $C_6F_{12}O$ is 0.6% of the calculated values. This indicates that even at 8.5% of $C_6F_{12}O$ concentration, the observed combustion is incomplete and weak.

## ACKNOWLEDGEMENT

This work has been funded by Air Liquide, Contract N° AIR LIQUIDE – CNRS, LSP 195656.

## REFERENCES

[1] J. Zhao, F. Xue,Y. Fu, Y. Cheng, H. Yang, S. Lu A comparative study on the thermal runaway inhibition of 18650 lithium-ion batteries by different fire extinguishing agents. Iscience 24 (2021),102854 (1-15).

[2] A. Kim, G. Crampton, Performance of Novec1230 in electronic facility fire protection. Fire Suppression and Detection - A Technical Working Conference Proceedings of SUPDET 2010, Orlando, Florida (2010), 1-6.

[3] U.S. Environmental Protection Agency. (2017, November 7). Substitutes in streaming agents. Retrieved from https://www.epa.gov/snap/substitutes-streaming-agents

[4] J. Gordon, No fire in the hole SEand V division oversees successful testing of new fire supression system, Robins Rev-Up 57 (2012), 1

[5] M. A. Enlow, Hangar Fire Suppression Utilizing Novec 1230, AFCEC-CX-TY-TP-2018-007, Technical Report,16 Jun 2017,15 Sep 2017

[6] N. Taniguchi, T.J. Wallington, M.D. Hurley, A.G. Guschin, L.T. Molina, M. J. Molina, Atmospheric chemistry of C2F5C(O)CF(CF3)(2): photolysis and reaction with Cl atoms, OH radicals, and ozone, J. Phys Chem. A 107 (2003) 2674–2679,

[7] J. Casey, Full-scale evaluation of novec™ 1230. DOT and FAA report number DOT/FAA/TC-19/27, 2019.

[8] J. Reinhardt, The Evaluation of FK-5-1-12 as a Halon 1301 Replacement for Aircraft Cargo Compartment Fire Protection Application, International Aircraft Systems Fire Protection Working Group Meeting, 2006.

[9] G. T. Linteris, F. Takahashi, V. R. Katta, H. K. Chelliah, O. Meier, Thermodynamic analysis of suppressant-enhanced overpressure in the FAA aerosol can simulator, in: Fire Safety Science -Proceedings of the Tenth International Symposium, International Association for Fire Safety Science (2011), 307-320.

[10] G. T. Linteris, D. R. Burgess, V. R. Katta, F. Takahashi, H. K. Chelliah, O. Meier, Stirred reactor calculations to understand unwanted combustion enhancement by potential halon replacements, Combust. Flame 159 (2012) 1016-1025.

[11] G. T. Linteris, V. I. Babushok, P. B. Sunderland, F. Takahashi, V. R. Katta, O. Meier, Unwanted combustion enhancement by C6F12O fire suppressant, Proc. Combust. Inst. 34 (2013), 2683-2690.

[12] J. L. Pagliaro, G. T. Linteris, P. B. Sunderland, P. T. Baker, Combustion inhibition and enhancement of premixed methane–air flames by halon replacements, Combust. Flame 162 (2015), 41-49.

[13] W. Xu, Y. Jiang, X. Ren, Combustion promotion and extinction of premixed counterflow methane/air flames by C6F12O fire suppressant, J. Fire Sci. 34 (2016). 289-304.

[14] G.T. Linteris, J. L. Pagliaro, Burning Velocity Measurements and Simulations for Understanding the Performance of Fire Suppressants in Aircraft. NIST Technical Note 1904, National Institute of Standards and Technology, US Department of Commerce : Washington, DC, USA. 2016

[15] Y.N. Shebeko, V.V. Azatyan, I. A. Bolodian, V. Y. Navzenya, S. N. Kopylov, D. Y. Shebeko, E.D. Zamishevski, The influence of fluorinated hydrocarbons on the combustion of gaseous mixtures in a closed vessel, Combust. Flame 121 (2000) 542-547.

[16] I.O. Moen, S.A. Ward, P.A. Thibault, J.H. Lee, R. Knystautas, T. Dean, C.K. Westbrook, The influence of diluents and inhibitors on detonations, Symposium (International) on Combustion 20 (1985) 1717-1725.

[17] L. A. Lovachev, V. T. Gontkovskaya, N. I. Ozerkovskaya, Part 2: Hydrogen Bromide Both as Inhibitor and Catalyst of Self-Ignition, Combust. Sci. Technol. 17 (1977) 143-151.

[18] J.L. Pagliaro, G.T. Linteris, Hydrocarbon flame inhibition by C6F12O (Novec 1230): Unstretched burning velocity measurements and predictions, Fire Safety Journal 87 (2017) 10-17.

[19] V. I. Babushok, G.T. Linteris, O. C. Meier, Combustion properties of halogenated fire suppressants, Combust. Flame 159 (2012), 3569-3575

[20] A. Hariharan, I.S. Wichman, Premixed flame propagation and morphology in a constant volume combustion chamber, Combust. Sci. Technol. 86(2014) 1025-1040.

[21] Cosilab combustion simulation laboratory manual, version 2.0

[22] H. Wang, X. You, A. V. Joshi, S. G. Davis, A. Laskin, F. Egolfopoulos, C. K. Law, USC Mech Version II. High-Temperature Combustion Reaction Model of H2/CO/C1-C4 Compounds. http://ignis.usc.edu/USC_Mech_II.htm, May 2007.

[23] V. I. Babushok, G.T. Linteris, D.R. Burgess Jr, P.T. Baker, Hydrocarbon flame inhibition by C3H2F3Br (2-BTP). Combust. Flame 162 (2015), 1104-1112.

[24] B. A. Williams, M. Drew, J. W. Fleming, Intermediate species profiles in low-pressure methane/oxygen flames inhibited by 2-H heptafluoropropane: Comparison of experimental data with kinetic modeling. Combust. Flame 120 (2000), 160-172.

# EFFECT OF INERT GAS DISCHARGE TIME ON WOOD CRIB FIRES IN REDUCED-SCALE AND FULL-SCALE EXPERIMENTS

**Zimak, J.[1*], Cuevas, J.[1], Senecal, J.[2], Pierce, J.[2], Penden, F.[2], Puchovsky, P.[1], Simeoni, A.[1]**

[1] *Worcester Polytechnic Institute, Department of Fire Protection Engineering, Worcester, MA, USA.*
[2] *Kidde-Fenwal, Inc. Ashland, MA, USA.*
**Corresponding author's email: jzimak@wpi.edu*

## ABSTRACT

In 2012, the NFPA 2001, *Standard on Clean Agent Fire Extinguishing Systems*, was revised to allow a maximum two-minute discharge duration for systems that protect class A fire hazards with inert gases. With this change, UL 2127 and FM 5600 also began testing and certifying systems over both 60- and 120-second discharge durations. Wood cribs are one of the fuel sources used to represent class A fire hazards. The effect on wood crib extinguishment and enclosure dynamics over the permitted discharge times was the focus of this study. Following the UL 2127 methodology at the longer 120-second discharge duration, fundamental changes in suppression dynamics due to bulk flow affect the time to reach wood crib extinguishment. The impact of bulk flow was studied with IG-100 (Nitrogen) on both reduced- and full-scale test arrangements. Observations and measurements included changes in oxygen content, near crib velocity, and temperature as well as test article mass. These quantities also support the validity of a novel ¼ reduced-scale crib and enclosure developed in this study.

**KEYWORDS:** Inert Gas, Approval Testing, Scaling, Nitrogen.

## NOMENCLATURE

| | |
|---|---|
| $A$ | area ($cm^2$) |
| $b$ | stick thickness (cm) |
| c | wood species constant (mg/ sec $cm^{1.5}$) |
| H | enclosure height (m) |
| $l$ | stick length (cm) |
| $\dot{m}$ | mass loss rate or MLR (kg/s) |
| n | number of sticks per layer |
| N | number of stick layers |
| r | stoichiometric oxygen to fuel ratio (-) |
| $s$ | stick spacing (cm) |
| $T$ | temperature (K) |
| $t$ | time (s) |
| $V$ | enclosure volume ($cm^3$) |

**Greek**

| | |
|---|---|
| $\varphi$ | porosity (cm) |
| $\nu$ | viscosity ($m^2/s$) |
| $\rho$ | density ($g/cm^3$) |

**Subscripts**

| | |
|---|---|
| E | enclosure |
| $s$ | crib surface |
| $v$ | crib vent |

## INTRODUCTION AND BACKGROUND

Total flooding clean agents are often used where water-based fire suppression (sprinkler, water spray, etc.) systems are not compatible with the protected assets or when the cost of damage due to discharged water is prohibitive [1]. These agents are electrically nonconductive and leave no residue after discharge. Halon 1301 was the main gas of choice for this type of application until 1993 when the Montreal Protocol banned ozone-depleting agents. Inert gas agents are a popular type of clean agent. Among them, nitrogen has received recent attention as a halon replacement agent [2-5], especially as the airline industry phases out the installation of halon fixed fire suppression systems in new aircraft cargo compartments by 2040. Nitrogen poses significant advantages as a halon replacement, as it is naturally occurring, has zero global warming potential, and does not thermally

decompose [6]. Nitrogen has also been recently studied for use in hybrid extinguishing systems combined with water mist sprays [7].

The two common extinction mechanisms for clean agent suppression are oxygen reduction [8] and temperature reduction [1]. Inert gasses extinguish fires by reducing the oxygen concentration below the required flammability limit. The quantity needed to suppress combustion is the minimum extinguishing concentration (MEC) and is often defined as the minimum concentration of inert gas necessary to suppress a cup-burner flame [9-11]. The MEC is then used by system manufacturers as a baseline to define the design concentrations for full-scale suppression systems [9] designed to protect a variety of different commodity classifications.

Currently, inert gas suppression systems are tested in a 100 $m^3$ enclosure as per UL 2127 [12] or FM 5600 [13] to determine the minimum extinguishment concentration used for total-flooding suppression systems. In these standardized tests, a test article is placed within the enclosure, burned and subjected to a suppression event to determine the required extinguishment agent concentration. It is important to notice that, for a class A test article (wood crib), both UL and FM standards follow equivalent extinction test methodologies.

Recently, system manufacturers have been allowed to choose the time it takes to fully discharge the inert gas suppressant agent to typically be either 60 seconds or 120 seconds per NFPA 2001 [9]. The change in discharge time has led to system-approved extinguishing concentration test results that surprise industry experts (including the authors of this work) and create confusion in the inert gas industry regarding how to utilize the longer discharge time safely. To answer this question, the underlying physics of the extinction dynamics must be better understood within the test enclosure utilizing the approved extinguishing test methodology.

This research article presents the methodology and results for the full-scale test method and a novel ¼ scale test used to study the difference in the two discharge periods, focusing on the MEC determination and reignition potential of a class A test article (wood crib). A series of measurements were made to better understand the time to suppression and extinguishing concentration for each discharge period and scale. The reduced-scale methodology and derivation are presented as a tool for future research. As previously mentioned, due to the equivalence in UL and FM methodologies, only UL will be referenced in this study for brevity.

## METHODOLOGY

Full- and reduced-scale tests were used to investigate the effects of a longer discharge time (120 s) on the extinction of a class A test article (wood crib) and compare them to the 60 s discharge. The full-scale test method followed the UL 2127 procedure with the addition of several near-field measurements. The reduced-scale test enclosure and instrumentation locations were scaled according to the reduced-scale crib. Both inert gas discharge systems were designed by Kidde-Fenwal, Inc. through their proprietary system design software. The suppression system consisted of one or three bottles of IG-100 (nitrogen) at 200 Bar, depending on the scale, connected to a manifold of schedule 40 piping terminating at a centrally-located discharge nozzle on the enclosure ceiling. Several initial discharge tests without a wood crib were performed at each scale and for each discharge period to confirm the discharge agent quantity and proper system function.

### Full-Scale Experimental Set-Up

Full-scale test data was required to validate the reduced-scale test methodology and investigate the changes in wood crib extinguishment at the longer discharge times. For the full-scale experiments, the enclosure dimensions were 5.2 m x 5.2 m x 3.6 m (L x W x H) to comply with the UL 2127 requirements, as shown in Fig. 1.

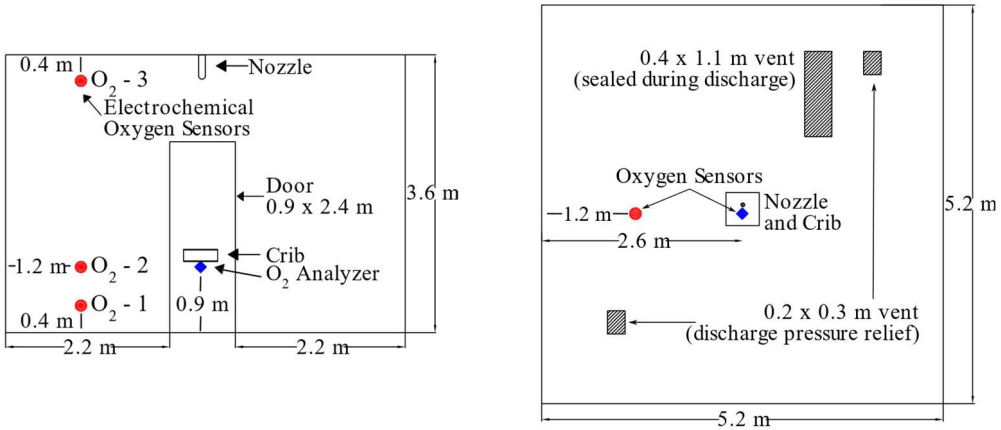


**Fig. 1.** Full-scale enclosure (a) elevation view (b) plan view, detailing the enclosure construction, ventilation location, and UL 2127 oxygen sampling locations. All dimensions are rounded to the first decimal place.

The full-scale enclosure had three rooftop vents and a single door with a window for access and observation. The vents and door provided fresh makeup air to the crib before suppression and were closed before discharge. Two vents were left unsealed to allow enclosure pressure regulation during discharge but still prevented backflow to avoid oxygen from reentering the enclosure.

Three oxygen sensors with a delay time of 15 ± 1 s were mounted equidistant between the wood crib and the left-most wall, at 36 cm above the floor and 36 cm below the ceiling, and at 81 cm above the floor (at the crib base) following UL 2127 requirements. A fourth sensor located directly under the crib (81 cm above the floor) was characterized to have a 29 ± 2 s delay time. Additional instrumentation placed in the near field of the crib will be presented in the following section.

## Full-Scale Test Article and Instrumentation

The UL 2127 Class A test protocol requires four different test articles, including a wood crib and three arrays of plastic sheets. As the potential for test article reignition was of interest, the porous wooden crib was chosen over the plastic sheet arrays.

Wood cribs are specified as an array of regular, three-dimensional wooden sticks [8]. Each stick has a square cross-section $b$, and a length $l$, significantly larger than its thickness. The sticks are arranged with uniform edge-to-edge spacing $s$, on each layer. Each layer is laid 90 degrees from the previous layer and attached with a staple or nail as required to prevent the sticks from moving during testing [12]. The total number of layers $N$, defines how tall the crib will be and $n$ is the number of sticks per layer. The crib surface area $A_s$, is the total area of the crib that can support combustion. The ventilation area $A_v$, is the area of the vertical shafts that run through the cribs when viewed from above. Both areas can be calculated from the crib construction parameters [14-15]. The UL 2127 crib has construction parameters of $N$=4, $n$=6, $b$=3.8 cm, and $l$=45.72 cm. The crib construction values and areas are used to calculate the crib porosity φ (see Eq. 1), which is the ratio of airflow through the shafts ($A_v * s^{0.5}$) to the stick burning rate ($A_s * b^{-0.5}$). Crib porosity is crucial to calculating the burning rate and is a key characteristic of the crib [14, 16-19].

$$\varphi = s^{.5} b^{.5} \frac{A_v}{A_s} \quad (1)$$

The porosity determines if the burning of the crib will be limited by the available crib surface area or by the transport of fresh air into the crib [20]. The porosity of the UL 2127 crib was calculated to be 0.153 and is therefore in the surface area-controlled regime (fuel-controlled) as defined by Block [17].

Thermocouples, bidirectional probes, and additional oxygen sensors were installed in and around the crib, as shown in Fig. 2.

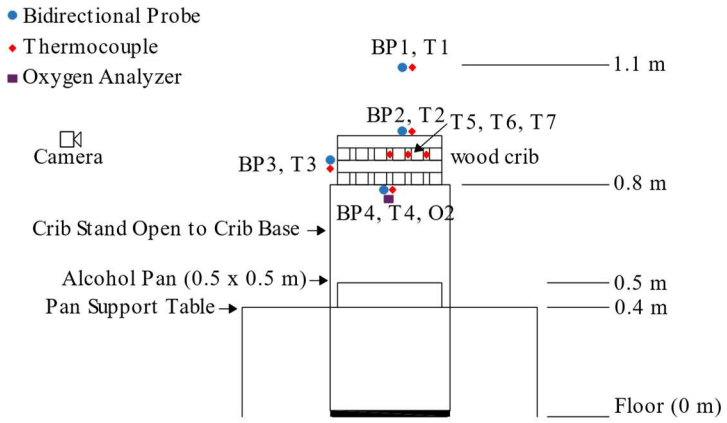


**Fig. 2.** Full-scale crib instrumentation. The oxygen sensors prescribed by UL 2127 are not shown (see Fig. 1a).

The three oxygen sensors at UL 2127 prescribed locations were electrochemical oxygen probes with a T90 response time of 8-10s and a resolution of 0.1%. Additional instrumentation included a paramagnetic oxygen gas analyzer with an error of less than 0.15% O2 and a T90 response time of less than 15 s, located 2.5 cm below the center of the crib. Four 2.5 cm diameter bidirectional probes were located directly above (BP2), below (BP4), on the side of (BP3), and 30 cm above the crib (BP1). Three 1-mm thick exposed-junction type-K thermocouples were located inside the crib (T5, T6, and T7). Each bidirectional probe had a thermocouple mounted near its opening. Thermocouple temperature corrections were performed to account for thermal inertia and emissivity [21-22]. The crib was placed on mass balance with an accuracy of 0.2 g according to its manufacturer's specifications.

UL 2127 specifies heptane as the starter fuel, but ethanol was used due to its reduced costs and similar use in wood crib ignition studies [14]. 850 mL of ethanol was used in the full-scale tests as this assured a burning time of 3 minutes, equivalent to the time delivered by 1500 mL of heptane as specified by UL 2127.

**Reduced-scale experimental set-up**

For reduced scaling of the wood crib, the objective was to maintain similarity in two key parameters: the wood crib porosity $\varphi$, and the representative mass loss rate (MLR). The representative MLR was calculated by dividing the steady-state mass-loss rate by the initial crib mass. The enclosure size was based on the crib scale and oxygen consumption, as mentioned later in this article.

The wood crib was scaled according to the methodology proposed originally by Heskestad and further expanded by Croce and Xin [16,18]. In this method, the different geometric parameters of the wood crib are scaled as functions of the enclosure height $H$, as shown in Eq. 2.

$$b \propto H^{\frac{1}{2}};\ l \propto H^{\frac{9}{8}};\ N \propto H^{\frac{1}{2}};\ n \propto H^{\frac{5}{8}} \qquad (2)$$

Through this method, the crib porosity was conserved. Several crib combinations were tested in a free burning environment to determine the remaining geometrical parameters. The selected crib maintained a similar representative MLR and steady-state burn time, as shown in Table 1. All cribs were constructed of kiln-dried Douglas fir. Observed crib free burning mass loss rates were on average 36% lower than the theoretical value calculated though Eq. 3 in the next section, likely due to discrepancies in the $c$ value between the theoretical wood and the actual Douglas fir used.

For the reduced-scale experiments, 200 mL of ethanol were used as the starter fuel, which provided 3.5 minutes of burning as per UL 2127 in a reduced-scale square 30.5 cm pan.

**Table 1. Steady state burning characteristics of full- and reduced-scale Douglas fir cribs.**

| Scale | Crib dimensions (N, n, b, l) | Porosity (cm) | MLR (g/s) | Steady State Burn Time (s) | MLR/$M_0$ (1/s x10^3)[a] |
|---|---|---|---|---|---|
| 1/4 -scale | 3, 4, 3, 23.5 cm | 0.15 | 1.2 ± .2 | 600 | 0.84 ± 0.02 |
| Full-scale | 4, 6, 3.8, 45.7 cm[b] | 0.15 | 5.4 ± .31 | 660 ± 120 | 0.66 ±.048 |

[a] representative MLR was used to gauge the percentage of the cribs mass lost every second
[b] UL 2127 full-scale crib, an average of 3 free burns

The reduced-scale enclosure was dimensioned such that the theoretical amount of oxygen consumed by the crib over a 60-second discharge would be equal to a 0.5% change in average oxygen concentration, corresponding to the UL 2127 standard maximum oxygen content deviation allowed before discharge. The theoretical mass-loss rate of the crib was calculated following Eq. 3 [17], which was derived using Spalding's B-number analysis, and it depends on the fuel properties and crib geometry. As cribs are in a surface area-controlled regime, the burning rate is approximated as several individual burning sticks burning with turbulent free convective boundaries.

$$\frac{\dot{m}}{A_s} = cb^{-0.5} \tag{3}$$

In this expression, $\dot{m}$ is the mass loss rate of the crib (mg/s), $A_s$ is the surface area of the crib ($cm^2$), and $c$ is a constant relating to the crib species (mg/sec $cm^{1.5}$). Values for $c$ vary between 0.87 and 1.33 mg/ sec $cm^{1.5}$ depending on the type of wood species, density, and moisture content [17]. The whitewood $c$ value of 1.11 mg/ sec $cm^{1.5}$ was used due to its similar density to the UL 2127 prescribed fir or spruce lumber, which was unavailable. The total mass of oxygen needed within the enclosure was calculated using the modified stoichiometric conversion [23] presented in Eq. 4, where the ratio of oxygen to fuel consumed, $r$, is equal to 1.32 for Douglas fir [1] and $\Delta t$ is the discharge time.

$$m_{O2} = \dot{m}_{Fuel} * r * \Delta t \tag{4}$$

Combining Eqs. 3 and 4, the volume of an enclosure based on the crib construction can be calculated by Eq. 5, assuming a maximum deviation of .5% oxygen content:

$$V_E = \frac{\Delta t * c * b^{-0.5} * A_s * r}{0.005 * \rho_{O2}} \tag{5}$$

Where $V_E$ is the volume of the enclosure in $cm^3$, and $\rho_{O2}$ is the density of oxygen. Using the UL 2127 full-scale crib values with a 60 s discharge time delivers an enclosure volume equivalent to the one specified by the UL 2127 (98 $m^3$). A 60 s discharge period was used, leading to a 22 $m^3$ reduced-scale enclosure with dimensions of 3m x 3m x 2.5m, as shown in Fig. 3. Both the reduced-scale and full-scale enclosures were constructed with plywood to UL construction standards. Heat transfer though the walls was not considered due to the realitivly low temperature of the enclosure during discharge, 56 ± 6 $^{O}$C for the full scale.

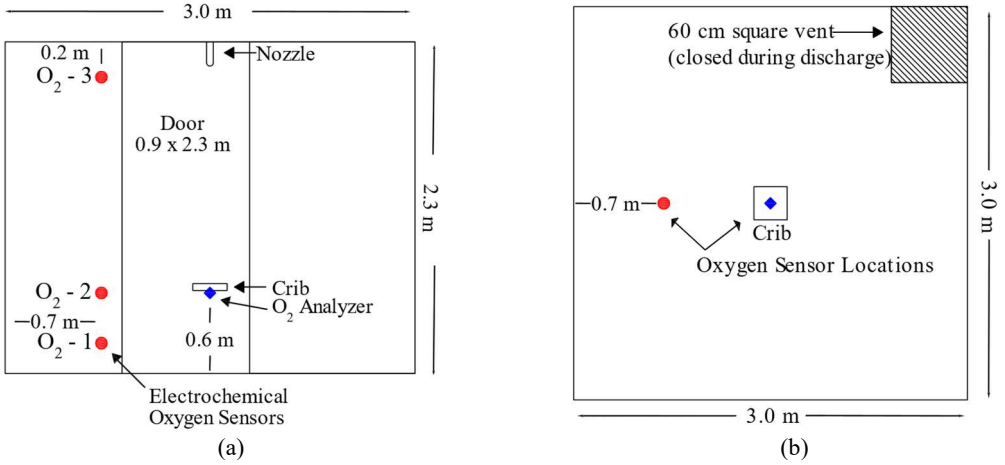


**Fig. 3.** Reduced-scale enclosure and gas sampling layout (a) elevation view and (b) plan view.

Both the reduced-scale and full-scale enclosures were constructed with plywood to UL construction standards. Heat transfer though the walls was not considered due to the realitivly low temperature of the enclosure during discharge, 56 ± 6 $^{O}$C for the full scale.

**Experimental procedure**

The full-scale and reduced-scale experiments were conducted per UL 2127. The protocol is presented below, along with the results of an exemplary experiment (Fig. 4).

- Each full-scale wood crib was dried using an electric convective heater for at least 12h to an average moisture content between 9 and 13% and then stored in a doubled-up and sealed polyethylene bag. The reduced-scale wood cribs were conditioned in a drying oven at 95ºC for at least 12h. The average dry masses of the full- and reduced-scale cribs were 7.06 ± 0.27 kg and 1.0 ± 0.08 kg, respectively.
- Six minutes before the start of discharge and with all the vents and door of the compartment open, a pan with ethanol was ignited under the crib at a distance of twice the crib height. The wood crib ignited and began burning briefly assisted by the pan fire for 3.5 minutes.
- Once ignited, the crib was allowed to burn freely in the enclosure until a steady state was achieved. This condition was confirmed by evaluating the average mass-loss rate over a one-minute period. From preliminary experiments, it was found that a period of 6min was sufficient to ensure that the crib reached steady-state burning.
- During this initial period, the door and the vents remained open, allowing for the evacuation of the combustion products and the supply of fresh air. Despite this, it was found that the oxygen concentration within the compartment decreased slightly due to the partial accumulation of combustion products but that it remained within the 0.5% of original oxygen concentration limit, as measured by the $O_2$ - 2 sensors shown in Fig. 1 and Fig. 3 as per UL 2127 [12].
- After reaching steady-state burning and 15s before the start of discharge, the ceiling vents and door were closed. The beginning of the discharge is shown by the vertical red line in Fig. 4.
- Shortly after the start of discharge, the average oxygen concentration began to drop, the upwards velocity at the top of the crib increased, and the crib's mass decreased due to the effects of the bulk flow. As the oxygen concentration approached the extinguishing concentration, the crib top velocity and mass approached a steady-state value as shown in Fig. 4.

- Extinction was defined by visual observation of flame disappearance and consistently occurred at the end of the discharge period for the full-scale tests. Shortly after crib extinguishment and the end of discharge (t =120 s in Fig. 4), the velocity, mass, and oxygen concentration values stabilized. Later, the oxygen concentration slowly increased as fresh air leaked in and the agent mixture leaked out and began to stratify toward the upper portion of the enclosures.
- Ten minutes after the end of discharge, the enclosure vents and door were opened to allow fresh air to enter the enclosure, and the crib was checked for signs of reignition.

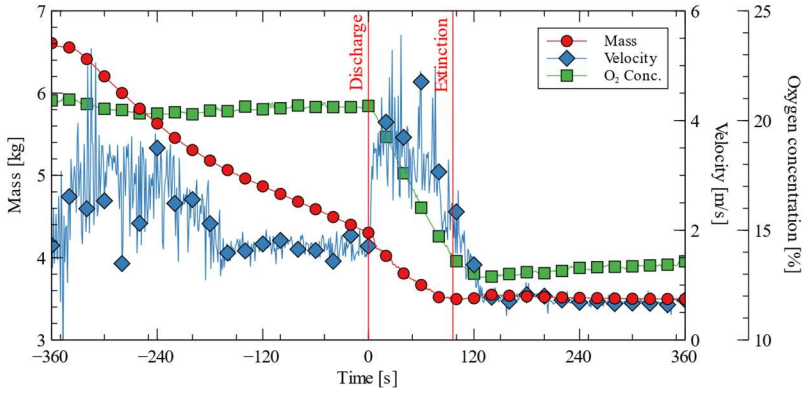


**Fig. 4.** Exemplary experiment (full-scale test F7).

### Experimental Matrix

The duration of agent discharge, 60 seconds and 120 seconds, and its effects are the main focus of this study. Ten reduced-scale experiments (R), five for each discharge period, and seven full-scale experiments (F) were conducted, as shown in Table 2.

**Table 2. Experimental matrix for full- and reduced-scale suppression tests.**

| Test # | Average Mass of Agent Discharged (kg) | Discharge Period (s) |
|---|---|---|
| F1, F2, F3 | 51.1 ± 7.1 | 60 |
| F4, F5, F6, F7 | 50.9 ± 6.8 | 120 |
| R1, R2, R3, R4, R5 | 11.5 ± 1.4 | 60 |
| R6, R7, R8, R9, R10 | 11.1 ± 0.4 | 120 |

## RESULTS AND DISCUSSION

Both the full- and reduced-scale cribs ignited uniformly across the base shortly after pan ignition and, on average, became fully involved 30 and 14s after pan ignition, respectively. After the alcohol in the pan was consumed, the cribs quickly transitioned to a steady-state burning rate. During this period, the MLR, velocity at the top of the crib, and temperature immediately above the crib were constant for each scale, as shown in Table 3. These values set the baseline for comparison between discharges.

The ratios of steady-state MLR and velocity between the full- and reduced-scale presented in Table 3 quantify the reduced-scale enclosure to a ¼ scale. The ¼ scale quantification is further supported by the ratio of enclosure volumes, 22/ 100 cubic meters.

**Table 3. Average steady-state values before discharge for full- and reduced-scale cribs**

| | MLR (g/s) | HRR (kW) | Vel. at top of crib (m/s) | Central Crib Temp. at TC5 (°C) |
|---|---|---|---|---|
| Full-scale | 4.7±0.24 | 68.5±3.5 | 1.6±0.1 | 478 ±23 |
| Reduced-scale | 1.13±.09 | 16.6±1.6 | .35±0.2 | 406±42 |

## Discharge

Agent from the 200-bar tank(s) was released into the enclosure through a ceiling-mounted nozzle. It is assumed that the change in oxygen content within the enclosure is only due to the discharged agent and not from residual products of combustion as per the FM 5600 test [13]. This assumption was confirmed through analysis of the average combined buildup of CO and $CO_2$ at the base of the crib which was consistently less than 0.5% and 0.9% by volume for the full and reduced scales respectively at the end of discharge. Good repeatability of test data, as shown in Fig. 5(a), allowed the discharge periods to be averaged at each scale for comparison of the discharge periods at both scales.

The tapering of the full-scale curves at the end of discharge, as seen in Fig. 5, occurs as the agent bottles reach a state of depletion. The more linear agent concentration curves of the reduced-scale discharges occurred as a significant amount of agent remained in the bottle at the end of discharge, which was not needed to reach the desired agent concentration. Nevertheless, the final agent concentration at the end of discharge was always above the system manufacturer's approved FM Global minimum design concentration and only differed by 3% between scales. The higher agent concentrations for the full- scale experiments did result in faster times to extinguishment, which will be discussed in the next section.

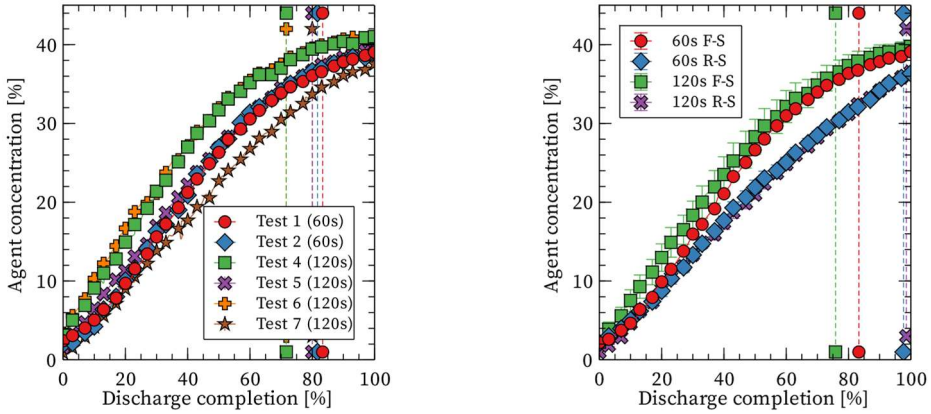


**Fig. 5.** Agent discharge. (a) Full-scale agent concentration curves. (b) Average concentration curves for all discharge times and scales. Vertical lines indicate the time of crib extinction. The data from Test F3 was removed due to gas analysis failure

The discharge event affected the gas-phase velocity and temperature through the crib and greatly influenced the mass of the crib. These effects result from the bulk flow created as the high-pressure agent was discharged into the enclosure, creating currents of agent and entrained air. The effects of bulk flow are visible across all measured quantities, including the temperature of the crib, T5, and the velocity through the top of the crib, BP2, as shown below in Fig. 6. As the bulk flow interacted with the crib, there was a significant increase in gas velocity through it, which accompanied the change in flame boundary location, that was observed to retreat into the crib, as shown by the significant increase in central crib temperature after the start of discharge.

The effects of bulk flow were also prevalent on the crib mass during discharge. While the bulk flow velocity through the crib increased, an upward force produced a sudden decrease in the apparent mass of the crib during the first few seconds of discharge, as can be seen in Fig. 7. Preliminary calculations indicate this force is likely caused by the increased gas velocity, (see Fig. 6 (b)). For example, an idealized flow of air at 9 m/s can cause an aerodynamic load of approximately 0.57 kg over the 0.15

$m^2$ crib. An apparent mass gain of the crib in the full-scale 60s-discharge experiments around 50% discharge completion occurred as the velocity through the crib decreased and the upward force began to subside. The variable upward bulk flow and the resulting force acting on the crib mass assembly prevented the actual mass of the crib and the MLR from being accurately measured during discharge.

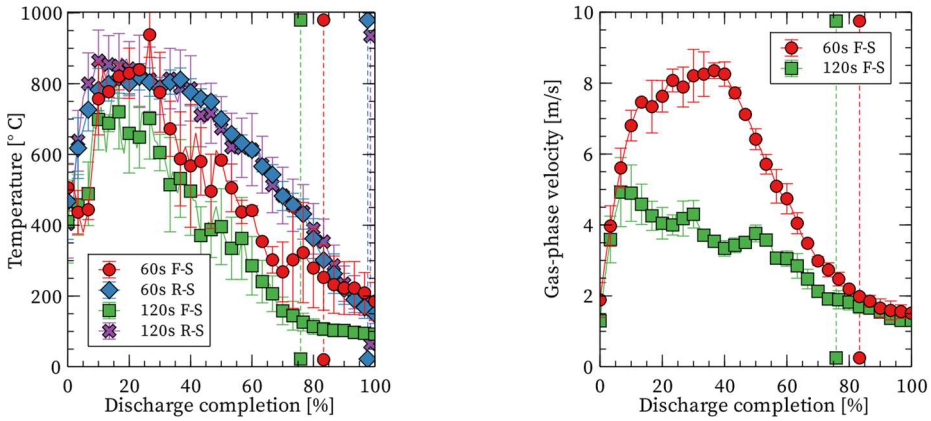


**Fig. 6.** Bulk flow effects. (a) full- and reduced-scale agent average crib temperatures during discharge for each discharge period. (b) Full-scale average velocity through the crib top (V2) during each discharge period. Vertical lines indicate the time of crib extinction.

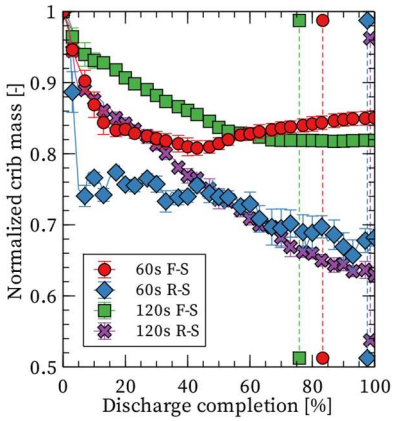


**Fig. 7.** Mass of the crib during the period of discharge. Vertical lines indicate the time of crib extinction.

It is proposed that this bulk flow must have been from the center bottom to the center top of the enclosure to cause the effects shown in the previous figures. It is also hypothesized that the bulk flow followed the 200 Bar agent discharge profile and moved from the top center of the enclosure where the nozzle was mounted outward to the enclosure walls. These two phenomena would create a recirculating concurrent axial flow profile within the enclosure, as shown in Fig. 8.

The effects of bulk flow were dependent on the rate of agent discharged, and therefore a function of both scale and discharge time, as visible by the higher velocities for the 60 s discharge (see Fig. 6) and larger 60 s discharge mass losses at the start of discharge (see Fig. 7) compared to the longer 120 s discharge period. The bulk flow effects were strongest at the shorter 60 s discharge period across scales and more prevalent at the full-scale, where five times more agent was discharged per test compared to the reduced-scale tests.

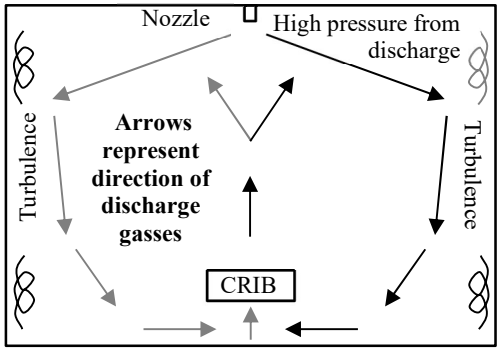


**Fig. 8.** Hypothesized bulk flow profile during discharge.

## Extinction

For the full- and reduced-scale experiments, the concentration of suppressing agent was found to be uniformly distributed within the enclosure approximately five seconds after the start of discharge. A uniform agent concentration also supports the bulk flow hypothesis as concentration uniformity requires rapid mixing, accomplished by continuous stirred tank reactor style recirculating concurrent axial flow. During discharge or shortly after, the wood crib was extinguished by the rising agent concentration. The oxygen concentration at extinction as a function of time after discharge is presented in Fig. 9. The time to extinction is defined by the disappearance of flame by visual observation or by video.

The range in extinction times increased as the bulk flow effects within the enclosure decreased from either reduction of scale or increase in discharge time. Variations in time to extinguishment for the full-scale were 2 and 5 s for the 60- and 120-seconds discharge, respectfully, and 5 and 72 s for the reduced-scale, respectfully. The increase in time to extinguishment dispersion is likely due to a higher surface-to-enclosure surface ratio at the reduced scale.

The average oxygen concentration at extinction was found to be independent of the scale and took the values of 13.3% ± 0.2% and 13.4% ± 0.4% for discharge periods of 60 and 120 s, respectively. In terms of the discharged agent, extinction was found to occur when the agent concentration within the compartment was approximately 36% ± 0.8% for all scales and discharge times tested. The measured agent extinguishment value is equal to the system's manufacturer's approved FM Global minimum design concentration and slightly higher than the accepted cup burner extinguishment concentration for heptane [24], as expected.

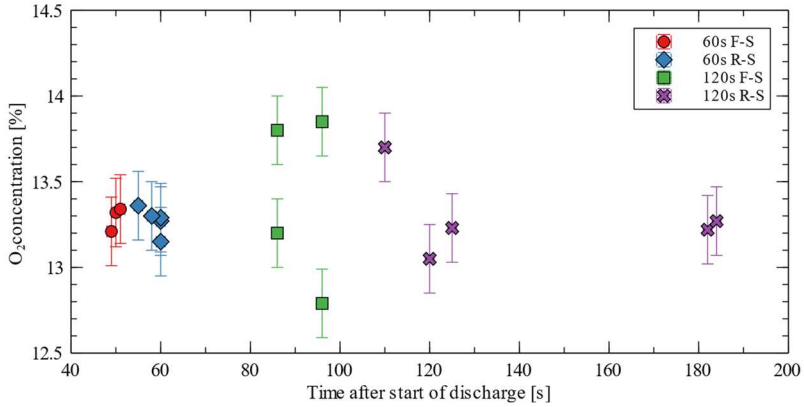


**Fig. 9.** Time to extinguishment versus extinguishing concentration.

## CONCLUSIONS

Wood crib fire suppression over a 60 second and 120 second discharge period was examined using full scale and reduced scale experiments modeled after UL 2127 and FM 5600 for the inert gas agent IG-100, nitrogen. In addition to the required observations and measurements, the mass loss of the wood crib and various temperatures and velocities near the crib were recorded. The range of additional data collected supports the reduced-scale testing methodology in replicating the full-scale test results. Furthermore, agent concentrations and the average extinguishment concentration obtained through the reduced-scale tests directly correlate to the full-scale test results. The results from the reduced-scale enclosure demonstrate that this approach can be used as a cost-effective research and development tool to understand the dynamics and effects of discharge better.

The change in discharge time from 60 to 120 s had a negligible effect on the average test article performance and extinguishment concentration, and results support the recent changes to the NFPA 2001 standard regarding the increase in discharge period. The 120 s discharge period maintained the same agent extinguishment concentration as the 60 s discharge period at the full- and reduced-scale. No crib reignited after suppression and the prescribed ten-minute soak period.

The longer discharge time significantly reduced the effects of bulk flow over both scales, leading to lower gas velocities through the crib and weaker interactions with the mass balance assembly. The reduction of bulk flow is also linked to a more extensive range in extinguishment.

Future research includes expanding the reduced-scale test method for plastic fuel array testing, investigation of other inert gas agents at both scales and discharge periods, and leakage characterization of future enclosures to maintain consistency between scales. To better understand the effects of bulk flow, a detailed characterization of the flow near the crib will be performed. This characterization will also support the development of Computational Fluid Dynamics (CFD) modeling of inert gas agent discharges in different realistic occupancies during discharge and suppression.

## ACKNOWLEDGEMENTS

The authors would like to thank Ray Ranellone, Fritz Brokaw, Abhinandan Singh, and Peter Guertin from Worcester Polytechnic Institute for their assistance in the conduction of the experiments, and Richard Lupien from Kidde-Fenwal, Inc. for his support in this project.

## REFERENCES

[1] Philip J. DiNenno and Eric W. Forssell, Clean Agent Total Flooding Fire Extinguishing Systems, in: Hurley MJ (ed) SFPE Handbook of Fire Protection Engineering, 5th edn. Society of Fire Protection Engineering, New York, NY.

[2] A. Dinesh, C.M. Benson, P.G. Holborn, S. Sampath, Y. Xiong, Performance evaluation of nitrogen for fire safety application in aircraft, Reliability Engineering & System Safety, Volume 202, 2020, 107044, ISSN 0951-8320.

[3] Xiong, Y., Diakostefanis, M., Dinesh, A., Sampath, S., & Nikolaidis, T. (2021). Numerical assessment for aircraft cargo compartment fire suppression system safety. Journal of Fire Sciences, 07349041211003208.

[4] Pathak A, Norrefeldt V, Pschirer M. Validation of a Simulation Tool for an Environmentally Friendly Aircraft Cargo Fire Protection System. Aerospace. 2021; 8(2):35.

[5] European Aviation Safety Agency. Update of CSs in order to comply with EC regulations. Notice of Proposed Amendment (NPA) No 2011-14, 2011.

[6] Moore, T. A., & Yamada, N. (1998, May). Nitrogen gas as a halon replacement. In Halon Options Technical Working Conference (pp. 330-338).

[7] Gałaj, J., & Drzymała, T. (2018). Assessment of extinguishing efficiency of hybrid system using water mist and inert gas during class A fires. In MATEC Web of Conferences (Vol. 247, p. 00013). EDP Sciences.

[8] Zhou, X., Xin, Y., & Dorofeev, S. (2019). Evaluation of an oxygen reduction system (ORS) in large-scale fire tests. Fire Safety Journal, 106, 29–37.

[9] NFPA 2001, Standard on Clean Agent Fire Extinguishing Systems, 2018 Edition. In NFPA National Fire Codes Online. Retrieved from http://codesonline.nfpa.org .

[10] Senecal, J. A. (2005). Flame extinguishing in the cup-burner by inert gases. Fire Safety Journal, 40(6), 579-591.

[11] ISO 14520-1, "Gaseous Fire Extinguish Systems – Physical Properties and System Design, Part 1: General Requirements," International Standards Organization, 2006.

[12] UL 2127, Inert Gas Clean Agent Extinguishing System Units, 2017 Edition.

[13] FM 5600, Examination Standard for Clean Agent Extinguishing Systems, 2021 Edition.

[14] Gross, D. (1962). Experiments on the burning of cross piles of wood. Journal of Research of the National Bureau of Standards, Section C: Engineering and Instrumentation, 66C(2), 99.

[15] Croce, P., & Xin, Y. (2005). Scale modeling of quasi-steady wood crib fires in enclosures. Fire Safety Journal, 40(3), 245-266.

[16] Heskestad, C. (1973). Modeling of enclosure fires. Symposium (International) on Combustion, 14(1), 1021-1030.

[17] Block, J. A. (1971). A theoretical and experimental study of nonpropagating free-burning fires. Symposium (International) on Combustion, 13(1), 971-978.

[18] Croce, P., & Xin, Y. (2005). Scale modeling of quasi-steady wood crib fires in enclosures. Fire Safety Journal, 40(3), 245-266.

[19] McAllister, S., & Finney, M. (2015). Burning rates of wood cribs with implications for wildland fires. Fire Technology, 52(6), 1755-1777.

[20] Babrauskas, V. (1986). Free burning fires. Fire Safety Journal, 11(1-2), 33-51.

[21] Shaddix, C R. Correcting thermocouple measurements for radiation loss: A critical review. United States: N. p., 1999.

[22] Ajay V. Singh, Michael J. Gollner, A methodology for estimation of local heat fluxes in steady laminar boundary layer diffusion flames, Combustion and Flame, Volume 162, Issue 5, 2015, Pages 2214-2230, ISSN 0010-2180.

[23] Drysdale, D. (2011) An Introduction to Fire Dynamics. 3rd Edition, John Wiley & Sons, Hoboken.

[24] Tapscott, R. E. (1999, April). Best Values of Cup-Burner Extinguishing Concentrations. In Proceedings of the 1999 Halon Options Technical Working Conference.

# Wildland Fires

# Estimation of Smoldering Peat Fire CO and $CO_2$ Emission Factors by Multidimensional Spread and Elemental Variables

**Bintang Farhan Muhammad.[1], Hafizha Mulyasih.[1], Ridho Irwansyah.[1], Yulianto Sulistyo Nugroho.[1,*]**

*[1] Fire Safety Engineering Research Group, Department of Mechanical Engineering, Universitas Indonesia, Kampus UI Depok 16424, Indonesia.*
**Corresponding author's email: yulianto.nugroho@ui.ac.id*

## ABSTRACT

Total peatland fire emission commonly estimated by the burned area that is measured with remote sensing. Given that smoldering peatland fire is a multidimensional phenomenon, estimates of burned area alone produce uncertainties. In addition, peatlands in different locations have different characteristics. This inhomogeneity produces uncertainty in trying to estimate the amount of emission onsite with the value that has been deducted from lab-scale experiments. This paper gives a novel approach to predict emission factor (EF) by the depth of burn (DoB), area (A), subsidence rate (SR), and time (t) to address the multidimensional spread uncertainty. Peat samples were collected from four locations in Indonesia, from Jambi, Papua, and two locations in Palangkaraya (PKY-1 & PKY-2). Dried peat samples were then placed on a reactor of 400 by 400 mm cross-section and 50 mm in depth which then smoldered on a buoyancy calorimeter apparatus, in which the burned depth and area, emission mass flow rate, and weight were measured. Throughout the experiment, the burned depth was measured by an IR proximity sensor, and the burned area was measured from IR thermal camera imaging. Calculated transient EFs were then linearly regressed with DoB, A, SR, t, and peat soil elemental variables (C, H, O, & N content). From this research, we are able to estimate transient EF from different samples, which vary in characteristics with the one regression equation. The $R_2$ given by this model for $CO_2$ and CO EFs reaches 0.94 and 0.96, respectively. Elimination of DoB from the regression variable reduces the accuracy of estimation in each sample significantly. Initially, the average $R_2$ for CO and $CO_2$ EFs are 0.91 and 0.89. After excluding DoB, it goes down to 0.8 for both CO and $CO_2$. This confirms that using the only area to estimate emission produces some degree of uncertainty. The estimation method presented in this paper enables better EF estimation as we address both multidimensional and inhomogeneity uncertainty.

**KEYWORDS:** Emission factor, peat, smoldering, modeling.

## NOMENCLATURE

| | | | |
|---|---|---|---|
| $EF$ | Emission factor (g/kg) | $H$ | Hydrogen content (%) |
| $\dot{m}_i^{''}$ | Emission mass flow rate (g/s) | $O$ | Oxygen content (%) |
| $\dot{m}^{''}$ | Fuel mass loss rate (kg/s) | $N$ | Nitrogen content (%) |
| $AC$ | Ash content (%) | $S$ | Sulfur content (%) |
| $VM$ | Volatile matter (%) | $DoB$ | Burned depth (mm) |
| $GFC$ | Gross calorific value (Kcal/kg) | $SR$ | Subsidence rate (mm/min) |
| $FC$ | Fixed carbon (%) | $A$ | Burned area ($cm^2$) |
| $C$ | Carbon content (%) | $t$ | Burning duration (min) |

## INTRODUCTION

Smoldering peatland fire has been a regular phenomenon and one of the significant contributors to atmospheric emissions from biomass burning. Peat is defined as organic soil with less than 20-35% mineral content composed of partially decomposed plant debris [1]. Although it only covers 2-3% of the Earth surface's, peatland stores 25% of the world's carbon soil [2]. Peatland can be categorized as

boreal and tropical peatland. Boreal peat covers 4,000,000 $km^2$ of the land, stores 50-60 billion tons of carbon. It is located mainly in high northern latitudes. At the same time, tropical peatland covers roughly 400,000 $km^2$ with additional 10 billion tons of carbon, 50% of it located in South East Asia [2,3]. The bulk of peat in pristine peatlands are usually very high in moisture in nature due to the accumulation in a water-saturated environment, especially in the tropics, thus making them resistant to fire. Nevertheless, current human activities have changed this condition, reducing the water table on peatlands and making them prone to fire..

With the humid climate and high precipitation in the tropical area, the amount of water input usually exceeds the loss of moisture by evaporation from the peat [4]. Nonetheless, recent human activities, like plantation development and logging, have caused the water to be lowered and made them susceptible to fire. Even during dry seasons, there was usually only an occasional wildfire that occurred, and there was enough time gap between fire phenomena to allow the recovery of the forest cover. But, with an accumulation of dry fuel (peat) and lessening humidity due to the absence of a tree canopy, it becomes more combustible. Countries like Indonesia, Malaysia, Brazil, and Peru, are densely populated, in which anthropogenic activities and increased activity of human-caused ignition have turned many peatlands prone to fire [1].

The majority of peat fire happens on the smoldering regime due to its char-forming nature and porous medium. Smoldering combustion is a flameless fire that occurs on a porous char-forming fuel [5]. When above the water table, the large surface area of the peat structure allows the in-depth transfer of oxygen and facilitates oxidation, thus making it vulnerable to smoldering fire [6]. With relatively low temperatures, peaking around 550-650$^oC$, smoldering combustion tends to spread slower compared to flaming combustion. However, it spreads in a multidimensional fashion and could reach the lower level of peats and last for weeks or even months [7]. Throughout the fire event, smoldering peatland fire emits more than 100 gas species, with the five most abundant are $CO_2$, CO, $NH_3$, $CH_4$, and HCN, with CO and $CO_2$ as the two most abundant in terms of mole fraction [8]. One of the huge fire events happened in 1997 in Indonesia, which came with huge consequences, financial and health [9,10,11]. Nonetheless, the estimation of peatland emissions is still not very well understood despite all the negative consequences.

One of the current issues on emission estimation is discussed thoroughly in a recent review article written by Hu [12]. The obstacles to peatland fire emission estimation studies are mainly on the scaling from lab experiments to estimate the total emission on the field. Inhomogeneity (e.g., the difference in composition, cracks, and permeability) exists on each peat sample. Peat samples that are brought to experiment in the lab will differ from the peat on the field. Uncertainties are also produced in trying to estimate the total emission on the field via remote sensing of the burned area. Given that peatland emission spread both lateral and vertically, estimated by the area alone produces uncertainties since the estimation does not take the vertical spread into account. Additionally, trying to scale up lab-gathered values does not take into account the ever-changing environmental condition that affects the rate of burning. Advances in detection technology are needed to eliminate this uncertainty.

One method to reduce the uncertainty of emission estimation is to estimate it by burned volume. Methods of the depth of burn measurement have been reviewed previously [13]. It was identified that there is four categories of method in the depth of burn measurement, which are LiDAR, soil core, soil moisture, and adventitious root techniques in which the author concludes that LiDAR is the most efficient and accurate. By knowing the combusted peat volume, derived from depth and area, and the bulk density, the carbon emission could then be estimated. Previously, the effort on trying to estimate field peat fire carbon emission has been made by measuring the burned depth with LiDAR as well as the area [14]. However, the author admits that there is uncertainty coming from the unaccounted emission factor (EF) in their total emission estimation. This paper aims to design a novel method to estimate the transient EF of CO and $CO_2$ by the depth of burn (DoB), burned area (A), subsidence rate (SR), and burning duration (t) to reduce the uncertainties given from area-based estimation.

Afterward, the regression model will be improved by including peat elemental variables, hence able to estimate multiple types of peat samples. This is done to address the problem of uncertainty given by peat inhomogeneity. The result in this paper enables us to estimate CO and $CO_2$ EFs for multiple types of peat, hence making field estimation through the depth of burn measurement more accurate

## METHODOLOGY

A lab-scale tropical peatland fire experiment was conducted on a buoyancy calorimeter apparatus with continuous weight and emission mass flow rate measurements. Throughout the experiment, peat depth of burn was also measured using infrared (IR) sensors that are located 20cm above the unburned fuel bed surface. The burned area was also measured using image processing of a thermal camera. The values are logged from time to time and used to create an estimation model of CO and $CO_2$ EFs along with other peat elemental variables (C, H, N, & O) that refer to the result of the ultimate analysis. A complete summary of peat sample proximate and ultimate analysis results can be seen in Table 1. The inclusion of these data on the estimation model is intended to depict the variation of emissions due to peat's inherent inhomogeneity in characteristics, while the area and depth are included to address the multidimensional spread estimation uncertainty. A detailed explanation of peat sampling, experimental setups, procedures, and EF modeling will be explained in the subsequent section.

**Table 1. Summary of fuel proximate and ultimate analysis results**

| Sampling Location | AC[a] (%) | MC[a] (%) | VM[a] (%) | FC[a] (%) | GCV[a] (Kcal/kg) | C (%) | H (%) | N (%) | O (%) | S (%) |
|---|---|---|---|---|---|---|---|---|---|---|
| PKY-1[b] | 7.5 | 8.20 | 49.8 | 34.5 | 4930 | 57.43 | 4.8 | 1.1 | 29.01 | 0.16 |
| Jambi | 6.81 | 15.19 | 49.8 | 28.19 | 4402 | 48.56 | 3.66 | 0.72 | 24.86 | 0.2 |
| Papua | 4.95 | 12.25 | 55.6 | 27.2 | 4695 | 50.62 | 6.07 | 1.69 | 36.42 | 0.25 |
| PKY-2[b] | 11.2 | 17.40 | 40.0 | 31.5 | 4274 | 47.79 | 5.16 | 0.7 | 35.02 | 0.13 |

[a]Abbreviations: AC: Ash content; MC: Moisture content before drying; VM: Volatile matter; FC: Fixed carbon; GCV: Gross calorific value.

[b]Both taken from the same site (Palangkaraya), but in different locations

### Sample Preparation

The peat sampling and processing method follow our previous work on peat fire dynamic study [15]. Four samples were collected from three locations, namely Jambi, Papua, and two samples from Palangkaraya (PKY-1 & PKY-2). These islands were selected as it represents the three main locations where peat deposit is concentrated in Indonesia [16]. Samples were taken at a depth of 60-120 cm with an undisturbed sampling method in order to obtain samples with suitable conditions until the experiment was conducted. Samples were then transferred to our lab inside a closed compartment to minimize changes in characteristics along with the delivery. Sub-samples from each sample categorized by locations were taken for proximate and ultimate analysis, which was conducted by a third party (SUCOFINDO Ltd.), similar to the process in our previous work [15]. While being stored, the samples were kept inside the storage, where it was taken from the field and tightly sealed to ensure minimum characteristic changes during storage. When about to be used for an experiment, sub-samples of the peat samples were taken into a tray. The tray will then be put inside an oven for 24 hours at $100^0$C temperatures, drying the peat soil. Dried peat will then be sieved with a 4mm mesh size. This is mainly to separate the peat from wood or grassroots debris since it might affect the smoldering spread [17]. Afterward, 2.25 kg of sieved peat sample was taken to the apparatus. Hence we have controlled bulk density at 281.2 kg/m$^3$. The scanning electron microscope (SEM) test was conducted, as shown in Figure 1, to visualize the physical structure and pore sizes of the peat samples. However, the study of physical structure, pore sizes, and particle size variation to fire behavior will

be for separate publication. Moisture for all samples are in the range of 7-8% after drying, hence making the sample to burn in smoldering regime.

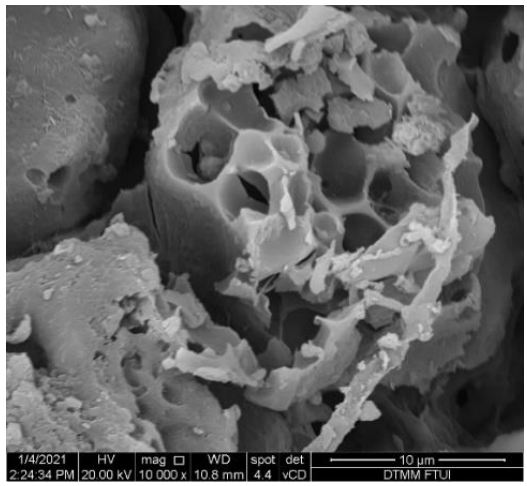


**Fig. 1.** Typical result of scanning electron microscope (SEM) test of PKY-1 sample, which has pore size approximately 2.5 µm

## Experimental Setups and Procedure

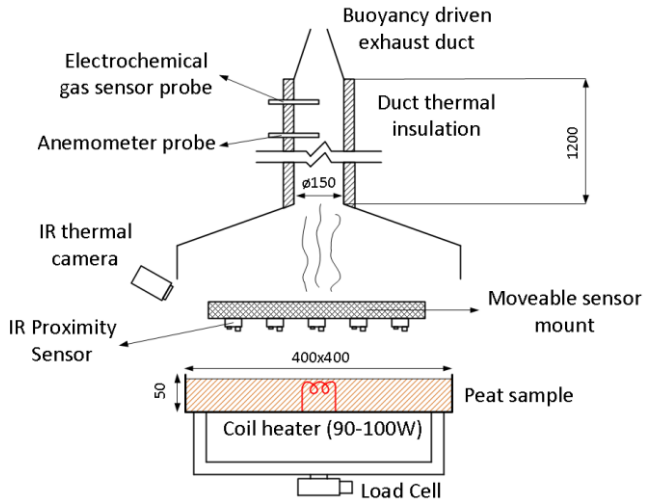


**Fig. 2.** Experimental setup illustration with dimensions given in millimeter.

After all the sample processing steps are done, it will then be placed on a reactor of 400 by 400 mm in cross-section and 50 mm in height to be tested under the buoyancy calorimeter apparatus. A buoyancy calorimeter was utilized to avoid extra oxygen supply to the fuel bed that is caused by the exhaust fan of the calorimeter. The parameter that is going to be measured on the apparatus is based on the emission factor formula, given in Eq. 1, with $\dot{m}_i''$ as the emission mass flow rate (g/s) and $\dot{m}''$ as the fuel mass loss rate (kg/s). Referring to a review article written by Hu et al. [12], EF is defined as the ratio between the mass of emitted species divided by the mass of dry fuel consumed. Usually, in peat fire EF studies, EF is expressed as the average throughout the experiment. On the reactor, the peat sample was ignited using a coil heater with a given power of 90-100 W. The location of the heater is in the middle of the reactor to minimize the edge effect, as the fire will start from the middle and spread outward gradually. The heater was kept on throughout the first hour of the experiment. Fuel mass loss rates were continuously logged with a load cell, while mass flow CO and $CO_2$ were

measured with an electrochemical gas sensor and hot wire anemometer. Measurement probes were cleaned using ultrasonic cleaner prior to each experiment to remove contaminants from the previous experiment. The electrochemical sensor that is used has acceptable accuracy within the measurement regime. With an assumption of plug flow, the velocity and gas concentration can be used to calculate EF with the density adjusted by temperature. The illustration of the experimental setups is shown in Figure 2. Temperature adjustment is needed due to the buoyant flow nature of the measurement. All devices will log the data continuously until the experiment ends 12-14 hours after ignition until the fuel is out. Continuous data logging allows the plotting of transient EF of CO and $CO_2$. Transient EFs were calculated by averaging the EFs from the start of the ignition to a particular point in time, giving the EFs for that corresponding time. These transient values will be estimated with both depth and area data measured with an IR proximity sensor and IR thermal camera.

$$EF = \frac{\dot{m}_i^{''}}{\dot{m}^{''}} \tag{1}$$

IR proximity sensors were placed 20 cm above the surface level of the pre-ignited fuel bed. It was mounted on a beam, with 15 sensors spread throughout the cross-section of the reactor. The mounting was also designed as a tray that can be pulled away from the top of the reactor, minimizing stack flow disturbance and avoiding sensor damage for prolonged heat exposure. Measurements were conducted in an interval of 30minutes, as the change in depth is not significant within shorter intervals. The depth of burn (DoB) measured with this device at any given time is expressed as the average of the depth measured by all 15 sensors. With this average method, it will approximate the equivalent depth if the peat is burned at the same vertical rate at every measurement point. Hence multiplying the DoB with the area (A) will result in its approximated burned volume. Subsidence rate (SR) is defined as the rate of change in DoB every 30 minutes. SR is included in the model to take into account the mass-loss rate at a different point in time in the experiment. For area (A) measurement, the imagery captured by the thermal infrared camera (FLIR A35) will be processed, with an interval of 10 minutes between image capturing, in which the camera was mounted with $30^0$ angles. Every frame of the video was converted to grayscale, binarized, and thresholded. The threshold was selected to be at $\geqslant$225$^o$C considering the uncertainty from the camera itself and also based on the temperature of smoldering peat, where the pyrolysis regime is dominant [17]. Depth and area data are used to address the problem of current multidimensional spread uncertainty in EF estimation.

**EF Modelling**

Both DoB and A will depict the burned volume, which should be related to the burned mass. As EF contains emission mass flow rate and fuel mass loss rate, SR will help represents the mass loss rate, and t will help represents the emission mass flow rate. These four variables, DoB, A, SR, and t, will be referred to as *multidimensional spread variables*. Two multivariable linear models were made, 1) Models with only multi-dimensional spread variables and 2) Models with both elemental (C, H, O, N) and multidimensional spread variables. The first model was made to show the ability of multidimensional spread to estimate EFs data of each sample. The second model was created to try to address the complexity of estimation due to the inhomogeneity of peat samples, thus, one linear equation was created to predict the EF of all four samples. Cross-validation was carried out to show the accuracy of the prediction. Backward elimination in the regression was performed to analyze the significance of each variable, mainly to compare the significance of A and DoB, whether using only one of which provides some degree of uncertainty

**Measurement Uncertainty**

Uncertainties for EF in this experimental setup come from a load cell, electrochemical gas sensors, thermocouples, and hot-wire anemometer. The electrochemical gas sensor has good accuracy in the measurement range. The measurement range of the sensor for CO and $CO_2$ are 100-2000 ppm(vol) and 0-20000 ppm(vol), respectively. Within that range, the uncertainty is both ±5%. During the time frame of the experiment, the typical value of CO and $CO_2$ ranged from 400-1800 ppm(vol) and 2000-

15000 ppm(vol), and thus the value measured from the electrochemical sensor in this regime is within acceptable uncertainty. Hot-wire anemometer and load cell have the uncertainty of ±0.015 m/s and ±2%, respectively. Thermocouples for emission temperature measurement to correct the density for EF calculation have the uncertainty of ±0.3%. Total uncertainty produced by all the measurement devices ranged from ±15-25%. Uncertainty for IR proximity sensor and IR thermal camera measurements is ±3.5% and ±5%, respectively.

## RESULTS AND DISCUSSION

Steady-state EF from each experiment was shown in Table 2, with the values being agreeable with previous experiments summarized in Hu's review [6]. Typical experiment emission mass flow rate, mass loss rate, and transient EF pattern are shown in Figures 3a and 3b. The steady-state burning period was determined on the period where mass flow rate was relatively constant with some degree of variation, as shown in Figure 3a within the two vertical black striped lines. Within the first two hours, the emission factor goes high relative to the latter values in each experiment. Other experiments show a similar pattern with different time scales. The soaring first two hours of EFs is because the effect of ignition heating was still significant, although the coil heater was turned off at the first-hour mark. After turning off the heating coil, the emission concentration goes down while the peat keeps smoldering.

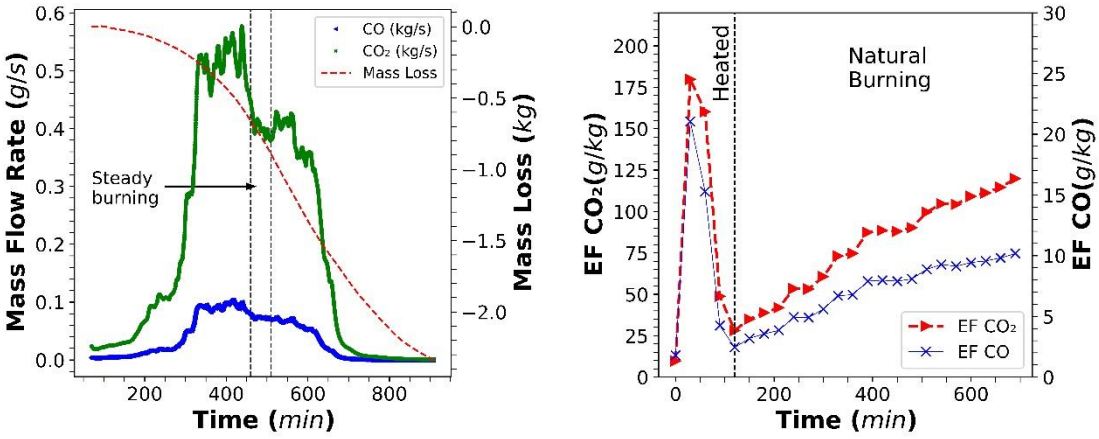


(a) (b)

**Fig. 3.** Typical pattern of (a) fuel mass loss and mass flow rate of CO and $CO_2$ (PKY-1); (b) transient EF of CO and $CO_2$ (Jambi).

**Table 2. Steady state EF comparison with previous research**

| Sample location | EF $CO_2$ | EF CO |
|---|---|---|
| PKY-1 | 1228 | 222.1 |
| Jambi | 1850.2 | 187.4 |
| Papua | 1611.1 | 105.4 |
| PKY-2 | 1503.2 | 165.4 |
| Experiment average | 1548.1 | 170.1 |
| Hu et al. (2018) average | 1615.4 | 248.06 |

The analysis of this research will consider the whole period of the experiment and not just the steady burning, except the first two hours since the ignition heating effect is still dominant. Although edge effect and non-steady burning do not represent the onsite phenomenon of smoldering peat, the main objective of this research is to establish the CO and $CO_2$ EFs estimation method. The transient EFs reported in the subsequent analysis are the average EF from ignition until the corresponding time, as explained in the experimental method section. However, the values that is going to be included in the linear model are post-heating period, as illustrated in Figure 3b, marked as the natural burning period, until 11-12$^{th}$ hour maximum to avoid a period where the edge effect is significant.

Typical transient DoB and A versus burning duration are shown in Figures 4a and 4b. The rate of increase on DoB and A varies in each sample. All samples show a bell-curve shape on transient A. Meanwhile, the DoB pattern is almost linear for Jambi and Papua, while for Palangkaraya, the shape approaches the S-shaped curve. This difference in DoB and A pattern can be explained by the difference in elemental and proximate analysis variables. Further analysis on transient DoB and A will be discussed in separate publications.

**Table 3. $R^2$ values for EF modelling with DoB, SR, A, and t for each sample**

| Sample location | $R^2$ EF $CO_2$ | $R^2$ EF CO |
|---|---|---|
| PKY-1 | 0.973 | 0.947 |
| Jambi | 0.991 | 0.989 |
| Papua | 0.954 | 0.952 |
| PKY-2 | 0.987 | 0.988 |
| Average | 0.976 | 0.969 |

The EFs trend on each sample was almost linear, except for Palangkaraya, which burns faster than the other two samples, as illustrated in Figures 5a to 5d. Approaching the end of the experiment time regime, both Palangkaraya samples decrease in gradient compared to the other two samples, as there is less fuel available due to the faster burning rate. The average mass loss rate, subsidence rate, and lateral spread rate for all four samples are 3.81 g/min, 0.08 mm/min, and 2.54 cm$^2$/min, with a standard deviation of 0.76 g/min, 0.02 mm/min, and 0.54 cm$^2$/min respectively. Modeling of EF CO and $CO_2$ with four variables, DoB, A, SR, and t, were shown in Figure 4c for the PKY-1 sample. It can be seen that the variability can be captured accurately, with $R^2$ of 0.973 and 0.947 for $CO_2$ and CO, respectively. The values of $R^2$ for other sample experiments are summarized in Table 3, with all $R^2$>0.9.

This indicates that these four variables, DoB, SR, A, and t, are a good estimate for EF. The regression is able to depict how much fuel is burned and how fast, or in other words, the mass-loss rate. However, trying to regress all samples with only these variables is inadequate, as some $R^2$ can be negative. Although the DoB pattern is similar, as shown in Figure 4a, the transient EFs can be five times higher. This can be explained by the inhomogeneity of each sample, hence raising the need to include the elemental variables to the regression model. The result of this regression is shown in Figures 5a to 5d. Cumulative $R^2$ given by this model is 0.975 and 0.982 for EF CO2 and EF CO, respectively. If broken down to each sample, the average $R^2$ is 0.91 and 0.89, with a standard deviation of 0.01 and 0.03 for $CO_2$ and CO EFs, respectively. Regression model equations are given in Eq. 2 and 3 for EF CO and EF $CO_2$. From the equation, we can infer that elemental-wise, EF will get higher with larger C and O content and lower with H and N content. For both equations, the influence of O content is more significant compared to C content. However, this trend is not apparent in the reported steady-state EFs, meaning that we cannot predict by the elemental characteristics alone. The volume burning rate, which is depicted by multidimensional spread variables, needs to be taken into account as well. For the amount of fuel burned, EF is increased by SR, A, and t, while DoB lessens the value of EFs. Additionally, we have tried adding other variables from the elemental and proximate analysis (e.g.,

gross calorific value, volatile matter, ash content, moisture, & S content), but it does not have any significant effect on the performance of the model.

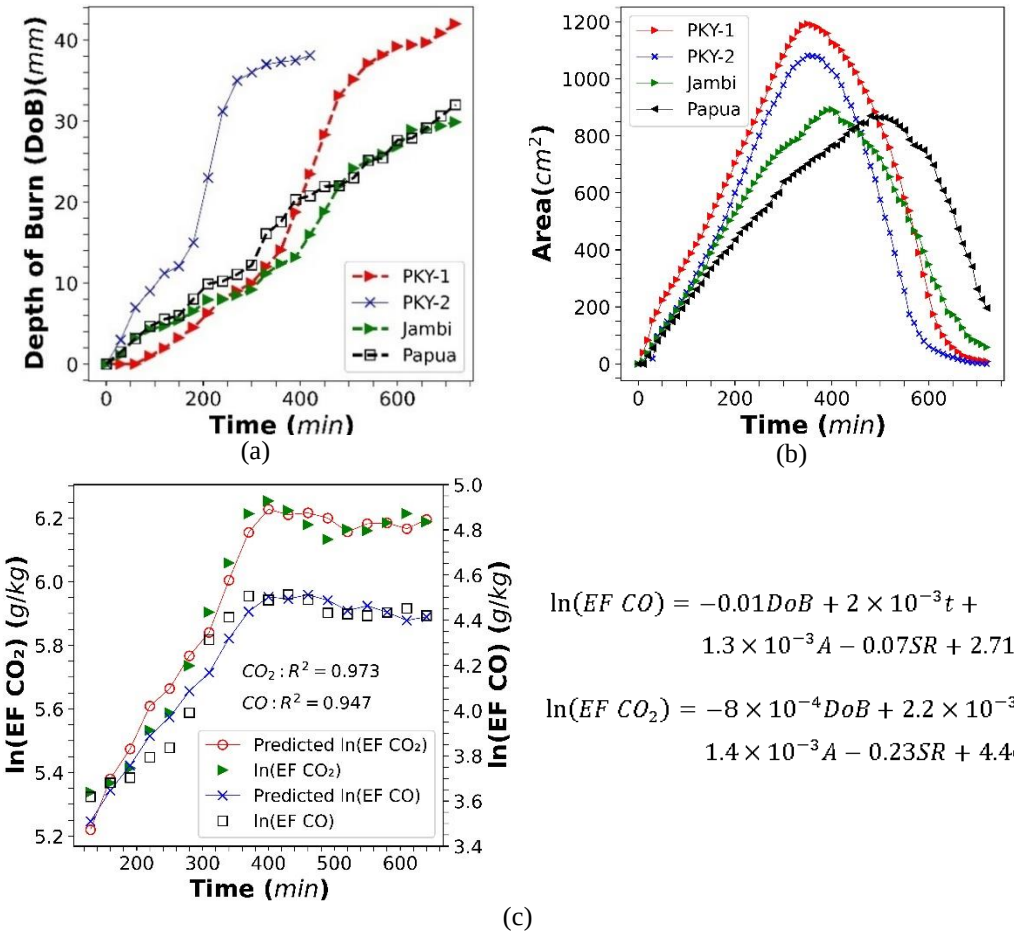


$$\ln(EF\ CO) = -0.01DoB + 2 \times 10^{-3}t + 1.3 \times 10^{-3}A - 0.07SR + 2.71$$

$$\ln(EF\ CO_2) = -8 \times 10^{-4}DoB + 2.2 \times 10^{-3}t + 1.4 \times 10^{-3}A - 0.23SR + 4.46$$

**Fig. 4.** The pattern of (a) transient depth of burn; (b) transient burned area; of all samples. Shown also prediction performance of multidimensional spread variable on PKY-1 sample (c).

To search for the uncertainty given by one dimensional estimation, backward elimination is done for DoB, SR, A, and t from both Eq. 2 and 3. The result is illustrated in Figure 5e for the PKY-1 sample only. Cumulative $R^2$ is the lowest if DoB is not included in the model, in which the $R^2$ is 0.938 and 0.96 for both EFs. On the PKY-1 sample itself, the $R^2$ of EF $CO_2$ goes down to 0.79. However, when A is eliminated from the regression model, the $R^2$ is increased to 0.973 and 0.980, respectively. The value is only slightly less than the all variable regression, but this indicates that A plays a positive role in the estimation if it is included. Additionally, it also indicates that A alone cannot be used as the sole predicting variable. Nonetheless, this experiment uses a thin fuel bed, in which thickness is only 50 mm. As the peat layer/fuel gets thicker we hypothesize that the predictive ability of A for EFs gets worse, and this can be a topic for future research. The summary of backward elimination is given in Table 4. To assess the predictive ability of this model, k-fold (k=5) shuffled cross-validation is conducted and produces an average score of 0.965 and 0.976 for $CO_2$ and CO, which implies good predictive ability. For EF CO, the maximum and minimum score is 0.985 and 0.967, while for EF $CO_2$, it is 0.981 and 0.935.

$$\ln(EF\ CO) = -0.04DoB + 3.5 \times 10^{-3}t + 7.7 \times 10^{-4}A + 0.28SR + 0.25C + 0.46O - 1.2H - 2.08N - 17.86 \quad (2)$$

$$\ln(EF\ CO_2) = -0.05DoB + 4.1 \times 10^{-3}t + 5.4 \times 10^{-4}A + 0.33SR + 0.15C + 0.41O - 0.93H - 1.62N - 10.29 \quad (3)$$

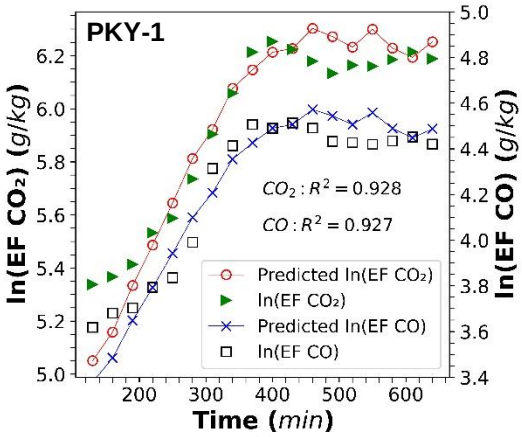


(a)

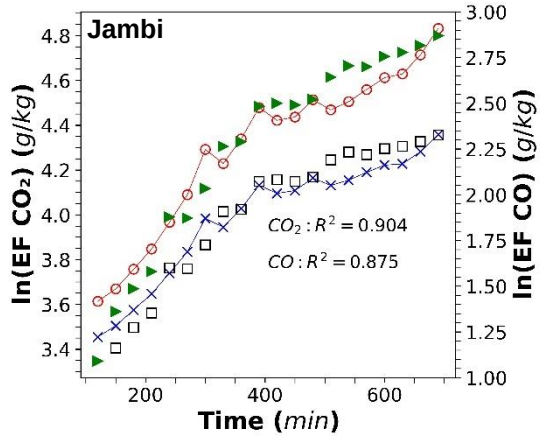


(b)

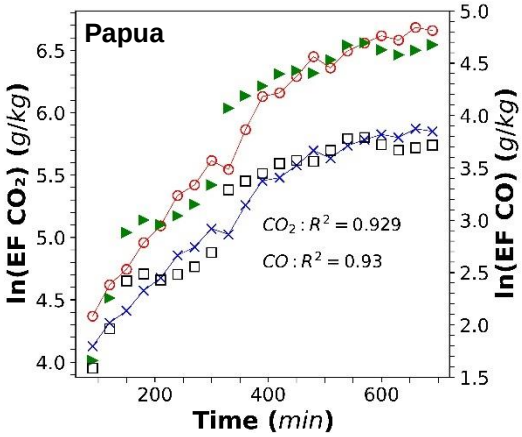


(c)

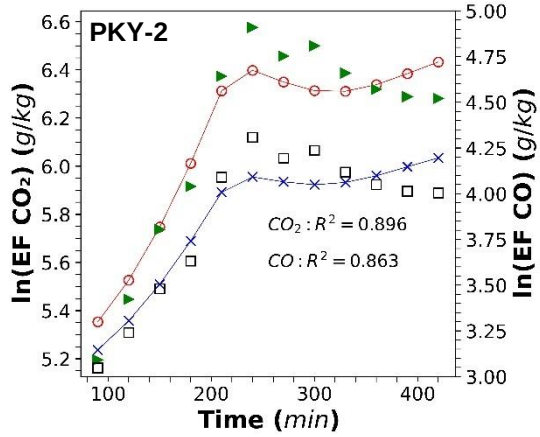


(d)

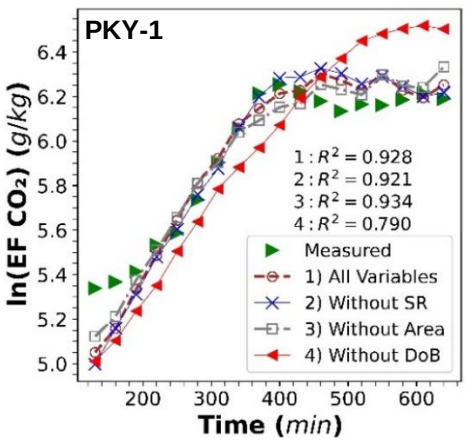


(e)

**Fig. 5.** Modeling result of ln(EF CO) and ln(EF $CO_2$) with DoB, SR, A, t, and peat characteristics (C, H, O, & N) for a) PKY-1; b) Jambi; c) Papua; and d) PKY-2. The example shown of EF $CO_2$ from PKY-1 sample experiment (e) for backward elimination of the model in Eq.2 and Eq.3

**Table 4. Cumulative $R^2$ values for backward elimination from Eq. 2 and 3**

| Sample location | $R^2$ EF $CO_2$ | $R^2$ EF CO |
|---|---|---|
| All variables | 0.975 | 0.982 |
| Without SR | 0.942 | 0.964 |
| Without A | 0.973 | 0.980 |
| Without DoB | 0.938 | 0.962 |

## CONCLUSIONS

Measurements of CO and $CO_2$ EFs were conducted on a buoyancy calorimeter apparatus. In this apparatus, weight and emission mass flux were continuously logged to calculate the transient EFs of both emissions. Multidimensional spread (DoB, A, SR, and t) and peat elemental variables (C, H, O, and N) were also measured and included in the estimation model for CO and $CO_2$ EFs. There are two main problems with the natural peat fire emission estimation method, in which uncertainty is caused by one-dimensional estimation and inhomogeneity of peatland characteristics. This causes complexity in EFs estimation. Thus, this research aims to address the problems by creating an estimation model from the multidimensional spread and elemental variables.

The estimation method using only DoB, A, SR, and t was satisfactory to estimate the corresponding sample in which it regressed while using the equation to other samples or trying to create one model for all produce a large amount of error. This is due to the inhomogeneity of peat from one location to another; hence, the inclusion of elemental variables into the model is necessary. After the inclusion of elemental variables to the model, $R^2$ larger than 0.9 can be produced, which indicates a good prediction ability of the model for both EFs. This is further supported by a k-fold cross validation average score >0.9 for both EFs. Elemental-wise, oxygen content has a more significant effect on EFs than carbon content, while hydrogen and nitrogen content reduces the EFs. Backward elimination shows that DoB is very important to be included in the model, as the exclusion of it reduces the $R^2$ the most, while the exclusion of A also reduces the $R^2$ but is not as significant. This confirms the uncertainty of the one-dimensional estimation method and gives a strong reason to develop a field two-dimensional emission estimation method. For future work, the model can be upgraded to include more environmental variables, such as wind, temperature, and humidity.

## ACKNOWLEDGEMENT

The authors would like to thank Universitas Indonesia for the financial assistance through Hibah Publikasi Artikel di Jurnal Internasional Kuartil Q1&Q2 2019 funding scheme with a contract number of NKB-0331/UN2.R3.1/HKP.05.00/2019 managed by Directorate for Research and Public Services (DRPM) Universitas Indonesia and Hibah PMDSU Kementerian Pendidikan, Kebudayaan, Riset, dan Teknologi Republik Indonesia with a contract number of NKB-352/UN2.RST/HKP.05.00/2021.

## REFERENCES

[1] M. R. Turetsky, B. Benscoter, S. Page, G. Rein, G.R. Van Der Werf, & A. Watts, Global vulnerability of peatlands to fire and carbon loss, *Nature Geoscience*. *8*(1) (2015) 11–14.

[2] Z. C. Yu, Northern peatland carbon stocks and dynamics: A review, *Biogeosciences*, *9*(10) (2012) 4071–4085.

[3] S. E. Page, J.O. Rieley, & C.J. Banks, Global and regional importance of the tropical peatland carbon pool, *Global Change Biology*, *17*(2) (2011) 798–818.

[4] T. J. Kelly, A.J. Baird, K.H. Roucoux, T.R. Baker, E.N. Honorio Coronado, M. Ríos, & I.T. Lawson, The

high hydraulic conductivity of three wooded tropical peat swamps in northeast Peru: Measurements and implications for hydrological function, *Hydrological Processes*, *28*(9) (2014) 3373–3387.

[5] D. Drysdale, An introduction to fire dynamics, third ed., John Wiley & Sons, Chicester, 2011.

[6] G. Rein, Smouldering Fires and Natural Fuels, in C. M. Belcher (Ed.), Fire Phenomena and The Earth System, John Wiley & Sons, Chichester, 2013, pp.15–34.

[7] X. Huang, F. Restuccia, M. Gramola, & G. Rein, Experimental study of the formation and collapse of an overhang in the lateral spread of smouldering peat fires, *Combustion and Flame*, *168* (2016) 393–402.

[8] C.E. Stockwell, R.J. Yokelson, S.M. Kreidenweis, A.L. Robinson, P.J. Demott, R.C. Sullivan, J. Reardon, K.C. Ryan, D.W.T. Griffith, & L. Stevens, Trace gas emissions from combustion of peat, crop residue, domestic biofuels, grasses, and other fuels: Configuration and Fourier transform infrared (FTIR) component of the fourth Fire Lab at Missoula Experiment (FLAME-4), *Atmospheric Chemistry and Physics*, *14*(18) (2014) 9727–9754.

[9] A. Heil, & J.G. Goldammer, Smoke-haze pollution: a review of the 1997 episode in Southeast Asia. *Regional Environmental Change*, *2*(1) (2001) 24–37.

[10] A.L. Hinwood, & C.M. Rodriguez, Potential health impacts associated with peat smoke: A review, *Journal of the Royal Society of Western Australia*, *88*(3) (2005) 133–138.

[11] O. Kunii, S. Kanagawa, I.T.S. Ismail, I. Yajima, Y. Hisamatsu, S. Yamamura, & T. Amagai, The 1997 haze disaster in indonesia: Its air quality and health effects, *Archives of Environmental Health*, *57*(1) (2002) 16–22.

[12] Y. Hu, N. Fernandez-Anez, T.E.L. Smith, & G. Rein, Review of emissions from smouldering peat fires and their contribution to regional haze episodes, *International Journal of Wildland Fire*, *27*(5) (2018) 293–312.

[13] A.N. Che Azmi, N. Mohd Apandi, & A.S. Ahmad, Carbon emissions from the peat fire problem—a review, Environmental Science and Pollution Research, 28(14) (2021) 16948–16961.

[14] U. Ballhorn, F. Siegert, M. Mason, & S. Limin, Derivation of burn scar depths and estimation of carbon emissions with LIDAR in Indonesian peatlands, Proceedings of the National Academy of Sciences of the United States of America, 106(50) (2009) 21213–21218.

[15] M.L. Ramadhan, P. Palamba, F.A. Imran, E.A. Kosasih, & Y.S. Nugroho, Experimental study of the effect of water spray on the spread of smoldering in Indonesian peat fires. Fire Safety Journal, 91(April) (2017) 671–679.

[16] S.R. Wahyunto, H.S. Suparto, Sebaran Gambut dan Kandungan Karbon di Sumatra dan Kalimantan, Wetlands International - Indonesia Programme & Wildlife Habitat Canada (WHC), Bogor, 2005, pp.1-2.

[17] A. Usup, Y. Hashimoto, H. Takahashi, & H. Hayasaka, Combustion and thermal characteristics of peat fire in tropical peatland in Central Kalimantan, Indonesia. *Tropics*, *14*(1) (2004) 1–19.

# Laboratory Scale Experiment of Vegetation Uprooting Phenomena during Smoldering of Peat

**Hapsari J.[1], Nugroho S. [1], Mulyasih H.[1], Nugroho Y.[1,*]**

*[1] Fire Safety Engineering Research Group Department of Mechanical Engineering, Faculty of Engineering Universitas Indonesia Kampus UI Depok, West Jawa, Indonesia.*
**Corresponding author's email: yulianto.nugroho@ui.ac.id*

## ABSTRACT

Smoldering peat has initiated the uproot of vegetation in a large area affected by peat fires. The phenomena have interfered with the post-fire revegetation efforts of peatlands and peat forests, which implicates their long-term ecosystem dynamics. The importance of the reforestation efforts should be supported through observing and quantifying the effect of smoldering propagation in peat soil on the stability of the vegetation. This study evaluates the impact of vegetation on smoldering propagation in an open-top reactor filled with peat samples and planted trees. The initial ignition condition that creates the smoldering front is essential to the success of this study. The peat sample was ignited by a heating power of 100 W for 1 hour to perform this measure. This study shows the comparison between smoldering combustion activities of peat samples with the presence of the tree and devoid of any trees as a control. The smoldering combustion activities could propagate devoid of any obstruction and create the same pattern of smoldering propagation in the control reactor until it was finally extinguished. The subsidence of peat surface in the smoldering area causes the mass of the soil to reduce and unable to support the tree leading to vegetation uprooting phenomena. In all experiments, surface subsidence occurred on peat soil due to the loss of moisture content and shrinkage in the peat's structure.

**KEYWORDS:** Peat, smoldering, propagation, vegetation, uprooting phenomena

## INTRODUCTION

The forest significantly impacts water circulation, precipitation, air circulation, and global and micro-climate. Linked with the multi-layered structure, the degradation of forests could amplify the disturbances that shape the structure and composition of the forest ecosystem. Forest fragmentation, fires, and windstorms can cause different levels of forest disturbance, significantly affecting tree mortality. Therefore, many believe restoring the damaged forest can be carried out through revegetation activities. However, many factors must be reconsidered before the revegetation efforts are conducted, including the risk of forest fires, especially in Indonesia.

Specifically, fires are considered a potential threat to forest sustainability, especially in Indonesia. The country is covered with 98 million hectares of tropical forests, representing 10% of the world's remaining tropical forests. However, Indonesia's forest fires occurred almost every year in the last three decades, and 1997/1998 (El Nino) forest fires were considered Indonesia's largest unprecedented ecological disaster. Over 9.7 million ha of Indonesian forest were burned during the El Nino event. Meanwhile, after 20 years (in 2019), Indonesian forest is still primarily degraded by the fire up to 1.6 million ha of land.

Forest fires mostly peaked during the dry season in the southern parts of Kalimantan and Sumatra Island, where a vast peatland forest was mainly located. Peat is a heterogeneous mixture of material that comes from organic matter or humus decomposition. The amount of decomposed organic matter is accumulated in a water-saturated environment without oxygen and is formed if the plant material does not fully decay in acidic and anaerobic conditions. A million hectares of virgin peat forest were converted into other functions (e.g., oil plantations), which led the peat area to lose its moisture content. Once ignited, the drained peat is highly flammable and becomes very difficult to extinguish.

Therefore, the occurrence of a forest fire leads to rapid changes in soil, which in turn affects the long-term ecosystem dynamics [1]. The tree planted as revegetation efforts of peatlands and peat forests can be disrupted if the smoldering in peatlands reoccurs. The high temperature from the smoldering combustion destroys the food source that comes through the roots of the plants, especially for small seed plants. In the case of forest fires in the peatland area, the moisture content of the soil was most likely to be different from the ordinary soil, causing a distinct characteristic of propagation during the smoldering combustion activities. Therefore, this research will quantify the effect of vegetation on the smoldering propagation in peat soil and then compare the result with the impact of windstorms on the fallen trees.

**Fig. 1.** Uprooted tree and other vegetations due to smoldering peat

## EXPERIMENTAL METHOD

The peat samples used in this study were collected from Palangka Raya, Indonesia, using the undisturbed sampling method in order to maintain its actual properties. The ultimate-proximate analysis shows that the C/H/N/S of the peat is 57.43/4.80/1.10/0.16 %, respectively. The raw peat sample was oven-dried at 100° C for 24 hours to achieve the dry peat conditions used for the experiments. After the oven-dry process, the peat lost a large amount of moisture content which is from 69.2% to 6%.

An open-top reactor with 20 cm x 20 cm in cross-section and 20 cm in depth was used to carry out the comprehensive smoldering propagation activities. The inner side of this stainless-steel reactor is covered with a Calcium Silicate board that acts as a heat insulator. This study's success depends on parameterizing the initial ignition condition, which creates the smoldering front zone. The peat sample was ignited by a 20 cm coiled heater placed at one side of the reactor and was buried at a 5 cm elevation below the surface of the peat sample with a heating power of 100 W for 1 hour. To obtain the temperature distributions, 39 sets of thermocouples were inserted through the bottom side of the reactor at four different heights; 15 cm, 12,5 cm, 10 cm, and 7,5 cm (as seen in Fig. 2).

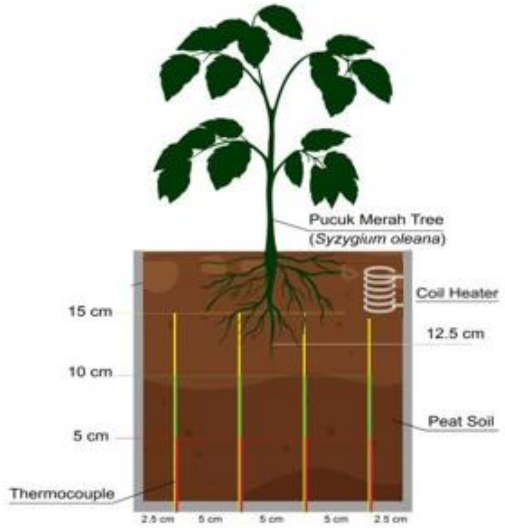


**Fig. 2.** Reactor set-up

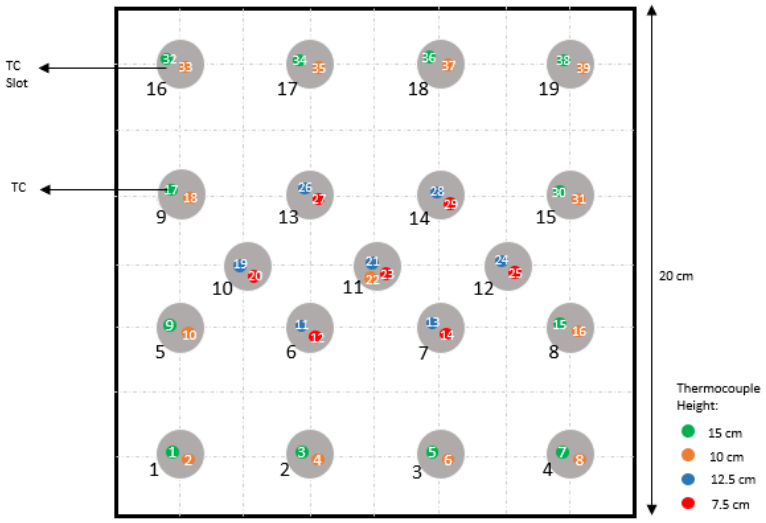


**Fig. 3.** Thermocouple configuration (Top view)

The reactor was filled with the dried peat sample loosely or without compaction. Then, a tap-rooted native Borneo tree species, namely Pucuk Merah (Syzygium oleana), was planted on the peat sample at 15 cm height from the base of the reactor (as seen in Fig. 2). Two sizes of tree diameter (3 cm and 1.5 cm) will be measured to compare different behavior by size. However, before the vegetation was placed inside the reactor, it was crucial to air-dry the tree under the sun for 2 hours to decrease the moisture content in the roots part. For comparison, baseline data or control experiment was conducted as the procedure above was repeated on a reactor devoid of any tree. Twice repetition was conducted for each data retrieval.

Data retrieval processes were started once the heat power successfully ignited the peat sample inside the reactor for one hour. Temperature distributions captured by the thermocouple inside the reactor were collected using two data logger units. Each data logger was connected to 20 and 19 thermocouples, respectively. A FLIR A35X thermal camera was used to obtain temperature data on the surface of smoldered peat inside the reactor. A schematic set-up for the experiment is presented in Fig. 4.

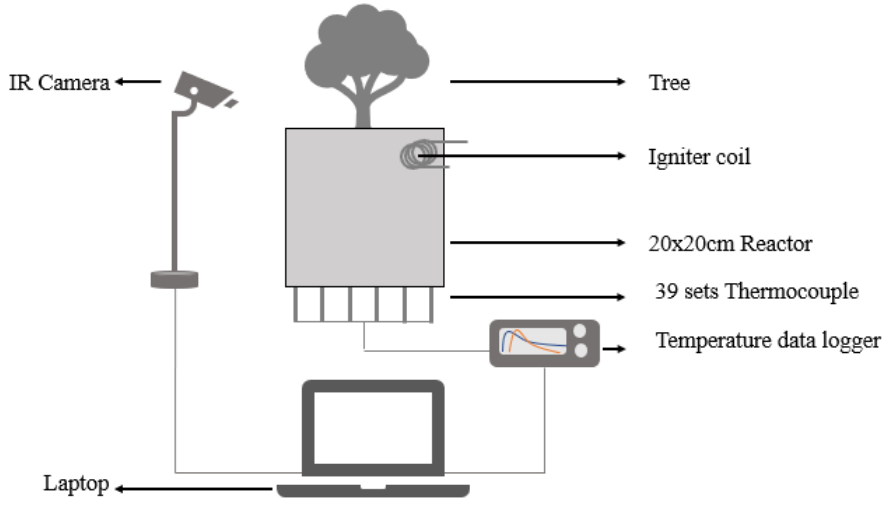


**Fig. 4.** Experimental set-up

## RESULTS AND DISCUSSION

Once ignited, smoldering peat fire spread unpredictably and became hard to extinguish. Previous studies [2] show that smoldering peat propagates horizontally from one layer to another without any obstruction, with the most combustion activity concentrated in the middle area of the sample reactor. The results of this experiment will quantify the effect of vegetation on smoldering propagation in peat soil.

### Baseline Data

Ignition successfully took place after one hour, and the smoldering distribution started to spread from the direction of the heat source. As the smoldering front spreads, peat was left to be self-sustained until it was extinguished after 69 hours later. During the smoldering fire, the temperature distribution spreads horizontally and vertically. The on-surface temperature distribution, which is captured by the FLIR camera every 5 minutes and thermocouple, shows that smoldering fire spreads in vertical and horizontal directions.

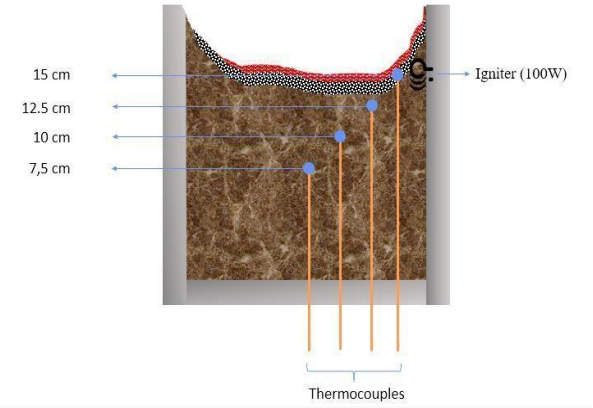


**Fig. 5.** Baseline test illustrations and thermocouple positions from the base of the reactor

During the ignition stages, the nearest thermocouple around the coil heater placed at the height of 15 cm captured a significant surge in peat temperature to 430° C. One hour later, the heat power was stopped. The temperature dropped slowly to 270 ° C. After 10 hours of smoldering, the hot spots were concentrated at the center area of the reactor. It resembles a circle shape with a diameter of 17 cm and a temperature of 450° C.

Due to the tendency of peat to find the combustible fuel to burn, the smoldering combustion activity inside the reactor showed two phases of peak temperature as seen in Fig. 6. The first phase rose from the first hour until the 30th hour and dropped at the 43$^{rd}$ hour. While the second phase was shown to increase from the 43$^{rd}$ hour, then dropped at the 45$^{th}$ hour until it was finally extinguished. As the smoldering propagated, the occurrence of land subsidence in peat soil started to be seen significantly at 33 hours with a 7-9 cm drop. The smoldering area was shrunk as the fuel left to burn was decreased, and the activities were finally extinguished after 69 hours.

To attain peat mass reduction, it is necessary to measure peat mass condition both before and after the smoldering activities. Table 1 shows that 2480 grams of peat filled the 20 cm height reactor with a moisture content of 6%. After the smoldering took place and was finally extinguished, the peat left only 5.5 cm due to the land subsidence with 3.84% of moisture content and a total mass of 735 grams.

**Table 1. Peat sample properties**

| Treatment | Peat height from the reactor base (cm) | | Moisture Content (%) | | Mass (gr) | |
|---|---|---|---|---|---|---|
| | Before | After | Before | After | Before | After |
| Baseline | 20 | 5.5 | 6 | 3.84 | 2480 | 735 |
| Vegetation (3 cm) | 20 | 7 | 6 | 4.1 | 2530 | 827 |
| Vegetation (1.5 cm) | 20 | 7.5 | 6 | 6.96 | 2403 | 842 |

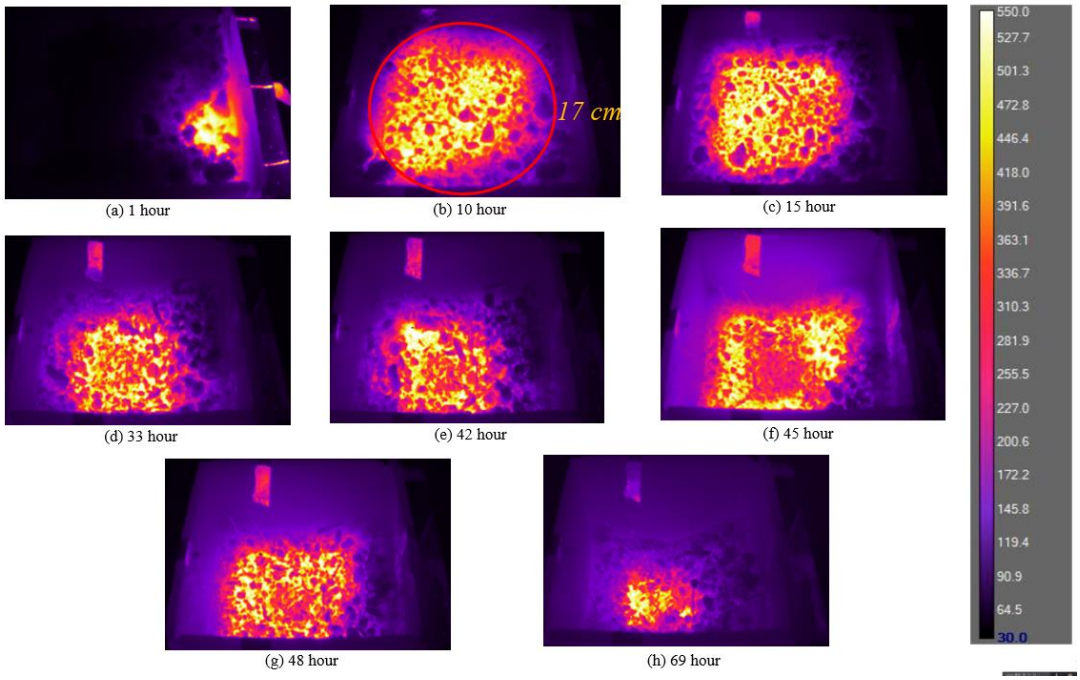


**Fig. 6.** Images of the smoldering process taken from the thermal camera

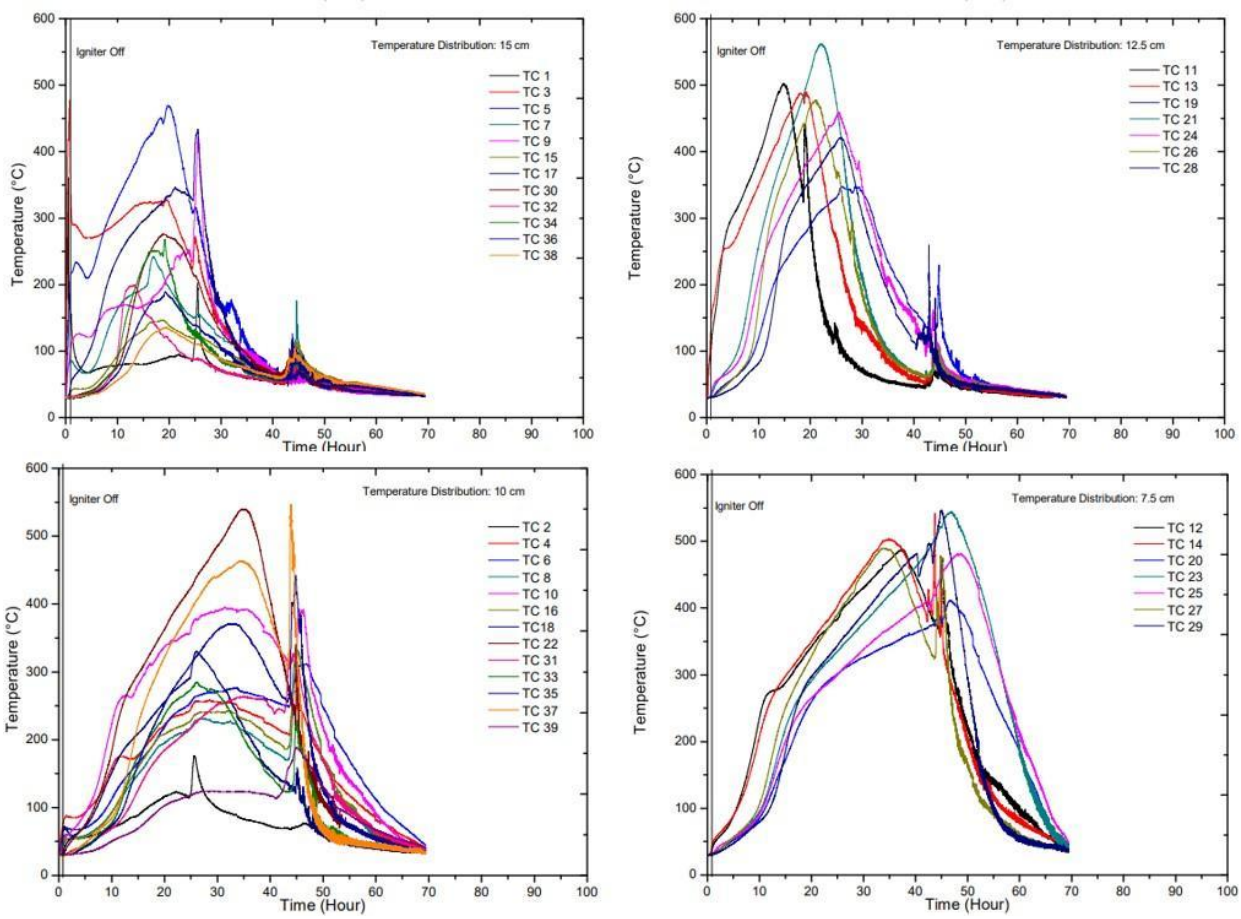


**Fig. 7.** Temperature distributions form thermocouples at different depth for baseline test

After the peat was finally extinguished, the ashes, char, and a small amount of unburned peat were seen as the final result of the burned peat. The gray to white powdery ashes were primarily concentrated in the middle area of the reactor; this indicates the place where the smoldering activities were mainly concentrated. In contrast, char production was shown as the result of the almost complete smoldering combustion process, which means that a similar amount of energy burned it in a shorter time than the ashes. Lastly, the unburn peat can be seen in the edges of the reactor, and it was indicated that this area does not have sufficient oxygen that flows around to create the smoldering process.

**Vegetation Treatment**

Vegetation located at the center of the reactor significantly affects smolder propagation activities in peat fire. For vegetation with a diameter of 3 cm, after 8 hours of combustion activities, the infrared-assisted visual observation showed that when the heat reached the tree location, the tree impeded further smolder propagation in the peat sample by 5 hours compared to smolder propagation in the control reactor. During the delay, heat propagated downward and caused significant damage to the tree's root system. At 400°C (peak temperature), the tree was uprooted and collapsed towards the heat source's direction after 9 hours of smoldering activity.

While for vegetation with a diameter of 1.5 cm, the heat was shown to reach the tree location after 4 hours of smoldering activities (Fig. 10). When the heat reached the tree location, the small-sized tree was directly uprooted since the root system was burned and could not hold the tree anymore. This is shown that the smoldering propagation was restrained due to the presence of the tree as an obstruction to the activities as can be seen on the delay on temperature distribution 15 cm and 12.5 cm depth (Fig. 9), meanwhile when there is no obstruction, the smoldering could propagate without any delay. After the tree was uprooted, the dynamics of the peat sample's smoldering propagation inside the reactor are similar to the 3 cm tree diameter until it is finally extinguished after 65 hours of smoldering activities (Fig. 10 (b)).

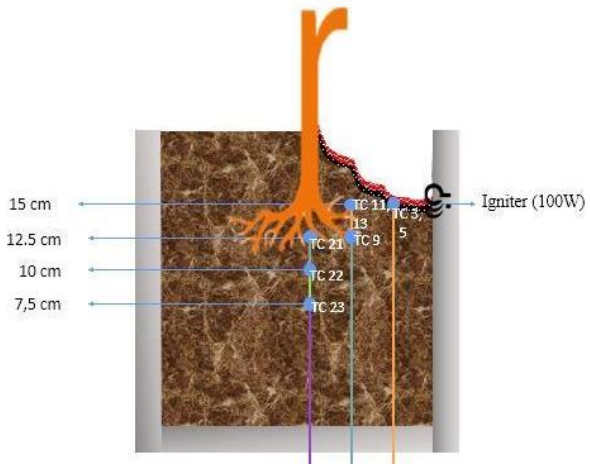


**Fig. 8.** Smoldering combustion activities for vegetation treatment

After the tree was finally uprooted, the smoldering combustion activities were seen to start to propagate similarly to the baseline experiment. The thermocouple reading has shown a rise in temperature after 10 hours with 580°C. Different from the baseline experiment, the temperature distribution in the reactor with vegetation treatment only showed one phase of temperature peak. Therefore, smoldering combustion activities could propagate devoid of any obstruction and create the same pattern of smoldering propagation in the control reactor until it was finally extinguished after 60 hours.

To attain peat mass reduction, it is necessary to measure peat mass condition both before and after the smoldering activities. Table 1 shows that 2530 grams of peat were filled the 20 cm height reactor with a moisture content of 6%. After the smoldering took place and was finally extinguished, the peat left only 7 cm due to the land subsidence with 4.1% of moisture content and a total mass of 827 grams.

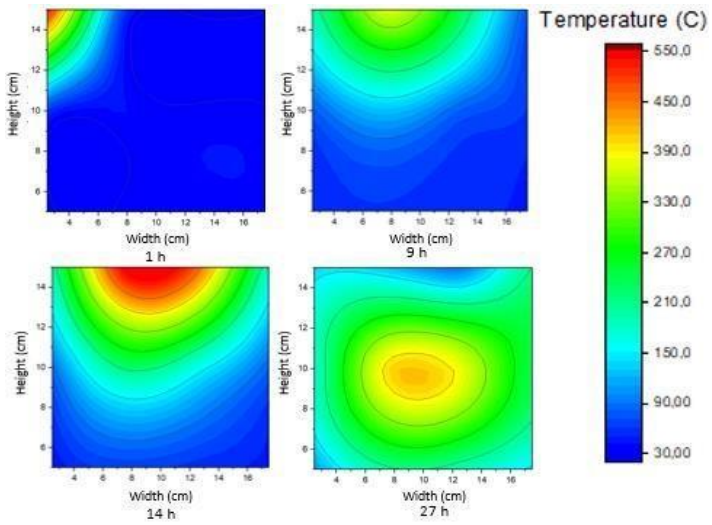


**Fig. 9.** Temperature contours of spread in peat sample for 3 cm (diameter) tree

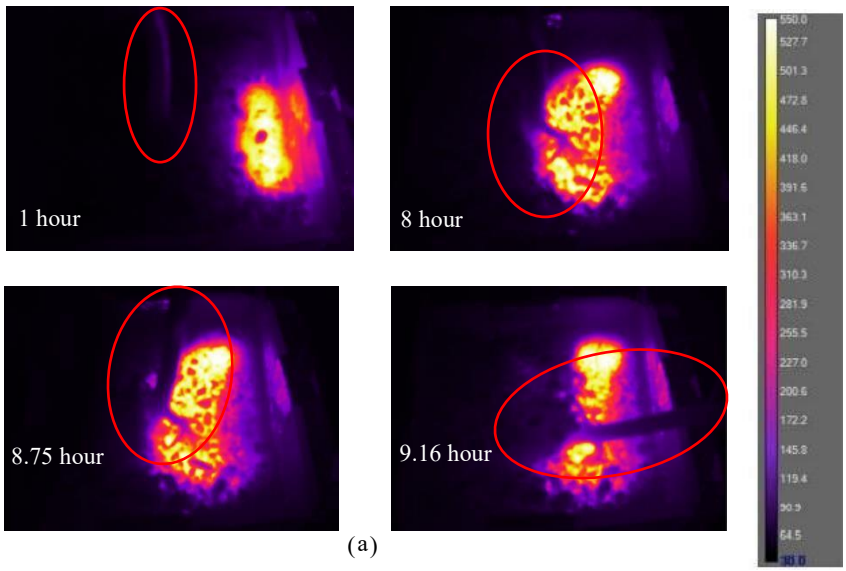


(a)

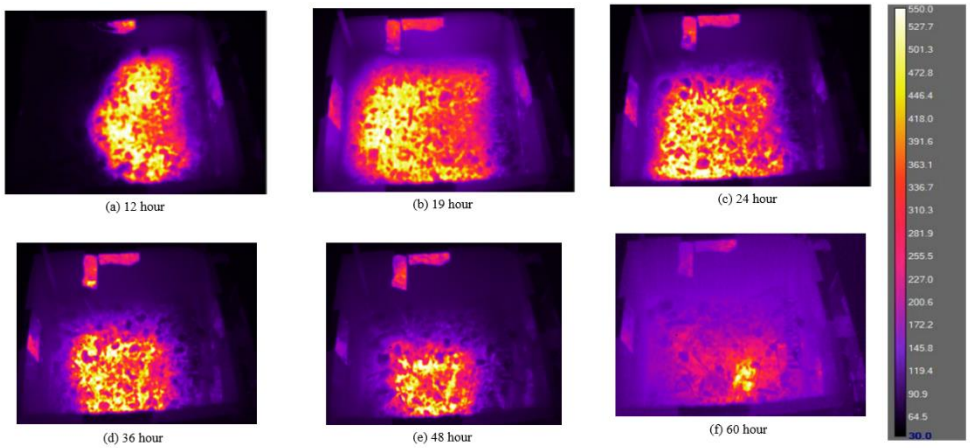


(b)

**Fig. 10**. The smoldering process from FLIR camera for 3 cm (diameter) tree. (a) uprooting process; (b) smoldering process after uprooted

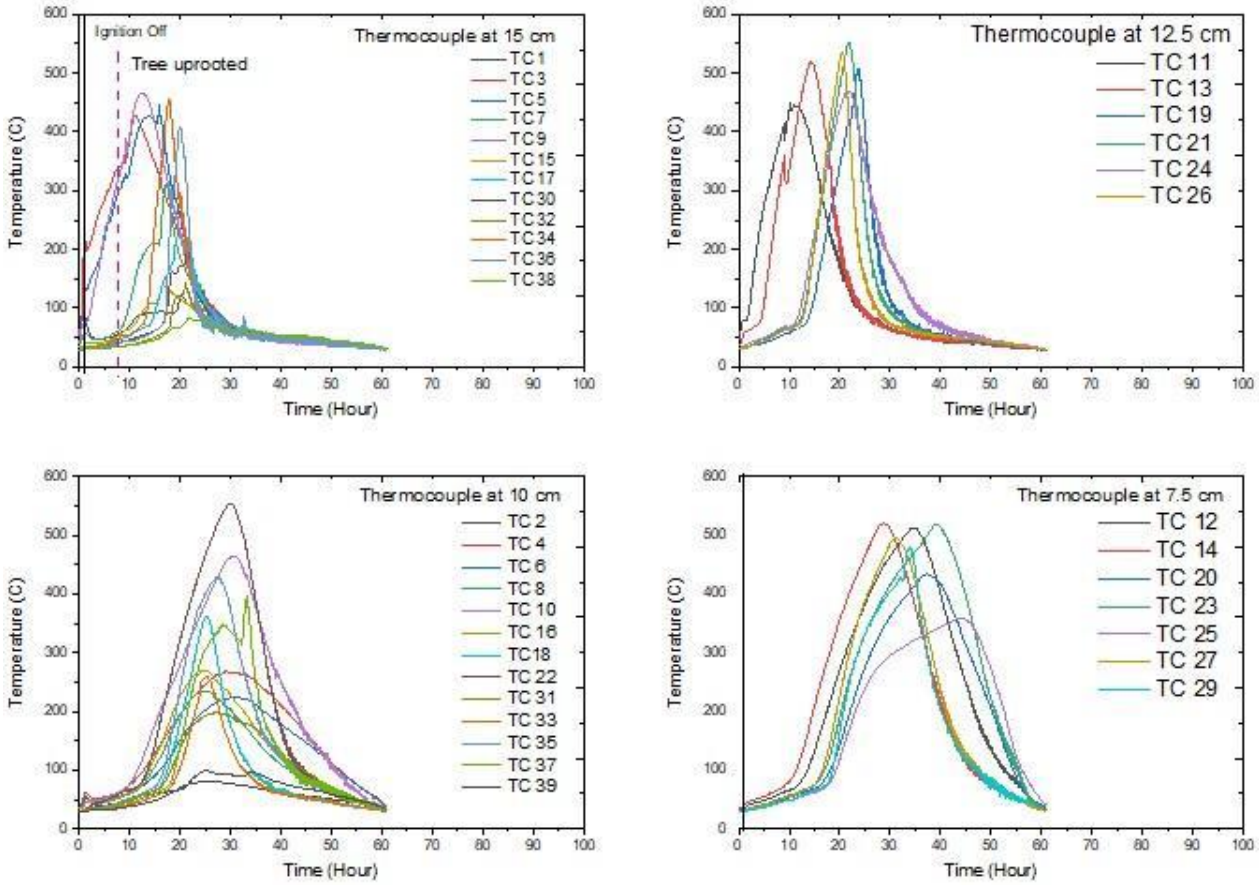


**Fig. 11.** Temperature distributions form thermocouple at different depth for vegetation treatment

**Fig. 12.** Smoldering residue seen inside the Reactor

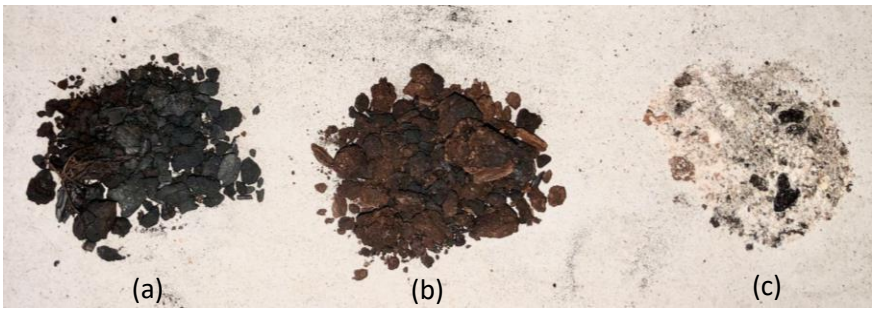


**Fig. 13.** Smoldering residue (a) Char (b) unburned peat (c) ashes

The smoldering combustion activities on the peat sample seem to leave the residue after it was finally extinguished (see Fig. 12) as similar to the baseline experiment. The grey to white powdery ashes was shown to be concentrated in the middle area of the reactor (Fig. 13 (c)), while char (Fig. 13 (b)) surrounded the ashes. The unburned peat (Fig. 13 (a)) can also be seen at the edges of the reactor due to the insufficient oxygen to create the smoldering process.

### Uprooting Phenomena

The phenomenon of the uprooted tree is shown in many occurrences, including windstorms [3], floods [7], and forest fires. The effect of stability disturbance has been shown to vegetation uprooting phenomena. From the experiment explained above, the smoldering propagation in peat soil tends to be in both vertical and horizontal directions of the peat. The underground fire inside the reactor caused the root system of the vegetation to be destroyed (as seen in Fig. 14). As the root of a tree performs many vital functions, including anchorage for the tree; therefore, once the root system is destroyed, the tree will not restrain the trunk's load and finally be uprooted.

Besides the destroyed root system, the disturbance in the peat soil also shows the effect on the uprooting of the tree. As is known, land subsidence occurs when smoldering fires propagate in peat soil (see Fig. 15). It occurs due to the loss of moisture content in the soil and leads to soil structural damage. This phenomenon also causes the tree to not be properly supported by the soil and finally uprooted after losing its stability.

**Fig. 14.** Destroyed Root System

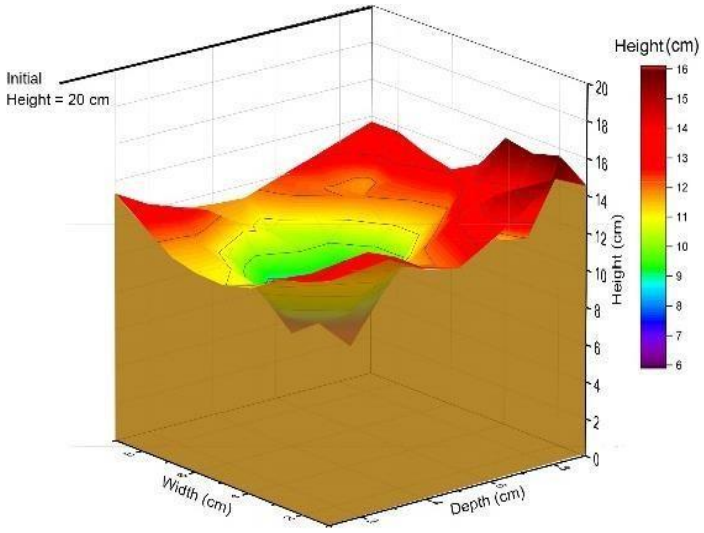


**Fig. 15.** Land subsidence in peat sample reactor after 60 hours of smoldering activity (for 3 cm in diameter tree)

In some flood occurrences, vegetation is often exposed to mortality due to uprooted phenomena [7]. A diminished mechanical anchoring in vegetation's root system, particularly for juvenile plants, the uprooting phenomena occurs as a consequence of a marked erosion gradually. Distinct from the fire and floods phenomena, which struck the stability of vegetation underground, the windstorm is known to damage trees directly above the ground. Based on a previous study [3], a study conducted in a 50-ha forest located in Amazonia Basin with the studied windstorm that occurred on October 25, 2012. About 11% of the trees were affected during the 90 km/h windstorm, with 70% being snapped, 20% uprooted, and 10% suffering a significant crown loss. Thus, both fires, floods, and storms can affect the tree and lead to forest damage from these results. Nevertheless, the mortality rate of the tree due to peatland fire is higher than the other event.

**Fig. 16.** Forest damage due to windstorm, Gardiner, et.al [6]

## CONCLUSION

Based on the experiment, the uprooting phenomena in peatlands due to peat fire can be depicted. The damaging effect of the smoldering phenomenon on the root system causes the root to lose its stability to support the tree until it was finally uprooted. The occurrence of land subsidence in the smoldering area causes the mass of the soil to reduce and unable to support the tree. For the peat fires that occur both underground and on-ground layers, the size of the tree events plays an essential role. This study indicates that the smaller tree was more susceptible to fire and uprooted easier. The smoldering propagation in peat soil tends to combust the vertical and horizontal area of the peat and is mainly concentrated in the middle area of the reactor. The smoldering combustion activities could propagate devoid of any obstruction and create the same pattern of smoldering propagation in the control reactor until it was finally extinguished after 60 until 65 hours.

## ACKNOWLEDGEMENT

The authors would like to thank the financial support provided by the Ministry of Education and Culture of the Republic of Indonesia through Penelitian Dasar Unggulan Perguruan Tinggi (PDUPT) 2022 managed by the Directorate for Research and Public Services (DRPM) Universitas Indonesia. The authors would also like to thank the Center for International Cooperation in Sustainable Management of Tropical Peatland (CIMTROP) Universitas Palangka Raya, and especially our colleague Mr. Kitso Kusin for their support in providing peat samples for this research.

## REFERENCES

[1] Schmoldt DL, DL Peterson, RE Keane, JM Lenihan, D Mckenzie, DR Weise, and DV Sandberg „Assessing the effects of fire disturbance on the ecosystem: a scientific agenda for research and management.“United States Department of Agriculture, Forest Service, General Technical Report (1999) PNW-GTR-455. 104pp

[2] Prat-Guitart, Nuria & Belcher, Claire & Hadden, Rory & Rein, Guillermo & Yearsley, Jon. (2015). A laboratory study of the effect of moisture content on the spread of smoldering peat fires. FLAMMA. 6. 35-38.

[3] Silvério, Divino & Brando, Paulo & Bustamante, Mercedes & Putz, F.E. & Magnabosco Marra, Daniel & Levick, Shaun & Trumbore, Susan. (2018). Fire, fragmentation, and windstorms: A recipe for tropical forest degradation. Journal of Ecology. 107. 10.1111/1365-2745.13076.

[4] Ramadhan, M.L., Palamba, P., Imran, F.A., Kosasih, E.A., Nugroho, Y.S. (2017). “Experimental study of the effect of water spray on the spread smoldering in Indonesian peat fires”. Fire Safety Journal 91 671 – 679

[5] Rein, Guillermo. “Smoldering Fires and Natural Fuels,” Fire Phenomena in the Earth System – An Interdisciplinary Approach to Fire Science. Ed. Belcher. Wiley and Sons, 2013. 15-34.

[6] Gardiner, Barry & Schuck, Andreas & Schelhaas, Mart-Jan & Orazio, Christophe & Blennow, Kristina & Nicoll, Bruce. (2013). Living with Storm Damage to Forests What Science Can Tell Us What Science Can Tell Us. 10.13140/2.1.1730.2400.

[7] K.Edmaier, P. Burlando, and P. Perona (2011). “Mechanicsms of vegetation uprooting by flow in alluvial non-cohesive sediment”. Hydrology and Earth System Science.

[8] Ming Yang, Pauline Defossez, Frederic Danjon and Thierry Fourcaud (2014). “Tree stability under wind: simulating uprooting with root breakage using a finite element method”. Oxford University Press.

[9] Fitter, A. and Stickland, T.: Fractal Characterization of Root System Architecture, Funct. Ecol., 6, 632–635, 1992

# KAPAS: Deterministic and Probabilistic Cellular Automata to Simulate Field-scale Flaming and Smouldering Wildfires in Tropical Peatlands

**Purnomo D. M. J., Muliawan C., Rein G.***

*Department of Mechanical Engineering and Leverhulme Centre for Wildfires, Environment and Society, Imperial College London, London, SW7 2AZ, United Kingdom.*
**Corresponding author's email: g.rein@imperial.ac.uk*

## ABSTRACT

Peatland wildfires involve flaming and smouldering combustion, releasing ancient carbon and create a positive feedback to climate change. While flaming consumes the surface vegetation, smouldering consumes the peat, the organic soil underneath the vegetation. The complexity of these two combustion types and the scale of wildfires, cause physics-based models to be too computationally expensive. Cellular automata, discrete computational models which use simple rules to simulate complex phenomena, were proved in our previous work to simulate peatland wildfires at the field-scale while remaining computationally light. This model ($KAPAS_P$), which use probabilistic rules, was calibrated in a computational domain with a specific cell size and time-step, thus, it is inacurrate for simulations in a domain with different cell size or time-step. These issues are important because the various size of peatland wildfires and the available data for model's input parameters require different spatial and temporal resolution. Here, we develop a deterministic cellular automata model for simulating peatland wildfires at the field scale ($KAPAS_D$), that can be used with any cell size and time-step. The flaming and smouldering spread rate prediction of $KAPAS_D$ have good agreement (less than 20% error) with experiments and benchmark model at different wind speed and moisture content. We validated the model against airborne footage of a peatland wildfire in Borneo in 2015, and found it has 80% accuracy in term of the number of smouldering hotspots. We found that the $KAPAS_D$ is similarly accurate to $KAPAS_P$ in term of burnt area (20% difference), thus, deterministic cellular automata offer potential for simulating peatland wildfires at any spatial and temporal resolution with similar accuracy to the probabilistic model. This work provides insights and tools for simulating peatland wildfires that can help mitigate them.

**KEYWORDS:** Wildfires, peatland, cellular automata, modelling.

## INTRODUCTION

Peatland wildfires are the largest fires on Earth which involve flaming and smouldering types of combustion [1]. Compared to flaming, smouldering is flameless, spreads slower, and has lower temperature. However, smouldering is more persitent and release higher amount of emission than flaming [2, 3, 4]. Fig. 1 shows the visual comparison between flaming and smouldering wildfires on peatland, which were obtained from a field-scale experiment in Indonesia in 2018. Peatland wildfires typically start with flaming wildfires which burn the surface vegetation. The flaming vegetation could ignite the organic soil (peat) underneath and create smouldering hotspots [1]. These hotspots spread and remain active for a long time even after the flaming wildfires extinghuish [5, 6]. The smouldering peat could rekindle the flaming vegetation at different locations when the environmental conditions are favourable [7]. The peat in peatland ecosystem is typically in wet condition [2], which deter its ignition via flaming vegetation. However, due to climate change and antropogenic activities, the wetness of the peat fail to preserve, facilitating smouldering peat wildfires [2]. For instance, in 1997, wildfires in peatlands in Indonesia intiate smouldering wildfires which sustained for weeks and released approximately 2.57Gt of carbon emission to the atmosphere [3]. The increasing trend of climate change and antrhopogenic activities in peatlands, indicate that the issues on peatland wildfires become emergent. Despite these, limited studies are dedicated to understand the phenomena on peatland wildfires.

Part of the reasons for the limited studies on peatland wildfires is the involved complexities in the phenomena. In computational study, state-of-the-art wildfire models do not facilitate the coexistence of flaming and smouldering wildfires, whereas physics-based models suffer from high computational demands, especially for field-scale modelling [1]. Alternative methods have been proposed to simulate field-scale peatland wildfires: cellular automata [1] and agent-based [8] models. While both the methods accurately simulate field-scale peatland wildfires which involve flaming and smouldering, the method of [8] is computationally more expensive than [1] due to the optimisation process of the model parameters in the model development. Model parameters optimisaition could also lead to an overfit for the calibration data, and consequently, relatively poor fit when the model is implemented for other cases.


**Fig. 1.** Comparison between flaming and smouldering wildfires. These photos are from field-scale experiment of flaming and smouldering wildfires on peatland. Photo taken by Wuquan Cui.

In this work we use cellular automata to simulate field-scale peatland wildfires. Cellular automata are discrete computational models which use simple rules, to simulate complex phenomena while remaining computationally light [1]. We improved our previous model [1] by implementing deterministic rules, instead of probabilistic. By using deterministic rules, the models can adapt to any spatial and temporal extent of the domain. The model in [1] can only be used with the one pair of cell size and time-step, otherwise its accuracy plummets. The usage of different cell size or time-step can only be implemented after a recalibration process. This inflexibility is undesirable since the data available, such as from satellites, are with different spatial and temporal resolution [9]. When deterministic rules are used, the change of cell size and time-step can be easily implemented by using simple mathematical operations.

This work has two main studies comprising a real peatland wildfire simulation and a comparison between deterministic and probabilistic cellular automata for peatland wildfire modelling. The real peatland wildfire simulation aims to develop deterministic cellular automata for a domain-flexible tool to simulate peatland wildfires which is based on a real peatland wildfire in Borneo. The comparative study aims to compare between deterministic and probabilistic cellular automata on their fidelity, accuracy, and computational efficiency to simulate flaming and smouldering wildfires on peatlands.

## METHODS

### Cellular automata

Cellular Automata (CA) are discrete computational models that use simple rules to simulate complex phenomena [9, 10]. These models consider a grid of cells domain, where each cell is in one of $k$ discrete states. The states of the cells update over discrete time-steps. The update of the cells' states is governed by a set of rules which are based on cells inside the neighbourhood. By choosing

representative states and rules, CA models can simulate complex physical phenomena while remain computationally light.

Different states and governing rules have been used in CA models for simulating wildfires [11, 12, 13, 14]. In this work, we integrate the deterministic rules in [11] into our previous model ($KAPAS_P$) [1] to develop a deterministic CA model for peatland wildfires. The rules in [11] stem from the change on the intrinsic value of a cell when cells within neighbourhood have different intrinsic values. When the intrinsic value of a cell reach a certain threshold, the state of the cell change. This rule mimics the accumulation of heat. Once the heat of an entity reach a certain level, the state of the entity change. We use a Moore neighbourhood – the eight cells directly surrounding the considered cell in a 3 × 3 square grid – which is the same neighbourhood used in [1, 11] due to its simplicity and accuracy. For simplicity, the deterministic model in this work will be referred to as $KAPAS_D$, which represents the modification of the model in [1] ($KAPAS_P$), by considering deteminisitc rules (D) instead of probabilistic rules (P).

**States and rules of the model**

There are 5 possible states for each cell in $KAPAS_D$: *surface vegetation (SV), flaming vegetation (FV), exposed peat (EP), smouldering peat (SP),* and *burned peat (BP)* (see Fig. 2a), which is the fewest number of states that can still enable the modelling of flaming and smouldering wildfires. Exposed peat represents a bare but unignited peat soil, because flaming has consumed the corresponding surface vegetation but it does not initiate smouldering peat. The flaming peat is not considered in $KAPAS_D$ because this phenomenon rarely happens [2].

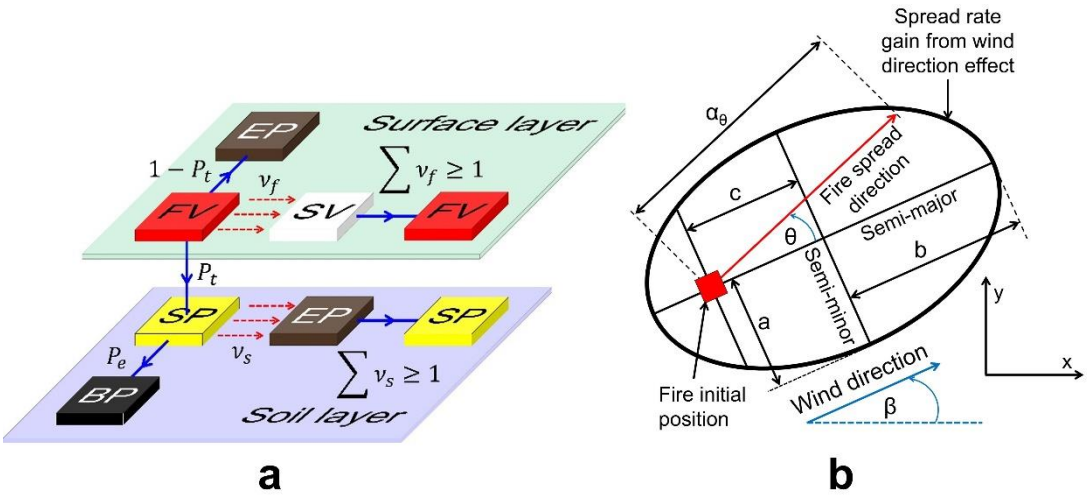


**Fig. 2.** (a) The states and rules in the model. The blue arrows represent the transition of states. The red dashed arrows represent the transfer of intrinsic values. *SV*, *FV*, *EP*, *SP*, and *BP* are surface vegetation, flaming vegetation,exposed peat, smouldering peat, and burned peat respectively. (b) The schematic of fire-wind angle factor ($\alpha_\theta$) in the model. The red square is a burning cell, which is also the focus of the ellipse, which spread the fire to its neighbors. The magnitude of the wind effect at the direction of $\theta$ relative to wind direction is equal to the length of the red arrow. a, b, and c are the ellipse parameters which are found based on [16].

$KAPAS_D$ considers three different surface vegetation: live vegetation, dead vegetation, and firebreak, which complies with the available data [1]. Live and dead vegetation facilitate the spread of flaming wildfire, with different spread rate, whereas firebreak stops the flaming spread. However, we assume that smouldering wildfire could still spread underneath the firebreak due to an overhang phenomenon where smouldering peat favour spread underground instead of on the surface [16]. To enable these rules, we use two separate layers of cellular automata: surface and soil layers, following [1] (Fig. 2a). By using this multi-layer approach, although the firebreaks are still intact in the surface layer,

smouldering peat can spread underneath which is captured in the soil layer. This multi-layer approach also facilitates the simulation of smouldering peat underneath intact surface vegetation. While the surface vegetation in the surface layer is undisturbed by the flaming, the peat can smouldering underneath in soil layer. This phenomenon has been observed in Artic peatland wildfire, which lead to overwintering wildfires [7]. However, the transition from smouldering peat to flaming vegetation when smouldering peat encounter intact surface vegetation is not considered in our model due to lack of scientific knowledge in the topic, whereas in the real phenomena, this transition did happen [7].

At the beginning, cells at particular location in the surface layer (based on the observation data) are set to be *FV*. Cells with *FV* states have intrinsic values of 1, whereas cells with *SV* states have intrinsic values of 0. When *FV* cells encounter *SV* cells within their neighbourhood, fraction of their intrinsic values ($\nu_f$) are transferred to the *SV* cells (Fig. 2a). While the intrinsic values of *SV* cells increase, the intrinsic values of *FV* cells are kept constant (i.e. 1) for simplicity. Once the intrinsic values of *SV* cells exceed 1, the *SV* cells transition to *FV* cells. *FV* cells could also ignite the cells in soil layer, with a probability of $P_t$, which facilitate the transition from *FV* to *SP*. If *FV* cells fail to ignite the peat underneath, these cells transition to *EP*. The *SP* cells in the soil layer are projected onto the surface layer. Therefore, *SP* cells in the soil layer correspond to *SP* cells in the surface layer. However, when the state of the corresponding cells in the surface layer are not *EP* (either vegetation or firebreak), the *SP* cells are not projected onto the surface layer. In the soil layer, *EP* cells have intrinsic values of 0, whereas *SP* cells have intrinsic values of 1. When *SP* cells encounter *EP* cells within their neighbourhood, fraction of their intrinsic values ($\nu_s$) are transferred to the *EP* cells (Fig. 2a). When the intrinsic values of *EP* cells exceed 1, these cells transition to *SP* cells. This rule is executed in the soil layer and independent of the surface layer. *SP* cells transition to *BP* cells with a probability of $P_e$.

**The variables in the model**

The value of $\nu_f$ (Eq. 1) is formulated based on Rothermel model [17] and Huygen's principle of wave propagation [16]. $\nu_f$ is a function of flaming spread rate ($R_f$), fire-wind angle factor ($\alpha_\theta$), spatiotemporal resolution ($\lambda$), neighbourhood factor ($\alpha_n$), and wind adjustment factor ($\alpha_w$). Spatiotemporal resolution contains the information of the domain which is formulated as the division between cell size ($\Delta x$) and time-step ($\Delta t$), i.e. $\lambda = \frac{\Delta x}{\Delta t}$. $R_f$ is determined following Rothermel model with corresponding vegetation type and wind speed ($U$). We assume a flat landscape which contains live and dead shrubs. We obtained the data of wind speed and direction ($\beta$) from local weather station. $\alpha_\theta$ is determined based on ellipse function of [16] (see Eq. 2). In Eq. 2, $\theta$ is fire spread direction relative to $\beta$, whereas $a$, $b$, and $c$ are the ellipse semi minor axis, semi major axis, and eccentricity respectively (see Fig. 2b). $a$, $b$, and $c$ are formulated in Eq. 3 to Eq. 5. $\alpha_n$ is considered to accommodate the effect of more than one affecting neighbouring cells to avoid overestimation of the spread rate. Therefore, since a Moore neighbourhood (8 surrounding cells) is selected, $\alpha_n$ is set to be 0.125. This neighbourhood also affect the accuracy of the spread rate in the simulation compared to the calculated spread rate when wind condition is considered. To resolve this issue, $\alpha_w$ is introduced to the model which is determined based on a calibration process with 10 different $U$. $\alpha_w$ is formulated as shown in Eq. 6. Athough the calibration proccess was only performed with one $\lambda$ (constant cell size and time-step), $\alpha_w$can be used for any $\lambda$. Fig. 3a shows the sensitivity analysis of the flaming spread rate of the simulation with 9 different $\lambda$, where the simulation has a maximum error of 21% when compared to the Rothermel model.

$$\nu_f = \alpha_w \cdot \alpha_n \cdot \alpha_\theta \cdot R_f / \lambda \tag{1}$$

$$\alpha_\theta = \left(\frac{a^2}{b - c\cos\theta}\right) \tag{2}$$

$$a = \left(\frac{r_H + 1}{2 r_L r_H}\right);\ b = \left(\frac{r_H + 1}{2 r_H}\right);\ c = \left(b - \frac{1}{r_H}\right) \tag{3}$$

$$r_L = 0.936 e^{0.2566U} + 0.461 e^{-0.1548U} - 0.397 \tag{4}$$

$$r_H = \frac{r_L + (r_L{}^2 - 1)^{0.5}}{r_L - (r_L{}^2 - 1)^{0.5}} \quad (5)$$

$$\alpha_w = -0.04U^2 + 0.59U + 1.59 \quad (6)$$

$P_t$ is formulated following [1] (Eq. 7) which is based on the experiment of [18], where it is a function of the peat moisture content (MC). $\nu_s$ (Eq. 8) is a function of smouldering spread rate ($R_s$), $\lambda$, and $\alpha_n$. $R_s$ is determined based on the interpolation from the experiments of smouldering spread rate at different peat MC [19, 20]. Fig. 3b shows the sensitivity analysis of the smouldering spread rate of the simulation with 7 different $\lambda$, where the simulation has a maximum error of 19% compared to the spread rate from experiments. $P_e$ is selected arbitrarily to enable smouldering fire that remain active for a long time after flaming has extinguished, following the value used in [1] ($5 \times 10^{-7}$).

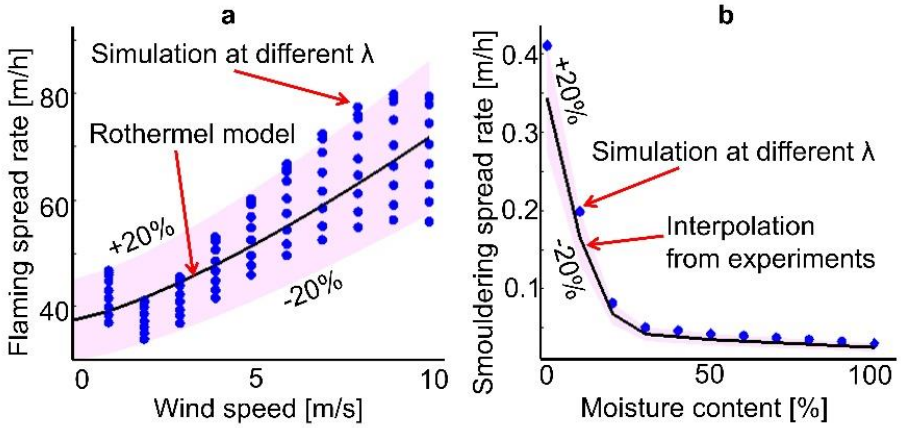


**Fig. 3.** (a) The comparison of flaming spread rate with different wind speed between Rothermel model and the simulation of $\text{KAPAS}_\text{D}$ at different spatiotemporal resolution ($\lambda$). (b) The comparison of smouldering spread rate with different moisture content between experiments and the simulation at different spatiotemporal resolution.

The spread to the diagonal neighbours in both flaming and smouldering requires an additional factor [11]. This factor is derived from the ratio between triangle and rectangular area [11]. The diagonal spread corresponds to the triangle burnt area, whereas the non-diagonal spread correspond to rectangular burnt area. Therefore, from a simple arithmetical operation, the $\nu_f$ and $\nu_s$ are multiplied by 0.83 when the fire spread to the diagonal neighbours, following [11].

$$P_t = (1 + 0.17e^{0.12MC})^{-1} \quad (7)$$

$$\nu_s = \alpha_n \cdot R_s/\lambda \quad (8)$$

## RESULTS AND DISCUSSION

We used $\text{KAPAS}_\text{D}$ to simulate a peatland wildfire in Borneo in 2015. This wildfire was chosen because we obtained a fuel map and airborne footage of the wildfire from [21]. Fig. 4a shows the footage of the peatland wildfire, where from the drone footage, smouldering hotspots are observed (see red dots in Fig. 4a). There are four plots at which the flaming wildfire initiated (region 1 to 4). Flaming wildfires in these four plots initiate 47 smouldering hotspots at randomly distributed locations. We used a $\Delta x$ of 5m and a $\Delta t$ of 180s to simulate this peatland wildfire. We used this computational domain because this domain is the most course domain at which Courant–Friedrichs–Lewy (CFL) condition is still satisfied. CFL condition limits the cell size and time-step to avoid the diffusion of an entity exceeding one cell at one time-step. Therefore, the maximum value of $R_f/\lambda$ in Eq. 1 should be less than 1. The course domain is selected to minimize the computational time. Fig.

4b shows the simulation results of the model. The model is run to simulate 90 days of the wildfire, however, Fig. 4b shows the result on 40 days of the wildfire (for visualization purposes). We found that the total number of smouldering hotspots (57 hotspots) in the simulation with peat MC of 75%, a typical MC in tropical peatland [21], has a good agreement with the footage (21% error). The difference in the hotspots distribution between footage and simulation can be caused by the variability in the nature. Our model assume a uniform peat MC across the landscape. However, in the natural peatland, the MC of the peat soil vary spatially and temporally [23]. Therefore, while the smouldering hotspots in the simulation are distributed similarly within and across plots, the hotspots in the footage are concentrated to some areas. We predicted that in 90 days 114 ha of peat could burn from these hotspots.

We then compared $KAPAS_D$ with our previous model ($KAPAS_P$) [1], firstly, using a hypothetical domain, and secondly, using the domain of the peatland wildfire in Borneo. In the hypothetical domain, we use a grid of 400 × 400 cells (with same cell size and time-step) to simulate flaming and smouldering wildfires independently. We found that the main difference between $KAPAS_D$ and $KAPAS_P$ is the burnt scar where $KAPAS_D$ has smooth fire front and $KAPAS_P$ has irregular front both in flaming and smouldering (see Fig. 5). The shape of the burnt scar in $KAPAS_D$ and $KAPAS_P$ are similar, in which they have ovoid shape of burnt scar in the flaming simulation and circular in the smouldering simulation. The circular shape of the burnt scar in smouldering simulation is to be expected, since in uniform fuel condition, the fire spread to the eight direction (the Moore neighbourhood) with similar rate. Meanwhile, the ovoid shape of burnt scar in flaming simulation is because of the anisotropy caused by the wind effect. The fire spread with downwind direction is strengthen by the wind, whereas the upwind direction is weakened by the wind. The ovoid shape, instead of ellipse, resulted in the simulation is caused by the limited number of fire spread direction, which is determined by the neighbourhood. If the number of spread direction in the simulation is sufficient, the simulation will result an ellipse shape of burnt scar, on which the governing rules of the model for flaming wildfires are based. The difference in fire front between $KAPAS_D$ and $KAPAS_P$ is caused by the uncertainty of the spread of the $KAPAS_P$. While $KAPAS_D$ always results the same burnt scar, $KAPAS_P$ has uncertainty in the burn scar resulted. This uncertainty is visualized by the non-smoothness (irregularities) of the fire front in both flaming and smouldering simulations.

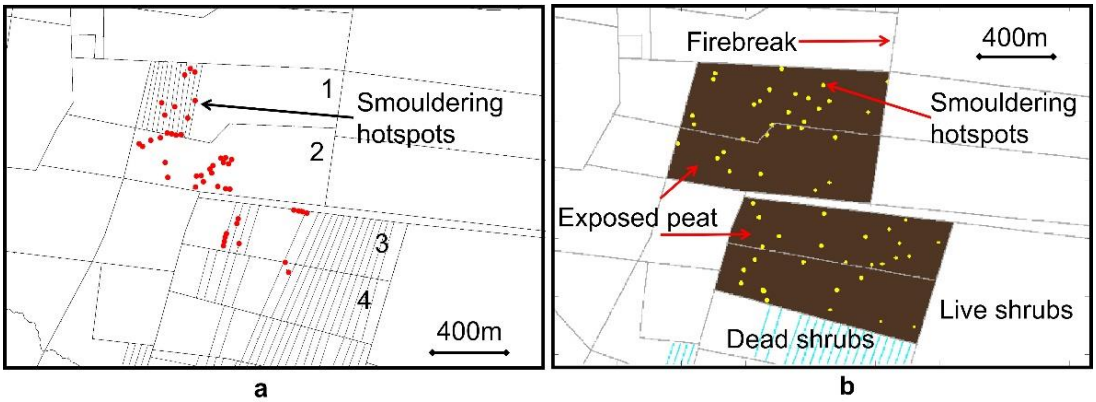


**Fig. 4.** (a) Smouldering hotspots in a peatland wildfire in Borneo in 2015, based on airborne footage. Flaming are initiated at region 1 to 4. The red dots are the locations of the smouldering hotspots observed from a drone. (b) Simulation of the peatland wildfire in (a). The yellow dots are the predicted locations of the smouldering hotspots.

The non-smoothness of the fire front and the uncertainty of the burnt scar shape is required to model a real peatland wildfire. The variability of nature, such as caused by landscape heterogeneity, cause the shape of the burnt scar unlikely to be a smooth Euclidean geometry (e.g. circle, ellipse). Therefore, while the results form $KAPAS_D$ and $KAPAS_P$ are similar, $KAPAS_P$ is more realistic than $KAPAS_D$ due the consideration of the variability of nature.

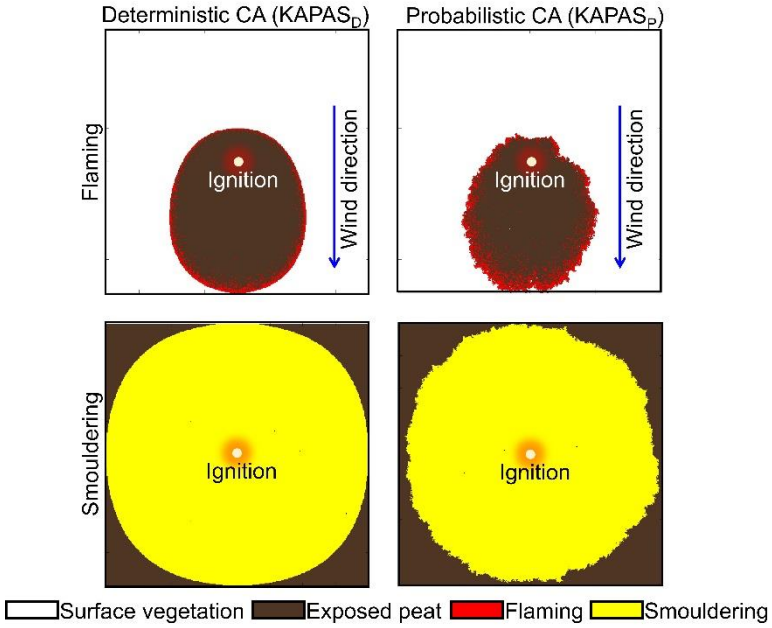


**Fig. 5.** The comparison of burnt scar of flaming and smouldering wildfires between deterministic CA (KAPAS$_D$) and probabilistic CA (KAPAS$_P$) in a hypothetical domain. The red glowing white circle is the location of the ignition and the blue arrow is the direction of the wind for flaming wildfire simulation.

Fig. 6 shows the comparison between KAPAS$_D$ and KAPAS$_P$ when the models are applied to simulate the Borneo peatland wildfire. On day 1 when the flaming was just started, the shape of flaming burnt scars from both the models conform with the finding in Fig. 4, where although both the models result in ovoid shape, the fire front in KAPAS$_P$ is not smooth, unlike the KAPAS$_D$. On day 2 when the flaming spreads relatively distant from the ignition location, the fire front of KAPAS$_D$ simulation form a curve (circular wedge), whereas KAPAS$_P$ form a non-smooth straight line. This finding indicates that KAPAS$_D$ is stronger than KAPAS$_P$ in maintaining its basic shape of flaming burnt scar (ovoid). Another observable difference between KAPAS$_D$ and KAPAS$_P$ found on day 2 is the present of unburned vegetation in KAPAS$_P$. While the noise-like dots in the KAPAS$_D$ on day 2 represent the smouldering hotspots which were initiated, the noise-like dots in the KAPAS$_P$ on day 2 comprises both smouldering hotspots and patches of unburned vegetation. These unburned patches are commonly observed in the real event of wildfire, which then indicate that KAPAS$_P$ can simulate peatland wildfires more realistically than KAPAS$_D$. However, the time required by the flaming wildfire to completely sweep the landscape between KAPAS$_D$ and KAPAS$_P$ are similar (within 10% difference) on each plot. Therefore, KAPAS$_D$ and KAPAS$_P$ have similar accuracy on flaming wildfire simulation in term of flaming spread rate.

The more realistic result of KAPAS$_P$ is also observed on day 40, where the growing smouldering hotspots in KAPAS$_D$ are almost perfect circles, whereas the hotspots in KAPAS$_P$, shape more irregularly. However, the number of smouldering hotspots from KAPAS$_D$ and KAPAS$_P$ are similar with less than 20% difference. This similarity is due to the same concept used for transition from flaming vegetation to smouldering peat. Meanwhile, the difference is caused by the slightly different behaviour of the flaming vegetation which initiated the smouldering peat.

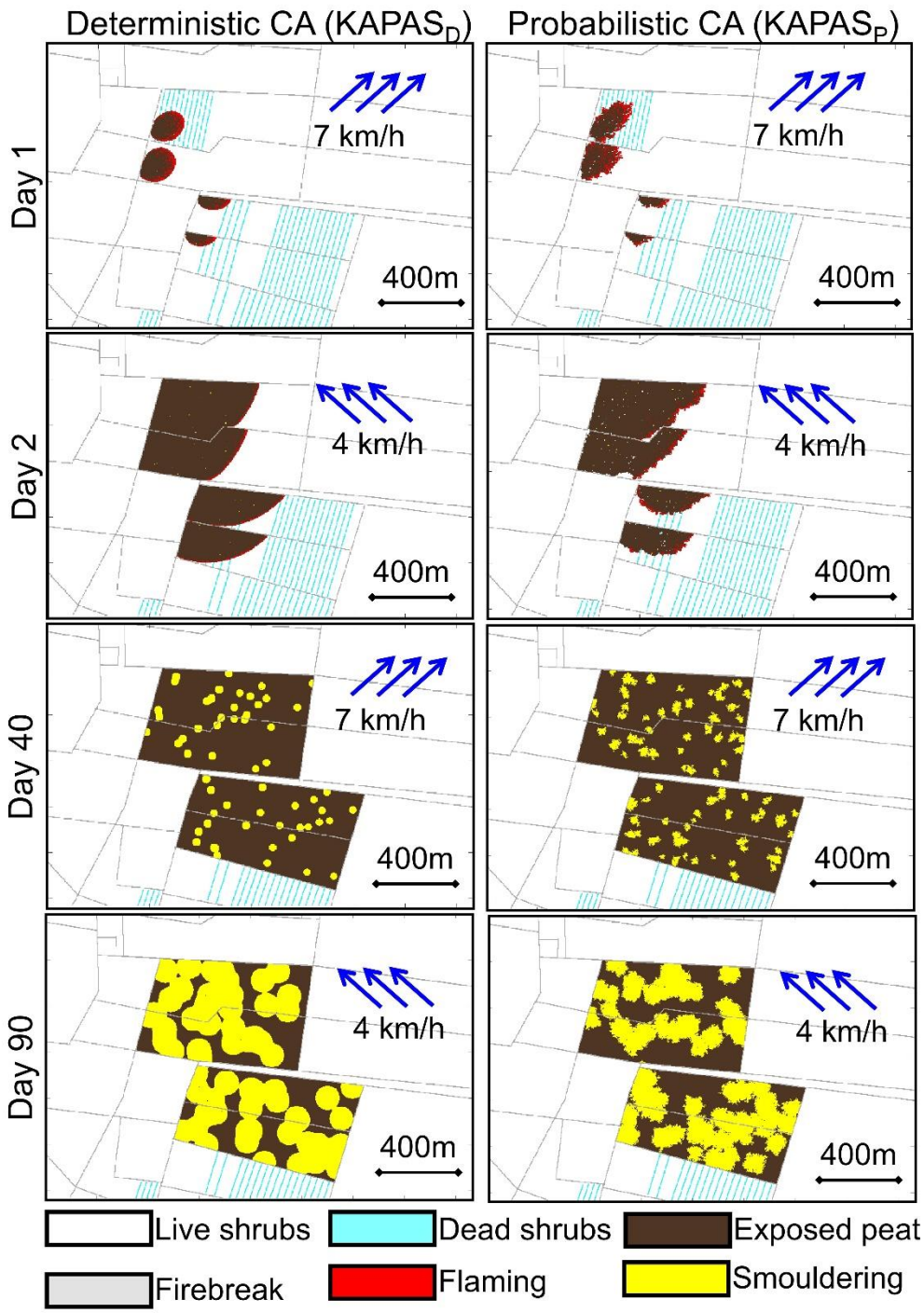


**Fig. 6.** The comparison of the simulation of Borneo peatland wildfire between deterministic CA (KAPAS$_D$) and probabilistic CA (KAPAS$_P$) at different times. The blue arrows are the direction of the wind for flaming wildfire simulation. Day 1 represents the start of flaming wildfire, day 2 represents the spread of flaming wildfire and the creation of smouldering hotspots, day 40 represents the spread of smouldering hotspots, and day 90 represents the merging of smouldering hotspots.

Both $KAPAS_D$ and $KAPAS_P$ successfully simulate merging phenomena of smouldering hotspots (see day 90), where number of individual hotspots merge and become larger hotspots which significantly increase the difficulty of the firefighting attempts. At the end of the simulation, the total smouldering burnt area from $KAPAS_D$ and $KAPAS_P$ differs by 28%. This difference is the largest difference on simulation results between $KAPAS_D$ and $KAPAS_P$. Other differences in results between the two models are less than 28%. Therefore, $KAPAS_D$ is similarly accurate to $KAPAS_P$. The computational efficiency of $KAPAS_D$ is also similar to $KAPAS_P$ with computational time of 1.61h and 1.93h respectively. Although the results from $KAPAS_P$ are more realistic, $KAPAS_D$ benefits from its ability to be implemented to any spatial and temporal extent without recalibration processes. Therefore, $KAPAS_D$ offers potential to simulate peatland wildfires at any spatial and temporal resolution with similar accuracy and computational efficiency to $KAPAS_P$.

We further run the models to simulate Borneo peatland wildfire when the peat moisture content is different, from 0% to 160% moisture contents with 20% increment. We found that $KAPAS_D$ and $KAPAS_P$ result in similar number of hotspots and smouldering burnt area at any moisture content (see Fig. 7). The largest difference of number of hotspots between the two models are at MC higher than 100%. At MC higher than 100%, $KAPAS_D$ do not create any smouldering hotspot, whereas $KAPAS_P$ successfully initiate few smouldering hotspots (see Fig. 7a). This finding indicates that the critical MC of smouldering hotspot creation in $KAPAS_D$ is lower than in $KAPAS_P$. Therefore, at a high MC, $KAPAS_D$ could underestimate the damage caused by smouldering wildfire. Fig. 6b clearly shows this underestimation when the peat MC is higher than 100%. While the burnt areas in $KAPAS_D$ are zero at high MC, the burnt areas in $KAPAS_P$ are close to 1ha. Only at MC of 160% $KAPAS_P$ result in zero smouldering burnt area.

While the creation of smouldering hotspots are stronger in $KAPAS_P$, the growth of these hotspots are stronger in $KAPAS_D$, especially at MC between 50% and 80% (see Fig. 7b) which is the typical MC in tropical peatland [21]. With similar number of hotspots, the smouldering burnt area in $KAPAS_D$ is 10% - 20% larger than in $KAPAS_P$ at MC between 50% and 80%. These findings infer that the flaming in $KAPAS_P$ more strongly initiate smouldering hotspots than in $KAPAS_D$. However, once the smouldering hotspots are created, their growth are stronger in $KAPAS_D$ than in $KAPAS_P$.

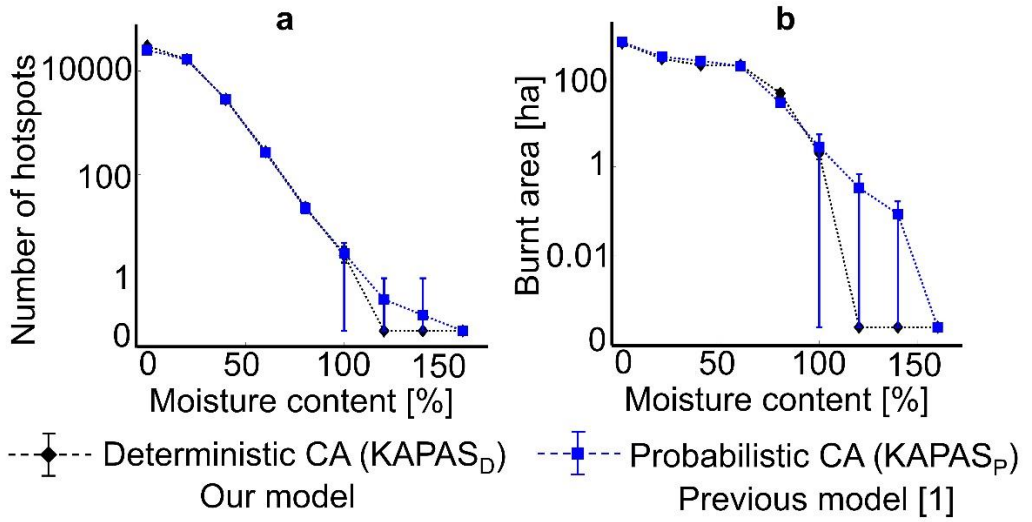


**Fig. 7.** The comparison of (a) number of hotspots and (b) smouldering burnt area between deterministic CA ($KAPAS_D$) and probabilistic CA ($KAPAS_P$) at different peat moisture contents. Each of the simulation was repeated 5 times to capture the uncertainties in the models.

## CONCLUSIONS

We developed here the first deterministic cellular automata model to simulate peatland wildfires at the field-scale, $KAPAS_D$. The model is validated against drone footage (over 523 ha of landscape) of a peatland wildifre in Borneo in 2015, and result in 80% accuracy on the number of smouldering hotspots. The growth of these hotspots for 90 days, the typical duration of wildfire season in Indonesia, could burn 114 ha of the peat. During the 90 days of the simulation time, $KAPAS_D$ simulated the multiple ignitions of flaming wildfires, the spread of these wildfires that also nucleate smouldering hotspots, the extinction of flaming wildfires and the growth of smouldering hotspots, and the merging of smouldering hotspots when its growth are sufficiently large. We compared the deterministic CA model ($KAPAS_D$) with probabilistic CA model from our previous work ($KAPAS_P$) [1], and found that both the models have similar computational time (10% difference) and similar accuracy in number of smouldering hotspots and smouldering burnt area (within 20% difference). Although both $KAPAS_D$ and $KAPAS_P$ have ovoid shape for flaming burn scar and circular shape for smouldering burn scar, the perimeter of these burn scars are smooth in $KAPAS_D$ but irregular in $KAPAS_P$. This finding indicates that $KAPAS_D$ has a more realistic result than $KAPAS_P$, since the perimeter of the burn scar is unlikely to be smooth due to the variability in nature. However, $KAPAS_D$ benefits from its ability to be used in any spatial and temporal extent, which is of utmost important due to the variability of spatial and temporal extent of peatland wildfires. $KAPAS_D$ and $KAPAS_P$ were further used to predict the burnt area of smouldeirng peat when the peat moisture content are varied. We found an exponential relationship between burnt area and peat moisture content obtained from both the models. However, the nucleation of smouldering hotspots were stronger in $KAPAS_P$, whereas its growth were stronger in $KAPAS_D$. This finding indicates that although $KAPAS_D$ and $KAPAS_P$ are similarly accurate, the difference in rules between the models influence the dynamics of the flaming and smouldering spread, especially near the critical conditions such as critical peat moisture content to initiate smouldering hotspots, emphasizing the importance of the comparison between the models. This work provides analysis and insights on the development of modelling tools for simulating peatland wildfires.

## ACKNOWLEDGEMENT

This research was funded by European Research Council (ERC) Consolidator Grant HAZE (682587), and Indonesian Endowment Fund for Education (LPDP).

## REFERENCES

[1] D. M. J. Purnomo, M. Bonner, M. Samaneh and G. Rein, "Using cellular automata to simulate field-scale flaming and smouldering wildfires in tropical peatlands," *Proceedings of the Combustion Institute*, 2020. doi: 10.1016/j.proci.2020.08.052.

[2] X. Huang and G. Rein, "Computational study of critical moisture and depth of burn in peat fires," *International Journal of Wildland Fire*, vol. 24, p. 798–808, 2015. doi: 10.1071/WF14178.

[3] G. Rein, "Smouldering Fires and Natural Fuels," in *Fire Phenomena in the Earth System – An Interdisciplinary Approach to Fire Science*, Wiley and Sons, 2013, pp. 15-34. doi: 10.1002/9781118529539.ch2.

[4] Y. Hu, N. Fernandez-Anez, T. E. L. Smith and G. Rein, "Review of emissions from smouldering peat fires and their contribution to regional haze episodes," *International Journal of Wildland Fire*, vol. 27, p. 293–312, 2018.

[5] M. R. Turetsky, B. Benscoter, S. Page, G. Rein, G. R. van der Werf and A. Watts, "Global vulnerability of peatlands to fire and carbon loss," *Nature Geoscience*, vol. 8, pp. 11 - 14, 2015.

[6] G. Rein and X. Huang, "Smouldering wildfires in peatlands, forests and the arctic: Challenges and perspectives," *Current Opinion in Environmental Science & Health,* vol. 24, 2021. doi: 10.1016/j.coesh.2021.100296.

[7] R. C. Scholten, R. Jandt, E. A. Miller, B. M. Rogers and S. Veraverbek, "Overwintering fires in boreal forests," *Nature,* vol. 593, p. 399–404, 2021. doi: 10.1038/s41586-021-03437-y.

[8] K. Widyastuti, M. A. Imron, S. T. Pradopo, H. Suryatmojo, B. M. Sopha, A. Spessa and U. Berger, "PeatFire: an agent-based model to simulate fire ignition and spreading in a tropical peatland ecosystem," *International Journal of Wildland Fire,* vol. 30, p. 71–89, 2021. doi: 10.1071/WF19213.

[9] C. Burke, S. Wich, K. Kusin, O. McAree, M. E. Harrison, B. Ripoll, Y. Ermiasi, M. Mulero-Pázmány and S. Longmore, "Thermal-Drones as a Safe and Reliable Method for Detecting Subterranean Peat Fires," *Drones,* vol. 3. doi:10.3390/drones3010023, 2019.

[10] S. Wolfram, "Cellular automata as models of complexity," *Nature,* vol. 311, pp. 419-424, 1984. doi: 10.1038/311419a0.

[11] J. von Neumann, Theory of Self-Reproducing Automata, Urbana: University of Illinois Press, 1966.

[12] I. Karafyllidis and A. Thanailakis, "A model for predicting forest fire spread using cellular automata," *Ecological Modelling,* vol. 99, pp. 87-97, 1997. doi: 10.1016/S0304-3800(96)01942-4.

[13] C. Favier, "Percolation model of fire dynamic," *Physics Letters A,* vol. 330, no. 5, pp. 396-401, 2004. doi: 10.1016/j.physleta.2004.07.053.

[14] C. M. Belcher, J. M. Yearsley, R. M. Hadden, J. C. McElwain and G. Rein, "Baseline intrinsic flammability of Earth's ecosystems estimated from paleoatmospheric oxygen over the past 350 million years," *Proceedings of the National Academy of Sciences of the United States of America,* vol. 107, no. 52, p. 22448–22453, 2010. doi: 10.1073/pnas.1011974107.

[15] N. Fernandez-Anez, K. Christensen, V. Frette and G. Rein, "Simulation of fingering behavior in smoldering combustion using a cellular automaton," *Physical Review E,* vol. 99, p. 023314(13), 2019. doi: 10.1103/PhysRevE.99.023314.

[16] X. Huang, F. Restuccia, M. Gramola and G. Rein, "Experimental study of the formation and collapse of an overhang in the lateral spread of smouldering peat fires," *Combustion and Flame,* vol. 168, pp. 393-402, 2016. doi: 10.1016/j.combustflame.2016.01.017.

[17] M. Alexander, "Estimating the length-to-breadth ratio of elliptical forest fire patterns," in *Pages 287-304 in Proceedings of the 8th Conference on Fire and Forest Meteorology*, Detroit, MI. Bethesda, MD: Society of American Foresters, 1985.

[18] R. C. Rothermel, "A mathematical model for predicting fire spread in wildland fuels," USDA Forest Service Research Paper INT-115, Washington, DC, 1972.

[19] W. H. Frandsen, "Ignition probability of organic soils," *Canadian Journal of Forest Research,* vol. 27, pp. 1471-1477, 1997. doi: 10.1139/x97-106.

[20] N. Prat-Guitart, G. Rein, R. Hadden, C. Belcher and J. Yearsley, "Propagation probability and spread rates of self-sustained smouldering fires under controlled moisture content and bulk density conditions," *International Journal of Wildland Fire,* vol. 25, no. 4, pp. 456-465, 2016. doi: 10.1071/WF15103.

[21] W. Eyal, S. Moafi, J. Men, N. Czyz and N. Ahmed, "Ecocide in Indonesia," Forensic Architecture, 2017. [Online]. Available: https://forensic-architecture.org/investigation/ecocide-in-indonesia.

[22] R. W. Nusantara, R. Hazriani and U. E. Suryadi, "Water-table Depth and Peat Subsidence Due to Land-use Change of Peatlands," in *IOP Conference Series: Earth and Environmental Science,* 2018. doi :10.1088/1755-1315/145/1/012090.

[23] M. Bechtold, G. De Lannoy, R. Reichle, D. Roose, N. Balliston and I. Burdun, "Improved groundwater table and L-band brightness temperature estimates for Northern Hemisphere peatlands using new model physics and SMOS observations in a global data assimilation framework," *Remote Sensing of Environment,* vol. 246, 2020. doi: 10.1016/j.rse.2020.111805.

# KAPAS: Deterministic and Probabilistic Cellular Automata to Simulate Field-scale Flaming and Smouldering Wildfires in Tropical Peatlands

**Purnomo D. M. J., Muliawan C., Rein G.***

*Department of Mechanical Engineering and Leverhulme Centre for Wildfires, Environment and Society, Imperial College London, London, SW7 2AZ, United Kingdom.*
**Corresponding author's email: g.rein@imperial.ac.uk*

## ABSTRACT

Peatland wildfires involve flaming and smouldering combustion, releasing ancient carbon and create a positive feedback to climate change. While flaming consumes the surface vegetation, smouldering consumes the peat, the organic soil underneath the vegetation. The complexity of these two combustion types and the scale of wildfires, cause physics-based models to be too computationally expensive. Cellular automata, discrete computational models which use simple rules to simulate complex phenomena, were proved in our previous work to simulate peatland wildfires at the field-scale while remaining computationally light. This model ($KAPAS_P$), which use probabilistic rules, was calibrated in a computational domain with a specific cell size and time-step, thus, it is inacurrate for simulations in a domain with different cell size or time-step. These issues are important because the various size of peatland wildfires and the available data for model's input parameters require different spatial and temporal resolution. Here, we develop a deterministic cellular automata model for simulating peatland wildfires at the field scale ($KAPAS_D$), that can be used with any cell size and time-step. The flaming and smouldering spread rate prediction of $KAPAS_D$ have good agreement (less than 20% error) with experiments and benchmark model at different wind speed and moisture content. We validated the model against airborne footage of a peatland wildfire in Borneo in 2015, and found it has 80% accuracy in term of the number of smouldering hotspots. We found that the $KAPAS_D$ is similarly accurate to $KAPAS_P$ in term of burnt area (20% difference), thus, deterministic cellular automata offer potential for simulating peatland wildfires at any spatial and temporal resolution with similar accuracy to the probabilistic model. This work provides insights and tools for simulating peatland wildfires that can help mitigate them.

**KEYWORDS:** Wildfires, peatland, cellular automata, modelling.

## INTRODUCTION

Peatland wildfires are the largest fires on Earth which involve flaming and smouldering types of combustion [1]. Compared to flaming, smouldering is flameless, spreads slower, and has lower temperature. However, smouldering is more persitent and release higher amount of emission than flaming [2, 3, 4]. Fig. 1 shows the visual comparison between flaming and smouldering wildfires on peatland, which were obtained from a field-scale experiment in Indonesia in 2018. Peatland wildfires typically start with flaming wildfires which burn the surface vegetation. The flaming vegetation could ignite the organic soil (peat) underneath and create smouldering hotspots [1]. These hotspots spread and remain active for a long time even after the flaming wildfires extinghuish [5, 6]. The smouldering peat could rekindle the flaming vegetation at different locations when the environmental conditions are favourable [7]. The peat in peatland ecosystem is typically in wet condition [2], which deter its ignition via flaming vegetation. However, due to climate change and antropogenic activities, the wetness of the peat fail to preserve, facilitating smouldering peat wildfires [2]. For instance, in 1997, wildfires in peatlands in Indonesia intiate smouldering wildfires which sustained for weeks and released approximately 2.57Gt of carbon emission to the atmosphere [3]. The increasing trend of climate change and antrhopogenic activities in peatlands, indicate that the issues on peatland wildfires become emergent. Despite these, limited studies are dedicated to understand the phenomena on peatland wildfires.

Part of the reasons for the limited studies on peatland wildfires is the involved complexities in the phenomena. In computational study, state-of-the-art wildfire models do not facilitate the coexistence of flaming and smouldering wildfires, whereas physics-based models suffer from high computational demands, especially for field-scale modelling [1]. Alternative methods have been proposed to simulate field-scale peatland wildfires: cellular automata [1] and agent-based [8] models. While both the methods accurately simulate field-scale peatland wildfires which involve flaming and smouldering, the method of [8] is computationally more expensive than [1] due to the optimisation process of the model parameters in the model development. Model parameters optimisaition could also lead to an overfit for the calibration data, and consequently, relatively poor fit when the model is implemented for other cases.


**Fig. 1.** Comparison between flaming and smouldering wildfires. These photos are from field-scale experiment of flaming and smouldering wildfires on peatland. Photo taken by Wuquan Cui.

In this work we use cellular automata to simulate field-scale peatland wildfires. Cellular automata are discrete computational models which use simple rules, to simulate complex phenomena while remaining computationally light [1]. We improved our previous model [1] by implementing deterministic rules, instead of probabilistic. By using deterministic rules, the models can adapt to any spatial and temporal extent of the domain. The model in [1] can only be used with the one pair of cell size and time-step, otherwise its accuracy plummets. The usage of different cell size or time-step can only be implemented after a recalibration process. This inflexibility is undesirable since the data available, such as from satellites, are with different spatial and temporal resolution [9]. When deterministic rules are used, the change of cell size and time-step can be easily implemented by using simple mathematical operations.

This work has two main studies comprising a real peatland wildfire simulation and a comparison between deterministic and probabilistic cellular automata for peatland wildfire modelling. The real peatland wildfire simulation aims to develop deterministic cellular automata for a domain-flexible tool to simulate peatland wildfires which is based on a real peatland wildfire in Borneo. The comparative study aims to compare between deterministic and probabilistic cellular automata on their fidelity, accuracy, and computational efficiency to simulate flaming and smouldering wildfires on peatlands.

## METHODS

### Cellular automata

Cellular Automata (CA) are discrete computational models that use simple rules to simulate complex phenomena [9, 10]. These models consider a grid of cells domain, where each cell is in one of $k$ discrete states. The states of the cells update over discrete time-steps. The update of the cells' states is governed by a set of rules which are based on cells inside the neighbourhood. By choosing

representative states and rules, CA models can simulate complex physical phenomena while remain computationally light.

Different states and governing rules have been used in CA models for simulating wildfires [11, 12, 13, 14]. In this work, we integrate the deterministic rules in [11] into our previous model ($KAPAS_P$) [1] to develop a deterministic CA model for peatland wildfires. The rules in [11] stem from the change on the intrinsic value of a cell when cells within neighbourhood have different intrinsic values. When the intrinsic value of a cell reach a certain threshold, the state of the cell change. This rule mimics the accumulation of heat. Once the heat of an entity reach a certain level, the state of the entity change. We use a Moore neighbourhood – the eight cells directly surrounding the considered cell in a 3 × 3 square grid – which is the same neighbourhood used in [1, 11] due to its simplicity and accuracy. For simplicity, the deterministic model in this work will be referred to as $KAPAS_D$, which represents the modification of the model in [1] ($KAPAS_P$), by considering deteminisitc rules (D) instead of probabilistic rules (P).

**States and rules of the model**

There are 5 possible states for each cell in $KAPAS_D$: *surface vegetation (SV), flaming vegetation (FV), exposed peat (EP), smouldering peat (SP),* and *burned peat (BP)* (see Fig. 2a), which is the fewest number of states that can still enable the modelling of flaming and smouldering wildfires. Exposed peat represents a bare but unignited peat soil, because flaming has consumed the corresponding surface vegetation but it does not initiate smouldering peat. The flaming peat is not considered in $KAPAS_D$ because this phenomenon rarely happens [2].

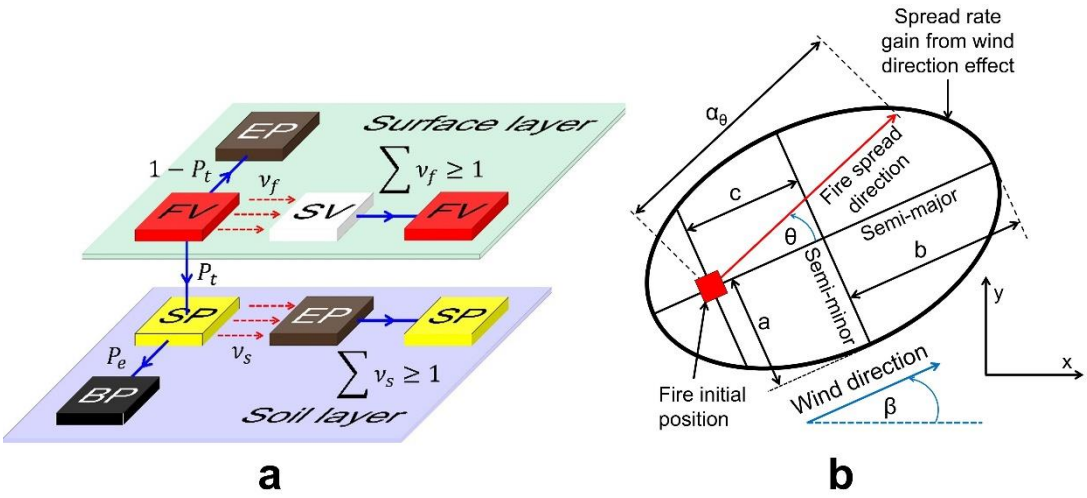


**Fig. 2.** (a) The states and rules in the model. The blue arrows represent the transition of states. The red dashed arrows represent the transfer of intrinsic values. *SV*, *FV*, *EP*, *SP*, and *BP* are surface vegetation, flaming vegetation,exposed peat, smouldering peat, and burned peat respectively. (b) The schematic of fire-wind angle factor ($\alpha_\theta$) in the model. The red square is a burning cell, which is also the focus of the ellipse, which spread the fire to its neighbors. The magnitude of the wind effect at the direction of $\theta$ relative to wind direction is equal to the length of the red arrow. a, b, and c are the ellipse parameters which are found based on [16].

$KAPAS_D$ considers three different surface vegetation: live vegetation, dead vegetation, and firebreak, which complies with the available data [1]. Live and dead vegetation facilitate the spread of flaming wildfire, with different spread rate, whereas firebreak stops the flaming spread. However, we assume that smouldering wildfire could still spread underneath the firebreak due to an overhang phenomenon where smouldering peat favour spread underground instead of on the surface [16]. To enable these rules, we use two separate layers of cellular automata: surface and soil layers, following [1] (Fig. 2a). By using this multi-layer approach, although the firebreaks are still intact in the surface layer,

smouldering peat can spread underneath which is captured in the soil layer. This multi-layer approach also facilitates the simulation of smouldering peat underneath intact surface vegetation. While the surface vegetation in the surface layer is undisturbed by the flaming, the peat can smouldering underneath in soil layer. This phenomenon has been observed in Artic peatland wildfire, which lead to overwintering wildfires [7]. However, the transition from smouldering peat to flaming vegetation when smouldering peat encounter intact surface vegetation is not considered in our model due to lack of scientific knowledge in the topic, whereas in the real phenomena, this transition did happen [7].

At the beginning, cells at particular location in the surface layer (based on the observation data) are set to be *FV*. Cells with *FV* states have intrinsic values of 1, whereas cells with *SV* states have intrinsic values of 0. When *FV* cells encounter *SV* cells within their neighbourhood, fraction of their intrinsic values ($\nu_f$) are transferred to the *SV* cells (Fig. 2a). While the intrinsic values of *SV* cells increase, the intrinsic values of *FV* cells are kept constant (i.e. 1) for simplicity. Once the intrinsic values of *SV* cells exceed 1, the *SV* cells transition to *FV* cells. *FV* cells could also ignite the cells in soil layer, with a probability of $P_t$, which facilitate the transition from *FV* to *SP*. If *FV* cells fail to ignite the peat underneath, these cells transition to *EP*. The *SP* cells in the soil layer are projected onto the surface layer. Therefore, *SP* cells in the soil layer correspond to *SP* cells in the surface layer. However, when the state of the corresponding cells in the surface layer are not *EP* (either vegetation or firebreak), the *SP* cells are not projected onto the surface layer. In the soil layer, *EP* cells have intrinsic values of 0, whereas *SP* cells have intrinsic values of 1. When *SP* cells encounter *EP* cells within their neighbourhood, fraction of their intrinsic values ($\nu_s$) are transferred to the *EP* cells (Fig. 2a). When the intrinsic values of *EP* cells exceed 1, these cells transition to *SP* cells. This rule is executed in the soil layer and independent of the surface layer. *SP* cells transition to *BP* cells with a probability of $P_e$.

**The variables in the model**

The value of $\nu_f$ (Eq. 1) is formulated based on Rothermel model [17] and Huygen's principle of wave propagation [16]. $\nu_f$ is a function of flaming spread rate ($R_f$), fire-wind angle factor ($\alpha_\theta$), spatiotemporal resolution ($\lambda$), neighbourhood factor ($\alpha_n$), and wind adjustment factor ($\alpha_w$). Spatiotemporal resolution contains the information of the domain which is formulated as the division between cell size ($\Delta x$) and time-step ($\Delta t$), i.e. $\lambda = \frac{\Delta x}{\Delta t}$. $R_f$ is determined following Rothermel model with corresponding vegetation type and wind speed ($U$). We assume a flat landscape which contains live and dead shrubs. We obtained the data of wind speed and direction ($\beta$) from local weather station. $\alpha_\theta$ is determined based on ellipse function of [16] (see Eq. 2). In Eq. 2, $\theta$ is fire spread direction relative to $\beta$, whereas $a$, $b$, and $c$ are the ellipse semi minor axis, semi major axis, and eccentricity respectively (see Fig. 2b). $a$, $b$, and $c$ are formulated in Eq. 3 to Eq. 5. $\alpha_n$ is considered to accommodate the effect of more than one affecting neighbouring cells to avoid overestimation of the spread rate. Therefore, since a Moore neighbourhood (8 surrounding cells) is selected, $\alpha_n$ is set to be 0.125. This neighbourhood also affect the accuracy of the spread rate in the simulation compared to the calculated spread rate when wind condition is considered. To resolve this issue, $\alpha_w$ is introduced to the model which is determined based on a calibration process with 10 different $U$. $\alpha_w$ is formulated as shown in Eq. 6. Athough the calibration proccess was only performed with one $\lambda$ (constant cell size and time-step), $\alpha_w$can be used for any $\lambda$. Fig. 3a shows the sensitivity analysis of the flaming spread rate of the simulation with 9 different $\lambda$, where the simulation has a maximum error of 21% when compared to the Rothermel model.

$$\nu_f = \alpha_w \cdot \alpha_n \cdot \alpha_\theta \cdot R_f / \lambda \tag{1}$$

$$\alpha_\theta = \left(\frac{a^2}{b - c\cos\theta}\right) \tag{2}$$

$$a = \left(\frac{r_H + 1}{2 r_L r_H}\right);\ b = \left(\frac{r_H + 1}{2 r_H}\right);\ c = \left(b - \frac{1}{r_H}\right) \tag{3}$$

$$r_L = 0.936 e^{0.2566U} + 0.461 e^{-0.1548U} - 0.397 \tag{4}$$

$$r_H = \frac{r_L + (r_L{}^2 - 1)^{0.5}}{r_L - (r_L{}^2 - 1)^{0.5}} \quad (5)$$

$$\alpha_w = -0.04U^2 + 0.59U + 1.59 \quad (6)$$

$P_t$ is formulated following [1] (Eq. 7) which is based on the experiment of [18], where it is a function of the peat moisture content (MC). $\nu_s$ (Eq. 8) is a function of smouldering spread rate ($R_s$), $\lambda$, and $\alpha_n$. $R_s$ is determined based on the interpolation from the experiments of smouldering spread rate at different peat MC [19, 20]. Fig. 3b shows the sensitivity analysis of the smouldering spread rate of the simulation with 7 different $\lambda$, where the simulation has a maximum error of 19% compared to the spread rate from experiments. $P_e$ is selected arbitrarily to enable smouldering fire that remain active for a long time after flaming has extinguished, following the value used in [1] ($5 \times 10^{-7}$).

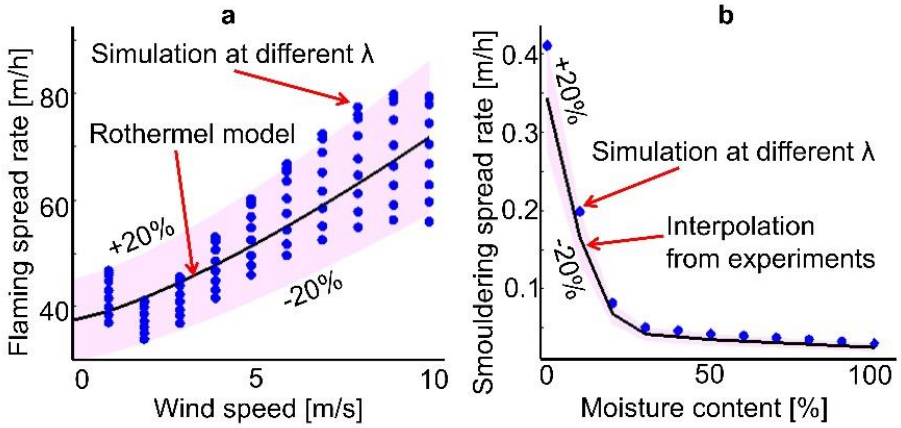


**Fig. 3.** (a) The comparison of flaming spread rate with different wind speed between Rothermel model and the simulation of $\text{KAPAS}_\text{D}$ at different spatiotemporal resolution ($\lambda$). (b) The comparison of smouldering spread rate with different moisture content between experiments and the simulation at different spatiotemporal resolution.

The spread to the diagonal neighbours in both flaming and smouldering requires an additional factor [11]. This factor is derived from the ratio between triangle and rectangular area [11]. The diagonal spread corresponds to the triangle burnt area, whereas the non-diagonal spread correspond to rectangular burnt area. Therefore, from a simple arithmetical operation, the $\nu_f$ and $\nu_s$ are multiplied by 0.83 when the fire spread to the diagonal neighbours, following [11].

$$P_t = (1 + 0.17e^{0.12MC})^{-1} \quad (7)$$

$$\nu_s = \alpha_n \cdot R_s/\lambda \quad (8)$$

## RESULTS AND DISCUSSION

We used $\text{KAPAS}_\text{D}$ to simulate a peatland wildfire in Borneo in 2015. This wildfire was chosen because we obtained a fuel map and airborne footage of the wildfire from [21]. Fig. 4a shows the footage of the peatland wildfire, where from the drone footage, smouldering hotspots are observed (see red dots in Fig. 4a). There are four plots at which the flaming wildfire initiated (region 1 to 4). Flaming wildfires in these four plots initiate 47 smouldering hotspots at randomly distributed locations. We used a $\Delta x$ of 5m and a $\Delta t$ of 180s to simulate this peatland wildfire. We used this computational domain because this domain is the most course domain at which Courant–Friedrichs–Lewy (CFL) condition is still satisfied. CFL condition limits the cell size and time-step to avoid the diffusion of an entity exceeding one cell at one time-step. Therefore, the maximum value of $R_f/\lambda$ in Eq. 1 should be less than 1. The course domain is selected to minimize the computational time. Fig.

4b shows the simulation results of the model. The model is run to simulate 90 days of the wildfire, however, Fig. 4b shows the result on 40 days of the wildfire (for visualization purposes). We found that the total number of smouldering hotspots (57 hotspots) in the simulation with peat MC of 75%, a typical MC in tropical peatland [21], has a good agreement with the footage (21% error). The difference in the hotspots distribution between footage and simulation can be caused by the variability in the nature. Our model assume a uniform peat MC across the landscape. However, in the natural peatland, the MC of the peat soil vary spatially and temporally [23]. Therefore, while the smouldering hotspots in the simulation are distributed similarly within and across plots, the hotspots in the footage are concentrated to some areas. We predicted that in 90 days 114 ha of peat could burn from these hotspots.

We then compared $KAPAS_D$ with our previous model ($KAPAS_P$) [1], firstly, using a hypothetical domain, and secondly, using the domain of the peatland wildfire in Borneo. In the hypothetical domain, we use a grid of 400 × 400 cells (with same cell size and time-step) to simulate flaming and smouldering wildfires independently. We found that the main difference between $KAPAS_D$ and $KAPAS_P$ is the burnt scar where $KAPAS_D$ has smooth fire front and $KAPAS_P$ has irregular front both in flaming and smouldering (see Fig. 5). The shape of the burnt scar in $KAPAS_D$ and $KAPAS_P$ are similar, in which they have ovoid shape of burnt scar in the flaming simulation and circular in the smouldering simulation. The circular shape of the burnt scar in smouldering simulation is to be expected, since in uniform fuel condition, the fire spread to the eight direction (the Moore neighbourhood) with similar rate. Meanwhile, the ovoid shape of burnt scar in flaming simulation is because of the anisotropy caused by the wind effect. The fire spread with downwind direction is strengthen by the wind, whereas the upwind direction is weakened by the wind. The ovoid shape, instead of ellipse, resulted in the simulation is caused by the limited number of fire spread direction, which is determined by the neighbourhood. If the number of spread direction in the simulation is sufficient, the simulation will result an ellipse shape of burnt scar, on which the governing rules of the model for flaming wildfires are based. The difference in fire front between $KAPAS_D$ and $KAPAS_P$ is caused by the uncertainty of the spread of the $KAPAS_P$. While $KAPAS_D$ always results the same burnt scar, $KAPAS_P$ has uncertainty in the burn scar resulted. This uncertainty is visualized by the non-smoothness (irregularities) of the fire front in both flaming and smouldering simulations.

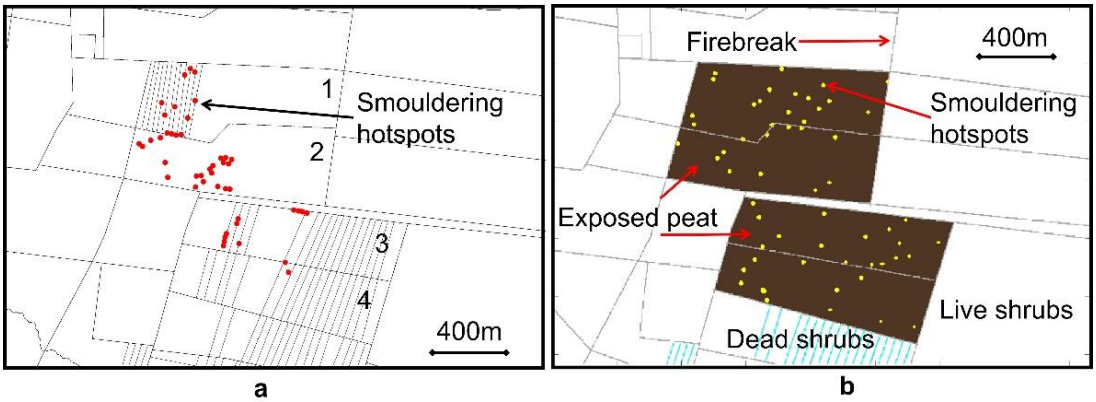


**Fig. 4.** (a) Smouldering hotspots in a peatland wildfire in Borneo in 2015, based on airborne footage. Flaming are initiated at region 1 to 4. The red dots are the locations of the smouldering hotspots observed from a drone. (b) Simulation of the peatland wildfire in (a). The yellow dots are the predicted locations of the smouldering hotspots.

The non-smoothness of the fire front and the uncertainty of the burnt scar shape is required to model a real peatland wildfire. The variability of nature, such as caused by landscape heterogeneity, cause the shape of the burnt scar unlikely to be a smooth Euclidean geometry (e.g. circle, ellipse). Therefore, while the results form $KAPAS_D$ and $KAPAS_P$ are similar, $KAPAS_P$ is more realistic than $KAPAS_D$ due the consideration of the variability of nature.

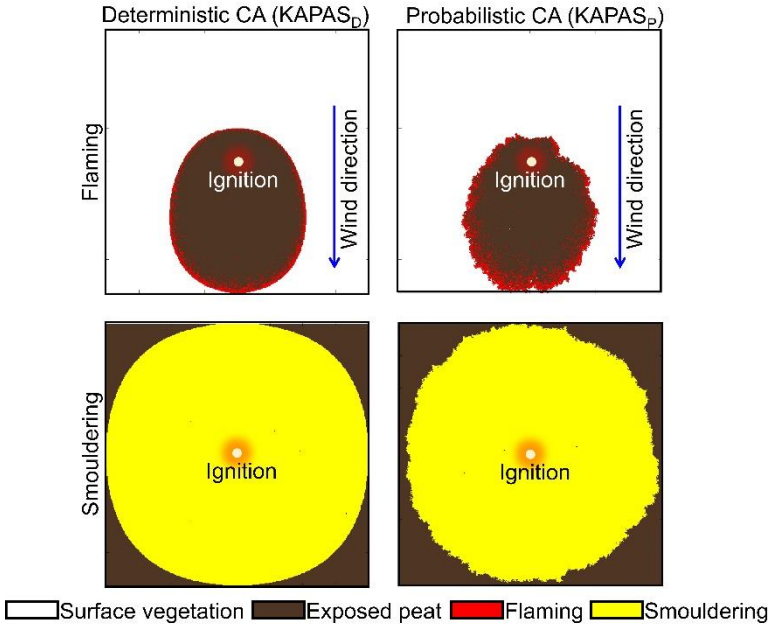


**Fig. 5.** The comparison of burnt scar of flaming and smouldering wildfires between deterministic CA (KAPAS$_D$) and probabilistic CA (KAPAS$_P$) in a hypothetical domain. The red glowing white circle is the location of the ignition and the blue arrow is the direction of the wind for flaming wildfire simulation.

Fig. 6 shows the comparison between KAPAS$_D$ and KAPAS$_P$ when the models are applied to simulate the Borneo peatland wildfire. On day 1 when the flaming was just started, the shape of flaming burnt scars from both the models conform with the finding in Fig. 4, where although both the models result in ovoid shape, the fire front in KAPAS$_P$ is not smooth, unlike the KAPAS$_D$. On day 2 when the flaming spreads relatively distant from the ignition location, the fire front of KAPAS$_D$ simulation form a curve (circular wedge), whereas KAPAS$_P$ form a non-smooth straight line. This finding indicates that KAPAS$_D$ is stronger than KAPAS$_P$ in maintaining its basic shape of flaming burnt scar (ovoid). Another observable difference between KAPAS$_D$ and KAPAS$_P$ found on day 2 is the present of unburned vegetation in KAPAS$_P$. While the noise-like dots in the KAPAS$_D$ on day 2 represent the smouldering hotspots which were initiated, the noise-like dots in the KAPAS$_P$ on day 2 comprises both smouldering hotspots and patches of unburned vegetation. These unburned patches are commonly observed in the real event of wildfire, which then indicate that KAPAS$_P$ can simulate peatland wildfires more realistically than KAPAS$_D$. However, the time required by the flaming wildfire to completely sweep the landscape between KAPAS$_D$ and KAPAS$_P$ are similar (within 10% difference) on each plot. Therefore, KAPAS$_D$ and KAPAS$_P$ have similar accuracy on flaming wildfire simulation in term of flaming spread rate.

The more realistic result of KAPAS$_P$ is also observed on day 40, where the growing smouldering hotspots in KAPAS$_D$ are almost perfect circles, whereas the hotspots in KAPAS$_P$, shape more irregularly. However, the number of smouldering hotspots from KAPAS$_D$ and KAPAS$_P$ are similar with less than 20% difference. This similarity is due to the same concept used for transition from flaming vegetation to smouldering peat. Meanwhile, the difference is caused by the slightly different behaviour of the flaming vegetation which initiated the smouldering peat.

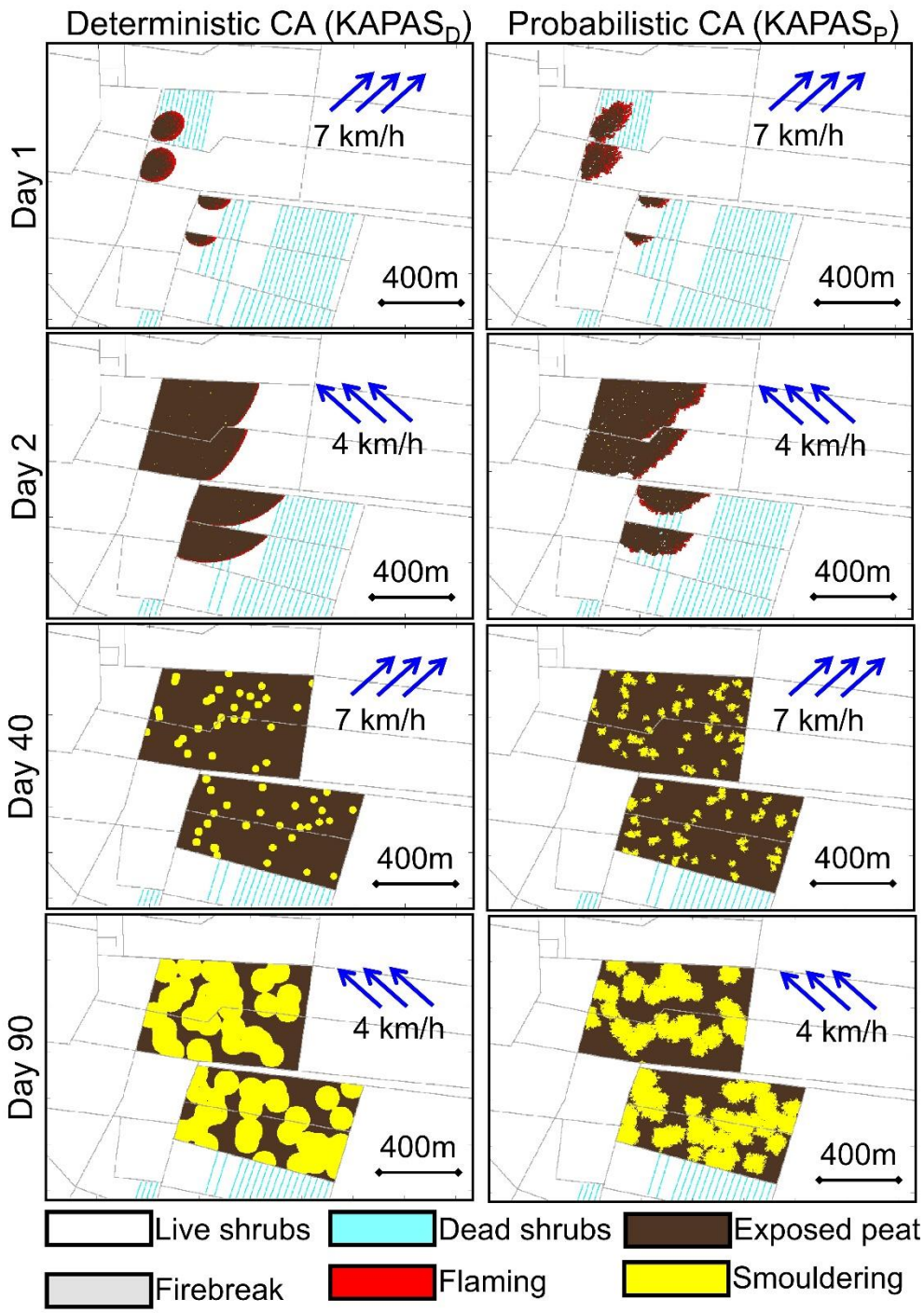


**Fig. 6.** The comparison of the simulation of Borneo peatland wildfire between deterministic CA (KAPAS$_D$) and probabilistic CA (KAPAS$_P$) at different times. The blue arrows are the direction of the wind for flaming wildfire simulation. Day 1 represents the start of flaming wildfire, day 2 represents the spread of flaming wildfire and the creation of smouldering hotspots, day 40 represents the spread of smouldering hotspots, and day 90 represents the merging of smouldering hotspots.

Both $KAPAS_D$ and $KAPAS_P$ successfully simulate merging phenomena of smouldering hotspots (see day 90), where number of individual hotspots merge and become larger hotspots which significantly increase the difficulty of the firefighting attempts. At the end of the simulation, the total smouldering burnt area from $KAPAS_D$ and $KAPAS_P$ differs by 28%. This difference is the largest difference on simulation results between $KAPAS_D$ and $KAPAS_P$. Other differences in results between the two models are less than 28%. Therefore, $KAPAS_D$ is similarly accurate to $KAPAS_P$. The computational efficiency of $KAPAS_D$ is also similar to $KAPAS_P$ with computational time of 1.61h and 1.93h respectively. Although the results from $KAPAS_P$ are more realistic, $KAPAS_D$ benefits from its ability to be implemented to any spatial and temporal extent without recalibration processes. Therefore, $KAPAS_D$ offers potential to simulate peatland wildfires at any spatial and temporal resolution with similar accuracy and computational efficiency to $KAPAS_P$.

We further run the models to simulate Borneo peatland wildfire when the peat moisture content is different, from 0% to 160% moisture contents with 20% increment. We found that $KAPAS_D$ and $KAPAS_P$ result in similar number of hotspots and smouldering burnt area at any moisture content (see Fig. 7). The largest difference of number of hotspots between the two models are at MC higher than 100%. At MC higher than 100%, $KAPAS_D$ do not create any smouldering hotspot, whereas $KAPAS_P$ successfully initiate few smouldering hotspots (see Fig. 7a). This finding indicates that the critical MC of smouldering hotspot creation in $KAPAS_D$ is lower than in $KAPAS_P$. Therefore, at a high MC, $KAPAS_D$ could underestimate the damage caused by smouldering wildfire. Fig. 6b clearly shows this underestimation when the peat MC is higher than 100%. While the burnt areas in $KAPAS_D$ are zero at high MC, the burnt areas in $KAPAS_P$ are close to 1ha. Only at MC of 160% $KAPAS_P$ result in zero smouldering burnt area.

While the creation of smouldering hotspots are stronger in $KAPAS_P$, the growth of these hotspots are stronger in $KAPAS_D$, especially at MC between 50% and 80% (see Fig. 7b) which is the typical MC in tropical peatland [21]. With similar number of hotspots, the smouldering burnt area in $KAPAS_D$ is 10% - 20% larger than in $KAPAS_P$ at MC between 50% and 80%. These findings infer that the flaming in $KAPAS_P$ more strongly initiate smouldering hotspots than in $KAPAS_D$. However, once the smouldering hotspots are created, their growth are stronger in $KAPAS_D$ than in $KAPAS_P$.

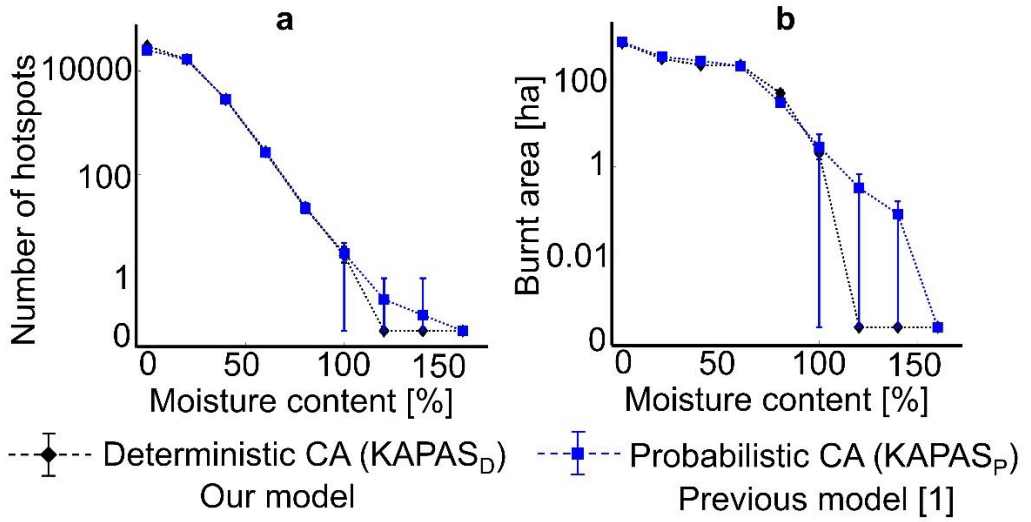


**Fig. 7.** The comparison of (a) number of hotspots and (b) smouldering burnt area between deterministic CA ($KAPAS_D$) and probabilistic CA ($KAPAS_P$) at different peat moisture contents. Each of the simulation was repeated 5 times to capture the uncertainties in the models.

## CONCLUSIONS

We developed here the first deterministic cellular automata model to simulate peatland wildfires at the field-scale, $KAPAS_D$. The model is validated against drone footage (over 523 ha of landscape) of a peatland wildifre in Borneo in 2015, and result in 80% accuracy on the number of smouldering hotspots. The growth of these hotspots for 90 days, the typical duration of wildfire season in Indonesia, could burn 114 ha of the peat. During the 90 days of the simulation time, $KAPAS_D$ simulated the multiple ignitions of flaming wildfires, the spread of these wildfires that also nucleate smouldering hotspots, the extinction of flaming wildfires and the growth of smouldering hotspots, and the merging of smouldering hotspots when its growth are sufficiently large. We compared the deterministic CA model ($KAPAS_D$) with probabilistic CA model from our previous work ($KAPAS_P$) [1], and found that both the models have similar computational time (10% difference) and similar accuracy in number of smouldering hotspots and smouldering burnt area (within 20% difference). Although both $KAPAS_D$ and $KAPAS_P$ have ovoid shape for flaming burn scar and circular shape for smouldering burn scar, the perimeter of these burn scars are smooth in $KAPAS_D$ but irregular in $KAPAS_P$. This finding indicates that $KAPAS_D$ has a more realistic result than $KAPAS_P$, since the perimeter of the burn scar is unlikely to be smooth due to the variability in nature. However, $KAPAS_D$ benefits from its ability to be used in any spatial and temporal extent, which is of utmost important due to the variability of spatial and temporal extent of peatland wildfires. $KAPAS_D$ and $KAPAS_P$ were further used to predict the burnt area of smouldeirng peat when the peat moisture content are varied. We found an exponential relationship between burnt area and peat moisture content obtained from both the models. However, the nucleation of smouldering hotspots were stronger in $KAPAS_P$, whereas its growth were stronger in $KAPAS_D$. This finding indicates that although $KAPAS_D$ and $KAPAS_P$ are similarly accurate, the difference in rules between the models influence the dynamics of the flaming and smouldering spread, especially near the critical conditions such as critical peat moisture content to initiate smouldering hotspots, emphasizing the importance of the comparison between the models. This work provides analysis and insights on the development of modelling tools for simulating peatland wildfires.

## ACKNOWLEDGEMENT

This research was funded by European Research Council (ERC) Consolidator Grant HAZE (682587), and Indonesian Endowment Fund for Education (LPDP).

## REFERENCES

[1] D. M. J. Purnomo, M. Bonner, M. Samaneh and G. Rein, "Using cellular automata to simulate field-scale flaming and smouldering wildfires in tropical peatlands," *Proceedings of the Combustion Institute*, 2020. doi: 10.1016/j.proci.2020.08.052.

[2] X. Huang and G. Rein, "Computational study of critical moisture and depth of burn in peat fires," *International Journal of Wildland Fire*, vol. 24, p. 798–808, 2015. doi: 10.1071/WF14178.

[3] G. Rein, "Smouldering Fires and Natural Fuels," in *Fire Phenomena in the Earth System – An Interdisciplinary Approach to Fire Science*, Wiley and Sons, 2013, pp. 15-34. doi: 10.1002/9781118529539.ch2.

[4] Y. Hu, N. Fernandez-Anez, T. E. L. Smith and G. Rein, "Review of emissions from smouldering peat fires and their contribution to regional haze episodes," *International Journal of Wildland Fire*, vol. 27, p. 293–312, 2018.

[5] M. R. Turetsky, B. Benscoter, S. Page, G. Rein, G. R. van der Werf and A. Watts, "Global vulnerability of peatlands to fire and carbon loss," *Nature Geoscience*, vol. 8, pp. 11 - 14, 2015.

[6] G. Rein and X. Huang, "Smouldering wildfires in peatlands, forests and the arctic: Challenges and perspectives," *Current Opinion in Environmental Science & Health,* vol. 24, 2021. doi: 10.1016/j.coesh.2021.100296.

[7] R. C. Scholten, R. Jandt, E. A. Miller, B. M. Rogers and S. Veraverbek, "Overwintering fires in boreal forests," *Nature,* vol. 593, p. 399–404, 2021. doi: 10.1038/s41586-021-03437-y.

[8] K. Widyastuti, M. A. Imron, S. T. Pradopo, H. Suryatmojo, B. M. Sopha, A. Spessa and U. Berger, "PeatFire: an agent-based model to simulate fire ignition and spreading in a tropical peatland ecosystem," *International Journal of Wildland Fire,* vol. 30, p. 71–89, 2021. doi: 10.1071/WF19213.

[9] C. Burke, S. Wich, K. Kusin, O. McAree, M. E. Harrison, B. Ripoll, Y. Ermiasi, M. Mulero-Pázmány and S. Longmore, "Thermal-Drones as a Safe and Reliable Method for Detecting Subterranean Peat Fires," *Drones,* vol. 3. doi:10.3390/drones3010023, 2019.

[10] S. Wolfram, "Cellular automata as models of complexity," *Nature,* vol. 311, pp. 419-424, 1984. doi: 10.1038/311419a0.

[11] J. von Neumann, Theory of Self-Reproducing Automata, Urbana: University of Illinois Press, 1966.

[12] I. Karafyllidis and A. Thanailakis, "A model for predicting forest fire spread using cellular automata," *Ecological Modelling,* vol. 99, pp. 87-97, 1997. doi: 10.1016/S0304-3800(96)01942-4.

[13] C. Favier, "Percolation model of fire dynamic," *Physics Letters A,* vol. 330, no. 5, pp. 396-401, 2004. doi: 10.1016/j.physleta.2004.07.053.

[14] C. M. Belcher, J. M. Yearsley, R. M. Hadden, J. C. McElwain and G. Rein, "Baseline intrinsic flammability of Earth's ecosystems estimated from paleoatmospheric oxygen over the past 350 million years," *Proceedings of the National Academy of Sciences of the United States of America,* vol. 107, no. 52, p. 22448–22453, 2010. doi: 10.1073/pnas.1011974107.

[15] N. Fernandez-Anez, K. Christensen, V. Frette and G. Rein, "Simulation of fingering behavior in smoldering combustion using a cellular automaton," *Physical Review E,* vol. 99, p. 023314(13), 2019. doi: 10.1103/PhysRevE.99.023314.

[16] X. Huang, F. Restuccia, M. Gramola and G. Rein, "Experimental study of the formation and collapse of an overhang in the lateral spread of smouldering peat fires," *Combustion and Flame,* vol. 168, pp. 393-402, 2016. doi: 10.1016/j.combustflame.2016.01.017.

[17] M. Alexander, "Estimating the length-to-breadth ratio of elliptical forest fire patterns," in *Pages 287-304 in Proceedings of the 8th Conference on Fire and Forest Meteorology*, Detroit, MI. Bethesda, MD: Society of American Foresters, 1985.

[18] R. C. Rothermel, "A mathematical model for predicting fire spread in wildland fuels," USDA Forest Service Research Paper INT-115, Washington, DC, 1972.

[19] W. H. Frandsen, "Ignition probability of organic soils," *Canadian Journal of Forest Research,* vol. 27, pp. 1471-1477, 1997. doi: 10.1139/x97-106.

[20] N. Prat-Guitart, G. Rein, R. Hadden, C. Belcher and J. Yearsley, "Propagation probability and spread rates of self-sustained smouldering fires under controlled moisture content and bulk density conditions," *International Journal of Wildland Fire,* vol. 25, no. 4, pp. 456-465, 2016. doi: 10.1071/WF15103.

[21] W. Eyal, S. Moafi, J. Men, N. Czyz and N. Ahmed, "Ecocide in Indonesia," Forensic Architecture, 2017. [Online]. Available: https://forensic-architecture.org/investigation/ecocide-in-indonesia.

[22] R. W. Nusantara, R. Hazriani and U. E. Suryadi, "Water-table Depth and Peat Subsidence Due to Land-use Change of Peatlands," in *IOP Conference Series: Earth and Environmental Science,* 2018. doi :10.1088/1755-1315/145/1/012090.

[23] M. Bechtold, G. De Lannoy, R. Reichle, D. Roose, N. Balliston and I. Burdun, "Improved groundwater table and L-band brightness temperature estimates for Northern Hemisphere peatlands using new model physics and SMOS observations in a global data assimilation framework," *Remote Sensing of Environment,* vol. 246, 2020. doi: 10.1016/j.rse.2020.111805.

# Poster Abstract

# Organoboron-Based Smoke Suppressant Flame Retardants for Natural Fibre Reinforced Composites

**Danielsiek D.[1]*, Ali W.[1,2], Gutmann J.S.[1,2], Mayer-Gall T.[1,2]**

*[1] German Textile Research Centre North-West (DTNW), Krefeld (Germany).*
*[2] Department of physical Chemistry and Center for Nanointegration Duisburg-Essen (CENIDE), University Duisburg-Essen, Essen (Germany)..*
**Corresponding author email: danielsiek@dtnw.de*

Natural fibre-based textiles, such as cotton and linen, as well as regenerated cellulose (rayon) find broad application not only for apparel and home textiles, but also in construction and automotive applications. Due to their tensile strength and flexibility, they are commonly used as textile reinforcements in high-performance composites and offer a green alternative to artificial polymer fibres.[1] Natural fibre reinforced composites however exhibit an inherent flammability. Additionally, the synthetic polymer matrix in composite materials often facilitates a strong smoke production during combustion.

Highly effective classical flame retardants, containing organohalogen substances or volatile organic compounds (VOC) like formaldehyde, are classified as toxic and environmentally concerning, hence need to be replaced by halogen-free substitutes.[2] As green alternatives for textile flame retardants several organophosphorus and organonitrogen compounds have been developed but lack a smoke suppression capability. Boric acid and its salts, in contrast, are very effective smoke suppressant additives, but are classified as substances of very high concern (SVHC) under REACH.[3] In order to develop a safer solution to provide boron's smoke suppression effect, halogen-free organoboron compounds (not concerned by SVHC rating) containing phosphorous and nitrogen are investigated as flame retardants for cotton, rayon, and flax fabrics. The chemical integration of the boronic acid moiety in the organic compound, combined with chemical and physical immobilization of the flame retardants on the textile fibre as well as the embedding of the textile in the composite polymer matrix are expected to mean very low potential environmental exposure while providing smoke suppressant and flame retardant properties to the composite.

*Acknowledgement of financial support - The research project (IGF Nr. 21318 N) is funded by the Bundesministerium für Wirtschaft und Technologie within the program Industrielle Gemeinschaftsforschung (IGF) by the Arbeitsgemeinschaft industrieller Forschungsvereinigungen e. V. (AiF)*

[1] Gholampour, A., Ozbakkaloglu, T. A review of natural fiber composites: properties, modification and processing techniques, characterization, applications. *J Mater Sci* 2020, **55,** 829–892
[2] de Wit, C. A. An Overview of Brominated Flame Retardants in the Environment. *Chemosphere* 2002, **46** (5), 583–624
[3] ECHA (2021, July 30), *Boric acid*. https://echa.europa.eu/de/substance-information/-/substanceinfo/100.030.114

**KEYWORDS:** Composites, Flame retardant, Natural fibre, Smoke suppressant.

# Impact of Si/P/triazine-based hybrid flame retardants on the flammability of textile fabrics

**Shabani V.[1,2*], Ali W.[1,2], Kamps L.[1], Wallmeier R.[1], Gutmann J.S.[1,2] and Mayer-Gall Th.[1,2]**

[1] *Deutsches Textilforschungszentrum Nord-West gGmbH, Krefeld, Germany.*
[2] *Department of Chemistry and Center for Nanointegration Duisburg-Essen (CENIDE), University Duisburg-Essen, Essen (Germany).*
* shabani@dtnw.de

Due to their wide range of applications, textiles, both natural fibers and man-made fibers, are ubiquitous in our everyday lives. However, they pose a high hazard potential due to their easy flammability.[1, 2]

Currently, halogenated flame retardants continue to be used very frequently, and although they are effective, they themselves and their degradation products are toxic, bioaccumulative, and a hazard to humans and the environment.[3, 4] Therefore, the development of halogen-free alternatives is essential for a safe future.

Past work has shown that N-P silanes are effective alternatives to halogen-containing flame retardants.[5] The aim of this work is to increase the efficiency of flame retardant by introducing triazine moities (Tria-N-P silanes). Our results indicate a synergistic effect of the new flame retardants.

The flame retardants are applied to various textiles (cotton and blended fabrics) using the sol-gel process. The phosphorus content is determined by ICP-OES. The flammability as well as the thermal stability are investigated according to DIN EN ISO 15025, micro-scale combustion calorimetry (MCC) and thermogravimetric analysis (TGA). The surface properties of the burnt areas and the coated textiles were also examined by scanning electron microscopy (SEM).

## *References*

[1] C. A. Wilkie, A. B. Morgan, *Fire Retardancy of Polymeric Materials*, Second Edition, CRC Press Taylor & Francis Group, 725-726, **2010**.
[2] P.M. Visakh, Y. Arao (eds.), *Flame Retardants, Polymer Blends, Composites and Nanocomposites, Springer International Publishing Switzerland*, 262-279, **2015**.
[3] X. Zhen, Y. Li, J. Tang, X. Wang, L. Liu, M. Zhong, C. Tian. *Environ. Sci. Technol*. 55, 11, 7376–7385, **2021**.
[4] https://www.flameretardants-online.com/flame-retardants/market?web=1&wdLOR=c7F4B4FDA-7F38-4345-8DCD-A9084621295D
[5] W. Ali, V. Shabani, O. Etemad-Parishanadeh, A. Salma, T. Textor, J. S. Gutmann, T. Mayer-Gall, *Technical Textiles* 1, 29-31, **2021**.

**KEYWORDS:** Flame-retardant, N-P-Silane, Triazine, Sol-Gel.

# Flame protection by polarity-adapted silanization of functional materials

**Shabani V.[1,2*], Ali W.[1,2], Kamps L.[1], Wallmeier R.[1], Pithan F. Th.[3], Schreiner J.[3], Gutmann J.S.[1,2] and Mayer-Gall Th.[1,2]**

[1] *Deutsches Textilforschungszentrum Nord-West gGmbH, Krefeld, Germany.*
[2] *Department of Chemistry and Center for Nanointegration Duisburg-Essen (CENIDE), University Duisburg-Essen, Essen (Germany).*
[3] *Kunststoff-Institut Lüdenscheid (KIMW) GmbH, Lüdenscheid, Germany.*
* shabani@dtnw.de

The highest demands are placed on plastics, especially when it comes to safety aspects such as fire protection, which are used in the field of electronic devices, in the textile industry, in construction and in the automotive sector.

In addition to efficiency, aspects such as health, the environment and sustainability must also be considered during development. Especially since the halogenated flame retardants frequently used in the past, such as TCEP (tris(2-chloroethyl) phosphate), as well as the brominated flame retardants called penta- and octa-BDE (penta- and octabromodiphenyl ether, respectively) and also the currently still frequently used deca-BDE (decabromodiphenyl ether), have proven to be of great concern[1-3].

It is equally important that the properties of the material (polymer) are not changed and negatively affected. Often, high percentages of flame retardants are added to the plastic matrix in order to meet the required regulations. As a result, the mechanical properties such as tensile strength and impact resistance are often affected.

Previous work has shown that N-P silanes are a good alternative to the flame retardants mentioned above.[4] The aim of this work is the targeted surface modification of fillers (e.g. aluminum trihydroxide, glass beads, wood flour) with novel N-P silanes in order to adapt the polarity to the respective matrix polymer (PE, PA, PP). This should not only improve the flammability of the novel composites, but also give the composite additional properties such as improved compatibility.

## *References*

[1] M. Alaee, R.J. Wenning, *Chemosphere*, 46 579–582, **2002**.
[2] D.F.S. Linda S Birnbaum, *Environmental Health Perspectives*. 112, 9-17, **2004**.
[3] H.M. Stapleton, N.G. Dodder, *Environ Toxicol Chem*. 27, 306, **2008**.
[4] W. Ali, V. Shabani, O. Etemad-Parishanadeh, A. Salma, T. Textor, J. S. Gutmann, T. Mayer-Gall, *Technical Textiles* 1, 29-31, **2021**.

**KEYWORDS:** Composites, Flame-retardant, N-P-Silane, Polymer.

# Novel halogen free flame retardants for textiles

**Ali W.[1,2,*], Shabani V.[1], Opwis K.[1], Textor T.[3], Gutmann S. J.[1,2], Mayer-Gall T.[1,2,*]**

[1] *Deutsches Textilforschungszentrum Nord-West gGmbH, Krefeld, Germany.*
[2] *Department of Chemistry and Center for Nanointegration Duisburg-Essen (CENIDE), University Duisburg-Essen, Essen, Germany.*
[3] *Reutlingen University–Textile Chemistry, Faculty of Textiles & Design, Reutlingen, Germany*
*: ali@dtnw.de / Mayer-gall@dtnw.de

## ABSTRACT

Natural and synthetic polymers such as cotton (CO), polyester (PET), or polyamide (PA) are used for textiles and are omnipresent in our daily life. However, they must be modified to overcome some disadvantages such as flammability. Conventional halogen-based flame retardants are highly effective but several of them have been restricted by REACH legislation or have been classified as SVHC-compounds. Therefore, there is a need to substitute them.

A variety of alternative flame retardants have been developed, and some of them are commercially available, but they are not performing as the conventional ones, especially for textile sectors, where is still a lack of suitable and durable substitutes.

Our researching group @DTNW established different types and routes for flame retardant textile finishing. The new flame retardants are based on different building blocks including phosphazenes and nitrogen- and phosphorous-containing silanes (N-P-silane). Figure 1 shows examples of our tested flame retardants. The broad compound-library were applied at different fabrics and their flammability performance and thermal behaviour were assessed through different ISO standards.

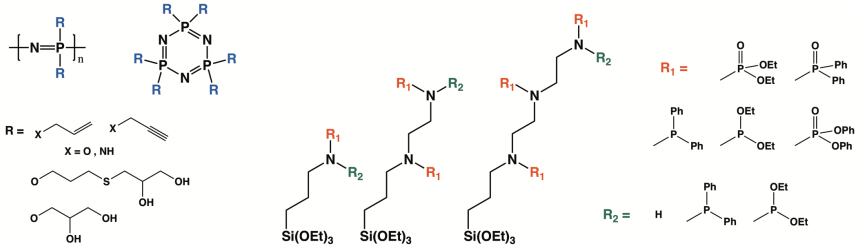


**Fig. 1.** Examples of halogen-free flame retardants including poly- and cyclophosphazene and N-P-silanes prepared and tested @DTNW.

**KEYWORDS:** flame retardants, halogen-free, textile, washing resistance.

**Acknowledgement**

The authors would like to express appreciation for the support of the AIF for IGF project no. 19739N, 19617 N, 18213 N, 16780 N.

# Blast wave from a vessel containing superheated water

**HEYMES F.[1], ANTONELLI A.G.[2], CHANUT C.[1], HOORELBEKE P.[3]**

*[1] Laboratoire des Sciences des Risques (LSR), IMT Mines Ales, Ales, France*
*[2] Laboratory of Industrial Safety and Environmental Sustainability, University of Bologna, Italy*
*[3] Total Energies, Paris, France*
**Corresponding author email: frederic.heymes@mines-ales.fr*

## ABSTRACT

Tanks containing superheated liquids may produce a BLEVE if a loss of containment leads to a sudden pressure drop in the vessel. Hazards from a BLEVE are mainly fragments and blast. A fireball may occur if the commodity is flammable.

Most previous works aiming at predicting the blast wave are based on the TNT curve with energy equivalence considerations. Some recent CFD works modelled the blast in 3D by a full set of Euler equations and achieved detailed blast propagation results, but it remains difficult to determine exactly how the pressure peak is produced by BLEVE phenomenon.

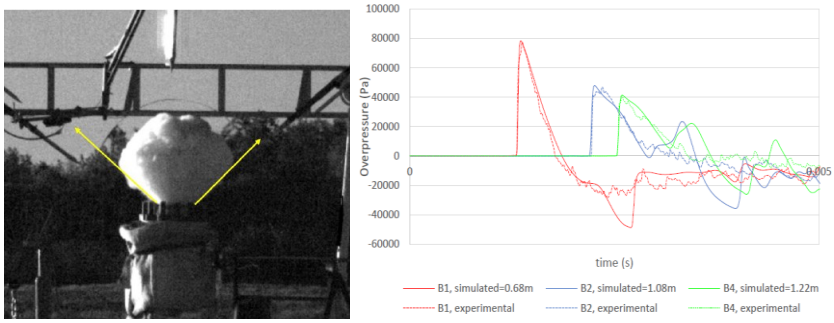


**Fig. 1.** Experimental BLEVE (left) and comparison between experiment and modelling for the blast (right)

This work is based on large scale water BLEVE tests in a 1D (pipe) apparatus equipped with a rupture disk. This device avoids any consideration about rupture dynamics: the opening area is perfectly known. CFD simulations by FLUENT show that the first and main pressure peak is successfully modelled by considering only the pressurized vapour release. Future work will investigate if, and how, the liquid phase contributes to the blast.

**KEYWORDS:** BLEVE, Blast, Superheated water

# Illustration of the potential of a PID-based real-time ventilation control system to prevent smoke back-layering in tunnel fires

**Hong Y.[1,2], Merci B.[2,*], Fu C.[1,**]**

[1] *Peking University, LTCS and Department of Mechanics and Engineering Science, Beijing, China*
[2] *Ghent University, Department of Structural Engineering and Building Materials, Ghent, Belgium*
**Corresponding author email: Bart.Merci@UGent.be*
***Corresponding author email: cjfu@pku.edu.cn*

## ABSTRACT

In order to prevent smoke back-layering, longitudinal ventilation systems are widely employed in tunnels. Correlations for critical velocity, predicting the minimum velocity for preventing back-layering, have already been extensively studied, for given fire size and tunnel (cross-sectional) dimensions. However, the air flow can feed under-ventilated fires with fresh oxygen. Moreover, the fire size can vary over time. Therefore, this work studies the concept of an automatic ventilation system based on the PID (proportional-integral-differential) controller. The proposed ventilation system automatically controls the fire smoke not to spread upstream in real-time, using feedback data of temperature sensors. This approach is numerically studied by coupling CFD calculations and a PID algorithm. Simulation results show that the approach can control the smoke well, preventing back-layering in real-time. The dimensionless critical velocity as predicted by the proposed method agrees well with the simulation results and correlations. Results also indicate that the average ventilation velocity with the PID method may be slightly higher than the constant ventilation for the larger fire size. In addition, due to the impact of turbulence fluctuations on the PID control system, the ceiling temperature distributions for the case of no back-layering are similar, but not identical, for the PID based and the constant ventilation system.

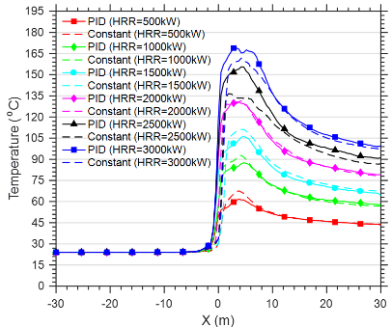


**Fig. 1.** Comparison of PID based and constant ventilation system: ceiling temperature distributions for different fire heat release rates.

**KEYWORDS:** smoke control, back-layering, tunnel fire, automatic ventilation

# Evaluating the Mechanical Energy of Liquid Hydrogen Tank Explosions

**Ustolin F.[1,*], Giannini L.[1,2], Pio G.[2], Salzano E.[2],Paltrinieri N.[1,2]**

*[1] Norwegian University of Science and Technology NTNU, Department of Mechanical and Industrial Engineering, Trondheim, Norway.*
*[2] University of Bologna, Dipartimento di Ingegneria Civile, Chimica, Ambientale e dei Materiali, Bologna, Italy.*
**Corresponding author email: scientist@institution.com*

## ABSTRACT

Hydrogen can play a central role in the energy transition in the post COVID-19 pandemic era thanks to its unique properties. However, its low density is one of the main drawbacks. The liquefaction process can drastically increase its storage capacity. The safety knowledge gap on physical explosions is still broad in the case of liquid hydrogen ($LH_2$). For instance, it is unclear what are the consequences yields as well as the probabilities of a catastrophic rupture of an $LH_2$ tank. A boiling liquid expanding vapour explosion (BLEVE) might arise after this top event. In this case, the expansion of the compressed gaseous phase is followed by the flashing of part of the liquid. Moreover, hydrogen would easily ignite due to its high flammability and lead to different combustion phenomena such as fire or fireball. This complex phenomenon was not widely explored for $LH_2$ yet.

This study focussed on the physical explosion by considering the combustion process as well. Many integral models were adopted to estimate the mechanical energy developed by the explosion. The hydrogen lower heating value was considered to estimate the contribution of the combustion to the energy generated by the explosion and its effect on the blast wave overpressure. The influences of the filling degree of the tank (liquid level) on the mechanical energy were analysed. The results were compared with the ones of previous studies where similar models were employed to estimate the mechanical energy of an $LH_2$ tank with different initial conditions. The aim of this study is to conduct a comparison between different models and assess which are the most and the least conservative. Moreover, the influence of the combustion process on the energy generated by the explosion is investigated. The outcomes of this work provide critical suggestions on the consequence analysis of cryogenic liquefied gas vessels explosions.

**KEYWORDS:** liquid hydrogen, explosion, BLEVE, combustion.

# Simulation of hydrogen explosions in congested geometries with an alternative burning model

**Arntzen B.J.[1,2,*], Lucas M.[1,2]**

[1] *University of Bergen, Dep. Of Physics and Thecnology, Bergen, Norway.*
[2] *Gexcon AS, Bergen, Norway.*
**Corresponding author email: bjorn.arntzen@uib.no*

Accurate CFD modelling of gas explosions requires that the flame moves with a representative velocity into the reactants due to a proper turbulent burning velocity model. These models depend on both the turbulence field and the chemical reactivity of the fuel-air mixture. A more fundamental chemical time scale calculated from fuel and oxygen concentrations and an Arrhenius equation based on product-temperatures is introduced. The result is an improved turbulent burning velocity model with less requirement for correction functions to adjust for; deviation in pressure, reactant temperature, Markstein (or Lewis) number, fuel mixtures, equivalence ratio, fuel and oxygen concentrations.

The burning model is compared with turbulent burning velocities from experiments presented by Kitagawa et al. [1] for a range of equivalence ratios, velocity fluctuations and initial pressures.

Results from explosion simulations with this burning model in FLACS-CFD are compared with explosion experiments in a congested geometry (Fig. 1) presented by Shirvill et al. [2] for four equivalence ratios and $H_2$-$CH_4$ mixtures.

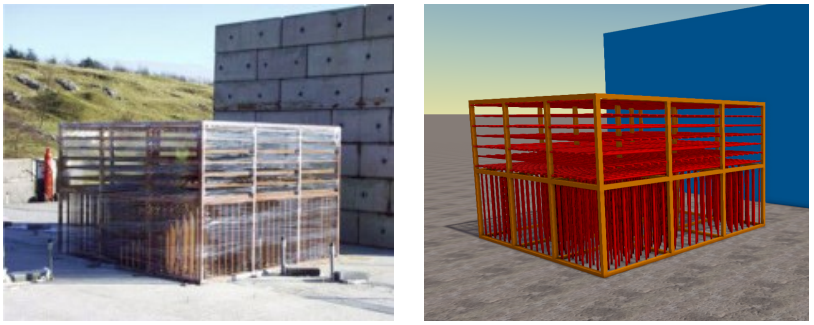

**Fig. 1.** Experimental configuration (left) and geometry model in FLACS-CFD (right).

1. Kitagawa T et al. (2008) *Turbulent burning velocity of hydrogen–air premixed propagating flames at elevated pressures*, International journal of hydrogen energy 33

2. Shirvill et al. (2019) *Experimental study of hydrogen explosion in repeated pipe congestion - Part 1*: Effects of increase in congestion, International Journal of Hydrogen Energy, 44

**KEYWORDS:** Turbulent burning, Experiments, FLACS CFD, Hydrogen.

# Changes in smouldering behaviour of wood pellets with the adition of solid inerts

**Fernandez-Anez N.[1,*], Hagen B.C.[1]**

*[1] Western Norway University of Applied Sciences, Department of safety, chemistry and biomedical laboratory sciences, Haugesund, Norway..*
** Corresponding author email: nieves.fernandez@hvl.no*

## ABSTRACT

Wood biomass is one of the key contributors to the green policy adopted by the European Union in their fight against climate change. This important role is translated in the production of larger amounts of wood pellets every year, meaning an increase on the dimension of both these facilities and the ones needed to store the final produced products, as well as the development of new pellets composed by different woods and even combinations of them. These two factors, the increase on the facilities and the development of new materials, have shown the urgency of determining the risks associated to the production and storage of wood pellets, including the risk of self-heating and smouldering.

Moreover, this situation requires the development of new design measurements to avoid, or at least decrease, the risk of wood pellet's smouldering. To this end, different procedures have been studied during the past years, focusing on the need of not changing the composition and energy efficiency of the fuels. One of the possible options would be mixing the pellets with solid inerts, which could be easily separated after their storage or burned together without any additional risk.

One of the existing solid inerts are PyroBubbles, environmentally friendly mineral agent sold in the form of round particles with an average grain size of 0.5 to 5 mm. The influence of this material in the smouldering tendency of wood pellets have been studied by the development of a series of tests in a lab-scale silo-shaped device. This device, a vertical cylinder 15 cm diameter and 30 cm high, is heated at the bottom with a hot-plate, and sample weight and temperatures are measured. Different amounts of PyroBubbles have been homogeneously mixed with the wood pellets and the delay in smouldering has been determined.

**KEYWORDS:** inertization, pellets, smouldering, wood biomass.

# DRYADS - Holistic Fire Management Ecosystem for Prevention, Detection and Restoration of Environmental Disasters

**Velanas P.[1], Margariti K.[1], Arsava K.S.[2,*], Li T.[2], Mikalsen R.F.[2]**

*[1] ACCELIGENCE LTD, Nicosia, Cyprus.*
*[2] RISE Fire Research AS, Trondheim, Norway.*
**Corresponding author email: kemal.sarp.arsava@risefr.no*

## ABSTRACT

Considering the socio-ecological transition of Europe 2030, and towards a more resilient and informed community, focusing on the forests that are near wildfire risk, DRYADS aims to build upon state-of-the-art high TRL products and unite them in a holistic Fire Management platform that optimize and reuse per phase the available Socio-technological Resources in all three main phases of Wildfires. For the prevention and preparedness DRYADS propose the use of a real-time risk evaluation tool that can receive multiple classification inputs and work with a new proposed neural network-powered Risk factor indicator. To create a model of Fire adapted communities (FAC) in parallel to insurance incentives, DRYADS will use alkali activated construction materials (AAM) integrating post-wildfires wood ashes (PWA) for fire-resilient buildings and infrastructure. DRYADS also uses a variety of technological solutions such as the Copernicus infrastructure, and a swarm of small drones customized for accurate forest supervision. In the area of Detection DRYADS propose a variety of toolsets that will accommodate most needs. Stemming from Virtual reality for the training, wearables for the protective equipment of the emergency responders. to UAV (drones), UAG and airships for improving capacity in temporal and spatial analysis as well as to increase the inspected area coverage. Last, DRYADS will build a new land and field-based restoration initiative that will use all modern techniques such as agroforestry, drones for seed spread, Internet of things sensors that will be able to adapt the seeding process based on the ground needs and on the same time with the help of AI to determine post-fire risks factors. DRYADS solution will be demonstrated and validated under real operating conditions. Demonstration will involve eight complex pilot implementations executed in seven EU countries and in Taiwan.

**KEYWORDS:** AI for Fire and Forest Management, Holistic Fire Management System, Restoration Technologies.

**ACKNOWLADGEMENT:** This project has received funding from the European Union's Horizon 2020 research and innovation programme under grant agreement No 10103692.

# The level of contamination of fire water after extinguishing Li batteries

**Karl J.[1,*], Suchý O.[1], Martinec M.[2]**

[1] *Technical Institute of Fire Protection, Prague, Czech Republic.*
[2] *University of Chemistry and Technology Prague, Prague, Czech Republic.*
**Corresponding author email: jan.karl@tupo.izscr.cz*

## ABSTRACT

Today, lithium batteries are widespread in all industries, and we use them in various devices. Lithium batteries are in different types and have different safety features. Li-ion and Li-pol batteries are the most common types of batteries. These batteries have excellent capacity and some other parameters, but they are also potentially dangerous. Charged batteries show explosive behavior or very rapid process of burning when they are mechanically damaged, short-circuited or exposed to heat. That is the reason why the risk of fire increases and it is necessary to solve the extinguishing procedure. Current procedures recommended by battery manufacturers define the extinguishing procedure by immersing the battery in a large amount of water. It is not yet known that a manufacturer would describe a more efficient and simpler procedure. That is the reason why we focused on the contamination of fire water caused by immersing batteries in water. Is it necessary to dispose of fire water as hazardous waste? This is the primary question of our research described in this paper.

We focused on water contamination with cylindrical as well as prismatic Li batteries. The batteries were immersed in water either in their original undamaged condition or after destruction caused by exposing the batteries to flames of flammable liquid. Samples of water were taken at 24 hours, 48 hours, 1 week and 1 month. A comprehensive analysis of firewater samples was performed with a main focus on heavy metals. Based on these results, the assessment was made of whether it is necessary to treat fire water as hazardous waste, or recommendations for its disposal.

**Fig. 1** Li batteries immersed in water

**KEYWORDS:** Li batteries, contamination of water, extinguishing

# Computational modelling of fire spread through informal settlements

**Stevens S.[1,*], Rush D.[1]**

[1] *University of Edinburgh, School of Engineering, Edinburgh, UK.*
**Corresponding author email: s.stevens@ed.ac.uk*

## ABSTRACT

An estimated 1 billion people live in informal settlements globally [1]. These are often characterised by densely-packed homes of highly combustible construction materials. Inevitably, rapid fire spread thus becomes a common problem.

Recent experimental research (e.g. [2]) has quantified novel fire behaviour in informal homes, where the unique challenges include fast fire growth and rapid heat transfer through thermally-thin metal walls. This has also enabled new research in the computational domain, particularly using CFD models (e.g. [3]).

Yet given that an informal settlement fire may affect hundreds of homes, CFD modelling is hugely intensive to operate at such scale. This poster will present recent work towards an alternative settlement-scale fire spread model for informal settlements. The core of the work is to calibrate an existing fire spread model [4] for use in informal settlements. Notable updates to the model include:

- Heat transfer through thermally-thin compartment walls, and corresponding accelerated growth of the pre-flashover fire,
- External flame intermittency and impingement on neighbouring structures,
- New construction materials with different thermal properties.

As preliminary testing with the unedited base model shows, minor interventions can produce drastically divergent outcomes in probabilistic multi-simulation tests (Fig. 1). A successful and well-constructed model should, in future, provide an experimental domain for interventionist measures against fire spread, without the need for costly and intensive physical experimentation.

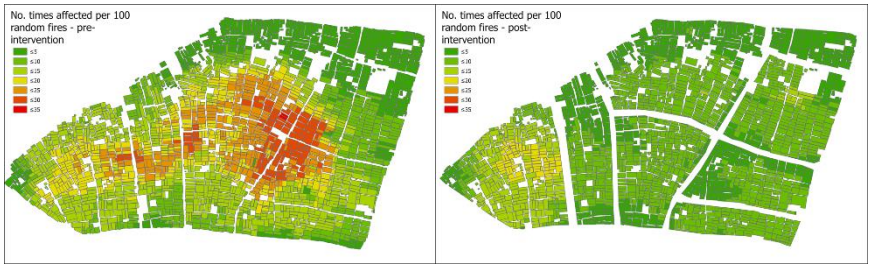


**Fig. 1.** 100 Monte Carlo simulations of random fires before and after road-widening intervention in Mukuru, Nairobi, Kenya

**KEYWORDS:** Computational modelling, Informal settlements, Urban fire.

## REFERENCES

[1] UN Habitat, World Cities Report 2020: The Value of Sustainable Urbanization, Nairobi, 2020.

[2] A. Cicione, R. Walls, S. Stevens, Z. Sander, N. Flores, V. Narayanan, D. Rush, An Experimental and Numerical Study on the Effects of Leakages and Ventilation Conditions on Informal Settlement Fire Dynamics, Fire Technol. (2021). doi:10.1007/s10694-021-01136-8.

[3] M. Beshir, M. Mohamed, S. Welch, D. Rush, Modelling the Effects of Boundary Walls on the Fire Dynamics of Informal Settlement Dwellings, Fire Technol. (2021). doi:10.1007/s10694-020-01086-7.

[4] K. Himoto, T. Tanaka, Development and validation of a physics-based urban fire spread model, Fire Saf. J. 43 (2008) 477–494. doi:10.1016/j.firesaf.2007.12.008.

# Influence of droplet drag reduction on the numerical modelling of the interaction between water sprays and hot air jets

**Thielens M.[1,*], Merci B.[1], Beji T.[1]**

[1] *Ghent University, Departement of Structural Engineering and Building Materials, Ghent, Belgium*

**Corresponding author email: Martin.Thielens@UGent.be*

## ABSTRACT

Recent investigations have highlighted the potential underprediction of droplet drag reduction in Computational Fluid Dynamics (CFD) simulations of dense water sprays [1]. In the Fire Dynamics Simulator (FDS, the current drag reduction model is based on the Ramirez correlation [2] that is developed for an idealized case of two droplets placed in tandem. This correlation mimics the wake effect on the trailing particle induced by a perfectly aligned leading particle. However, other interactions occurring in a full spray (such as lateral interactions) are not accounted for, which might explain (partially) the underestimation of drag reduction.

Based on these observations, a novel expression for the drag reduction has been developed. The latter is based on a functional form with a predefined asymptomatic behaviour for very dilute and very dense spray, and a smooth transition in between. The proposed expression reads:

$$F_D/F_{D0}=(1-B)\exp[-(\alpha+1-A)^n]+B$$

where $F_D/F_{D0}$ is the drag force reduction, $\alpha$ is the local droplet volume fraction and $A$,$B$ and $n$ are three parameters that have been determined using available experimental data for several sprays ($A=5\times10^{-5}$,$B=0.11$,$n=10^6$).

The development and the analysis of this novel expression against multiple water sprays (in the absence of fire-driven flows), with variable level of density has been described in a paper that is currently under revision. That previous study has shown that – for a very dense spray – by substantially reducing the drag force in dense regions of the spray, the spray expands more and leads to simulations results that are much closer to the experimental data.

The present work aims at further consolidating the previous analysis by considering an additional test case examined experimentally in [3] and where a dense water spray is interacting with a hot air jet. Two simulations are carried out with FDS 6.7.6. In the first simulation, the default drag reduction model is used. In the second simulation, a modified version of the code is used and in which the novel drag reduction has been implemented. The preliminary simulation results show that by using the novel correction function, the interaction height between the water spray and the hot air jet is better predicted.

[1] Liu Y., Beji T., Thielens M., Tang Z., Fang Z. and Merci B (2022) Numerical analysis of a water mist spray: The importance of various numerical and physical parameters, including the drag force, Fire Safety Journal, 127:103515, https://doi.org/10.1016/j.firesaf.2021.103515

[2] Ramírez-Muñoz J., Soria A. and Sadinas-Rodríguez E. (2007) Hydrodynamic force on interactive spherical particles due to the wake effect, Int. J. of Multiphase Flow, 33:802-807 https://doi.org/10.1016/j.ijmultiphaseflow.2006.12.009

[3] Zhou X. (2015) Characterization of interactions between hot air plumes and water sprays for sprinkler protection, 35 – 3:2723-2729, https://doi.org/10.1016/j.proci.2014.05.078

**KEYWORDS:** CFD, Drag Reduction, Modelling, Water Sprays

# Theoretical study of solid laminar combustion under forced flow

**Fuhai Gou, Huahua Xiao*, Manman Zhang, Jinhua Sun***

*State Key Laboratory of Fire Science, University of Science and Technology of China, Hefei, Anhui, China.*
**Corresponding author's email: xiaoh@ustc.edu.cn; sunjh@ustc.edu.cn*

## ABSTRACT

In this study, the laminar combustion characteristics of solid plates under forced flow have been studied. The steady combustion experiments of PMMA plates of different sizes under forced flow have been carried out. The theory of solid plate combustion under forced flow is developed based on the boundary layer theory. It can also be seen from the experiments that the combustion state of PMMA plate is stable laminar combustion. Based on the boundary layer theory, the flow function equation is solved and the theoretical expressions of flame thickness and Nusselt number are obtained. Based on the experimental results and theoretical analysis, multiple physical parameters related to combustion are discussed. Flame standoff distance is related to the wind speed, position, and mass transfer number. Figure.1 shows the relationships between flame standoff distance and flame length, which can be describe by:

$$y_f = Ax^{1/2} \tag{1}$$

The relationship of Nusselt number and Reynolds number under forced flow can be obtained through experimental data and calculated using boundary layer theory, which can be describe by:

$$Nu = C\sqrt{Re} \tag{2}$$

And, the result shows that Nu and are not simply proportional, which is different from previous studies. In analysis, the mass transfer number is found not to be constant for different positions in the flame area.

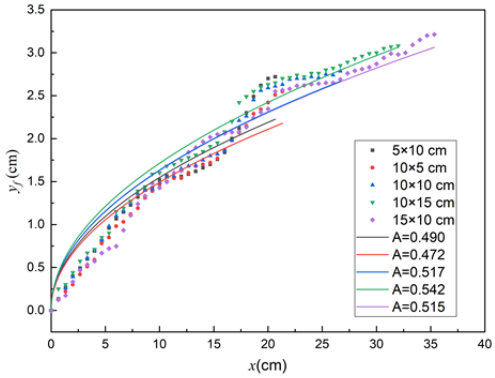


**Fig. 1.** The flame standoff distance of five sizes of PMMA plates.

**KEYWORDS:** Laminar combustion, boundary layer, flame, heat transfer.

# Flame Propagation in a Semiconfined Layer of Stratified Cryogenic Hydrogen-Air Mixture

**Veser A.[1], Friedrich A.[2], Necker G.[2], Kuznetsov M.[2,*], Jordan T.[2]**

[1] *Pro-Science GmbH, 76275 Ettlingen, Germany;*
[2] *Karlsruhe Institute of Technology, 76131 Karlsruhe, Germany.*
**Corresponding author email: kuznetsov@kit.edu*

## ABSTRACT

In the frame of the PRESLHY project, more than 100 combustion experiments with cryogenic hydrogen-air mixtures were made in a semi-confined obstructed channel. The horizontal channel has a length of 3 m, a height of 40 cm and a width of 60 cm. In order to reproduce the scenario of flame propagation over a spill of LH2, a stratified layer of hydrogen-air mixture with a vertical gradient of temperature (from 100 to 300K) and a gradient of hydrogen concentration from 0.1 to 0.6 %H2/cm were created in a semiconfined channel. Then, the mixture was ignited by the electric spark at the upper corner, in the area of a higher hydrogen concentration and a lower temperature.

In the experiments, a maximum H2-concentration at the ceiling from 8 vol% to 55 vol% as well as different blockage ratios (BR = 0, 30 and 60%) were investigated with respect to flame propagation velocity and maximum combustion pressure. Besides the main experiment series at cryogenic temperatures (about 100 K inside the channel), a part of the experiments was also performed at ambient temperature for comparison.

The comparison shows not so significant difference between warm and cold experiments because the temperature of the cold mixture increases fast with air dilution down to the channel height. Higher combustion pressure of cold part is not affected the combustion process because of too thin layer and the over-pressure discharge through the opening. For instance, the quasi-detonation was only achieved for cryogenic mixture with hydrogen concentration changing from 29.6 to 12.1% at BR=60%. Maximum pressure of 12-14 bar and a velocity of 1300 m/s were measured almost at the same conditions as for warm experiment at ambient temperature.


**Fig. 1.** Side view of experimental facility (left); front view of channel cross section (right).

**KEYWORDS:** Combustion, cryogenic hydrogen, semi-confined layer, stratified atmosphere

# Fire REsistaNce of External Thermal Insulation Composite Systems

*Coppalle A.[1],J. VaheJ.[1], Bourbigot S.[2], Bensabath T.[2] ,Tang M [2]., Rogaume T. [3], Batiot B. [3], Drean D.[4], Girardin B.[4]*
*[1]CORIA, INSA Rouen, France,*
*[2]UMET, Université Lille, France,*
*[3]P-PRIME, ENSMA Poitiers, France*
*[4]Efectis France.*
**Corresponding author email: alexis.coppalle@coria.fr*

## ABSTRACT

The increase of the energy performance of buildings may have an impact on fire safety. For example, fires associated with insulation façade systems for high-rise buildings may have dramatic consequences. In France, there is an evolution of the constructive methods implemented in recent years, in particular thanks to the current thermal regulations (RT 2012). In this context, external thermal insulation (ETI) has many advantages and has developed strongly . This potentially translates into an increase in the fuelmass and fire propagation on the façades, involving complex and insufficiently understood phenomena. The purpose of the project is to acquire the scientific and technical knowledges necessary to the control of the fire safety of façades and to reinforce the research for new materials having a low flammability. Using both experimental methods and CFD simulations, the studies will be carried out at small (matter ), intermediate (panel ) and large (system) scales.

**KEYWORDS:** façade fires, small tests, panel tests, LEPIR and BS tests, modelisation

# Effect of ventilation on temperature rise due to fire in a large-scale residential structure

**Chaudhari D.M.[1],*, Weinschenk. C.[1]**

[1] *Fire Safety Research Institute, Columbia, Maryland, U.S.A - 21043.*
**Corresponding author email: Dushyant.Chaudhari@ul.org*

## ABSTRACT

This study aims to investigate the impact of heating, ventilation, and air conditioning (HVAC) system on temperature rise in a large-scale residential structure from propane-fuelled gas burner fires. A total of 29 experiments were conducted in a purpose-built, ranch-style, two-story residential structure consisting of 3 bedrooms (BR_1, BR_2, and BR_3), living-room (LR), dining-room (DR), and kitchen (Kit) on the first floor and an open basement (Ba_A through Ba_D regions). Experimental conditions such as locations of the gas burner, HVAC status (on or passive), and interior door positions (opened or closed) were varied systematically. Temperature, gas concentration, differential pressure data collected during these experiments were used quantify the changes to the aforementioned variables.

Peak temperature data are compared here (Fig. 1) for basement fire (steady HRR of 280 kW) experiments for different regions where thermocouples were installed. The lines indicate average temperatures in the respective region. The peak temperature distributions across the entire residential structure are statistically different (Wilcoxon signed-rank test, p-value $< 0.01$) for experiments with HVAC on versus with HVAC in the passive state, regardless of whether the basement stairwell door was opened or closed. Further, transport of combustion products was reduced when the stairwell door was closed (Exp. 25, 26) resulting in a reduction of peak temperature by about 30°C in living room and by about 10°C in the bedrooms when compared to the case when the door is open (Exp. 23, 24). This study also aims to investigate the ability of CFD models to accurately predict the effect of a residential HVAC system.

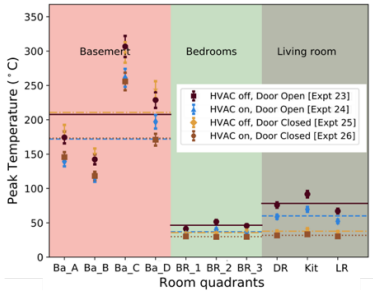


**Fig. 1.** Comparison of peak tempreature observed in different regions of the residential structure for different ventilation conditions.

**KEYWORDS:** Compartment fires; Gas burners; HVAC; Door effect